NASA/CP—2002–211783

The Twelfth Thermal and Fluids Analysis Workshop

Alok Majumdar, Compiler
Marshall Space Flight Center, Marshall Space Flight Center, Alabama

Proceedings of a workshop hosted and organized by the
NASA Marshall Space Flight Center and held at the
Bevill Center, The University of Alabama in Huntsville,
Huntsville, Alabama, September 10–14, 2001

July 2002

The NASA STI Program Office…in Profile

Since its founding, NASA has been dedicated to the advancement of aeronautics and space science. The NASA Scientific and Technical Information (STI) Program Office plays a key part in helping NASA maintain this important role.

The NASA STI Program Office is operated by Langley Research Center, the lead center for NASA's scientific and technical information. The NASA STI Program Office provides access to the NASA STI Database, the largest collection of aeronautical and space science STI in the world. The Program Office is also NASA's institutional mechanism for disseminating the results of its research and development activities. These results are published by NASA in the NASA STI Report Series, which includes the following report types:

- TECHNICAL PUBLICATION. Reports of completed research or a major significant phase of research that present the results of NASA programs and include extensive data or theoretical analysis. Includes compilations of significant scientific and technical data and information deemed to be of continuing reference value. NASA's counterpart of peer-reviewed formal professional papers but has less stringent limitations on manuscript length and extent of graphic presentations.

- TECHNICAL MEMORANDUM. Scientific and technical findings that are preliminary or of specialized interest, e.g., quick release reports, working papers, and bibliographies that contain minimal annotation. Does not contain extensive analysis.

- CONTRACTOR REPORT. Scientific and technical findings by NASA-sponsored contractors and grantees.

- CONFERENCE PUBLICATION. Collected papers from scientific and technical conferences, symposia, seminars, or other meetings sponsored or cosponsored by NASA.

- SPECIAL PUBLICATION. Scientific, technical, or historical information from NASA programs, projects, and mission, often concerned with subjects having substantial public interest.

- TECHNICAL TRANSLATION. English-language translations of foreign scientific and technical material pertinent to NASA's mission.

Specialized services that complement the STI Program Office's diverse offerings include creating custom thesauri, building customized databases, organizing and publishing research results…even providing videos.

For more information about the NASA STI Program Office, see the following:

- Access the NASA STI Program Home Page at ***http://www.sti.nasa.gov***

- E-mail your question via the Internet to help@sti.nasa.gov

- Fax your question to the NASA Access Help Desk at (301) 621–0134

- Telephone the NASA Access Help Desk at (301) 621–0390

- Write to:
  NASA Access Help Desk
  NASA Center for AeroSpace Information
  7121 Standard Drive
  Hanover, MD 21076–1320
  (301)621–0390

NASA/CP—2002–211783

The Twelfth Thermal and Fluids Analysis Workshop

Alok Majumdar, Compiler
Marshall Space Flight Center, Marshall Space Flight Center, Alabama

National Aeronautics and
Space Administration

Marshall Space Flight Center • MSFC, Alabama 35812

July 2002

Available from:

NASA Center for AeroSpace Information
7121 Standard Drive
Hanover, MD 21076–1320
(301) 621–0390

National Technical Information Service
5285 Port Royal Road
Springfield, VA 22161
(703) 487–4650

FOREWORD

The 2001 Thermal and Fluids Analysis Workshop (TFAWS) was held from September 10–14 at the Tom Bevill Center, The University of Alabama in Huntsville, Huntsville, Alabama. Organized by Marshall Space Flight Center, the theme of this year's workshop was "Engineering Excellence and Advances in the New Millenium." This yearly workshop focused on applications of themal and fluids analysis in the aerospace field. Its purpose is to bring industry, academia, and Government together to share information and exchange ideas about analysis tools and methods. We had a successful workshop despite the terrible tragedy of September 11 that shook our Nation during the week.

Paper sessions were classified into four categories: Thermal Spacecraft/Payload, Thermal Propulsion/Launch Vehicles, Interdisciplinary, and Fluids. One of the highlights of this year's workshop was to include a general session on TPSX material database and a panel discussion on Multidisciplinary Analysis.

There were several hands-on classes on Thermal and Fluid Flow software including grid generation and solid modeling. In addition, several short courses and product overview lectures were delivered during the workshop. This document, however, only includes the papers from four paper sessions and panel discussions on Multidisciplinary Analysis (http://tfaws01.msfc.nasa.gov/).

The organizers of this year's workshop consider it a privilege to participate in such an event. I would like to thank all the authors, presenters, and industry representatives who contributed to this year's success.

Bruce Tiller
Chairperson
TFAWS 2001 Organizing Committee
Marshall Space Flight Center
Huntsville, Alabama

TABLE OF CONTENTS

SPACECRAFT and VEHICLE FLUID SYSTEMS DESIGN, ANALYSIS, and TEST PAPER SESSION

Determining Dynamic Stiffness of a Pressurized Bearing Using 3D CFD Code with Experimental Verification
Robert F. Blumenthal, AEA Technology Engineering Software and Wes Franklin, Bently Rotor Dynamics Research Corporation

Launch Vehicle Ascent Stage Separation Wind Tunnel Test
Wayne Bordelon, Alonzo Frost, and Victor Pritchett, NASA MSFC

Advances in Turbulence and Plume Thermo-Chemistry on the Prediction of Missile Plume Structure
W.H. Calhoon, J.L. Papp, S.M. Dash, CRAFT Tech

Comparison of Full and Partial Admission Flow Fields in the Simplex Turbine
Daniel J. Dorney, Lisa W. Griffin and Douglas L. Sondak, NASA MSFC

Pre- and Post-Processing Tools to Streamline the CFD Process
Suzanne Miller Dorney, Ph.D., NASA MSFC

Stage Separation CFD Tool Development and Evaluation
Alan Droege and Ten-See Wang, NASA MSFC, Reynaldo Gomez, NASA JSC

Time-Dependent Simulations of Turbopump Flows
Cetin Kiris, Dochan Kwak, and William Chan, NASA Ames Research Center, Robert Williams, NASA MSFC

CFD Prediction of the BEAGLE 2 Mars Probe Aerodynamic Database
Peter A. Liever and Sami D. Habchi, CFD Research Corporation, Simon I. Burnell and Steve J. Lingard, Martin Baker Aircraft, Ltd.

Extension of a System Level Tool for Component Level Analysis
Alok Majumdar, NASA MSFC, and Paul Schallhorn, Sverdrup Technology, Inc.

Approximating Fluid Flow from Ambient to Very Low Pressures – Modeling *ISS* Experiments that Vent to Vacuum
Robert Minor, NASA MSFC, Stuart Nelson and Andy Johnston, Sverdrup Technologies, Inc.

Incorporation of Condensation Heat Transfer in a Flow Network Code
Miranda Anthony and Alok Majumdar, NASA MSFC

Status of Nozzle Aerodynamic Technology at MSFC
Joseph H. Ruf, David M. McDaniels, NASA MSFC, Bud Smith, Plumetech, and Zachary Owens, University of Virginia

Aero-Heating Analysis For Davinci Space Project Rocket Ballute
Brian Feeney, ORVA Corp, and Vladimir Kudriavtsev, CFD Canada

Experimental Study of Unshrouded Impeller Pump Stage Sensitivity to Tip Clearance
Robert W. Williams, Thomas Zoladz, Anne K. Storey, and Stephen E. Skelley, NASA MSFC

INTERDISCIPLINARY ANALYSIS and INTEGRATION PAPER SESSION

Thermal Response Modeling System for a Mars Sample Return Vehicle
Y.-K. Chen and F.S. Milos, NASA Ames Research Center

Advances in Thermal Model Data Exchange Using Open Standards
Hans Peter De Koning, ESA/ESTEC – The Netherlands

Use of Thermplot Software for Quick Evaluation of Thermal Model Results
Hume Peabody, Swales Aerospace

Integrated Turbopump Thermo-Mechanical Design and Analysis Tools
Mike Platt, Concepts NREC

How to Quickly Import CAD Geometry into Thermal Desktop
Shonte Wright, JPL California Institute of Technology and Emilio Beltran, Microsoft Corporation

PROPULSION and LAUNCH VEHICLE THERMAL SYSTEMS DESIGN, ANALYSIS, and TEST PAPER SESSION

Steady State Transportation Cooling in Porous Media Under Local, Non-Thermal Equilibrium Fluid Flow
Alvaro Che Rodriguez, NASA JSC

Heat Flux Sensor Testing
D.W. Clark, NASA MSFC

Thermal/Fluid Analysis of a Composite Heat Exchanger for Use on the RLV Rocket Engine
Dalton Nguyen, NASA MSFC

Thermal Analysis in Support of the Booster Separation Motor Crack Investigation
Darrell Davis and Terry Prickett, NASA MSFC

Fundamental Boiling and RP-1 Freezing Experiments
Brian Goode, NASA MSFC

Thermal and Chemical Characterization of Non-metallic Materials Using Coupled Thermogravimetric Analysis and Infrared Spectroscopy
Timothy L. Huff, NASA MSFC

Thermal Analysis of the MC1 Engine Turbopump
Jose Roman, NASA MSFC

Thermal Analysis of a Carbon Fiber Rope Barrier for Use in the Reusable Solid Rocket Motor Nozzle Joint-2
J. Louie Clayton, NASA MSFC

Corrections of Heat Flux Measurements on Launch Vehicles
Dr. Thomas R. Reinarts, Monique L. Matson, and Laurie K. Walls, NASA KSC

MDA PANEL DISCUSSION SESSION

Introduction
Robert Garcia, NASA MSFC

Loci: Logic Programming for Computational Field Simulations
Edward Luke, Mississippi State University

MDICE An Integrated Framework for Multidisciplinary Engineering Simulations
V. Sarathy, M. Underwood, and V. Harrand, CFD Research Corporation

NPSS Overview to TAFW Multidisciplinary Simulation Capabilities
Karl Owen, NASA Glenn Research Center

Recipe© Collaborative Engineering Environment
International Space Systems, Inc.

Rethinking the Design Process iSIGHT Framework
Mark Prow and Dr. Therese Rhodes, Engineous Software

iMAN
Mitchell Bailey, UGS

Robust Design Computational System (RDCS)
Kadambi (Raj) Rajagopal, Boeing

SPACECRAFT and PAYLOAD THERMAL SYSTEMS DESIGN, ANALYSIS, and TEST PAPER SESSION

Assessment and Accommodation of Thermal Expansion of the Internal Active Thermal Control System Coolant During Launch to On-Orbit Activation of *International Space Station* Elements
J. Darryl Edwards, Sverdrup Technology, Inc., Eugene K. Ungar, Ph.D., NASA JSC, and James M. Holt, NASA MSFC

Thermal Technology Development Activities at the Goddard Space Flight Center–2001
Dan Butler, NASA GSFC

Analysis of Pool Boiling in Microgravity During Loss of Cooling for the Quench Module Insert (QMI)
Richard D. Horton, Tec-Masters, Inc.

Thermal Examination of an Orbiting Cryogenic Fuel Depot
Patrick V. Hull and Steven L. Canfield, Tennessee Technological University, Connie Carrington and John Fikes, NASA MSFC

X–38 Deorbit Propulsion Stage MLI Performance Test
Ken Kittredge, NASA MSFC

Space Station Environmental Control and Life Support System Pressure Control Pump Assembly Modeling and Analysis
R. Gregory Schunk, NASA MSFC

Thermal Analysis of Next-Generation Space Telescope (NGST) Mirrors During Optical Testing in the X-Ray Calibration Facility (XRCF)
Tim Page, NASA MSFC and Steven Sutherlin, Raytheon ITSS

Comparison of Analytical and Numerical Performance Predictions for an *International Space Station* Node 3 Internal Active Thermal Control System Regenerative Heat Exchanger
Stephen A. Wise, Qualis Corporation and James M. Holt, NASA MSFC

Thermal Design, Analysis, and Testing of the Quench Module Insert Bread Board
Shawn Breeding and Julia Khodabandeh, NASA MSFC

Thermal Design Overview of the Mars Exploration Rover Project
Glenn Tsuyuki, Jet Propulsion Laboratory, California Institute of Technology

Use of Blackbody Optical Fiber Thermometers in High-Temperature Environments
Matthew R. Jones and David G. Baker, Brigham Young University

Determining Dynamic Stiffness of a Pressurized Bearing Using 3D CFD Code with Experimental Verification

Problem Statement

- Existing Methods of Pressurized Bearing Dynamic Stiffness Prediction Not Generally Applicable for All Geometries

- 1-D, 2-D Bulk Flow Methods Require Analytical/Geometric Approximations

A Generalized 3D Approach Applicable to All Geometries and Operating Conditions is Highly Desirable

CFX-TASCflow

- General 3-D Navier-Stokes Fluid Flow Solver Developed By AEA Technology Engineering Software

- Applicable to Laminar/Turbulent, Compressible/Incompressible, Steady/Transient Flow

- Flexible Fluid Properties (Constant, Variable)

- Uses Multi-block, Locally Structured Grids with Arbitrary Block Connectivity

- **Unique "Moving Grid" Feature Allows Motion of Walls in Computational Model. Modeling of Positive Displacement Pumps, Hydrostatic Bearings, and Seals Now Possible**

“Moving Grid” Approach

- User Provides Mathematical Model of Time-Dependent Position of Each Node On Moving Boundary Via User-FORTRAN Subroutine
- User Defines Nodes in Model Which Will Not Move (Frozen Nodes)
- All Other Nodes Will Move Based On A Laplacian Diffusion Solution
- The Entire Grid is Smoothly Adjusted In A Shape-Preserving Manner
- A Transient Solution is Created Based on The Time-Dependant Position of the Moving Boundary

Moving Grid Example:
"Piston" Grid

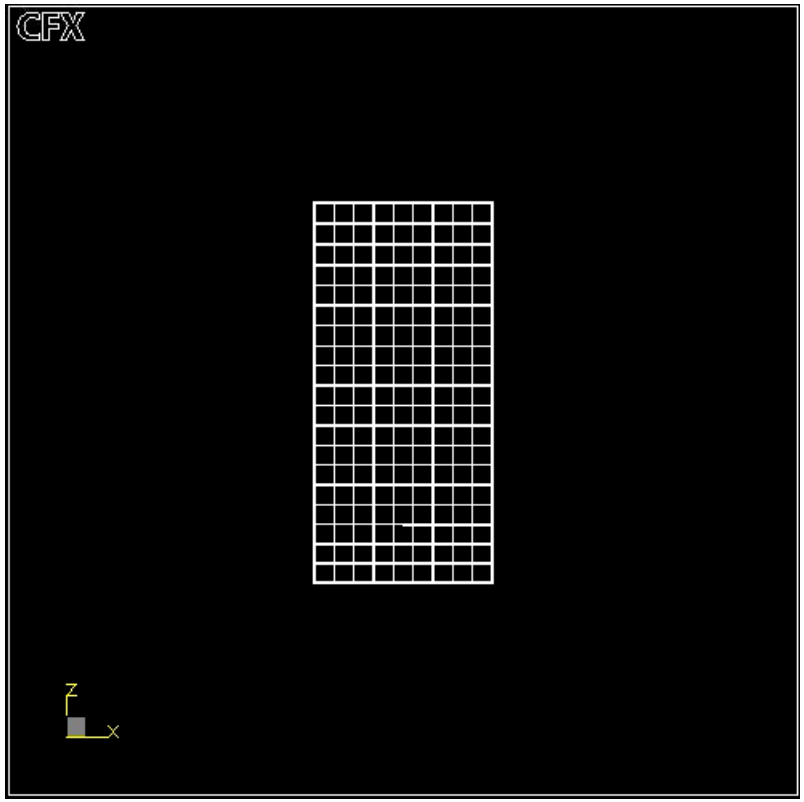

Pressurized Bearing Model

- Four Pocket Fixed-Ring Orifice-Compensated Bearing
- Half Bearing Modeled (No Mis-alignment Assumed)
- Model Size: 177K Nodes
- Fluid: ISO 32 Oil at T=89 deg F
- Rotational Speed: 8000 RPM

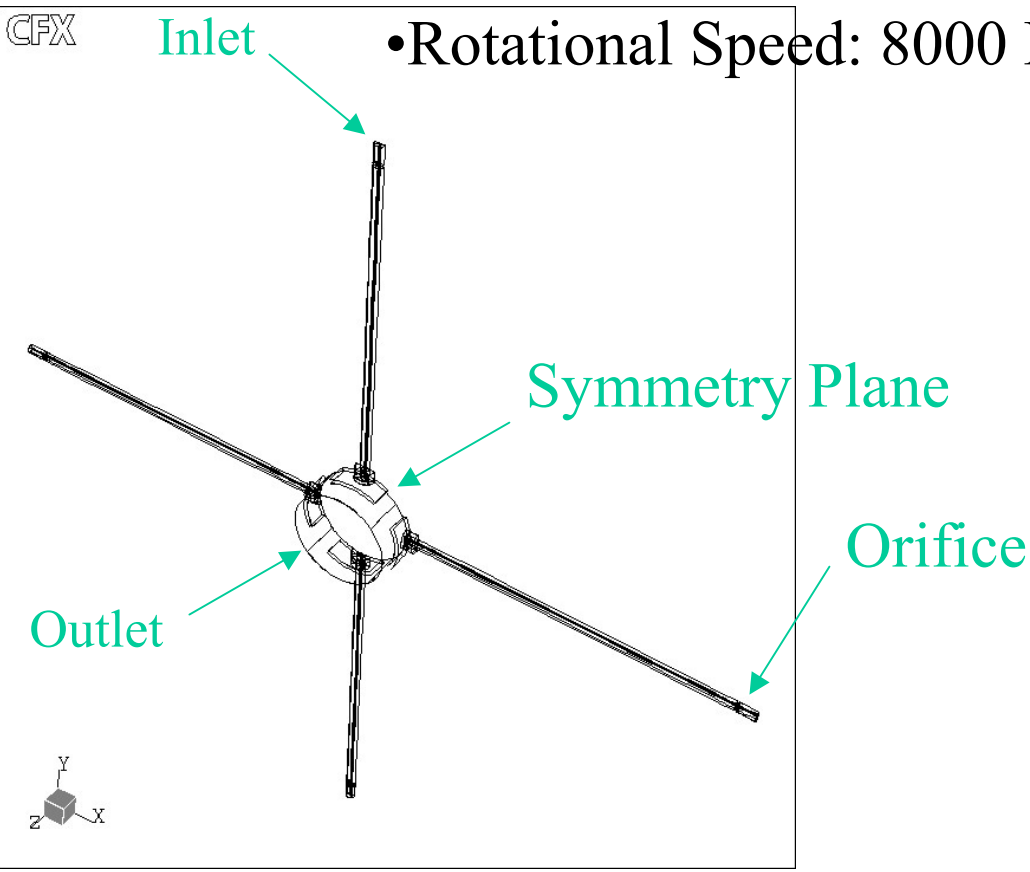

Bearing CFD Model

- Multi-Block Structured Grid
- Generalized Grid Interface (GGI) Allows Arbitrary Block Connections, Reduces Overall Node Count

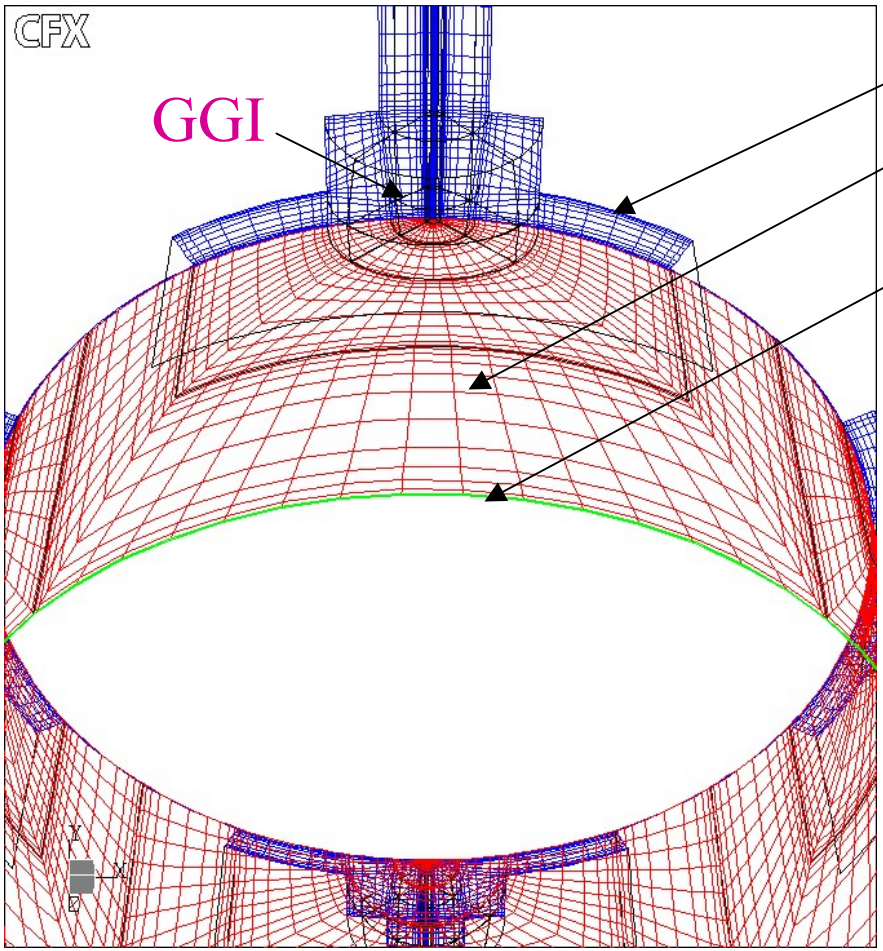

Boundary Conditions

Symmetry Plane

Rotor (Spinning Wall)

Outlet (Ps=14.7 psia)

Bearing CFD Model - "Moving Grid" Feature

- User Specifies Two Nodal Regions:
  - "Moved" Nodes - Nodes which follow a user-prescribed motion as a function of time (e.g. elliptical orbit)
  - "Frozen" Nodes - Nodes which are fixed

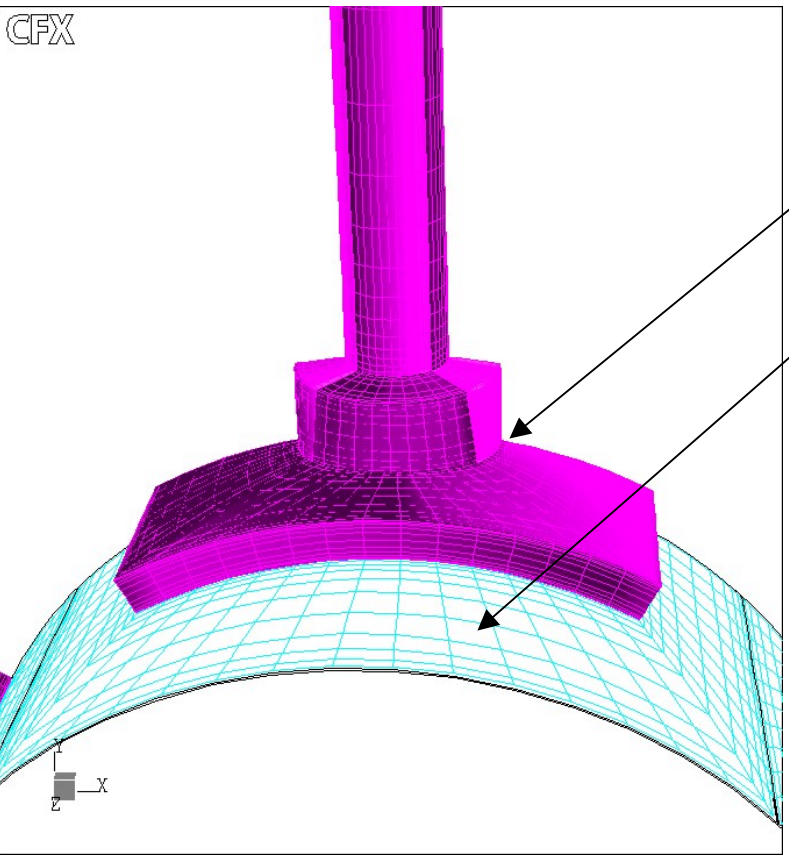

"Frozen Nodes" - Feed Tube, Recess

"Moved" Nodes - Rotor Surface

All Other Nodes (Land Region, Region Between Rotor and Recess) Will Move To Accommodate Motion Of The Rotor

“Moving Grid” Boundary Conditions

- Four Perturbation Speeds Analyzed: 1500,3000,4500,6000 RPM

- Circular Orbit of Journal Center Specified:

  XNODE,YNODE: New Position of Nodes on Journal Surface[in]
  RO: Journal Eccentricity [in]
  OMEGA: Perturbation Circular Frequency [sec]
  STIME: Current Solution Time [sec]
  DTIME: Time Step Size [sec]
  OFF: Journal Offset At Time=0

```
XNODE=X(INODE,JNODE,KNODE)+RO*(COS(OMEGA*STIME)-
     &                                  COS(OMEGA*(STIME-DTIME)))+OFF
YNODE=Y(INODE,JNODE,KNODE)+RO*(SIN(OMEGA*STIME)-
     &                                  SIN(OMEGA*(STIME-DTIME)))
```

Pressurized Bearing CFD Results

Bearing Static Pressure as a Function of Time

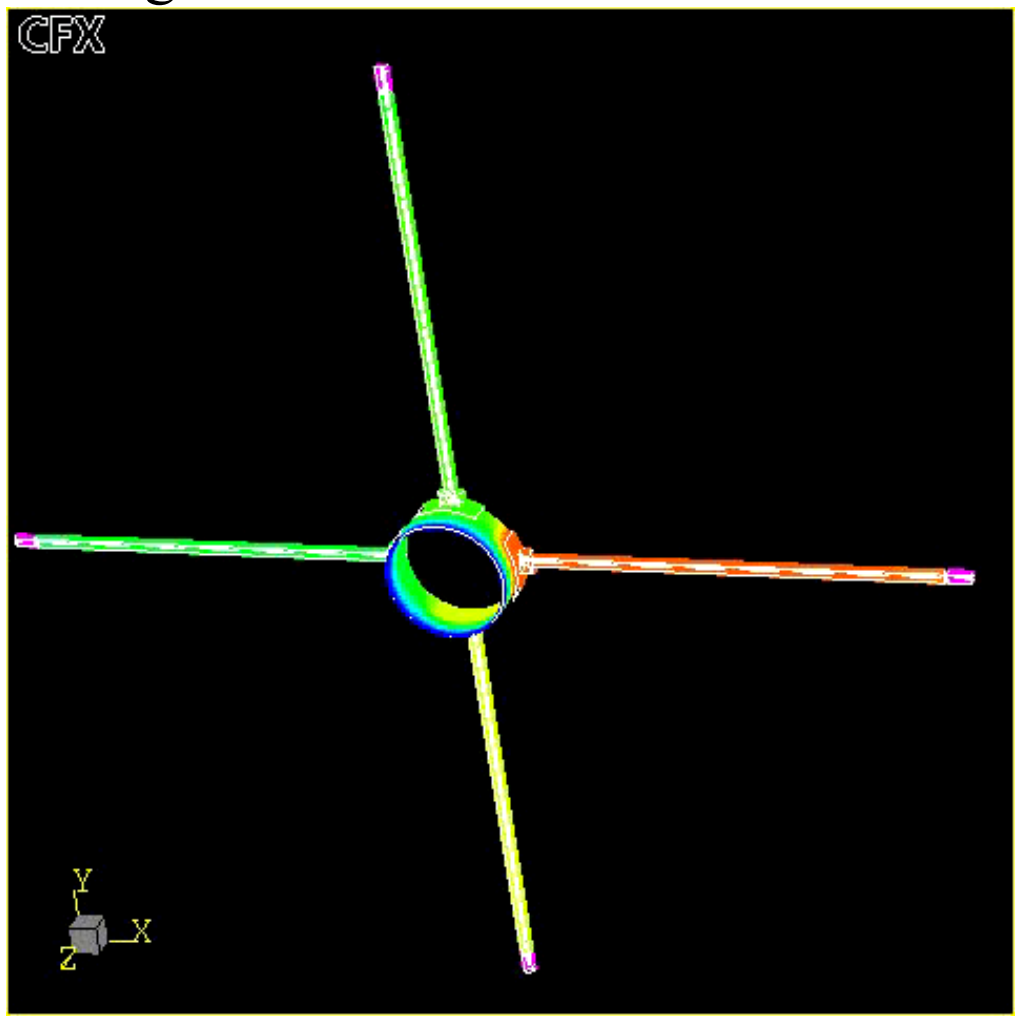

Pressurized Bearing CFD Results

Bearing Static Pressure as a Function of Time

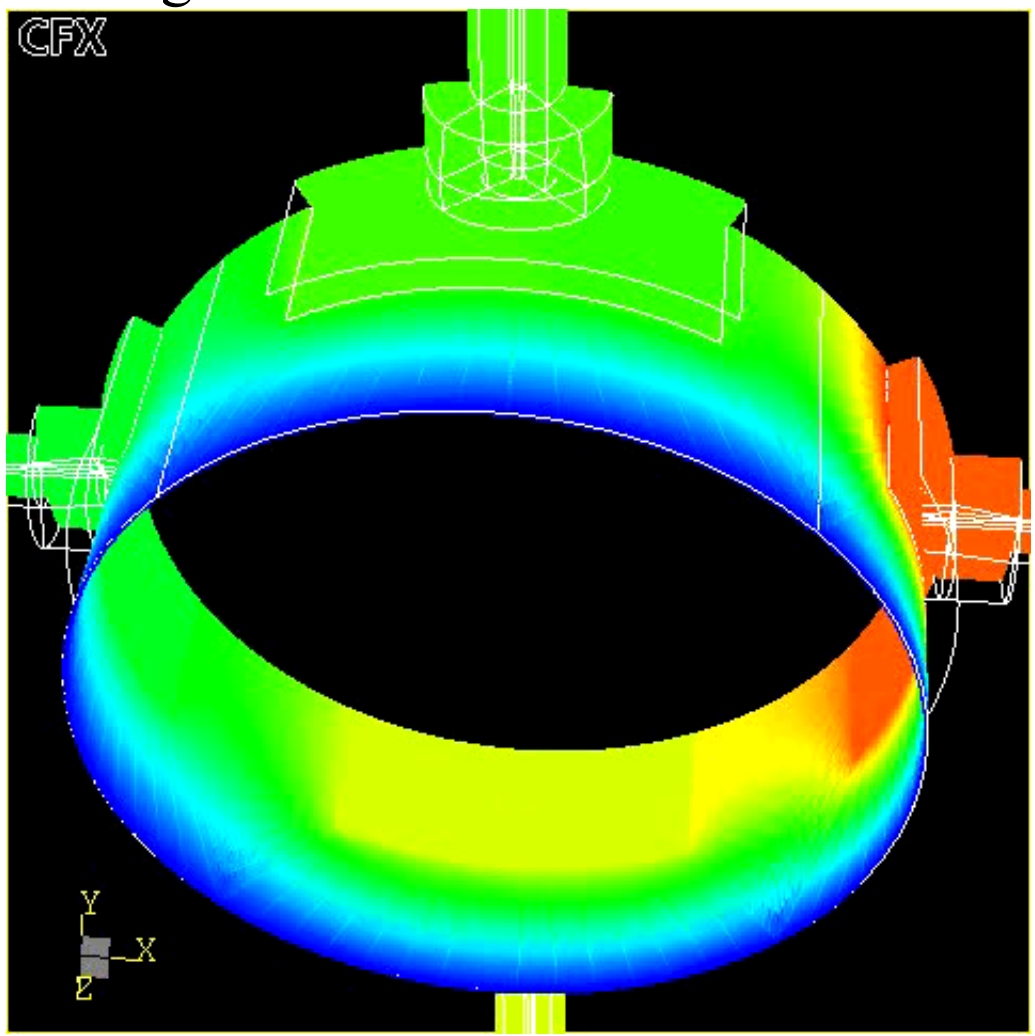

Pressurized Bearing CFD Results

Time-Dependant Journal Forces Used to Calculate Direct and Quadrature Dynamic Stiffness

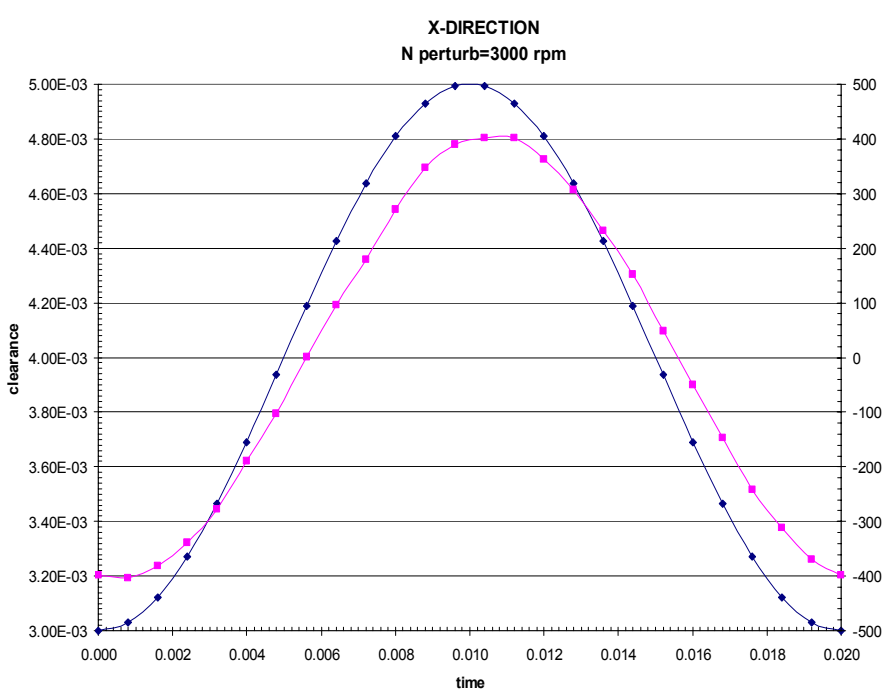

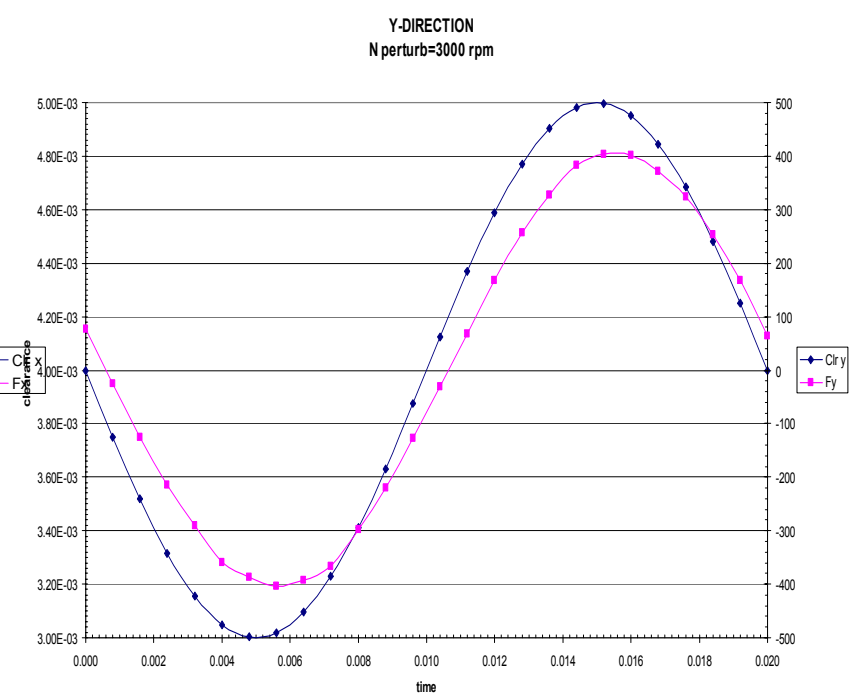

Calculation of Bearing Dynamic Stiffness from CFD Solution

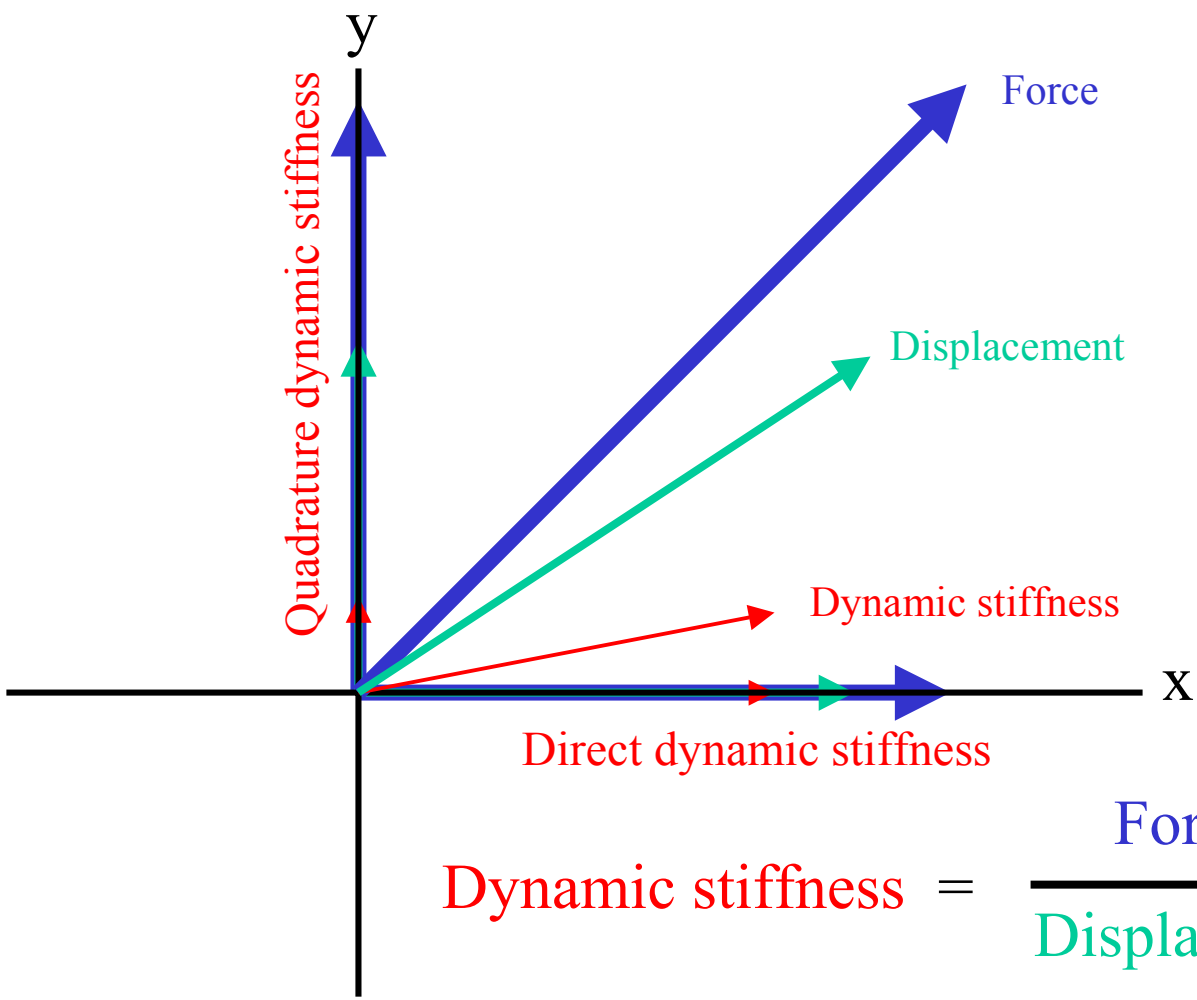

$$\text{Dynamic stiffness} = \frac{\text{Force}}{\text{Displacement}}$$

Bearing

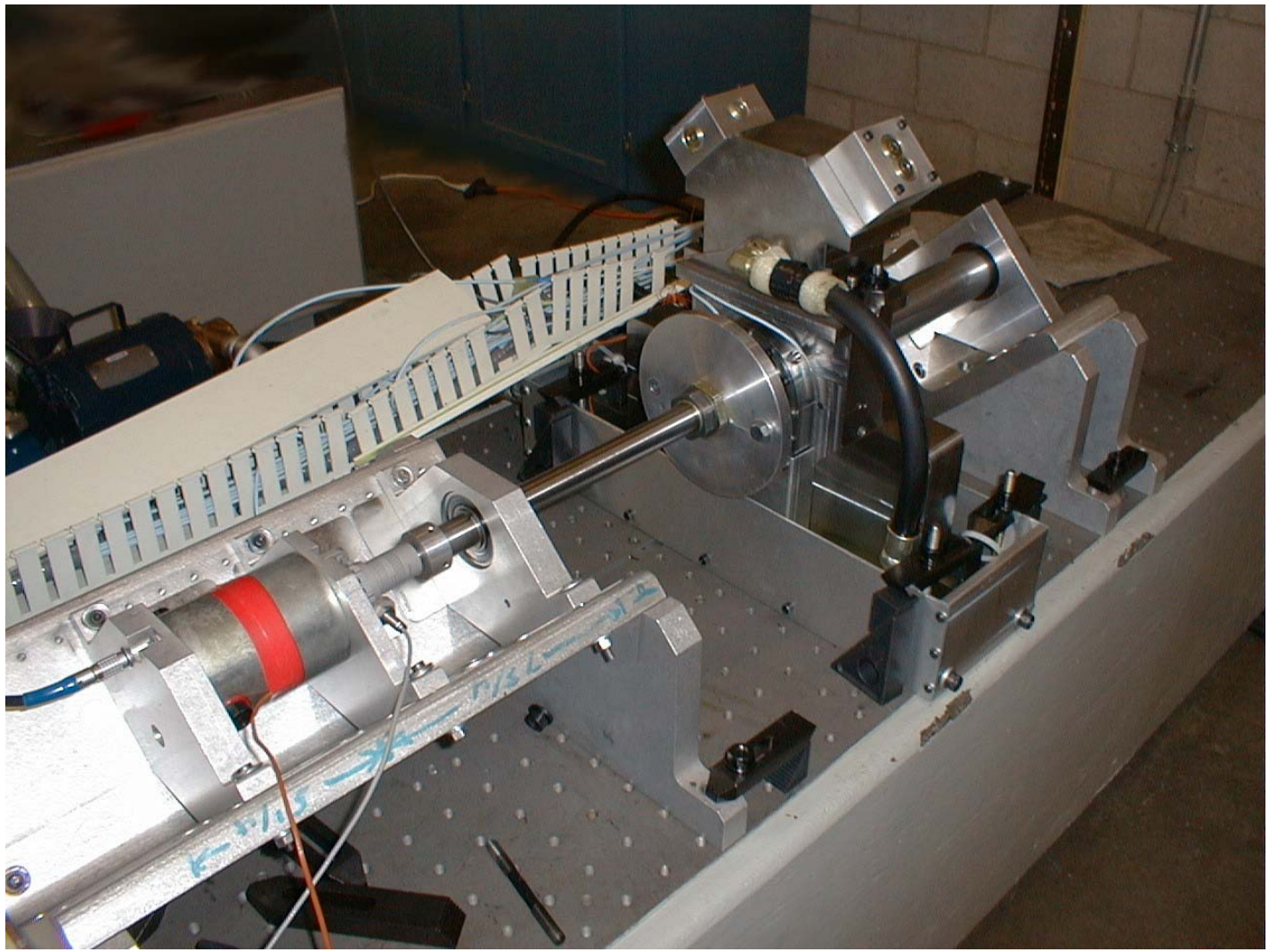

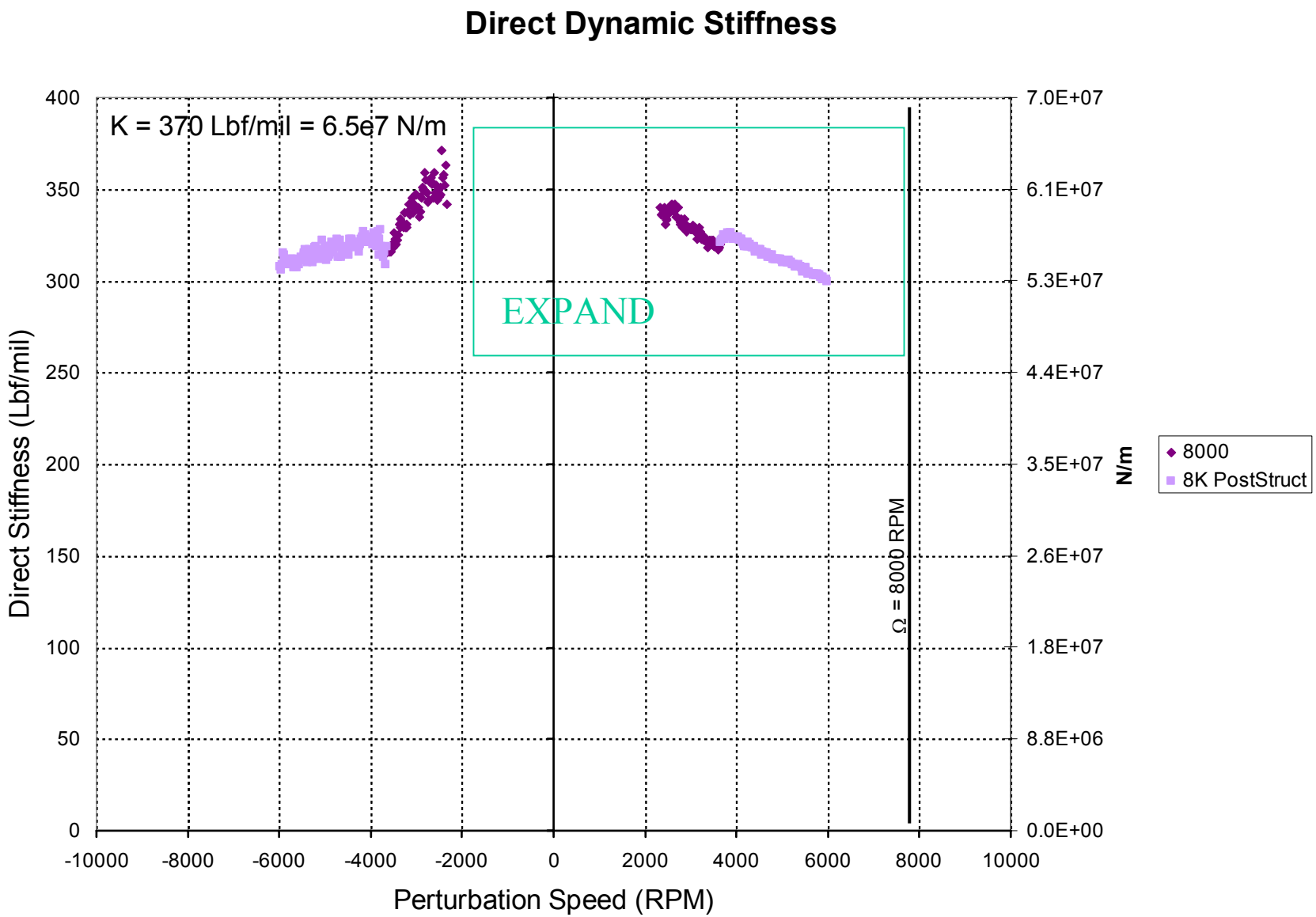
Direct Dynamic Stiffness
K = 370 Lbf/mil = 6.5e7 N/m
EXPAND
Ω = 8000 RPM
Direct Stiffness (Lbf/mil)
Perturbation Speed (RPM)
N/m
400
350
300
250
200
150
100
50
0
-10000
-8000
-6000
-4000
-2000
0
2000
4000
6000
8000
10000
7.0E+07
6.1E+07
5.3E+07
4.4E+07
3.5E+07
2.6E+07
1.8E+07
8.8E+06
0.0E+00
8000
8K PostStruct

Direct Dynamic Stiffness

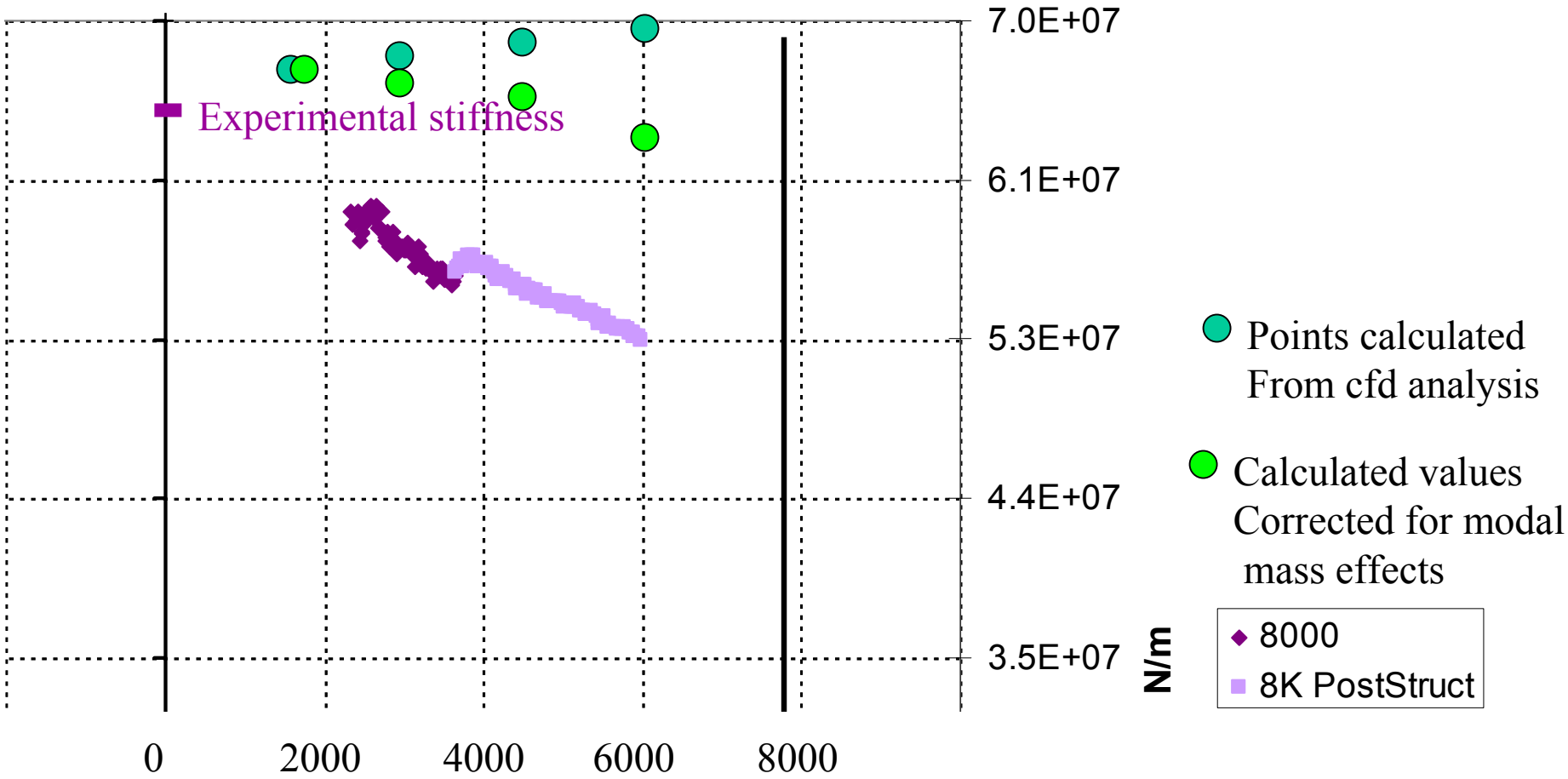

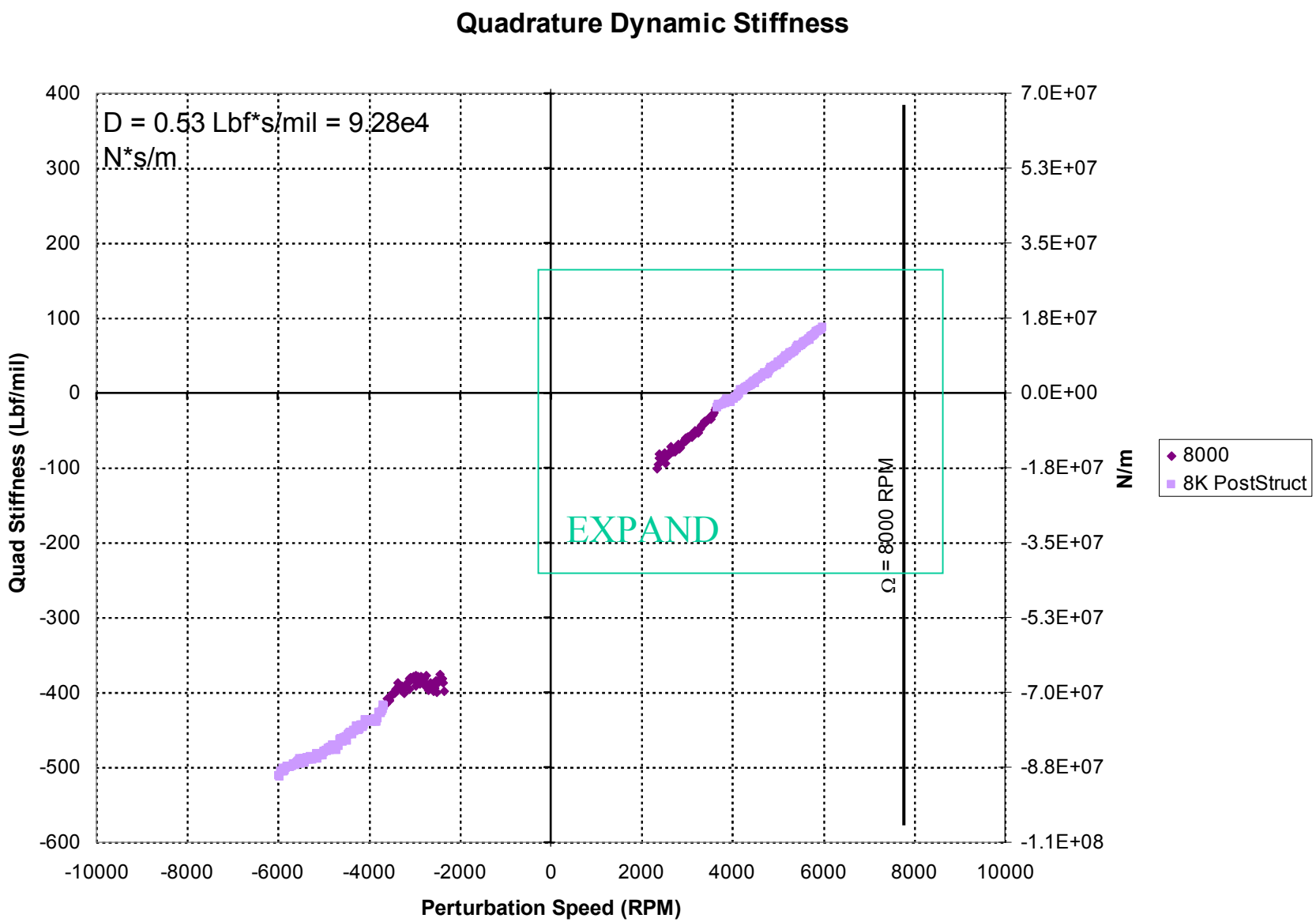
Quadrature Dynamic Stiffness
D = 0.53 Lbf*s/mil = 9.28e4 N*s/m
EXPAND
Ω = 8000 RPM
Quad Stiffness (Lbf/mil)
N/m
Perturbation Speed (RPM)
400
300
200
100
0
-100
-200
-300
-400
-500
-600
7.0E+07
5.3E+07
3.5E+07
1.8E+07
0.0E+00
-1.8E+07
-3.5E+07
-5.3E+07
-7.0E+07
-8.8E+07
-1.1E+08
-10000
-8000
-6000
-4000
-2000
0
2000
4000
6000
8000
10000
8000
8K PostStruct

Quadrature Dynamic Stiffness

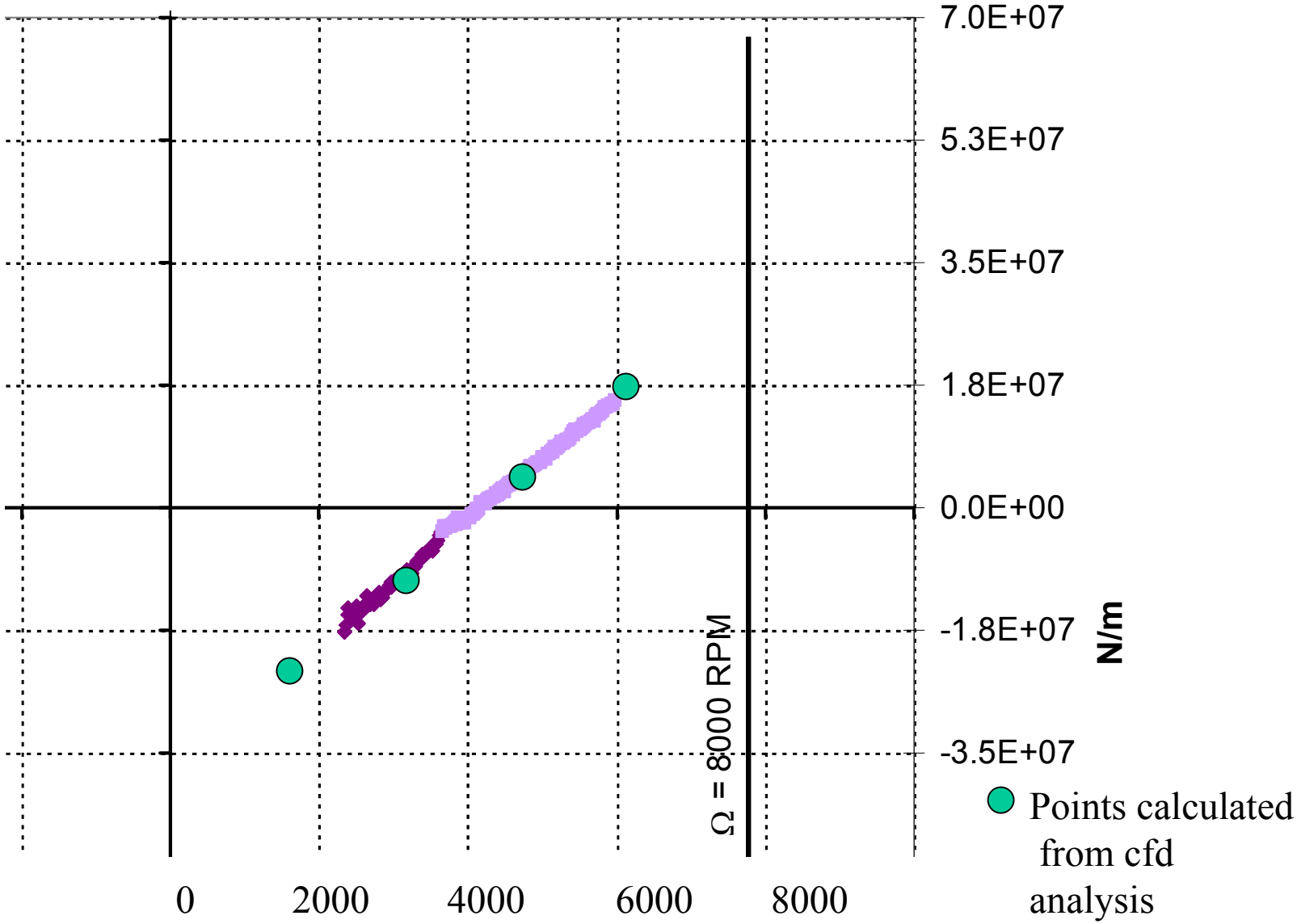

Summary

- A New Method of Simulating Pressurized Bearing Operation using Computational Fluid Dynamics was Presented

- "Moving Boundary" Feature Allows Time-Accurate Modeling of Journal Motion Within Bearing

- Good Comparison of Predicted vs Measured Dynamic Stiffness

- **New Approach is Applicable to Any Bearing/Seal Geometry**

Launch Vehicle Ascent Stage Separation Wind Tunnel Test

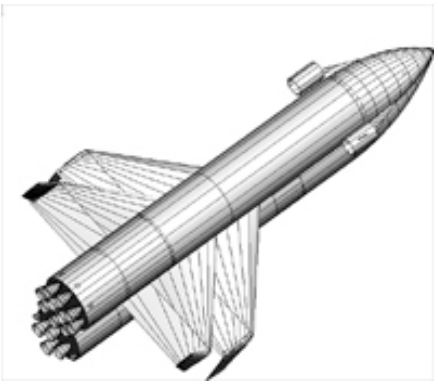

Wayne Bordelon/MSFC
Alonzo Frost/MSFC
Victor Pritchett/MSFC

12th Thermal and Fluids Analysis Workshop

September 10 – 14, 2001

Presentation Overview

- Background
- Objectives
- LGBB Configuration
- Approach
  - Test Facility
  - Instrumentation
  - Tests Conducted
- Preliminary Results
  - Pressure Sensitive Paint
  - Schlieren Video
  - Force and Moment
- Observations
- Summary
- Acknowledgements

Background

- 2nd Gen NASA Led Risk Mitigation Activities Call:
  - 1st round call – June, 2000
  - Goal: advance technologies, mitigate risks, and conduct advanced development activities to enable RLV decision/development

- Stage Separation and Ascent Aerothermodynamics Task Selected as part of the Airframe Project
  - Develop tools and databases to address TSTO stage sep
  - Multi-center team (JSC, LaRC, MSFC)
  - Wind tunnel testing and CFD development and application
  - LGBB bimese was selected as initial reference configuration
  - FY01 testing at MSFC and LaRC

MSFC Aero Research Facility Test Objectives

- Measure Force and Moment Data for Isolated and Bimese Configurations
- Record Schlieren Data for Aerodynamic Analysis
- Develop Pressure Sensitive Paint Test Methodology and Determine Feasibility
- Develop and Test Stage Separation Envelope using Manual Stage Separation Sting
- Develop Reference Databases to Validate Tools and Support Preliminary Design
- Develop NASA In-House Expertise and Capability to Support 2nd Gen Insight

LGBB Configuration

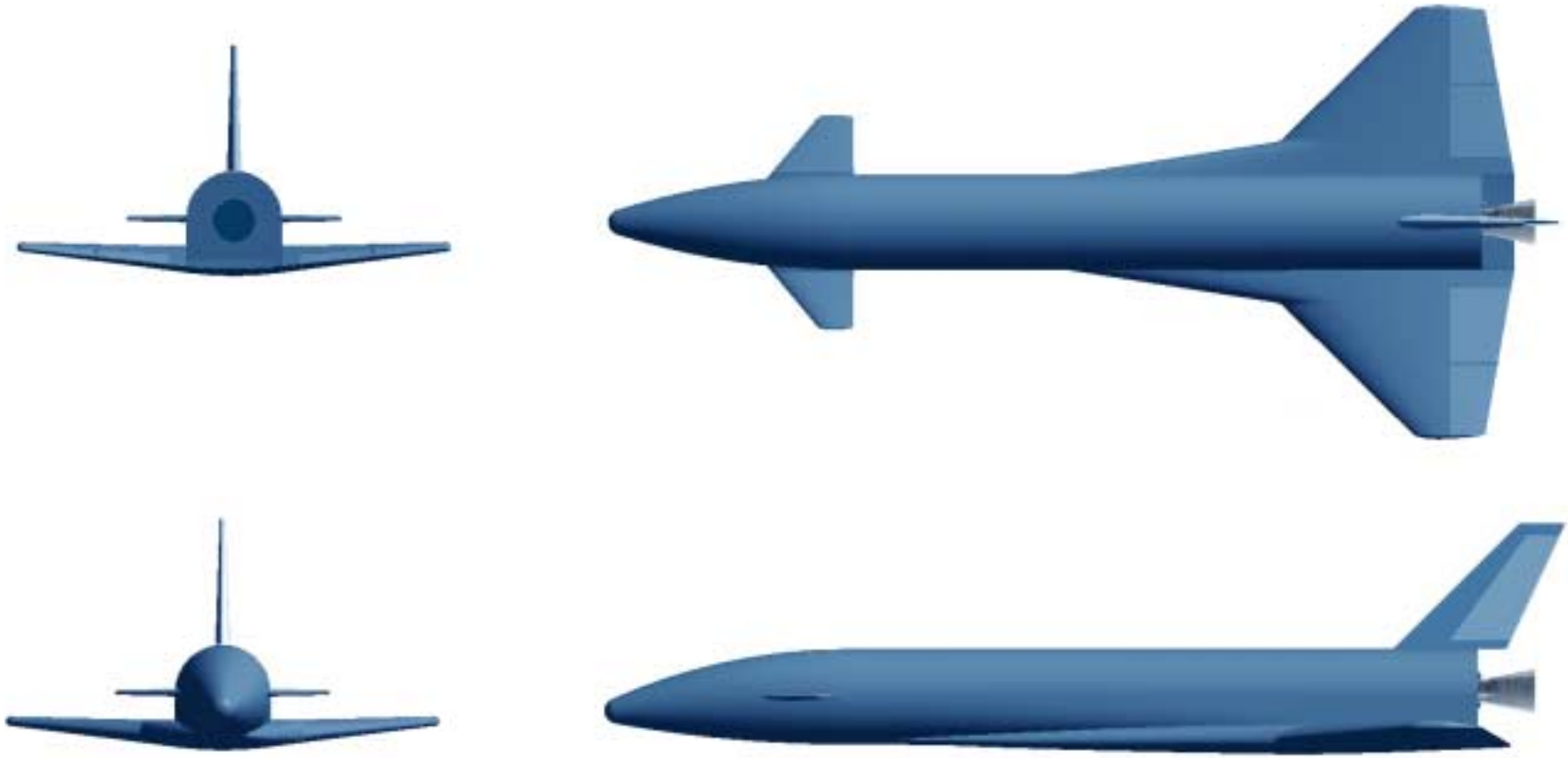

LGBB Configuration

BIMESE ARRANGEMENT

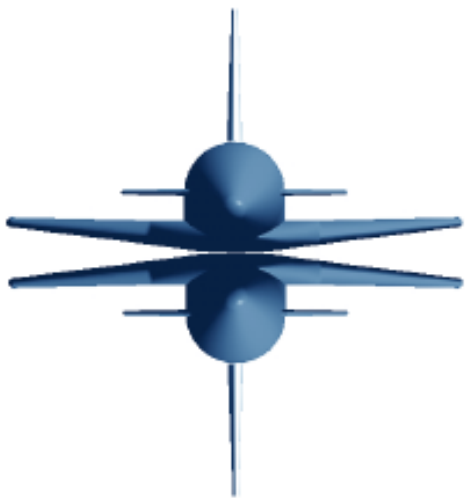

Aerodynamic Research Facility Test Approach

- Test Conducted at MSFC's 14" Aerodynamic Research Facility
- Design and Fabricate 0.0121 Scale LGBB Model
- Pressure Sensitive Paint Feasibility Test
- Isolated Orbiter Force and Moment Data
- Develop Stage Separation Test Envelope
- Bimese Configuration Force and Moment Data using Manual Stage Separation Test Rig
- Schlieren Video to Analyze Aerodynamic Environment

MSFC Aerodynamic Research Facility

MSFC Aerodynamic Research Facility

Type of Tunnel	Blowdown to atmosphere or vacuum
Test Section Size	Height 14 inches Width 14 inches Length 24 inches
Mach Number	Transonic test section with controllable diffuser, perforated walls, and interchangeable nozzle blocks. Mach 0.25 to 1.3, 1.46, 1.96 Supersonic test section with movable fixed contour nozzle blocks. Mach 2.74 to 4.96
Reynolds Number	1 to 18 million per foot
Stagnation Pressure	22 to 105 psia
Dynamic Pressure	2 to 20 psia
Stagnation Temperature	Ambient to 200 F; normally 100 F
Air Storage	6000 cubic feet at 515 psia and 100 F
Vacuum Storage	42,000 cubic feet at 0.1 psia
Run Time	60 to 90 seconds (transonic) 45 to 50 seconds (supersonic)
Recharge Time	10-20 minutes nominally for transonic and 15-20 minutes nominally for supersonic. Supplemental charging may be done with 3500 psi plant air when needed.
Run Rate	20 to 30 runs per 8-hour shift
Angle of Attack	-10 to +10 degrees with added range provided by offset stings up to 90 degrees

Courtesy of MSFC's Web Site

LGBB - 0.0121 Scale Model

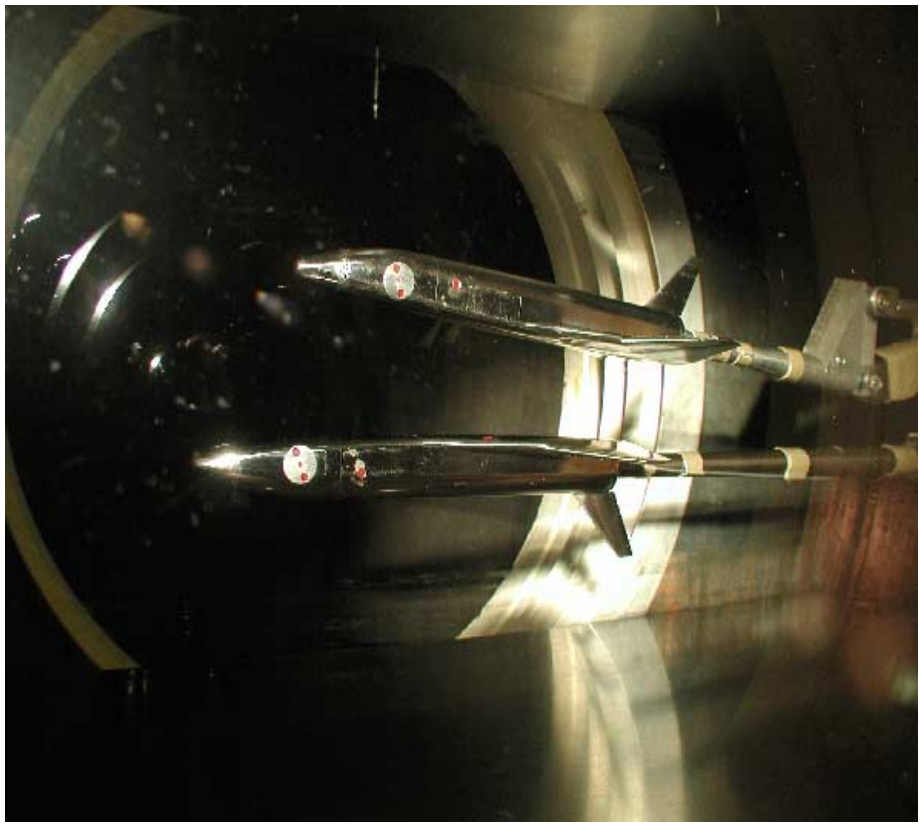

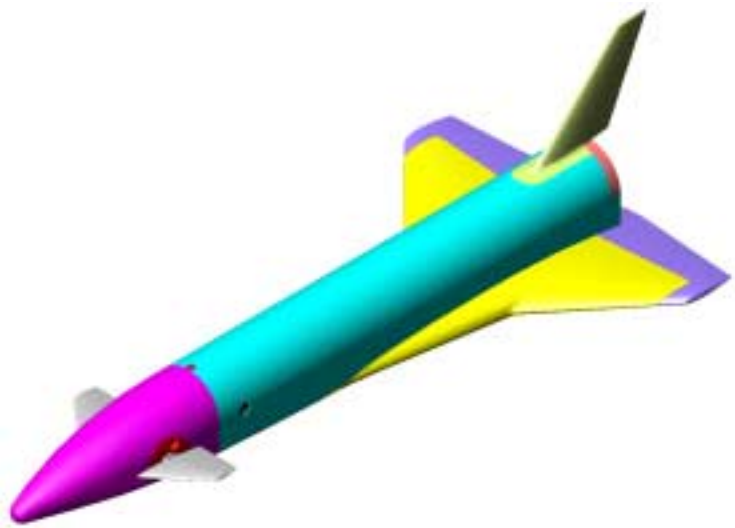

Stage Separation Test Instrumentation

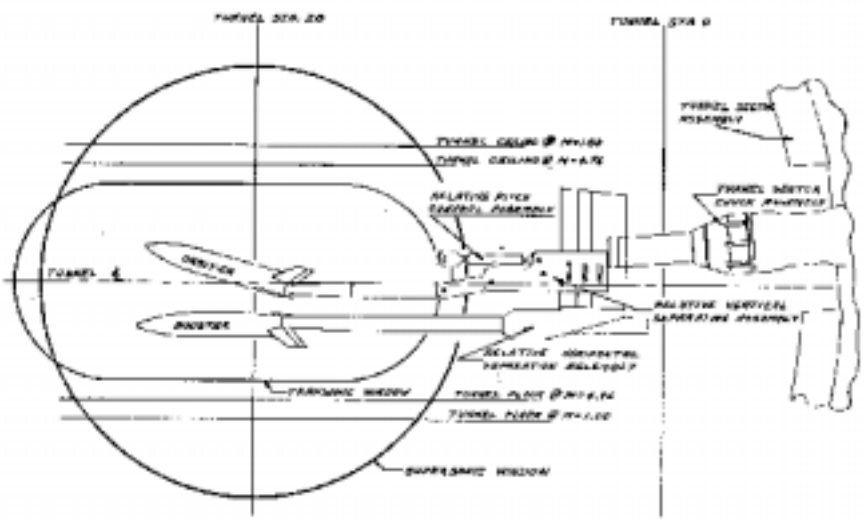

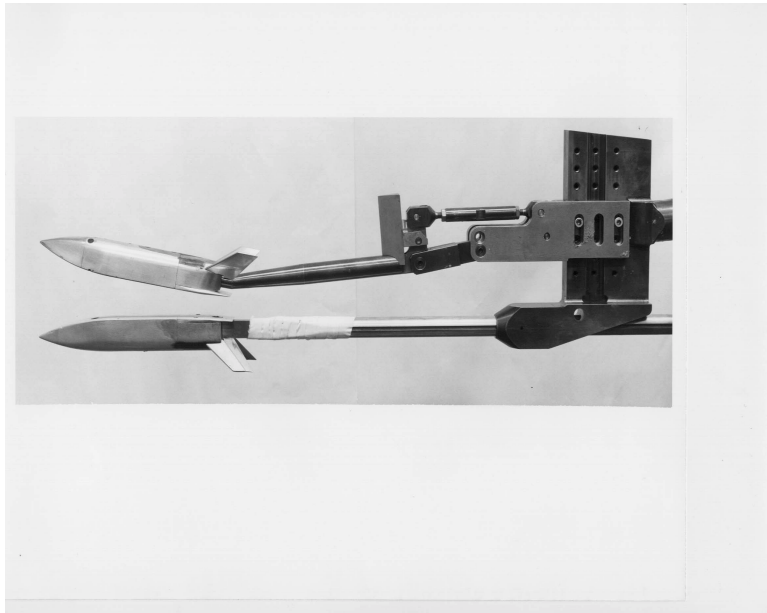

Wind Tunnel Separation Testing
(Phase A Shuttle Concept)

Pressure Sensitive Paint Test

STS Orbiter Inside TST and PSP Imager Outside Tunnel

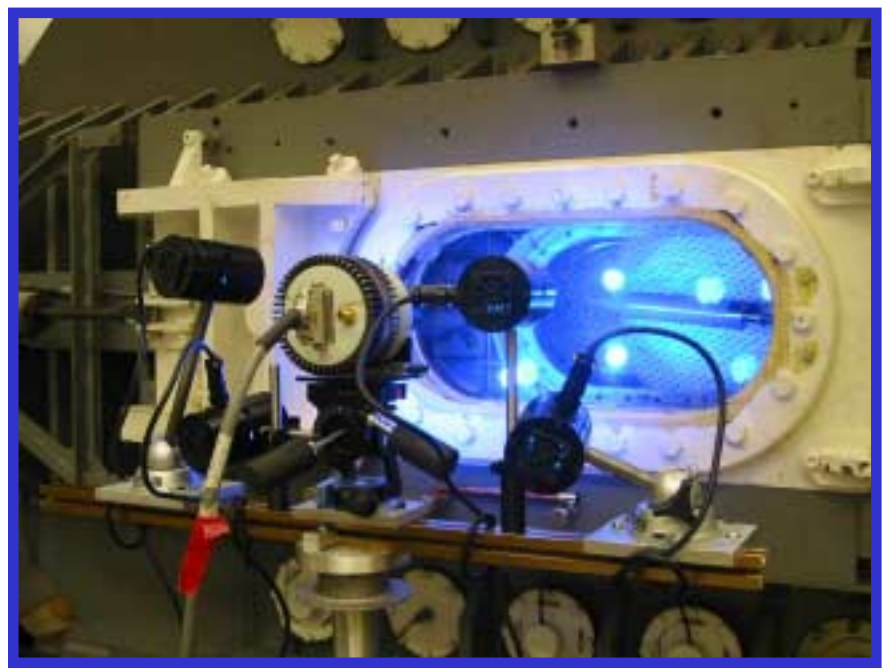

Isolated LGBB PSP Sample Results

Mach 3.48, Alpha = 0°

$\beta = 0$ deg

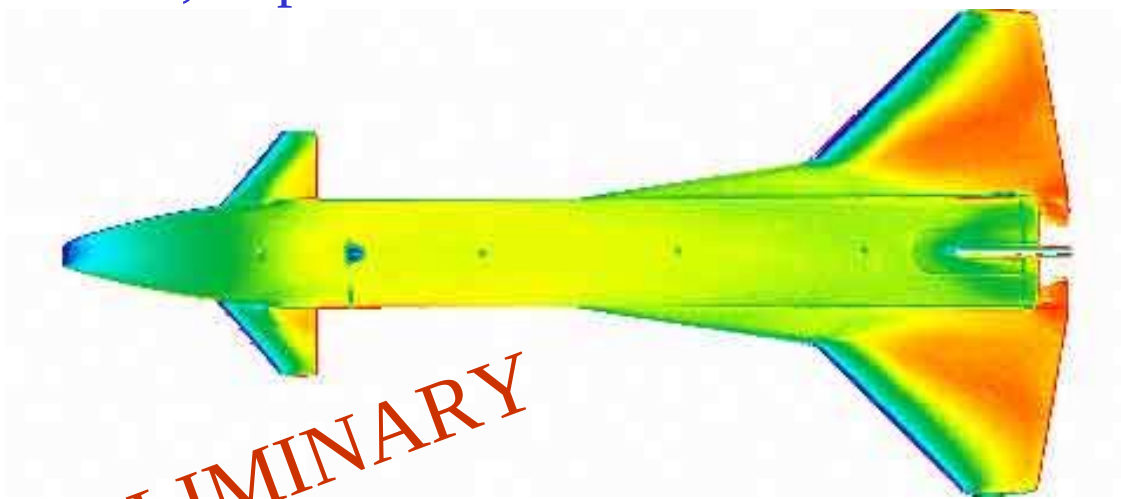

PRELIMINARY

$\beta = 8$ deg

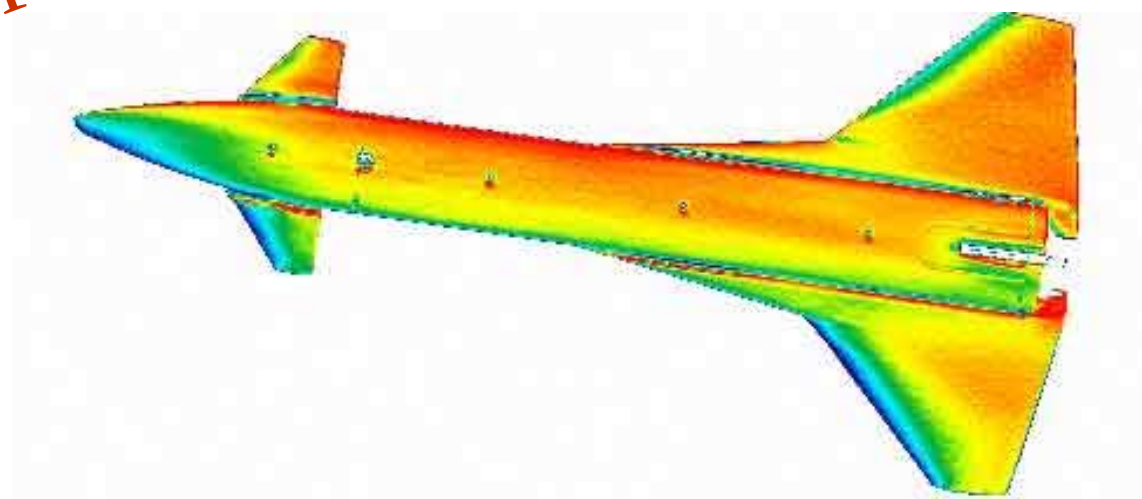

Isolated LGBB PSP Sample Results

Mach 3.48, Alpha = 0°

Top View

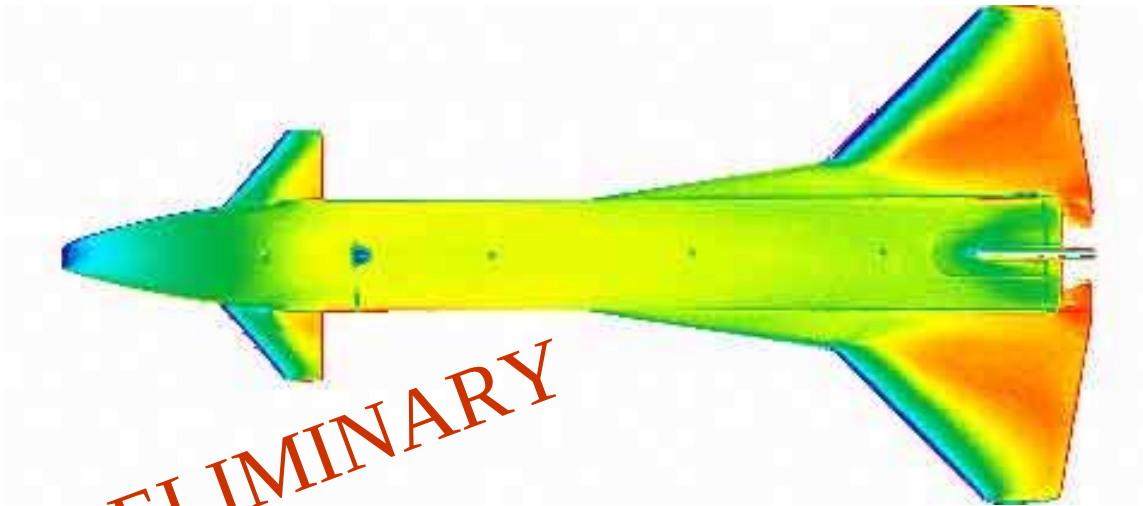

PRELIMINARY

Bottom View

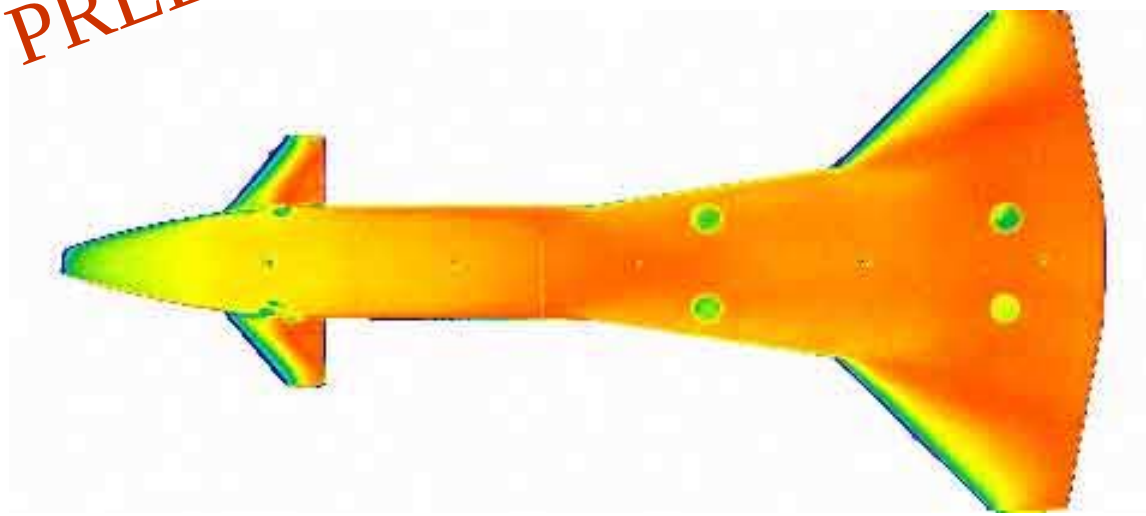

Stage Separation LGBB Test Envelope

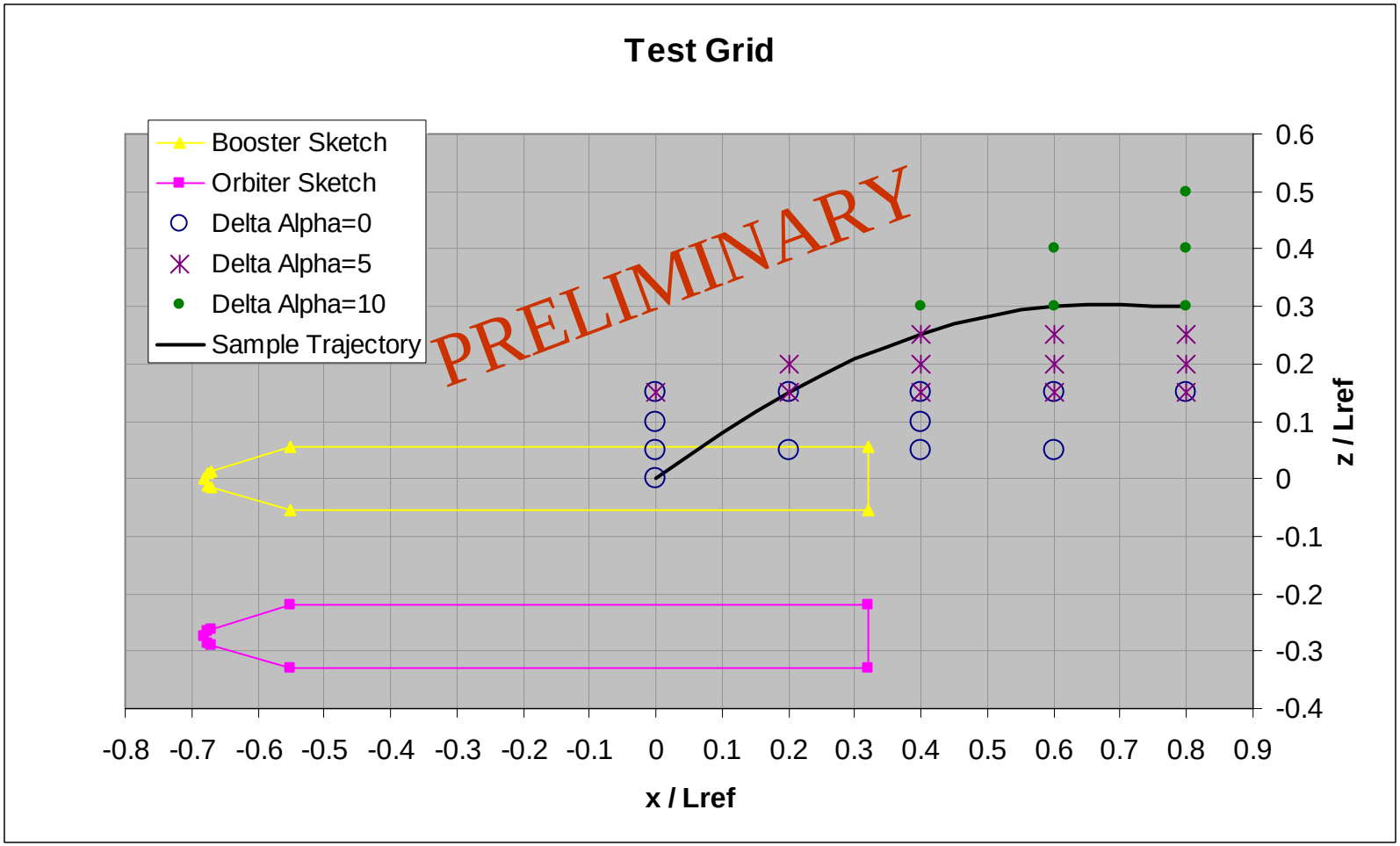

Sample Stage Separation Trajectory

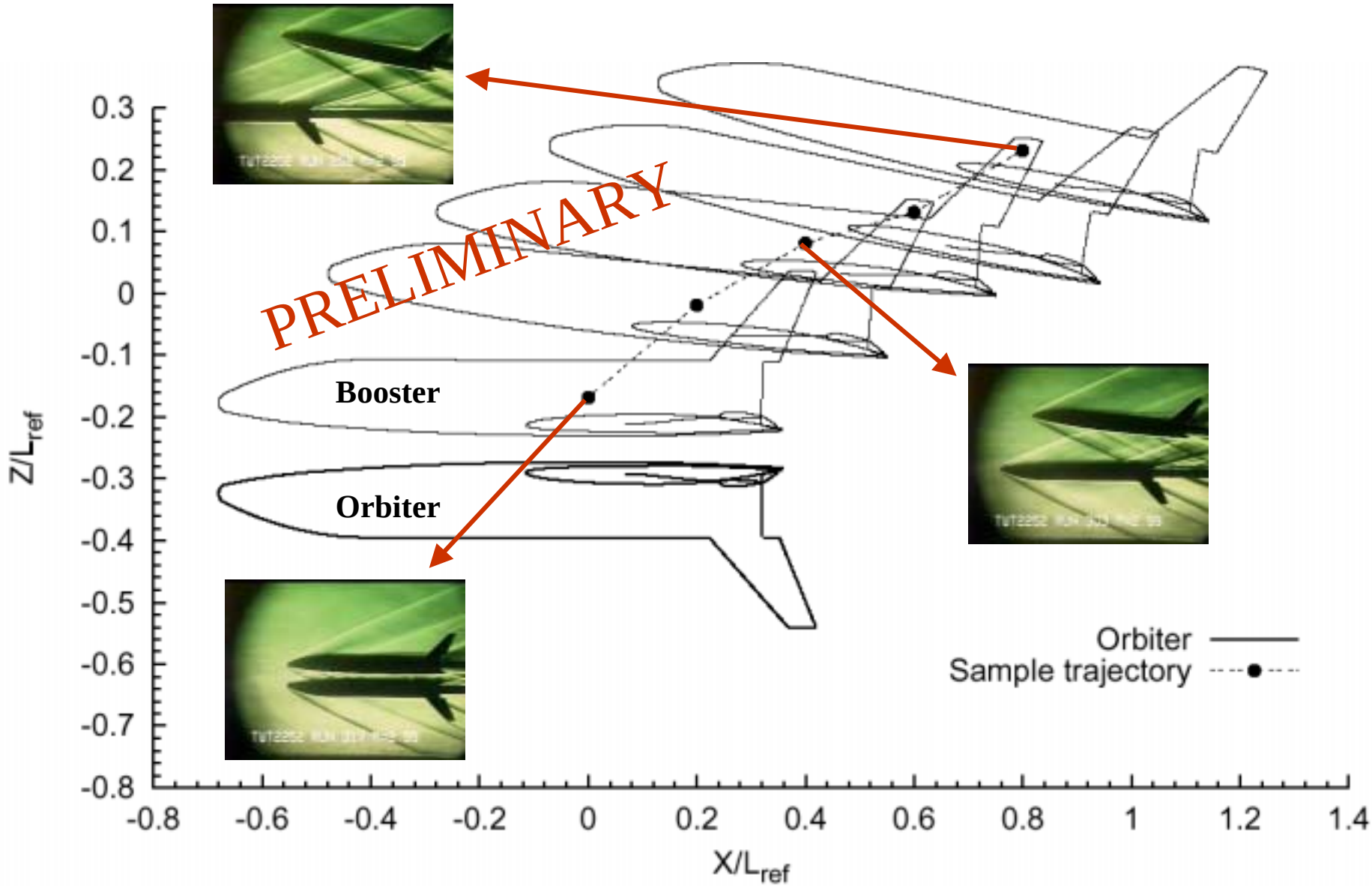

Schlieren Photos of Sample Trajectory

PRELIMINARY

ARF 0.0121 Scale LGBB Test (Frost – MSFC)

-- Schlieren Video, Stack Proximity Location

ARF 0.0121 Scale LGBB Test (Frost – MSFC)

-- Schlieren Video, Separated Location

Schlieren Results to OVERFLOW Comparison

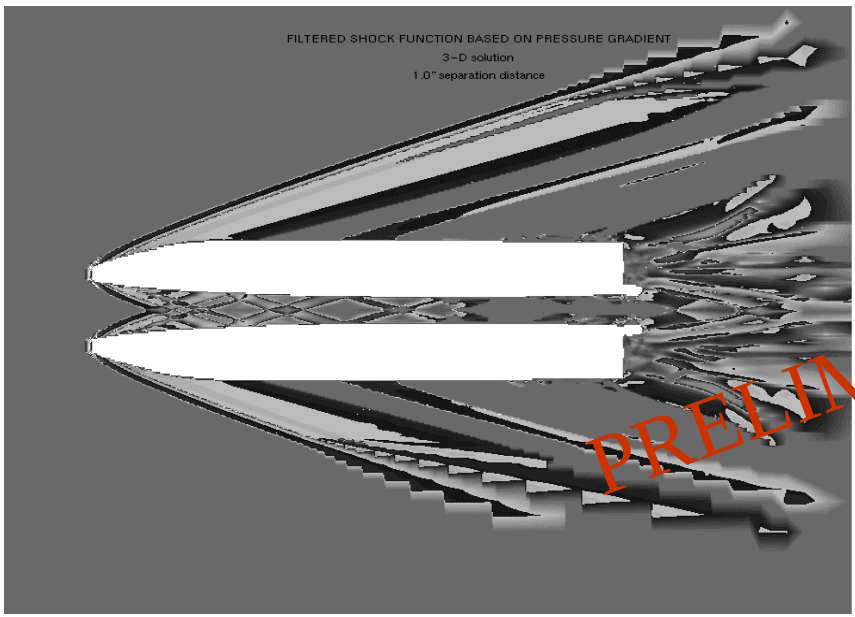

PRELIMINARY

Preliminary Results – Normal Force vs AOA

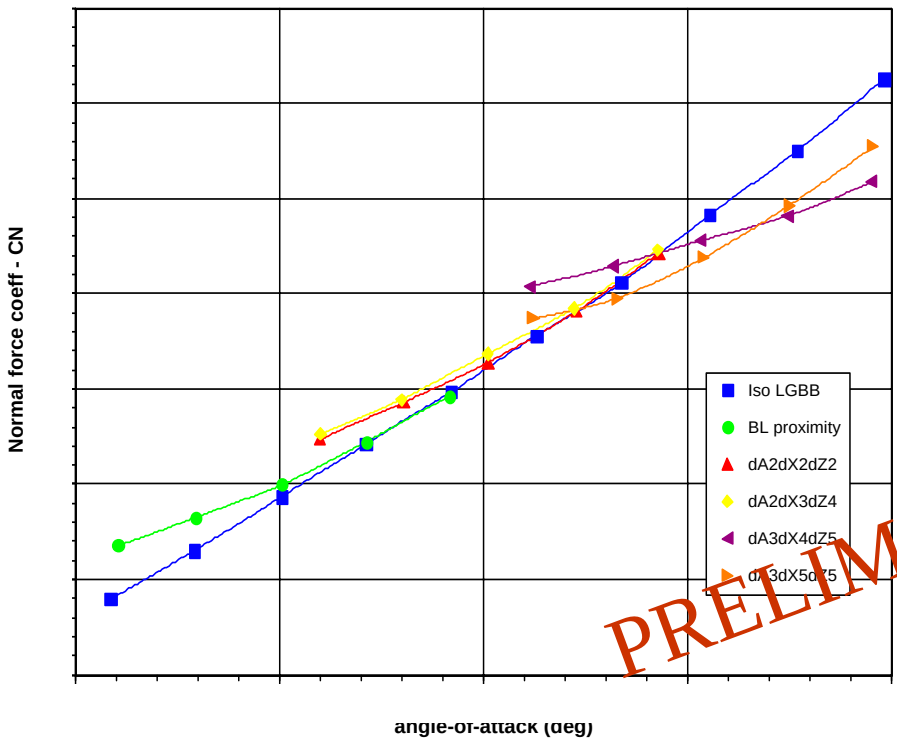

Booster

Orbiter

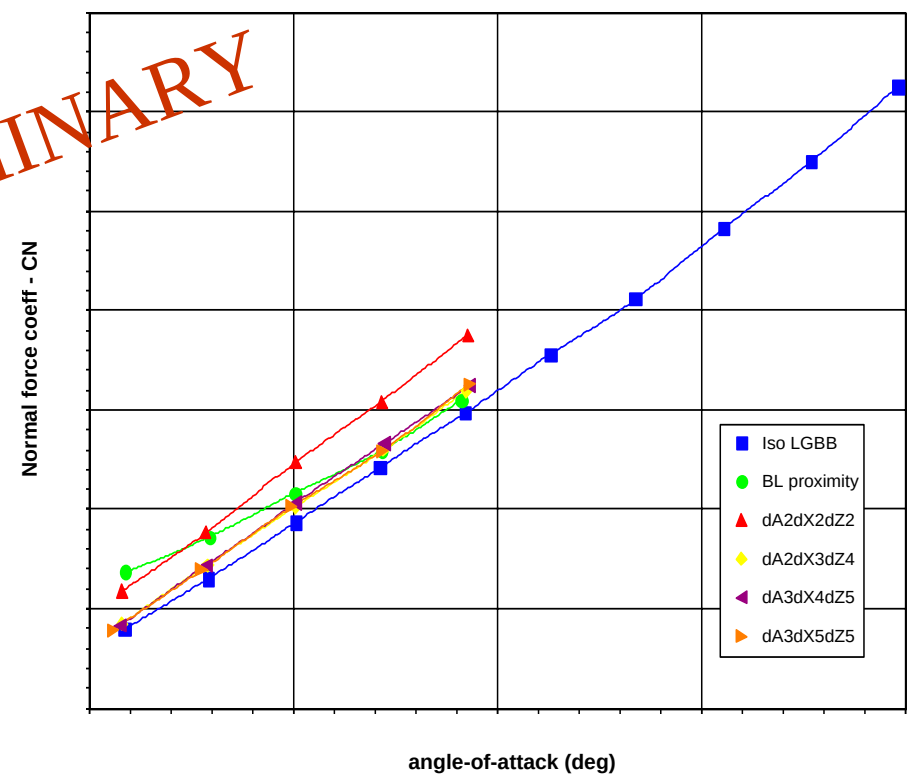

PRELIMINARY

Preliminary Results – Axial Force vs AOA

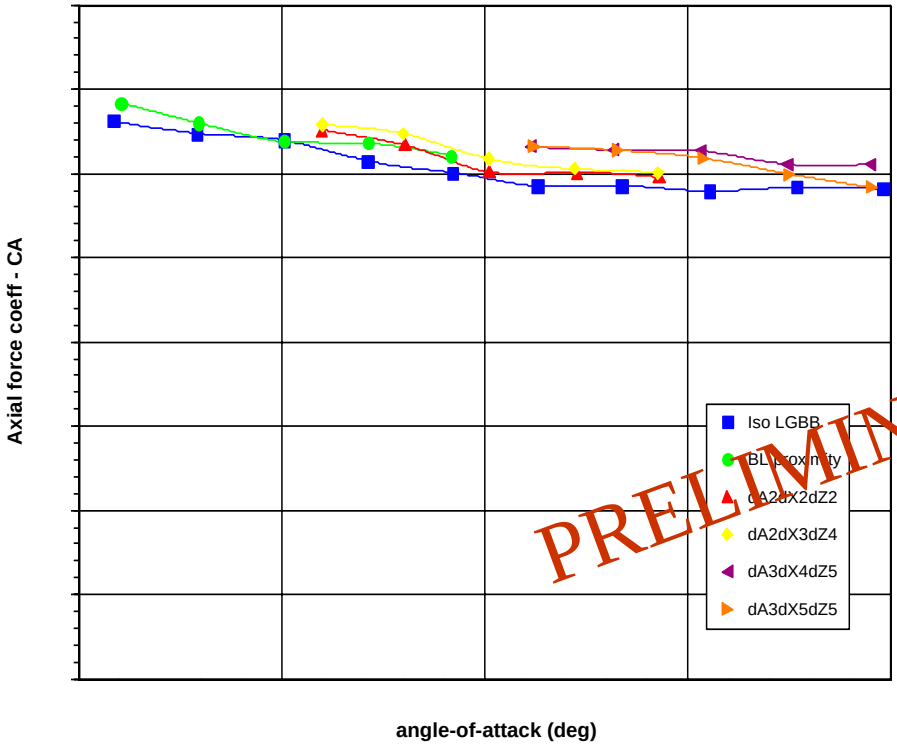

Booster

PRELIMINARY

Orbiter

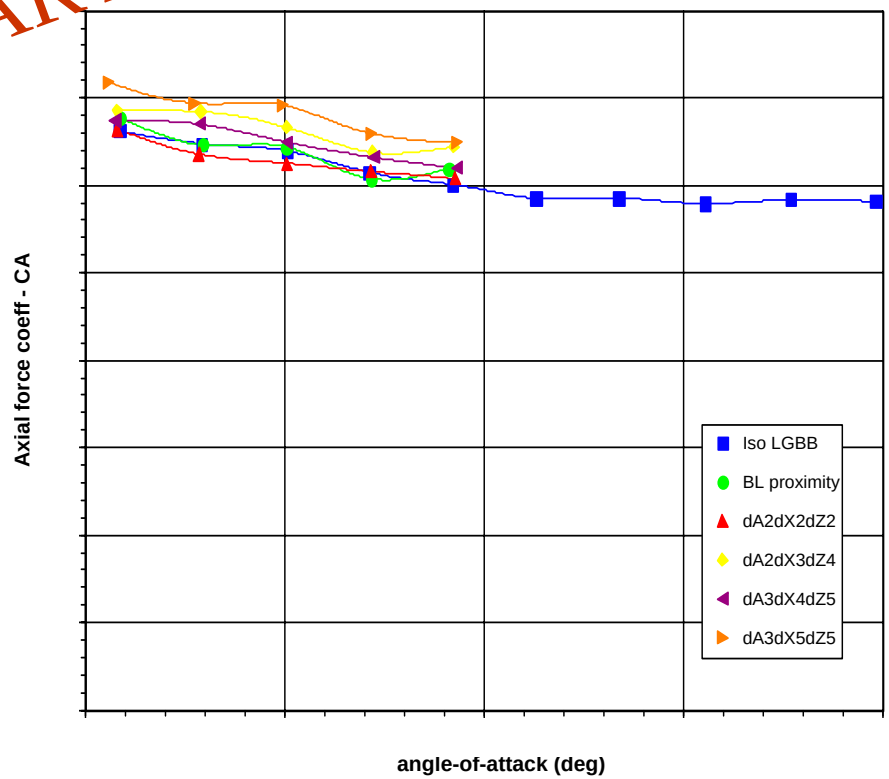

Preliminary Results – Pitching Moment vs AOA

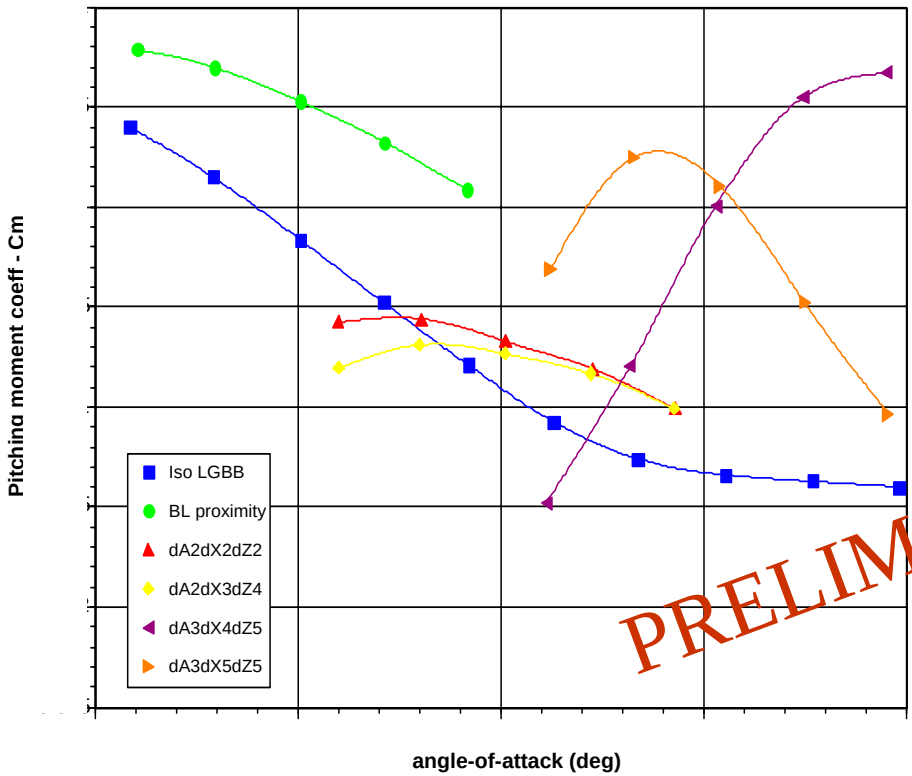

Booster

Orbiter

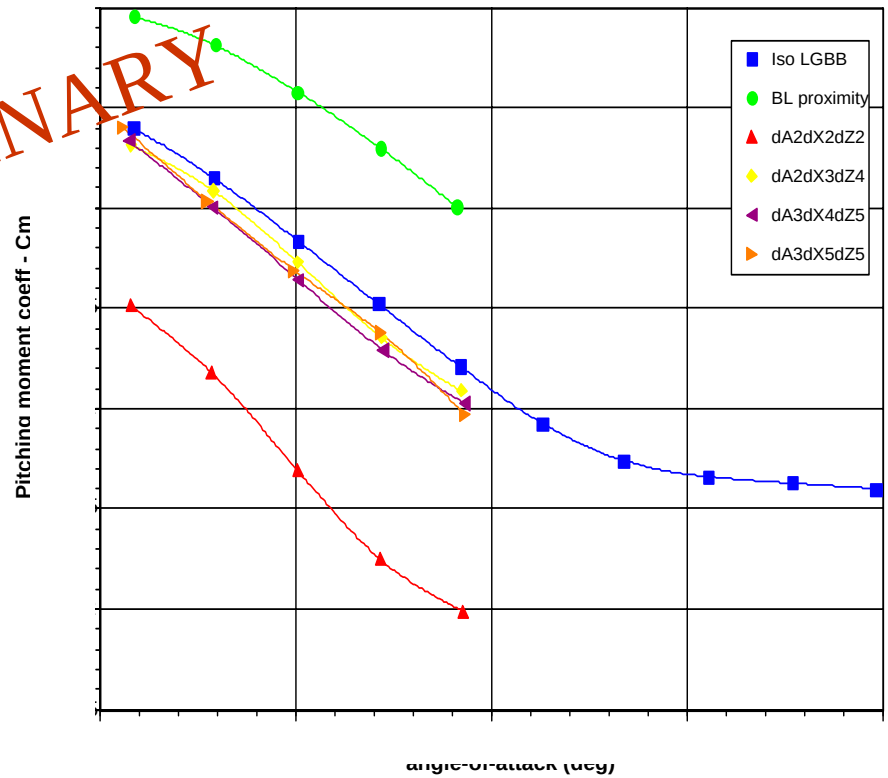

PRELIMINARY

Observations

- Pressure Sensitive Paint Test
  - Preliminary Results Promising
  - Methodology Understood
  - Verification of Results
- Isolated Orbiter Force/Moment Data
  - Baseline Data
  - Interference Effects
- Stage Separation Force/Moment Data
  - Experience Using Stage Separation Sting
  - Shock Impingement Effects on Aerodynamic Forces
- Schlieren Video Data
  - Shock Reflections Between Bodies in Proximity Location – “Shock Train”
  - Separate Nose Bow Shocks for Bimese LGBB Configuration at Mach 3
  - Qualitative Agreement with CFD Results

Summary

- Aerodynamic Research Facility LGBB Stage Separation Test part of Multi-Center 2nd Gen In-House Tool Development Task
- ARF LGBB Stage Separation Test Completed at MSFC
  - PSP Feasibility Test
  - Isolated Force/Moment Data
  - Bimese Configuration Force/Moment Data
  - Schlieren Video
- LGBB Bimese Reference Configuration Analyses and Test Results In-Work to Develop Tools and Database
- Preliminary Results Showed Qualitative Agreement with CFD Aerodynamic Predictions
- Preliminary Results Exhibiting Complex Nature of Stage Separation Aerothermal Problem

Acknowledgements

- Stage Separation Test Team:
  - Wayne Bordelon -- MSFC/TD63
  - Alonzo Frost -- MSFC/TD63
  - Victor Pritchett -- MSFC/TD63
  - Alan Droege -- MSFC/TD64
  - Tara Polsgrove -- MSFC/TD30

- Aerodynamic Research Facility (ARF) Test Team:
  - Henry Brewster -- MSFC/TD74
  - John Galloway -- MSFC/TD74
  - Richard Norman -- MSFC/TD74
  - Herb Bush -- MSFC/TD74
  - Holly Walker -- MSFC/TD74

Advances in Turbulence and Plume Thermo-Chemistry on the Prediction of Missile Plume Structure

September 11, 2000

W.H. Calhoon, J.L. Papp, S.M. Dash

Combustion Research and Flow Technology
(CRAFT Tech)

CRAFT Tech

INTRODUCTION

CHARACTERISTICS OF MANY ROCKET PROPULSION SYSTEMS:

- RUN FUEL RICH FOR PERFORMANCE REASONS
- EXHIBIT STRONG AFTERBURNING OF EXHAUST WITH THE ATMOSPHERE
- HIGH RADIATIVE EMISSIONS
- SIGNIFICANT BASE FLOW RECIRCULATION AND/OR BODY FLOW SEPARATION AT HIGH ALTITUDES

CRAFT Tech

INTRODUCTION

PLUME AFTERBURNING CHARACTERISTICS IMPORTANT TO:

- MISSILE BASE COMPONENT DESIGN
  - PLUME RADIANT HEAT TRANSFER
  - HEAT TRANSFER FROM BASE FLOW COMBUSTION
- MISSILE STABILITY AND CONTROL
  - PLUME INDUCED BODY FLOW SEPARATION
- MISSILE DEFENSE SYSTEM DEVELOPMENT

INTRODUCTION

ILLUSTRATION OF PLUME TOTAL INTENSITY VARIATION WITH ALTITUDE

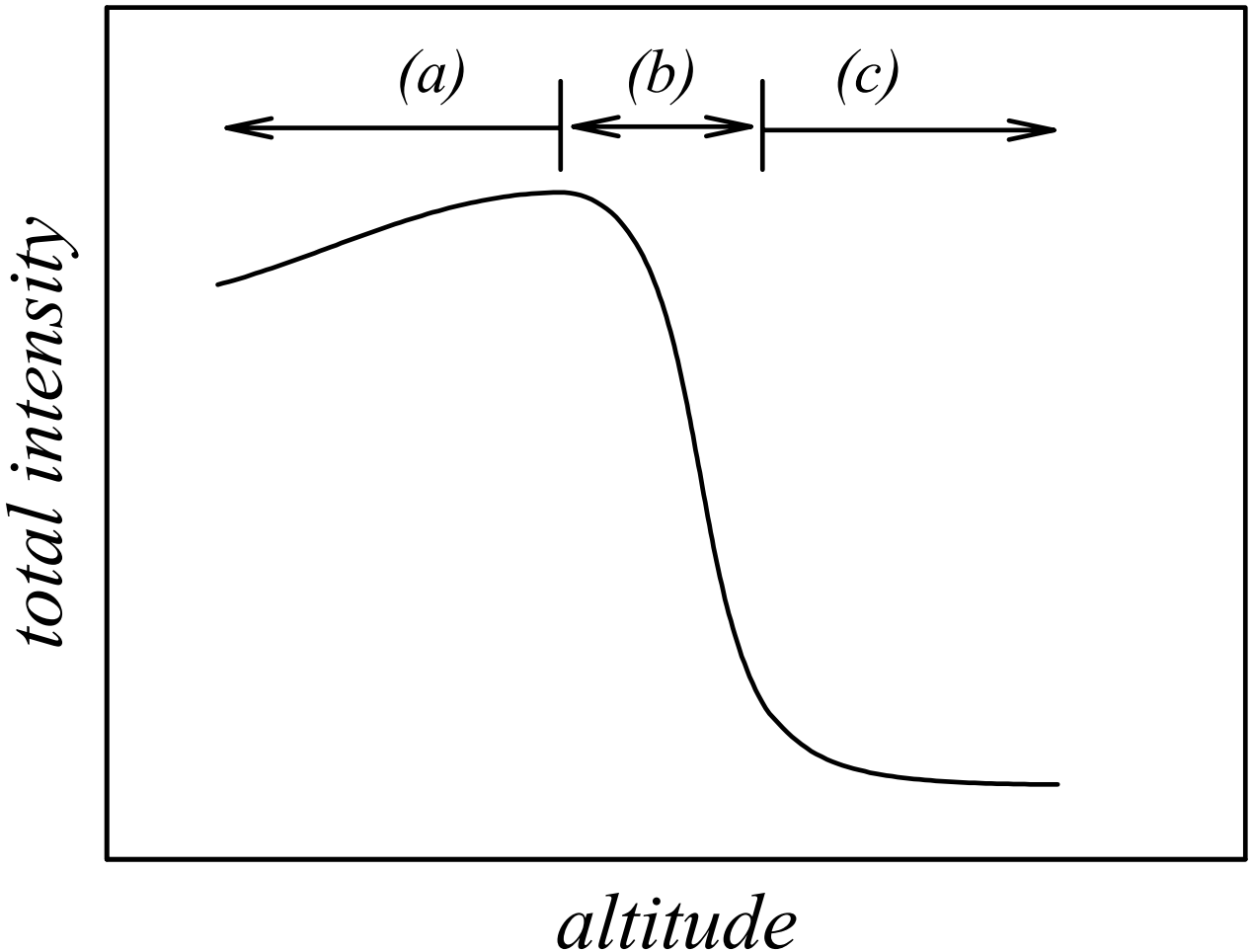

CRAFT Tech

INTRODUCTION

COMPUTATIONAL CHALLENGES FOR THE ACCURATE PREDICTION OF MISSILE BODY AND PLUME FLOWS:

- TURBULENCE MODELING
  - HIGHLY COMPRESSIBLE TURBULENT FLOW
  - TURBULENT TRANSITION
  - STRONG FLOW CURVATURE – TURBULENT ANISOTROPY
- COMBUSTION MODELING
  - TURBULENCE-CHEMISTRY INTERACTIONS
  - TURBULENT FLAME EXTINCTION
  - BASE FLOW/SEPARATION ZONE FLAME HOLDING

CRAFT Tech

TURBULENCE MODELING

MODELING EFFORTS FOCUSED ON:

A. HIGH SPEED BOUNDARY LAYER TRANSITION MODELING

BODY FLOW SEPARATION COMBUSTION AND MISSILE HEATING

B. COMPRESSIBILITY AND AXISYMMETRIC CORRECTIONS FOR HIGH SPEED FLOWS

PLUME ENTRAINMENT RATE/COMBUSTION AND SIGNATURE

C. EXPLICIT ALGEBRAIC REYNOLDS STRESS MODELING

FLOW CURVATURE EFFECTS IN THE NEAR PLUME REGION

CRAFT Tech

COMPRESSIBILITY AND AXISYMMETRIC CORRECTION MODELING

PLUME MIXED SUBSONIC/SUPERSONIC FLOW:

- REQUIRES A UNIFIED TURBULENCE MODEL TO CAPTURE BOTH THE LOW AND HIGH SPEED FLOW REGIMES

MISSILE PLUME FLOW GEOMETRIC TRANSITION:

- HIGHLY 3-D BASE FLOW TO AXISYMMETRIC HIGH SPEED JET
- REQUIRES A COMPRESSIBLE AXISYMMETRIC CORRECTION

BASELINE TURBULENCE MODEL: STANDARD K-E

HIGH SPEED COMPRESSIBILITY CORRECTION

- EXTRA DISSIPATION EXHIBITED THROUGH PRESSURE AND VELOCITY FLUCTUATIONS
- TURBULENT MACH NUMBER, M_T, RELATING TURBULENT VELOCITY TO MEAN VELOCITY SCALE USED TO MODEL PRESSURE/VELOCITY FLUCTUATION
- IMPROVED MODEL USES ZEMAN TYPE LAG, λ, TO BRIDGE THE LOW AND HIGH SPEED REGIMES
- RECALIBRATION MODEL COEFFICIENTS FOR HIGH SPEED PLANAR JETS

$$SS_k = -\alpha_1 \tilde{M}_T^2 P_k - \alpha_2 \tilde{M}_T^2 \rho\varepsilon, \qquad \tilde{M}_T = max\left(M_T - \lambda, 0\right)$$

$$\alpha_1 = 2.5, \;\; \alpha_2 = 2.0, \;\; \lambda = 0.2$$

TURBULENT COMPRESSIBILITY CORRECTION

SHEAR LAYER GROWTH RATE PARAMETER AS A FUNCTION OF MACH NUMBER

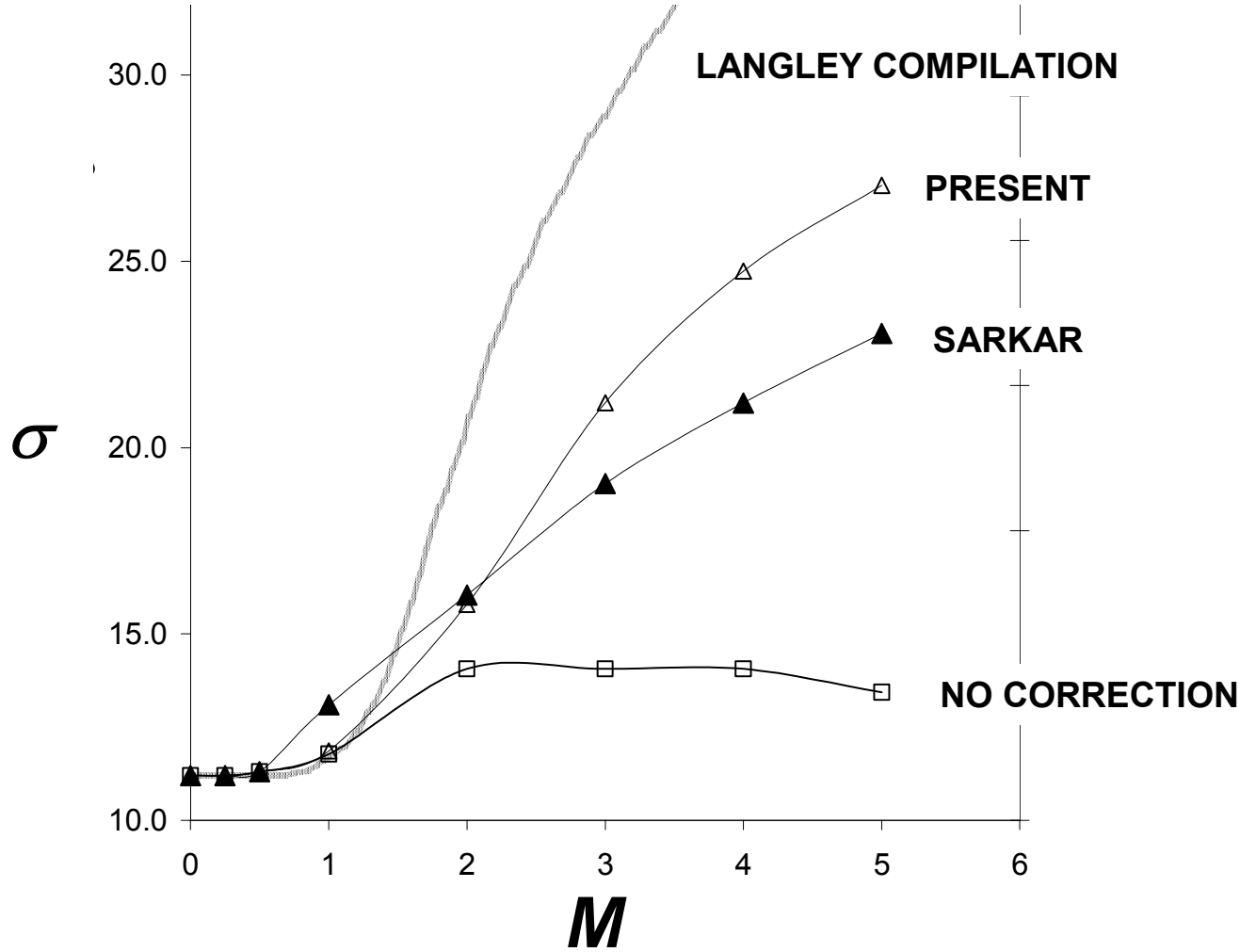

TURBULENT COMPRESSIBILITY CORRECTION

- FOR AXISYMMETRIC FLOWS, VORTEX STRETCHING LEADS TO DECREASED TURBULENT SCALES AND INCREASED DISSIPATION

- POPE (1978) DEVELOPED INCOMPRESSIBLE MODEL BASED ON TURBULENT VORTEX STRETCHING INTERPRETATION:

$$SS_\varepsilon = C_{\varepsilon_3} \rho \varepsilon \left(\frac{k}{\varepsilon} \right)^2 \omega_{ij} \omega_{jk} \left(\frac{\partial u_k}{\partial x_i} + \frac{\partial u_i}{\partial x_k} \right)$$

- COMPRESSIBLE EXTENSION:

$$SS_\varepsilon = C_{\varepsilon_3} \exp\left(-\beta \tilde{M}_T^2 \right) \rho \varepsilon \left(\frac{k}{\varepsilon} \right)^2 \omega_{ij} \omega_{jk} \left(\frac{\partial \rho u_k}{\partial x_i} + \frac{\partial \rho u_i}{\partial x_k} \right)$$

$$\beta = 75.0, \; C_{\varepsilon_3} = 0.79$$

TURBULENT COMPRESSIBILITY CORRECTION

CENTERLINE VELOCITY DECAY FOR SEINER M_{JET} = 2.0 HOT JET EXPERIMENT

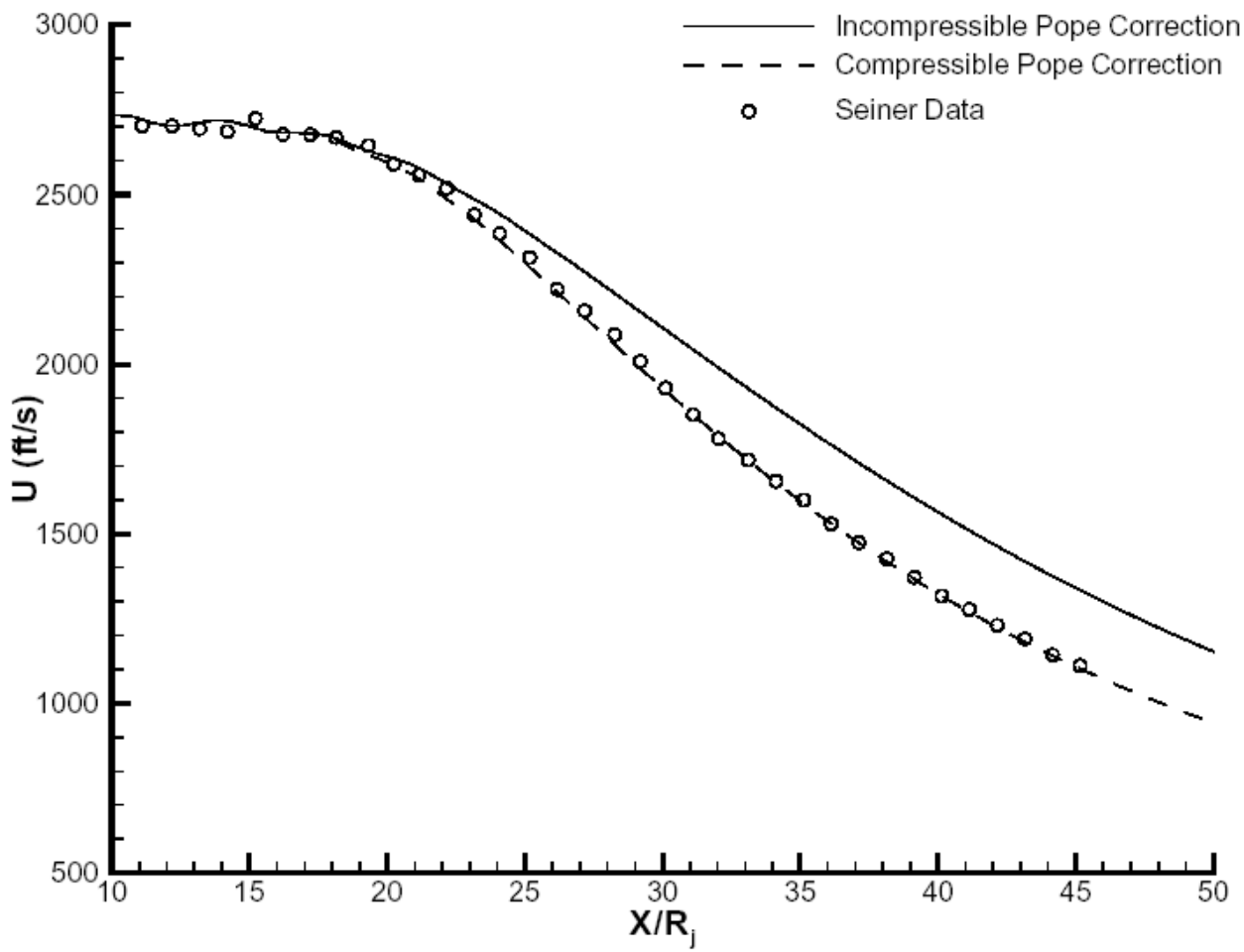

CRAFT Tech

MISSILE PLUME COMBUSTION MODELING

MODELING EFFORTS FOCUSED ON:

A. HIGH SPEED TURBULENCE-CHEMISTRY INTERACTION MODELING

- **PLUME AFTERBURNING IGNITION AND SUSTAINMENT HIGHLY DEPENDENT ON TURBULENCE-CHEMISTRY INTERACTIONS**

B. TURBULENT FLAME EXTINCTION MODELING

- **PLUME AFTERBURNING SHUTDOWN MECHANISMS**
  - ***DAMKOHLER NUMBER REDUCTION – GRADUAL SHUTDOWN***
  - ***TURBULENT FLAME EXTINCTION – RAPID SHUTDOWN***

HIGH SPEED TURBULENT-CHEMISTRY INTERACTION MODELING

- **CLOSURE MODELING REQUIRED FOR:**
  - **MEAN REACTION RATE:** $\overline{w'_{k,dot}} = \int_0^\infty \int_0^\infty \int_0^1 \ldots \int_0^1 w'_{k,dot} P(\rho', T', Y'_k) dY'_1 \ldots dY'_k d\rho' dT'$
- $P(\rho, T, Y_k)$ **REPRESENTS THE COMBINED EFFECTS OF:**
  - **TURBULENT TRANSPORT (LARGE AND SMALL SCALE)**
  - **MOLECULAR DIFFUSION**
- $P(\rho, T, Y_k)$ **MODELED USING AN ASSUMED PDF FOR SPECIES AND TEMPERATURE:**
  - **REQUIRES TURBULENT TRANSPORT EQUATIONS FOR SPECIES AND TEMPERATURE FLUCTUATIONS**

CRAFT Tech

HIGH SPEED TURBULENT-CHEMISTRY INTERACTION MODELING

- **MODELED TRANSPORTS EQUATIONS TO SPECIES AND TEMPERATURE FLUCTUATIONS:**

$$\frac{D\bar{\rho}Q}{Dt} = \frac{\partial}{\partial x_j}\left((\bar{D} + D_Y)\frac{\partial Q}{\partial x_j} \right) + 2D_Y \sum_{k=1}^{K} \left(\frac{\partial < Y_k >}{\partial x_j} \right)^2 - 2C_Q \bar{\rho}\frac{Q}{\tau} + 2\sum_{k=1}^{K} \overline{w'_{k,dot}\, Y''_k}$$

$$\frac{D\bar{\rho}g}{Dt} = \frac{\partial}{\partial x_j}\left(\bar{\gamma}(\bar{D}_T + D_{T,t})\frac{\partial g}{\partial x_j} \right) + 2\bar{\gamma}D_{T,t}\left(\frac{\partial < e >}{\partial x_j} \right)^2 - 2C_g \bar{\rho}\frac{g}{\tau}$$

$$- 2(\bar{\gamma} - 1)\bar{\rho}g\frac{\partial < u_j >}{\partial x_j}$$

- **HIGH SPEED SCALAR FLUCTUATION DATA UNAVAILABLE**

- **MODEL COEFFICIENTS CALIBRATED USING AVAILABLE LOW SPEED DNS AND EXPERIMENTAL DATA**

TEMPERATURE CONTOURS FOR LAMINAR AND PDF RATE MODELS AT 30 KM

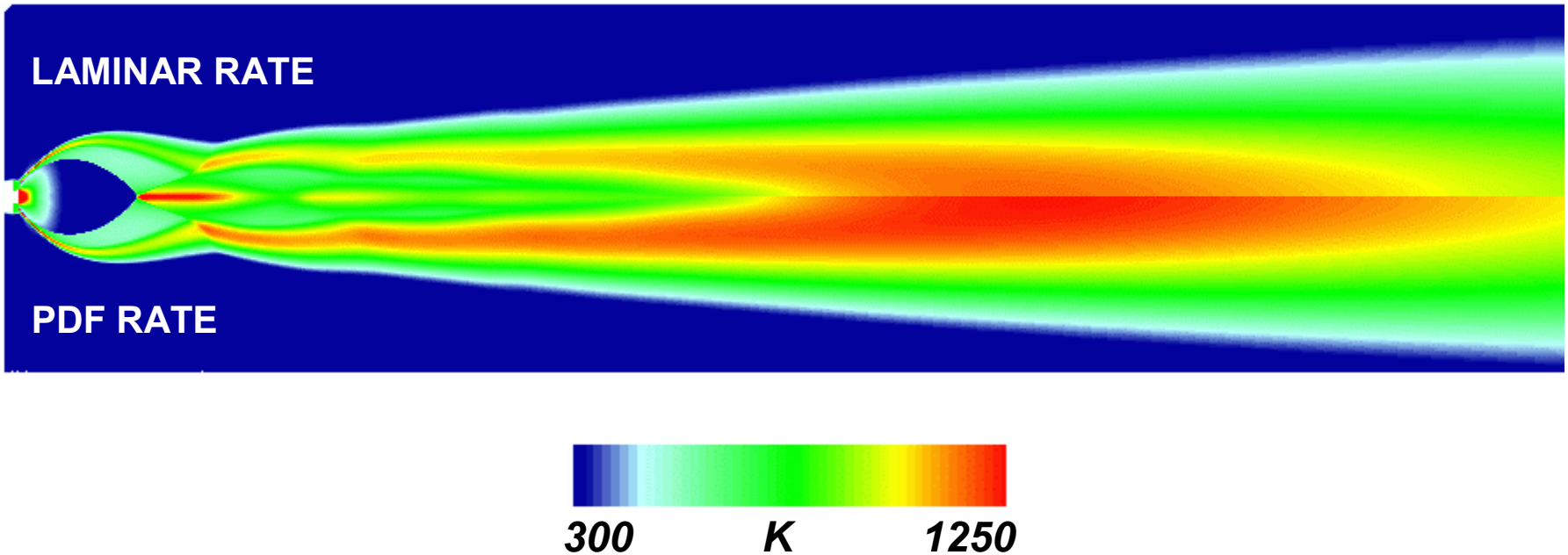

CO_2 MOLE FRACTION CONTOURS FOR LAMINAR AND PDF RATE MODELS AT 30 KM

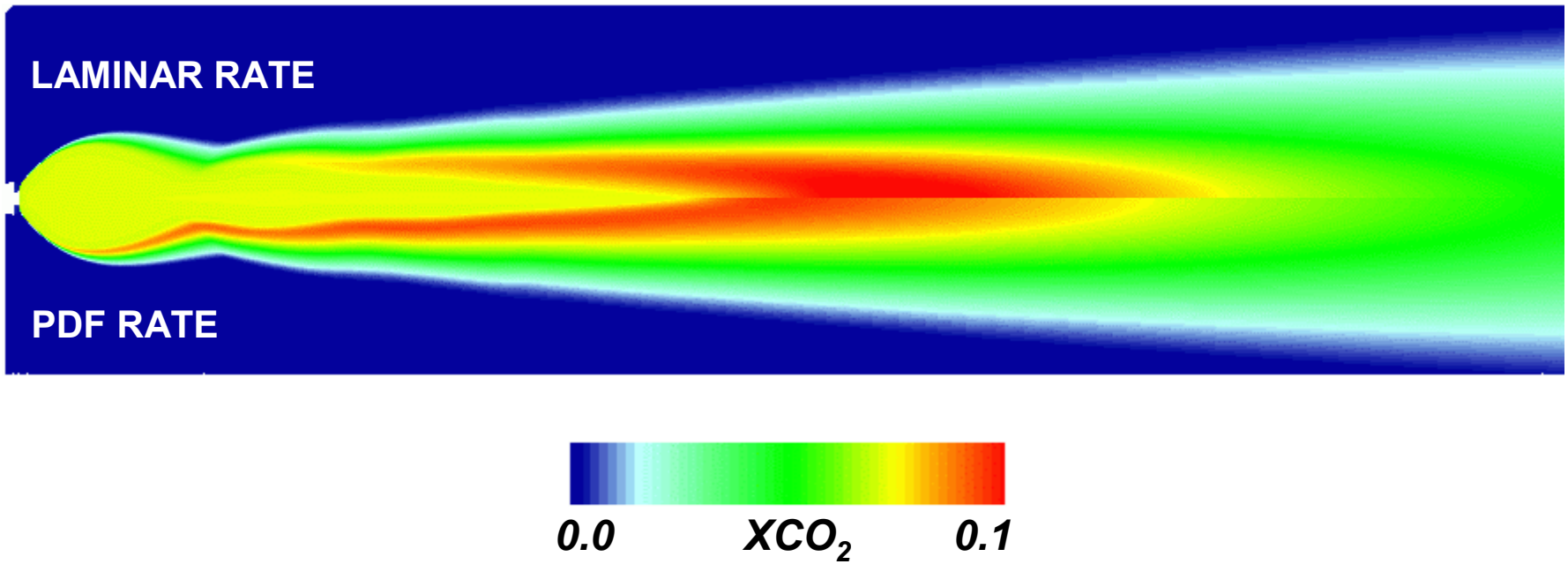

COMPARISON OF LAMINAR AND PDF RATE MODELS FOR SHEAR LAYER TEMPERATURE, $x/x_{refl} = 3$

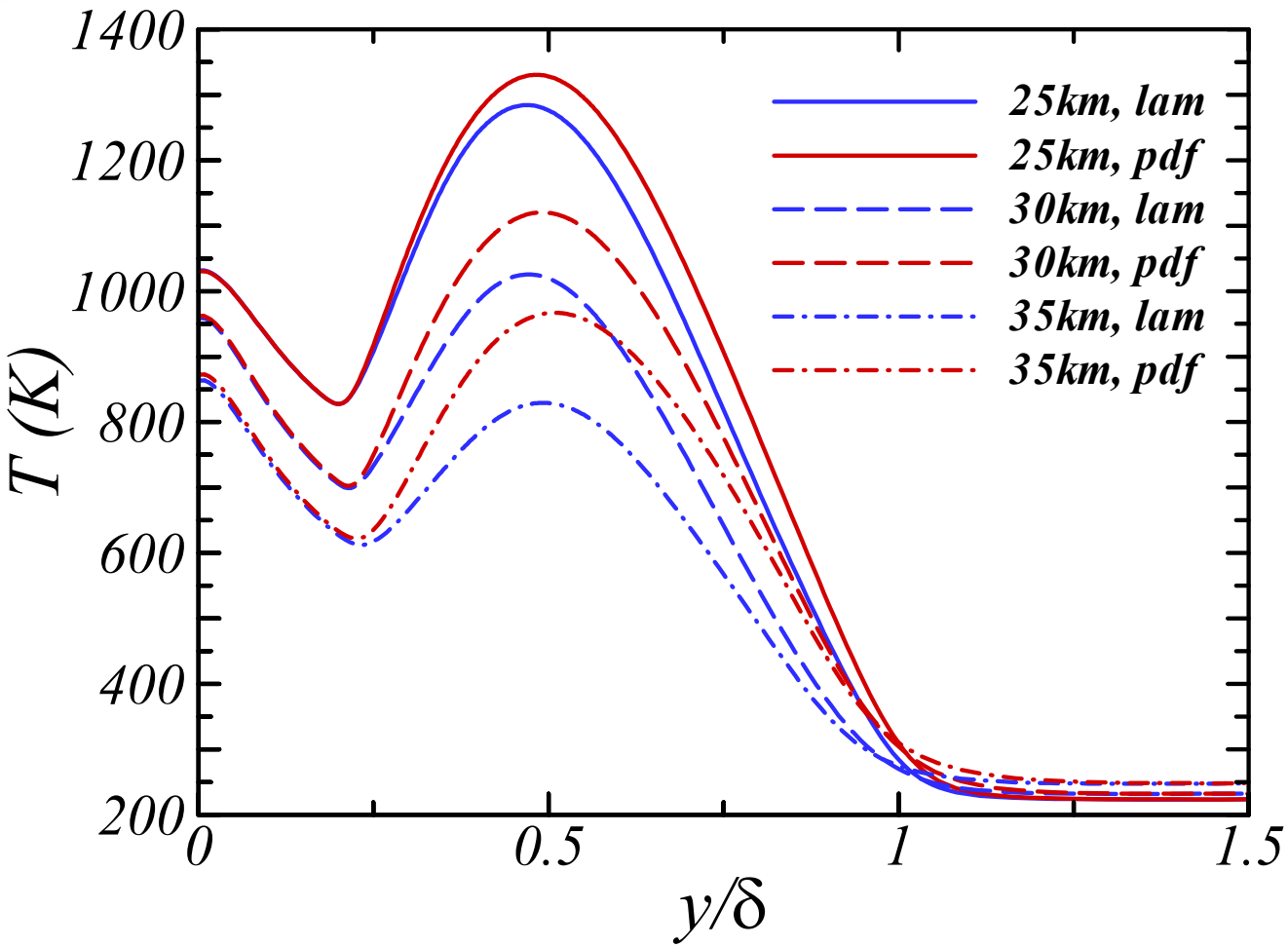

PREDICTED TEMPERATURE INTENSITY AT $x/x_{refl} = 3$

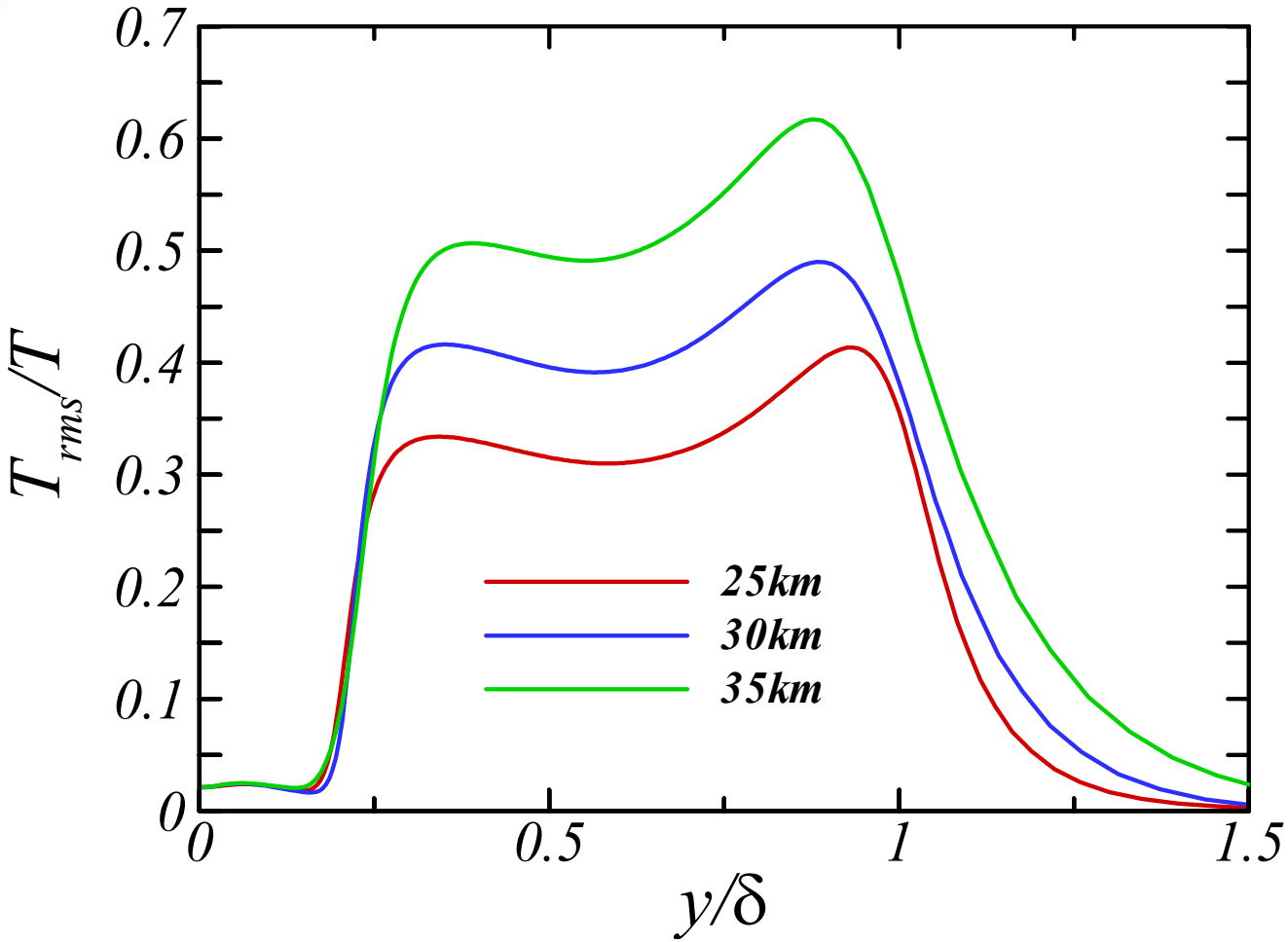

CRAFT Tech

PDF MODEL SCALAR FLUCTUATIONS

- LOW SPEED CALIBRATION OVERPREDICTED SCALAR FLUCTUATION LEVELS BY ~ 40 %
- AD-HOC COEFFICIENT ADJUSTMENT REQUIRED TO REPRESENT FLIGHT DATA
- NO SCALAR FLUCTUATION DATA AVAILABLE FOR HIGH SPEED FLOWS
- LARGE-EDDY SIMULATION (LES) CAN PROVIDE DATA IN FLOW REGIMES UNSUPPORTED BY EXPERIMENTS
- SCALAR FLUCTUATION MODELING EFFORTS FOCUSED ON USING LES TO PROVIDE REQUIRED DATA AND PHYSICAL INSIGHT

LES PLANAR SHEAR LAYERS

THREE FLOW REGIMES FOR PLANAR SHEAR LAYERS:

- LOW COMPRESSIBILITY: $M_C < 0.6$
  - DOMINATED BY 2-D MODAL INSTABILITIES
- MODERATE COMPRESSIBILITY: $0.6 < M_C < 1.0$
  - DOMINATED BY 2-D AND 3-D MODAL INSTABILITIES
- HIGH COMPRESSIBILITY: $M_C > 1.0$
  - DOMINATED BY 3-D MODAL INSTABILITIES

LES PLANAR SHEAR LAYER CONDITIONS

ALL CASES USED:

- $U_1/U_2 = 6.1$
- $\rho_1/\rho_2 = 0.3$
- $T_1 = 1000$ K, $T_2 = 300$ K

LOW COMPRESSIBILITY CASE:

- $M_C = 0.27$
- $M_1 = 0.5$, $M_2 = .15$

HIGH COMPRESSIBILITY CASE:

- $M_C = 1.3$
- $M_1 = 2.41$, $M_2 = 0.72$

SPANWISE VORTICITY CONTOURS

$M_c = 0.27$

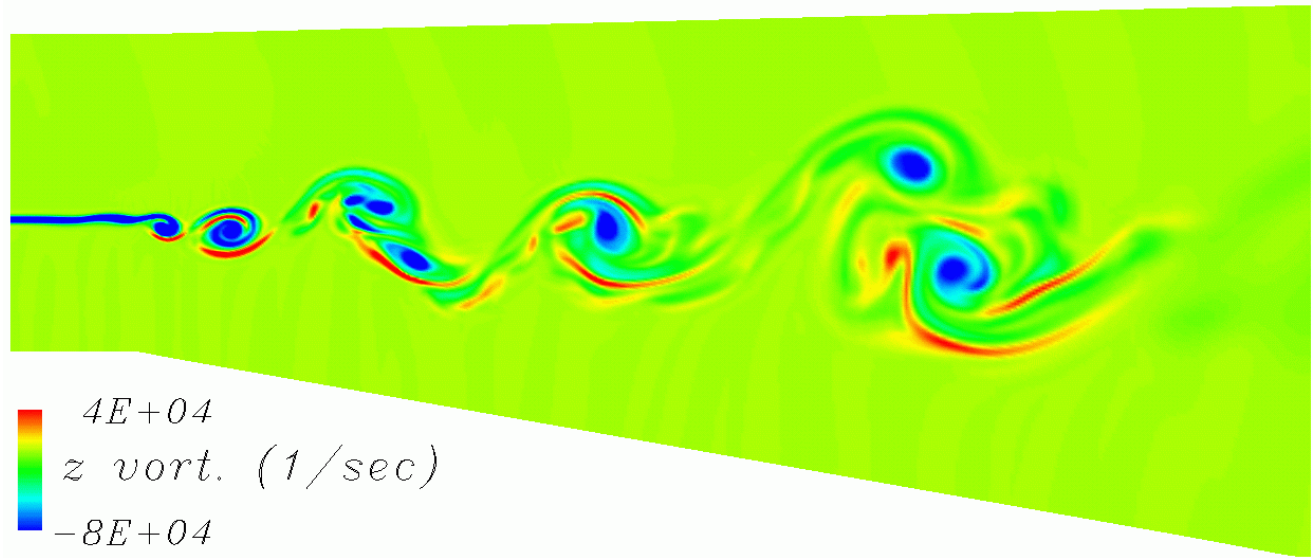

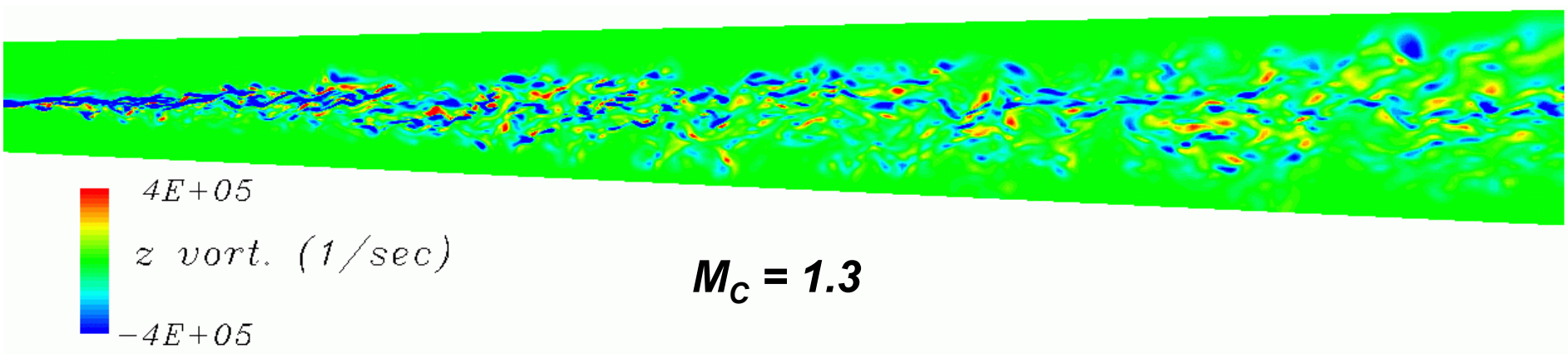

$M_c = 1.3$

TEMPERATURE CONTOURS

$M_c = 0.27$

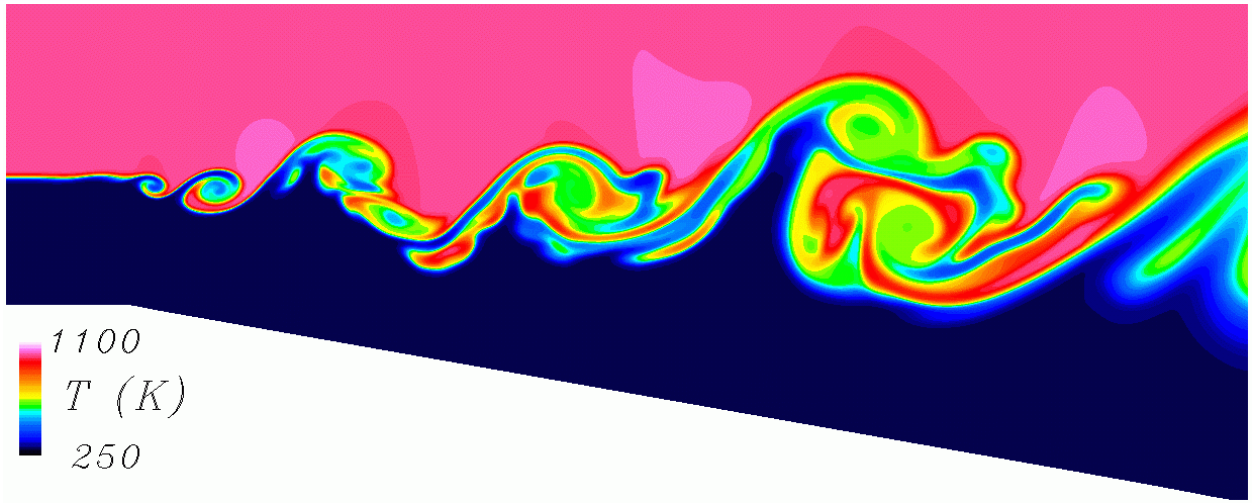

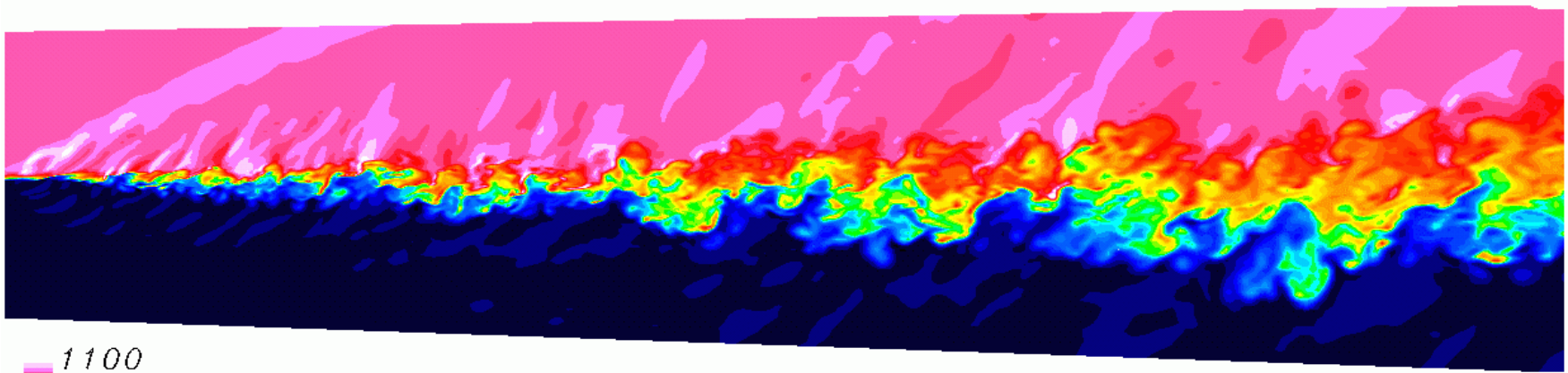

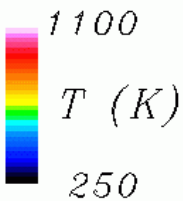

$M_c = 1.3$

SELF-SIMILAR TEMPERATURE PROFILES

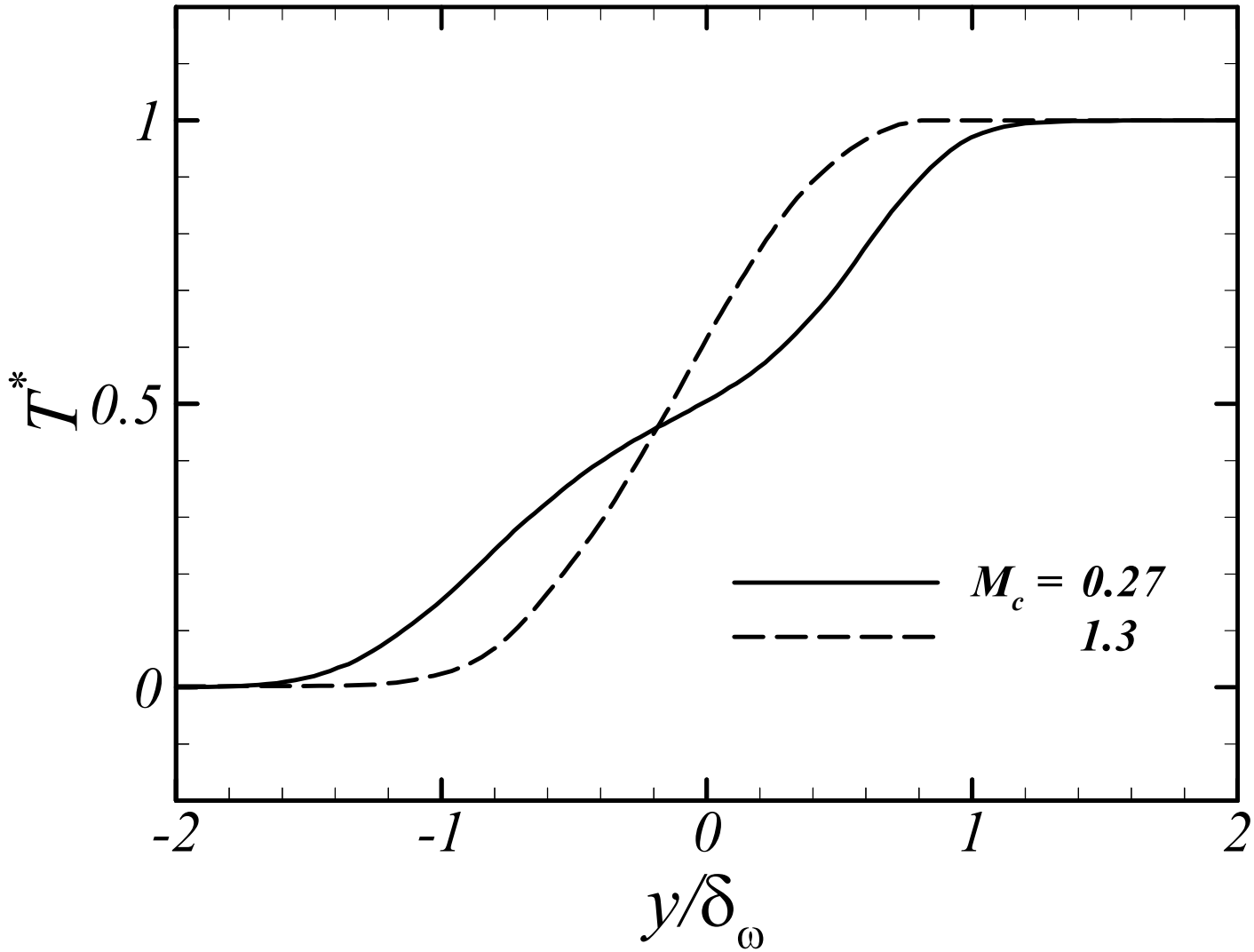

SELF-SIMILAR TURBULENT PRANDTL NUMBER PROFILES

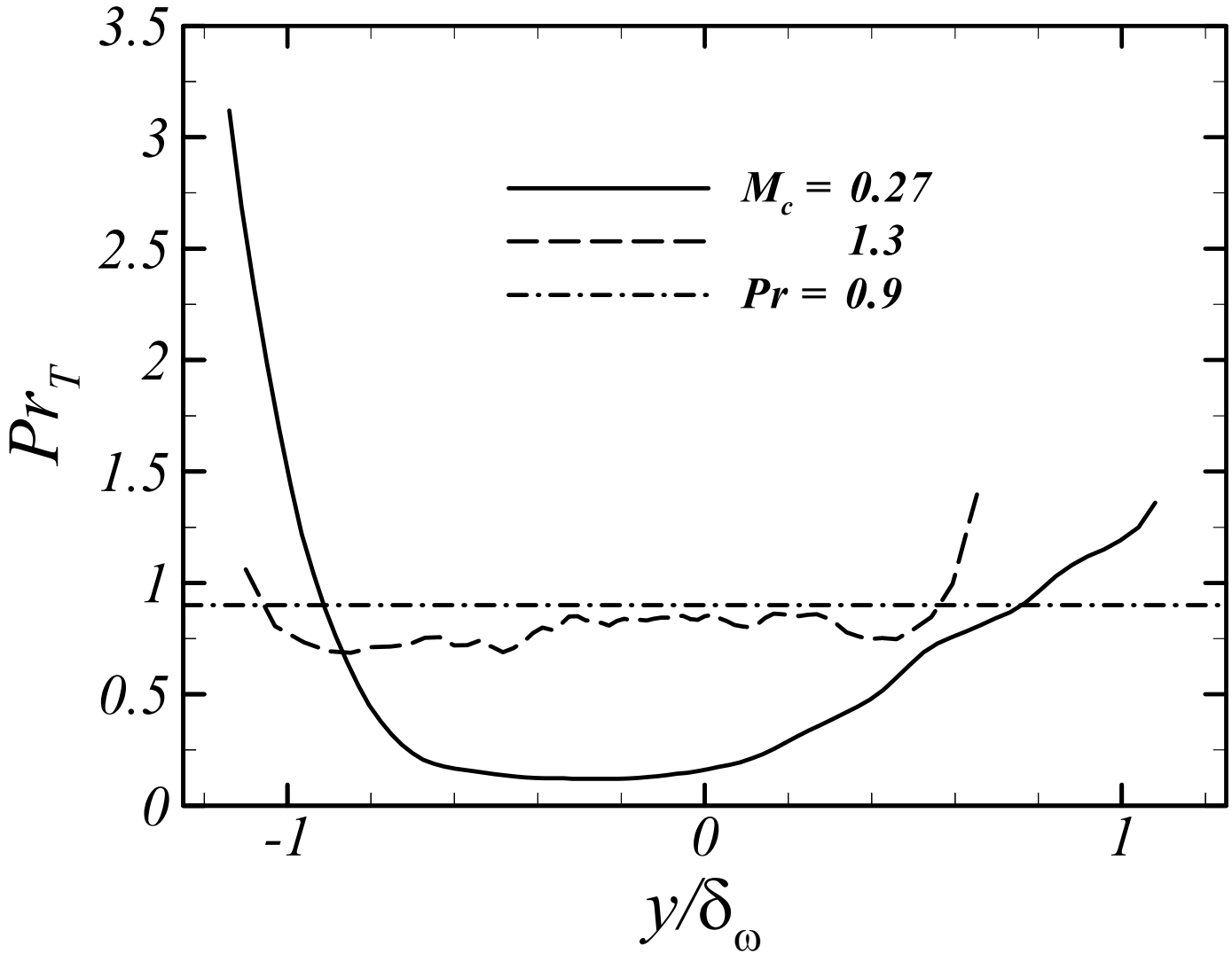

SELF-SIMILAR TEMPERATURE INTENSITY PROFILES

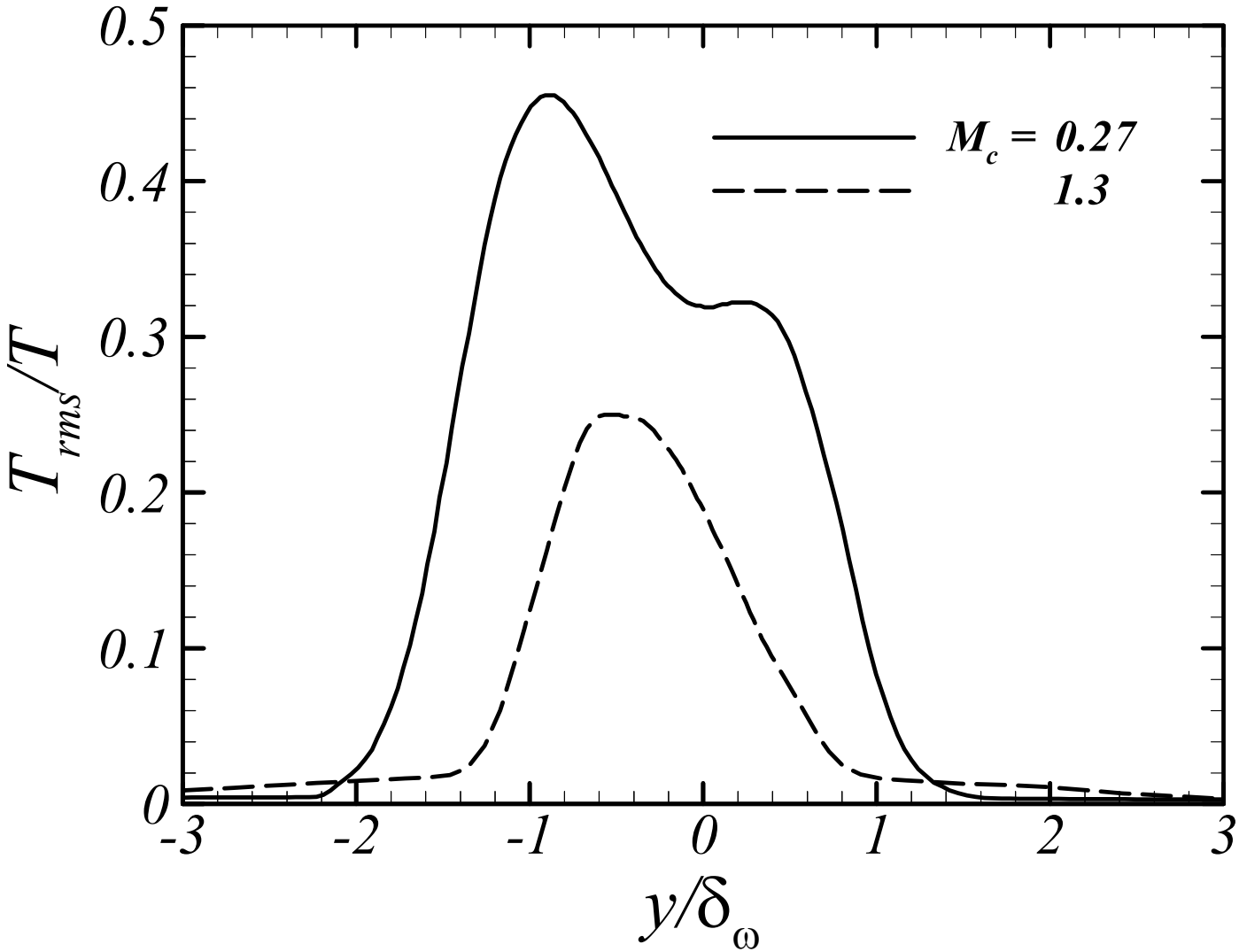

CRAFT Tech

CONCLUSIONS

- **MISSILE EXHAUST PLUME FLOWFIELD AND SIGNATURE PREDICTION IS A VERY COMPLEX PROBLEM**

- **AN ADVANCED TURBULENCE AND COMBUSTION MODELING FRAMEWORK IS REQUIRED TO MAKE ACCURATE PREDICTIONS**

- **ONGOING RESEARCH AT CRAFT TECH FOCUSED ON IMPROVING PREDICTIVE CAPABILITIES FOR:**
  - HIGH SPEED TURBULENT TRANSITION
  - ROTATING TURBULENCE AND ANISOTROPY
  - SCALAR FLUCTUATIONS
  - TURBULENT FLAME EXTINCTION
  - TURBULENT PARTICULATE DISPERSION

Comparison of Full and Partial Admission Flow Fields in the Simplex Turbine

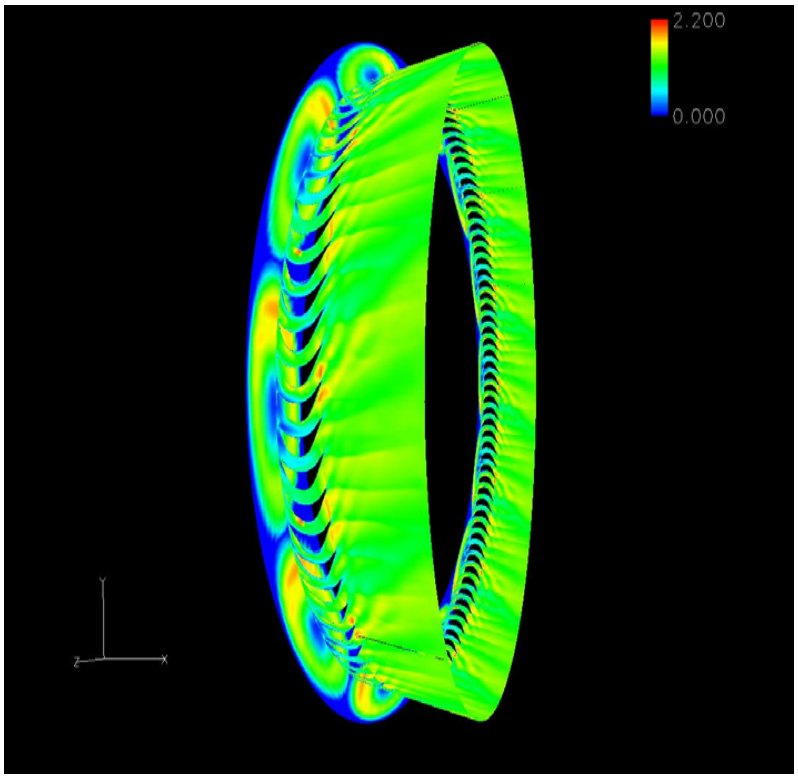

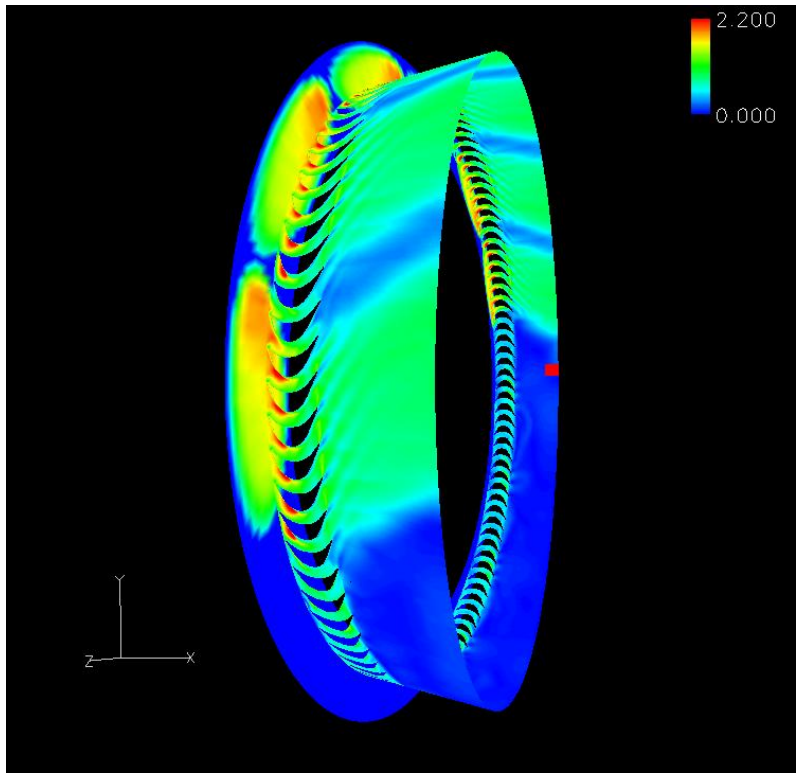

Daniel J. Dorney, Lisa W. Griffin and Douglas L. Sondak
NASA Marshall Space Flight Center
Applied Fluid Dynamics Analysis Group
MSFC, AL 35812

10 September 2001

Outline

- **Motivation**
- **Flow code description - CORSAIR**
  - Capabilities
  - Future directions
- **Results**
  - Full admission Simplex turbine
  - Partial admission Simplex turbine
- **Conclusions**

Motivation

- **Determine the effects of partial admission flow on:**
  - rotor performance as a function of circumferential location
  - unsteady rotor loading
- **Provide an efficient technique for determining turbine performance**

Flow Code Capabilities - I

- **CORSAIR**
  - Unsteady time-dependent equations of motion
  - Full Navier-Stokes, thin-layer Navier-Stokes or Euler
  - Variable fluid properties (Cp, gamma)
- **Third-order spatial discretization of inviscid fluxes**
  - Roe's scheme
- **Second-order spatial discretization of viscous fluxes**
  - Standard central differences
- **Second-order temporal accuracy**
- **Multi-block O-H grid topology**
  - O-grids around airfoils and in tip clearance regions
  - H-grids for remainder of flow field and nozzles
  - Well-suited for medium-to-fine grain parallel simulations

Flow Code Capabilities - II

- **Turbulence models**
  - Highly-modified Baldwin-Lomax model
- **Transition models**
  - Abu-Ghannam and Shaw (natural)
  - Mayle (natural)
  - Modified Roberts' correlation (bubble)
- **Boundary conditions**
  - Steady and unsteady inlet and exit
  - Specified wall temperature or heat flux
  - Film cooling/mass injection
  - Actuator disk
  - Component linking
- **Grid Motion**
  - Arbitrary translation/rotation
  - Blade vibration

Flow Code Capabilities - III

- **MPI and OpenMP used for parallel simulations**
  - decomposition by blade row
  - decomposition by blade passage
  - decomposition by O- and H-grids
  - decomposition by component
  - user specified decomposition
- **Graphical User Interface**
  - Grid generation
  - Flow solver
  - Error checking
  - Design page
  - User's manual/help facility
  - Post-processing
- **Miscellaneous capabilities**
  - Conjugate heat transfer capability
  - Provides unsteady pressure file for stress analysis
  - Provide Fourier decomposition of unsteady pressures
  - Will run on any Unix, Linux or Windows NT platform

CORSAIR Future Directions

- **Modifying code for pump geometries**
  - incorporating incompressible flow physics
- **Incorporate two-phase flow modeling**
- **Incorporate cavitation modeling**

Simplex Turbine Simulations

- **Objective - determine the effects of partial admission on the rotor unsteady load and performance as a function of circumferential location**
- **Full-Admission simulation (FA)**
  - 1 nozzle and 8 rotors modeled
  - 750,000 grid points
  - 8 full cycles (one complete rotor revolution) completed
- **Partial-Admission simulation (PA)**
  - 6 nozzles and 95 rotors modeled
  - 7 million grid points
  - 0.95 revolutions completed
  - PA-IN - in region of nozzle flow
  - PA-OUT - outside the region of nozzle flow

Simplex Turbine Rotors

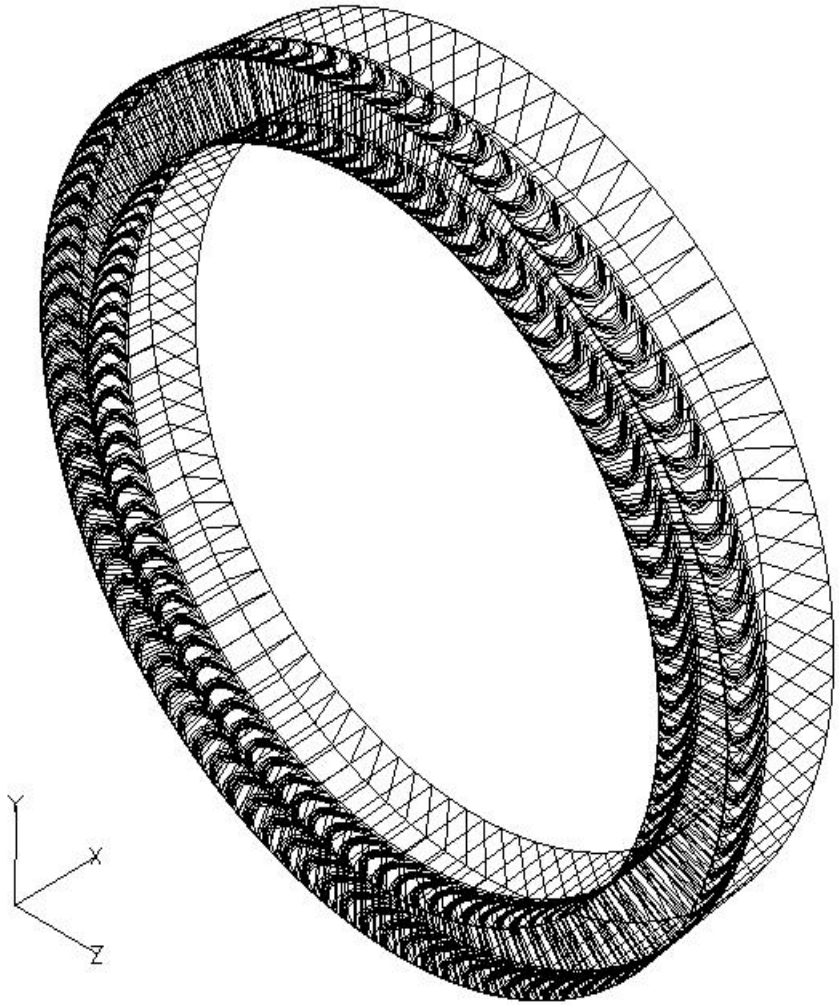

Simplex Turbine Nozzles

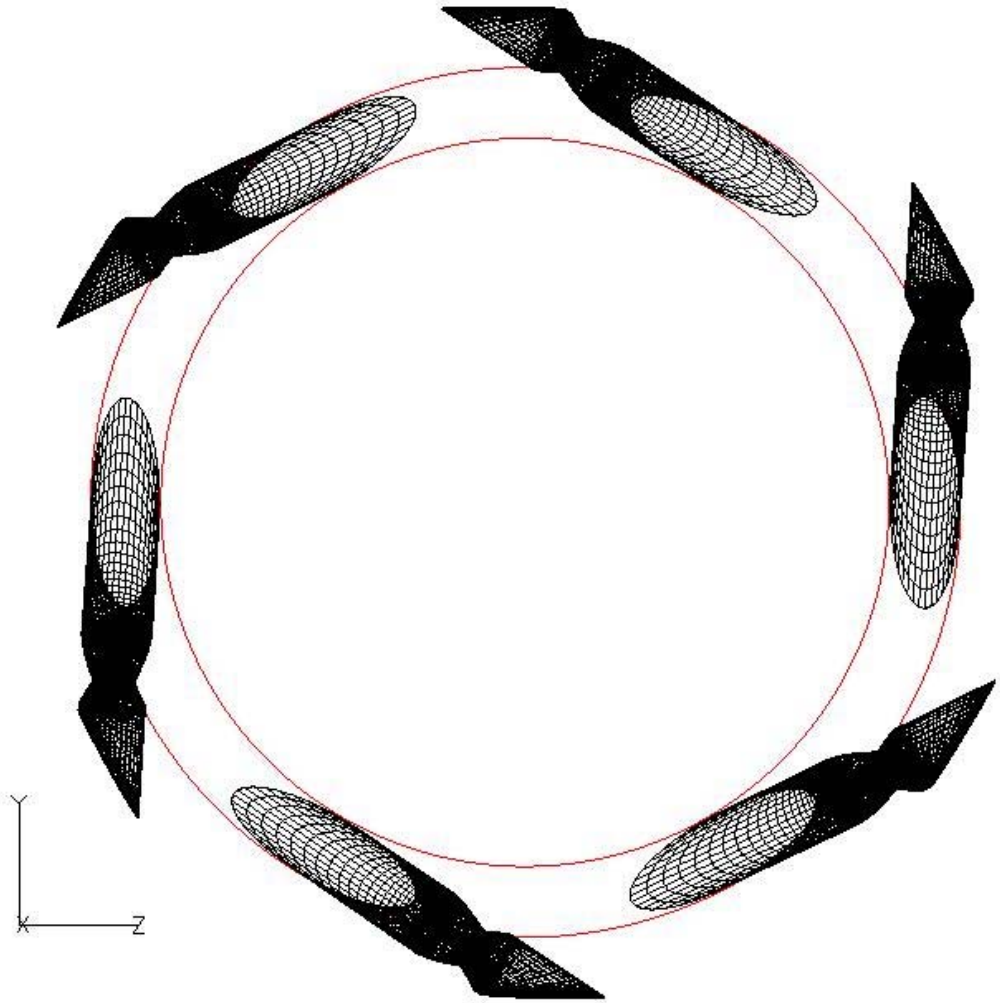

Computational Grids - Rotor

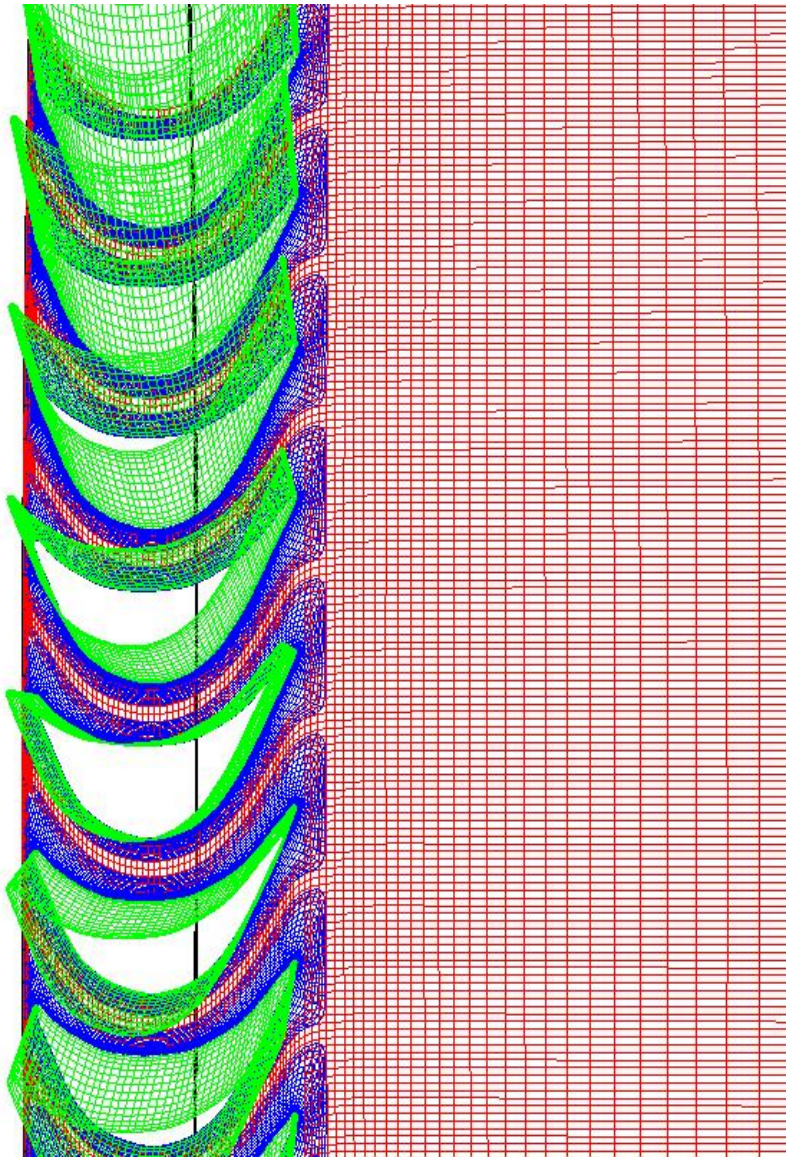

Nozzle/Rotor Interface - Mach Number (PA)

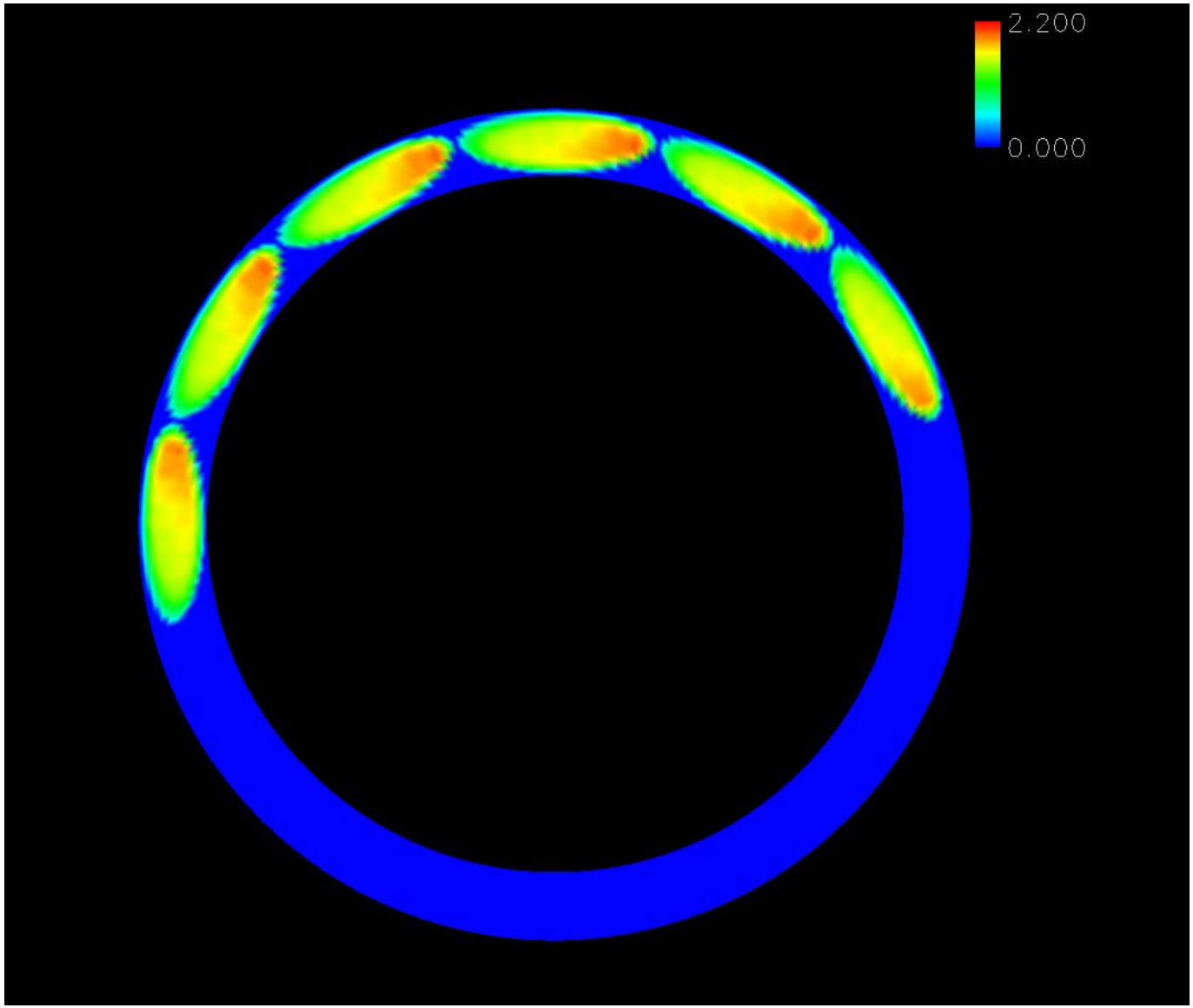

Instantaneous Mach Number - Nozzle

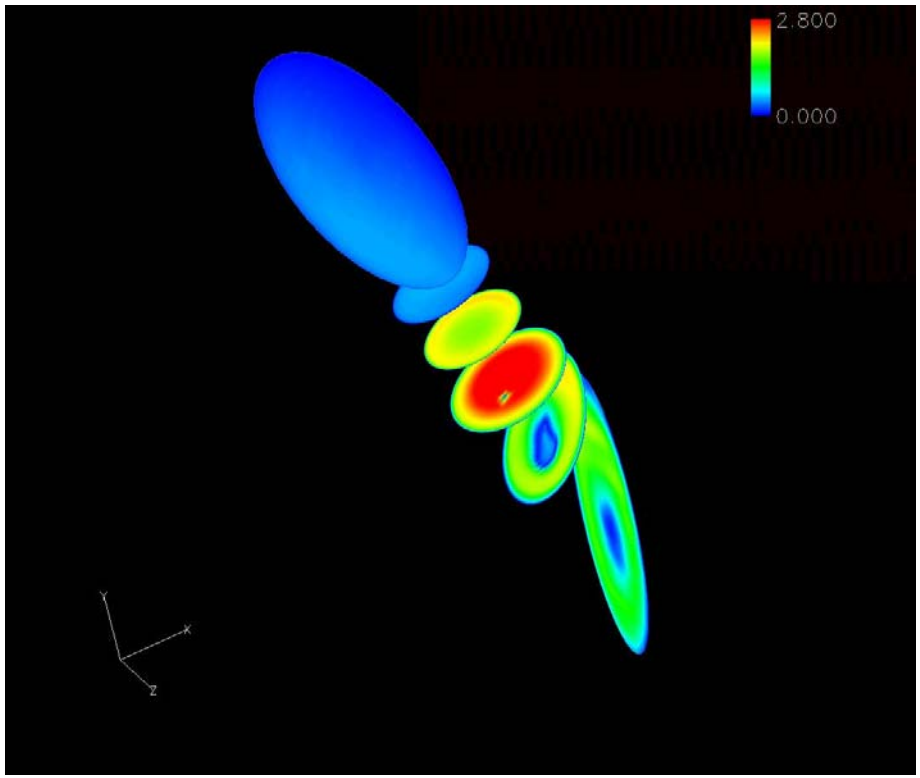

FULL ADMISSION

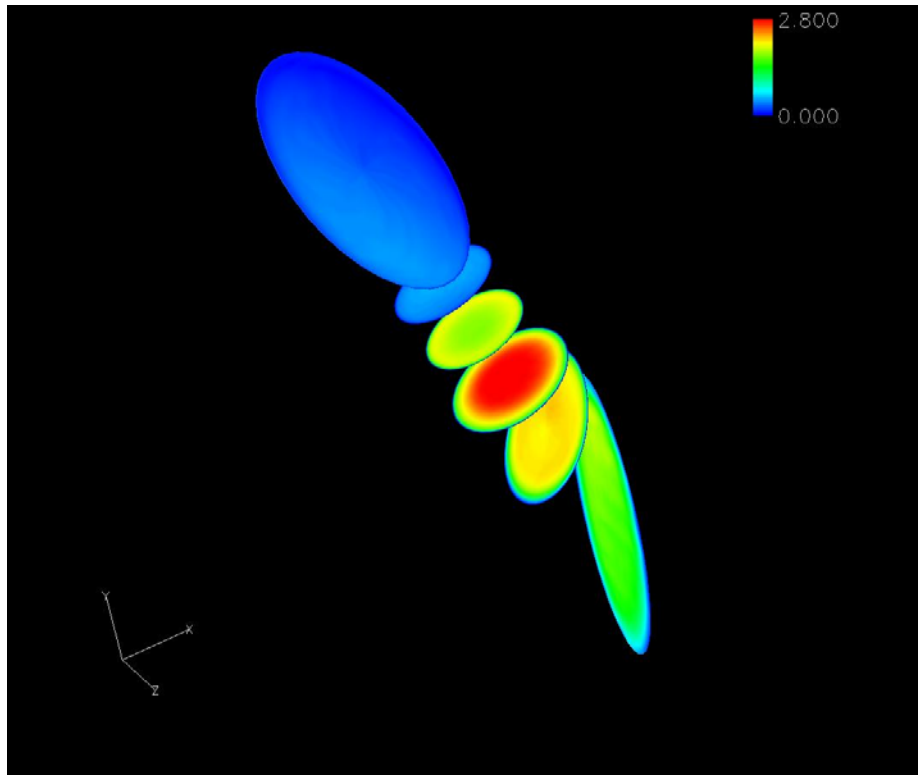

PARTIAL ADMISSION

Instantaneous Mach Number - Nozzle

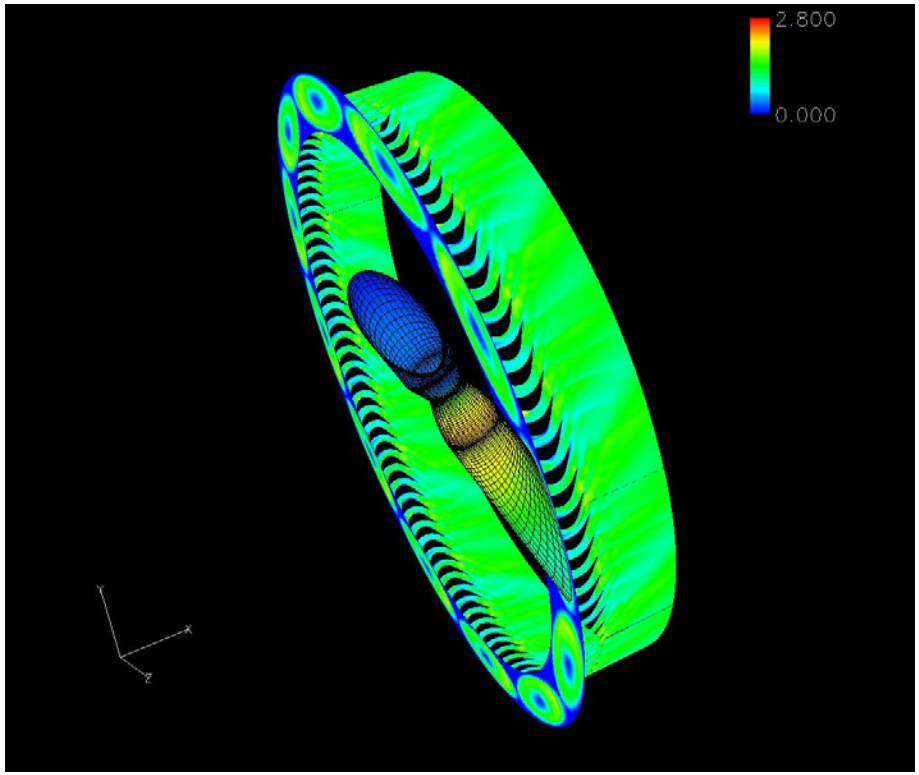

FULL ADMISSION

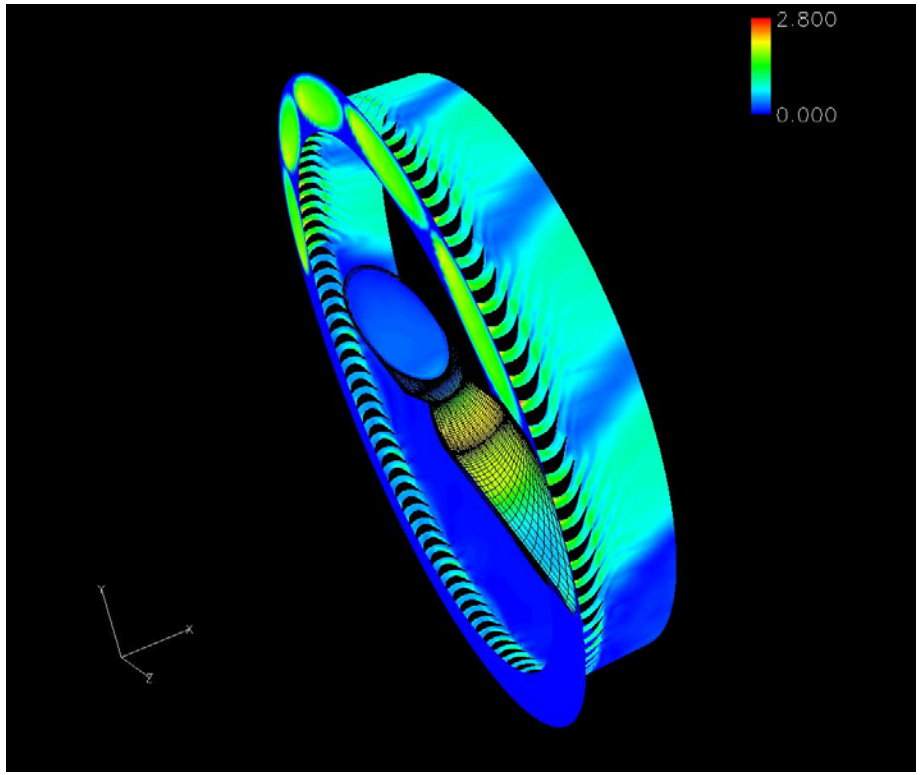

PARTIAL ADMISSION

Instantaneous Mach Number

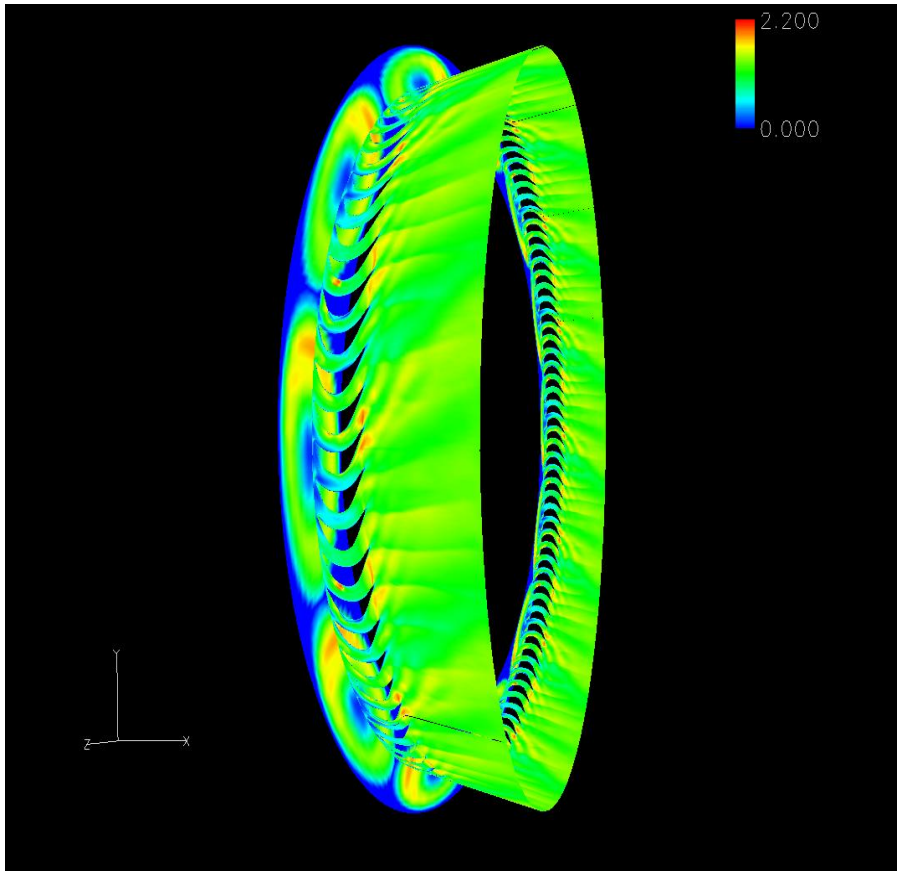

FULL ADMISSION

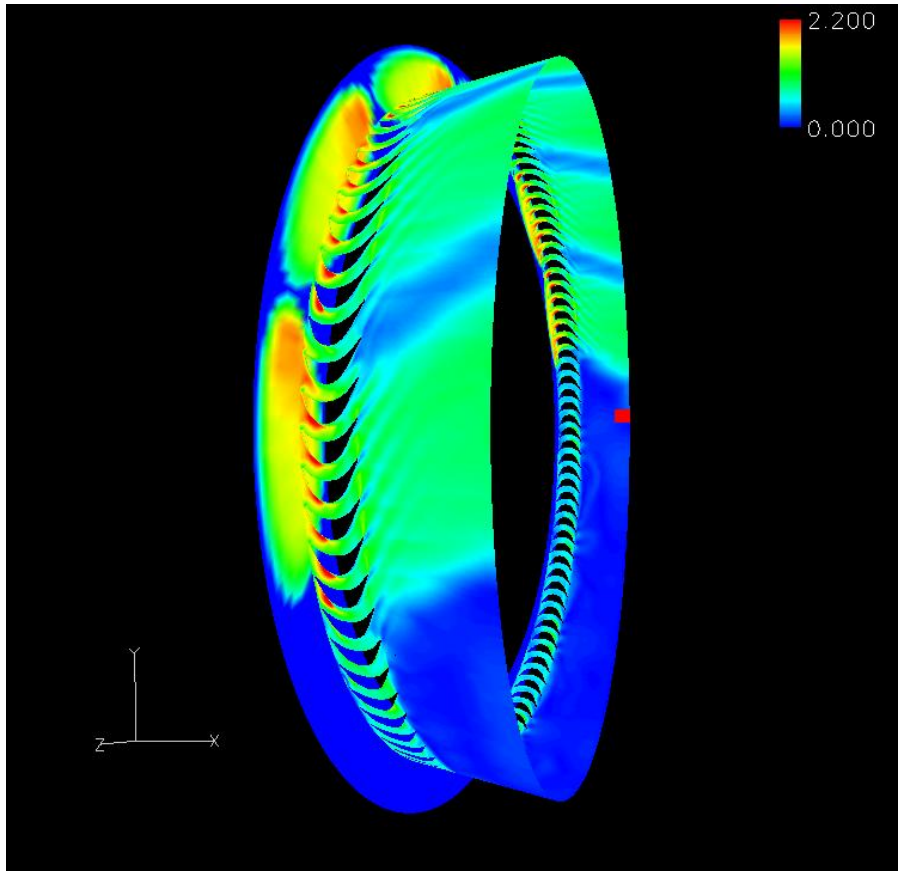

PARTIAL ADMISSION

Instantaneous Mach Number - Rotor Exit

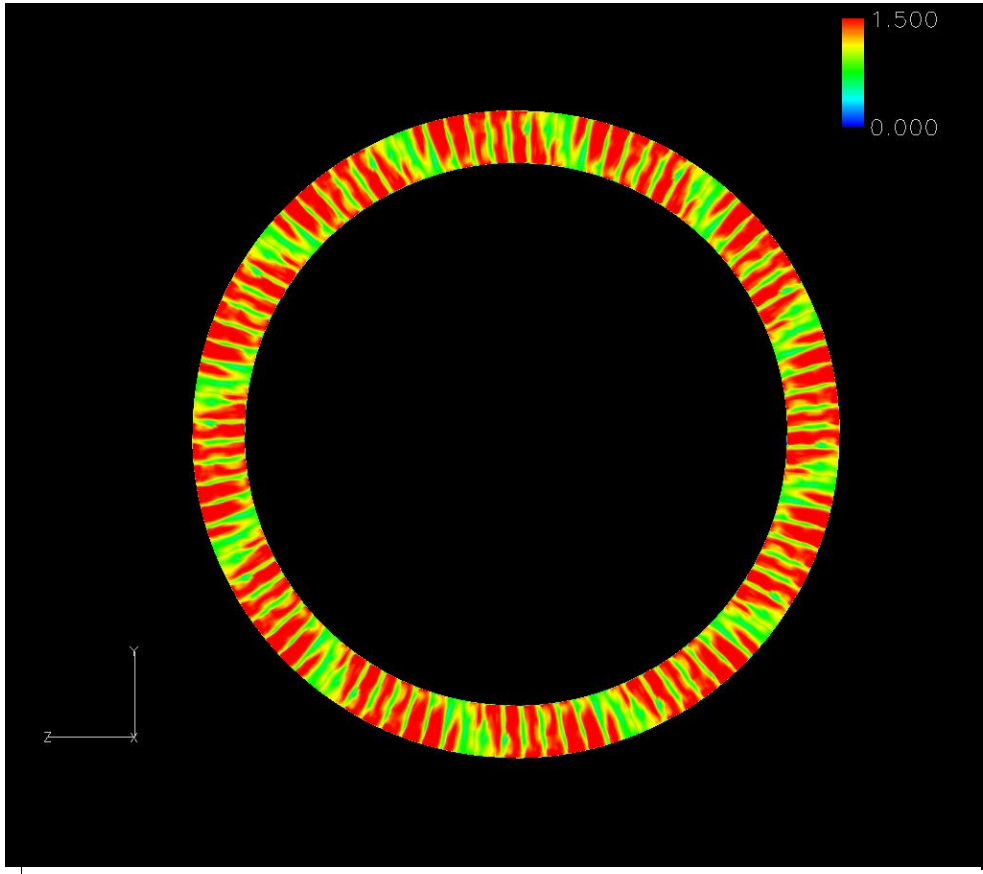

FULL ADMISSION

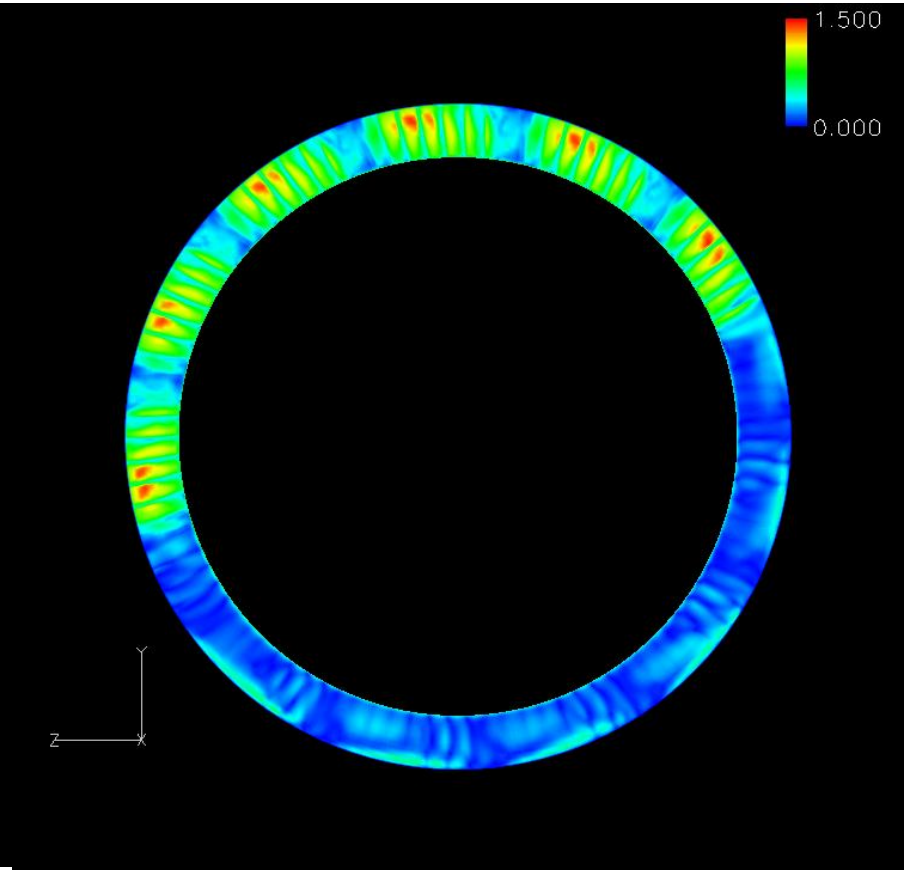

PARTIAL ADMISSION

Unsteady Rotor Pressure Envelopes (FA)

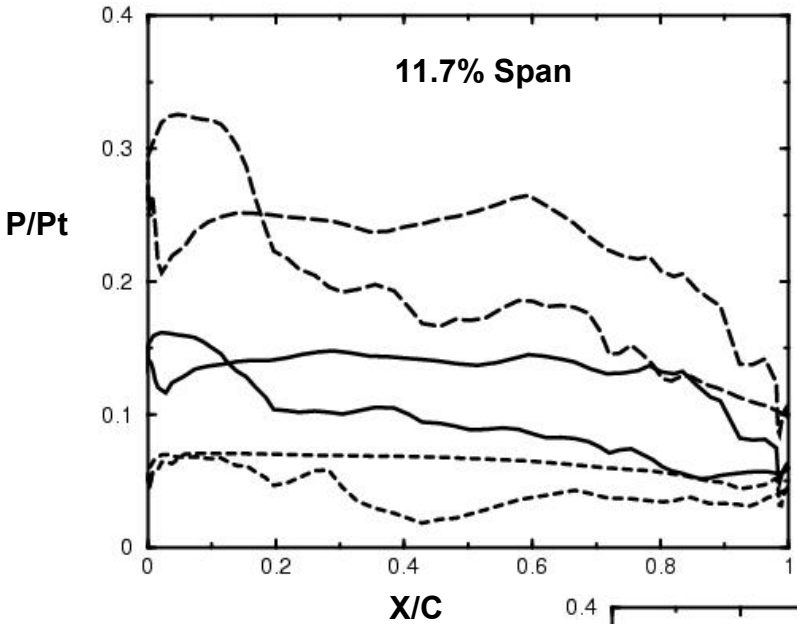

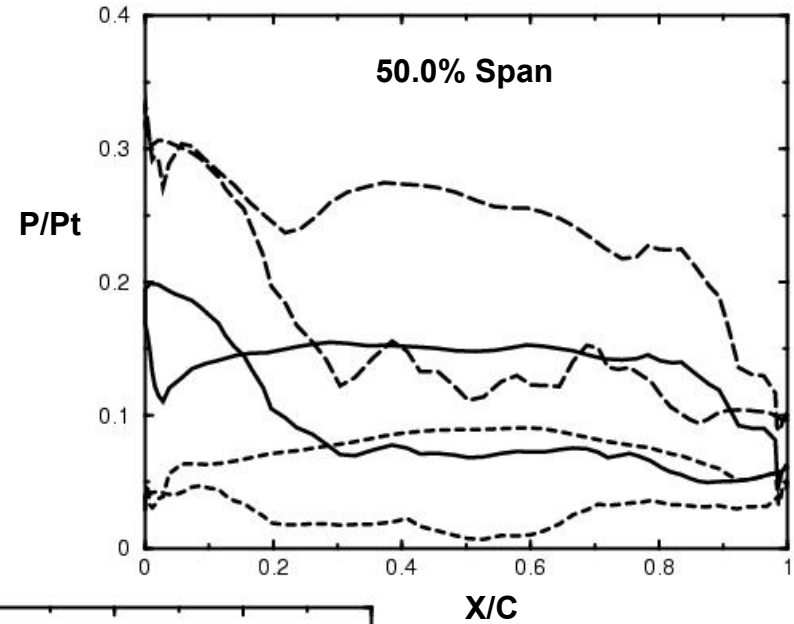

- - - - - - Minimum
-- -- -- -- Maximum
---------- Time-Avg

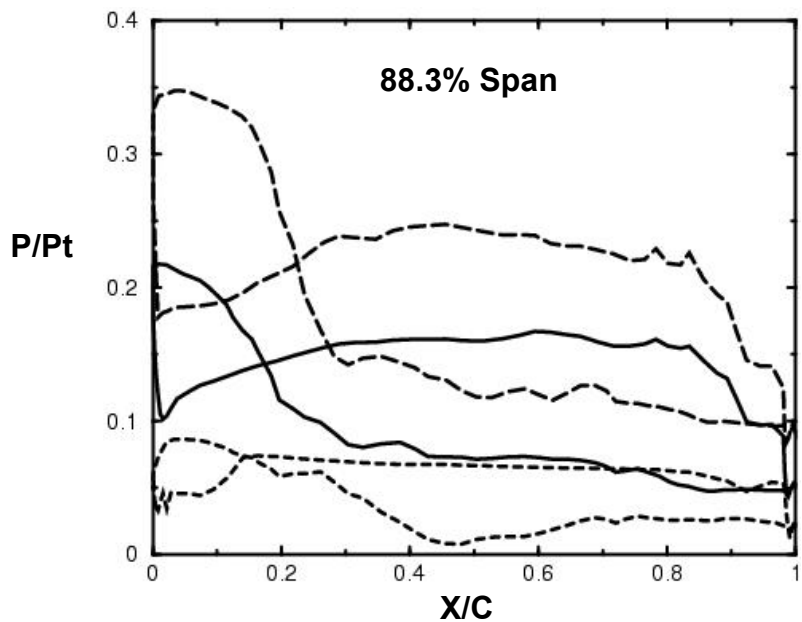

Unsteady Rotor Pressure Envelopes (PA-IN)

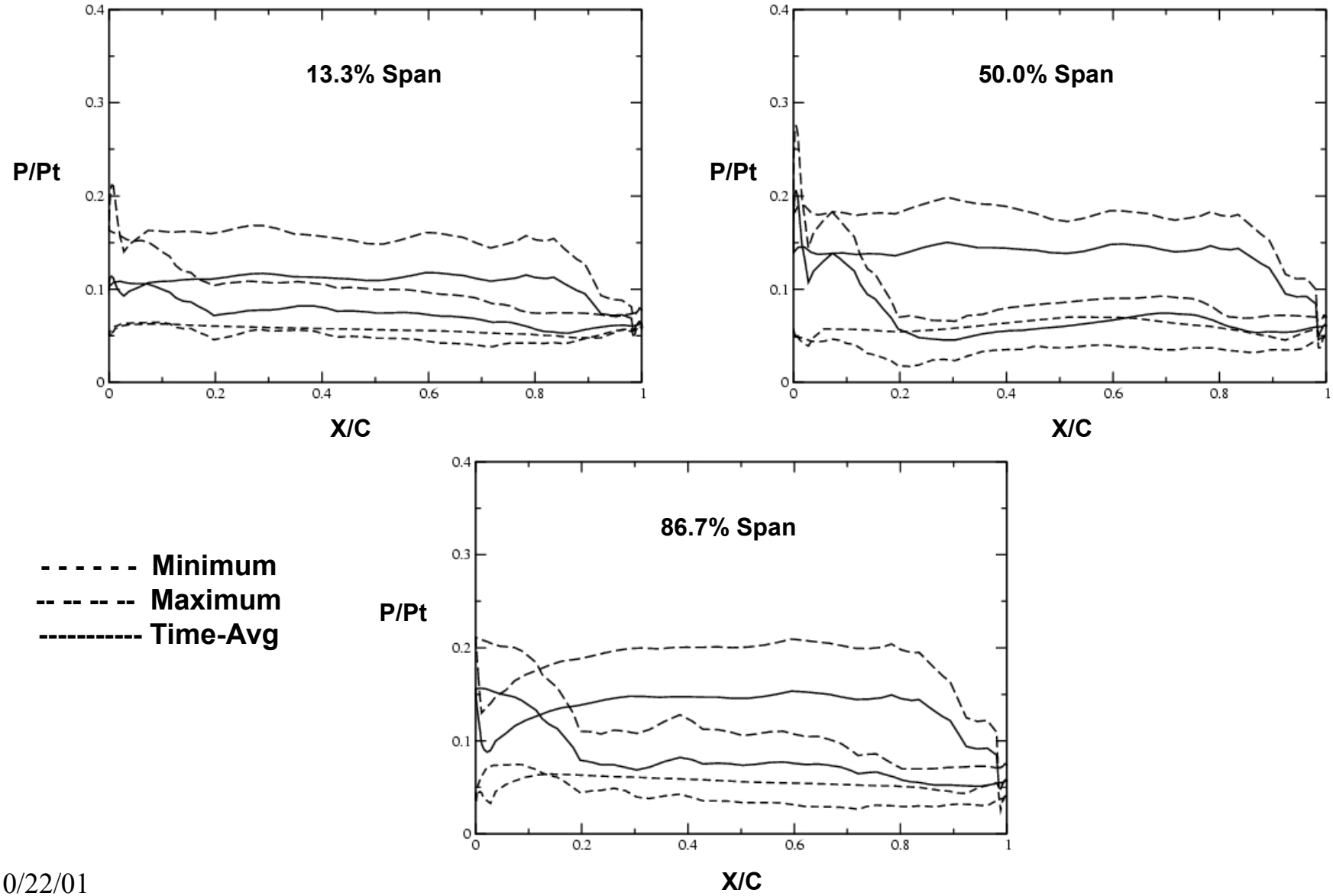

Unsteady Rotor Pressure Envelopes (PA-OUT)

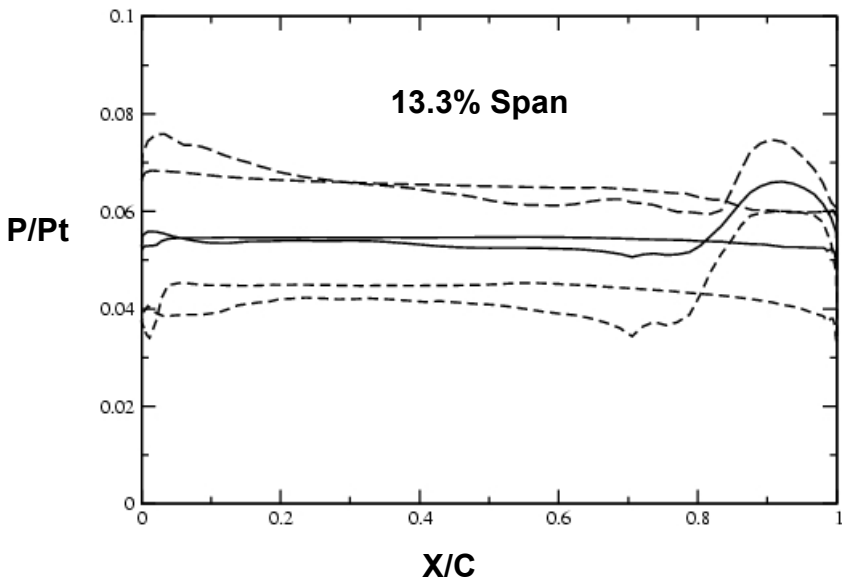

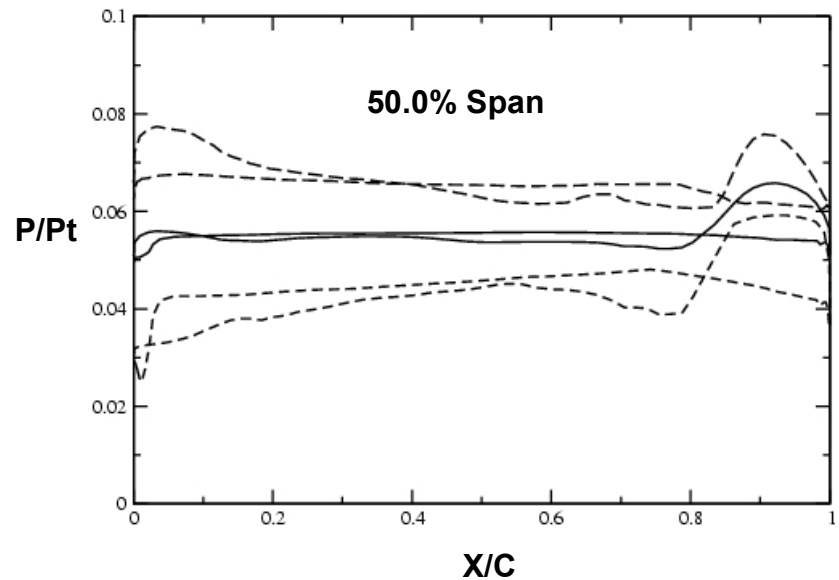

- - - - - - Minimum
-- -- -- -- Maximum
---------- Time-Avg

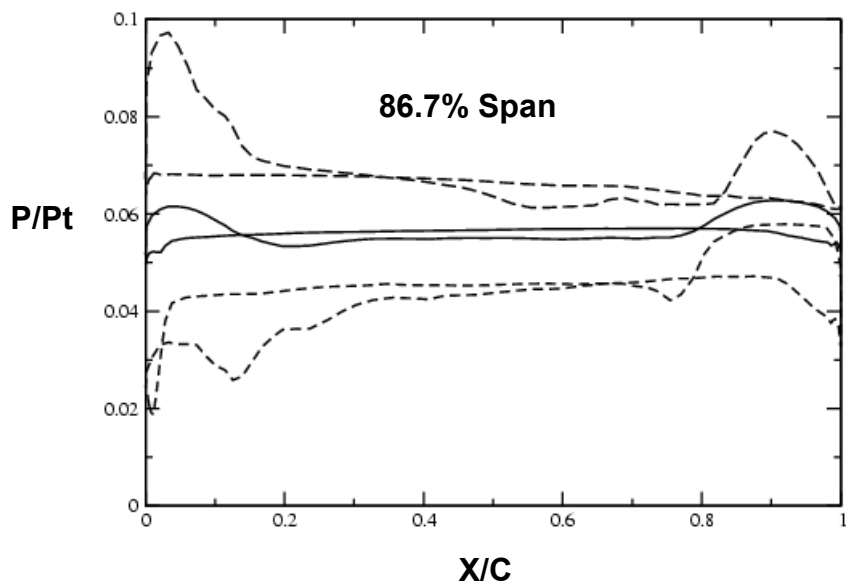

Unsteady Pressure - 11.7% Span (FA)

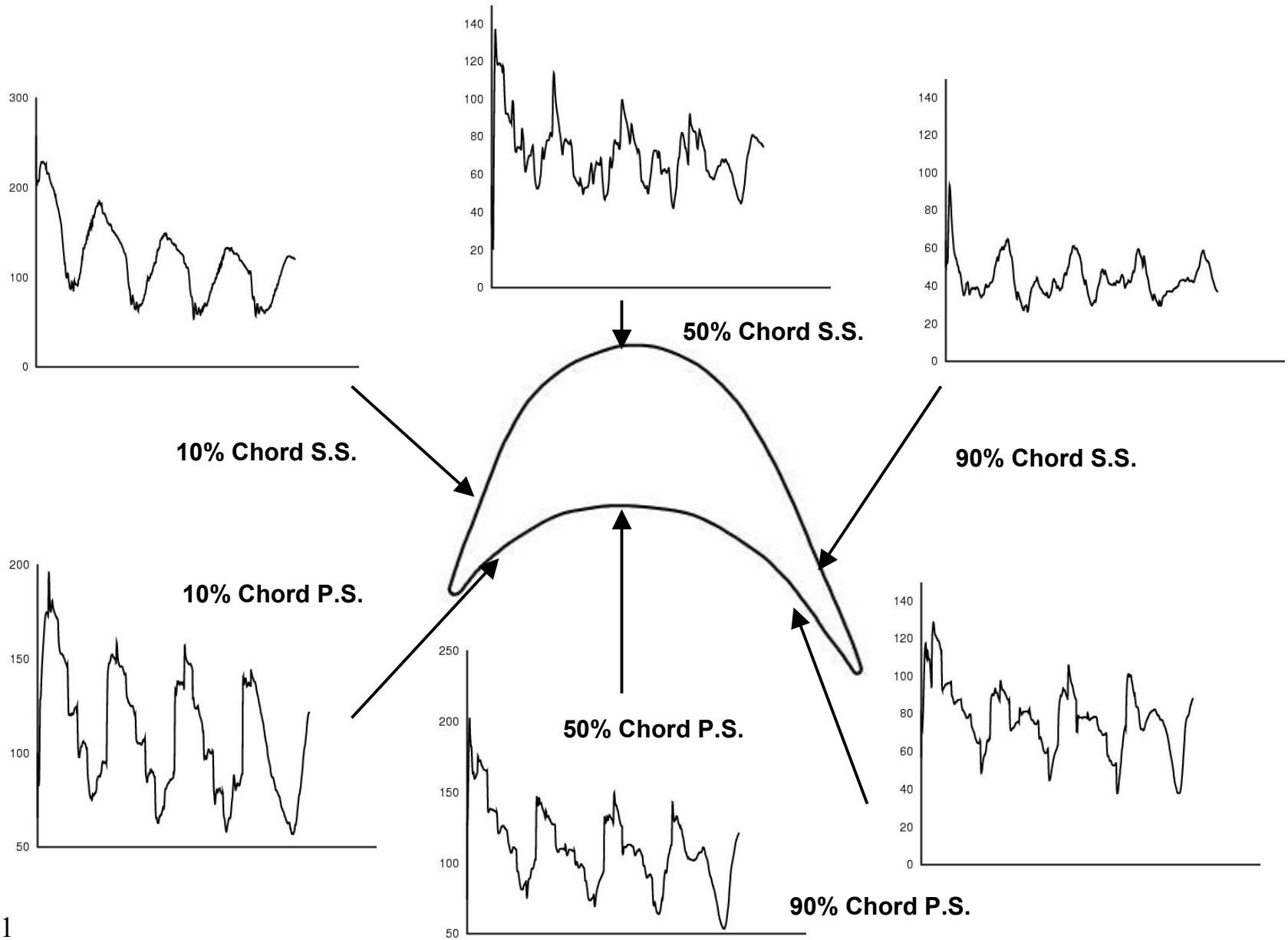

Unsteady Pressure - 13.3% Span (PA)

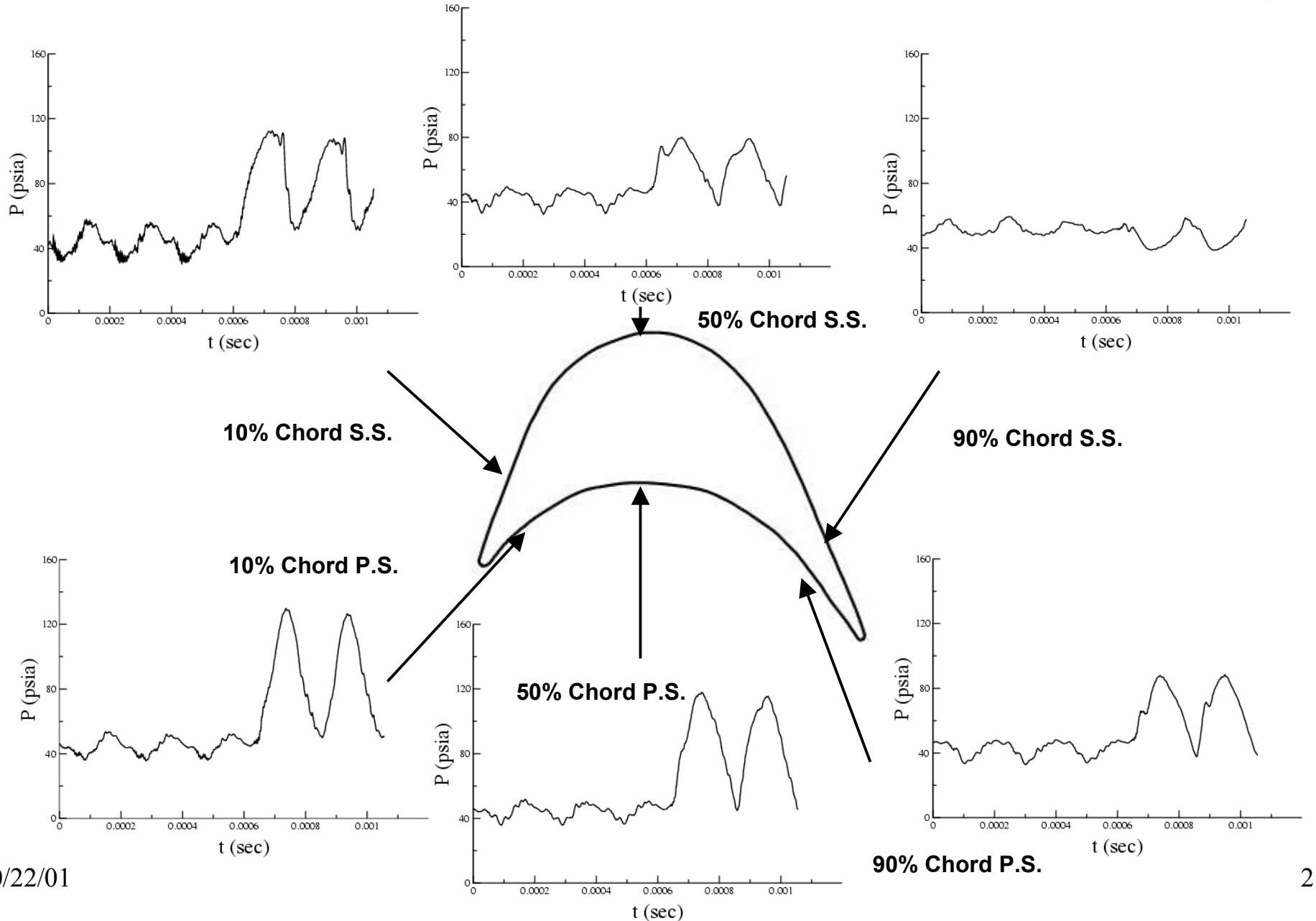

Unsteady Decomposition - 11.7% Span (FA)

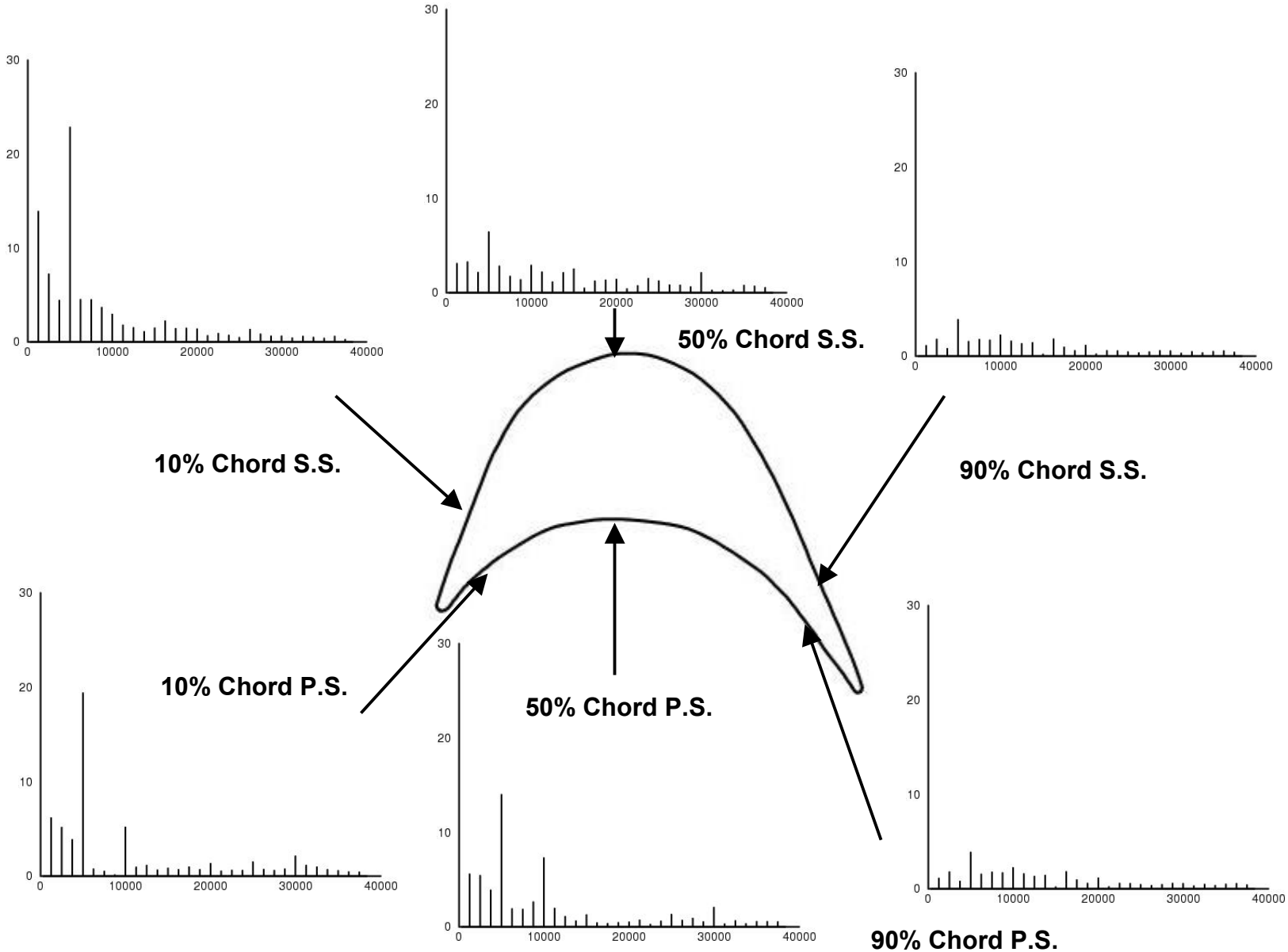

Unsteady Decomposition - 13.3% Span (PA)

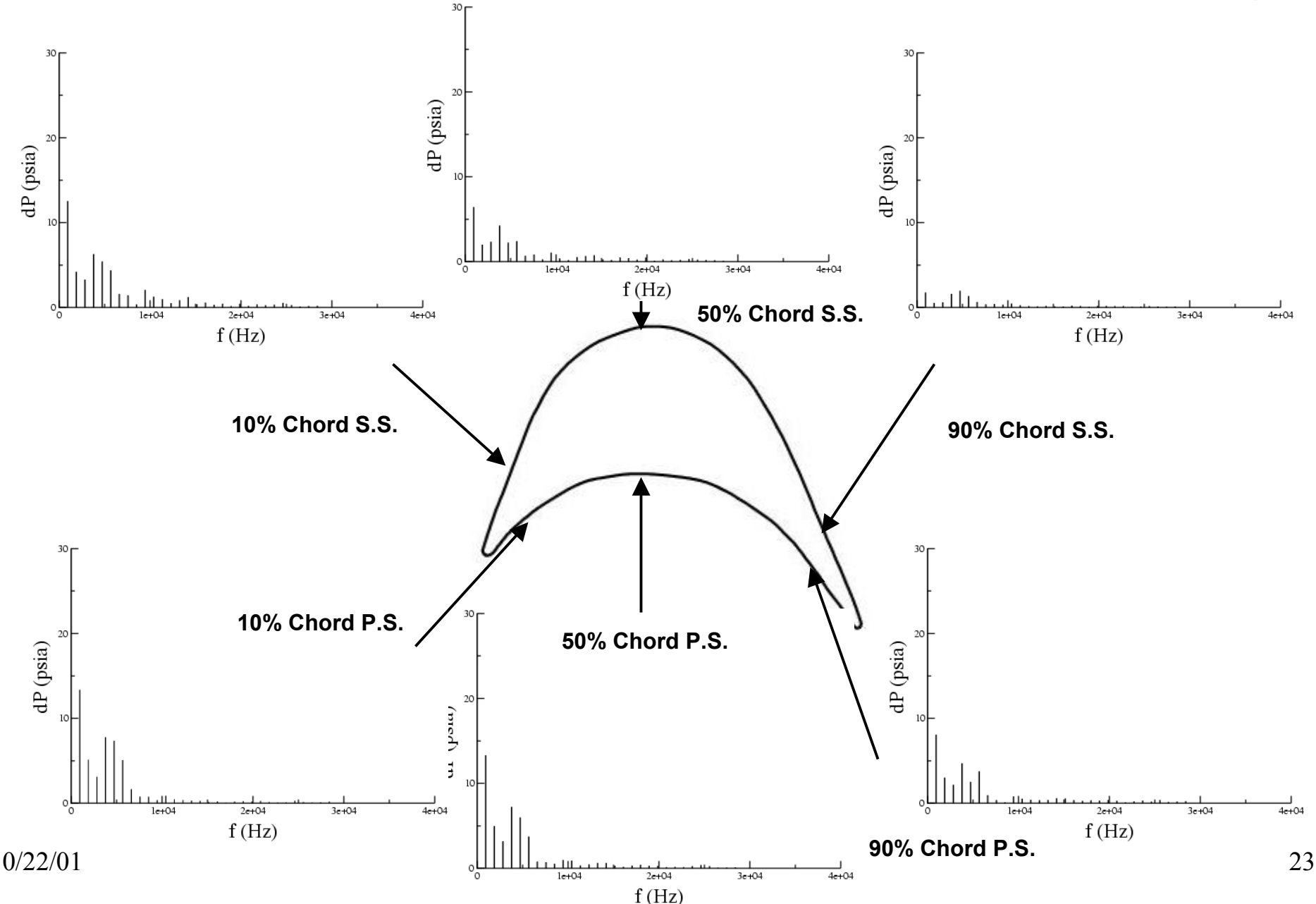

Unsteady Pressure - 50.0% Span (FA)

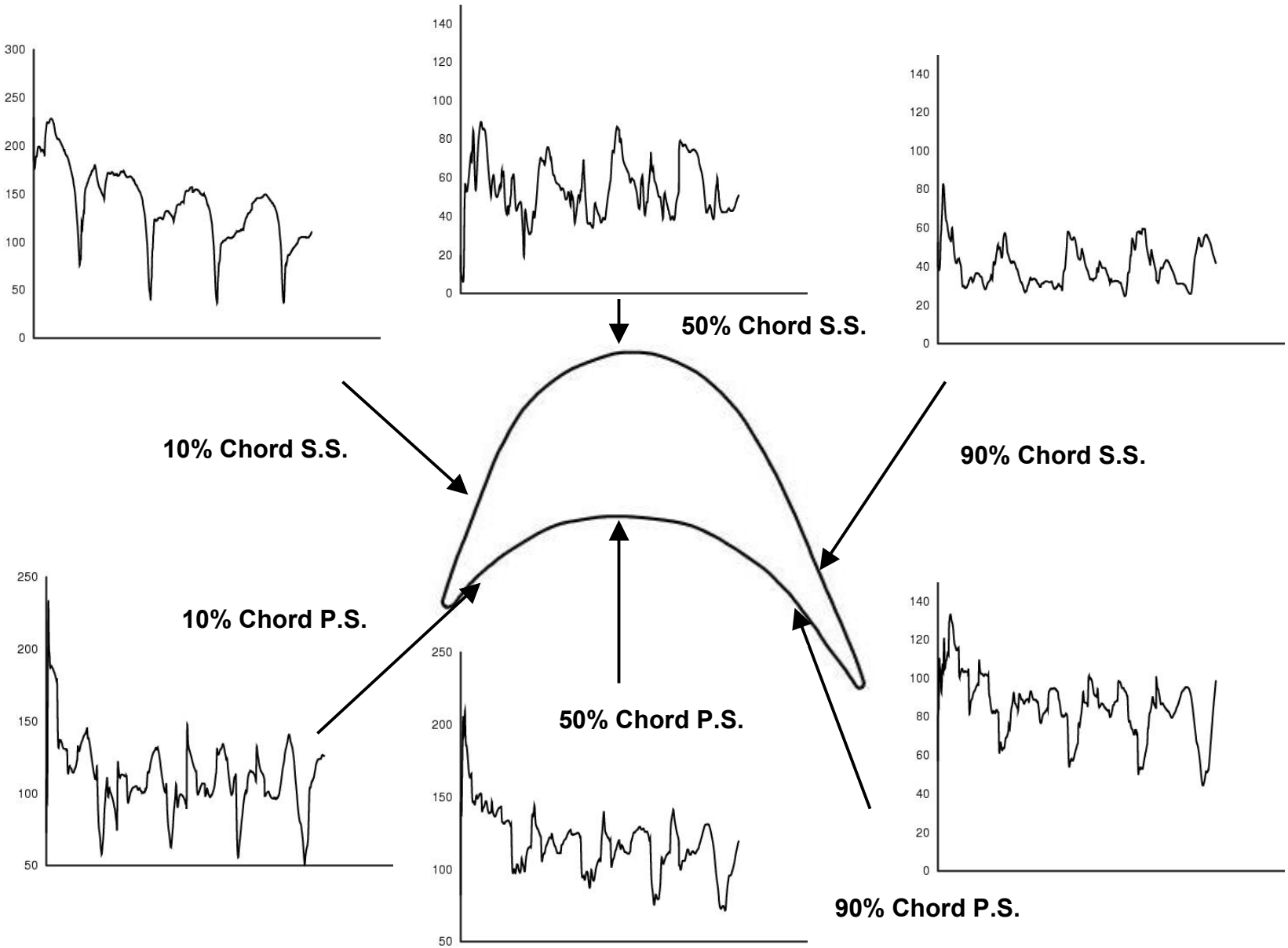

Unsteady Pressure - 50.0% Span (PA)

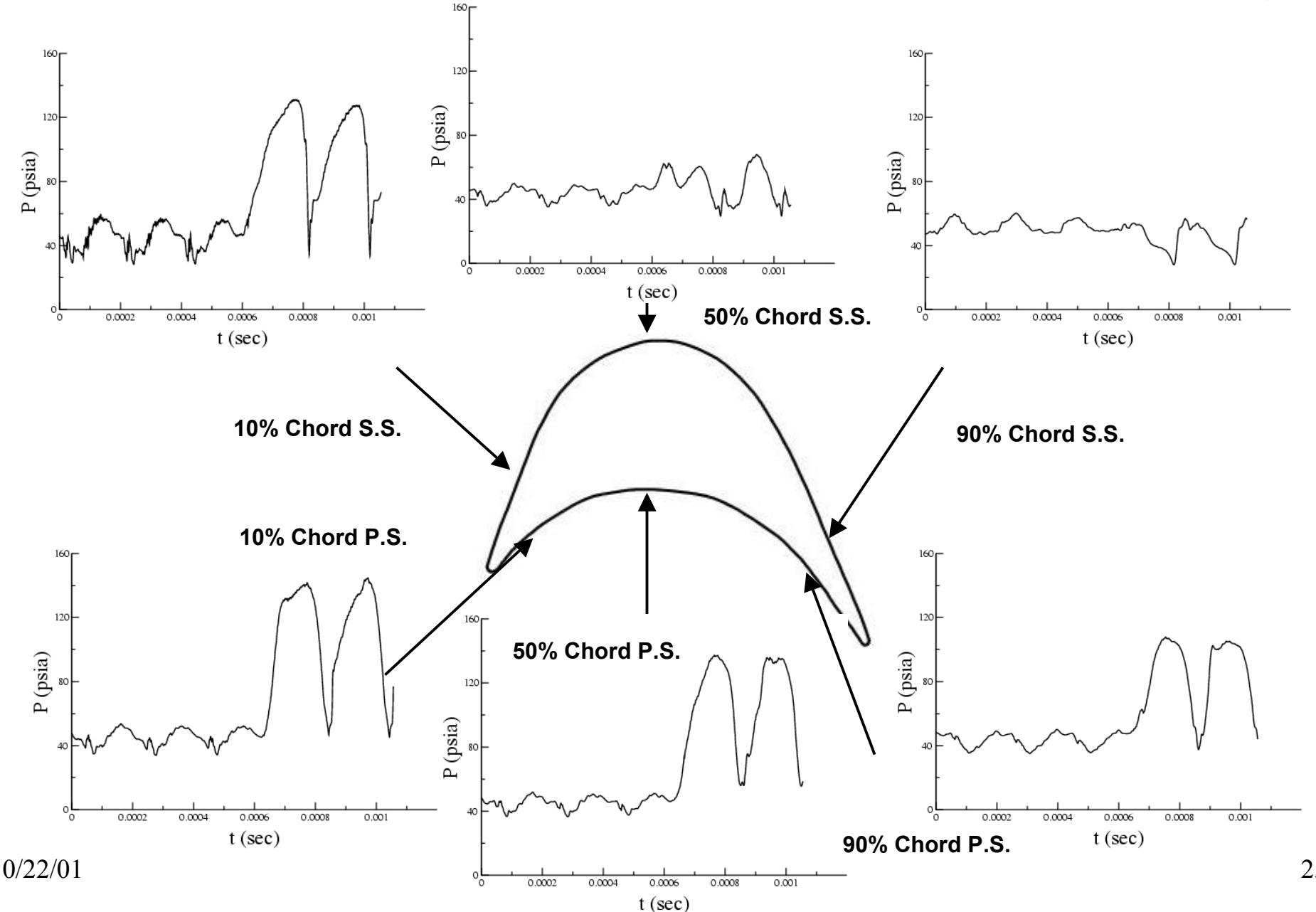

Pressure Decomposition - 50.0% Span (FA)

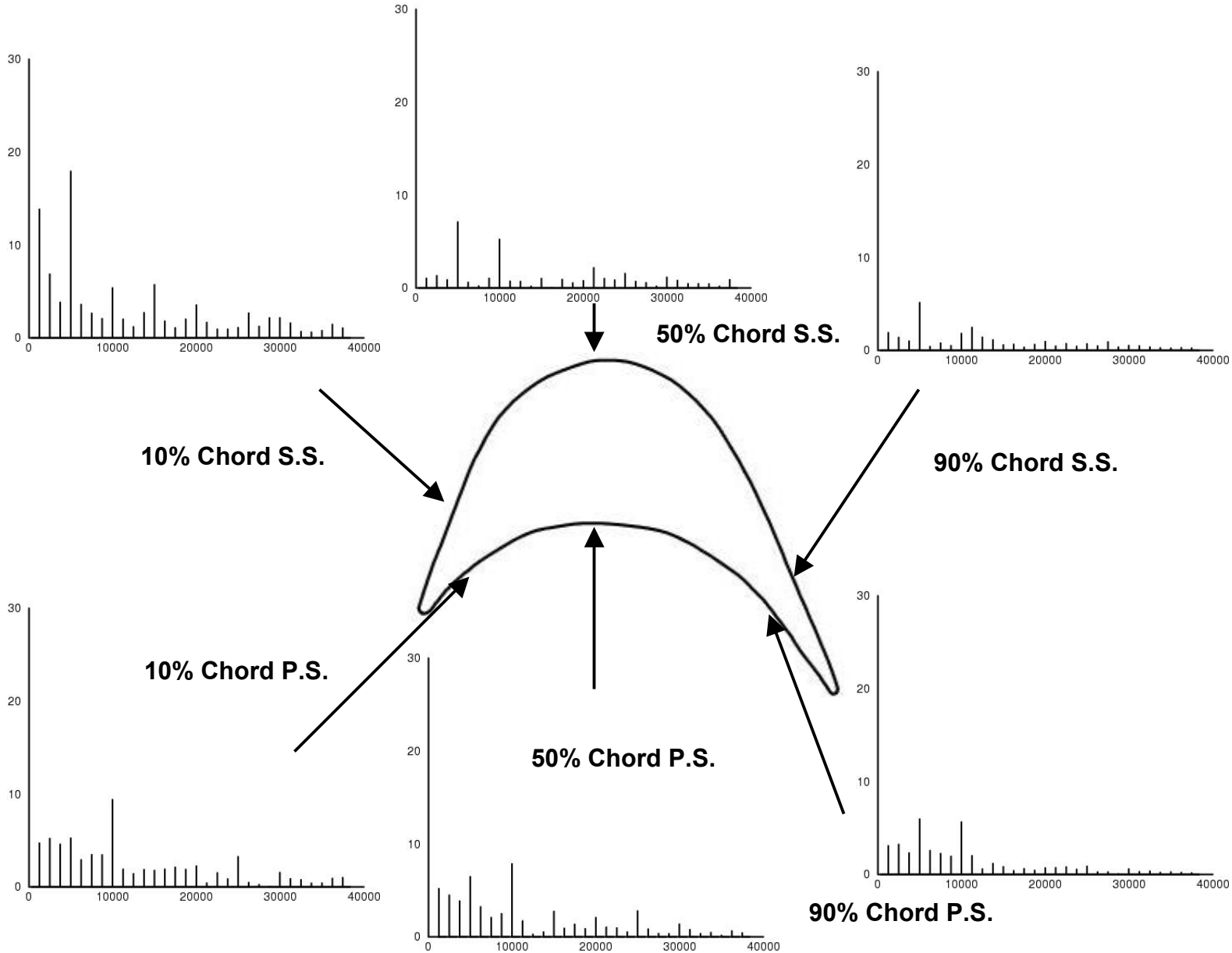

Pressure Decomposition - 50.0% Span (PA)

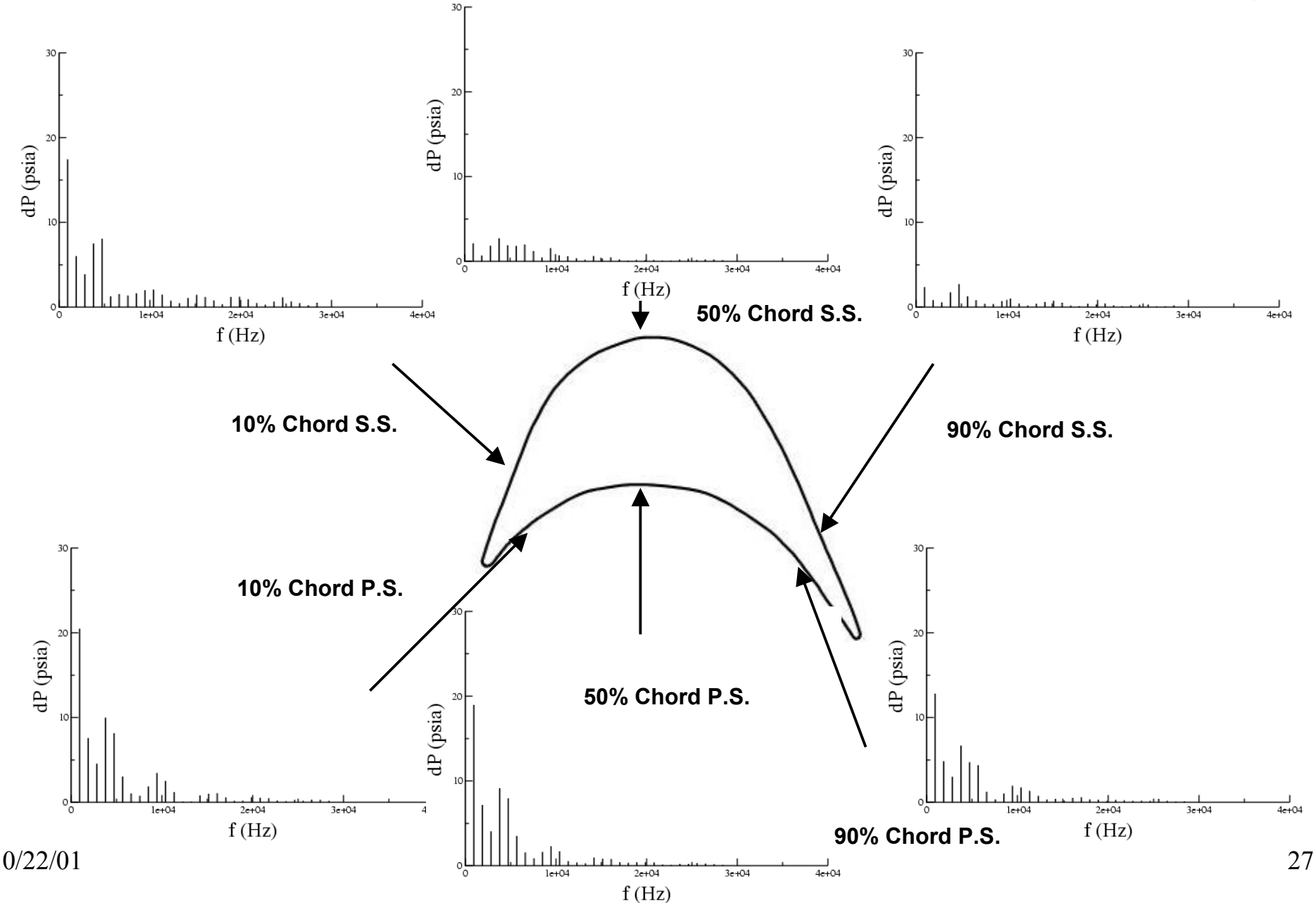

Unsteady Pressure - 88.3% Span (FA)

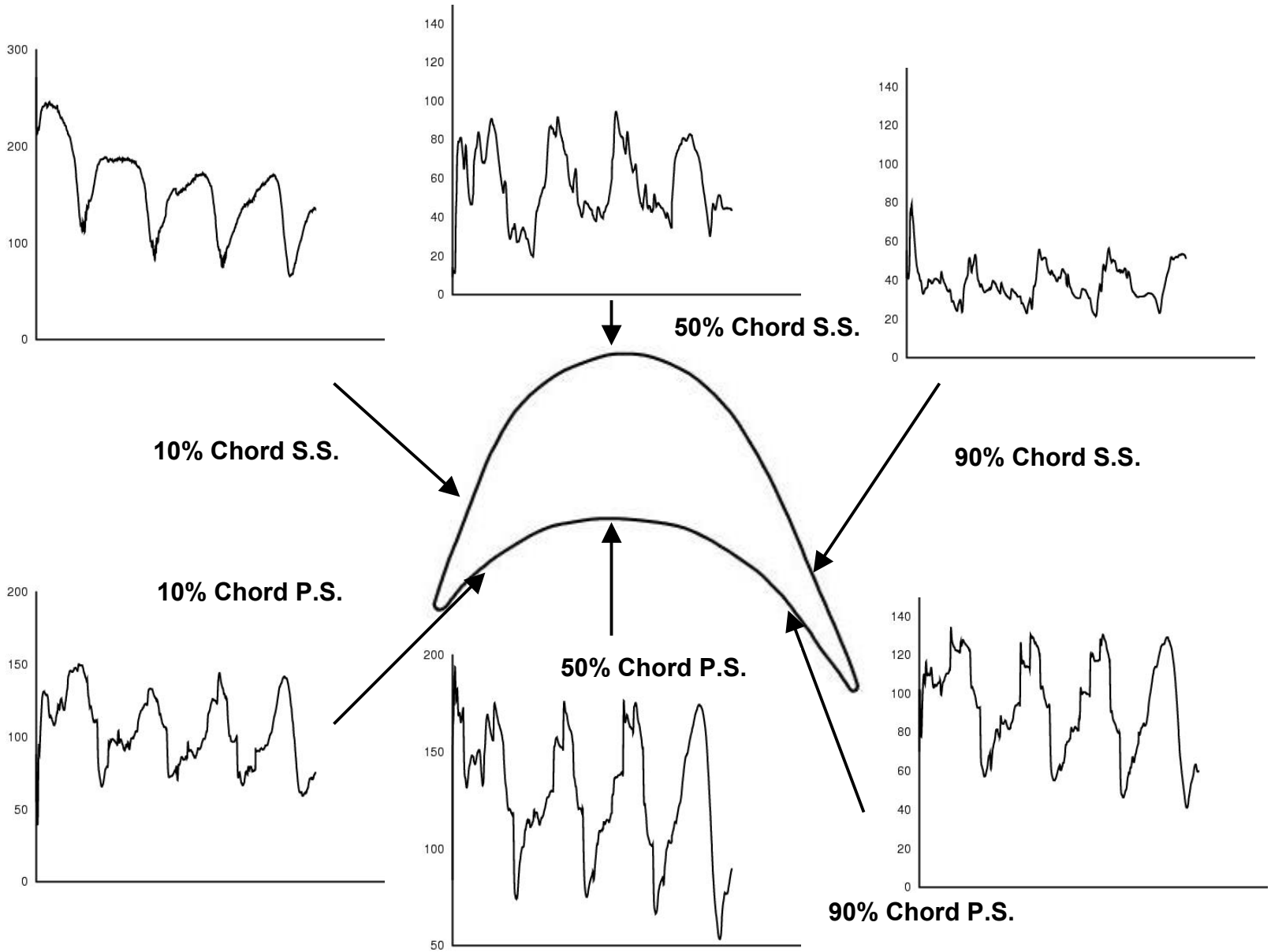

Unsteady Pressure - 86.7% Span (PA)

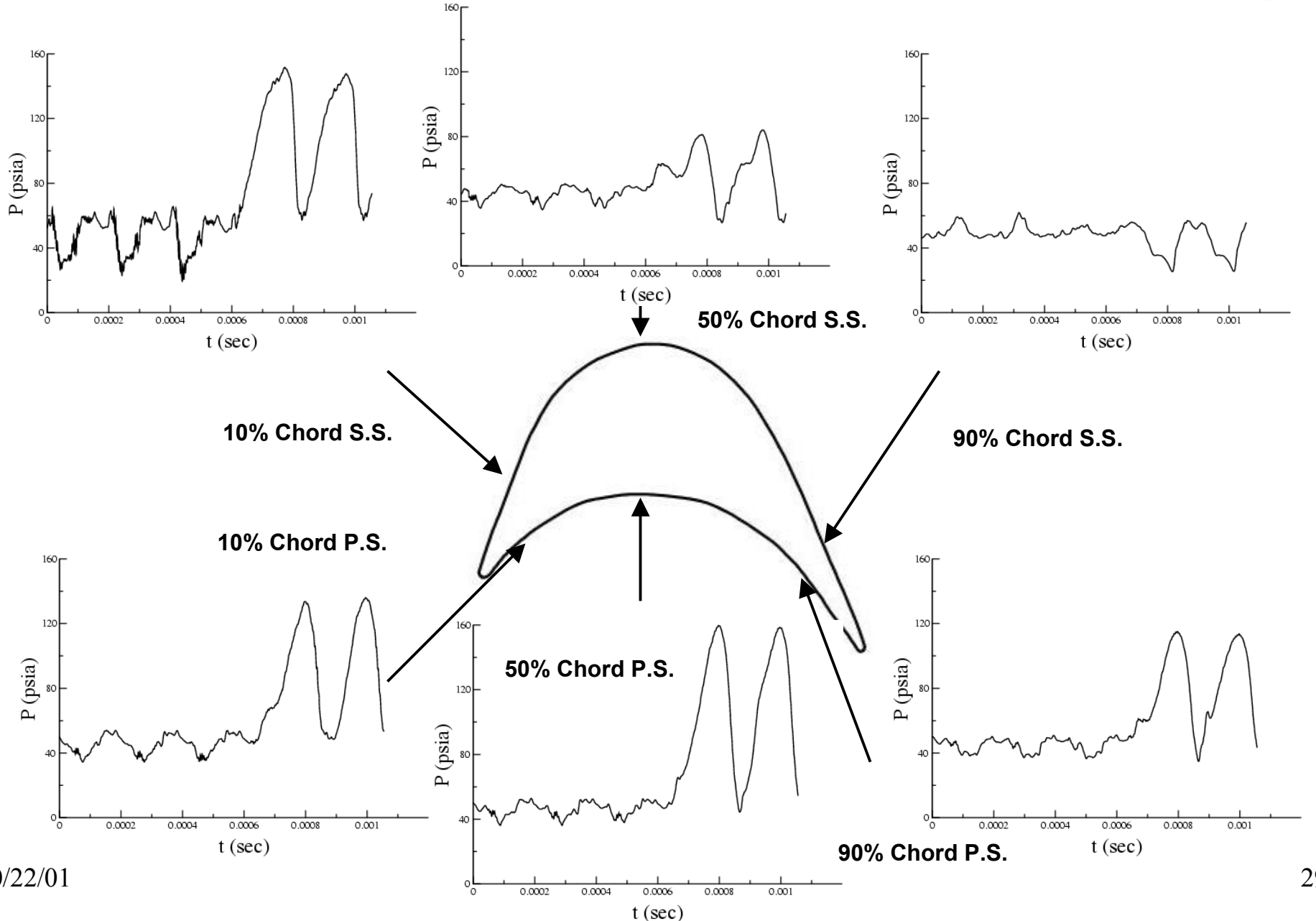

Pressure Decomposition - 88.3% Span (FA)

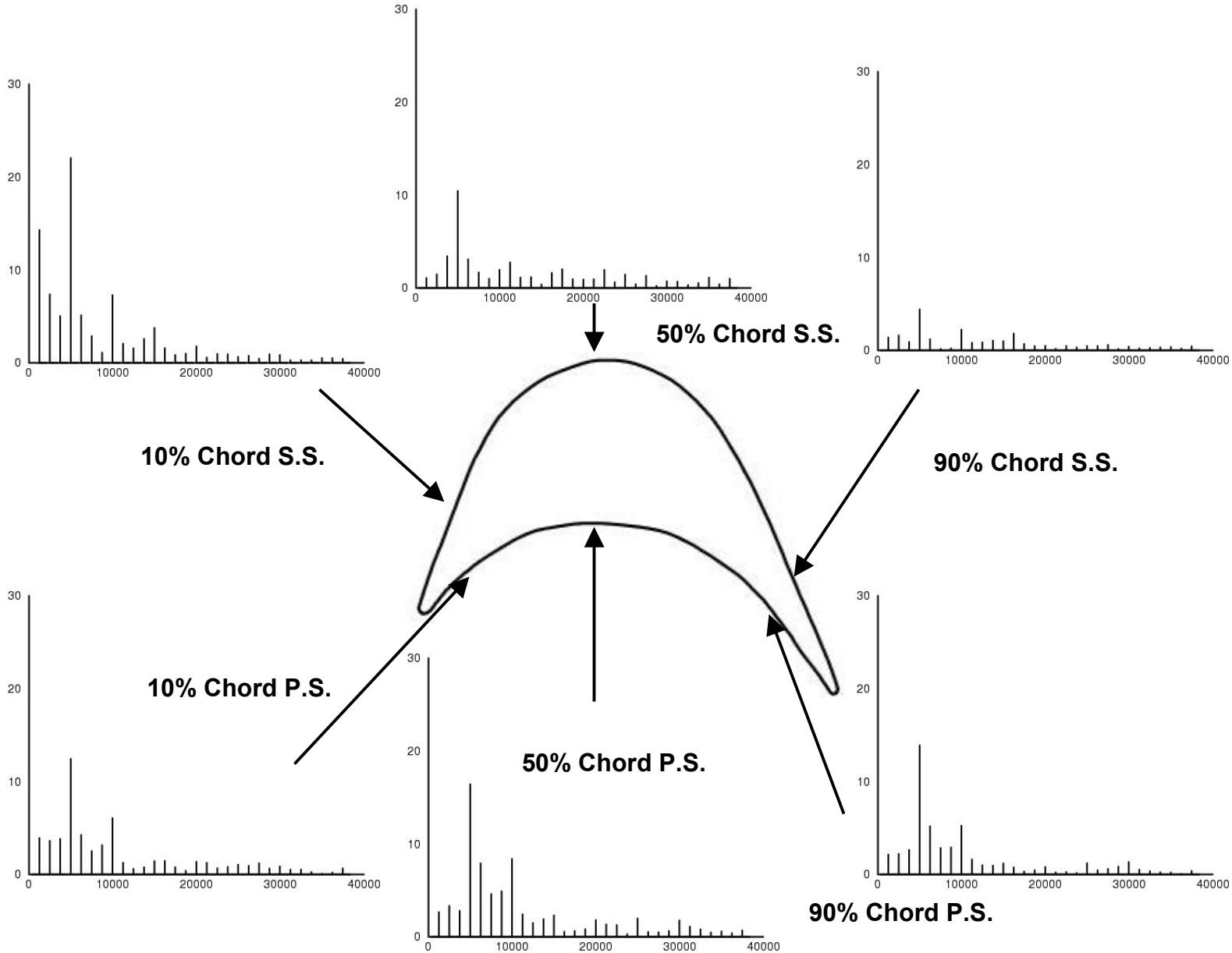

Pressure Decomposition - 86.7% Span (PA)

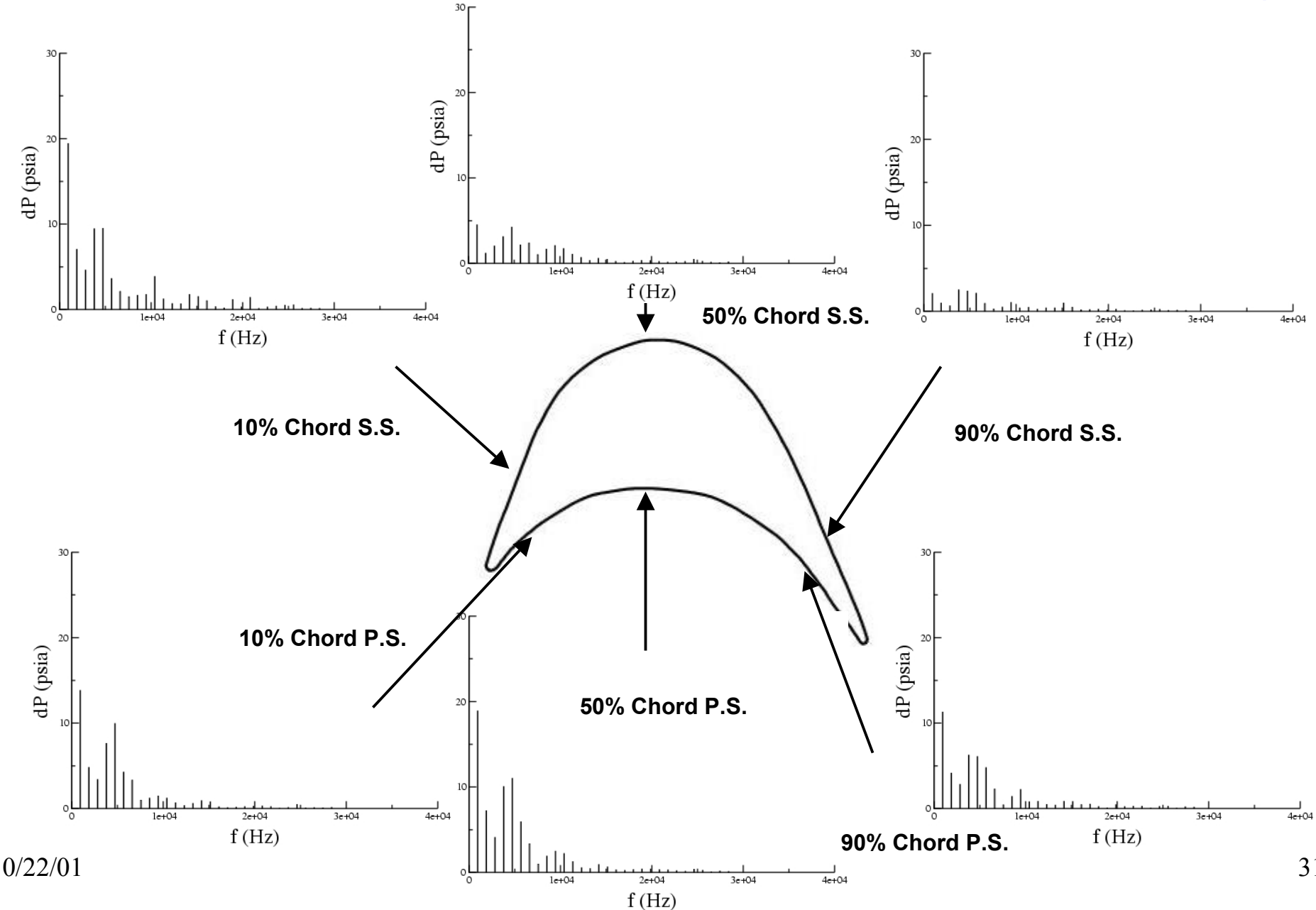

Unsteady Integrated Forces (FA)

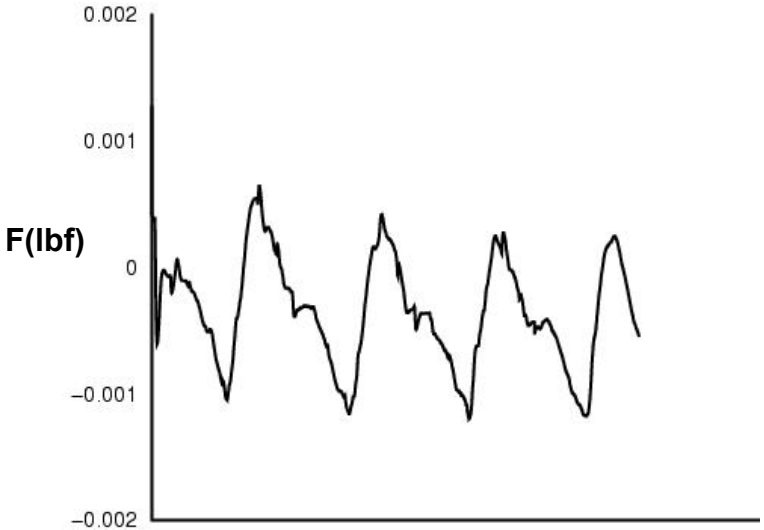

Axial Force

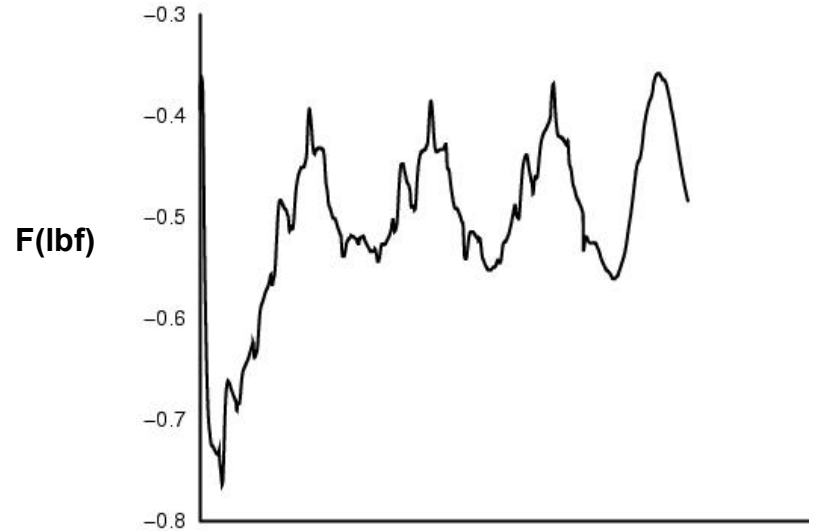

Radial Force

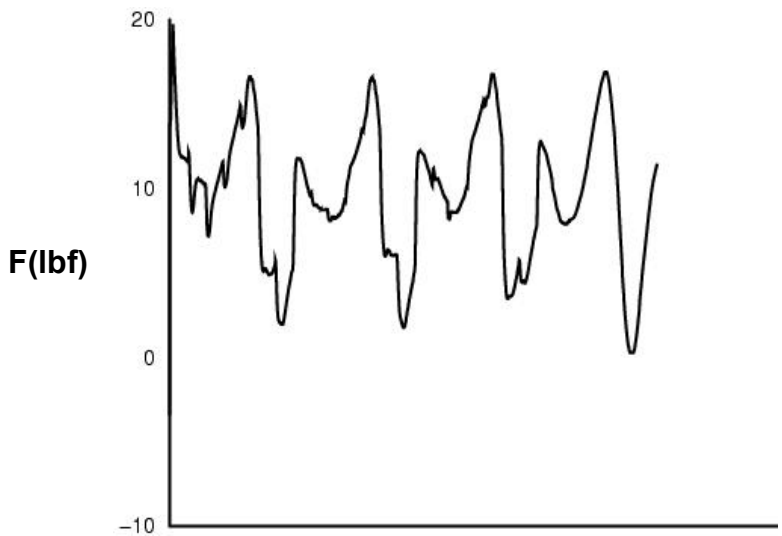

Tangential Force

Unsteady Integrated Forces (PA)

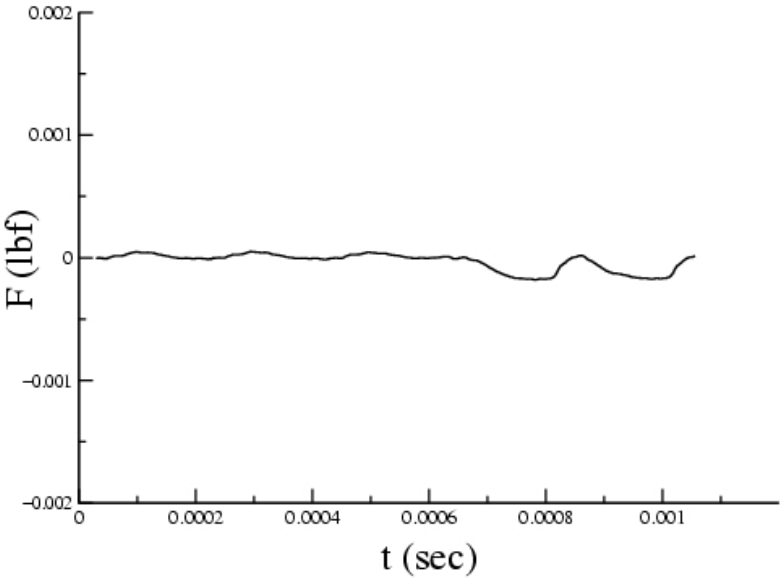

Axial Force

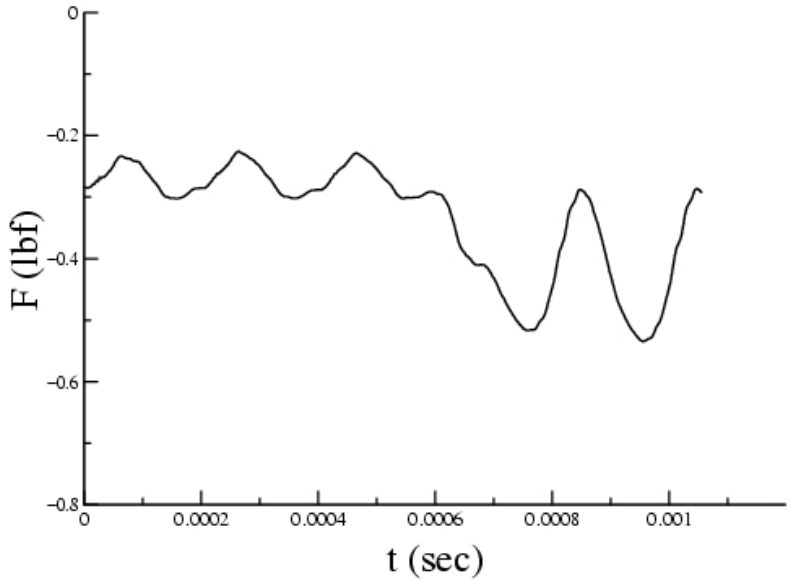

Radial Force

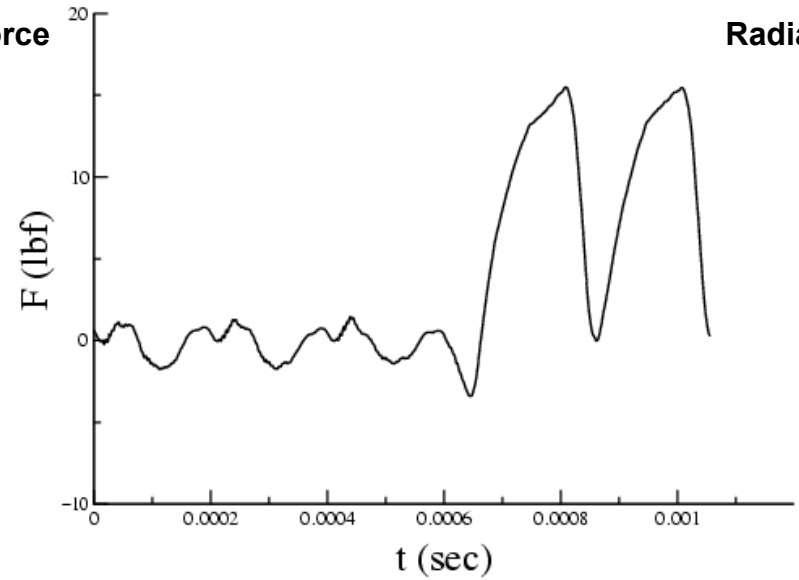

Tangential Force

Conclusions

- **Full admission simulation performed for the Simplex turbine**
  - models one nozzle and 12 rotors
  - Mach number of flow exiting nozzle low
  - Mach number at rotor exit too high
  - unsteadiness predominantly a nozzle-passing and twice nozzle-passing frequency
- **Partial admission simulation underway for Simplex turbine**
  - models all nozzles and rotors
  - design Mach number obtained at nozzle exit
  - design Mach number obtained at rotor exit
  - unsteadiness at nozzle-passing and lower frequencies

Pre- and Post-Processing Tools to Streamline the CFD Process

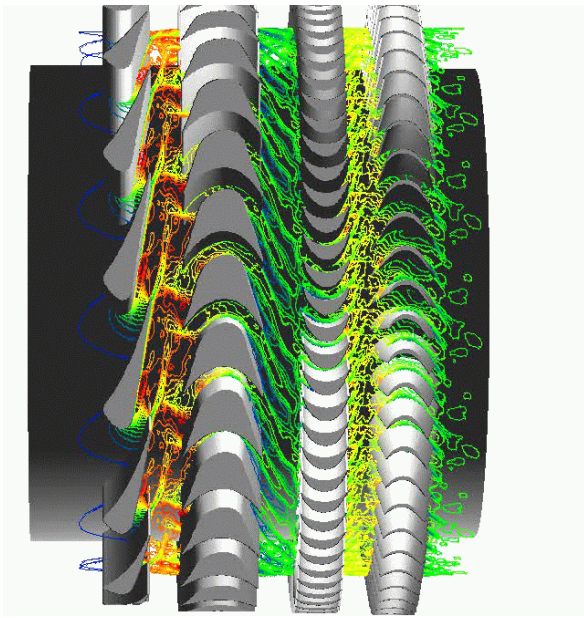

Suzanne Miller Dorney, PhD
Applied Fluid Dynamics Analysis Group
NASA Marshall Space Flight Center
MSFC, AL 35812

September 10, 2001

Support of CFD

- **Pre-processing**
- **Interim-processing**
- **Post-processing**

CFD Codes

- **FDNS**
  - general purpose CFD code
  - combustion, pump, and external flow simulations
- **CORSAIR**
  - code for unsteady turbomachinery simulations
  - turbines, compressors, and internal flow simulations

Pre-Processing Support for FDNS

- **Geometry specification**
  - generated by GridGen
  - obtained by another source
  - standard plot3d format
- **Boundary condition specification**
  - generated by GridGen
  - generated by hand

FDNS Boundary Conditions

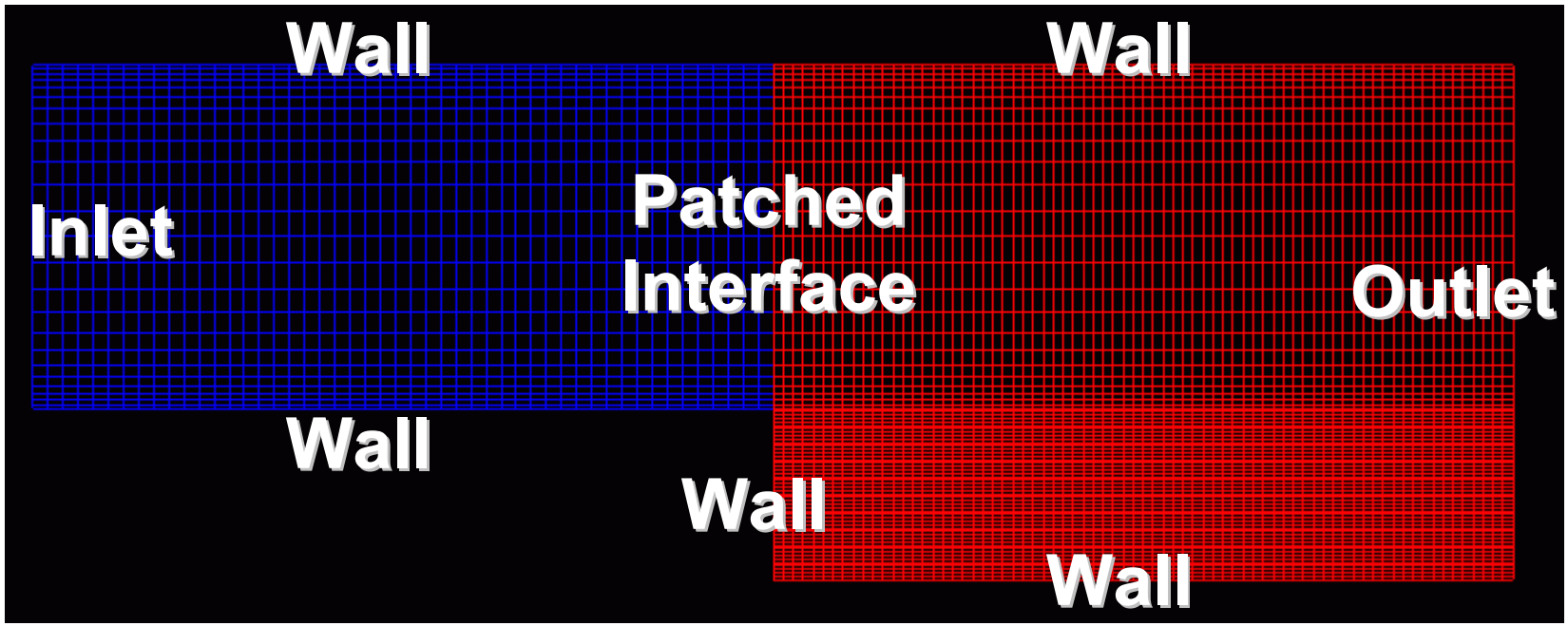

Specification of Boundary Conditions

```
#IDIM
2
#IZON,IZFACE,  IBND,   ID, ISNGL, INPNT
    2      2      2      5      0      0
# IZT,  JZT,  KZT,LPROC,        CBG1,        CBV2
   50     25      1      1  0.000e+00  0.000e+00
   75     75      1      1  0.000e+00  0.000e+00
#THCYCX, IZB1, IZF1,IJZ11,IJZ12,JKZ11,JKZ12,INONUF,IPROC1
#        IZB2, IZF2,IJZ21,IJZ22,JKZ21,JKZ22,IDFACE,IPROC2
 0.00      1      2      1     25      1      1     21      1
           2      1     51     75      1      1      0      1
#IBCZON,IDBC,ITYBC,IJBB,IJBS,IJBT,JKBS,JKBT,IVFINT,PRAT,IPZ,IPI,IPJ,IPK
    1   1   0    1    1   25    1    1    0 -1.000e+00   1   1   1   1
    2   2   2   75    1   75    1    1    0 -1.000e+00   1   1   1   1
#IWBZON, L1,   L2,   M1,   M2,   N1,   N2,IWTM,   HQDOX,IWALL,   DENNX,   VISWX
    1     1    50     1     1     1     1    1 0.000e+00    0 1.000e+00 1.000e+00
    1     1    50    25    25     1     1    1 0.000e+00    0 1.000e+00 1.000e+00
    2     1     1     1    51     1     1    1 0.000e+00    0 1.000e+00 1.000e+00
    2     1    75     1     1     1     1    1 0.000e+00    0 1.000e+00 1.000e+00
    2     1    75    75    75     1     1    1 0.000e+00    0 1.000e+00 1.000e+00
          :
          :
          :
```

3D 22-Grid Case

Type	# Values Needed	Occurances	Total Values
Grid Dimensions	3	22	66
Patched Interfaces	17	37	629
Flow Boundaries	14	51	714
Walls	12	56	672
Total Values			2081

PreViewer

- Visualization tool designed specifically for FDNS
- Interactive tool to visually inspect input files
- Automated error checking of input files

Patched Interface Panel

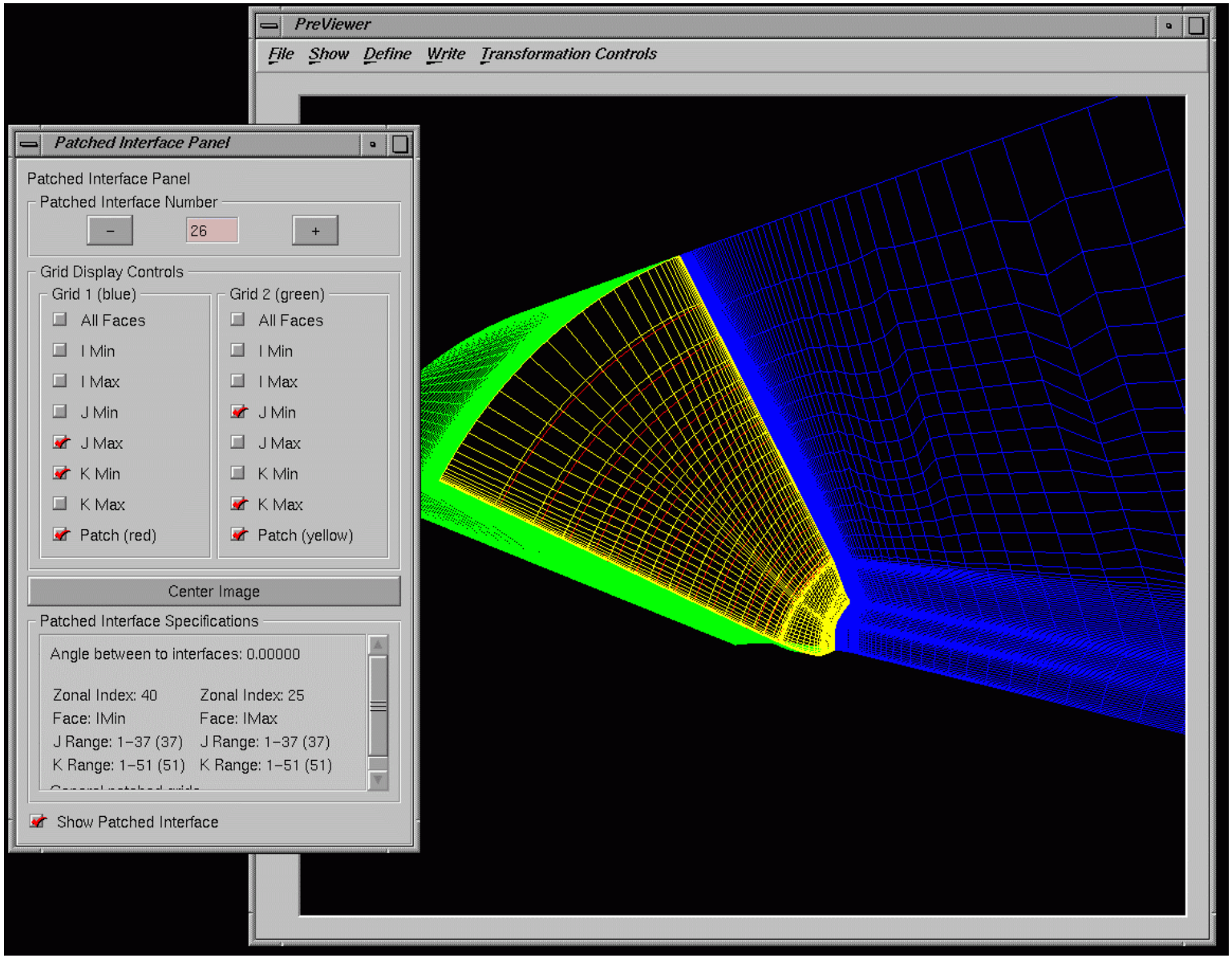

Combined Panel

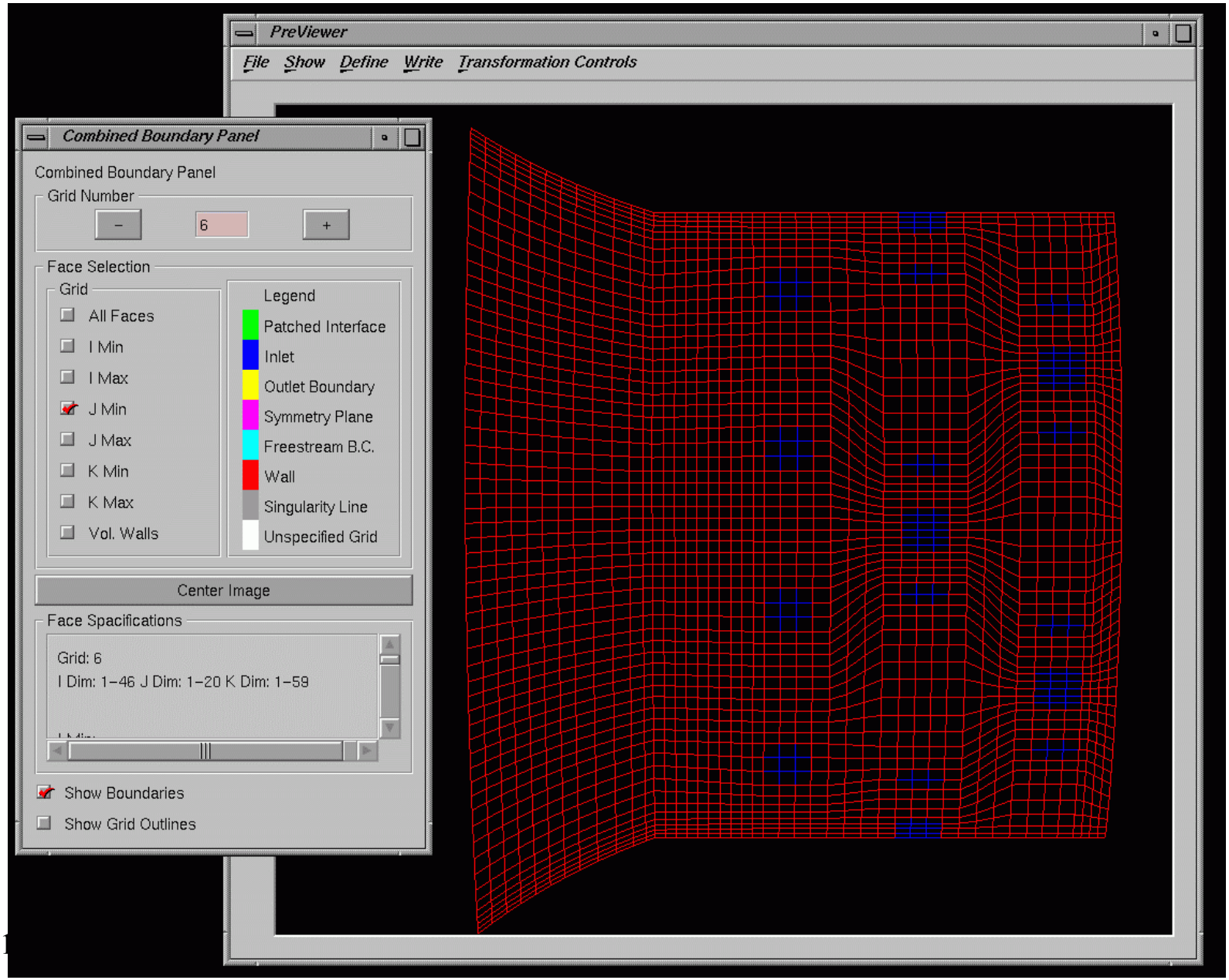

Error Report Panel

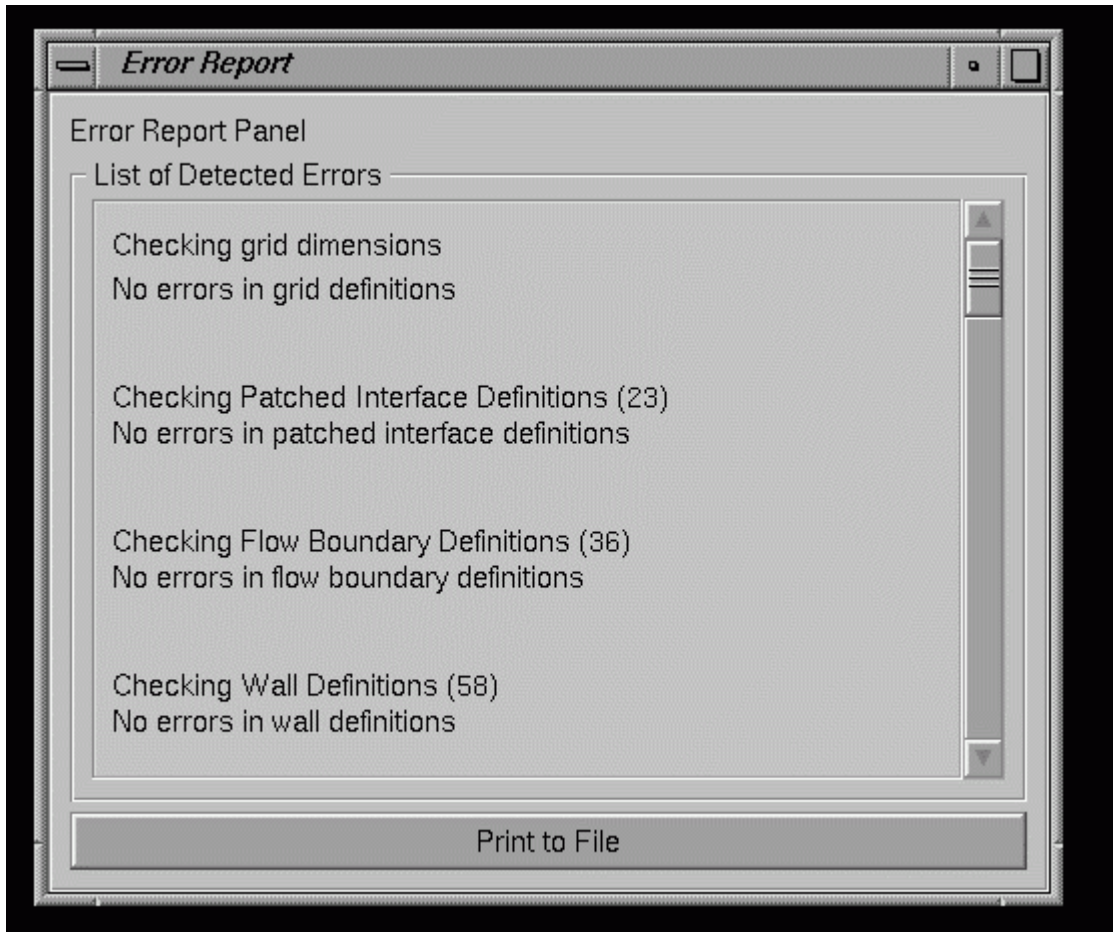

Future Plans for PreViewer

- **Expand Error Checking**
- **Expand ability to define boundary conditions**
- **Set up specification files for interim- and post-processing tools**

Interim-Processing

- **Process**
  - generates line plots of results while the solution is forming
- **FlowShow**
  - generates an animation of contour or vector plots of solution while it is forming
- **Monitor**
  - updates screen images of mass conservation, delta, contours, vectors, and line plots of a solution while it is forming

General Method for Interim-Processing

- Track a file that is being written by the flow solver during execution
- Processing is triggered each time file is updated/written
- Specified data is extracted from the file
- Line plots or images are updated, or new frames are generated

Process: Check for Convergence

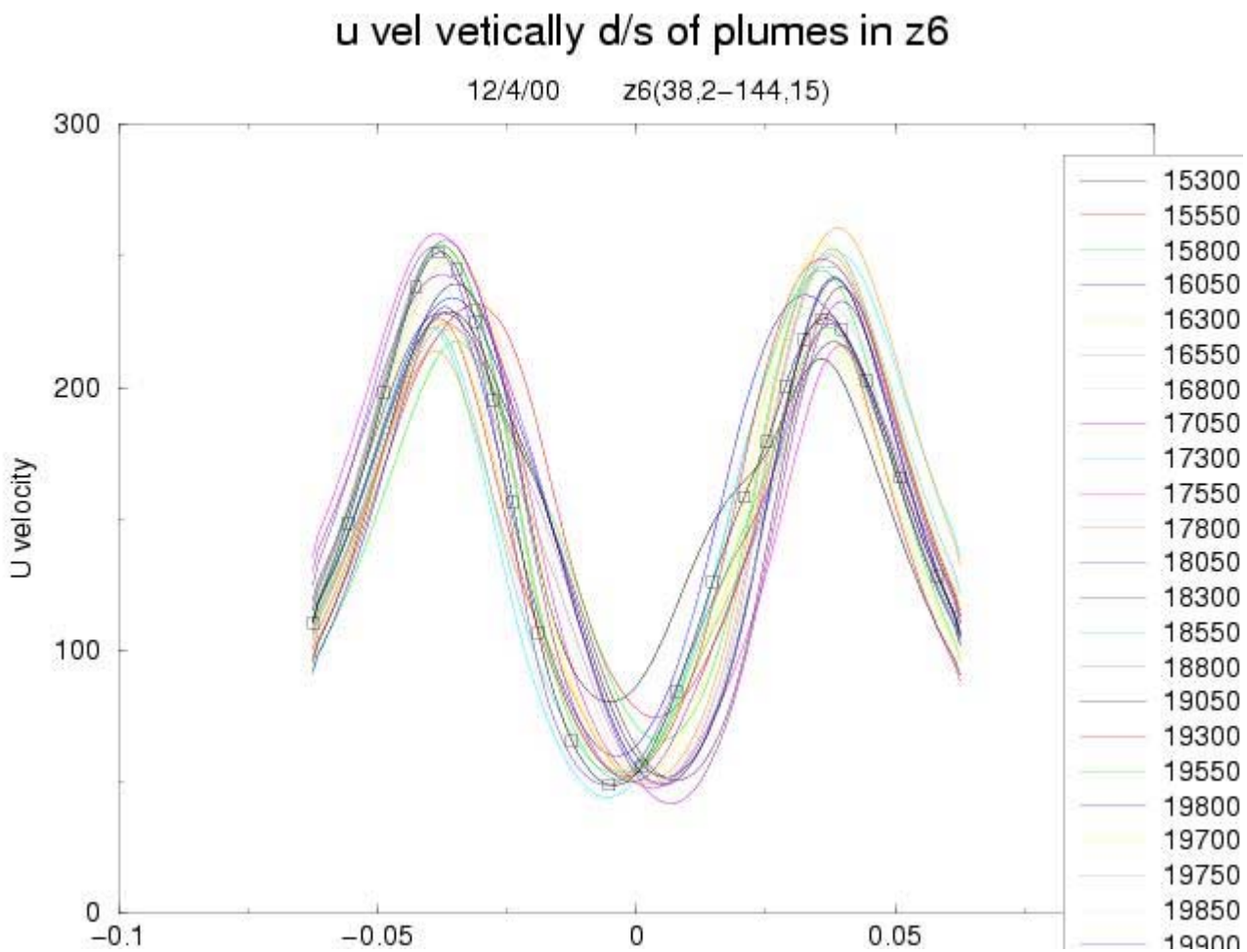

FlowShow: Super-Sonic Back Facing Step

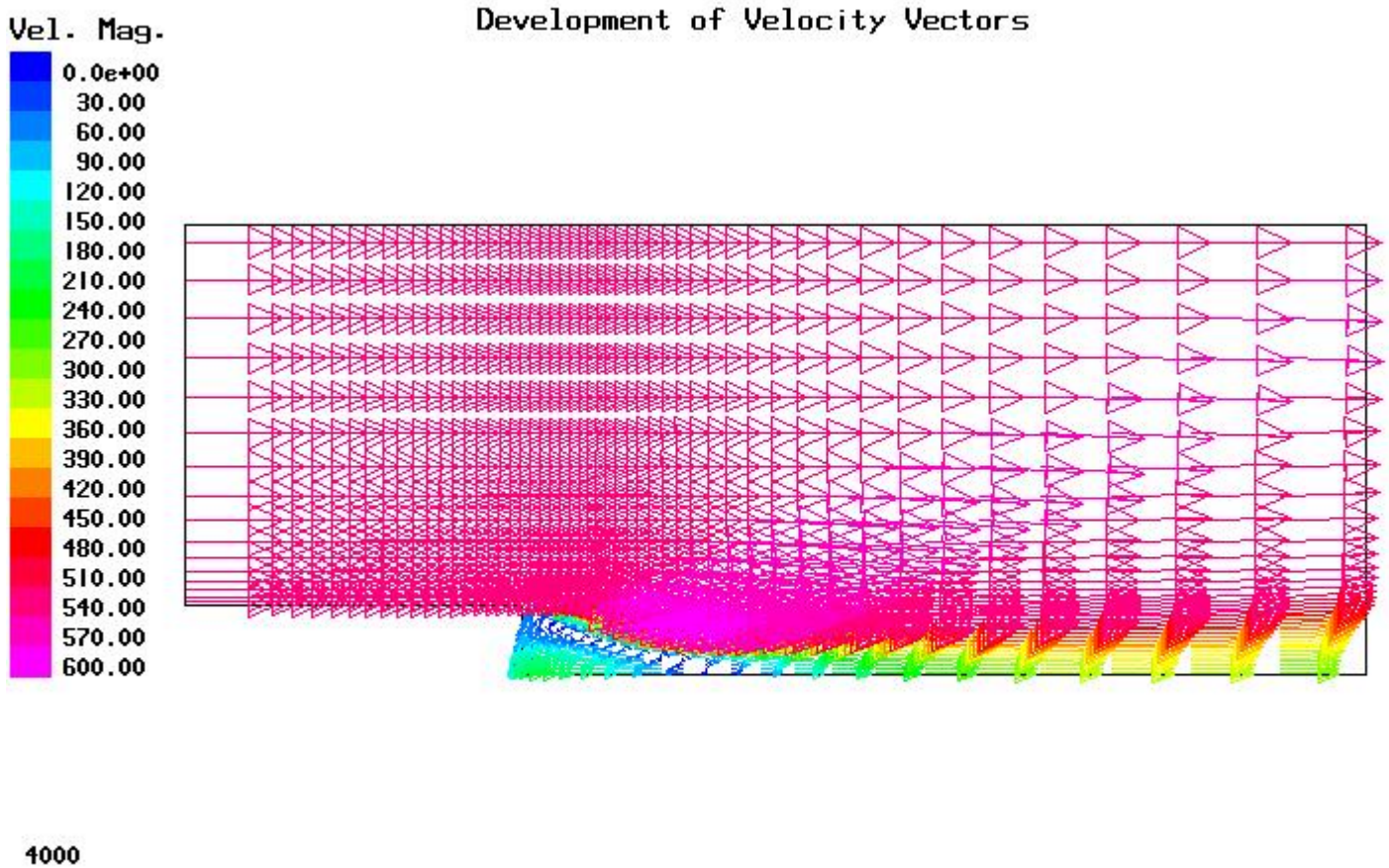

Monitor: Super-Sonic Back Facing Step

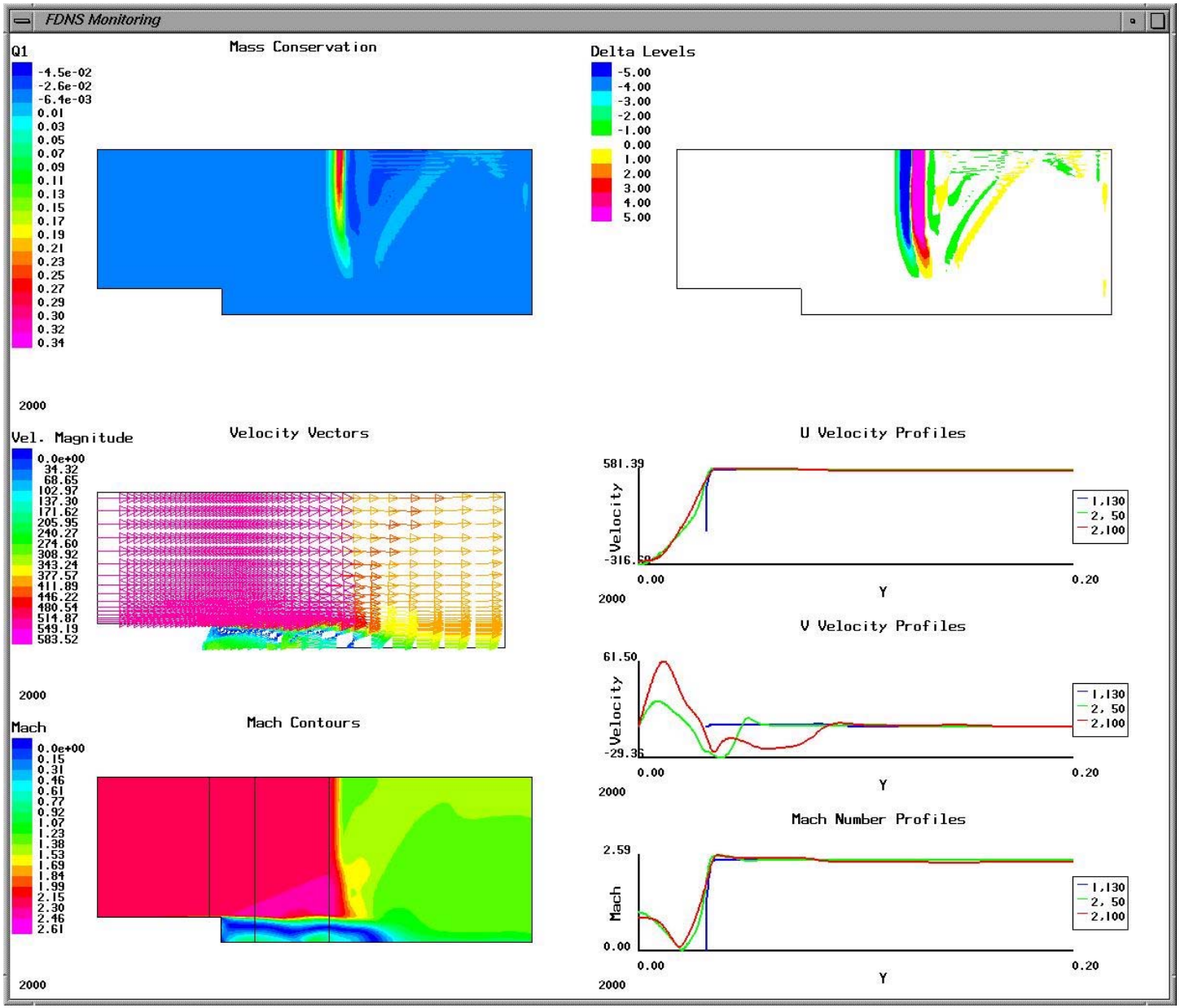

Future Plans for Interim-Processors

- Generate GUI's for specification of input files
- Combine functionality between tools
- Add display of experimental data

Post-Processing

- Animations
  - simple format specifications
  - runs in batch mode
  - engineer friendly

Instantaneous Mach Contours

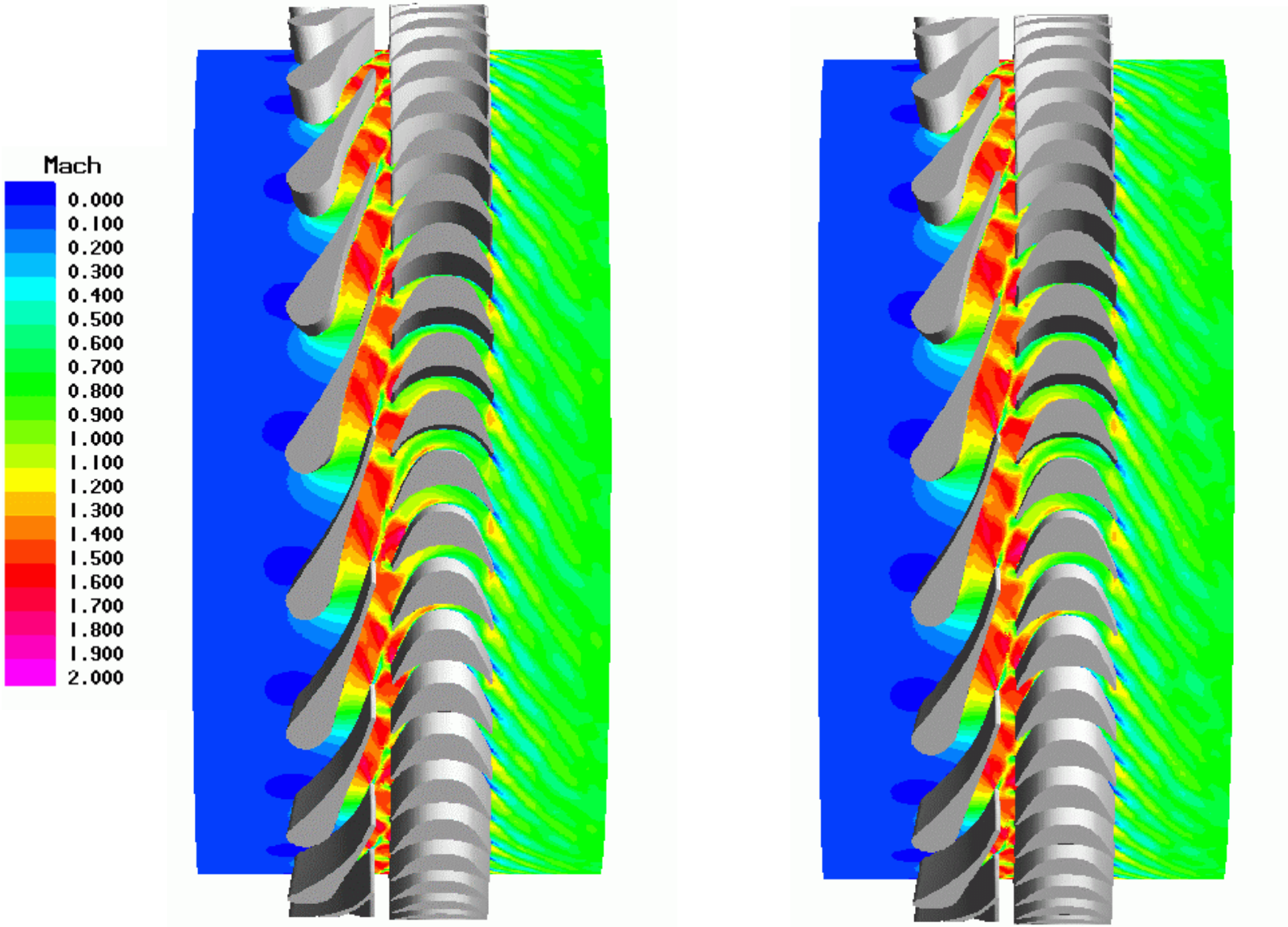

Timestep 0 **Timestep 16**

Animator

- **Generates MPEG animation files in batch mode**
- **Allows input files to be compressed**
- **Input Data Files**
  - CORSAIR - customized output files
  - General Codes
    - **standard Plot3D files**
    - **xy point files**
- **Types of Animations**
  - envelopes
  - line plots
  - contours
  - vectors
- **Customization of animations**

2-Stage Turbine Pressure Contour

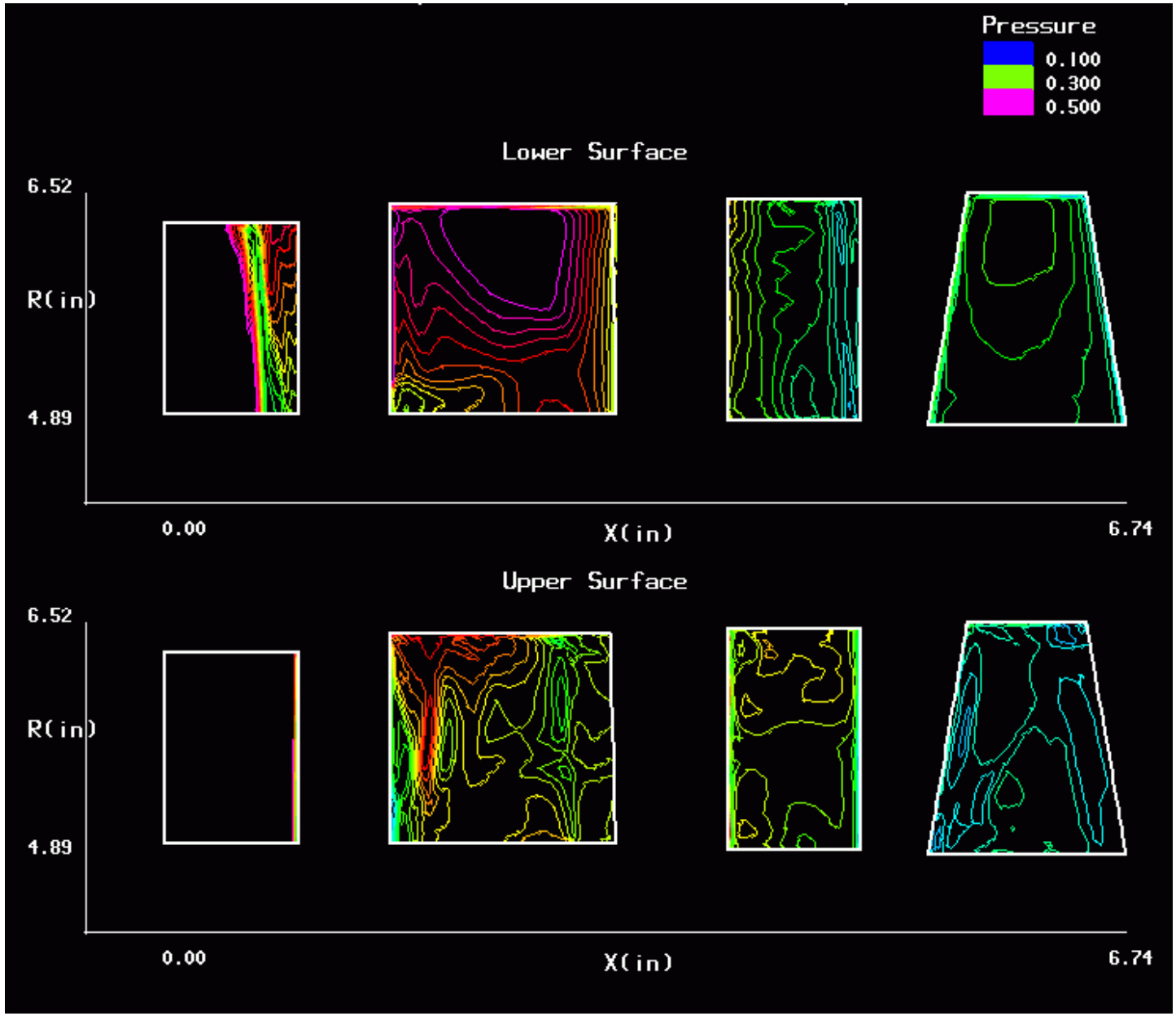

Future Plans for Animator

- Add the calculation of streamlines/streaklines
- Include a GUI to specify the view in 3D
- Include automated feature extraction

Conclusions

- **Pre-Processing**
  - significantly reduced time needed for error checking
  - eliminate ambiguities in input files
- **Interim-Processing**
  - improved ability to detect convergence
  - improved understanding of underlying flow mechanisms
- **Post-Processing**
  - improved understanding of underlying flow mechanisms
  - improved technology transfer
- **Improved Designs**

Stage Separation CFD Tool Development and Evaluation

9/11/01

Alan Droege

NASA-MSFC

Reynaldo Gomez

NASA-JSC

and Ten-See Wang

NASA-MSFC

Stage Separation CFD Tool Development and Evaluation

- Background
- Flow Solver Descriptions
- Initial Results
- Lessons Learned
- Future Work

A. Droege, R. Gomez, and T-S Wang

Background

- Second generation reusable launch vehicle (2nd gen. RLV)
  - Space shuttle was the 1st gen. RLV.
  - 2nd gen. RLV concepts - two stages to orbit
  - Risk reduction tasks in FY01 through FY05. Architecture downselect in FY03, full scale development decision in FY06.
- Stage Separation of two lifting/winged bodies - issues
  - Possible recontact after separation, plume impingement, or other unforeseen separation behavior
  - Therefore, aerodynamic and plume data is needed for separation and control system designs.
- Some CFD tools are available and others are being developed. They need to be benchmarked for this type of problem.

Background (continued)

- Purpose of this task - CFD tool demonstration and validation for second generation RLV stage separation
- Little work has been done in CFD for side by side separation of large lifting/winged bodies
- CFD is needed to expand experimental databases and to cover flow regimes not covered in testing
- Data for multiple configurations is needed to screen 2nd gen. RLV designs in the early design phases - CFD will be faster than test

Langley Glide Back Booster Bimese Configuration

- LGBB concept developed by the Vehicle Analysis Branch of Langley Research Center
- Bimese configuration uses OML of two LGBBs belly to belly without canards
- Bimese configuration chosen for aerodynamic tool development because it is a representative 2nd gen. configuration but is not a “real” configuration.

Flow Solver Descriptions

- Cart3D
- Overflow/Overflow-D
- Unic

Cart3D

- Cartesian mesh, Euler solver
- Advantages: Automated meshing, highly parallel, rapid turnaround
- Disadvantages: inviscid, single species, no automatic 6-DOF capability
- Under development: automatic adaption, propulsive flow boundary conditions, viscous capabilities
- Potential 2nd gen. RLV application: early development phases

Overflow/Overflow-D

- Body fitted mesh near body, Cartesian mesh in far field, Chimera, Navier-Stokes solver
- Advantages: Parallel, viscous, moving body, large user base, some grid adaption, multi-species
- Disadvantages: no automatic grid generation, no chemistry
- Under development: Overflow and Overflow-D are being combined to get a code with Overflow's multigrid, grid sequencing, improved turbulence models, and Fortran 90 coding and Overflow-D's moving body 6-DOF, adaptive Cartesian background grid, and MPI capabilities.
- Potential 2nd gen. RLV application: all but the earliest development phases

A. Droege, R. Gomez, and T-S Wang

Unic

- Unstructured mesh, Navier-Stokes solver
- Advantages: Parallel, viscous, reacting flow chemistry, easy grid generation, mesh adaption, 6-DOF using assumed trajectory
- Disadvantages: code is still under development
- Under development: MPI, multi-body 6-DOF, mesh refinement
- Potential 2nd gen. RLV application: all development phases

Overflow grid system
Generated using Gridgen v13 + CGT

Single LGBB overset grid system

17 zones

4.3 x 10^6 volume points

46 x 10^3 surface points

Wall spacing: y+ < 1 at UPWT conditions

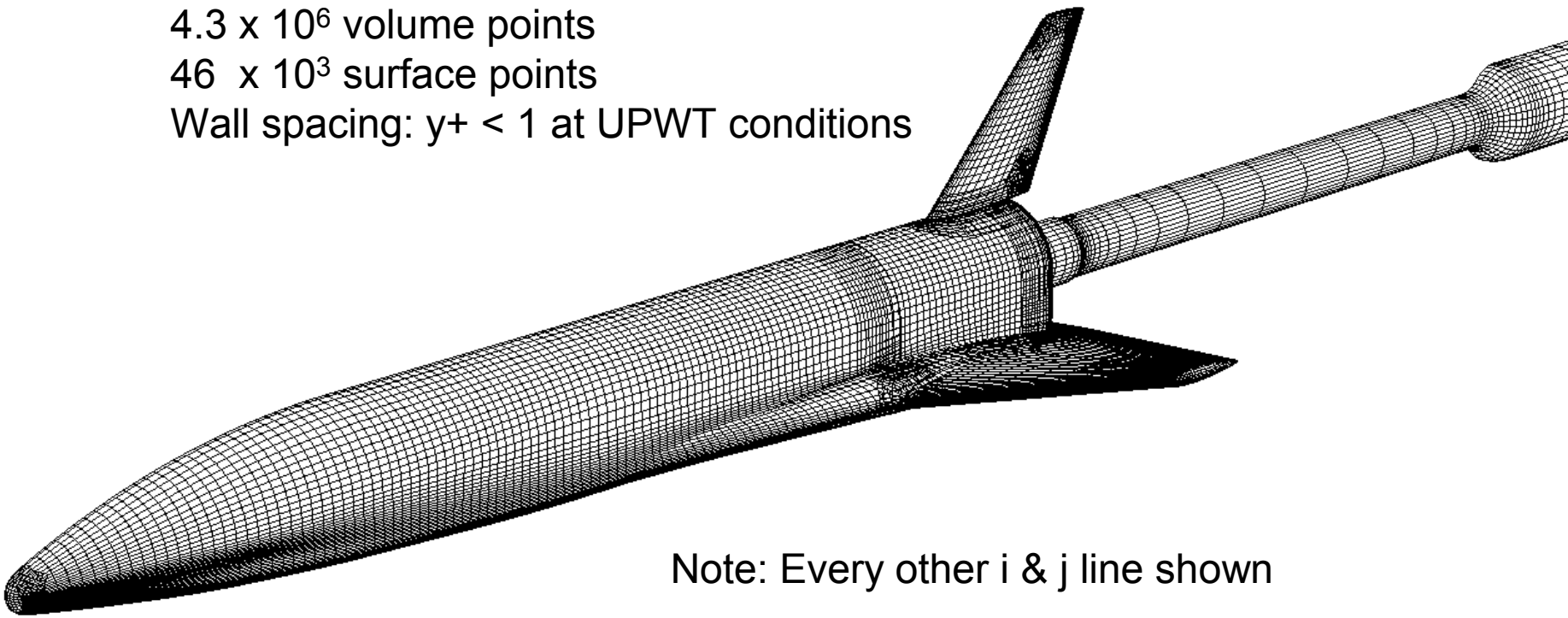

Note: Every other i & j line shown

A. Droege, R. Gomez, and T-S Wang

Overflow solution

Mach 3.0 UPWT

- 1.75% LGBB
- No wind tunnel stings
- 0.8” separation distance
- Cp on vehicle surface
- Mach number on y = 0 plane

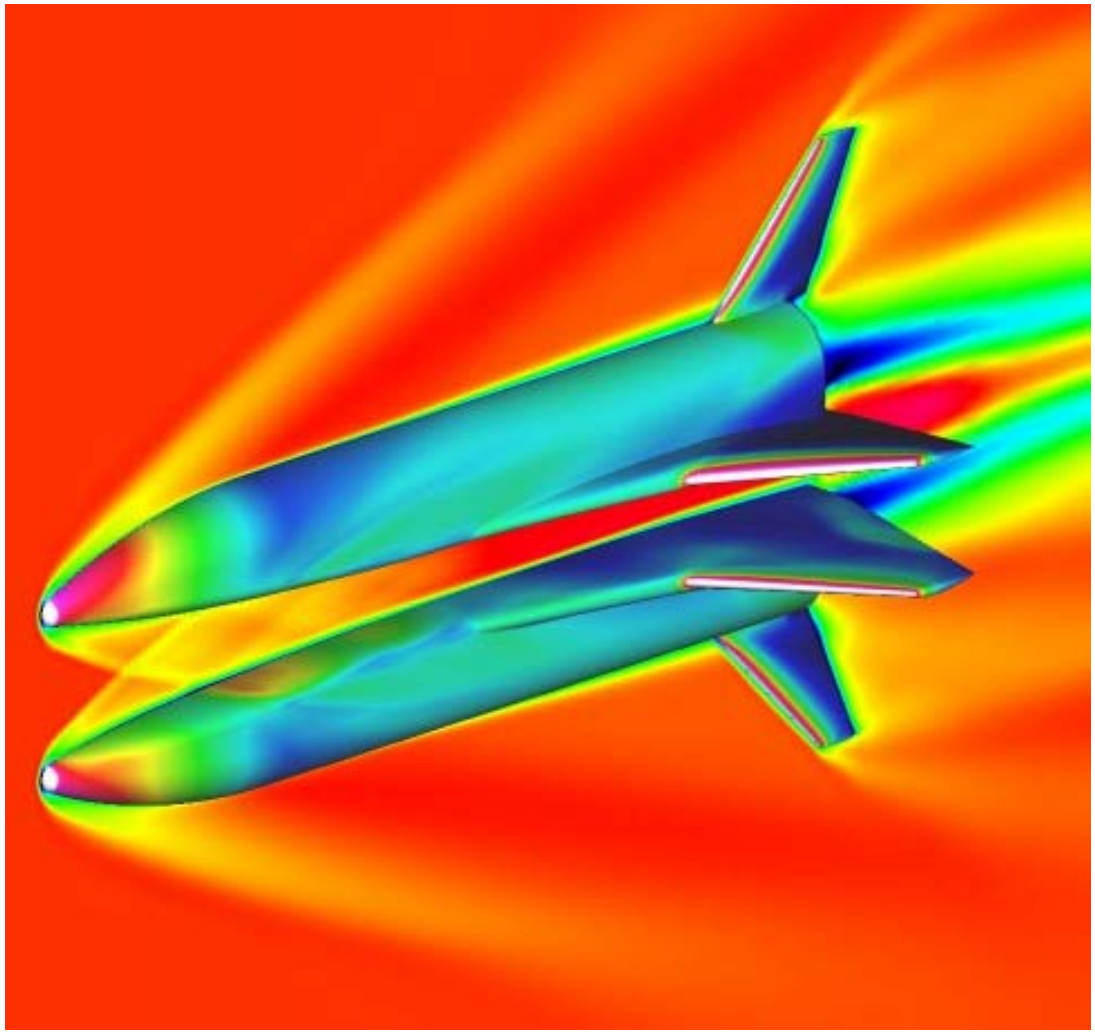

A. Droege, R. Gomez, and T-S Wang

Cart3D grid system

Sample LGBB Cartesian grid system

1.1 x 10^6 cells

7 levels of grid refinement

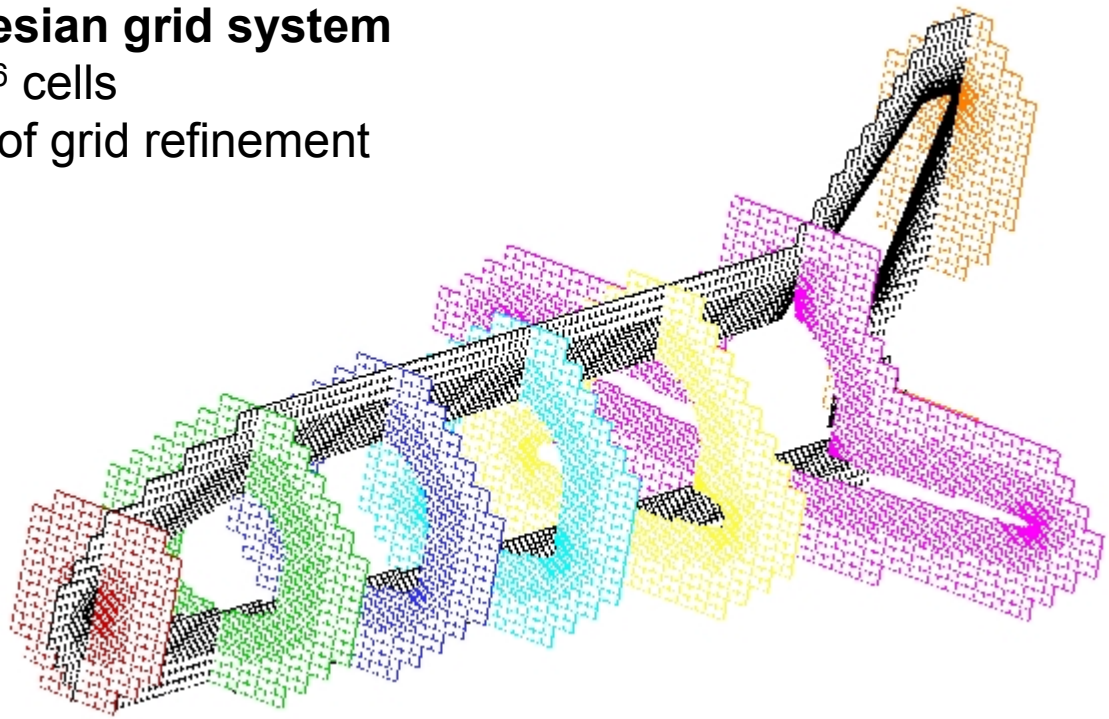

Note: 3 coarsest levels of refinement not shown

A. Droege, R. Gomez, and T-S Wang

Cart3D solution

Upper Surface

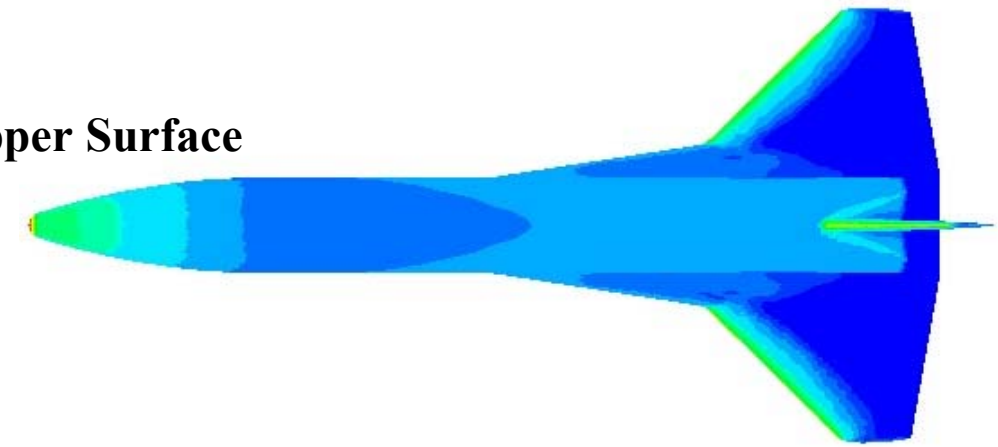

Mach 3.0

- 1.75% LGBB
- No wind tunnel stings
- 0.42” separation distance
- Cp on vehicle surface

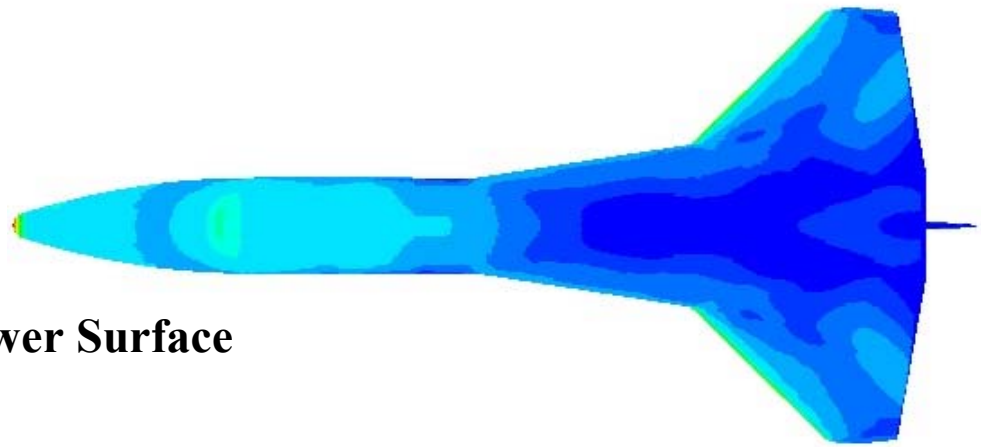

Lower Surface

A. Droege, R. Gomez, and T-S Wang

Lessons Learned

- Massively parallel computers and flow solvers have helped bring CFD into the realm of preliminary design tools for vehicle aerodynamics.
- Automated and semi-automated meshing tools in the hands of experienced users have yielded good meshes in a significantly reduced amount of time when compared to work done just a few years ago - Faster, Better, Cheaper.
- Automation of run set-up, convergence checking, and postprocessing is needed. It exists, but is not tightly coupled with the codes investigated in this study.
- Terabytes of storage needed for storage of all files associated with a single CFD aerodynamic database. Question: Is it cheaper to keep restart files or just rerun cases of interest later?

Future Work

- Cart3D
  - Work on new flow solver (add capabilities)
  - Exercise new flow solver and compare results to old flow solver
  - Compute more cases for comparisons
- Overflow
  - Completion of the integration of Overflow and Overflow-D
  - Exercise the combined flow solver
  - Compute more cases for comparisons

Future Work

- Unic
  - Code completion
  - Single and bimese benchmark calculations and comparisons
  - Plume/vehicle interaction simulations
- All
  - Do an apples-to-apples comparison (between CFD codes and between analytical and experimental results)
  - Investigate sting effects
  - Apply codes to downselected configurations
  - Use CFD tools to impact all phases of the 2nd gen. RLV design process

Time-Dependent Simulations of Turbopump Flows

Cetin Kiris
Dochan Kwak
William Chan
NASA Ames Research Center

Robert Williams
Marshall Space Flight Center

Thermal and Fluids Analysis Workshop
September 10-14, Hunstville AL

Outline

- INTRODUCTION
  - Major Drivers of the Current Work
  - Objective
- SOLUTION METHODS
  - Summary of Solver Development
  - Formulation / Approach
  - Parallel Implementation
- UNSTEADY TURBOPUMP FLOW
  - Scripting Capability
  - Fluid /Structure Coupling
  - Data Compression
- SUMMARY

Major Drivers of Current Work

- To provide computational tools as an economical option for developing future space transportation systems (i.e. RLV subsystems development)

Impact on component design ⇒ Rapid turn-around of high-fidelity analysis
Increase durability/safety ⇒ Accurate quantification of flow
(i.e. prediction of flow-induced vibration)

Impact on system performance ⇒ More complete systems analysis
using high-fidelity tools

- Target

Turbo-pump component analysis ⇒ Entire sub-systems simulation

Computing requirement is large:
⇒ The goal is to achieve 1000 times speed up over what was possible in 1992

Objectives

- To enhance incompressible flow simulation capability for developing aerospace vehicle components, especially, unsteady flow phenomena associated with high speed turbo pump.

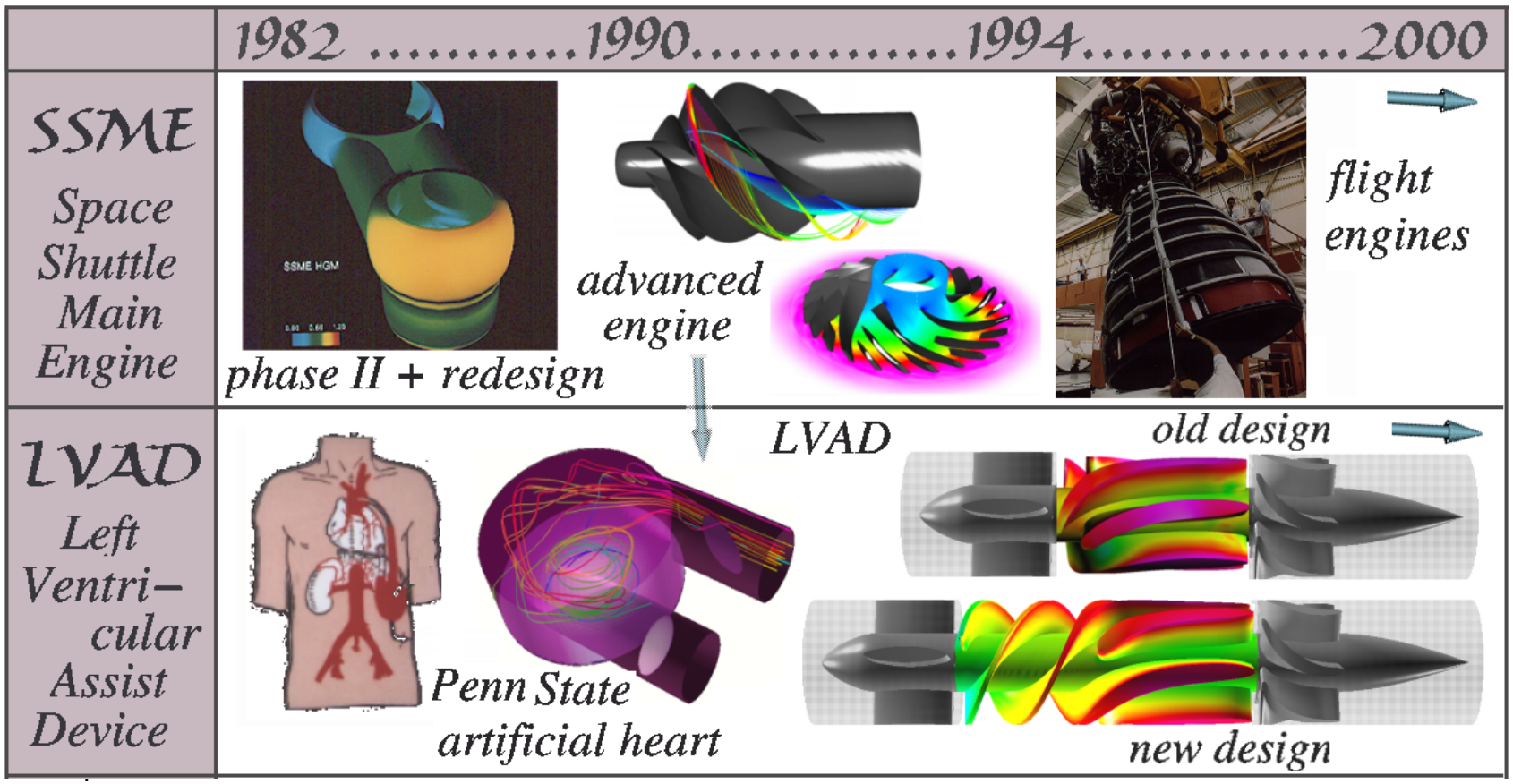

Current Challenges

- Challenges where improvements are needed
  - Time-integration scheme, convergence
  - Moving grid system, zonal connectivity
  - Parallel coding and scalability

- As the computing resources changed to parallel and distributed platforms, computer science aspects become important.
  - Scalability (algorithmic & implementation)
  - Portability, transparent coding, etc.

- Computing resources
  - "Grid" computing will provide new computing resources for problem solving environment
  - High-fidelity flow analysis is likely to be performed using "super node" which is largely based on parallel architecture

INS3D – Incompressible N-S Solver

** ***Parallel version :***

- MPI and MLP parallel versions
- Structured, overset grid orientation
- Moving grid capability
- Based on method of artificial compressibility
- Both steady-state and time-accurate formulations
- 3rd and 5th-order flux difference splitting for convective terms
- Central differencing for viscous terms
- One- and two-equations turbulence models
- Several linear solvers : GMRES, GS line-relaxation, LU-SGS, GS point relaxation, ILU(0)..,..

- HISTORY

** 1982-1987 Original version of INS3D – Kwak, Chang

** 1988-1999 Three different versions were devoped :

INS3D-UP / Rogers, Kiris, Kwak
INS3D-LU / Yoon, Kwak
INS3D-FS / Rosenfeld, Kiris, Kwak

Time Accurate Formulation

- Time-integration scheme

Artificial Compressibility Formulation

· Introduce a pseudo-time level and artificial compressibility
· Iterate the equations in pseudo-time for each time step until incompressibility condition is satisfied.

Pressure Projection Method

· Solve auxiliary velocity field first, then enforce incompressibility condition by solving a Poisson equation for pressure.

Impulsively Started Flat Plate at 90°

- Time History of Stagnation Point

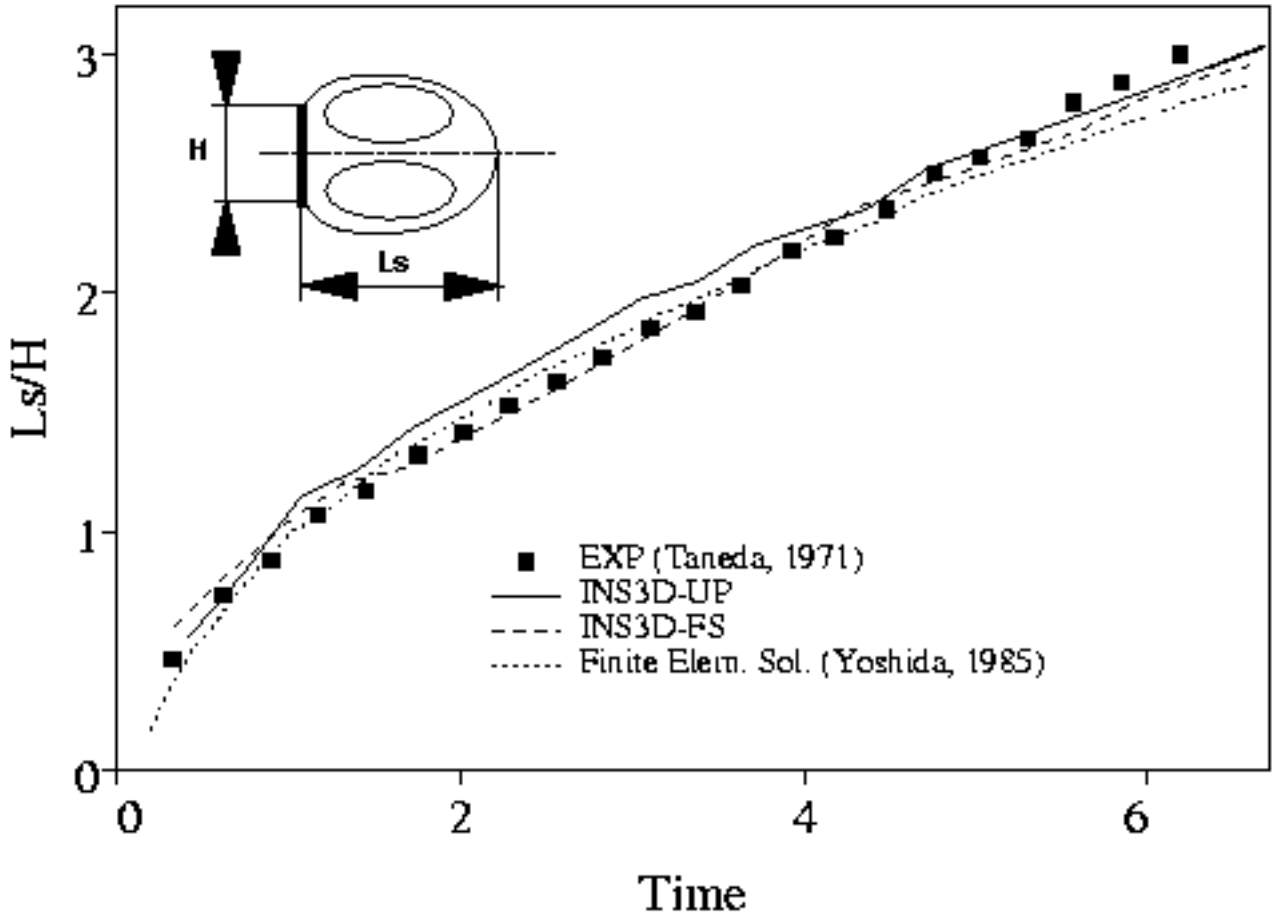

INS3D Parallelization

- INS3D-MPI
  (coarse grain)

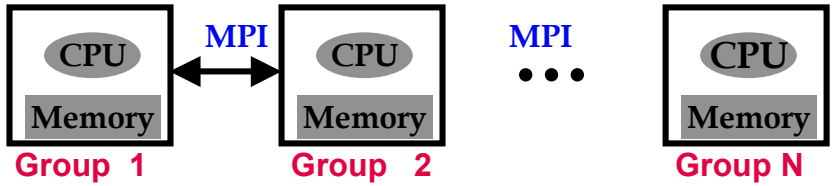

- INS3D-MPI / Open MP
  MPI (coarse grain) + OpenMP (fine grain)
  Implemented using CAPO/CAPT tools

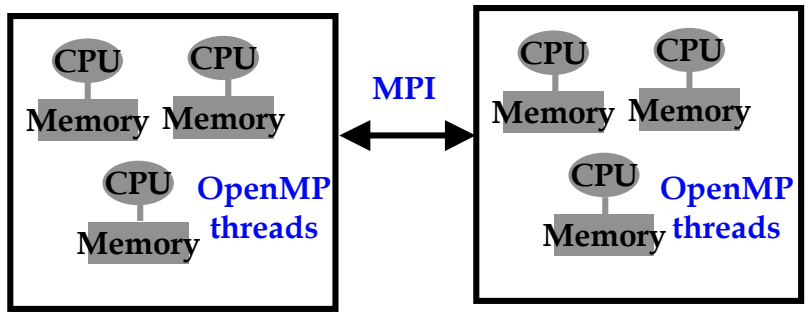

- INS3D-MLP

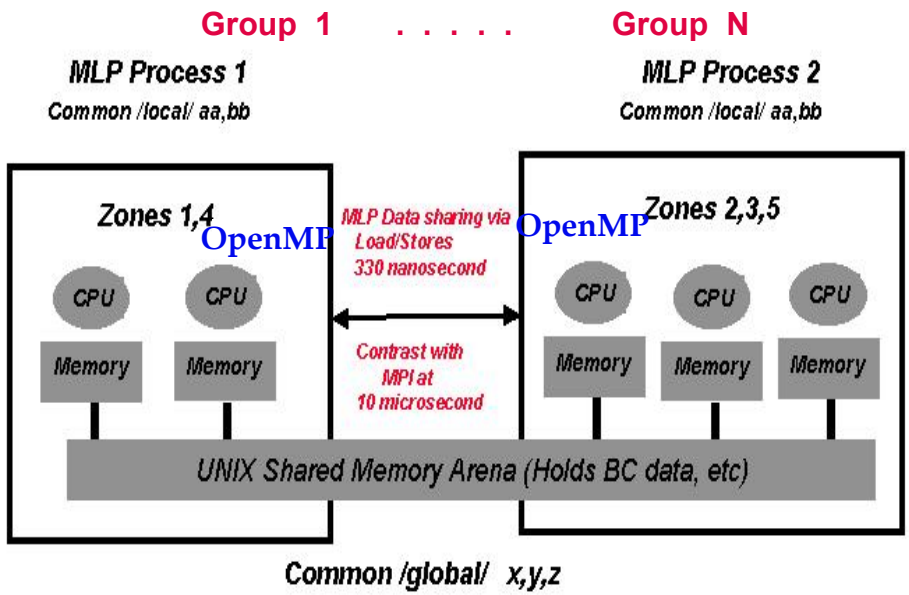

Previous Work (SSME Impeller)

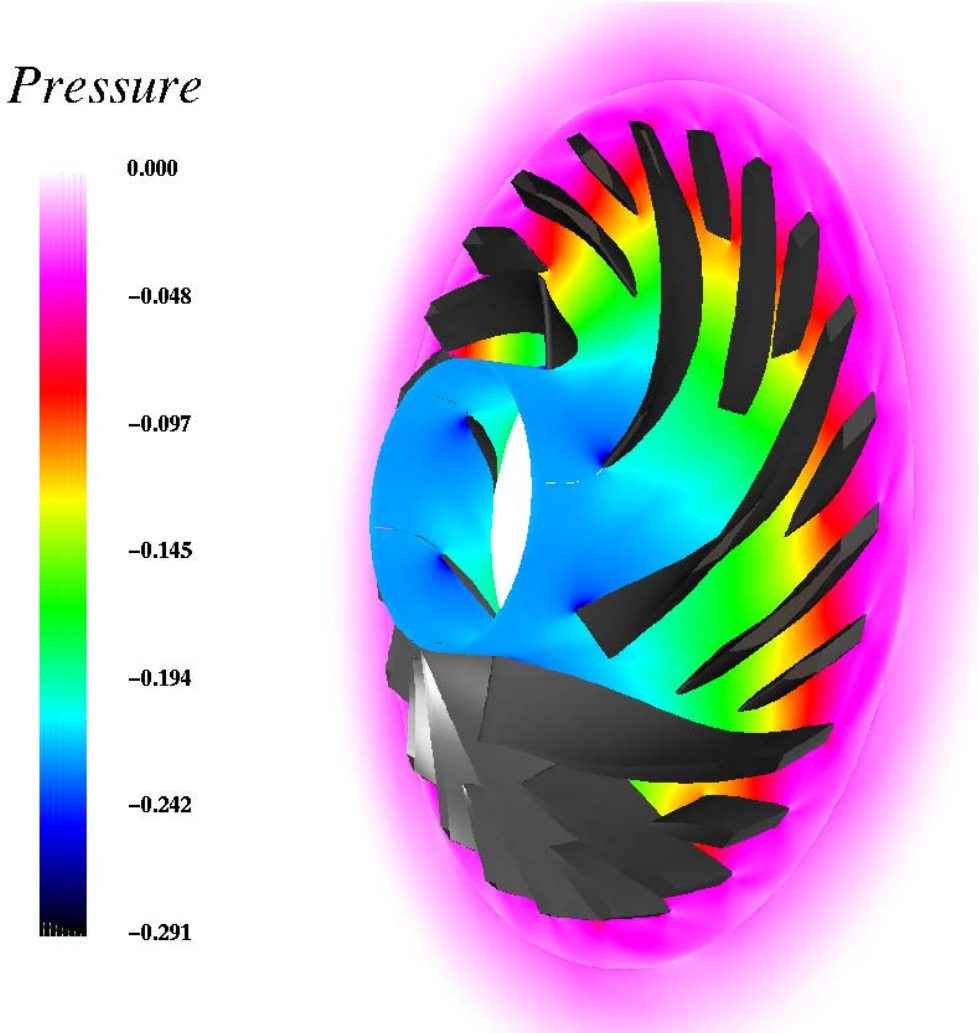

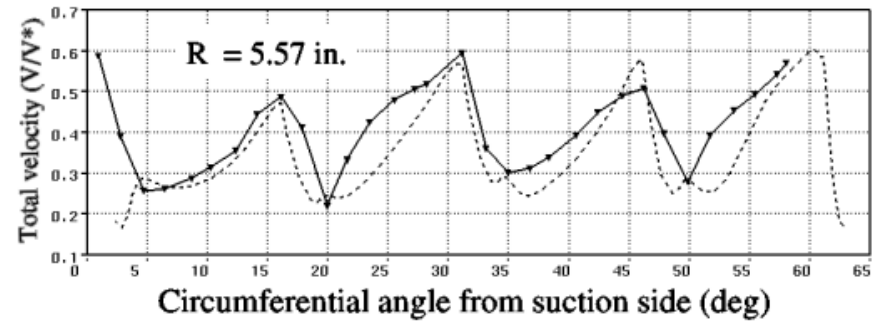

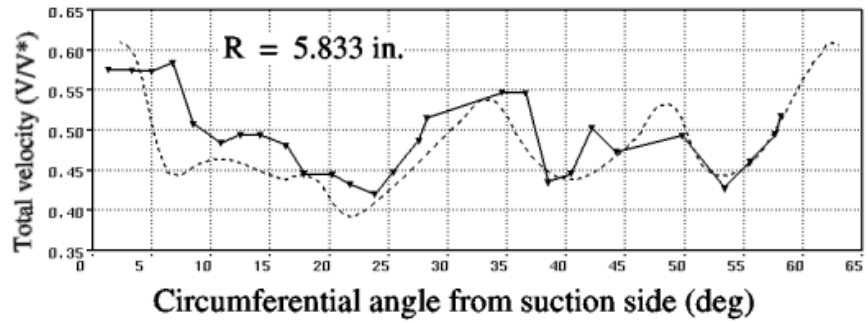

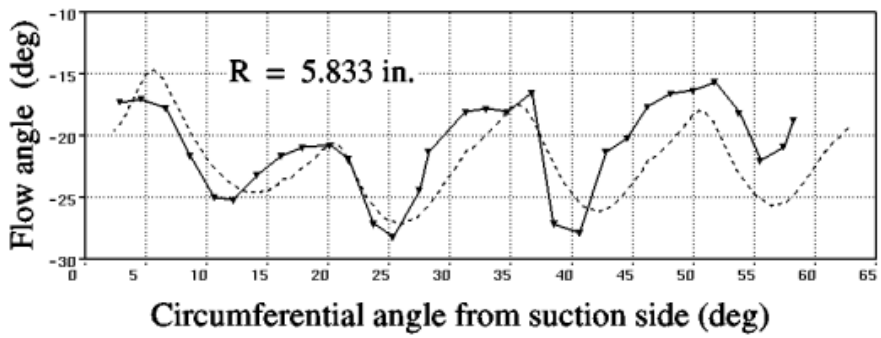

Space Shuttle Main Engine Turbopump

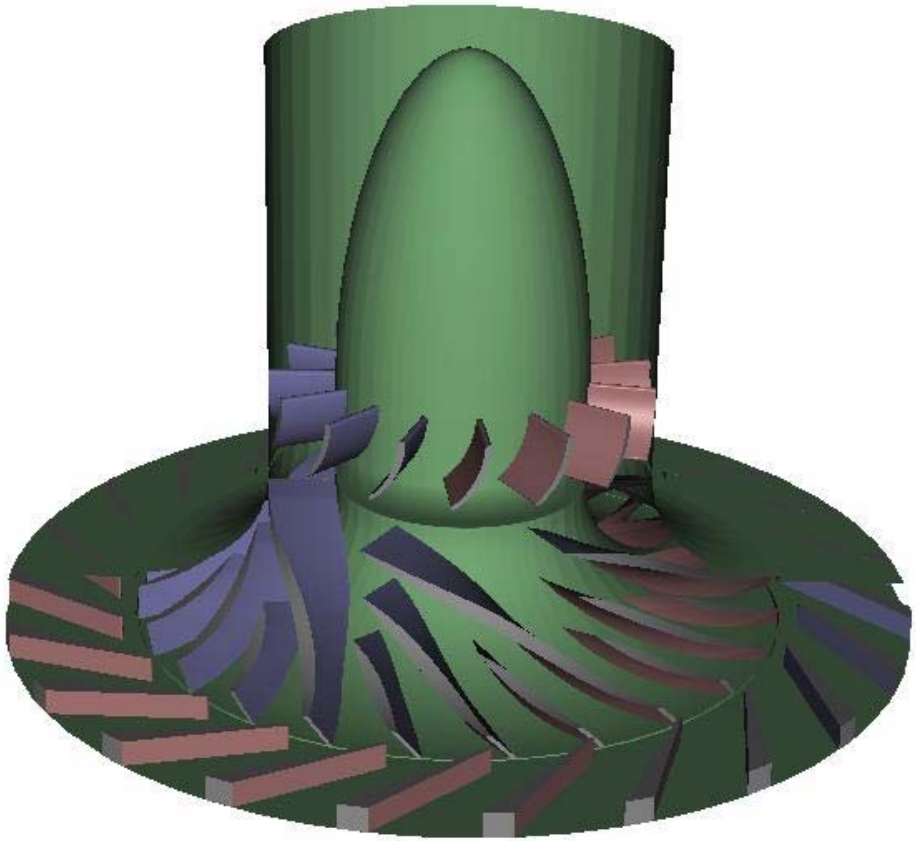

Impeller Technology Water Rig

Baseline SSME/ATD HPFTP Class Unshrouded Impeller

Inlet Guide Vane (IGV)
- **15 Blades**
- **Pitch, p = 24 degrees**
- **Blade Inlet Angle (mean), $\beta_{IGV,1}$ = 90 degrees**
- **Blade Exit Angle (mean), $\beta_{IGV,2}$ = 45 degrees**

Clearance between IGV and Impeller, x = 0.12 inches

Impeller
- **6+6+12 Unshrouded Design**
- **Pitch, p = 60 degrees**
- **Blade Inlet Angle (mean), $\beta_{imp,1}$ = 23 degrees**
- **Blade Exit Angle (mean), $\beta_{imp,2}$ = 65 degrees**
- **Clearance between blade LE and Shroud, r = 0.0056 inches**
- **Clearance between blade TE and Shroud, x = 0.0912 inches**

Clearance between Impeller and Diffuser, r = 0.050 inches

Diffuser
- **23 Blades**
- **Pitch, p = 15.652 degrees**
- **Blade Inlet Angle (mean), $\beta_{dif,,1}$ = 12 degrees**
- **Blade Exit Angle (mean), $\beta_{dif,,2}$ = 43 degrees**

INS3D Parallelization

INS3D-MLP/OpenMP vs. -MPI/OpenMP

TEST CASE : SSME Impeller
60 zones / 19.2 Million points

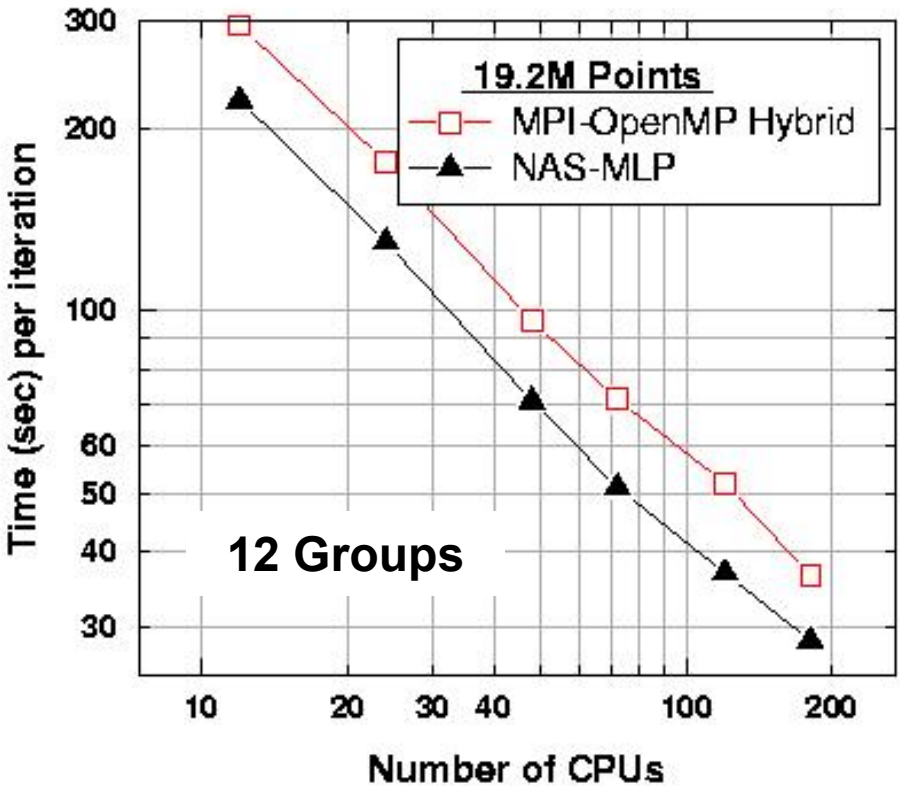

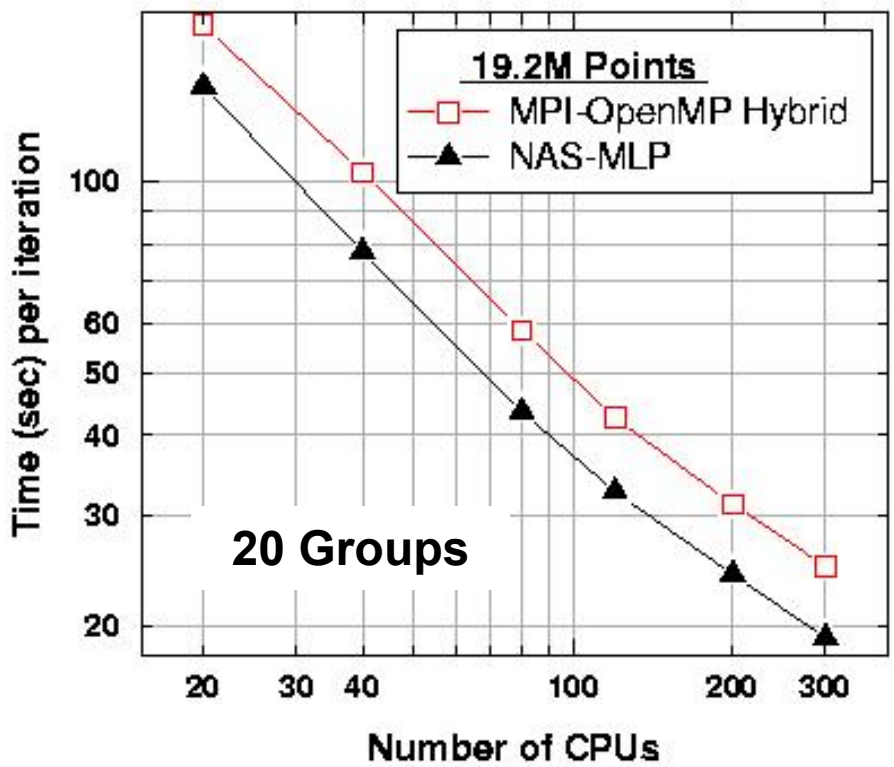

RLV 2nd Gen Turbopump (SSME Rig1)

Impeller Technology Water Rig

Baseline SSME/ATD HPFTP Class Impeller

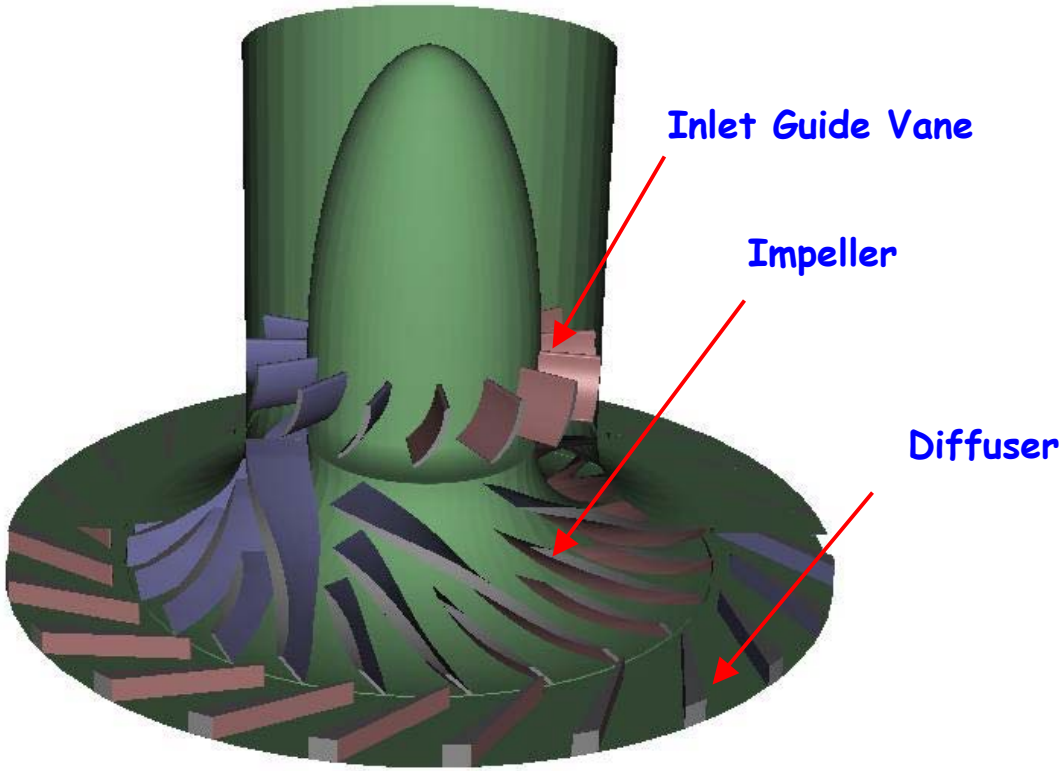

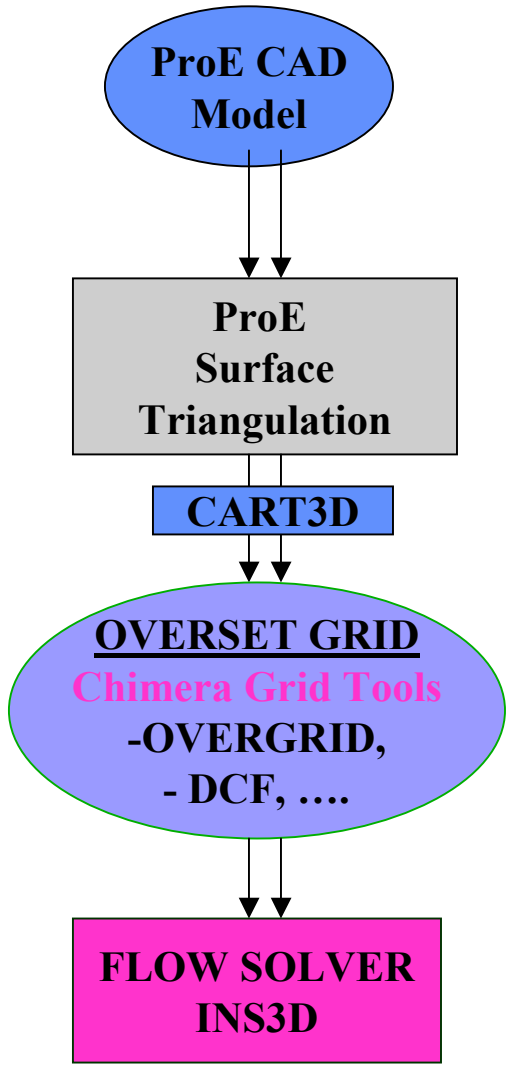

RLV 2nd Gen Turbopump

Overset Grid System

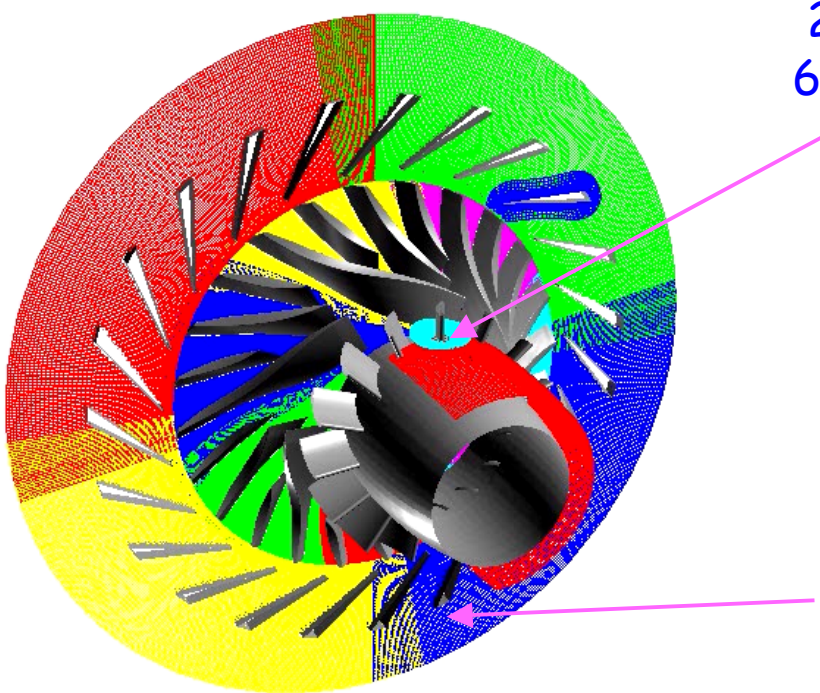

Inlet Guide Vanes
15 Blades
23 Zones
6.5 M Points

Diffuser
23 Blades
31 Zones
8.6 M Points

RLV 2nd Gen Turbopump

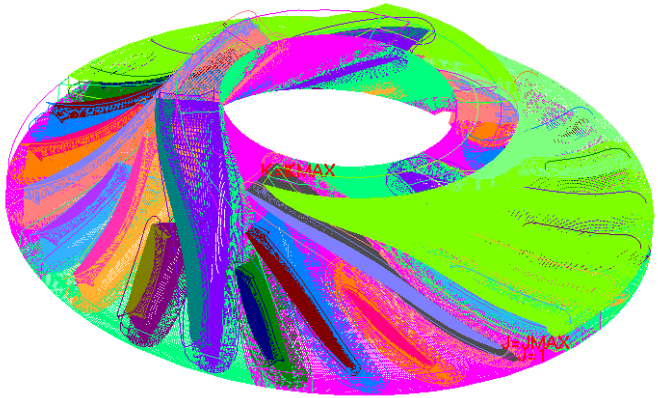

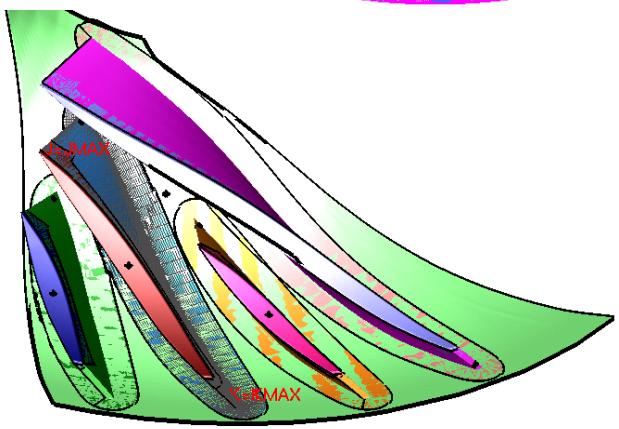

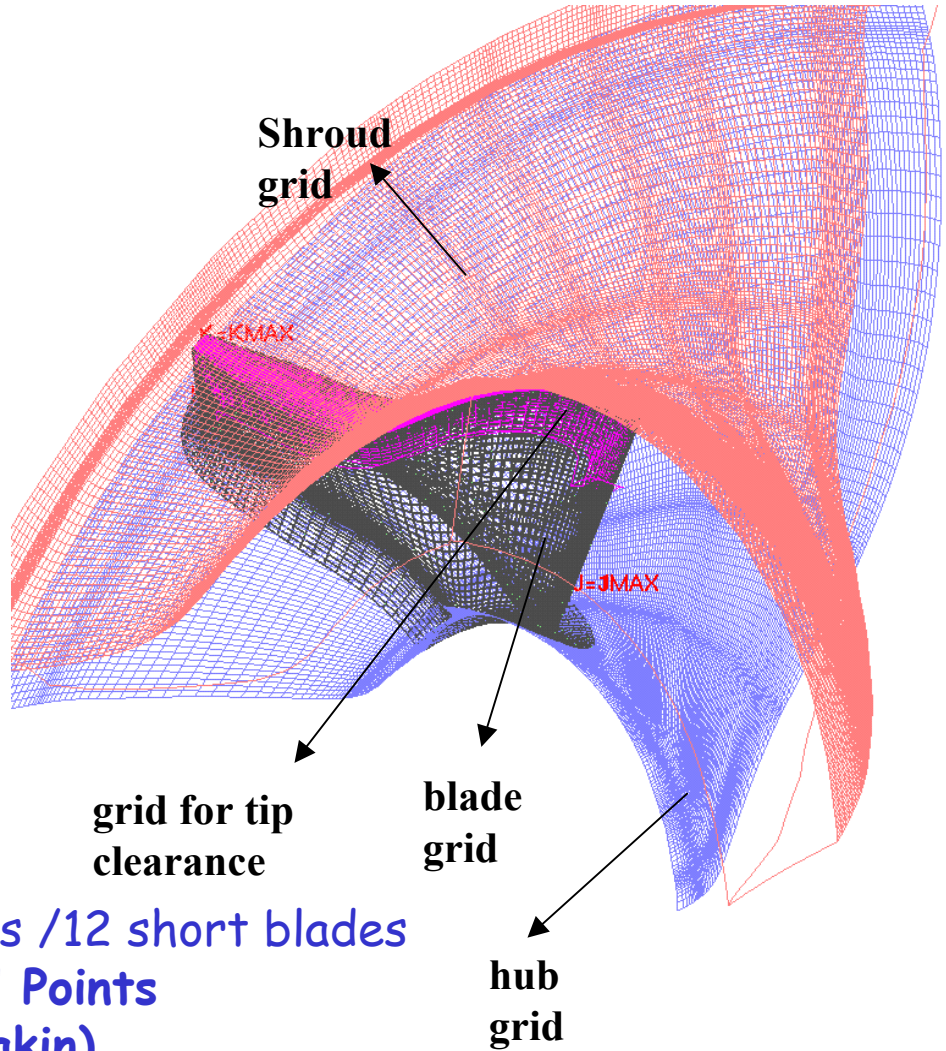

Unshrouded Impeller Grid :

6 long blades / 6 medium blades /12 short blades

60 Zones / 19.2 Million Grid Points

Overset connectivity : DCF (B. Meakin)

Less than 156 orphan points.

Impeller Overset Grid System

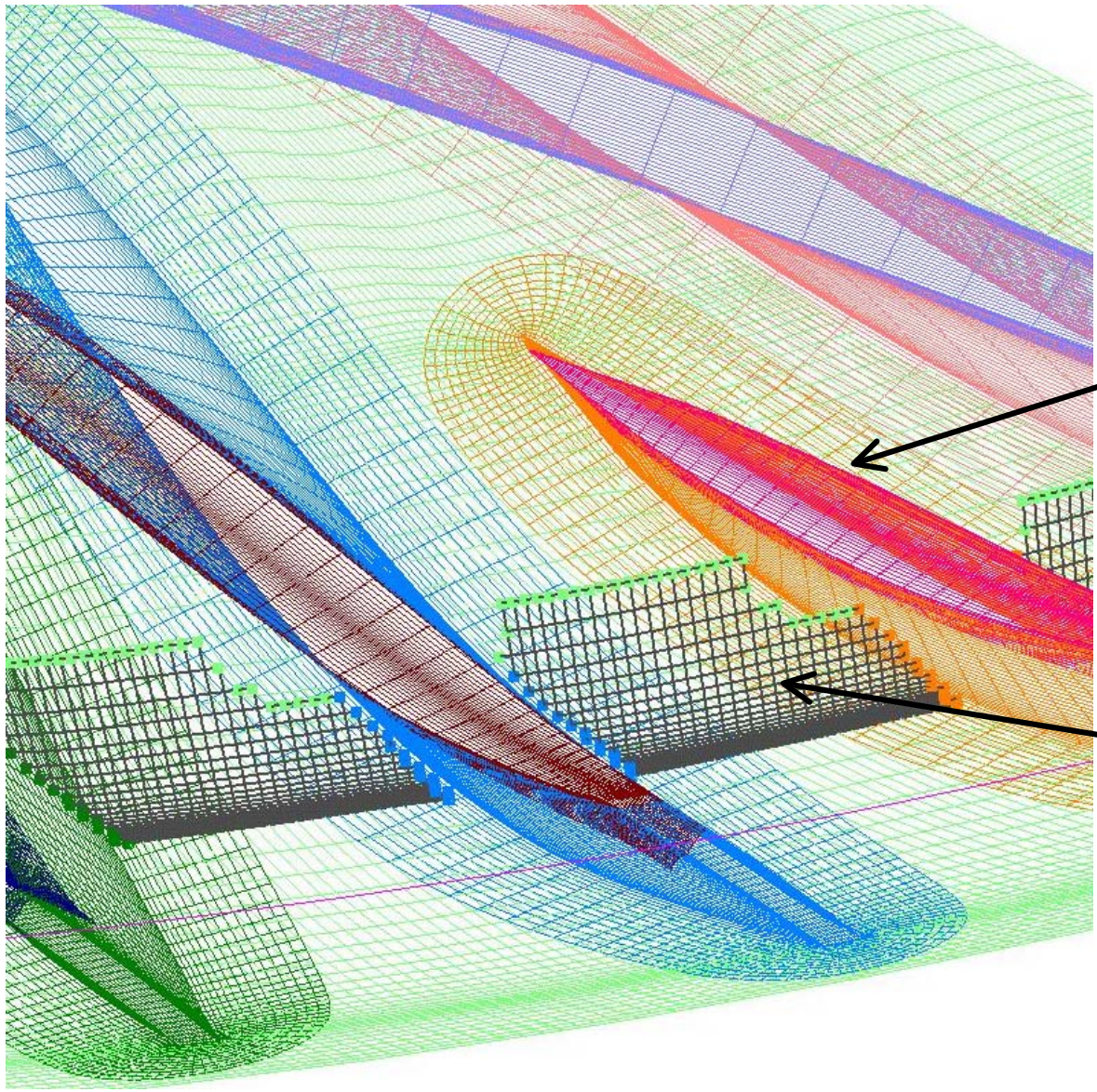

Scripting Capability

SCRIPTING CAPABILITY FOR GRID GENERATION

> Require expertise to build scripts the first time

> Allow rapid re–run of entire grid generation process

> Easy to do grid refinement and parameter studies

> Easy to try different gridding strategies

> Documentation of gridding procedure

> Written in Tcl scripting language

  > works on UNIX, LINUX and WINDOWS

  > integer and floating point arithmetic capability

  > modular procedure calls

  > easy to add GUI later if needed

Scripting Capability

INPUT AND OUTPUT

Current example: one script for each component
(IGV, Impeller and Diffuser)

Input

> profile curve for hub and shroud in PLOT3D format
(rotated by script to form surface of revolution)

> blade and tip surfaces in PLOT3D format

> Parameters that can be changed
- global surface grid spacing (on smooth part of geometry)
- local surface grid spacing (leading/trailing edges, etc.)
- normal wall grid spacing (viscous, wall function)
- marching distance
- grid stretching ratio
- number of blades
- ...

Output

> overset surface and volume grids for hub, shroud, blades

Scripting Capability

INLET GUIDE VANES AND DIFFUSER

	Old IGV	New IGV	Old DIFF	New DIFF
No. of points (million)	7.1	1.1	8.0	1.6
Time to build	1/2 day	10 sec.	1/2 day	8 sec.

Script timings on new grids based on SGI R12k 300MHz processor

Time to build script = 1 day for IGV, 1 day for DIFF

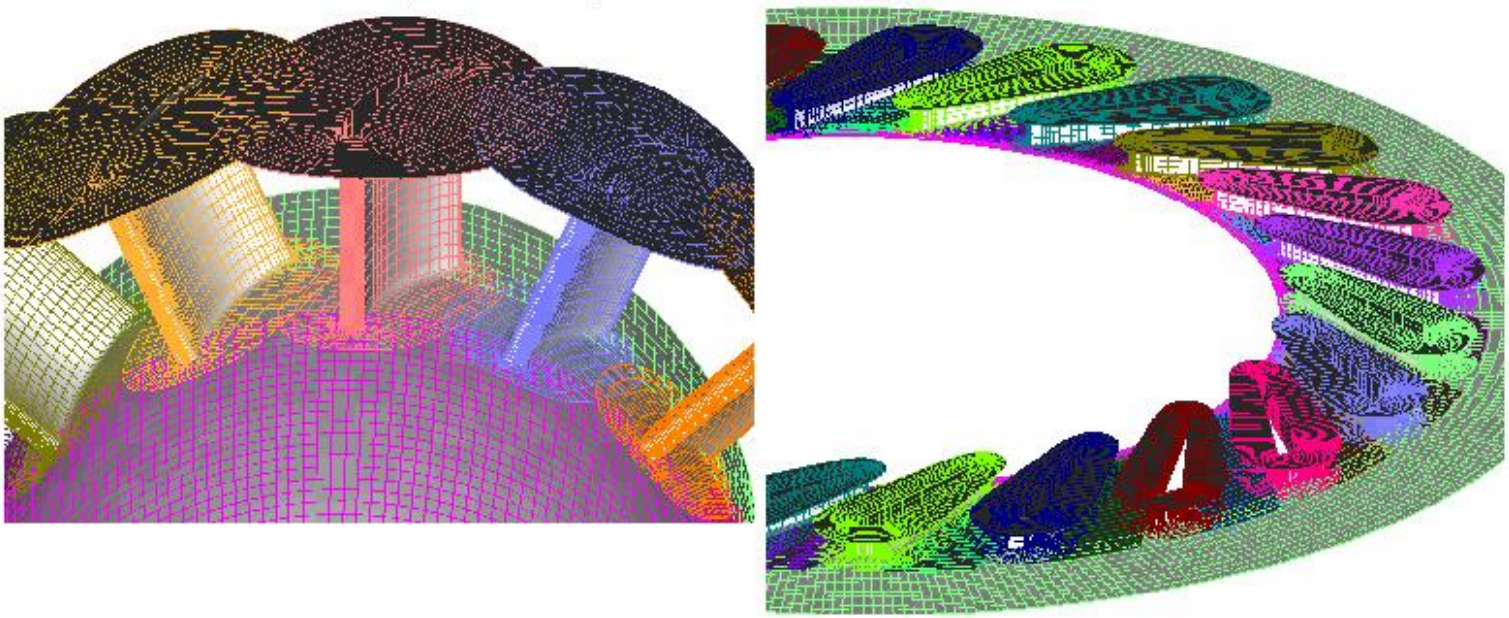

Scripting Capability

IMPELLER

	Old IMP	New IMP	Old TOT	New TOT
No. of points (million)	19.2	5.7	34.3	8.4
Time to build	~ 2 weeks	50 sec.		

Time to build IMP script : 3 to 4 weeks

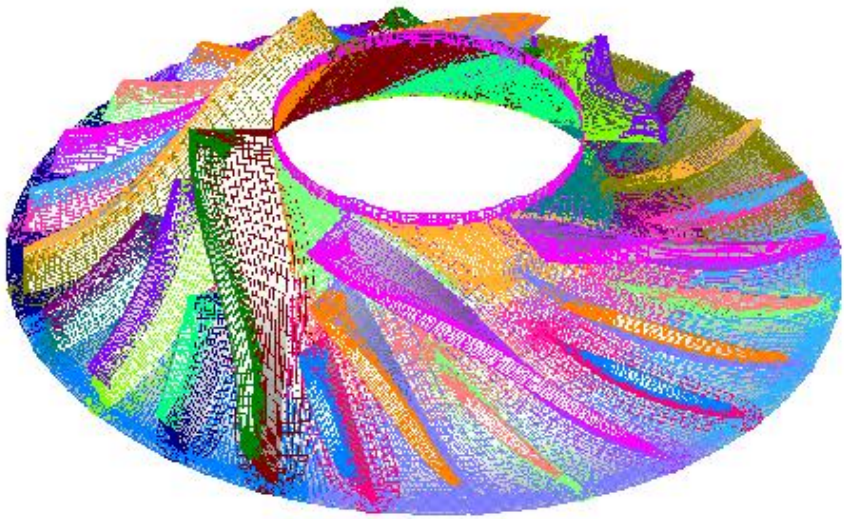

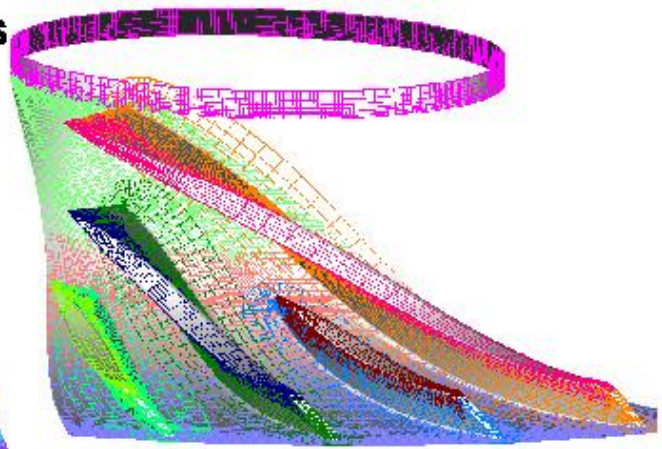

Scripting Capability

FUTURE PLANS FOR SCRIPTING

> Complete domain connectivity capability in scripts (X–ray maps and DCF input file creation)

> Flow solver input creation in scripts

> Perform more tests on different parameters

> Perform tests on different geometries, e.g., volute, inducer

> Improve robustness (error traps, wider range of cases)

> Generic template for each component

> Graphical interface front end

RLV 2nd Gen Turbopump (baseline)

FIRST Rotation : Impeller rotated 30-degrees

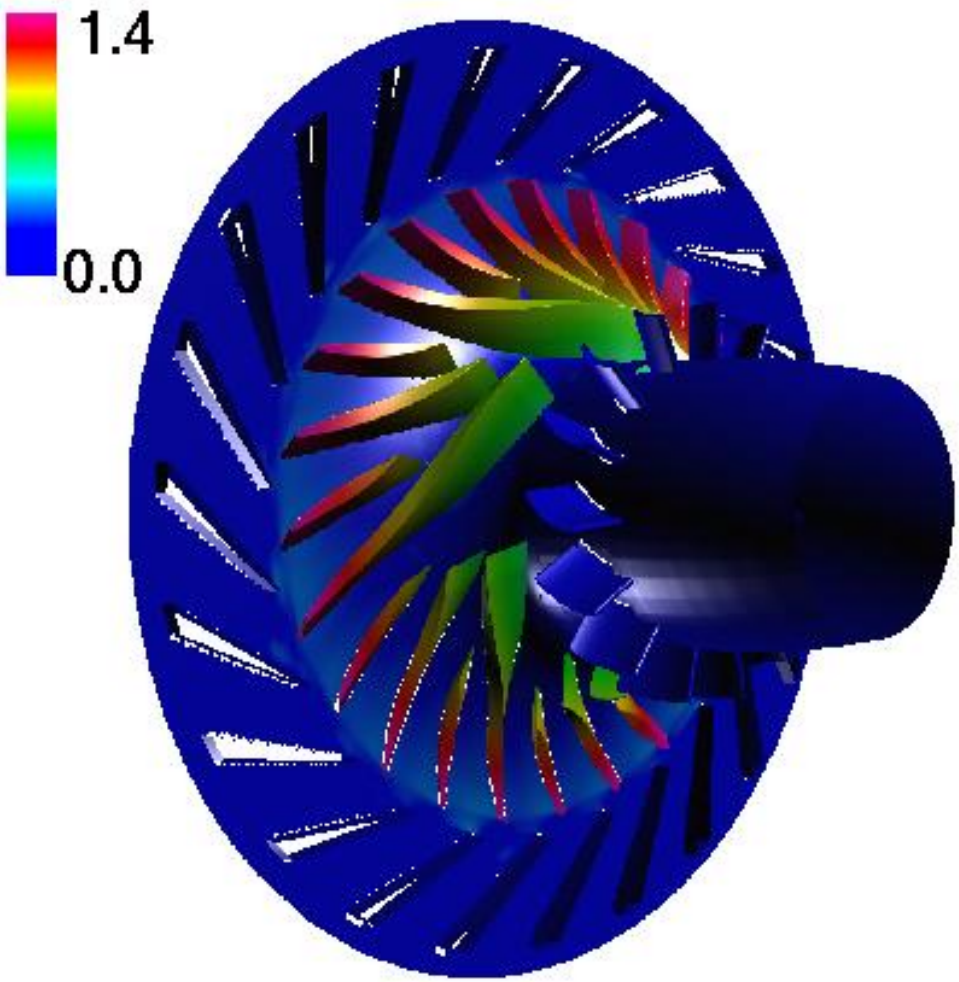

VELOCITY MAGNITUDE

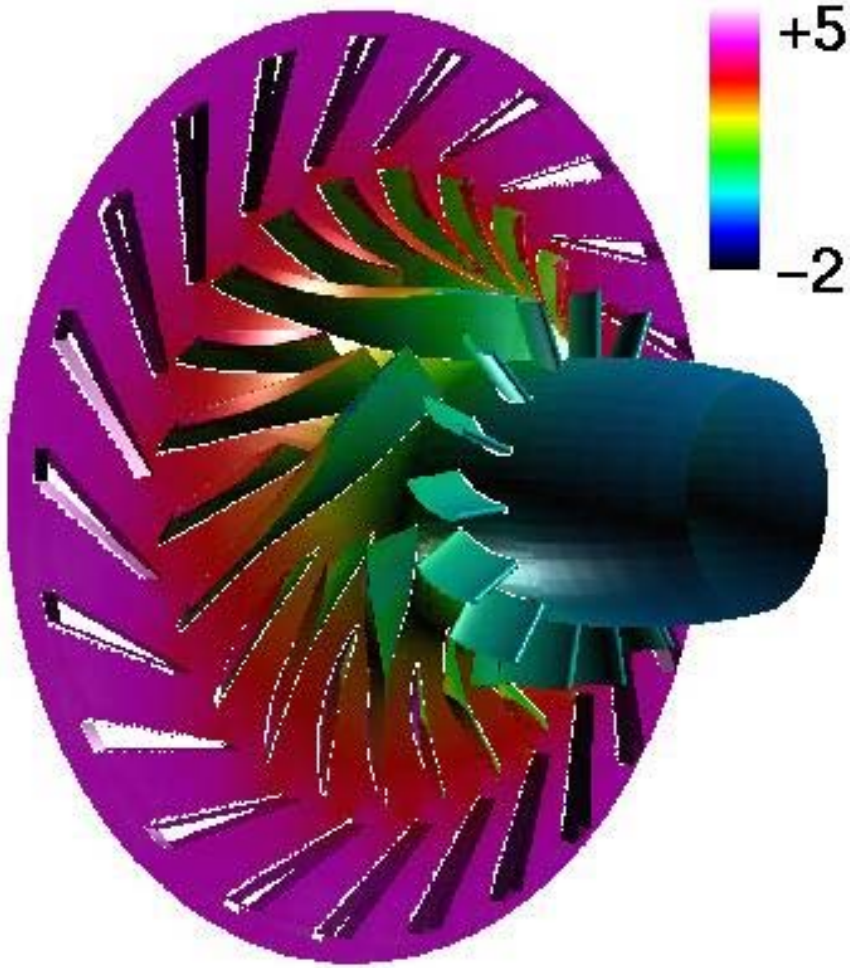

PRESSURE

RLV 2nd Gen Turbopump (baseline)

FIRST Rotation : Impeller rotated 125-degrees

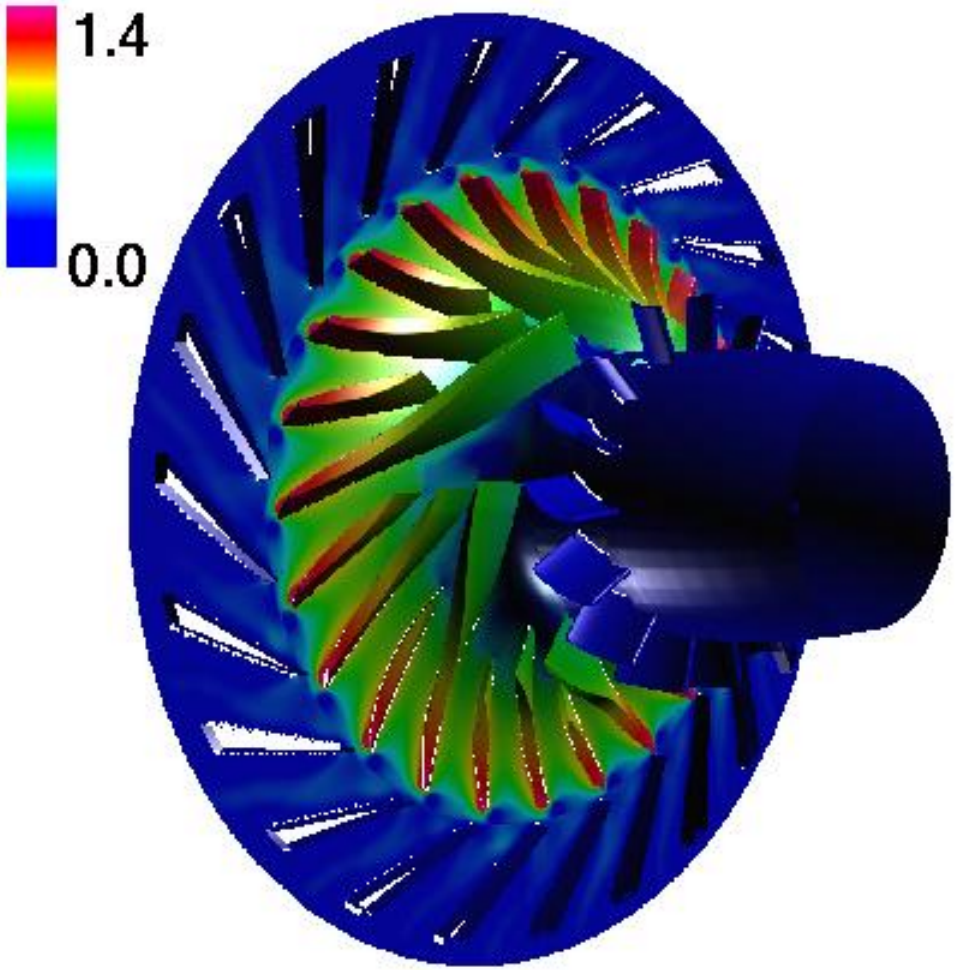

VELOCITY MAGNITUDE

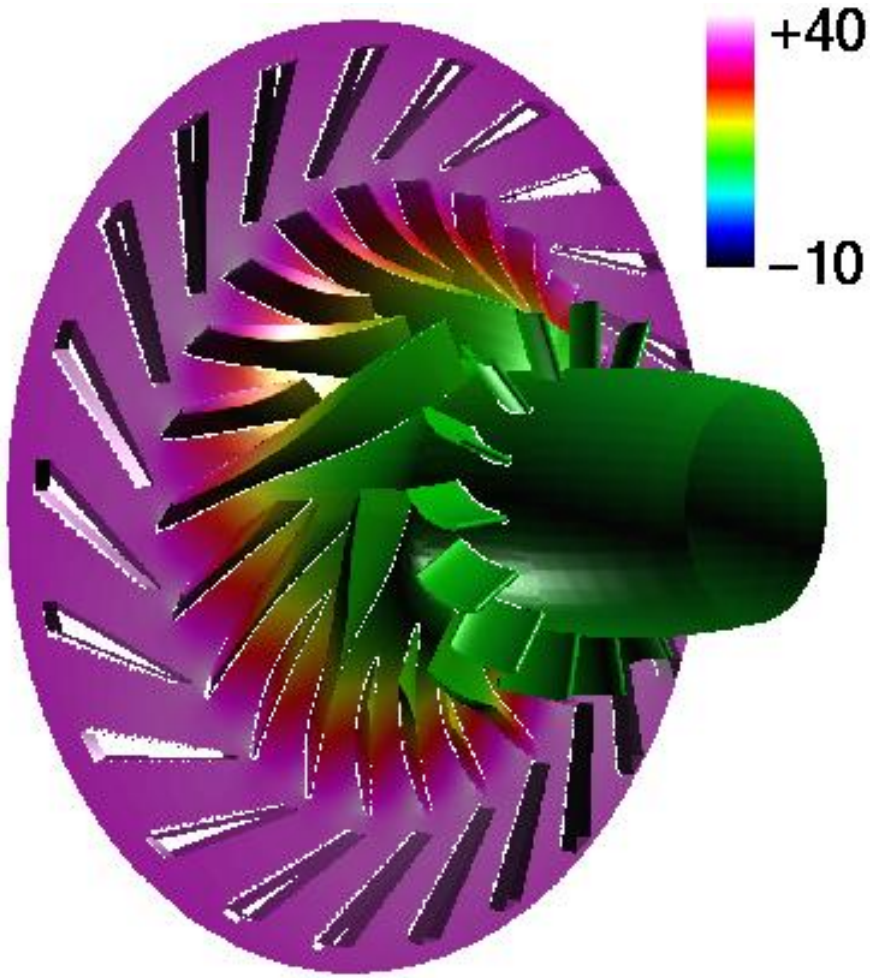

PRESSURE

RLV 2nd Gen Turbopump (baseline)

FIRST Rotation : Impeller rotated 160-degrees

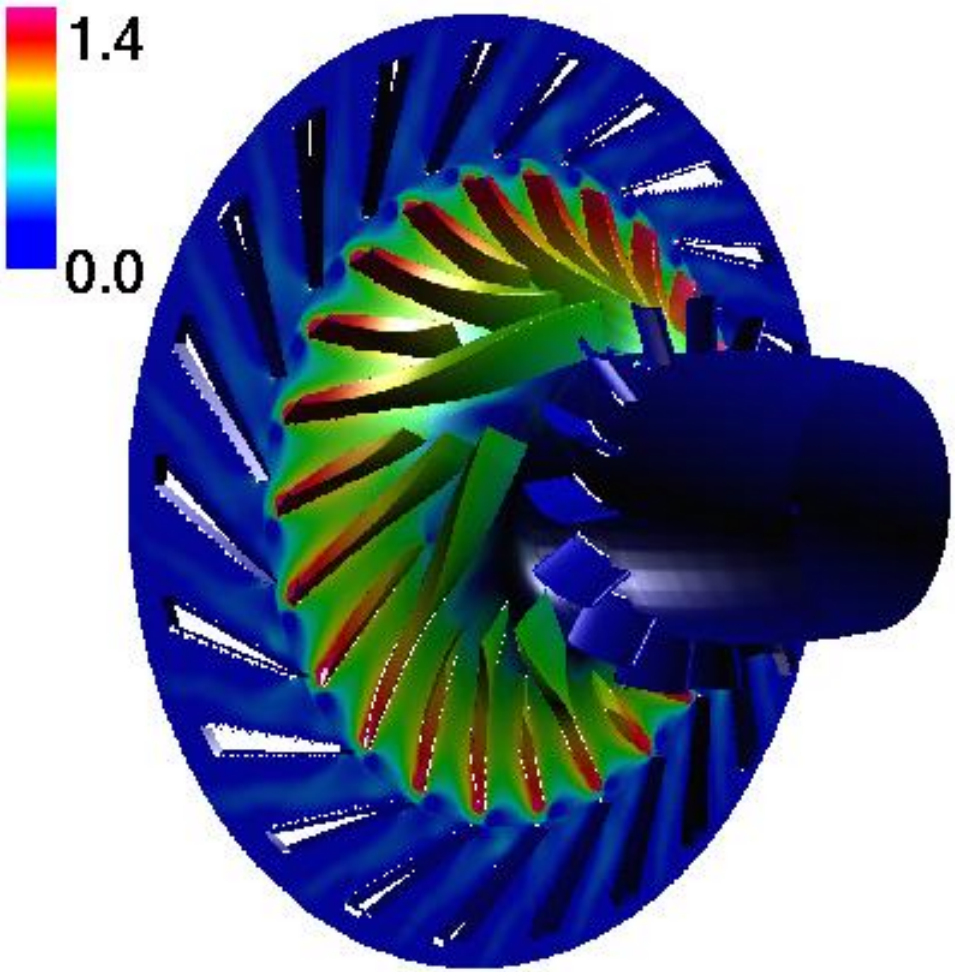

VELOCITY MAGNITUDE

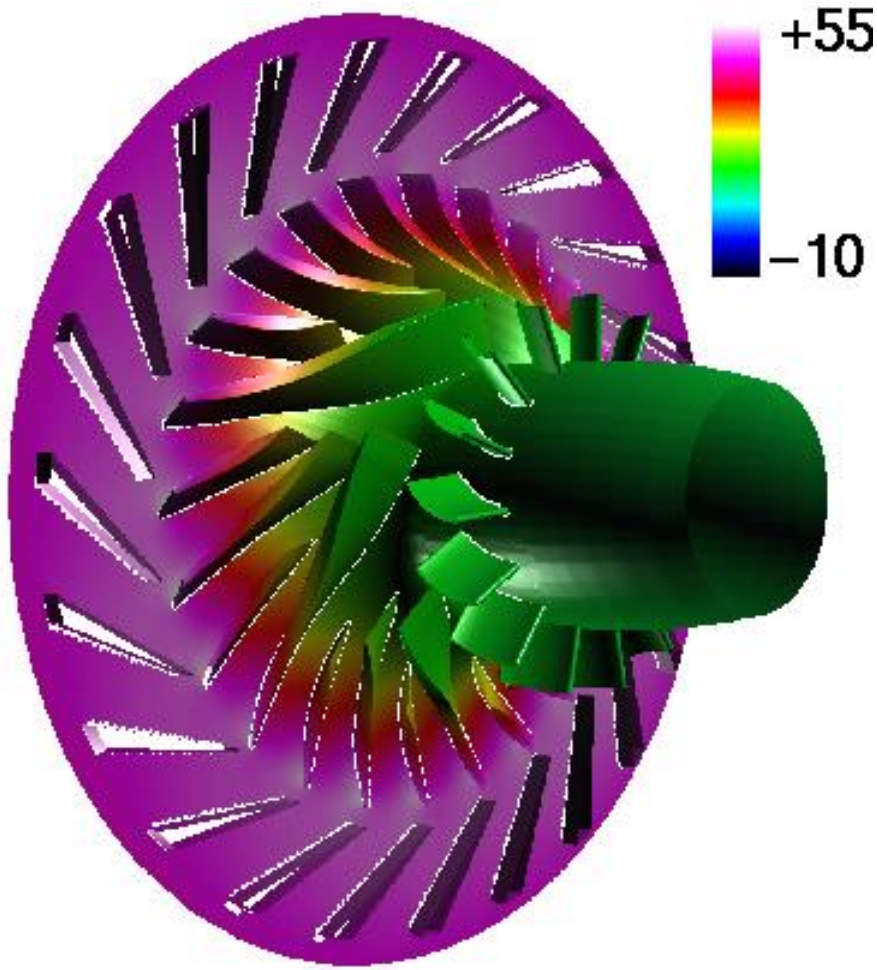

PRESSURE

RLV 2nd Gen Turbopump (baseline)

FIRST Rotation : Impeller rotated 230-degrees

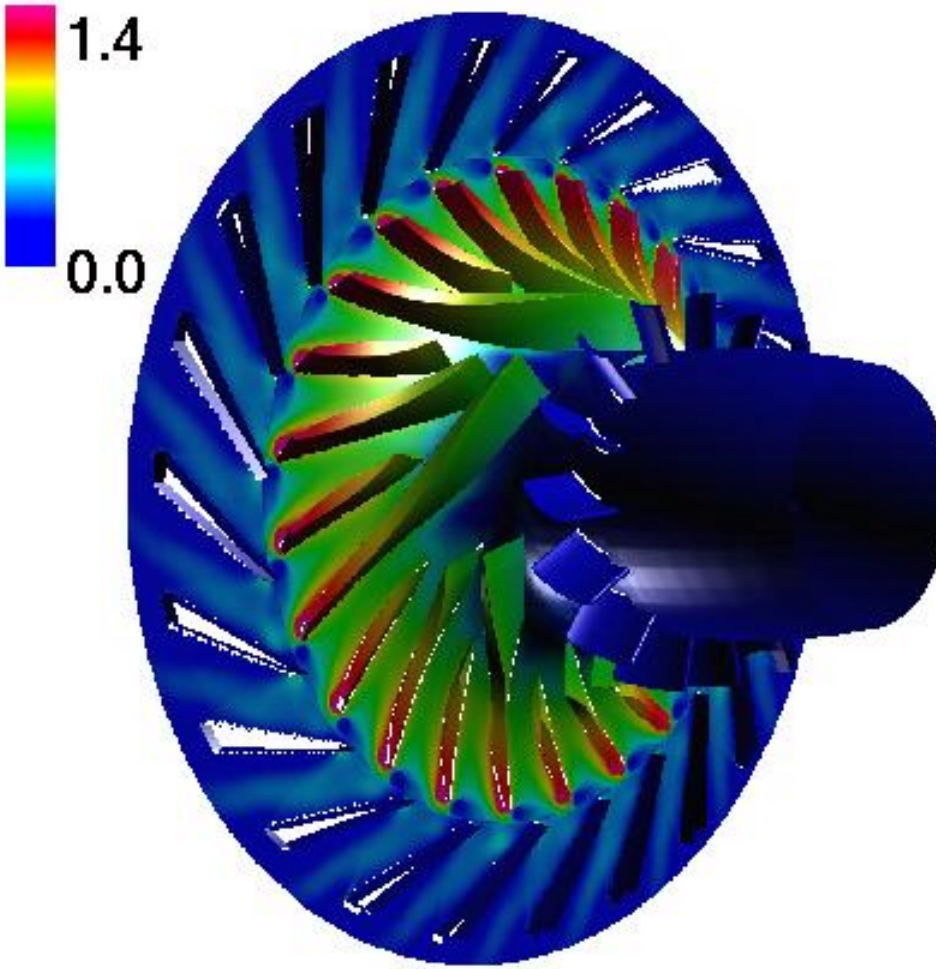

VELOCITY MAGNITUDE

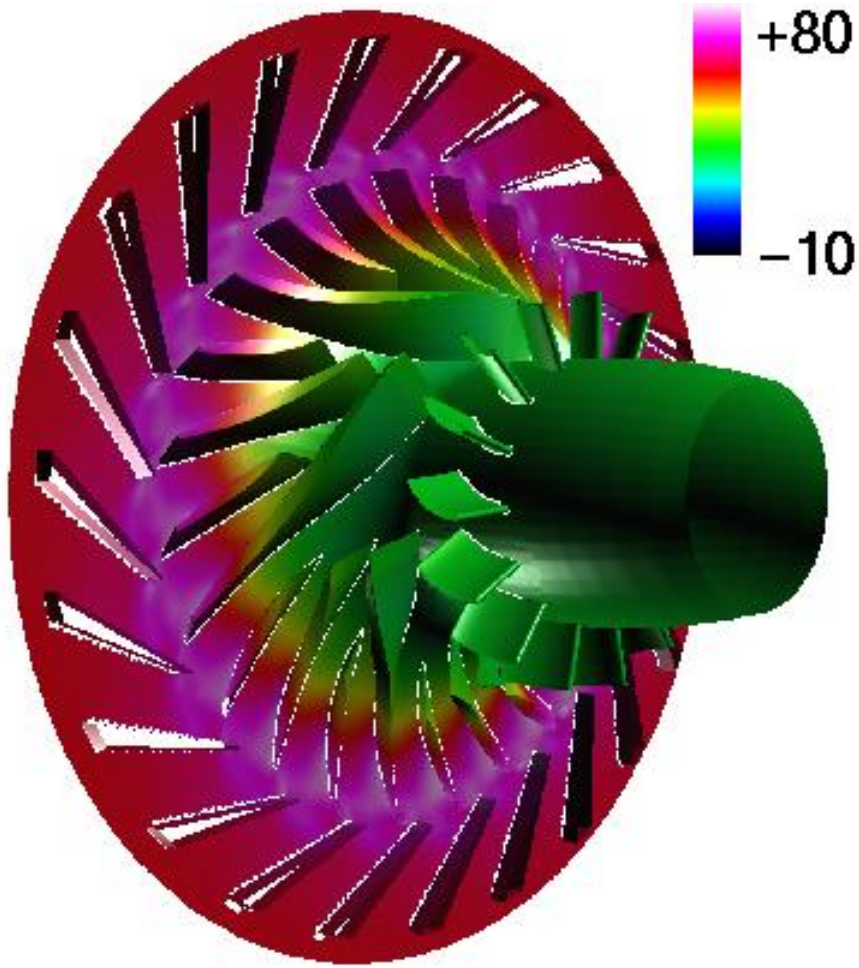

PRESSURE

SSME-rig1 / Initial start

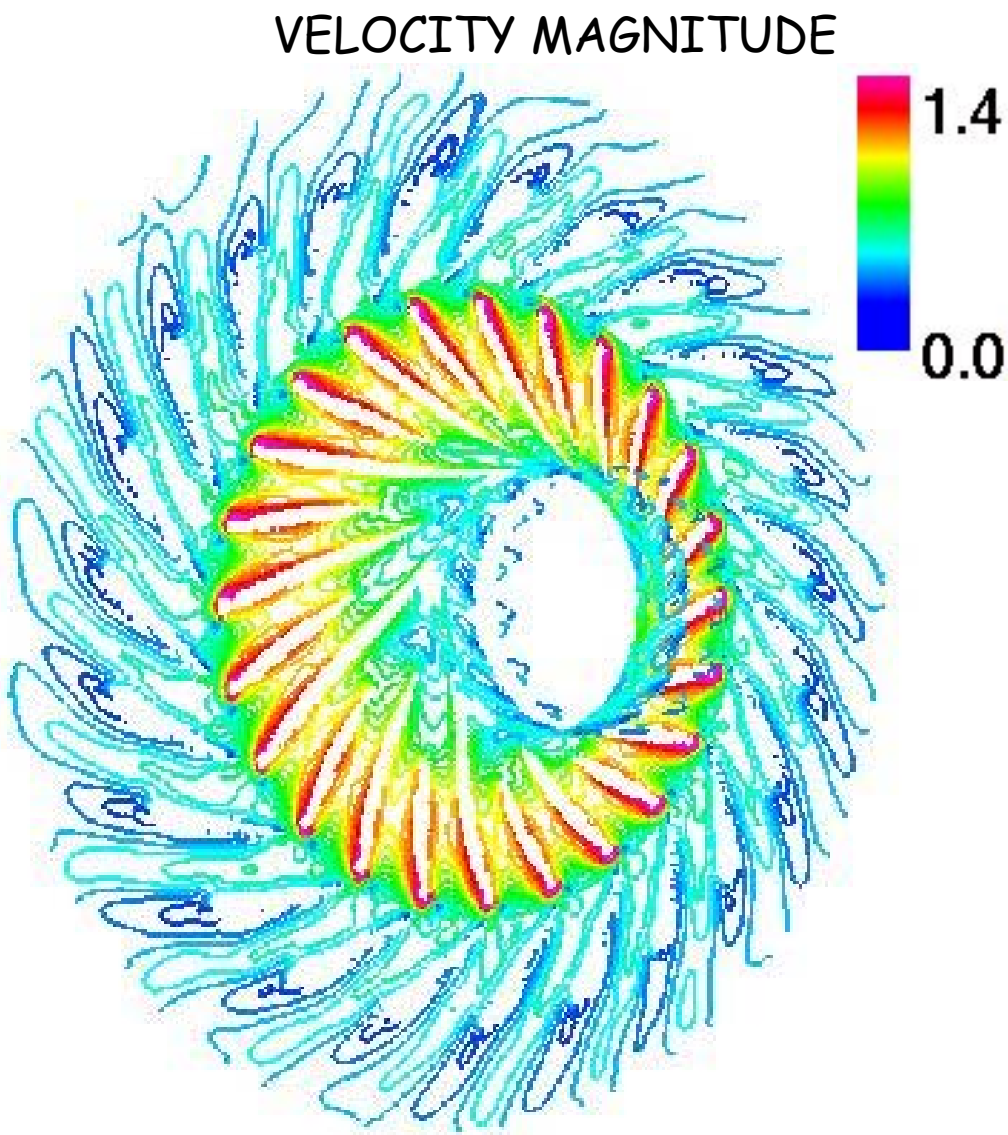

- 34.3 Million Points
- 800 physical time steps in one rotation. One and a half impeller rotations are completed.

*One physical time-step requires less then 20 minutes wall time with 128 CPU's on SGI Origin platforms. One complete rotation requires one-week wall time.

*Code optimization is currently underway. For small case, 50% improvement is obtained by employing a better cash usage in the code. Less than 10 minutes per time step will be obtained by the end of September 2001.

Data Compression using

Data compression by J. Housman & D.Lee

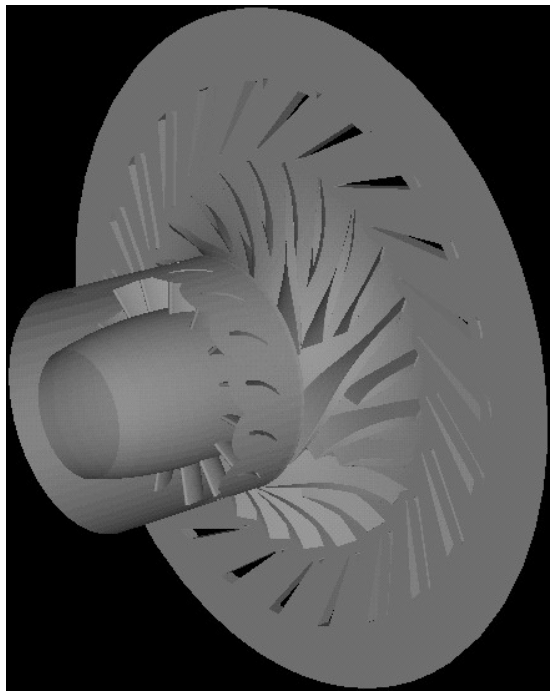

Before Compression

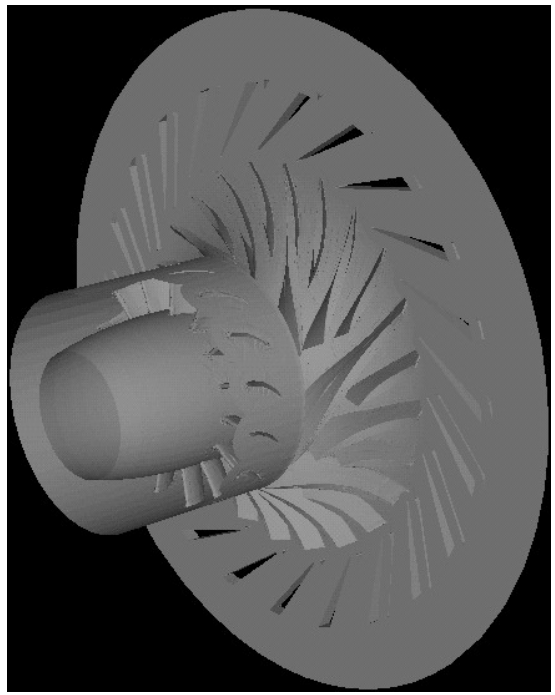

After Reconstruction

Grid File Compression

Data Compression

- **Data compression by J. Housman & D.Lee**

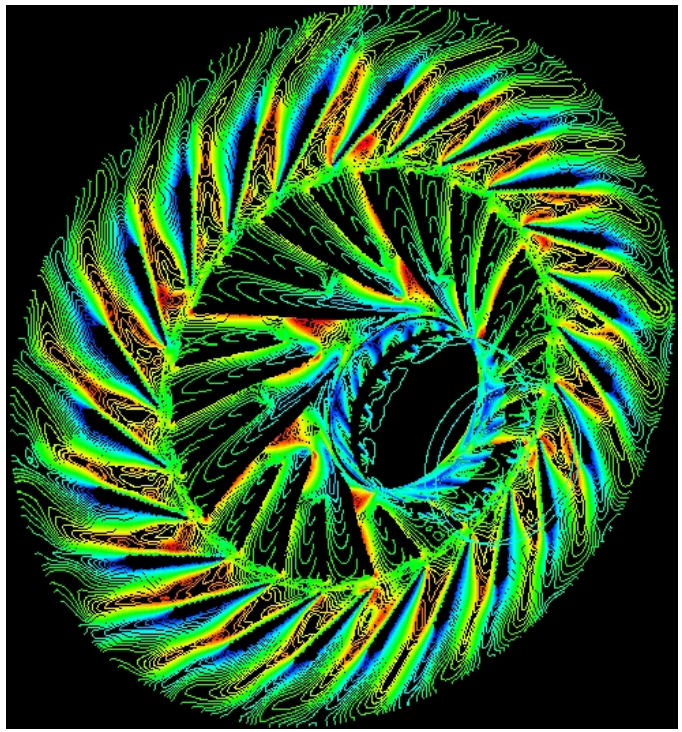

Before Compression

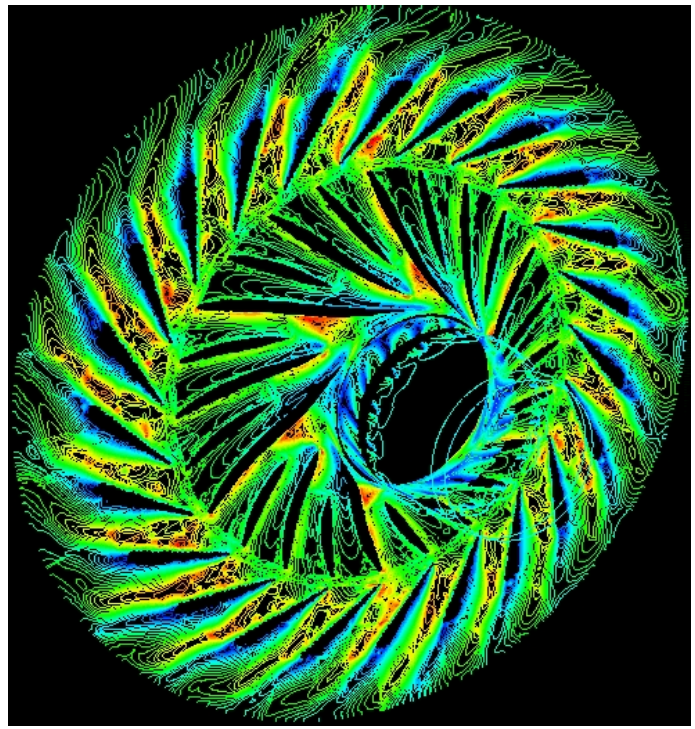

After Reconstruction

Total Velocity Contours

STATIC/DYNAMIC STRESS ANALYSIS FOR TURBOPUMP SUB-SYSTEMS

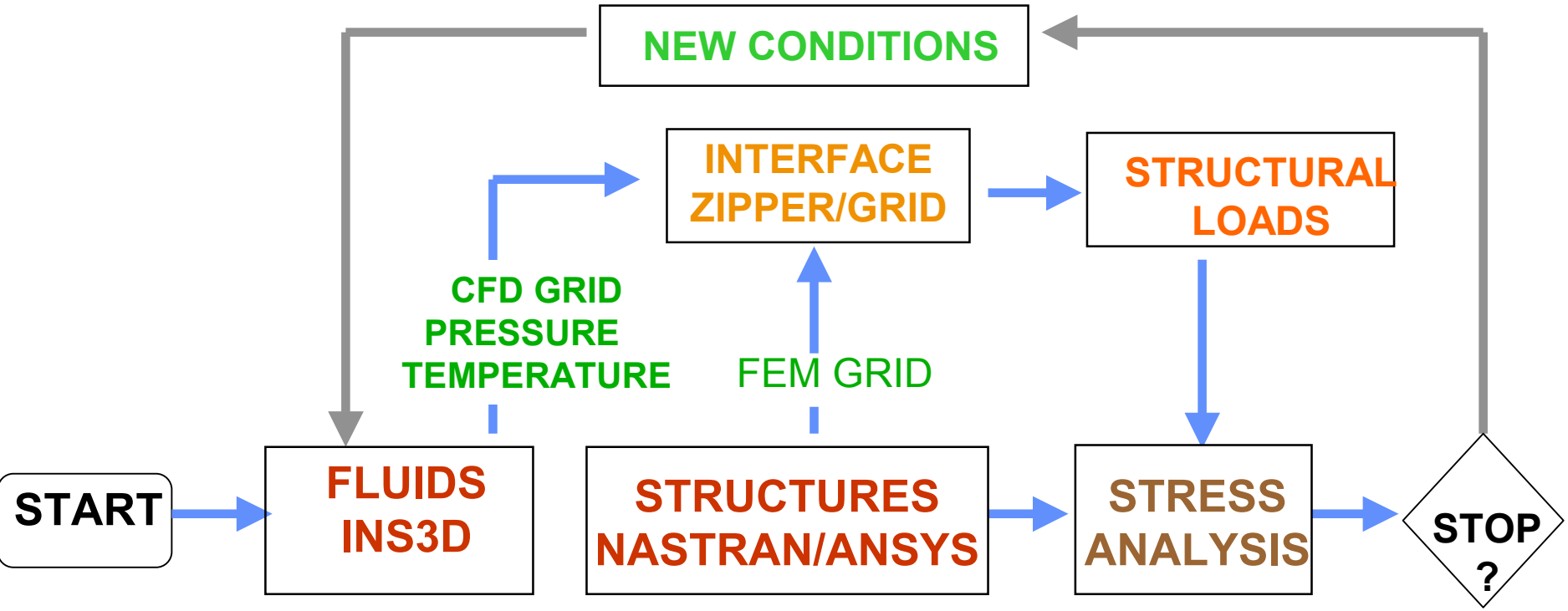

FLUID/STRUCTURE INTERFACE

- **LUMPED LOAD APPROACH**
  - FAST, NEEDS FINE GRIDS, ADEQUATE FOR UNCOUPLED METHOD

- **CONSISTENT LOAD APPROACH (CONSERVES LOADS)**
  - ACCURATE FOR COUPLED METHODS, EXPENSIVE

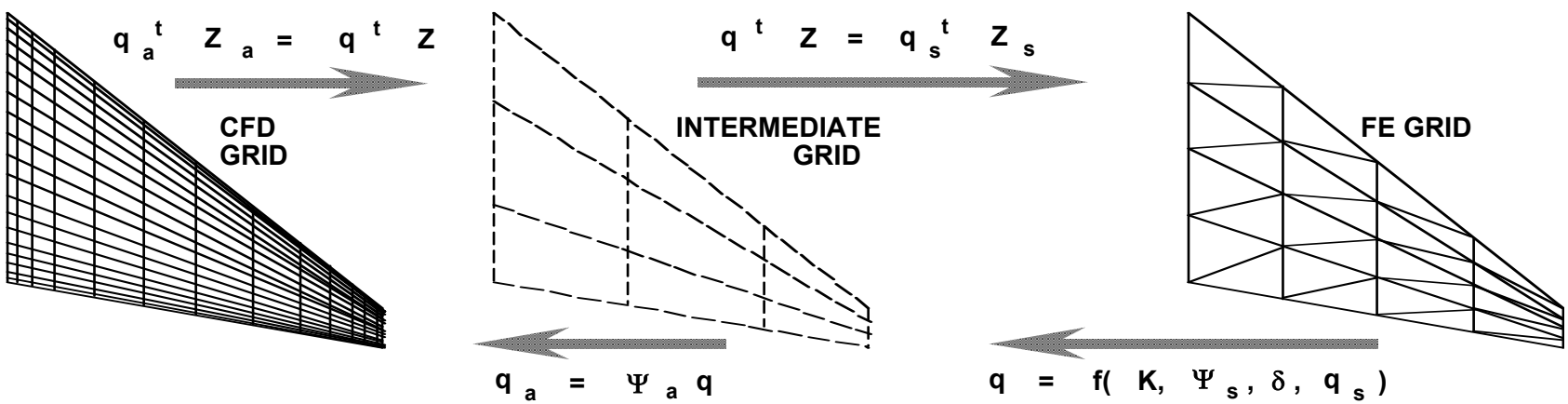

CONSISTENT LOAD APPROACH USING VIRTUAL SURFACE VALIDATED IN ENSAERO

By Guru Guruswamy

STRUCTURES

- **STRUCTURES WILL BE MODELED USING BEAM, PLATE, SHELL AND SOLID FINITE ELEMENTS**

- **INHOUSE AND COMMERCIAL FEM CODES WILL BE USED**

PRELIMINARY RESULTS FOR HUB USING 3D PLATE FEM

COARSE GRID
230 NODES
414 FE
1196 DOF

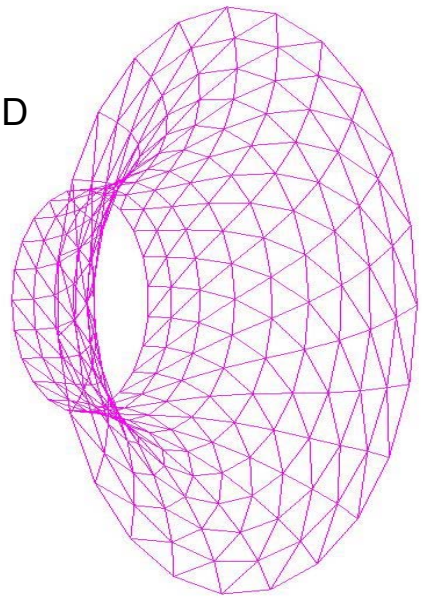

TYPICAL
STRUCTURAL
MODE AT 12KHz

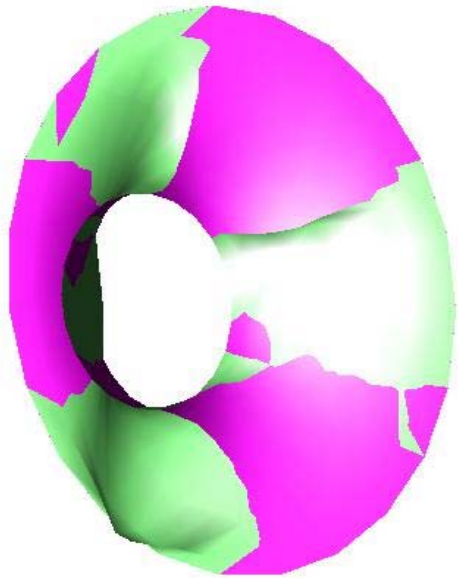

By Guru Guruswamy

Summary

- Unsteady flow simulations for RLV 2nd Gen baseline turbopump for one and half impeller rotations are completed by using 34.3 Million grid points model.

- MLP shared memory parallelism has been implemented in INS3D, and benchmarked. Code optimization for cash based platforms will be completed by the end of September 2001.

- Moving boundary capability is obtained by using DCF module.

- Scripting capability from CAD geometry to solution is developed.

- Data compression is applied to reduce data size in post processing.

- Fluid/Structure coupling is initiated.

CFD Research Corporation
215 Wynn Dr. , Huntsville, AL 35805 (256) 726-4800 FAX: (256) 726-4806 www.cfdrc.com

CFD PREDICTION OF THE BEAGLE 2 MARS PROBE AERODYNAMIC DATABASE

Peter A. Liever and Sami D. Habchi
CFD Research Corporation

Simon I. Burnell and Steve J. Lingard
Martin Baker Aircraft, Ltd

Presented at
Thermal and Fluids Analysis Workshop 2001

September 11, 2001

Overview

- Beagle 2 Mars Mission
- Aeroshell Design Approach
- Aerodynamic Database Approach
- CFD-FASTRAN Flow Solver
- CFD Analysis and Flow Features
- Static Aerodynamic Database
- Pitch Stability Analysis
- Summary

Beagle 2 Mission

- Beagle 2 Lander Part of ESA Mars Express Orbiter, Launch in June 2003
- Named After Charles Darwin's Ship, HMS Beagle
- Martin-Baker Part of UK Beagle 2 Consortium
- Deliver Science Package to Mars Surface and Search for Signs of Life
  (Atmospheric Composition, Soil, Water, Organic Material)

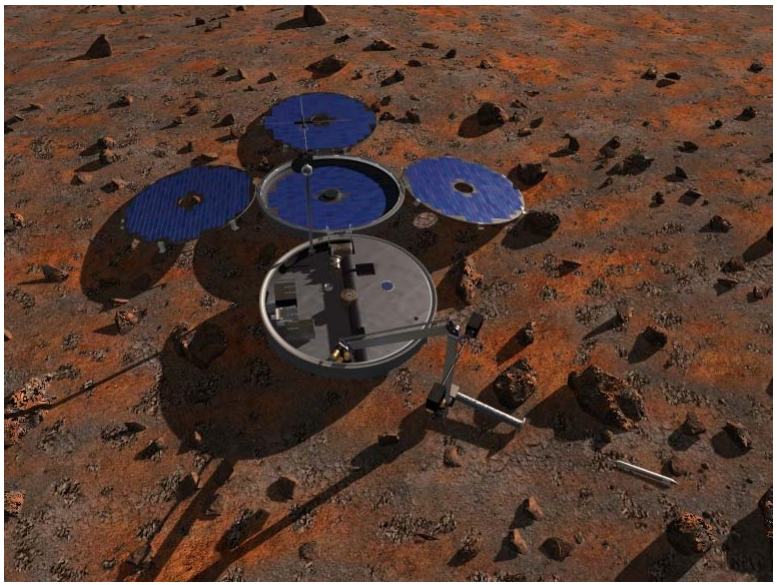

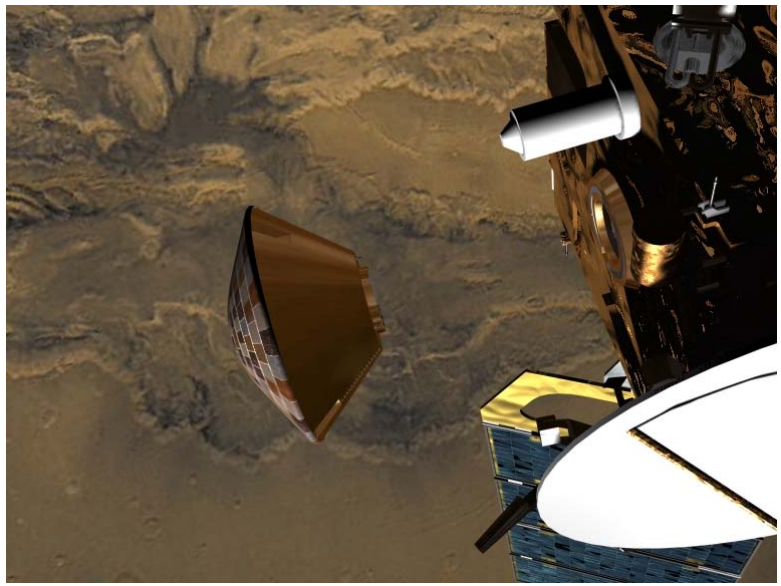

Martin Baker Role in Beagle 2 Program

- Martin-Baker Responsible for Beagle 2 Entry, Descent and Landing System (EDLS)
  - Entry Vehicle
  - Parachute Deployment
  - Transonic Deceleration
  - Aeroshell Separation
  - Airbag Inflation
  - Landing
  - Airbag Release

- Previous Experience Developing Cassini/Huygens Descent Control System

Beagle 2 EDLS

- Beagle 2 Ejected From Mars Express 5 Days Prior to Entry
- Enters Atmosphere at Mach=31.5, Altitude=120km
- Aerobraking to M=1.5 Where Pilot Chute Deploys
- Main Chute Deployed at M=0.4
- Airbag Inflation
- Landing and Deployment of Experiments

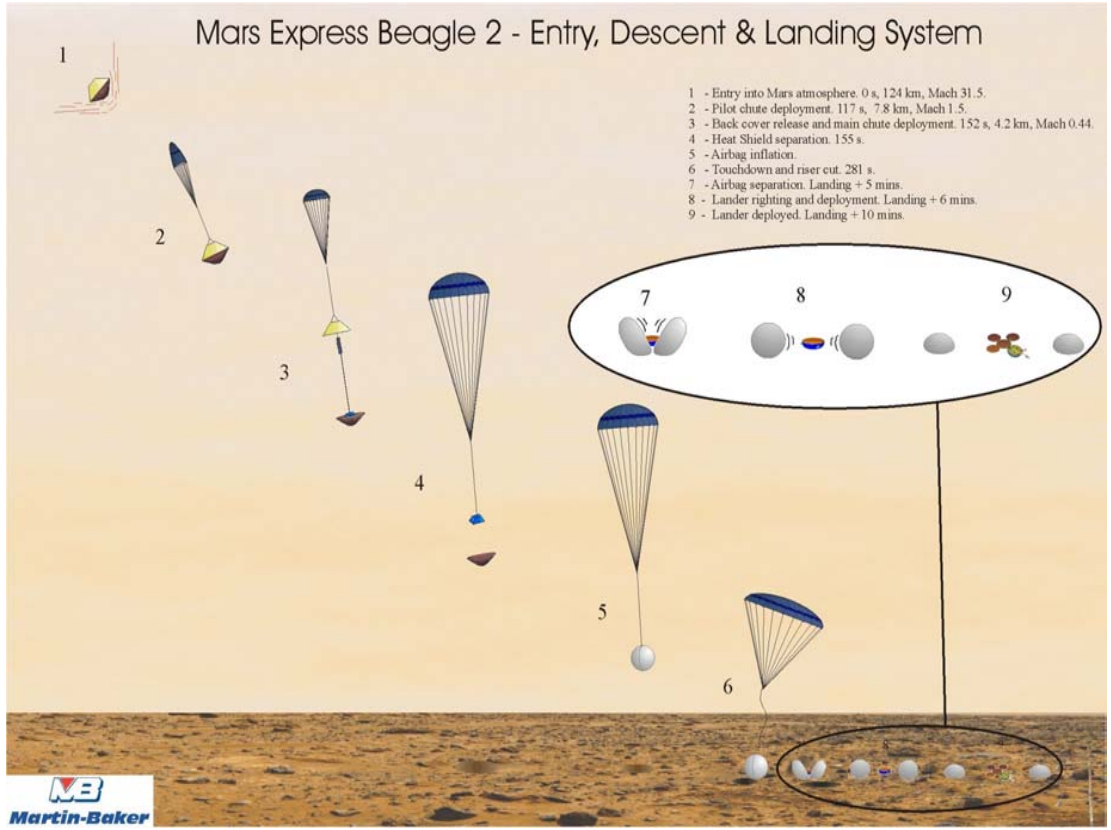

Beagle 2 Aeroshell Design Approach

- Simple Generic Shape to Take Maximum Advantage of Existing Aerodynamic Data, and to Simplify Analysis
- Use of Existing Aerodynamic Databases (Huygens, Stardust, Viking, Pathfinder)
- Adoption of ballistic entry
- Minimum ballistic coefficient
- High Drag Shapes Consistent with Stability Constraints and Existing Databases (Large Angle Sphere Cone)
- Nose Radius For Minimum Mass, Maximum Drag
- Minimum Corner Radii for Maximum Drag, Limited by Structural/Thermal Requirements
- Base Diameter Maximum for Minimum Ballistic Coefficient

Beagle 2 Aeroshell Design Approach

- Constraints on Project Budget and Time to Launch Opportunity
- Reuse Existing Database
- Limited Wind Tunnel Experiments
- Apply CFD to Develop Transonic-Supersonic-Hypersonic Aerodynamic Database
- Develop Blended Aerodynamic Database From Existing Scaled Data, CFD Predictions and Wind Tunnel Experiments

Role Of CFD In Beagle 2 Development

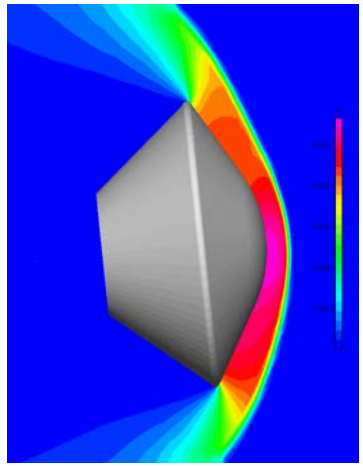

- CFD Now Mature Enough for Reliable Use for Entry Bodies
  - Reduction of Wind Tunnel Testing Costs, Time Savings
- Martin Baker Utilize CFD-FASTRAN for Entry Body Flow Prediction
  - Static Aerodynamic Coefficient Derivation
  - Localized Flow Effects
  - Heat Flux
  - Dynamic Coefficient Derivation
- US Navy, CFDRC, and Martin-Baker Have Used CFD for a Wide Range of Escape System Related R&D
  - Seat and Occupant Aerodynamic Database Development
  - Evaluation of Seat Stability Enhancements

Beagle 2 Aeroshell Geometry

- Geometrically Similar to Huygens Probe
  (To Maximize Data Reuse From Huygens Program)
- Addition of Backshell Frustrum Enclosing Payload
- 60° Half Angle Blunted Cone
- Maximum Diameter D=0.9m (Huygens D=2.7m)
- Mass 60kg (17% Science Payload)

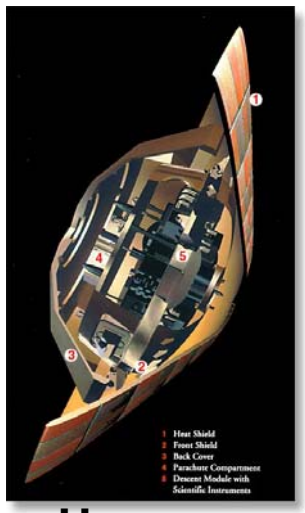

Huygens

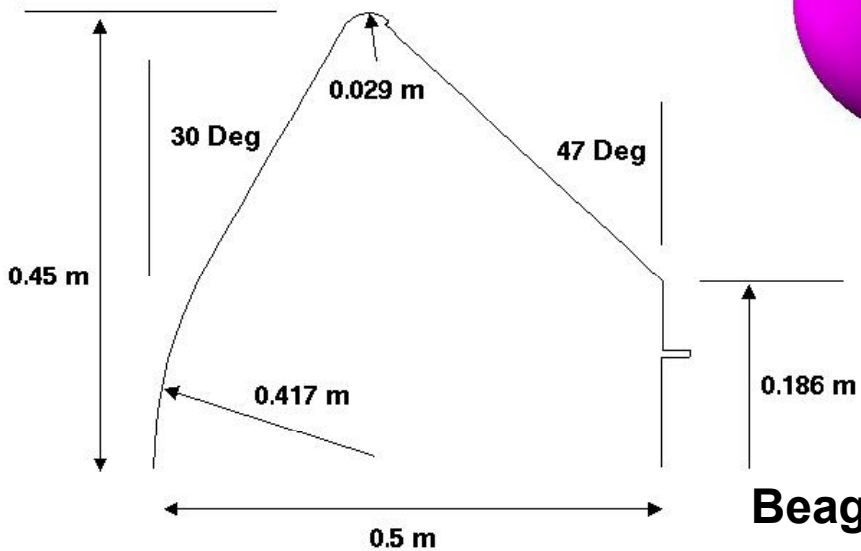

Beagle 2

Beagle 2 Aerodynamic Database Matrix

CFD Database Matrix selected from Nominal Trajectory

- Martin-Baker 6-DoF Trajectory Code
  - NASA MarsGRAM Atmosphere
  - Newtonian Aerodynamics
  - Derived Aerodynamic Databases
  - Monte Carlo Dispersion
- Nominal Trajectory
  - Entry Angle of γ = -18º
  - Altitude 120 km
- Nine Trajectory Points Selected for CFD Analysis

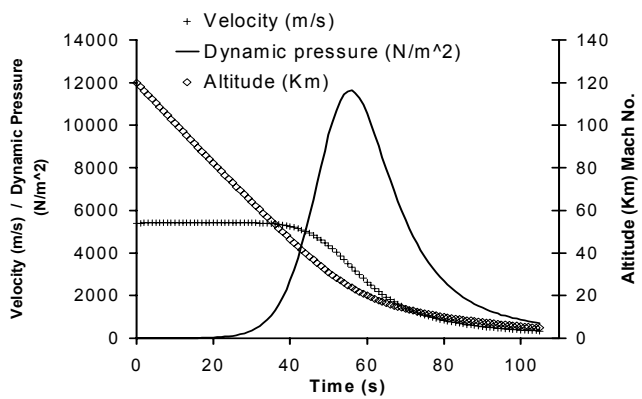

Mach No.	Velocity (m/s)	Temp (K)	Pressure (Pa)
28	5386	156.8	1.4
25	5061	170.8	8.9
20	4248	184.5	29.1
15	3256	191.1	59.3
10	2200	195.6	104.0
7	1552	198.3	144.9
5	1117	200.6	185.7
3	677	204.3	257.7
1.5	345	209.2	398.3

CFD-FASTRAN Flow Solver

- Density-Based Finite Volume Formulation
- Euler and Navier-Stokes for 2D, 3D and Axisymmetric
- Multi-Zone Structured/General Unstructured/Hybrid Grids
- Chimera Overset Grids
- Laminar, Turbulent (Baldwin-Lomax, K-ε, K-ω, Spalart-Allmaras)
- Generalized Finite Rate Chemistry and Thermal Non-Equilibrium
- Roe Approximate Riemann Solver and Van Leer Flux Vector Splitting
- Explicit, Point Implicit and Fully Implicit Time Integration
- Distributed Parallel Computing Capability

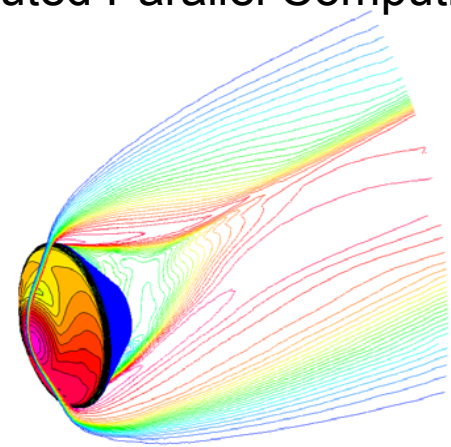

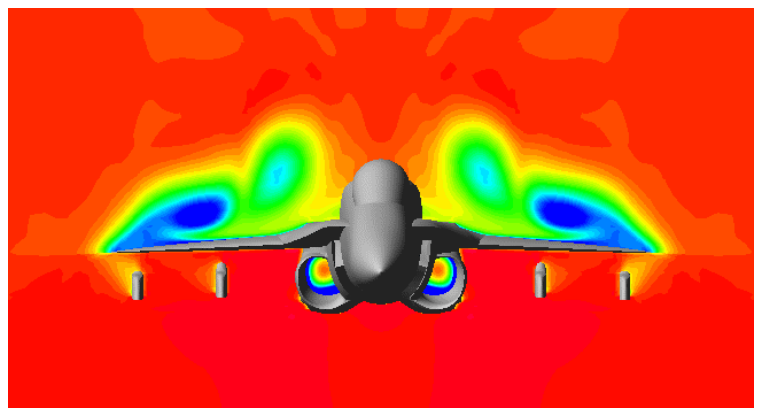

CFD-FASTRAN Multi-Body Dynamics

- Fully-Automated Chimera/Overset Grid Methodology
- Fully Coupled 6-DOF Solution for Multiple Body Motion
- Closed Loop Control Models Including Autopilot, Motor Ignition/Firing, Thrust Profiles, Point Forces
- Comprehensive Output of Forces, Moments, Angular Velocities, Accelerations and Body Orientations in any User Defined Axis System
- Easy-to-use GUI for Fast Model Set-Up (Physics, Chimera Hole Cutting)

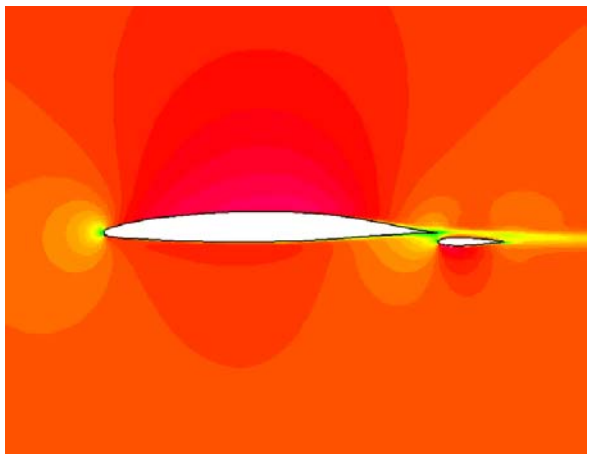

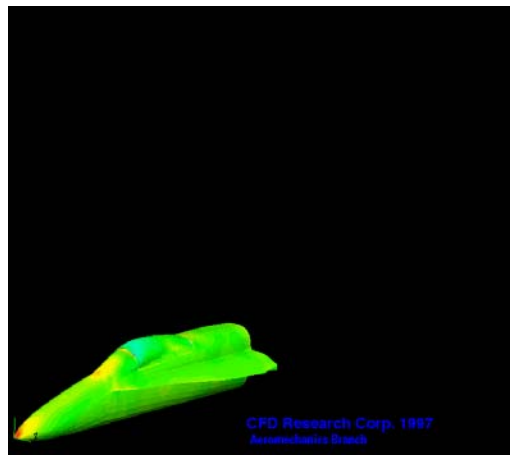

CFD-FASTRAN Thermochemistry

- Two Databases for Thermodynamics
  - Curve fit database for 300K to 6000K
  - Spectroscopic Database for Thermal Non-Equilibrium
- General Finite Rate Reactions
  - Handles Arbitrary Number of Species and Reactions
- Multiple Energy Modes
  - Thermal Equilibrium or Two-Temperature Non-Equilibrium
- Applications
  - Entry or Re-entry Physics
  - High Speed Missile Applications

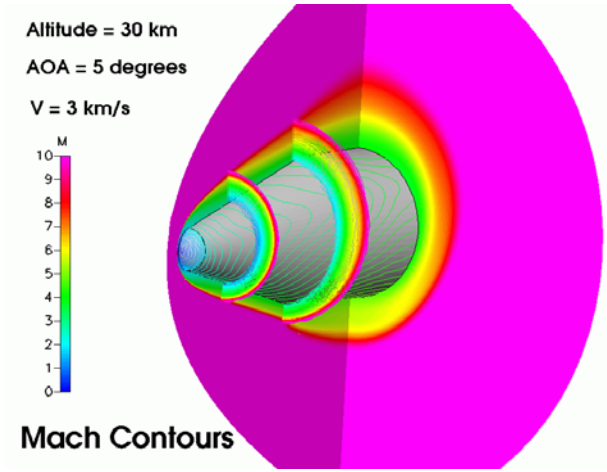

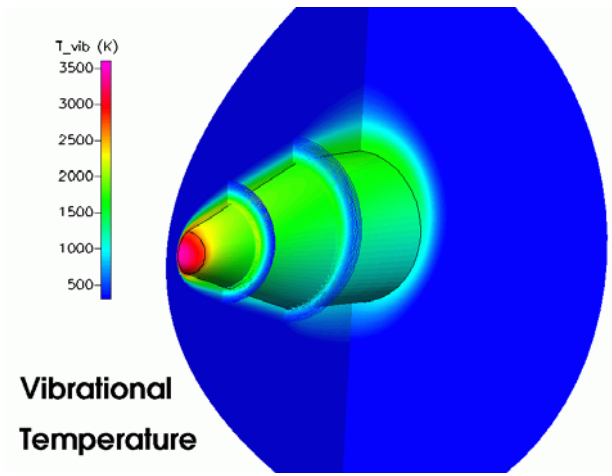

CFD-FASTRAN Applications

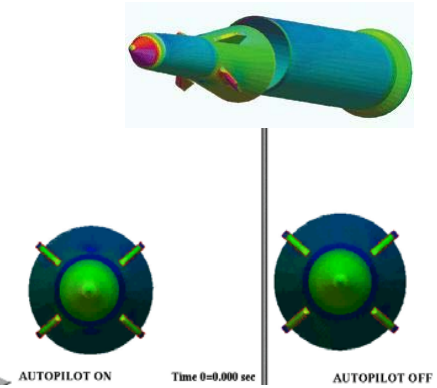

Missile Staging/Maneuvering

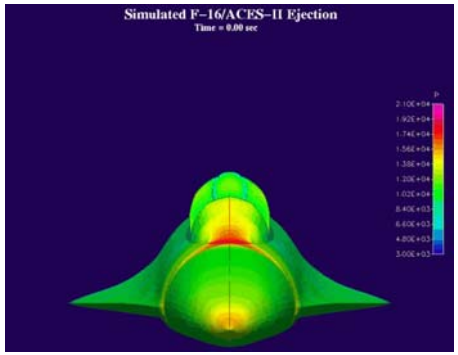

Escape Systems

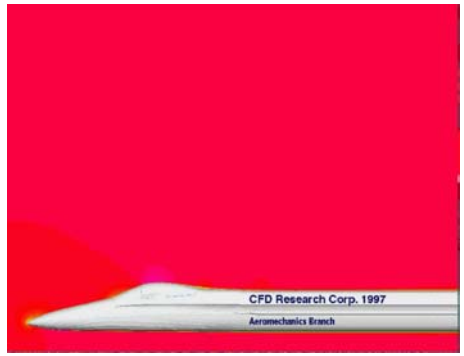

Canopy Trajectory

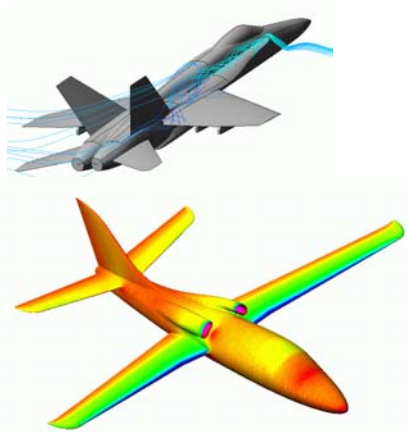

Aircraft Aerodynamics

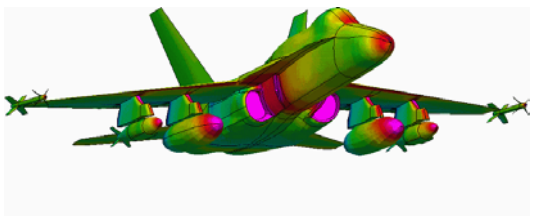

Store Separation

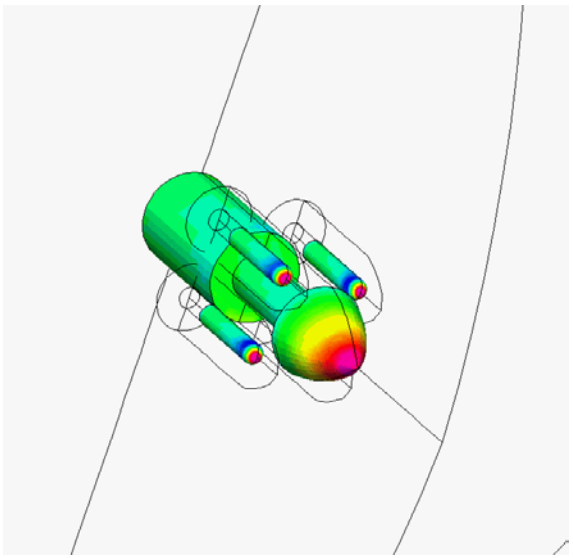

Ammunition Dispenser

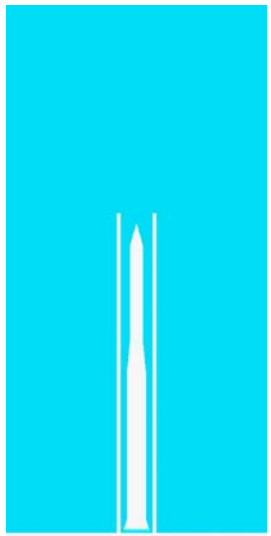

Tube Launch

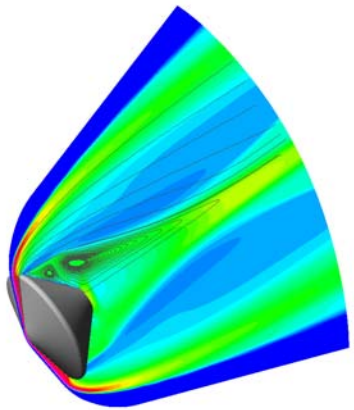

Aerothermochemistry

Mars Atmosphere CFD Model

- Laminar
- Fixed Wall Temperature
- Martian Atmosphere: 97% CO_2, 3% N_2 (Mass Fraction)
- Below Mach=7:
  - Nonreacting Mixture of Thermally Perfect Gases (CO_2, N_2)
- Above Mach=7:
  - Finite-Rate Chemical Reactions
  - Eight Species (CO_2, CO, N_2, O_2, NO, C, N, O), No Ablation Products
  - Nine Reactions (Park, 1994)
- Analyze Reacting and Nonreacting Cases at Mach=7 to Verify Consistency

Mach No.	Angle-of-Attack (Degrees)					Gas Chemistry
	0	2	5	8	11	
28		●	●	●	●	Reacting
25		●	●	●	●	Reacting
20	●	●	●	●	●	Reacting
15		●	●	●		Reacting
10		●	●	●		Reacting
7	●	●	●			Reacting
7	●	●	●			Nonreacting
5		●	●			Nonreacting
3	●	●	●	●	●	Nonreacting
1.5	●	●	●	●	●	Nonreacting

Beagle 2 Computational Grid

- Half Body Model (180 Degree), Assume Flow Symmetry
- Resolve Shock Layer and Wake
- Avoid Grid Singularities
- Hypersonic Grid: 305,000 Grid points, 9 Domains.
- Transonic Grid: 507,000 Grid points, 9 Domains
- Near Wall Grid Clustering With y^+ Range of 1.0 to 5.0

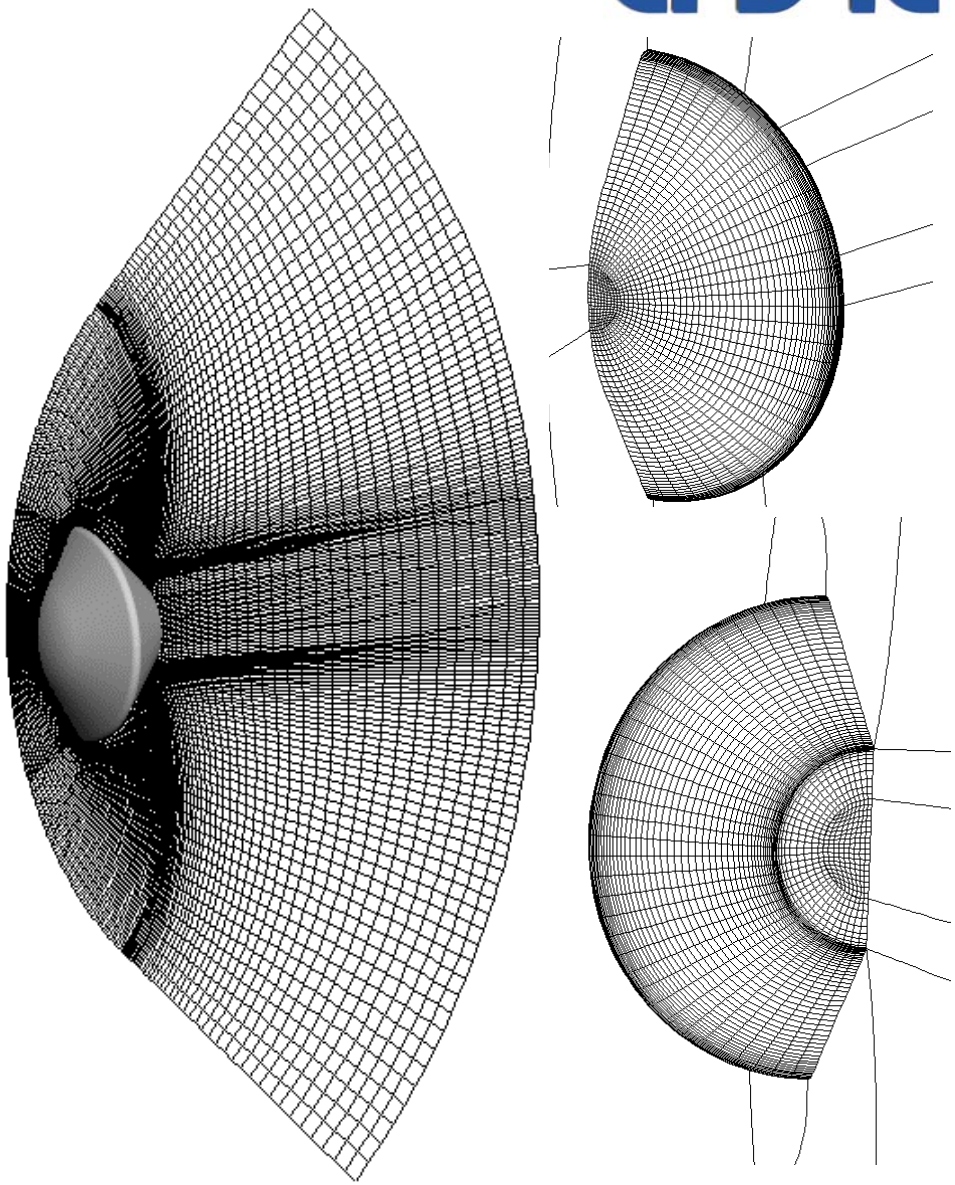

Beagle 2 Grid Refinement Study

Axisymmetric Grid Refinement Study to Ascertain Grid-Independent Solution for Aerodynamic Forces

	Grid Density	C_A
Mach = 3 Nonreacting	Axisymmetric, Baseline Grid	1.5094
	Axisymmetric, Refined Grid	1.5095
	3-D, Baseline Grid, α=0°	1.5085
Mach = 20 Reacting	Axisymmetric, Baseline Grid	1.4598
	Axisymmetric, Refined Grid	1.4600
	3-D, Baseline Grid, α=0°	1.4596

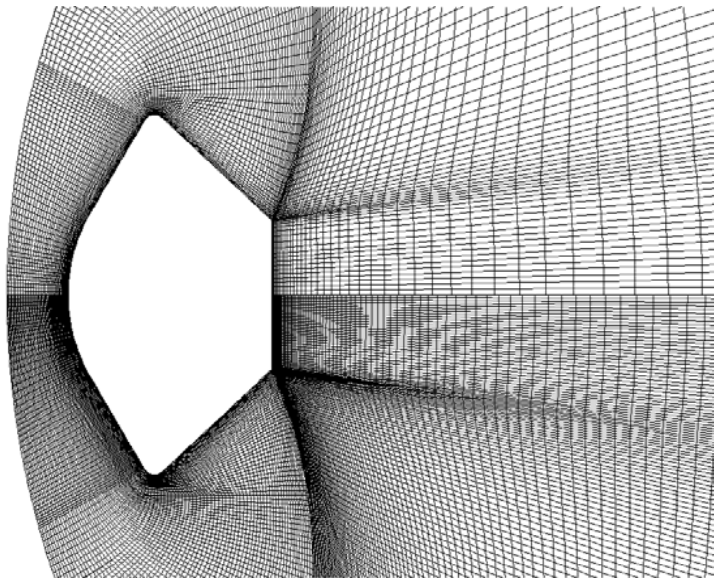

CFD Validation Against Experiment

Validation of Aerodynamic Force Predictions Against Experiment

- 60 mm Diameter Beagle 2 Model
- Oxford University Gun Tunnel
- CO_2 gas
- Mach=6

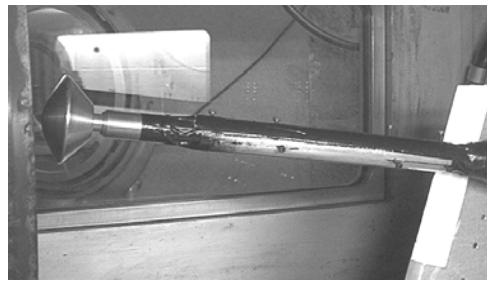

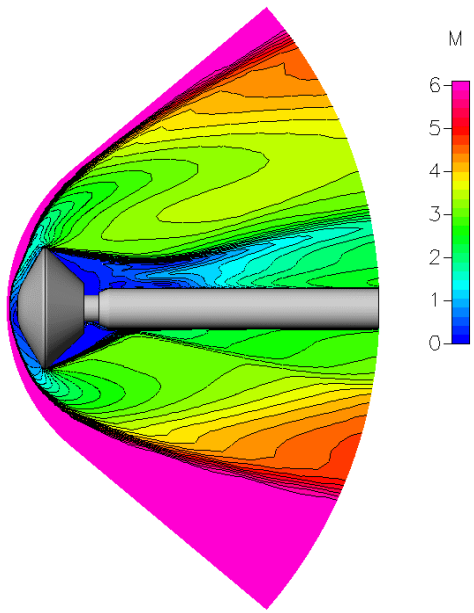

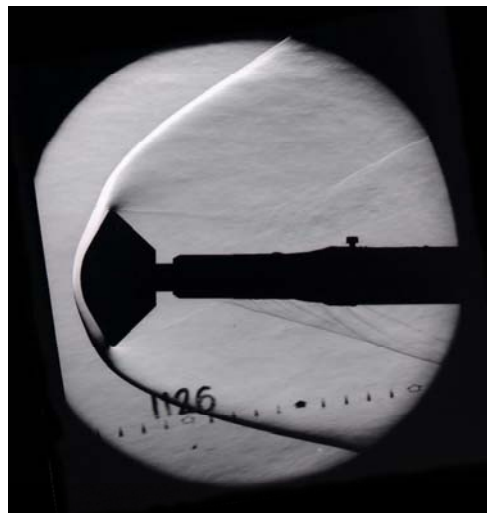

Beagle 2 Flow Field Characteristics

Aerodynamics Affected by Shift of Sonic Line, Effect of CO_2 Gas

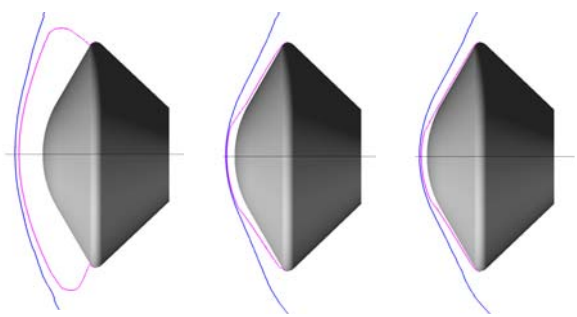

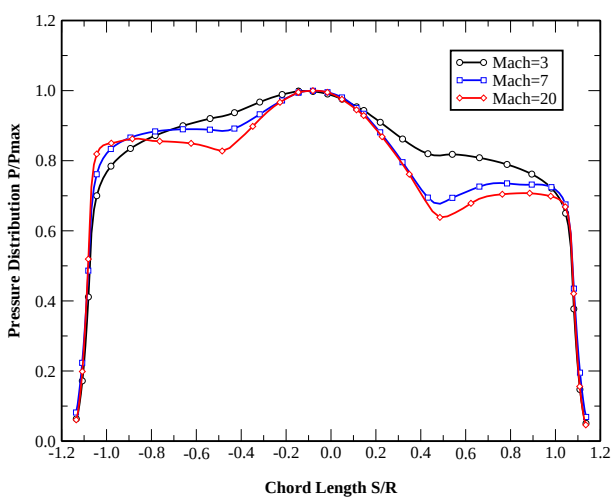

Evolution of Wake Over Trajectory: Reattachment Point Moves Forward

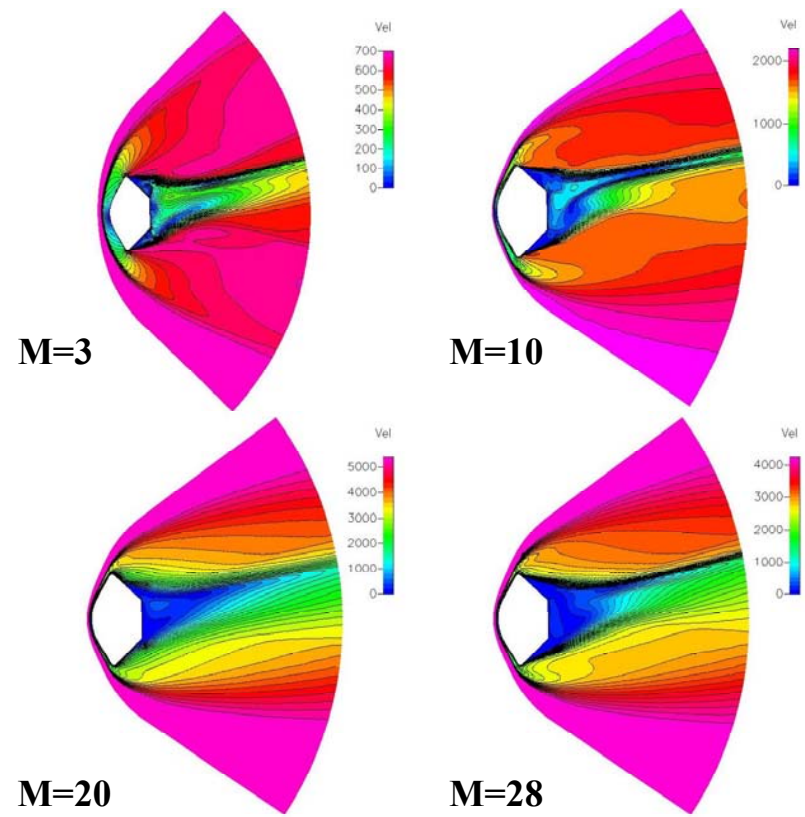

Beagle 2 Flow Field Characteristics

- Base Flow at Mach=1.5 Unsteady
- Oscillations Result From Interaction of Separated Shear Layer and Strong Reverse Base Flow

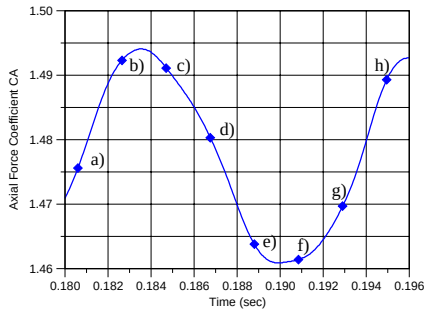

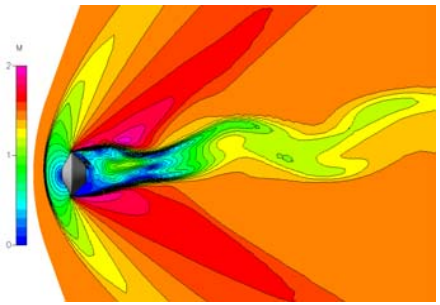

(a) time = t_o

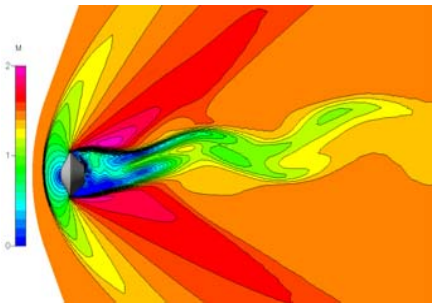

(b) time = t_o + 0.002 sec

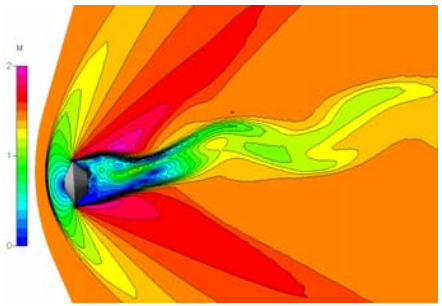

(c) time = t_o + 0.004 sec

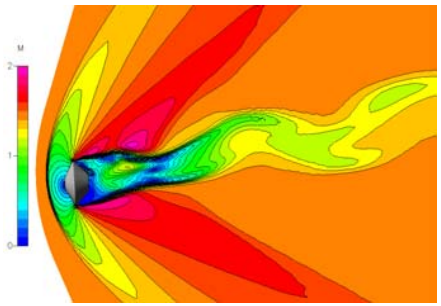

(d) time = t_o + 0.006 sec

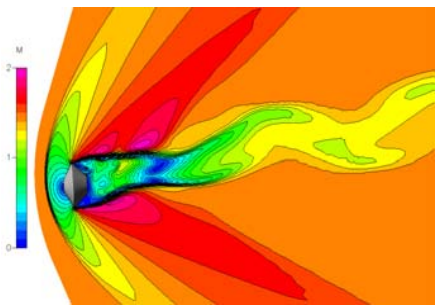

(e) time = t_o + 0.008 sec

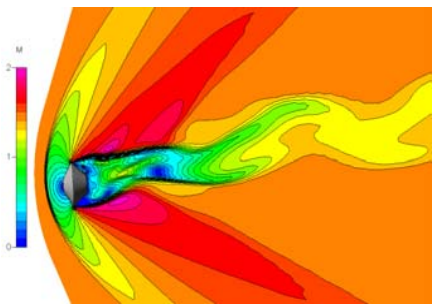

(f) time = t_o + 0.010 sec

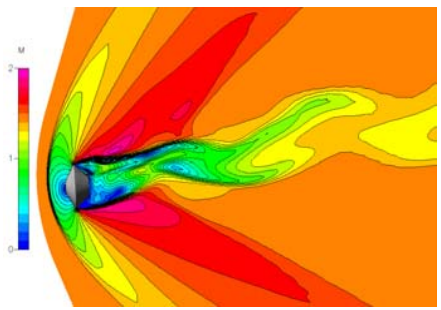

(g) time = t_o + 0.012 sec

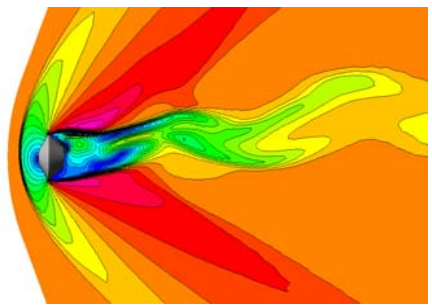

(h) time = t_o + 0.014 sec

Beagle 2 Aerodynamic Coefficients

- Newtonian Flow Approximations Hold Very Well for Mach Numbers Above 10
- Rise for Mach=28 Due to Transitional Flow (Knudsen Number=0.01)
- Below Mach 10, Transition to Half Newtonian Level for Normal Force and Moment Coefficients, Axial Force Components Rise Sharply
- Transition to Half Newtonian Level in CO_2 Occurs at Lower Mach Number Compared to Air

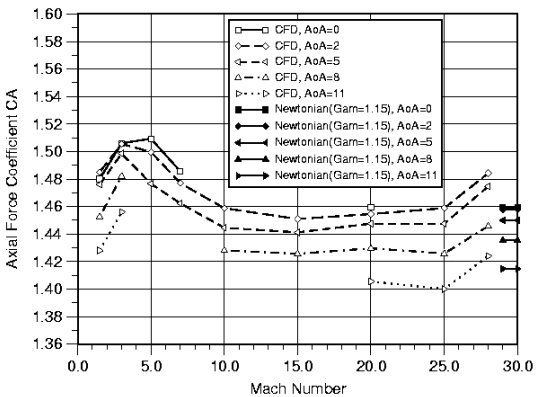

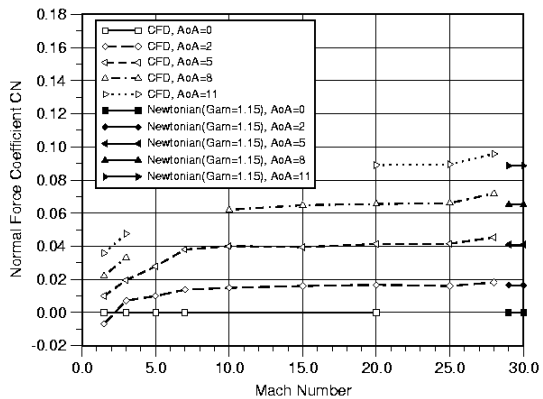

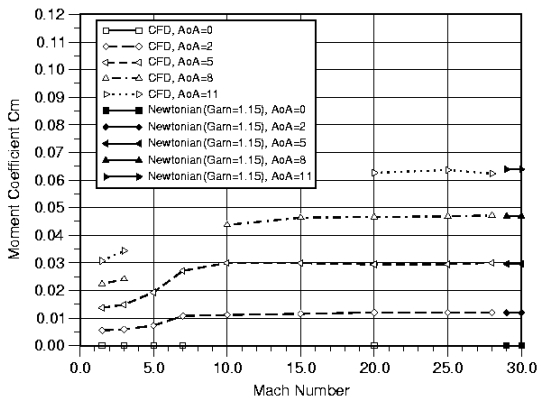

Beagle 2 Blended Database

Several Datasets Employed in Construction of Blended Database

- Current CFD Based Data
- Huygens Phase A2 Data, Scaled to Beagle 2 (Air)
- Huygens Wind Tunnel Data (Air)
- Stardust Sample Return Capsule Wind Tunnel and CFD Data (Air)
- Mars Pathfinder Data
- Scaled NASA Experimental Data for 60° Cone (Air)

Total Angle of Attack Range from 0 to 30°, Mach Number Range from 0.4 to 28.

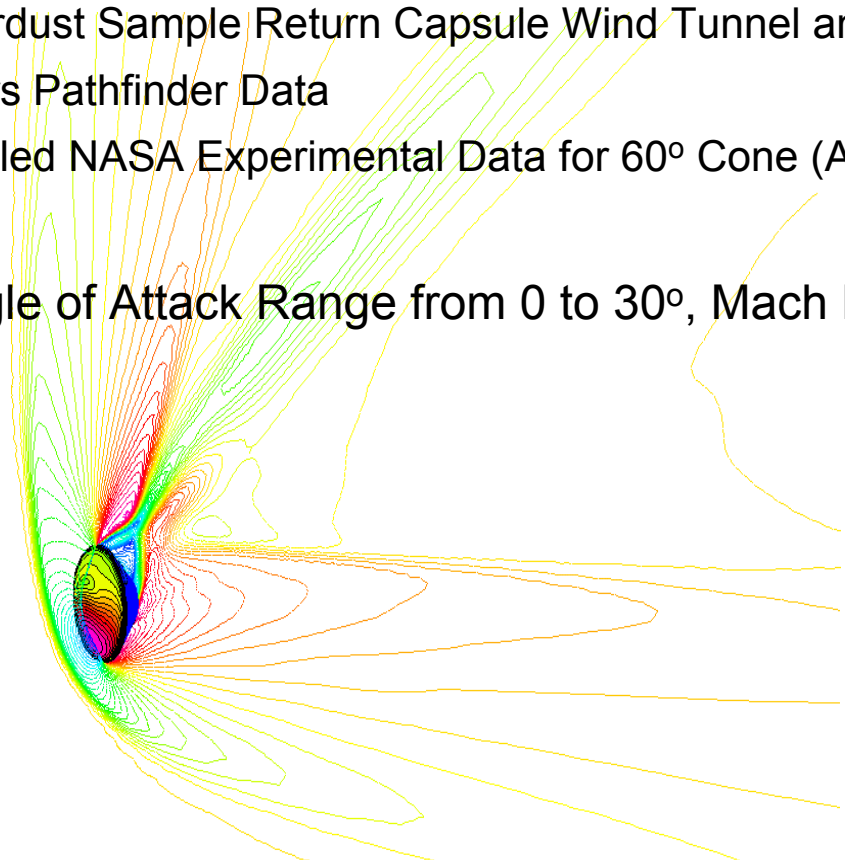

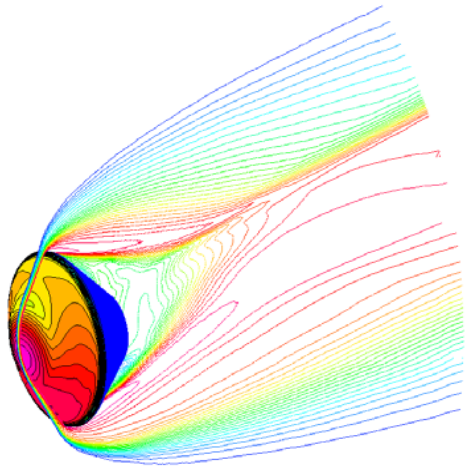

Beagle 2 Dynamic Stability Database

Assess Stability of Beagle 2 at Pilot Chute Release

- Well Known Pitch Instability of Blunt Bodies in Transonic Regime
- Dynamic Behaviour Driven by Unsteadiness in Base Region
- Dynamic Instability Likely to Occur Near Pilot Chute Deployment, M >1.5

Wind tunnel tests:

- Oxford University CO_2 Tunnel, Mach=2

CFD Analysis

- CFD-FASTRAN, Time-Accurate, 6-DOF

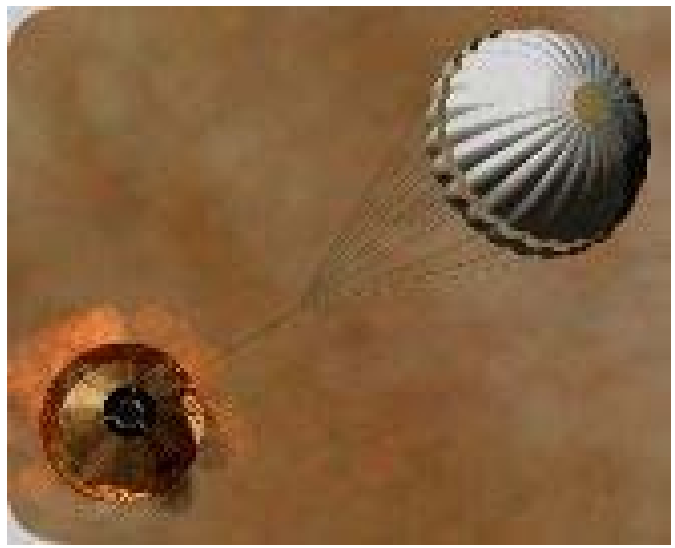

Beagle 2 Pitch Stability Experiment

- Oxford University Tunnel
- Mach=2, CO_2 Gas
- Model 20 mm Diameter
- Run Time Greater Than 10 sec
- Mounted on Flexible Pivot
- AoA Perturbation by Push Rod
- Model Movement Measured by Accelerometers

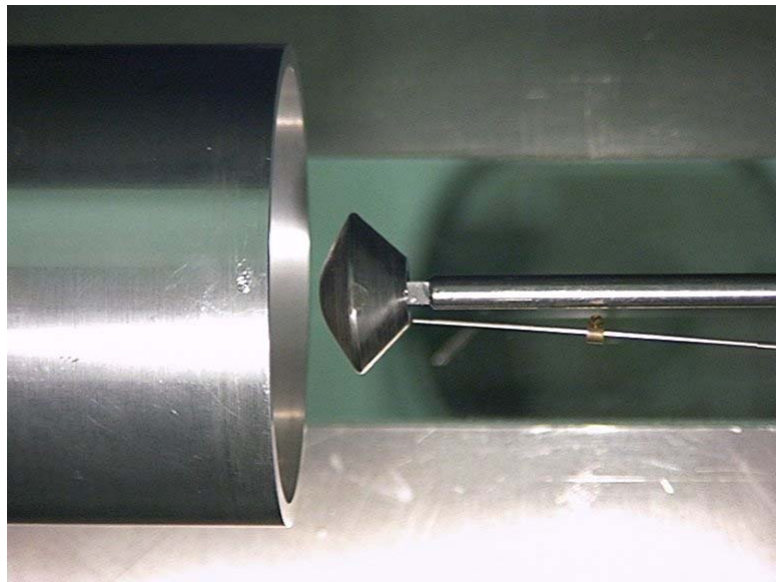

CFD Pitch Damping Analysis

CFD-FASTRAN Calculations

- Time-Accurate, 6-DOF (Constrained to Pitch Motion Only)
- Chimera Overset Grids: Sting Fixed, Model Moving
- Flexure Mount Resistive Torque Modeled
- Mach = 2, CO_2 Gas
- Initial Perturbation $\Delta\alpha$ = 2 Degrees
- Modeled Sting/No-Sting Configurations to Assess Sting Interference Effects

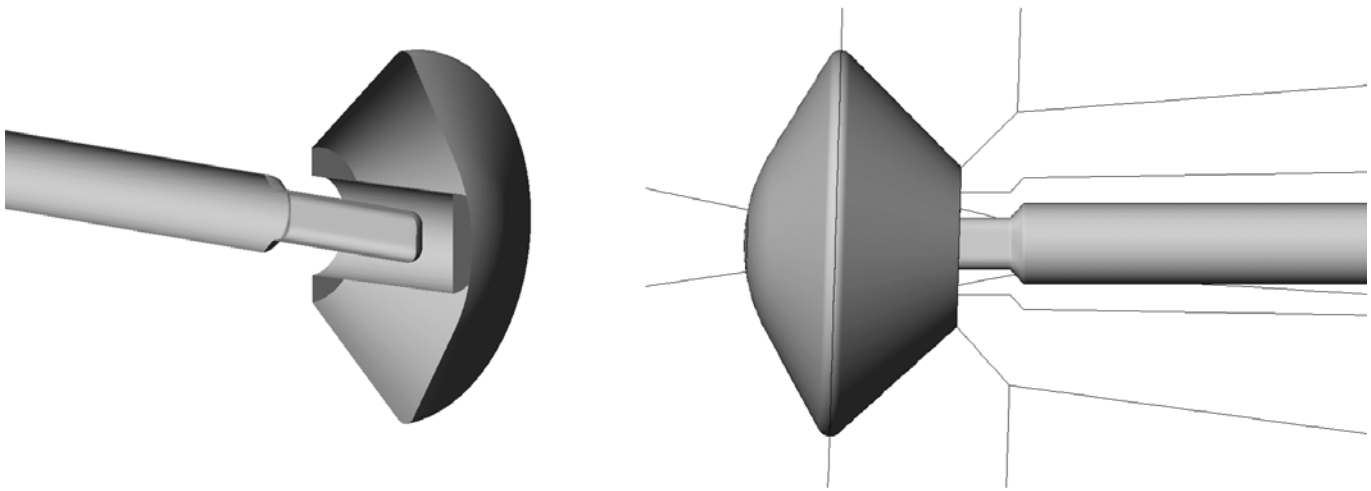

CFD Based Pitch Damping Results

- Pitch Damping Analysis is Work in Progress
- Insufficient Data Available to Extract Damping Coefficients
- Significant Effects of Sting Interference and Flexure Mount

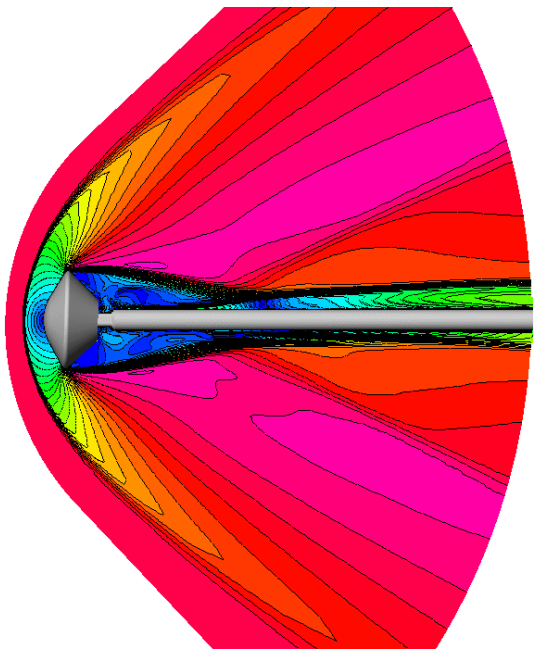

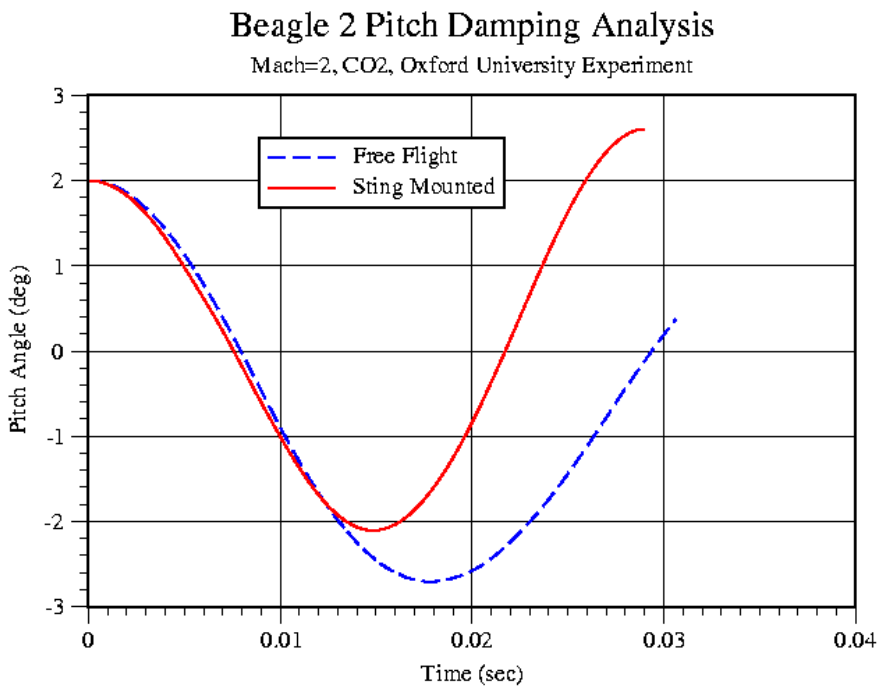

Summary

- CFD Has Matured to Provide Reliable Planetary Entry Vehicle Aerodynamic Predictions
- CFD Provides Substantial Time And Cost Savings
- CFD-FASTRAN Applied Over Entire Trajectory (Entry to Chute Deployment)
- Valuable Insight Gained Into Vehicle Flow Characteristics (Examples: Wake and Base Flow Structure,Transonic Wake Unsteadiness)
- Blended Aerodynamic Database Generated by Combining CFD Data, Scaled Existing Data, and Wind Tunnel Test Data
- CFD Based Pitch Damping Analysis Provides Insight Into Dynamic Stability Characteristics Not Easily Obtained From Wind Tunnel Tests

Extension of a System Level Tool for Component Level Analysis

Alok Majumdar
NASA Marshall Space Flight Center
MSFC, AL

Paul Schallhorn
Sverdrup Technology, Inc.
Edwards, CA

This paper presents an extension of a numerical algorithm for network flow analysis code to perform multi-dimensional flow calculation. The one dimensional momentum equation in network flow analysis code has been extended to include momentum transport due to shear stress and transverse component of velocity. Both laminar and turbulent flows are considered. Turbulence is represented by Prandtl's mixing length hypothesis. Three classical examples (Poiseuille flow, Couette flow and shear driven flow in a rectangular cavity) are presented as benchmark for the verification of the numerical scheme.

1.0 Introduction

Traditionally, fluid network codes have been used for system level analyses, whereas Navier-Stokes(NS) codes have been used for component level analyses. Until recently, most attempts to merge the two methodologies have come from the NS side (i.e. using a NS code to perform a system level analysis). This approach brings the enormous overhead associated with such a code. The current approach, on the other hand, begins from the fluid network side. The system level code utilized in the current study is the Generalized Fluid System Simulation Program (GFSSP) [1].

The Generalized Fluid System Simulation Program was developed for the purpose of calculating pressure and flow distribution in a complex flow network associated with secondary flow in a liquid rocket engine turbopump. The code was developed to be a general purpose flow network solver so that generic networks could be modeled. A given fluid system is discretized into the nodes and branches. This practice is conceptually similar to the "staggered grid" practice of SIMPLE algoritm of Patankar & Spalding[2]. GFSSP employs a finite volume formulation of mass, momentum, and energy conservation equations in conjunction with the thermodynamic equations of state for real fluids. Mass, energy and specie conservation equations are solved at the nodes; the momentum conservation equations are solved in the branches. The system of equations describing the fluid network is solved by a hybrid numerical method that is a combination of the Newton-Raphson and successive substitution methods. Eighteen different resistance/source options are provided for modeling momentum sources or sinks in the branches. Two thermodynamic property programs, GASP-WASP[3,4] and GASPAK[5]

are integrated with the code to provide thermodynamic and thermophysical properties of real fluid. GFSSP's system level capability has been extensively verified by comparing with test data [6-10].

2.0 Unstructured Finite Volume Grid

The unstructured finite volume grid network for GFSSP is shown in Figure 1, which shows connectivity of five nodes with four branches. In this figure node-i is connected with four neighboring nodes (j = 1 to 4) . In structured coordinate systems the number of neighboring nodes are restricted to 2, 4 and 6 for one, two and three dimensional systems respectively. On the other hand for an unstructured system, there is no such restriction on the number of neighboring nodes. The index k represents fluid species.

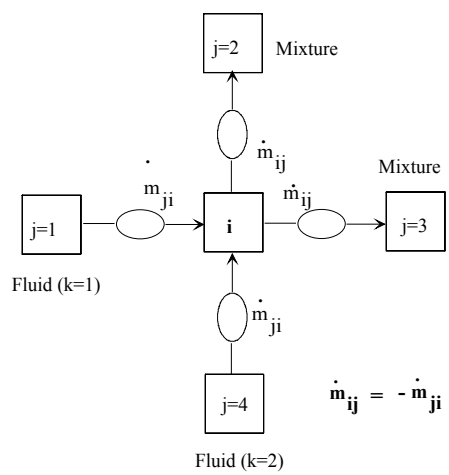

Figure 1: Schematic of Nodes and Branches for an Unstructured Finite Volume Grid

3.0 Conservation Equations

3.1 Mass Conservation Equation

The mass conservation equation for the ith node can be represented by:

$$\sum_{j=1}^{n} \dot{m}_{ij} = 0 \tag{1}$$

Equation 1 implies that the net mass flow from a given node must equate to zero. In other words, the total mass flow rate into a node is equal to the total mass flow rate out of the node.

3.2 Momentum Conservation Equation

The one dimensional form of momentum equation for every branch takes the following form:

$$\frac{m_{ij,dot}}{g_c}\left(u_i - u_u\right) = \left(p_i - p_j\right)A + \frac{\rho g V \cos\theta}{g_c}$$
$$- K_f m_{ij,dot}\left|m_{ij,dot}\right| A + \frac{\rho K_{\text{rot}}^2 \omega^2 A}{2 g_c}\left(r_j^2 - r_i^2\right) + S$$
(2)

Equation 2 represents the balance of fluid forces acting on a given branch. Inertia, pressure, gravity, friction and centrifugal forces are considered in the conservation equation. In addition to five forces, a source term S has been provided in the equation to input pump characteristics or to input power to pump in a given branch. If a pump is located in a given branch, all other forces except pressure are set to zero. The source term S is set to zero in all other cases. Figure 2 shows the schematic of a branch control volume.

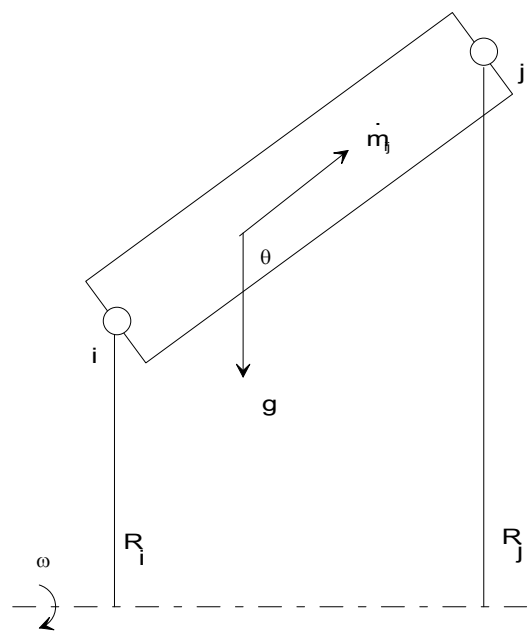

Figure 2: Schematic of a Branch Control Volume Showing the Gravity and Rotation

Multi-dimensional conservation equations must account for the transport of mass, momentum and energy into and out of the control volume from all directions in space. Mass conservation equations (Equation 1) can account for such transport because each internal node can be connected with multiple neighboring nodes located in space in any arbitrary location (Figure 1). On the other hand, the momentum conservation equation (Equation 2) is one dimensional. Multi-dimensional momentum transport can be accounted for by incorporating two additional terms in the momentum equation. These

terms include: a) momentum transport due to shear, and b) momentum transport due to the transverse component of velocity.

These two terms can be identified in the two-dimensional steady state Navier-Stokes equation which can be expressed as:

$$\rho\left(u\frac{\partial u}{\partial x}+v\frac{\partial u}{\partial y}\right) = \frac{\partial(\rho uu)}{\partial x}+\frac{\partial(\rho vu)}{\partial y}$$
$$= -\frac{\partial p}{\partial x}+\rho g_x+\mu\left(\frac{\partial^2 u}{\partial x^2}+\frac{\partial^2 u}{\partial y^2}\right) \tag{3}$$

The first term on the left hand side of Equation 3 corresponds to the current inertia term described in Equation 2. The second term on the left hand side of Equation 3 corresponds to the transverse momentum exchange. The first term on the right hand side corresponds to the pressure term in Equation 2. The second term on the right hand side of Equation 3 corresponds to the gravity term. The third term on the right hand side of the equation is negligible (based on an order of magnitude argument). The fourth term on the right hand side represents momentum transport due to shear. The next two sub-sections describe the implementation of shear and transverse momentum transport into the momentum equation of GFSSP. A more detailed description of the implementation of these terms for laminar flow is detailed by Schallhorn [11].

3.3 Momentum Transport Due to Shear

3.3.1 Laminar Flow

Begin by examining the shear term (fourth term) of the Navier-Stokes Equation in more detail. First, consider the shear as a force instead of a force per unit volume by multiplying the volume by the shear term.

$$\mu\frac{\partial^2 u}{\partial y^2}V \approx \mu\frac{\Delta u}{(\Delta y)^2}(\Delta x)(\Delta y)(\Delta z) = \mu\frac{\Delta u}{\Delta y}\Delta x\Delta z = \mu\frac{\Delta u}{\Delta y}A_{shear} \tag{4}$$

Figure 3 represents a set of nodes and branches for which shear forces are exchanged. Let branch 12 represent the branch for which the shear force is to be calculated. Branches N12 and S12 represent the parallel branches which will be used to calculate the shear force on branch 12. Let YS be the distance between branches 12 and S12, and let YN be the distance between branches 12 and N12. Let AS be the shearing area between branches 12 and S12, while AN is the shearing area between branches 12 and N12.

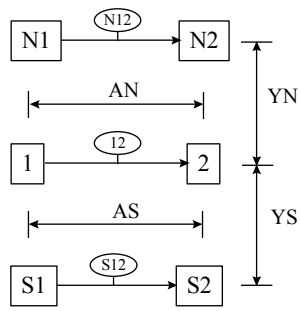

Figure 3: Branch and Node Schematic for Shear Exchange

A differencing scheme that can account for non-orthogonality in node structure was used. Equation 5 represents the shear term for branch 12. The angle θ represents the angle that adjacent branches make with respect to the referenced branch.

$$\mu \frac{\partial u}{\partial y} A_{\text{Branch 12 shear}} \approx \left[\left(\mu \frac{u_{N12} \cos\theta_{N12} - u_{12}}{YN} AN \right) + \left(\mu \frac{u_{12} - u_{S12} \cos\theta_{S12}}{YS} AS \right) \right] \tag{5}$$

Equation 5 can be generalized to n-number of parallel branches at any position around branch 12 as shown in Equation 6.

$$\mu \frac{\partial u}{\partial y} A_{\text{Branch 12 shear}} \approx \sum_{i=1}^{n} \left(\mu \frac{u_{i12} \cos\theta_{i12} - u_{12}}{Yi} Ai \right) \tag{6}$$

Where the summation subscript i represents the ith parallel branch to branch 12.

Next, the shear interaction with a neighboring parallel wall should be addressed. Suppose that adjacent to branch 12 is a wall that is approximately parallel to the branch. The angle θ_{wall} represents the angle between branch 12 and the wall. The wall has a velocity v_{solid}. The distance between the centerline of branch 12 and the wall is y_{wall} and the shear area is A_{wall}. The expression for the shear effect of the wall on branch 12 is given in Equation 7.

$$\mu \frac{\partial u}{\partial y} A \Big|_{\text{Branch 12 - wall}_{\text{shear}}} \approx \mu \frac{u_{wall} \cos\theta_{wall} - u_{12}}{y_{wall}} A_{wall} \tag{7}$$

If there were multiple walls adjacent to branch 12, then Equation 7 could be generalized into Equation 8.

$$\mu \frac{\partial u}{\partial y} A \Big|_{\text{Branch 12 - wall}_{\text{shear}}} \approx \sum_{i=1}^{n} \left(\mu \frac{u_{wall_i} \cos\theta_{wall_i} - u_{12}}{y_{wall_i}} A_{wall_i} \right) \tag{8}$$

Finally, combining the adjacent branch and the wall shear equations into one generalized equation for the ith branch for which shear is to be calculated. Equation 9 represents the actual laminar shear formulation incorporated into GFSSP, where i is the current branch, np_i is the number of parallel branches to branch i, and ns_i is the number of parallel solid walls to branch i.

$$\mu \frac{\partial u}{\partial y} A_{\text{Branch i shear}} \approx \sum_{j=1}^{np_i} \left(\mu \frac{u_{ij} \cos\theta_{ij} - u_i}{Y_{ij}} A_{ij} \right) + \sum_{k=1}^{ns_i} \left(\mu \frac{u_{\text{wall}\,ik} \cos\theta_{\text{wall}\,ik} - u_i}{y_{\text{wall}\,ik}} A_{ik} \right) \tag{9}$$

3.3.2 Turbulent Flow

To model shear stress in a turbulent flow, a turbulence model must be employed. Separate methods must be used to model the interaction between adjacent branches and between branches and adjacent walls. The following two sections provide the details for the modeling of these interactions.

3.3.2.1 Branch-Branch Interaction

Turbulent shear stress interaction between a branch and one of its neighboring branches is modeled using a modified form of the Mixing Length algebraic model proposed by Prandtl (see reference 5 for a description of Prandtl Mixing Length model). Referring to Figure 3 again, shear interaction between branch 12 and branch N12 is determined by their relative mean velocities, the shear area (AN) and the distance between the two branches (YN). In the original mixing length turbulence model proposed by Prandtl, viscosity (beginning with Equation 3) is replaced by an effective viscosity. This effective viscosity is defined as the sum of the viscosity and a "turbulent" viscosity:

$$\mu_{\text{effective}} = \mu + \mu_{\text{turbulent}} . \tag{10}$$

The turbulent viscosity, proposed by Prandtl, is defined by Equation 11, below.

$$\mu_{\text{turb}} = \rho(\kappa y)^2 \left| \frac{\partial u}{\partial y} \right| \tag{11}$$

where, ρ = local density of the fluid,
κ = Prandtl's mixing length constant (0.4),
y = distance from the wall,
u = local fluid velocity parallel to the wall.

Prandtl's formulation requires knowledge of local positioning with respect to a wall(s); however, GFSSP's formulation (outlined earlier) is fully unstructured. In order to implement the above approach into GFSSP, either additional information is required in the input file, or a modification to the definition of "y" in Equation 11 is needed. Based upon a desire to easily allow for an individual model to provide results for both laminar and turbulent approaches with minimal input change by the user, the latter approach of

modifying the definition of "y" was chosen. The new definition of "y" for Equation 11 is the distance between the branches, which is a required input for the laminar approach already. Therefore, for turbulent flow, Equation 4, 5, and 6 become Equations 12, 13, and 14.

$$\mu \frac{\partial^2 u}{\partial y^2} V \bigg|_{Turbulent} \approx \left(\mu + \left\{ \rho (\kappa \Delta y)^2 \left| \frac{\Delta u}{\Delta y} \right| \right\} \right) \frac{\Delta u}{\Delta y} A_{shear} \tag{12}$$

$$\mu \frac{\partial u}{\partial y} A_{Branch12\,shear} \approx \left[\begin{array}{l} \left(\left\{ \mu + \left[\rho (\kappa \cdot YN)^2 \left| \frac{u_{N12} \cos\theta_{N12} - u_{12}}{YN} \right| \right] \right\} \frac{u_{N12} \cos\theta_{N12} - u_{12}}{YN} AN \right) \\ + \left(\left\{ \mu + \left[\rho (\kappa \cdot YS)^2 \left| \frac{u_{12} - u_{S12} \cos\theta_{S12}}{YS} \right| \right] \right\} \frac{u_{12} - u_{S12} \cos\theta_{S12}}{YS} AS \right) \end{array} \right] \tag{13}$$

$$\mu \frac{\partial u}{\partial y} A_{Branch12\,shear} \approx \sum_{i=1}^{n} \left(\left\{ \mu + \left[\rho (\kappa \cdot Y_i)^2 \left| \frac{u_{i12} \cos\theta_{i12} - u_{12}}{Y_i} \right| \right] \right\} \frac{u_{i12} \cos\theta_{i12} - u_{12}}{Y_i} Ai \right) \tag{14}$$

Equation 14 represents the actual branch-branch turbulent shear formulation put into GFSSP.

3.3.2.2 Branch -Wall Interaction

Turbulent shear stress interaction between a solid (wall) and an adjacent branch is modeled using the log law of the wall [12]. The log law of the wall utilizes a characteristic turbulence distance from the wall (y^+) and a characteristic velocity (u^+). y^+ is a function of wall shear stress, and u^+ is a function of y^+ and wall shear stress; therefore an iterative scheme is required to calculate wall shear stress. Equations 15, 16, and 17 are the three equations that are iterated upon until a converged value for wall shear stress is achieved.

$$y^+ = \frac{\rho y \left(\frac{\tau}{\rho} \right)^{\frac{1}{2}}}{\mu} \tag{15}$$

where, ρ = local fluid density
μ = local fluid viscosity
y = local distance from wall

$$u^+ = \begin{cases} y^+ & \text{if } y^+ < 5.0 \\ -3.05 + 5.0\left(\log\left(y^+\right)\right) & \text{if } 5.0 \le y^+ < 30.0 \\ 5.5 + 2.5\left(\log\left(y^+\right)\right) & \text{if } y^+ \ge 30.0 \end{cases} \tag{16}$$

$$\tau = \mu \left.\frac{\partial u}{\partial y}\right| = \rho\left(\frac{u}{u^+}\right)^2 \tag{17}$$

where, u = local velocity parallel to the wall

In order to initiate the iterative process, a seed value of the wall shear stress must be provided. The seed value of wall shear stress utilized is given by Equation 18:

$$\tau_{\text{initial guess}} = \frac{\mu u}{y} \tag{18}$$

Equations 15-18 represent the actual branch-wall turbulent shear stress formulation incorporated into GFSSP.

3.4 Transverse Momentum Transport

The transverse momentum component of Equation 3 can be expressed in terms of a force per unit volume.

$$\frac{\partial \rho v u}{\partial y} V \approx \frac{(\rho v \Delta u)}{(\Delta y)} (\Delta x)(\Delta y)(\Delta z) = (\Delta x)(\Delta z)(\rho v \Delta u) = m_{\text{trans,dot}} \Delta u \tag{19}$$

Figure 4 represents a set of nodes and branches for which transverse momentum exchange will take place. Let the branch 12 represent the current branch which will receive transverse momentum from the surrounding branches. Branch S12 represents an adjacent parallel branch, while branches S1 and S2 represent the adjacent normal branches.

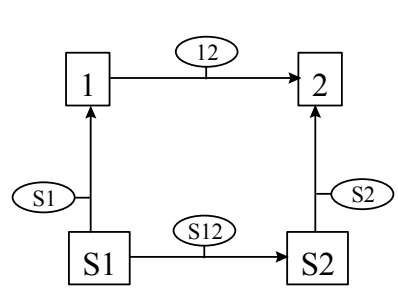

Figure 4: Branch and Node Schematic for Transverse Momentum Exchange

Now, examine the formulation for calculating the transverse momentum term for branch 12. First, calculate the average mass flow rate for the adjacent normal branches:

$$\mathrm{m}_{\mathrm{S,dot}} = \frac{1}{2}\left(\mathrm{m}_{\mathrm{S1,dot}} + \mathrm{m}_{\mathrm{S2,dot}}\right) \tag{20}$$

Examining Figure 4, a positive transverse mass flow rate is defined as flow into the nodes corresponding to the branch in question. Based on this definition of transverse mass flow rate, calculate the transverse momentum term:

$$\left.\frac{\partial \rho v u}{\partial y} V\right|_{12} \approx \left(\mathrm{m}_{\mathrm{S,dot}} u_{12} - \mathrm{m}_{\mathrm{S,dot}} u_{S12}\right) = \mathrm{m}_{\mathrm{S,dot}}\left(u_{12} - u_{S12}\right) \tag{21}$$

The parallel branch (S12) will contribute to the transverse momentum term of branch 12 when $\dot{\mathrm{m}}_{12} \geq 0$ (since a positive transverse flow rate begins at S12 and ends at 12), and should have a negligible contribution when $\dot{\mathrm{m}}_{12} < 0$ (i.e. transverse flow rate begins at 12 and ends at S12). Equation 22, is the upwinding representation of the transverse momentum term for branch 12.

$$\left.\frac{\partial \rho v u}{\partial y} V\right|_{12} \approx u_{12}\left(\max\left\|-\mathrm{m}_{\mathrm{S,dot}}, 0\right\|\right) - u_{S12}\left(\max\left\|0, \mathrm{m}_{\mathrm{S,dot}}\right\|\right) \tag{22}$$

Equation 22 can be generalized for m-parallel branches around branch i, each with an angle θ_{ij} with respect to branch i, and n_{ij} corresponding transverse connecting branches, each transverse branch with an angle of θ_{ijk} with respect to branch i. Equation 23 represents this generalized version of Equation 22.

$$\left.\frac{\partial \rho v u}{\partial y} V\right|_{i} \approx \sum_{\mathrm{j}=1}^{m_i}\left[u_i\left(\max\left\|-\sum_{\mathrm{k}=1}^{\mathrm{n}_{\mathrm{ij}}}\left\{\frac{1}{\mathrm{n}_{\mathrm{ij}}}\mathrm{m}_{\mathrm{ijk,dot}}\cos\theta_{ijk}\right\}, 0\right\|\right) - \left(u_{ij}\cos\theta_{ij}\right)\left(\max\left\|0, \sum_{\mathrm{k}=1}^{\mathrm{n}_{\mathrm{ij}}}\left\{\frac{1}{\mathrm{n}_{\mathrm{ij}}}\mathrm{m}_{\mathrm{ijk,dot}}\cos\theta_{ijk}\right\}\right\|\right)\right] \tag{23}$$

Equation 23 represents the actual transverse momentum formulation put into GFSSP, where i is the current branch for which transverse momentum is being calculated, m_i is the number of parallel branches which will be used to calculate transverse momentum, and n_{ij} is the number of connecting transverse branches between the current branch i, and the jth parallel branch.

4.0 Verification Results

In order to verify proper implementation of the shear and transverse momentum components into GFSSP, three models were identified and developed. Two verification

models were benchmarked for both laminar and turbulent flow. These two models are: two dimensional Poiseuille flow and two dimensional Couette flow. The third model was benchmarked with the laminar flow solution only. This third model is the two dimensional shear driven flow in a square cavity. The following sections describe the models and presents the results.

4.1 Poiseuille Flow Model

Consider the flow between two fixed flat plates shown in Figure 5. The flow is pressure driven and assumed to be fully developed. The analytical solution for this situation can easily be derived for laminar flow. Figure 6 shows an approximate velocity profile for the laminar situation.

A simple 3 node, 10 branch model (two sets of 5 parallel branches) was constructed to model the physical situation described above. The model is shown schematically in Figure 7.

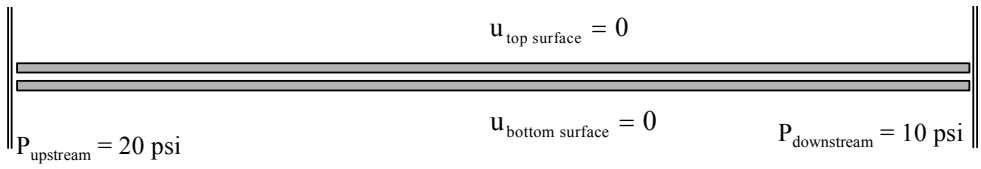

Figure 5: Poiseuille Flow Physical Situation

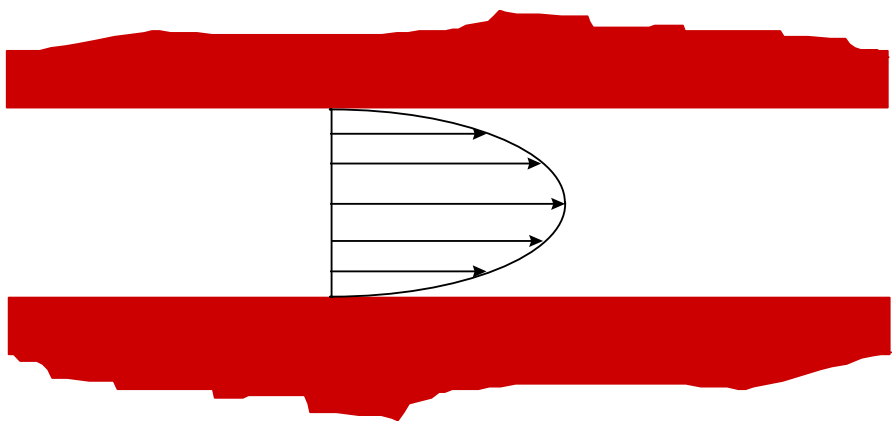

Figure 6: Poiseuille Flow Velocity Profile

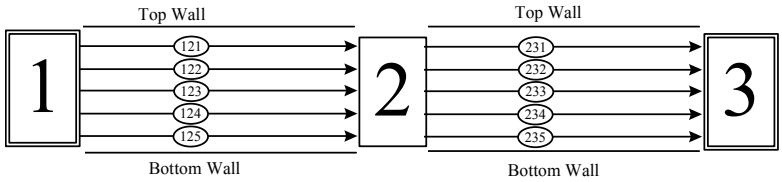

Figure 7: GFSSP Poiseuille Flow Model

The GFSSP's flow through a restriction resistance option was used in the initial flow field calculation (for the first Newton-Raphson iteration, after which the shear will replace the friction factor calculation) for each of the branches. The bottom and top walls are fixed.

Figure 8 shows a comparison between the velocity profiles for the known solutions (analytical for laminar and experimental for turbulent) and the GFSSP 3 node, 10 branch (5 parallel branch) model. As can be seen in Figure 8, the results of this crude GFSSP model compare vary favorably with the analytical solution.

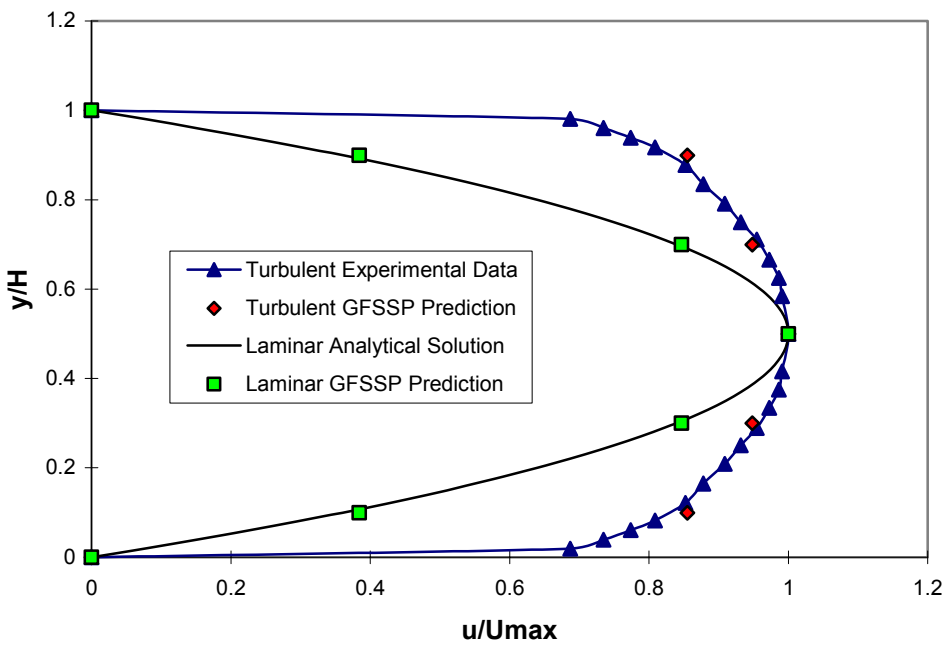

Figure 8: Poiseuille Flow Velocity Distribution

4.2 Couette Flow

Consider the flow between two fixed flat plates shown in Figure 9. The flow is shear driven and assumed to be fully developed. The solution to the laminar case is a linear velocity profile, illustrated in Figure 10.

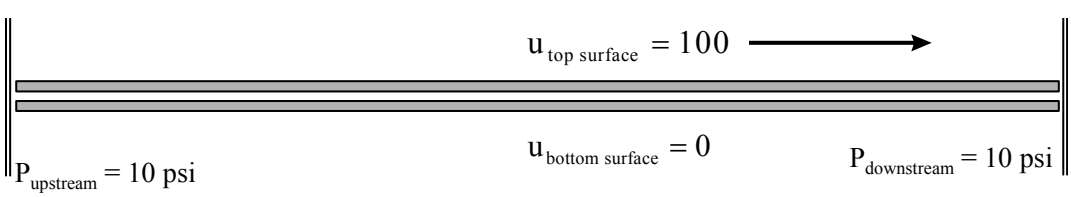

Figure 9: Couette Flow Physical Situation

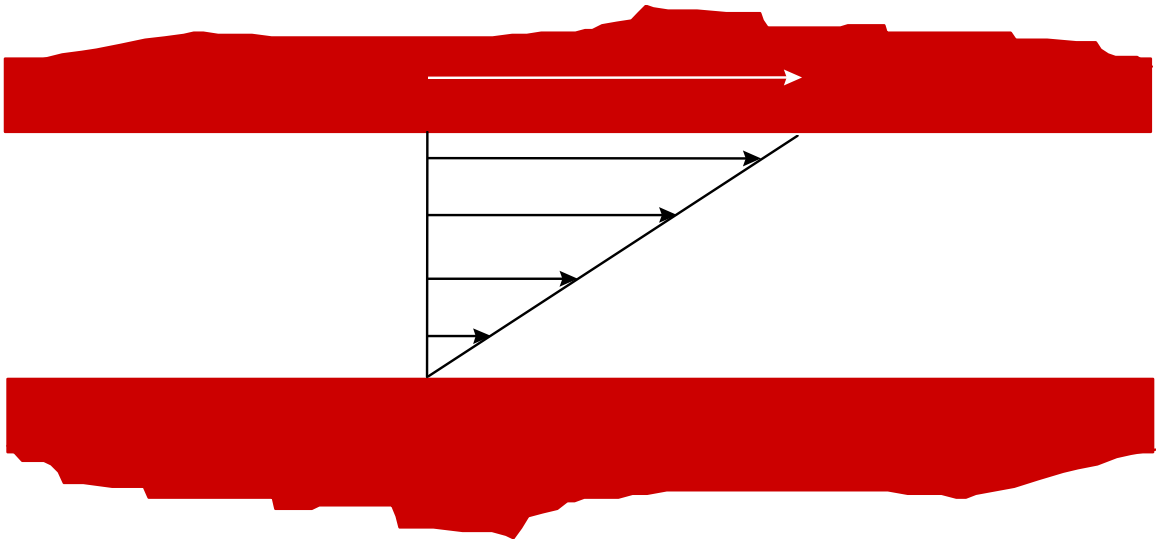

Figure 10: Laminar Couette Flow Velocity Profile

A simple 3 node, 10 branch model (two sets of 5 parallel branches) was constructed to model the physical situation. The model is shown schematically in Figure 11.

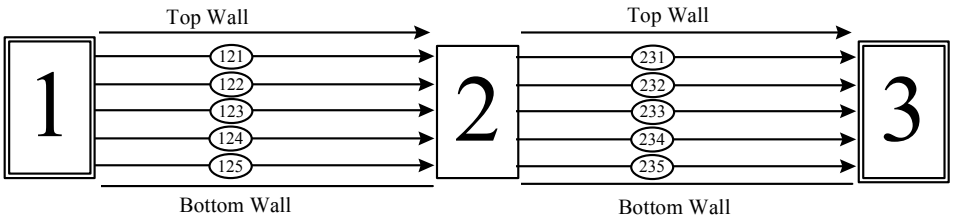

Figure 11: GFSSP Couette Flow Model

As with the Poiseuille flow case, resistance option -02 was used in the initial flow field calculation (for the first Newton-Raphson iteration, after which the shear will replace the friction factor calculation) for each of the branches. The bottom walls are fixed, and the top walls are moving at a known velocity.

Figure 12 shows the comparison between the velocity profiles for the known solutions (analytical for the laminar case, experimental results for the turbulent case) and the GFSSP 3 node, 10 branch (5 parallel branch) model. As can be seen in Figure 12, the results of this crude GFSSP model compare nearly identically with the analytical solution.

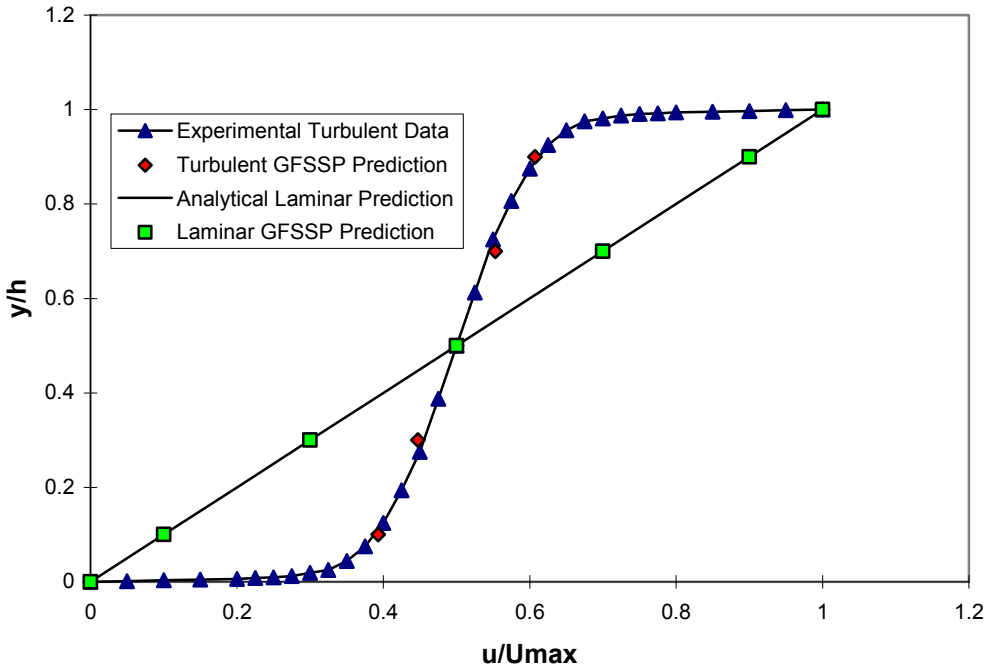

Figure 12: Couette Flow Velocity Distribution

4.3 Shear Driven Flow in a Square Cavity

Consider a square cavity as shown in Figure 13. The flow is induced by shear interaction at the top wall. The bottom and side walls are fixed. The top wall is moving to the right at constant speed. The corresponding Reynolds number for this situation is Re = 100.

4.3.1 Benchmark Numerical Solution

Due to the non-linearity of the governing differential equations, an analytical solution of this situation is not available. Instead of an analytical solution, a well known numerical solution by Odus Burggraf [13] was used as the benchmark. Burggraf used a 51x51 grid in his model of the square cavity.

4.3.2 GFSSP Driven Cavity Model

The GFSSP model of the driven cavity consists of 49 nodes (48 of which are internal) and 84 branches.

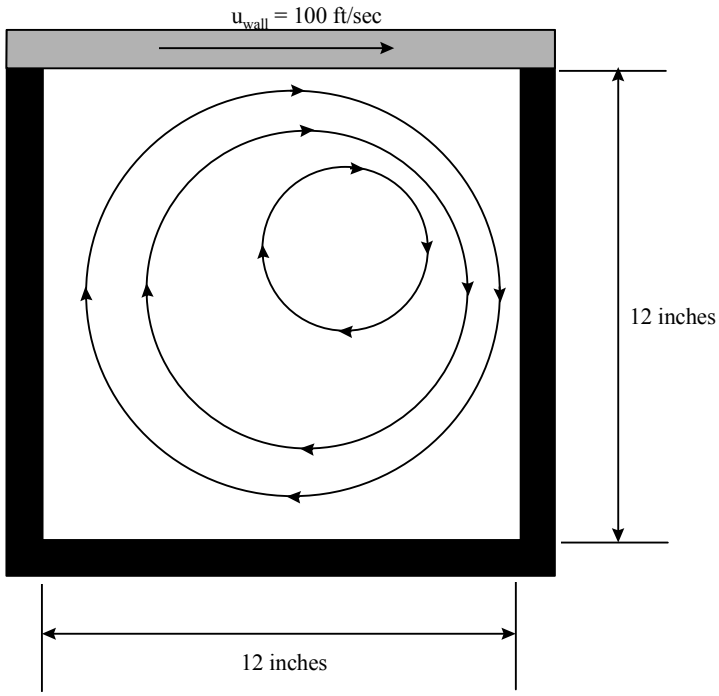

Figure 13: Flow in a Shear Driven Square Cavity

For numerical stability, one node (Node 1) was assigned to be a boundary node with an arbitrary pressure. A unit depth was assumed for the required areas. The model is shown schematically in Figure 14. As in the previous cases, GFSSP's flow through a restriction resistance Option was used in the initial flow field calculation for all of the branches. The bottom and side walls are fixed. The top walls are moving to the right at known velocity. All parallel angles are 0°, and all transverse angles are 90°.

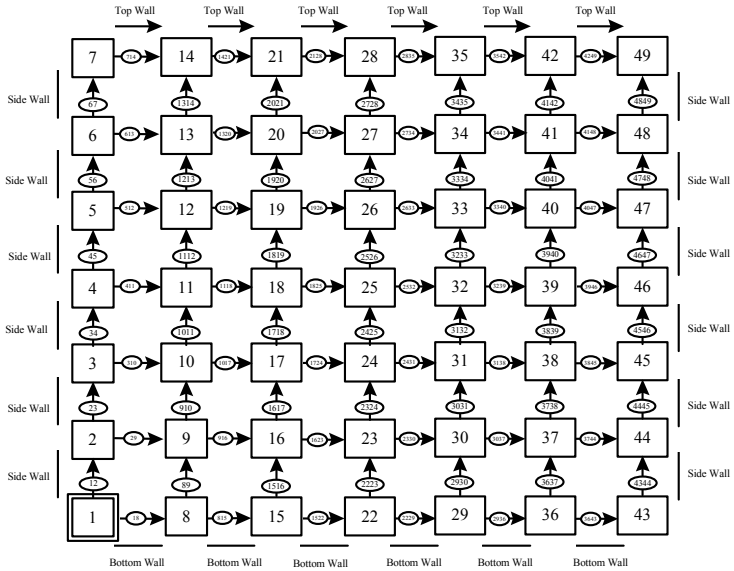

Figure 14: GFSSP Flow in a Shear Driven Square Cavity Model

4.3.3 Results

Figure 15 shows a comparison between the benchmark numerical solution and GFSSP 7x7 node model velocity profiles along a vertical plane at the horizontal midpoint. As can be seen in Figure 15, the results of this crude GFSSP model compare very favorably with the benchmark numerical solution of Burggraf [13].

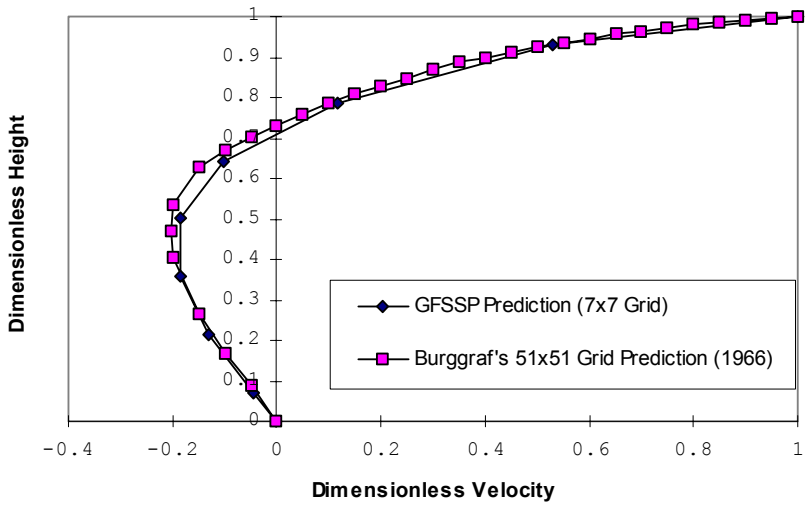

Figure 15: Shear Driven Square Cavity Centerline Velocity Distribution

5.0 Conclusions

This paper presents a numerical algorithm to extend a system level flow network code that was designed to solve one dimensional momentum equation to perform multi-dimensional flow calculation. The algorithm uses an identical mathematical framework for both system and component level analysis. The multi-dimensional features were incorporated by including additional momentum sources due to shear stress and transport of momentum due to transverse component of velocity. The simplicity and ease of the formulation can largely be attributed to the use of unstructured co-ordinate system. Excellent agreement with analytical solution was obtained for laminar flow in three benchmark problems: Poiseuille Flow, Couette flow and shear driven flow in a square cavity. Turbulence is modeled by an effective viscosity which is calculated from Prandtle's mixing length theory. Numerical predictions compared well with turbulent Couette flow data.

6.0 Acknowledgements

The work was performed at Sverdrup Technology (MSFC Group) under contract NAS8-40386, Task Directives 611-022, 550-5500-0500.

7.0 References

1. Majumdar, A.K.: *A Generalized Fluid System Simulation Program to Model Flow Distributions in Fluid Networks*, (User's Manual) Report No. MG-99-290, NASA MSFC Contract No. NAS 8-40836, November 1999.
2. Patankar, S., *Numerical Heat Transfer and Fluid Flow,* Hemisphere Publishing Co., New York, 1980.
3. Hendricks, R. C., Baron, A. K., and Peller, I. C., "GASP - A Computer Code for Calculating the Thermodynamic and Transport Properties for Ten Fluids: Parahydrogen, Helium, Neon, Methane, Nitrogen, Carbon Monoxide, Oxygen, Fluorine, Argon, and Carbon Dioxide", NASA TN Dd-7808, February, 1975.
4. Hendricks, R. C., Peller, I. C., and Baron, A. K., "WASP - A Flexible Fortran IV Computer Code for Calculating Water and Steam Properties", NASA TN D-7391, November, 1973.
5. Cryodata Inc., "User's Guide to GASPAK, Version 3.20", November 1994.
6. Van Hooser, Bailey John and Majumdar Alok, "Numerical Prediction of Transient Axial Thrust and Internal Flows in a Rocket Engine Turbopump", Paper No. AIAA 99-2189, 35th AIAA/ASME/SAE/ASEE Joint Propulsion Conference and Exhibit, June 21, 1999, Los Angeles, CA.
7. Holt, Kimberly, Majumdar, Alok, Steadman Todd, and Hedayat, Ali, Paper No. AIAA 2000-3719 "36th AIAA/ASME/SAE/ASEE Joint Propulsion Conference and Exhibit, July 16-19, 2000, Huntsville, AL.
8. Schallhorn, Paul, Elrod, David, Goggin, David and Majumdar, Alok, "A Fluid Circuit Model for Long Bearing Squeeze Film Damper Rotordynamics", AIAA Journal of Propulsion and Power, Vol. 16, No. 5, pp 777-780, Sept-Oct 2000.
9. Majumdar, Alok and Steadman, Todd, "Numerical Modeling of Pressurization of a Propellant Tank", AIAA Journal of Propulsion and Power, Vol. 17, No. 2, March-April 2001.
10. Cross, Matthew, F, Majumdar Alok K, Bennett, Jr., John C., and Malla, Ramesh B., "Modeling of Chill Down in Cryogenic Transfer Lines", Accepted for publication in AIAA Journal of Spacecraft and Rocket.
11. Schallhorn, P.: *Development of the Generalized Fluid System Simulation Program for Multidimensional Flow*, Sverdrup Report No. 661-022-97-003, April 1997.
12. Schlicting, H., Boundary Layer Theory, 6th Edition, McGraw-Hill, 1964 .
13. Burggraf, O.R.: "Analytical and Numerical Studies of the Structure of Steady Separated Flows", Journal of Fluid Mechanics, Vol. 24, part 1, pp. 113-151, 1966.

Approximating Fluid Flow from Ambient to Very Low Pressures – Modeling ISS Experiments that Vent to Vacuum.

September 11 2001

Robert Minor

MSFC TD 62/NASA

Background

- Two ISS experiment payloads will vent a volume of gas overboard via either the ISS Vacuum Exhaust System or the Vacuum Resource System. A system of ducts, valves and sensors, under design, will connect the experiments to the ISS systems.

Background

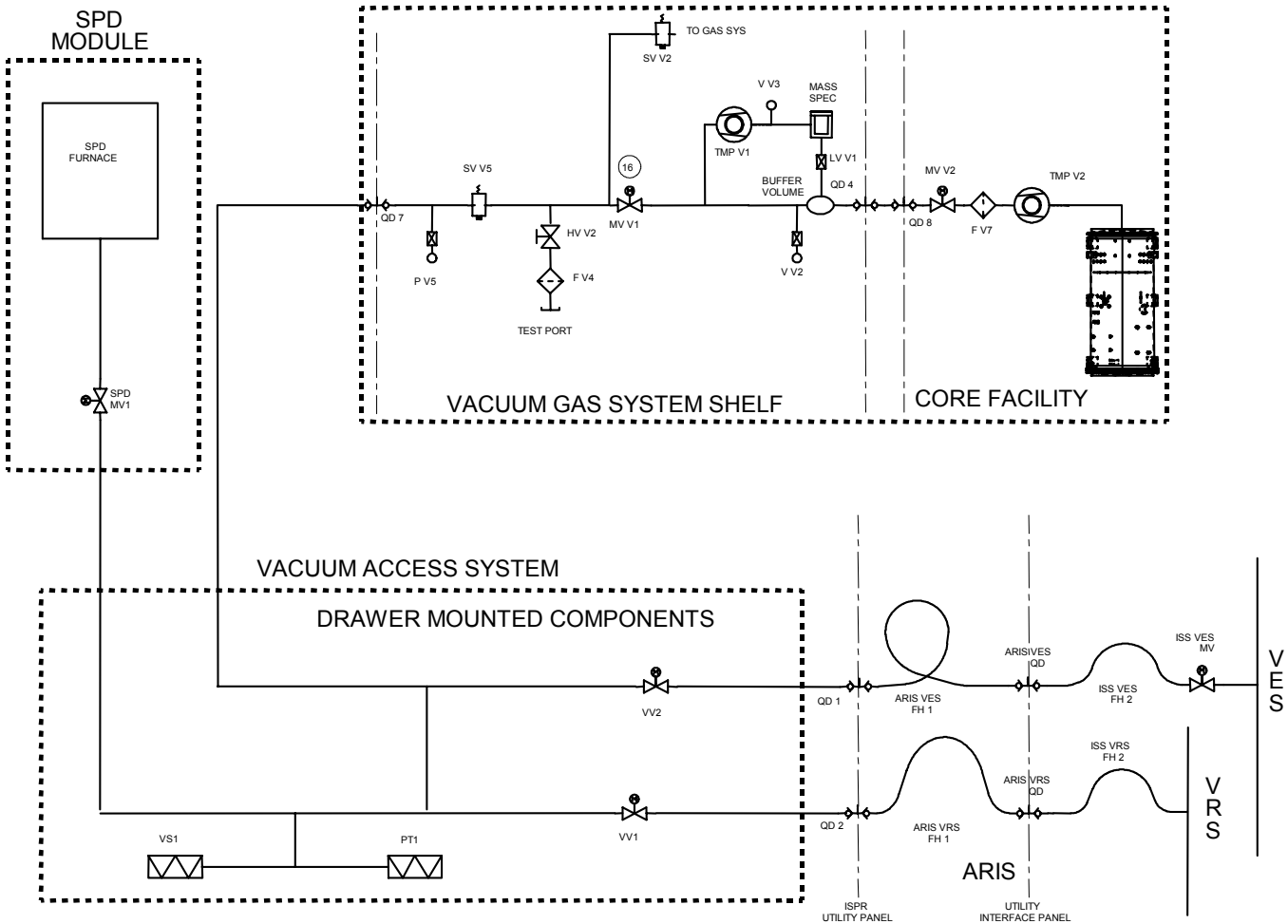
SPD MODULE
SPD FURNACE
SPD MV1
TO GAS SYS
SV V2
V V3
MASS SPEC
TMP V1
LV V1
16
SV V5
BUFFER VOLUME
QD 4
MV V2
TMP V2
QD 7
HV V2
MV V1
QD 8
F V7
P V5
F V4
V V2
TEST PORT
VACUUM GAS SYSTEM SHELF
CORE FACILITY
VACUUM ACCESS SYSTEM
DRAWER MOUNTED COMPONENTS
ARIS VES QD
ISS VES MV
VV2
QD 1
ARIS VES FH 1
ISS VES FH 2
VES
ISS VRS FH 2
ARIS VRS QD
VRS
VS1
PT1
VV1
QD 2
ARIS VRS FH 1
ARIS
ISPR UTILITY PANEL
UTILITY INTERFACE PANEL

The Task

- Create an analysis tool that will verify the rack vacuum system design with respect to design requirements, more specifically approximate pressure at given locations within the vacuum systems.
- Determine the vent duration required to achieve desired pressure within the experiment modules.
- Update the analysis as systems and operations definitions mature.

Unknowns

- Final configuration of rack based vacuum system.
- Some material specific characteristics of the ISS vacuum system, particularly off-gas rates for components with company proprietary material specifications.
- Gas to be vented.
- Gas temperature, pressure and volume.
- Operations scenarios which could impact pressure and temperature of downstream systems.

Known

- Final Configurations of ISS Vacuum Exhaust and Vacuum Resource Systems.
- At some point, in all operations scenarios, there will be a venting of an experiment chamber from ambient to very low pressure.
- Pressure outside ISS is ~1.2e-7 torr.
- Volume outside ISS is infinite.

Three Regimes of Fluid Flow

- Continuum (viscous) flow can be laminar or turbulent, and can be predicted by the laws of conservation of mass and energy.

- Transitional flow has characteristics of both molecular and continuum and is approximated with a conductance method.

Fluid Flow (Continued)

- Molecular flow can be characterized by the mean free path of the molecule (λ). The mean free path is the distance a molecule is predicted to travel with out colliding with another molecule or vessel wall. Molecular flow occurs when λ is relatively large so the likelihood that a molecule will collide with a vessel wall is greater than the likelihood that there will be intermolecular collisions. Molecular flow will be analyzed using a conductance method.

Determining Flow Regime

- Predicting flow regime is accomplished with Knudsen number (Kn).
  - A Knudsen number greater than zero and less than 0.01 indicates a continuum flow regime.
  - The transitional regime will occur where K*n* is greater than or equal to 0.01 and less than or equal to 1.0.
  - A Knudsen number greater than 1.0 identifies the flow regime as molecular flow.
- Knudsen number is calculated by:
  - Kn=0.066/(D*P)
  - Derivation for this equation can be found in the paper.

Determining Pressure

- Two distinct methods of determining the change in pressure over time are employed in order to evaluate performance over all flow regimes
  - Pressure changes through the viscous flow regime are evaluated using the Generalized Fluid System Simulation Program (GFSSP).
  - Flow in the low continuum, transitional, and molecular regimes is predicted using a conductance method.

GFSSP

- Assumes a Newtonian, non-reacting and one-dimensional flow.
- Requires resolution of the system into nodes (internal and boundary) and branches.
- Pressures, temperatures, and concentrations of fluid species are specified at the boundary nodes
- Flow rates are computed in the branches.
- Results are in english units.

Conductance Method

- Flow for the molecular and transitional regimes are predicted by measuring the ability of a gas to flow through a control volume, called conductance.
- In a manner similar to GFSSP analysis a conductance model is developed as a series of connected nodes.
- Control volumes are modeled in terms of pipe and orifice.
- Control volume conductances can be added, in a manner analogous to electrical resistance, so that systems with parallel or series branches can be simplified into single volumes.

Conductance Method (Continued)

$$\mathring{P}_j = \frac{1}{V_j}\left[G_j + L_j + C_{ij} * (P_i - P_j) - C_{jk} * (P_j - P_k)\right]$$

Where: $\mathring{P}_j$ = Change in pressure in control volume j (torr/sec)

V = Volume (L)

G = Off-gas rate (torr L/sec)

L = Leak (torr L/sec)

C = Conductance (L/sec)

P = Pressure (torr)

i and k are upstream and down stream respectively from j.

Meshing the Models

- GFSSP output becomes the conductance model input file.
  - Design both models so node information mesh.
  - GFSSP calculates in english units, conductance code in SI, be sure to convert.
  - Expect a settling in period, the duration will depend on step size.

Helpful Assumptions for ISS Venting Approximations

- The experiment will either fly at ambient pressure to the station or at some point an on-orbit operation will fill an experiment chamber with station air. This allows for the following assumptions:
  - The gas to be vented is air.
  - Gas temperature and pressure are standard.
- If the valve configuration is under study, let valves open instantaneously.
- Station vacuum systems are vented from ambient pressure along with experiment modules.

Helpful Assumptions for ISS Venting Approximations

- Seals
  - All seals, within the system under design, will leak, the maximum allowable amount, per seal specification.
  - Seals leaking the maximum allowable amount, will not impact continuum pressures, i.e. GFSSP model.
  - Seals within Vacuum Exhaust and Vacuum Resource systems do not leak.
  - Other experiments connected to these vacuum systems do not leak.

Helpful Assumptions for ISS Venting Approximations

- Off-gassing is described by an exponential decay function.
  - Pressure must be low enough for the escape of entrained gases to be significant, which won't occur to a noticeable degree in continuum regime.
  - When off-gassing rates are unavailable use a known rate for a material with chemical similarities.

Conclusions

When designing a new analysis tool:

- Gather information from system designers, operations planners, and principal investigators,
- Fill in the blanks with assumption,
- Create modular software,
- Share results,
- Iterate.

Incorporation of Condensation Heat Transfer in a Flow Network Code

Miranda Anthony & Alok Majumdar

NASA/Marshall Space Flight Center

Huntsville, Alabama

Content

- Introduction
- Problem Description
- Generalized Fluid System Simulation Program
- Condensation Heat Transfer
- Solid to Fluid Heat Transfer
- Numerical Model Results
- Conclusions
- References & Acknowledgements

Introduction

- Pure water is distilled from waste water in International Space Station
- Distillation assembly consists of evaporator, compressor and condenser
- Vapor is periodically purged from the condenser to avoid vapor accumulation
- Purged vapor is condensed in a tube by coolant water prior to entering purge pump
- The paper presents a condensation model of purged vapor in a tube

UPA Distillation Assembly

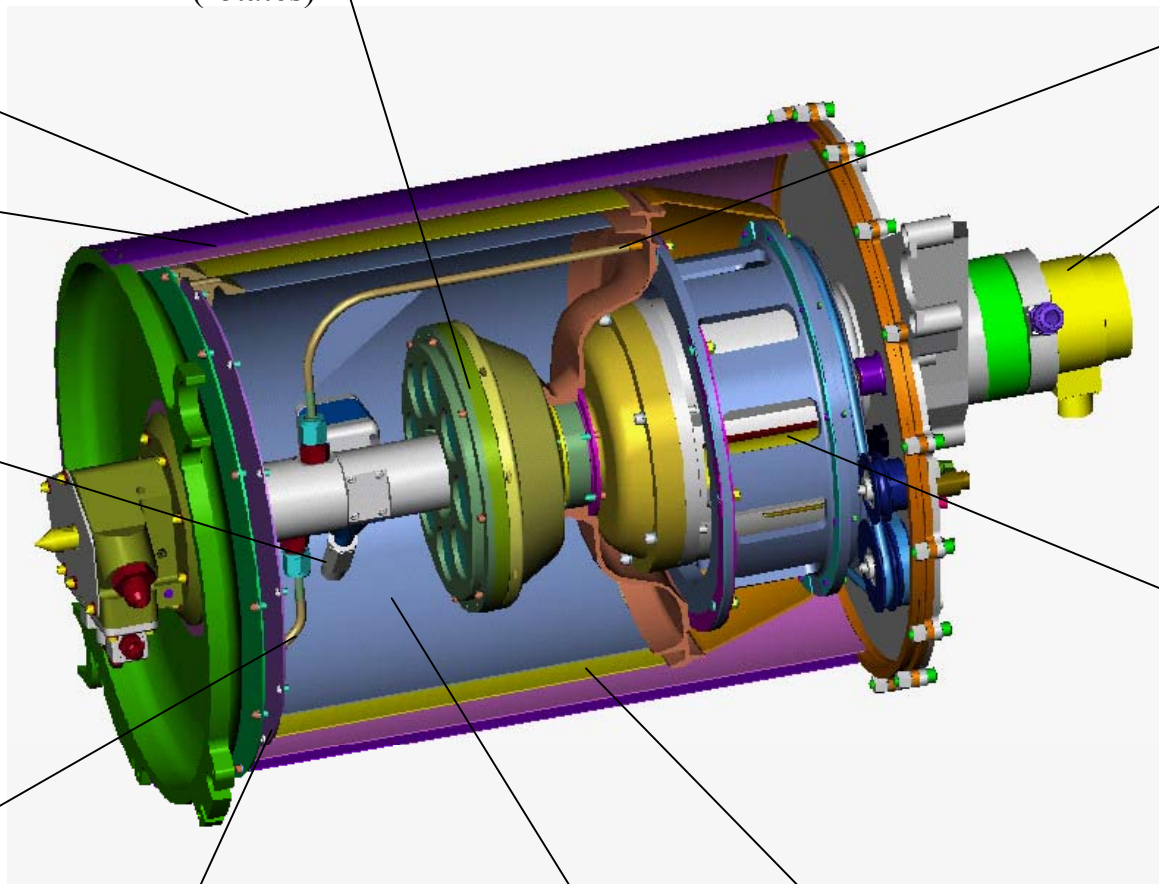

UPA Simplified Schematic

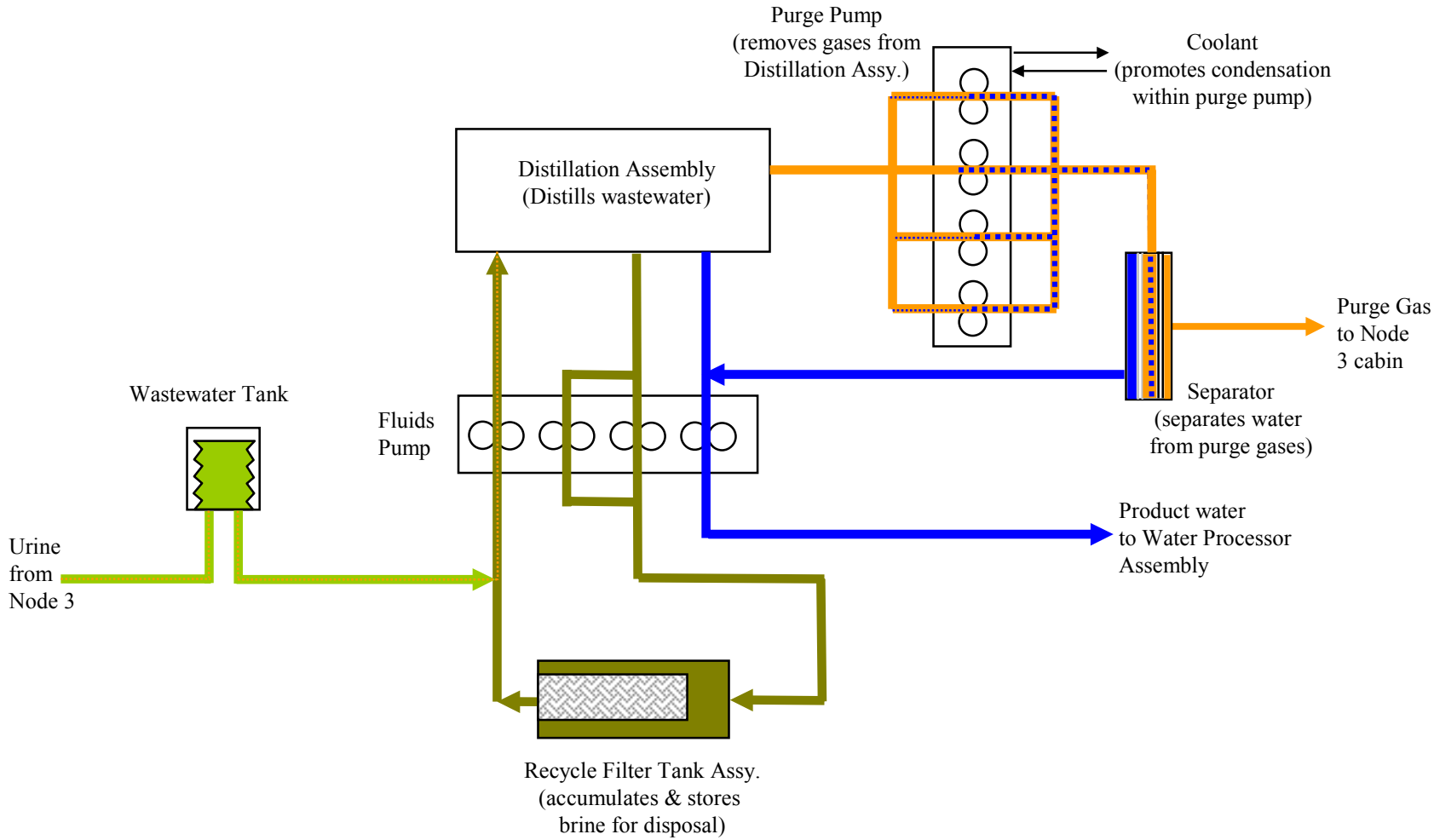

Problem Description

Superheated
Water Vapor
P_{inlet} = 0.95 psia
T_{inlet} = 101°F

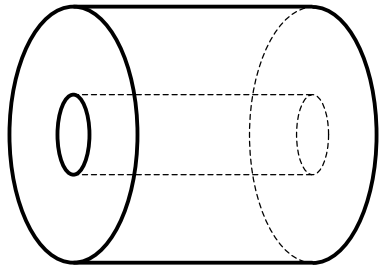

Saturated
Water Vapor
P_{outlet} = 0.5 psia

$T_{outer\ wall}$ = 65°F

Inner Tube Diameter = 0.125 inch
Outer Tube Diameter = 1 inch
Length = 4 inches
Material is Titanium

Calculate the Quality and Heat Transfer Properties of the Water as it Condenses in the Pipe

Model consists of 2 Boundary Nodes and 28 Internal Nodes and Models Conduction through the Tube Wall

Generalized Fluid System Simulation Program (GFSSP)

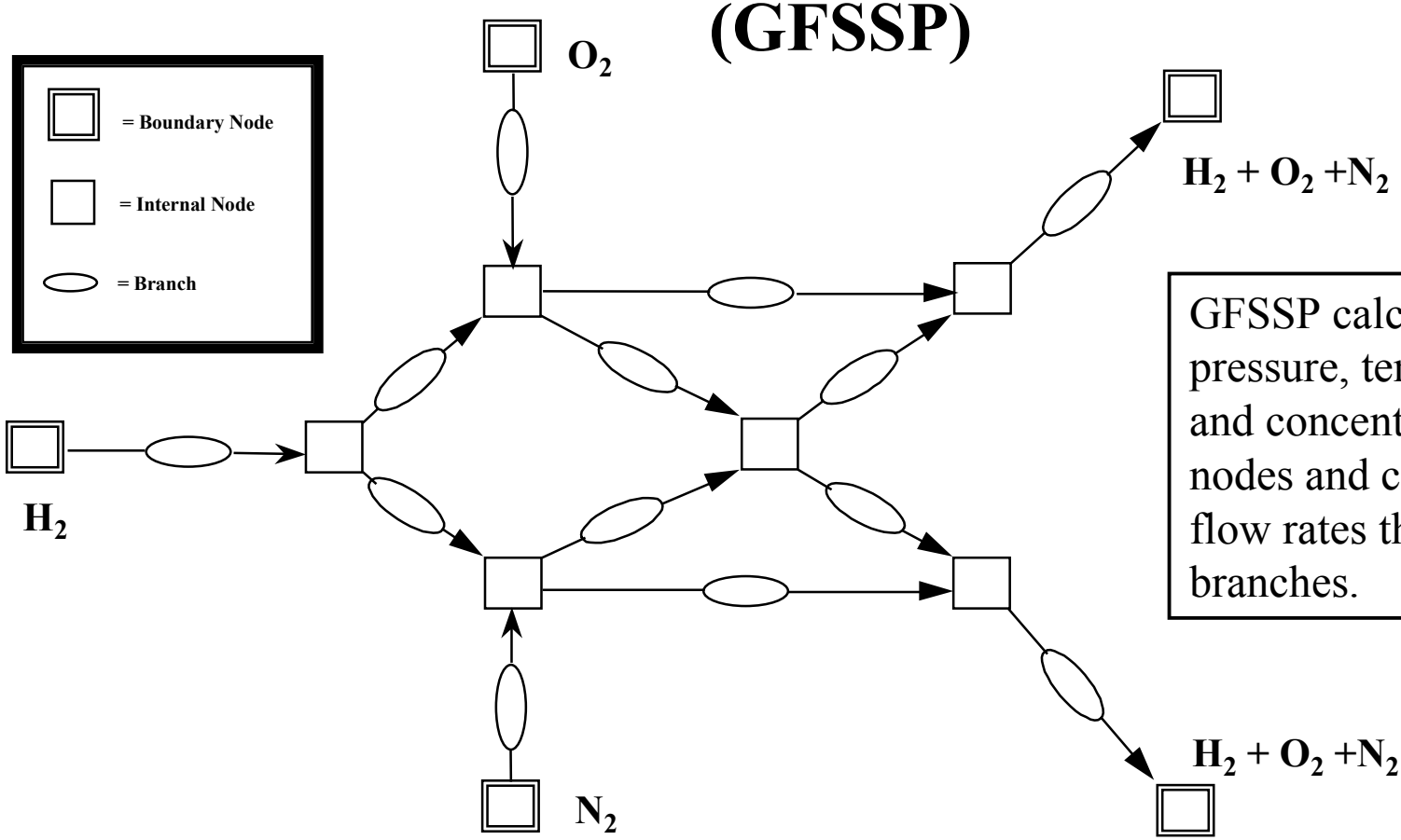

GFSSP calculates pressure, temperature, and concentrations at nodes and calculates flow rates through branches.

GFSSP
Finite Volume Method

- Finite Volume Method is based on conservation principle of Thermo-Fluid Dynamics
- In Classical Thermodynamics we analyze a single control volume
- In Finite Volume Method, flow domain is discretized into multiple control volumes and a <u>simultaneous</u> analysis is performed
- Finite Volume Method can be classified into two categories:
  - Navier-Stokes Solution (Commonly known as CFD)
  - Network Flow Solution (NFS)

GFSSP
Finite Volume Method

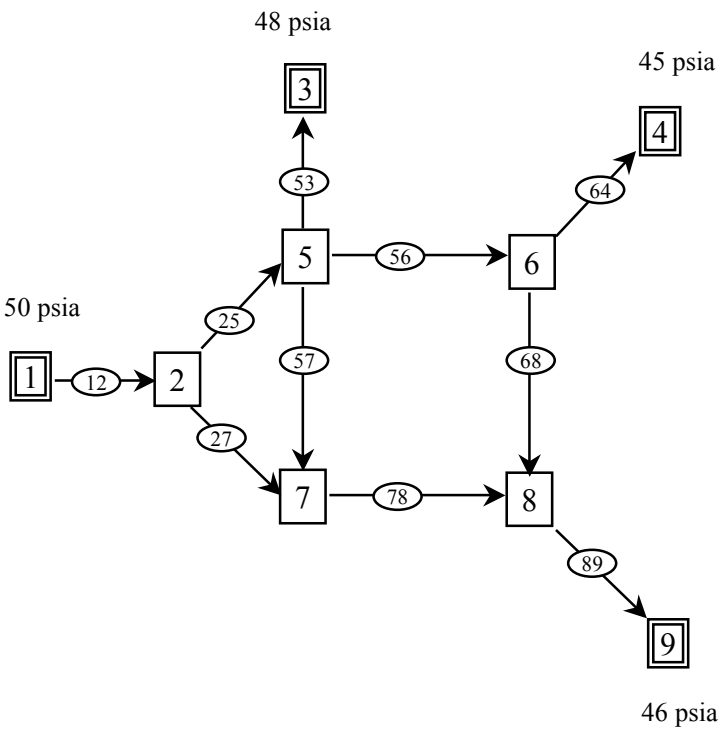

Network Flow Solution (NFS)

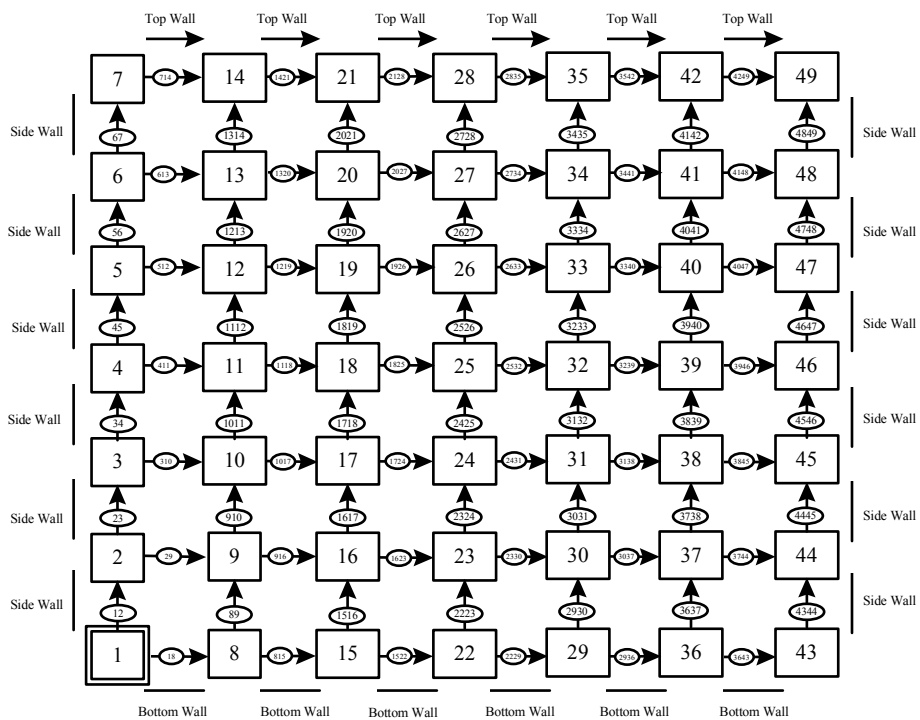

Navier-Stokes Solution (CFD)

GFSSP Process Flow Diagram

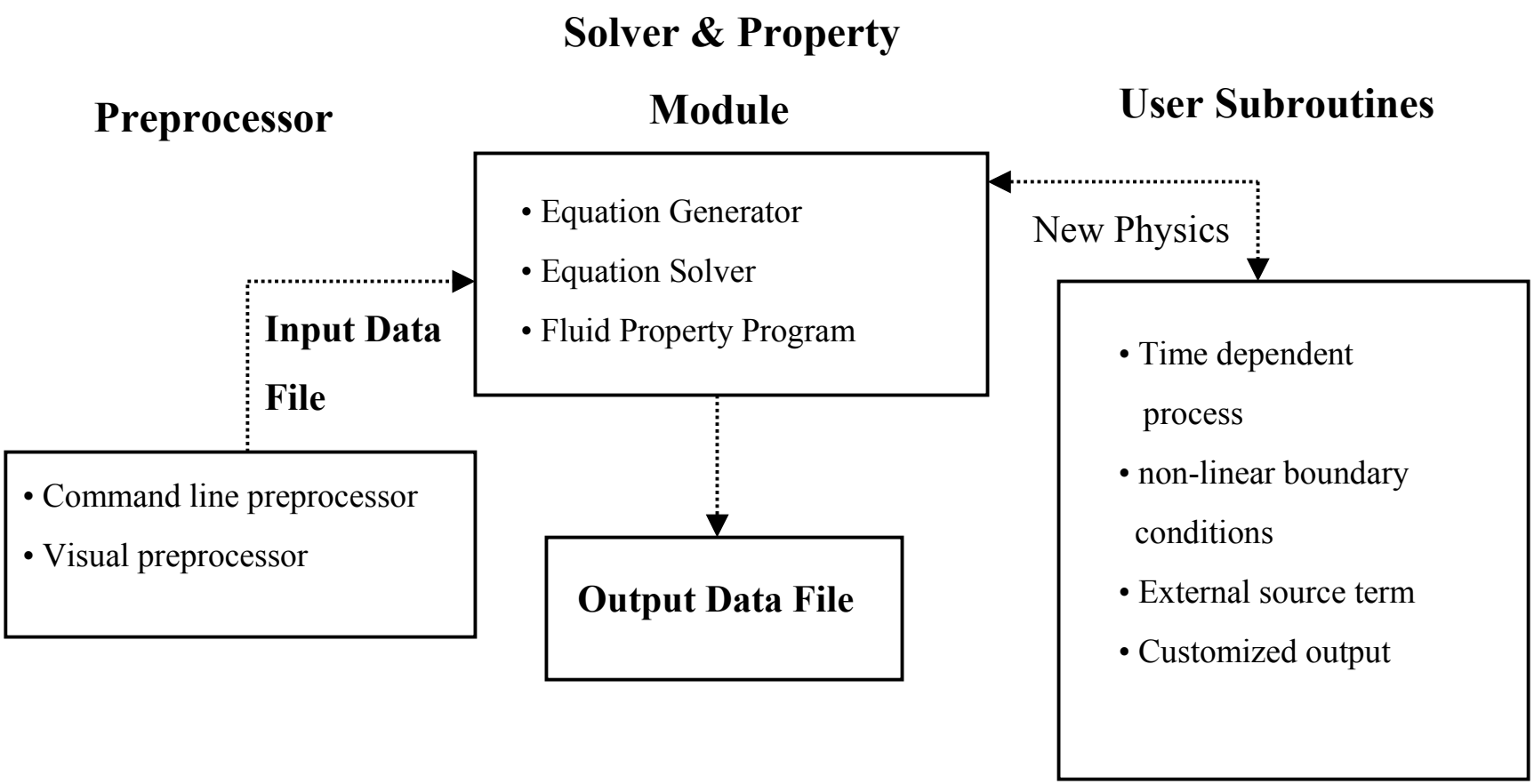

Coupling of Thermodynamics & Fluid Dynamics

p – Pressure

$\dot{m}$ - Flowrate

h - Enthalpy

c - Concentration

ρ - Density

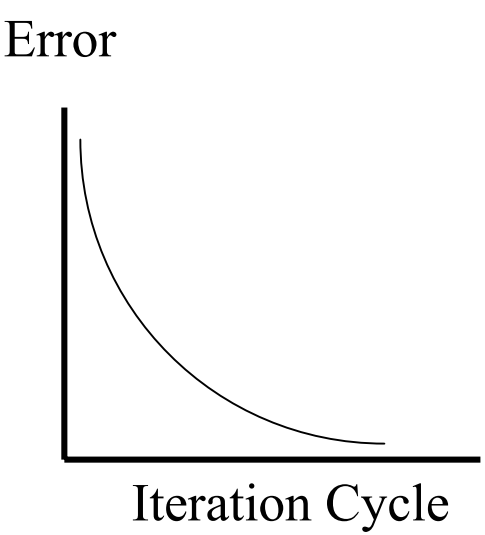

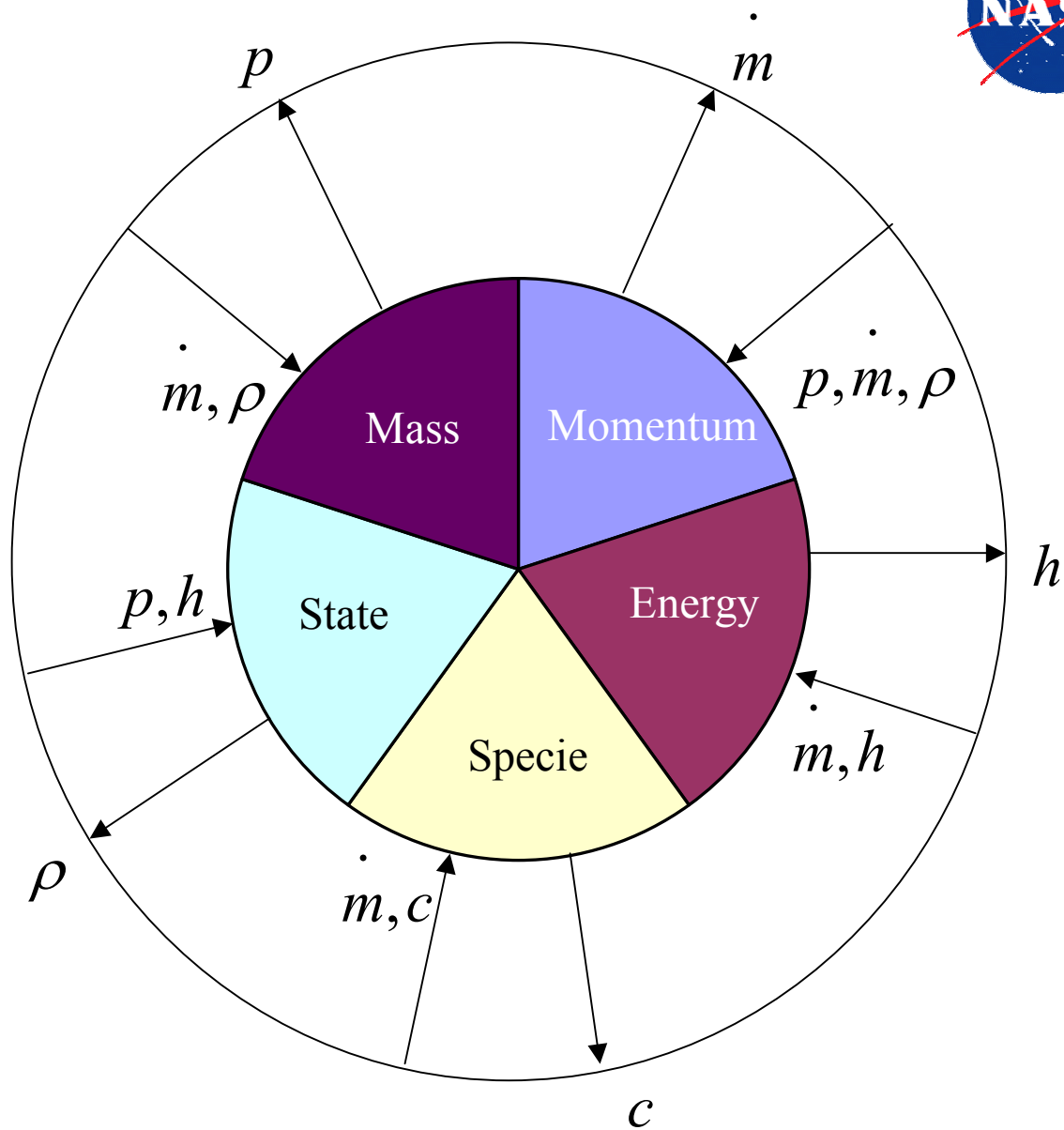

GFSSP Solution Scheme

SASS : **S**imultaneous **A**djustment with **S**uccessive **S**ubstitution

Approach : Solve simultaneously when equations are strongly coupled and non-linear

Advantage : Superior convergence characteristics with affordable computer memory

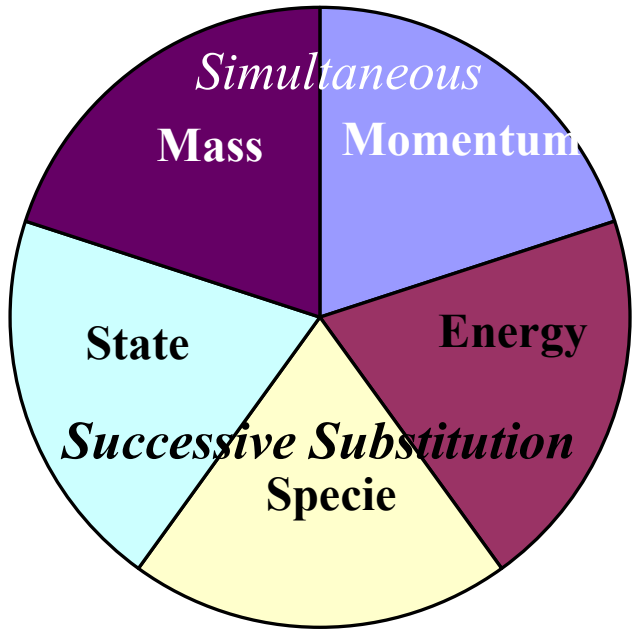

Condensation Heat Transfer

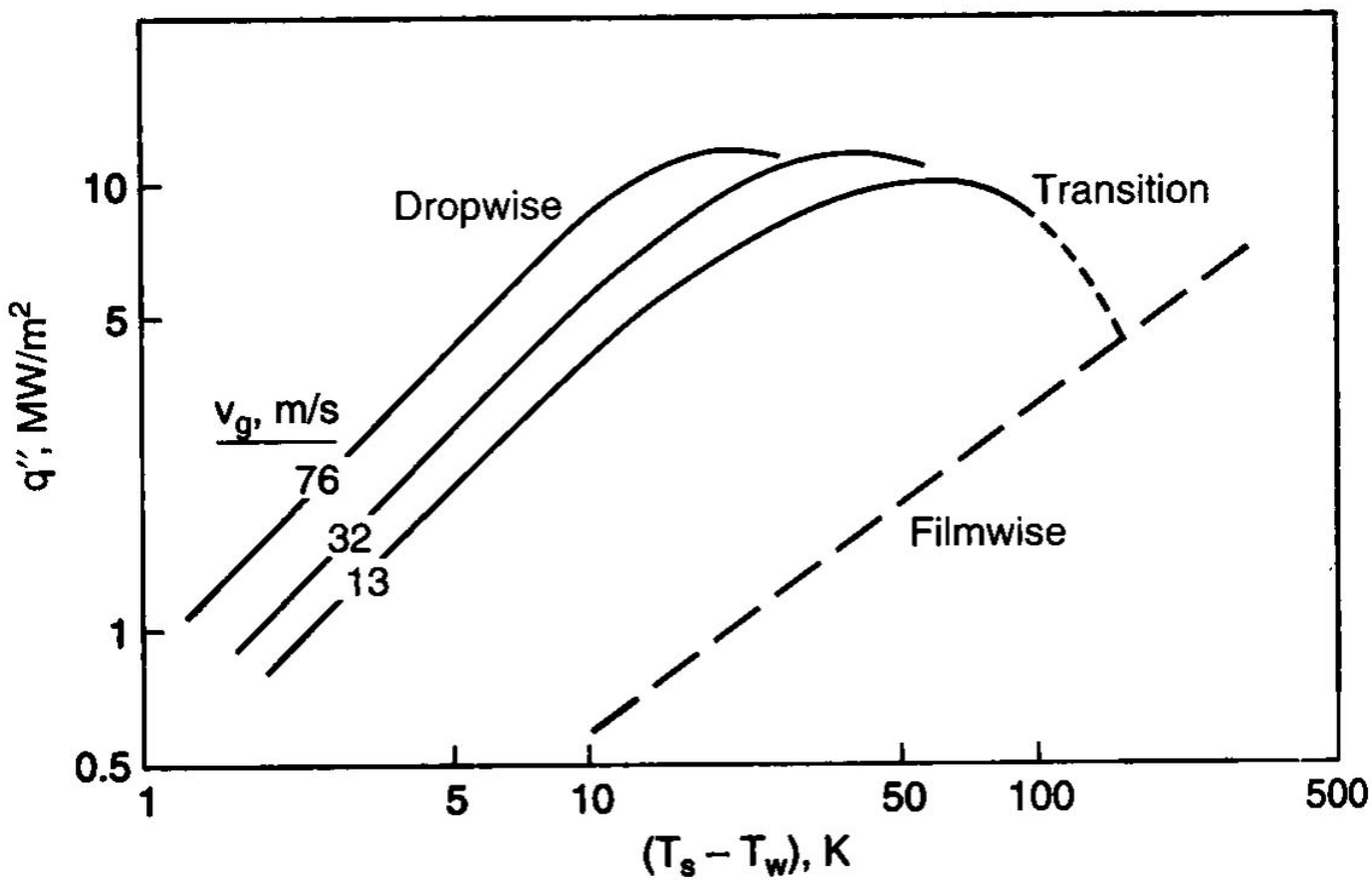

Heat transfer correlations

Akers, et al, 1959 – Annular Correlation
Boyko and Kruzhulin, 1967 – Annular Correlation
Chato, 1962 – Stratified Correlation
Soliman, et al, 1968 – Generalized Correlation

Chose Soliman correlation for its stability and generality

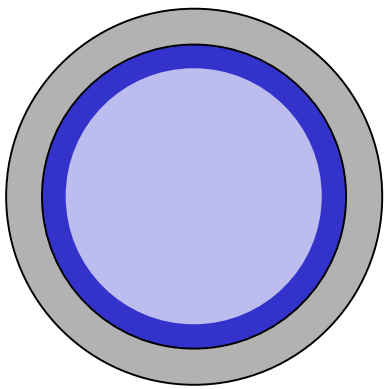

Annular Condensation

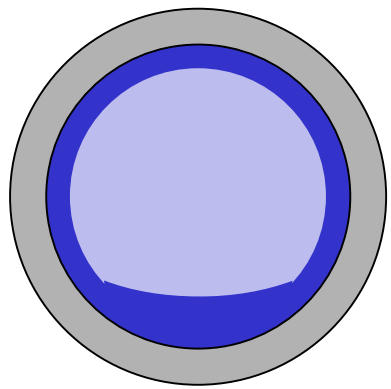

Stratified Condensation

Soliman Correlation for Heat Transfer Coefficient for Annular Flow Condensation

$$h = 0.036\,\mathrm{Pr}^{0.65}\,F_0^{0.5}\left[\frac{k_l \rho_l^{0.5}}{\mu_l}\right]$$

$$F_0 = F_f + F_m \pm F_a$$

$$F_f = 0.045\,\mathrm{Re}_T^{-0.2}\left[\frac{\pi^2 \rho_v D^4}{8W_T^2}\right]\left[x^{1.8} + 5.70\left(\frac{\mu_l}{\mu_v}\right)^{0.0523}(1-x)^{0.470}x^{1.33}\left(\frac{\rho_v}{\rho_l}\right)^{0.261} + 8.11\left(\frac{\mu_l}{\mu_v}\right)^{0.105}(1-x)^{0.940}x^{.860}\left(\frac{\rho_v}{\rho_l}\right)^{0.522}\right]$$

$$F_m = 0.5\left(D\frac{dx}{dz}\right)\left[\frac{\pi^2 \rho_v D^4}{8W_T^2}\right]\left[2(1-x)\left(\frac{\rho_v}{\rho_l}\right)^{2/3} + \left(\frac{1}{x} - 3 + 2x\right)\left(\frac{\rho_v}{\rho_l}\right)^{4/3} + (2x - 1 + \beta x)\left(\frac{\rho_v}{\rho_l}\right)^{1/3} + \left(2\beta - \frac{\beta}{x} - \beta x\right)\left(\frac{\rho_v}{\rho_l}\right)^{5/3} + 2(1 - x - \beta + \beta x)\left(\frac{\rho_v}{\rho_l}\right)\right]$$

$$F_a = 0$$

F_f: Effect of two-phase friction
F_m: Effect of momentum changes in the flow
F_a: Effect of axial gravitational field on the wall shear stress

Solid-to-fluid heat transfer

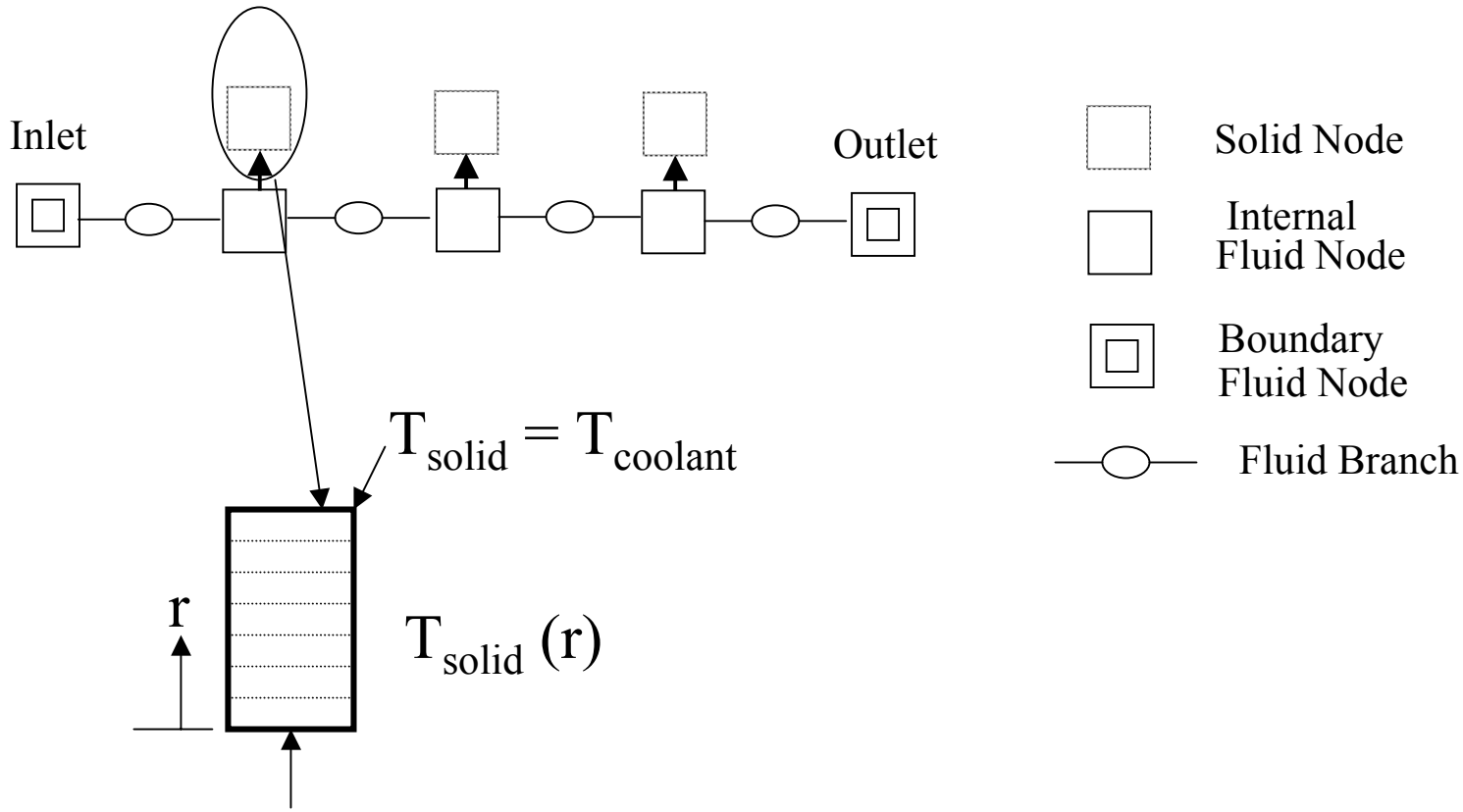

$$Q_{condensation} = h\,A\,(T_{fluid} - T_{solid})$$

Plot of Quality vs. Pipe Location for Selected Heat Transfer Correlations

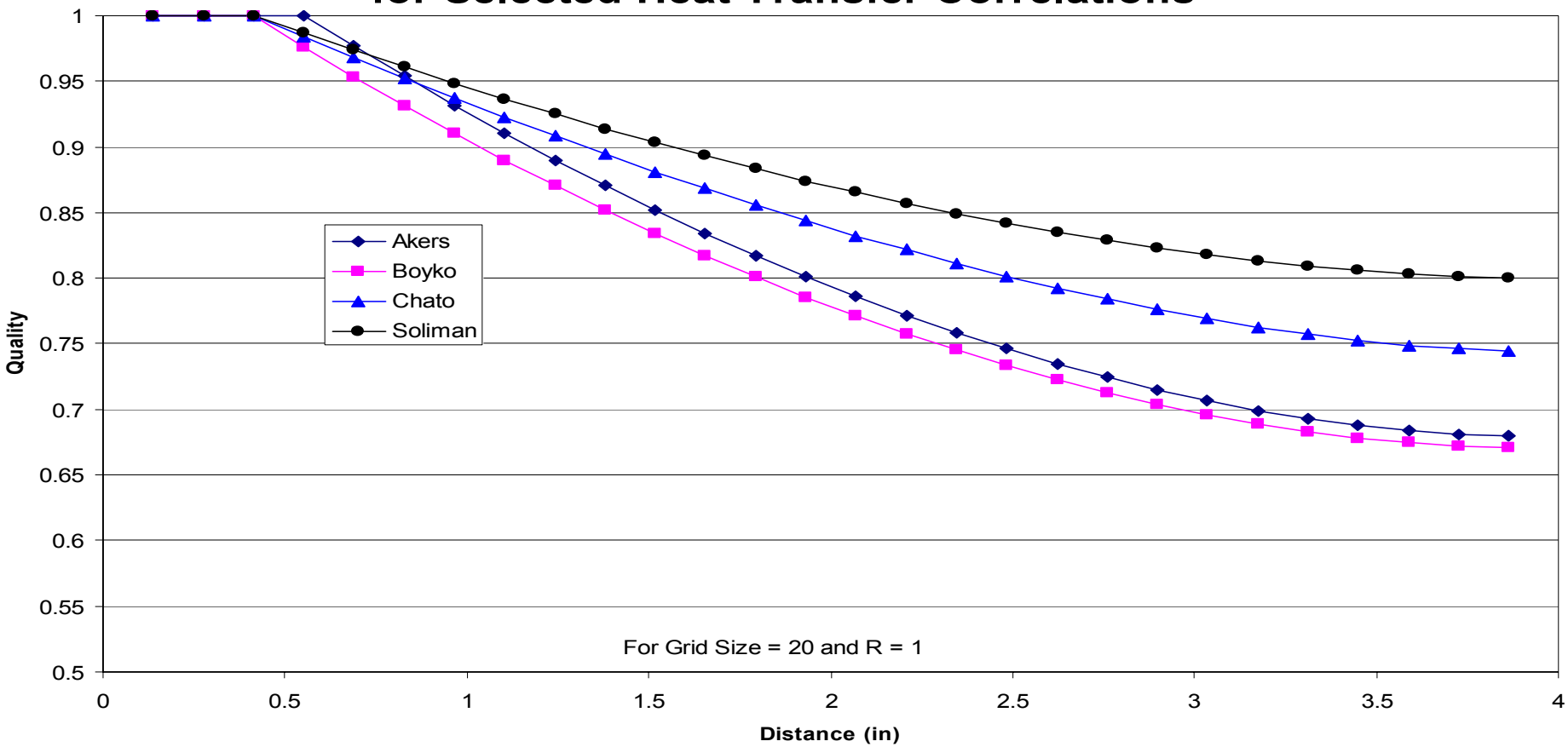

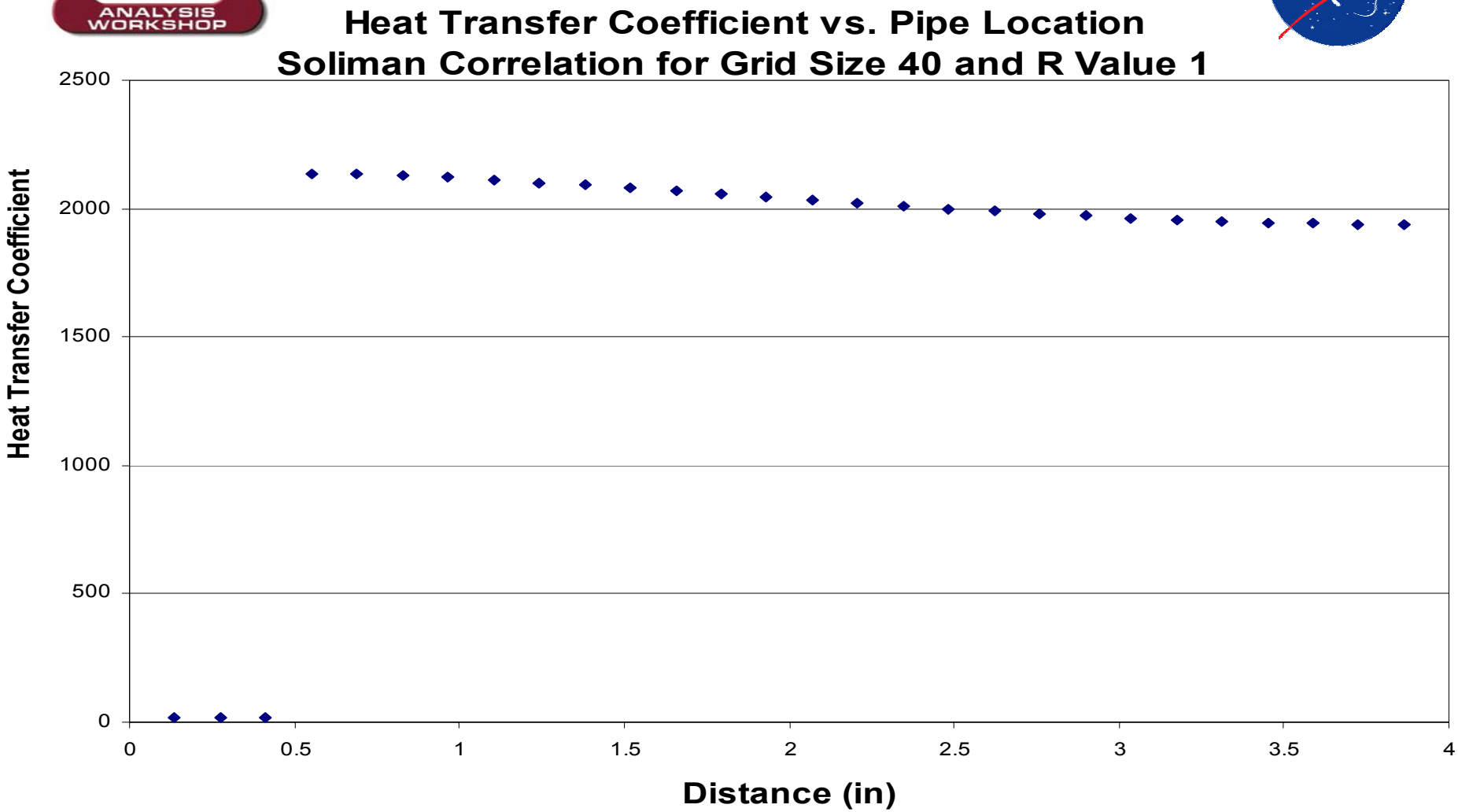
Heat Transfer Coefficient vs. Pipe Location
Soliman Correlation for Grid Size 40 and R Value 1
Heat Transfer Coefficient
2500
2000
1500
1000
500
0
0
0.5
1
1.5
2
2.5
3
3.5
4
Distance (in)

Quality Comparison for Different Tube Grid Resolution (Soliman Correlation)

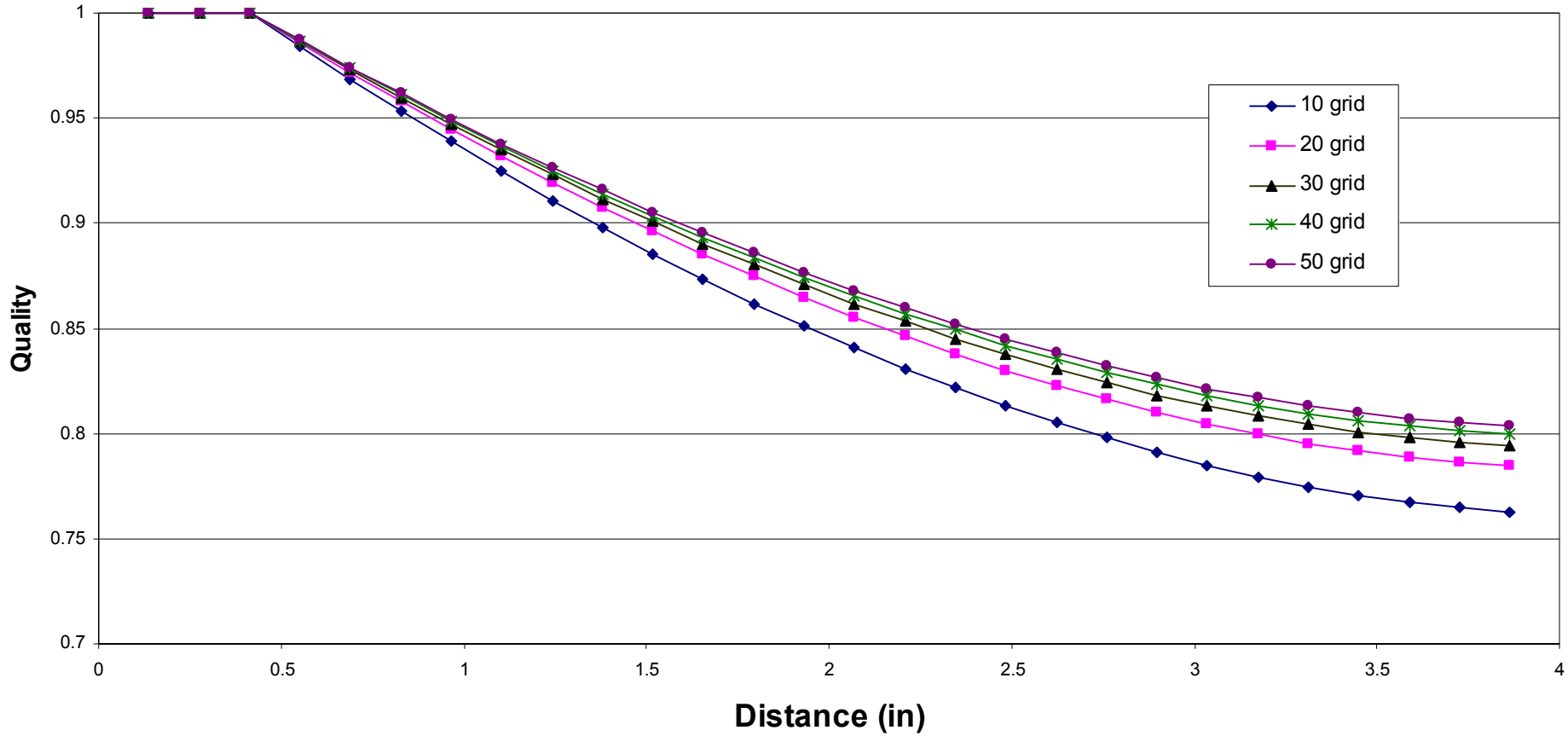

Outer Wall Temperature Comparison for Different Tube Grid Resolution (Soliman Correlation)

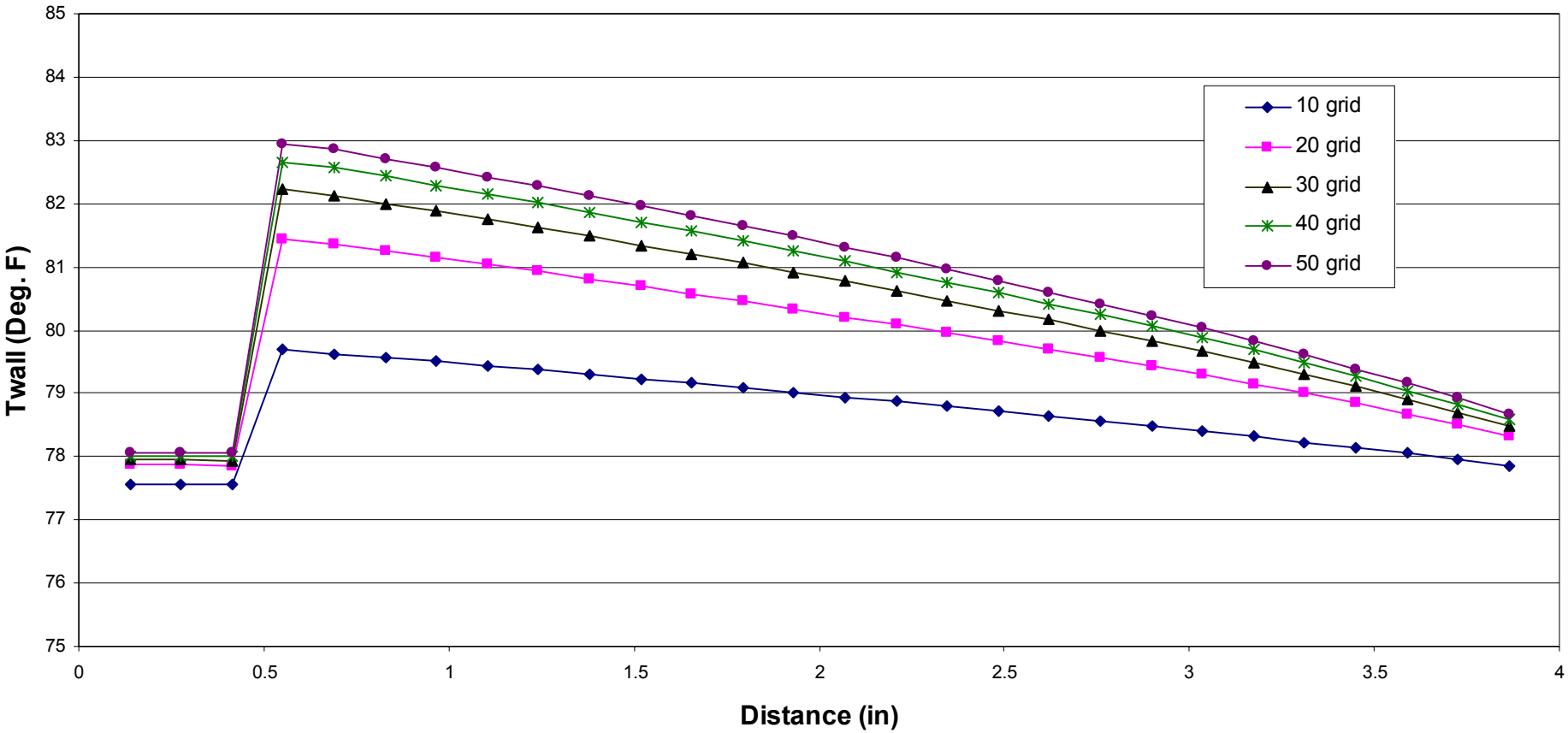

Conclusions

- A condensation heat transfer model was successfully incorporated in a general purpose flow network code
- The numerical model considers solid-to-fluid heat transfer
- Soliman et al's correlation of condensation heat transfer is recommended due to its generality and stability

References & Acknowledgements

References:

1. Don Holder, “Urine Processor Assembly Condensate Issue”, NASA/Marshall Space Flight Center, Environmental Control and Life Support System Group, August 31, 2001, Huntsville, Alabama.
1. Rohsenow, W. M., Hartnett, J. P. and Cho, Y. I., “Handbook of Heat Transfer”3rd Edition, McGraw Hill, 1998
2. Soliman, M., Schuster, J. R. and Berenson, P. J., “A General Heat Transfer Correlation for Annular Flow Condensation”, Journal of Heat Transfer, ASME, May, 1968.
3. Majumdar, A. “Generalized Fluid System Simulation Program (GFSSP) Version 3.0” Sverdrup Technology Report No. MG-99-290, November, 1999.

Acknowledgement:

Authors would like to acknowledge Mr. Bruce Tiller and Mr. Richard Schunk of MSFC for their suggestions and comments

Status of Nozzle Aerodynamic Technology at MSFC

Joseph H. Ruf/TD64
David M. McDaniels/TD63
Bud Smith/Plumetech
Zachary Owens/U. of Virginia

Thermal and Fluid Workshop
September, 2001
Huntsville, AL.

- Overview
  - Objectives
  - Analytical Tool Development
  - Cold Flow Nozzle Test Hardware
  - Analytical TVC Model
  - Related Work

- Objectives
  - Of this Presentation: Provide Insight Into MSFC In-house Nozzle Aerodynamic Technology; Design, Analysis & Testing
  - CDDF 'Altitude Compensating Nozzle Technology'
    - Develop In-house ACN Aerodynamic Design Capability
    - Build In-house Experience for all aspects of ACN via End-to-End Nozzle Test Program
    - Obtain Experimental Data for Annular Aerospike: Thrust η, TVC capability and surface pressures

Status of Nozzle Aerodynamic Technology At MSFC

- Analytical Tool Development
  - To support selection/optimization of future Launch Vehicle propulsion we needed a parametric design and performance tool for ACN
  - Chose Aerospike Nozzles as the ACN to Start With
  - Aerospike Design And Performance Tool (ADAPT)
    - Developed by Bud Smith/Plumetech
    - Parametrics on:
      - Aerospike Configuration
        - » Linear
        - » Annular
        - » Axisymmetric
      - Thruster Configuration
        - » 2D/Slot, or Clustered-Axisymmetric
        - » Rao, Ideal, Truncated Ideal

Aerospike Nozzle Terminology

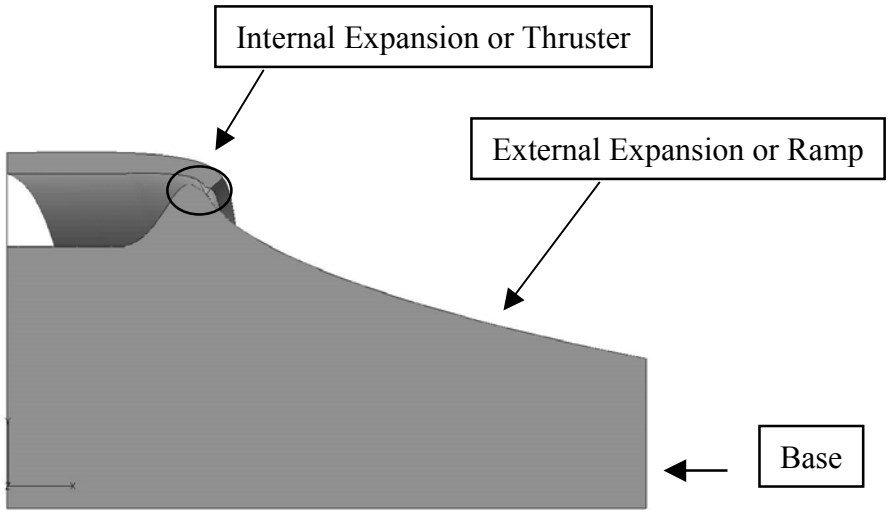

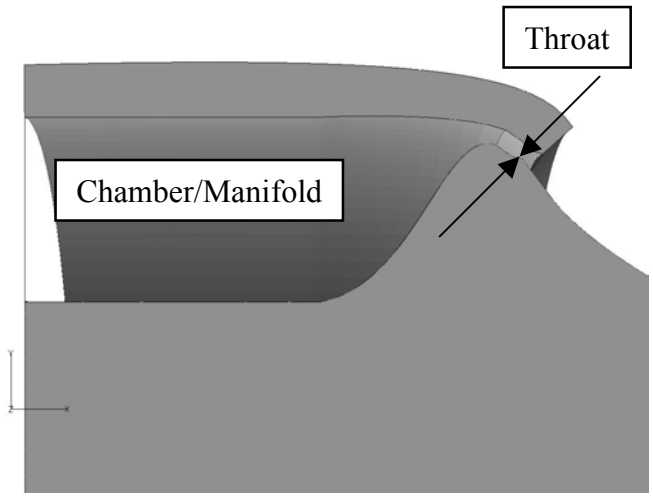

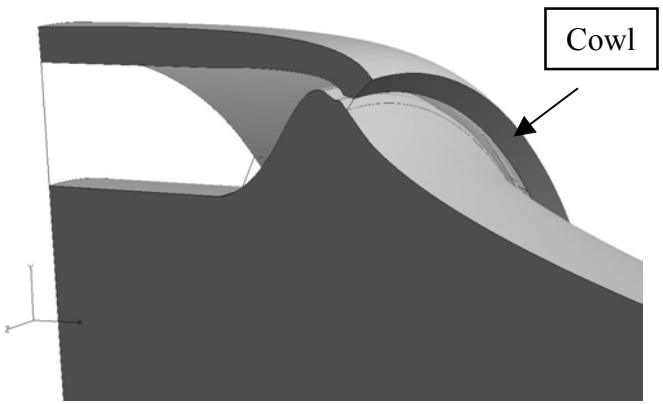

Aerospike Nozzle Terminology

Low Altitude or NPR

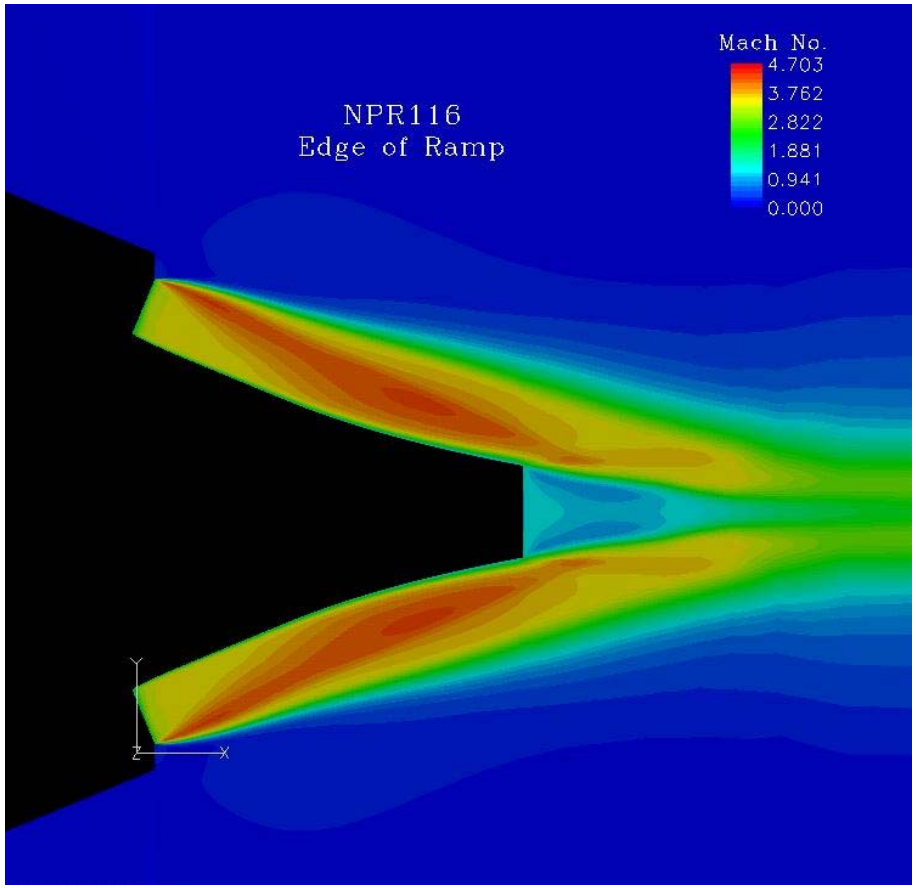

High Altitude or NPR

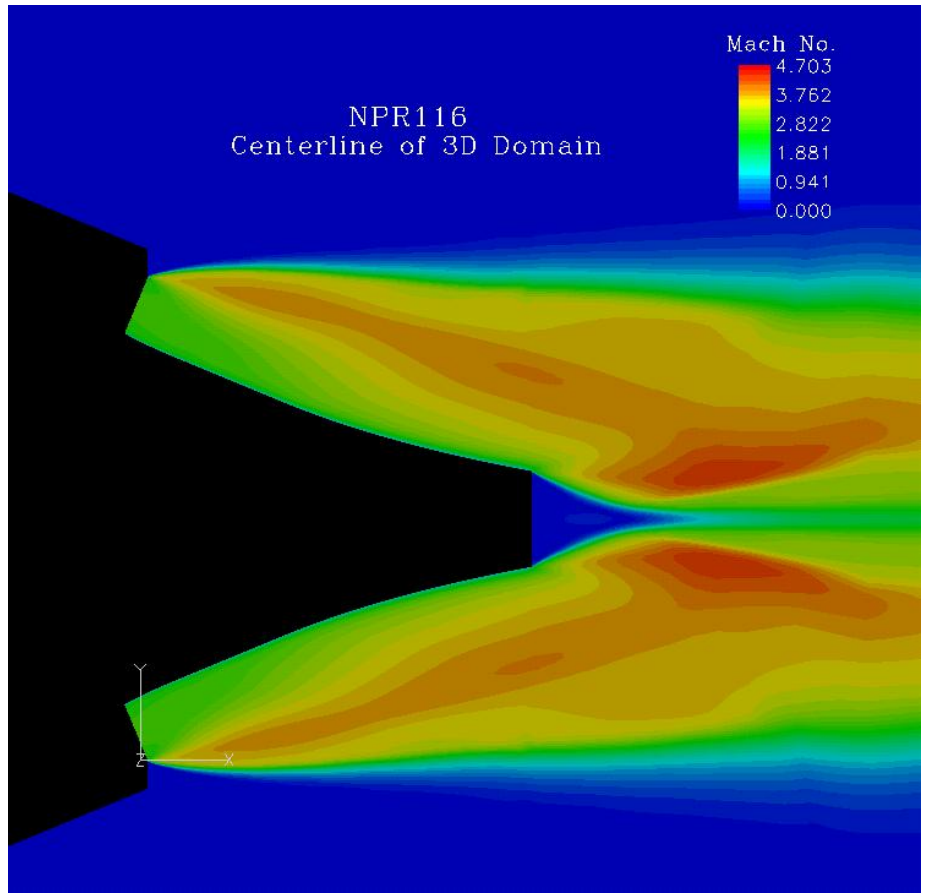

- Analytical Tool Development
  - Chose Aerospike Nozzles as the ACN to Start With
  - To support future propulsion selection we needed a parametric design and performance tool for ACN
  - Aerospike Design And Performance Tool (ADAPT)
    - Developed by Bud Smith/Plumetech
    - Parametrics
      - Aerospike Configuration
        - » Linear
        - » Annular
        - » Axisymmetric
      - Thruster Configuration
        - » 2D/Slot, or Clustered-Axisymmetric
        - » Rao, Ideal, Truncated Ideal

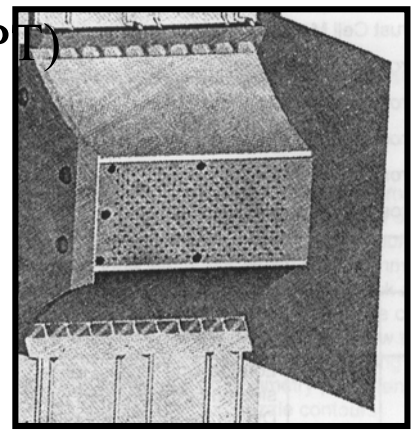

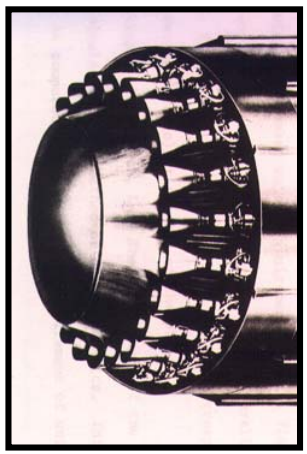

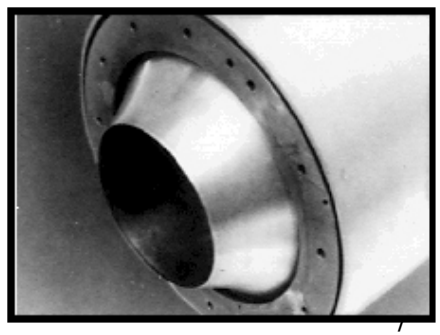

Status of Nozzle Aerodynamic Technology At MSFC

- Analytical Tool Development
  - Chose Aerospike Nozzles as the ACN to Start With
  - To support future propulsion selection we needed a parametric design and performance tool for ACN
  - Aerospike Design And Performance Tool (ADAPT)
    - Developed by Bud Smith/Plumetech
    - Parametrics
      - Aerospike Configuration
        - » Linear
        - » Annular
        - » Axisymmetric
      - Thruster Configuration
        - » 2D/Slot, or Clustered-Axisymmetric
        - » Rao, Ideal, Truncated Ideal

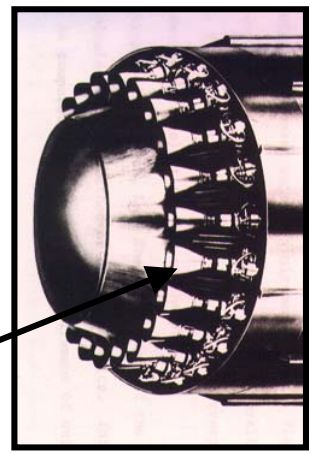

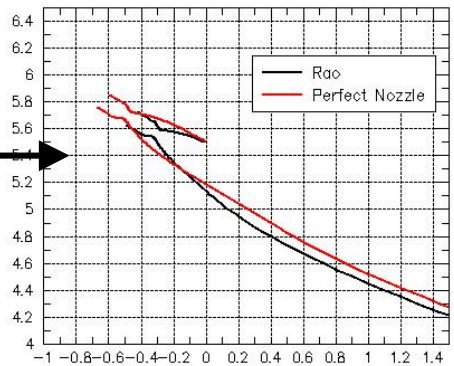

- Analytical Tool Development, cont.
  - Parametrics, cont.
    - Sizing and Design Point
      - » Radius, Area Ratio or NPR_{design}(10)
      - » Mass Flow or Throat Area
      - » P_c, P_{a_des}(10), Expansion Split(10)
    - Working Fluid; Air, Lox/RP, Lox/H2, Others
    - Performance
      - » Each Geometric Combinations Performance Calculated at up to 10 Altitudes (NPR)
      - » Nozzle Ramp Truncation(10)
      - » Outputs;P vs. X, a Summary Table, Thrust, I_{sp}, C_f ...

- Analytical Tool Development, cont.

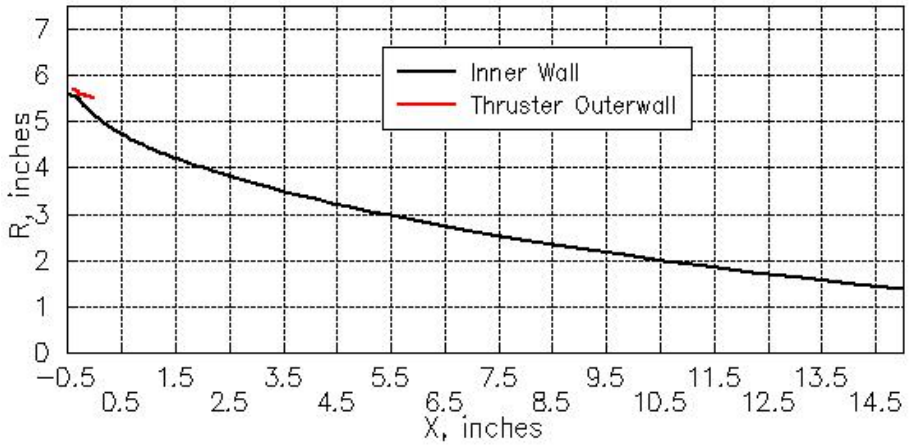

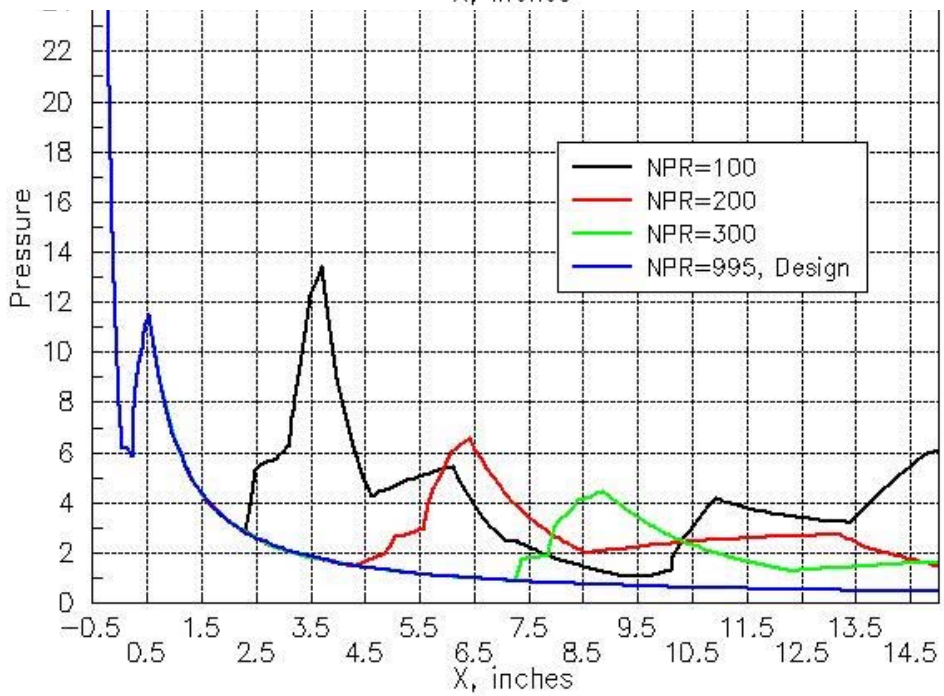

- Analytical Tool Development, cont.
  - Example Table Output

```
Summary of Aerospike Design And Analysis Results For ' Problem: case1ra

Case1 Rao

Case Number - 0101

Cluster Design Pressure     =       0.3014 psia
Cluster Design Area Ratio   =      38.6300
Thruster Design Pressure    =      11.0742 psia
Thruster Design Area Ratio =        3.4962

Case Number                                0101


Cluster - 1-D
Area Ratio                                38.630
Cluster Radius (in)                       5.5000
Area (in**2)                              95.033
Length (in)                              29.9768
Mass Flow Rate lbm/s                     14.2361
Prandtl-Meyer Ang (deg)                  81.8045
Mach Number                               5.5621
Pressure (psia)                           0.3014
Temperature (R)                           105.74
Density (lbm/ft**3)                    0.769E-02
Velocity (ft/sec)                      2803.6414
Specific Heat Ratio                       1.4000
Molecular Weight                         28.9700
Equivalent 15 deg noz length  - in        17.224

Thruster - 1-D
Area Ratio                                 3.496
Exit Height (in)                          0.2548
Throat Height (in)                        0.0704
Throat Area (in**2)                       2.4601
Exit Area - in**2                          8.641
Nozzle Length - in                         0.283
Prandtl-Meyer Ang (deg)                  45.7879
Mach Number                               2.7988
Pressure (psia)                          11.0742
Temperature (R)                           296.10
Density (lbm/ft**3)                    0.101E+00
Velocity (ft/sec)                      2360.8020
Specific Heat Ratio                       1.4000
Molecular Weight                         28.9700
Tilt Angle (Deg)                         36.0166
```

- Analytical Tool Development, cont.
  - Example Table Output, Page 2

Case Number	010100	010101	010102	010103	010
Ambient Pressure - psia	0.3014	6.0300	3.0150	1.5080	1.0
Pressure Ratio - Pc/Pa	995.3800	49.7512	99.5025	198.9390	298.5
Performance					
Thruster					
1-D Vacuum Thrust (no tilt) - lbf	1140.0	1140.0	1140.0	1140.0	114
1-D Delivered Thrust (no Tilt) - lbf	1137.4	1088.1	1114.1	1127.0	113
1-D Vacuum Isp (no tilt) - sec	80.067	80.067	80.067	80.067	80.
1-D Delivered Isp (no Tilt) - sec	79.885	76.424	78.245	79.156	79.
1-D Vac. Thrust Coefficient(no tilt)	1.5447	1.5447	1.5447	1.5447	1.5
1-D Del. Thrust Coefficient(no Tilt)	1.5412	1.4744	1.5095	1.5271	1.5
1-D Vacuum Thrust (tilt) - lbf	926.3	926.3	926.3	926.3	92
1-D Delivered Thrust (tilt) - lbf	924.2	884.1	905.2	915.7	91
1-D Vacuum Isp (tilt) - sec	64.762	64.762	64.762	64.762	64.
1-D Delivered Isp (tilt) - sec	64.614	61.815	63.288	64.025	64.
1-D Vac. Thrust Coefficient(tilt)	1.2551	1.2551	1.2551	1.2551	1.2
1-D Del. Thrust Coefficient(tilt)	1.2522	1.1980	1.2265	1.2408	1.2
Boundary Layer Thrust loss - lbf	1.442	1.444	1.443	1.443	1.
Vacuum Thrust - lbf	916.0	916.0	916.0	916.0	91
Delivered Thrust - lbf	914.5	885.8	900.9	908.4	91
Vacuum Isp - sec	64.478	64.478	64.478	64.478	64.
Delivered Isp - sec	64.372	64.372	64.372	64.372	64.
Vac. Thrust Coefficient	1.2411	1.2411	1.2411	1.2411	1.2
Del. Thrust Coefficient	1.2391	1.2002	1.2207	1.2309	1.2
Nozzle Efficiency(cf_del/cf_1d_del)	0.9895	1.0019	0.9952	0.9920	0.9
Cluster					
1-D Vacuum Thrust - lbf	1269.2	1269.2	1269.2	1269.2	126
1-D Delivered Thrust - lbf	1240.5	1240.5	1240.5	1240.5	124
1-D Vacuum Isp - sec	89.152	89.152	89.152	89.152	89.
1-D Delivered Isp - sec	87.140	87.140	87.140	87.140	87.
1-D Vac. Thrust Coefficient	1.7197	1.7197	1.7197	1.7197	1.7
1-D Del. Thrust Coefficient	1.6809	1.6809	1.6809	1.6809	1.6
Boundary Layer Thrust loss - lbf	10.102	0.000	15.263	12.673	11.
Delivered Thrust - lbf	1223.0	1120.3	1142.9	1173.5	118
Delivered Isp - sec	86.084	86.081	86.081	86.079	86.
Del. Thrust Coefficient	1.6571	1.5179	1.5486	1.5901	1.6
Nozzle Efficiency(cf_del/cf_1d_del)	0.9858	0.9031	0.9213	0.9460	0.9

Results for Cluster **Truncation of** **25.00 Percent**(X = 4.31 INCHES)

Case Number	010100	010101	010102	010103	010
Ambient Pressure - psia	0.3014	6.0300	3.0150	1.5080	1.0
Pressure Ratio - Pc/Pa	995.3800	49.7512	99.5025	198.9390	298.5
Performance					
Cluster					
Delivered Thrust - lbf	1215.5	1093.5	1134.4	1143.7	117
Delivered Isp - sec	85.552	76.968	79.848	80.500	82.
Boundary Layer Thrust loss - lbf	8.047	11.288	9.340	8.039	8.
Base Drag Thrust Loss - lbf	0.000	0.000	0.000	0.000	0.

Status of Nozzle Aerodynamic Technology At MSFC

- Analytical Tool Development, cont.
  - Methodology
    - Namelist Driven
    - Runs in Seconds on PC or Unix
    - Bud Smith Wrote Aerospike Specific Driver Routines Around the Standard Nozzle Aero Codes
      - » CEC, MOC, Rao and Perfect Nozzle Design, BLIMPJ
    - External Expansion, Lee & Thompson Method
  - Verification & Validation - In Work
    - Currently Testing ADAPT's Functionality
    - ADAPT Used to Design Cold Flow Test Article - Design & Performance Validation
  - Future Growth
    - Base Pressure Correlation
    - Reverse MOC to Design the External Expansion Ramp with the Thruster Exit Conditions
    - Input Specific Geometries for Analysis
    - Other ACN Concepts; Single Expansion Ramp Nozzles, Expansion-Defection

- Cold Flow Test Hardware Design
  - Objective of Test Article
    - Validation of ADAPT Design & Performance Methods
    - Exercise Skills from End-to-End. Learn by Doing
      - Aero Design, Mechanical Design, Build, Cold Flow Test, Data Interpretation, Validation of Design Tools
    - Axial Thrust and TVC Force Test Data for an Annular Aerospike
    - CFD Validation Data Set - Lots of Static Pressure Measurements
  - Model Description
    - Area Ratio = 38.6, NPR_{des}=995, P_{c_des}=250psi
    - Throat = 0.072 in., R_e = 5.5 in.
    - Mass Flow ~11 lbm/s, Thrust ~ 1000lbf
    - TVC, +/- 10% and 20% Differential Throttling
  - Status: Mechanical Design is Nearly Complete, Testing in Jan. 2002

Cold Flow Nozzle Test Hardware
Annular Aerospike with TVC Capability

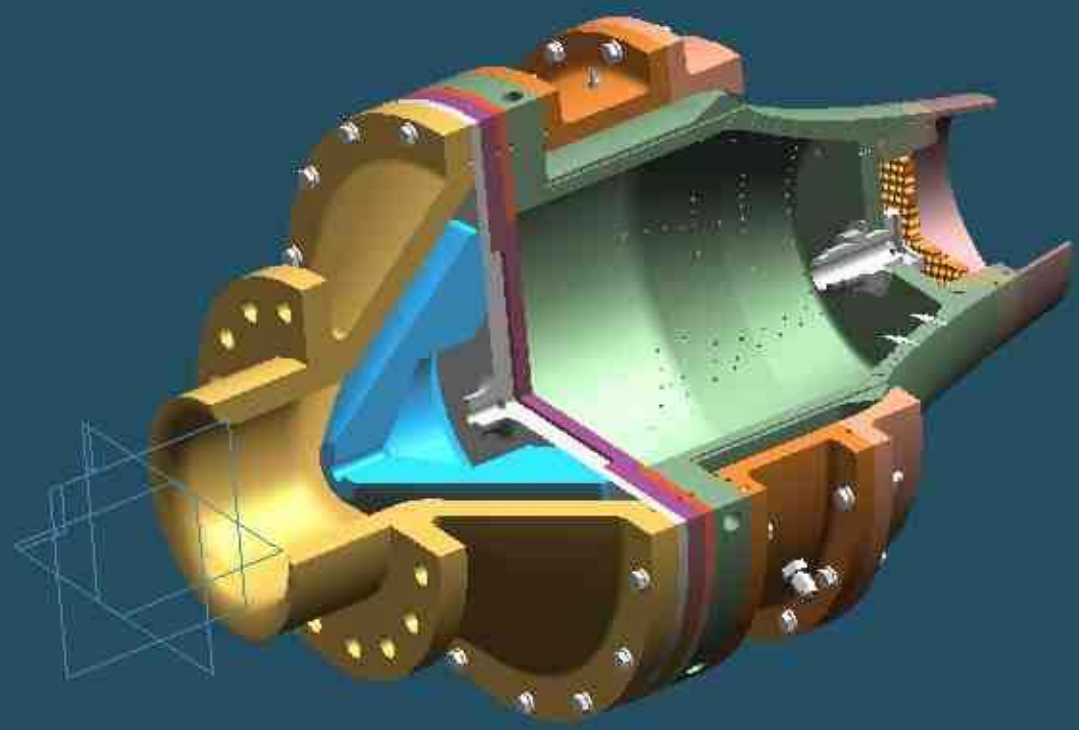

Cold Flow Nozzle Test Hardware
Annular Aerospike with TVC Capability

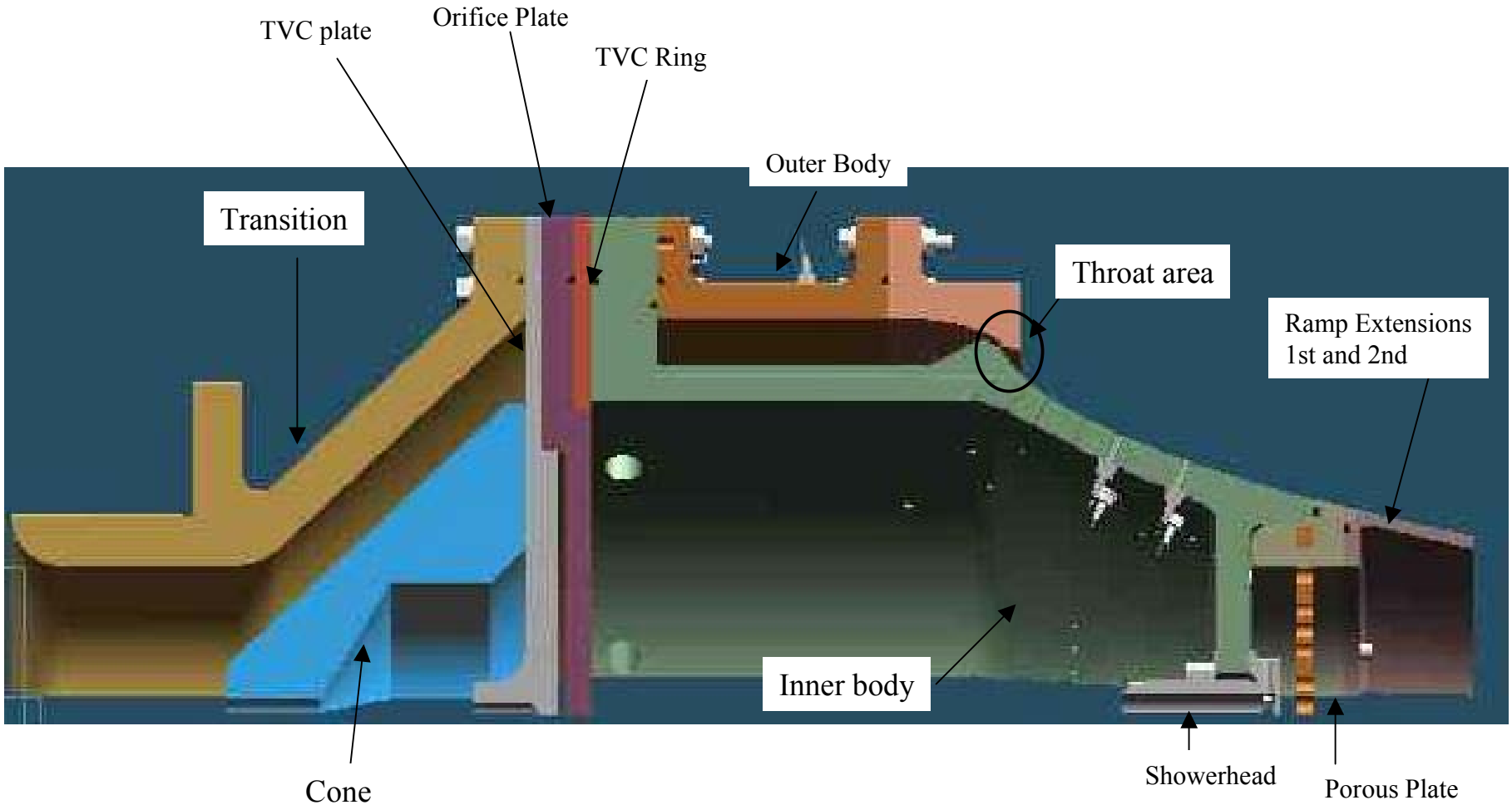

Note: the splitter plates are not shown

- Analytical TVC Model
  - Objective: Estimate thrust vector control capability (TVC) of an annular aerospike via differential throttling.
  - Approach
    - Use ADAPT to define the forces acting on an aerospike.
    - Processed ADAPT output to parametrically assesses TVC capabilities in terms of an equivalent gimbal angle of a Bell Nozzle.
      - vehicle geometry, CG/Cowl Radius
      - spike length, % truncation
      - nozzle pressure ratio, effect of altitude
      - throttle setting, +/- 30%, +/-15% of P_c

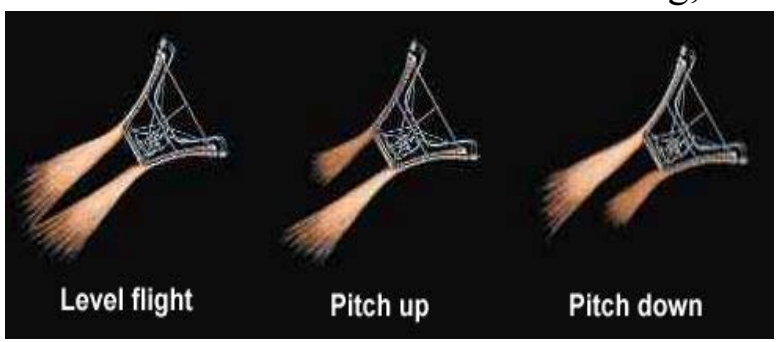

Status of Nozzle Aerodynamic Technology At MSFC

Modular thrusters allow differential throttling as a means for TVC.

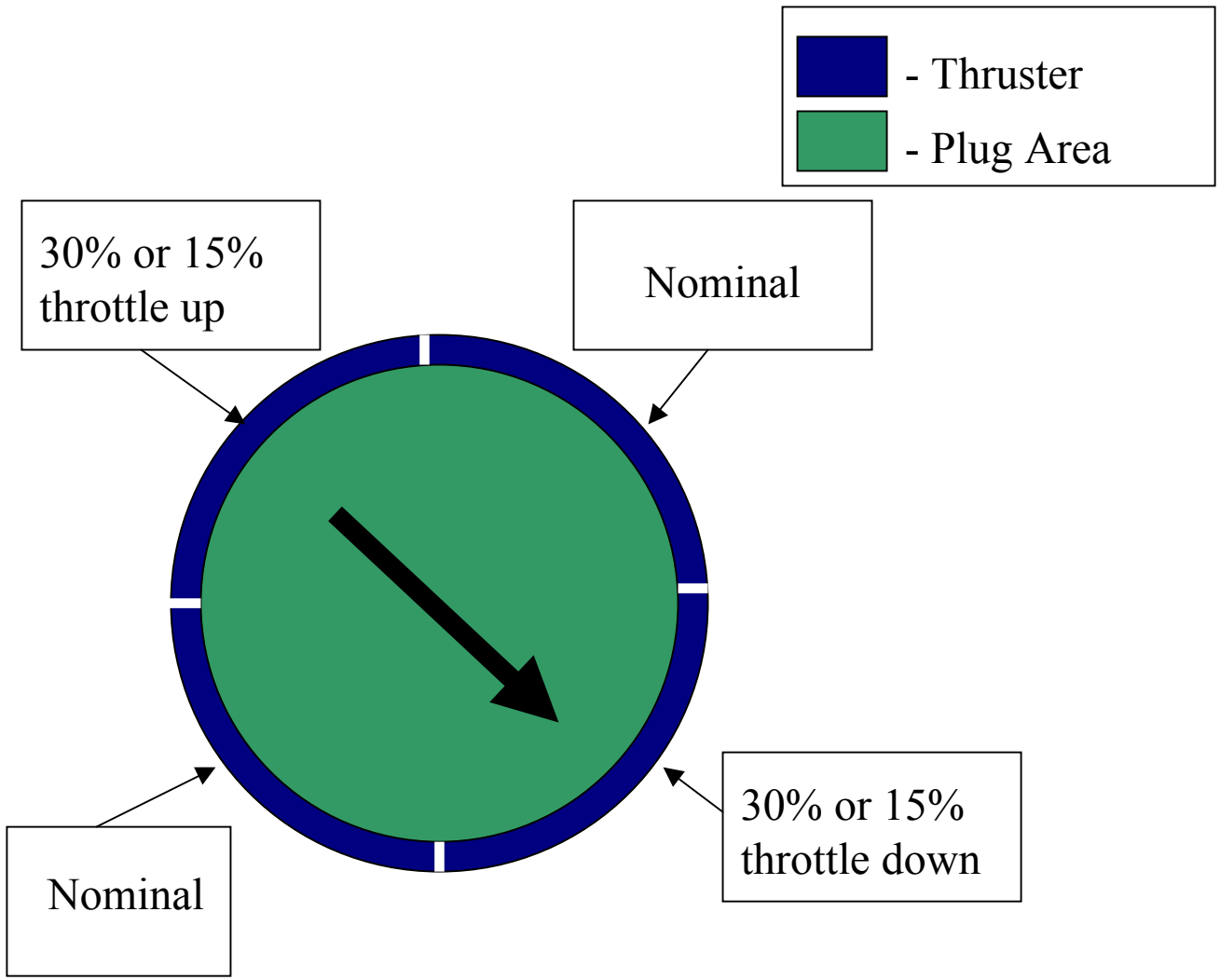

Aerospike Forces & Moments

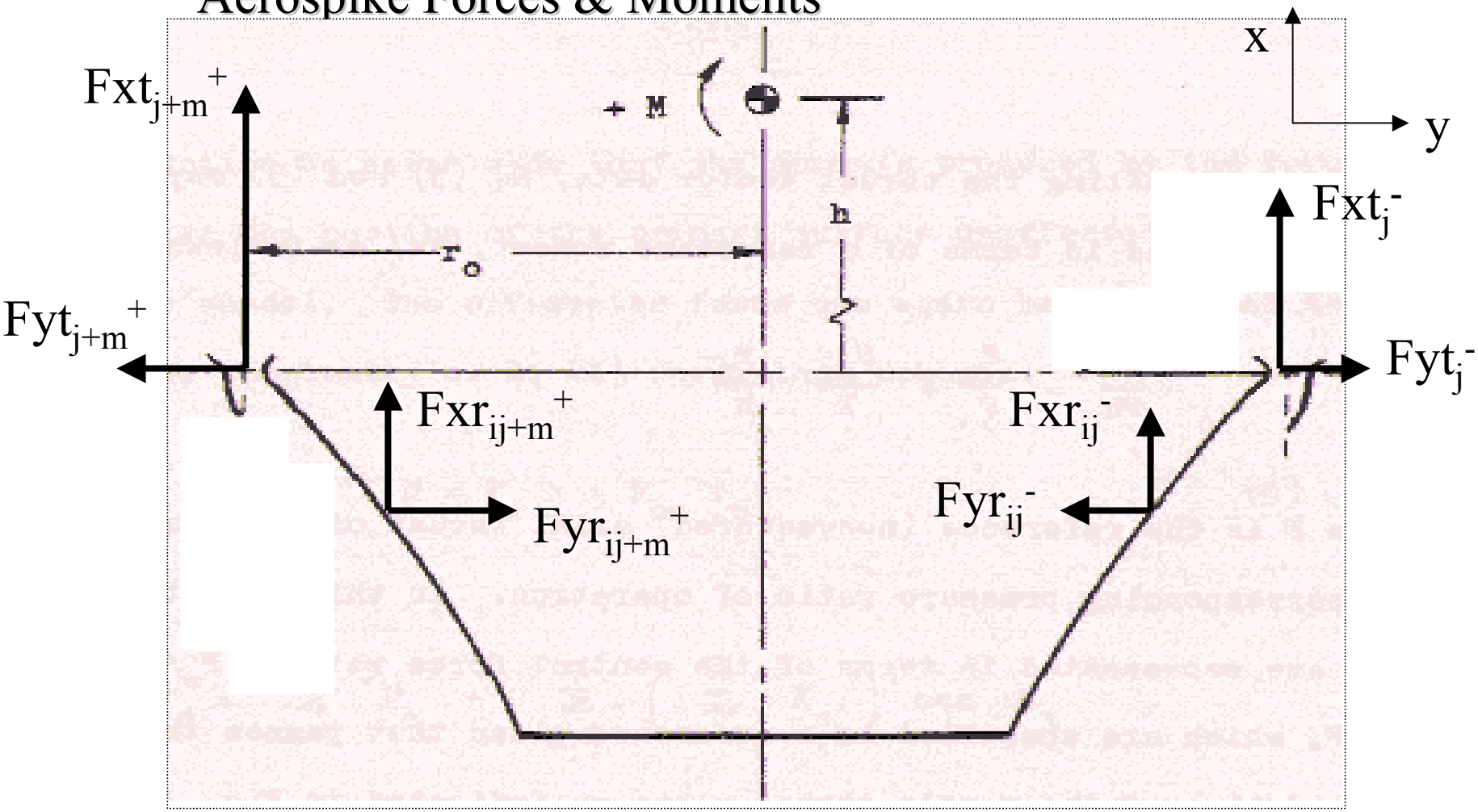

$$M = \sum_{j=1}^{j\max}\left[\left(Fxt \times r_o\right) + \left(Fyt \times h\right) + \sum_{i=1}^{i\max}\left[\left(Fxr_i \times r_i\right) + \left(Fyr_i \times h_i\right)\right]\right]$$

Status of Nozzle Aerodynamic Technology At MSFC

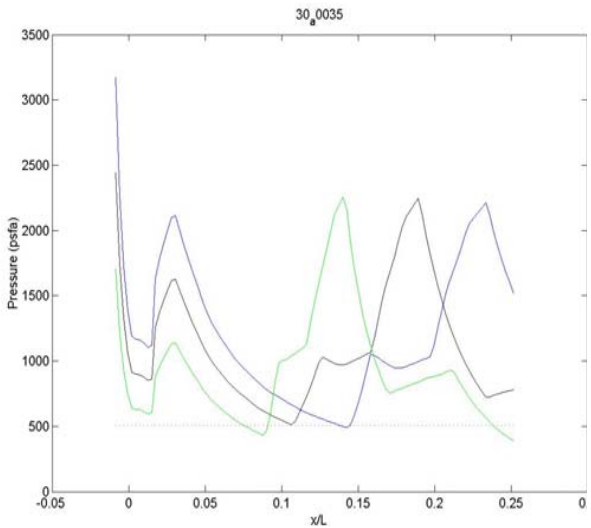

NPR=86

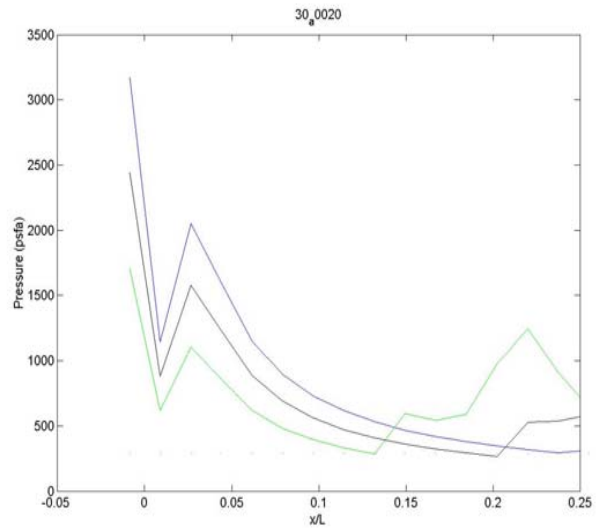

NPR=150

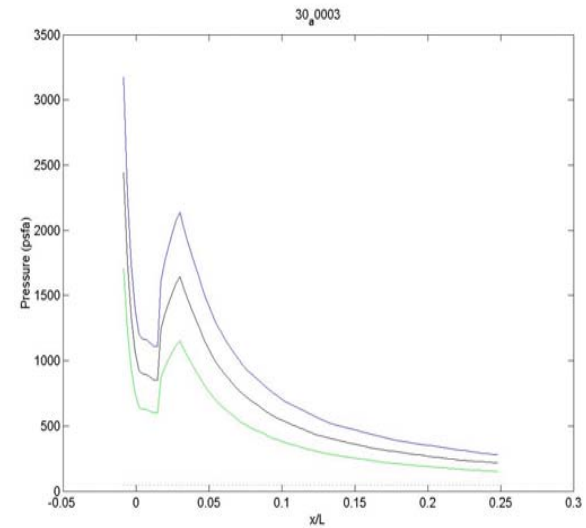

NPR*=1000

- Green curve represents ramp pressure on throttled down quadrant. Positive contribution to overall moment.
- Black curve represents ramp pressure on nominal ramp quadrants. No effect on overall moment.
- Blue curve represents ramp pressure on throttled up quadrant. Negative effect on overall moment.

Sample Output, NPR=86

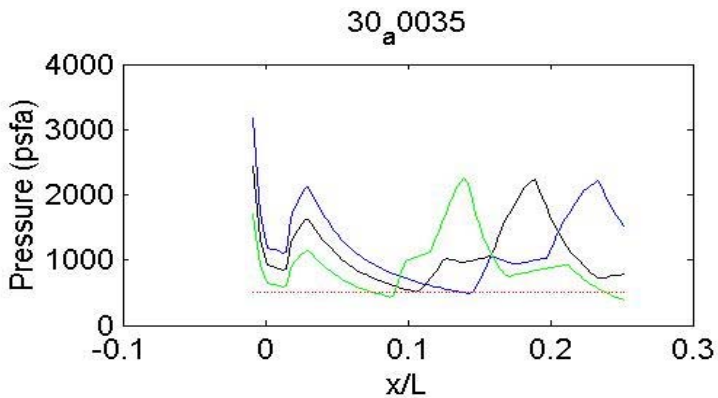

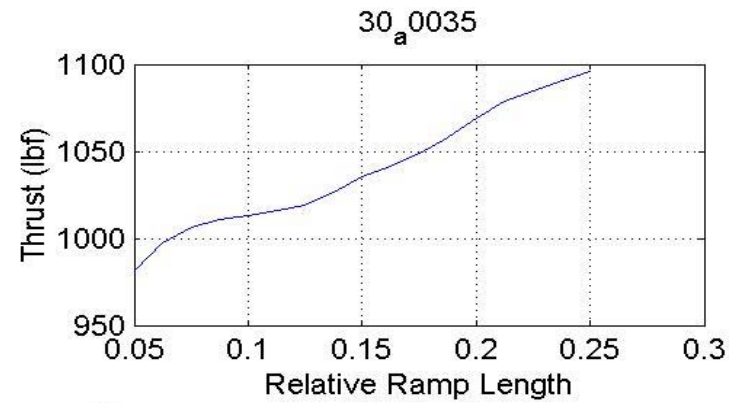

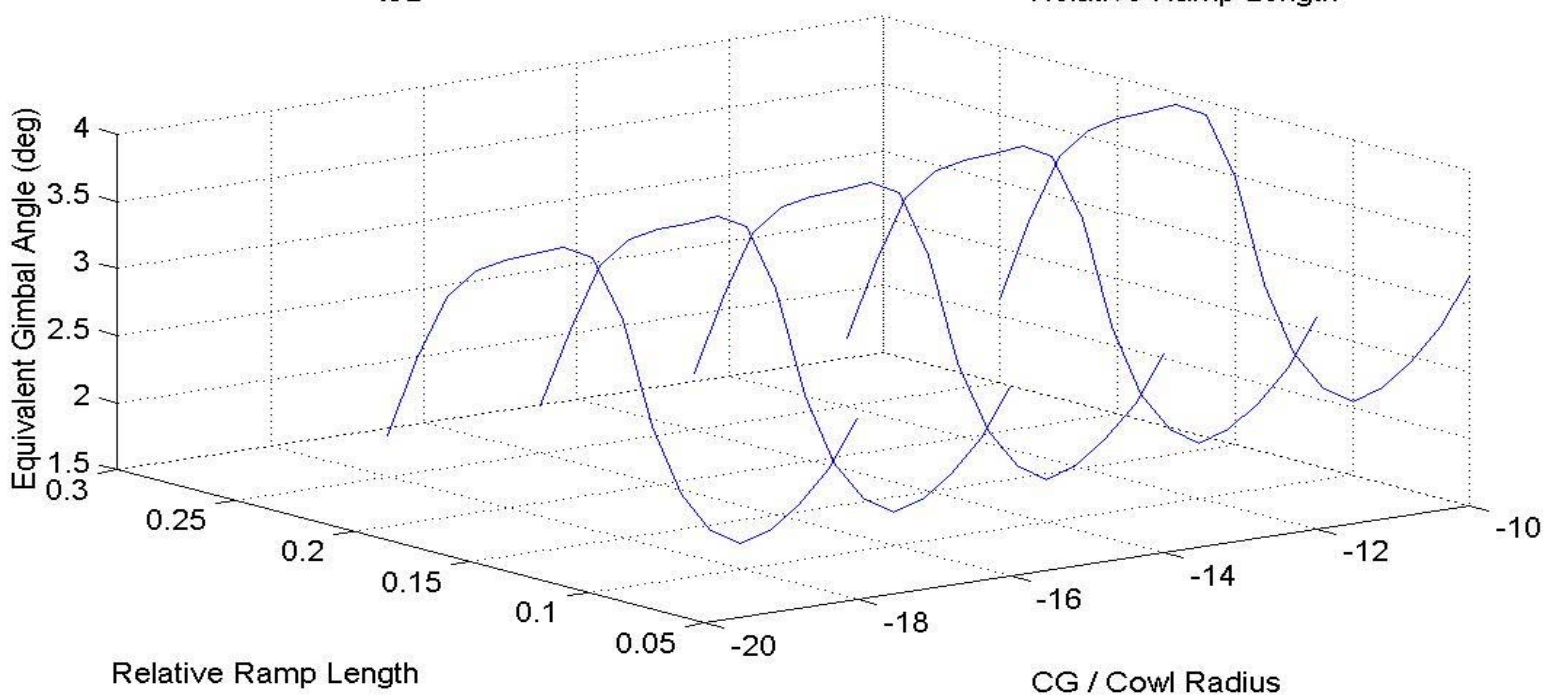

Analytical TVC Model
Conclusions

- Lateral forces, particularly the thruster's, dominate the solution
- The ramp's lateral force opposes the desired moment
- Ramp recompressions should factor into ramp length selection
- Differential throttling +/-30% on annular aerospikes yields 1 to 4 degrees of equivalent gimbal angle.

- Axial Thrust Performance of an Aerospike warrants further study of TVC methods

Status of Nozzle Aerodynamic Technology At MSFC

- Related Work
  - A Cold Flow Test is About to Start With a Set of ACN All Designed to the Same NPR.

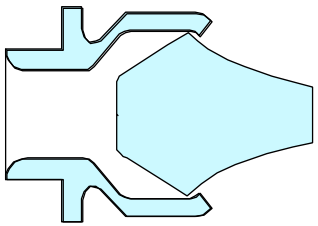

Plug: AR=22.3, 35% full plug length

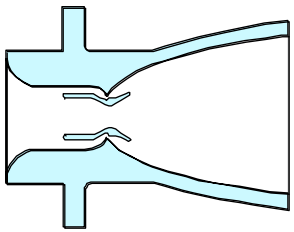

Dual-Expander: AR=22.08/40.25

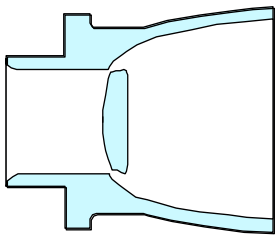

Expansion-Deflection: AR=18.2

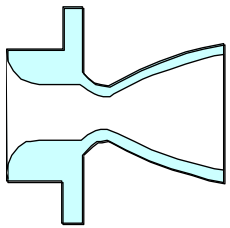

Small Reference Bell: AR=12.2

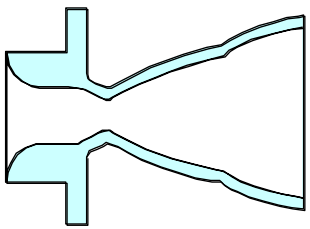

Dual Bell: AR=12.2/27.1

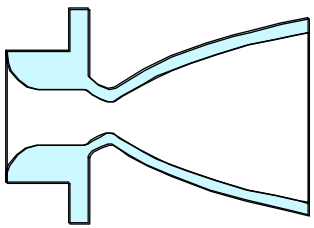

Large Reference Bell: AR=27.1

da Vinci
PROJECT
Canada's PRIZE Contender

50 Graydon Hall Drive, # 401 ■ Toronto, ON M3A 3A3 ■ PH/FAX (416) 441-0803 ■ http://www.cfdcanada.com

AERO-HEATING ANALYSIS FOR DAVINCI SPACE PROJECT ROCKET BALLUTE

Brian Feeney, ORVA Corp (Toronto, CANADA)
Vladimir Kudriavtsev, CFD Canada, Toronto, ON

http://www.davinciproject.com

Prepared for NASA Thermo-Fluids Workshop
Huntsville, Alabama, Sept 10-14, 2001

DaVinci Project --- Introduction

<u>X-Project:</u> objective is to fly a spacecraft with the three astronauts, to elevation >100 km and to do it TWICE during the two week period. No government funding is allowed.
Award: 10 million $$$, 20 teams are now registered

<u>DaVinci Project:</u> to meet this objective using "off-the shelf" commercial technologies. Utilize helium balloon for delivery to 80,000 ft, rocket on the tether, commercial multi-use engines. Rocket is returned using pressurized ballute to be deployed during the re-entry.

Basic Idea of the Design

Follows Leonardo da Vinci parachute idea (see first title slide)

Rocket

Ballute 1:
Peak
temperatures

Ballute 2:
High to medium
Temperatures

Example: Shock wave visualization

Bow shock wave is formed in front of the vehicle, internally pressurized ballutes assume thermal and pressure loads and protect the rocket and astronauts (rear) from excessive heat during re-entry.

Vehicle in Launch and re-entry mode

a)

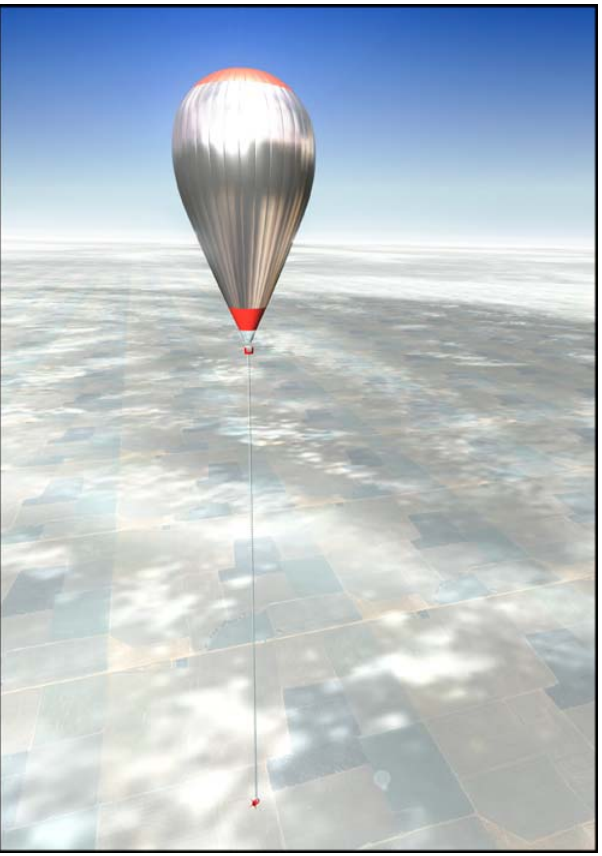

b)

c)

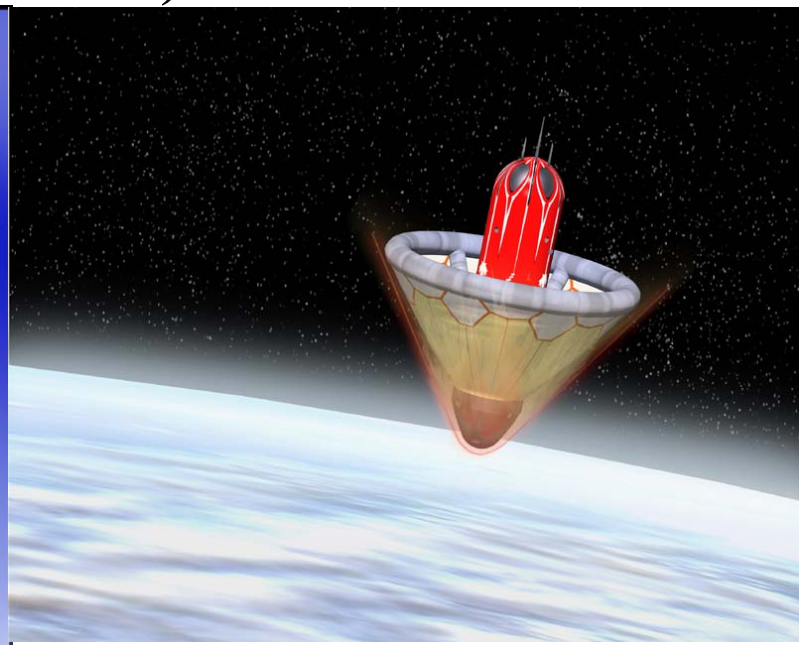

a) Vehicle tethered below the balloon
b) Close-up view of Vehicle
c) Vehicle re-entry with ballute deployed

Vehicle at Toronto Air Show (May, 2001)

Brian Feeney - Project Director

First conceptual prototype

Full scale prototype

daVinci Team

Assembled ballutes

In the exhibit hall

CONCEPTUAL DESIGN AND CFD

A)CFD REQUIRED ADDITIONAL DATASETS THAT DESIGNERS DID NOT HAVE INITIALLY, OR HAVE NOT CONSIDERED INITIALLY(ballute thickness, configuration, velocity estimations)
B) CFD ANSWERED SOME QUESTIONS THAT DESIGNERS HAD RAIZED (Cd, Pressure)
C)CFD RAIZED SET OF NEW QUESTIONS FOR DESIGNERS TO THINK ABOUT (STABILITY, LOADS, OVERHEATING)
D) CFD REQUIRED NEW AND MORE ACCURATE DATA (TRAJECTORY, GEOMETRY), ELEVATED DESIGN PROCESS TO A NEW LEVEL

MAJOR "PRACTICAL" CFD DILLEMA → CHOICE OF CFD SOFTWARE and MODELS
ULTIMATELY WE USED WHAT WE COULD AFFORD AND WHAT WE KNEW.
CFD-ACE+ software package was utilized during the phase of conceptual design.
According to software developer (CFDRC) it can predict supersonic flows up to Mach =4.

We estimated air and flow conditions, temperature distributions, pressure field and drag coefficient Cd. These data helped to further modify the trajectory and to make new apogee and altitude estimations for the overall mission. These changes allowed us to minimize external thermal loads and to meet and exceed ballute material limitations.
At this point minor changes in ballute shape are no longer mission critical due to safety factor on material properties. Pressure forces on ballute were also estimated and weight requirements for helium gas were established.
MODE OF OPERATION: DESIGNERS PROVIDE INPUT--->CFD--->DISCUSSIONS ---> NEW INPUT --→ more CFD

Ballutes - NASA JPL Conceptual Studies

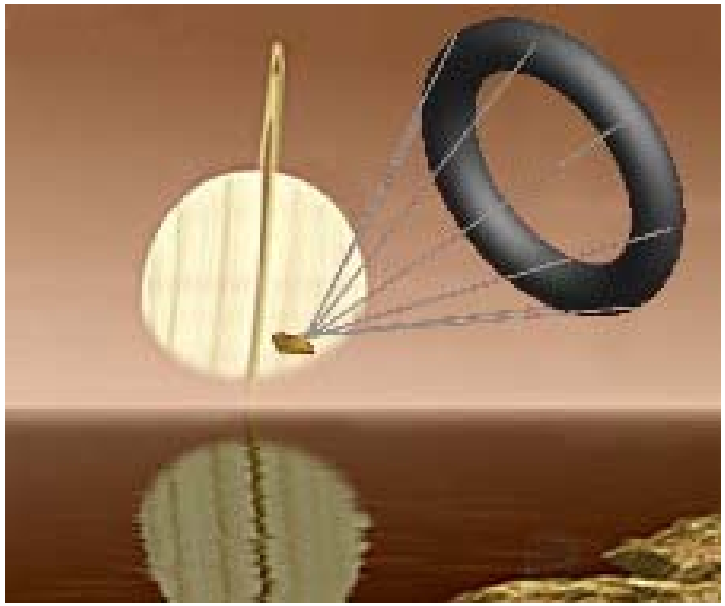

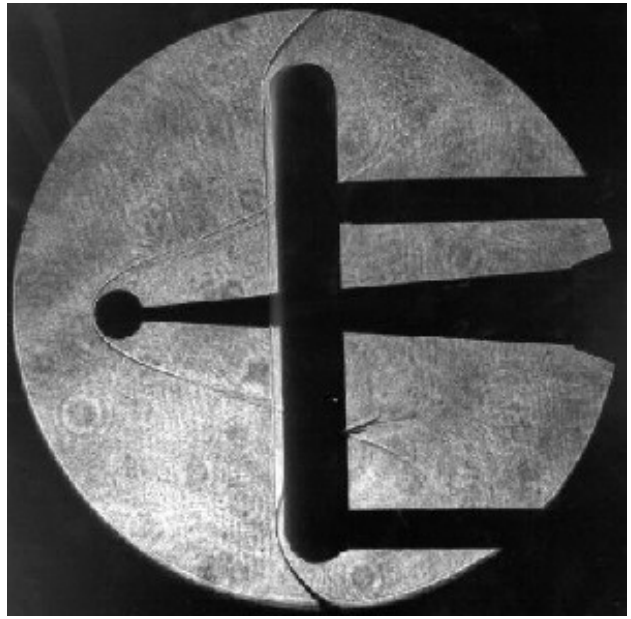

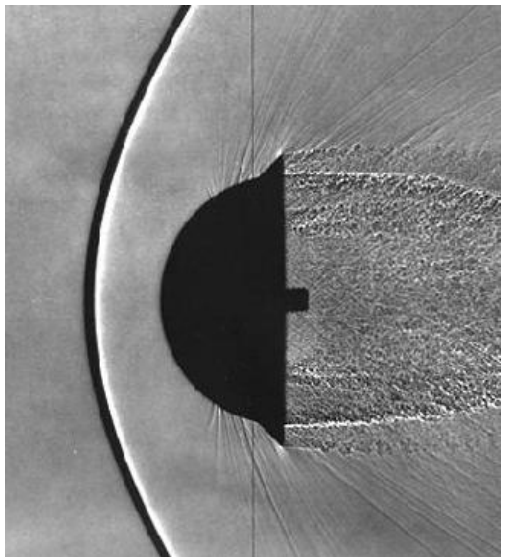

Bow shock visualization

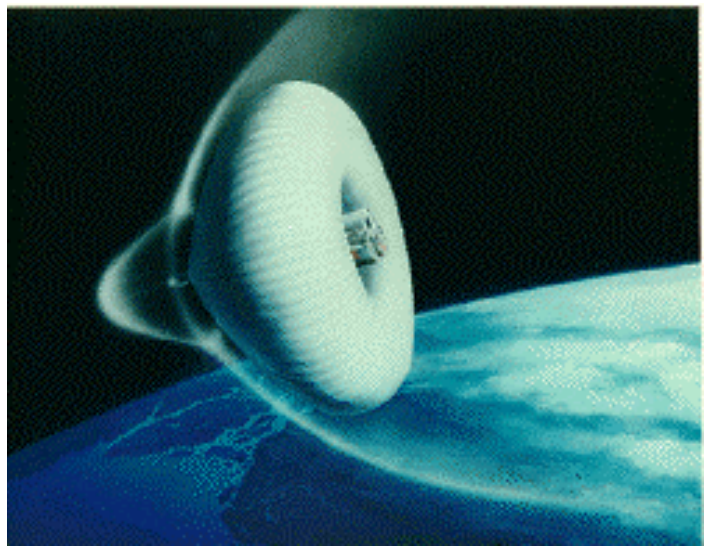

Rocket Ballute - Present Design

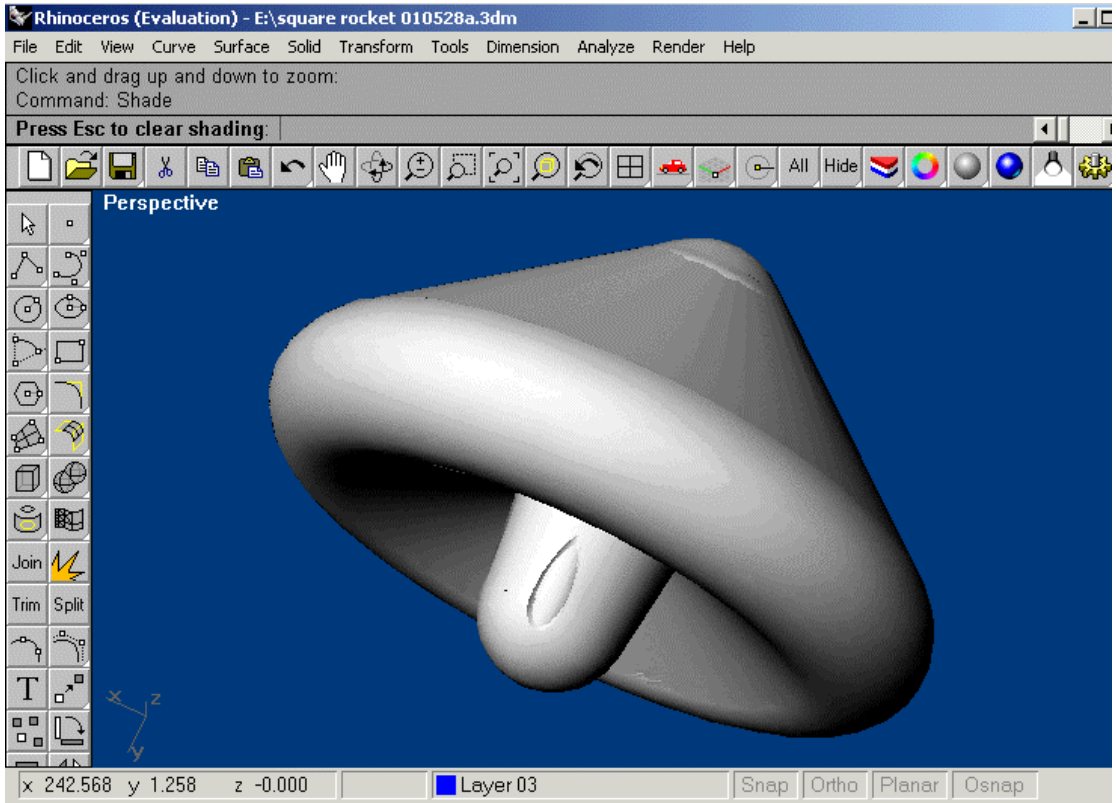

New Conceptual Configuration evolved as a result of engineering evaluation that followed CFD studies -- SECOND ITERATION OF CONCEPTUAL DESIGN

Rocket Ballute-Present Design

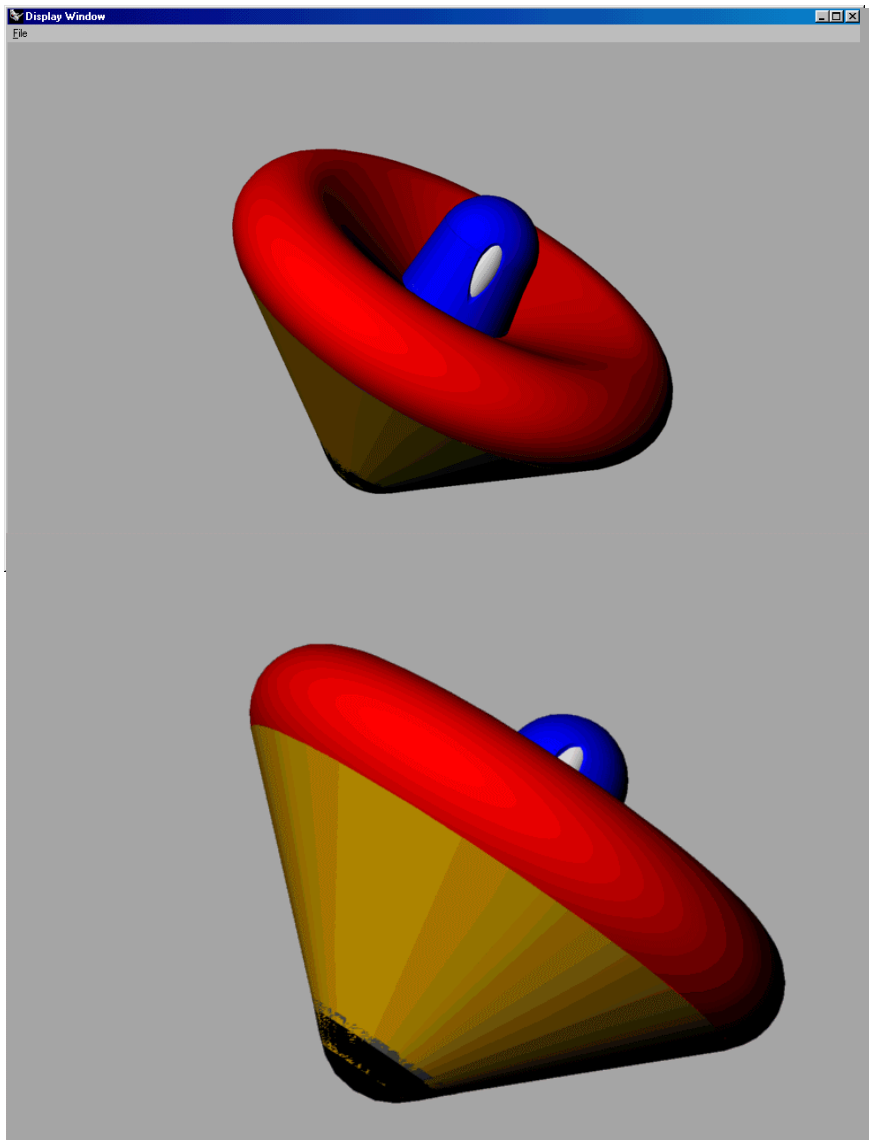

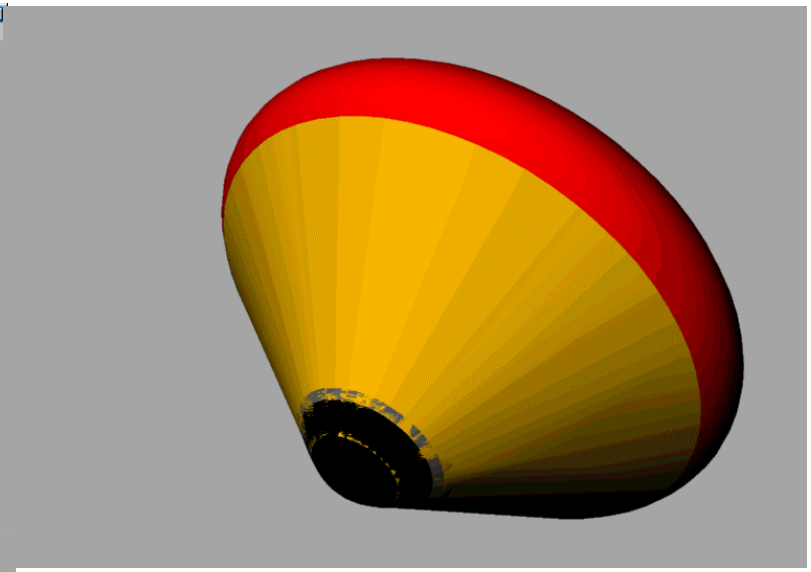

CHANGES:
-larger OD for ballute
-larger filled volume (front)
-longer to avoid
“wake closure” on capsule
-longer to move center of pressure away from center of mass
<<CONFIGURATION IS FINALIZED>>

Rocket --- Present Design

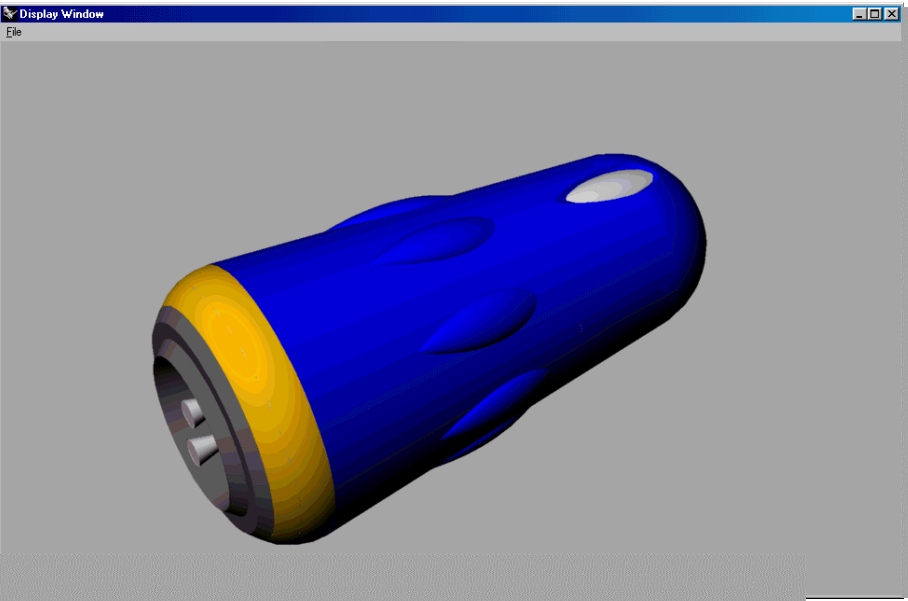

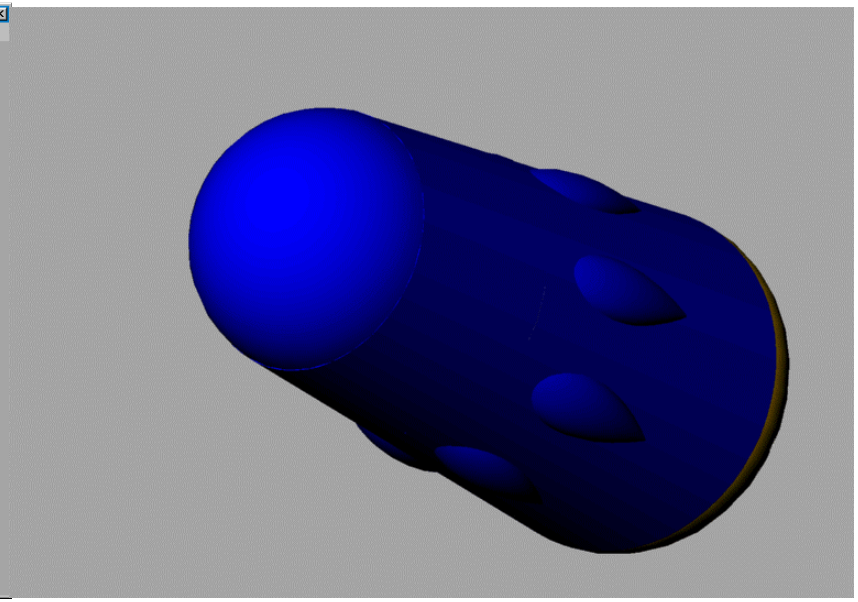

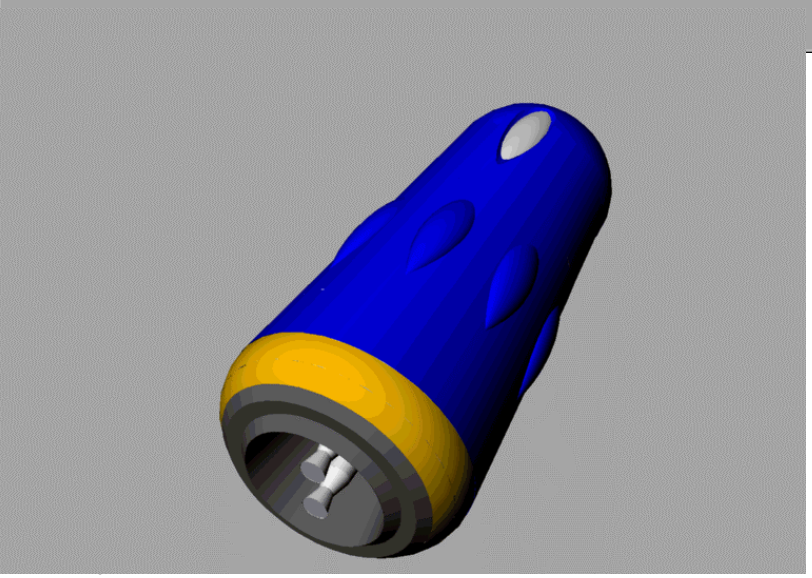

CHANGES:
-larger OD for rocket "base"
-larger front nose diameter and angle
SUBJECT TO SUBSEQUENT EVALUATION

Computational Setup

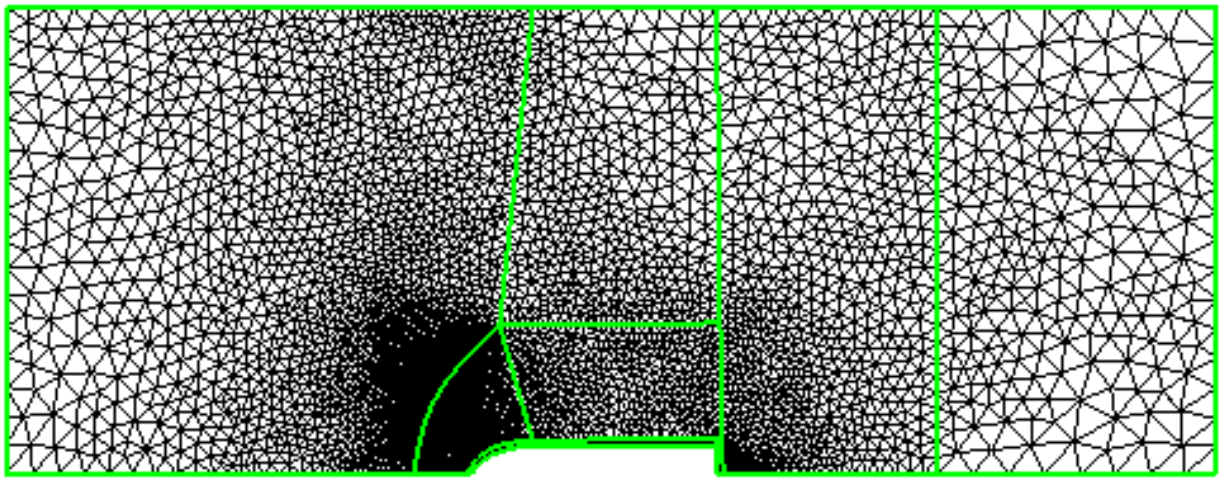

Rocket

Hybrid S-U Gridding

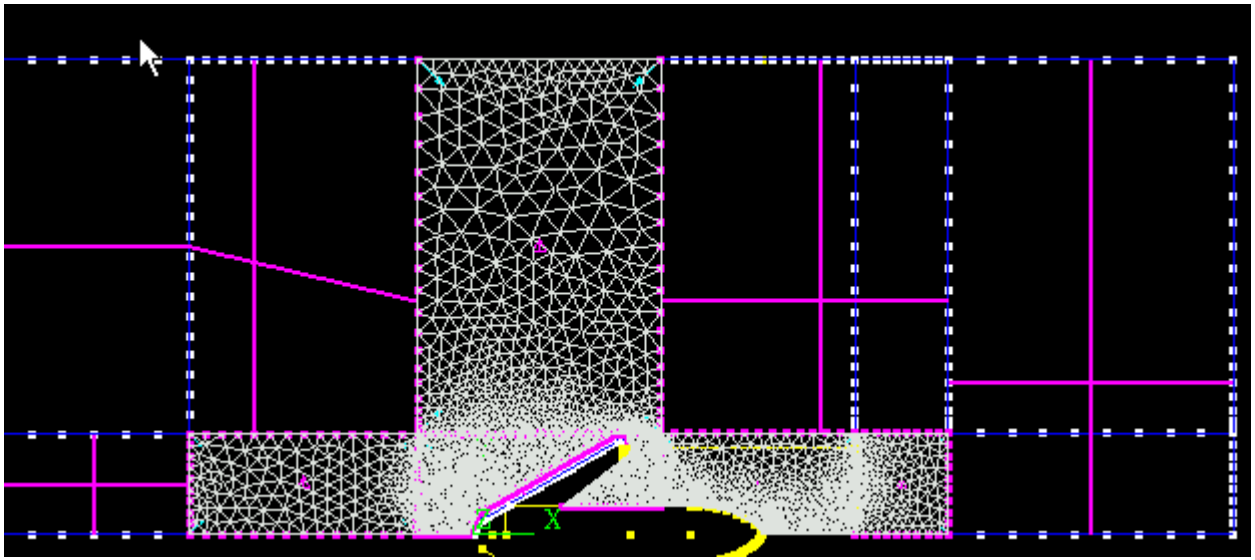

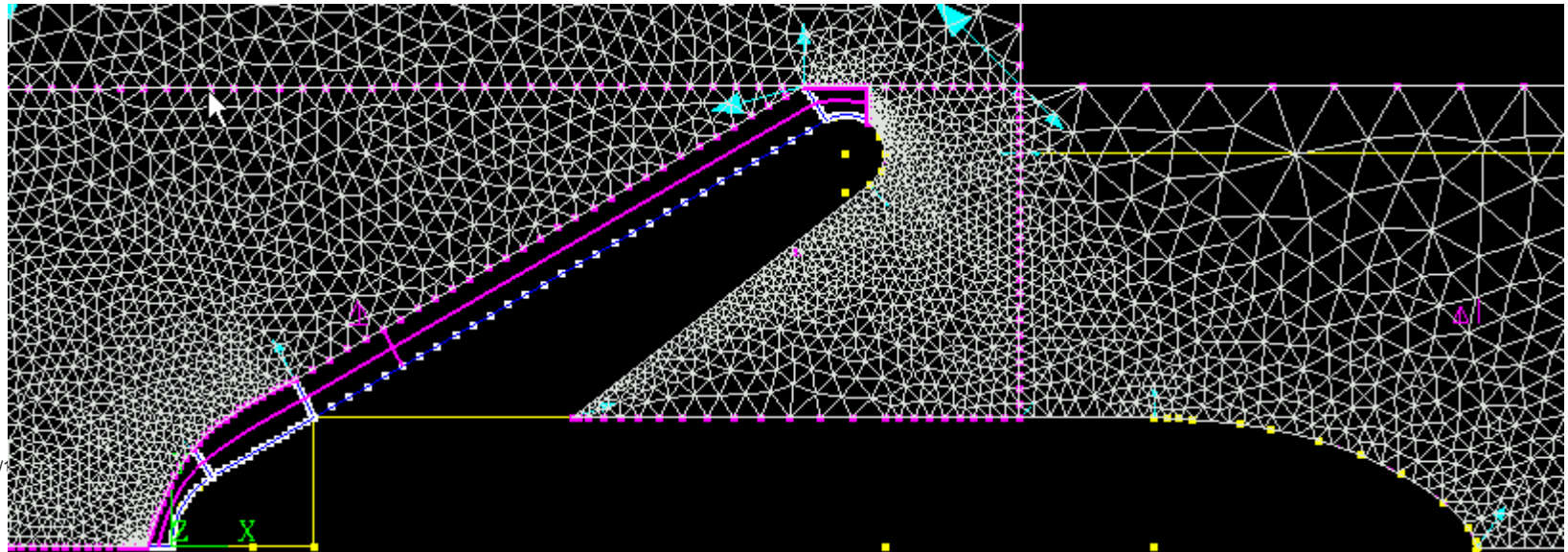

Setup- Rocket Ballute

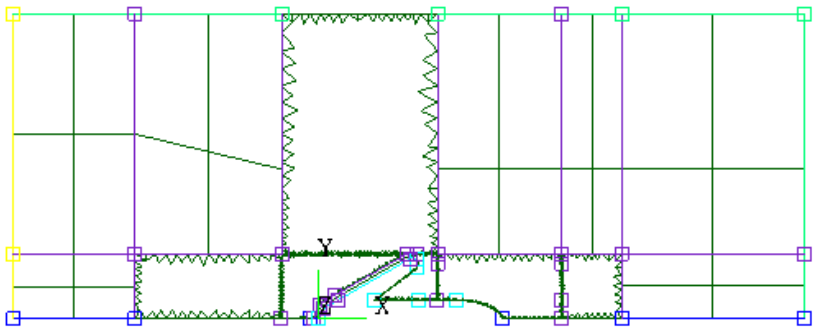

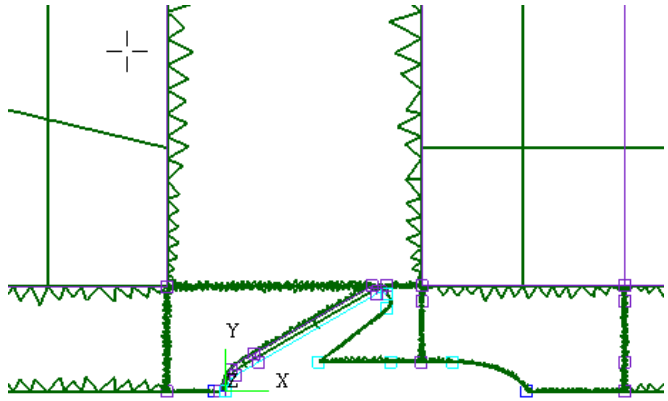

Output

Pressure Forces

	Name	Key	Type	X-axis	Y-axis
4	b1	464	Wall	1.722654E+04	-1.191149E+04
7	b1	471	Wall	1.861155E+04	-3.223037E+04
9	b2	491	Wall	2.857052E+05	-4.947670E+05
11	b3	492	Wall	5.738700E+03	-1.255066E+04
62	rb	583	Wall	-4.191336E-12	9.547799E+03
64	rbrear	585	Wall	3.005454E+03	1.291571E+04
75	rb	542	Wall	0.000000E+00	2.260614E+04
76	rb	543	Wall	-4.279382E-12	9.828310E+03
77	b4	598	Wall	1.397867E+04	6.904508E+02
78	b5s	599	Wall	3.215643E+04	-4.123918E+04

Shear Forces

	Name	Key	Type	X-axis	Y-axis
4	b1	464	Wall	2.884109E+01	2.981358E+01
7	b1	471	Wall	1.435156E+02	8.290480E+01
9	b2	491	Wall	1.887833E+03	1.088571E+03
11	b3	492	Wall	1.684699E+02	2.881604E+01
62	rb	583	Wall	-3.849444E+00	3.784508E-01
64	rbrear	585	Wall	-2.980826E+00	3.375424E-01
75	rb	542	Wall	-2.468475E+00	8.473813E-02
76	rb	543	Wall	-3.492539E+00	-2.613778E-02
77	b4	598	Wall	1.106551E+01	-6.542686E+00
78	b5s	599	Wall	2.188292E+00	1.945553E+00

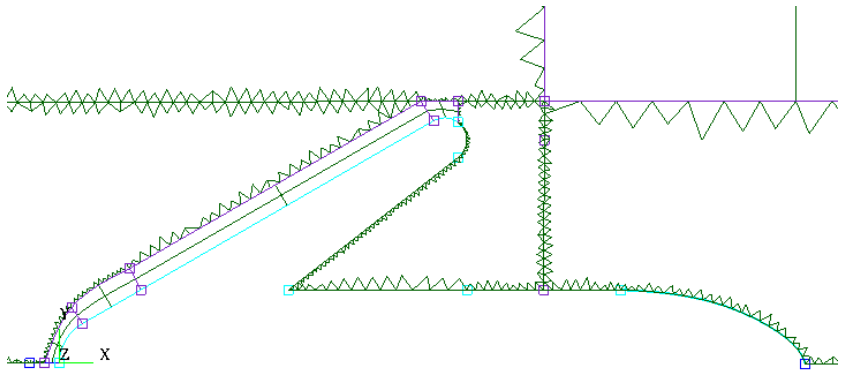

Problem Setup -velocities

K-eps RNG Turbulence Model, with the following inlet conditions: example P=20E3 Pa, T=245 (low altitude)

P, Pa	T, K	mu	RHO	Beta	Tu_free	Velocity	M	K	D
20,000	245	1.56885E-05	0.284732	0.2	0.01	350	1.11611	6.125	3.064E+05
20,000	245	1.56885E-05	0.284732	0.2	0.01	450	1.434999	10.125	8.373E+05
20,000	245	1.56885E-05	0.284732	0.2	0.01	550	1.753888	15.125	1.868E+06
20,000	245	1.56885E-05	0.284732	0.2	0.01	650	2.072776	21.125	3.645E+06
20,000	245	1.56885E-05	0.284732	0.2	0.01	750	2.391665	28.125	6.460E+06
20,000	245	1.56885E-05	0.284732	0.2	0.01	850	2.710554	36.125	1.066E+07
20,000	245	1.56885E-05	0.284732	0.2	0.01	950	3.029442	45.125	1.663E+07
20,000	245	1.56885E-05	0.284732	0.2	0.01	1000	3.188887	50	2.042E+07
20,000	245	1.56885E-05	0.284732	0.2	0.01	1100	3.507775	60.5	2.989E+07
20,000	245	1.56885E-05	0.284732	0.2	0.01	1200	3.826664	72	4.234E+07
20,000	245	1.56885E-05	0.284732	0.2	0.01	1400	4.464441	98	7.844E+07

Inlet velocity conditions:

we start computations with lower flow (V=350..450 m/s) and then use converged solutions from lower velocity case as strart-up for higher velocity case.
For a given altitude (pressure, Temperature) we run range of velocity conditions between 350…1400 m/s

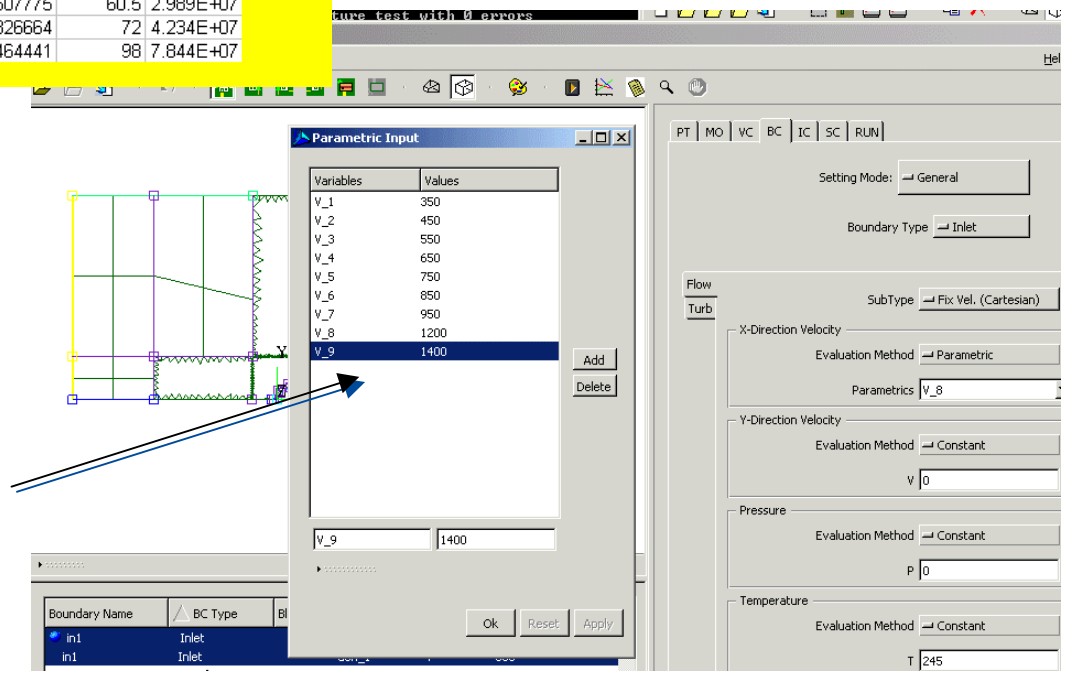

Boundary Conditions

Computational Domain: approximately 12K nodes

Most Robust model:
IC: previous solution for all fields
inlet: fixed inlet velocity Vfree
outlet2: fixed far filed velocity Vfree
outlet1: extrapolated pressure

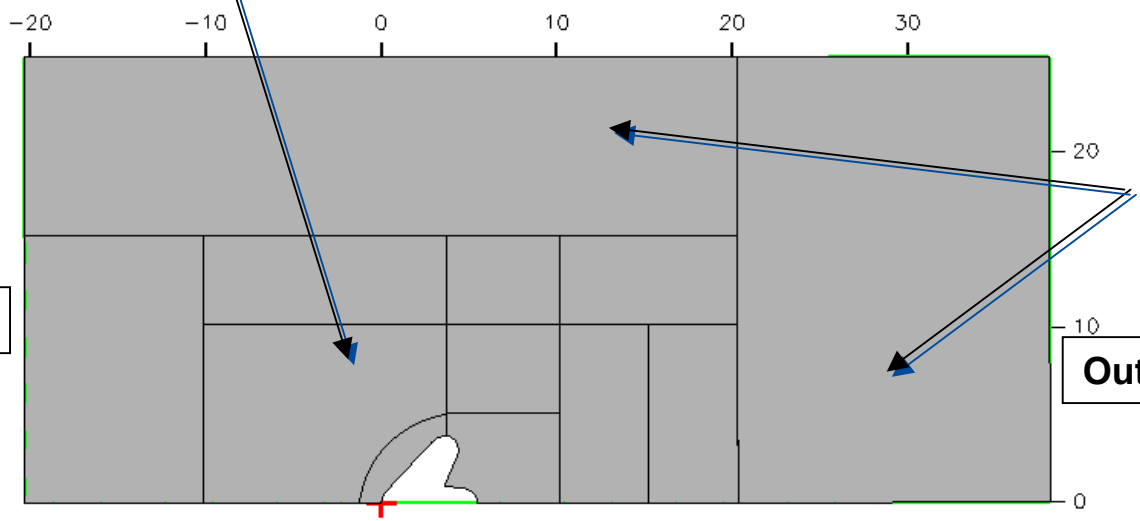

"extra" segments were added in process to better support far field conditions

Also considered:
outlet2: fixed pressure, P=0, or extrapolated pressure
outlet1: fixed pressure, P=0
If any node at the outlet has velocity <M, extrapolated condition will lead to divergence

BCs, Solution and Relaxation

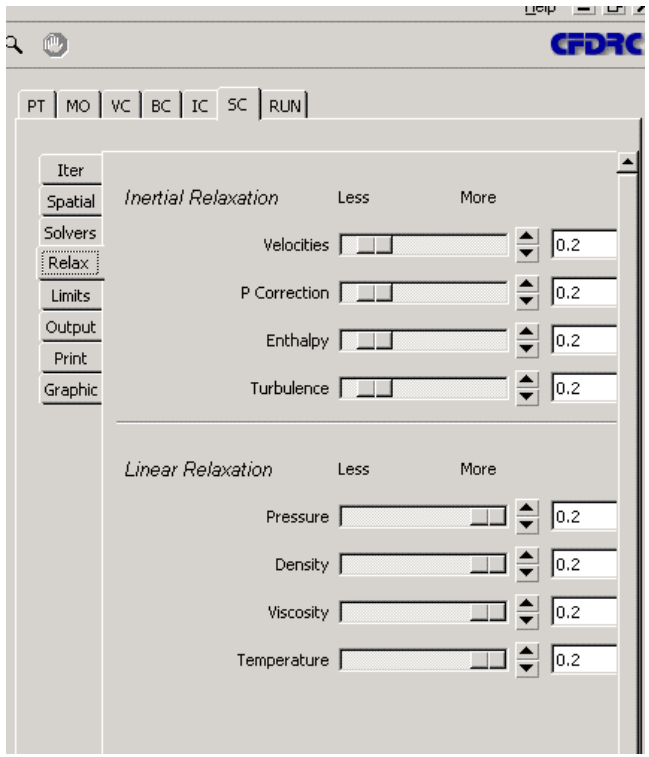

-OUTLET BOUNDARY CONDITIONS and CONVERGENCE at different velocities
-startup solution with 100 m/s ramp
-linear relaxation for pressure, density, viscosity and temperature in the range 0.7…0.2
[note that we use pressure based code in this study]

First Results: Vinlet=550 m/s

Pressure fields

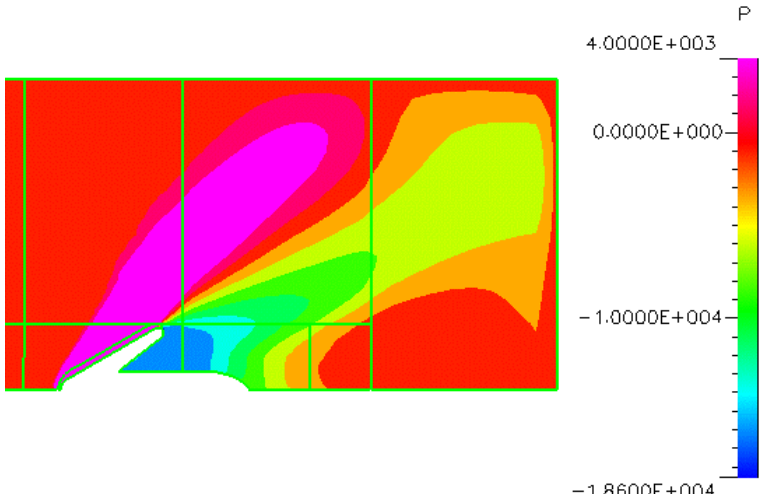

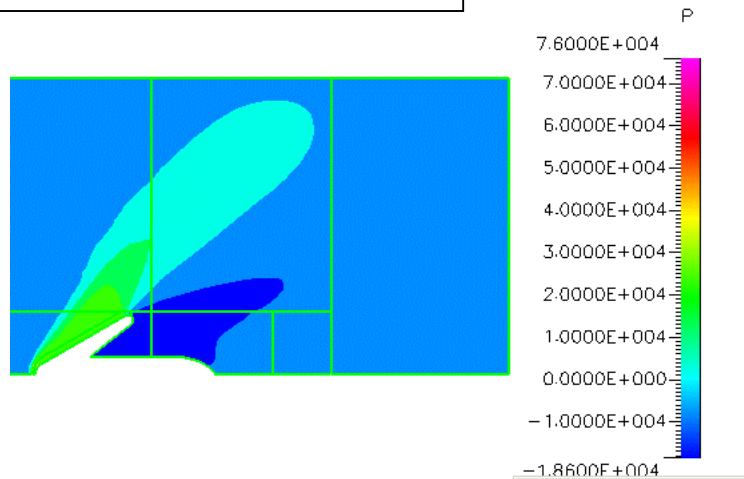

Turbulence parameters: K & D

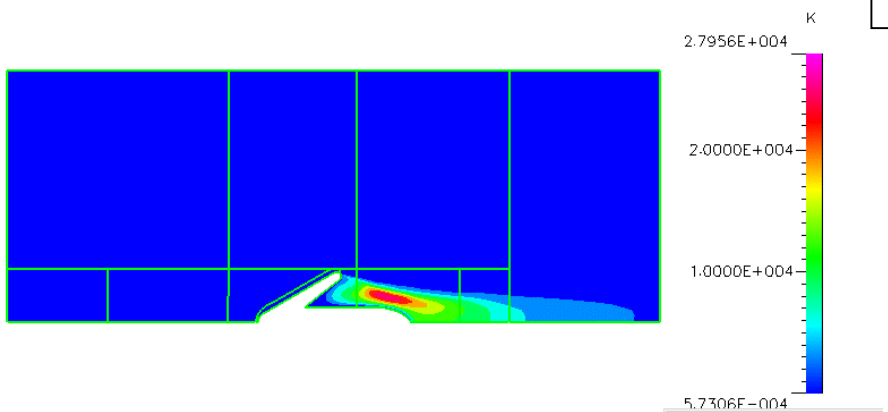

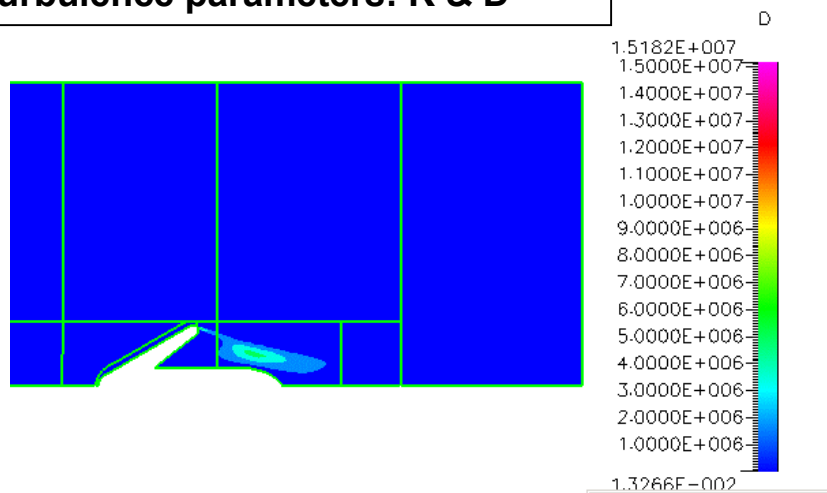

Mach Numbers and Temperatures

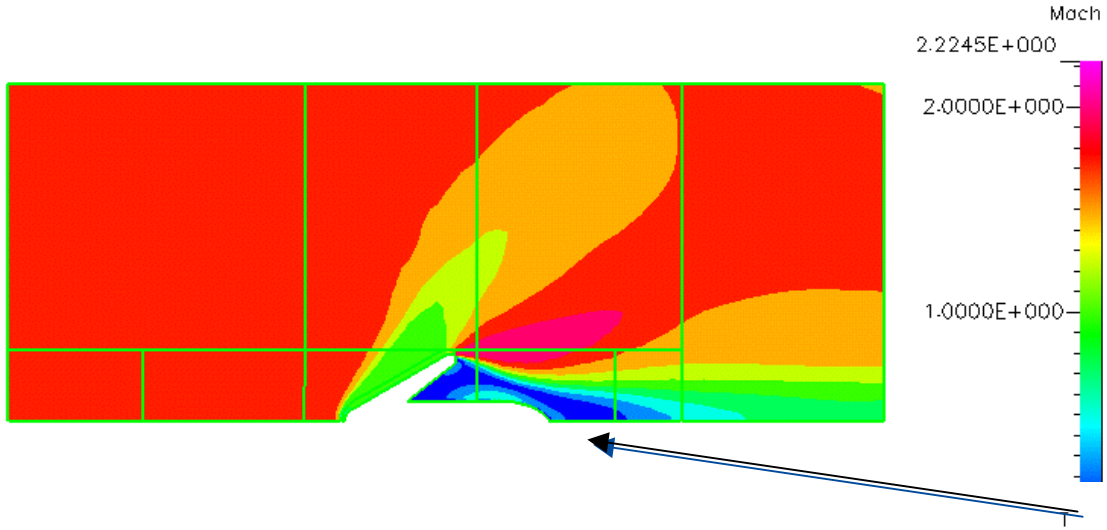

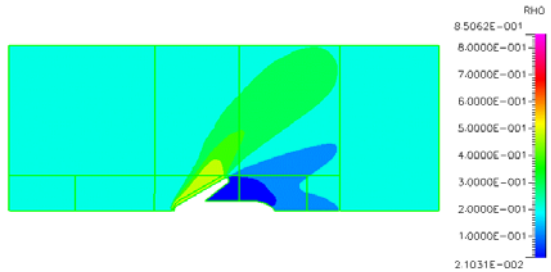

Recirculation Zone --flow impingement on the capsule. Consequently this finding lead to rocket ballute re-design.

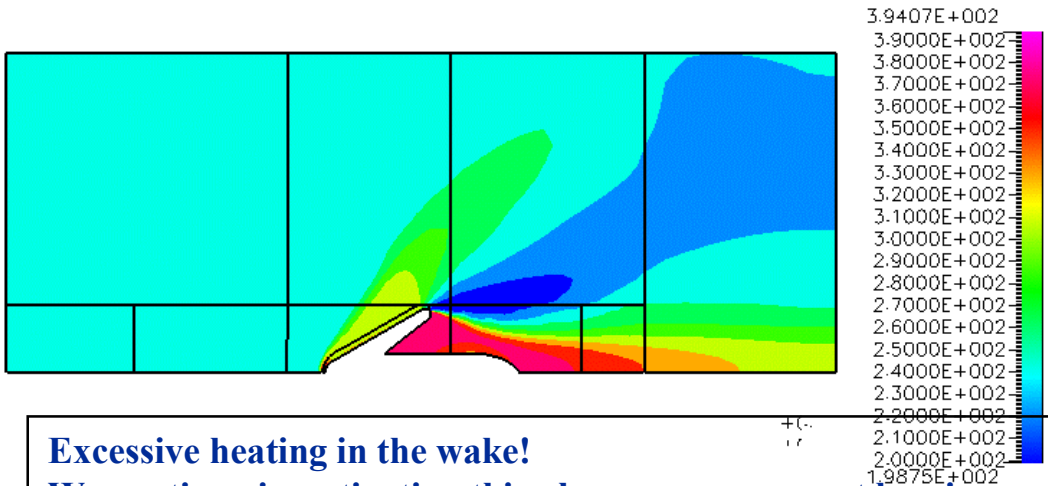

Excessive heating in the wake!
We continue investigating this phenomena , suspect bug in software or in our model setup.

Second Design Iteration, Rballute=1.5meters

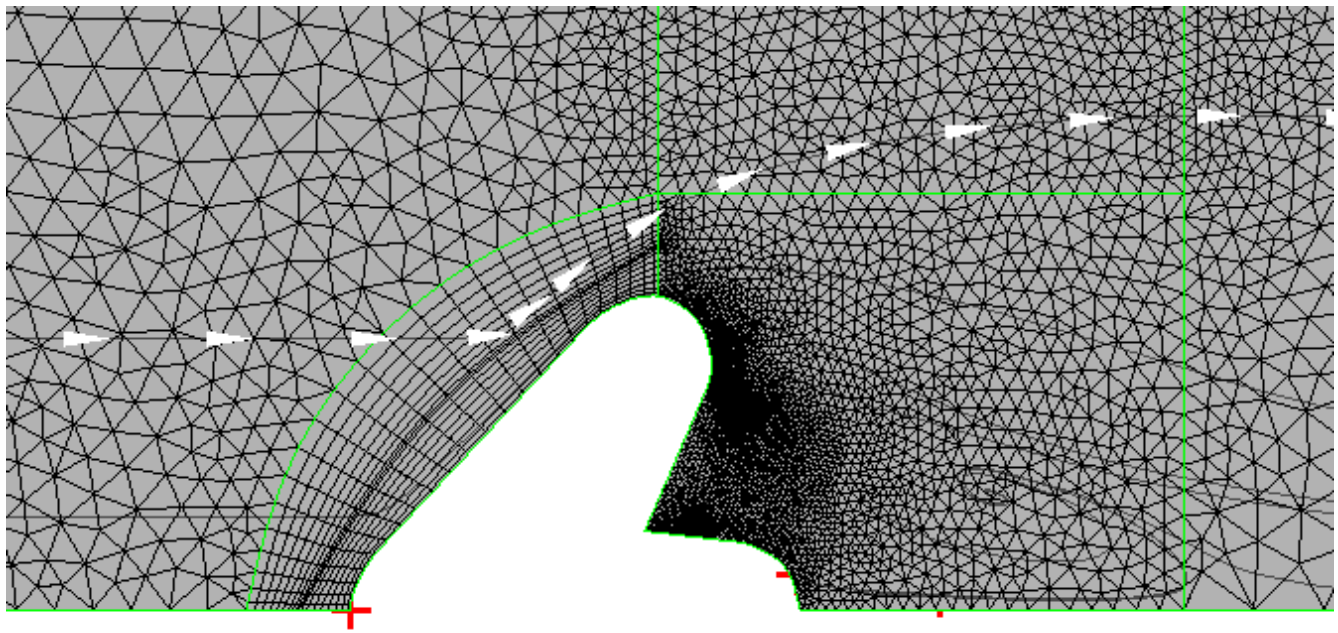

Hybrid structured-unstructured grid near ballute

Bow Shock (pressure) distribution

Worst case scenario considered: M=4.5 at H=35 km

Max pressure is close to 15 psi: defines requirements for ballute pressurization , helim mass for on-board storage

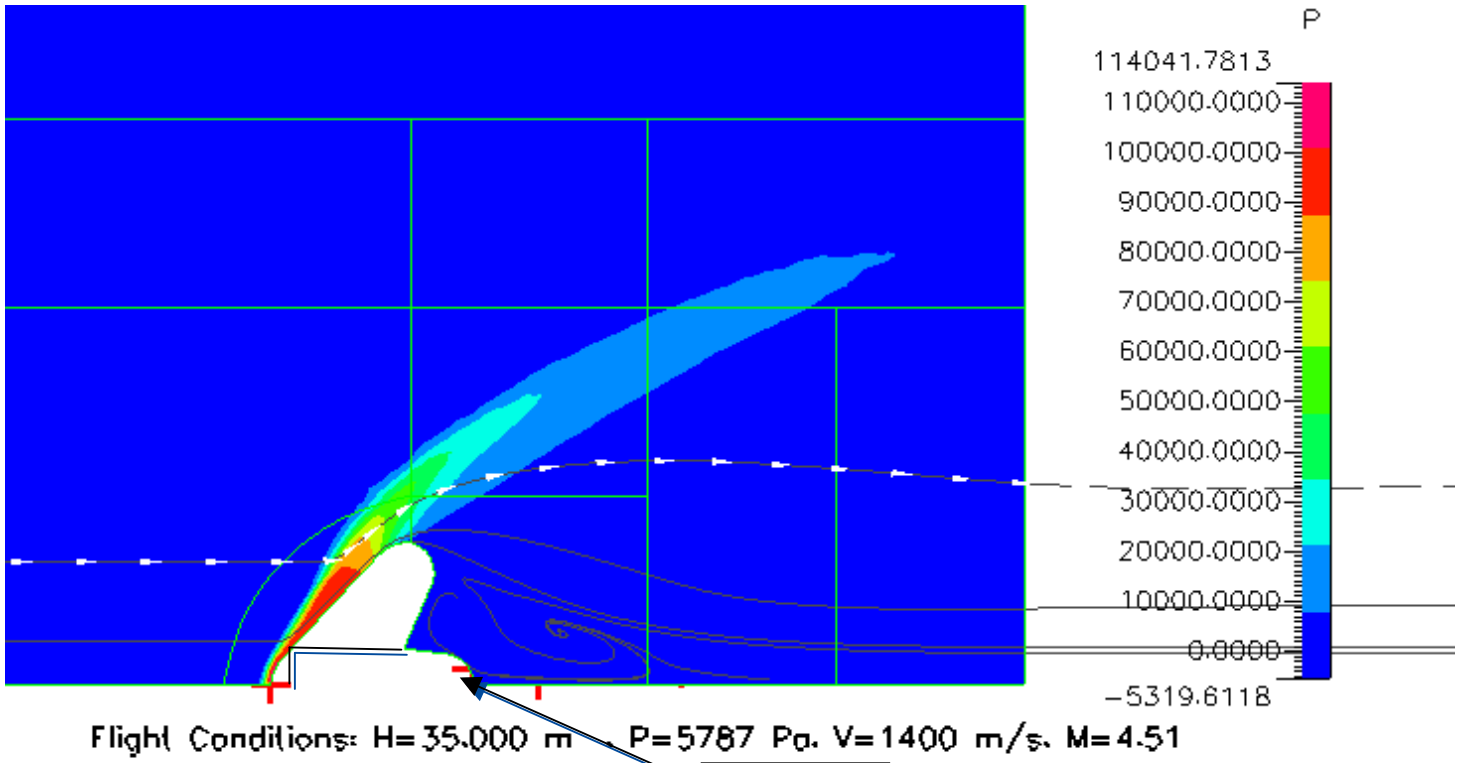

capsule

Note much shorter rocket body and larger aspect ratio. Correspondingly wake is now much larger and covers entire capsule with astronauts.

Pressure Loads for Ballute Calculation

Worst case scenario considered: M=4.5 at H=35 km

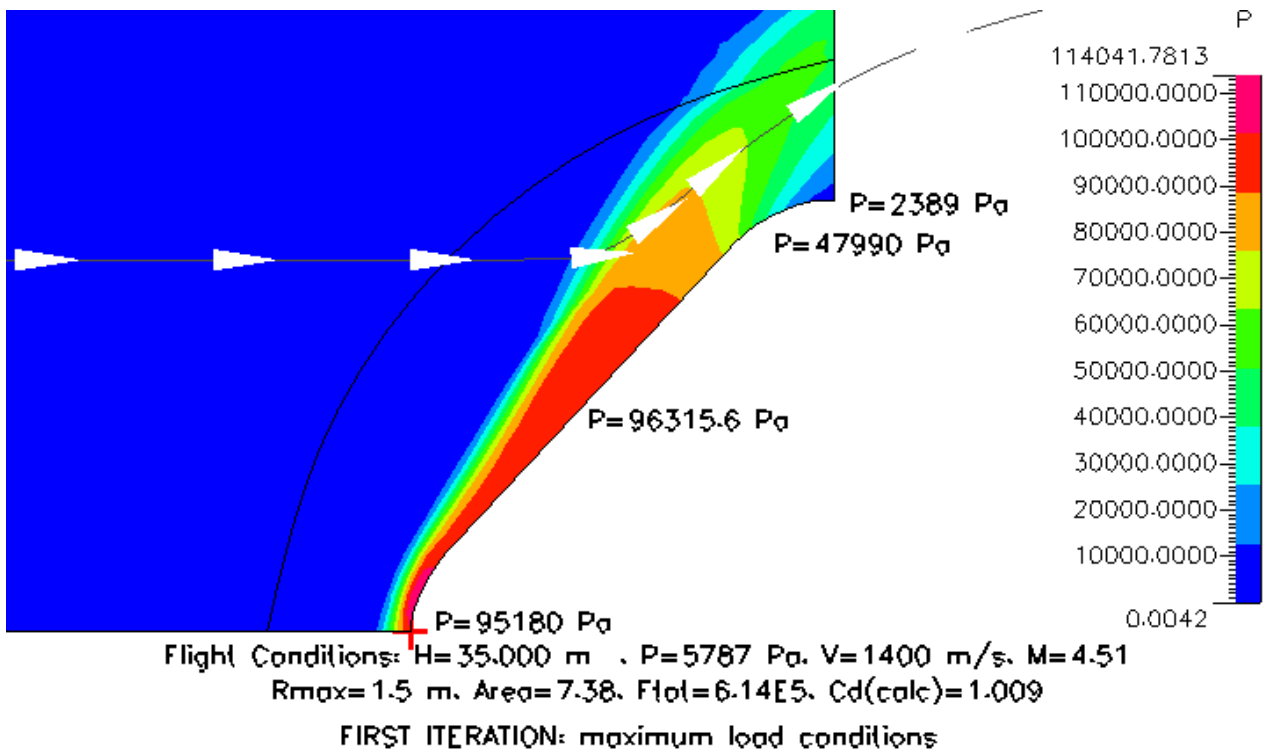

Aerodynamics - Cd estimation

Peak Flight Conditions
Zone

H (km)	P[Pa]	T [K]
30	11680	230
35	5730	244
40	2920	258
44	1750	267

Cd=2F/A/[RHO*V2]**

Forces, N on segments, for 1 radian

1.27E+03						1.08E+03
2.04E+02						1.9872
5.90E+02						5.81E+02
6.44E+02						6.63E+02
1.92E+03						2.12E+03
5.08E+01						5.80E+01
1.72E+02						2.11E+02
3.00E+02						3.03E+02
9.54E+04	Newton	Total				**9.78E+04**
Total=6.28*9.54E4		**599112**				6.14E+05
Area=	7.38				Velocity=1400 m/s	
Cd=2F/[RHO*V**2]		0.984915				**1.009966**
0.08281	Rho_BY_SA		RHO_CODE		0.084106	

Total force

Cd

Forebody Heating - Ballute

Worst case scenario considered: M=4.5 at H=35 km

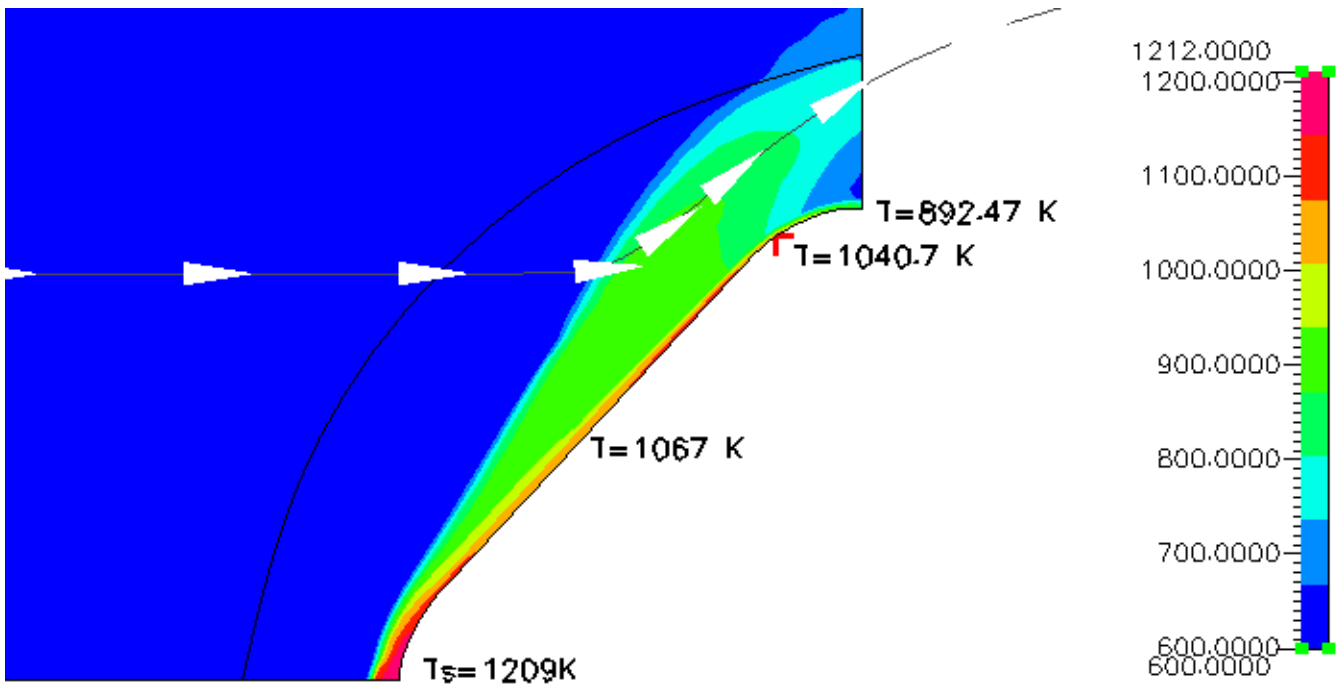

Flight Conditions: H=35.000 m , P=5787 Pa, V=1400 m/s, M=4.51
Rmax=1.5 m, Area=7.38, Ftot=6.14E5, Cd(calc)=1.009

FIRST ITERATION: maximum load conditions

Mach Number

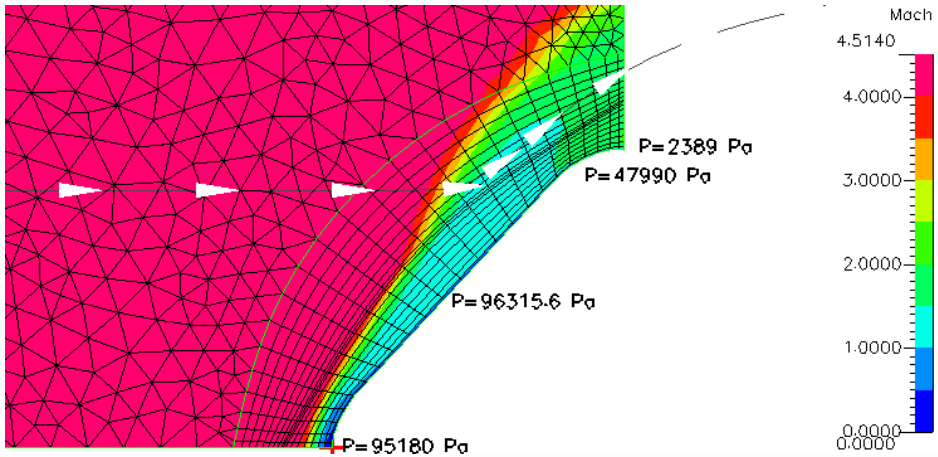

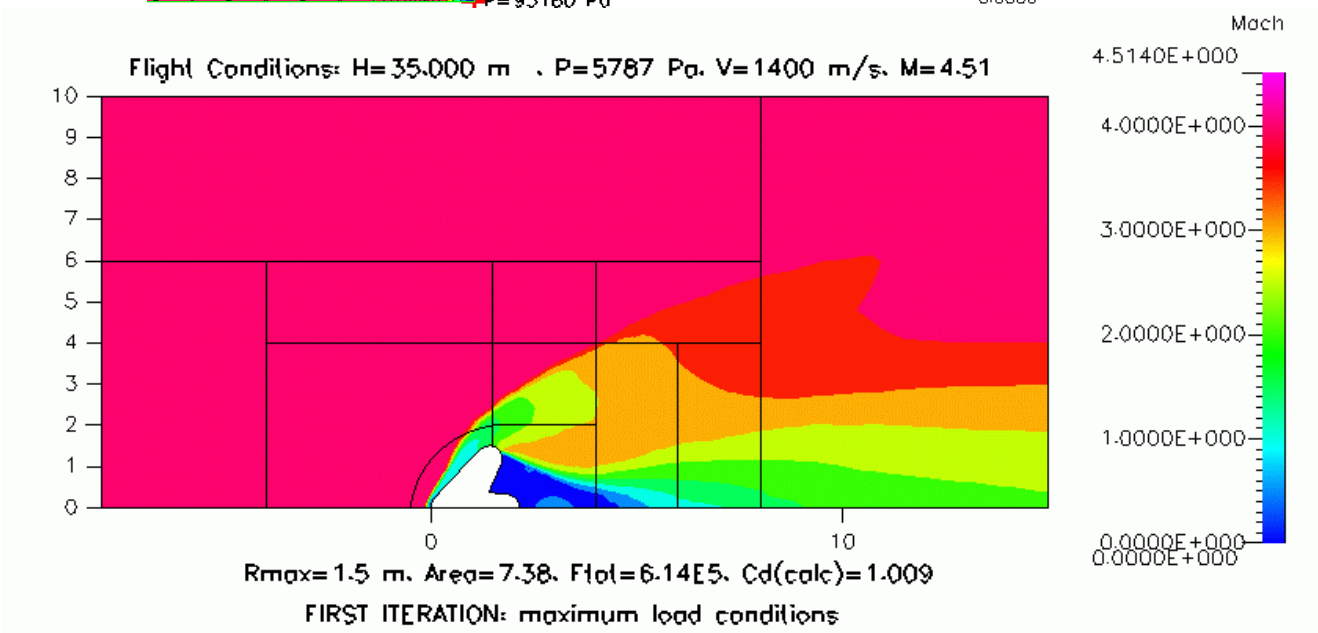

PR-12-02/25

Worst case scenario considered: M=4.5 at H=35 km

Density and Total Pressure

Worst case scenario considered: M=4.5 at H=35 km

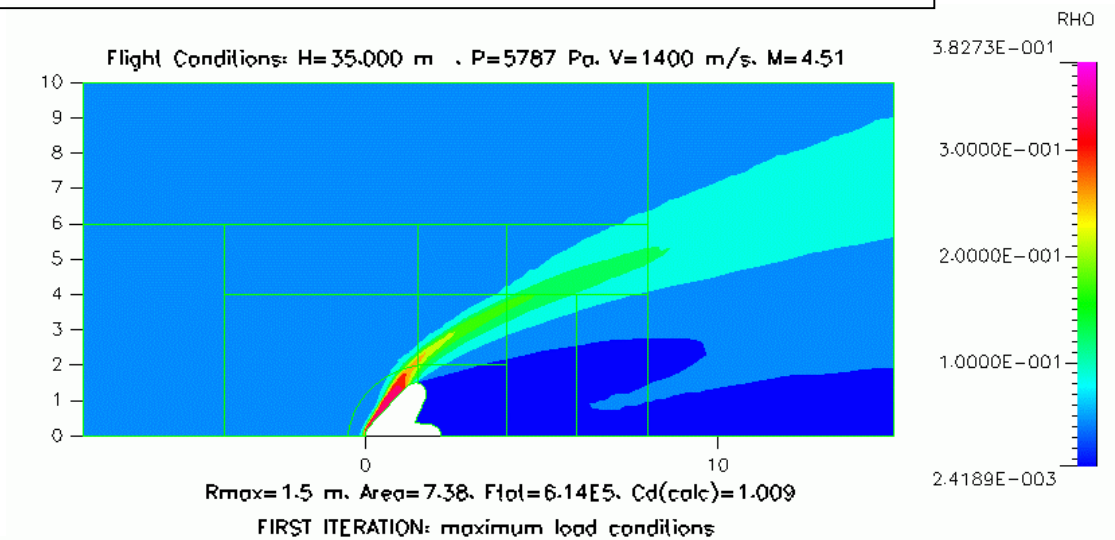

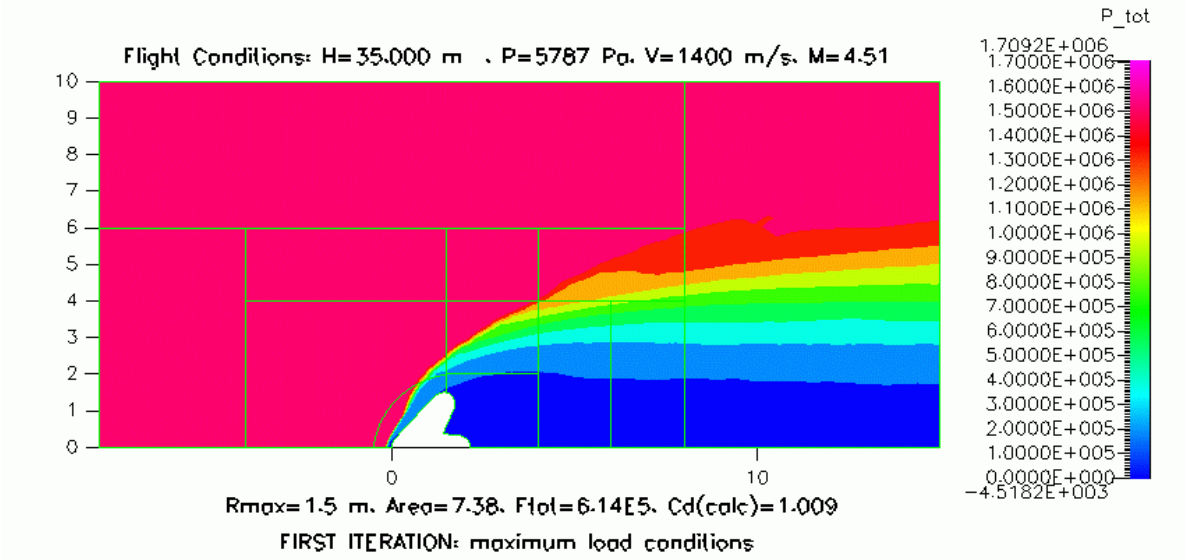

Third Iteration: Increased Ballute Outer Radius Rmax=3.78 meters

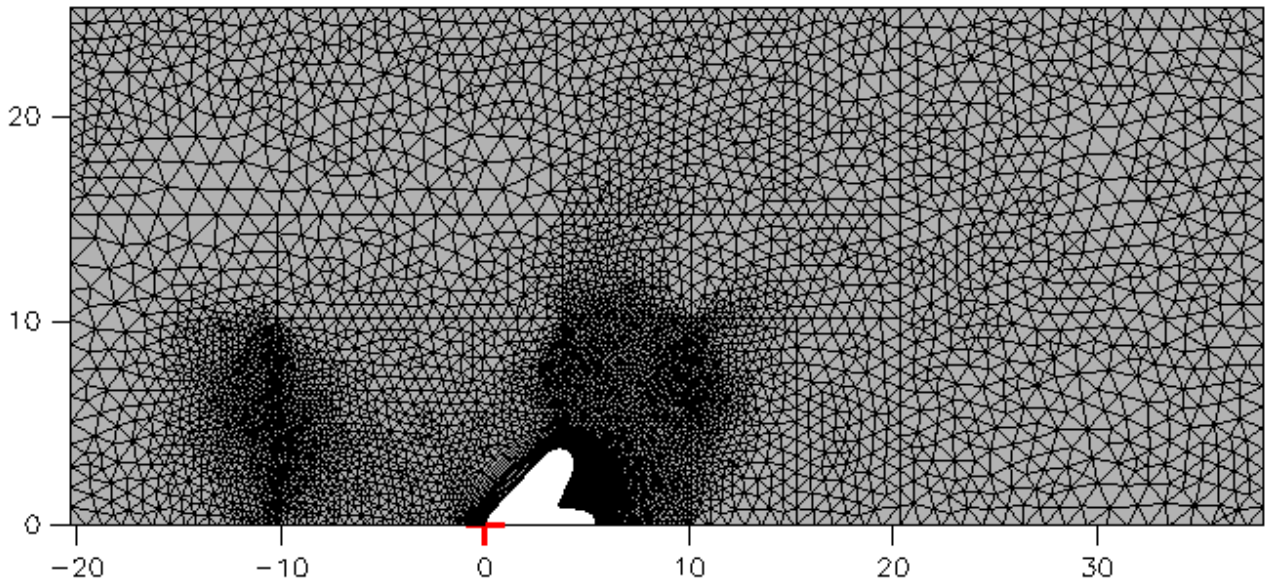

Worst case scenario considered: M=4.5 at H=35 km

Pressure distribution

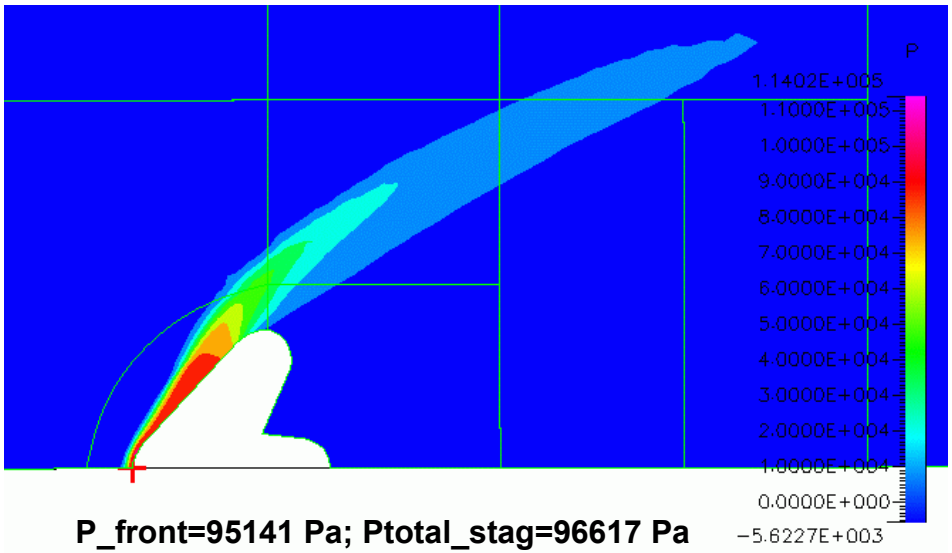

P_front=95141 Pa; Ptotal_stag=96617 Pa

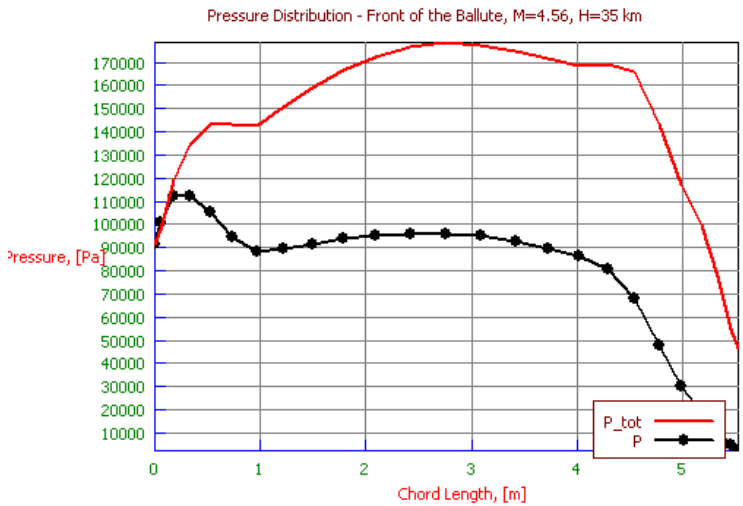

Forebody Heating - Ballute

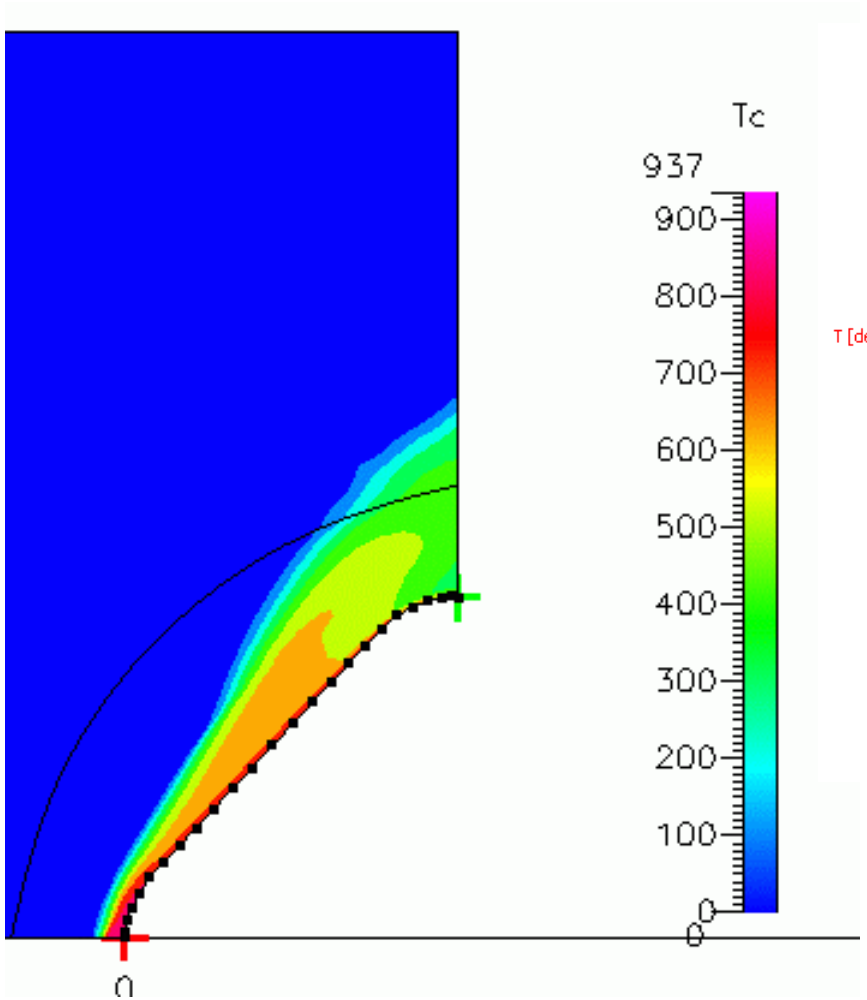

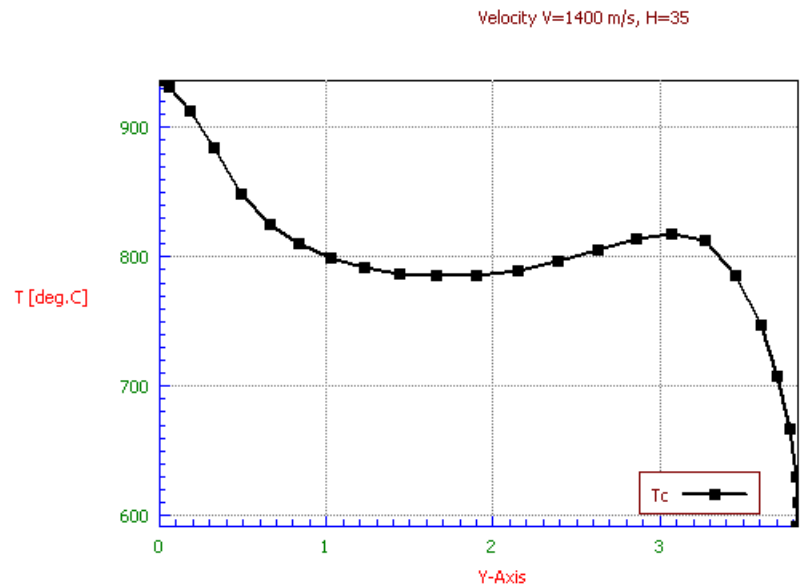

Tmax=1209K, Tmax=936.2 C;

Peak loads shown in previous section are on the limit of available resources and material properties.
Here we present results for three different trajectories:
with apogees of 110, 120 and 130 km. According to preliminary ballistic analyses this corresponds with maximum velocities of 925 , 110 and 1091 m/s at approximate altitude of 47 km.

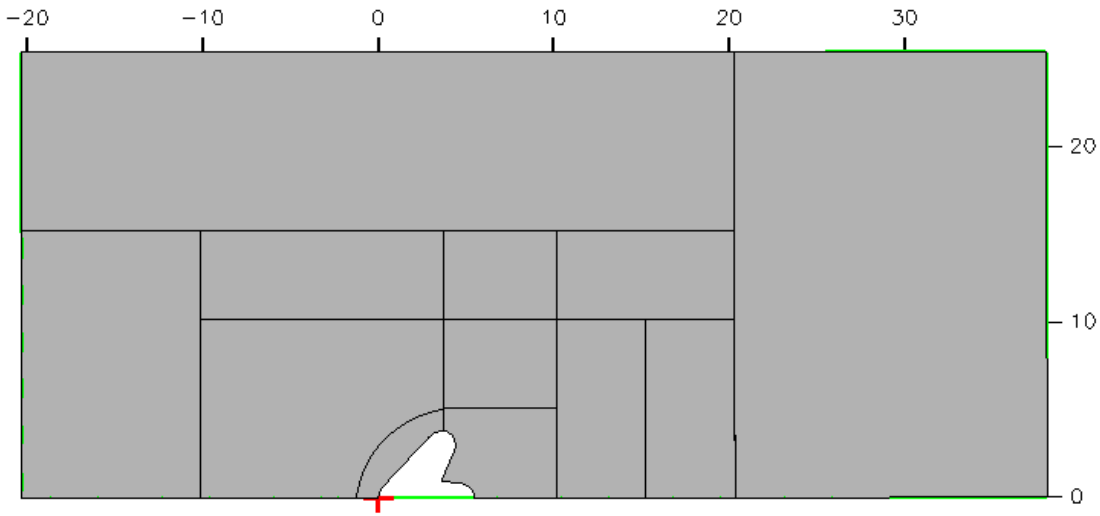

Comparison of Trajectories

Ballistic analyses utilized Cd=1, estimated from previous CFD studies for rocket ballute.
For considered trajectories maximum velocities were reached at 43..48 km range.
For the "first cut" we assumed that velocities of 925 m/s, 1010 m/s and 1095 m/s were all reached at 47 km altitude. Standard Atmosphere table for this altitude shows pressure of 1207 Pa and temperature T=274K
We performed external flow CFD simulations for on-design max.velocities.
These velocities are 925 m/s for 110 km trajectory, 1010 m/s for 120 km trajectory and 1091 m/s for 130 km trajectory.

In order to perform analysis using ACE+ at high supersonic speeds lower velocity supersonic solution must be obtained first (for example at Ufreestream=500 m/s), and then used as "initial field" for conditions with higher velocities. We used intermediate solutions at 500, 650, 700 and 850 m/s.

Summary: AeroHeating

110 km apogee: T peak=373 C

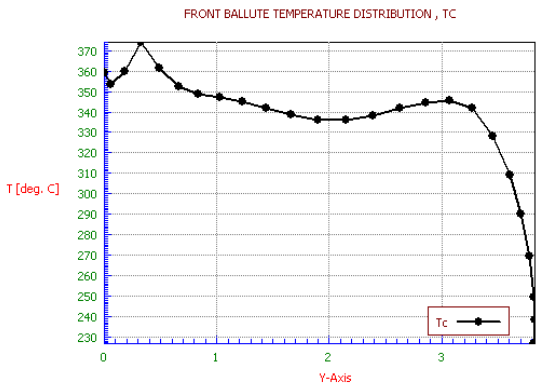

120 km apogee: T peak=461 C

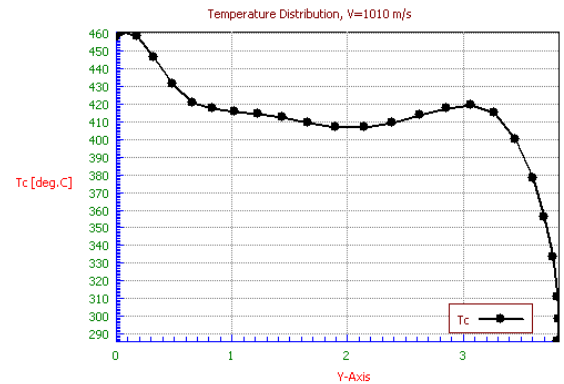

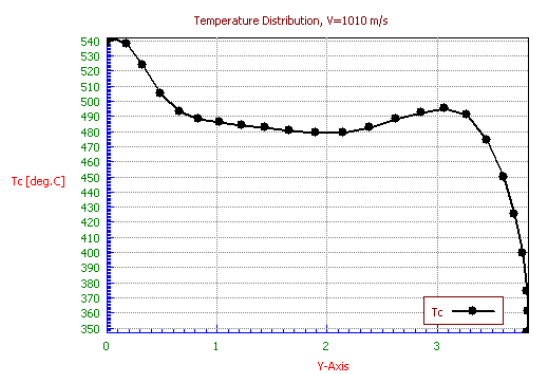

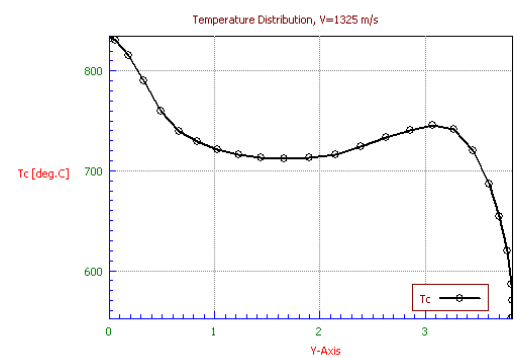

Vmax=1325 m/s; T peak=834C

130 km apogee: T peak=543C

MACH - V=925 m/s, H=110 km

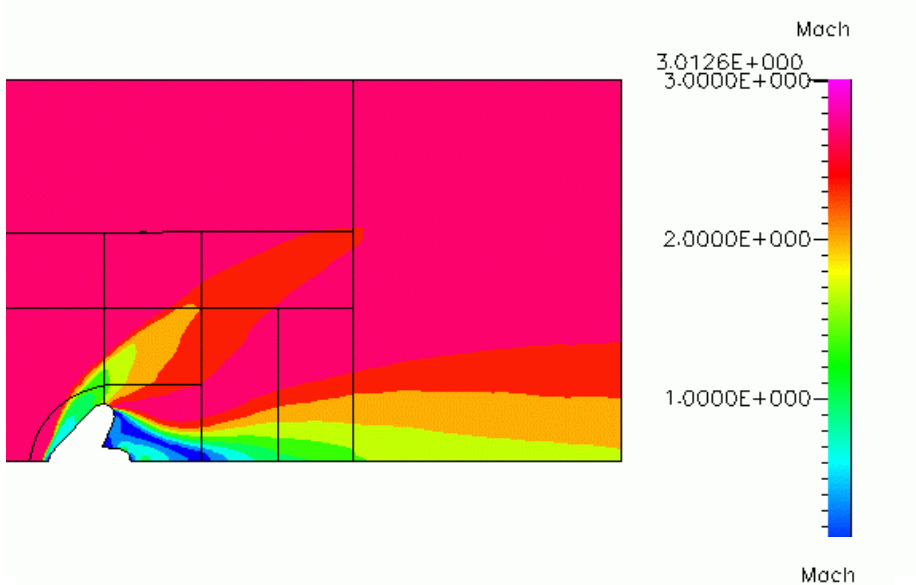

110 km apogee, V=925 m/s

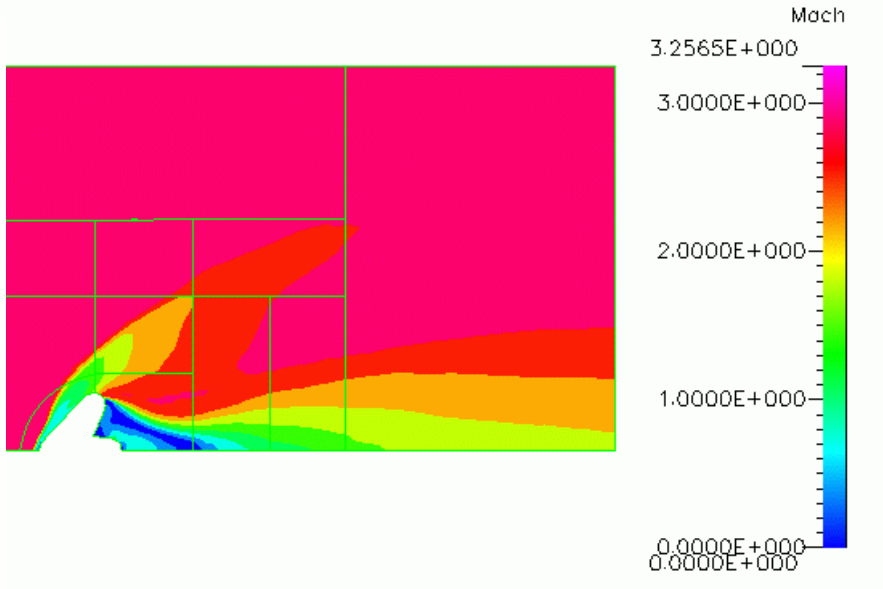

120 km apogee, V=1010 m/s

SUMMARY AND CONCLUSIONS

Comparison of aero-heating (air temperature in front of the ballute) shows significant reduction of thermal loads down to Tmax=372 C for the trajectory with 110 km apogee. This trajectory meets X-Prize requirements.
Trajectory with 120 apogee is also meeting X-prize requirements and material limitations for ballute. Our main design objective will be to achieve velocities below 1000 m/s at altitudes below 45 km. Our preliminary analysis show that we can meet this objective.

-we utilized CFD-ACE+ to analyze several consecutive iterations for the design of daVinci rocket ballute;
- using CFD we were able to "zero-in" on a conceptual configuration, flight scenario and trajectory requirements that will meet X-prize objectives and also minimize thermal loads;
-estimated thermal loads (Tmax<500C) can be met with commercially available materials used by ballute manufacturers

CFD Heads-up:
-coupled flow, heating shell simulation
-density-based gas flow and heating simulations
-wake heating issues
-transient mission profile simulations
-capsule transient heating analysis
-ballute and air heating analysis
-coupled flow --ballute fluid-structure interaction

Experimental Study of Unshrouded Impeller Pump Stage Sensitivity to Tip Clearance

September 10, 2001

Robert W. Williams, Thomas Zoladz, Anne K. Storey, and Stephen E. Skelley
NASA Marshall Space Flight Center, AL 35812

Background

- A turbopump develops required head by spinning very fast
  - The faster the pump rotates, the more head is generated
- A shroud is a heavy metal casing which covers blade passages
  - Shrouds help maintain performance and control axial thrust
- As a pump spins faster, stresses due to centrifugal force increase
  - The weight of the shroud increases the stress on the blades
  - This stress limits the speed at which a pump can operate
- A pump impeller without a shroud has less centrifugal force
  - Unshrouded Impellers operate at higher speeds with lower stress
  - Higher speeds allow Unshrouded impellers to generate more head
  - Use of unshrouded impellers allows for reduction of pump stages
- Tip clearance affects performance of unshrouded impeller
  - Experimentally quantify tip clearance effects on pump performance

Unshrouded Team Members

- MSFC Support
  - TD63 - Test Engineer, *Skelley*; Unsteady Data Reduction, *Zoladz*; Test Article Build Engineer, *Branick*
  - TD64 - Impeller Design, Analysis, Test Engineer, and Mgmt, *Williams*
  - TD74 - Facility Engineering and Facility Operations, *Storey & Jones*; Instrumentation and Controls, *Bush, Norman & McBride*; Calibration Wind Tunnel, *Gerry*; and Data Acquisition, *Kirkpatrick*
- Contractor Support
  - Pratt & Whitney - IGV, Baseline Impeller, and Diffuser Design, *Erler*
  - Boeing, Rocketdyne - Advanced Impeller Design, Analysis, and Tool Development, *Prueger, Chen, & Williams*
  - $A^2 I^2$ (Micro Craft Inc.) - Rig Mechanical Design and Fabrication, *Tyler*

Experiment Objectives and Approach

- Objective:
  - Experimentally determine unshrouded impeller performance sensitivity to tip clearance
- Approach:
  - Determine impeller efficiency at scaled operating conditions in water at MSFC's Pump Test Equipment (PTE) Facility
  - Test unshrouded impeller at three different tip clearances
  - Test each tip clearance configuration at on- and off-design conditions
  - Collect unsteady- and steady-state data in each configuration
  - Determine impeller efficiency directly using drive line torquemeter and pump inlet and exit total pressure measurements

Facility Description

- Test was conducted at MSFC's PTE Facility
  - PTE is a closed-loop water flow facility with 10,000 gallon reservoir
  - Deaeration and pressurization systems, facility flow meter, flow control valve, torquemeter, and 350 horsepower drive motor

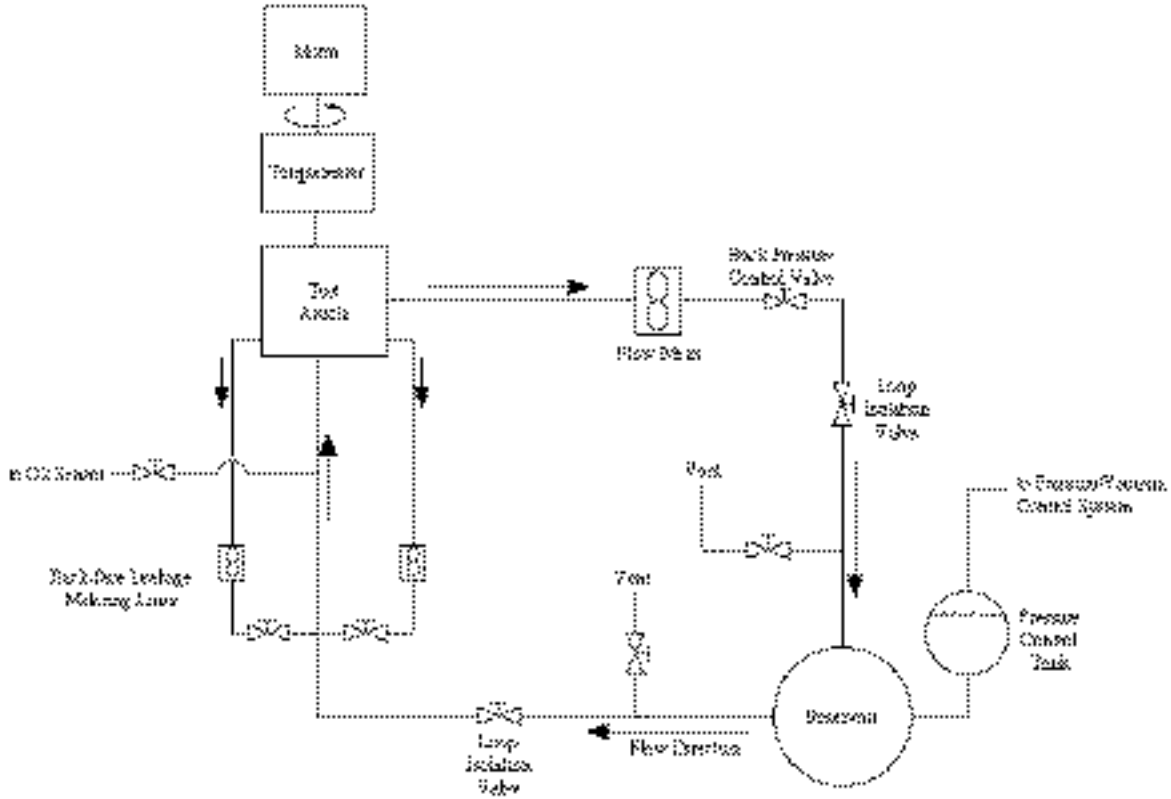

Unshrouded Impeller Technology Water Rig

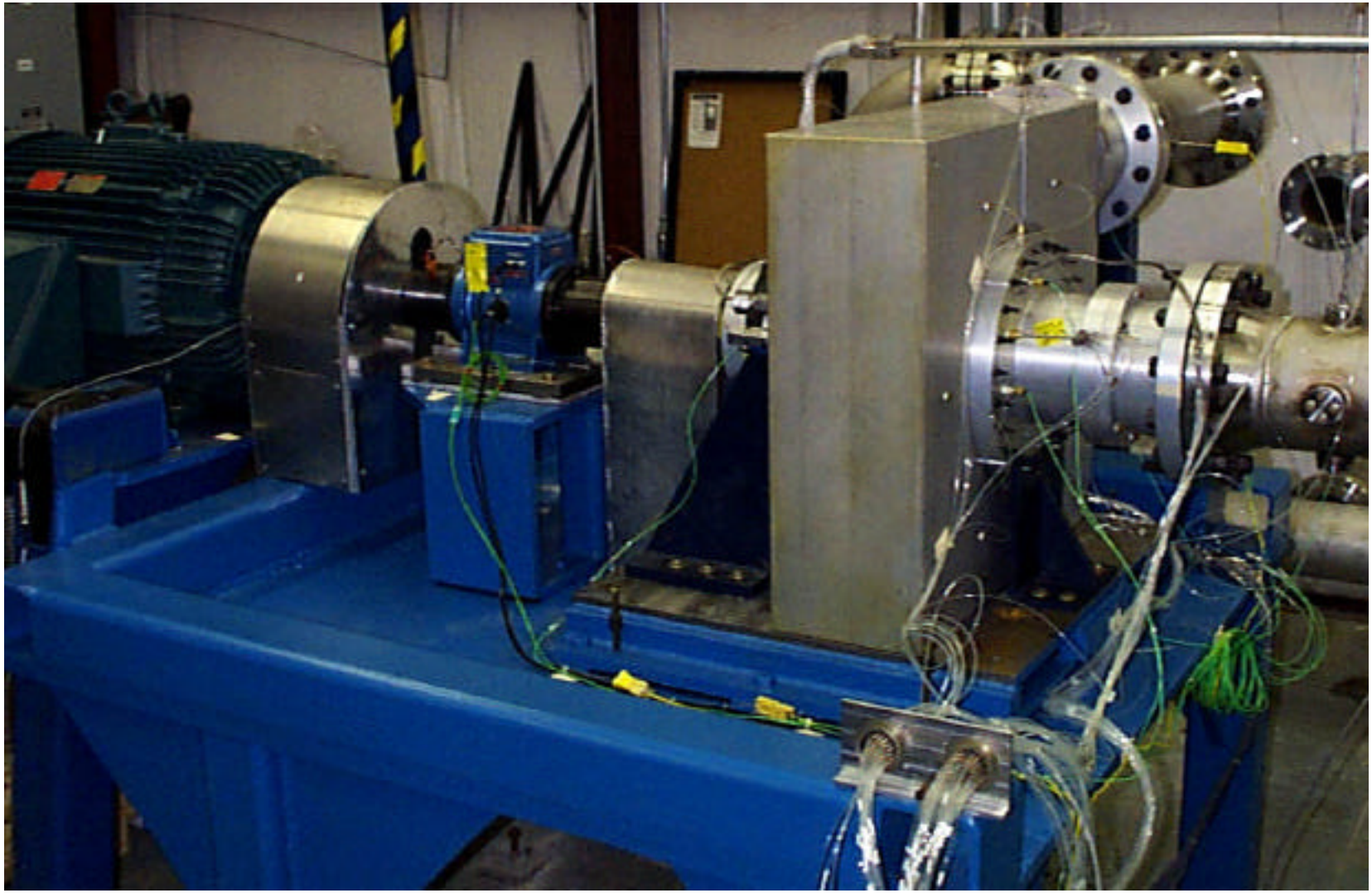

PTE Test Stand and Instrumentation Rack

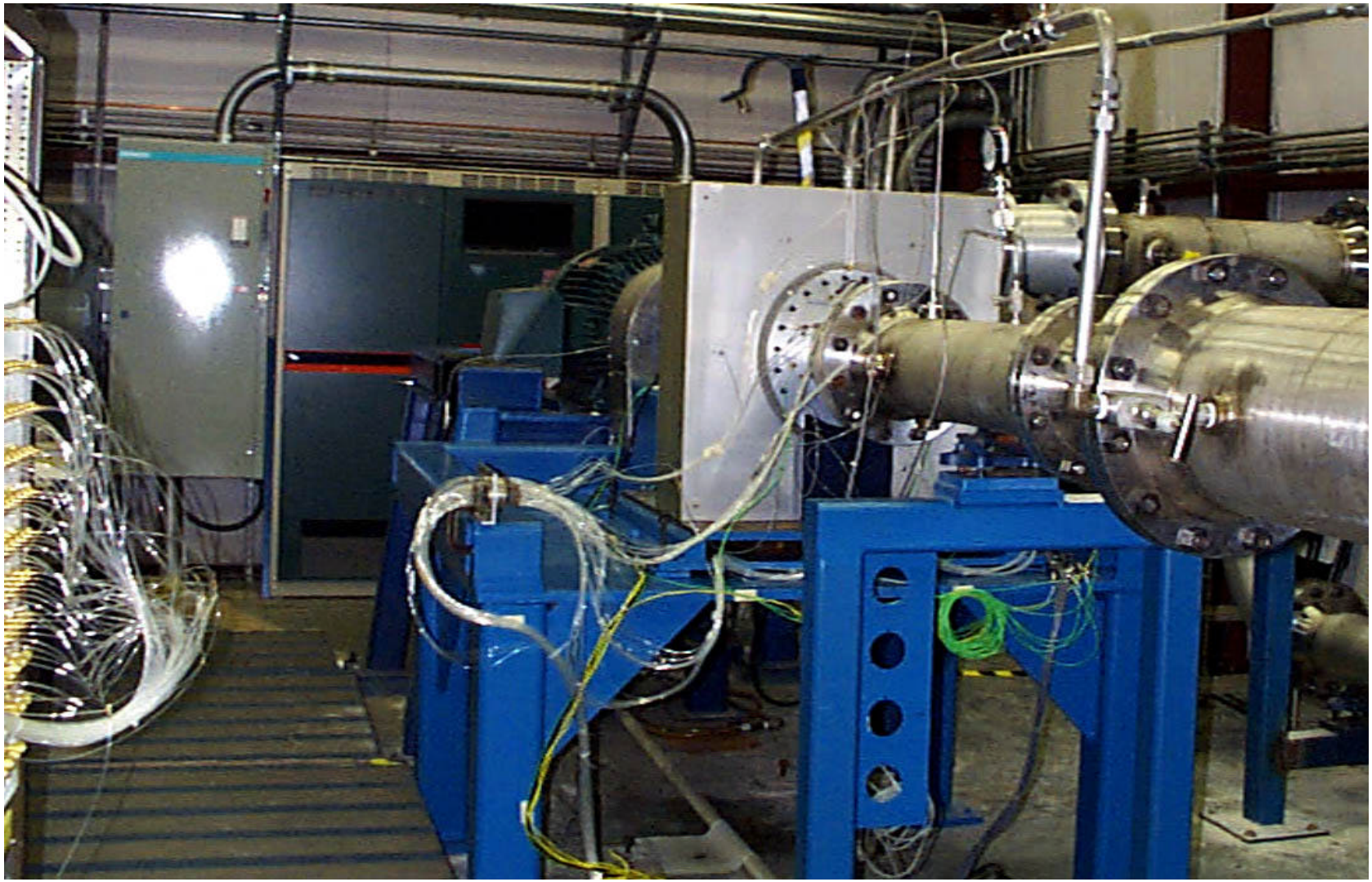

Instrumentation Rack

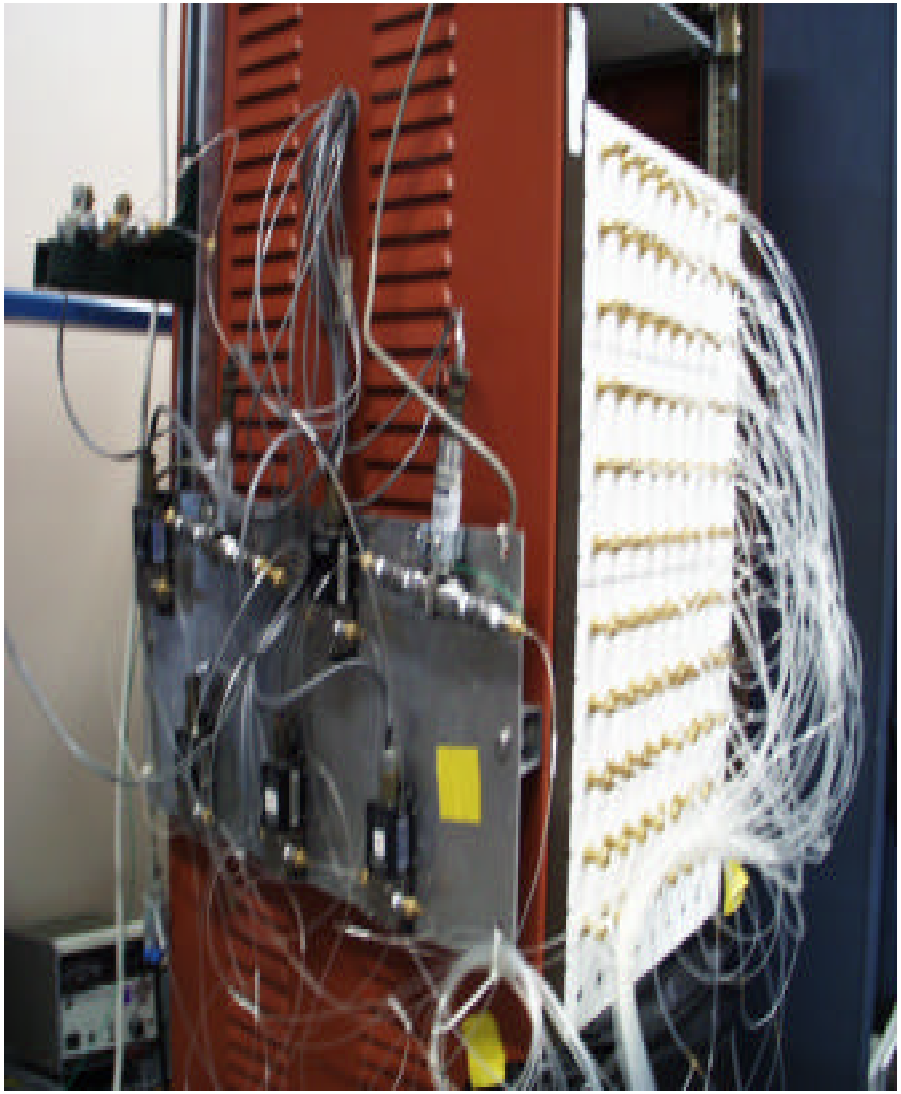

- Housing for pressure transducers, SCXI modules, and power supplies
- Transducers selected for application, accuracy, and range
  - Honeywell
  - Validyne
  - Druck
  - Sensotec

Real Time Data Display Reduction

- LabVIEW measurement and display system
  - Continuously update and display the set point parameters
  - health monitoring measurements
    - Temperature
    - Leakage flow
- LabVIEW data storage system
  - Pressures
  - Flow rates
  - Temperatures
  - Speed
  - Torque
- Detailed reduction and analysis
  - Completed later by test engineer using stored data
  - Reduction performed using excel spreadsheet

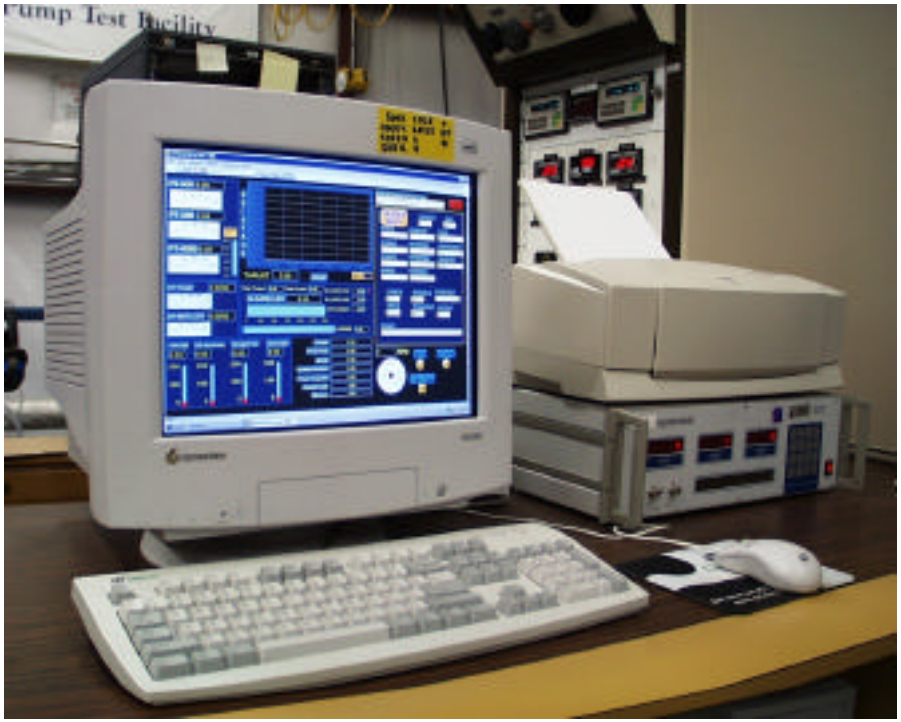

PTE Facility Operation Panel

- Control pump operation
  - Speed
  - Flow
  - Inlet pressure
- Maintain test set points
- Pump health monitoring
  - Bearing temperature

Test Article Description

- Modular Design of the Test Article Allows for Use With a Variety of Inlet, Impeller, and Diffuser Configurations
  - Inlet Adapter
  - Inlet Guide Vane Assembly
  - 6+6 Impeller
  - Front Shroud
  - Shims
  - Diffuser

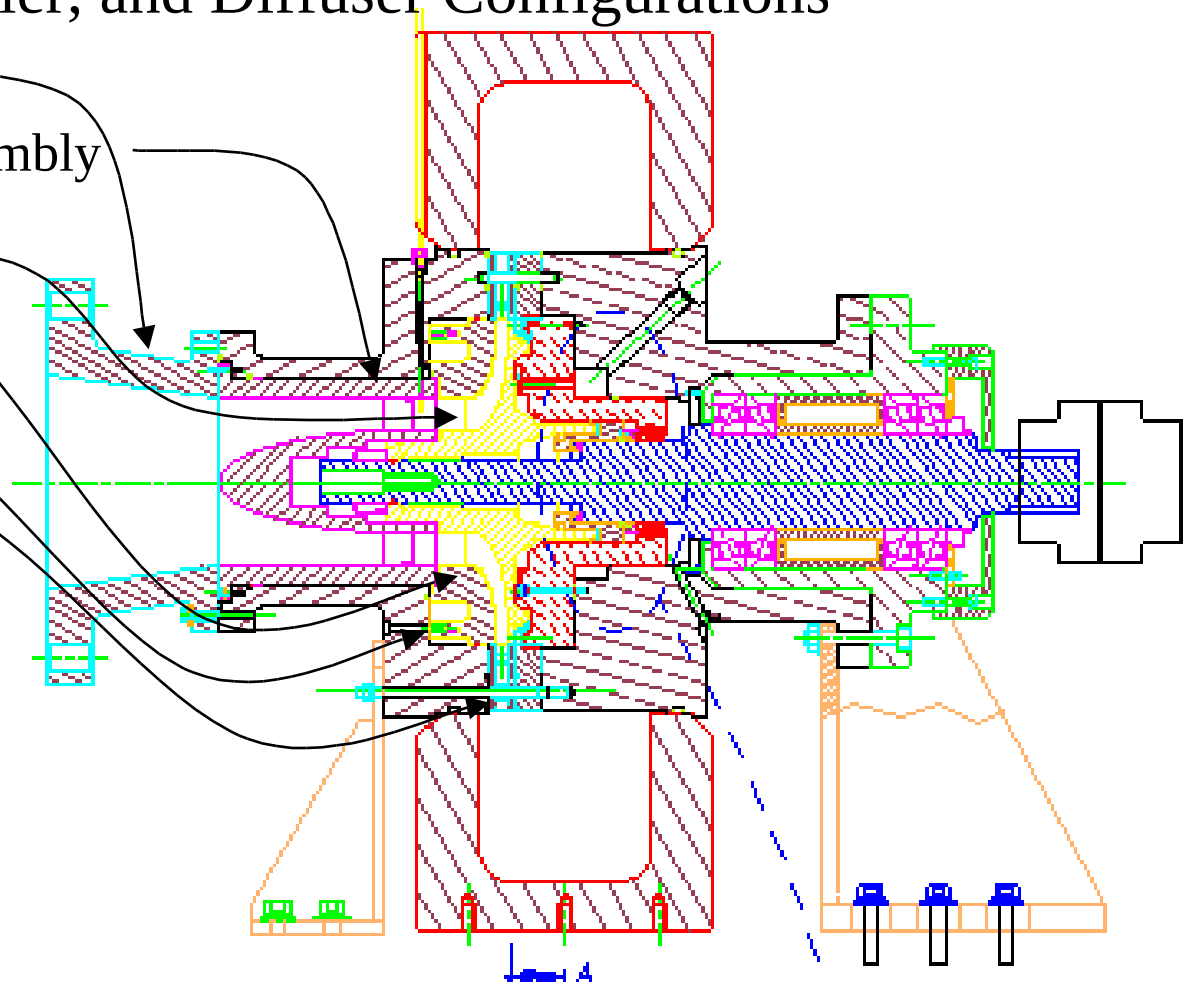

Unshrouded Impeller Test Article Cross Section

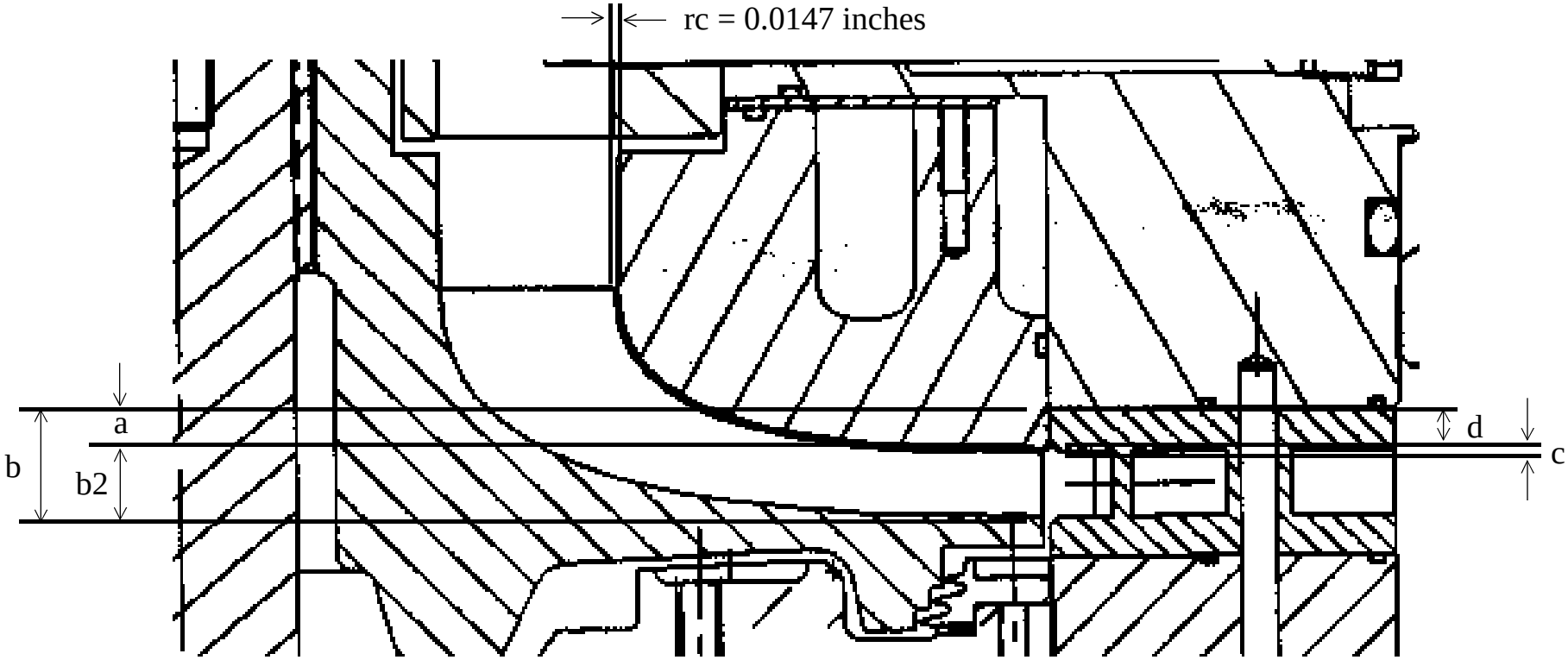

Clearance 1
a = 0.3123 inches
b = 0.7526 inches
b2 = b-a = 0.4393 inches
d = 0.2591 inches
c = a-d = 0.0532 inches
%b2 = c/b2 = 12.11%

Clearance 2
a = 0.3123 inches
b = 0.7526 inches
b2 = b-a = 0.4393 inches
d = 0.2358 inches
c = a-d = 0.0765 inches
%b2 = c/b2 = 17.41%

Clearance 3
a = 0.3123 inches
b = 0.7526 inches
b2 = b-a = 0.4393 inches
d = 0.3003 inches
c = a-d = 0.0120 inches
%b2 = c/b2 = 2.73%

Test Measurements

- Steady-state measurements
  - Surface static pressure taps are grouped into 27 measurement planes
    - Static pressure taps concentrated at: front shroud, diffuser, rear shroud, and discharge housing
  - Total pressure probes are located in the facility inlet and exit spools
  - Flow direction probes are located just downstream of the inlet guide vanes and impeller discharge
  - Facility flow rate and the leakage flows in 2 external metering lines
  - Shaft speed and shaft torque measured directly
  - Water and bearing temperatures measured
  - Dissolved oxygen measured
- Unsteady measurements
  - High frequency pressure transducers located in facility inlet and exit spools
  - Three high frequency pressure transducers located at impeller discharge
  - Single accelerometer mounted on bearing housing

Measurement Locations

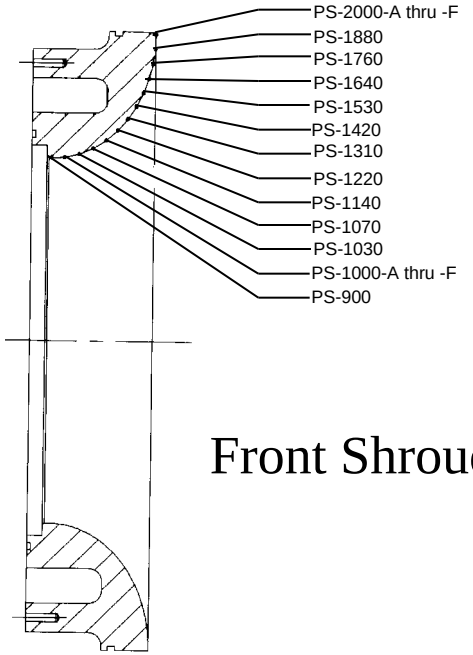

Front Shroud

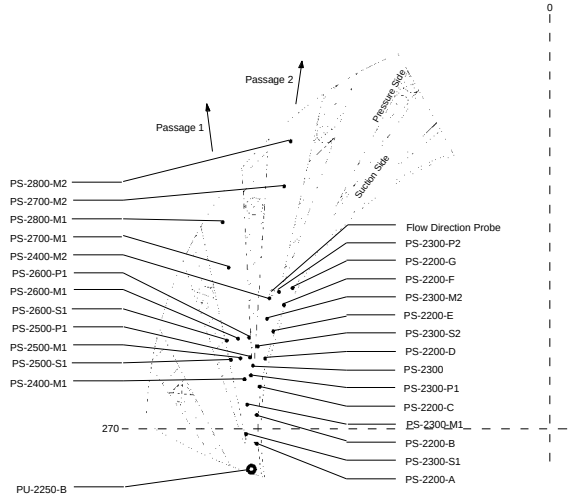

Diffuser

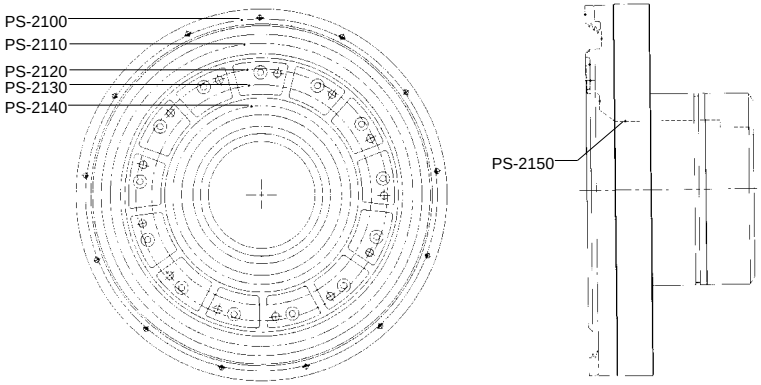

Rear Shroud

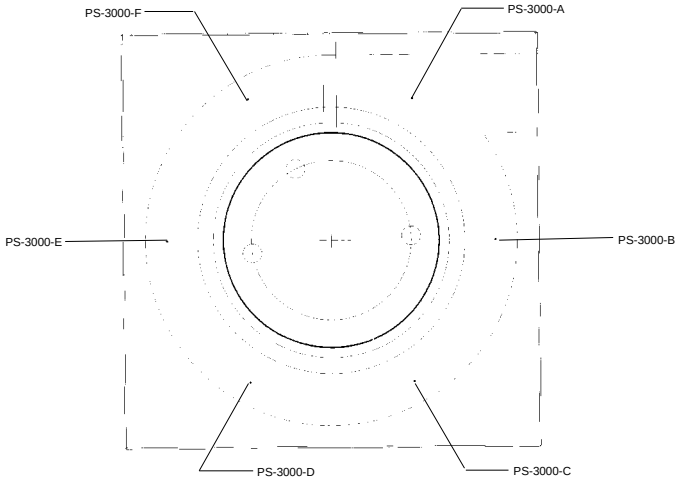

Discharge Collector

Test Matrix

- Performance evaluated over range of scaled operating conditions at constant shaft speed of 3000 RPM
  - Three test series were conducted to fully map pump performance at different clearances
  - Series included definition of the basic head-flow curve at constant suction specific speed
  - Suction performance mapping across a wide range of flow rates
  - Unsteady pressures and accelerations were recorded during inlet pressure and speed ramps at selected flow coefficients

Stage Head Coefficient

Noncavitating Stage Head Coefficient vs Normalized Impeller Flow/Speed Ratio

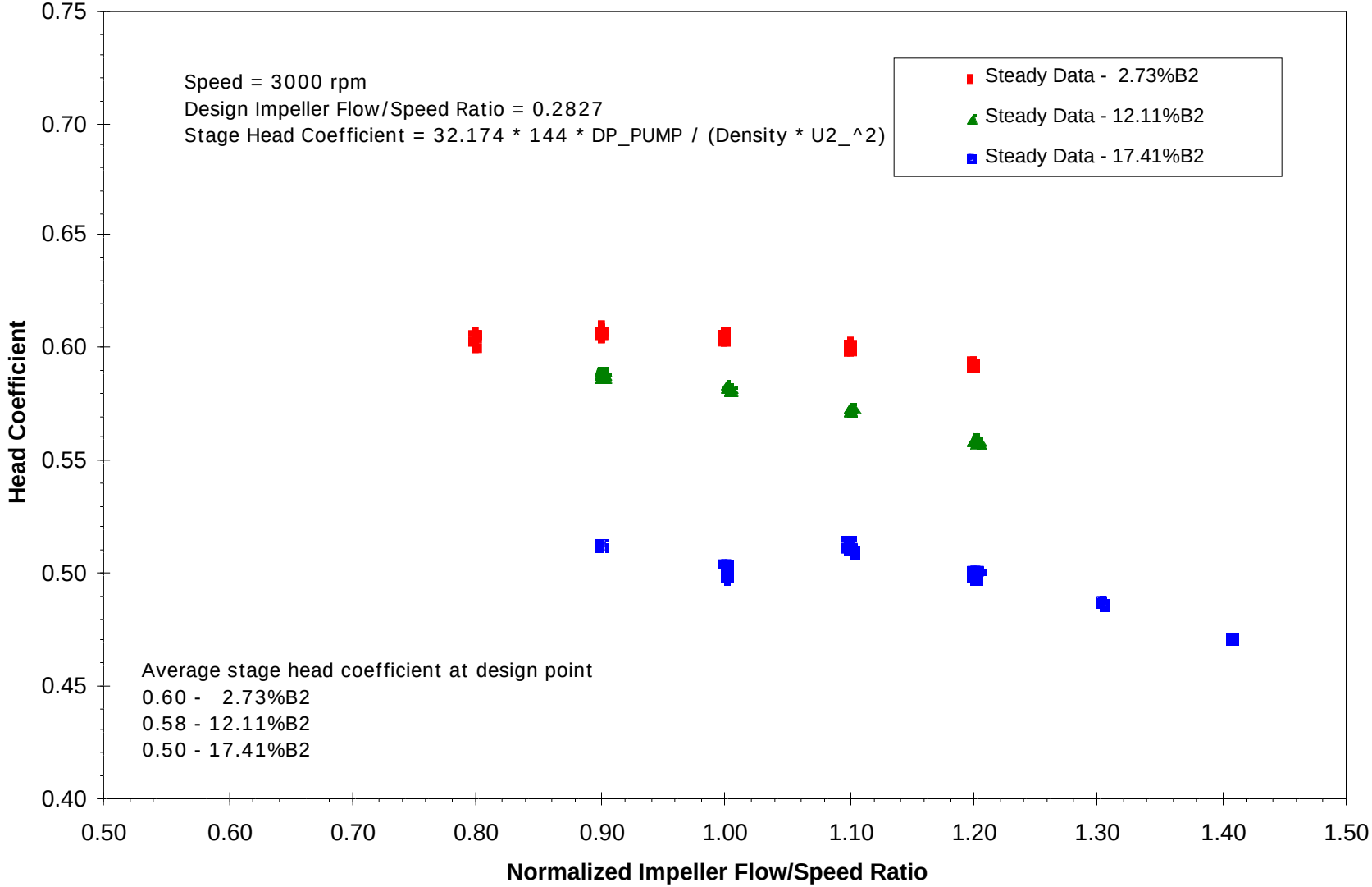

Impeller Head Coefficient

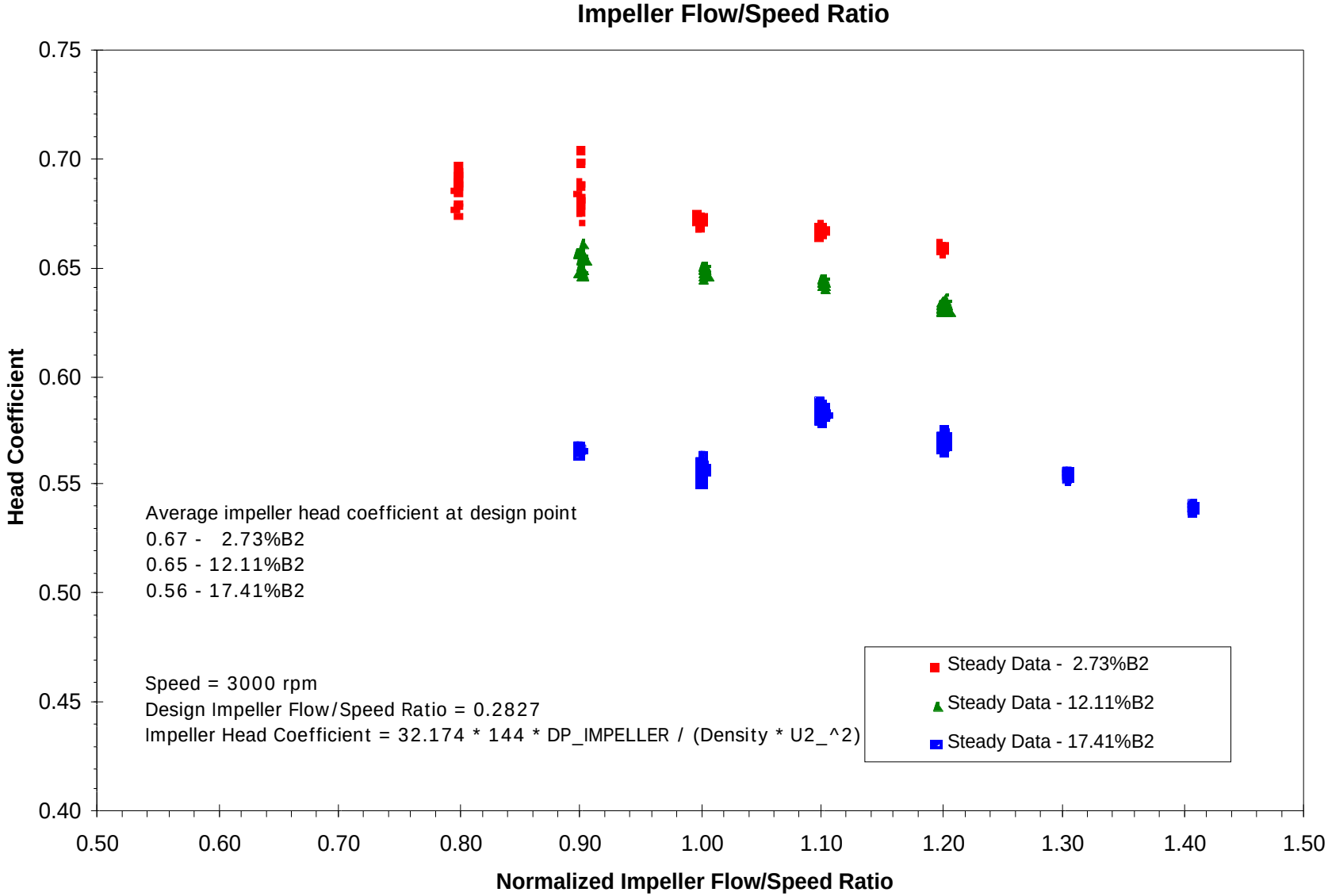

Stage Efficiency

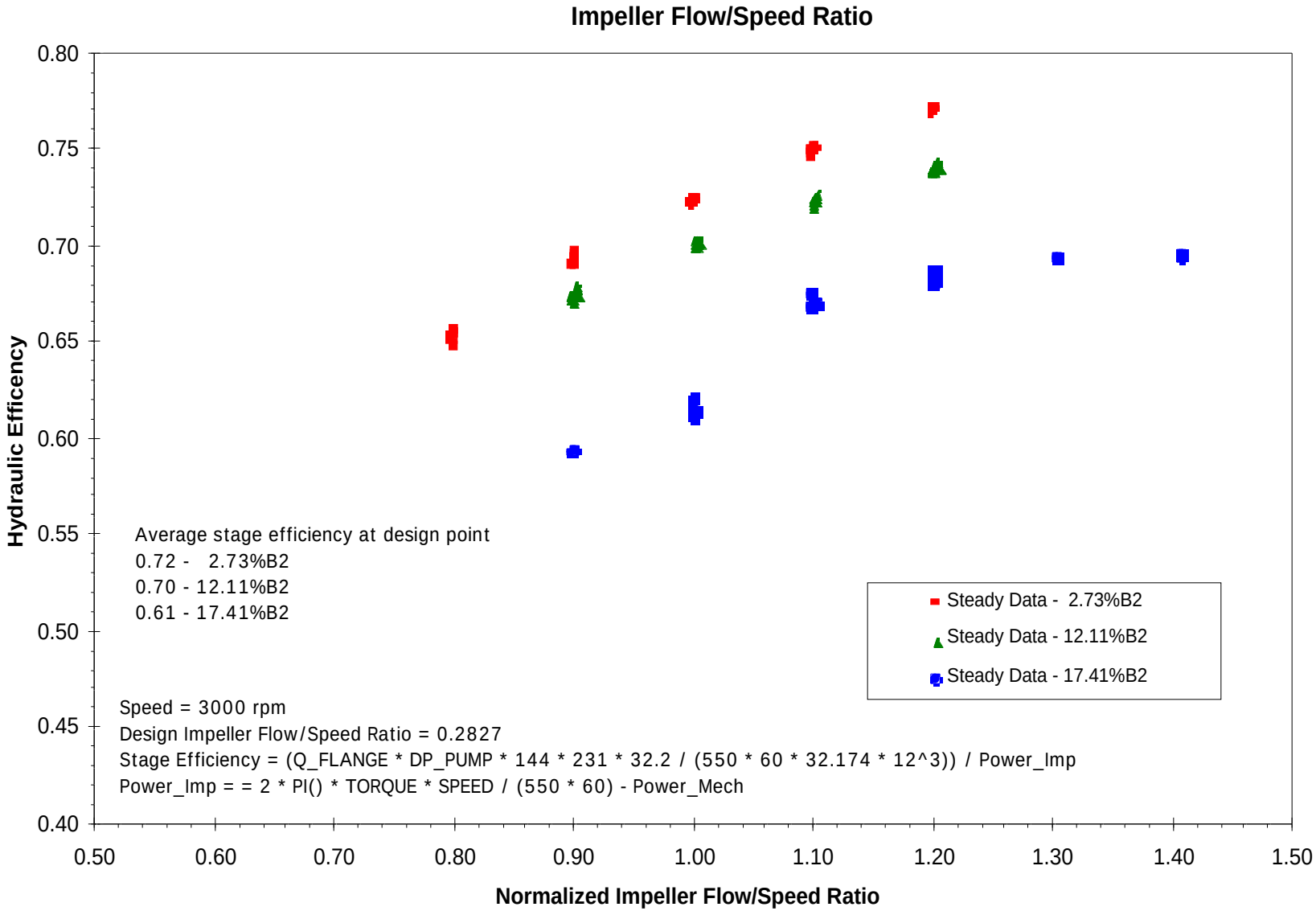

Impeller Efficiency

Noncavitating Impeller Efficiency vs Normalized Impeller Flow/Speed Ratio

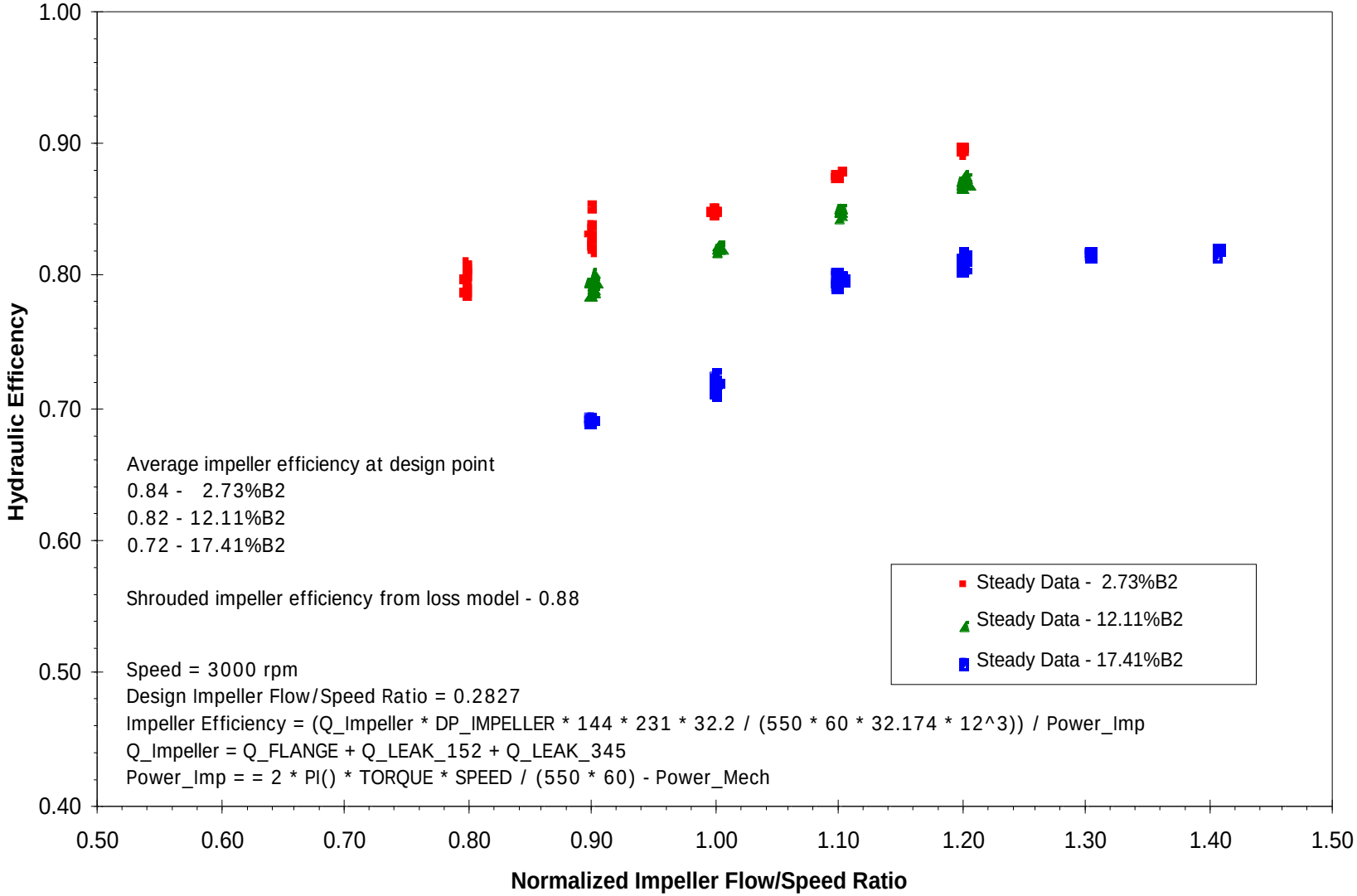

Unsteady Data Overview

- determine impeller / diffuser fluctuating pressure sensitivity to tip clearance
  - over Nss
  - across Q/N
  - correlate unsteady data to stage performance
- identify / map unsteady flow features which could inhibit the development of unshrouded pump technology
  - rotating diffuser / impeller stall
  - rotating cavitation
  - rotor / stator interaction loads (synchronous - impeller wake)

Unsteady Data Overview - baseline clearance

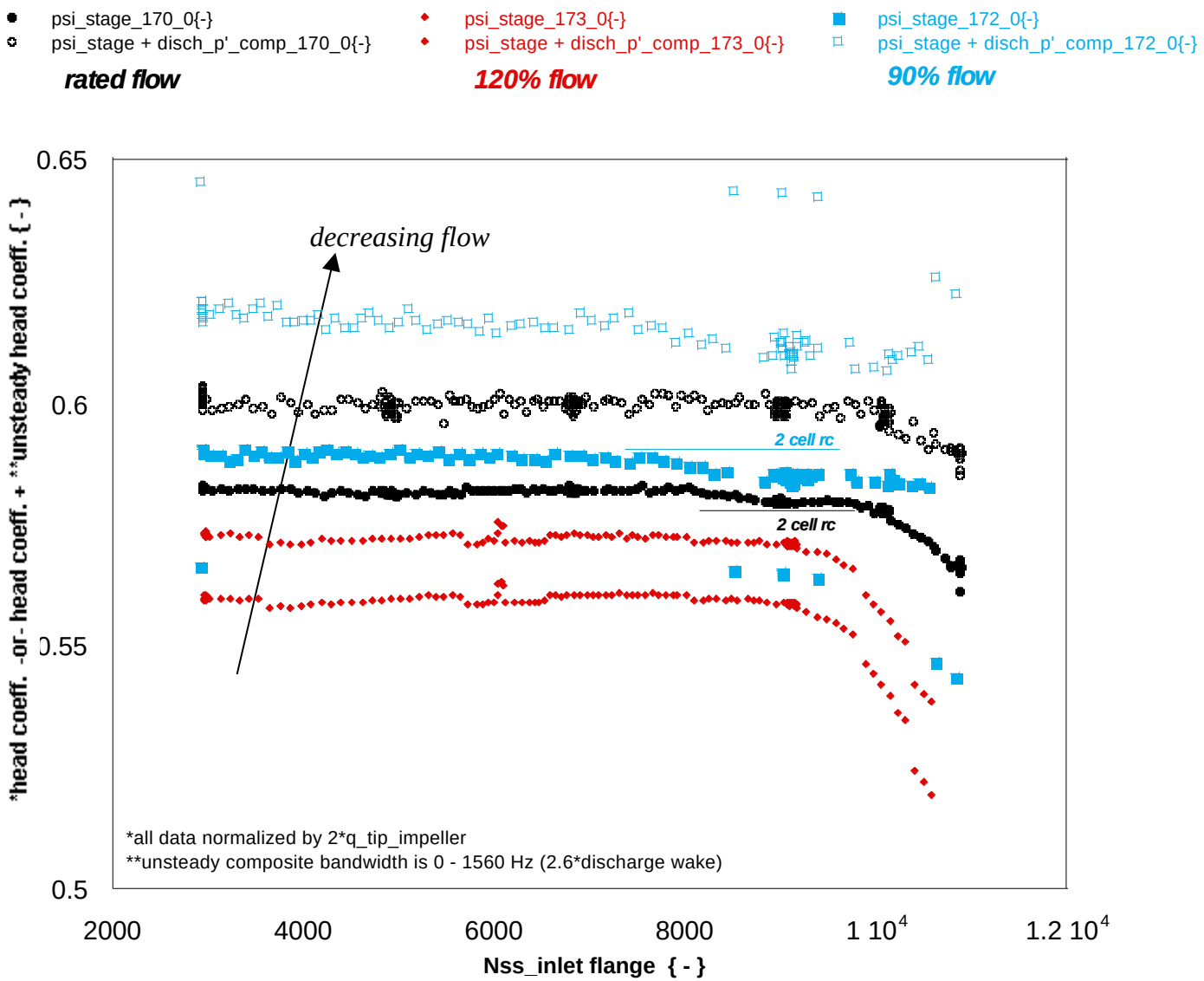

Unsteady Data Overview - across build (rated flow)

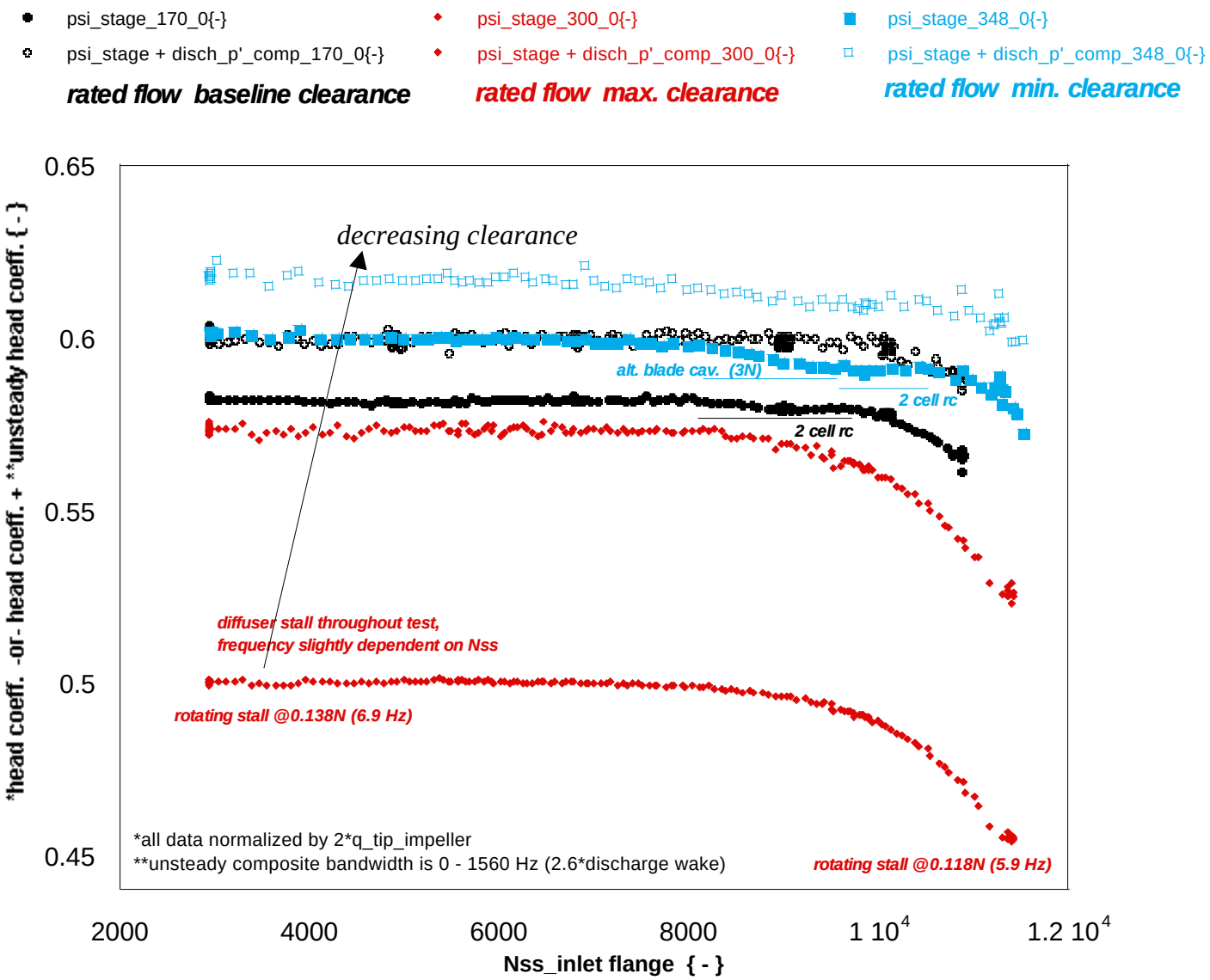

Unsteady Data Overview - cavitation induced oscillations

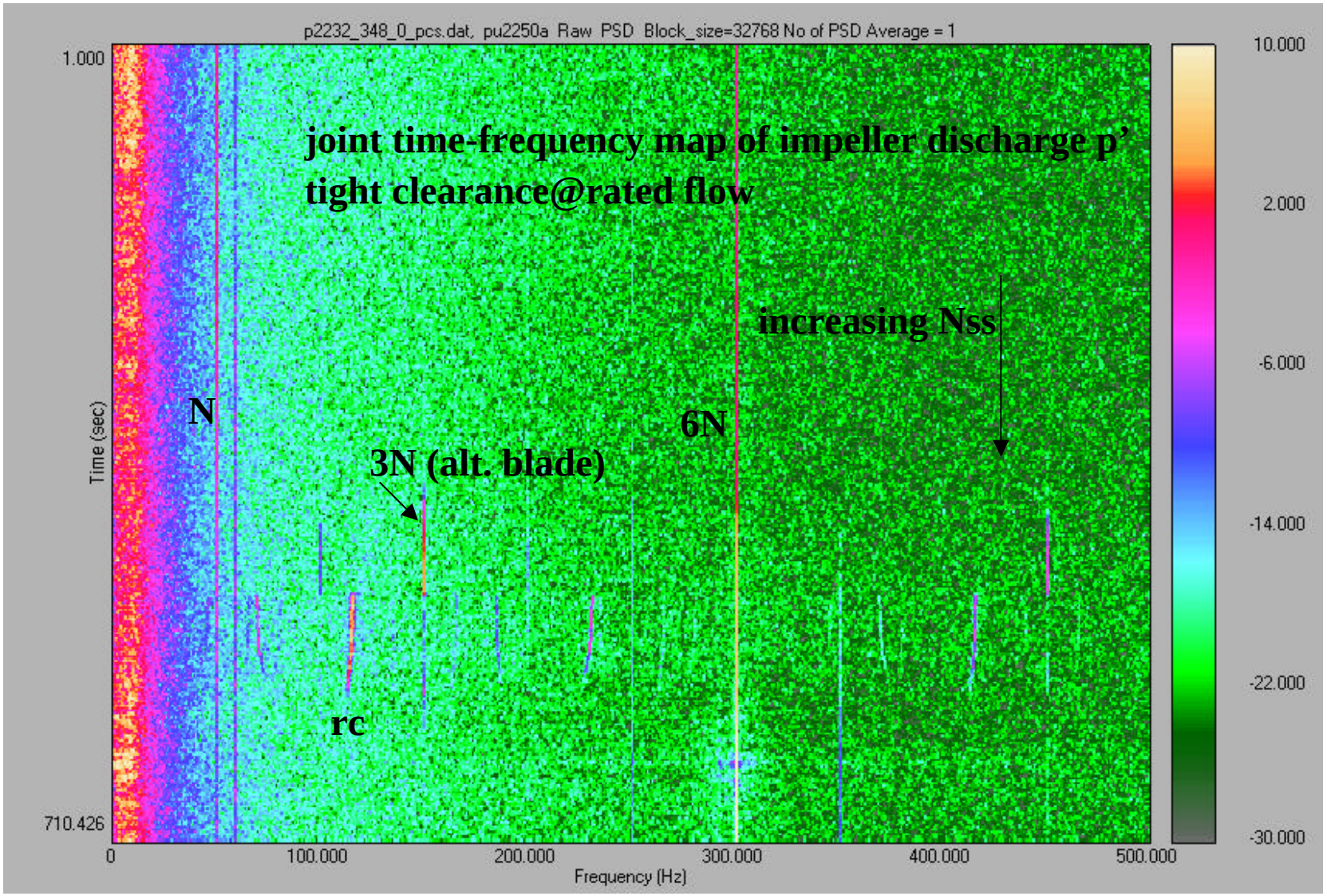

Unsteady Data Overview - flow excursion - baseline clearance

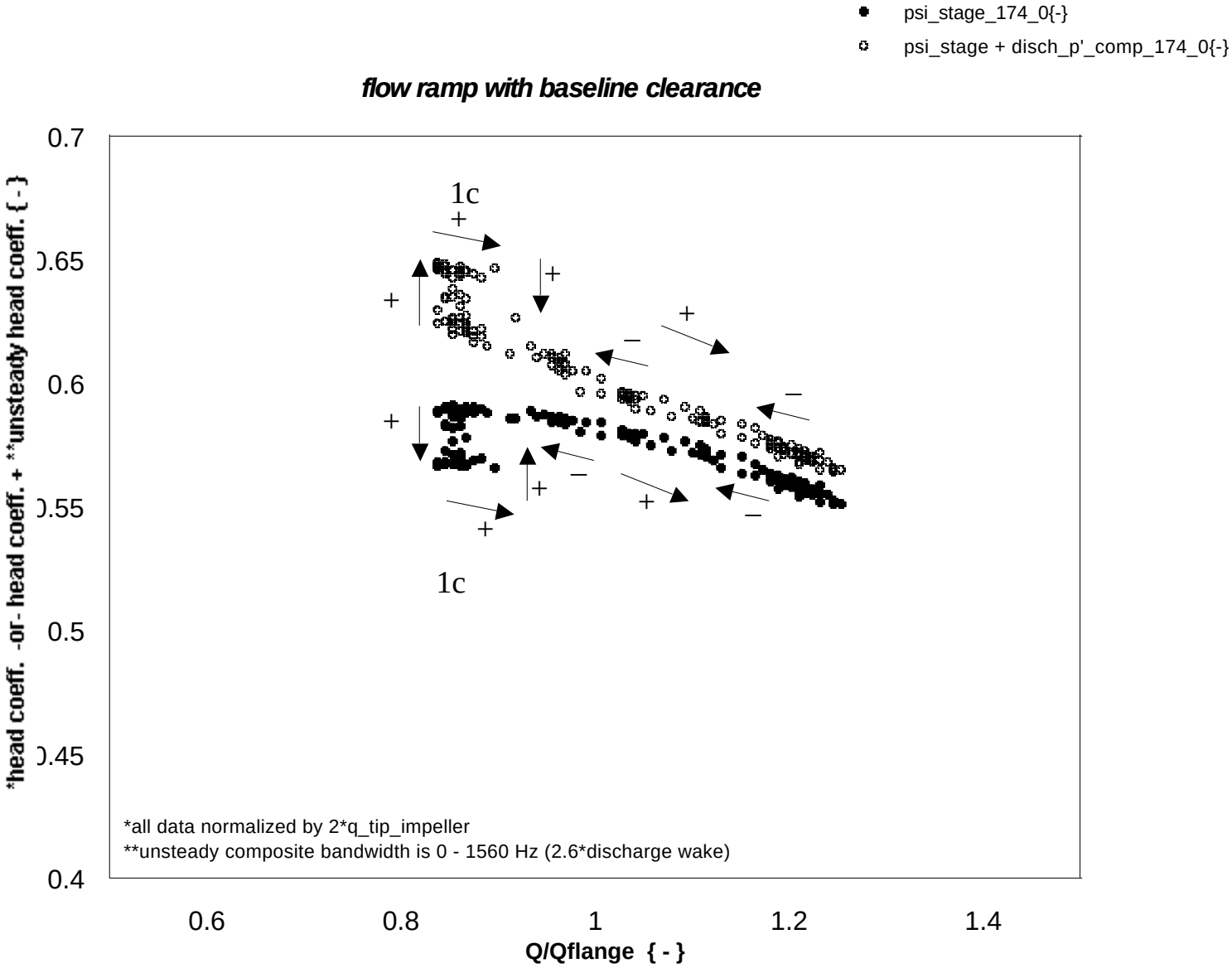

Unsteady Data Overview - flow excursion - opened clearance

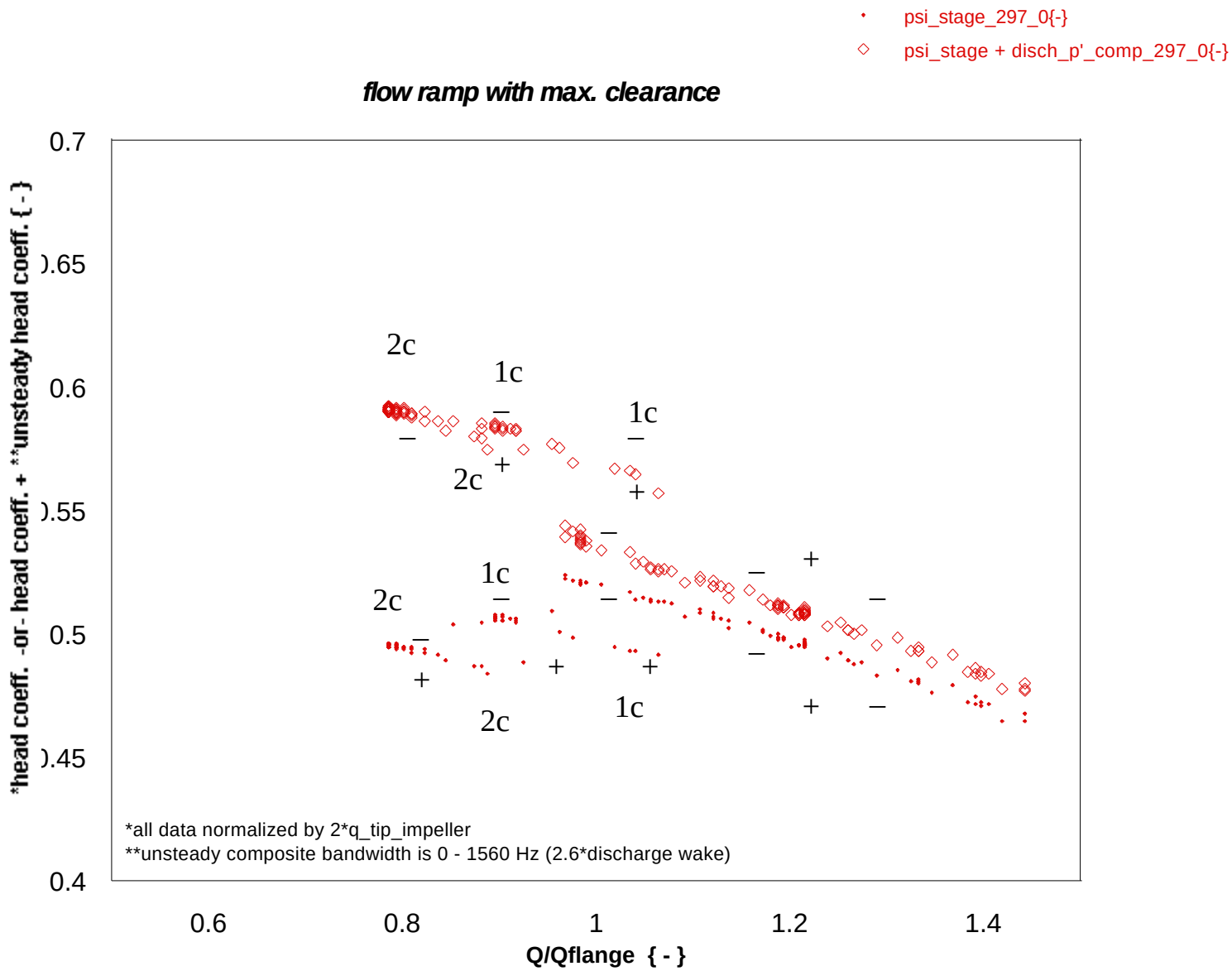

Unsteady Data Overview - rotating stall

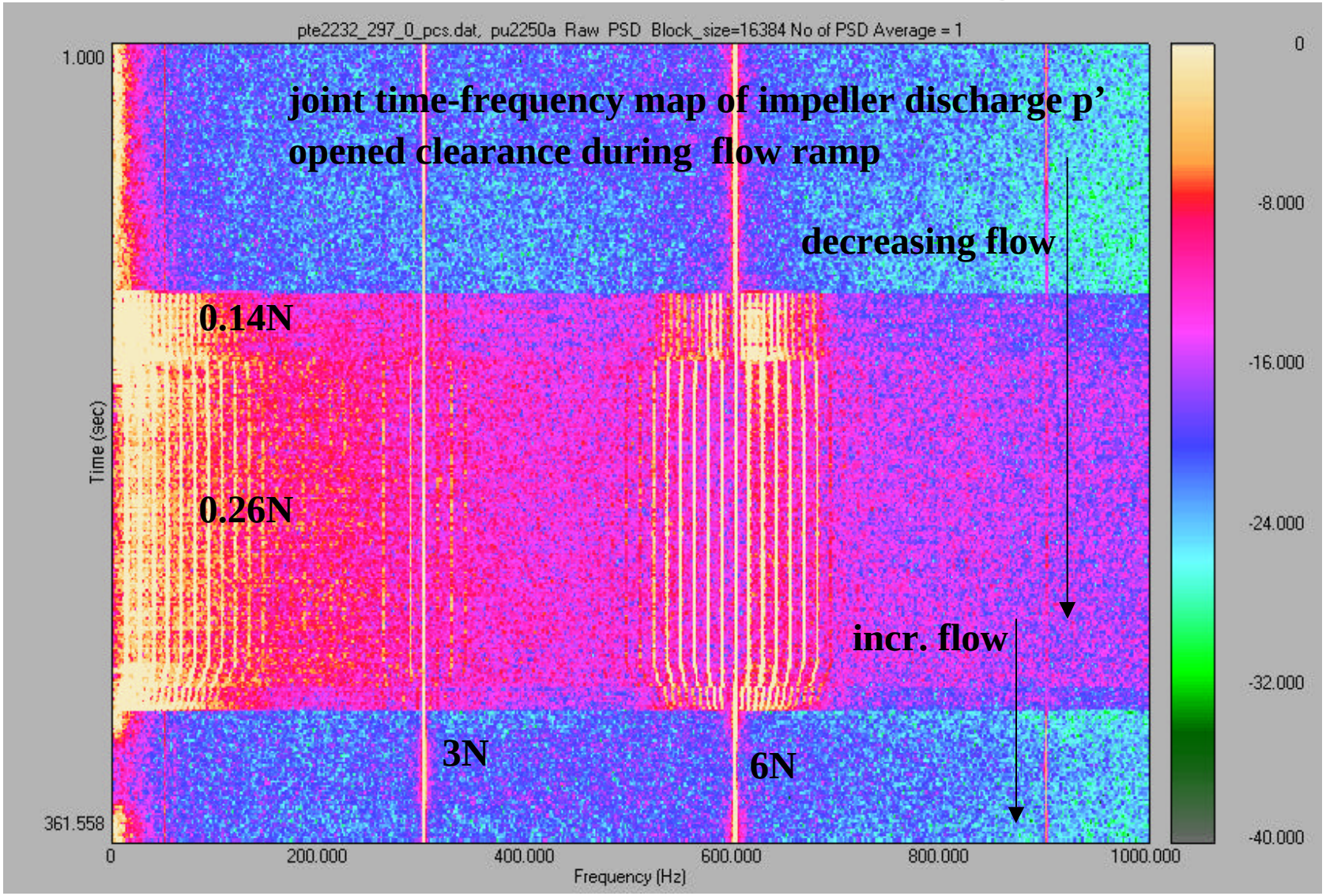

Unsteady Data Overview - flow excursion - tight clearance

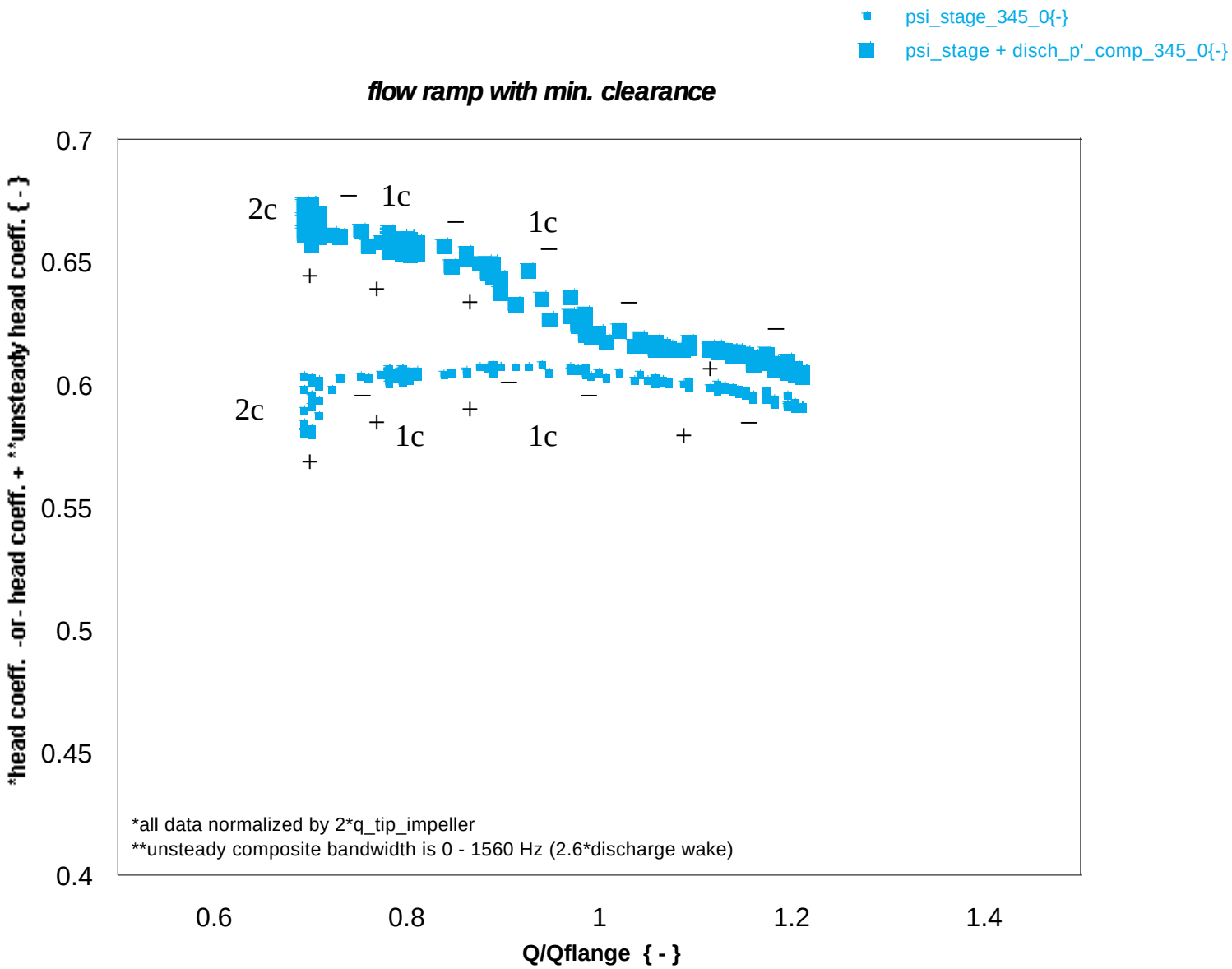

Unsteady Data Overview - rotor_stator interaction

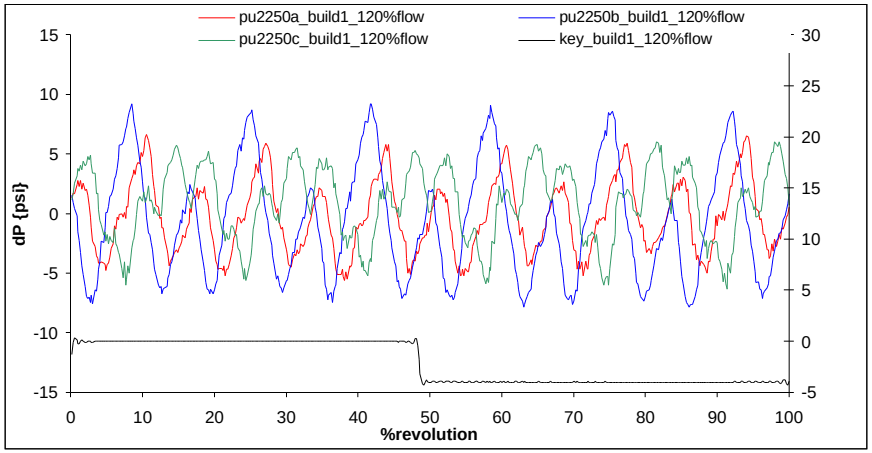

120% flow across locations

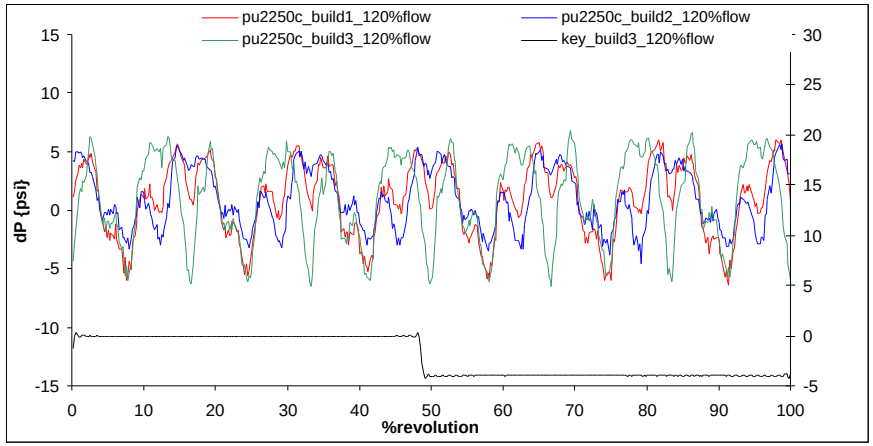

120% flow across builds_location C (vane l.e. suction)

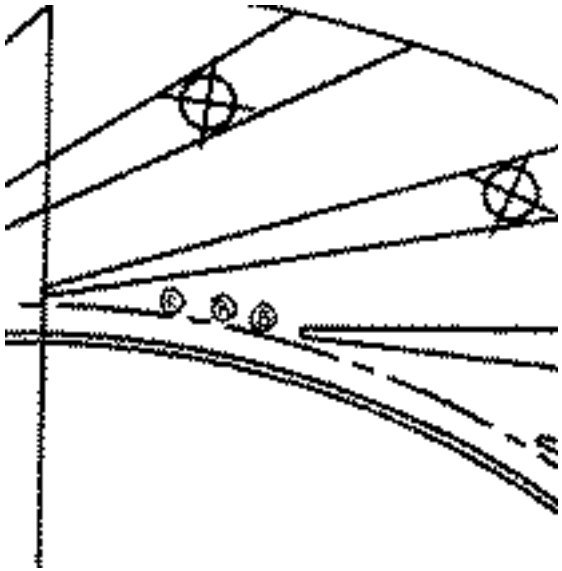

- map impeller wake across diffuser channel versus Q/N and axial clearance
- use synchronous time averaging process
- build data set for time-accurate CFD

Unsteady Data Overview - rotor_stator interaction

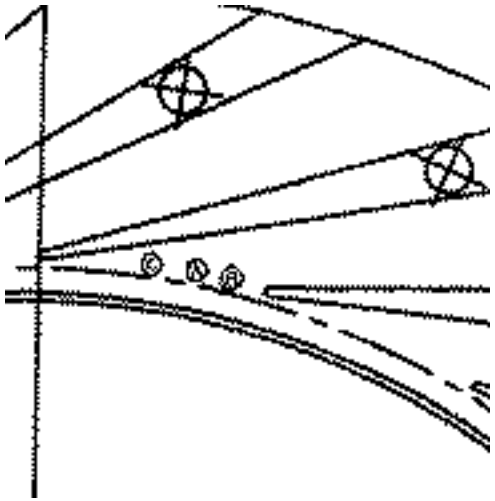

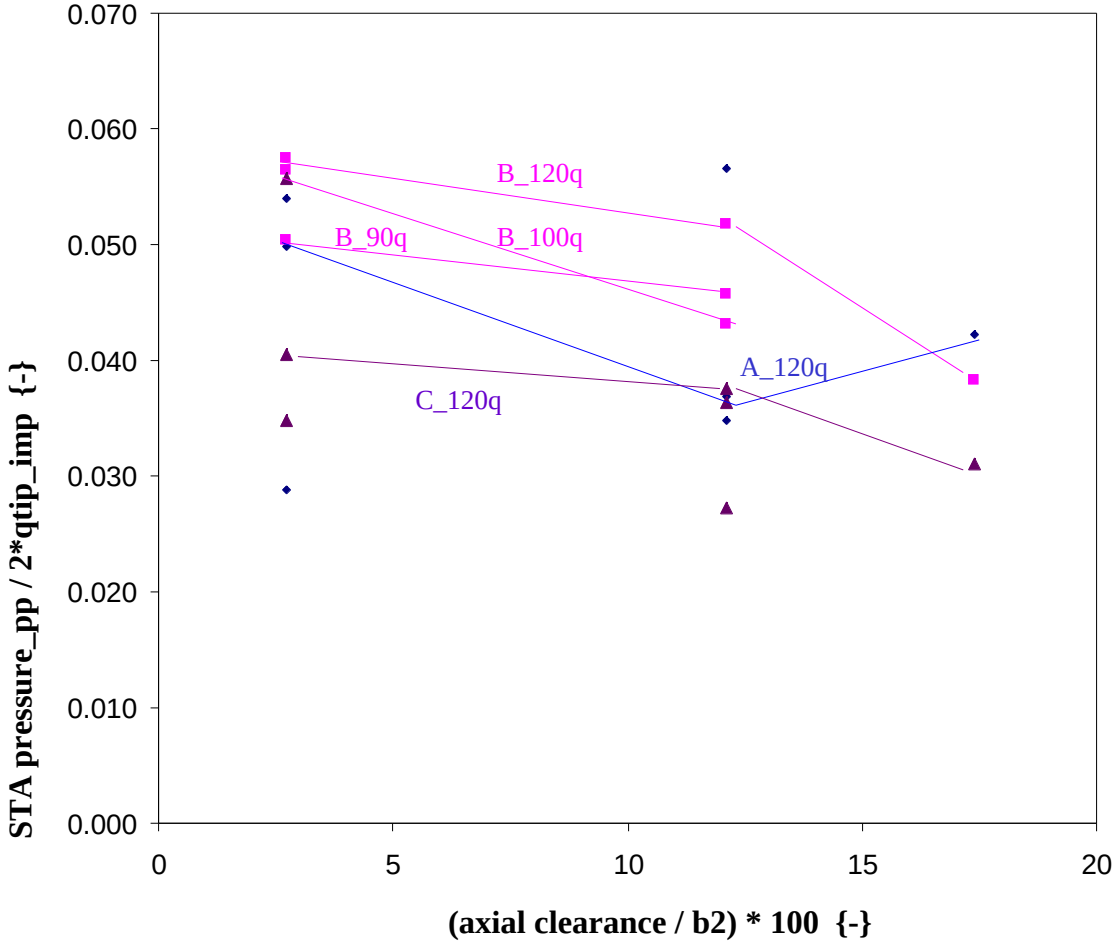

Unsteady Data Summary

- determine impeller / diffuser fluctuating pressure sensitivity to tip clearance
  - Nss not a major influence on overall composite unsteady pressure at impeller discharge
  - Q/N excursions identified both single and dual-cell rotating stall at impeller / diffuser interface
    - hysteresis (w/r to flow) and axial clearance dependence identified
  - unsteady data to stage performance correlation (head loss) most pronounced during rotating stall with some correlation during rotating cavitation (2-cell) and alternate blade (3N) cavitation
- identify / map unsteady flow features which could inhibit the development of unshrouded pump technology
  - rotating diffuser / impeller stall mapped
  - rotating and alternate-blade (attached) cavitation mapped
  - rotor / stator interaction loads characterized versus Q/N and axial clearance

THERMAL RESPONSE MODELING SYSTEM FOR A MARS SAMPLE RETURN VEHICLE

Y.-K. Chen and F.S. Milos
Thermal Protection Materials & Systems Branch
NASA Ames Research Center, MS 234-1
Moffett Field, CA 94035-1000

ABSTRACT

A multi-dimensional, coupled thermal response modeling system for analysis of hypersonic entry vehicles is presented. The system consists of a high fidelity Navier-Stokes equation solver (GIANTS), a two-dimensional implicit thermal response, pyrolysis and ablation program (TITAN), and a commercial finite-element thermal and mechanical analysis code (MARC). The simulations performed by this integrated system include hypersonic flowfield, fluid and solid interaction, ablation, shape change, pyrolysis gas generation and flow, and thermal response of heatshield and structure. The thermal response of the heatshield is simulated using TITAN, and that of the underlying structural is simulated using MARC. The ablating heatshield is treated as an outer boundary condition of the structure, and continuity conditions of temperature and heat flux are imposed at the interface between TITAN and MARC. Aerothermal environments with fluid and solid interaction are predicted by coupling TITAN and GIANTS through surface energy balance equations. With this integrated system, the aerothermal environments for an entry vehicle and the thermal response of the entire vehicle can be obtained simultaneously. Representative computations for a flat-faced arc-jet test model and a proposed Mars sample return capsule are presented and discussed.

INTRODUCTION

Spacecraft heatshields typically use thermal protection system (TPS) materials that pyrolyze and ablate at high temperature for mass-efficient rejection of the aerothermal heat load. Pyrolysis is an internal decomposition of the solid that releases gaseous species, whereas ablation is a combination of processes that consume heatshield surface material (including chemical reactions, melting, and vaporization). For design and sizing of ablating spacecraft TPS materials, it is important to have a reliable numerical procedure that can predict surface recession rate, in-depth pyrolysis, and internal temperature history. The thermal properties and the boundary conditions of the heatshield also must be precisely defined to perform an accurate prediction.

A simplified schematic diagram of the geometry is shown in Figure 1. The outer face of the heatshield is exposed to an aerothermal heating environment that can be predicted using a high fidelity computational fluid dynamics (CFD) code with surface-thermochemistry boundary conditions. The inner face of the heatshield is attached to a structure that contains various other components. The structure often should be included in the thermal response simulation to correctly predict the bond-line temperature history. The maximum allowable bond-line temperature is typically the key parameter that drives the TPS thickness. The structure and its interior can have a complicated geometry, but the thermal response is relatively simple compared with that of the TPS.

A number of programs have been written to simulate ablating heatshields. The CMA code,[1] developed by Aerotherm Corporation in the 1960's, was one of the first one-dimensional codes. CMA solved internal energy balance and decomposition equations coupled with general surface energy balance boundary (SEB) conditions to simulate the response of pyrolyzing and ablating heatshields in hypersonic flows. In 1997, the FIAT code was developed at NASA Ames Research Center to support the development of lightweight ceramic ablators. FIAT is numerically more stable and solves a wider range of problems than CMA, and it has been used for TPS sizing calculations in various NASA space missions.[2] However, the governing equations solved in both CMA and FIAT are one-dimensional. Thus, neither of these two codes is applicable for conditions in which a one-dimensional assumption is not true, such as the nose-tip of a slender hypersonic reentry vehicle or around the shoulder of a blunt vehicle.

For axisymmetric or planar geometries, Aerotherm also developed ASCC,[3] an engineering code for fully-coupled fluid/solid simulation of ablating heatshields. In ASCC the thermal diffusion equation is solved using a finite-difference scheme with overlaid grids. A two-dimensional ablation code developed at Sandia National Laboratories uses the finite-control-volume method with unstructured grids.[4] In this code, mesh motion (owing to ablation) is modeled by assuming the mesh behaves as a linear elastic solid. In both of these codes the effect of pyrolysis gas is not considered. Recently the TITAN program was developed to perform two-dimensional thermal response and shape change simulations for pyrolyzing ablators.[5] The governing equations, which include energy conservation and a three-component decomposition model with a moving grid, are discretized using a finite-volume approximation and general body-fitted coordinates. Time-accurate solutions are achieved by an implicit time marching technique using Gauss-Siedel line relaxation with alternating sweeps.[6] In many cases, a coupled fluid and solid simulation is required for

accurate prediction of shape change, because shape change can not be correctly determined without appropriate aerothermal heating, but aerothermal heating is very sensitive to the geometry of the solid. To this end, the Navier-Stokes solver, GIANTS,[7] was successfully coupled with TITAN using a loosely coupled method for simulating the fluid/solid interaction. TITAN uses an external zone with a moving grid and internal grid that is fixed. This two-zone approach can handle some simple geometries but is not sufficiently flexible to model a complicated interior structure.

To address this deficiency, the purpose of the present work is to integrate GIANTS and TITAN with the MARC finite-element code.[8] The three codes are integrated through the use of MARC's user-supplied boundary condition subroutines. TITAN is used for the heatshield analysis because the physics of pyrolysis and ablation is too complicated for available commercial finite-element codes to accurately simulate. The structural materials beneath the heatshield experience relatively benign heat loads, and are usually multi-dimensional with complicated geometry. A commercial finite-element code, such as MARC, can perform thermal and structural analyses of the interior of a space vehicle. This integrated system can predict, simultaneously, two-dimensional aerothermal heating, ablation, shape change, and thermal response of heatshield and structure. The integrated simulation program should significantly reduce the computational and human effort required to design and analyze a spacecraft heatshield and attached structure. To demonstrate the capability of this modeling system, representative computations for an arc-jet model and a proposed Mars sample return capsule are presented and discussed.

INTEGRATED MODELING SYSTEM

Figure 2 presents the flow chart for integrated thermal response modeling system. The MARC, TITAN, and GIANTS codes are the three major components in the system. A brief description of each code is listed in the following subsections. The accuracy of each code has been studied previously.[5,7,9] This modeling system is integrated around the MARC code. The front end of MARC, known as Mentat,[10] is a graphical user interface program. The material properties are provided by TPSX,[11] a material properties database developed at NASA Ames Research Center.

MARC and TITAN are interfaced through MARC's heat-flux boundary condition routine. The continuity conditions of heat flux and temperature are imposed at the interface:

$$q_{MARC}^{l+1} = -k\nabla T\,|_{TITAN}^{l} \tag{1}$$

$$T_{TITAN}^{l+1} = T_{MARC}^{l} \tag{2}$$

At each time increment (from l to $l+1$) the front-face heat flux boundary condition of MARC is updated using the temperature gradient calculated by TITAN using Eq. (1), and the back-face temperature boundary condition of TITAN is equal to the temperature computed by MARC using Eq. (2) at each interface point.

TITAN and the flow environment code GIANTS are interfaced using MARC's surface energy balance boundary condition. The conditions at the ablating surface are determined by convective and radiative heating and by surface thermochemical interactions with the boundary layer gases. The SEB equation employed is of the convective transfer coefficient type and takes the form:[12]

$$\rho_e u_e C_h\left[H_r - (1+B')h_w\right] + \dot{m}_c h_c + \dot{m}_{gw} h_{gw} + \alpha_w q_{Rw} - F\sigma\varepsilon_w T_w^4 - q_{Cw} = 0 \tag{3}$$

The sum of the first three terms in Eq. (3) is the convective heat flux plus the heat of ablation. The fourth and fifth terms are the radiative heat fluxes absorbed and reradiated by the wall, respectively, and the last term represents the rate of conduction into material. Here B' is a nondimensionalized mass blowing rate. Tables of B' for charring materials can be generated using ACE[13] or MAT.[14]

A blowing correction accounts for the reduction in transfer coefficients due to the transpiration or blowing effect of gases from pyrolysis and surface ablation being injected into the boundary layer. The blowing correction equation for convective heat transfer is:

$$\frac{C_h}{C_{h1}} = \frac{\ln(1+2\lambda B')}{2\lambda B'} \tag{4}$$

where λ is blowing reduction parameter and C_h/C_{h1} is the ratio of blown (ablating) to unblown (nonablating) heat transfer coefficients. With $\lambda = 0.5$, Eq.(4) reduces to the classical laminar-flow blowing correction.[15] A variable λ is used for cases with transitional or turbulent flow.

The computation starts with the MARC code. At each time increment, MARC calls TITAN to compute a new heat flux boundary condition. At the same time TITAN obtains its back-face temperature boundary condition from MARC and, if necessary, calls the flow environment code to update the front-face SEB boundary condition. When the maximum local surface recession exceeds a predefined criterion since the last surface convective heating was calculated,

a new flow-field grid is generated based on the current body geometry, and the flow simulation routine is called to compute the aerothermal heating environment. Each call to the flow environment routine is a steady-state calculation. The non-ablating surface heating is calculated by the flow code, and the blowing reduction parameter is used in TITAN to take into account the laminar flow blockage due to surface blowing. As expected, the GIANTS calculation is much more computationally intensive than the thermal response computation. For a coupled GIANTS/TITAN/MARC simulation, most of the CPU time is consumed by flow environment calculations. Thus, the CPU time required for a simulation is primarily determined by the efficiency of the GIANTS code.

MARC

Structural material thermal response and thermal stress analysis are performed using the commercial finite-element code, MARC. The heat transfer and mechanical analyses can be coupled or performed separately. The internal energy conservation law is

$$\rho c_p \frac{\partial T}{\partial t} - \nabla \cdot (k \nabla T) = Q . \tag{5}$$

The boundary conditions include prescribed temperature, heat flux, and convective heat transfer coefficient to the environment. For transient analysis, the initial temperature is specified to start the calculation. To perform thermal stress analysis, MARC uses an instantaneous thermal expansion coefficient defined as

$$d\varepsilon_{kl}^{th} = \alpha_{kl}\, dT \ . \tag{6}$$

In most cases, however, thermal expansion data are given with respect to a reference temperature T_0, as

$$\varepsilon^{th} = \overline{\alpha}(T - T_0) . \tag{7}$$

Hence, the conversion of the expansion data to the instantaneous thermal expansion coefficient becomes

$$\alpha = \overline{\alpha} + \frac{d\overline{\alpha}}{dT}(T - T_0) . \tag{8}$$

TITAN

Ablating heatshield thermal response and shape change computations are performed using TITAN. The governing equations include energy conservation and three-component decomposition model. The SEB condition, Eq. (3), is solved with a moving grid to calculate the shape change due to surface recession. The internal energy balance is a transient thermal conduction equation with additional pyrolysis terms:[5]

$$\rho c_p \frac{\partial T}{\partial t} = \nabla \cdot (k \nabla T) - (h_g - \overline{h}) \nabla \cdot \dot{m}_g + \dot{m}_g \cdot \nabla h_g + \dot{s} \rho c_p \nabla T \tag{9}$$

The individual terms in Eq. (9) may be interpreted as follows: rate of storage of sensible energy, net rate of thermal conductive heat flux, pyrolysis energy-consumption rate, net rate of energy convected by pyrolysis, and convection rate of sensible energy due to coordinate system movement.

A three-component decomposition model is used. The resin filler is presumed to consist of two components which decompose separately, while the reinforcing material is the third component which can decompose. The instantaneous density of the composite is given by:

$$\rho = \Gamma(\rho_A + \rho_B) + (1 - \Gamma)\rho_C \tag{10}$$

where A and B represent components of the resin, and C represents the reinforcing material. Γ is the volume fraction of resin and is an input quantity. Each of the three components can decompose following the relation:

$$\frac{\partial \rho_i}{\partial t} = -B_{ai} \exp\left(\frac{-E_{ai}}{RT}\right) \rho_{vi} \left(\frac{\rho_i - \rho_{ri}}{\rho_{vi}}\right)^{\Psi_i} + \dot{s} \nabla \rho_i , \qquad i = A, B, C \tag{11}$$

where ρ_{vi} and ρ_{ri} and are the original and the residual (or terminal) density, respectively, of component *i*. The motion of pyrolysis gas is assumed to be one-dimensional along the surface-normal (η) direction, and thus the pyrolysis gas mass flux is calculated using the following approximation:

$$\dot{m}_g A = -\int_{\eta_0}^{\eta} \left(\frac{\partial \rho}{\partial t}\right) A \, d\eta \tag{12}$$

The governing equations are discretized using a finite-volume approximation with a general body fitted coordinate system. A time accurate solution is achieved by the implicit time marching technique using Gauss-Siedel line relaxation with alternating sweeps. The computational grid is compressed during the course of computation to account for surface recession.

GIANTS

The flow simulation over a large angle blunt body is performed using a Navier-Stokes solver. The GIANTS code solves the time-dependent conservation equations of mass, momentum, and energy for chemical and thermal non-equilibrium flow-field. The species mass conservation equation is given by[6]

$$\frac{\partial \rho_j}{\partial t} + \frac{\partial}{\partial x_k}(\rho_j u_k) = -\frac{\partial}{\partial x_k}(\rho_j v_{jk}) + w_j \ , \tag{13}$$

the momentum conservation is written as

$$\frac{\partial}{\partial t}(\rho u_l) + \frac{\partial}{\partial x_k}(\rho u_l u_k) = -\frac{\partial \tau_{lk}}{\partial x_k} \ , \tag{14}$$

and the energy conservation as

$$\frac{\partial E}{\partial t} + \frac{\partial}{\partial x_k}((E+p))u_k) = -\frac{\partial q_k}{\partial x_k} - \frac{\partial}{\partial x_k}(u_l \tau_{lk}) - \sum_j \frac{\partial}{\partial x_k} v_{jk} h_j \ . \tag{15}$$

The governing equations are discretized using a finite-volume method. The numerical method used to solve these discretized equations is exactly the same as that used in the TITAN code. This fully implicit, Gauss-Seidel line relaxation technique has been shown to yield steady-state results efficiently. A bifurcation diffusion model[16] was also implemented in this version of GIANTS to correctly compute multi-species mass diffusion.

ARC JET TEST MODEL

The first test case is a simulation of the flat-faced cylindrical arc-jet test model shown in Figure 3. The TPS material is phenolic-impregnated carbon ablator[17] (PICA) with a body radius of 3.81 cm and corner radius of 0.381 cm. The PICA is bonded to a piece of aluminum honeycomb structure, and this assembly is inserted into a copper model holder. The copper is protected from high temperature by a ring of TPS tile material (AETB) and disk of TPS blanket material (FRSI). The length of arc-jet heat pulse is 35 s. The TPS is sized to keep the structure below a specified temperature for several minutes.

The PICA material is divided into 2 computational zones. Zone I is the region right next to structural materials, where temperature should remain sufficiently low so that resin decomposition can be ignored. Zone II is the region directly exposed to hot arc-jet stream, where surface recession and pyrolysis gas effects must be considered in the simulation. PICA zone II is finite-volume meshed for TITAN; the rest of the model is finite-element meshed for MARC. Because a large subsonic region forms in front of the flat-faced cylinder, the flowfield is simulated using the Navier-Stokes solver GIANTS. The flow simulation is limited to the region in front of the PICA for simplicity. The exterior surfaces of the AETB and copper are assumed to be adiabatic.

Predicted heat flux distributions (from GIANTS) along the PICA surface at various times are presented in Figure 4, and the recession history (from TITAN) is shown in Figure 5. The predicted Mach contours at the beginning and the end of the heat pulse are depicted in Figure 6. Initially the heat flux is very high on the relatively sharp corner and significantly lower at the centerline. Therefore the ablation rate is highest near the corner, and the corner gradually rounds off. As the corner rounds, the bow shock moves closer to the surface, and consequently the heat flux around the stagnation region increases.

Fluid and solid temperature contours at 35 s are shown in Figure 7 (for clarity, different temperature scales are used for the fluid and solid). The maximum shock and solid temperature reaches about 6800 K and 2900 K, respectively. At 200 s there is no flowfield because the arc jet is turned off, so only the solid temperature is plotted. The PICA surface continuously cools down through surface radiation, and as heat is conducted into the model the maximum temperature is at an interior location. Thus, at 200 s the hottest spot (about 650 K) is located at a depth of about 0.6 cm from the front surface.

MARS SAMPLE RETURN VEHICLE

The second test case is simulation of a Mars sample return capsule. The purpose of the Mars Sample Return Mission is to return samples of material collected at Mars to Earth so that they can be studied here. The final phase of the

mission uses an Earth entry, descent, and landing capsule (Figure 8) that has a 0.9-m diameter, spherically blunted, 60° half-angle cone forebody.[18] This Earth Entry Vehicle (EEV) is designed to transport the samples safely through the Earth's atmosphere to a recoverable location on the surface, while maintaining the Martian samples at a temperature below 323 K. To minimize system complexity and the number of potential failure modes, the EEV design relies on a non-parachuted capsule that decelerates solely by aerodynamic forces during entry. A passive energy-absorbing material is used to cushion the Mars samples from excessively large deceleration during landing. The assumed trajectory is shown in Figure 9. The entry velocity is 11.6 km/s at angle of -25°. Peak heating occurs at 17 s, and peak deceleration is about 130 **g** at 20 s. Ground impact ("landing") occurs at about 41 m/s at 360.5 s.

A complete Pro/E model of the EEV contained 57 different types of parts including numerous small, non-axismmetric features such as antennas, bolts, cable connections, latches, springs, and vents.[19] Suppression of these features resulted in the model, shown in Figure 8, that contains 19 axisymmetric parts and volumes. The samples are located in region 19 inside an aluminum sample canister, parts 13-14. This can is held within a titanium containment vessel, parts 15-16. This assembly resides in a spherical structure called the impact shell, parts 4-5. This shell is made of carbon-carbon composite, as is the rest the vehicle substructure, parts 1-3. Volume 17 contains an energy absorbing composite structure that is assembled in a soccer-ball construction. The remainder of the vehicle interior is filled with various insulating materials, air gaps, and silicone rubber. The forebody heatshield is 1.2-cm thick chopped-molded and tape-wrapped carbon phenolic, and the aft heatshield is 1.0-cm thick SLA 561-V. Materials properties were obtained from NASA Langley and from the TPSX database.

The TITAN code is used for analysis of the heatshield materials only, and the rest of the vehicle is solved in MARC. The MARC material map is presented in Figure 10, and the three grids are illustrated in Figure 11. A very fine grid is needed in both the fluid and the solid to resolve the steep temperature gradients and complicated physics near the surface of the vehicle. A relatively coarser grid is adequate in the interior of the vehicle where temperature gradients are lower and time scales are longer.

Predicted forebody pressure distributions at selected times are shown in Figure 12. The peak pressure, which occurs at about 20 s, is about 1.15 atm. The pressure decreases gradually on the nose, with a slight minimum near the sphere-cone tangency point. The pressure increases slightly along the conical frustrum, then decreases rapidly as the flow accelerates around the shoulder of the vehicle. Predicted forebody convective heat flux distributions are presented in Figure 13. The heat flux decreases steadily, except for a local maximum near the shoulder during part of the trajectory. The peak heat convective flux is about 1.1 kW/cm^2 at 17 s. The stagnation point heat flux is shown in Figure 14. The vehicle decelerates rapidly owing to its bluntness, thus the heat pulse is fairly narrow, with 95% of the heating occurring in 14 s. The radiative heat flux over the forebody is estimated using the NOVAR code.[20] The peak radiative heat flux is about 0.22 kW/cm^2 at 16.4 s. The total heat load at the nose is about 9.2 kJ/cm^2 of which 8.5 kJ/cm^2 is convective and 0.7 kJ/cm^2 is radiative.

The forebody heat flux and pressure histories are imposed as boundary conditions of the integrated TITAN/MARC code. Owing to the large uncertainties in predicting afterbody heating, afterbody flowfields were not simulated using the Navier-Stokes solver. Instead, the heating is assumed to be uniform over the entire aft surface and equal to 5% of the time-dependent forebody stagnation point heating. This procedure is imprecise but possibly conservative in estimating the overall heat load experienced by the aft heatshield.

The blowing reduction parameter of 0.5 is used in the boundary conditions, Eqs. (3-4) for TITAN. Predicted peak surface temperature and total recession are shown in Figure 15. The peak temperature is 2500 to 3200 K over most of the forebody. However, the total recession is relatively low (under 1 mm) owing to the high density of the carbon phenolic heatshield. Because the surface recession is much smaller than the nose and shoulder radii, the effect of shape change on the aerothermal heating is insignificant for this problem. The surface and bond line temperatures in the TPS at the stagnation point are presented in Figure 16. The surface temperature increases with total heat flux, but after peak heating the temperature decreases more gradually by reradiation as heat is conducted back toward the surface from the interior of the TPS. The bond line temperature begins to rise at 50 s, and has reached 500 K at 300 s. The stagnation point blowing rates are shown in Figure 17. The carbon phenolic initially pyrolyzes in response to the aerothermal heating, then when the heat flux is sufficiently high, ablation also occurs.

In-depth temperature contours computed by TITAN and MARC at various times are presented in Figure 18. At 40 s, all the heat is contained within the heatshield. The peak surface temperature has cooled to 950 K, but the internal temperatures are unchanged from the assumed initial value of 250 K. At 100 s, most of the thermal energy is still confined within the heatshield, but some heat has penetrated into the forebody structure and foam insulations. At later times the TPS continues to cool by reradiation and conduction to the interior. The air gap at the nose is effective in preventing heat conduction, and the main conduction paths are along the skirt structure and through the body foam. A small amount of heat conduction through the aft TPS is also visible at the later times. At 500 s (if the vehicle is intact) the sample canister is safely below the design limit of 323 K.

The vehicle impacts the ground at about 360 s. Depending on the angle of the collision and the ground characteristics at the impact site, the containment vessel is displaced some distance through the energy absorbing material toward the nose structure, and other vehicle damage can occur as well. It is not obvious what assumptions are conservative for continuing the thermal analysis in the post-landing (pre-recovery) phase. Various scenarios can be simulated using MARC, including an impact simulation using assumed mechanical properties for the various materials. Future work will consider contact resistances between materials, and mechanical analyses such as calculation of thermal and deceleration stresses in the carbon-carbon structure.

CONCLUSIONS

A multi-dimensional fully coupled fluid/heatshield/structure thermal response modeling system has been developed. The system consists of a two-dimensional implicit thermal response and ablation program (TITAN), a commercial finite-element thermal and mechanical analysis code (MARC), and a high fidelity Navier-Stokes equation solver (GIANTS). This system can simultaneously predict aerothermal environments, heatshield ablation and shape change, and structural material thermal response for hypersonic entry vehicles as well as test models in hypersonic ground facilities. Representative computations for an arc-jet model and a proposed Mars sample return capsule were demonstrated. This integrated system can substantially reduce the computational effort required for multi-dimensional thermal analysis of ablative heatshield and structural materials, and thus should simplify the design cycle for future vehicles.

ACKNOWLEDGEMENTS

Ruth Amundsen and Robert Dillman at NASA Langley provided the Pro/E model for the EEV, an EEV material-properties spreadsheet, and other useful information. Joe Olejniczak at NASA Ames provided CFD and NOVAR results for the EEV trajectory.

REFERENCES

1. Moyer, C.B., and Rindal, R.A., "Finite Difference Solution for the In-Depth Response of Charring Materials Considering Surface Chemical and Energy Balances," Aerotherm Corporation, Mountain View, California, Final Report 66-7, Part II, March 1967 (also NASA CR-1061, June 1968).
2. Chen, Y.-K., and Milos, F.S., "Ablation and Thermal Analysis Program for Spacecraft Heatshield Analysis," *J. of Spacecraft and Rockets*, Vol. 36, No. 3, 1999, pp. 475-483.
3. Rafinejad, D., Dahm, T.J., Brink, D.F., Abbett, M.J., and Wolf, C.J., "Passive Nosetip Technology (Pant II) Program, Volume II, Computer User's Manual: ABRES Shape Change Code (ASCC)" Report SAMSO-TR-77-11, Acurex Corp., Mountain View, CA, Oct. 1986.
4. Hogan, R.E., Blackwell, B.F. and Cochran, R.J., "Numerical Solution of Two-dimensional Ablation Problems Using the Finite Control Volume Method with Unstructured Grids," AIAA Paper 94-2085, June 1994.
5. Chen, Y.-K., and Milos, F.S., "Two-Dimensional Implicit Thermal Response and Ablation Program for Charring Materials on Hypersonic Space Vehicles," *J. of Spacecraft and Rockets*, Vol. 38, No. 4, 2001, in press.
6. Candler, G. V., "The Computation of Hypersonic Ionized Flows in Chemical and Thermal Nonequilibrium," AIAA Paper 88-0511, Jan. 1988.
7. Chen, Y.-K., Henline, W.D., "Analysis of Hypersonic Arcjet Flowfields and Surface Heating of Blunt Bodies," AIAA Paper 93-0272, Jan. 1993.
8. Anon., *Users Manual, MARC Analysis Research Corporation, Volume A: Users Information*, MARC Analysis Research Corporation, Palo Alto, CA, 1994.
9. Chen, Y.-K., Milos, F.S., Bull, J.D., and Squire, T.H., "Integrated Analysis Tool for Ultra-High Temperature Ceramic Sharp-Body Reentry Vehicles," AIAA Paper 99-0350, Jan. 1999.
10. Anon., "Users Manual, Mentat II," MARC Analysis Research Corporation, Palo Alto, CA, 1995.
11. Squire, T.H., Milos, F.S., Hartlieb, G.C., and Rasky, D.J., "TPSX: Thermal Protection Systems Expert and Material Properties," *ICCE Fourth International Conference on Composites Engineering*, edited by D. Hui, ICCE and College of Engineering, University of New Orleans, July 1997, pp. 937-938.
12. Anon., *User's Manual: Aerotherm Charring Material Thermal Response and Ablation Program*, Report UM-87-11/ATD, Acurex Corporation, Mountain View, CA, Aug. 1987.

13. Anon., *User's Manual: Aerotherm Chemical Equilibrium Computer Program*, Report UM-81-11/ATD, Acurex Corporation, Mountain View, CA, Aug. 1981.

14. Milos, F.S., and Chen, Y.-K., "Comprehensive Model for Multi-Component Ablation Thermochemistry," AIAA Paper 97-0141, Jan. 1997.

15. Kays, W.M., and Crawford, M.E., *Convective Heat and Mass Transfer*, 2nd Edition, McGraw-Hill, 1980, pp. 355-357.

16. Bartlett, E.P., Kendal, R.M., and Rindal, R.A., "An Analysis of the Coupled Chemically Reacting Boundary Layer and Charring Ablator: Part IV – A Unified Approximation for Mixture Transport Properties for Multi-component Boundary-Layer Applications," NASA CR-1063, June 1968.

17. Tran, H., Johnson, C, Rasky, D., Hui, F., Chen, Y.-K., and Hsu, M., "Phenolic Impregnated Carbon Ablators (PICA) for Discovery Class Missions," AIAA Paper 96-1911, June 1996.

18. Mitcheltree, R.A., Braun, R.D., Hughes, S.J., and Simonsen, L.C., "Earth Entry Vehicle for Mars Sample Return," IAF Paper IAF-00-Q.3.04, Oct. 2000.

19. Amundsen, R.M., Dec, J.A., and Lindell, M.C., "Thermal Analysis Methods for an Earth Entry Vehicle," Eleventh Thermal and Fluids Analysis Workshop, Cleveland, OH, Aug. 2000.

20. Olynick, D.R., Henline, W.D., Chambers, L.H., and Candler, G.V., "Comparison of Coupled Radiative Navier-Stokes Flow Solutions with the Project Fire II Flight Data," AIAA Paper 94-1955, June 1994.

NOMENCLATURE

A = area, m^2
B' = $\dot{m} / \rho_e u_e C_h$, nondimensional mass flux
B_a = pre-exponential constant in Eq.(11), s^{-1}
C_h = Stanton number for heat transfer
c_p = heat capacity, J/kg-K
E = internal energy in Eq.(15), J/kg
E_a = activation energy in Eq.(11), J/kmol
F = view factor
$\boldsymbol{g}$ = Earth standard gravity, 9.81 m/s^2
H_r = recovery enthalpy, J/kg
h = enthalpy, J/kg
$\bar{h}$ = partial heat of charring in Eq.(9), J/kg
k = thermal conductivity, W/m-K
$\dot{m}$ = mass flux, kg/m^2-s
p = pressure, N/m^2
Q = heat source term, J/m^3
q = heat flux, W/m^2
q_C = conductive heat flux, W/m^2
q_R = radiative heat flux, W/m^2
R = universal gas constant, J/kmol-K
R_b = maximum body radius, m
R_c = corner radius, m
R_n = nose radius, m
s = stream length, m
$\dot{s}$ = surface recession rate, m/s
T = temperature, K
t = time, s
u = velocity, m/s
v = diffusion velocity, m/s
w = mass source term, kg/m^3
x = general coordinate variable, m
α = surface absorptance
$\bar{\alpha}$ = thermal expansion coefficient, 1/K
ε = surface emissivity
ε^{th} = thermal strain
Γ = volume fraction of resin
λ = blowing reduction parameter
ρ = total density, kg/m^3
σ = Stefan-Boltzmann constant, W/m^2-K^4
τ = CFD shear stress, N/m^2
Ψ = decomposition reaction order
η = surface -normal coordinate, m

subscripts

c = char
e = boundary-layer edge
g = pyrolysis gas
i = density component (A, B, and C)
j = gas phase species
k, l = coordinate directions
v = virgin
w = surface
0 = reference value

superscript

ℓ = time level index

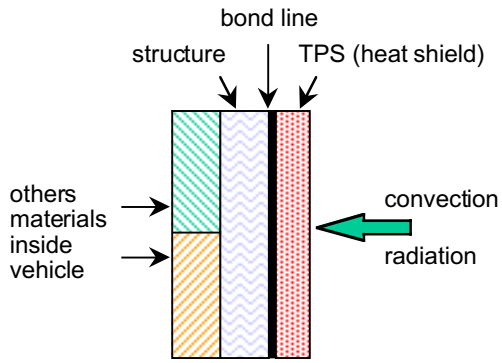

Figure 1. Schematic diagram of thermal analysis problem for a space vehicle.

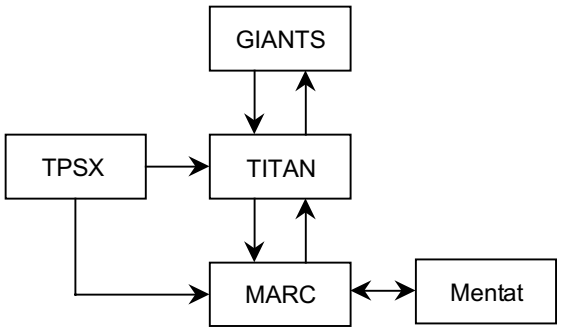

Figure 2. Flow chart for integrated thermal response modeling system.

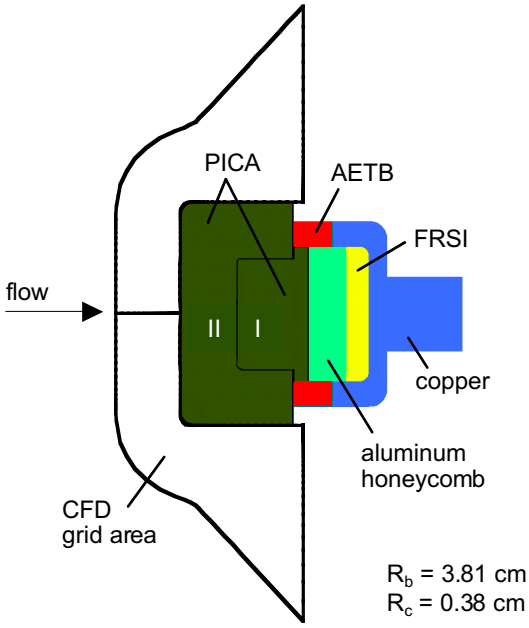

Figure 3. Flat faced arc-jet test model geometry.

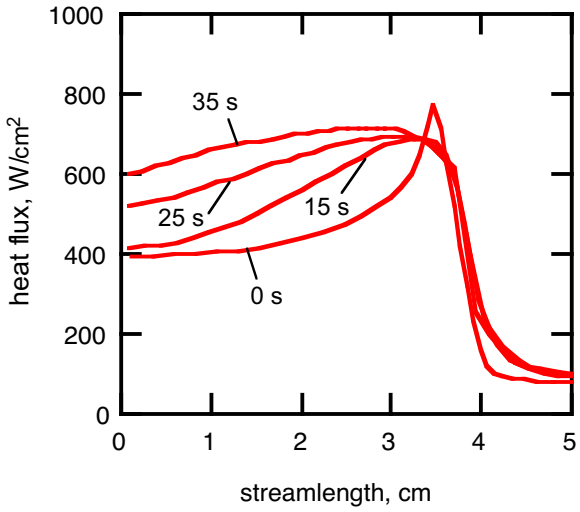

Figure 4. Heat flux on arc-jet model at various times.

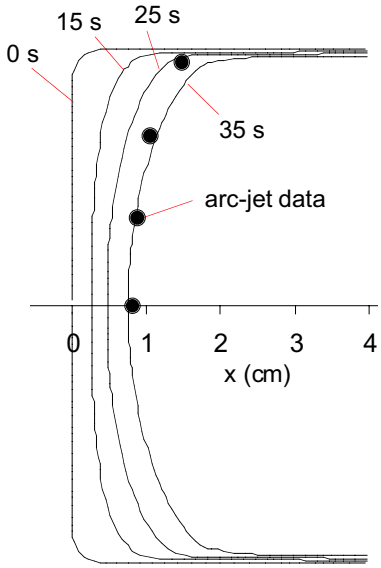

Figure 5. Recession history of arc-jet model.

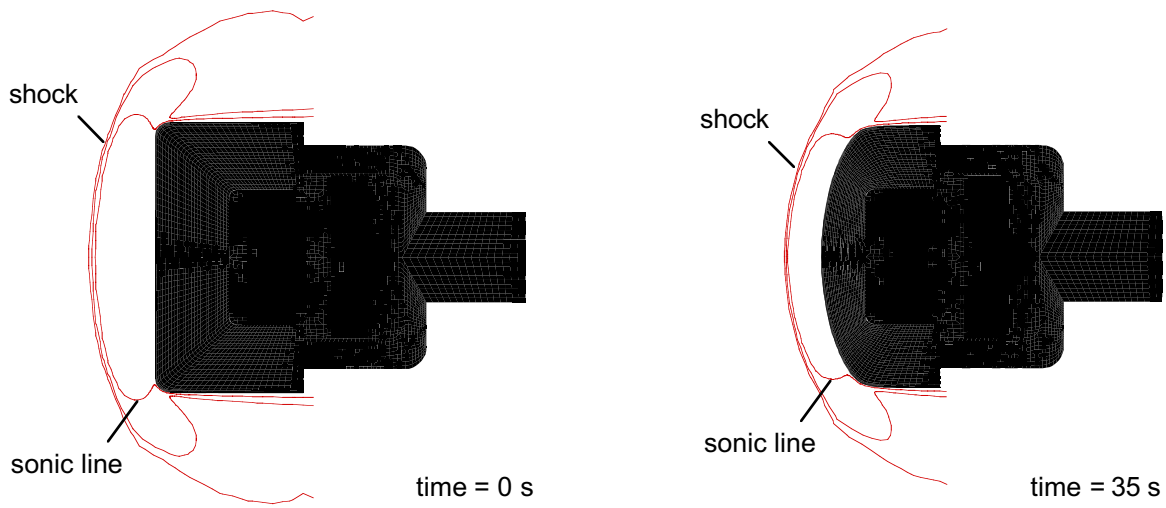

Figure 6. Mach contours for flow past arc-jet model at beginning (0 s) and end (35 s) of heating.

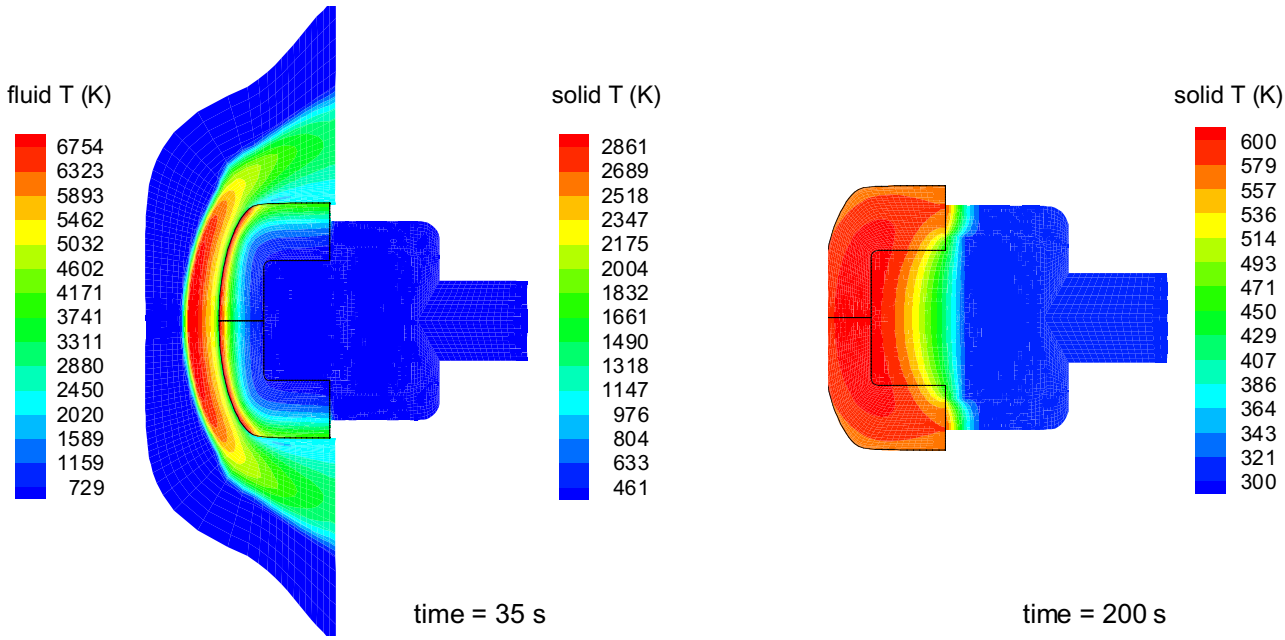

Figure 7. Temperature contours for arc-jet model.

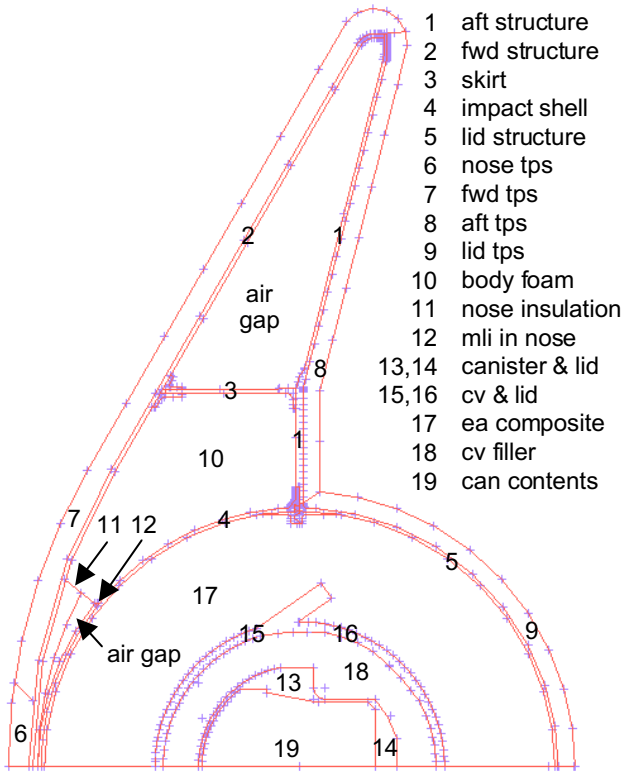

Figure 8. Axisymmetric EEV geometry.

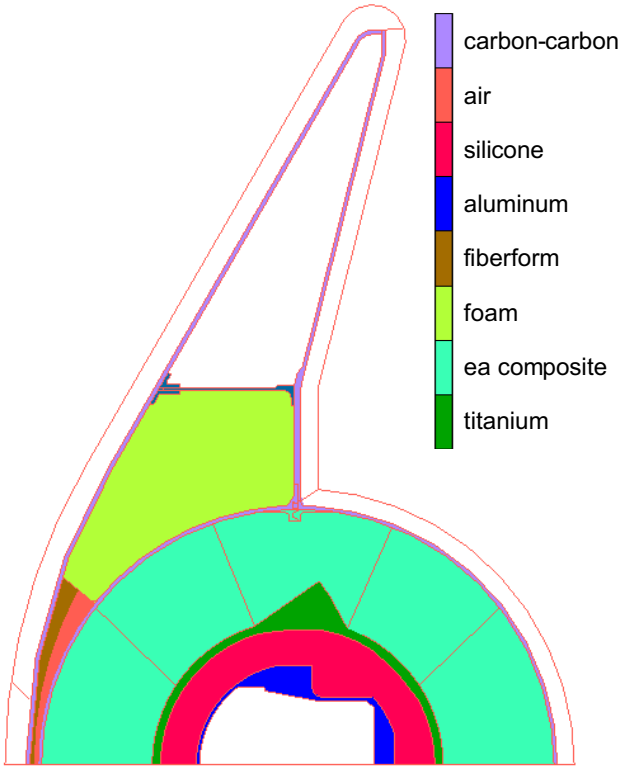

Figure 10. MARC geometry and material map.

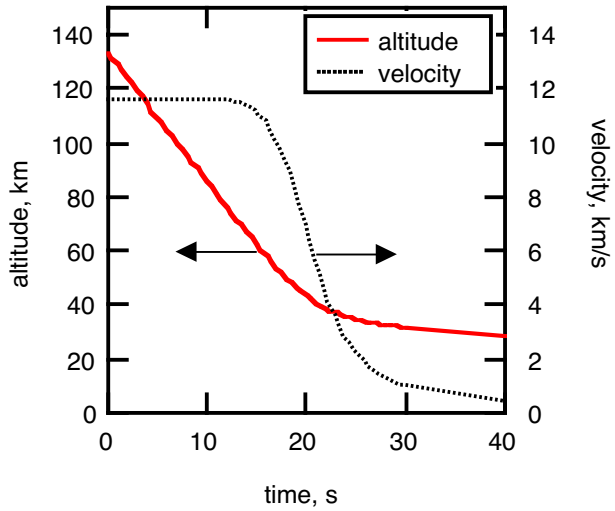

Figure 9. EEV trajectory.

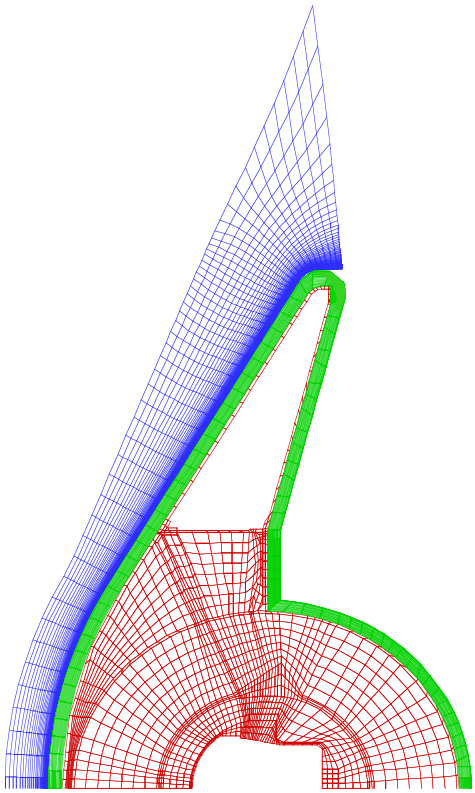

Figure 11. GIANTS grid (blue), TITAN grid (green), and MARC grid (red).

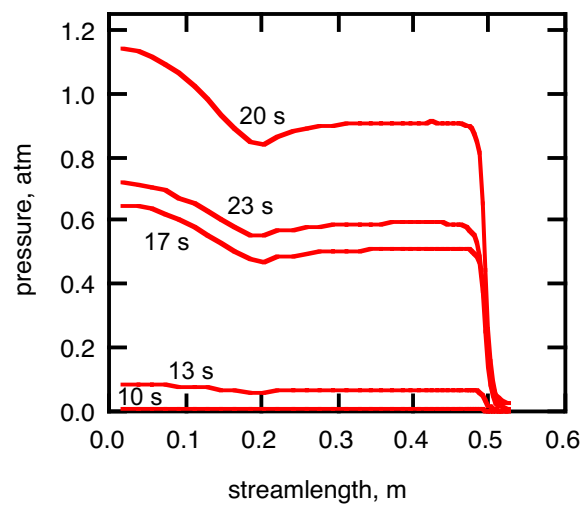

Figure 12. Surface pressure distribution at selected times.

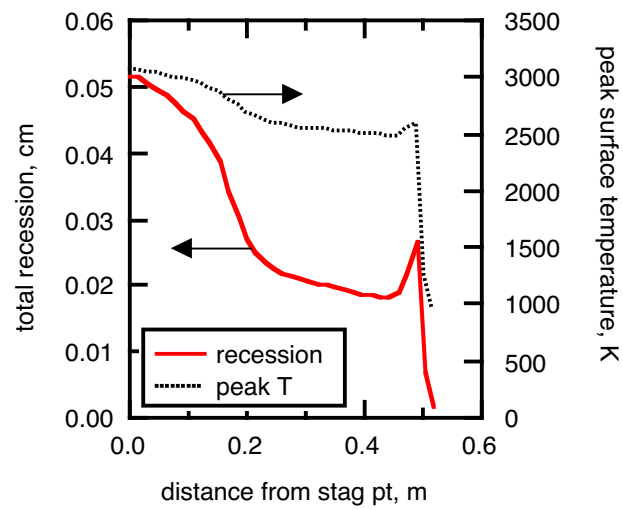

Figure 15. Surface peak temperature and recession.

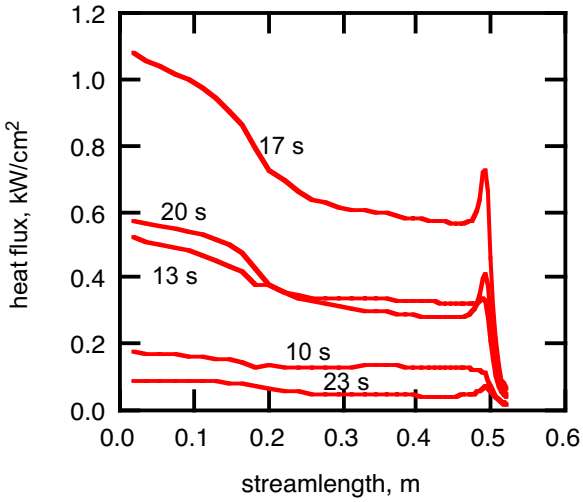

Figure 13. Surface heat flux distribution at selected times.

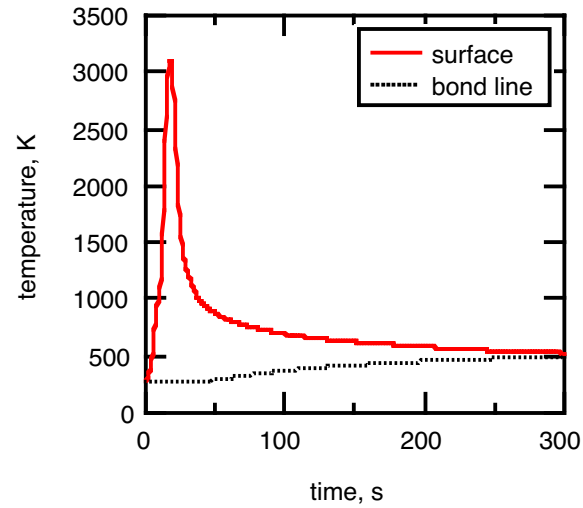

Figure 16. TPS temperature histories at stagnation point.

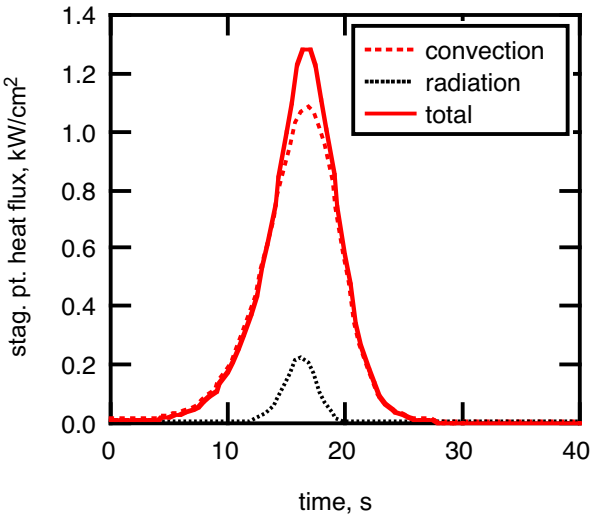

Figure 14. Stagnation point heat flux.

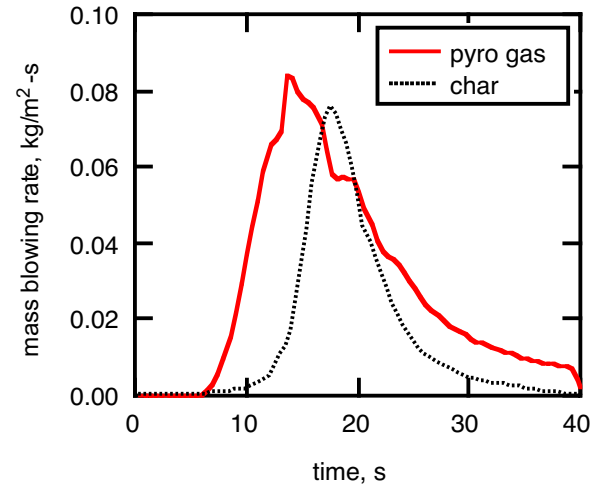

Figure 17. Surface mass flux at stagnation point.

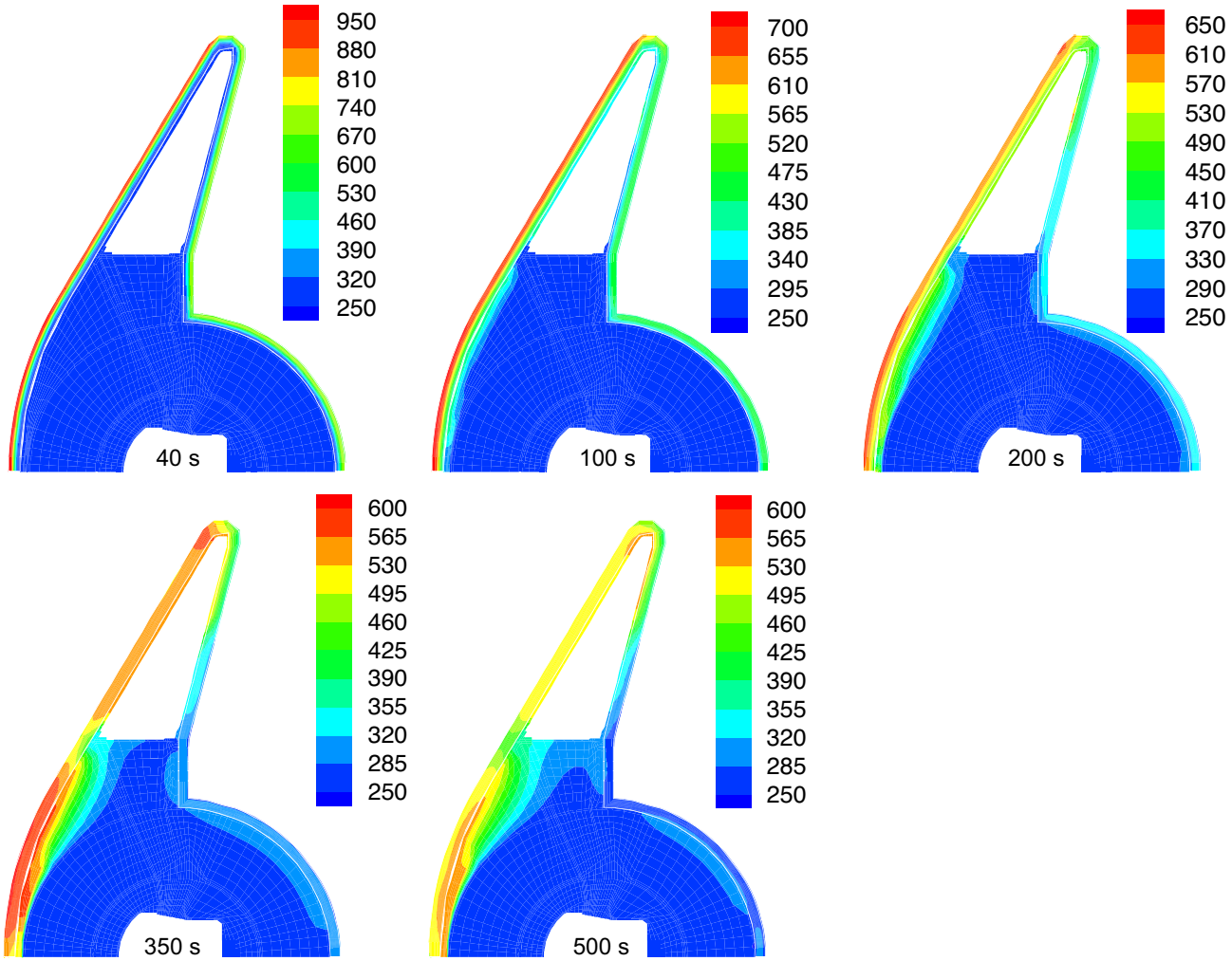

Figure 18. EEV temperature contours at selected times, K.

Advances in thermal model data exchange using open standards

Hans Peter De Koning - ESA/ESTEC - The Netherlands
Hans-Peter.de.Koning@esa.int

NASA Thermal and Fluids Analysis Workshop 2001
Huntsville, AL, USA, September 10-14, 2001

Background

- In more and more space projects - in particular international programmes - routine exchange of thermal analysis model data between different tools is necessary
- Conversion processes are inefficient
  - Mostly with direct point-to-point converters - costly to maintain
  - Supplemented with significant manual work
  - SI / US-English unit conversion a problem in itself
- Conversion processes are mostly informal
  - Not very reliable - no thorough validation - no certification
- Open standards are emerging: STEP, STEP-TAS, XML, XSL

Background - Old situation
Exchange of thermal analysis models in Europe

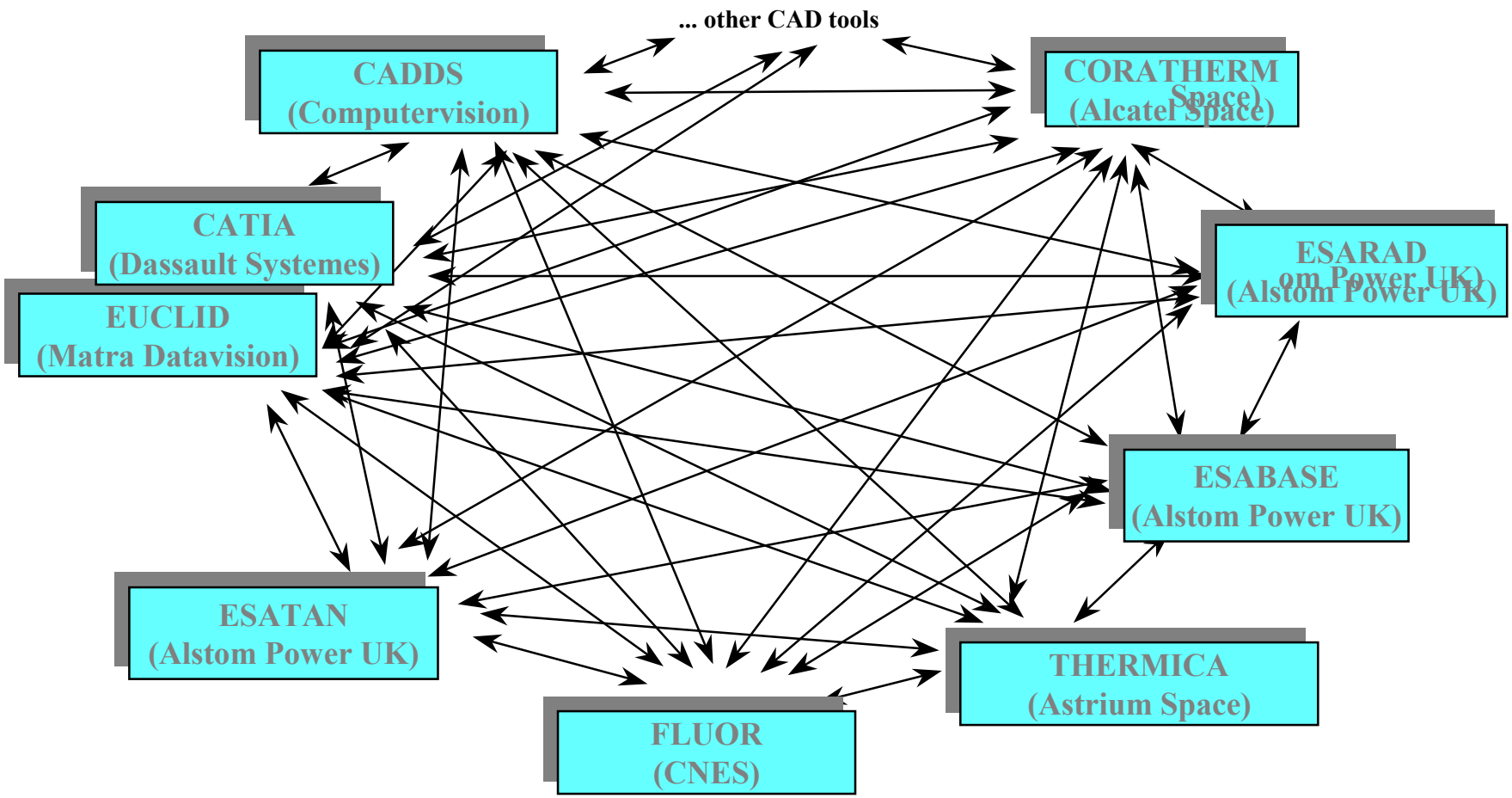

Background - New emerging situation: Use of STEP / ISO 10303

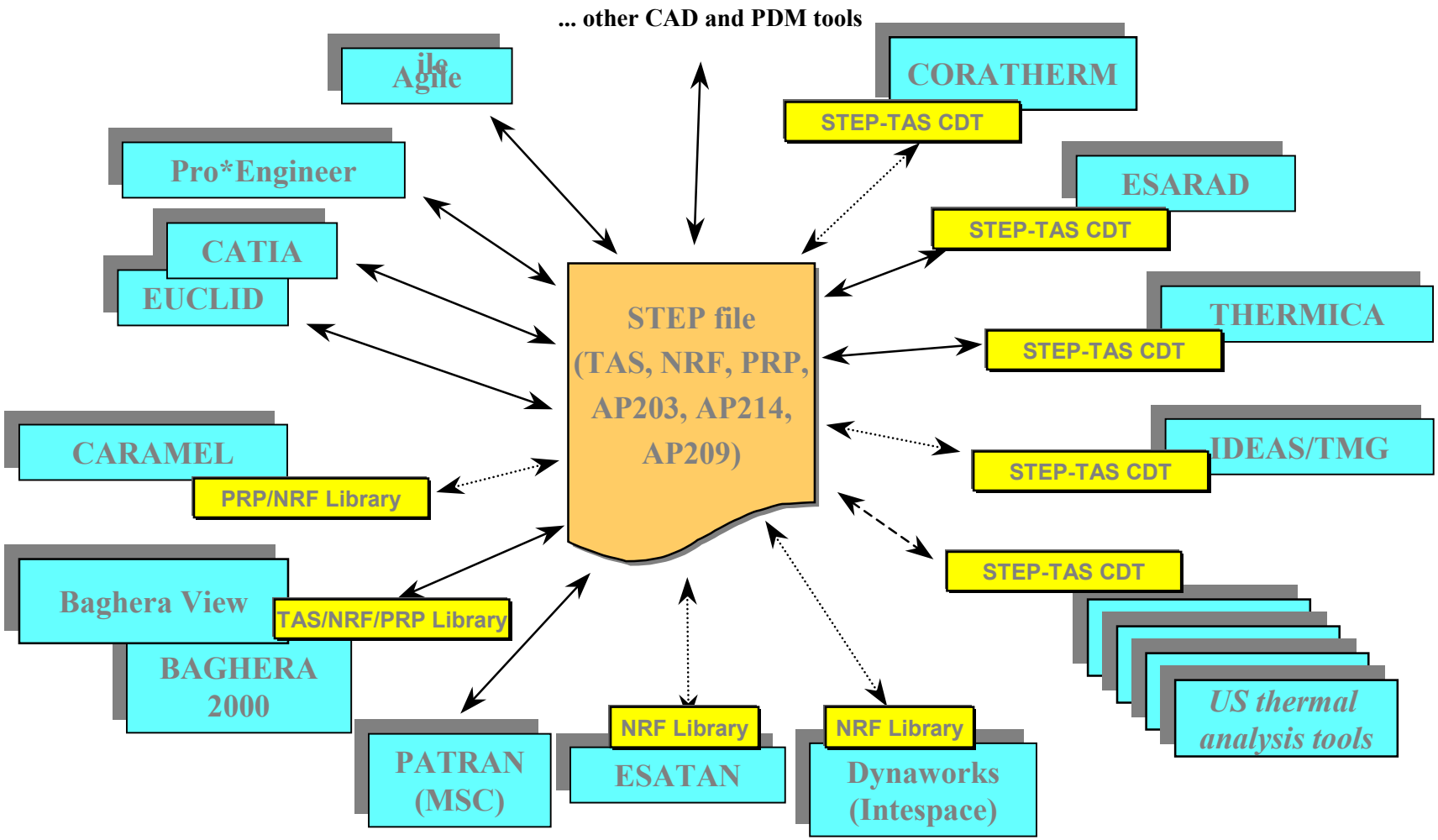

Objective of STEP / ISO 10303

- STEP = STandard for the Exchange of Product model data
  = casual name for ISO 10303
- "ISO 10303 is an International Standard for the computer-interpretable representation and exchange of product data. The objective is to provide a mechanism that is capable of describing product data throughout the life cycle of a product, independent from any particular system. The nature of this description makes it suitable not only for neutral file exchange, but also as a basis for implementing and sharing product databases and archiving."

(From ISO 10303 Part 1)

The (Aero)Space STEP Protocols Map

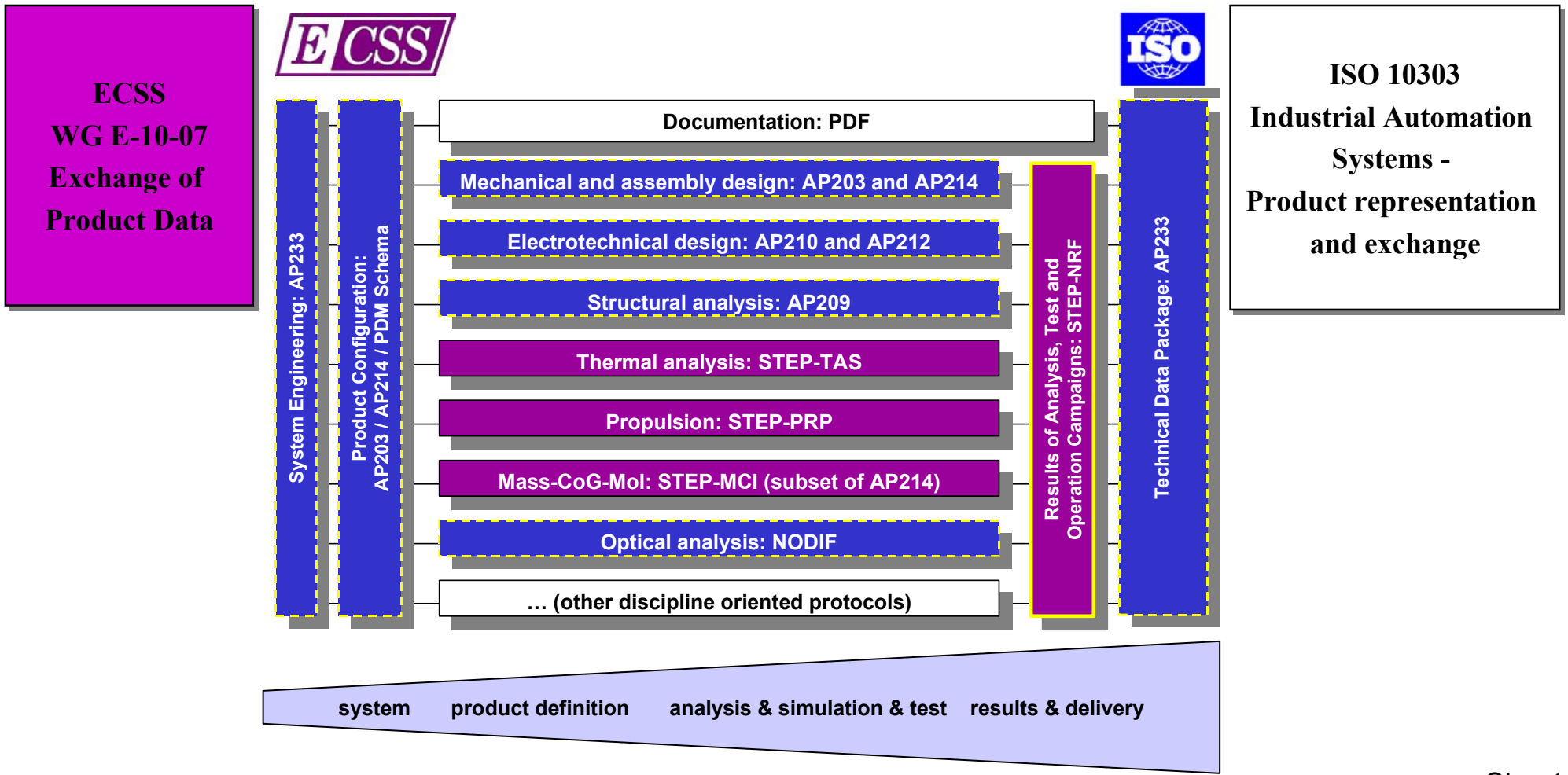

Disciplines in space projects
and examples of possible exchange

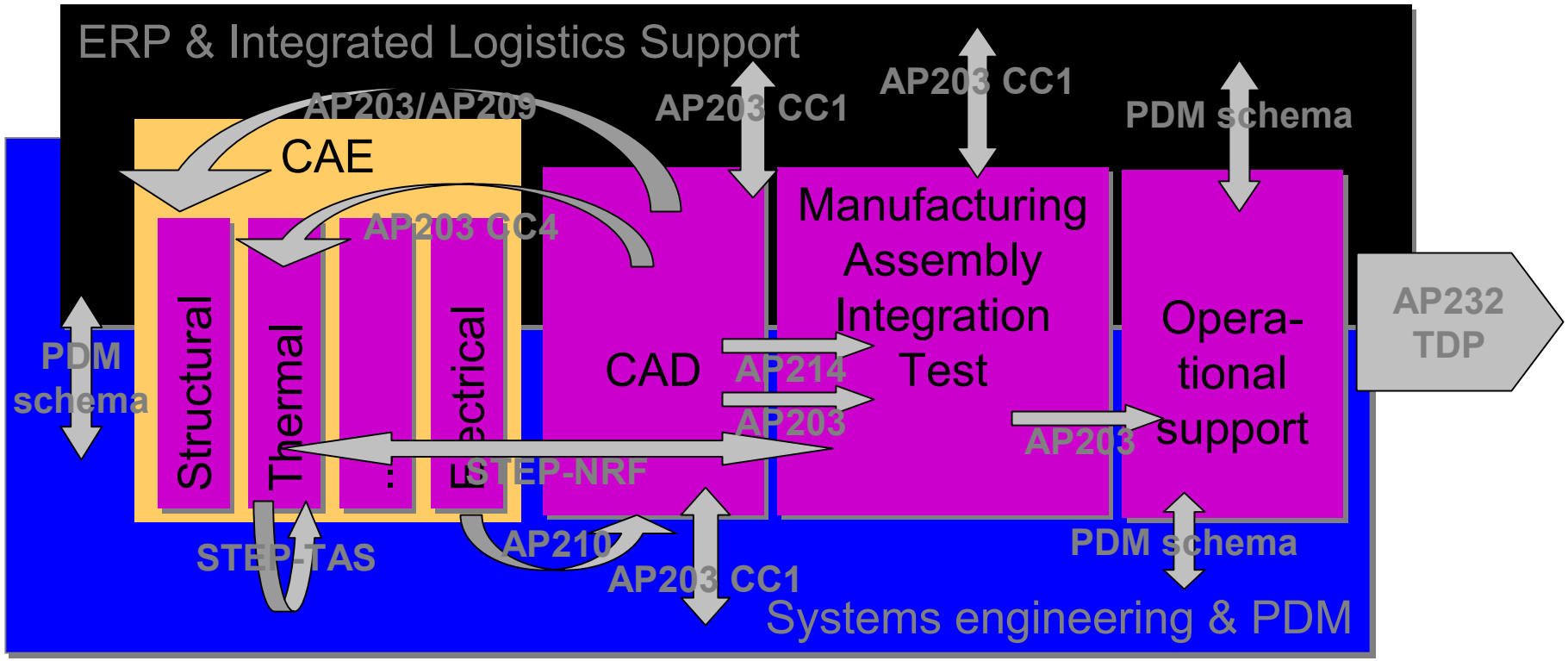

TAS = Thermal Analysis for Space
NRF = Network-model Results Format

Brief history TAS and NRF

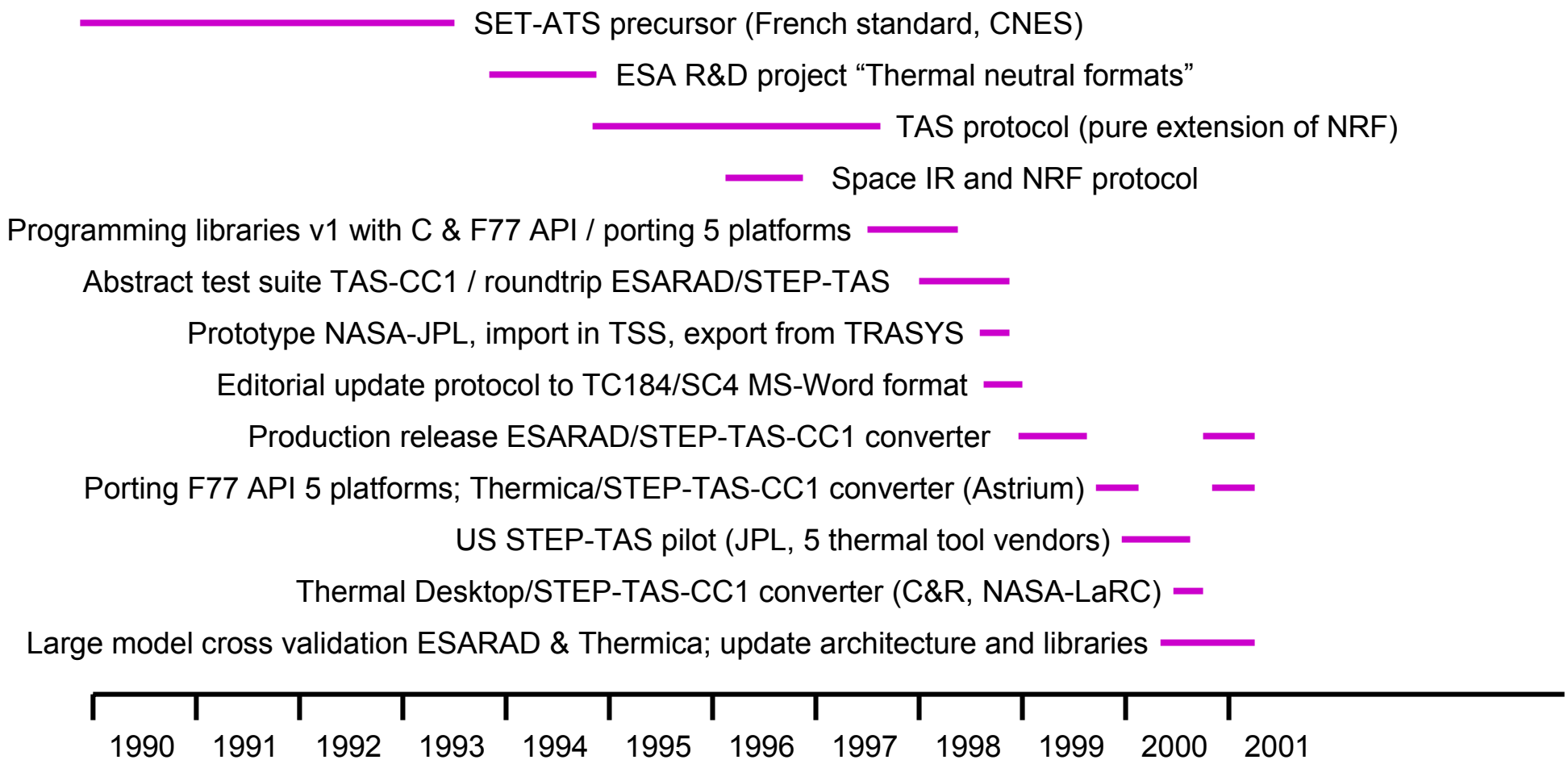

STEP-TAS initial steps

- Initial steps taken
- Almost all tools / vendors on-board
  - Europe: ESARAD, THERMICA
  - US: Thermal Desktop/RADCAD, NEVADA, TSS, TRASYS, ATM, MSC-Patran, I-Deas TMG
- STEP-TAS converters in industrial release ESARAD and THERMICA (2000, 2001)
- Successful US pilot implementations in 2000

Update of STEP-TAS architecture

- Lessons learned from initial development and implementation
  - It takes too long …
    - To upgrade / correct the protocol or Converter Development Toolkit
    - To validate converter implementation
  - Web-based Implementors Forum is necessary
    - Including Converter Development Toolkit distribution
    - Problem reporting / tracking
    - Discussion Forum
    - Test suites / benchmarks

Main characteristics of STEP-TAS (1)

- Self contained, complete Application Protocol
  - AAM, ARM, Mapping Table, AIM, Express-G (586 pages)
  - Conforms to TC184/SC4 methods and guidelines
- Geometry defined as AP203 CC4 surfaces
- Thermal-radiative model faces added as associated features
  - Including possibility to support hierarchical submodel tree
  - Associated notional thickness, surface material and bulk material
  - Thermo-optical, thermo-physical properties for named material
  - Concept of material property environment (Part 45)
- Kinematic model conform STEP Part 105
  - for articulated rigid bodies (e.g. rotating solar arrays, gimballed antennas)

Main characteristics of STEP-TAS (2)

- Space mission aspects
  - orbit arc (Keplerian and discrete ephemeris)
  - space co-ordinate system, celestial bodies
  - orientation, general and named pointing, spinning, linear rotation rates
  - space thermal environment, including constant or lat/long dependent albedo / planetshine tables
- Boolean construction surfaces available for advanced tools
- STEP-TAS CC1 Abstract Test Suite
  - conform STEP Part 3xx series
  - test suite has been used in validation of TAS processors

STEP-TAS geometry and thermal-radiative models

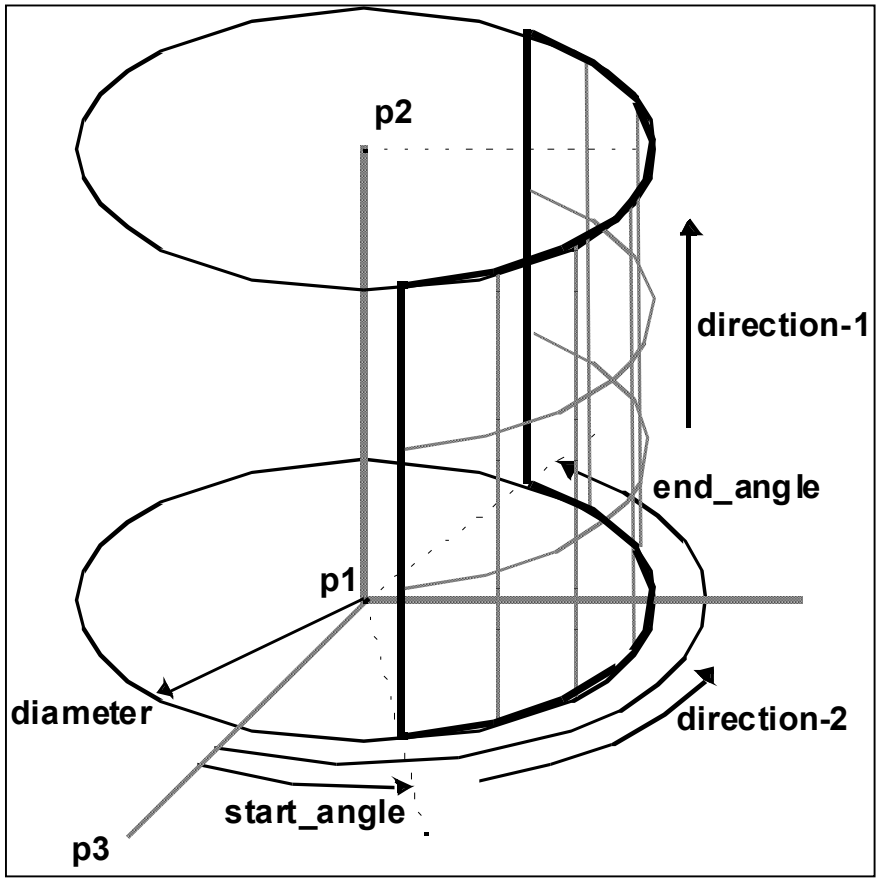

- Shapes
  - Primitives: triangle, rectangle, quadrilateral, disc, cylinder, cone, sphere, paraboloid
  - Compound shapes
  - Shapes conform to AP203 CC4 non-manifold surfaces
- Thermal-radiative model
  - associates thermal-radiative faces with surface shapes
  - thermal mesh (uniform and non-uniform)
  - surface and bulk material properties by reference to material

Illustration of basic STEP-TAS Keplerian orbit definition

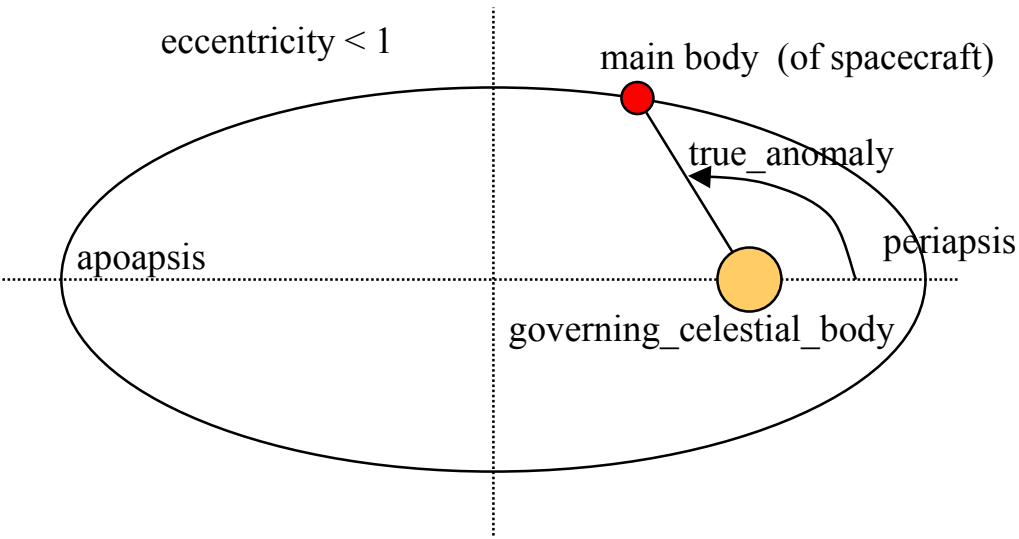


```
ENTITY keplerian_orbit_arc
    SUBTYPE OF (orbit_arc);
    kepler_parameters : kepler_parameter_set;
END_ENTITY;

ENTITY kepler_parameter_set;
  semi_major_axis : length_measure;
  eccentricity : REAL;
  inclination : plane_angle_measure;
  right_ascension_of_ascending_node :
    plane_angle_measure;
  argument_of_periapsis : plane_angle_measure;
  true_anomaly_at_start : plane_angle_measure;
WHERE
  wr1: semi_major_axis >= 0.0;
  wr2: eccentricity >= 0.0;
  wr3: (-180.0 < inclination) AND
       (inclination <= 180.0);
  wr4: (-360.0 < right_ascension_of_ascending_node)
    AND (right_ascension_of_ascending_node <=
    360.0);
  wr5: (0.0 <= argument_of_periapsis) AND
    (argument_of_periapsis < 360.0);
  wr6: (-360.0 < true_anomaly_at_start) AND
    (true_anomaly_at_start <= 360.0);
END_ENTITY;
```

STEP-TAS :
Product structure and kinematic

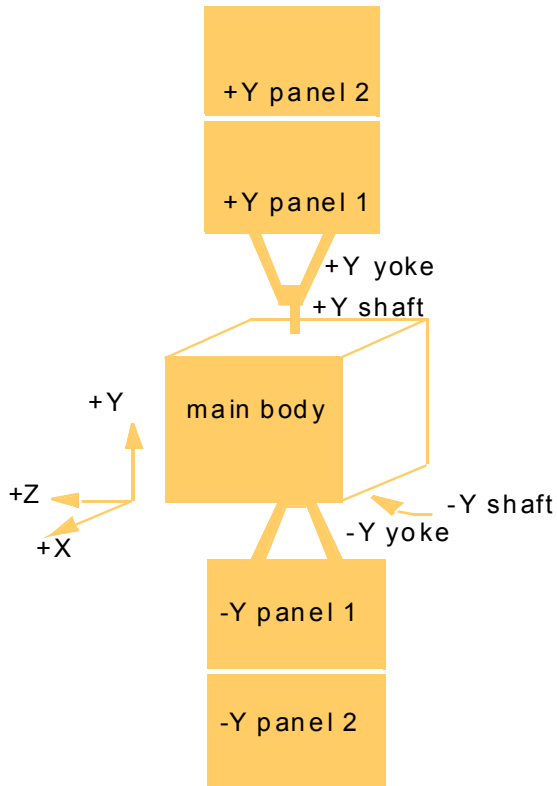

(a) Schematic shape model of a typical communications satellite with two fully deployed solar array wings

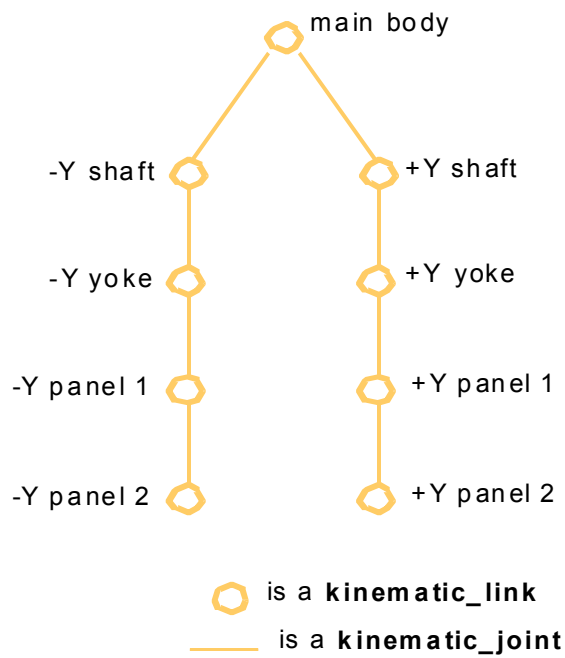

(b) The corresponding **kinematic_model** presented as a topological graph

STEP-TAS Conformance Classes

	thermal-radiative model with basic geometry	kinematic model	constructive geometry	space mission aspects
CC-1	✓			
CC-2	✓	✓		
CC-3	✓		✓	
CC-4	✓	✓	✓	
CC-5	✓	✓		✓
CC-6	✓	✓	✓	✓

Main characteristics NRF (1)
Network-model Results Format

- Targets engineering-discipline independent exchange of bulk results data from analysis, test or operation
  - Representation of engineering objects by network models consisting of discrete nodes and node-relationships
  - Hierarchical tree of network models / submodels
  - Definition of properties
    - Quantitative, descriptive and functional properties
    - Scalar, vector and tensor property values
    - Property values only at discrete locations / discrete states
  - Full annotation of analysis / test / operation context
    - Campaign, case, phase, run
    - Facility/tool, environment, date and time, organisation, person, ...

Main characteristics NRF (2)

NRF dataspace

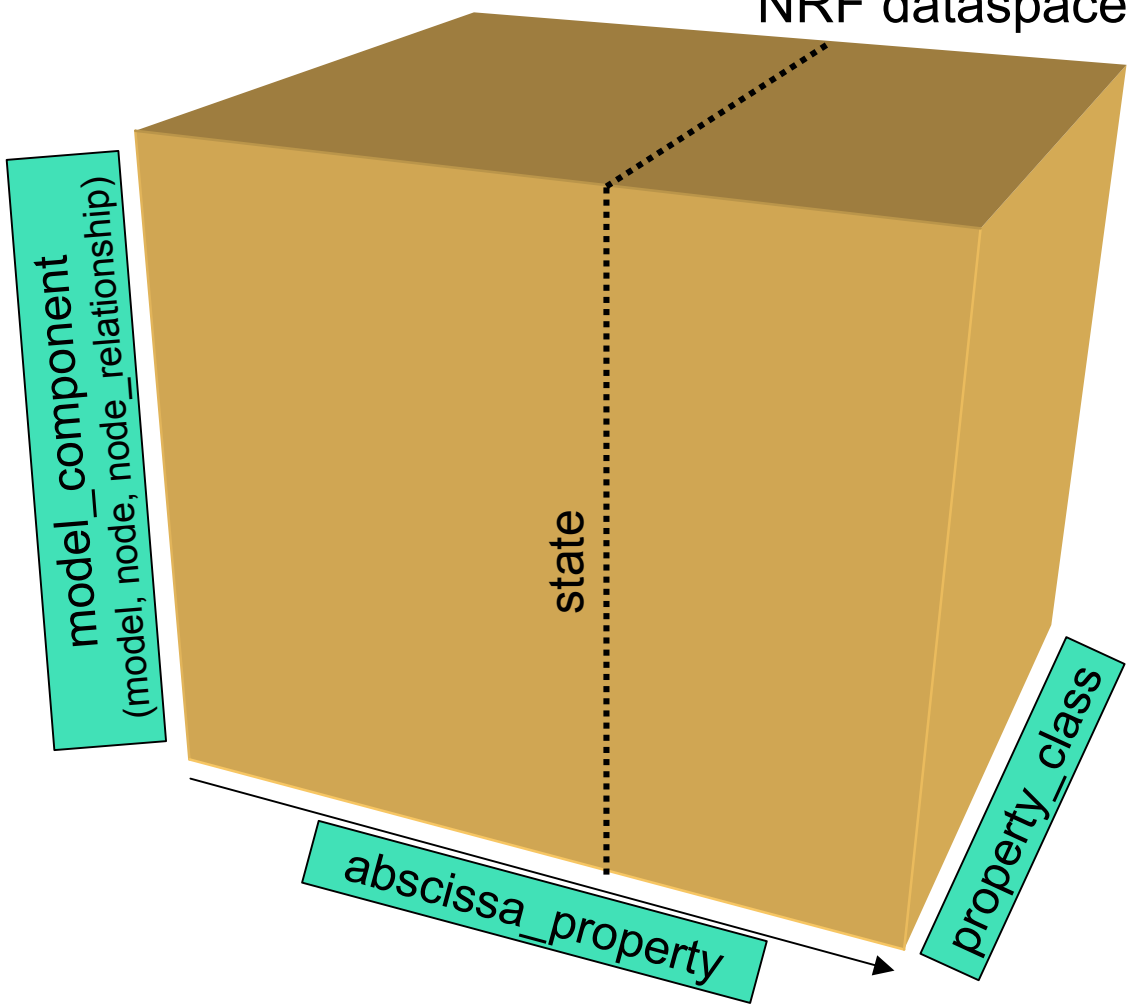

Each gridpoint in the 3D dataspace is a property value

Each can be scalar, vector, tensor

Data model and implementation designed to handle sparsely populated dataspace efficiently

Main characteristics NRF (3)
Proposed NRF/HDF architecture

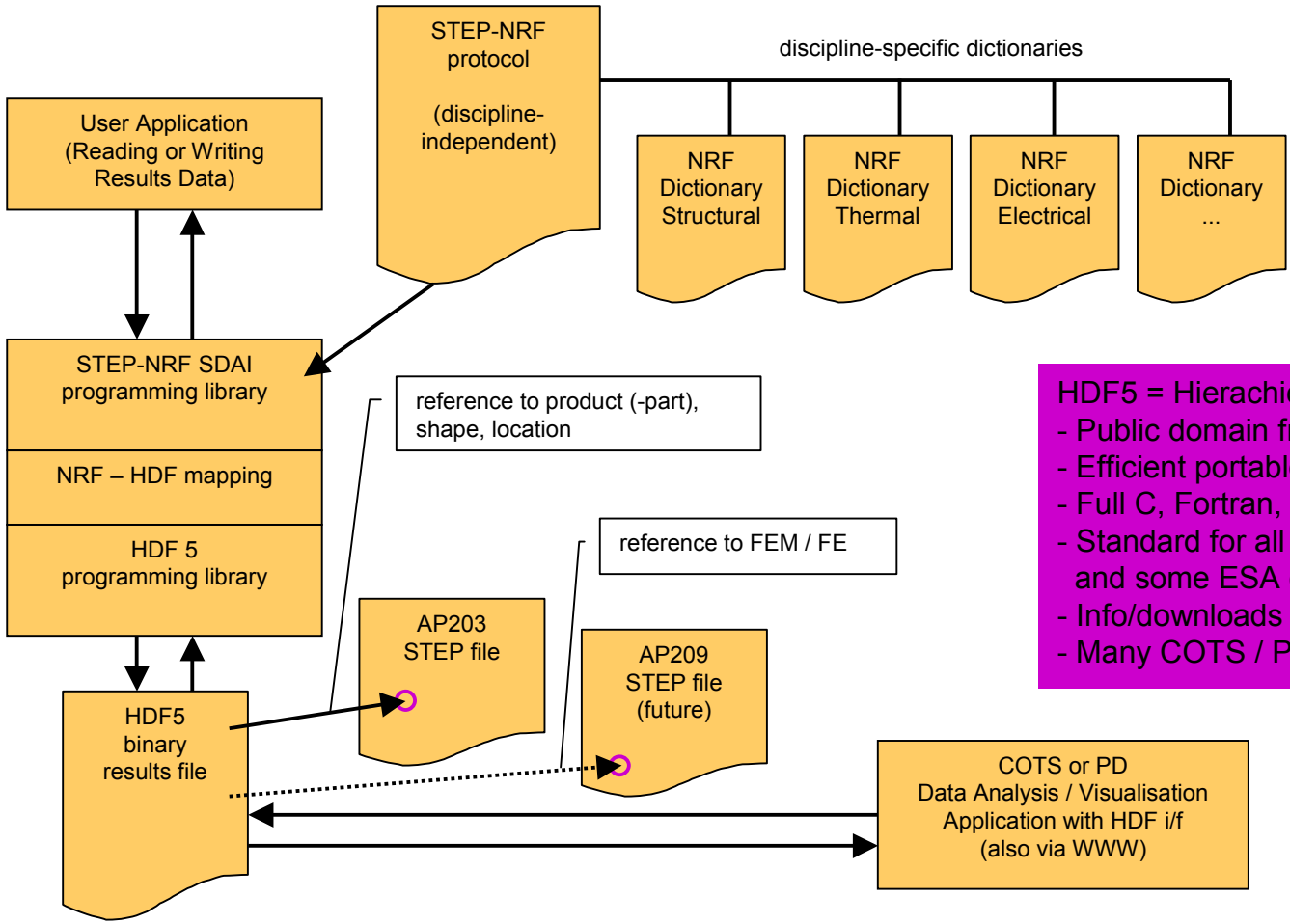

HDF5 = Hierachical Data Format v5
- Public domain from NCSA
- Efficient portable binary storage format
- Full C, Fortran, Java libraries on >10 platforms
- Standard for all NASA EOS missions and some ESA earth observation
- Info/downloads at hdf.ncsa.uiuc.edu
- Many COTS / PD tools with HDF interface

HDF5 is an efficient alternative for Part21 for large amounts of similar data

STEP-TAS CDT
Converter Development Toolkit

- High-level API (Application Programming Interface)
  - ARM concepts - close to thermal tools - hides STEP complexity
  - Full set of reading/writing functions in ANSI-C and F77
  - With documentation, examples and test suite
  - With Baghera-View to perform independent visual inspection
- Advantages:
  - Available to tool developers at nominal cost (from Simulog)
    - Platforms: Windows, Sun/Solaris, HP-UX, Compaq/Tru64, SGI/Irix
  - Enables to jumpstart converter implementation
  - Reduces converter validation / verification effort
  - All converters share reading/writing approach - increased reliability
  - Extensibility at affordable cost - e.g. add HDF or XML encoding

STEP-TAS Converter Architecture

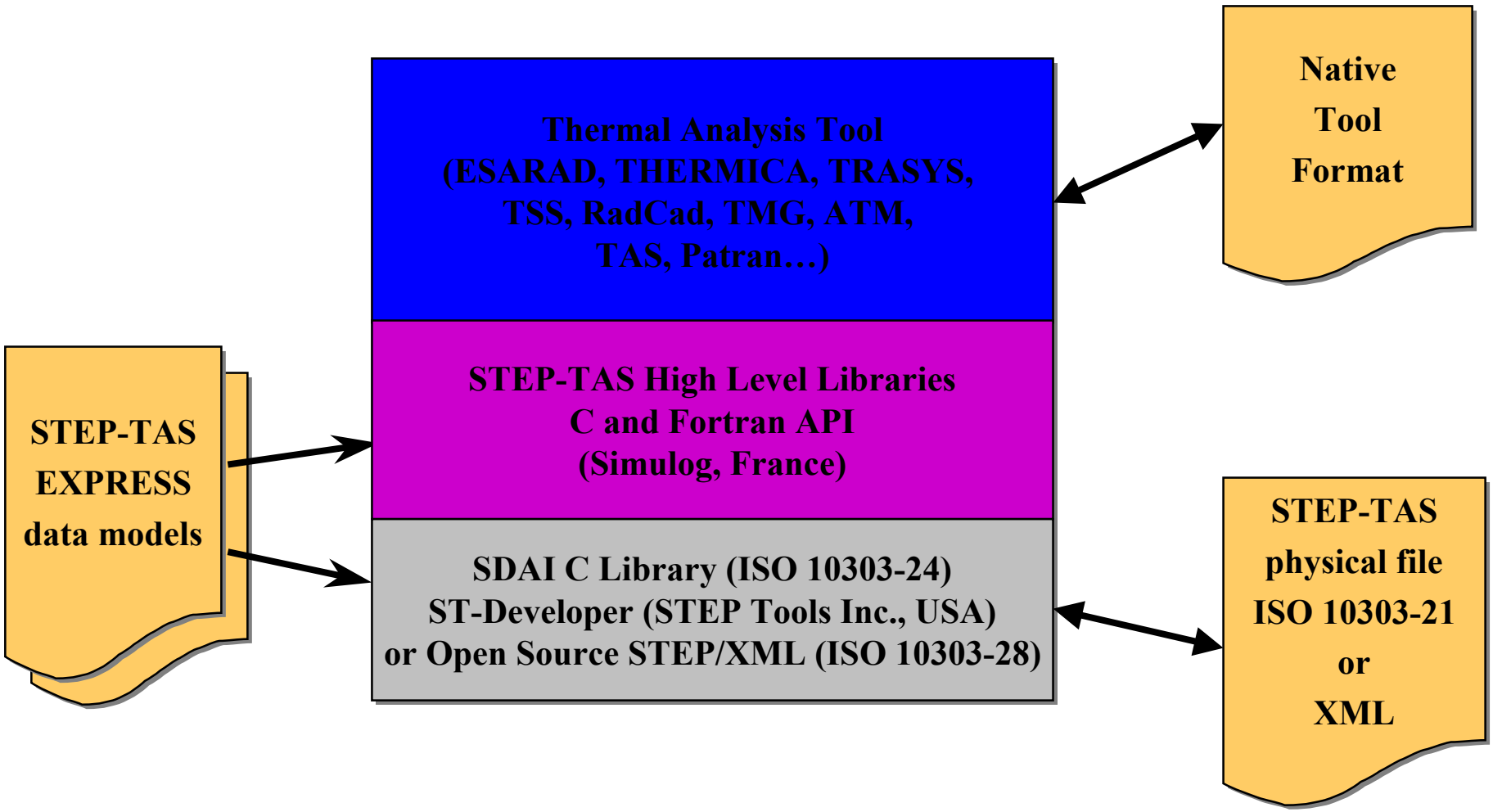

The STEP-TAS roadmap - Sep 2001

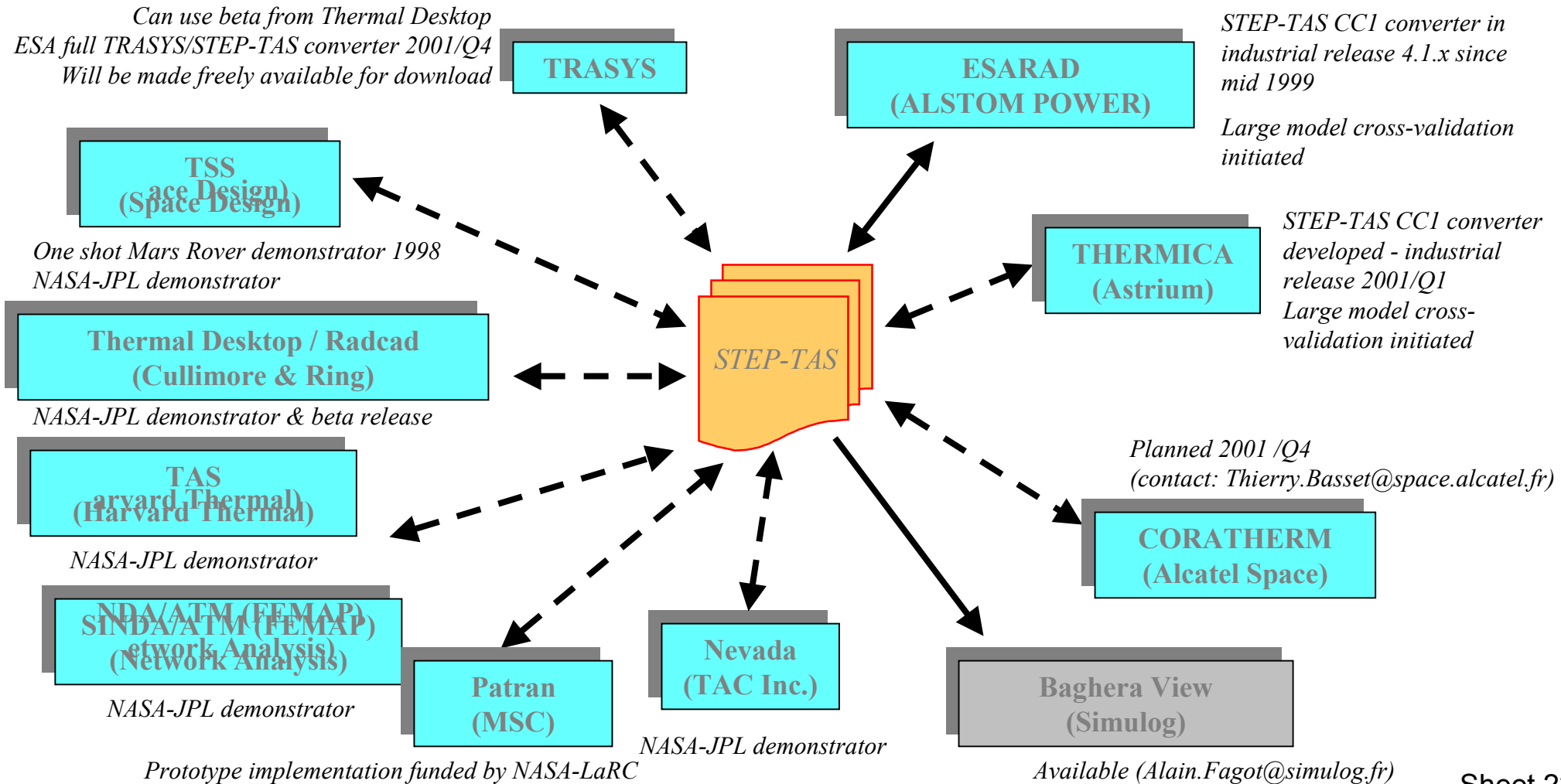

Status of STEP-TAS interfaces on European side

- ESARAD (ALSTOM POWER, ESA)
  - CC1 bi-directional interface in industrial release since mid 1999
- THERMICA (Astrium/Toulouse)
  - CC1 bi-directional interface in industrial release since 2001/Q1
- Large model cross-validation ESARAD / THERMICA
  - Currently in progress
  - Thousands of thermal-radiative faces
  - Resolving performance / memory management issues
  - Import of models is slow - still issues with reliability
- Coratherm (Alcatel Space)
  - Converter development expected to start 2001/Q4

Status of STEP-TAS interfaces on US side

- Bi-directional demonstrator development funded by NASA-JPL
  - 2000-Q1/Q3 on limited scope by 5 vendors:
    - Thermal Desktop (Cullimore and Ring Inc.)
    - TSS (Space Design)
    - TAS (Harvard Thermal)
    - SINDA-G/ATM (Network Analysis Inc.)
    - Nevada (TAC Inc.)
- Bi-directional converter development funded by NASA-LaRC
  - Thermal Desktop (C&R) - beta released 2000-Q3/Q4
  - MSC/Patran - currently in progress
  - Using STEP-TAS converter development toolkit from Simulog
- Cross validation US tools / European tools being planned

NASA-JPL STEP-TAS Demonstrator

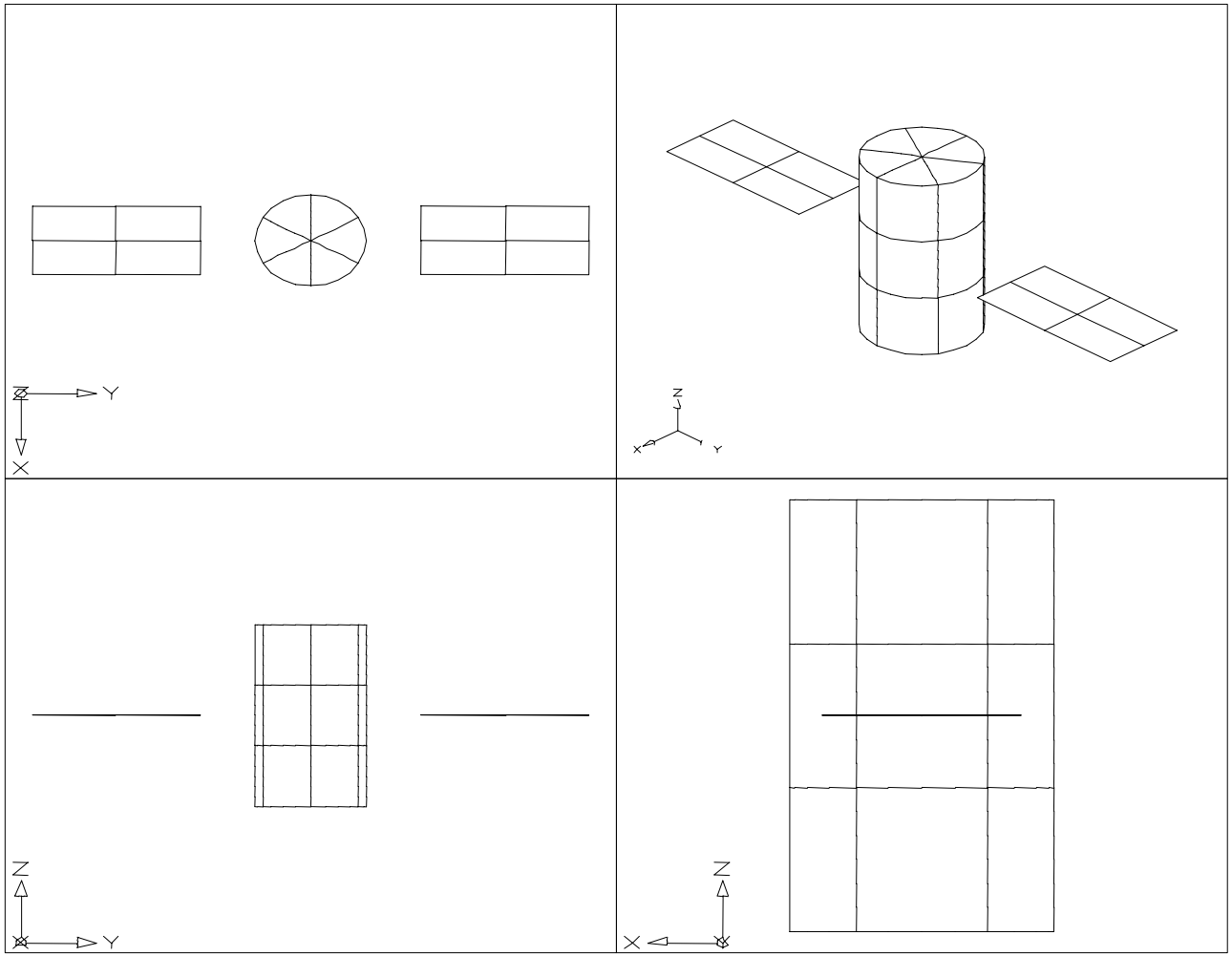

- A feasibility and familiarisation study
- Objective: to develop a limited bi-directional STEP-TAS prototype converter

Examples of STEP-TAS exchanges

ROSETTA in ESARAD

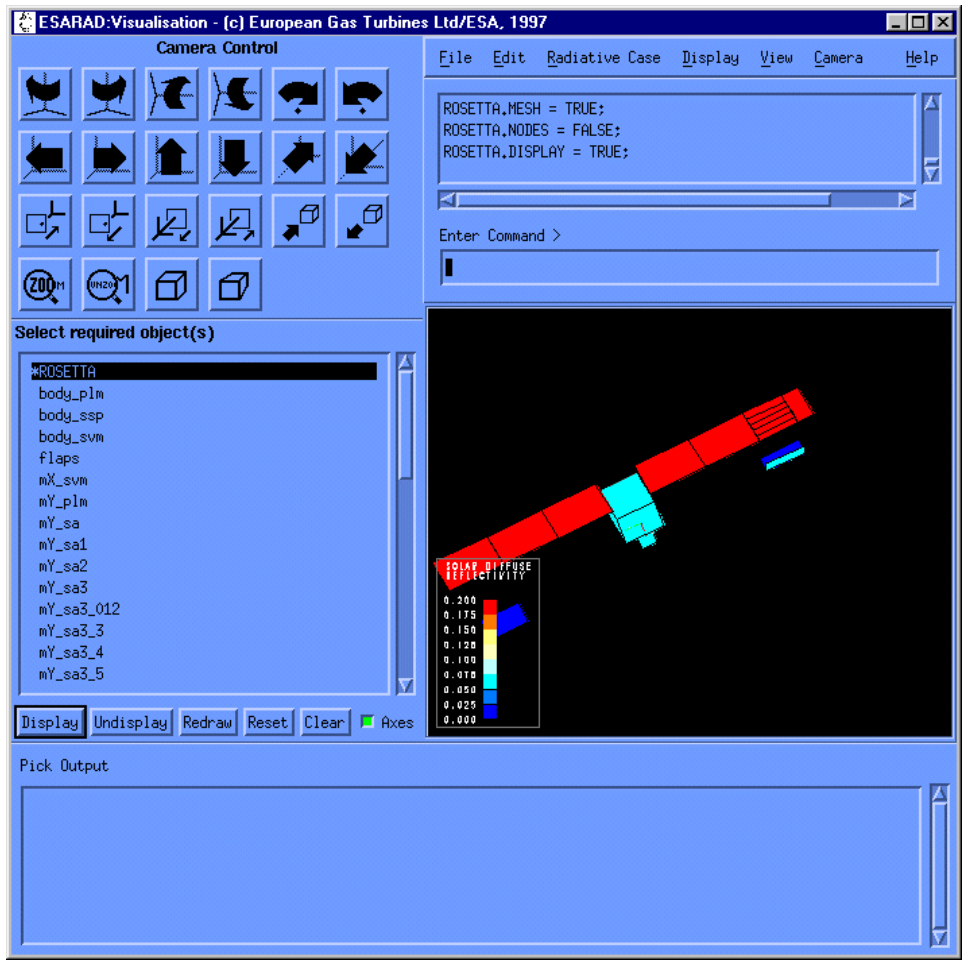

ROSETTA in Baghera View

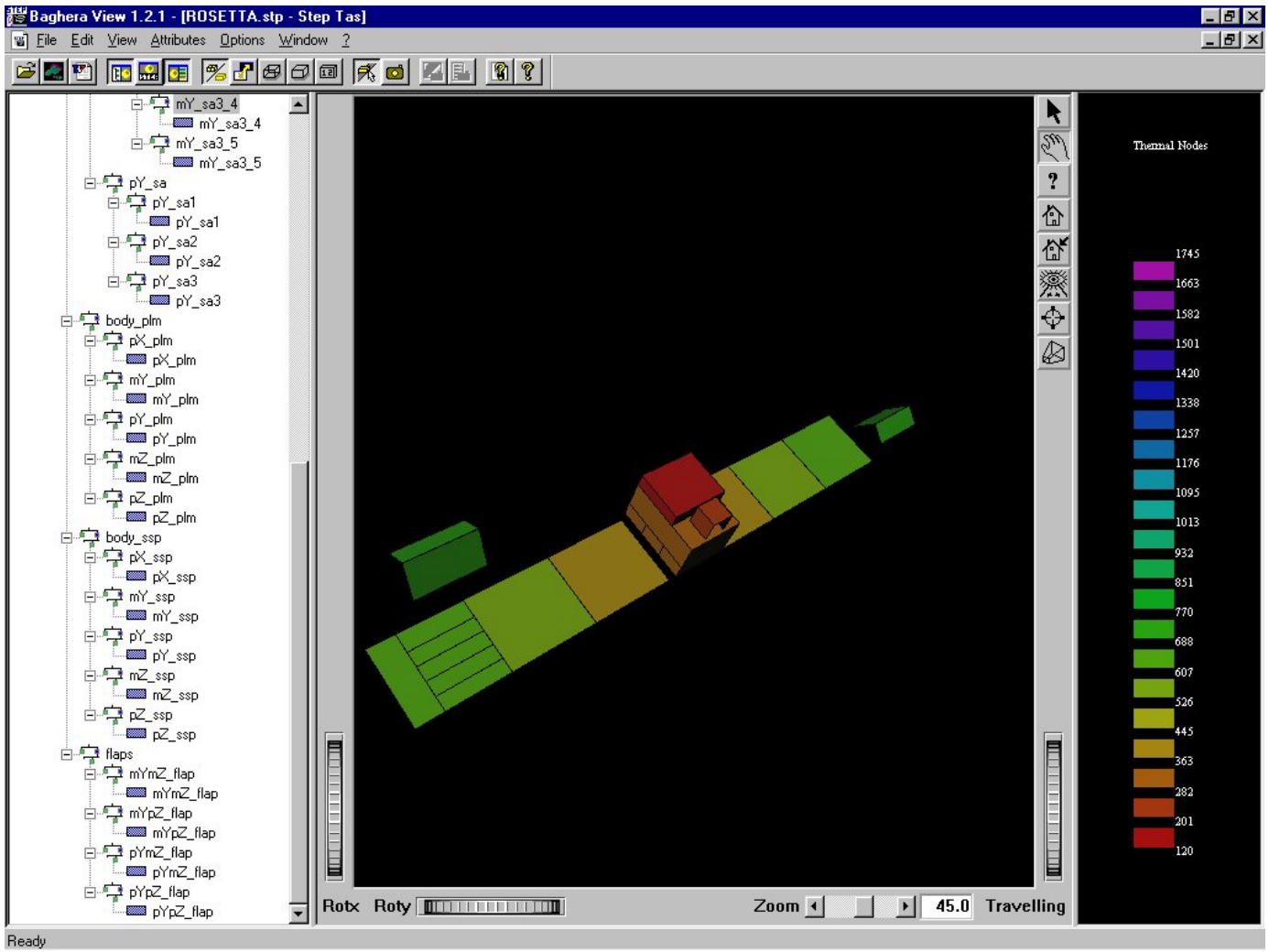

ROSETTA in THERMICA

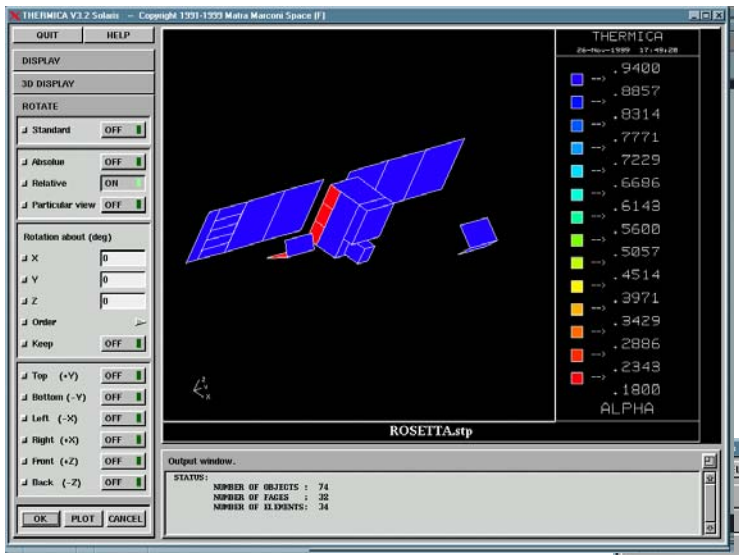

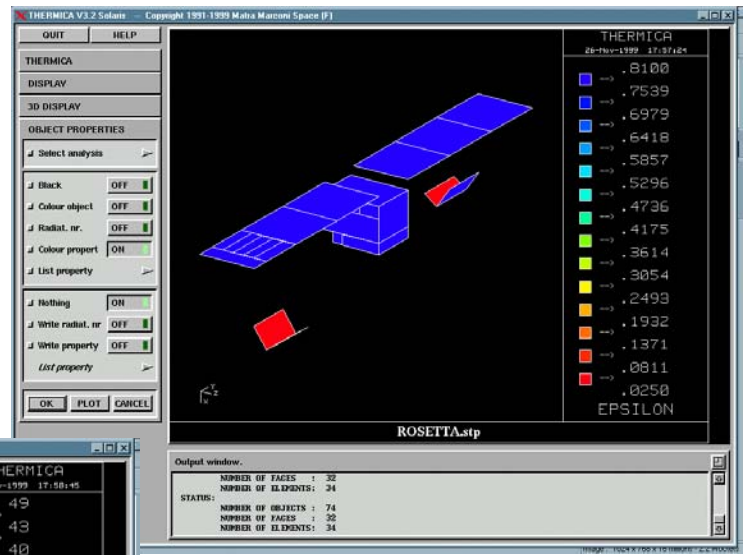

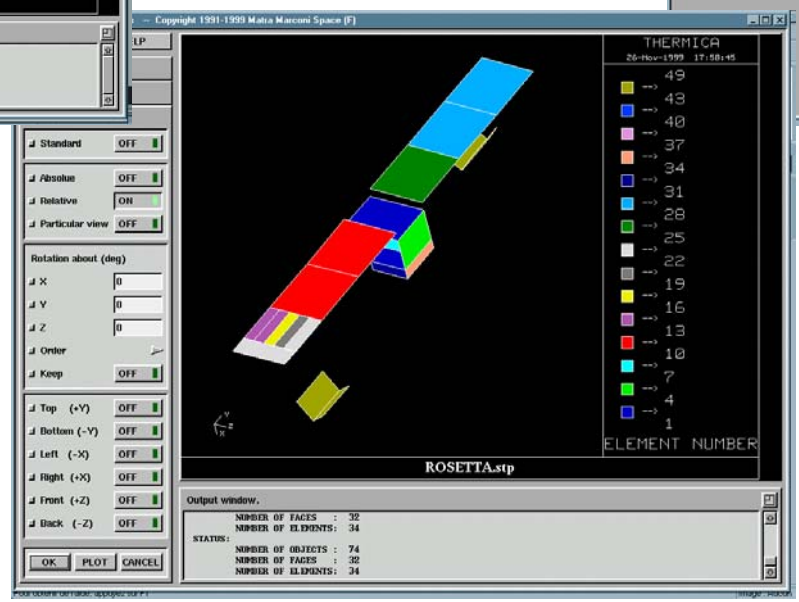

Doris in THERMICA

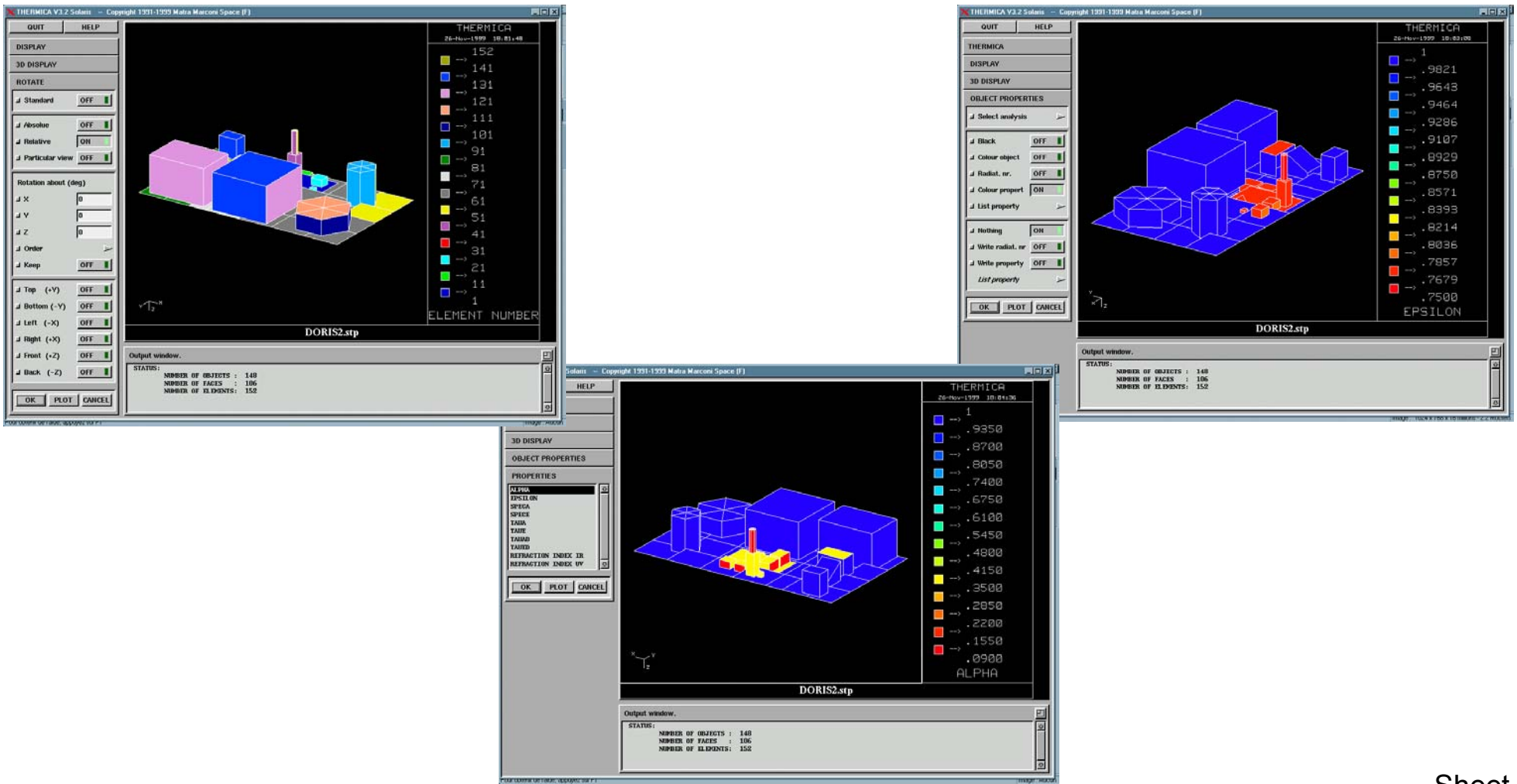

Doris in Baghera-View

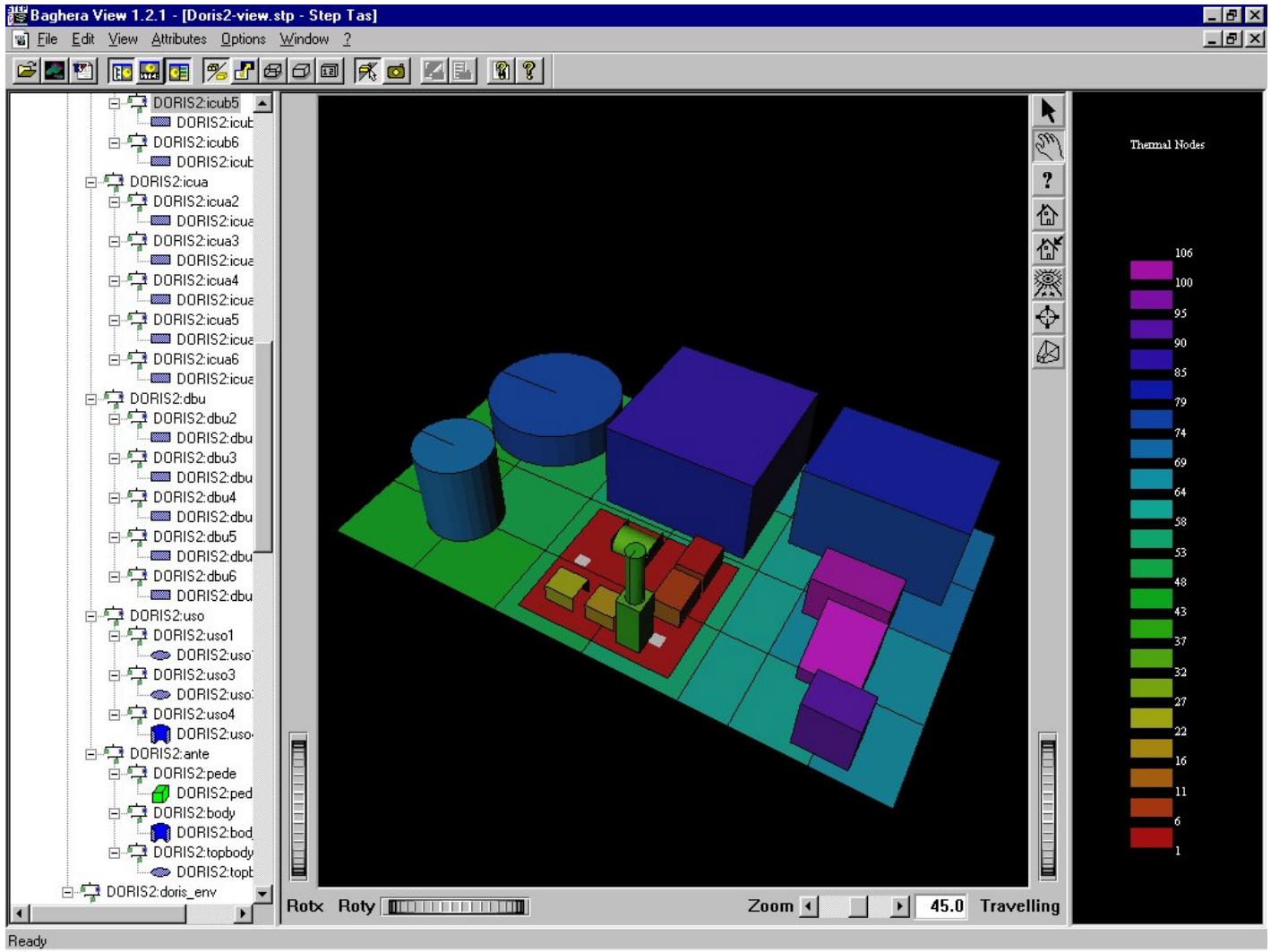

DORIS in ESARAD

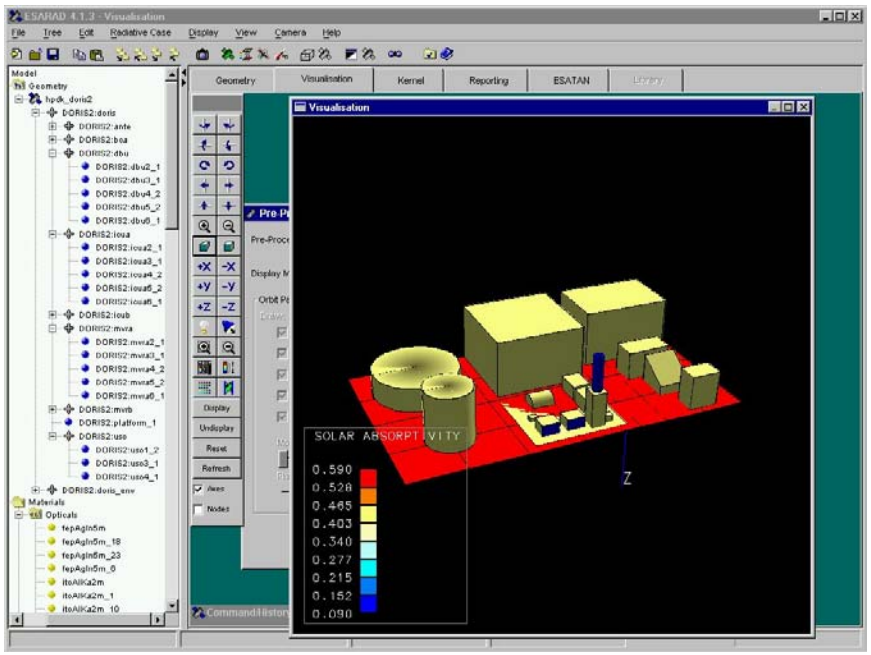

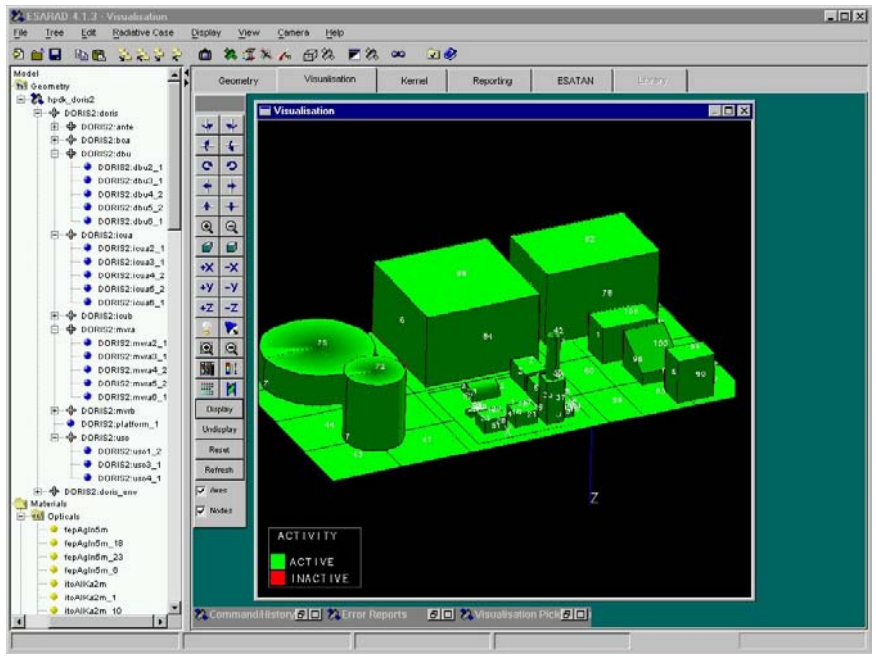

NASA-JPL demonstrator in ESARAD

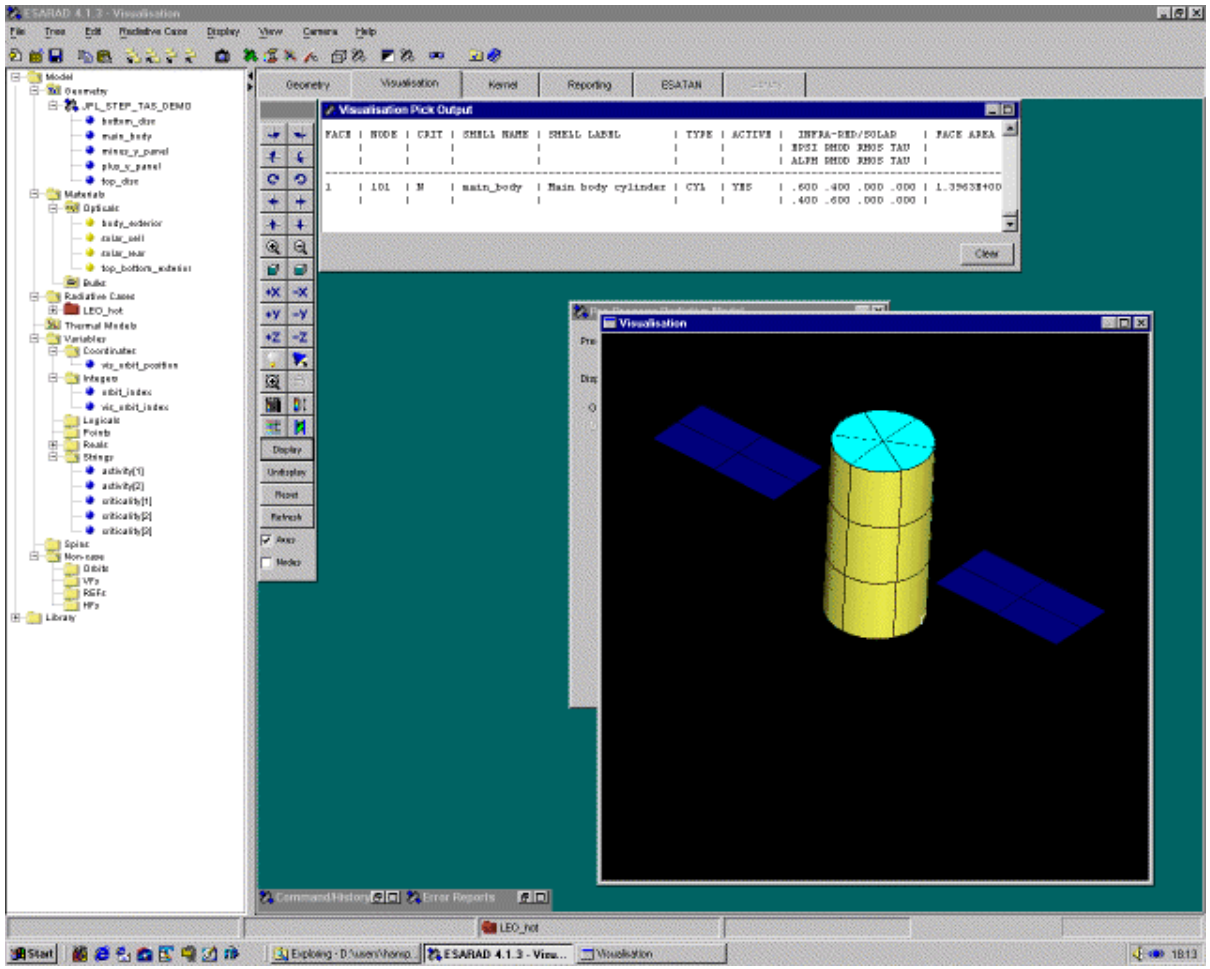


```
ISO-10303-21;
HEADER;
...
#109=TYPE_QUALIFIER('diffuse');
#110=TYPE_QUALIFIER('infra_red');
#111=ATR_PROPERTY_NAME('transmittanc
    e');
#112=ATR_PROPERTY_QUANTITATIVE(#111,
    .SYMMETRICAL.);
#113=ATR_PROPERTY_USAGE(#71,#112,#11
    4);
#114=ATR_PROPERTY_MEANING((#109,#110
    ));
#115=SI_UNIT(*,$,.METRE.);
#116=SI_UNIT(*,$,.DEGREE_CELSIUS.);
#117=GLOBAL_UNIT_ASSIGNED_CONTEXT('
    ,'',(#115,#116));
#118=GLOBAL_UNCERTAINTY_ASSIGNED_CON
    TEXT('','',(#119,#120));
#119=UNCERTAINTY_MEASURE_WITH_UNIT(L
    ENGTH_MEASURE(1.E-008),#115,
...
```

Details available at ftp://ftp.estec.esa.nl/pub/yc/step/JPL_STEP_TAS_DEMO/index.htm

Lessons learned

- Iterative, incremental development necessary
  - Can not get things right in one go …
- High level programming library very useful
  - Greatly reduces converter development effort
  - Speeds up standard penetration & increases exchange reliability
  - Chosen API close to old SET-ATS interface needs reconsideration
- Continuous resource / funding level is needed
  - To meet vendor expectations by providing timely support and library updates resolving SPRs
- Communication must be improved
  - Start a ‘STEP-TAS implementors forum’

Road Ahead (1)

- Web-based collaboration on further development:
  STEP-TAS Implementors' Forum
  - ftp://ftp.estec.esa.nl/pub/step-tas/index.html as a start
  - Will use sourceforge.net open source software development set-up for distribution of documentation and code, bug tracking, configuration control, test suite(s) - start 2001/Q4
  - E-mail tech support
- Take European / US collaboration to a next stage
  - Action ESA and NASA together with Simulog
  - Clarify/establish intellectual property rights and support

Road Ahead (2)

- Trade-off for best 'Return on Investment' next 5 years
  - Appropriate level of formal publishing (ISO, ESA and NASA)
  - Much simplified ARM based exchange
  - Start support of XML physical file (STEP part 28)
  - Upgrade high level API to support all STEP-TAS constructs
    - e.g. submodelling, non-uniform meshing and node numbering
- Upgrade STEP-TAS Converter Development Toolkit
  - Resolve all reported issues / bugs
  - Use open source software approach
- Upgrade converter options
  - Consistently support length unit selection / conversion

Road Ahead (3)

- TRASYS/STEP-TAS-CC1 bi-directional converter
  - Stand-alone tool by Simulog on ESA funding
  - Will be made available freely
- Upgrade BagheraView capabilities
  - By Simulog sponsored by CNES
  - Release v1.3 beta ready 5-Sep-2001 (supports Windows 2000)
- Revive NRF developments
  - HDF5 binding (co-operation with EDF, NCSA and others)
  - Assess links with Engineering Analysis modules, ISO 10303-50
  - Pilot web-based remote consultation of structural test results

Acknowledgements

- STEP-TAS and STEP-NRF were developed under ESA contract by an industrial consortium consisting of
  - Simulog (F, prime)
  - Fokker Space (NL)
  - Association GOSET (F)
  - Epsilon Ingénierie (F)
  - Alstom Power (UK)
- Special acknowledgement to Georg Siebes of NASA-JPL who is and has been the driving force for the development and acceptance of STEP-TAS in the US

USE OF THERMPLOT SOFTWARE FOR QUICK EVALUATION OF THERMAL MODEL RESULTS

Hume Peabody
Swales Aerospace
5050 Powder Mill Road
Beltsville, MD 20705

Abstract

Recently, advances have been made in graphical displays of thermal modelers, allowing color contour temperature plots and animations. While these are useful for presentations, they do little to help debug or identify areas of a model that may be out of design limits. Often, a thermal engineer needs hard data for analysis or debugging.

Swales Aerospace has developed a tool called ThermPlot that runs in the familiar Windows environment. ThermPlot reads output files from many of the popular thermal analysis packages (SindaFluint, Sinda/G®, ESATAN, TMG) and stores the data in a Microsoft Excel® workbook. This allows the user access to ***all*** time dependent thermal data for post processing, rather than a simple plot or image.

Features included in ThermPlot are: inclusion of node descriptions from thermal model file, multiple file capabilities for trend studies and comparisons, creation of tables and plots of selected data, grouping of nodes, and generation of post run-time calculated heatmaps. Once the desired options have been selected, the data is read from the thermal model output files and written directly into an Excel® workbook. Tables and plots are also created in the workbook as defined by the user. The user is also free to perform any additional analysis using the wide range of functions offered in Microsoft Excel®.

This paper describes the features of ThermPlot in greater detail. It also provides some examples of real-world applications where use of ThermPlot resulted in quicker data reduction and analysis of model conversions, parametric studies, and heat flow analysis.

1 INTRODUCTION

In this age of faster computers and quick information transfer, the trends have been towards larger, more detailed models and shorter project timelines. With many thermal solvers actually creating models, including conduction and radiation effects, it becomes more difficult for the thermal analyst to fully understand a model's behavior. Combined with a customers desire for results in a shorter amount of time, it can be a quite daunting task to process vast quantities of data to isolate the relevant data subset. Unfortunately, as the thermal solvers have gotten more advanced, the same cannot be said for the post-processing tools.

ThermPlot is a post-processing tool developed by Swales Aerospace to allow a thermal analyst to quickly take output and select the most crucial pieces of data for evaluation. While each company may have particular scripts and utilities to process data, none offer the power and simplicity of ThermPlot. It creates an interface between many popular thermal analysis solvers and Microsoft Excel® by reading data from the standard output routines from the thermal solver output and storing it on a worksheet in an Excel® file. It also has the capabilities to create customizable tables and plots of pertinent data. Combined with its abilities to process multiple files, it is an ideal tool for analyzing results from parametric studies. But perhaps its most powerful option is the ability to create interactive heatmaps within Excel® which allow the analyst to evaluate not only the temperature of critical nodes, but also the heat paths connected to them. ThermPlot can greatly reduce the time required to evaluate thermal model results thereby, allowing the thermal analysts to quickly respond to a customer's needs or questions. Figure 1 shows the main screen from ThermPlot.

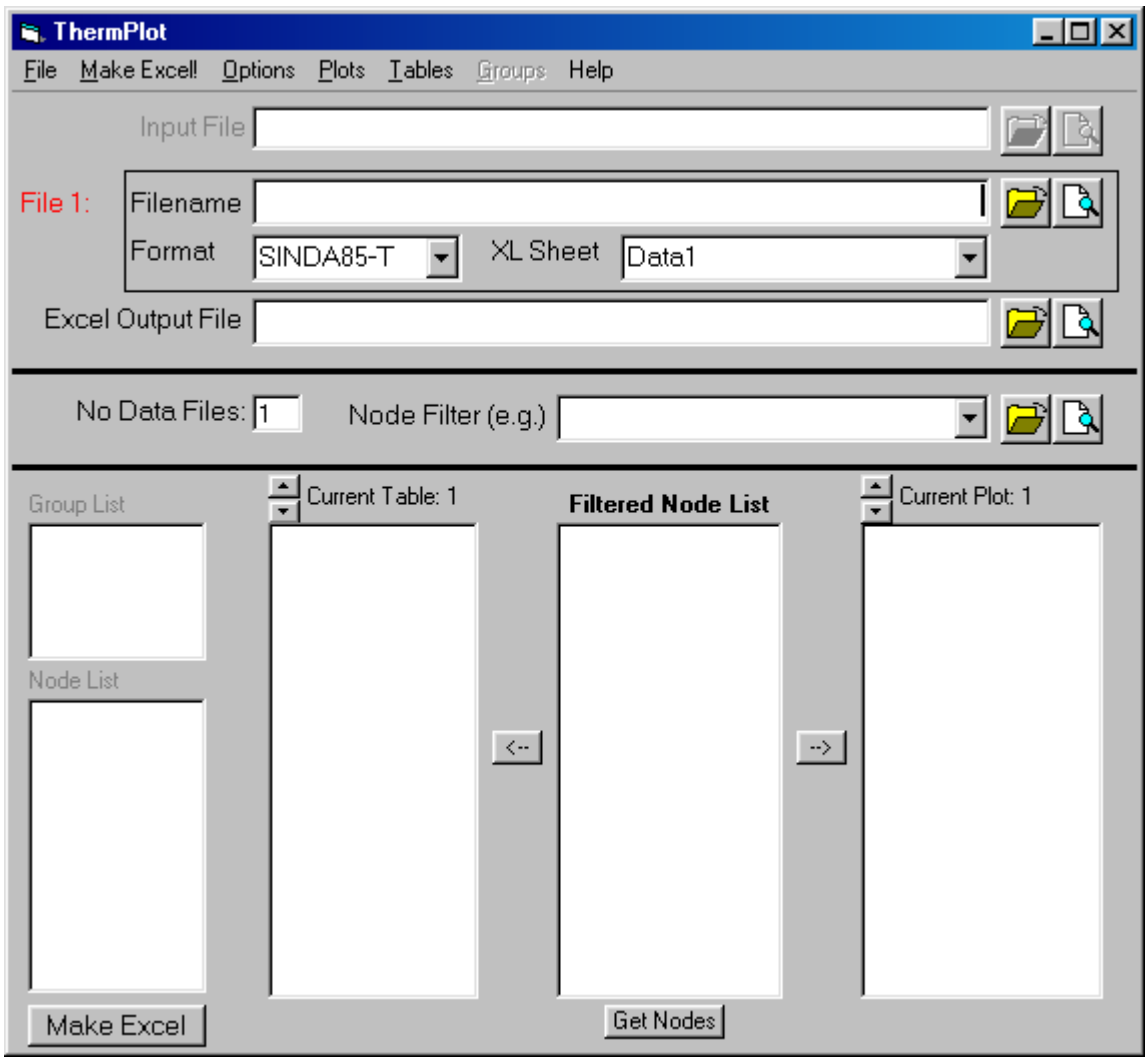

Figure 1 – ThermPlot Main Screen

2 FEATURES

2.1 Formats

ThermPlot supports the following thermal solver packages: SINDA85 (or SINDA/Fluint), SINDA/G®, TMG, and ESATAN. Additional thermal solver formats may be added in the future if demand warrants. Table 1 shows the supported outputs for each solver as well as the required output call within the solver.

Table 1 - Supported Thermal Solvers

Solver	Parameter	Calling Command	Format Selection	Comment
SINDA-85	T	TPRINT	SINDA85-T	
	Q	QPRINT	SINDA85-Q	No Time header is printed*
	G	GPRINT	SINDA85-G	No Time header is printed*
SINDA/G®	T	TPRINT	SINDA/G-T	
	Q	QIPRNT	SINDA/G-Q	No Time header is printed*
	G	GPRINT	SINDA/G-G	No Time header is printed*
	C	CPRINT	SINDA/G-C	No Time header is printed*
	C(Q)	QFPRNT	SINDA/G-C(Q)	Heat flow through conductor
ESATAN	T	PRNDTB	ESABLK-T	
	Q	PRNDTB	ESABLK-Q	Sum of QS, QA, QE, QI, QR
	QS	PRNDTB	ESABLK-QS	
	QA	PRNDTB	ESABLK-QA	
	QE	PRNDTB	ESABLK-QE	
	QI	PRNDTB	ESABLK-QI	
	QR	PRNDTB	ESABLK-QR	
ESATAN	T	PRNDBL	ESATBL-T	
	Q	PRNDBL	ESATBL-Q	Sum of QS, QA, QE, QI, QR
	QS	PRNDBL	ESATBL-QS	
	QA	PRNDBL	ESATBL-QA	
	QE	PRNDBL	ESATBL-QE	
	QI	PRNDBL	ESATBL-QI	
	QR	PRNDBL	ESATBL-QR	
TSS	Heat Load/Flux	HeatRate	TSS-HRT	
TMG	T		TMG-T	Tempf file
	Q		TMG-Q	Qnodef file
Generic CSV			GEN. CSV	Comma Delimited
Generic SDF			SPC DELIM	Space Delimited

** ThermPlot requires that the time header be printed for each timestep. This is not done for the highlighted commands. Therefore, if **only** a GPRINT is called, the data may not be processed correctly.*

2.1.1 Multiple Files

One useful feature of ThermPlot is the ability to post process multiple output files for comparison. Multiple output files may be compared using Tables in various ways. Two common comparison styles are: (1) compare the same parameter (e.g. Min, Max, etc) for multiple cases (Compare Results) or (2) compare cases based on the specified parameters (Multiple Cases). This is discussed in greater detail in Section 2.4.1. Multiple files also allows the user to plot data from different sources (e.g. thermal vacuum data versus model data).

2.2 Options

2.2.1 Node descriptions

Often in large spacecraft models, it is difficult to remember which nodes represent which components. As such, thermal analysts often include a comment after the node definition or around a block of nodes. Thermplot allows these values to be read from the thermal model and associated with the corresponding node in Excel®. Two types of node descriptions are included: Block Description and Node Description. The block description refers to the comments before a node definition (e.g. "C MLI Nodes"). The node description is anything after the line comment character ('$' for SINDA and '#' for ESATAN). If no node description is given, the block description is used. The node descriptions are used exclusively in tables.

2.2.2 Filtering of output

At times, the user may wish to output only a subset of the complete data set. This may be accomplished in two ways: only selected nodes may be output or only nodes that meet specified criteria may be output. "Selected Nodes Only" will only output nodes that are (1) Included in a table or Plot, (2) Included in a group (discussed in Section 2.3), or (3) Selected in the Filtered Node List. This is a much quicker algorithm since the search parameters are already known. Conversely, the user may also specify a range of nodes to output. This method requires as much processing time as the default of reading the entire file, since each line must be evaluated to determine if it satisfies the criteria. However, it does provide an easy way to output particular nodes within a specified range. It supports single nodes, ranges of nodes, or any combination thereof. Each criterion should be separated by commas; range start values and end values should be separated by a dash. (e.g. MOTOR.1-MOTOR.15, PANEL.1-15, ELEC.32, 15). If only a node number is specified, the submodel is ignored and any thermal node with the specified node number is included regardless of its submodel.

2.2.3 Update Existing Data

A user may have defined a particular format or style for an existing spreadsheet and wish to retain it (e.g. plot style, table formats, etc). Assuming the data on the data sheets remains in ***exactly*** the same format, it is possible to update only the data and bypass the Table and Plot creation phases. This requires the new data to have the identical order of nodes and timesteps to assure that formulas apply to the correct cells. If a node type in SINDA is changed (e.g. from diffusion to boundary or arithmetic), this may change the output order of the nodes. If the data location has been modified (i.e. column or row inserted, etc) the formulas may no longer apply to the correct cells.

2.2.4 Transpose Output

At times, a user may have output for more than 250 timesteps. Due to the 256 column limitation in Excel®, it is impossible to have more than 256 timesteps **and** nodes. If the user requires more than 250 timesteps (or 247 if using groups) to be output, the data may be transposed such that each row represents a timestep rather than the default of each column. However, unless the model contains less than 255 nodes, a subset of less than 256 nodes must be selected using the filtering options (discussed in Section 2.3.2) or nodes beyond the 255th will be truncated.

2.2.5 Unit Conversion

Data from different models may not be in units compatible for direct comparison. ThermPlot provides the capability to convert the data from one unit system to another so that direct comparisons may be made. Time, Temperature, Heat and Flux conversions are provided for the most commonly used systems of units. Table 2 lists the units that are supported; any one of these may be converted to another for a given parameter. The conversion is done through a formula for each cell so that the original output value is preserved.

Table 2 – Supported Units for Conversion

Parameter	Units Supported
Time	s, min, hr
Temperature	°C, °F, K, R
Heat	W, J/min, BTU/min, BTU/hr
Flux*	$/cm^2$, $/m^2$, $/in^2$, $/ft^2$

** To convert a heat flux, both the heat conversion and flux conversion must be selected*

2.3 Groups

Detailed models typically have many more nodes to represent components that may be more simply modeled in a reduced model. It can be difficult to directly compare results from the two models. To simplify this comparison, the average temperature (or total heat load) may be calculated for a selection of nodes. These are referred to as Groups in ThermPlot.

Groups can be very useful when comparing a bulk temperature or total heat applied for a region or component in a detailed model to the equivalent section in a reduced model. Groups are also very useful when combined with the heatmap option as they allow the user to quickly see what areas have an effect on the node or group of interest. Heatmaps are discussed in detail in Section 2.7.

2.4 Tables

Commonly, tabular form is the best way to present a concise summary of thermal data. A table of relevant nodes would represent each instrument or major component of a spacecraft. Often the maximum and minimum are of the most interest to determine if the design is within limits. However, sometimes it is also desirable to know the orbit average (from a transient run) or the steady state temperatures as well. The Table Builder allows the user to create tables customized to each analysis. The Table Builder screen is shown in Figure 2.

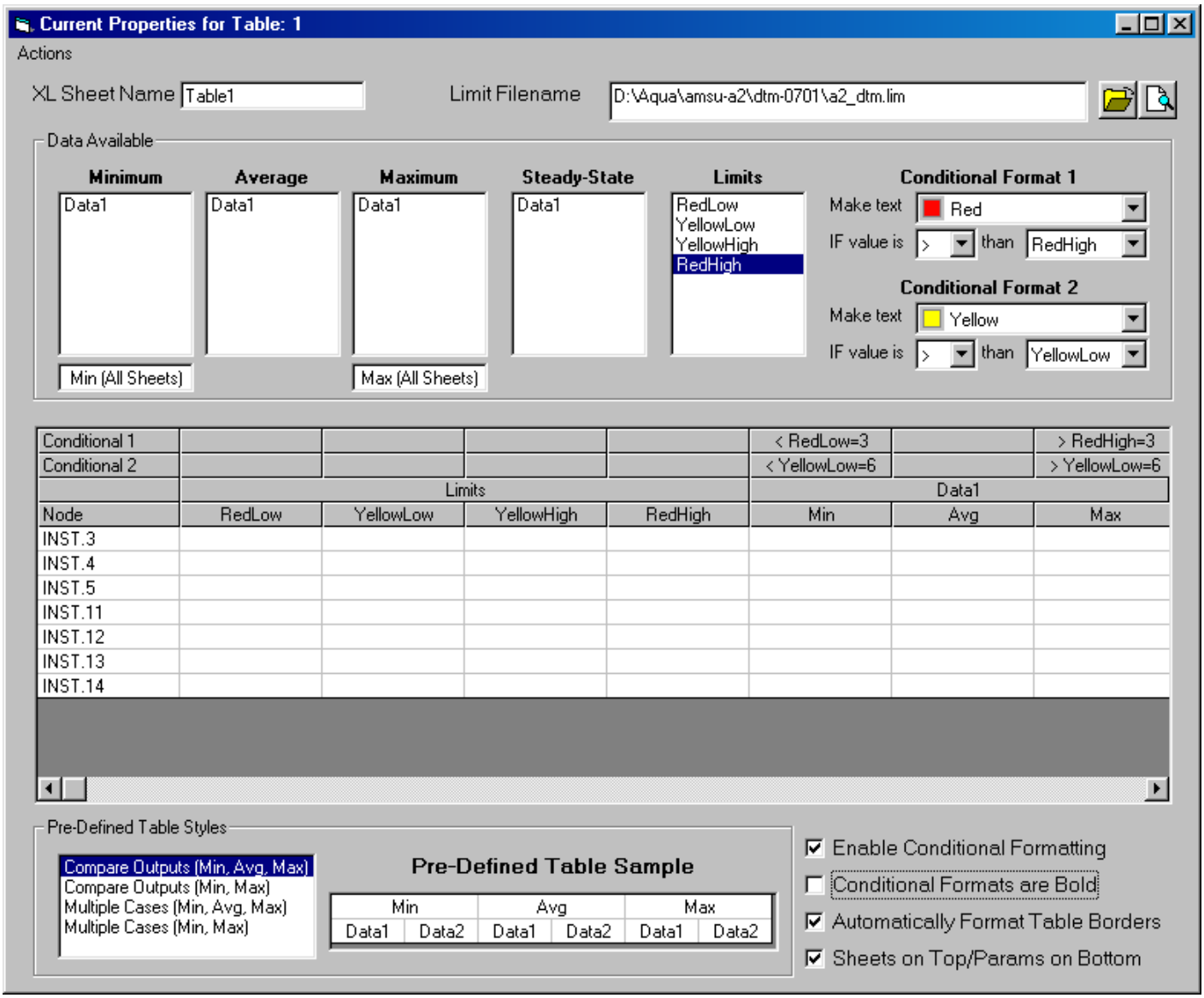

Figure 2 – Table Builder Form

2.4.1 Table Properties

Tables may include any of the following information for any group or node from any dataset (i.e. sheet): minimum, average, maximum, or steady-state value. The minimum, maximum, and average values are calculated over the last orbit defined as follows: the range over which the timesteps are continuously increasing. For example, a model run for ten, 6000 second orbit periods starting at TIMEO=0 and TIMEND=60000 would calculate the values over the entire 60000 seconds. Conversely, a model run for ten, 6000 second orbits with each orbit starting at TIMEO=0.0 and ending at TIMEND=6000, would calculate the value over the last 6000 seconds only. The user may define any combination of parameters (e.g. Min, Max, etc.) and datasets (i.e. sheets) for each table by simply double clicking a single selection from the appropriate list box or by Alt-Dragging a selection to the table Preview.

Some predefined table styles may also be quickly created. The "Compare Results" style is most applicable for thermal model verification after conversion from one format to another, providing quick confirmation that the thermal model in the "new" format provides the same behavior as the thermal model in the "old" format. The "Multiple Cases" is best suited for determining the effects of changing parameters within the model (i.e. heater power, conductance, etc.) This style provides a quick look at specified parameters on a case by case basis. A sample of the "Compare Outputs" and "Multiple Cases" style headings are shown in **Table 3** and **Table 4** respectively.

Table 3 – Sample of Compare Results Table Headings

Min		Avg		Max	
Case1	Case2	Case1	Case2	Case1	Case2

Table 4 – Sample of Multiple Cases Table Headings

Case1			Case2		
Min	Avg	Max	Min	Avg	Max

2.4.2 Table Formats

Limits may also be defined for each node. These should be in an external, comma-separated value file, which is loaded onto a new sheet within the workbook. The user can then add any of the defined limits in the same manner as adding any other parameter. Once a limit has been added to a table, the user may define a highlight format (i.e. color and bolding) based on the value compared to the limit (Conditional Format). For example, values for the Min on sheet 1 may be colored red if they are less than the "RedLow" limit. The borders for the table may also be automatically formatted, with heavier lines dividing similar sheets or parameters.

2.5 Plots

Transient results are often presented in a graphical plot format. Many existing packages provide for this already, ThermPlot included. The user may plot data from various sources (i.e. different files) onto any plot and even mix formats (i.e. T and Q). This may be useful for plotting a heater's behavior and the transient temperature behavior of the sensing node to ensure it is cycling properly. Each data set may be plotted on the primary or secondary axis as desired. Groups and/or nodes may also be plotted together. Excel® supports up to 256 data series of up to 4096 data points each. Each individual plot is stored on a separate Excel® worksheet which can be named by the user. The Plot Properties screen is shown in Figure 3.

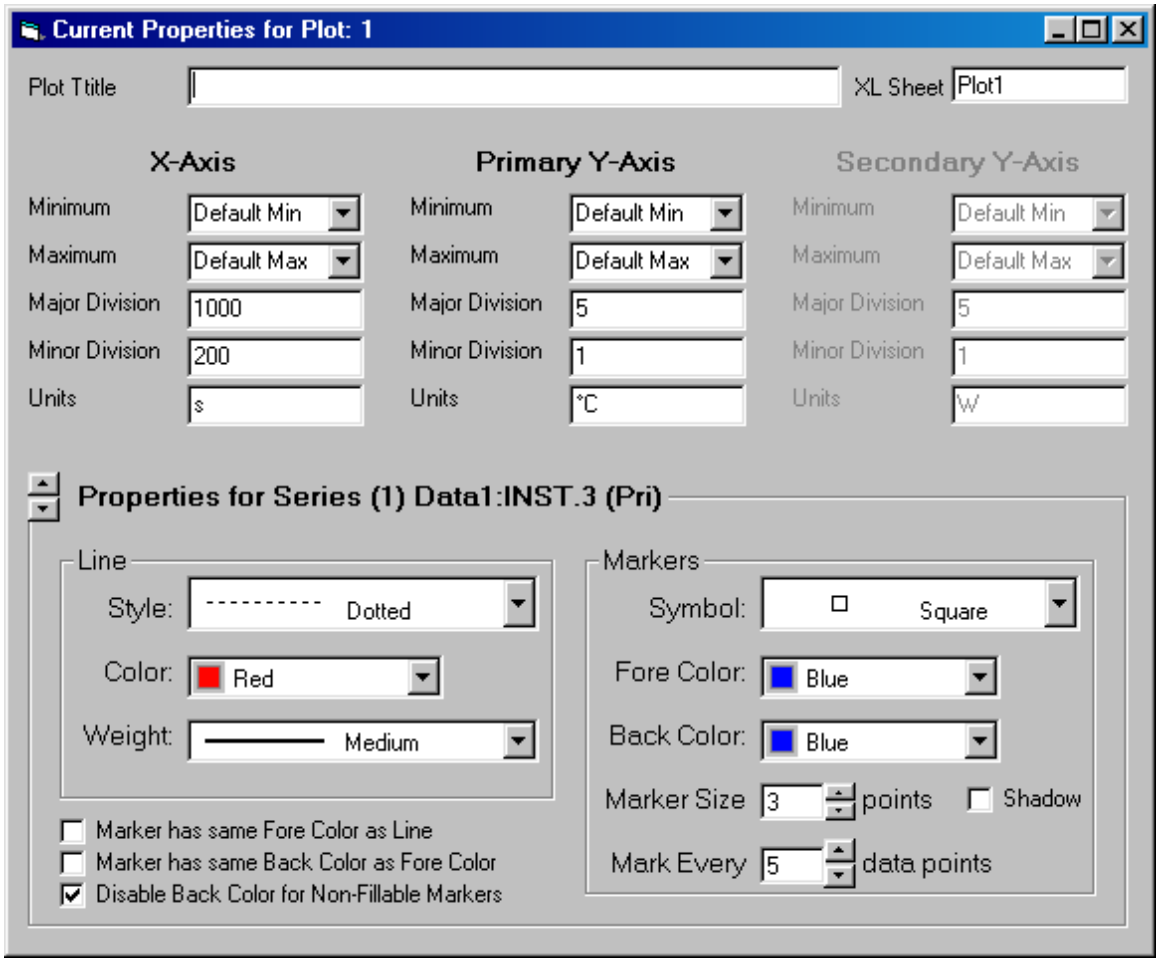

Figure 3 – Plot Properties Form

2.5.1 Plot Properties

The user may define the maximum and minimum values for each axis, as well as the spacing of major and minor gridlines. The Plot Title and axis units may also be specified. If any data series is to be plotted on a secondary axis, the properties for the secondary axis are enabled.

2.5.2 Plot Formats

The user has full control over the line for each data series including both line style and marker style. For the line style, the user may change the color, line type, and weight. For the marker, the user may change the symbol, symbol foreground color, symbol background color (if a fillable marker, e.g. square, circle, but not X or dash), and marker size and shadowing. The user may also determine the data point spacing between markers for dense marker patterns.

2.6 Heatmaps

Perhaps the most powerful feature of ThermPlot is the ability to create heatmaps for an entire thermal model. These heatmaps are calculated at the time of request rather than simply loading in data output from the thermal solver. As such, they require the following information at each output timestep: temperatures, applied heat loads, and conductance values. For SINDA, the conductor node pairs are determined by reading the input file; for ESATAN conductor values are currently read from the ESATAN model input file (i.e. time varying conductances are not yet supported). All of the data is stored on appropriate sheets within an Excel® template, which is then saved as an Excel® workbook. Once this workbook is opened, the user may set appropriate parameters (e.g. Stefan-Boltzman constant, Timestep, etc) for calculation of heatflows. Table 5 shows a sample of the heatmap worksheet along with letters denoting particular sections referenced later.

Table 5 - Sample of Heatmap Table

	Description	OCCULTER TIP			
(A)	**Node i**	COR1.500		**Temp**	143.88
(B)	**Time**	SS		**Time Col**	C
(C)	**Sigma**	5.67E-12	*(E)*	**Min Heat**	0.0005
(D)	**Toffset**	273.15	*(F)*	**Heat to**	Node

(G)	**SUMMARY:**	**In**	**Out**
	Conduction	0.000	0.234
	Radiation	0.000	0.017
	Source	0.252	-
	Sum	0.252	0.251

High (In) to Low (Out):						***Low (Out) to High (In):***					
Description j	**Node j**	**Type**	**Cond**	**Temp j**	**Heat j**	**Description j**	**Node j**	**Type**	**Cond**	**Temp j**	**Heat j**
OCCULTER TOP	COR1.501	Lin	3.86E-02	137.82	-0.23	OCCULTER TOP	COR1.501	Lin	3.86E-02	137.82	-0.23
	COR1.35	Rad	5.67E-02	30.59	-0.01		COR1.15	Rad	6.49E-03	30.57	0.00
	COR1.5	Rad	2.51E-02	30.53	0.00	OCCULTER BAFFLE (LIGHT TRAP)	COR1.600	Rad	2.40E-02	43.44	0.00
	COR1.25	Rad	2.46E-02	30.65	0.00		COR1.25	Rad	2.46E-02	30.65	0.00
OCCULTER BAFFLE (LIGHT TRAP)	COR1.600	Rad	2.40E-02	43.44	0.00		COR1.5	Rad	2.51E-02	30.53	0.00
	COR1.15	Rad	6.49E-03	30.57	0.00		COR1.35	Rad	5.67E-02	30.59	-0.01

2.6.1 Post Run-Time Calculated Heatmaps

Because the heatflows are calculated for a user specified (variable) timestep, massive amounts of heatflow data need not be stored in the thermal model output file (i.e. QMAP, QDUMP,etc). Upon changing the timestep *(B)*, the worksheet will calculate the entire set of heat flows for all node/group interactions for the selected timestep, Stefan-boltzman constant *(C)*, and absolute temperature offset *(D)*. Models with hundreds of thousands of conductor can quickly create workbooks that may exceed limitations in Excel®. The heatmap option currently supports 131066 [(65536 rows – 3 header rows) x 2 worksheets] conductors. If demand warrants, additional conductor capability may be added.

2.6.2 Heatflows between Nodes and/or Groups

Heat flow between nodes and groups may be displayed for any of the following combinations: node-to-node, node-to-group, group-to-node, and group-to-group. The option is determined by combining the "Heat to" selection *(F)* with the Node/Group entered by the user *(A)*. Once the user has entered a node or group name for "Node i", the worksheet will output all nodes/groups connected to the specified node/group, the description for the node, the conductance value, the temperature of the adjoining node, and the heat flow through the conductor. The data will then be sorted from High to Low (i.e. In to Out where heat in is defined as positive). The data will be repeated on the right side of the spreadsheet and sorted from Low to High. The temperature and description of the specified node/group will also be calculated. A summary of the node/group heat balance is provided in the upper right including total heat flow in and out by conduction and radiation, the heat applied to the node and the overall balance *(G)*.

2.6.3 Show only relevant heatflows

For large models with thousands of nodes, many heat paths to a single node can exist. However, many of these may contribute negligible amounts of heat to the node. A "Min Heat" setting *(E)* allows the user to specify a minimum threshold value to be output; anything less than the threshold will not be displayed. This eliminates negligible heat paths from being displayed.

3 APPLICATIONS

3.1 File conversion

3.1.1 Quick comparison of converted file format results

Many projects receive models in formats used by instrument suppliers, which may not be compatible with the software used by the spacecraft contractor. The provided instrument models must therefore be converted to the format used by the spacecraft contractor for incorporation into the spacecraft model. This is an arduous task unto itself, but once converted, it must be assured that the converted model behaves the same as the original model.

The "Compare Outputs" option provides a quick look at the minimum, maximum, and average between various stages of the model conversion. Assuming that each of these parameters is within acceptable errors, it can be concluded that the model conversion is a success.

Table 6 - Sample Table For Model Conversion Comparison

	Min				Avg				Max			
Node #	TMG	SINDA	ESA	RAD	TMG	SINDA	ESA	RAD	TMG	SINDA	ESA	RAD
1	13.1	12.7	13.1	13.5	13.3	12.9	13.3	13.8	13.6	13.4	13.7	14.1
2	13.7	13.3	13.7	14.2	14.0	13.7	14.1	14.6	14.8	14.6	14.9	15.3
3	13.6	13.1	13.6	14.1	13.7	13.3	13.7	14.4	13.9	13.6	14.0	14.7
4	13.6	13.3	13.6	14.1	13.6	13.4	13.6	14.1	13.7	13.4	13.7	14.1
5	13.1	12.9	13.1	13.6	13.1	12.9	13.1	13.7	13.2	13.0	13.2	13.7
6	12.2	11.9	12.2	12.7	12.3	12.0	12.3	12.8	12.3	12.1	12.4	12.9
7	14.9	14.3	14.8	15.6	15.1	14.6	15.1	16.0	15.4	15.1	15.6	16.4
8	15.1	14.4	15.0	15.8	15.3	14.8	15.4	16.3	15.8	15.5	16.0	16.8

3.2 Parametrics

3.2.1 Comparison of effects of changing parameters compared to baseline

Parametric studies are another common task of a thermal analyst. Often exact values are unknown for particular parameters in a model (conductance, heater power, dissipation, MLI effective emissivity). Varying these parameters can create many output files that may be tedious to compare. By using the Multiple Files or Compare Outputs options, the effects of varying these parameters can be quickly established.

For a small satellite, the batteries were predicted to run warmer than allowed. By varying the conductance to the top of the battery box and the emissivity of the top, it was possible to quickly determine the overall effect of each change.

Table 7 - Sample Table for Parametric Case Study

		Min				Max			
Desc	Node #	Case1	Case2	Case3	Case4	Case1	Case2	Case3	Case4
BATTERY 1	HOKIES.1001	38.8	35.7	35.1	35.0	45.1	42.2	41.8	42.4
BATTERY 2	HOKIES.1002	39.0	35.9	35.2	35.2	45.3	42.4	41.9	42.6
BATTERY 3	HOKIES.1003	39.1	35.9	35.3	35.2	45.5	42.4	42.0	42.6
BATTERY 4	HOKIES.1004	39.2	35.9	35.3	35.2	45.5	42.4	42.0	42.7
BATTERY 5	HOKIES.1005	39.2	35.9	35.2	35.2	45.5	42.4	42.0	42.7
BATTERY 6	HOKIES.1006	38.9	35.7	35.1	35.0	45.2	42.1	41.8	42.4
BATTERY 7	HOKIES.1007	39.0	35.7	35.1	35.1	45.3	42.2	41.8	42.5
BATTERY 8	HOKIES.1008	39.1	35.8	35.2	35.1	45.4	42.2	41.9	42.5

3.3 Heatmaps

3.3.1 Analyze heat flow instead of just temperature

For a thermal balance test, a particular instrument component was predicting colder that the instrument provider would allow. This component was a bonded composite/metal junction that was required to remain above –30°C; it was predicted at –50°C. To provide for the safety of the instrument, it was proposed to use the flight cover (instrumented with a heater) to provide a warm view for the component. Thermal analysis revealed that even with 50W of heater power on the cover, the temperature still did not reach an acceptable value.

By using the heatmap option of ThermPlot, it was discovered that much of the heat being added to the cover was simply conducting through the shaft to a nearby radiator for the motor! This path was certainly not evident from the temperatures. This new information led to the introduction of a second heater plate in view of the radiator and resulted in an acceptable temperature for the composite bond. Without knowledge of how the heat was flowing through the model, it would have been difficult to analyze this particular problem.

4 CONCLUSIONS

As models continue to grow in size and complexity, it is a difficult task to understand how a model will behave in a particular set of circumstances. Understanding and identifying the major contributing heat paths is crucial to debugging and understanding the physical behavior of the system. ThermPlot allows the thermal analyst to spend more time analyzing critical areas of a design rather instead of reducing massive amount of data to a subset of importance.

Integrated Turbopump Thermo-Mechanical Design and Analysis Tools

September 12, 2001

Mike Platt

Summary

- Steady and transient thermo-mechanical effects drive life, reliability, and cost
- Design cycle needs upfront consideration of:
  - fits, clearance, preload
  - cooling requirements
  - stress levels, LCF limits, HCF margin
- Data synthesis is needed from component design tools

3242R6 Simplified
CETI

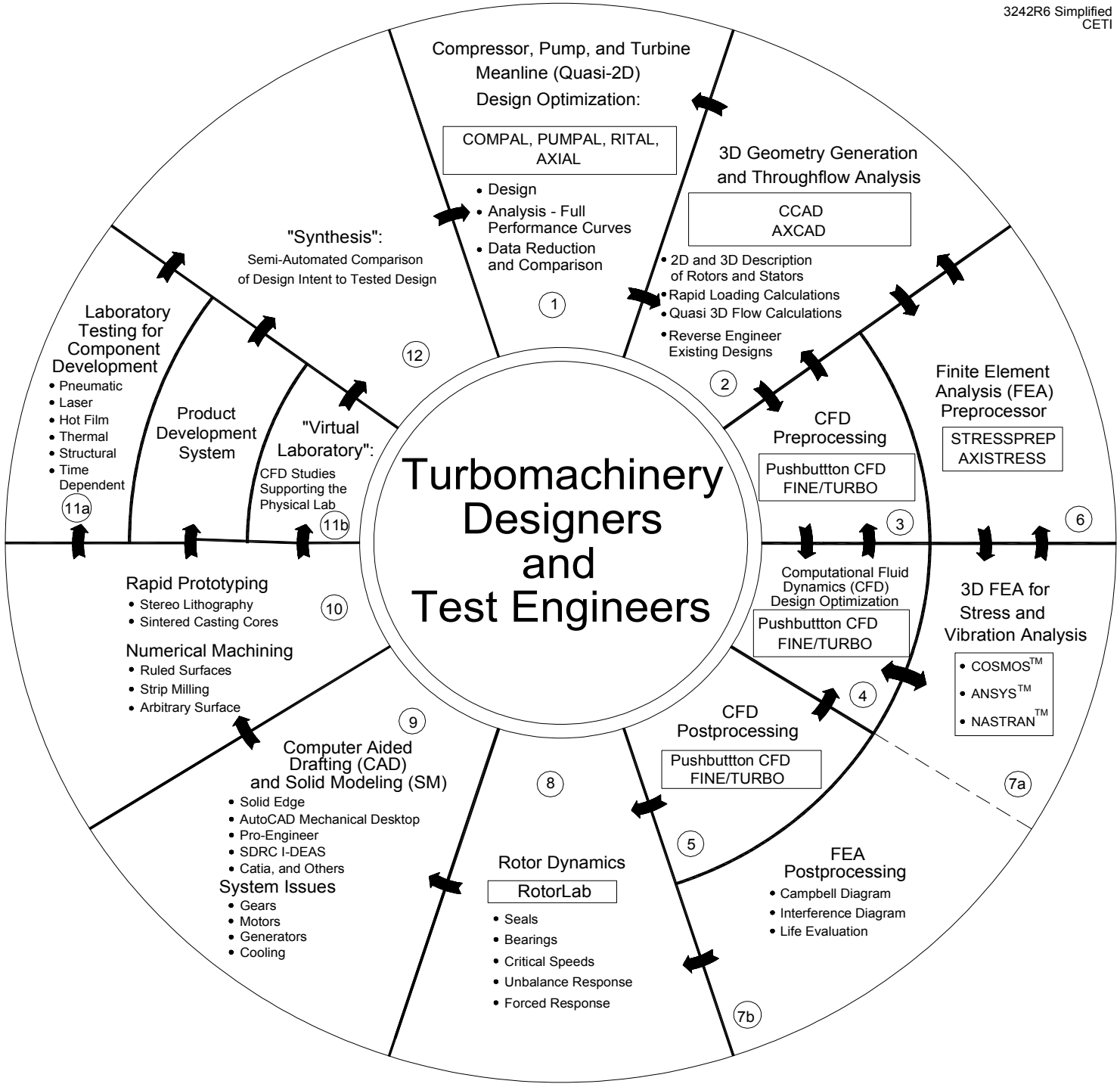

SBIR Tool Development

- Use LNG turbopump design during feasibility study
  - 630 gpm at 29.6 krpm
  - 37 lbm/s

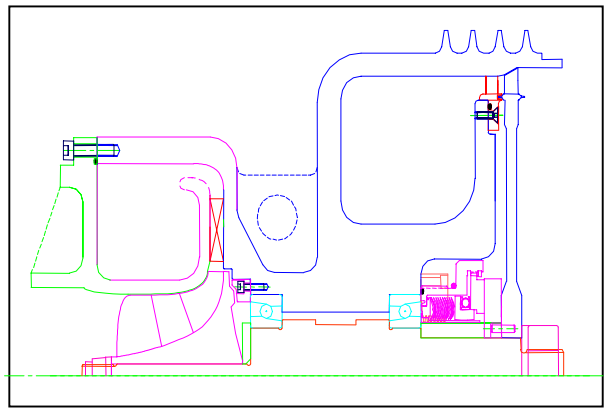

- Utilize existing component analysis tools to drive assembly models
- Integration into collaborative environment, not just interfacing separate tools

Current Design System

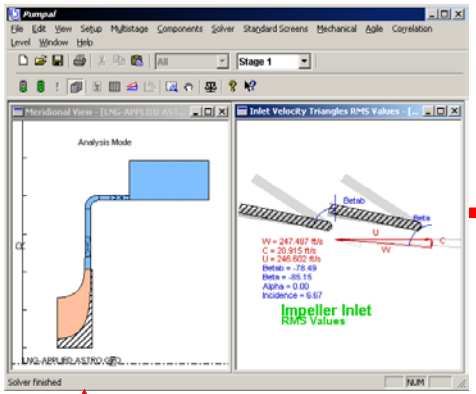

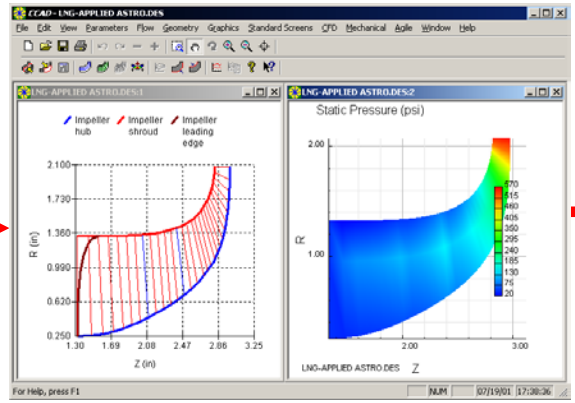

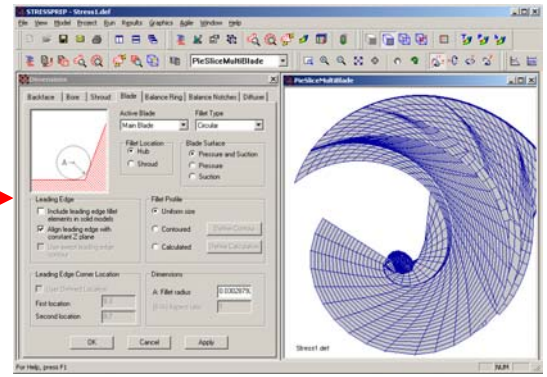

Meanline

3D Blading & CFD

Stress & Vibration

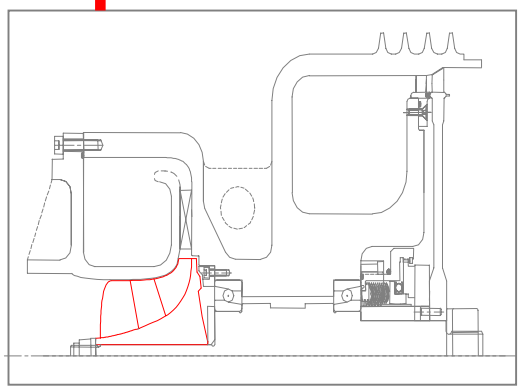

- Captures blade and disk stress, vibration, thermals
- Misses radial and axial preload effects, thermal conduction through bore

Current Design System

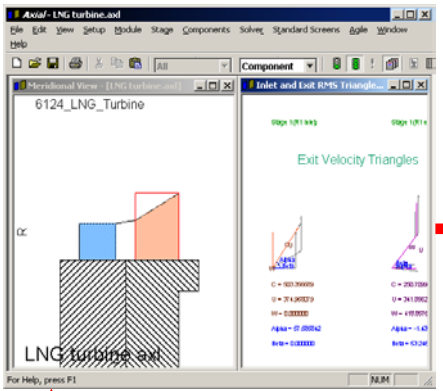

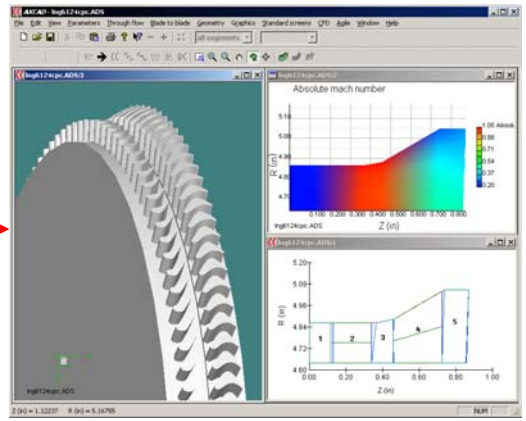

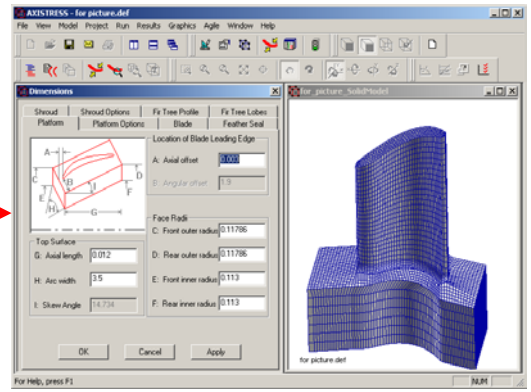

Meanline

3D Blading & CFD

Stress & Vibration

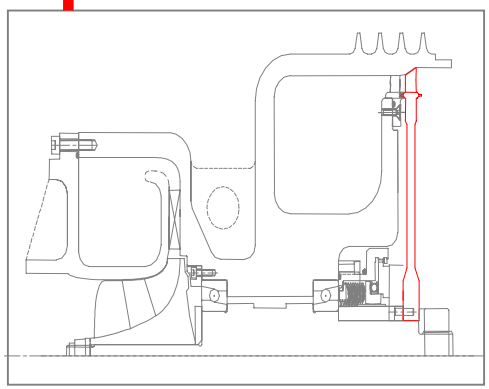

- Captures blade and disk stress, vibration, thermals
- Misses radial and axial preload effects, seal interaction, bore conduction

Current Design System

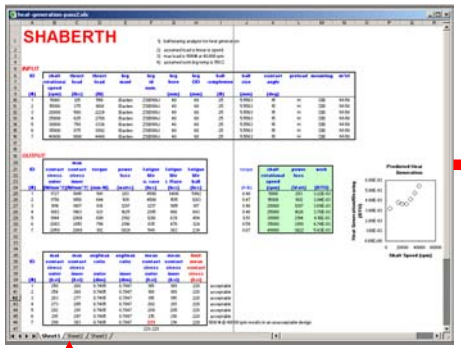

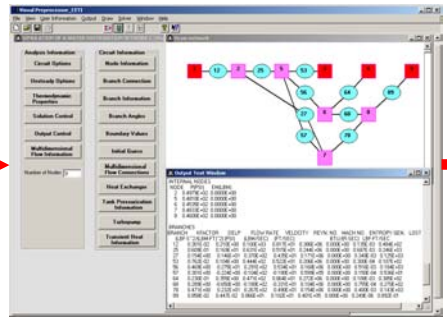

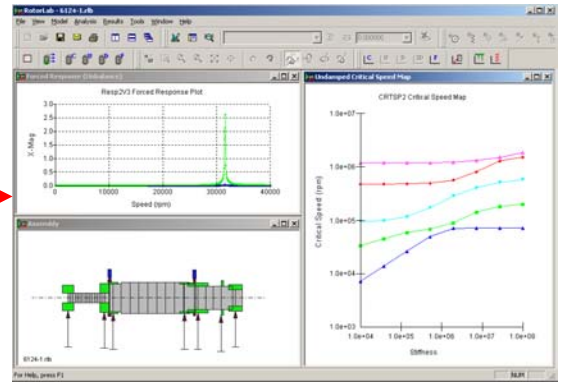

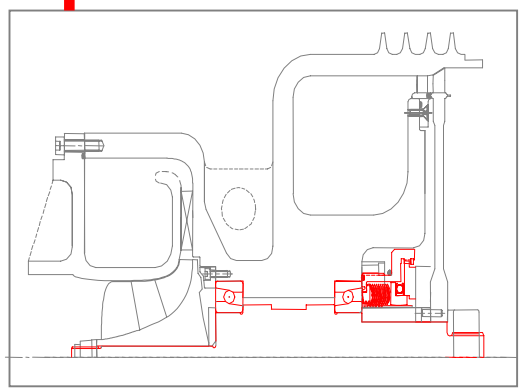

- Captures nominal bearing, seal, and shaft design
- Misses radial and axial preload effects

Thermo-Mechanical Design Tools

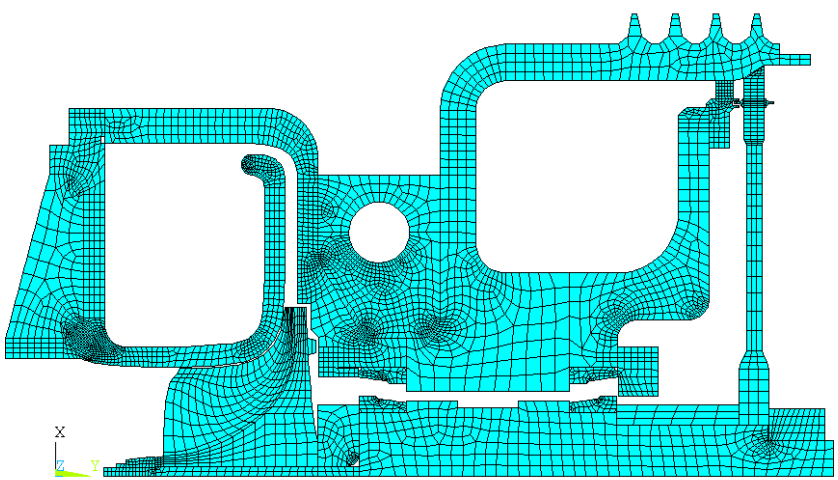

- Utilize data from component design tools
  - Rotor, shaft, housing geometry
  - Primary flow from pump and turbine
  - Internal cooling flow
  - Bearing, seal, and shaft design

Thermo-Mechanical Design Tools

- Temperature, stress, deflection
- Blade clearance, seal clearance, bearing race interference
- Thrust load, bearing preload
- Rotor clamp loads, shaft torque
- Stress results feed probabilistic models

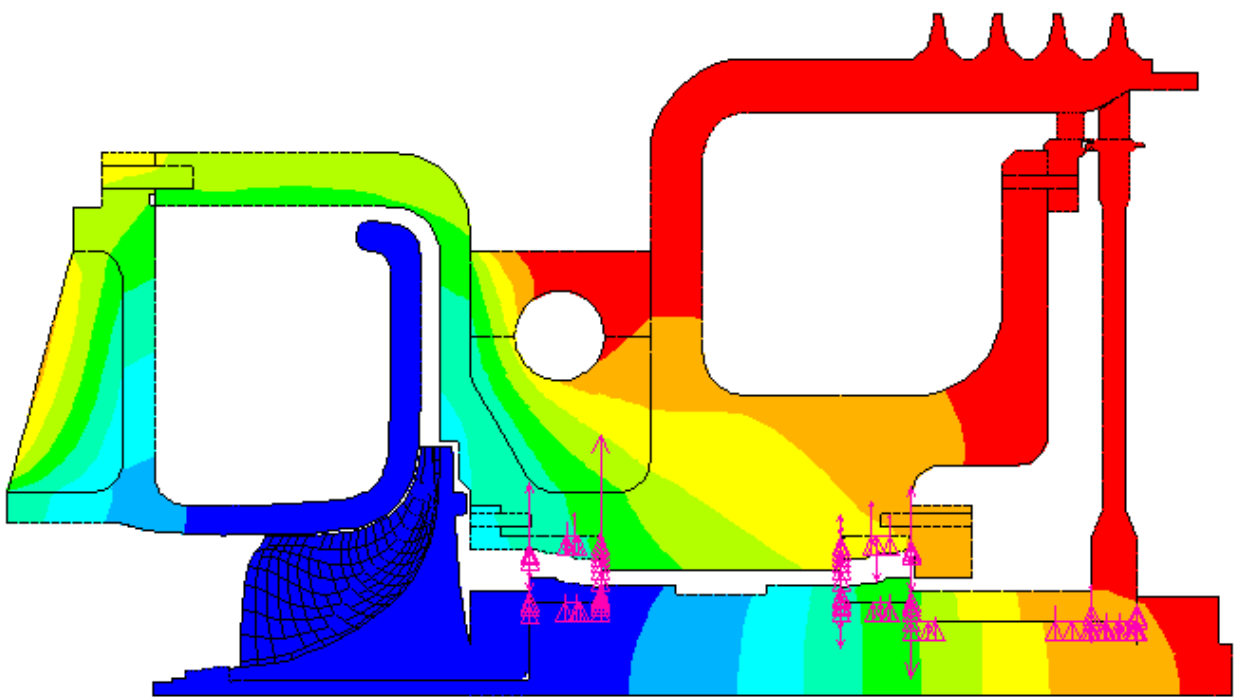

ANSYS 5.6.2
JUN 21 2001
08:03:11
NODAL SOLUTION
STEP=1
SUB =1
TIME=1
TEMP (AVG)
RSYS=0
PowerGraphics
EFACET=1
AVRES=Mat
SMN =-252
SMX =65.195
CE
NFOR

-252
-216.756
-181.512
-146.268
-111.024
-75.781
-40.537
-5.293
29.951
65.195

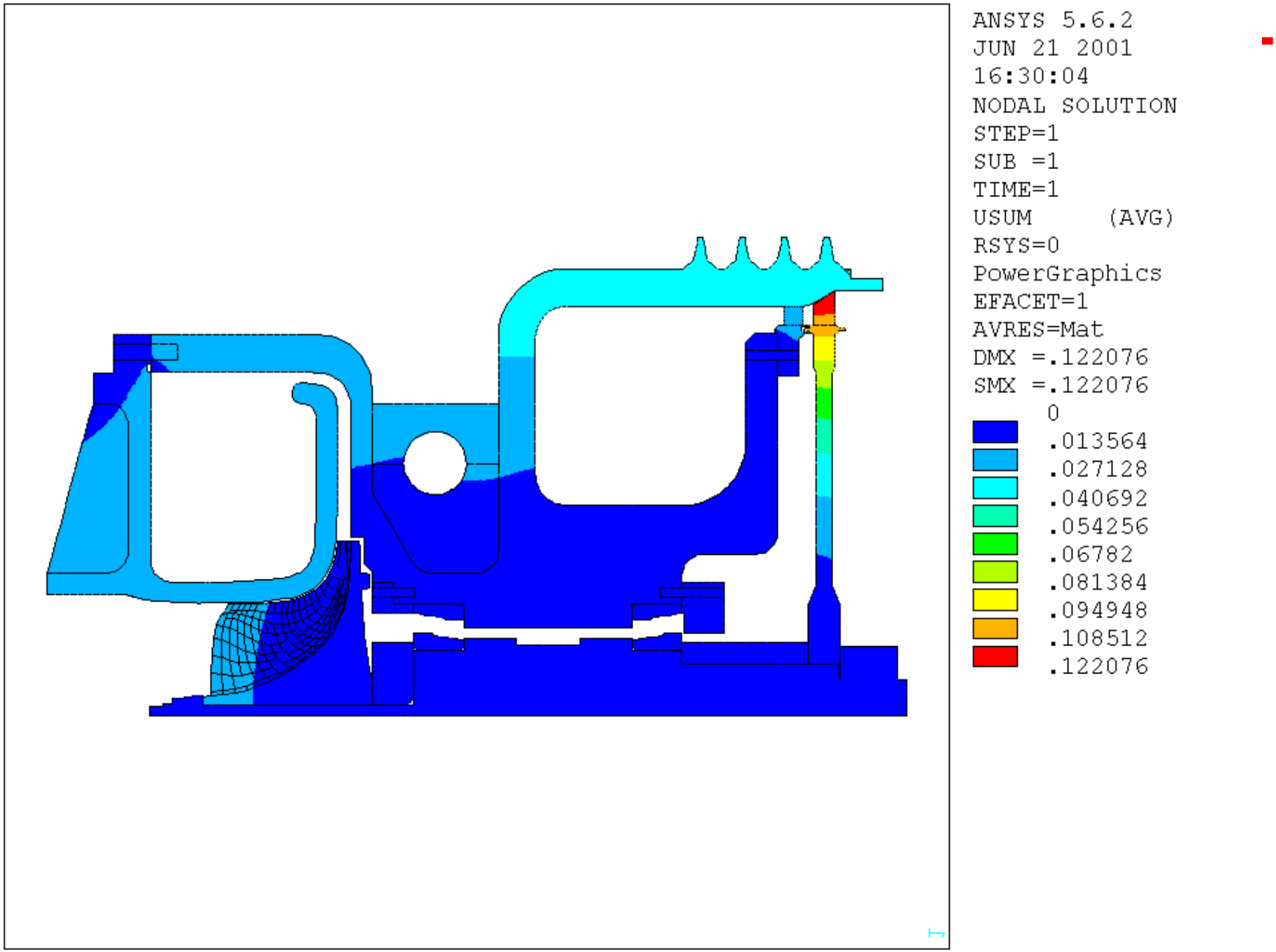
ANSYS 5.6.2
JUN 21 2001
16:30:04
NODAL SOLUTION
STEP=1
SUB =1
TIME=1
USUM (AVG)
RSYS=0
PowerGraphics
EFACET=1
AVRES=Mat
DMX =.122076
SMX =.122076
0
.013564
.027128
.040692
.054256
.06782
.081384
.094948
.108512
.122076

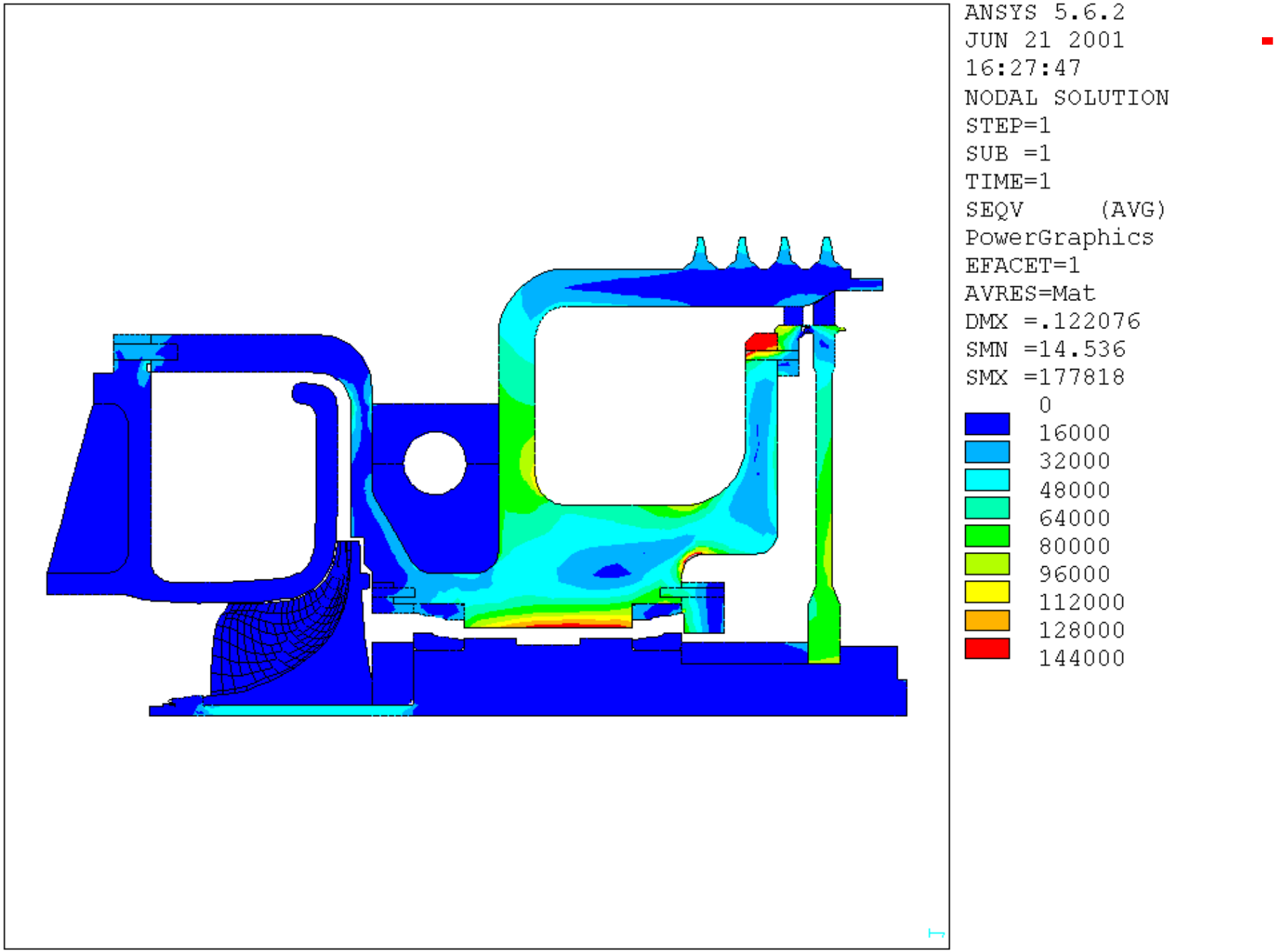
ANSYS 5.6.2
JUN 21 2001
16:27:47
NODAL SOLUTION
STEP=1
SUB =1
TIME=1
SEQV (AVG)
PowerGraphics
EFACET=1
AVRES=Mat
DMX =.122076
SMN =14.536
SMX =177818
0
16000
32000
48000
64000
80000
96000
112000
128000
144000

Life & Confidence Goals

Fixed Confidence Level

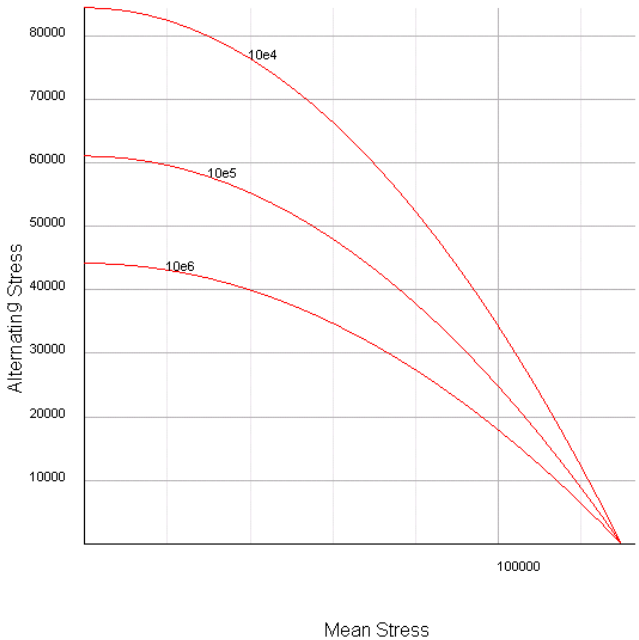

Fixed Number of Cycles

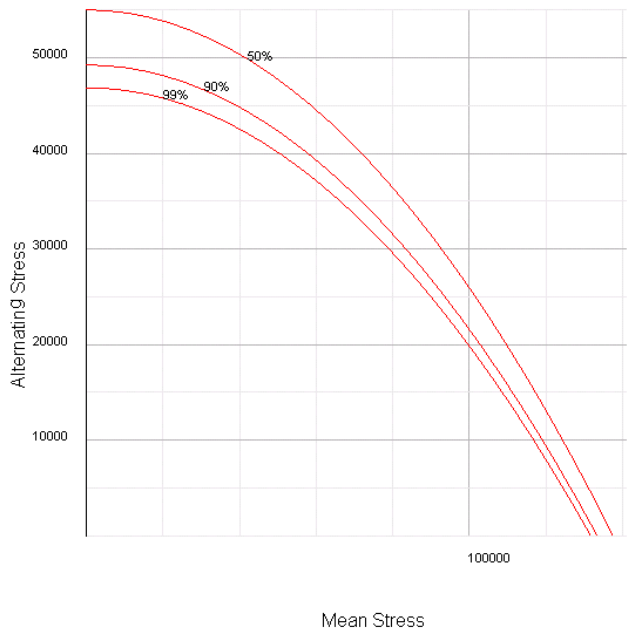

Typical Transient Results

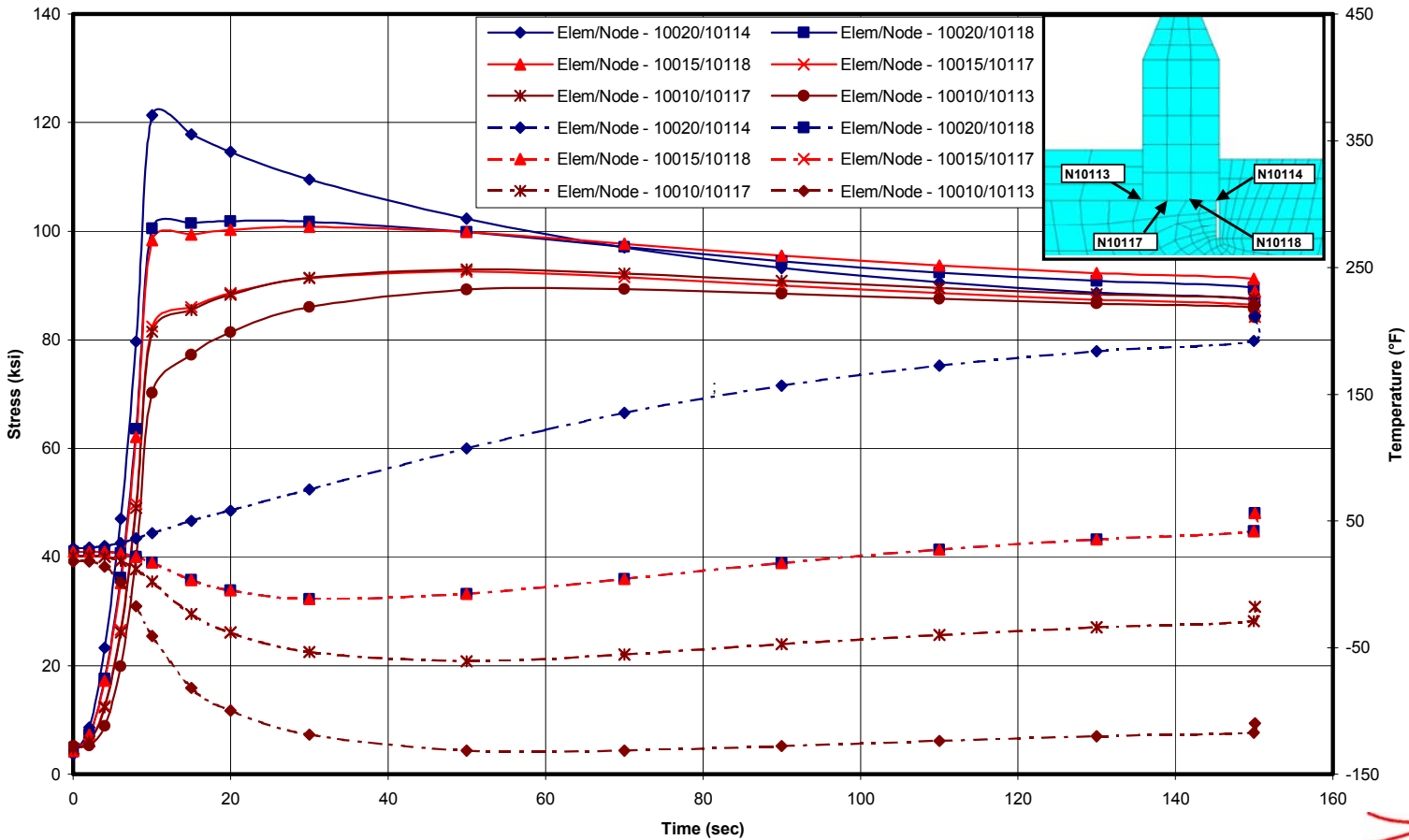

Goals for Design Tool Integration

- Collaborative working environment
- Integrate with existing component design and analysis tools
- Direct data sharing, including CAD files
- Extensible to other solvers and applications
- Preserve intellectual property

Integration with CAD Kernel

- Consistent and open data format
- Combine geometry and analytical results
- Direct support for native CAD files

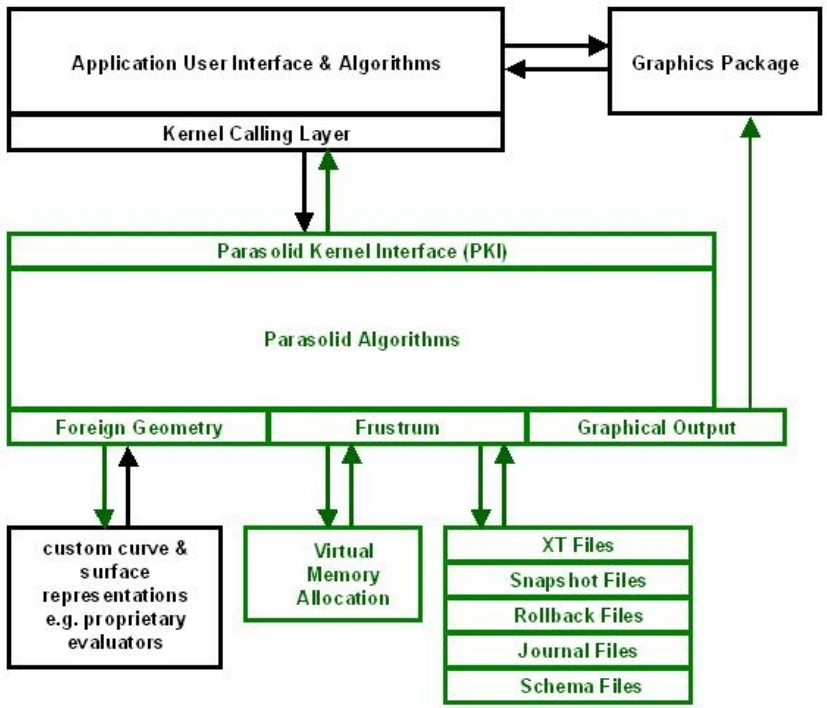

Design Tool Integration

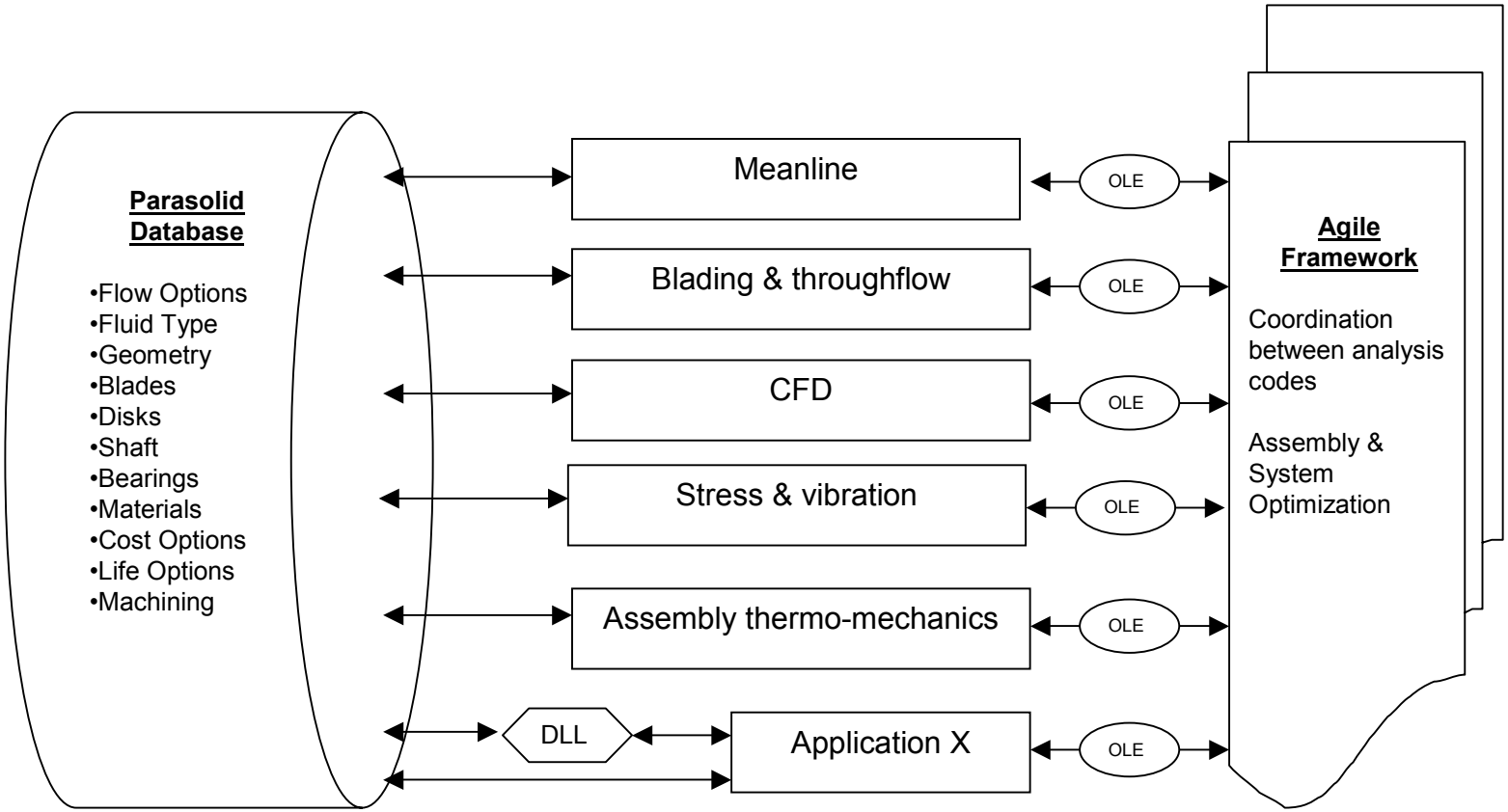

Integration with Parasolid Data

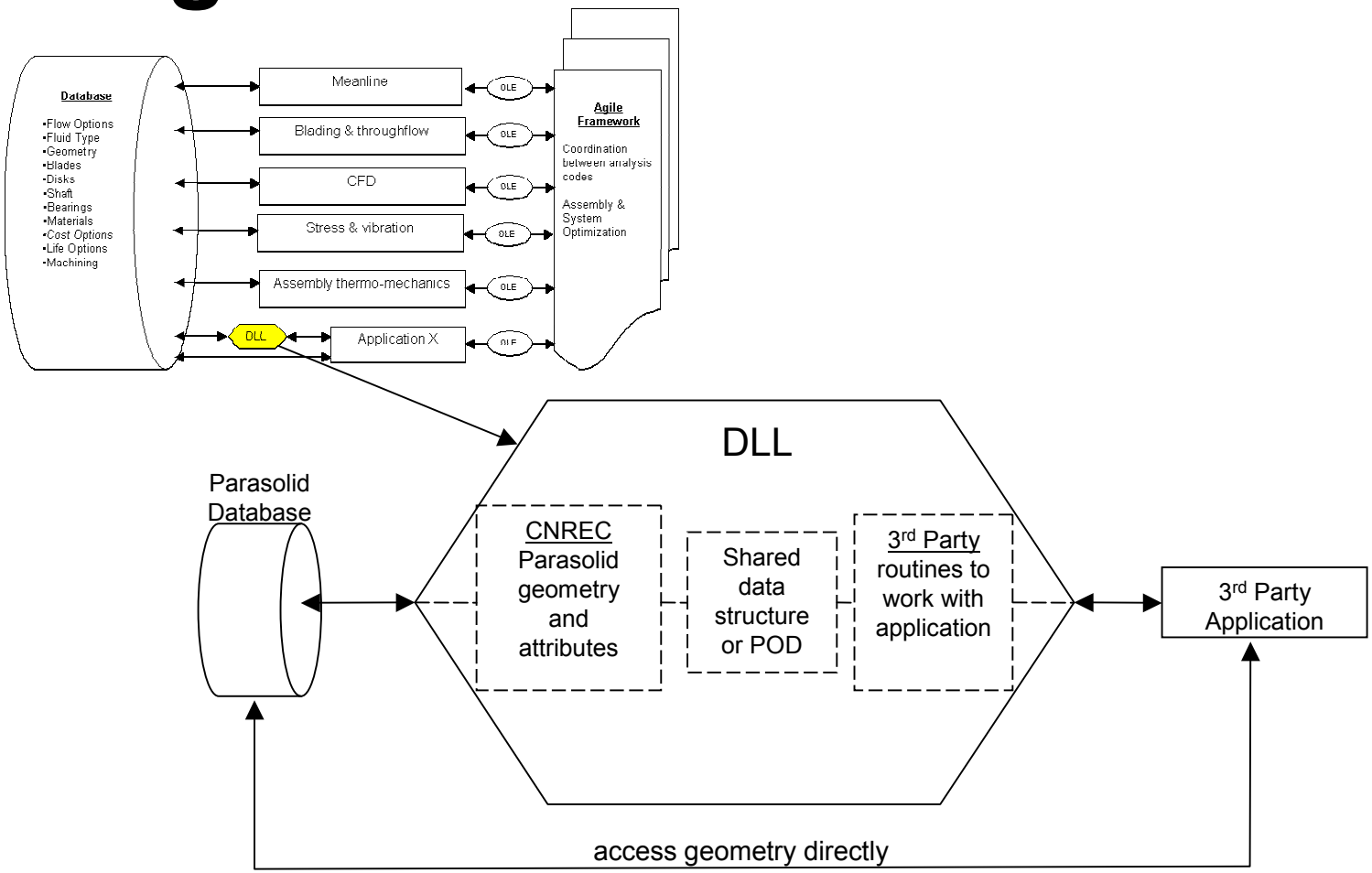

Integration with Design Framework

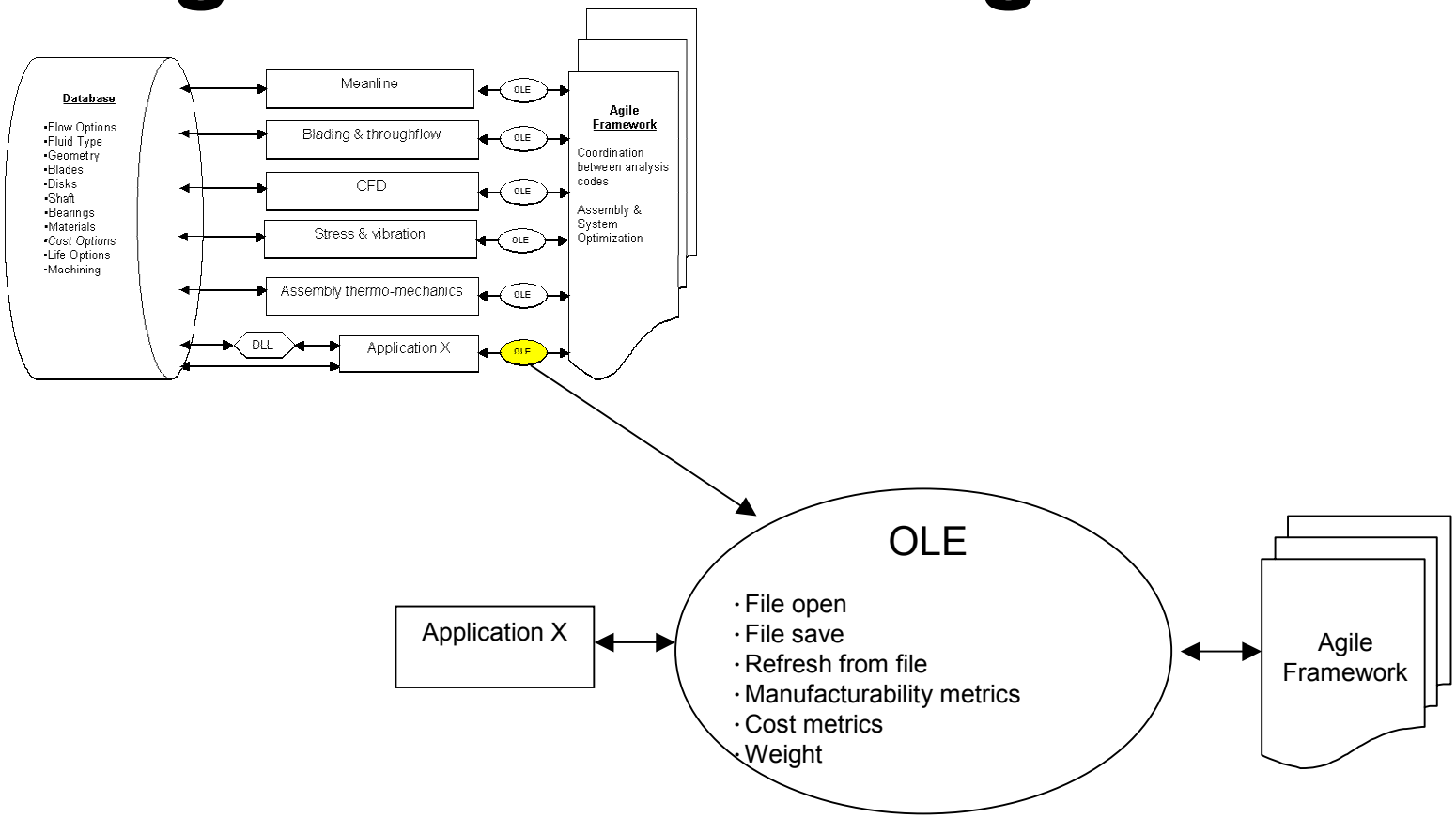

Conclusions

- Thermo-mechanical analysis tool provides upfront design capability
- Existing component design tools are effectively leveraged
- Dual-use capability will give a broad user base
- Parasolid kernel allows collaboration with a wide applications base

How to quickly import CAD geometry into Thermal Desktop

September 13, 2001

Shonte Wright
Jet Propulsion Laboratory
California Institute of Technology

Emilio Beltran
Microsoft Corporation

Presentation Outline

- JPL's Concurrent Design Environment
- Bridging the Gap
- The Import Process
- Model Reduction Methods
- Demonstration
- Acknowledgements

JPL's Concurrent Design Environment

There are several groups at JPL that are committed to concurrent design efforts, two are featured herein

- **Center for Space Mission Architecture and Design (CSMAD):**

  Enables the practical application of advanced process technologies in JPL's mission architecture process

- **Team I:**

  Functions as an incubator for projects that are in the Discovery, and even pre-Discovery proposal stages

JPL's Concurrent Design Environment (cont'd)

- JPL's concurrent design environment is to a large extent centered on the CAD file
- During concurrent design sessions CAD geometry is ported to other more specialized engineering design packages such as
  - ZeMax/Code V (for detailed optical design)
  - NASTRAN (for structural dynamics)
  - ADAMS (for rigid body dynamics)
  - *and now* Thermal Desktop (for thermal analysis)

Bridging the Gap

- Given Thermal Desktop's integration with AutoCAD 2000, it was believed to offer the highest potential for success and was selected over other thermal tools for use in the concurrent design environment

- Following some experimentation it was determined that CAD geometry exported as a 3D Studio file could be imported by AutoCAD 2000 and very easily converted to Thermal Desktop surfaces

Bridging the Gap (cont'd)

- Benefits of working with 3D Studio geometry include the speed and simplicity in which very complicated models can be imported into Thermal Desktop

- 3D Studio geometry is imported to AutoCAD 2000 by way of a translator (which is included as part of the standard installation of AutoCAD 2000); hence it is NOT necessary to have 3D Studio installed in order to take full advantage of this technique

The Import Process

In its most basic form, the import process uses only three steps:

1) Select “3D Studio” from among the file types listed under the *Insert* menu.

2) Select the 3D Studio filename and the pertinent file import options.

3) Use AutoCAD’s *Explode* command to reduce the object into individual elements (if it arrives as one single object)

Model Reduction Methods

The user is advised to exercise caution since CAD geometry imported using this method will be meshed, and even the most simple models can get very large, very quickly as illustrated below

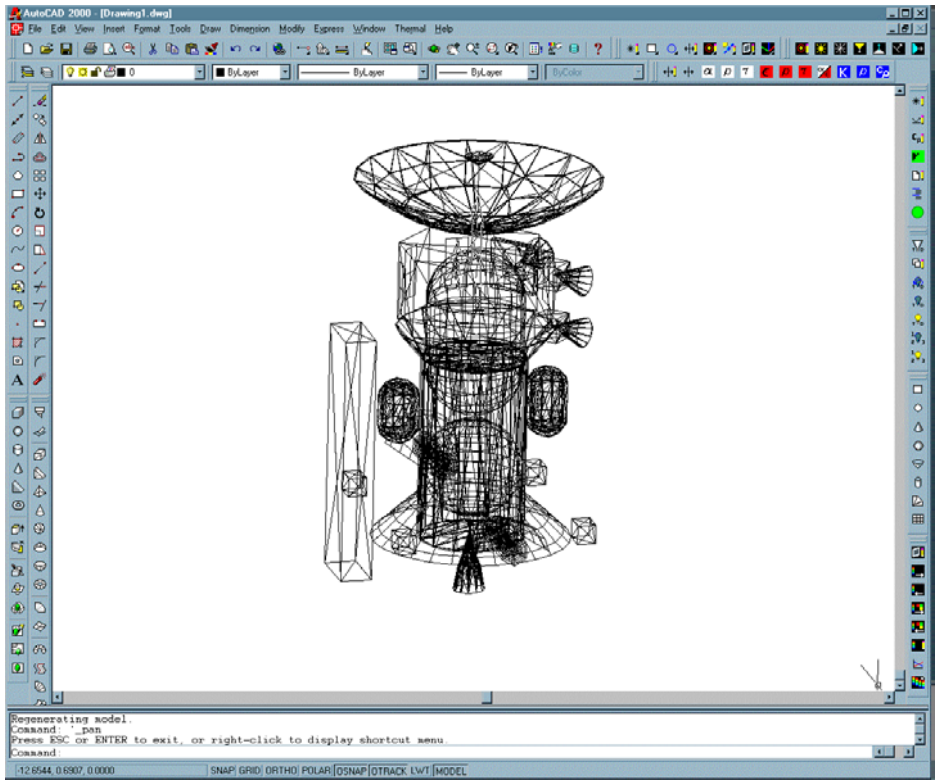

Model Reduction Methods (cont'd)

In these instances one of three approaches has been taken:

1) Deletion of inconsequential geometry prior to import

2) Using Thermal Desktop's "Super Node" capability

3) Replacing complex geometry with Thermal Desktop Primitives

Model Reduction Methods (cont'd)

By using a combination of the methods discussed, a model can be layered and reduced

From

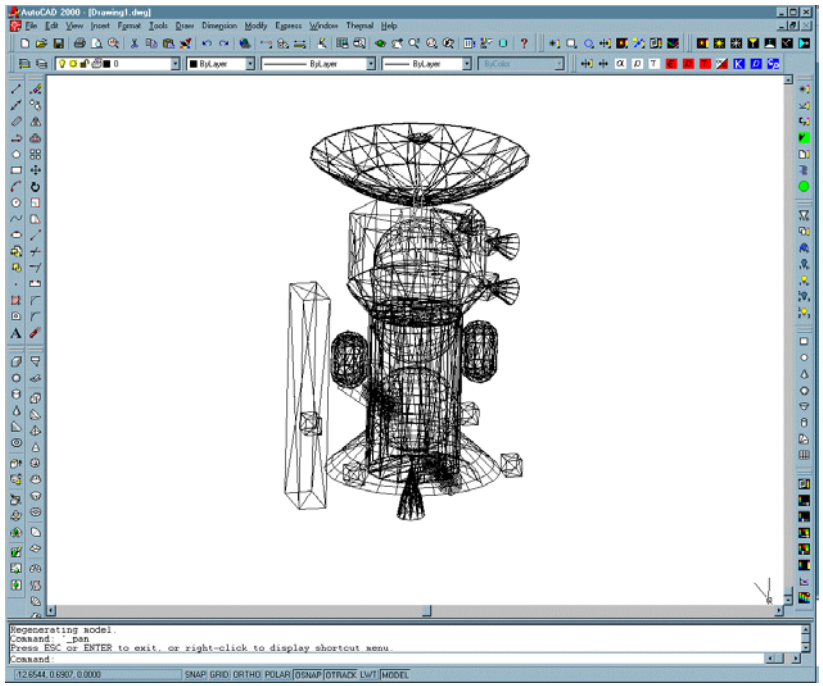

To

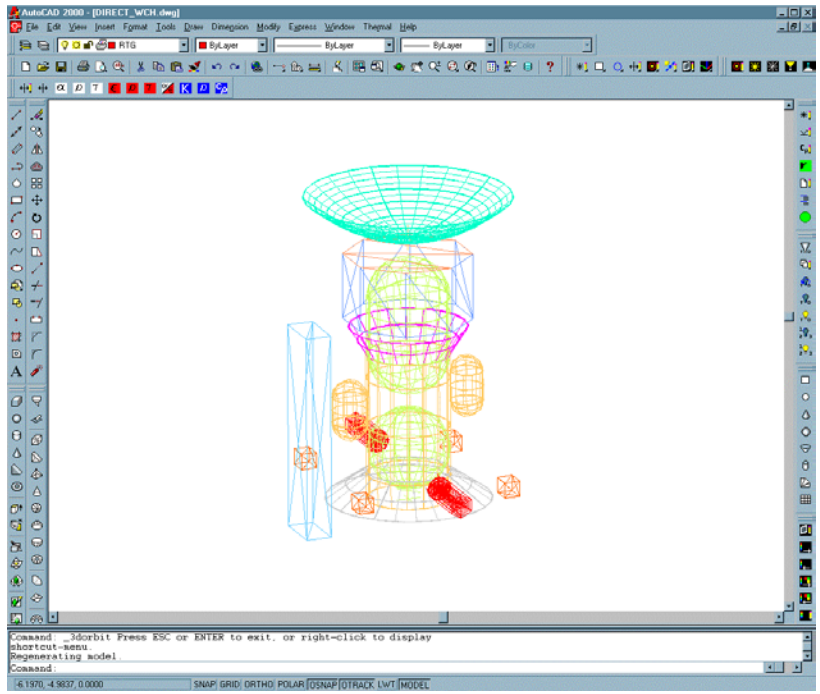

In a matter of minutes!!!

Demonstration

The following demonstration is based on work performed for JPL's Center for Space Mission Architecture and Design

Acknowledgements

I would like to thank Knut Oxnevad, Carlos Carrion, Stephen Wall, Bode Akisanya, and the co-author Emilio Beltran for their technical support in the completion of this work.

STEADY STATE TRANSPIRATION COOLING IN POROUS MEDIA UNDER LOCAL, NON-THERMAL EQUILBRIUM FLUID FLOW

Alvaro Che Rodriguez
NASA Johnson Space Center

Abstract

An analytical solution to the steady-state fluid temperature for 1-D transpiration cooling has been derived. Transpiration cooling has potential use in the aerospace industry for protection against high heating environments for re-entry vehicles. Literature for analytical treatments of transpiration cooling has been largely confined to the assumption of thermal equilibrium between the porous matrix and fluid. In the present analysis, the fundamental fluid and matrix equations are coupled through a volumetric heat transfer coefficient and investigated in non-thermal equilibrium. The effects of varying the thermal conductivity of the solid matrix and the heat transfer coefficient are investigated. The results are also compared to existing experimental data.

Introduction

Transpiration cooling is the process of injecting a fluid (generally serving as a coolant) into a porous matrix, which could serve as a protective barrier against high temperature environments for a re-entry vehicle. In order to utilize a transpiration cooling analysis approach to solving physical applications, a well-developed understanding of the heat transfer and fluid flow characteristics must be obtained. In the report by J.C.Y. Koh et. al. "Investigation of Fluid Flow and Heat Transfer in Porous Matrices for Transpiration Cooling", the fundamental equations for steady state transpiration cooling are stated [1]. However, the solution of the fluid temperature distribution generates results that are not consistent with the physical model requirements as a result of the lack of formal boundary conditions. The results of which can create conditions that violate energy conservation. Therefore, an investigation of the fluid temperature solution presented by Koh is conducted to understand the inconsistencies with the model, and derive an alternative fluid temperature solution. Once these steady state transpiration equations have been established, they can be used as a guide for understanding behavior of heat transfer in porous matrices and also for further transient studies of transpiration cooling.

Transpiration cooling has been treated in the literature by numerous authors. Heat conduction textbooks generally treat transpiration cooling with the assumption of thermal equilibrium between the matrix and fluid. The assumption leads to defining an effective conductivity for the fluid and solid matrix [2]. Curry and Cox conducted numerical studies of the transient effects of transpiration cooling [3]. Using a non-equilibrium solution, they determined that for a high conductivity of the solid matrix, the equilibrium solution is a valid assumption. However, the lower the conductivity of the solid, the more desperate the fluid solution diverges from that of the solid. Additionally, the volumetric

heat transfer coefficient does not affect the response significantly compared to the thermal conductivity of the solid matrix [3].

Transpiration Cooling Model

The physical model utilized in Koh's report is used in this analysis. A flat plate with finite thickness, L, shown in Figure 1, is used for the derivation of the steady state fluid and matrix temperature distributions. The analysis is based on a one-dimensional model with constant material properties.

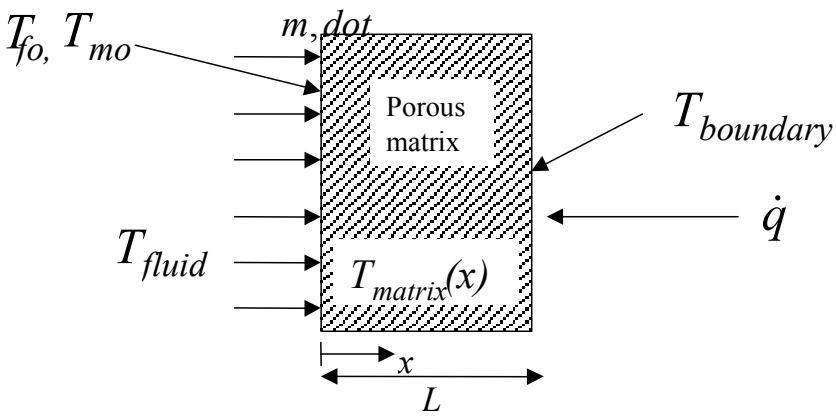

Figure 1: Transpiration Cooling Model

The boundary conditions for the transpiration cooling model are taken from Figure 1. A fluid is injected into porous matrix at a constant mass flow rate, m,dot, with a temperature T_{fo}. The temperature of the matrix at the entrance, x=0, is T_{mo}. A flux is imposed at x=L from the environment which induces a constant temperature boundary condition at the exit, T_{mw}.

The energy balance equations for the fluid and the matrix in non-dimensional form are used to define the governing differential equations for the transpiration cooling model. The energy equation for the fluid stated by Koh is,

$$\frac{d\theta_f}{d\eta} = \frac{h'L}{m,dotc_p}\left(\theta_m - \theta_f\right) = A\left(\theta_m - \theta_f\right) \tag{1}$$

where

$$\theta_f = \frac{T_f - T_{f,i}}{T_{mw} - T_{f,i}} \tag{2}$$

and c_p is the specific heat of the fluid, k_m is the effective conductivity of the matrix, h' is the heat transfer coefficient for internal convection, and $\eta = x/L$. Equation (1) states that

heat is transferred from the matrix to the fluid via convection [1]. Conduction from the matrix to the fluid raises the enthalpy of the fluid and is given by,

$$\frac{d\theta_m}{d\eta} = \frac{m, dotc_p L}{k_m}\theta_f = B\theta_f \tag{3}$$

where

$$\theta_m = \frac{T_m - T_{f,i}}{T_{mw} - T_{f,i}} \tag{4}$$

Matrix Temperature Distribution

From the energy balance equations for the transpiration cooling model, the steady state equations for the fluid and matrix temperature distributions are derived [1]. Equation (3) can be solved in terms of the fluid temperature and substituted into equation (1). The resulting equation is a linear homogeneous second order ordinary differential equation with constant coefficients previously solved by Koh, which describes the non-dimensional steady-state matrix temperature:

$$\frac{d^2\theta_m}{d\eta^2} + A\frac{d\theta_m}{d\eta} - AB\theta_m = 0 \tag{5}$$

The boundary conditions imposed upon the matrix are used to solve equation (5) which are given by,

$$\theta_m(\eta = 0) = \frac{T_{m,o} - T_{f,i}}{T_{mw} - T_{f,i}} = \theta_{m,o} \tag{6}$$

$$\theta_m(\eta = 1) = \frac{T_{mw} - T_{f,i}}{T_{mw} - T_{f,i}} = 1 \tag{7}$$

Imposing the boundary conditions on the solution of equation (5) results in the non-dimensional matrix temperature,

$$\theta_m = \frac{1 - \theta_{mo}e^{r_2}}{e^{r_1} - e^{r_2}}e^{r_1\eta} - \frac{1 - \theta_{mo}e^{r_1}}{e^{r_1} - e^{r_2}}e^{r_2\eta} \tag{8}$$

where, r_1 and r_2 are the roots of the characteristic equation defined by equation (5) shown here,

$$r_1 = \frac{A}{2}\left(-1+\sqrt{1+4B/A}\right) \tag{9}$$

$$r_2 = \frac{A}{2}\left(-1-\sqrt{1+4B/A}\right) \tag{10}$$

Equation (8) is the steady state transpiration cooling equation for the matrix temperature along the η coordinate. This equation, first derived by Koh, will be necessary for determining an alternative steady state equation for the fluid temperature distribution, which is discussed in the following section.

Derivation of Alternative Fluid Temperature Distribution

The fluid temperature distribution is determined by substituting the matrix temperature solution into one of the energy balance equations, equation (1) or (3). However, the results from this substitution produce different results based upon which equation is chosen for the substitution. The fluid temperature presented by Koh utilized equation (3). However, no boundary condition for the fluid at the entrance is required. Since, the results from this method do not permit entrance conditions from being incorporated, an alternative solution which imposes a fluid entrance boundary condition is derived.

Equation (1) can be used to solve for the fluid temperature. The fluid entrance boundary condition can be incorporated into the solution since equation (1) is a non-homogeneous first order differential equation of the form,

$$\frac{d\theta_f}{d\eta} + A\theta_f = A\theta_m \tag{11}$$

where θ_m is defined by equation (8). The solution to equation (11) is approached by first multiplying equation (11) by the function, $e^{A\eta}$, which produces,

$$e^{A\eta}\frac{d\theta_f}{d\eta} + e^{A\eta}A\theta_f = e^{A\eta}A\theta_m \tag{12}$$

Noting that the left-hand side of equation (12) is equivalent to the derivative $D_x\left[e^{A\eta}\cdot\theta_f\right]$, the following expression can be obtained,

$$e^{A\eta}\theta_f = \int e^{A\eta}A\theta_m d\eta + C \tag{13}$$

where C is a constant of integration and defined by the boundary condition imposed upon this problem. Substituting equation (8) into equation (12) and solving for θ_f yields,

$$\theta_f = e^{-A\eta}\left[\int e^{A\eta} A\left(\frac{1-\theta_{mo}e^{r_2}}{e^{r_1}-e^{r_2}}e^{r_1\eta} - \frac{1-\theta_{mo}e^{r_1}}{e^{r_1}-e^{r_2}}e^{r_2\eta}\right)d\eta + C\right] \tag{14}$$

which can be simplified to the following form,

$$\theta_f = A\left[\frac{1-\theta_{mo}e^{r_2}}{\left(e^{r_1}-e^{r_2}\right)\left(r_1+A\right)}\left(e^{r_1\eta}\right) - \frac{1-\theta_{mo}e^{r_1}}{\left(e^{r_1}-e^{r_2}\right)\left(r_2+A\right)}\left(e^{r_2\eta}\right) + \frac{C}{A}e^{-A\eta}\right] \tag{15}$$

The constant of integration is solved by imposing the fluid entrance boundary condition, which is defined as,

$$\theta_f(\eta=0) = \frac{T_{f,o}-T_{f,i}}{T_{mw}-T_{f,i}} = \theta_{f,o} \tag{16}$$

The boundary condition is imposed on equation (15) and results in the following expression for the non-dimensional fluid temperature distribution,

$$\theta_f = A\left[\frac{1-\theta_{mo}e^{r_2}}{\left(e^{r_1}-e^{r_2}\right)\left(r_1+A\right)}\left(e^{r_1\eta}\right) - \frac{1-\theta_{mo}e^{r_1}}{\left(e^{r_1}-e^{r_2}\right)\left(r_2+A\right)}\left(e^{r_2\eta}\right) + \left(\frac{\theta_{f,0}}{A} - \left(\frac{1-\theta_{mo}e^{r_2}}{\left(e^{r_1}-e^{r_2}\right)\left(r_1+A\right)} - \frac{1-\theta_{mo}e^{r_1}}{\left(e^{r_1}-e^{r_2}\right)\left(r_2+A\right)}\right)\right)e^{-A\eta}\right] \tag{17}$$

which simplifies to

$$\theta_f = A\left[\frac{1-\theta_{mo}e^{r_2}}{\left(e^{r_1}-e^{r_2}\right)\left(r_1+A\right)}\left(e^{r_1\eta}-e^{-A\eta}\right) - \frac{1-\theta_{mo}e^{r_1}}{\left(e^{r_1}-e^{r_2}\right)\left(r_2+A\right)}\left(e^{r_2\eta}-e^{-A\eta}\right) + \frac{\theta_{f,0}}{A}e^{-A\eta}\right] \tag{18}$$

Equation (18) states the steady state transpiration cooling equation for the fluid temperature. It is a function of primarily of the distance along the x direction, and based on the boundary condition of the matrix and fluid at the entrance of the porous matrix.

Results

The steady state transpiration cooling equations for the fluid and the matrix are functions of a single variable, η. In Figure 2, the alternative fluid temperature solution and steady state matrix temperature are plotted versus the non-dimensionalized coordinate, η. The entrance fluid boundary condition is assumed to be the temperature of the fluid reservoir with a temperature of T_{fo}=T_{fi}=600 °F and the matrix boundary condition at the entrance is T_{mo} = 500 °F. At the exit, T_{mw} is 1500 °F, which is due to the environmental heating.

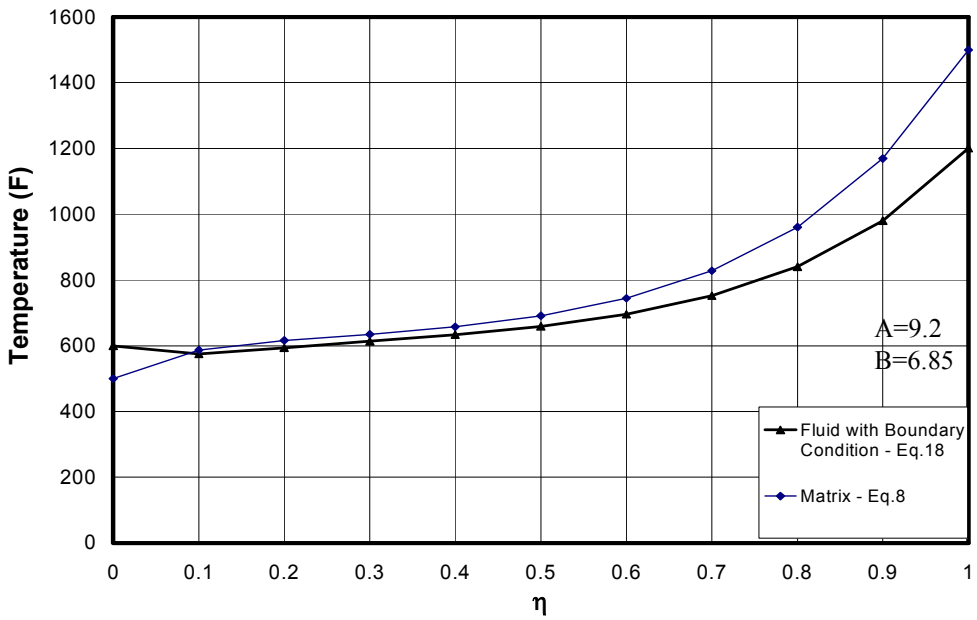

Figure 2: Fluid and Matrix Temperature Distributions along the Porous Matrix

Using equation (8) and (18), the alternative fluid temperature solution and the matrix solution are shown in Figure 2. The fluid and matrix temperature profiles along the η direction obey the conservation of energy and satisfy the physical boundary conditions imposed upon the model. A comparison of the results from the Koh study and the alternative method of calculating the fluid temperatures is shown in Figure 3.

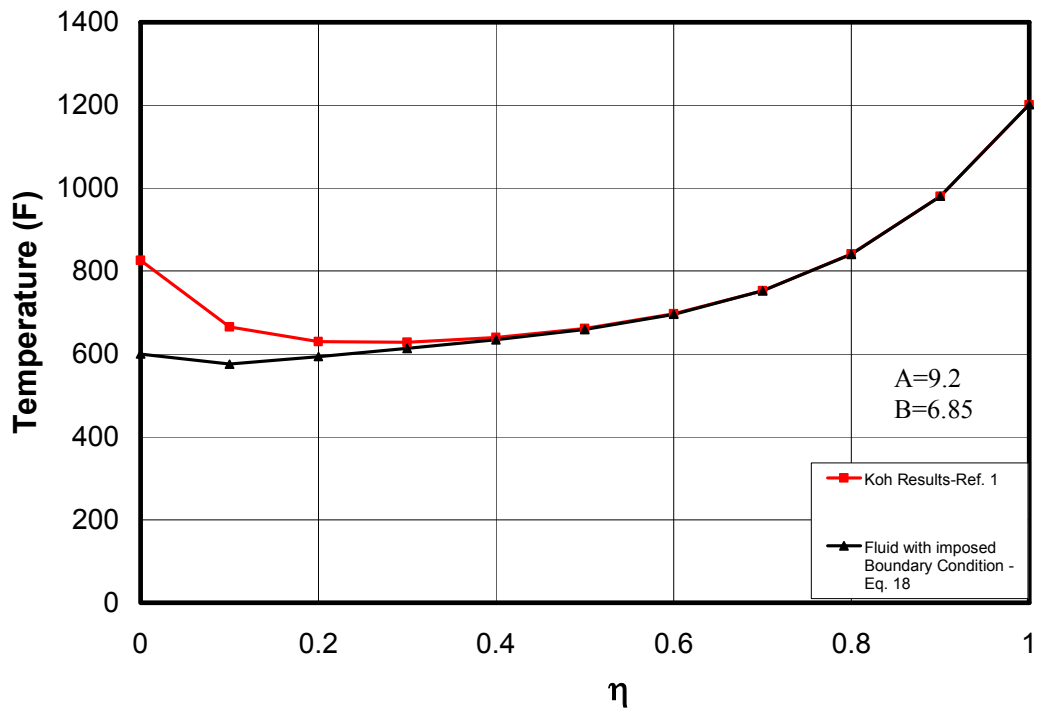

Figure 3: Fluid Temperature Solution Comparison

In Figure 3, the solution presented in [1] results in an entrance fluid temperature that does not adhere to the boundary conditions imposed upon the system. However, the alternative solution given by equation (18) has an imposed boundary condition, which satisfies the physical boundary conditions of the transpiration cooling model.

The parameters that govern the temperature distribution for the fluid and matrix are A and B defined in equations (1) and (3). The inverse of the thermal conductivity of the solid matrix is defined in parameter B. The effect of varying the thermal conductivity is shown in Figure 4.

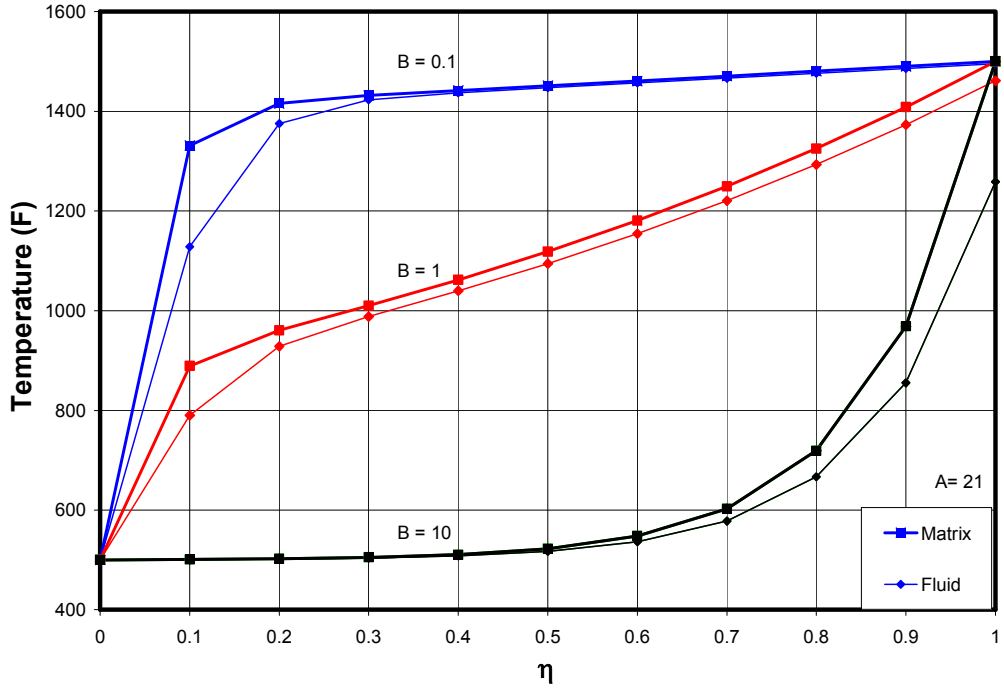

Figure 4: Predicted Temperature Distributions with Varying Thermal Conductivity

Since increasing the thermal conductivity results in a decreasing B, the temperature distribution changes dramatically with the amount of heat that is allowed to flow through the matrix. It is also clear that the temperature distribution is highly dependent on the solid matrix conductivity. The volumetric heat transfer coefficient is represented in parameter A. The effect of varying A is illustrated in Figure 5.

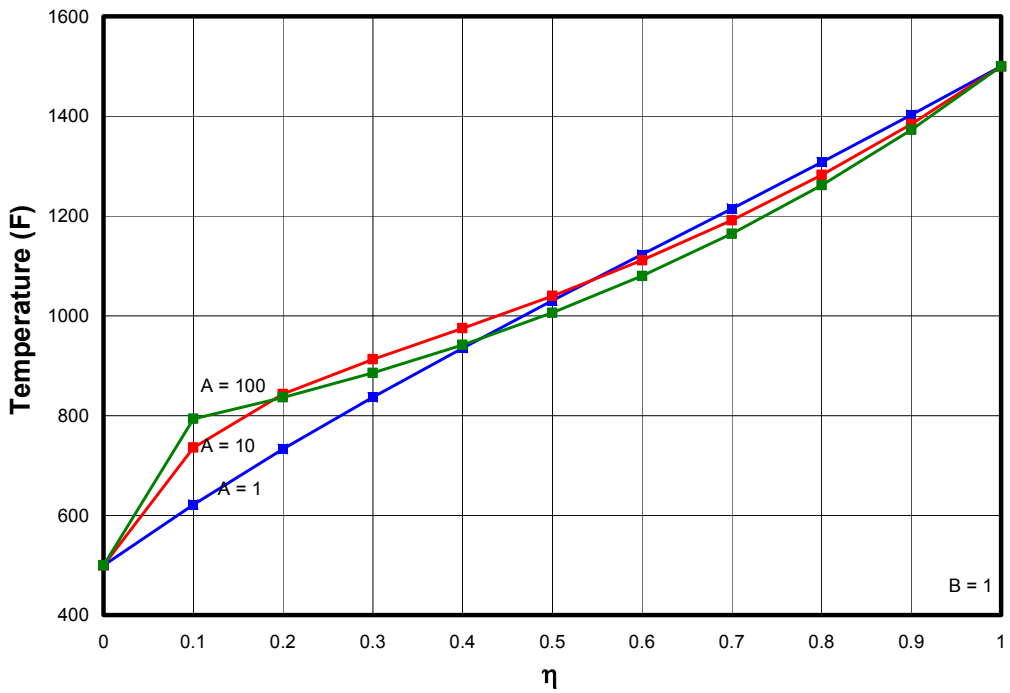

Figure 5: Predicted Temperature Distributions with Varying Heat Transfer Coefficient

The heat transfer coefficient does not significantly change the temperature distribution of the solid matrix. For increasing heat transfer coefficient, h', the fluid temperature (not shown in Figure 5) will converge on the matrix temperature solution, however it will not significantly affect the matrix temperature distribution. This phenomenon demonstrated by the present analysis therefore conforms to previous numerical studies of porous media heat transfer [3].

The results of the present analysis are also compared to previous experimental data [4]. The experimental data is based on air flowing through uniformly packed beds at various Reynolds numbers. Spheres were used in the experiment approximately .5 inch in diameter. However, for materials that would fit transpiration cooling applications, the porous matrix diameter would be reduced by several magnitudes of order. The reduction in the porous matrix diameter affects the mass flow rate, which is accounted for in the present analysis. Iron-constantan thermocouples were imbedded in the spheres to determine matrix temperatures. Gas temperatures were determined by an energy balance equation in finite difference form [1].

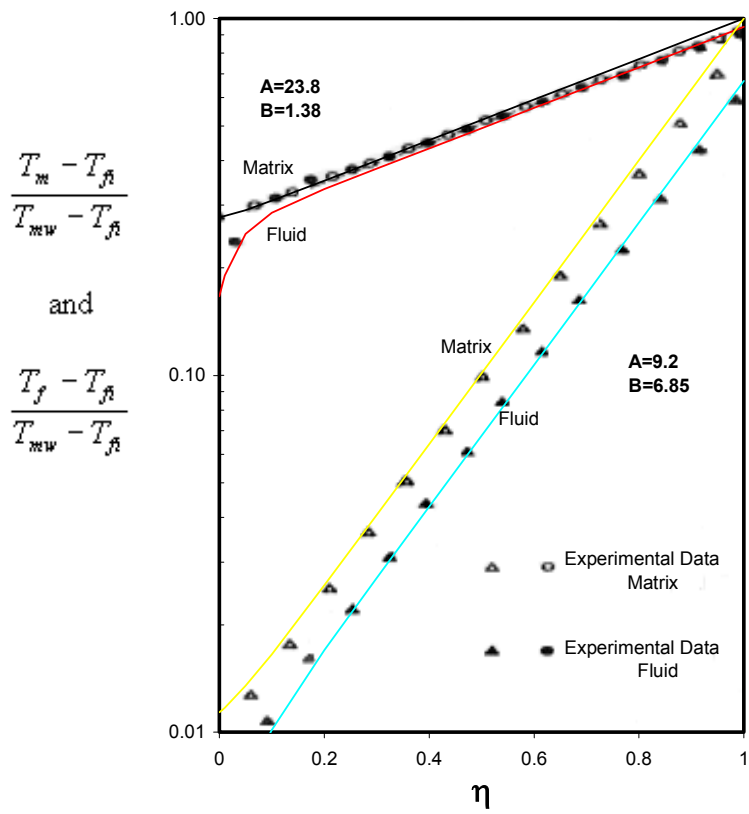

Figure 6: Comparison of Theoretical and Experimental Results

As illustrated in Figure 6, the analysis agrees well with the two sets of experimental data. For the large heat transfer coefficient condition, characterized by a higher value of A, it is seen that the difference between the matrix and fluid temperatures is small. For the small thermal conductivity condition, characterized by a higher value for B, the heat flow becomes significantly reduced agreeing with both the experimental data and previous numerical studies.

Conclusion

The fluid temperature solution presented by Koh produces results that are not physically realistic. An alternative method for deriving the steady state fluid temperature has been presented. This method allows for the inclusion of the entrance boundary condition for the fluid. Furthermore, the two solutions are compared to one another and the alternative fluid solution adheres to the physical system requirements. The effect of increased thermal conductivity of the solid matrix is significant. However, the effect of changing the volumetric heat transfer coefficient was small. The results also compared well to the existing experimental data. This analysis may further the understanding not only of steady state behavior, but also the transient responses in transpiration cooling.

References

1. Koh, J. C. Y, et al. "Investigation of Fluid Flow and Heat Transfer in Porous Matrices for Transpiration Cooling." Boeing Company Technical Report AFFDL-TR-65-228, 1968.

2. Gebhardt, B. Heat Conduction and Mass Transfer. New York: McGraw-Hill Inc., 1993.

3. Curry, D. M., and Cox, J. E. "The Effect of the Porous Material Characteristics on the Internal Heat and Mass Transfer." ASME, 73 HTD-49, 1973.

4. Turnacliff, R.D., "An Experimental Study of Local Convective Heat Transfer and Pressure Drop for Laminar and Turbulent Flow of Air within a Uniformly Packed Bed of Spheres," Ph.D. Thesis, University of Minnesota, 1957.

Acknowledgements

I would like to thank Dr. Donald Curry for inspiring the current analysis and serving as a mentor. I would also like to thank the Thermal Design Branch at NASA for encouraging activities such as these.

Nomenclature

A	eq. (12), dimensionless
B	eq. (13), dimensionless
c_p	specific heat (Btu/lb.-F)
h'	volumetric heat transfer coefficient (Btu/hr-ft^3-F)
k	thermal conductivity (Btu/hr-ft-F)
l	length (ft.)
m, dot	mass flow rate, (lb./hr)
T	Temperature, (F)
x	distance measured from inlet of matrix (ft.)
η	dimensionless variable, x/l
θ	dimensionless variable, $\dfrac{T - T_{fi}}{T_{mw} - T_{fi}}$

Subscripts

m	matrix solid
f	fluid
o	inlet (x=0)
fi	fluid reservoir
fo	fluid inlet (x=0)
w	wall (x=L)

Heat Flux Sensor Testing

TFAWS 2001 Conference

Huntsville, Al

September 13, 2001

D.W. Clark
ED25

Objectives

Develop secondary calibration capabilities for MSFC's Hot Gas Facility (HGF), a Mach 4 Aerothermal Wind Tunnel.

- Evaluate ASTM slug/ thinskin calorimeters against current HGF heat flux sensors
- Provide verification of baselined AEDC/ Medtherm gage calibrations
- Address future calibration issues involving NIST certified radiant gages

Why Are NIST Calibration Standards Valuable?

- Shuttle Safety
  - Thermal Protection Systems are developed, characterized, and qualified for flight using NIST radiant calibration standards at HGF
- Shuttle Performance
  - 26% of the Space Shuttle's weight is TPS
  - On the External Tank alone, a 15% reduction in TPS increases Shuttle payload capacity by 600 pounds, representing $6,000,000 in potential payload cost savings per Shuttle flight

MATERIALS ENVIRONMENT TEST COMPLEX (METCO)

Improved Hot Gas Facility

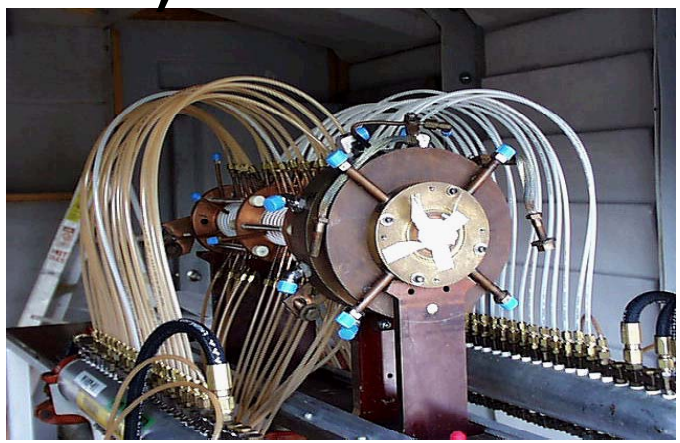

Hyperthermal Tester

Thermal Acoustics Facility

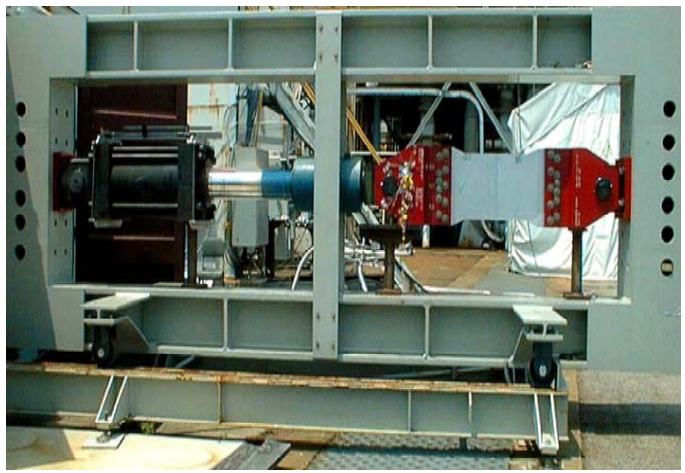

Large Scale Tensile Tester

HGF Layout

REMTECH Inc.

RTR 170-03

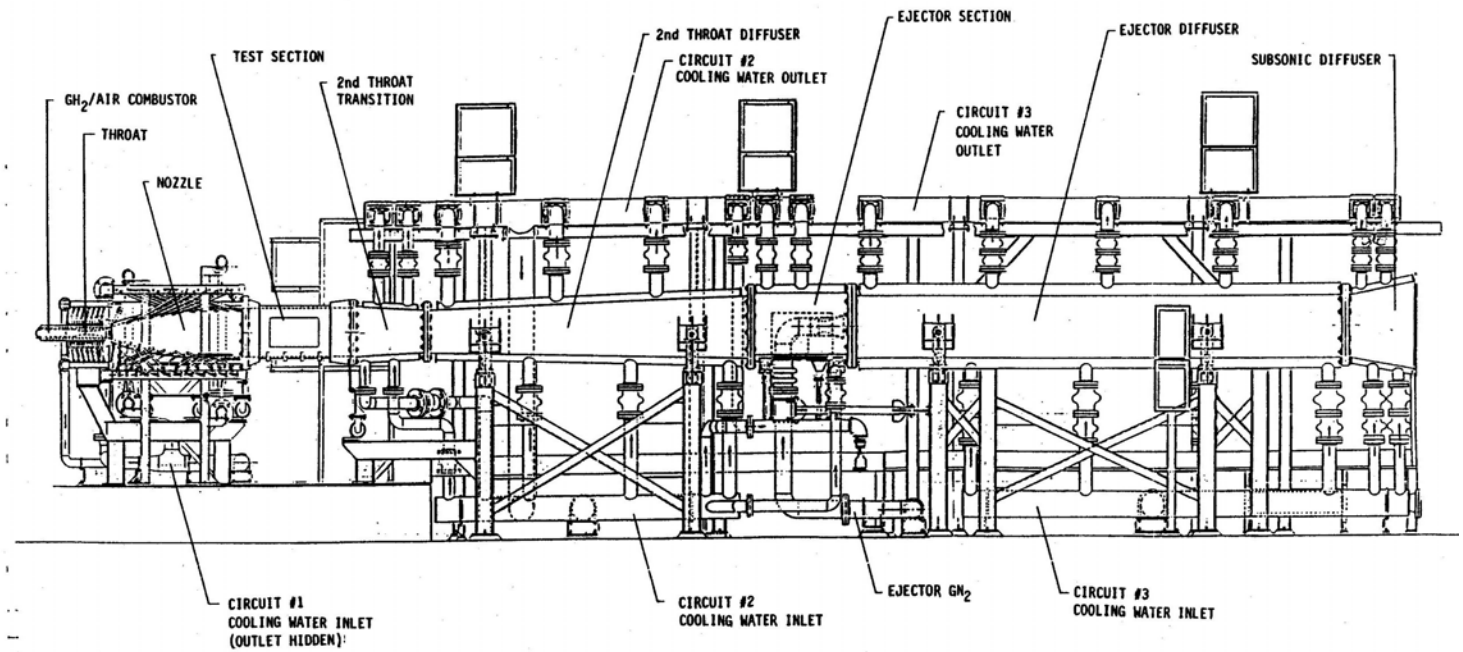

Fig. 88 MSFC Improved Hot Gas Facility

119

HGF Facility Description

- The Marshall Space Flight Center's Improved Hot Gas Facility (IHGF) is an aerothermodynamic testing facility ideal for Thermal Protection System materials characterization and qualification.
  - A combustion driven, Mach 4 wind tunnel, with a 16 x 16 inch test section.
  - Burns a lean mixture of gaseous hydrogen (GH_2) and missile grade air producing total temperatures of 1440 - 2400 ^oF with total pressures of 100 - 220 psia.
  - A 300 kW radiant lamp system is available for plume environment simulation.
  - Infrared (IR) thermal imaging/ video capabilities used for collecting real-time surface temperature measurements
- The IHGF is reasonably small, inexpensive in operation, very flexible and efficient, and is operated with a small, highly experienced crew.
- Run times up to 300 seconds and up to 10 tests per day.
  - Variable wedge angle (up to 20 degrees) model insertion system for panels up to 12" x 19".
  - Can accommodate protuberance testing up to 7" x 12".
- The IHGF provides the opportunities for inexpensive screening, preliminary study, and technique development work.
  - It continues to provide MSFC and Industry with quick response capability during conceptual design phases as well as during flight vehicle problem resolution.
  - It is used for development and flight qualification of Space Shuttle External Tank and SRB TPS

Calorimeter Illustration

METCO Thin Skin:

Dia = 1.5”

L =0.065 & 0.095”

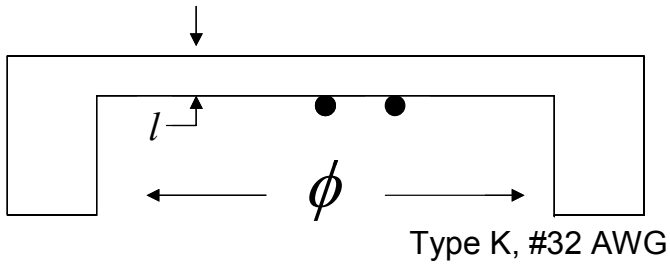

Section View of Thin Skin

Ames Slug:

Dia = 0.302”

L =0.35”

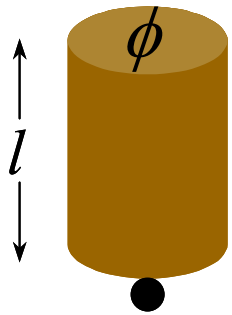

Slug Calorimeter

304 Stainless properties:

Density: 0.29 lbm/in3

Specific Heat: 0.12 Btu/lbm/F

Copper properties:

Density: 0.323 lbm/in3

Specific Heat: 0.092 Btu/ lbm/F

Schmidt-Boelter Gage Design

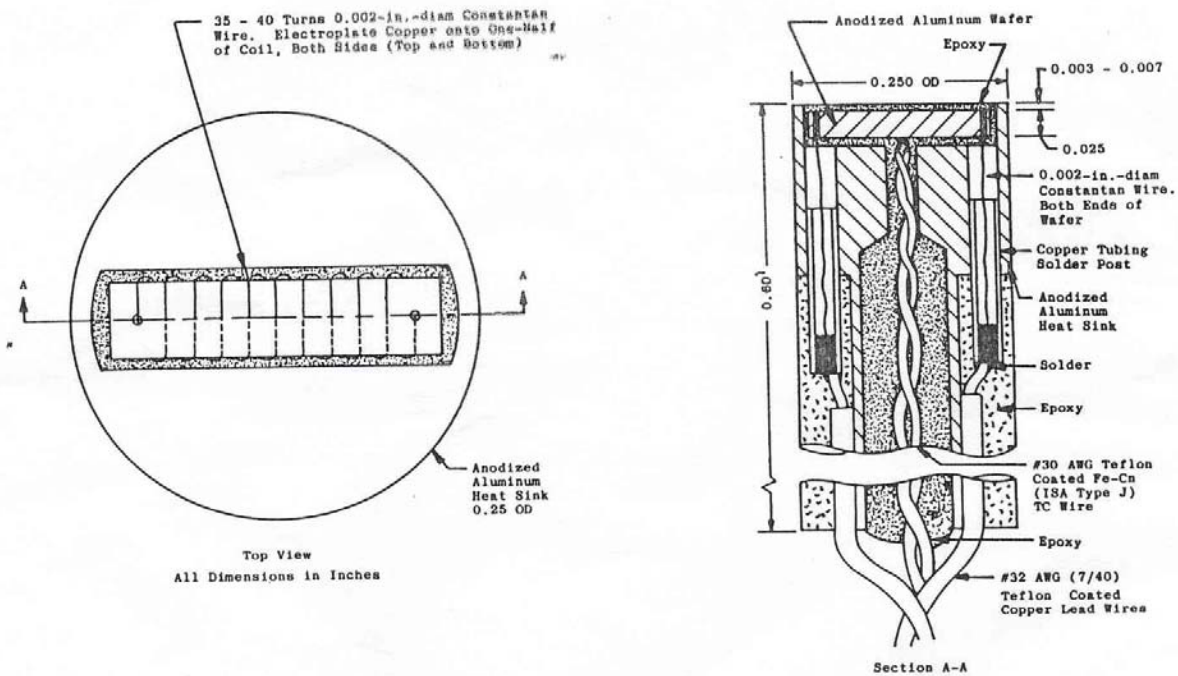

Figure 4. Section drawing of Schmidt-Boelter gage.

Slug Assembly Drawing

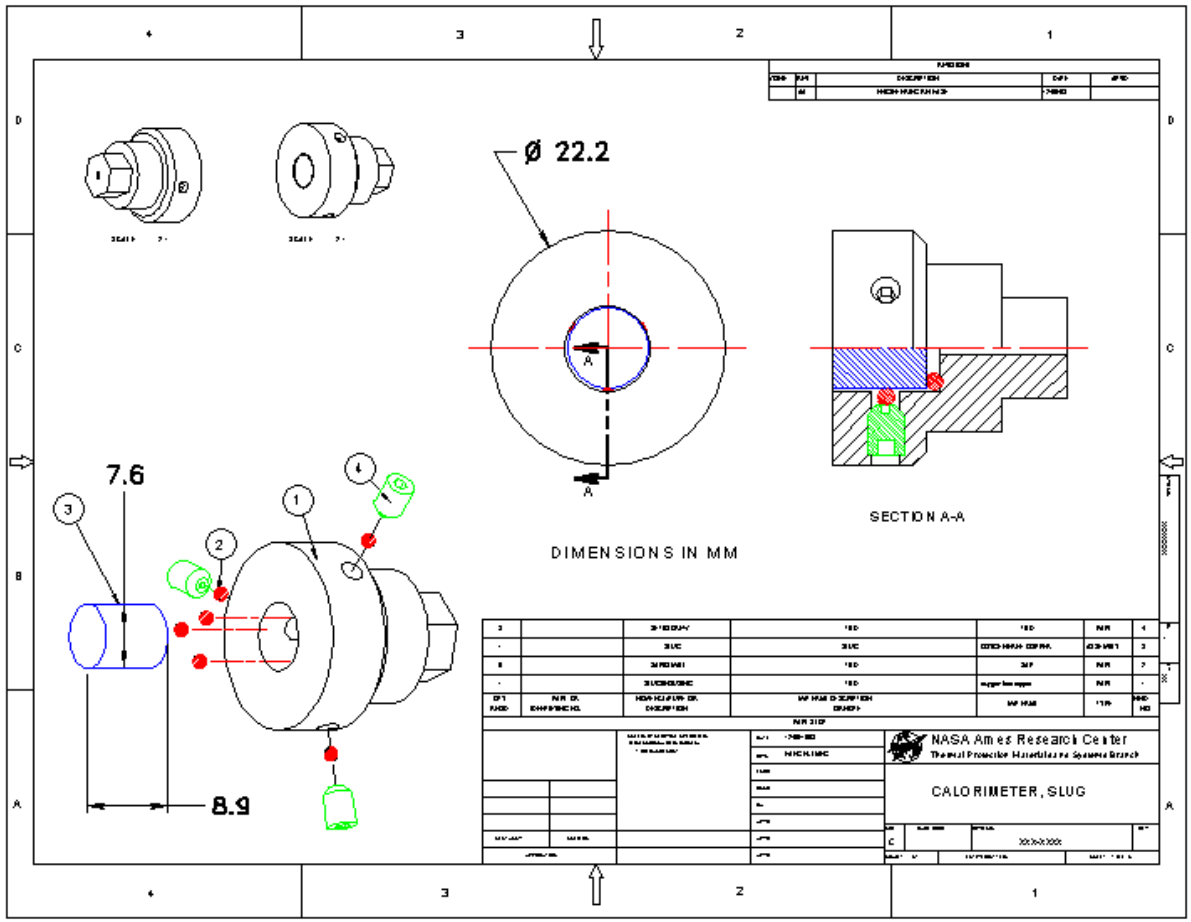

D.W. Clark
ED25

Calibration Plate

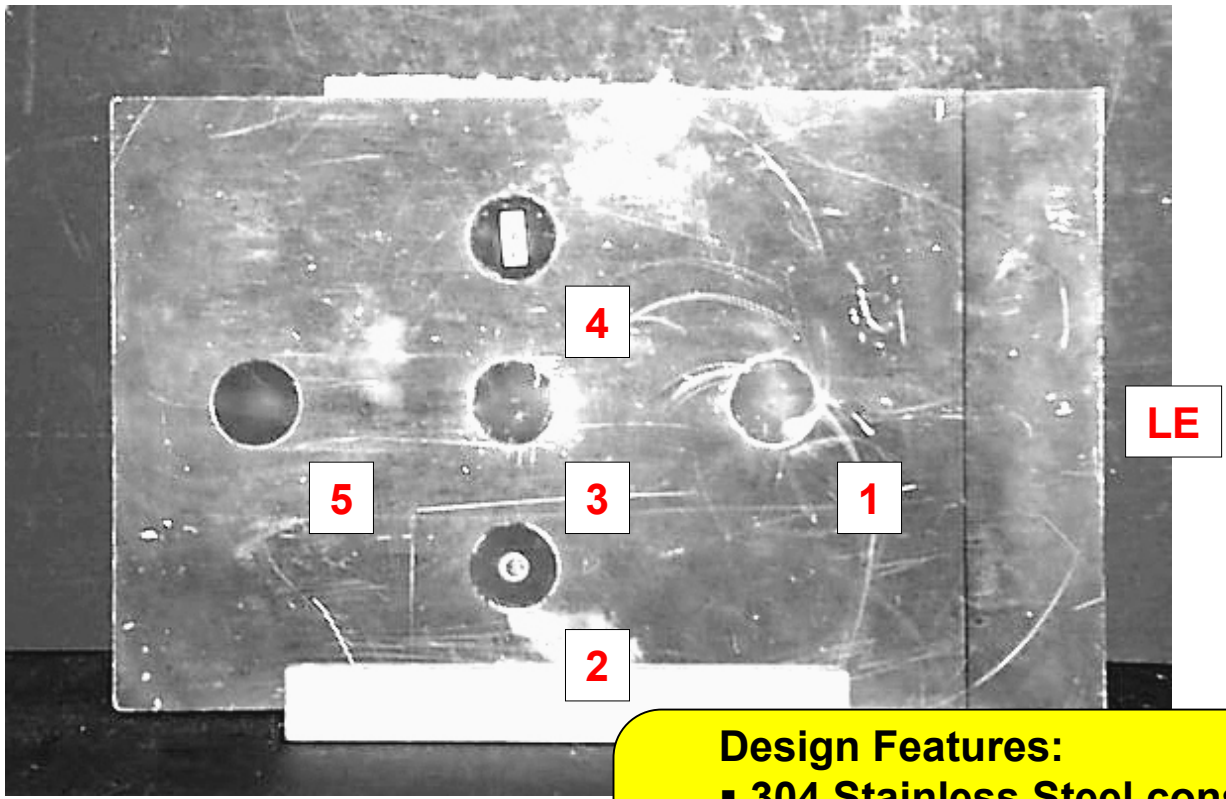

Design Features:

- 304 Stainless Steel construction
- Multiple mounting ports for simultaneous calorimeter/gage calibrations

Calorimetry Study Test Matrix And Chronology

Position > Test	1	2	3	4	5	Tunnel Condition
1 2 3	MT	0.095	3 HF	0.065	SLUG	125 psia / 1600°F / 0°
4 5 6	MT	0.095	3 HF	0.065	SLUG	125 psia / 1600°F / 15°
7 8	MT	0.065	SLUG	0.095	3 HF	125 psia / 1600°F / 0°
9 10	MT	0.065	SLUG	0.095	3 HF	125 psia / 1600°F / 15°
11 12	MT	3 HF	0.065	SLUG	0.095	125 psia / 1600°F / 0°
13 14	MT	3 HF	0.065	SLUG	0.095	125 psia / 1600°F / 15°
15 16	MT	SLUG	0.095	3 HF	0.065	125 psia / 1600°F / 0°
17 18	MT	SLUG	0.095	3 HF	0.065	125 psia / 1600°F / 15°

Calorimeter Legend
MT = 1/2" Medtherm S/N 107641
(Gage "MT" is always in Position 1)
0.065 = Thin Thin Skin Gage
0.095 = Thick Thin Skin Gage
SLUG = Ames Furnished Slug S/N TBD
3 HF #1 = 1/4" Medtherm S/N 667121
3 HF #2 = 3/16" Medtherm S/N 79455
3 HF #3 = AEDC S/N 2679

Test	First Runs HGF No.	First Runs Date	Repeat Runs HGF No.	Repeat Runs Date		Tunnel Condition
1	337	14-Jun	552	30-Jul		125 psia / 1600°F / 0°
2	338	14-Jun	550	30-Jul		125 psia / 1600°F / 0°
3	341	14-Jun	549	30-Jul		125 psia / 1600°F / 0°
4	342	14-Jun	546	30-Jul		125 psia / 1600°F / 15°
5	343	14-Jun	544	30-Jul		125 psia / 1600°F / 15°
6	344	14-Jun	543	30-Jul		125 psia / 1600°F / 15°
7	345	14-Jun	542	26-Jul		125 psia / 1600°F / 0°
8	346	14-Jun	541	26-Jul		125 psia / 1600°F / 0°
9	348	14-Jun	540	26-Jul		125 psia / 1600°F / 15°
10	349	14-Jun	539	26-Jul		125 psia / 1600°F / 15°
11	350	15-Jun	449	12-Jul		125 psia / 1600°F / 0°
12	351	15-Jun	450	12-Jul		125 psia / 1600°F / 0°
13	352	15-Jun	451	12-Jul		125 psia / 1600°F / 15°
14	353	15-Jun	453	12-Jul		125 psia / 1600°F / 15°
15	354	15-Jun	388	25-Jun		125 psia / 1600°F / 0°
16	355	15-Jun	391	25-Jun		125 psia / 1600°F / 0°
17	356	15-Jun	389	25-Jun		125 psia / 1600°F / 15°
18	357	15-Jun	390	25-Jun		125 psia / 1600°F / 15°

Miscellaneous Notes
Gage "MT" is always in Position 1
Tests 1 2 3 and 4 5 6 are intended to check for data repeatability.

D.W. Clark
ED25

Test Conditions

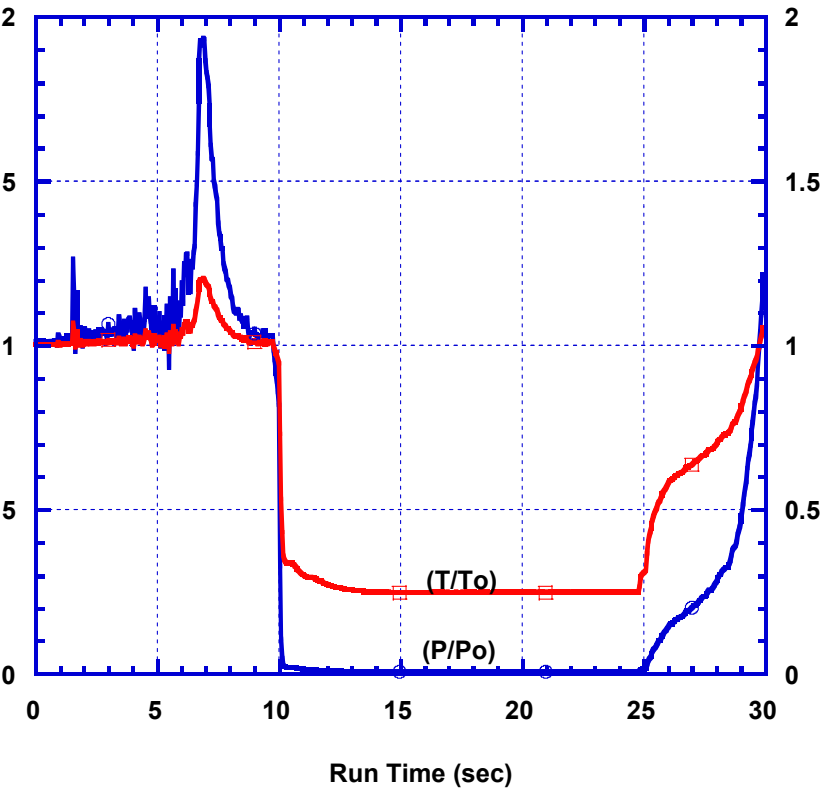

Tunnel Performance

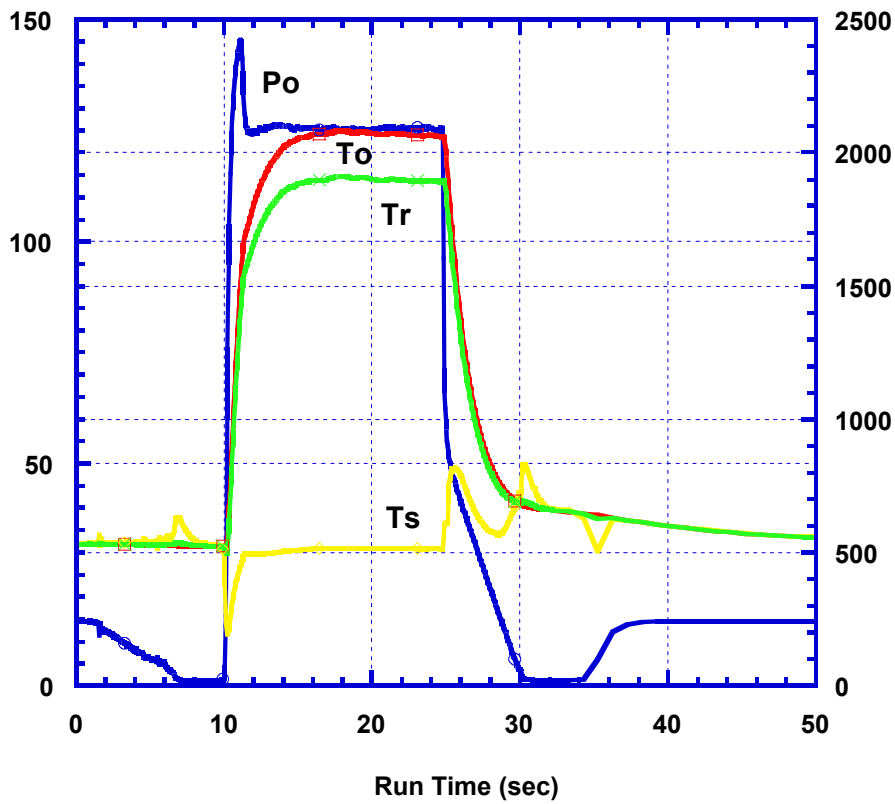

Tunnel Environments

D.W. Clark
ED25

Data Reduction Timeline

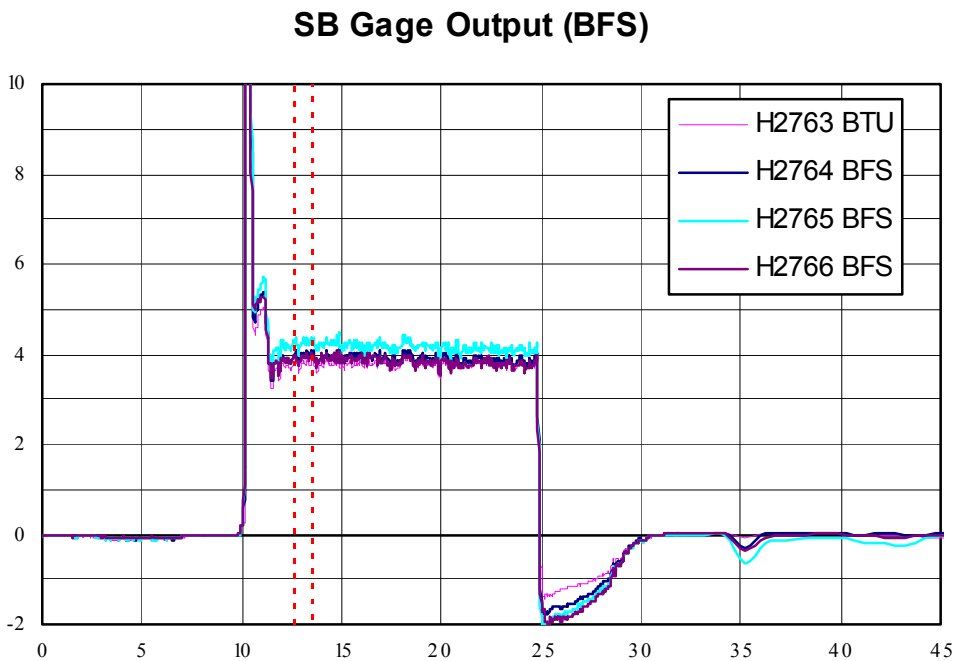

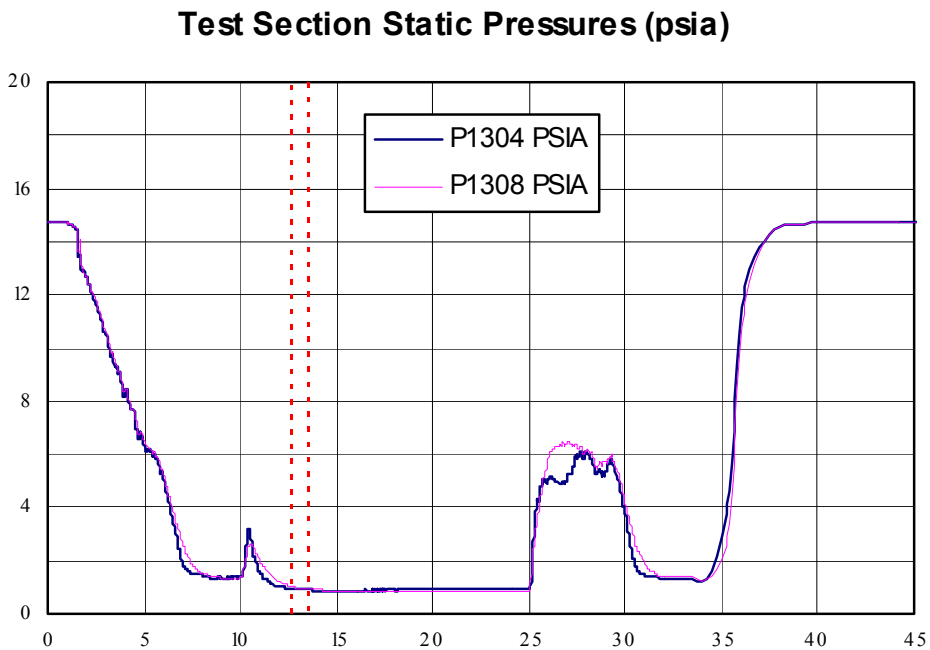

Calorimeter data evaluated when test section reaches steady flow. (~13 sec). Corresponding calorimeter/ gage comparisons made over one second time interval.

D.W. Clark
ED25

Calorimeter Data

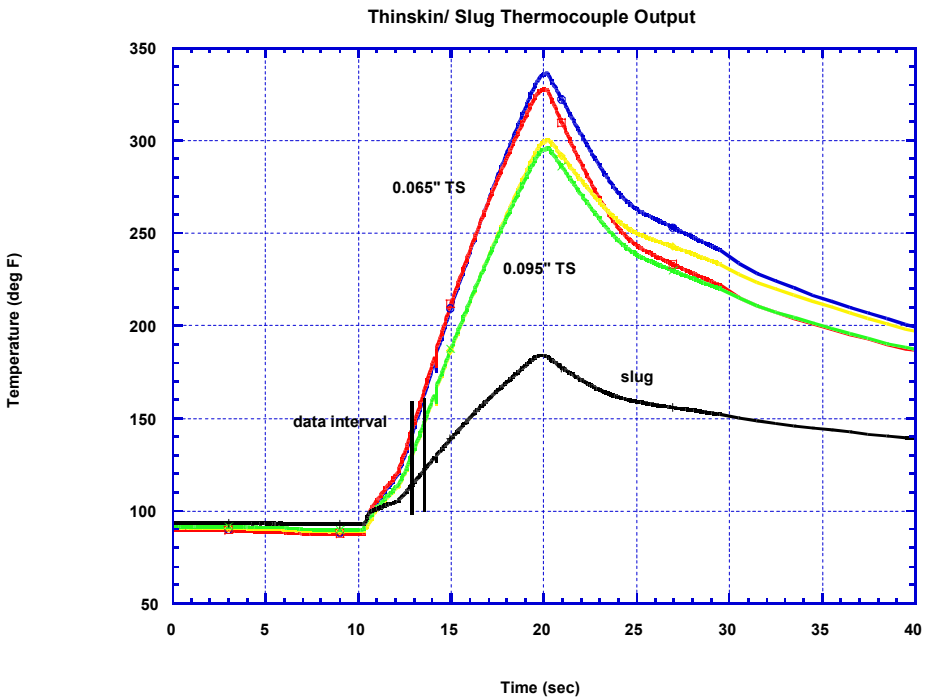

Calorimeter Temperatures

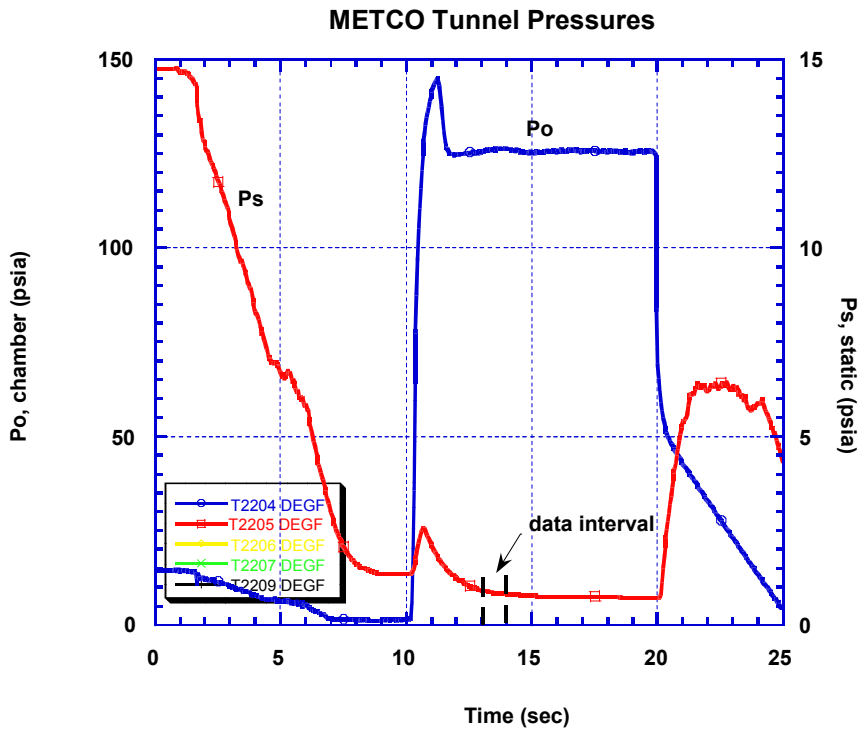

Static Pressures

D.W. Clark
ED25

Thin Skin Radial Conduction Errors

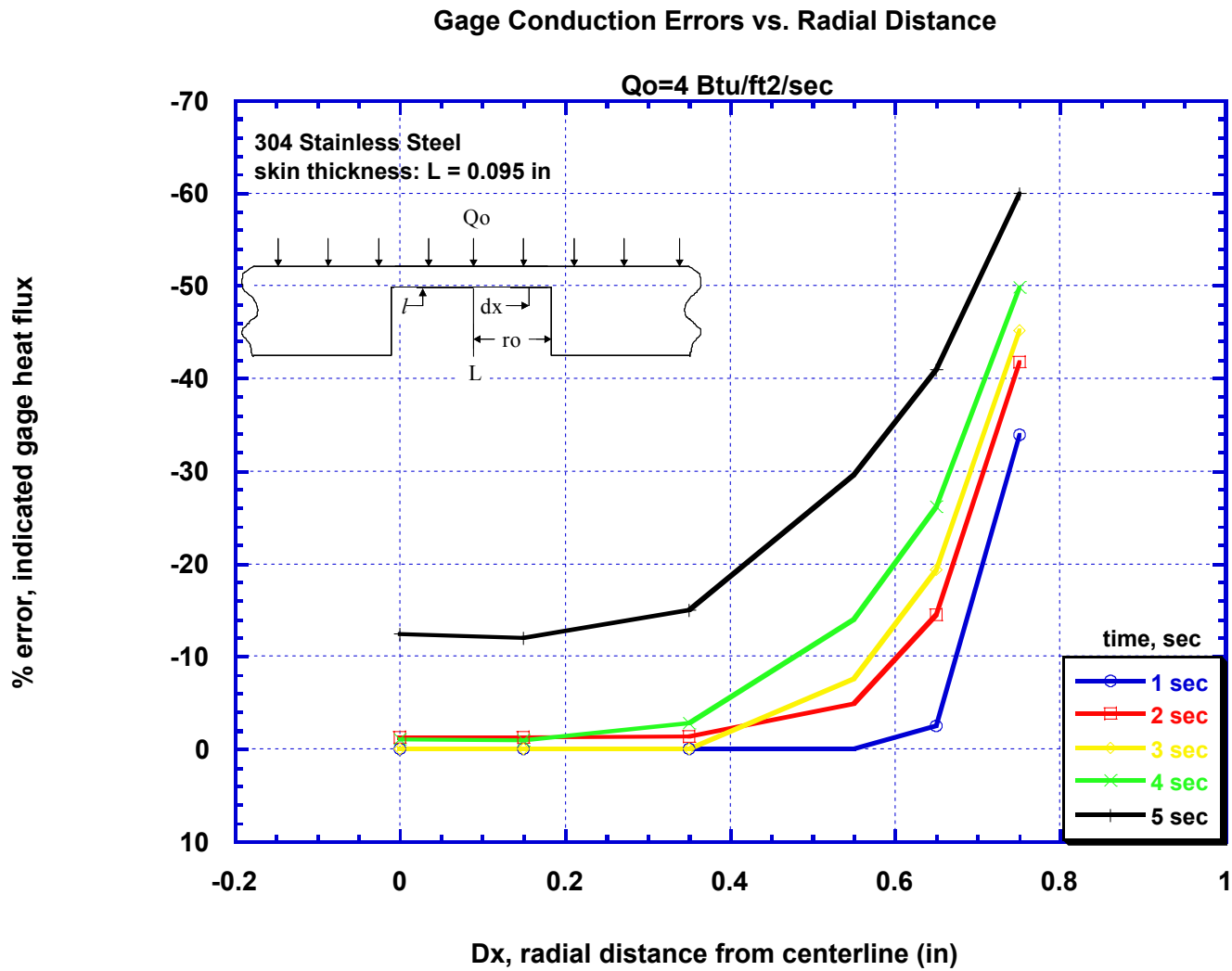

D.W. Clark
ED25

Thin Skin Temperatures

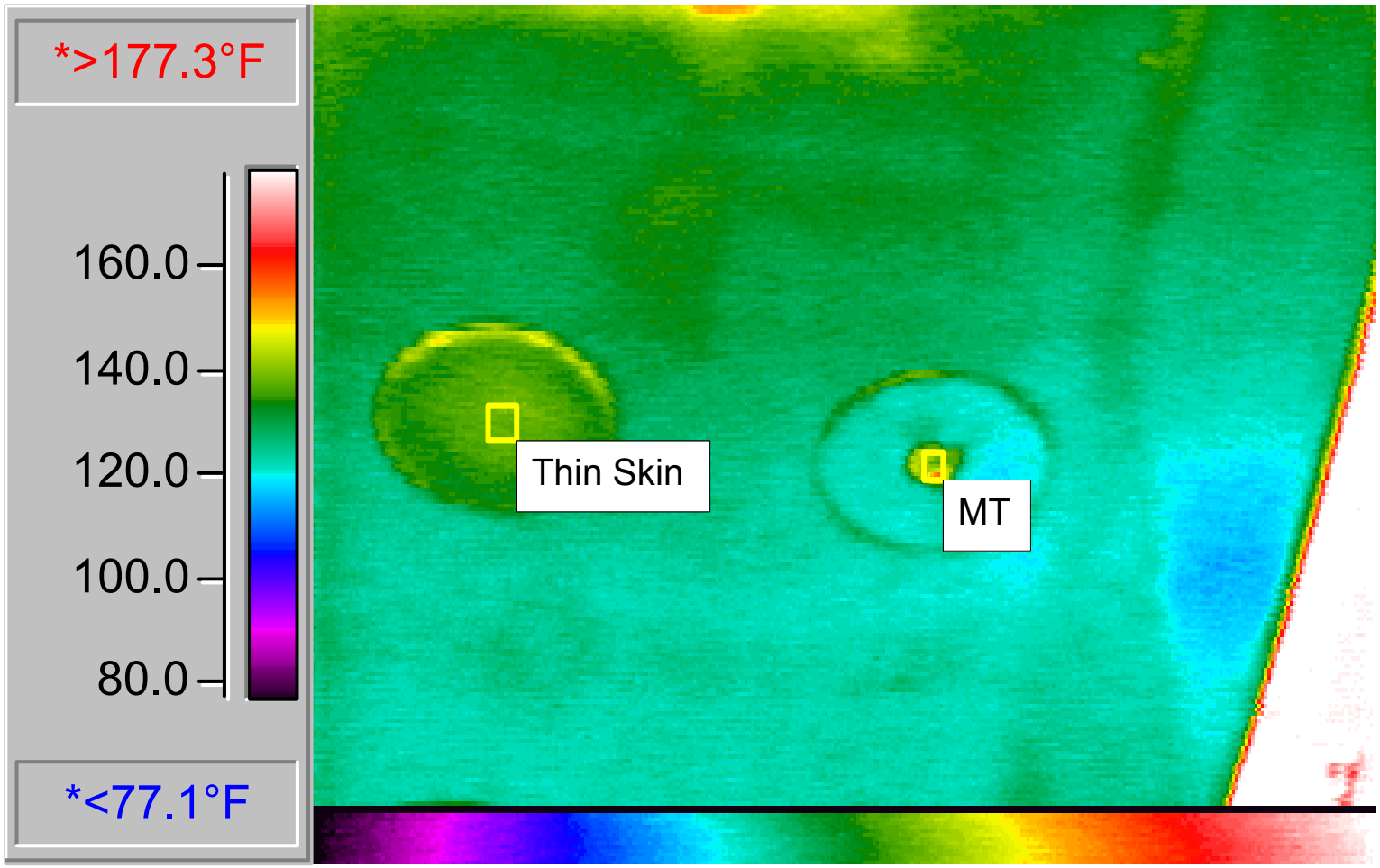

S-B Gage Temperatures

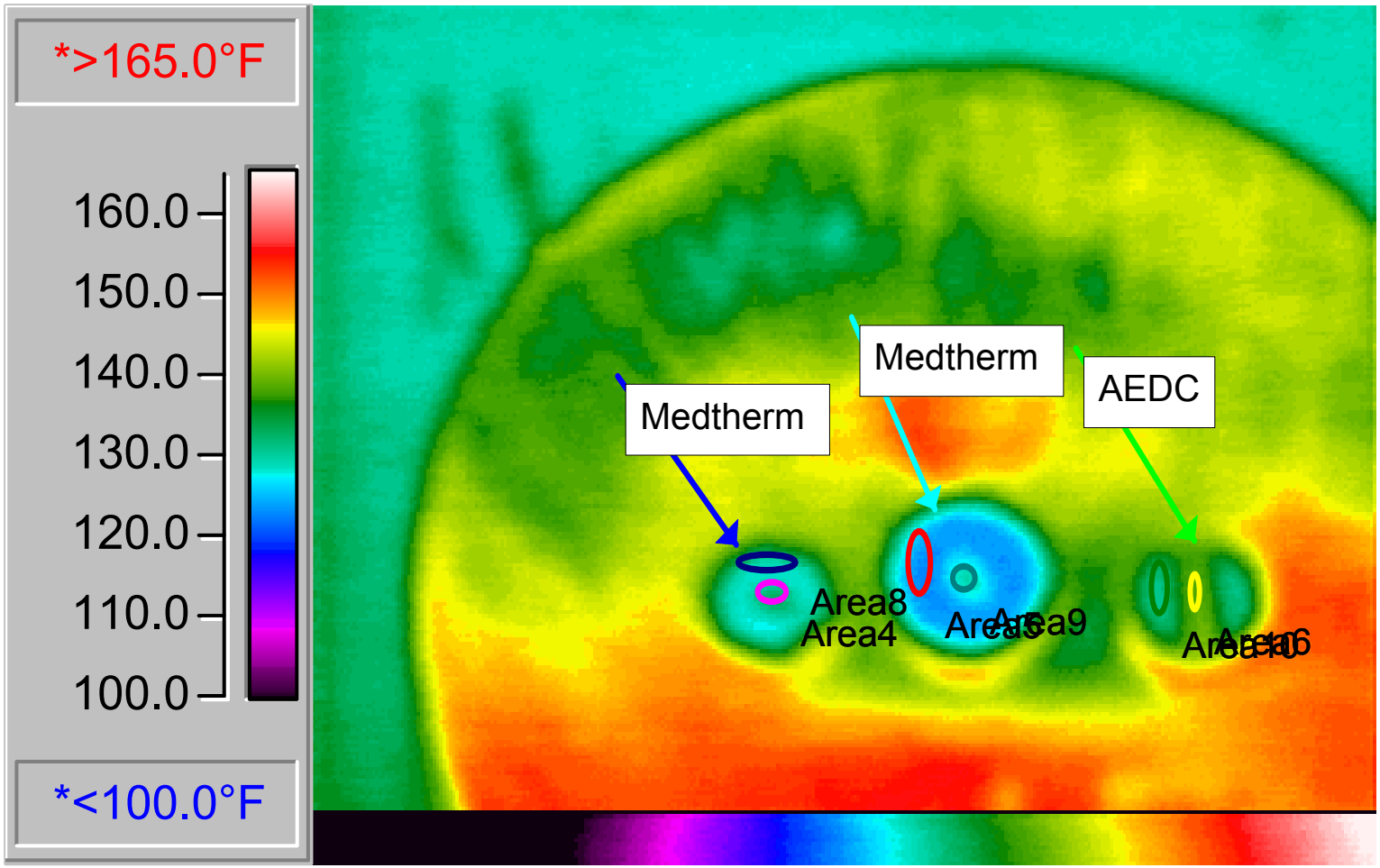

Calorimeter Heat Transfer

- Hot Wall Rates:

$$\dot{q} = \rho C_p l \frac{dT_c}{dt}$$

- Compressible Flow:

$$\frac{T}{T_o} = \left(\frac{P}{P_o}\right)^{\left(\frac{\kappa-1}{\kappa}\right)}$$ (temperature ratio)

$$T_r = \Pr^{1/3}\left(T_o - T\right) + T$$ (recovery temperature)

- Cold Wall Rates:

$$\dot{q}_{cw} = \dot{q}\frac{\left(T_r - 460.\right)}{\left(T_r - T_w\right)}$$

Measurement Repeatability

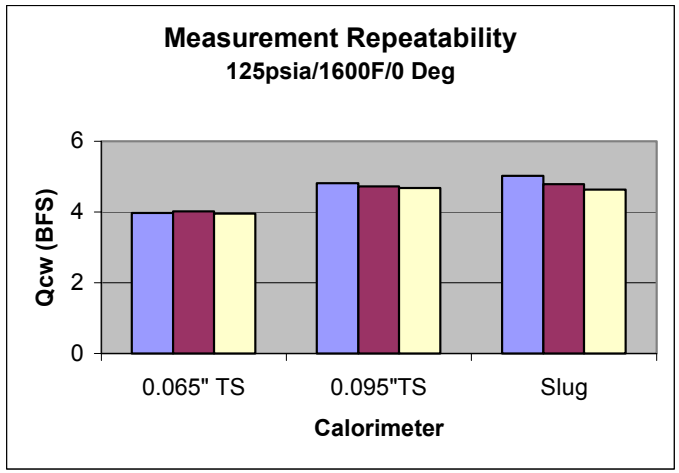

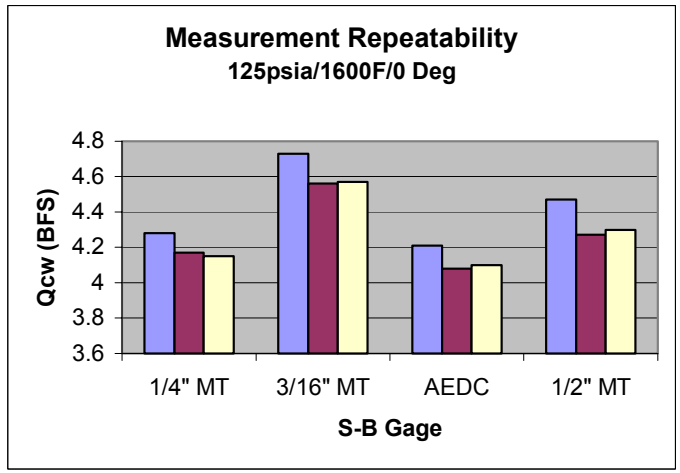

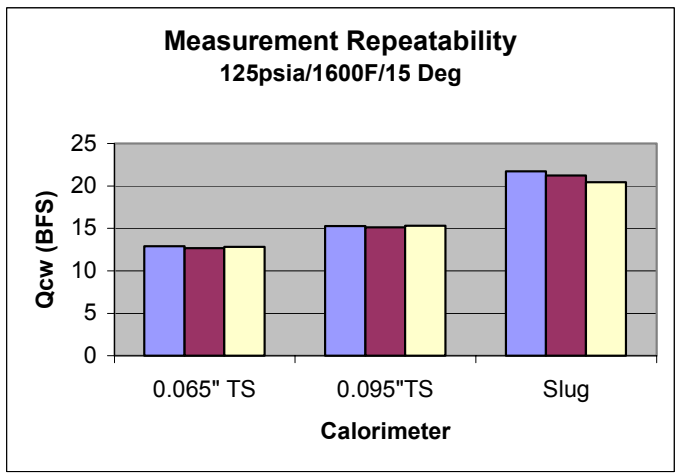

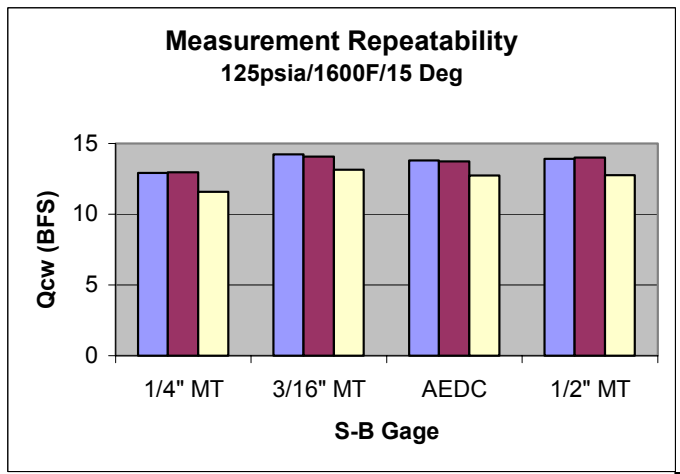

D.W. Clark
ED25

Measurement Comparisons

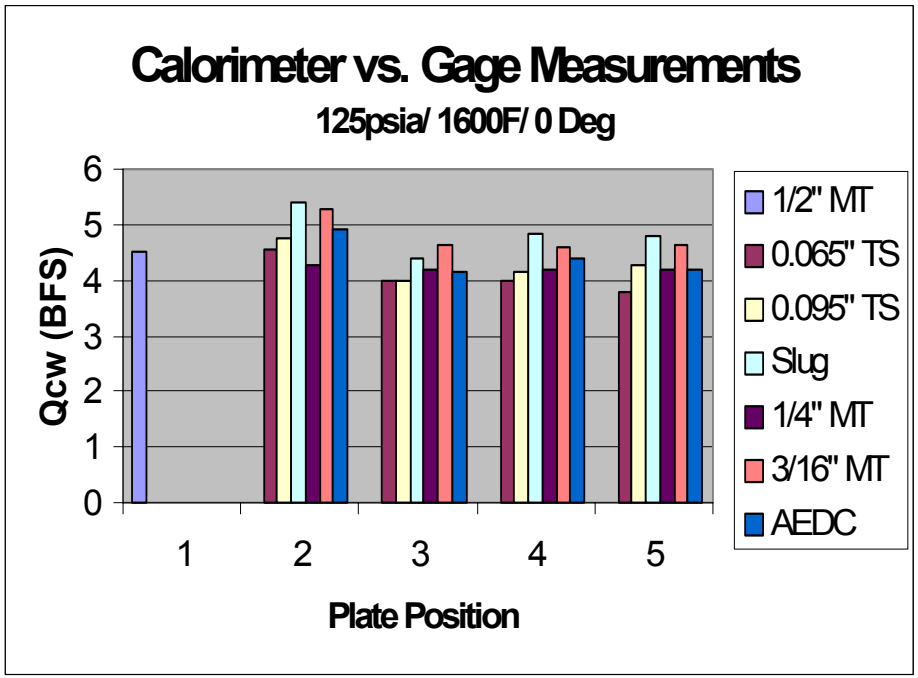

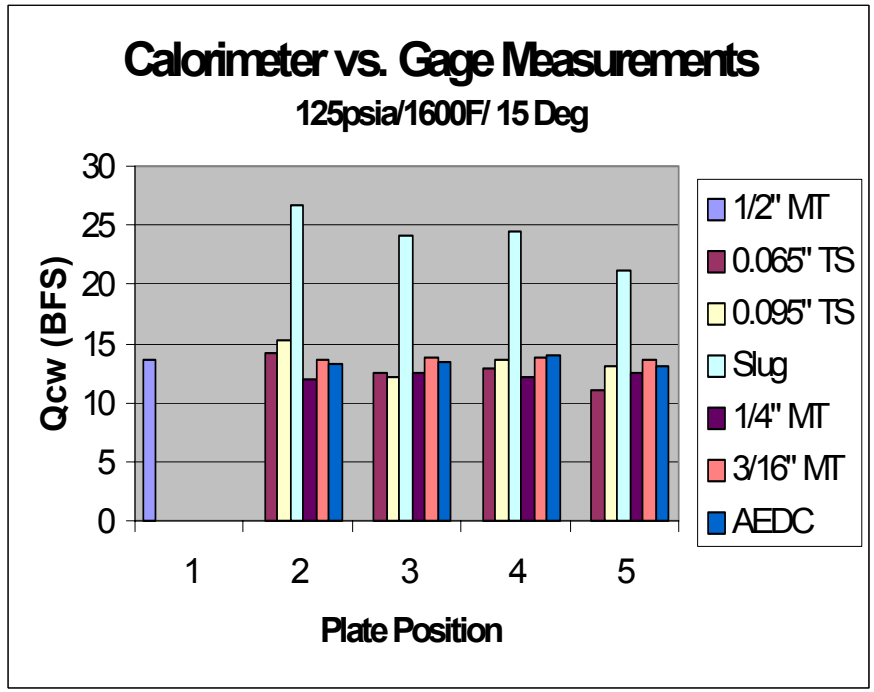

Test Condition: 125psia/ 1600F/ 0 & 15 Deg

D.W. Clark
ED25

Future Work Planned At MSFC HGF

- Continue to develop calorimeter database
- Study combined effects of supersonic convection and radiant heating on material response
- Calibrate In-flight measurements of heat fluxes with dissimilar material induced thermal mismatches between gage and surrounding TPS material
- Study radiant heat measurement in the presence of convective cooling

THERMAL/FLUID ANALYSIS OF A COMPOSITE HEAT EXCHANGER FOR USE ON THE RLV ROCKET ENGINE

Dalton Nguyen
ED25/MSFC

ABSTRACT

As part of efforts to design a regeneratively cooled composite nozzle ramp for use on the reusable vehicle (RLV) rocket engine, an C-SiC composites heat exchanger concept was proposed for thermal performance evaluation. To test the feasibility of the concept, sample heat exchanger panels were made to fit the Glenn Research Center's cell 22 for testing. Operation of the heat exchanger was demonstrated in a combustion environment with high heat fluxes similar to the RLV Aerospike Ramp. Test measurements were reviewed and found to be valuable for the on going fluid and thermal analysis of the actual RLV composite ramp. Since the cooling fluid for the heat exchanger is water while the RLV Ramp cooling fluid is LH2, fluid and thermal models were constructed to correlate to the specific test set-up. The knowledge gained from this work will be helpful for analyzing the thermal response of the actual RLV Composite Ramp. The coolant thermal properties for the models are taken from test data. The heat exchanger's cooling performance was analyzed using the Generalized Fluid System Simulation Program (GFSSP). Temperatures of the heat exchanger's structure were predicted in finite element models using Patran and Sinda. Results from the analytical models and the tests show that RSC's heat exchanger satisfied the combustion environments in a series of 16 tests.

INTRODUCTION

Nasa is developing Advanced Technology Composite Aerospike Nozzle Ramp for potential use on reusable launch vehicles (RLVs). The primary drivers for the high risk, high payoff composite ramp concept are reduced weight relative to current designs and increased high temperature performance. Thermal and fluid analyses were performed to find if any composite heat exchanger designs meet the RLV requirements. This independent study also provides potential design options that may lead to a feasible nozzle ramp design. To test the feasibility of the designs, sample heat exchanger[1] panels were made to fit the Glenn Research Center's cell 22 for testing. Operation of the heat exchanger was demonstrated in a combustion environment with high heat fluxes similar to the RLV Aerospike Ramp. Test measurements were reviewed and found to be valuable for the on going fluid and thermal analysis of the actual RLV composite ramp. Since the cooling fluid for the heat exchanger is water while the RLV Ramp cooling fluid is LH2, fluid and thermal models were constructed to correlate to the specific test set-up. The heat exchanger's cooling performance was analyzed using the Generalized Fluid System Simulation Program (GFSSP)[2]. Temperatures of the heat exchanger's structure were predicted in finite element models using Patran[3] and Sinda[4] codes.

COUPLE D FLUID/THERMAL ANALYSIS

The heat exchanger test article, shown in Figure1, includes 9 composite tubes, inlet and outlet manifolds, and instrumentation ports. Cooling performance the CMC panel was analyzed using the Generalized Fluid System Simulation program (GFSSP). Temperatures of the panel structure were predicted in finite element models using Patran and Sinda. A schematic of the GFSSP model is shown in Figure 2. The coolant thermal properties are taken from test data. From the inlet manifold to each of 9 tubes, the flow coefficient[6] is 0.6. At the 90 degree elbow, the flow restriction is defined by the 2k method[7] (k1 = 800 and k2 = 0.2.) The surface roughness inside the tubes is 0.0019 inches (50 μm). Heat transfer coefficients for the combustion gas, shown in Figure 3, were provided by the Rockwell Science Center from a series of calibration tests. Thickness of the CMC layer is 0.030 inches with a thermal conductivity of 5.8 BTU/hr-ft-^{o}F in the transverse direction, and 10 BTU/hr-ft-^{o}F in the longitudinal direction.

Results:

Figure 4 shows how the water mass flow rate depends on the water pressure difference between the water inlet and outlet ports. Pressure drops range from 4.63 psid to 22.95 psid for 16 tests. The water mass flow rate predictions are consistently higher than the test measurements. Average deviation was found to be 8.5% for a series of 16 tests. The source of this variation may be the accuracy of the interior surface roughness of 0.0019 inches that was used in the model.

Temperatures of the water outlet in tests 668, 671, and 672 in which the mass flow rates are about 1.5 lbm/sec are 123 ^{o}F, 136 ^{o}F, and 141 ^{o}F. When the water mass flow rates increased to 3.0 lbm/sec in tests 663, 664, and 665, the water outlet temperatures decreased to 97 ^{o}F, 99 ^{o}F, and 101 ^{o}F respectively.

The temperature of the outside surfaces were calculated for tests 668, 671, and 672 to be 2410 ^{o}F , 2630 ^{o}F, and 2860 ^{o}F respectively. They are below the use temperature limit[4] of 3000 ^{o}F. The Figures 6 to 8 show thermal elements and temperatures of the panel for tests 671, and 672. As the water mass flow rate increases to 3.0 lbm/sec, temperatures of the outside surface were found to be 1950 ^{o}F, 2040 ^{o}F, and 2580 ^{o}F for conditions of test 663, 664 and test 665 respectively. Overall the outside surface temperatures were below the limit temperature of 3000 ^{o}F for all cases.

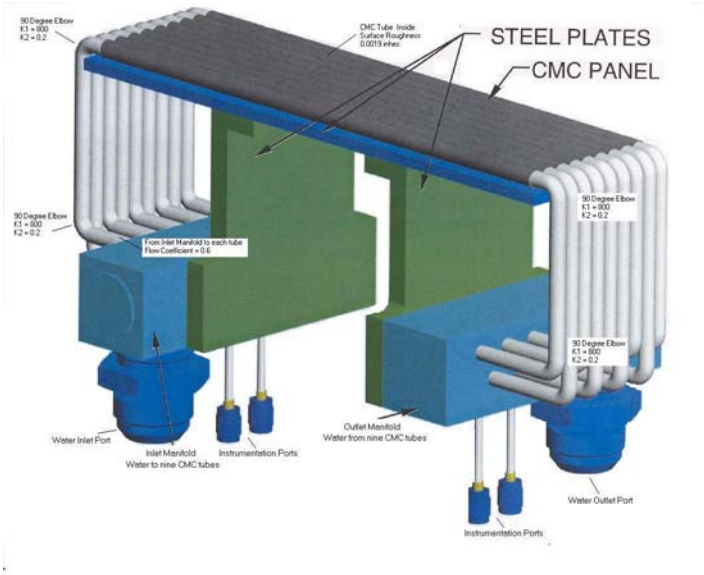

Figure 1:
Test Article Assembly with Instrumentation Ports

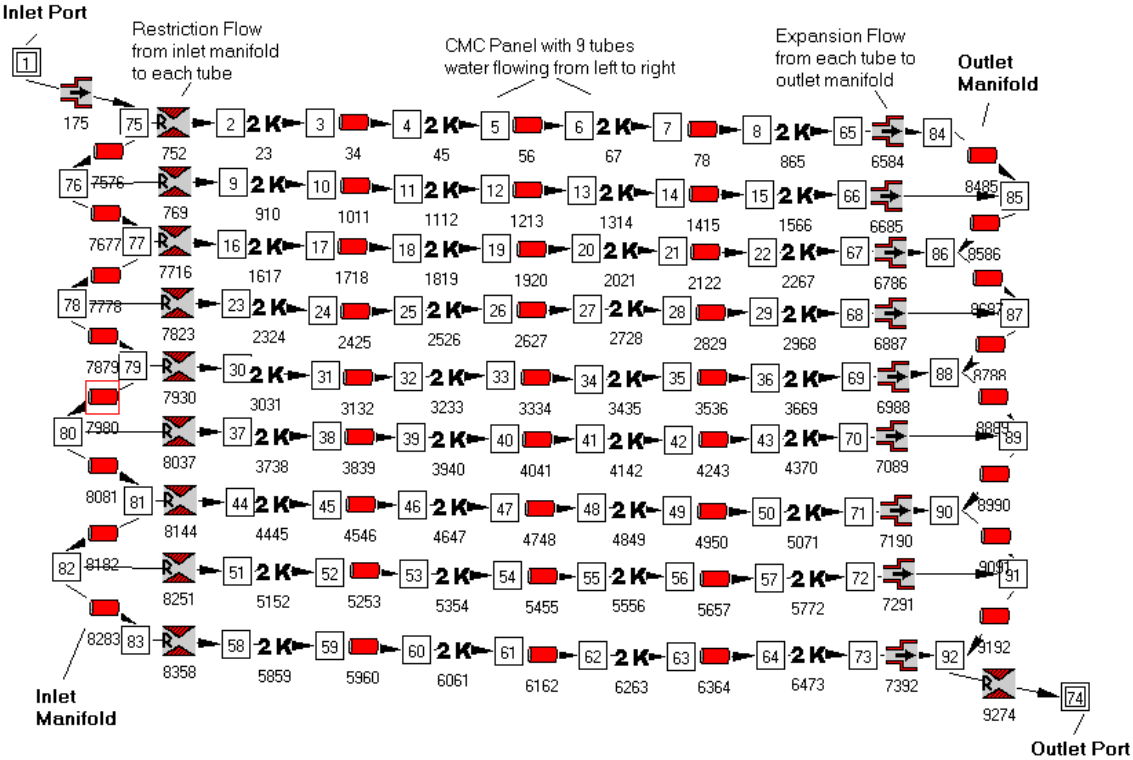

Figure 2: GFSSP model schematic of 9 tube panel
with inlet and outlet manifolds

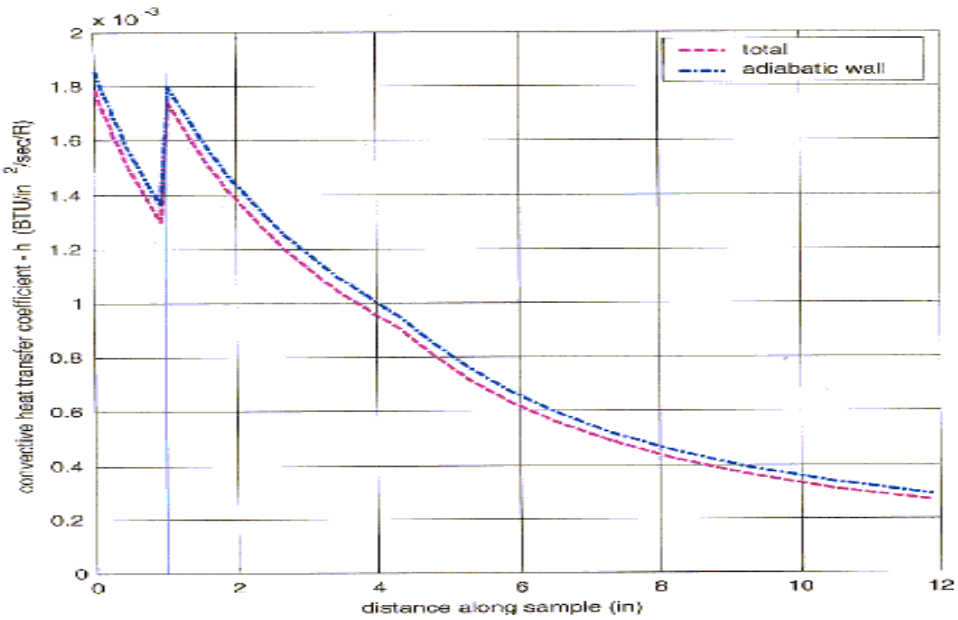

Figure 3: Heat Transfer Coefficient
Cell 22 Calorimeter test Results

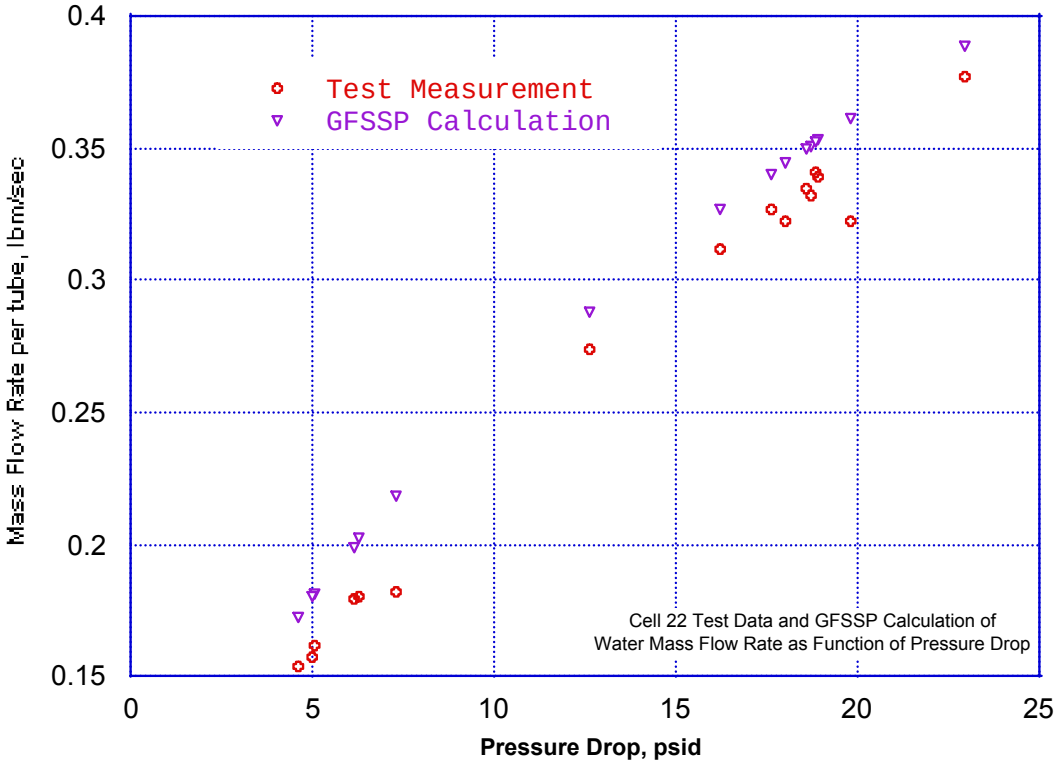

Figure 4: Test measurements and GFSSP calculation of
Water Mass Flow rate as Function of Pressure Drop

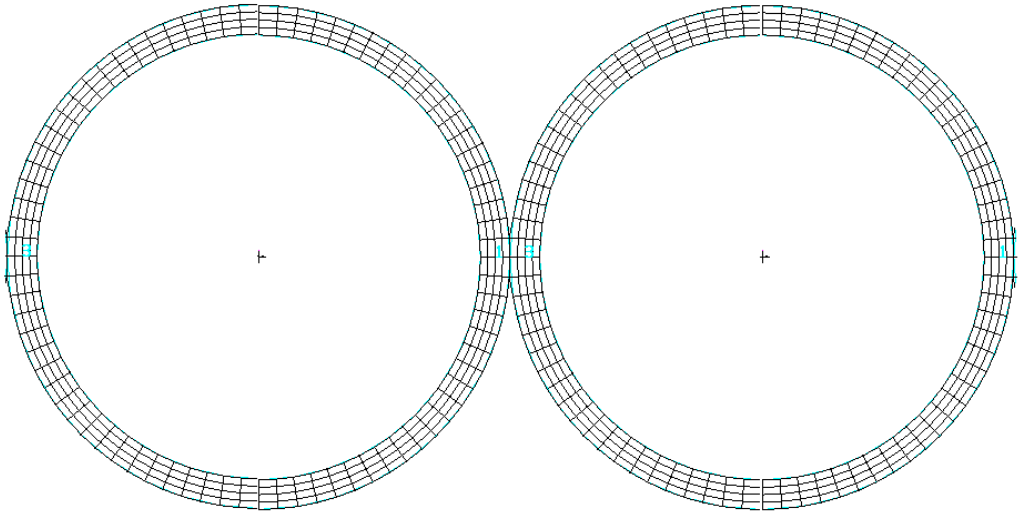

Figure 5: Thermal Element Model

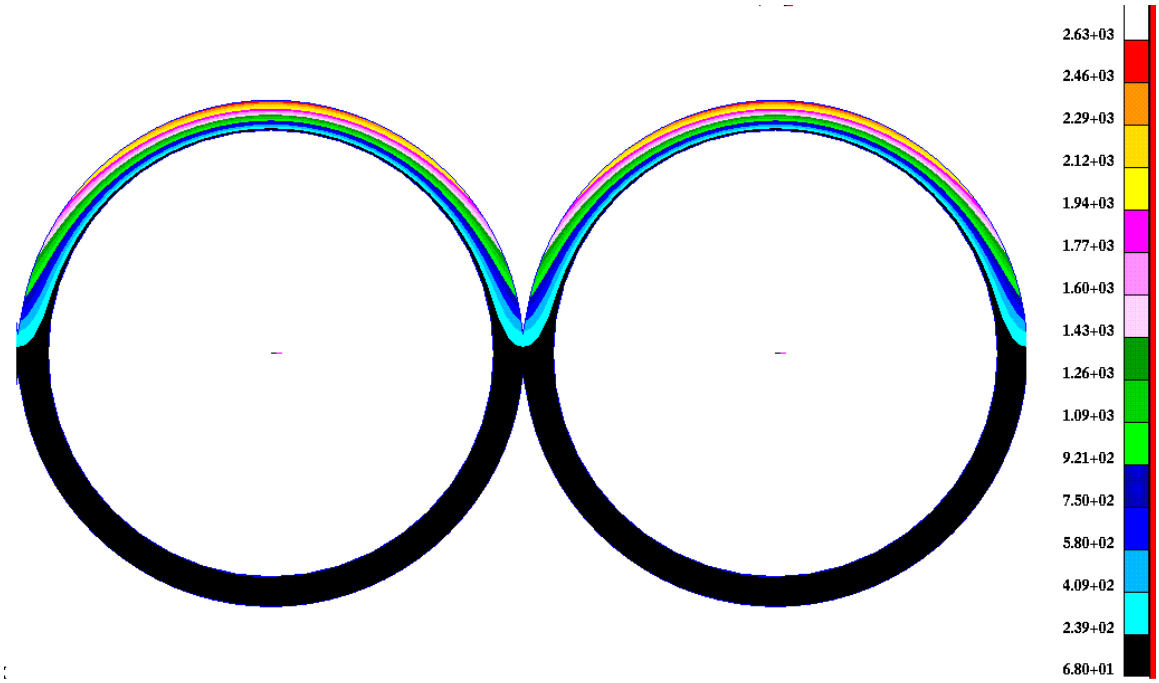

Figure 6: Temperatures of Composite Panel
for Test 671 Combustion Environment

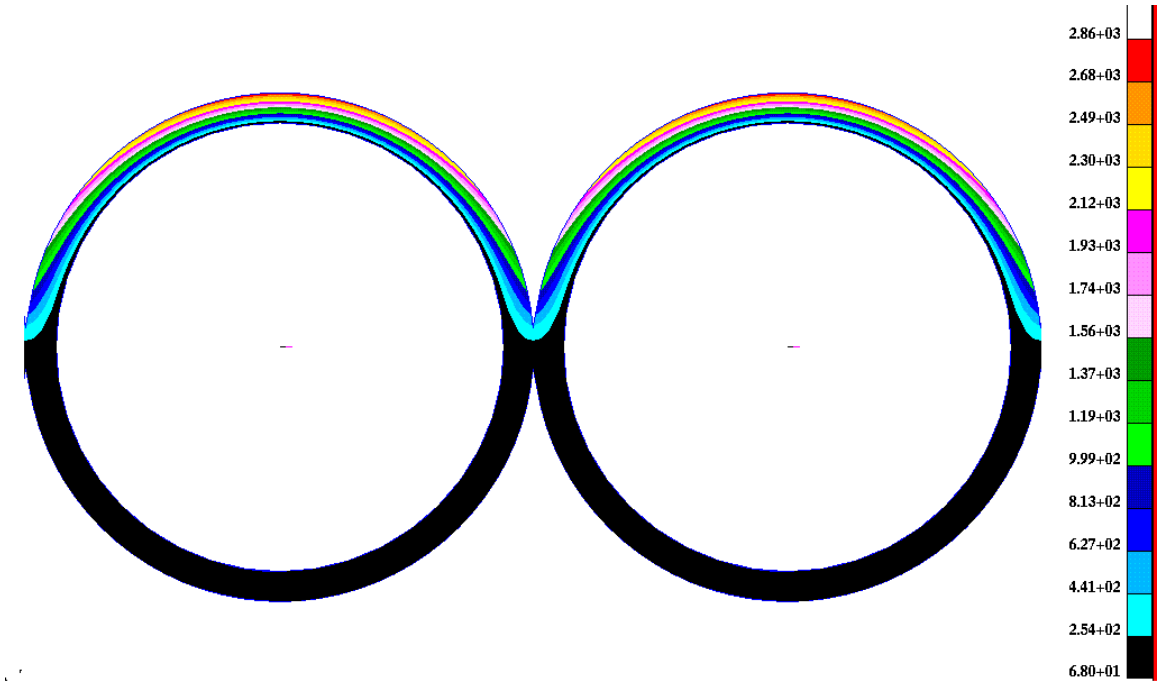

Figure 7: Temperatures of Composite Panel
for Test 672 Combustion Environment

CONCLUSIONS

The heat exchanger's cooling performance was analyzed using the GFSSP. Temperatures of the heat exchanger's structure were predicted in finite element models using Patran and Sinda. Results from the analytical models and the tests show that RSC's heat exchanger survived the combustion environments in a series of 16 tests. The outer surface temperatures of the heat exchanger were found to be below the use limit. The knowledge gained from this coupled fluid and thermal analysis will be helpful for analyzing the thermal response of the actual RLV Composite Ramp.

ACKNOWLEDGEMENTS

The author wish to acknowledge the contributions of J. Stout (Boeing-Rocketdyne), and D. Marshall (Rockwell Science Center).

REFERENCES

1. Rockwell Science Center: "Testing of Ceramic Composite Panels at NASA GRC's Cell 22." January 04, 2001.

2. Generalized Fluid System Simulation Program (GFSSP), Version 3.0

3. Patran Manual

4. Sinda/G User's Guide

5. Baumeister, T.: "Mark's Handbook…" 8thed, McGraw-Hill, New-York.

6. Hooper, W.B.:"The Two-K Method Predicts Heat Losses in Pipe Fittings." Chem. Engr., Aug 24 pp97-100, 1981.

THERMAL ANALYSIS IN SUPPORT OF THE BOOSTER SEPARATION MOTOR CRACK INVESTIGATION

Darrell Davis
NASA/MSFC/ED25
Thermodynamics and Heat Transfer Group

Terry Prickett
NASA/MSFC/ED25
Thermodynamics and Heat Transfer Group

ABSTRACT

During a post-test inspection of a Booster Separation Motor (BSM) from a Lot Acceptance Test (LAT), a crack was noticed in the graphite throat. Since this was an out-of-family occurrence, an investigation team was formed to determine the cause of the crack. This paper will describe thermal analysis techniques used in support of this investigation. Models were generated to predict gradients in nominal motor conditions, as well as potentially anomalous conditions. Analysis was also performed on throats that were tested in the Laser Hardened Material Evaluation Laboratory (LHMEL). Some of these throats were pre-cracked, while others represented configurations designed to amplify effects of thermal stresses. Results from these analyses will be presented in this paper.

INTRODUCTION

Booster Separation Motors (BSM) are small solid propellant motors attached to the Frustum and Aft Skirt of the Solid Rocket Boosters (SRB). These motors have a throat diameter of 3.13 inches and fire for approximately 0.8 seconds. The purpose of the motors is to provide a thrust vector to the SRBs at separation to guide them away from possible contact with the orbiter.

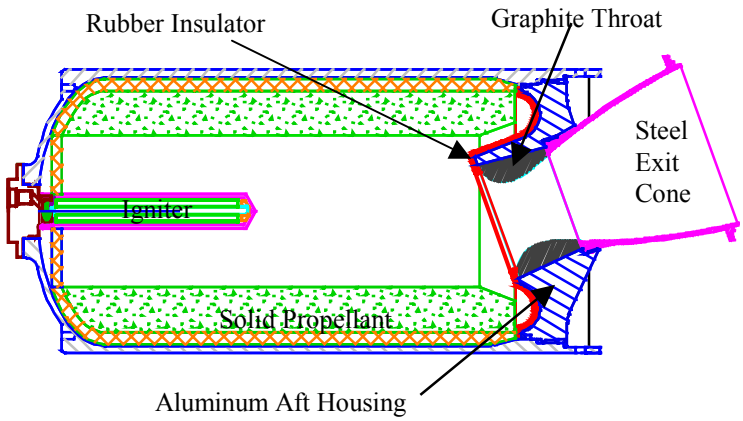

Figure 1: BSM Cross Section

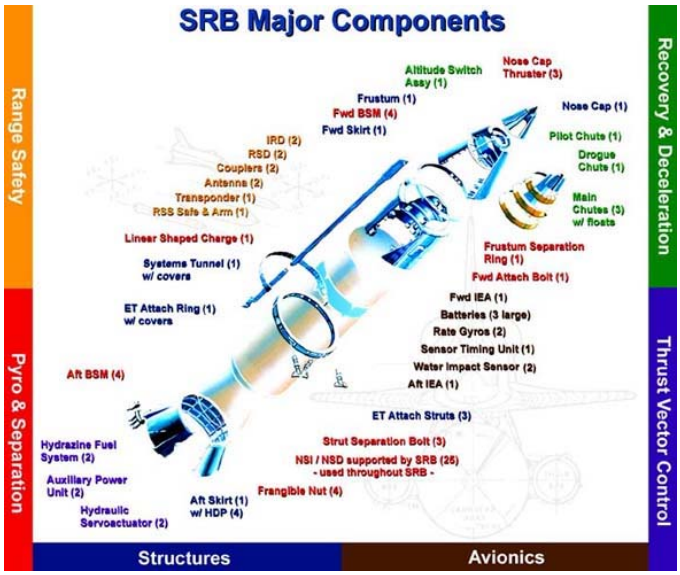

Figure 2: SRB Components Showing Location of BSMs

These motors are manufactured by Pratt & Whitney's Chemical Science's Division (CSD) near San Jose, California. A lot of BSMs consist of 160 motors manufactured with similar characteristics. From each lot, two motors are chosen for Lot Acceptance Tests (LAT). The motors are preconditioned hot and cold, 120F and 30F, and fired. The purchase of the lots is dependent on the results of the LAT. Testing of the lot designated ABM was performed in December 2000. Since it was near the Christmas holiday, the two BSMs were packed into crates and left under a overhang. In early January, the motors were removed and subjected to the post-test inspection. At that time it was noticed that the forward end of the graphite throat had a crack.

Figure 3: Crack in Graphite Throat

During the history of the BSM program, a crack had never been detected in a BSM throat. Since this was an out-of-family occurrence, an anomaly investigation team was formed. (Further investigation revealed that this might not have been as rare as was thought. Even though eight BSMs fly on each SRB, 16 per flight, very few had been subjected to the type of inspection that would have seen such a crack. Most of the throats on the aft BSMs are shoved into the BSM case at splashdown and are damaged beyond the point of reasonable inspection. The typical inspection routine for the forward BSMs was a simple visual inspection to ensure there was no catastrophic failure or out-of-family erosion of the throat. BSMs from the first three shuttle flights, the first two post-Challenger flights and every one of the LAT BSMs were inspected in-depth.)

MODEL DESCRIPTION

The Thermodynamics and Heat Transfer Group was tasked to generate thermal profiles to be used as an input to stress models. Although the throat is symmetric and could be modeled with a 2-D model, the aft housing in not symmetric and provides a non-uniform heat sink. Therefore it was decided to create a 3-D SINDA model. PATRAN was used for pre- and post-processing of the SINDA model. Figure 4 shows the elemental composition of the model as well as a graphic illustrating the locations of the different materials.

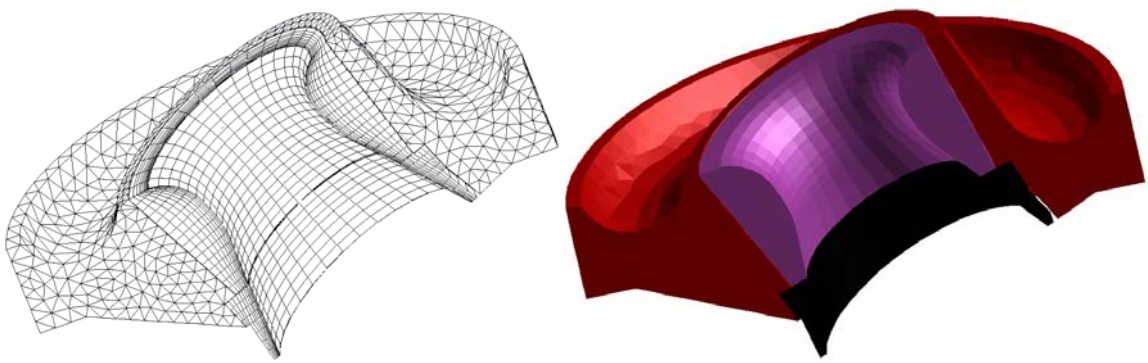

Figure 4: PATRAN Pre-processing Graphics

Boundary conditions and material properties were provided by CSD. The Aerothermal Chemical Equilibrium (ACE) code was used to calculate combustion gas properties within the chamber. UARLED was used to calculate gas static and recovery temperatures as well as boundary layer temperatures and heat transfer coefficients (HTCs). The HTCs were adjusted by empirical constants based on CSD's experience with actual measured responses from many similar programs. These boundary conditions have been used by CSD since the inception of the BSM program. Figure 5 shows recovery temperature as a function of axial location. The analysis assumed no circumferential variation in temperature at a specific location. Figure 6 shows a multiplying factor applied to the recovery temperature to account for the effect of Propellant Mean Bulk Temperature (PMBT) on the ballistics of the motor. Therefore the recovery temperatures used in the analysis to predict surface temperatures were functions of time and location. Figure 7 illustrates the values of the heat transfer coefficients as a function of time.

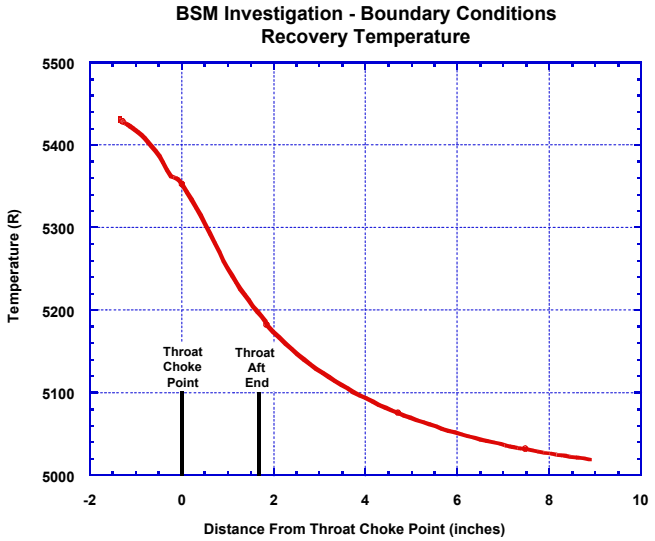

Figure 5: Recovery Temperature

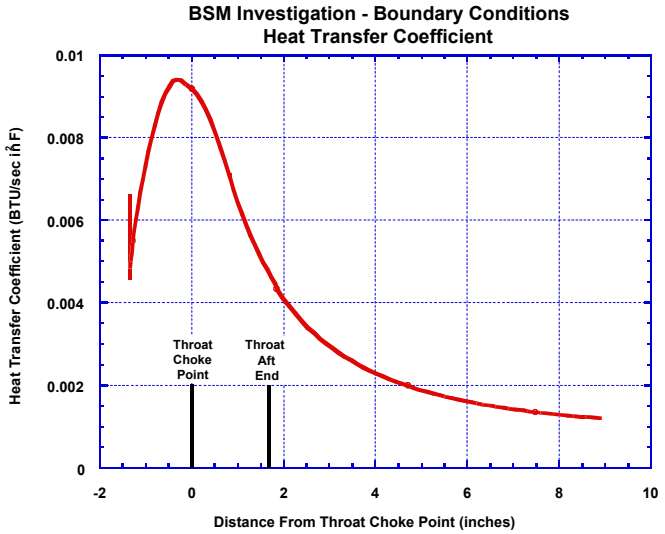

Figure 6: Heat Transfer Coefficient

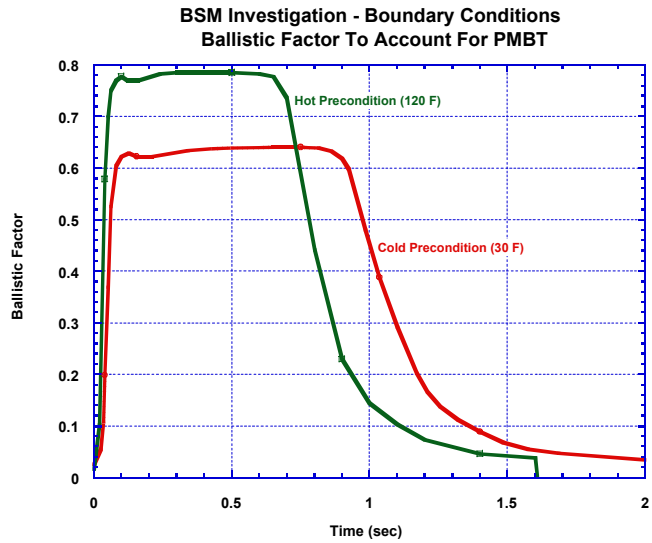

Figure 7: Ballistic Factor

The PATRAN model was translated into SINDA and the environments were applied to the model. The initial temperature of the BSM was assumed to be 120 F. A transient routine was used to generate in-depth thermal response through the throat. A two second simulation was run to investigate the isotherm propagation during soakback as well as during hot-fire. Results were recorded every 0.1 seconds. The data was read back into PATRAN for post-processing and a database of the results was sent to the stress group for structural analysis. The results in Figure 8 represent the results of the thermal analysis at 0.8, 1.2 and 2.0 seconds respectively.

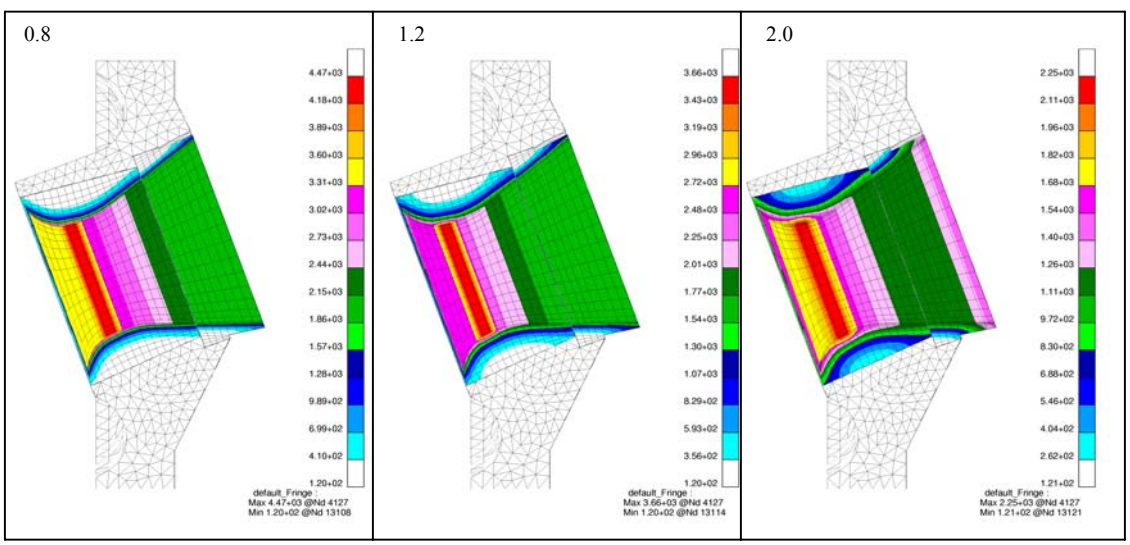

Figure 8: Results From Thermal Model at 0.8, 1.2, and 2.0 seconds. Temperature units are deg F.

Results from the structural analysis did not produce stresses high enough to generate a crack in the throat. Since the material properties of the AJT graphite are well known, the project questioned the accuracy of the thermal model and called upon the thermal community to produce a test that could correlate the model. CSD was able to run some hot-fire test with thermocouples in the adhesive between the graphite throat and the aft housing in an attempt to verify the backside predictions. However, it proved to be extremely difficult to ensure the thermocouple beads would be in contact with the graphite. Since the case is highly pressurized during testing, no holes could be drilled into the case or housing for the thermocouple leads. The only way to get the thermocouples into the gap was to attach them to the backside of the throat prior to assembly. However, during the assembly process, as the throat is slid into the housing, the frictional forces applied to the leads caused the beads to become disconnected from the surface. This made the actual location of the bead hard to verify and since the adhesive has a low conductivity, a thin layer of adhesive between the surface and bead would cause a large gradients to form. Because of this, thermocouple responses were not repeatable. They did, at the very least, indicate that our predictions were in the ballpark, but did not provide data that could be used to correlate the model.

The need to correlate the model still existed, and it appeared that hot-fire testing would not meet the requirements. The data was not conclusive, the boundary conditions could not be verified, testing was depleting valuable assets, and it was expensive. The investigation team began looking for a test facility that could simulate hot-fire test conditions. However, the test requirements were very stringent. To achieve reasonable model correlation, and verification of material properties, the facility had to be able to generate high heat rates very quickly. The stress analysts also wanted to be able to test an entire throat, rather than a sample. This would enable them to correlate hoop stresses and thermal expansion. It was eventually determined that the LHMEL (Laser Hardened Materials Evaluation Laboratory) facility at Wright-Patterson Air Force Base in Dayton, Ohio, would best fit the test requirements. The LHMEL facility was established in 1976 as a laboratory to research laser/material interaction of advanced materials for future aerospace systems. LHMEL 1, a 15-kilowatt continuous wave CO_2 electric discharge coaxial laser (EDCL), was installed at that time. In 1989, LHMEL II was dedicated. The largest CO_2 laser in the US, LHMEL II is a 150-kilowatt continuous wave CO_2 EDCL.

SRI (Southern Research Institute) in Birmingham, Alabama, as a subcontractor to CSD, was the organization in charge of designing the tests. Initial flux predictions were still lower than what the throat would experience in a hot-fire test. In an attempt to focus more energy on the throat, SRI contacted Union Carbide, the throat manufacturer, to check the availability of a 2/3-scale throat. Union Carbide provided the scaled throats to SRI for instrumentation. Three tests were designed to generate specific data to be useful in correlating thermal and stress models. The first test was a standard thermal test. It consisted of the 2/3-scale throat bonded into an aluminum housing. Thirteen Type K thermocouples were installed into the fixture by drilling in from the backside. Nine thermocouples were placed on the bondline, while four were placed at know depths within the throat. The second test was known as line-on-line tests. For these tests, the aluminum housing was machined-matched to provide an interference fit with the throat. While these were primarily structural tests, six thermocouples were included. For the third tests, SRI pre-cracked the graphite throat. The purpose of these tests was to determine the ability of the throat to generate debris if it was cracked prior to motor firing, as well as to empirically show the differential heating between the areas above and below the crack. There were eight thermocouples on these tests. Figure 9 shows the fixture for a standard thermal test.

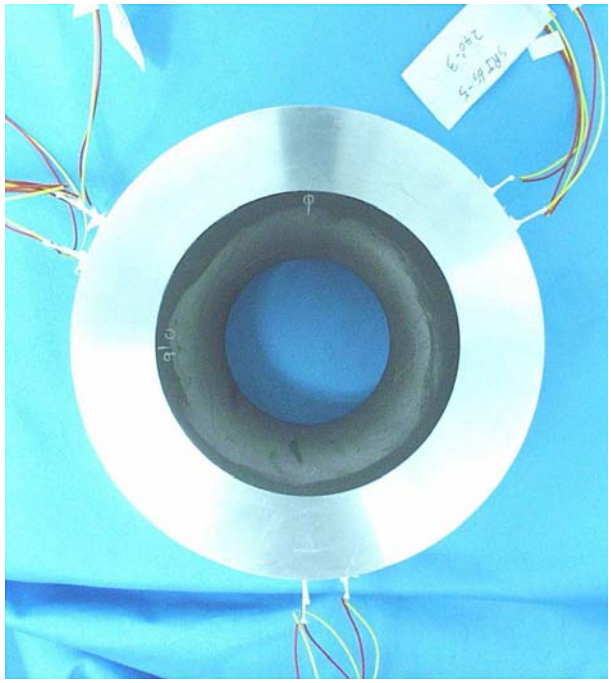

Figure 9: Top View of Standard Thermal Test Set-Up

SRI also designed a mirror to reflect the laser back to the top surface, providing a more uniform flux to the curved throat surface. Figure 10 shows the standard thermal fixture configured for testing. The crimped copper tube on the right side of the picture provided a small airflow above the fixture to remove smoke from the path of the laser. Figure 11 shows the test in process. Notice that the footprint of the laser is slightly elliptical. Also notice the smoke being generated at the top of the throat.

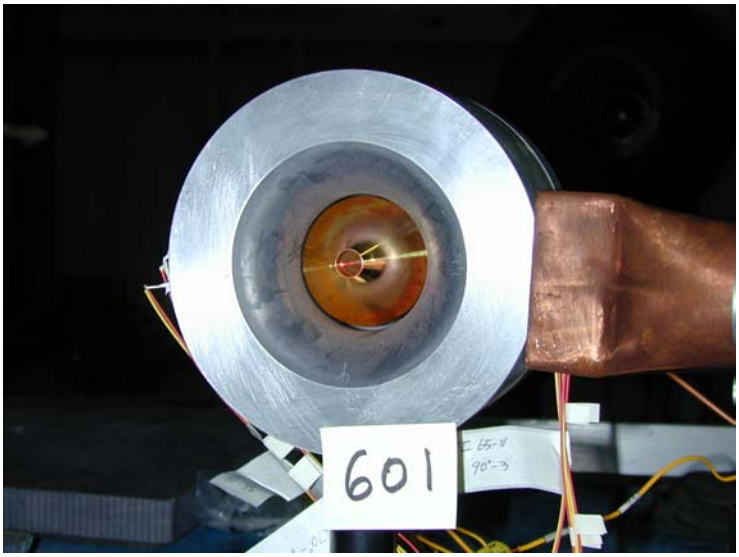

Figure 10: Standard Thermal Fixture Ready For Testing

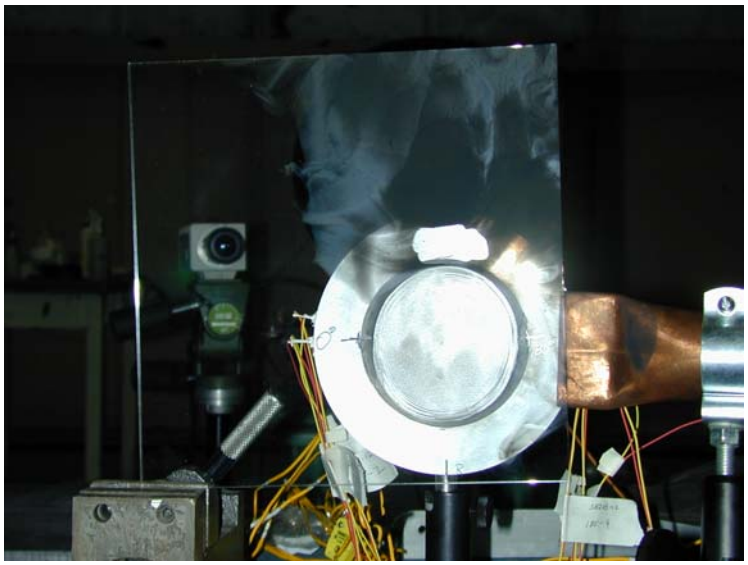

Figure 11: Standard Thermal Fixture During Testing

Since the cross-section of the fixture was constant, and the flux applied to the surface was uniform, a 2-D representation was sufficient. Again, PATRAN was used for pre-processing and interpreted into SINDA. A rendering of the model showing the grid and materials is given in Figure 12.

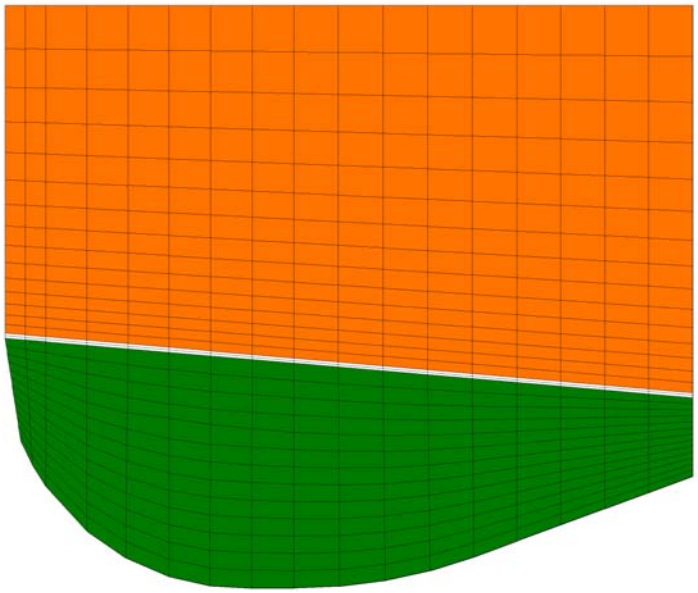

Figure 12: 2-D Model Used To Correlate Standard Thermal Tests

The material properties used for the LHMEL test model were the same properties used in the hot-fire model. The initial temperature was assumed to be the same as the ambient room temperature, 77 F. LHMEL test personnel provide the chart shown in Figure 13. It shows a fairly uniform total flux for all areas above the throat choke-point. In the model, a constant flux of 2100 W/cm2 (16.57 BTU/in2 sec) was applied to the nodes forward of the choke-point.

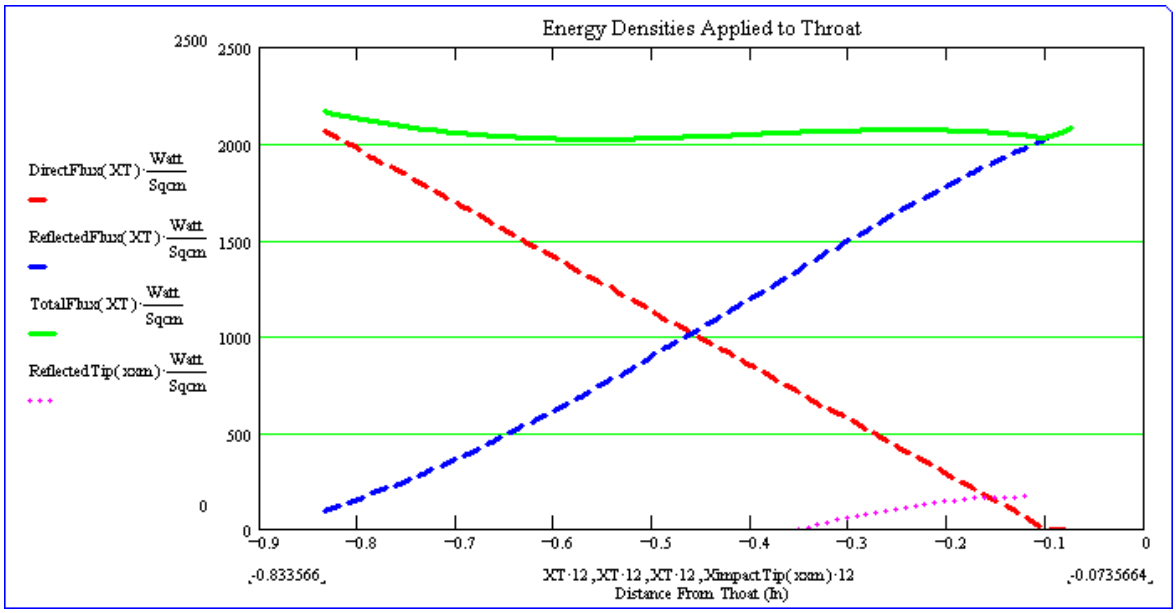

Figure 13: Flux Values From LHMEL Testing

Three one-second standard thermal tests were performed. It had been determined that the thermocouple located 0.500” down from the top surface and 0.200” inside of the bondline should produce the most uniform results. The thermocouple was surrounded by material with homogeneous properties, whereas the bondline thermocouples would likely have more variance in them depending on their location in the epoxy. Each test had a thermocouple 0.500” down and 0.200” inside, at three different radial locations, 60, 180 and 300 degrees. Figure 14 shows the results of the thermal model compared with the all nine thermocouples from the three on-second standard thermal tests.

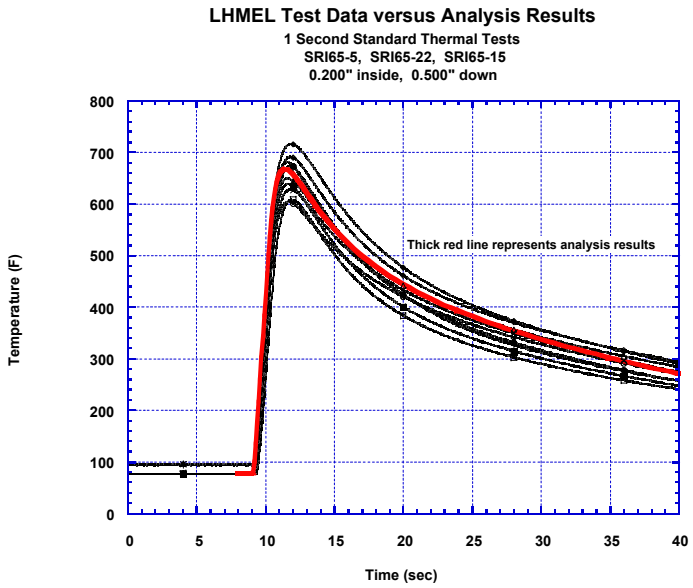

Figure 14: Model Predictions Versus Thermocouple Response For In-Depth Location

Another key correlation location was on the bondline and 0.500" down from the top. Each one second standard thermal test had three thermocouples at this location, clocked radially at 60, 180 and 300 degrees. As was expected, the response of the thermocouples in the bondline had larger variations than thermocouples embedded wholly within the graphite and was less than the model predicted at that location. However, when the predicted temperature of the first layer of epoxy (5 mils back from the back surface of the throat) was plotted along with the thermocouple response, most thermocouples fell with the predicted range. Figure 15 shows these results.

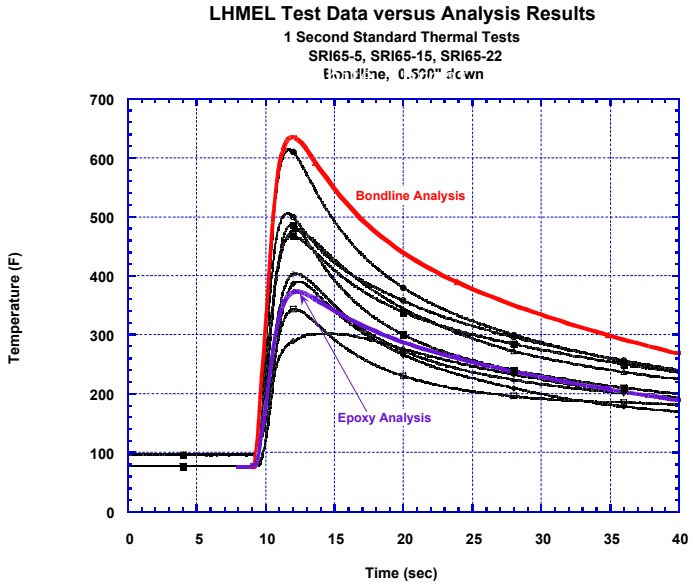

Figure 15: Model Predictions Versus Thermocouple Response For Bondline Location

The LHMEL tests produced data that was very useful in correlating the original thermal model. The model accurately predicted the test results without any changes to grid fidelity or material properties. Because of this we were able to stand by our original hot-fire predictions. The in-depth response was as good as the initial boundary conditions, which were assumed to be accurate for modeling purposes. Time and financial constraints did not allow for an in-depth testing program to verify combustion environments. However, because of CSD's vast experience with similar motors, and extensive testing and analysis during initial qualification of the BSM's, a high confidence exists in the environments.

Further confirmation of the thermal model came from the second round of LHMEL testing. Even though the first round was quite successful from a thermal standpoint, it did not produce all of the desired results. Also, there were two throats dedicated to gather thermal expansion data for the stress analyst. For this test, the throat was not contained by an aluminum housing and the only instrumentation were Linear Voltage Differential Transformers (LVDTs). These were called "free-thermal" tests. During this first round of LHMEL testing, the LVDTs did not work on either test. It was decided to go back to LHMEL for a second round of testing and do only free-thermal tests. Since this was primarily a structural test, and since there wasn't much time to install thermocouples, the throats were only instrumented with LVDTs. A single thermocouple was taped onto the outer surface simply to act as a monitor. Figure 16 shows the set-up for the free-thermal tests.

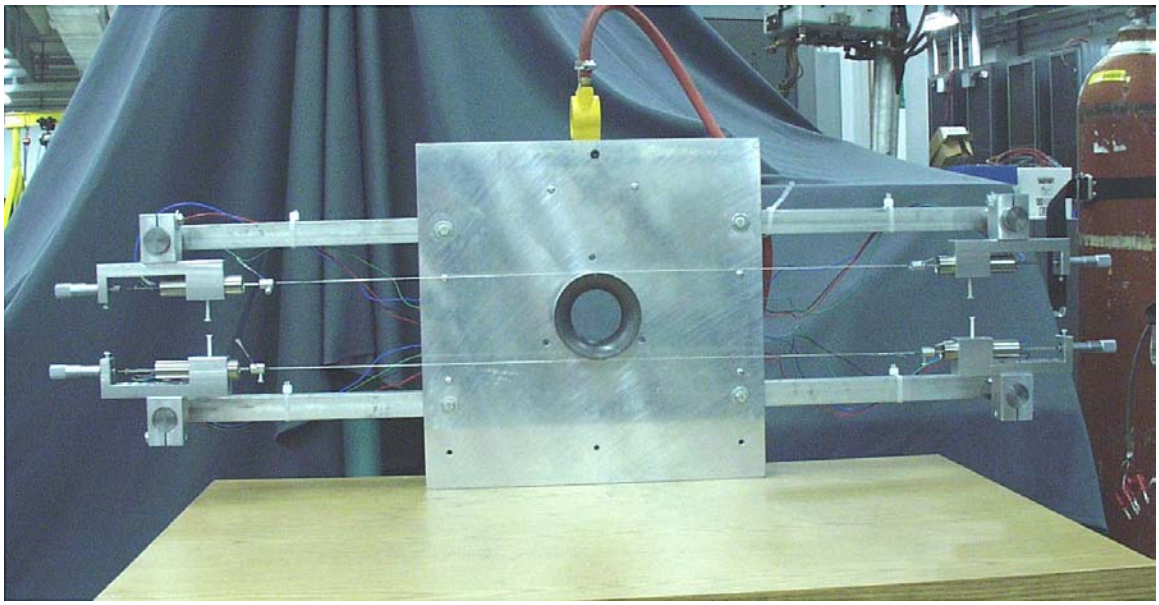

Figure 16: Free Thermal LHMEL Test Set-Up

For the free-thermal tests, the top backside of the throat had to be machined flat to allow better attachment of the LVDTs. Therefore, a new 2-D grid was developed.

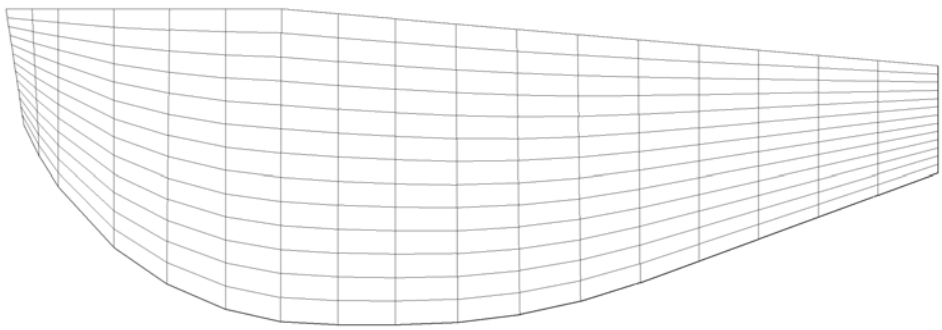

Figure 17: Finite Element Grid for Free-Thermal Tests

The same boundary conditions were applied to the model and the results were sent to stress for input into the structural model. Since there was no appreciable thermal instrumentation on the second round of free thermal tests, verification of the model would come from the results of the combined thermal-structural model. Figure 18 shows the results from that analysis.

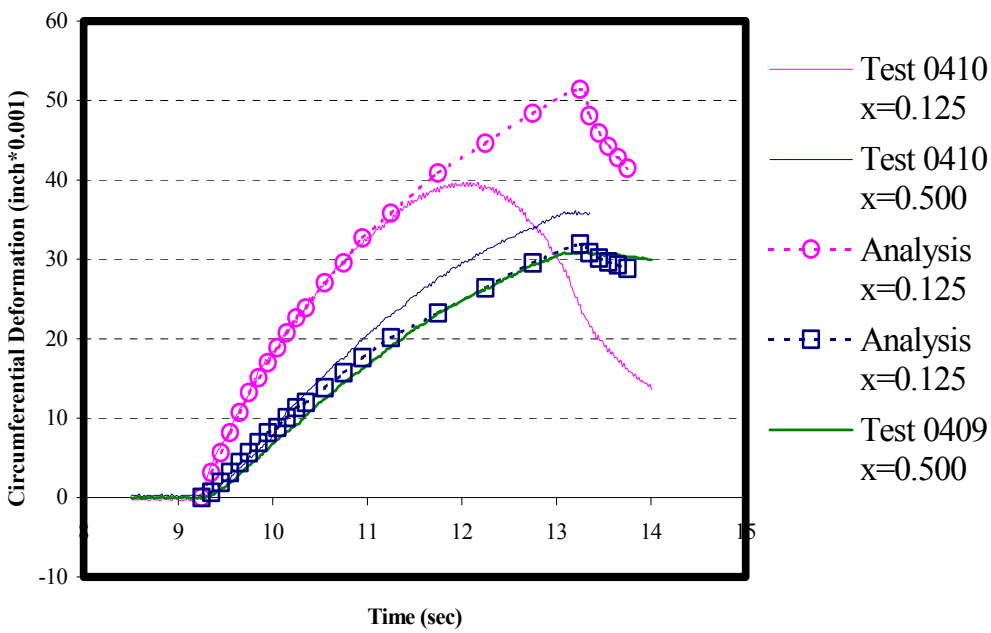

Figure 18: Results From Structural Deformation Model

Since the thermal expansion properties of the AJT graphite are well known, the main variable in the thermal-structural model was the thermal predictions. Since the results of the thermal-structural model matched test results so well, combined with results from the first round of the LHMEL testing indicate that we have high confidence in the model.

The purpose of this paper is to document the process involved in correlating a thermal and combined thermal-structural model. As it was mentioned, there were several LHMEL tests performed and predictions were made for each test. For brevity, the only data presented here was that which was sufficient to show model correlation. An entire data package was generated showing model-versus-test results. This is currently being submitted as a NASA memorandum and will eventually have a reference number.

The authors would like to acknowledge the contributions of the following people: Eric Poole from NASA/MSFC Strength Analysis Group for the structural analysis, John Koenig and Jacques Cuneo from SRI for excellent support in designing and performing LHMEL testing, Dave Bidwal from CSD for providing hot-fire boundary conditions and historical material properties, and all of the people at the LHMEL facility for having a world-class facility and for providing excellent test results.

FUNDEMENTAL BOILING AND RP-1 FREEZING EXPERIMENTS

1. LN2 Boiling Heat Transfer Coefficients

The prestart thermal conditioning of the hardware in LOX systems involve heat transfer between LOX and metal where boiling plays a large role. Information is easilly found on nucleate boiling, maximum heat flux, minimum heat flux and film boiling for common fluids like water. After looking at these standard correllations it was felt more data was needed for the cool down side transition boiling for the LN2 and LOX. In particular interest is the film boiling values, the temperature at which transition begins and the slope as peak heat flux is approached. The ultimate goal is an array of boiling heat transfer coeficient as a function of surface temperature which can be used in the chilldown model of the feed system, engine and bleed system for X-34.

The first experiment consisted of an actual MC-1 Lox Impeller which had been machined backwards, that was instrumented with 17 surface thermocouples and submerged in liquid nitrogen. The thermocouples were installed on metal thicknesses varying from the thin inducer to the thick hub. Table 1.1 shows the list of tests and impeller orientation. Table 1.2 shows the measurement list.

Table 1.1 Test Matrix
test 1, inducer down orientation
test 2, repeat inducer down orientation
test 3, inducer up orientation
test 4, horizontal 0 degrees up orientation
test 5, horizontal 180 degrees up orientation

Table 1.2 Measurement list

ID	description	thickness
1	exit, hub, 40deg	0.35
2	mid, hub, 40deg	0.70
3	inlet, hub, 40deg	0.35
4	exit, blademid, 5deg	0.07
5	mid, blademid, 35deg	0.07
6	inlet, blademid, 5deg	0.03
7	exit, hub, 220deg	0.35
8	mid, hub, 275deg	0.70
9	inlet, hub, 185deg	0.35
10	exit, blademid, 260deg	0.07
11	mid, blademid, 270deg	0.07
12	inlet, blademid, 260deg	0.03
13	inlet, bladeroot, 170deg	0.05
14	backface, r=1.625, 0deg	0.45
15	backface, r=0.625, 0deg	0.90
16	backface, r=0.625, 180deg	0.90
17	backface, r=1.625, 180deg	0.45

The impeller intial temperature was warm ambient. It was dropped into liquid nitrogen until completely chilled and the 17 transient temperatures were recorded. Figures 1.1 through 1.5 show different views of the impeller and the instrumentation locations. Figure 1.6 shows a chilled impeller in a vertical orientation. Figure 1.7 shows the impeller being submerged in liquid nitrogen in a horizontal orientation.

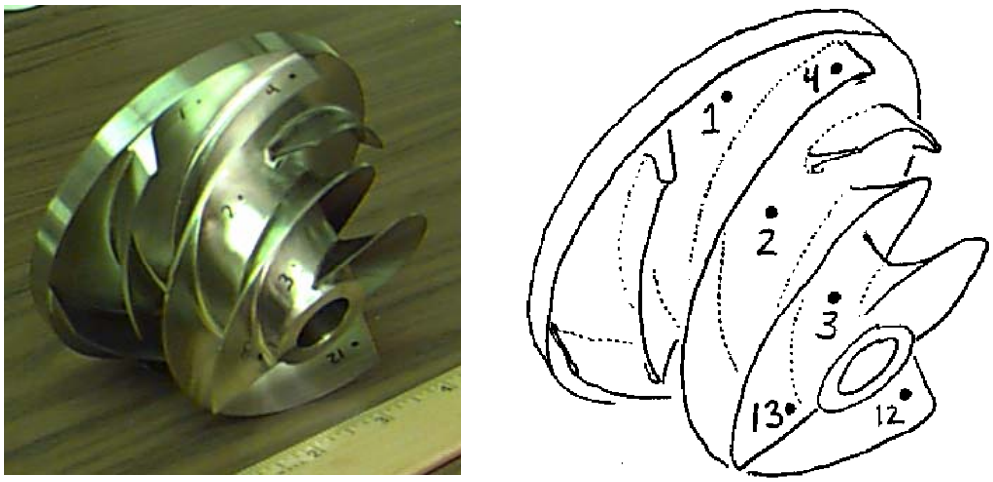

Figure 1.1 Impeller Instrumentation View 1

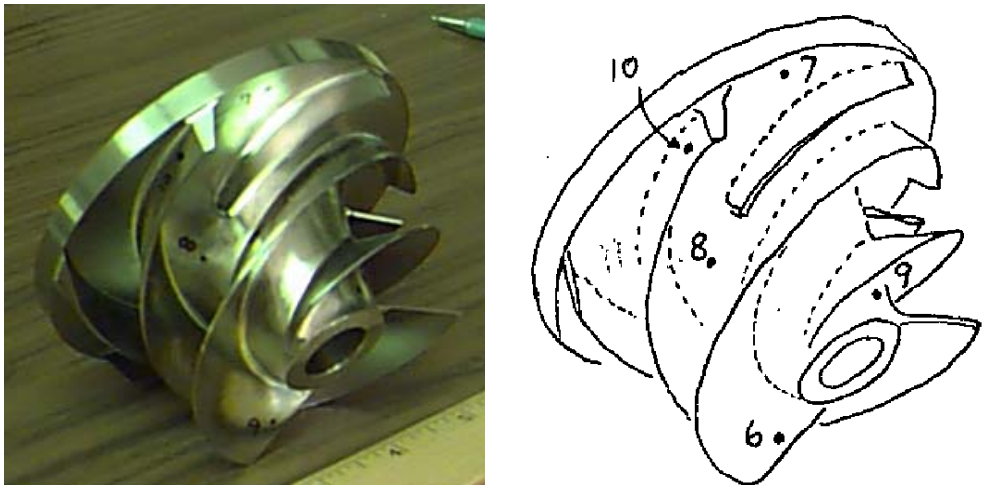

Figure 1.2 Impeller Instrumentation View 2

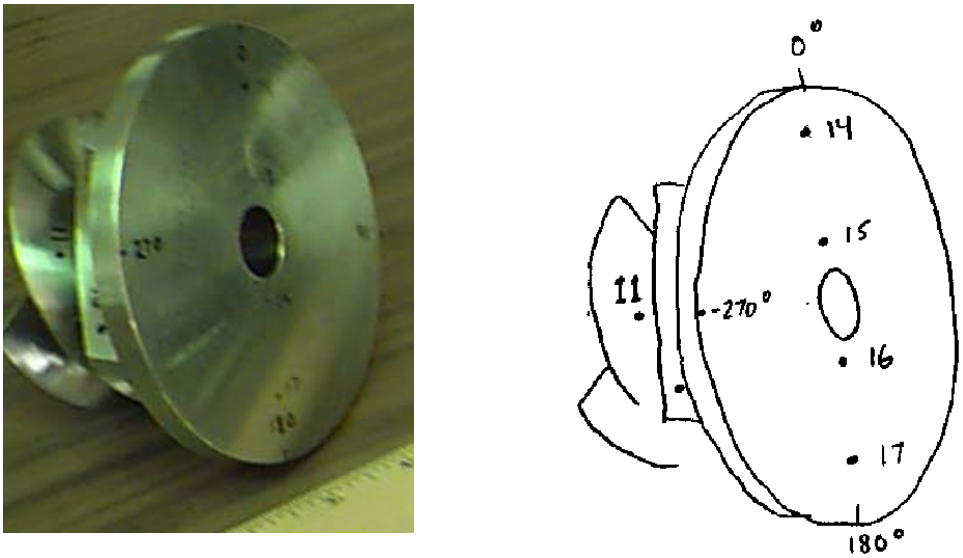

Figure 1.3 Impeller Instrumentation View 3

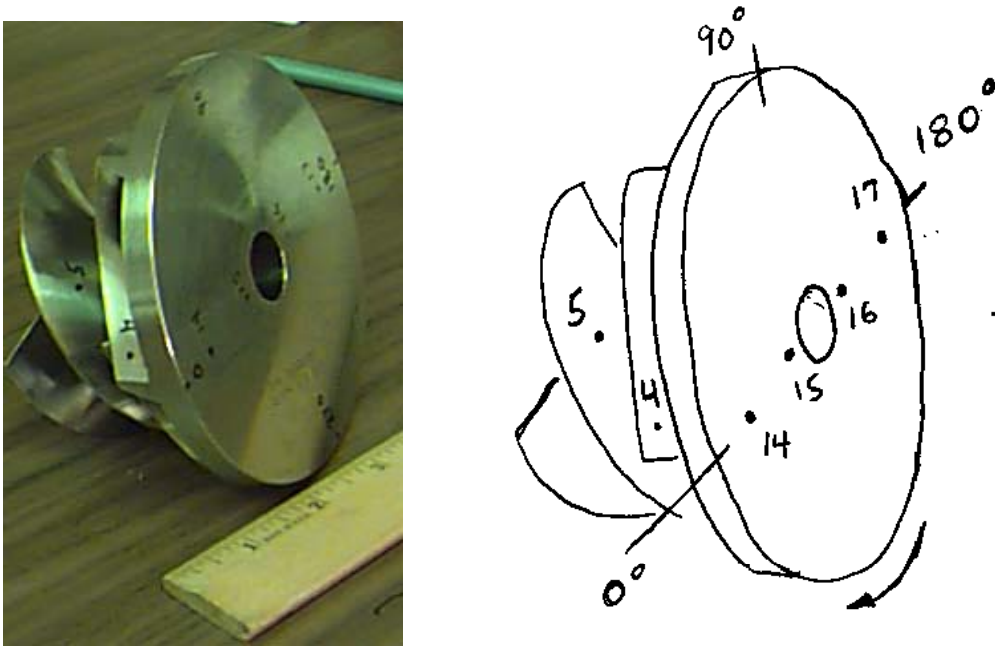

Figure 1.4 Impeller Instrumentation View 4

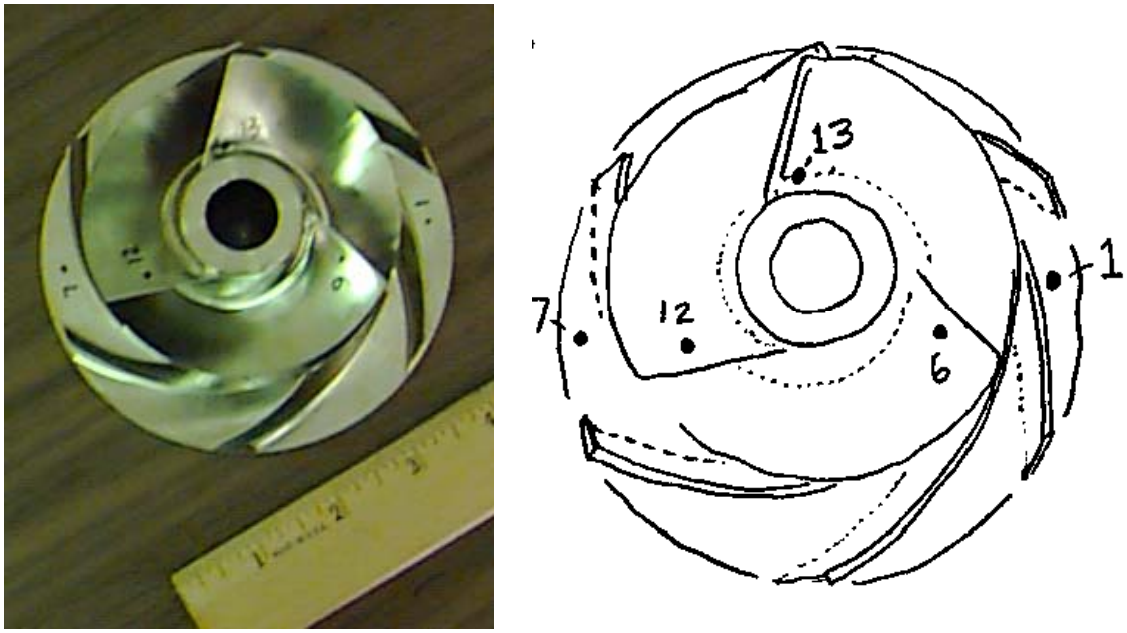

Figure 1.5 Impeller Instrumentation View 5

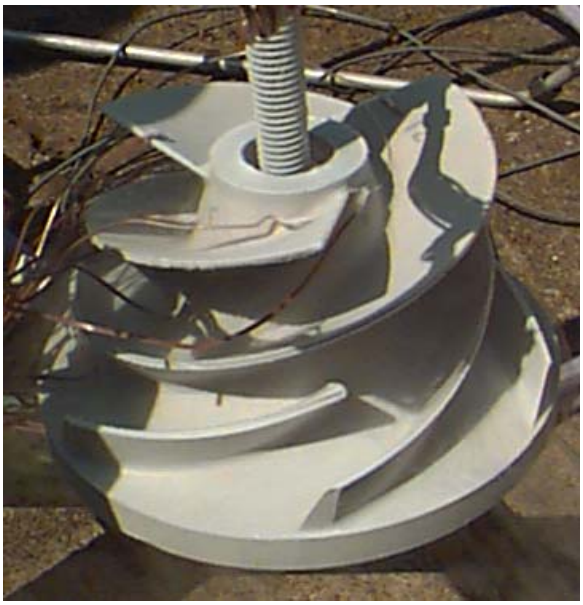

Figure 1.6: Chilled Lox Impeller

Figure 1.7: Chilling Lox Impeller in LN2

The results of the impeller chill test showed no significant variation with orientation. In general it can be said from this data that when LN2 envelopes the impeller, that all surfaces were chilled in 140 seconds. Figure 2.1.8 shows the measured data from an impeller test. Features to notice from the temperature curves are that for thick sections film boiling dominates the chill time until the surface gets to approximately –200 degrees F and then as soon as the transition to nucleate boiling begins to occur the chill time is very short from that point in time

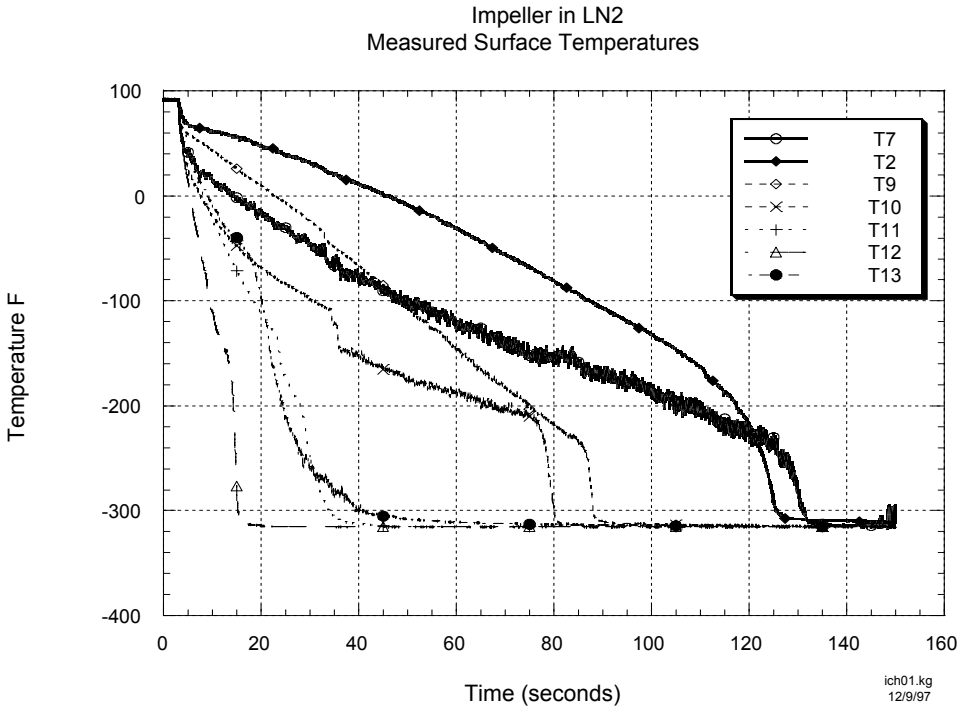

Figure:1.8: Measured Surface Temperatures, LN2 Impeller Test

With this data and a simple thermal model with varying thicknesses, the heat transfer coefficient that is required with time is derived. This is performed for a number of tests and for most of the well behaved thermocouples and averaged to establish a single array of boiling heat transfer coefficient as a function of surface temperature. As a final check this array is used to calculate surface temperature and compared to the measured data. The predictions in figure 1.9 may be compared to measured temperatures in figure 1.8 to see that the array is valid. This approach provided the needed information around the transition temperature that is not readilly found in literature.

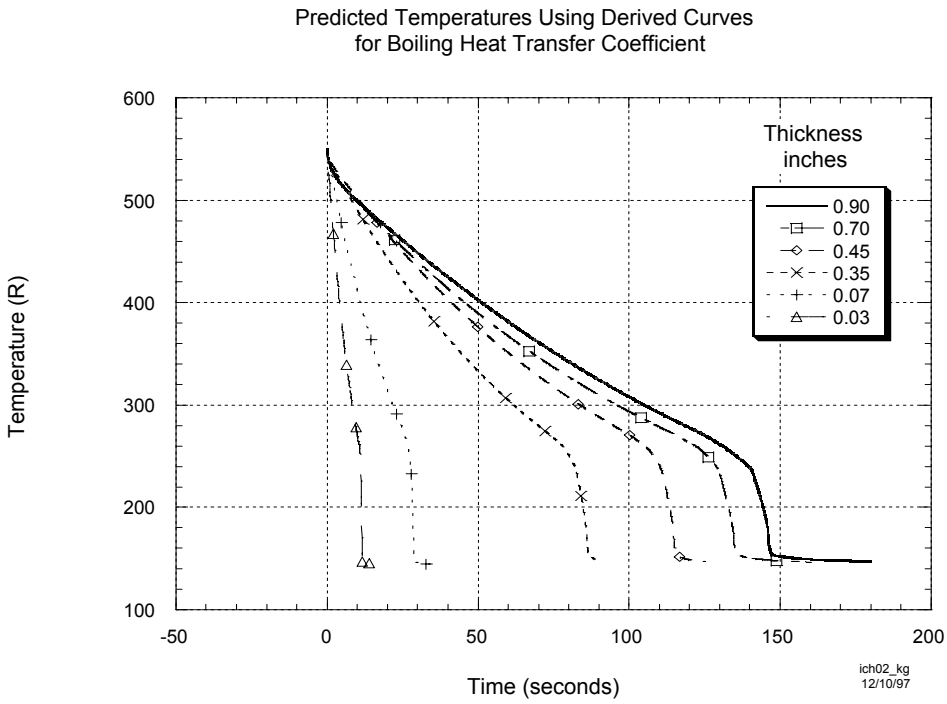

Figure 1.9: Predicted Impeller Surface Temperatures from Derived HTC Curve

2. LOX Boiling Heat Transfer Coefficients

The second experiment measured the surface temperatures of two steel plates chilled in liquid oxygen. The experience from chilling the impeller showed chilldown times sensitive to film boiling and transition boiling heat transfer coefficients and the transition temperature. The LOX testing was performed to get this information for LOX instead of extrapolating LOX from LN2. Figure 2.1 shows the plates in LOX and figure 2.2 shows the instrumented plates on the table. There were two plates 0.25 and 0.1 inches thick made from 304L stainless steel. This testing was performed in open air at a bearing materials and friction test facility operated by Phillip Hall in ED32. The surface temperature was measured and the same approach used from the impeller chill testing to obtain an array of boiling heat transfer coefficient as a function of surface temperature for LOX. Figure 2.3 shows some of the derived heat transfer coefficients before they were averaged. Features to notice on this plot are the two curves with a much lower peak. This occurs with the thin plate where the temperature drops so fast, data recording speed and thermocouple response effects the result. Next time this approach is used, thicker plates would yield better fidelity in the transition and peak boiling regions. Also notice the bump in the curves at the high temperatures when the plates are first dropped in the LOX. This phenomena was very repeatable and is evidence that it takes a finite time for film boiling to establish. This effect was included in the array for the chill model.

Figure 2.1: Chilling Steel Plates in Lox

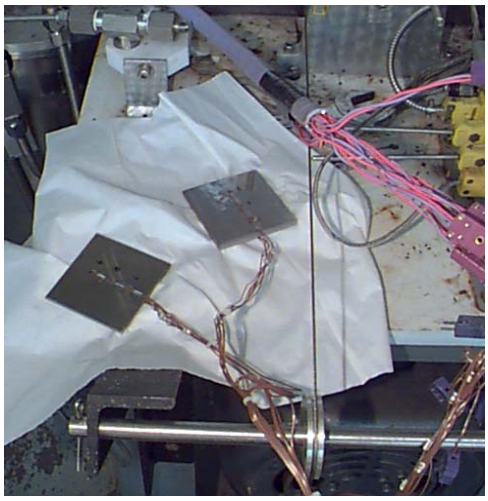

Figure 2.2: Instrumented Steel Plates

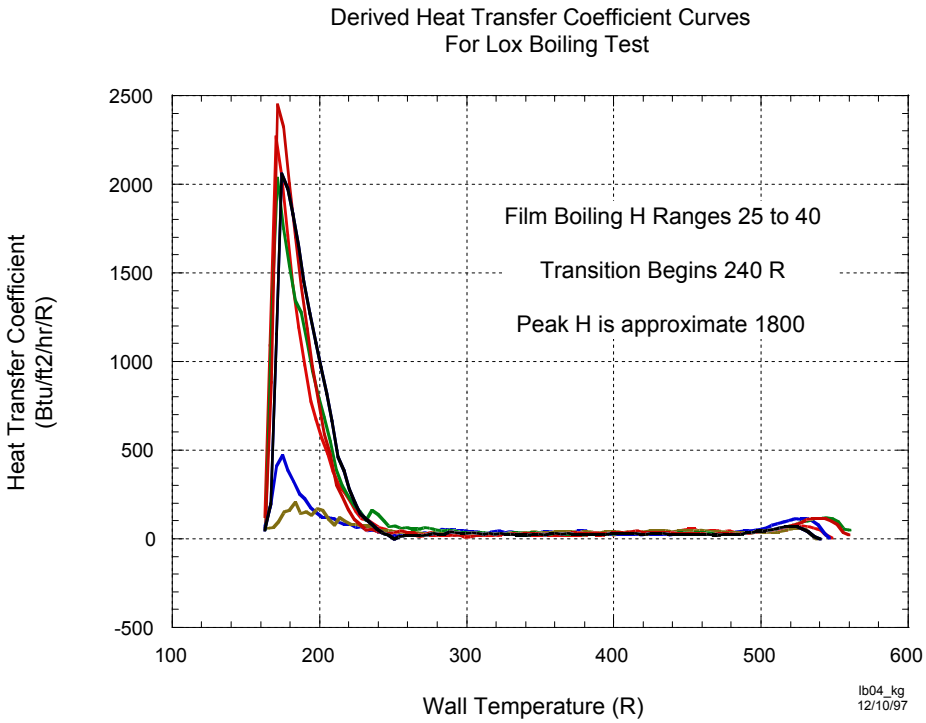

Figure 2.3: Derived HTC Curves from Steel Plates in Lox

The following are the SINDA arrays for boiling heat transfer and low pressures for LOX and LN2. These arrays may be applied for any pool boiling problem using these fluids.

```
C
            315 $ H DERIVED FROM STEEL PLATE IN LOX VS. DTE R
C                where DTE = t wall - t sat(162.3) ,h
               0.,100.,   1.7,200.,  5.7,1000.,  7.7,1800.
             17.7,1500., 27.7,1050.,  37.7,665.,  47.7,365.
              57.7,154.,   67.7,60.,   77.7,40.,   87.7,19.
              187.7,19.,  317.7,26.,  337.7,40.,  367.7,60.
              377.7,60.,  387.7,30.,  1000.,30.
            END
C
            316 $ H (btu/hr/ft2/r) FROM IMPELLER IN LN2 VS. TEMP DEGR
C                t wall - t sat(139.2) ,h
               0.,100.,   5.8,100.,   7.8,600., 9.8,2000.
             14.8,4000., 20.8,3000., 40.8,1000., 60.8,500.
             100.8,120.,  120.8,60.,  135.8,50., 1000.,50.
            END
C
```

3. RP-1 Freezing Temperature

To address the concern of RP-1 freezing in a turbopump more information on the freezing temperature was required. At the beginning of the Fastrac program a package was distributed on RP-1 properties from the Chemical Propulsion Information Agency dated 1966. This package in the general identification section lists the freezing point of RP-1 to be –55 deg F (405 deg R). In the military specification section it states that the freezing point must be –40 deg F (420 deg R) or less. A package distributed from Rocketdyne also lists –55 deg F as a typical value. An RP-1 freezing experiment was conceived to determine what the RP-1 freezing limit should be for our application and to observe the characteristics of the frozen fuel to determine at what temperature does RP-1 have the potential to damage hardware or stop flow in the bearing coolant passage.

RP-1 was frozen in an aluminum tray using liquid nitrogen and as the RP-1 thawed the temperature was measured and physical properties were observed. The results indicated that there is no discreet freezing temperature but a transition that occurs between the temperatures of 400 R and 350 R. As temperature is reduced below 350 R the solid wax increases in hardness. These temperatures are approximate because during thaw there were many phases, and temperatures existing simultaneously in the tray. This test showed conclusively that 400 R would be a safe lower limit, and that 335 R represents a significant risk to turbopump operation. RP-1 is shown in figure 1 with a temperature of 373 R (–87 F). Table 1 lists the temperatures and corresponding physical observations.

Figure 3.1: RP-1 at –87 deg F (373 deg R)

Table 3.1: Frozen RP-1 Observations

Temperature	Description
302 R	Hard wax
335 R	Solid wax, softening some
350 R	Soft wax
355 R	Gel
380 R	Gel, thick liquid, rapid warm up
420 R	Liquid RP-1 with some solid present

Based on the results of this test it was felt that –80 deg F (380 deg R) was a safe condition for fuel temperatures in the bearing coolant passage and the impeller backface cavity. In early testing we picked –60 deg F as a guideline. The operation of the turbopump was not effected in any way when Fuel Seal Drain temperatures were above –60 deg F (400 deg R). All ground test experience was with Fuel Seal Drain temperatures above –60 deg F (400 deg R). A discreet limit for this hazard was never identified however. The following is how the observer guideline was written in the test request for a LOX RP-1 Turbopump.

```
Observer Guidelines

1.  If during the pre-start phase both Fuel Seal Drain Temperatures
(E1T1032/1034) are above -65 F no action is required.  If one is between
-75 and -65 F raise IPS cavity pressure (E3P1028/1029) to 165 psia and
proceed.  If IPS supply is approximately 165 psia and one FSD
temperature is below -75 F do not start the engine.  If one temperature
is below -65 F, consult MSFC Turbomachinery if available and time
permits.
```

4. RP-1 Frozen Thickness

A second test was performed to determine how much frozen RP-1 would accumulate on a cold wall submerged in warm RP-1. LN2 flowed through the tube, and the wall temperature was measured to be 160 R. Again there was no solid liquid boundary but a transition that occurred as the distance from the wall increased. This made thickness measurements rather subjective. Because of this we had 4 different people measure the thickness and then take an average. The method for measuring the frozen thickness was to use calipers with one side hard against the tube wall and close the calipers until you think you hit frozen RP-1. This distance minus the measured tube diameter is the frozen thickness of RP-1. This test showed that if bulk RP-1 temperatures remained warm no significant buildup of solid RP-1 can take place. Figure 4.2 shows a thickness measurement being taken in this experiment and table 4.1 shows the values for four separate measurements and an average.

Figure 4.2: RP-1 Frozen Thickness

Table 4.1 Steady State Thickness Values

Measurement	Value
A.	.044 inches
B.	.082 inches
C.	.074 inches
D.	.024 inches
average	.056 inches

A conservative approach to calculating frozen thickness was developed using a thermal conductivity of .14 (Btu/ft/hr/degF) and a freezing temperature of -60 deg F (400 deg R). The following is an example using the approach to calculate the thickness on the tube test.

Assumptions

1. The freezing temperature is 400 deg R
2. Warm RP-1 Temperature is 520 deg R
3. The tube OD wall temperature is 160 deg R (Tsat Nitrogen is 144 deg R).
4. RP-1 Fluid properties from CPIA handout at film temperature 460 deg R.
5. Copper tube outer diameter is 0.35 inches

RP-1 Properties
Viscosty mu = 27.5 E-5 lbm/in/sec
Thermal conductivity k = 1.875 E-6 Btu/in/sec/R
Thermal conductivity for solid RP-1 k = 3.241 E-6 Btu/in/sec/R
Density = sp.grav * rho H20 = 0.83 * 0.03615 lbm/in3 = 0.03 lbm/in3
Prandtl Number = 65.

Calculate Grashov Number

$$Gr = \frac{g\ Beta\ (Tf\text{-}Ts)\ d3}{(mu/rho)2}$$

$$= \frac{386.4\ (in/sec2)\ (1/460)(1/R)\ (520\text{-}400)\ (.35)\text{^}3\ (in3)}{(27.5\ E\text{-}5/0.03)\text{^}2\ (in4/sec2)}$$

= 51433

Calculate Rayleigh Number
Ra = Gr Pr
= 51433 * 65
= 3,343,145

Calculate Nusselt Number from Emperical correllation Long Horizontal Cylinder
Nu = .48 Ra ^.25
= .48 (3344500) ^.25
= 20.5

Calculate Natural Heat Transfer Coeficient
H = k Nu/ d
= 1.875 E-6 * 20.5 / 0.35
= 1.098 E-4 Btu/in2/sec/R = 56.9 Btu/ft2/hr/R

Frozen thickness of RP-1 can be calculated by performing an energy balance at the freezing surface and by knowing that the conductivity of frozen RP-1 is 0.14 Btu/ft2/hr/F (3.241E-6 Btu/in2/sec/R)
Q/A = k/x (400 –160) = h (520- 400)
x = k(400-160)/h(520-400)
= 3.241E-6 Btu/in/sec/R * 240 R / (1.098E-4 Btu/in2/sec/R * 120)
= 0.059 inches

The conclusion that is reached from the investigations into frozen thickness is that as long as the bulk RP-1 is warm, approximately 500 deg R or higher, there should be no concern with RP-1 freezing no matter how cold the hardware is. Also it has been shown that the thickness can be calculated with reasonable accuracy for conditions other than what existed in the test. It is not supprising that we have not noticed any effects of RP-1 Freesing in the either of the injectors even though we predict annulus wall temperatures below the freezing point of RP-1 based on these experiments and calculations.

THERMAL AND CHEMICAL CHARACTERIZATION OF NON-METALLIC MATERIALS USING COUPLED THERMOGRAVIMETRIC ANALYSIS AND INFRARED SPECTROSCOPY

Timothy L. Huff
George C. Marshall Space Flight Center

ABSTRACT

Thermogravimetric analysis (TGA) is widely employed in the thermal characterization of non-metallic materials, yielding valuable information on decomposition characteristics of a sample over a wide temperature range. However, a potential wealth of chemical information is lost during the process, with the evolving gases generated during thermal decomposition escaping through the exhaust line. Fourier Transform-Infrared spectroscopy (FT-IR) is a powerful analytical technique for determining many chemical constituents while in any material state, in this application, the gas phase. By linking these two techniques, evolving gases generated during the TGA process are directed into an appropriately equipped infrared spectrometer for chemical speciation. Consequently, both thermal decomposition and chemical characterization of a material may be obtained in a single sample run. In practice, a heated transfer line is employed to connect the two instruments while a purge gas stream directs the evolving gases into the FT-IR. The purge gas can be either high purity air or an inert gas such as nitrogen to allow oxidative and pyrolytic processes to be examined, respectively. The FT-IR data is collected real-time, allowing continuous monitoring of chemical compositional changes over the course of thermal decomposition. Using this coupled technique, an array of diverse materials has been examined, including composites, plastics, rubber, fiberglass epoxy resins, polycarbonates, silicones, lubricants and fluorocarbon materials. The benefit of combining these two methodologies is of particular importance in the aerospace community, where newly developing materials have little available data with which to refer. By providing both thermal and chemical data simultaneously, a more definitive and comprehensive characterization of the material is possible. Additionally, this procedure has been found to be a viable screening technique for certain materials, with the generated data useful in the selection of other appropriate analytical procedures for further material characterization.

INTRODUCTION

Thermogravimetric (TG) analysis is a well-established procedure for determining non-metallic material properties such as percent moisture content, percent ash content, percent composition, oxidative induction time, and decomposition kinetics. These characteristics are measured as the change in mass of a sample as it is heated, cooled or held at a constant temperature under a controlled atmosphere, that can be oxidative, inert, or a combination of both. In decomposition studies, the obvious objective is to reach temperatures sufficient to decompose the material, and thus is destructive in nature. Conversely, Fourier Transform Infrared (FTIR) techniques are especially useful in the chemical speciation of non-metallic materials simply because they are non-destructive in nature, providing reproducible, quantitative data while preserving the sample for further testing. However, FTIR is also a proven technique for identifying chemical constituents in gas phase as well. Thus these two techniques can be complementary to each other, with the gases generated during material decomposition in the TG available for chemical speciation by FTIR techniques. Specific applications using these combined techniques are presented, with the versatility and limitations further discussed.

PRESENTATION

The coupled thermogravimetric analyzer (TGA) and FTIR are shown below. Briefly, evolving gas generated in the thermogravimetric analyzer (right side) during material decomposition is purged through a heated transfer line into a heated gas cell within the FTIR. The carrier gas may be either high purity air or an inert gas such as nitrogen to allow oxidative and pyrolytic processes to be examined, respectively. A liquid nitrogen-cooled detector is employed for identification of chemical groups, owing to specific functional group/wavelength interactions. For example, a non-aromatic carbon-hydrogen (C-H) group interacts in the infrared region at a wavelength range of 3000-2800 cm^{-1}.

Data generated during the TGA run is presented as a X-Y plot with the ordinate represented as the percent weight of the sample versus run time on the abscissa. This is shown graphically below. The two weight loss curves shown are of the same sample, the difference being the purge gas used for each run. As can be seen, initial decomposition of this sample was similar in both atmospheres, suggesting pyrolytic decomposition. As heating progressed a weight loss was again observed in the sample heated in the oxidative atmosphere, indicating an oxidative process.

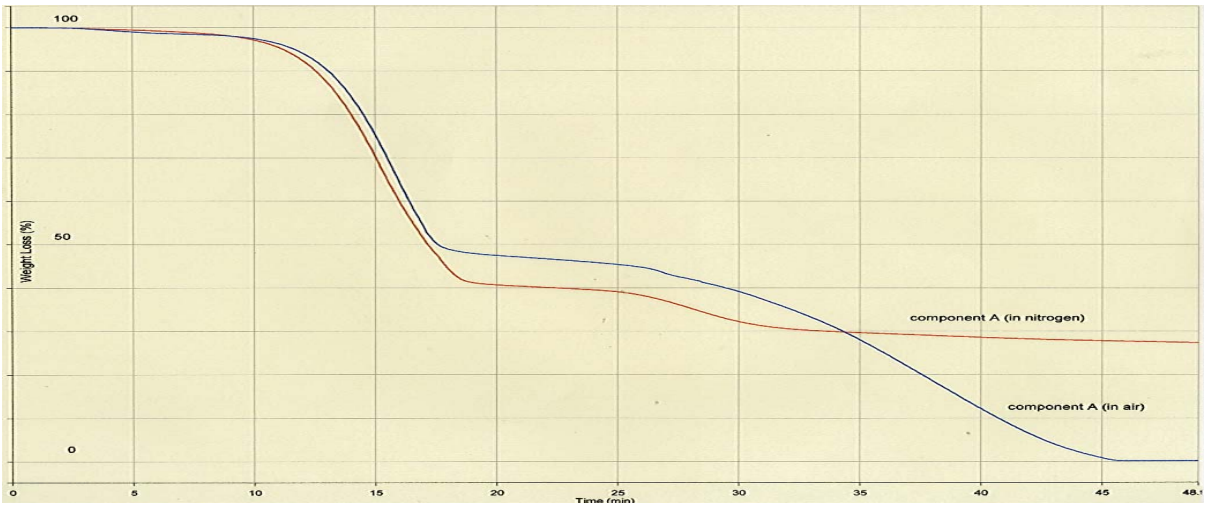

During the decomposition process, the evolving gases directed to the FTIR are analyzed real-time for chemical groups. At the end of a run, the data can be presented as a "stacked plot" that presents the spectral data plotted against time throughout the heating cycle for the sample. This allows for the observation of increases and decreases in individual chemical groups (based on peak height and location) as the run progresses. An example of such a plot is presented below.

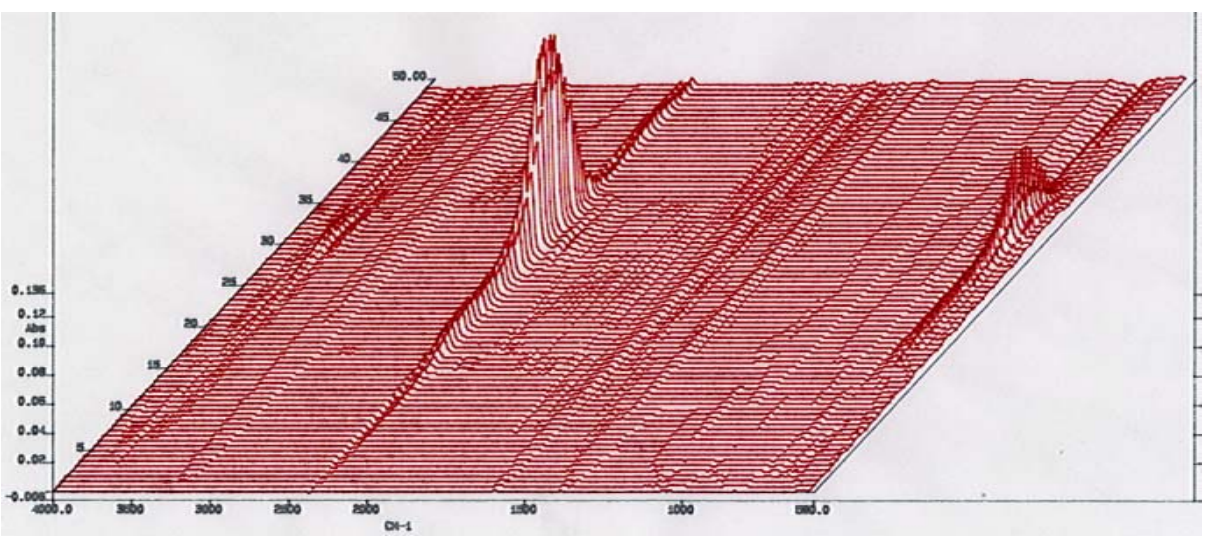

Additionally, weight loss data can be incorporated into the spectral data, with specific "slices" in the plot generated that correlate individual point-in-time spectra with observed weight changes. In the example below, a spectrum collected during a weight loss event occurring approximately 22 minutes into the run is shown. By observing the peak locations on the X-axis, information on the types of chemical groups evolving at that time can be attained. In this example, the observed peaks indicate the presence of nitrogen-hydrogen groups, non-aromatic carbon-hydrogen groups, carbon dioxide, carbon monoxide and carbonyl (C=O) groups.

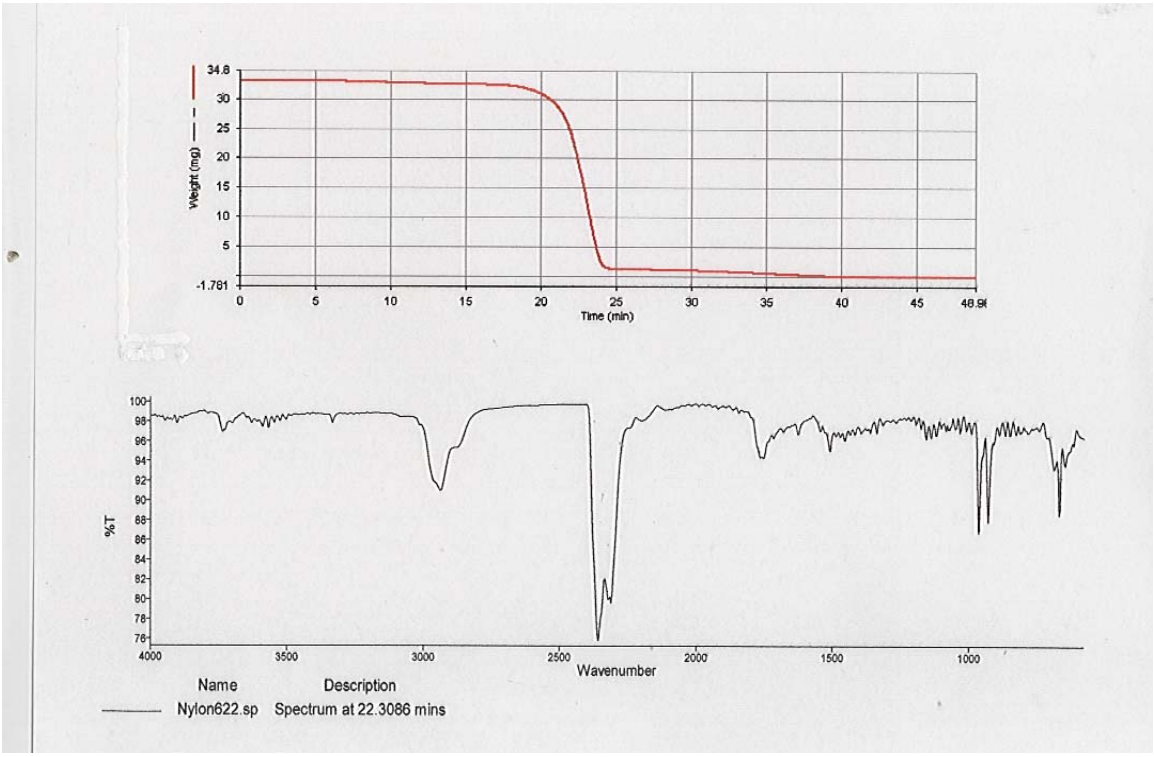

Interpretation of the spectra is usually qualitative with only the presence or absence of specific functional groups noted. However, semi-quantitative estimates of functional group concentrations can be made from spectral peak height and area information. From the example above, a strong peak is observed at approximately 2400 cm^{-1}. This region corresponds to the presence of carbon dioxide and is often observed in runs conducted in an oxidizing environment. This is commonly due to sample charring, with the resulting carbon being oxidized further to carbon dioxide. The reactive nature of this environment can also result in loss of functional group information if the group is susceptible to oxidative effects. In the first of two stacked plots below, the sample was run in an oxidative atmosphere with the expected prominent carbon dioxide peak at 2400 cm^{-1} observed. Sample charring is indicated by the recurrence of carbon dioxide in the latter stages of the run. The second plot, run in an inert atmosphere, shows small additional peaks at wavelengths just below that of carbon dioxide during the initial decomposition

step. These peaks are indicative of carbon monoxide, which are not seen in the oxidative environment due to rapid oxidation to carbon dioxide solely.

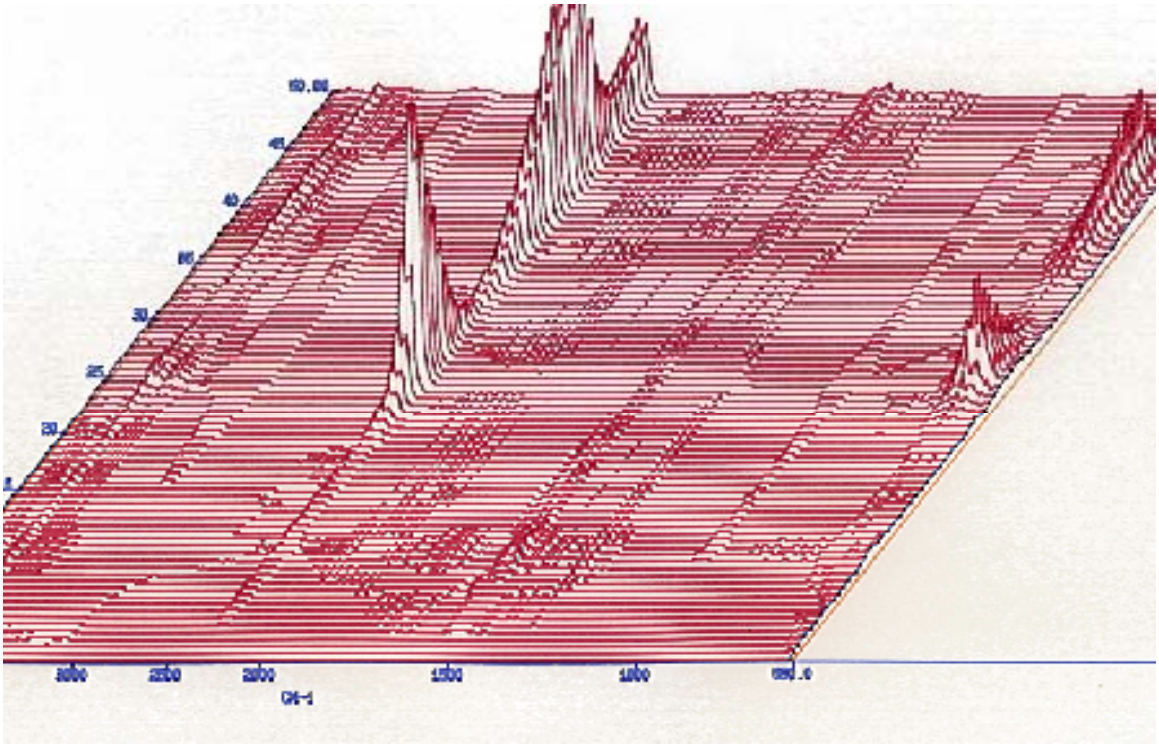

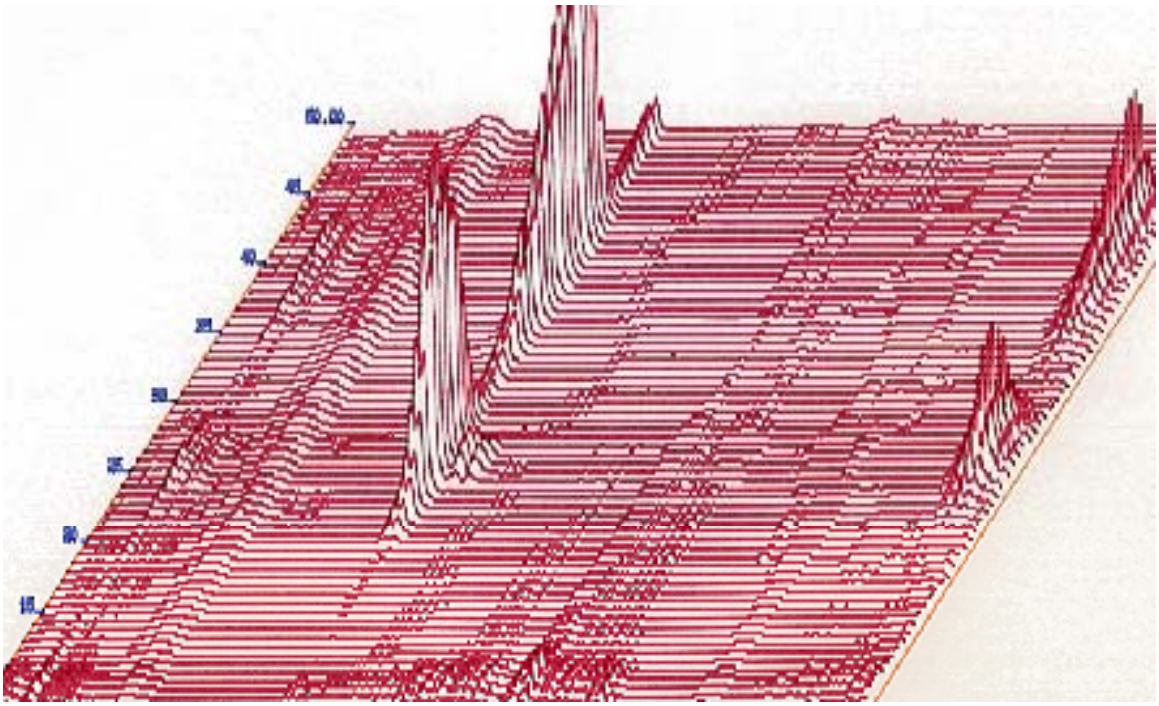

In some instances, the presence of carbon dioxide can also have a masking effect on other functional groups that locate closely to the carbon dioxide peak. Examination of the stacked plot below indicated that sample decomposition was largely associated with the release of carbon dioxide, again seen by the characteristic peak at 2400 cm^{-1}.

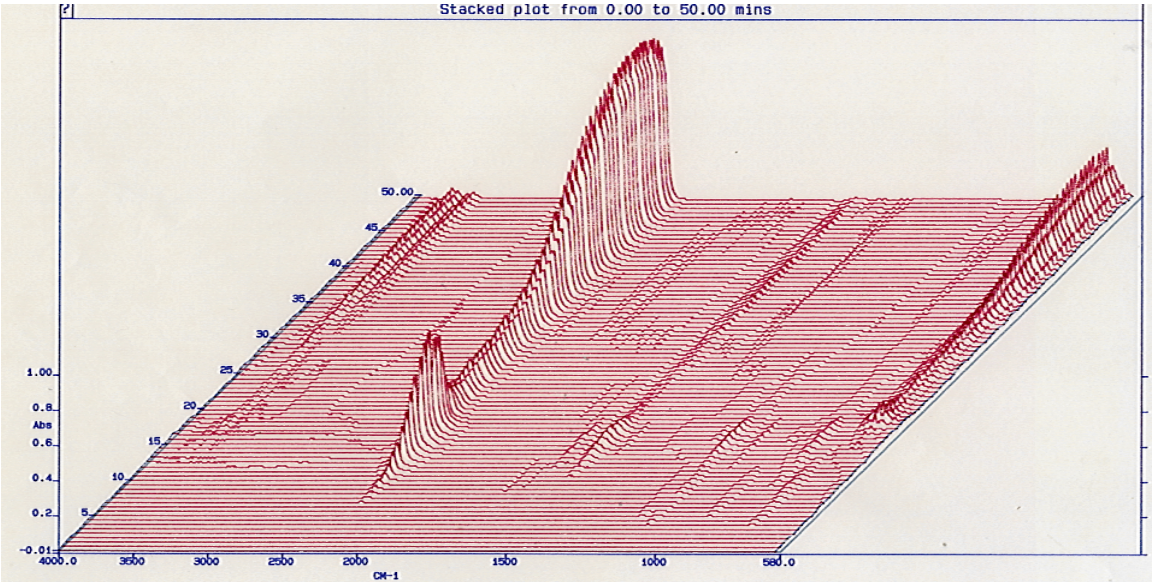

Closer examination of the spectra on a scan-by-scan basis actually revealed the presence of a carbon-nitrogen peak co-locating within the carbon dioxide region. The peak was short-lived and could have been easily overlooked.

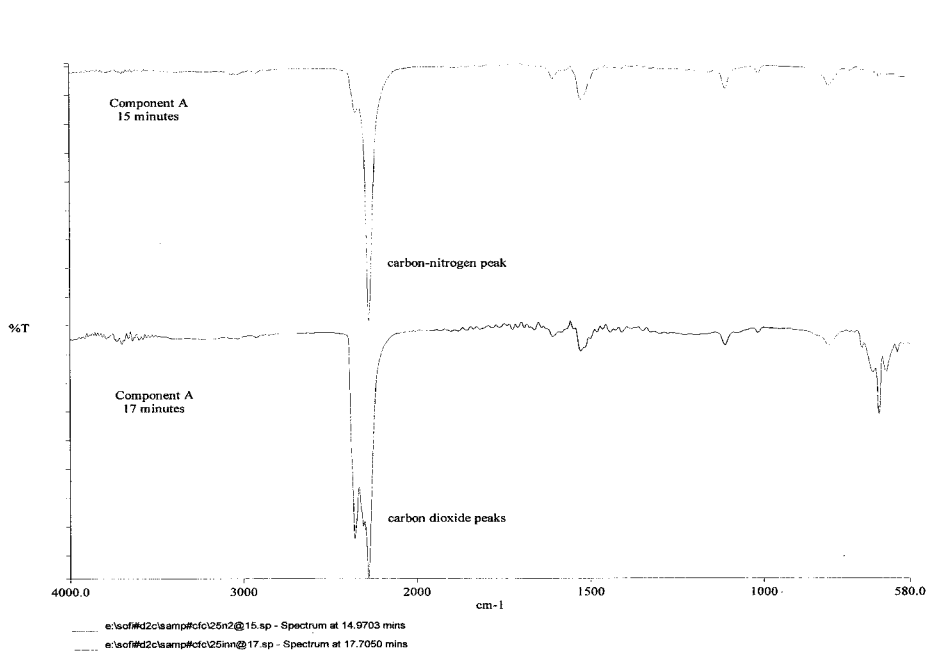

There are instances, however, when an oxidizing environment may actually provide more information than can be obtained in an inert purge atmosphere, as was observed in a sample containing disulfide groups. Diatomic groups such as these are largely infrared inactive and thus not readily identifiable by standard FTIR means. Analysis of this sample is shown below with runs in both nitrogen and air presented. In the inert nitrogen atmosphere multiple functional groups are observed, none of which are identified as disulfides. When run in air, however, the evolving disulfides reacted with the oxidizing atmosphere, producing sulfoxide groups. These groups are infrared active, producing strong spectral peaks at 1375 and 1339 cm^{-1}. By inference, the presence of sulfoxide peaks indicated decomposition of the disulfide groups.

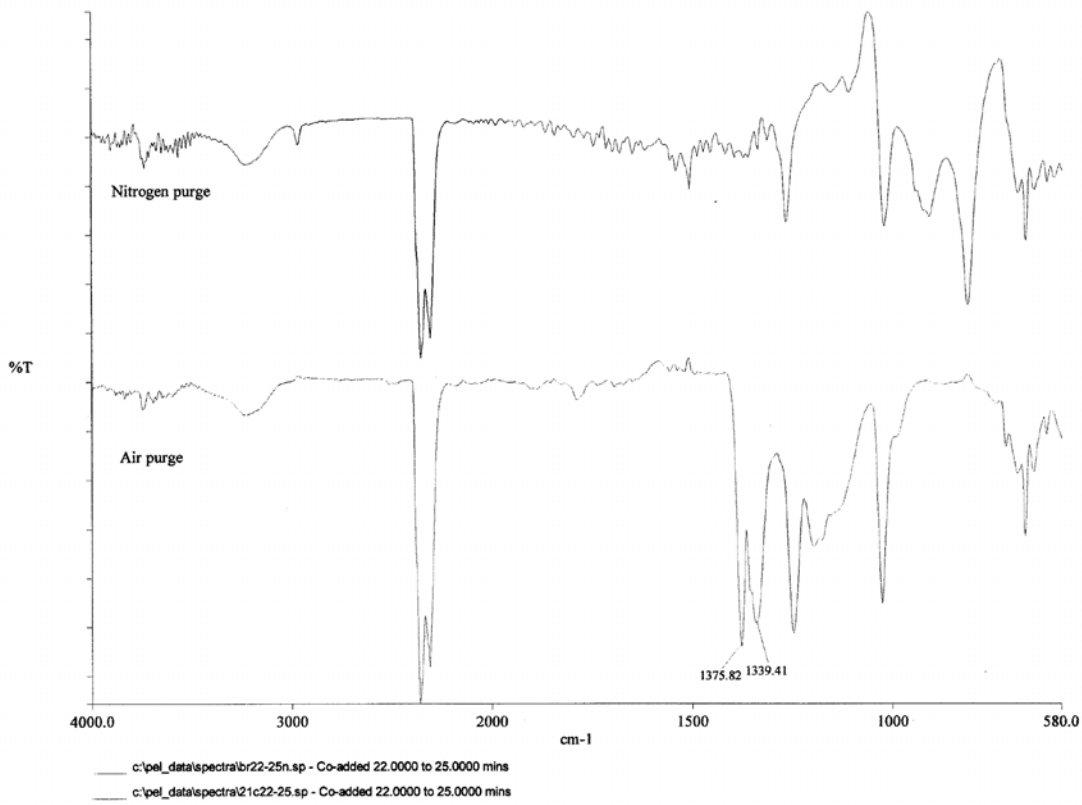

The example cited above represents a selective application of the TGA-FTIR, where specific information was required. This procedure has also been found useful in some instances as a screening tool, with the information obtained beneficial in the selection of other thermal test procedures. For example, a material exhibiting a low decomposition temperature would suggest a low melting point as well. If this information is required for a sample, Differential Scanning Calorimetry (DSC) may be an appropriate technique since the instrument can operate at subambient temperatures. Conversely, Differential

Thermal Analysis (DTA) may be preferred for materials exhibiting higher decomposition temperatures as this instrument has a higher operating temperature range. Examination of the spectral plot may determine if the decomposition event is due to breakdown of chemical constituents or sample charring, which may also influence the analysis chosen. Analysis of the spectral data will also provide some qualitative data regarding the organic and inorganic nature of the material, which can be useful in the selection of appropriate quantitative chemical procedures.

CONCLUSIONS

The use of thermogravimetric analysis in tandem with Fourier transform infrared spectroscopy allows for the determination of gaseous decomposition products evolved from nonmetallic materials during heating. Thus, not only are the thermal properties of a material examined, but also specific chemical species evolved during decomposition are identified. This can be accomplished in air or inert gas atmosphere, allowing either oxidative or pyrolytic processes to be studied. Spectra collected during an oxidative run are usually characterized by a predominant carbon dioxide peak due to oxidation of some evolving carbon constituents with the air or sample charring. An inert atmosphere generally provides more functional group information, as the evolving species do not react with the atmosphere. The spectral data is largely qualitative, although some semi-quantitative estimates can be made based on spectral intensity. Aside from its use as an analytical tool, this procedure has application as a screening technique in some instances; with the generated data useful in the selection of other appropriate procedures for further material characterization.

THERMAL ANALYSIS OF THE MC1 ENGINE TURBOPUMP

Jose Roman, MSFC NASA

ABSTRACT

The MC1 Engine turbopump supplied the propellants to the main injector. The turbopump consisted of four parts; lox pump, interpropellant seal package (IPS), RP pump and turbine. The thermal analysis was divided into two 2D finite element models; Housing or stationary parts and rotor or rotating parts. Both models were analyzed at the same boundary conditions using SINDA. The housing model consisted of; lox pump housing, ips housing, RP housing, turbine inlet housing, turbine housing, exit guide vane, heat shield and both bearing outer races. The rotor model consisted of the lox impeller; lox end bearing and id race, RP impeller, and RP bearing and id race, shaft and turbine disk.
The objectives of the analysis were to (1) verified the original design and recommend modifications to it, (2) submitted a thermal environment to support the structural analysis, (3) support the component and engine test program and (4) to support the X34 vehicle program.

INTRODUCTION

The MC1 Engine turbopump supplied the propellants to the main injector. The thermal analysis was divided into two 2D finite element models; housing or stationary parts and rotor or rotating parts. Both models were analyzed at the same boundary conditions. The housing model consisted of; lox pump housing, interpropellant seal package (IPS) housing, fuel housing, turbine inlet housing, turbine housing, exit guide vane, heat shield and both bearing outer races. The rotor model consisted of the lox impeller, lox end bearing and id race, fuel impeller, and fuel bearing and id race, shaft and turbine disk.

OBJECTIVES

The objectives of the analysis were to (1) verified the original design and recommend modifications to it, (2) submitted a thermal environment to support the structural analysis, (3) support the component and engine test program and (4) to support the X34 vehicle program.

DESIGN CONFIGURATION

The design configuration of the MC1 turbopump was to supply the propellants to the main injector using the turbine energy supplied by the gas generator. The turbine inlet housing is connected by bolted flange to the gas generator. The turbine exit diffuser was bolted to the turbine discharge duct. The lox pump inlet was connected to lox tank feed

line. The lox pump discharge was bolted to the discharge line which it was connected to the lox main valve. The fuel pump inlets are connected to fuel tank feed line, which it was divided into two lines for the two inlets of the pump. The fuel pump discharge was bolted to the discharge line, which was connected to the fuel main valve.
A lox secondary flow was required to maintain the lox pump end bearing at a low temperature during operation. A fuel secondary flow was required to keep the turbine end bearing at a low temperature during operation. Both flows are recirculated from the high pressure side of the pump, through a small line into the bearing cavity back to the main flow on the low pressure side of the pump.
The interpropellant seal package was design to maintain a positive pressure differential between the lox bearing cavity and the fuel impeller back face. This was achieved by using high pressure helium as a medium between the cavities and the used of a series of carbon seal and knife edge seals helped to keep the flow leaks to a minimum.
The turbine was composed of the turbine inlet manifold, 24 converging/diverging nozzle, the disk, 147 blades, and 67 turbine guide vanes. The pumps are both single stage shrouded impellers. The shaft is supported by two ball bearing packages, one at the lox pump end, behind the impeller, the other at the turbine end, between the fuel impeller and the turbine.

DESIGN REQUIREMENTS

The global design requirement conditions were base at steady state conditions and full power level. Several specific conditions in the design were related to the thermal analysis. The clearance between the fuel pump housing and the outer race of the turbine end bearing or bearing deadband was required not to exceed a limit of .002 inches during operation. The operating temperature of the bearing and races were limited to a specific range. The temperature of the fuel fluid was limited to be above its freezing point, introducing the necessity of heaters.
The X34 environmental conditions, the flight conditions of hot and cold day, the ability of start and operated at high altitude (low ambient air), and the iteration between the turbopump and the engine compartment were parts of the design requirements

THERMAL ANALYSIS

The analysis consisted of two finite element models; housing assembly and rotor assembly. They were solved using the SINDA thermal analyzer computer code. Cold day and Hot day X34 vehicle conditions, as predicted by OSC, were used for the environmental ambient conditions, air temperatures flow conditions, etc. These conditions varied with time from ground to flight back.
The internal pump environment was predicted by Brian Goode from time 18000 seconds to engine start, which included ground time, airplane flight until the lox pump chilldown. During engine chilldown heaters were used to keep the ips housing temperature above the freezing temperature (-40 F°) of the fuel.
At engine start, time 0, boundary conditions where base on the fuel reach start conditions predicted by Mike Martin of the System Analysis Group, Space Transportation Directorate. Mr. Martin predictions were also for the engine hot firing max. conditions as

well as engine cut off time, 150 sec., and shutdown. Internal flow Conditions were supplied by Katherine Van Hooser of the Functional Design Group of the Space Transportation Directorate.

Housing Model

A transient axisymmetric thermal model was solved using SINDA. The model was generated from a 2D finite element mesh obtained from Wayne Gregg of the Strenght Analysis Group. The model consisted of 13747 nodes and 51547 conductors. The thermal boundary conditions were applied in Patran. Corrected mass and conduction areas were simulated for exit guide vanes, radial pins, heat shield bolts, and bolt washers. Results were obtained for all X34 flight conditions. Figure 1 shows some of these results. Figure 1 shows the thermal gradient at the turbine inlet wall during the engine start transient. It reached steady state conditions on about 10 seconds.
A requirement of .002 inches, maximum turbine end bearing deadband was imposed by the rotodynamic analyst to maintained stability on the bearing. The following design changes were implemented to reach this requirement. The heat shield insulating the pump housing from the hot turbine environment, and the turbine inlet housing to pump housing joint pin, which reduced the conductive heat transfer between the hot turbine inlet and the pump housing.
The bearing temperature control is a critical issue on the thermal design of the turbopump. Mass averaged outer race temps were calculated and provided to Tim Jett of the Nondestructive Evaluation & Tribology Group for the bearing design. Simulation included flow through the bearing, which keep the outer races at fluid temperature. Maintaining the outer race at the same or closed temperature as the fluid and housing kept a constant gap between the outer race and the pump housing during the mission.

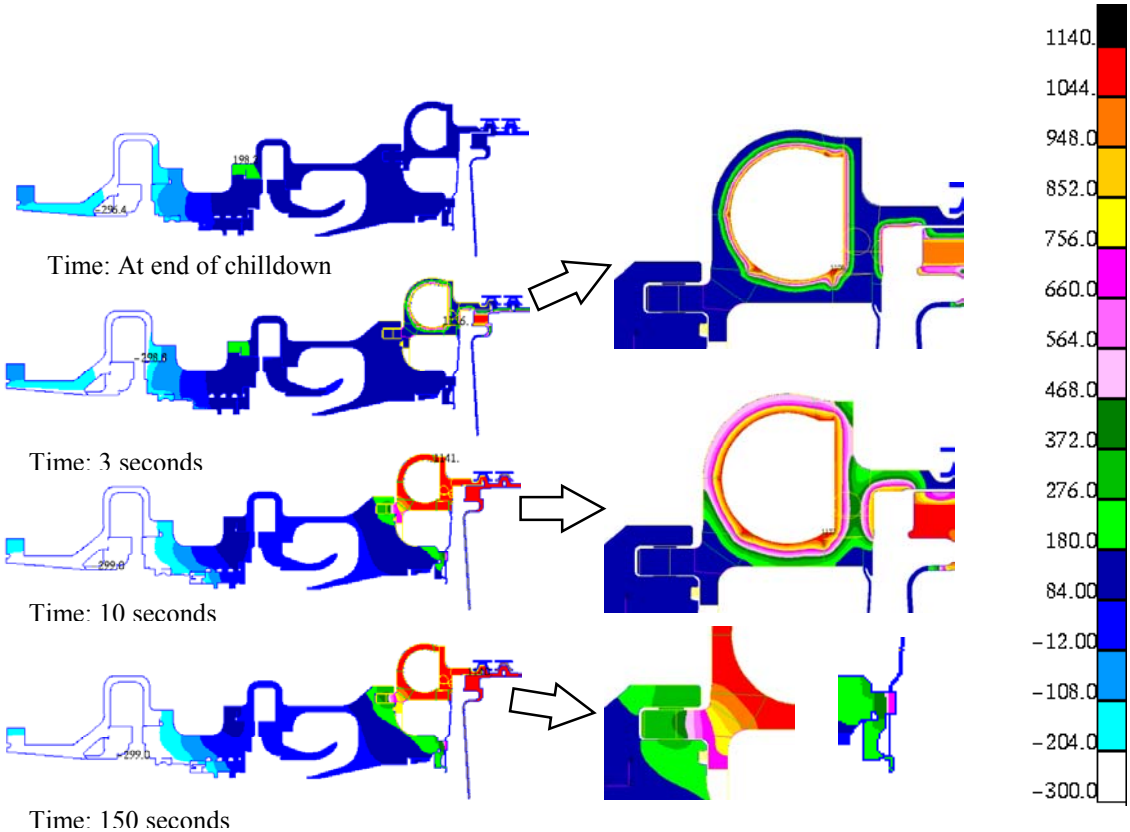

Figure 1: Composite of Housing Transient Result

Rotor Model

A transient axisymmetric thermal model was solved using SINDA. The model was generated from a 2D finite element mesh. The model consisted of 3125 nodes and 12331 conductors. The thermal boundary conditions were applied in Patran. Corrected mass and conduction areas were simulated for pump impellers, ball bearings, and turbine blades.

Results were obtained for all X34 flight conditions. Figure 2 shows some of these results Figure 2 shows the thermal gradient at the turbine disk during the engine start transient.

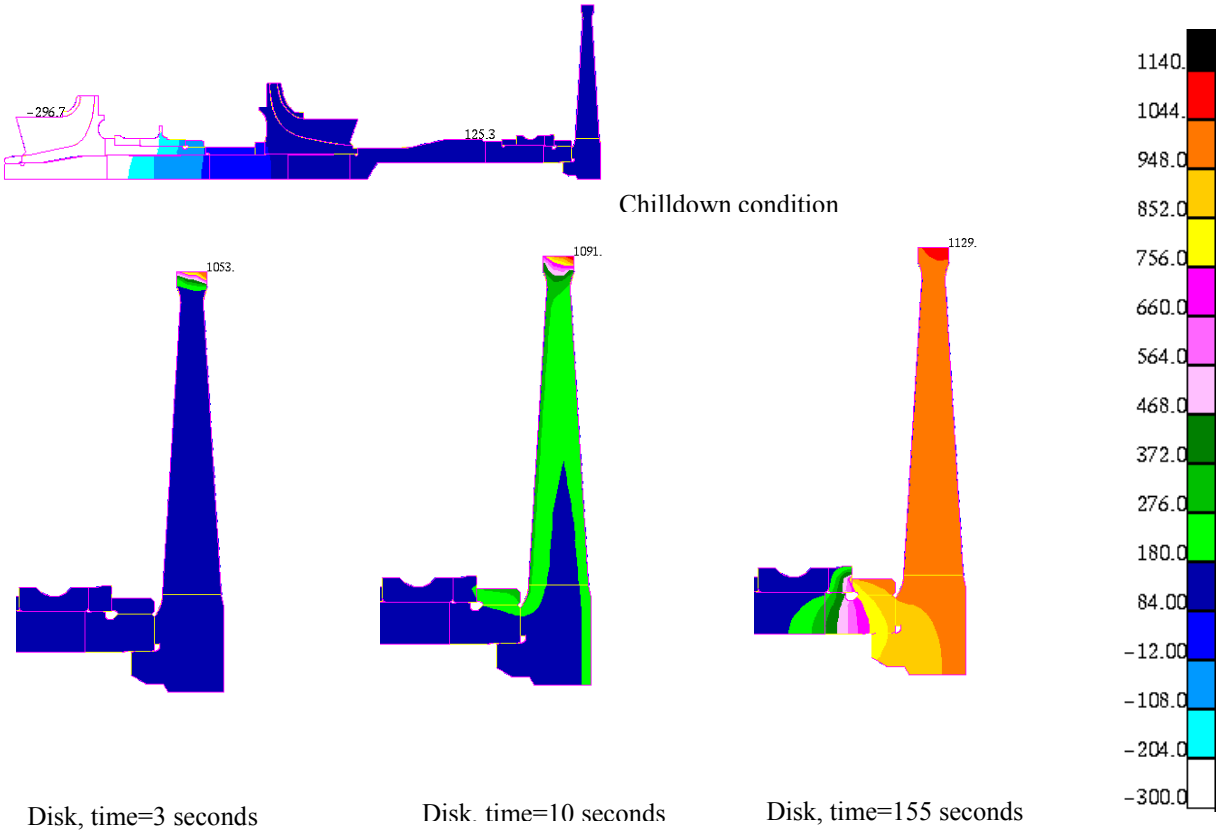

Figure 2: Rotor Model Results

CONCLUSIONS

As a result of the analysis a heat shield between the disk cavity and the fuel pump housing, and a radial pin joint, a minimum contact attachment, between the fuels pump housing and the turbine inlet housing were implemented into the base design.
Some of the areas of uncertainty included turbine housing cavity and heat shield disk cavity because of the unknown gas generator combustion gas properties. Conservative assumptions used to bind the possibilities. The used of the heat shield minimizes the impact of unknown environments.
Heaters are used during the engine pre-fire stage to prevented the fuel to reach freezing temperature (-40°F)
Average surface temperature was calculated in support of the engine aft compartment ambient assessment. This is an X34 system requirement. Environments of Hot & Cold day were used in support of this task.
The analysis results were used to support the structural analysis and the analysis of the post engine fire heat absorbed by the oxygen trapped in the pump to help sized relieve lines and valve.

Thermal Analysis of a Carbon Fiber Rope Barrier For Use in the Reusable Solid Rocket Motor Nozzle Joint–2

J. Louie Clayton
National Aeronautics and Space Administration
Thermodynamics and Heat Transfer Group / ED25
Marshall Space Flight Center
Huntsville, Alabama

Abstract

This study provides development and verification of analysis methods used to assess performance of a carbon fiber rope (CFR) thermal barrier system that is currently being qualified for use in Reusable Solid Rocket Motor (RSRM) nozzle joint-2. Modeled geometry for flow calculations considers the joint to be vented with the porous CFR barriers placed in the "open" assembly gap. Model development is based on a 1-D volume filling approach where flow resistances (assembly gap and CFRs) are defined by serially connected internal flow and the porous media "Darcy" relationships. Combustion gas flow rates are computed using the volume filling code by assuming a lumped distribution total joint fill volume on a per linear circumferential inch basis. Gas compressibility, friction and heat transfer are included in the modeling. Gas-to-wall heat transfer is simulated by concurrent solution of the compressible flow equations and a large thermal 2-D finite element (FE) conduction grid. The derived numerical technique loosely couples the FE conduction matrix with the compressible gas flow equations. Free constants that appear in the governing equations are calibrated by parametric model comparison to hot fire sub-scale test results. The calibrated model is then used to make full-scale motor predictions using RSRM aft dome environments. Model results indicate that CFR thermal barrier systems will provide a thermally benign and controlled pressurization environment for the RSRM nozzle joint-2 primary seal activation.

List of Symbols

A	normal surface area
C	specific heat
D	passage diameter
e	Euler constant
f	Moody friction factor
g_c	gravitational constant
GF	flow conductor
h	convective film coefficient
H	enthalpy
L	flow path length
M	molecular weight
m	mass
p	pressure
Q	heat rate
R	gas constant
T	temperature
U	internal energy
t	time
V	volume
W	work
x	coordinate direction

Greek

Δ	difference operator
α	Darcy constant
ρ	gas density
μ	gas viscosity

Subscripts

g	gas
h	hydraulic
i	inlet
o	outlet
p	constant pressure
w	wall
v	constant volume

Introduction

Current manufacturing procedures used for close out of RSRM nozzle joint–2, Fig 1, involves injection of a room temperature vulcanizing silicon material (RTV) into the assembly gap after the joint has been bolted together. The assembly gap dimension is about 45 mils nominal and RTV injection penetration is usually inboard to the housing, full circumference of the joint.

* Approved for Public Release: Distribution is Unlimited

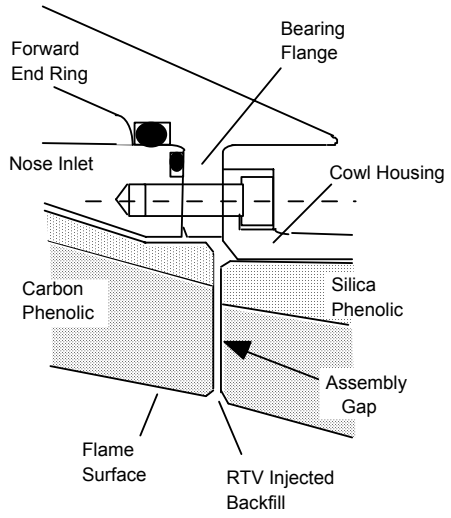

Fig 1- Current RSRM Nozzle Joint -2 Configuration

Due to structural deformations during pressurization of the motor, the assembly gap in the carbon phenolics open on the order of 10-20 mils with the largest deformation occurring at the flame surface. Typically the RTV backfill cannot track the deformation and fails to maintain a seal during motor operation. The result is an uncontrolled, hot gas pressurization of the joint free volume in the bearing vicinity (o-ring glands and bolt hole volumes). The exact nature of gas path geometry varies from confined and well-defined to large, circumferentially un-bonded areas. In general, if the gas path is more confined the local heating will be more severe.

The thermal problem with the current backfill process is the inherent randomness of the gas path geometry that is a result of process and hardware variation. The current back filling procedure results in gas path formation in virtually all motors (>90%) with resulting heat affected phenolics, adhesives and painted surfaces. Because of the peculiar sensitivity of heating severity to the gas path geometry, there exists a potential for exceeding the aluminum inlet and cowl housing reuse temperatures of 300°F.

Joint-2 has been analyzed thermally, Ref 1, by MSFC for worst case conditions and determined to be very robust in terms of thermal protection of primary and secondary seal. This particular metal housing design has several desirable features:

1. It is dynamically static which means the gland sealing surfaces remain essentially fixed when the motor pressurizes.
2. Metal to metal gaps leading to primary and secondary glands have a large (L/D) that serves to reduce the flow rate peak magnitude and provides significant cooling of the gas.
3. There is a large thermal capacitance at possible gas impingement points.
4. The joint does not have a large free volume available for pressurization.

Elimination of RTV and the use of a permeable CFR system in this joint will eliminate the random nature of gas path formation using the current procedure. This will allow for a controlled vented style pressurization of the joint free volume. In addition, compared to RTV backfill procedure, the CFR barrier system will be easier to use in terms of processing the joint and will result in a more streamlined assembly operation.

The following provides development and verification of analysis methods used to simulate the thermal performance of the CFR barrier system. Code development is derived from an existing base class of codes know as SINDA/JPR, Ref 2. Free constants that appear in governing equations are calibrated by parametric model comparison to hot fire, sub-scale test results. Finally, the calibrated model is then used to make full-scale motor thermal predictions using estimated RSRM aft dome environments.

Model Development

Fundamentally, model development begins with derived class capabilities from the base SINDA/JPR computer code. This code was developed at MSFC for thermal analysis of the joint pressurization process associated with a single gas path connecting to an o-ring gland. The approach uses 1-D gas dynamic flow equations for the determination of conditions along the gas path and applies bulk formulated mass and energy equations to the volume filling process in an o-ring gland. Detailed heat transfer is simulated using the SINDA code, Ref 3, concurrently with the flow calculation routines embedded in the JPR code. Gas flow and heat transfer couplings (wall heat-transfer, film coefficient, flow enthalpies, etc.) are explicitly computed in time over the transient solution of the pressurization process. This loose coupling

allows the flow solution to be partitioned in time on a finer scale than solution to the conduction grid. The stiffness in the flow matrix, for typical joint filling situations, usually can be resolved with time steps on the order of 0.01-0.1 milliseconds; An inherent numerical property that is fixed by geometry, gas properties and typical rates of pressurization. The implicit solution of the thermal FE grid is usually stable at time steps one/two orders of magnitude larger than required for the flow thus an explicit "marching" numerical technique allows for a loosely coupled solution of flow and conduction matrices.

In JPR, the equations that describe flow along the gas path are formulated in terms of familiar R-C analogous "parallel" networks. Gas temperature and pressure relationships, are applied to the computational grid points, expressed in terms of (*resistance)* x (*potential difference)*. The Darcy equation for compressible porous media flow can be simplified and cast in similar form and easily integrated into the existing JPR numerical scheme. Resistance contributions offered by the CFR are integrated into the overall system network resistance and simulated by the same nonlinear solution techniques used for convergence of the frictional internal flow resistances. JPR is numerically formulated as a point-to point solver (Gauss-Seidel) with partial back substitution.

As a result of the 1-D flow field associated with venting the joint symmetrically, the inlet normal flow areas, circumferential rope length and free volume available for pressurization are computed on a per unit depth basis. For this geometry, aspect ratios for flow and heat transfer calculations are similar to parallel flat plates. Hydraulic diameters that appear in the dimensionless heat transfer and flow relationships are assumed to be a function of gap dimension only. Porous media (Darcy) flow through the CFRs was also simplified via the 1-D assumption.

Geometry / Heat Transfer Modeling

Fig 2 provides a look at nozzle joint-2 configured with two CFRs in the assembly gap. This current design is referred to as the *dual face seal*.

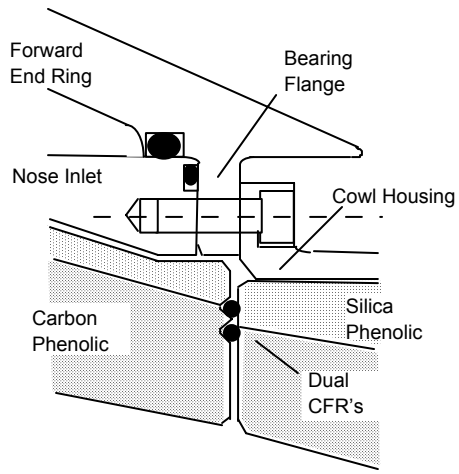

Fig 2 - Dual CFR Face Seal Nozzle Joint -2 Configuration

A thermal conduction finite element grid of the subject region, Fig 3, was constructed based on an idealized geometry. The grid is 2-D heterogeneous-anisotropic and contains approximately 4000 nodes and about 4200 isoparametric linear quad elements.

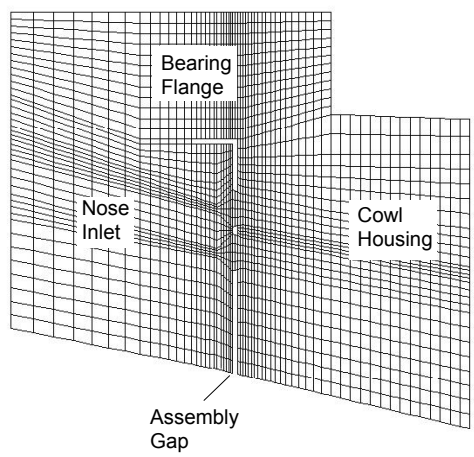

Fig 3 - 2-D Thermal Conduction Finite Element Grid of Nozzle Joint-2

Gas temperatures were calculated at 25 grid points along the flow path using a full up-winding scheme. These grid points were co-located with the FE nodes in the conduction grid. Convective boundary integrals were simplified to utilize a constant temperature distribution over the half element surfaces. The following detailed assumptions were applied to the FE grid and heat transfer modeling:

1. A simple 2-D grid (non-axisymmetric) was used because of the large radius of curvature relative to dimensions of the locally modeled region.
2. Material anisotropy was included for the carbon phenolics based on directional thermal conductivities for the given ply angle.
3. Material heterogeneity was simulated by variable property input as a function of temperature dependent char state. Char properties were used at temperatures above 1000°F.
4. Decomposition kinetics of the phenolic resins were not considered. The associated energies are typically small compared to sensible contributions of the advecting flow of the combustion gas.
5. Forced convective boundary conditions were applied along the assembly gap and through the CFR from inlet to stagnation points along the flex bearing. Effects of the hydrodynamic entry and variable gas properties were included.
6. Radiative loading (gas to wall) was not considered due to the small gap dimensions involved.
7. For the CFR, a non-equilibrium thermal situation exists for heat transfer, i.e., gas temperature not equal to solid media temperature. Nusselt relationships of the form:

$$\frac{\bar{h}}{D_h k} = Nu = C_1 Re^{0.5} Pr^{0.33} \qquad (1)$$

   were applied on a volumetric basis where the constant C_1 was estimated from model calibration with test data.
8. Exponents for the dimensionless parameters in Eq (1) were inferred from relationships derived for packed bed heat transfer applicable to cylinders in a cross-flow.
9. For the Reynolds number evaluation, superficial gas velocities were used where the characteristic dimension was taken as the square root of the permeability.
10. At impingement points along the flow path, augmentation of the heat transfer rates was estimated using relationships found in Ref 4.
11. Variable gas specific heats were used in the nodal energy balance. Gas properties data were taken from Ref 5.

Gas Flow Modeling

The flow network was 1-D and utilized a course descritization of the domain. Serial resistances were defined for the inlet, both CFR's, in-board portions of the assembly gap and metal gaps leading into the primary o-ring gland. Shown in Fig 4 is the basic arrangement of the network and locations of computed pressure points and assigned volumes.

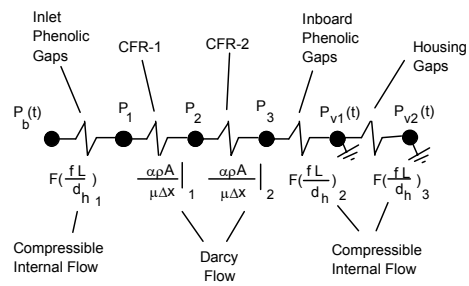

Fig 4 - 1-D Transient Internal / Darcy Flow Network

For test correlation, the flow model does not include the serial resistance offered by the primary o-ring metal gaps. These test, Ref 6, were conducted using an equivalent bulk volume appended to the end of a simulated joint-2 assembly gap.

Basic Equations for Flow Calculations

Calculation of the thermodynamic state in the assigned volumes was based on a bulk formulation of the unsteady form of mass and energy conservation equations. They are specified as:

$$\frac{dm}{dt} = \left(m_{i,dot} - m_{o,dot}\right) \qquad (2)$$

$$Q,dot + H_i = \frac{d}{dt}(mU) + H_o + W \qquad (3)$$

where;

$$Q,dot = \bar{h}A\left(T_w - T_g\right)$$
$$\Delta U = C_v \Delta T$$
$$\Delta H = C_p \Delta T$$
$$pV = mRT \qquad (4)$$

These equations are finite differenced by fully implicit methods and applied to the grid points capable of storing mass. At connect points along the assembly gap mathematical relationships for the primary variables are derived from the steady form of the conservation equations. From a functional

standpoint, these relationships take the form of simple weighted averages where the weight factors are the nonlinear conductance terms for the network, see Fig 4.

Derivation of conductance terms in the flow network is based on two separate methods of fluid transport: compressible-internal flow and porous media flow through the CFR's. In general, the computation boils down to the evaluation of an equation of the form:

$$GF_i = \frac{m, dot}{\Delta P} \qquad (4)$$

where the mass flow rate in numerator is computed by one of the following methods:

$$m, dot = p_i A \sqrt{\frac{g_c M}{eRT_i}} f(\frac{L}{D}, \frac{p_j}{p_i}) \qquad (5)$$

for internal flow, and

$$m, dot = \frac{\alpha \rho A}{\mu \Delta x}\left(P_i - P_j\right) \qquad (6)$$

for Darcy flow through the CFR. The weighted average formula applied to the grid points takes the transcendental form:

$$P_i = \frac{GF_{i-1}P_{i-1} + GF_i P_{i+1}}{GF_{i-1} + GF_i} \qquad (7)$$

The collection of weighted average formulas at the arithmetic grid points forms a system of non-linear simultaneous equations that are converged every iterative pass of the implicit solution to Eqs (2,3) . This procedure may be termed "quasi-steady" from the standpoint of formulation of equations along the flow path. For gas flow modeling, the following detailed assumptions were made:

1. Bulk control volumes were assigned on a cubic inch per circumferential linear inch basis of joint free volume. All flow calculations were 1-D.
2. Temperature and equilibrium composition specific heats derived for the propellant combustion gases were used for enthalpy and internal energy terms.
3. The ideal gas law used equivalent molecular weights where volume contents are perfectly mixed. Total pressures were computed from the relationship.
4. Thermally dependent properties used in Darcy resistance were evaluated at a CFR bulk mean temperature along the direction of flow. Porous media flow was assumed to be 1-D.

Model Calibration Procedure

Benchmarking for flow model calibration involved back fitting dynamic permeability to pressure trace data obtained from the Joint Environment Simulator (JES) series of tests, Ref 6. Internal flow losses were determined using standard textbook correlations; therefore, parametric optimization of "just" the permeability sufficed to give reasonable agreement with measured data. This outcome was considered likely due to the fact that the CFRs resistance controls the overall rate of gas flow into the joint.

Lab measured cold gas CFR permeability values were used for initializing the Darcy constant in the model. From observation of JES measured pressure response, several permeability dependences were discovered and incorporated. First was a sensitivity to initial gap size and hence initial squeeze on the CFR. At a minimum gap of 25 mils, the initial permeability was estimated to be ~ $3x10^{-10}$ in^2 and transitioned to ~$5x10^{-9}$ in^2 at the maximum assembly gap of 65 mils. This effect was attributed to the mechanical deformation of the microstructure of the CFR under different levels of compressive load as a function of CFR squeeze. This shift in permeability causes a significant difference in Δp's across the CFR for the various cases. A second dependency was observed in the form of a time based pressure lag in the measured data that could only be explained by the in-situ deposition of alumina (Al_2O_3) on the surface of the CFR during the transient. Permeability values had to be adjusted a full order of magnitude from the initial value over the fill transient. A simple accumulation model was devised to "dynamically" transition the permeability as a function of total deposition on the CFR surface. Post-test inspection shows significant alumina deposition on outboard surfaces of the CFR.

Also extracted from JES tests were gas temperatures useful in determination of system heat transfer rates. The convective heat transfer in the gaps is approximated well by standard internal flow correlations. For the CFR, temperature measurements

were necessary to calculate the effective porous media volumetric heat transfer coefficients. Model development included the potential for a non-equilibrium gas-solid situation in the CFR as discussed in previous sections. JES testing provided gas temperature data for several cases and heat transfer coefficient parametrics allowed for back fitting predicted response to observed gas temperatures.

The following section provides the calibrated model results comparison to the JES measured data.

JES-3 Single CFR, 25 mil Gap

Shown in Fig 5 are model-calibrated results for the JES-3 test. This case was a single CFR face seal configuration with the minimum 25 mil assembly gap.

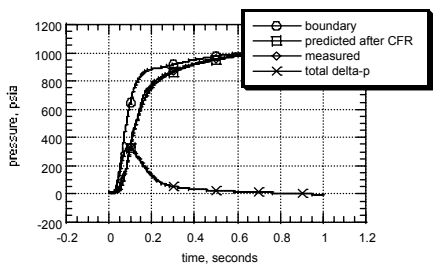

Fig 5 - JES-3 Single CFR Model Predicted vs. Measured Pressures, 25 mil Gap

Predicted pressure response is in excellent agreement with the measured values. Fill times are on the order of ½ second and pressure differentials of about 300 psi. Fig 6 shows the gas temperature comparisons for this case.

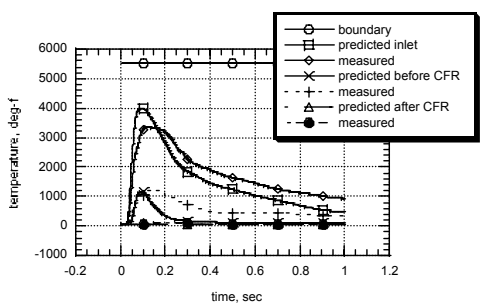

Fig 6 - JES-3 Single CFR, Model Predicted vs. Measured Temperature, 25 mil Gap

A constant boundary temperature of 5540°F was imposed at time zero. Computed gas temperatures at the inlet and in front of the CFR were in good agreement with the measured data. Differences in response decay times are attributed to thermocouple (TC) wall effects. Better comparison agreement could be obtained by thermally modeling the TC. The CFR backside gas temperature increase was <10°F. This TC measurement was present in all tests and was used for calibration of the volumetric heat transfer coefficient. The constant C_1 was adjusted until the desired backside ΔT was matched as a least squares best fit for all tests in the series.

JES-6 Dual CFRs, 25 mil Gap

Fig 7 provides a look at model predicted pressures versus the measured data for the dual CFR face seal at the minimum assembly gap.

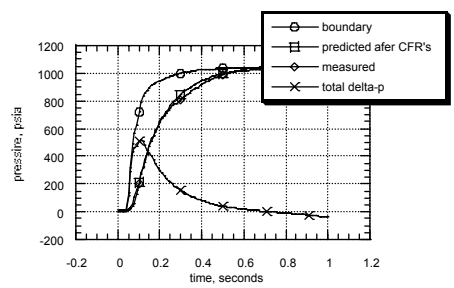

Fig 7 - JES-6 Dual CFR Model Predicted vs. Measured Pressures, 25 mil Gap

Again, the comparison shows very good pressure response agreement. Fill times (about 0.7 second) and total pressure differentials (about 450 psi) have increased over the single CFR case primarily due to doubling of the flow path resistance. Fig 8 shows the computed gas temperatures versus measured for the gap region outboard of CFRs (the inlet).

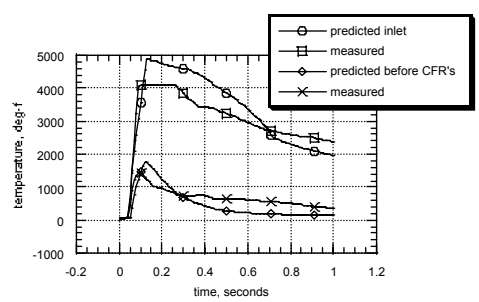

Fig 8 - JES-6 Dual CFR Model Predicted vs. Measured Inlet Temperatures, 25 mil Gap

Inlet temperature comparison is acceptable. Peak measured inlet temperatures saturated the type-K thermocouple at 4100°F with the model prediction closer to 5000°F. Gas temperatures in front of CFRs are in the 1500-1700°F range. Fig 9 shows the gas temperature results for in-between and after the CFRs.

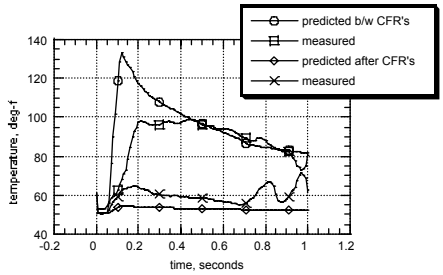

Fig 9 - JES-6 Dual CFR Predicted vs. Measured Temperatures, 25 mil Gap

For this case, measured gas temperatures between the CFRs increased about 50°F and backside temperature increase was <10°F. Model results compare well globally considering the overall range of computed temperatures in the model.

JES-6, Dual CFRs, 65 mil Gap

Fig 10 provides a look at model predicted pressures versus the measured values for a dual CFR system configured at the maximum assembly gap of 65 mils.

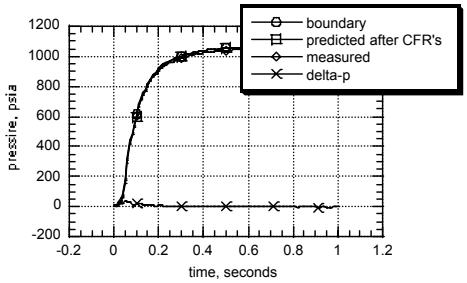

Fig 10 - JES-6 Dual CFR Model Predicted vs. Measured Pressures, 65 mil Gap

Model and measured pressures are in very good agreement for this case. For the large assembly gap, joint volume filling essentially follows chamber filling with little and/or no discernable fill time associated with the event. Pressure differentials are < 60 psi. Fig 11 shows the gas temperature comparisons for this case.

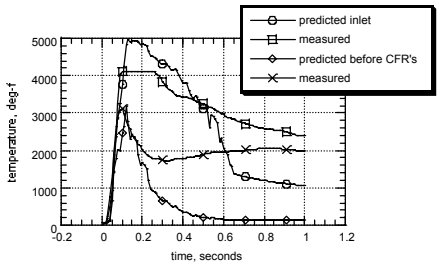

Fig 11 - JES-6 Predicted vs. Measured Temperatures Before CFRs in the Inlet Region, 65 mil Gap

There is very little gas sensible energy loss from chamber to inlet regions outboard of the CFR for this case. Temperatures are on the order of the 3000°-5000°F. Adjacent to the CFR, temperatures are considerably hotter than the minimum gap results due to higher peak flow rates (higher input heat rate) and wall heat transfer is less due to increased gap hydraulic diameter.

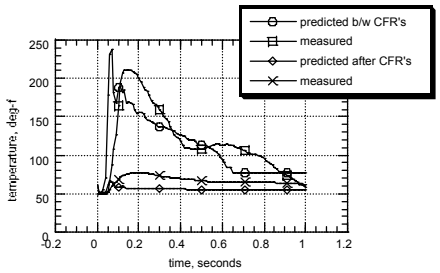

Fig 12 - JES-6 Predicted vs. Measured Temperatures Between and After CFRs, 65 mil Gap

For the larger gap spacing, in-between CFR gas temperatures can increase as much as ~160°F over start conditions. Temperature increase after the CFRs is approximately 20°-30°F. Again, model predictions are in fair agreement given overall magnitudes of the globally computed temperatures.

Flight Support Motor (FSM)-9 Assembly Gap Bounding Case

Predicted pressures for FSM-9 static test Joint-2 Dual CFR face seal are shown in Fig 13. For this case, the potential variation in volume filling transient is depicted by the shaded gray area where the boundaries are defined by results generated by max/min

assembly gaps. Results indicate a fill time variation of about 0.2 second with the quicker times occurring with larger gaps. Inferring a nominal response from Fig 13 would indicate joint filling is complete at about 0.6 second.

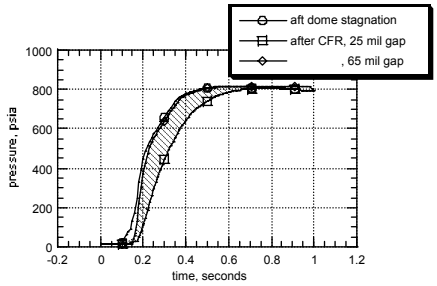

Fig 13 - FSM-9 Predicted Pressures

Joint-2 gas temperature predictions for FSM-9 are provided in Figs 14-16. Fig 14 shows that, as a function of assembly gap, inlet gas temperatures adjacent to the CFR range from 1800°-4000°F. A nominal estimation (45 mil gap) would be in the 2500°-3000°F range.

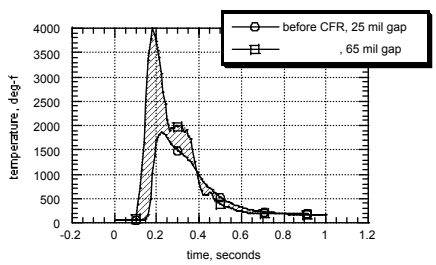

Fig 14 - FSM-9 Predicted Gas Temperatures in Assembly Gap Before CFRs

There is a significant reduction in temperature across the first CFR regardless of gap size. In-between temperatures are shown in Fig 15. Predicted variation in gas temperature increase, for this location, range from 60°F < ΔT < 350°F, depending on local gap.

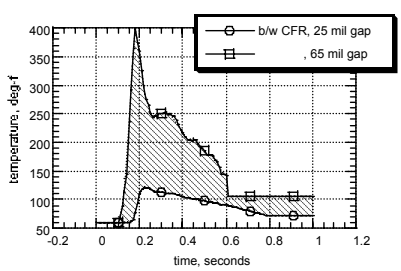

Fig 15 - FSM-9 Predicted Gas Temperatures in Assembly Gap Between CFRs

Fig 16 shows predicted temperatures for gasses that exit the in-board CFR and are headed for joint volumes. The effect of assembly gap variation on temperature magnitude has diminished to the point of inconsequential in terms of heating. Predicted variation in temperature increase for this location is about 3° < ΔT < 30°F.

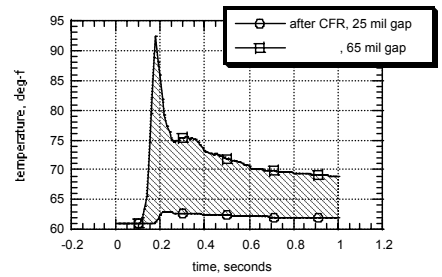

Fig 16 - FSM-9 Predicted Gas Temperatures in Assembly Gap After CFRs

Conclusions

The RSRM nozzle joint-2 CFR barrier system is predicted to perform in FSM-9 in a similar manner as demonstrated by JES model validation testing. This conclusion is based on the following considerations. JES test environments, i.e., ignition pressure rise rate, gas temperature and composition are similar to full-scale motor environments; thus, there is no issue with thermal boundary conditions. Further, the JES testing had a reasonable amount of geometric and kinematical similarity to full-scale hardware. The 1-D flow assumptions are approximately valid for a pressurization event of this joint. Circumferential flow can be addressed by steady Computational Fluid Dynamics (CFD) analyses if needed. Lumping of volumes in the test, to account for a more distributed situation in the full-scale hardware, is adequate if the controlling flow path resistance is the CFRs. This is believed to be the case based on the known "as-built" hardware housing gaps and overall assembly variation. Dynamic gap opening was not simulated in the JES test but was included in the FSM-9 model predictions. If the CFRs remain intact and seated, results indicate this effect is minimal in terms of gas temperature increase inboard of the barriers.

As a result of model calibration observations and review of the test data, the following general conclusions are drawn:

1. The excellent observed CFR thermal performance exploits the fact that the joint is vented. Pressurization rates for the free volumes behind the rope are rapid and total volume filling occurs by the time the chamber pressure trace is essentially neutral.

2. Another beneficial aspect of the CFRs is the filtering of the combustion gasses available for pressurization of joint free volumes. This will likely preclude any un-desirable molten slag deposition on seals or housing structures. During the numerous CFR tests, alumina / carbon deposition was always found on outboard surfaces of the rope.

3. CFR permeability had to be adjusted to account for initial squeeze. This effect is likely caused by the mechanical deformation of the CFR and resultant changes to the porous microstructure of the rope. Observed rope Δp's were on the order of 200-300 psi per rope for the minimum gap cases and decreased <60 psi for the larger gaps

4. CFR permeability is affected to some extent by the in-situ deposition of alumina and/or other condensables in the combustion gas as the joint pressurizes. This increases the Δp's across the rope during the later portion of the fill transient slightly increasing the fill times for the joint.

5. For the dual rope cases, CFR surface temperatures on the outboard side vary from 300-1100°F depending on the local gap. CFR surface temperature on the inboard side increase < 20°F for all cases with the gas in near thermal equilibrium with the solid carbon fibers. This outcome suggests that the CFR design provides more than sufficient thermal mass for quenching combustion gasses available for pressurization of the joint.

6. Large assembly gap joints will inherently have more free volume, higher peak flow rates and transfer less heat into the gap walls. As a result, both gas and CFR temperatures are significantly hotter on the outboard side of the barrier. Inboard of the CFRs, gas temperatures are relatively insensitive to initial gap.

7. For cases analyzed in this study where the CFRs remain fully seated and intact, predicted temperature rise in the metal housings was negligible. Primary seal pressurization environment will be thermally benign. There will be some irreversible recovery of gas temperature as the flow stagnates in dead ended regions of the joint but this effect will have no thermal impact on the structure.

References

1. RSRM Nozzle Joints Thermal Assessment, ED61, Memo ED63 (43-96), Marshall Space Flight Center, 1996

2. SINDA/JPR, "Joint Pressurization Routine (JPR) Theoretical Development and Users Manual", J. Louie Clayton, Memo ED66 (95-01), 1995

3. Systems Improved Numerical Differencing Analyzer (SINDA), JD Gaski, Network Analysis Associates Inc., 1987

4. O-Ring2: Volume Filling And O-ring Erosion Prediction Code, Improved Model Descriptions And Validation, Michael O'Malley, TWR-17030, August 1987

5. SRM Thermochemical Data, TP-H1148 Propellant, R. H. Whitesides, SRS Technologies, July 30, 1986

6. Carbon Fiber Rope (CFR) Joint Environment Simulator, A. Prince, Thiokol Corporation, ETP-1859, 1999

CORRECTIONS OF HEAT FLUX MEASUREMENTS ON LAUNCH VEHICLES

Dr. Thomas R. Reinarts
Monique L. Matson
Laurie K. Walls
NASA / ELV Mission Analysis Branch
VB – A3
Kennedy Space Center, Florida 32899

ABSTRACT

Knowledge of aerothermally induced convective heat transfer is important in the design of thermal protection systems for launch vehicles. Aerothermal models are typically calibrated via the data from circular, in-flight, flush-mounted surface heat flux gauges exposed to the thermal and velocity boundary layers of the external flow. Typically, copper or aluminum Schmidt-Boelter gauges, which take advantage of the one-dimensional Fourier's law of heat conduction, are used to measure the incident heat flux. This instrumentation, when surrounded by low-conductivity insulation, has a wall temperature significantly lower than the insulation. As a result of this substantial disturbance to the thermal boundary layer, the heat flux incident on the gauge tends to be considerably higher than it would have been on the insulation had the calorimeter not been there. In addition, radial conductive heat transfer from the hotter insulation can cause the calorimeter to indicate heat fluxes higher than actual. An overview of an effort to develop and calibrate gauge correction techniques for both of these effects will be presented.

INTRODUCTION

An instrument placed into a system to measure a given effect changes the environment simply by its addition to the system. Therefore, the measured value deviates by some amount from the undisturbed value, and it is important to understand the magnitude of this deviation. The deviation is small for many types of measurements, but can be substantial for heat flux gauges on launch vehicles. Since analytical models used to predict heat flux loads on launch vehicles are frequently calibrated by in-flight measurements from heat flux gauges, it is important to understand the contributing factors to sensor disturbance of the environment and its impact on sensor measurements. In areas with TPS, the dominating contributor is the potentially large temperature difference between the hotter, low conductivity insulation that surrounds the cooler gauge. This results in an incident heat flux indicated by the gauge that is higher than it would be on the insulation if the gauge had not been introduced into the system, potentially by factors of two or more. There are two causes of this (Figure 1). First, the near step change in wall temperature from TPS to sensor disturbs the thermal boundary layer, producing a higher incident flux on the sensor[1,2]. Second, the lower temperature gauge also acts as a heat sink, causing a

radial flow of energy through the sides of the gauge that moves through the epoxy/wafer and down the gauge body, which increases the indication of surface normal incident heat flux.

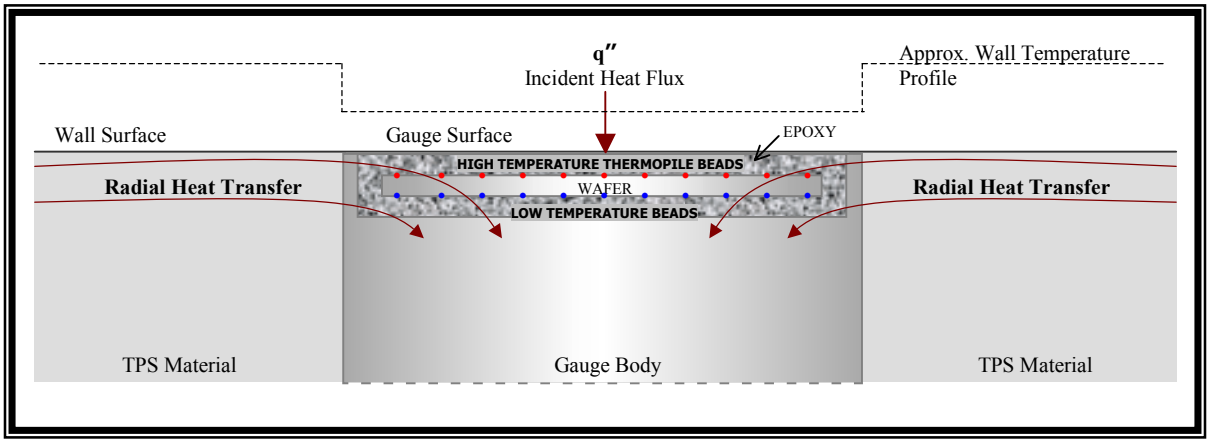

Figure 1: Diagram of Heat Transfer through a Schmidt-Boelter Gauge

An effort to quantify these effects has been undertaken in a three-part study, which includes modeling of the external velocity and temperature boundary layers, modeling of the conductive heat transfer within the sensor and from the surrounding TPS to the sensor, and testing in an aerothermal facility at Marshall Space Flight Center (MSFC). The overall modeling and calibration effort will eventually be used to quantify and correct the in-flight sensor errors. The expected result is an improved understanding of aerothermally induced convective heat transfer on launch vehicles, reduced design loads, and relaxed TPS requirements. While current data provide conservative factors of safety, there are potential benefits attainable from reduced conservatism via lower TPS mass and reduced TPS application requirements.

BOUNDARY LAYER ANALYSIS

In convective flow, dramatic thermal boundary layer changes can result from steep surface thermal gradients in the direction of flow. The heat transfer from a convective flow to the plate can be described by the following equation:

$$q'' = -k_f \nabla T_{f0} \tag{1}$$

where k_f is the thermal conductivity of the fluid, T_{f0} is the temperature of the fluid, and q'' is the fluid/wall heat-flux.

Thus, a dramatic change in wall surface temperature results in a change in the fluid thermal gradient at the wall interface, causing a changed heat flux into the wall. Schmidt-Boelter gauges are typically made of materials with relatively high specific heat and high thermal conductivity. When surrounded by a TPS with low conductivity, the surface temperature gradient from TPS to gauge can be steep. In this situation, the heat flux into the gauge is not the same as the heat flux into the same area if the gauge is not present. Attempts at modeling this phenomenon has been

performed by others[1,2,3,4]. These models assumed a step change in wall temperature, and constant fluid properties over the surface temperature gradients. A CFD effort has been undertaken to include fluid property variations and calculate the difference between the gauge incident and undisturbed heat fluxes.

Referencing Figure 2, the magnitude of this dissimilar material effect is dependent on fluid properties, flow conditions at the leading edge, flow development length, calorimeter size, and of course, the surface temperature gradient.

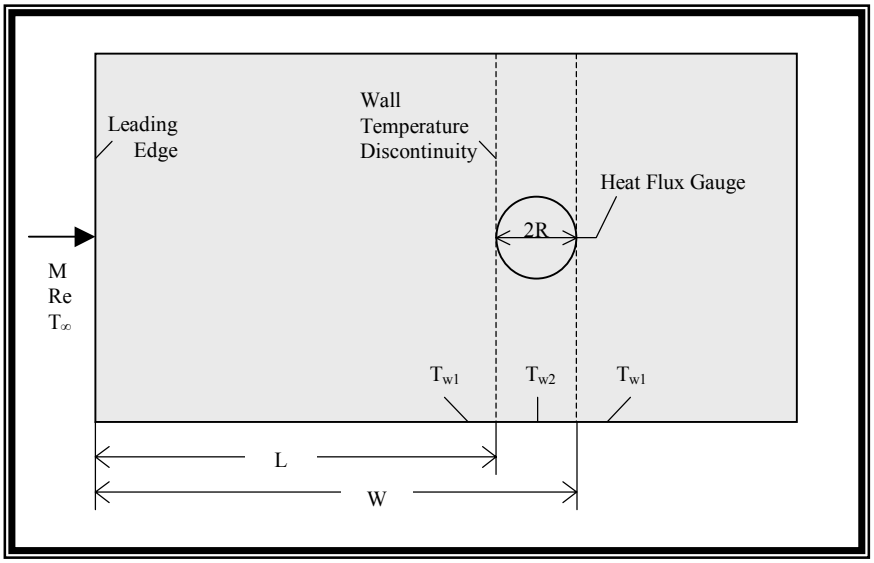

Figure 2: Diagram of CFD 2-D Plate Model

CONDUCTIVE HEAT TRANSFER ANALYSIS

In addition to boundary layer effects, hotter surrounding TPS can conduct energy into the calorimeter and cause the calorimeter to indicate a higher than actual surface incident heat flux. To understand the conductive heat transfer effects on a Schmidt-Boelter gauge, it is important to also understand the operation and construction of the gauge. The Schmidt-Boelter gauge includes a coiling of thermopile wire around a wafer, which is encased by a low conductivity epoxy. The thermopile beads are located on the top (high temperature thermopile) and bottom (low temperature thermopile) of the wafer surface. These thermopile beads provide a temperature gradient that, based on appropriate calibration and the one-dimensional Fourier's law of heat conduction (Equation 2), outputs the incident heat flux.

(2) $$q'' \propto \frac{\delta T}{\delta x}$$

Fourier states that, for steady state one-dimensional heat transfer through a given homogenous material, the heat flux, q'', is directly proportional to the differential temperature, δT, divided by the differential length, δx. Since the gauge's operation is based on this temperature difference

between the upper and lower surface of the wafer, the radial heat transfer directly increases the incident heat flux measurement. Previous models have been developed to study sensitivity and to assist in gauge design[5]. Yet, to the authors' knowledge, an investigation of the radial effects has not been pursued before. A detailed description of Schmidt-Boelter gauge design/operation can be found in Carl Kidd's AEDC report[5]. The design and development of the three-dimensional Schmidt-Boelter gauge model is presented next.

SCHMIDT-BOELTER MODEL DESIGN AND DEVELOPMENT

A Schmidt-Boelter (S-B) gauge comprises four major components, including the cylindrical conductive gauge body, the non-conductive epoxy, the conductive rectangular wafer and the thermopile (Figure 3). Note that the gauge body and the wafer are typically composed of the same conductive material, usually copper or aluminum.

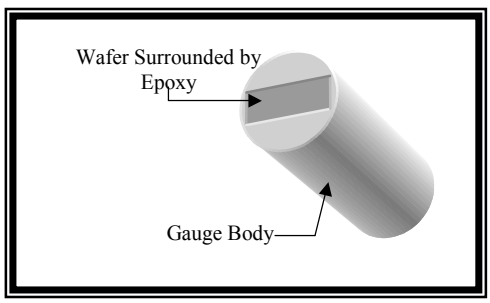

Figure 3: Basic Diagram of S-B Gauge

The gauge measures the temperature difference between the top and bottom surfaces of the wafer via the thermopile, outputting a signal proportional to the incident heat flux. The epoxy is exposed to the top surface of the gauge and completely encases the wafer and thermocouple wire. The idealizations incorporated by this 3-D model are shown in the figure below. Note that the thermocouple wire and beads are shown for explanation purposes only (Figure 4). Kidd analyzed the effects of the size and material of the thermocouple wire on heat transfer measurements, which show that wire having diameters less than 0.003 in (0.0762 mm) induce small errors[6]. Therefore, they are considered negligible for modeling construction because of their limited impact on the overall thermal environment.

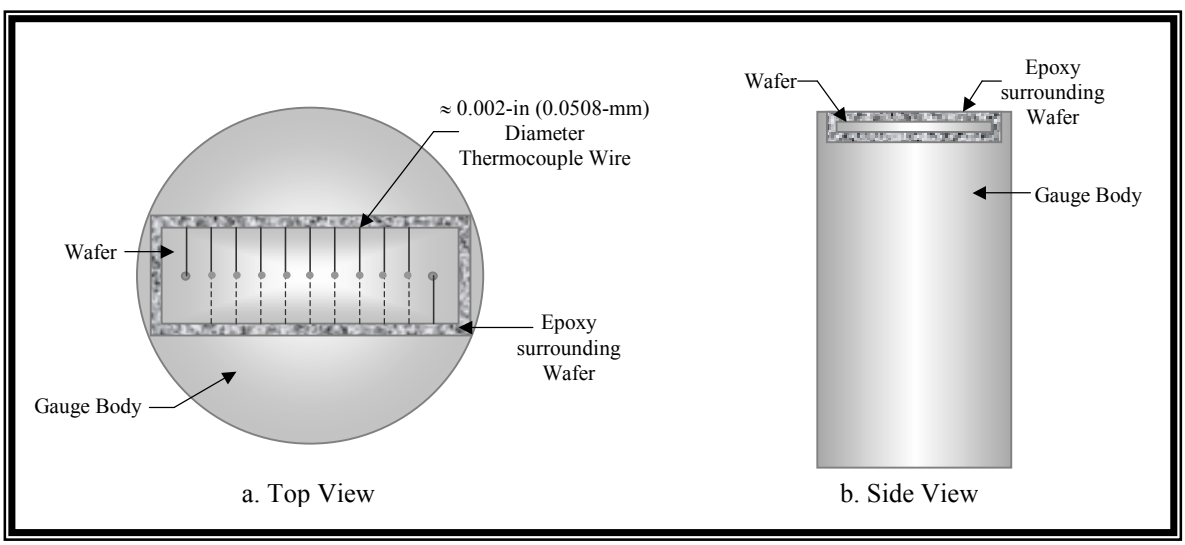

Figure 4: Idealization used for Modeling of the S-B Gauge

The software used to develop and analyze this model was SINDA/G 2.1, a finite-differencing thermal analyzer. Each node was manually generated in order to provide a customized model that focuses on the temperature differences measured by the gauge. The 3-D Schmidt-Boelter gauge model consists of over 3600 nodes, the densest mesh being in the epoxy/wafer area. There is a high concentration of detail there because the effect on the epoxy/wafer is the focus of this radial heat transfer study. Less detail is needed for those nodes that are composed of the same material and are not located near the relative vicinity of the wafer.

AEROTHERMAL TESTING AT MARSHALL SPACE FLIGHT CENTER

Both the CFD and the detailed gauge model calibrations will be achieved via testing of flat plates with thin skin calorimeters and copper and aluminum Schmidt-Boelter gauges. The thin skin calorimeters will indicate the actual heat flux, and the Schmidt-Boelter gauges will give readings that, when properly corrected by the calibrated models, will match the thin skin measurements. Test panels are shown in Figure 5 (Page 6), and will be tested in the Improved Hot Gas Facility (IGHF) at MSFC. Note that the diagrams are not to scale but the panels are 12 inches by 19 inches. There are two categories of test panels: with TPS and without TPS.

Three panels of different materials without TPS will be used. The materials include stainless steel, copper, and aluminum. Each will include one thin skin calorimeter of a material similar to the plate. The stainless steel panel will include two more thin skin calorimeters on the same flow path line as the first to determine incident heat rate variations as a function of location along the major plate axis. Each of these plates will also have two Schmidt-Boelter calorimeters of dissimilar materials, located as shown in Figure 5. The thin skin gauges will be made of the same material as the plate and will give an accurate assessment of the incident convective heat flux.

The fourth panel will be stainless steel, partially covered by an ablative, low thermal conductivity material (also shown in Figure 5). The ablative material will most likely be BTA, and will appear as rectangular strips on either side of a stainless steel strip centered and in the direction of flow. The ablative material will be approximately 0.125 in thick, and the stainless steel below the TPS will be machined out so the BTA is level with the center strip of stainless steel. Three thin skin calorimeters will be used, and will appear as in the stainless steel panel with no TPS. One copper and one aluminum S-B gauge will appear flush mounted with the TPS, each on a separate TPS strip. The TPS will be cured with the S-B's in situ, with no gap between the gauge and the TPS.

Summarizing, four different panels have been designed and are in fabrication: 1) a copper panel with one copper S-B gauge, two aluminum S-B gauges, and a thin skin calorimeter; 2) an aluminum panel with one aluminum S-B gauge, two copper S-B gauges, and one thin skin calorimeter; 3) a stainless steel panel with three thin skins, one copper S-B gauge, and one aluminum gauge; and 4) a stainless steel panel partially covered with an ablative with three thin skins, one copper S-B gauge, and one aluminum S-B gauge. The copper gauges are Medtherm Schmidt-Boelters and the aluminum gauges are AEDC Schmidt-Boelters.

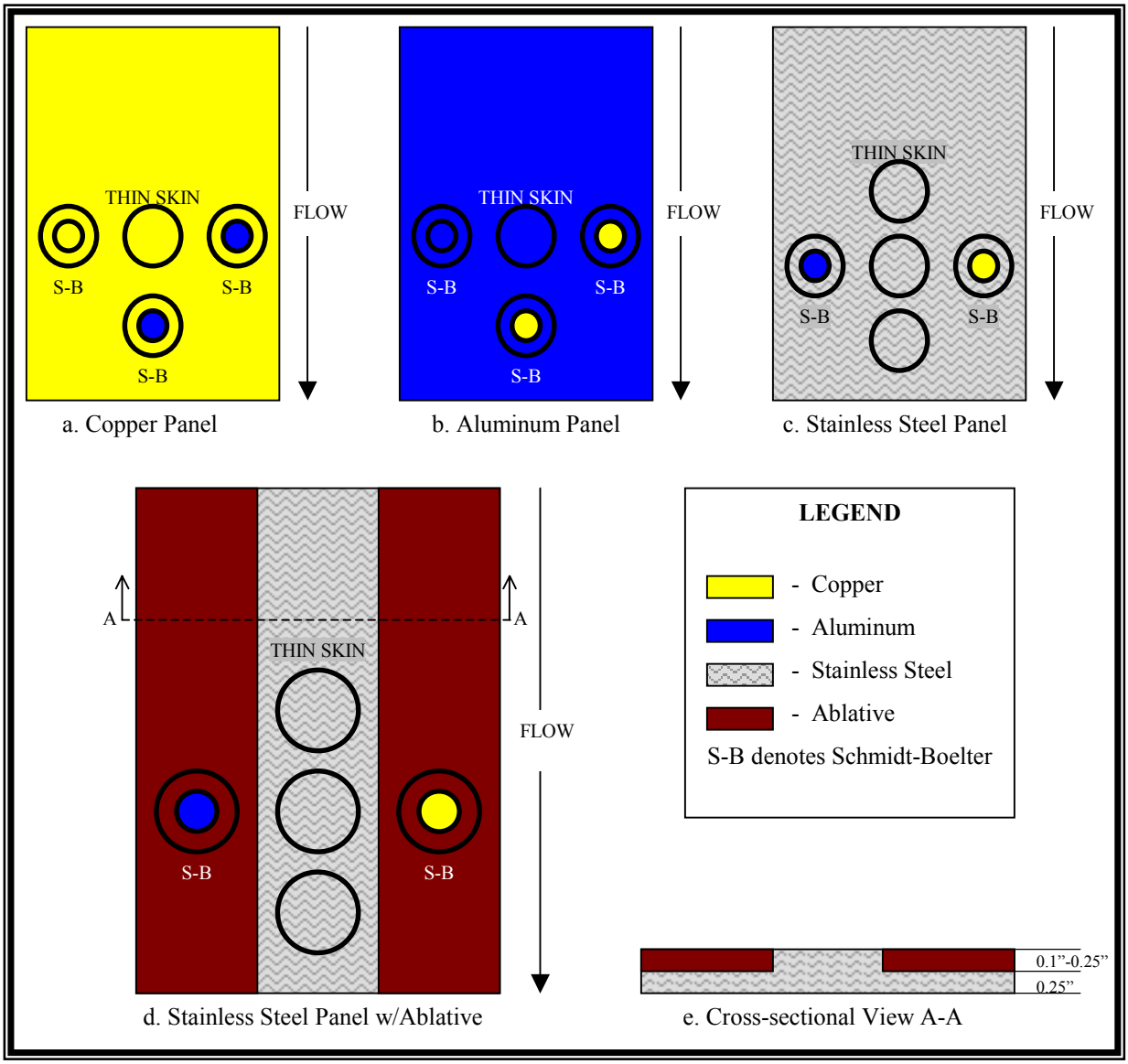

Figure 5: Testing Panel Configuration

The primary purpose of the study is determine dissimilar material effects, and the testing will be used for model calibration, that will build confidence for use of the models to correct in-flight data. In addition, the impact of gage/wafer orientation with respect to convective flow direction will also be studied in the testing program. The testing matrix shown in Table 1 (Page 7) also includes a couple of radiant test points that will eliminate thermal boundary layer effects and allow focus on radial heat transfer effects.

Table 1: Basic Testing Matrix

Test # (by priority)	Panel	Angle	Approx. HR ($Btu/ft^2/s$)	Comments	Time (s)
1	Stainless Steel Plate	0°	4.7	Baseline	20
2	Stainless Steel Plate	0°	4.7	Repeat Baseline	20
3	Aluminum Plate	0°	4.7	Baseline	20
4	Aluminum Plate	0°	4.7	Repeat Baseline	20
5	BTA/SS/Hypalon	0°	4.7	Baseline	20
6	BTA/SS/Hypalon	0°	4.7	Repeat Baseline	20
7	Copper Plate	0°	4.7	Baseline	20
8	Copper Plate	0°	4.7	Repeat Baseline	20
9	Stainless Steel Plate	0°	4.7	Baseline with Medtherm calorimeters rotated 120°	20
10	Stainless Steel Plate	0°	4.7	Repeat Baseline with Medtherm calorimeters rotated 120°	20
11	Stainless Steel Plate	0°	4.7	Baseline with Medtherm calorimeters rotated 240°	20
12	Stainless Steel Plate	0°	4.7	Repeat Baseline with Medtherm calorimeters rotated 240°	20
13	BTA/SS/Hypalon	TBD	8.0	Baseline	20
14	BTA/SS/Hypalon	TBD	8.0	Repeat Baseline	20
15	BTA/SS/Hypalon	0°	4.7	Baseline, radiant	20
16	BTA/SS/Hypalon	0°	4.7	Repeat Baseline, radiant	20
17	Aluminum Plate	0°	4.7	Baseline with Medtherm calorimeters rotated 120°	20
18	Aluminum Plate	0°	4.7	Repeat Baseline with Medtherm calorimeters rotated 120°	20
19	Aluminum Plate	0°	4.7	Baseline with Medtherm calorimeters rotated 240°	20
20	Aluminum Plate	0°	4.7	Repeat Baseline with Medtherm calorimeters rotated 240°	20
21	Copper Plate	0°	4.7	Baseline with Medtherm calorimeters rotated 120°	20
22	Copper Plate	0°	4.7	Repeat Baseline with Medtherm calorimeters rotated 120°	20
23	Copper Plate	0°	4.7	Baseline with Medtherm calorimeters rotated 240°	20
24	Copper Plate	0°	4.7	Repeat Baseline with Medtherm calorimeters rotated 240°	20

In addition to the usual IHGF measurements and the thin skin and S-B data, surface IR (Infrared) data will be important. Spot IR and surface plane IR data will be used to determine the surface temperature profile of the plate, focusing on the areas on and in the near vicinity of the S-B gauges. This information will be crucial in the model calibration efforts, especially for determining the boundary layer effects caused by the surface temperature differences between the panel and the S-B gauges.

Finally, it will be important to understand the contact resistances between the S-B gauges and the surrounding material. The easiest way to establish this is by making the contact resistance as close to zero as possible using high conductivity thermal grease for the panels with no TPS.

POST-TEST MODEL ANALYSIS

As mentioned previously, the primary goal of this study is to correct and better understand in-flight measurements of heat fluxes on launch vehicles. Test data from the aerothermal facility will be used to calibrate the analytical models. In addition, a sensitivity analysis will be performed to determine the impact of sensor orientation, wafer thickness, epoxy thickness, and contact conductance from the sensor to the surrounding material. Also, during manufacturing, several deviances from production specifications can occur. For instance, the thermopile beads could be separated unevenly, they may not be centered, etc. The sensitivity analysis will investigate all of theses types of variables and the effects they induce on the overall gauge measurement.

CONCLUSIONS

A three part program has been assembled that will produce a calibrated technique to correct material dissimilarity induced errors for in-flight Schmidt-Boelter heat flux measurements on launch vehicles. In general, the need for such corrections is greatest for aerothermal heating measurements. Two coupled models have been developed, one correcting boundary layer effects stemming from near step changes in the temperature from the surrounding material to the gauge, and the other accounting for radial heating errors. Testing in an aerothermal facility will provide the calibration. While this approach is more crucial to aerothermal heating measurements, the radial conduction effects model can also be applied to radiative measurement corrections, such as for plume radiation. While current uncorrected data provide conservative factors of safety, there are potential benefits attainable from reduced conservatism via lower TPS mass and reduced TPS application requirements.

ACKNOWLEDGEMENTS

The author(s) wish to acknowledge the help of the people at the MSFC Improved Hot Gas Facility, who have entered into a cooperative effort with us to obtain the necessary calibration data. Their assistance in fabricating the test panels and interfacing with heat flux gauge manufacturers and calibrators has been invaluable.

REFERENCES

1. Reynolds, W. C., Kays, W. M., and Kline, S. J., “Heat Transfer in the Turbulent Incompressible Boundary Layer, II – Step Wall-Temperature Distribution,” in *NASA Memorandum*, Washington, NASA, 1958, pp. 1-3.
2. Rubesin, Morris W., “The Effect of an Arbitrary Surface-Temperature Variation along a Flat Plate on the Convective Heat Transfer in an Incompressible Turbulent Boundary Layer,” in *NACA Technical Note 2345*, Moffett Field, CA, NACA, 1951, pp. 1-3, 24.

3. Westkaemper, John C., "On the Error in Plug-Type Calorimeters Caused by Surface-Temperature Mismatch," *Journal of the Aerospace Sciences*, November 1961, pp. 907-908.

4. Knox, E.C., "A Critique on Correcting Heat-Transfer Results for Temperature Mismatch," in *Remtech Inc. Technical Note RTN 158-02*, March 1987.

5. Kidd, C. T., "A Durable, Intermediate Temperature, Direct Reading Heat Flux Transducer for Measurements in Continuous Wind Tunnels," in *AEDC-TR-81-19*, Arnold AFS, TN, AEDC, 1981, pp. 7-15.

6. Kidd, C. T., "Thin-Skin Technique Heat-Transfer Measurement Errors Due to Heat Conduction into Thermocouple Wires," *ISA Transactions* **24**, no. 2, 1985, pp. 1-9.

CONTACT

Dr. Reinarts can be reached at the following e-mail address: Thomas.reinarts-1@ksc.nasa.gov.

NOMENCLATURE, ACRONYMS, ABBREVIATIONS

M	Mach Number
Re	Reynolds Number
T_∞	Free Stream Temperature
$T_{w1,w2}$	Wall Temperature
L	Running Length to Heat Flux Gauge
R	Radius of Heat Flux Gauge
W	L+2R
q''	Incident Heat Flux
δT	Differential Temperature
δx	Differential Length
TPS	Thermal Protection System
KSC	Kennedy Space Center
MSFC	Marshall Space Flight Center
IHGF	Improved Hot Gas Facility
AEDC	Arnold Engineering Development Center
S-B	Schmidt-Boelter
CFD	Computational Fluid Dynamics
k_f	Fluid thermal conductivity
∇T_{f0}	Temperature gradient of the fluid at the fluid wall interface
BTA	Low Conductivity Ablative
IR	Infrared

Panel Discussion on Multi-Disciplinary Analysis

Moderated by

Robert Garcia
Marshall Space Flight Center
Huntsville, Alabama

The Marshall Space Flight Center (MSFC) is hosting the Thermal and Fluids Analysis Workshop (TFAWS) during the week of September 10, 2001. Included in this year's TFAWS is a panel session on Multidisciplinary Analysis techniques. A description of that session is available below. The intent is to provide an opportunity for the users to gain information as to what product may be best suited for their applications environment and to provide feedback to you, the developers, on future desired developments.

Potential users of multidisciplinary analysis (MDA) techniques are often overwhelmed by the number of choices available to them via commercial products and by the pace of new developments in this area. The purpose of this panel session is to provide a forum wherein MDA tools available and under development can be discussed, compared, and contrasted. The intent of this panel is to provide the end-user with the information necessary to make educated decisions on how to proceed with selecting their MDA tool. It is anticipated that the discussions this year will focus on MDA techniques that couple discipline codes or algorithms (as opposed to monolithic, unified MDA approaches). The MDA developers will be asked to prepare a product overview presentation addressing specific questions provided by the panel organizers. The purpose of these questions will be to establish the method employed by the particular MDA technique for communication between the discipline codes, to establish the similarities and differences amongst the various approaches, and to establish the range of experience and applications for each particular MDA approach. The following approaches are on the agenda:

1. NPSS from NASA Glenn Research Center (Karl Owen)
2. MDICE from CFD Research (Vincent Harrand)
3. RECIPE from ISSI (Jerry Wittenstein, Troy Stanley)
4. iMAN from UGS (James (Nick) Nicholson)
5. iSIGHT from Engineous (Mark Prow, JP Evans)
6. RDCS from Boeing-Rocketdyne (Bill Follett)
7. LOCI from Mississippi State University (Ed Luke)

After the presentations by the MDA developers, there will be a discussion period that will include audience participation. The panel discussion will be moderated by Roberto Garcia, Georg Siebes, and Bruce Tiller from NASA. The presenters are requested to address the following points, not necessarily in this order, in their presentations:

1) In what aspect of the MDA process is your tool focused? For example, life cycle workflow management vs. analysis data exchange; level of fidelity (1D, 2D, or 3D); component vs. subsystem vs. system
2) Describe how your approach couples dissimilar discipline codes. For example, fine grain vs. coarse grain coupling; one way vs. two way communication amongst the disciplines; etc.
3) Distinguish current (operational) capabilities vs. future planned capabilities. Highlight how these capabilities are being used operationally.
4) Do you provide discipline specific modules or are you instead focused on the integration and coupling functions in the design and analysis process?
5) Does your approach include utilities to facilitate the coupling of legacy or third party codes?

6) Does the approach include any knowledge capture (expert system) or optimization capability? If so, describe these capabilities.
7) Does your product have the capability to run parallel jobs and/or make use of parallelization capability within the discipline codes?
8) Does your approach currently support linking directly with CAD? If so, to which packages?
9) Does your approach support coupling between analysis tools of varying levels of fidelity? For example, coupling of 1D analysis to 2D or 3D analysis.
10) Does your approach support time accurate MDA?
11) To what platforms has your method been ported?
12) Please provide a list of third party codes, discipline based codes that have been successfully run under your framework.

Loci: Logic Programming for Computational Field Simulations

Mississippi State University

Edward Luke

Motivation

- Complexity of numerical simulation software is increasing
- Current state-of-the-art with respect to parallel computing is labor intensive and prone to errors
- Concerns of reliability and rapid prototyping are important to domains where efficient means of modeling are unknown

Key Concepts

- Computations are performed with respect to numerical discretizations called meshes.
- Meshes can be represented as a collection of entities combined with a set of binary relations called maps.
- Computations are performed by binding values to entities.
- Many computations are based on values assigned to neighboring entities. The binary relations used to represent the mesh are invoked in the access of these neighboring entities.

Key Observations

- Entities can generally be partitioned into a set of entities categories. The number of these categories are relatively independent of grid density.
- Since values tend to bind to entities according to category, pre-sorting entities by category facilitates $O(1)$ computation of set intersections, unions, and complements.
- Many computations are of a declarative nature. For example: In an ideal gas, pressure is calculated using density and temperature.
- Simple and compose-able components facilitate reuse.

Paradigm: Programming by Rule Database

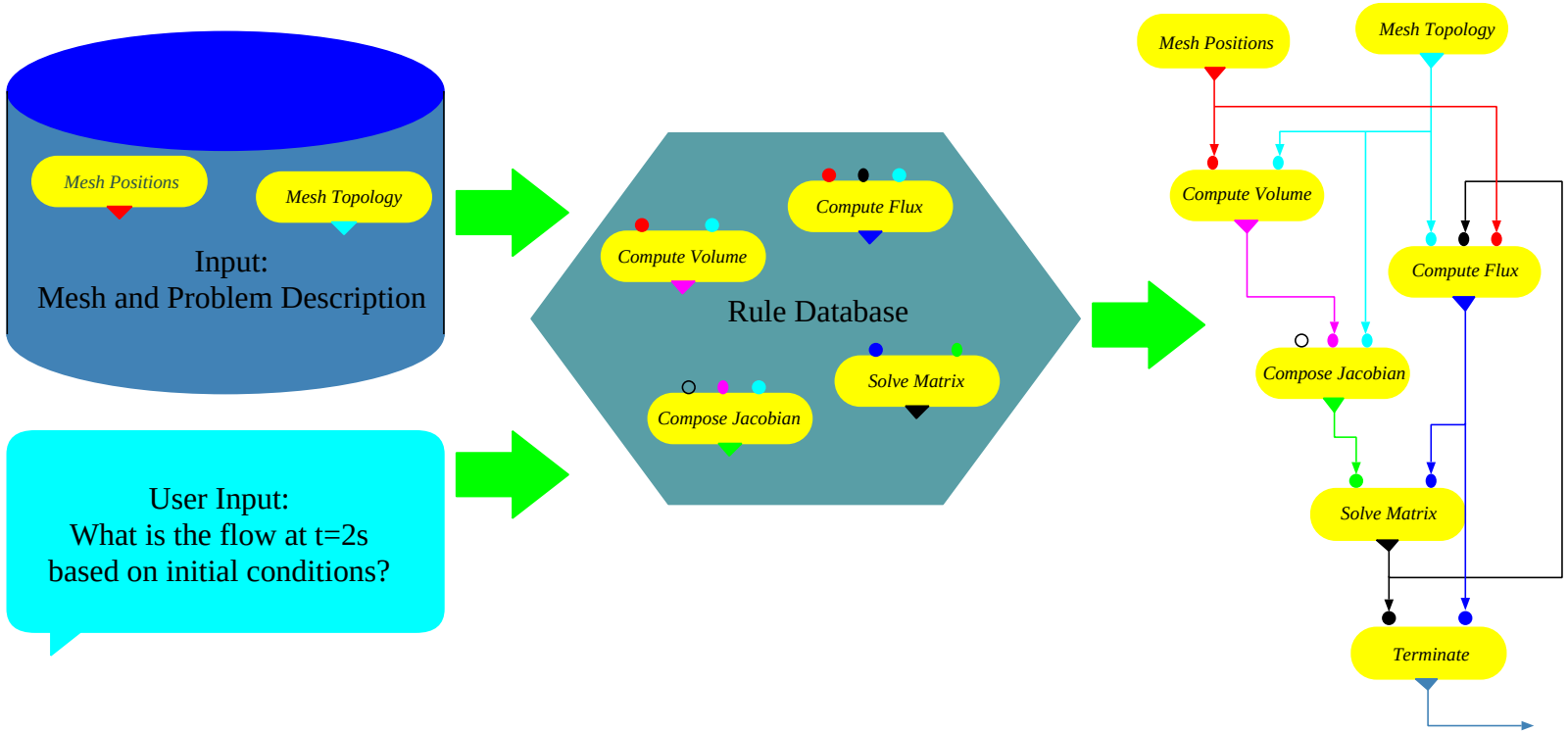

Rules Represent Annotations to Stateless Subroutines

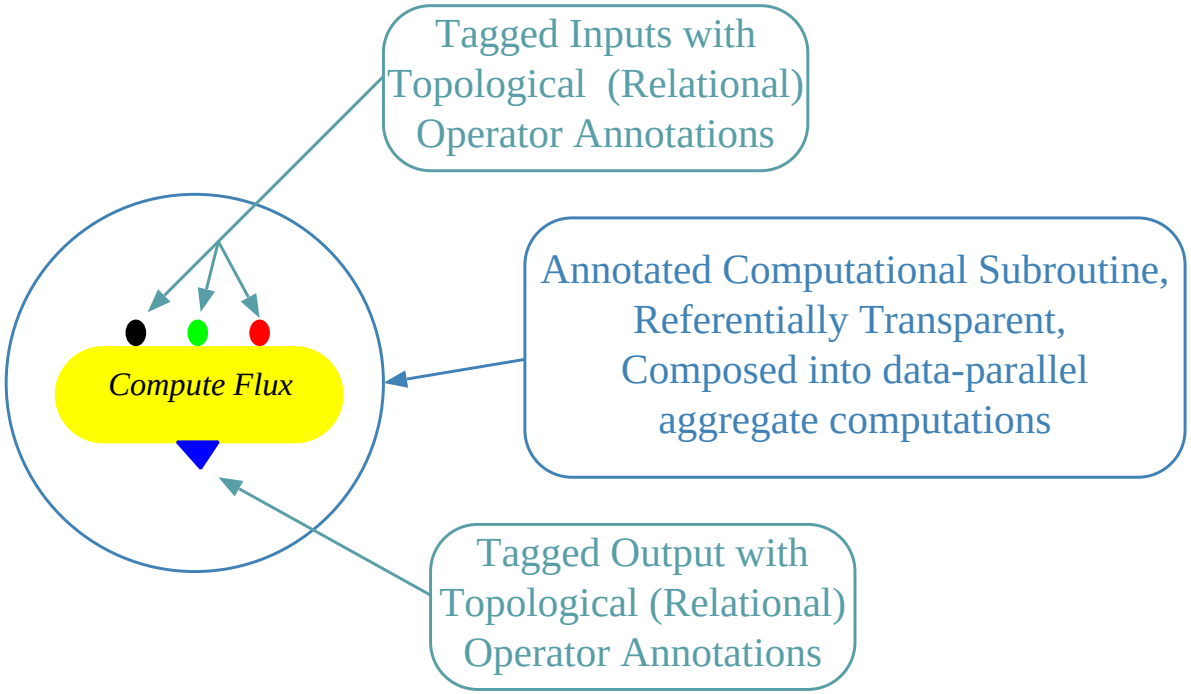

A Simple Example

Consider the ideal gas law for mixtures of thermally perfect gases:

$$p = \rho \tilde{R} T$$

This equation establishes a relationship of pressure to density, temperature, and mixture gas constant. This relationship is universal: it applies to any place where these properties are simultaneously available at any instant in time.

A Simple Example (cont)

The ideal gas law relation can be represented by the rule signature

$$p \leftarrow \rho, \tilde{R}, T$$

This rule signature signifies that a value for pressure can be generated from values for density, temperature, and mixture gas constant. It is described by the implication:

$$value(\rho) \wedge value(\tilde{R}) \wedge value(T) \Rightarrow value(p)$$

An Overview of the Chem Code

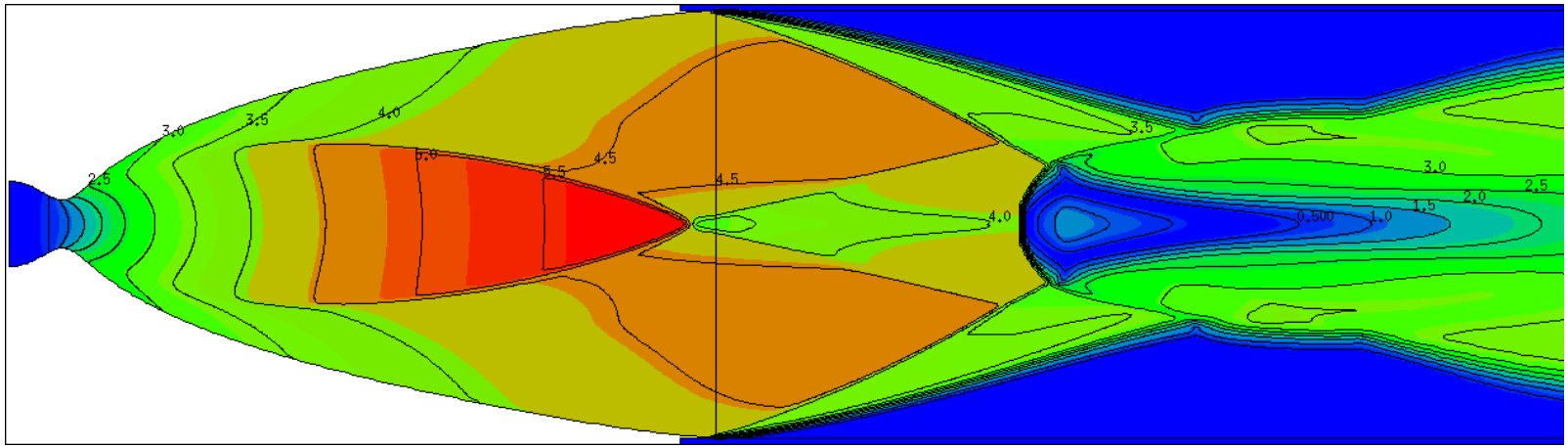

- General reaction kinetics, thermodynamic, and transport models
- High-Resolution Approximate Riemann Solvers
- Fully implicit, time-accurate and steady-state formulation
- Explicit Runge-Kutta integration formulation also supported
- Support for Generalized Grids (arbitrary polyhedra)
- 4th order MacCormack integration method supported for LES

Parallel Implementation

- Uses both MPI and POSIX-threads.
- Parallelization is automatic (No parallel directives are used in model specifications.)
- Parallelization supports arbitrary decompositions of entities.
- Future work will include dynamic load balancing both in the POSIX thread model and MPI.

Performance Benchmark

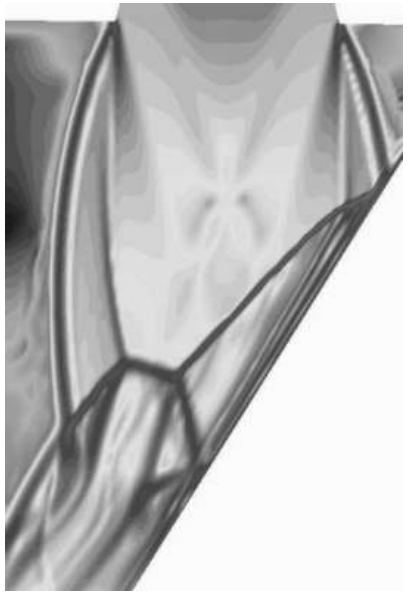

- Test case is a 3D inviscid non-reacting supersonic jet impingement problem.
- 600K cells in a structured multiblock grid.

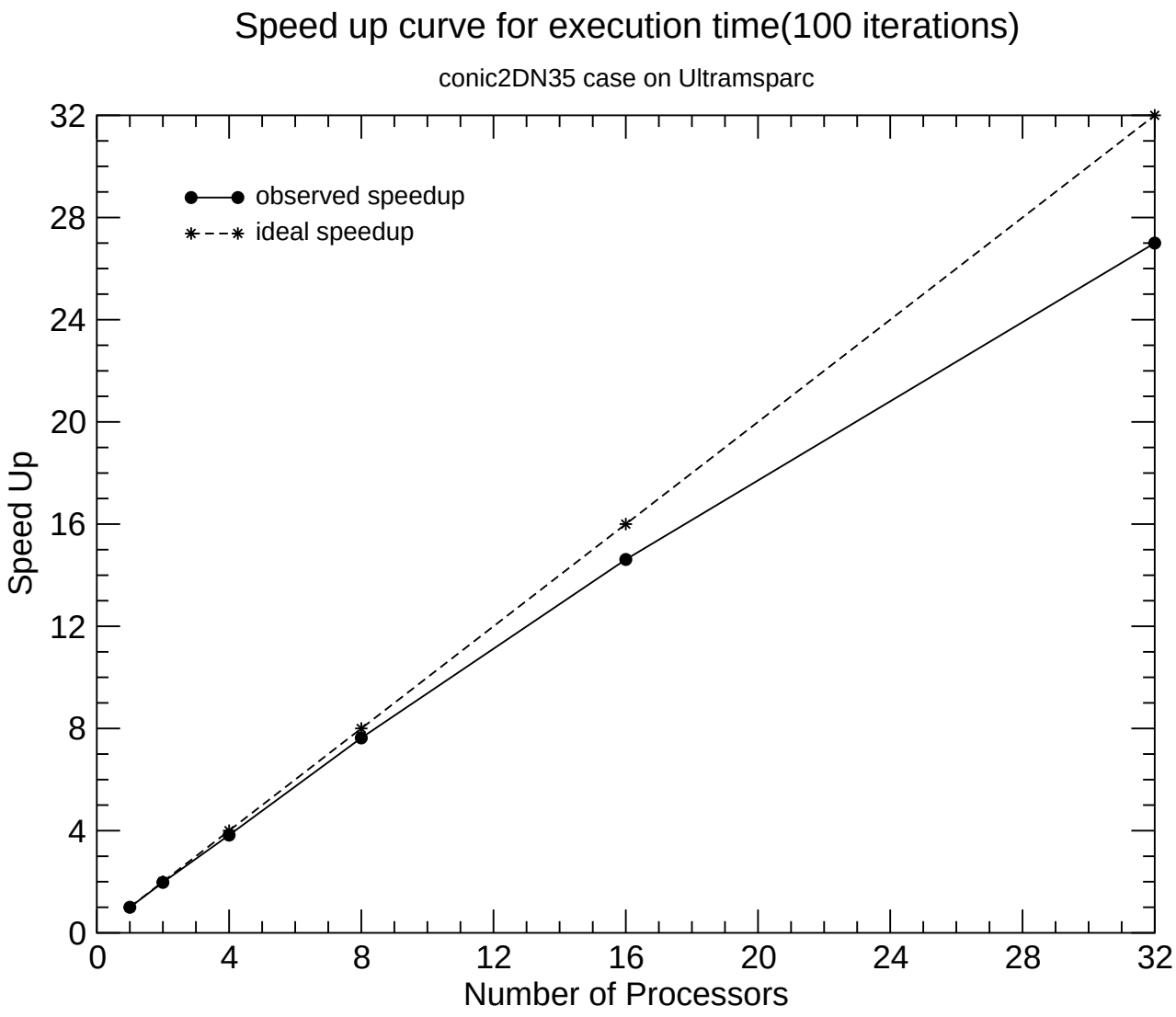
Speed up curve for execution time(100 iterations)
conic2DN35 case on Ultramsparc
observed speedup
ideal speedup
Speed Up
Number of Processors
0
4
8
12
16
20
24
28
32

Coupling Fluids and Solid Mechanics using Loci

Fracture and Fluid Mechanics

- Gas under high temperature and Pressure such as encountered in propulsion systems and high efficiency steam turbines.
- Concern: Failure of containment of these gases
- Fracture mechanics problems dominated by thermal and mechanical loads due to above gases. It is a multidisciplinary problem.
- MSU - Gas Phase Models
- Cornell - Fracture Mechanics Models

Model Problem

- Regeneratively Cooled curved pipe (Idealized Problem)
- Gas Phase: Chem Code provides model
- Solid Phase: FEM model for aniostropic non-linear thermal and mechanical response. (Under development at Cornell)

Unsteady thermal response at 10ms

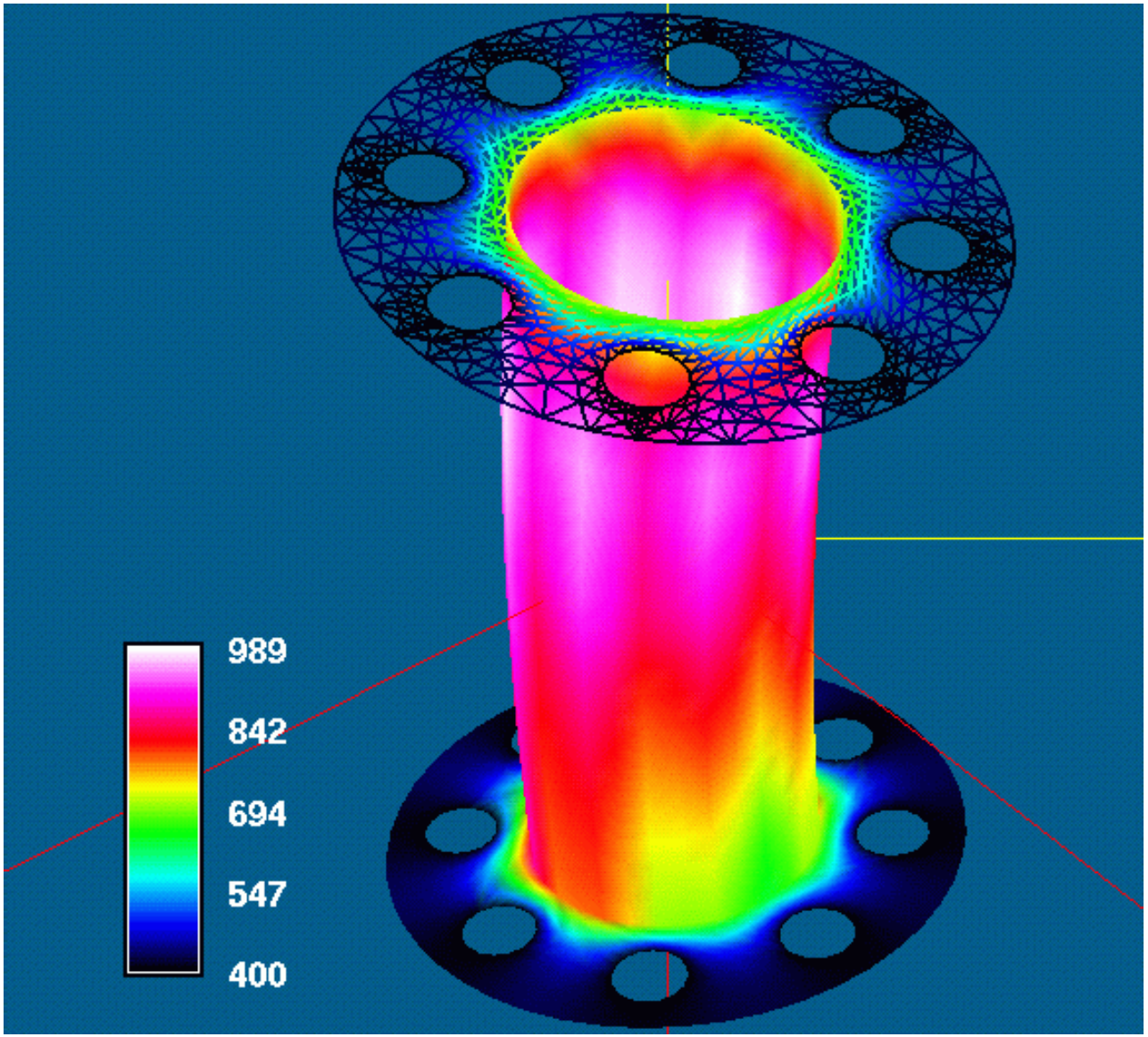

Loci for MD Topics

- Loci is a research tool that is currently under development
- Focused on Fine-Grained inter-operation of 3D models for time accurate MD simulations.
- Not constrained to 3D
- Coupling to external codes planned for next year.
- Provides automatic parallelization
- Ported to Unix and Linux Systems (SGI, Sun, x86)

MDICE
An Integrated Framework for Multi-disciplinary Engineering Simulations

Presented by
V. Sarathy, M. Underwood, and V. Harrand
CFD Research Corporation
Huntsville, AL

September 12, 2001
Thermal and Fluid Analysis, MDA Panel Session
NASA, Marshal Space Flight Center
Huntsville, AL

Motivation for Building Distributed Systems for MDA

- Monolithic Applications are too Unwieldy to Maintain
  - Promote Little Software Reuse
  - Poor Extensibility due to Tightly-Coupled Nature
  - Increase Software Maintenance Needs
  - Prohibitive Costs in Building Complex Applications ad hoc from Scratch

- Distributed Systems Lead to Separation of Concerns
  - Promote Software Component Reuse
  - Offer Plenty of Scope for Extensibility
  - Enable Plug-and-Play of Components due to Loosely-Coupled Nature
  - Facilitate Software Maintenance

- Lack of Integration Among the Various Software Analysis Components is the Major Obstacle in Multi-Disciplinary Analysis

Issues in Design of Distributed Simulation Environments

- Coping with Heterogeneity in Hardware Platforms, Programming Languages
- Collaboration among Applications from Dissimilar Disciplines and Technology Providers
- Handling Data Communication between Applications
- Security Issues in a Networked Environment

Requirements of a Framework for Distributed Applications

- What We Need is an Infrastructure Framework that Enables:
  - Applications to Interwork Seamlessly in Heterogeneous Environments
  - Components to Communicate with Each Other with Location Transparency, Using a Common Programming Model
  - Event-Driven Control Over Applications Using Remote Method Invocations; Most Engineering Applications have a Sequential Work Flow
  - Capability to Control the Level of Coupling Between Application Processes (Fine Grain *vs*. Coarse Grain, One-way *vs*. Two-way)
  - Dynamic Spawning/Removal of Application Processes
  - Hiding of Low-Level System Infrastructure Tasks from Application Developers

Conceptual Overview of MDICE

- MDICE - Multi-Disciplinary Computing Environment

- MDICE Enables Engineering Programs of Various Disciplines to Functions as One Multi-Disciplinary Application in a Distributed, Heterogeneous, Object-Oriented Framework

- MDICE is an ORB-like Middleware Designed to Bridge the Gap Between Application Programs and Lower-Level Hardware & Software Architecture and Coordinate their Interoperability.

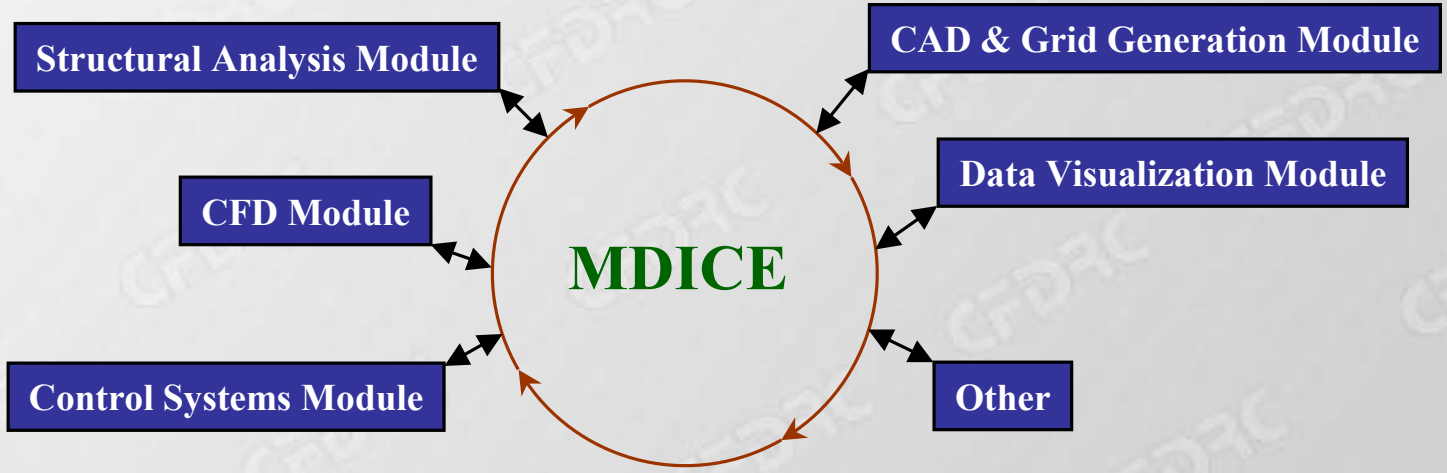

Salient Features of MDICE

- Workflow Management of a Multi-Disciplinary Simulation
- Dynamic Process Interactions by Virtue of Common Object Transfers Between Application Modules
- Temporal Synchronization of Application Modules for Time-Accurate Simulations
- Automatic Unit Conversions (Metric-SI) and Precision Conversion (Double-Single)
- Multi-Dimensional Coupling (1D, 2D, or 3D) Between Applications
- Special-Purpose Engineering Modules that are Integrated into the Environment

Creating an MDICE Compliant Application

- A Stub Provides Mechanisms to Enable the Application to Work in a Distributed Setting; Stub is Created Using a Declarative Language
- Middleware Components are Linked into the Application at Compile Time using the MDICE Library.
- Legacy Applications Integrated into MDICE Using Wrapper-based Approach

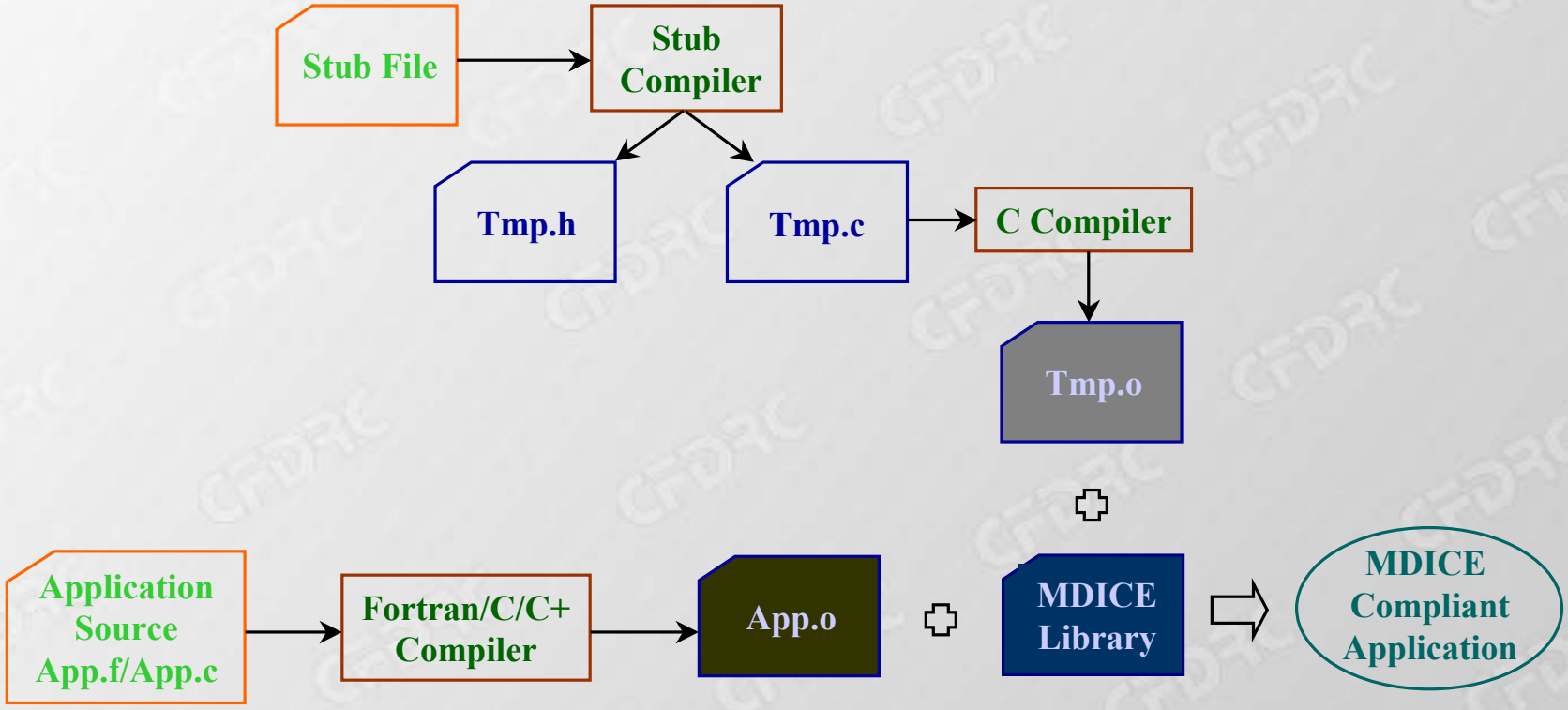

Components in MDICE Framework

- MDICE Controller Performs the Role of the Central Nervous System of the Environment
  - Controls the Workflow of the Simulation & Module Interactions
  - Delegates Tasks to the Modules via Remote Method Invocations

- Modules Interact with Each Other by Exchanging MDICE Objects

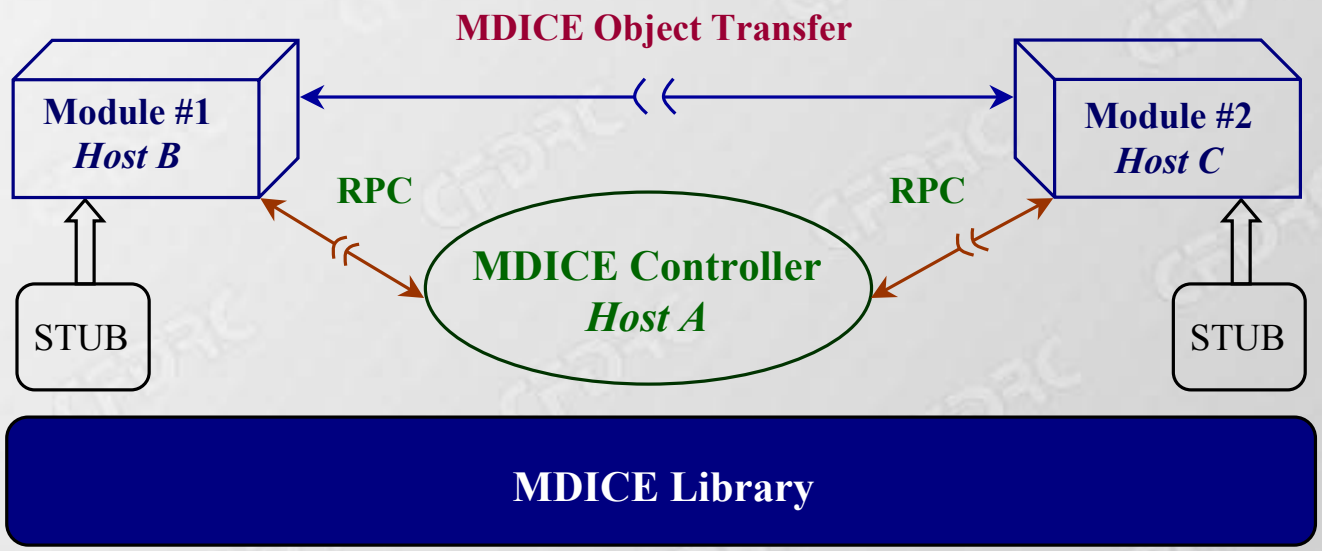

Layered Approach to Middleware

- Implement the Middleware as a Layered Architecture

Engineering Applications

Upper Level	**Services, Object Implementations for Engineering Disciplines, Data Unit Conversions, Data Type Conversion**
Mid Level	**Mechanisms to Enable Applications Interoperate without Dependencies on Location, OS Platform, Programming Language, Network Communication Protocols; Object Serialization/Deserialization, RPC**
Base Level	**Network Connection Management, IPC, TCP/IP Event De-multiplexing, Signal Handling, Other OS Mechanisms**

Composite Pattern to Implement MDICE Objects

- MDICE Objects Contain One or More Scalars, Arrays or Sub-Objects
- MDICE Object Allow Hierarchical Tree-Like Structure
- MDICE Library is Comprised of a Suite of Objects Suited for Engineering Applications.

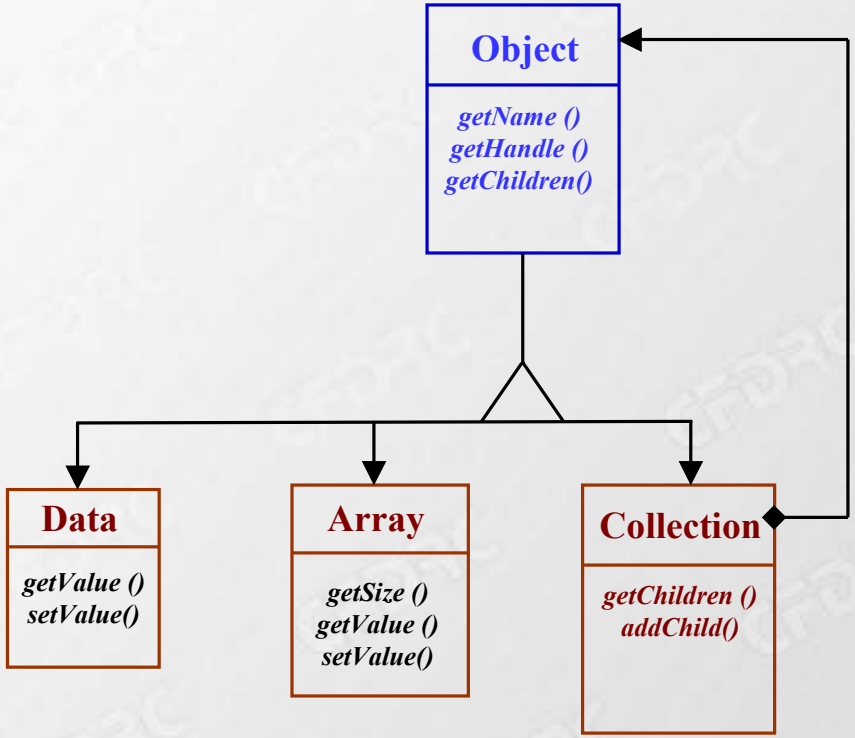

OMT Representation of MDICE Object

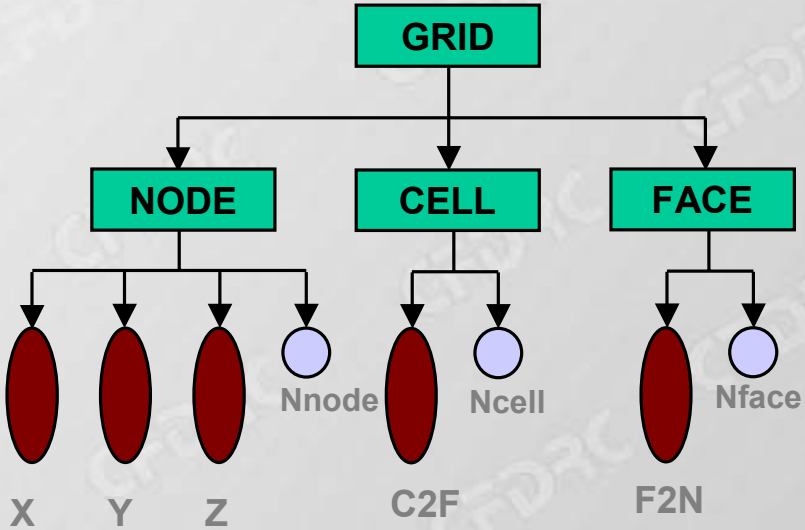

CFD Grid Representation

What is the Framework Good For ?

- The Goal is to Leverage Distributed Systems Design, Computer Networking Technology and Modern Software Architectures to Better Enable Multi-Disciplinary Engineering Simulations

- MDICE Applications have been Deployed in the Following Engineering Areas:
  - Parallelization of Large Scale CFD Applications
  - Aero-elastic Analysis
  - Semi-Conductor Manufacturing Process Modeling
  - Bio-Medical Device Modeling
  - Nuclear Industry Applications
  - Design Optimization
  - Aero-thermal-elastic Analysis

Available Platforms & Disciplines

- MDICE has been Ported to the Following Platforms:
  - Linux, IRIX, HP-UX, AIX, OSF, Solaris and Win32

- The Following Disciplines have been Integrated into MDICE and have been Successfully Employed for Multi-Disciplinary Simulations:
  - CAD – Unigraphics, Pro-Engineer
  - Grid Generation – CFD-GEOM
  - CFD Flow Solvers – CFD-FASTRAN, CFD-ACE, SPLITFLOW, ENS3DAE, ADPAC, COBALT, CORSAIR, GCNSfv
  - Structural Solvers – SI (Wrapper Interface for NASTRAN, ANSYS), ENS3DAE, EMS, CFD-ACE (Stress Module)
  - Post-Processing – CFD-VIEW, XMGR

MDICE Applications

- A Quick Overview of MDICE-Enabled Applications in Several Engineering Disciplines

- All Examples Represent Cases where Requisite Modeling Capabilities were not Available all in the Same Simulation Software
  - Necessitated Integrating & Coupling Several Software Components Together with MDICE

Aero-elastic Modeling of F18 Buffet

- Numerical Simulation of Buffet Phenomenon in a Twin-Tail F18 Configuration; Coupled Fluid-Structure Interaction (FSI) Simulation
- Mach Number= 0.243, Reynolds Number= 11 x $(10)^6$

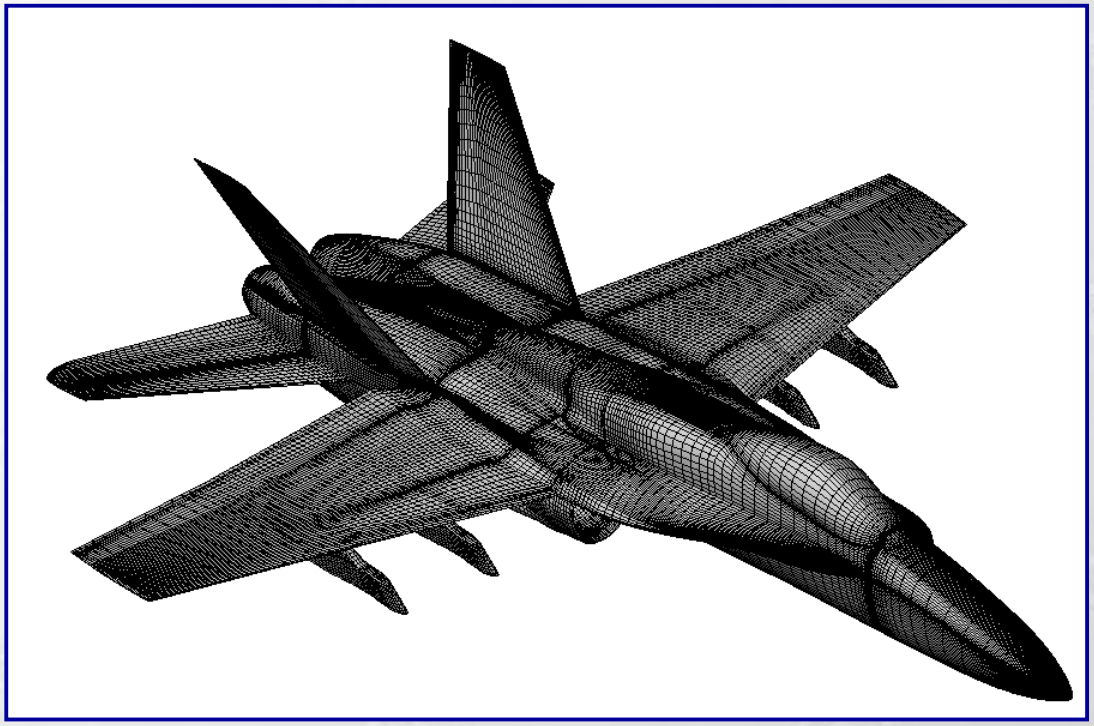

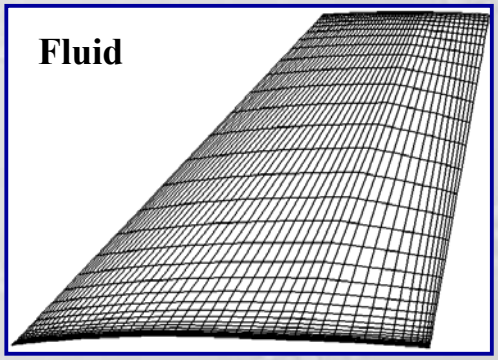

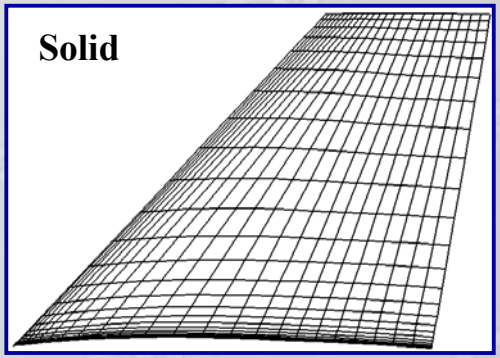

F18 Buffet Simulation

- Instantaneous Streamlines for Flow at an Angle of Attack of 40°

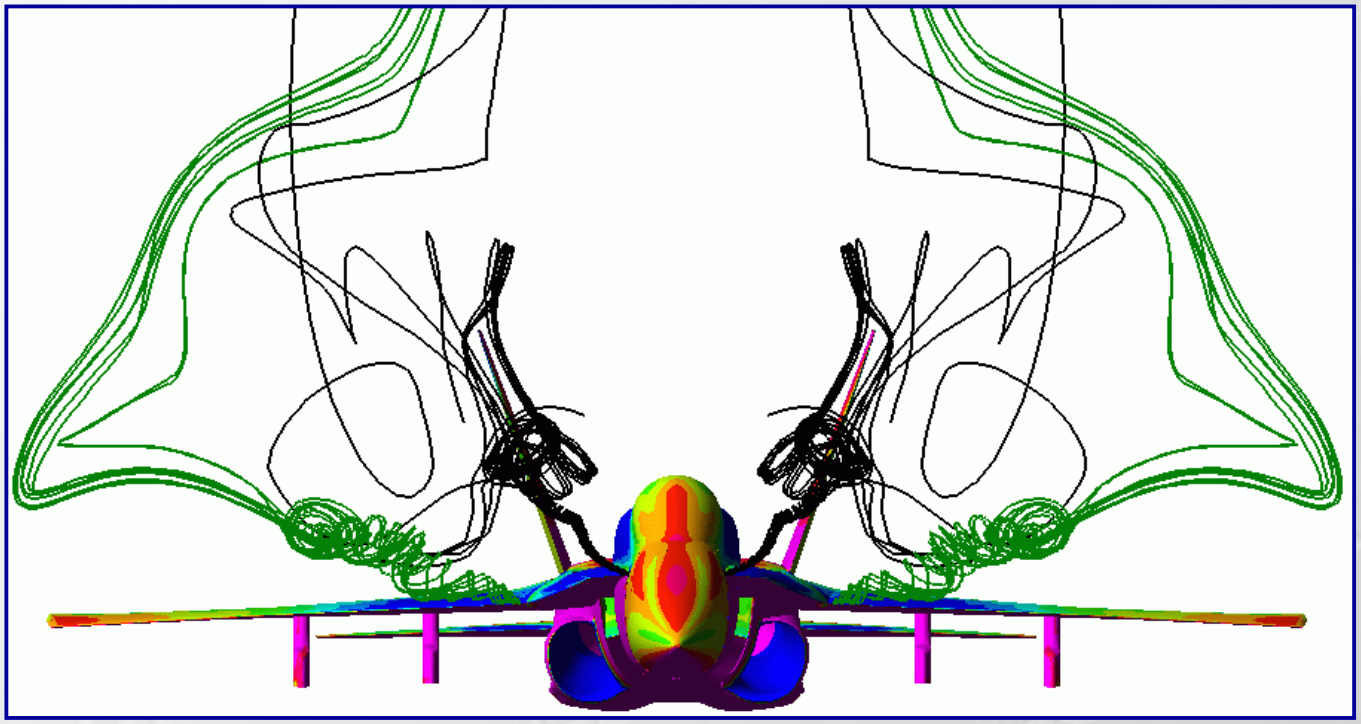

Module Interactions in MDICE

- Coupled FSI (Fluid-Structure Interaction) Performed in MDICE with Interactions Between 4 Instances of Flow Solver and 2 Instances of Structural Solve
- Proposal to Include Control Systems Module in the Framework to Enable Flow Control Using Piezoelectric Actuators

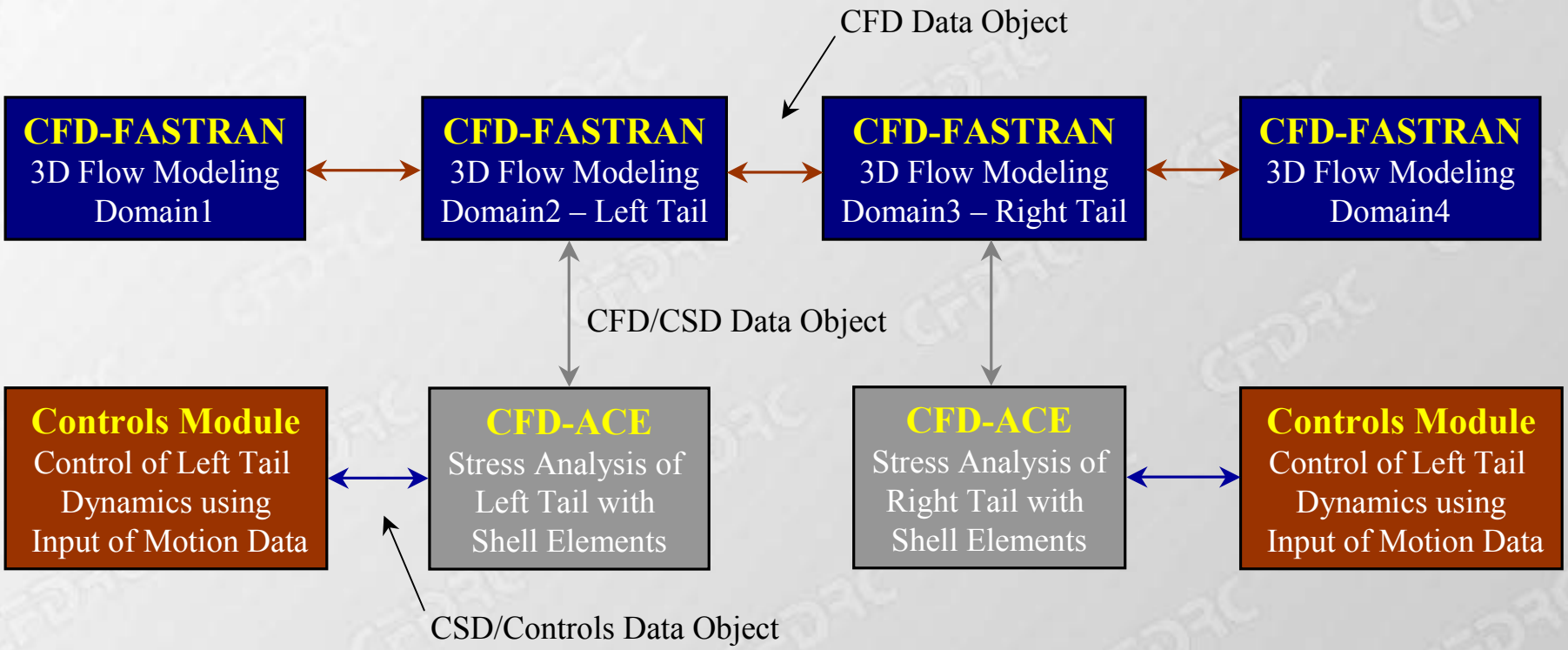

Virtual Reactor

- What is a Virtual Reactor
  - Customized Interactive Simulation Tool for Modeling Semi-conductor Manufacturing Process in a CVD Reactor
  - Integrated Physical Modeling of Flow, Heat Transfer, Chemistry, Visualization

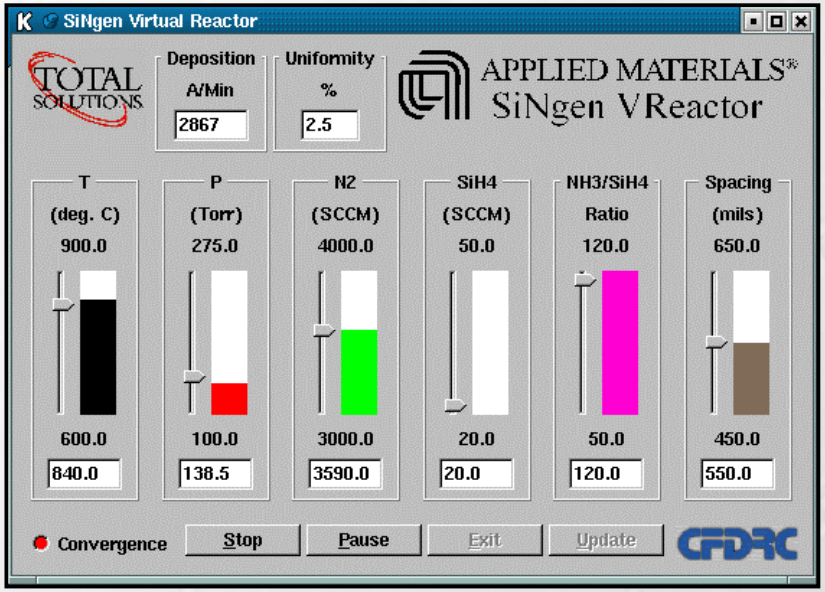

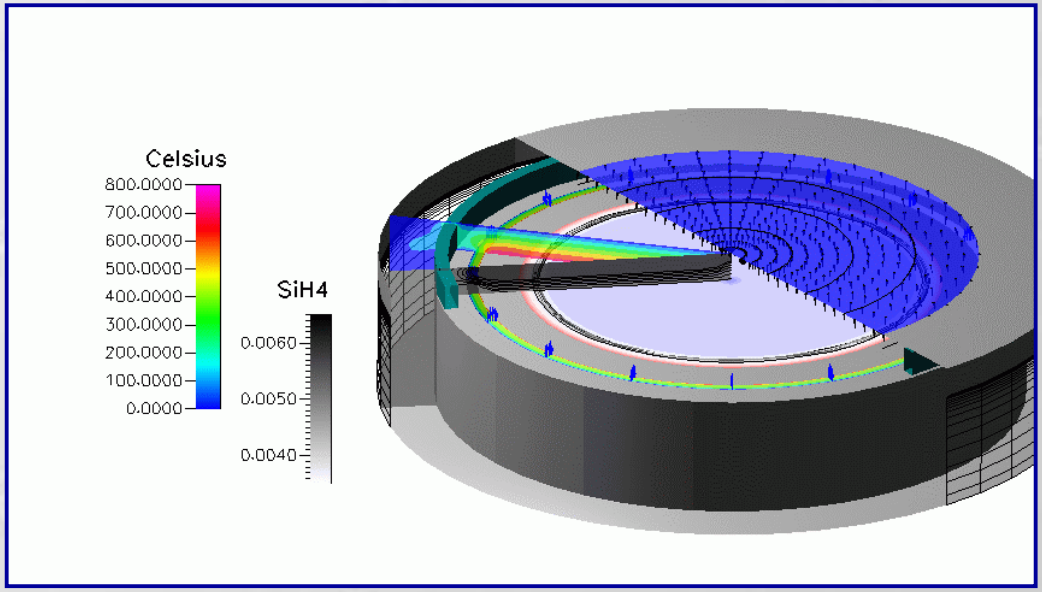

Virtual Reactor Architecture

- Application Module Interactions in Virtual Reactor
- User Drives the Entire Simulation from the Client GUI

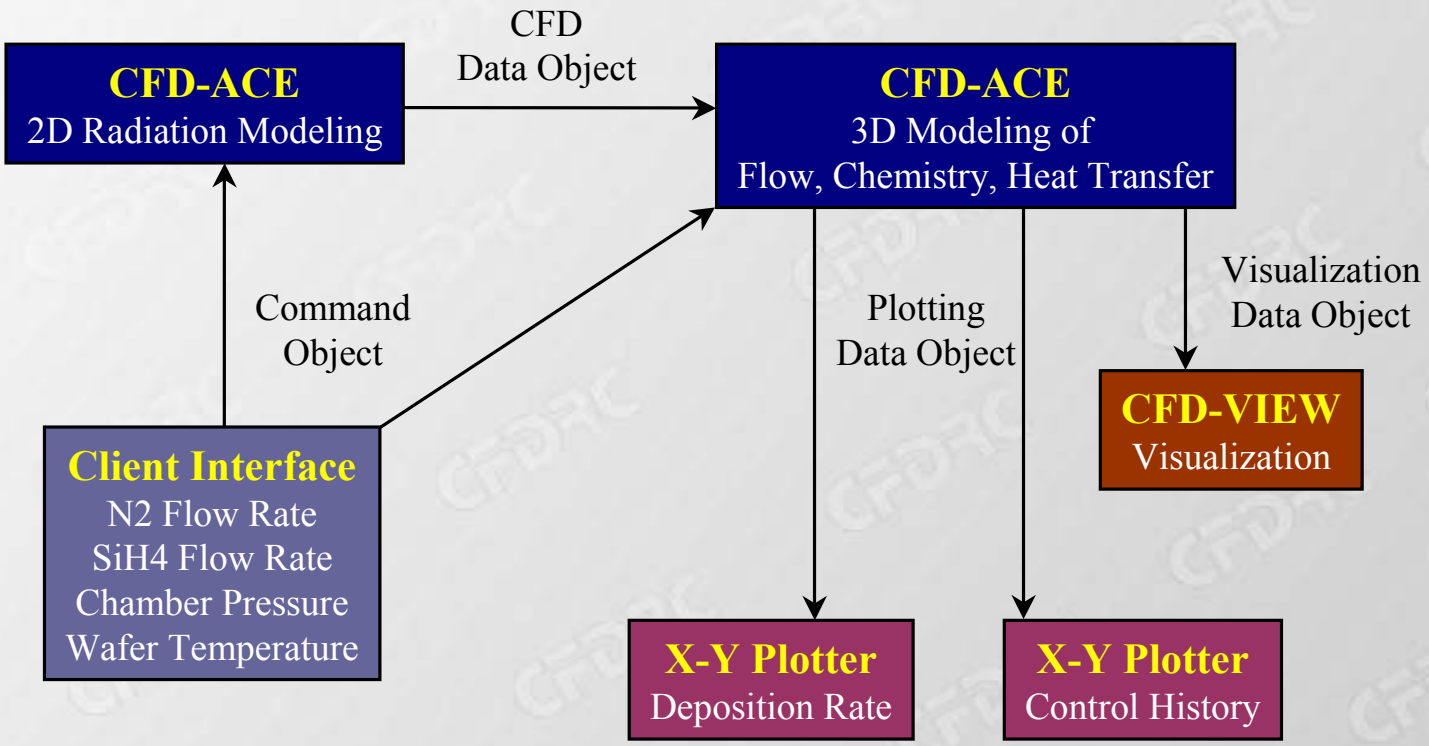

Simulation Tools for Direct Write of MICE

- MICE - Mesoscopic Integrated Conformal Electronics
- 3D Pulsed Model for Analyzing Thermal Profiles of Composite Layers as a Function of Translation Rate, Pulsing Profile, Intensity & Spot Size of Laser

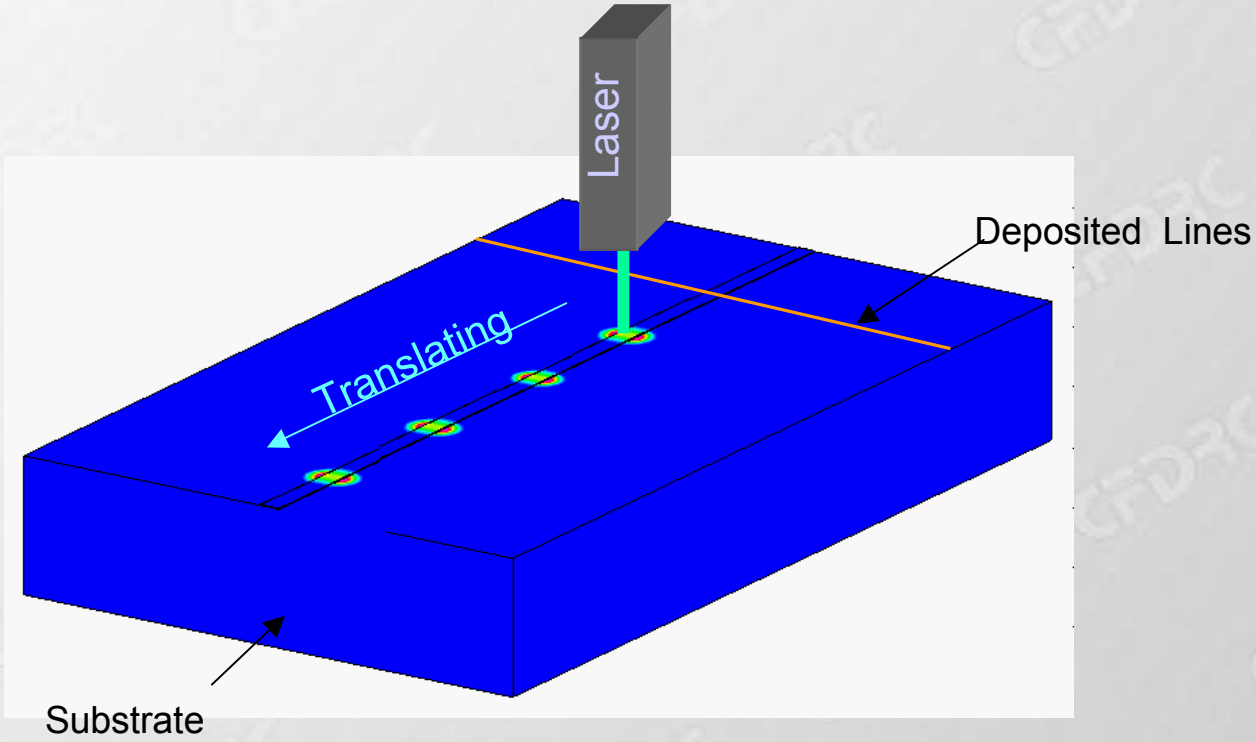

MDICE for MICE

- Integrated, Interactive Simulation Tool for MICE - Physical Modeling of Radiation, Chemistry/Sintering, Grid Adaptation & Visualization

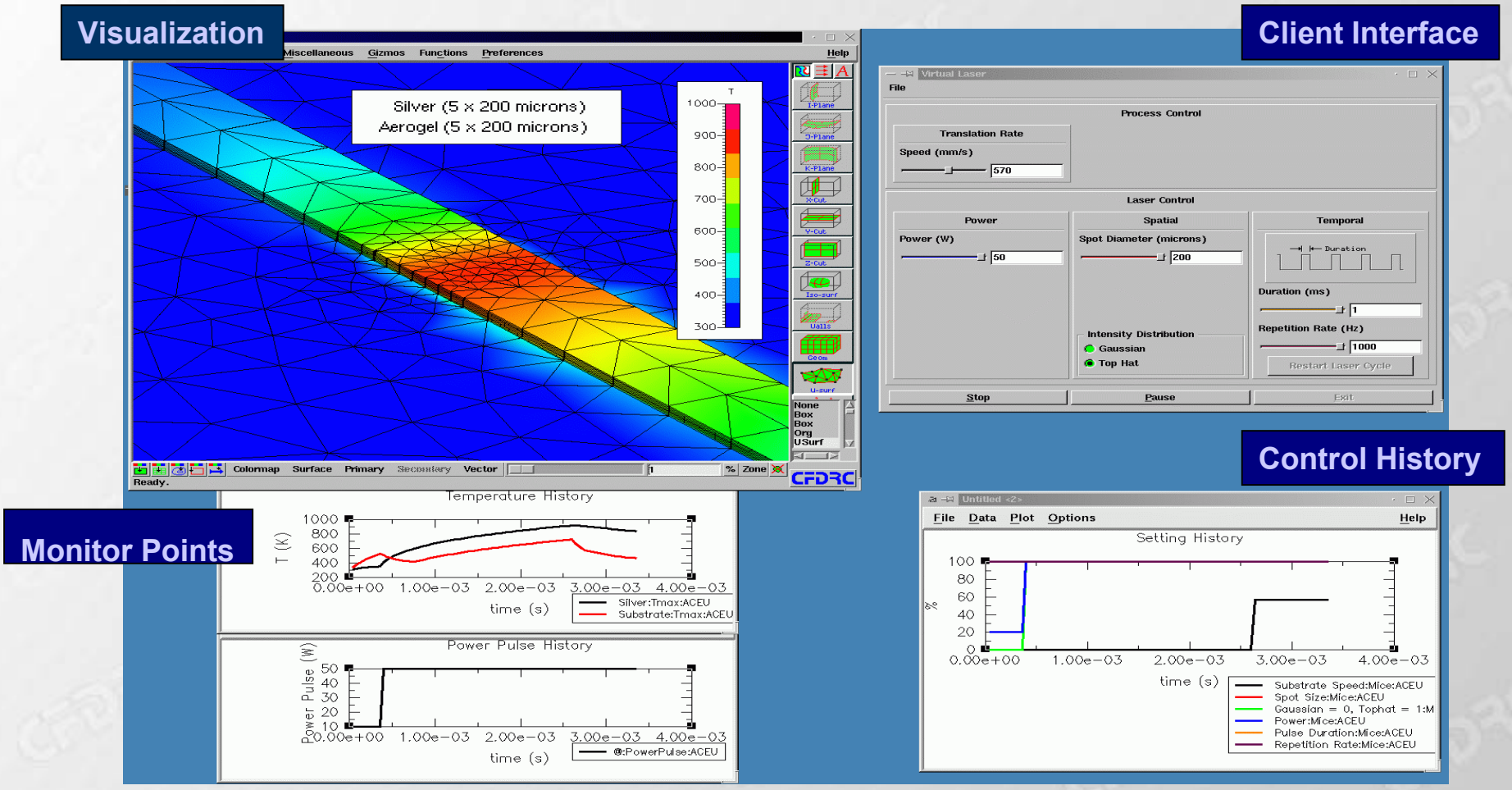

Bio-Medical Application

- Modeling Pulasatile Flow of Blood Through Mechanical Heart Valves due to Movement of the Ventricle
- Studying the Stresses in the Valves at Different Phases

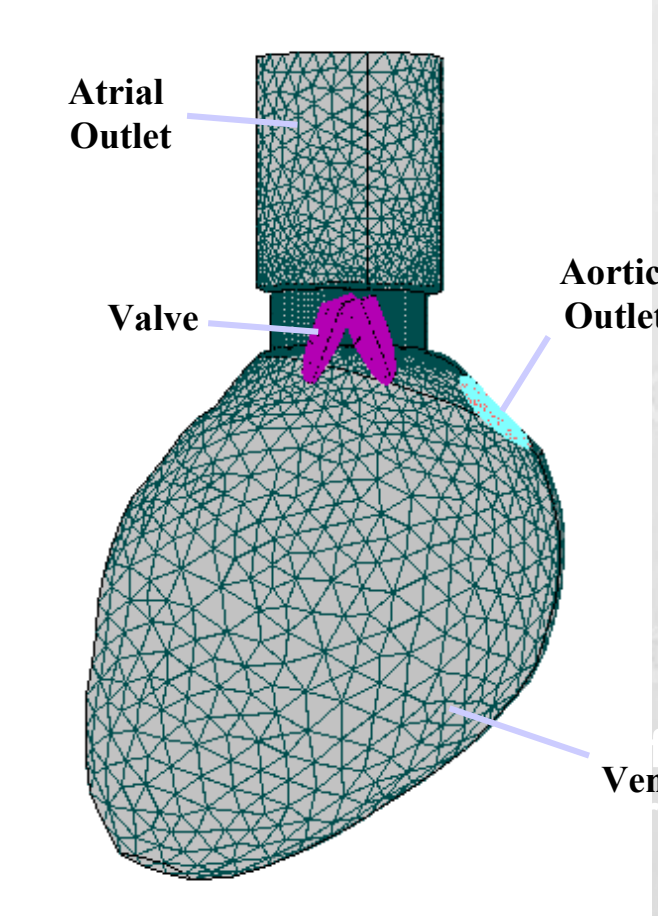

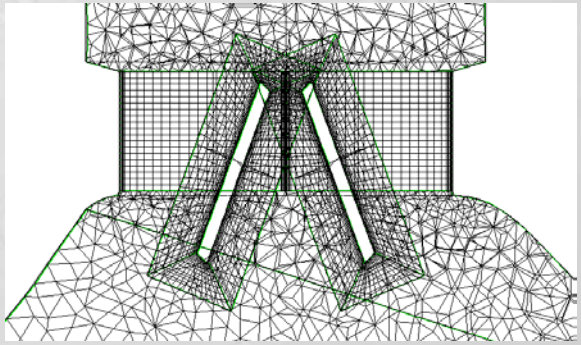

Heart-Valve Simulation

- Snap-Shots of a Transient Simulation at Fully-Open and Fully-Closed Position of the Valves

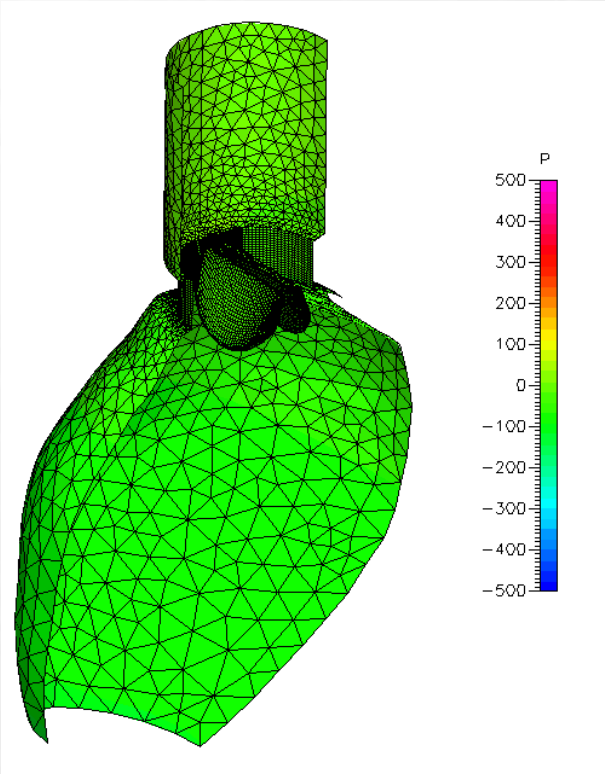

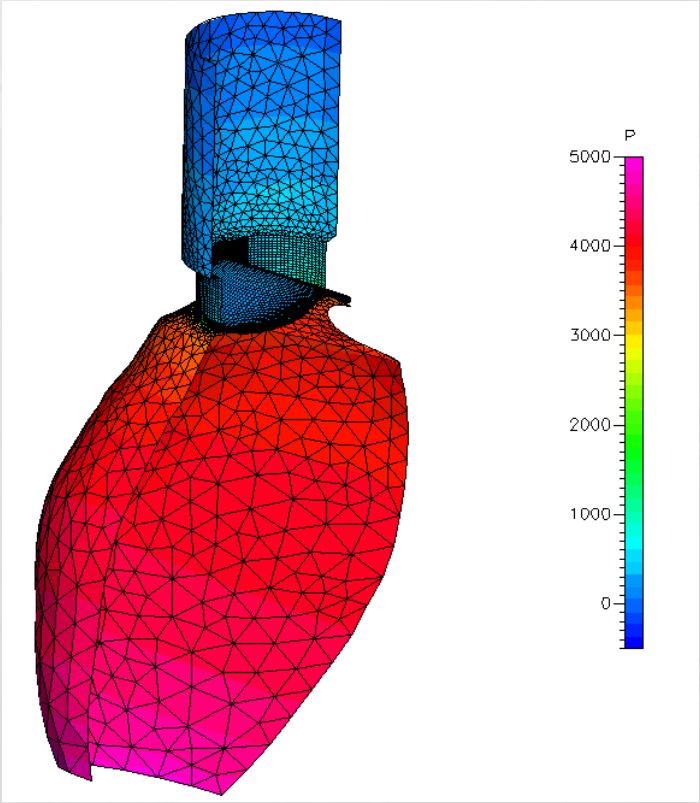

Heart-Valve Simulation

- MDICE Module Interactions in Heart Valve Simulation

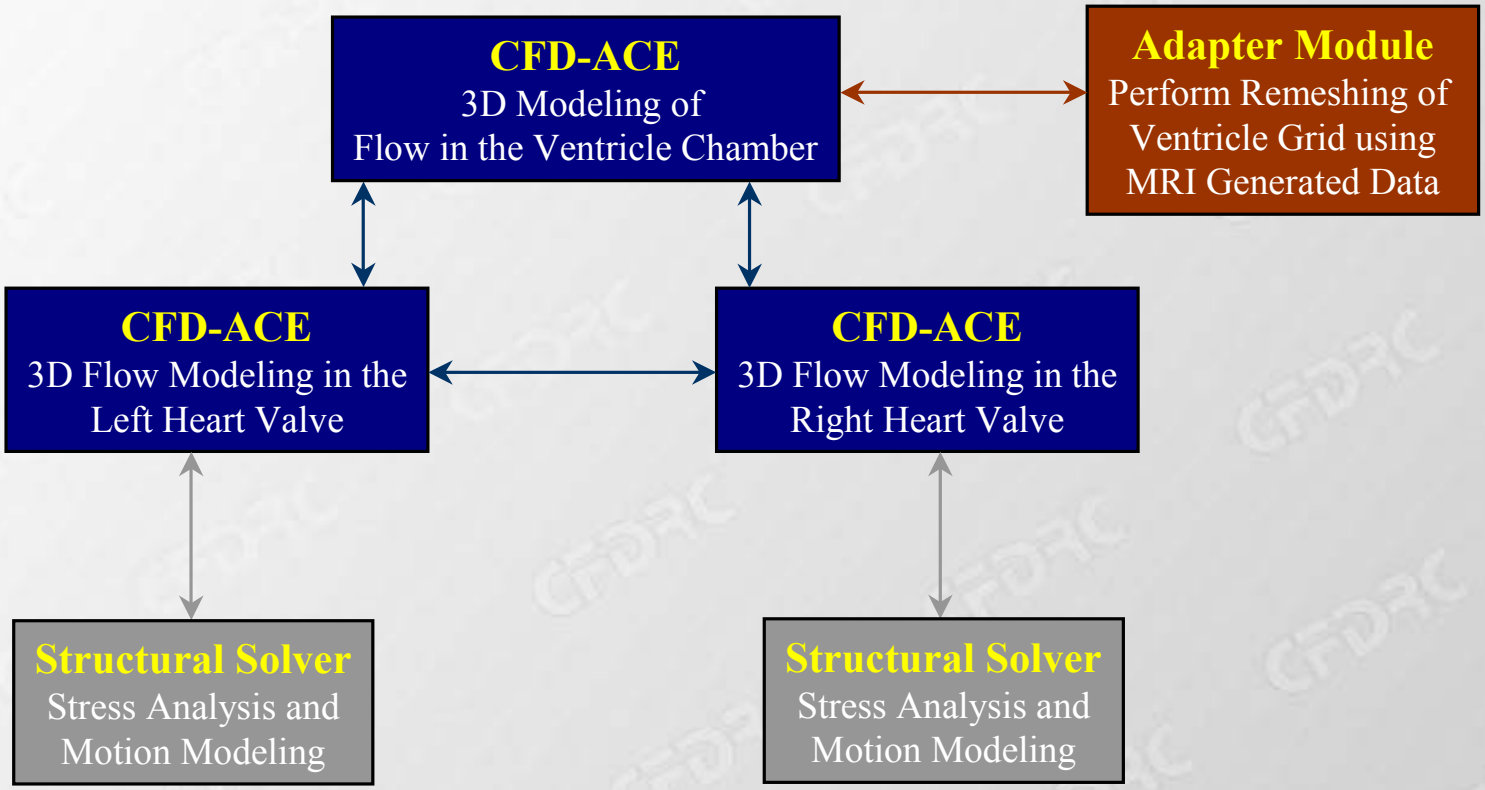

Nuclear Industry Application

- Vacuum Relief Valve Used for Nuclear Power Plant Storage Tanks
- During Emergency Cooling, Valve Opens to Allow Air into the Tank
- Simulation Results Lead to Improved Disk and Body Shape of the Valve

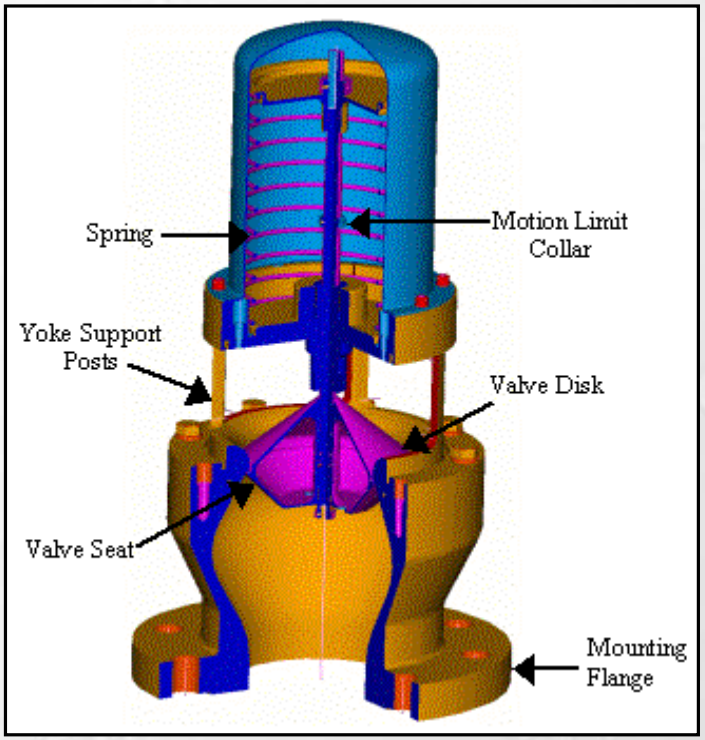

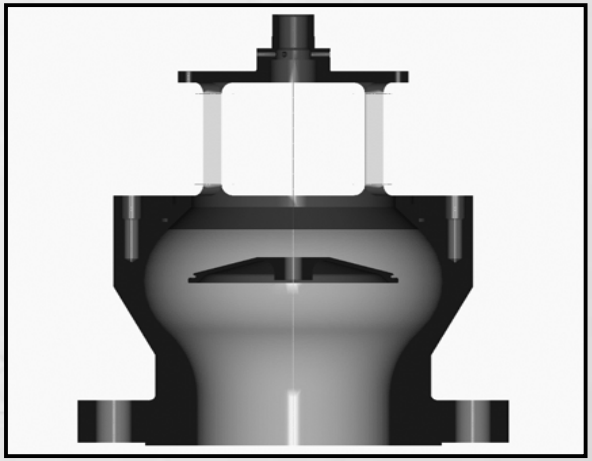

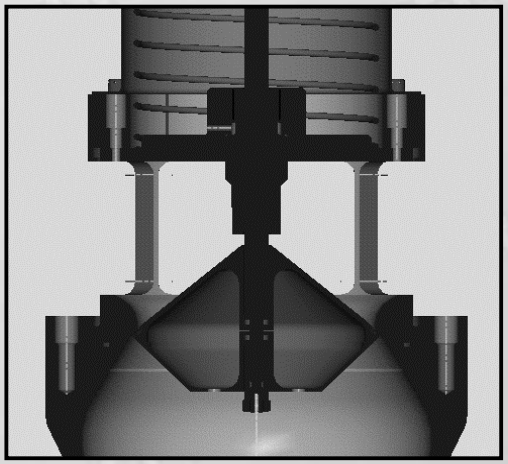

Vacuum Relief Valve Simulation

- Module Interactions in Coupled Fluid-Structure Interaction (FSI) Simulation

CFD-ACE
3D Modeling of Flow in Storage Tank

↔

CFD-ACE
3D Modeling of Flow Around Moving Valve

↕

Motion Analysis Module
Model the Dynamics & Kinematics of Valve Motion

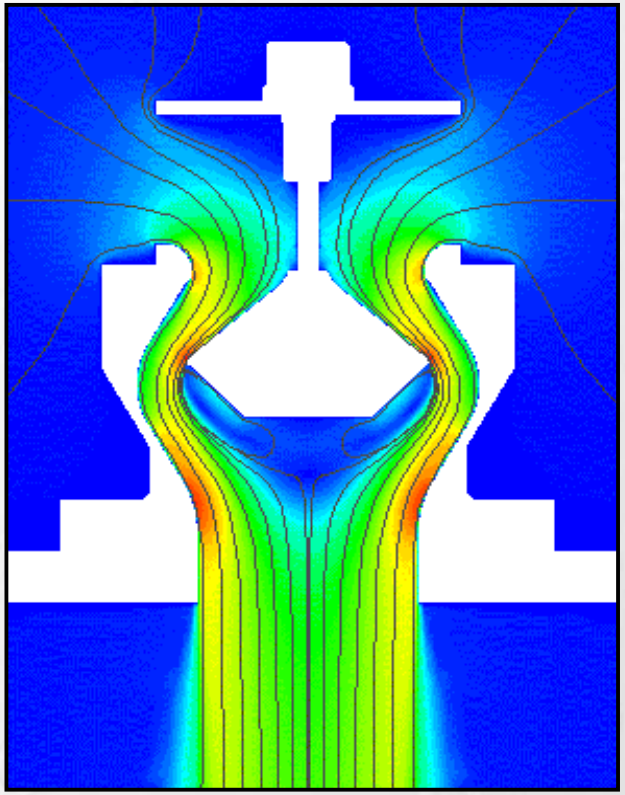

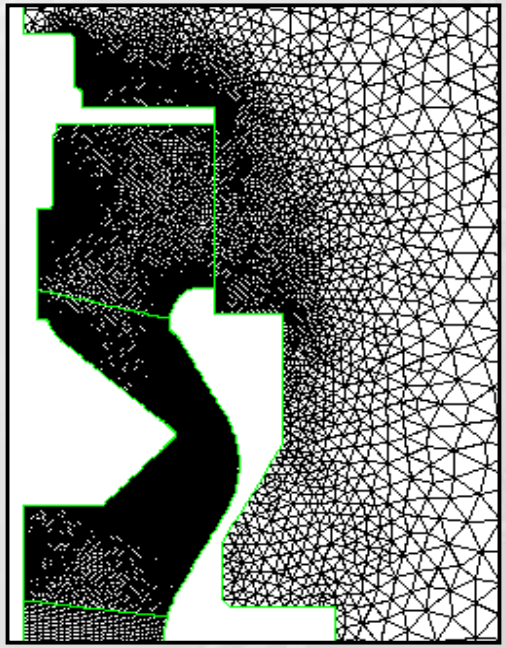

Concluding Comments

- MDICE Provides Middleware Technology for Integrating Applications at the Source Level; Legacy Applications Integrated Using Wrapper Approach

- MDICE Provides an Environment that Enables Workflow Management of a Simulation
  - Parallelization
  - Optimization
  - Multi-Disciplinary Analysis

- Coupling Between Applications Controlled Using Dynamic Data Exchange
  - User may Control the Level of Coupling (Fine *vs*. Coarse, One-way *vs*. Two-way)

- Turnkey Solutions Available in Conjunction with CFDRC's Software for Specific Engineering Disciplines

NPSS Overview to TAFW Multidisciplinary Simulation Capabilities

September 12, 2001

Presented by
Karl Owen
for the
NPSS Development Team

Computing and Interdisciplinary Systems Office
Glenn Research Center

Presentation Outline

- Definition of NPSS
- Current Status of NPSS
  - NPSSv1 Capabilities
  - Engineering Demonstrations
  - Planned Capabilities

Presentation Outline

- ***Definition of NPSS***
- Current Status of NPSS
  - NPSSv1 Capabilities
  - Engineering Demonstrations
  - Planned Capabilities

Definition of NPSS - the Numerical Propulsion System Simulation

NPSS is a concerted effort by NASA Glenn Research Center, the aerospace industry, and academia to develop an advanced engineering environment – or integrated collection of software programs - for the analysis and design of aircraft engines and, eventually, space transportation components.

NOTE: NPSS is now being applied by GE ground power to ground power generation with the view of expanding the capability to non-traditional power plant applications (example: fuel cells) and NPSS has an interest in in-space power and will be developing those simulation capabilities

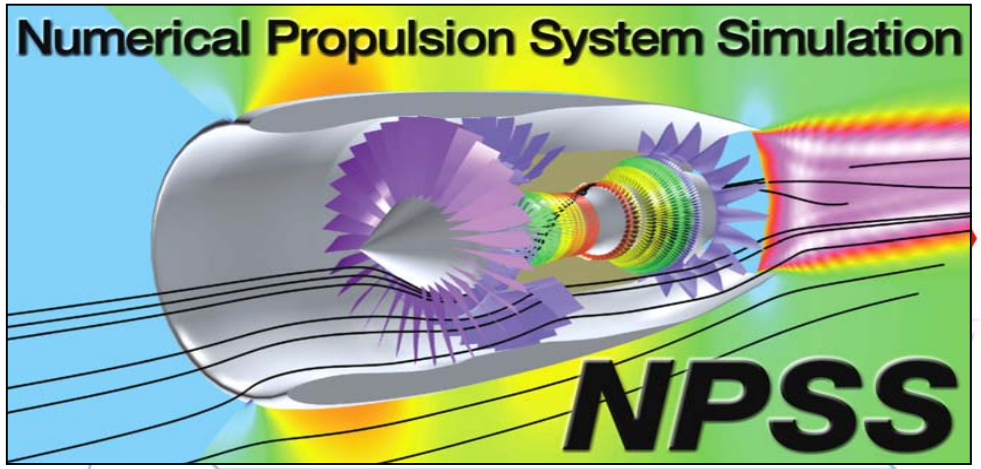

Validated Models

- Fluids
- Heat transfer
- Combustion
- Structures
- Materials
- Controls
- Manufacturing
- Economics

Integrated Interdisciplinary Analysis and Design of Propulsion Systems

High-Performance Computing

- Parallel processing
- Object-oriented architecture
- Expert systems
- Interactive 3-D graphics
- High-speed networks
- Database management systems

Rapid Affordable Computation of

- Performance
- Stability
- Cost
- Life
- Certification requirements

A Numerical Test Cell for Aerospace Propulsion Systems

Computing and Interdisciplinary Systems Office
Glenn Research Center

HPCCP/NPSS
Work Breakdown Structure

Simulation Environment

- Gov't/industry collaborative effort
- Object-oriented programming
- CAD geometry interface

Seamless integration of people, data, analysis tools, and computing resources

Engineering Applications

- Code Parallelization
- 3–D Subsystems/System

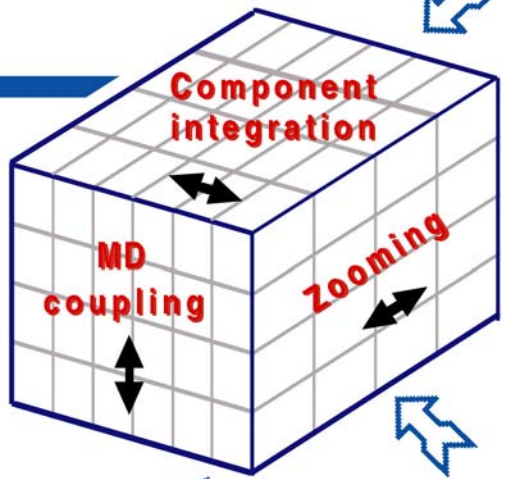

- Coupled aero-thermal-structural analysis
- Hierarchical methods

- 0-D engine/1-D compressor
- 0-D core/3-D LP subsystem

Computing Testbeds

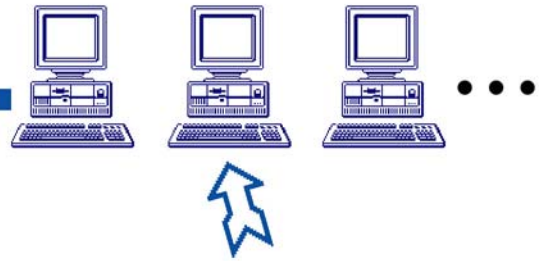

- High-speed networks
- PC cluster
- Distributed computing

Low-cost, distributed parallel computing

High-fidelity, large-scale simulations

NPSS Production and Simulation Architecture

NPSS Production 0-D Model

NPSS Dev. Kit supplies tools for integrating codes, accessing geometry, zooming, coupling, security.

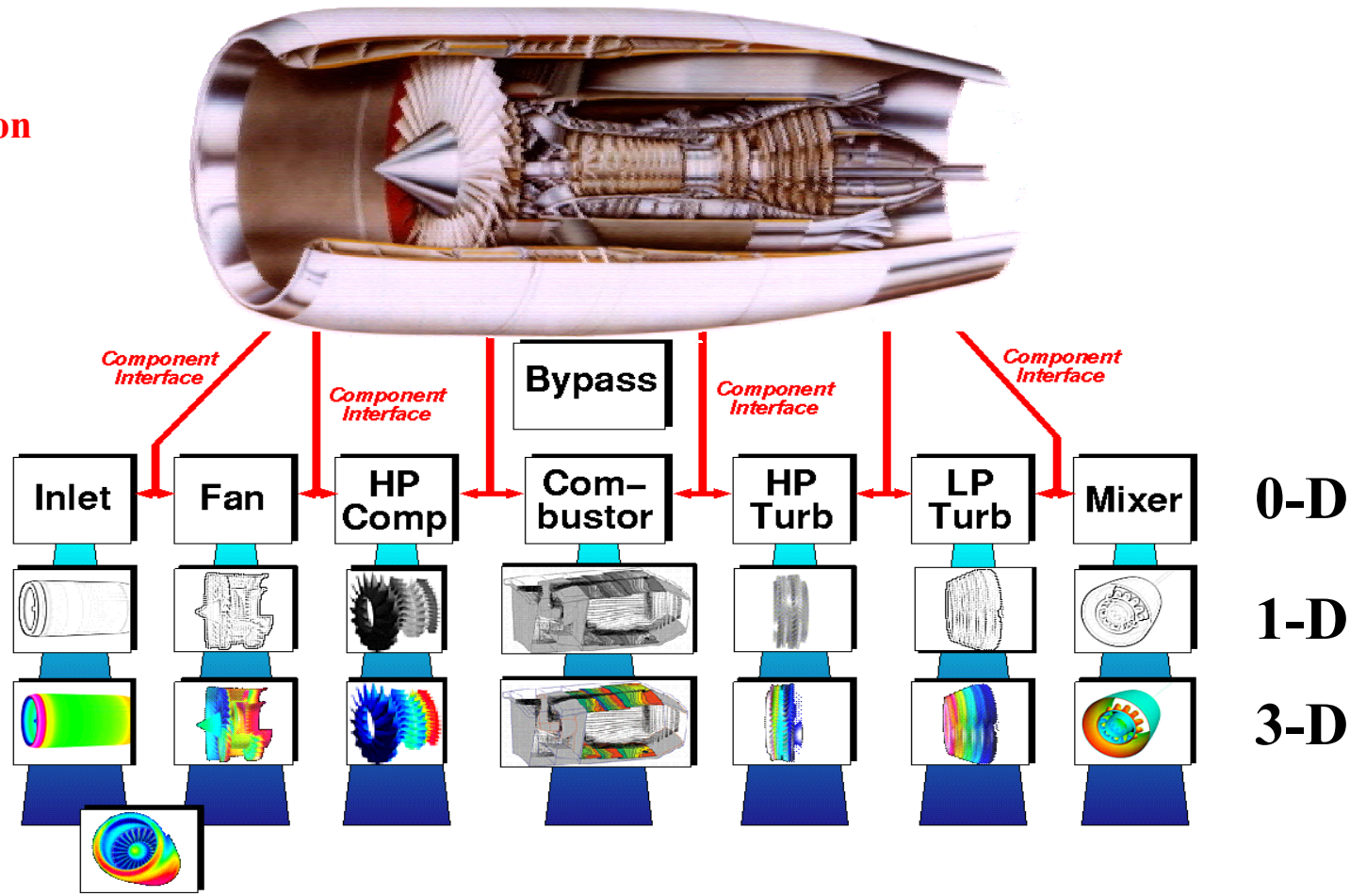

NPSS Object-Oriented Architecture

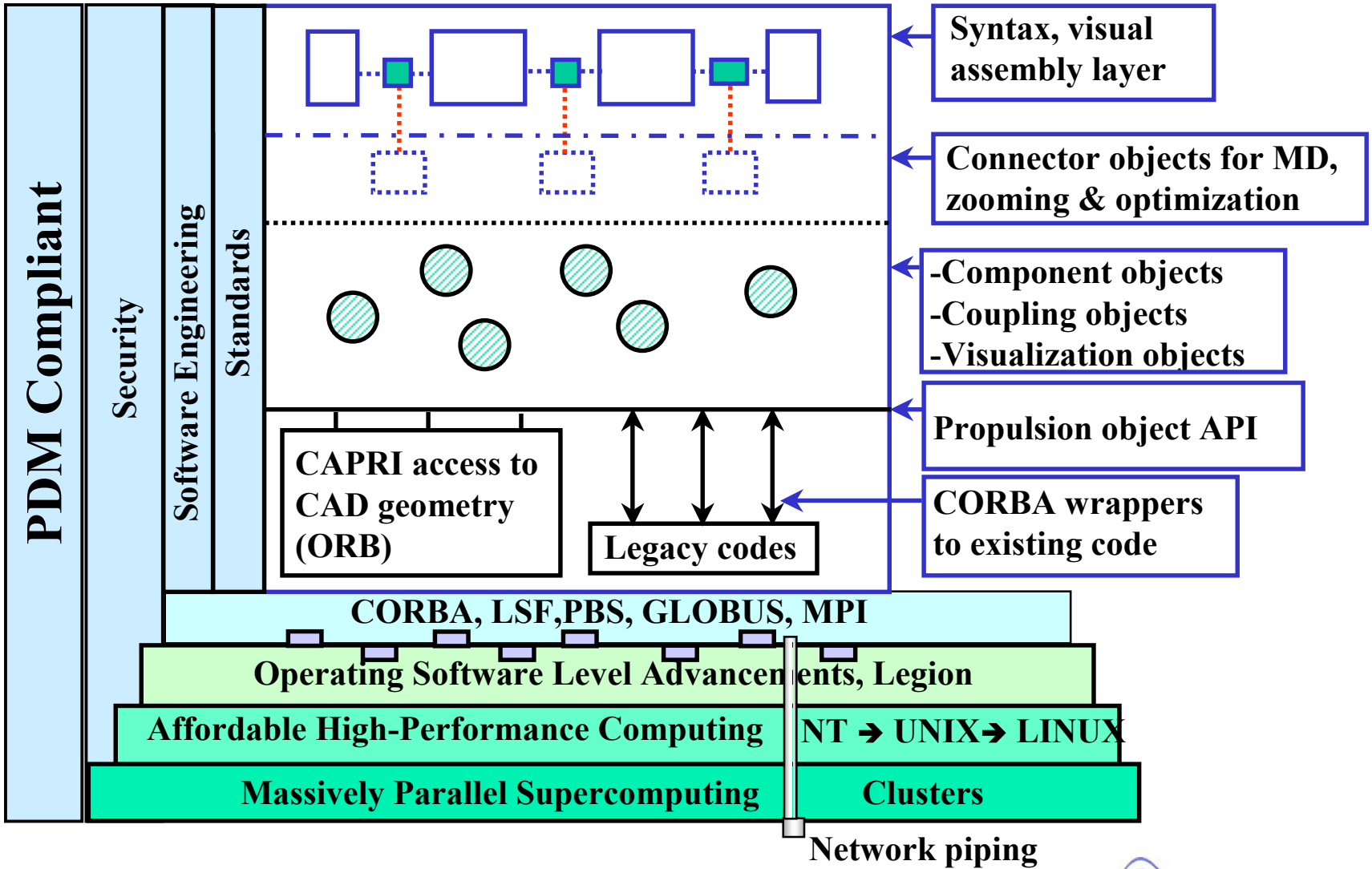

Presentation Outline

- Definition of NPSS
- ***Current Status of NPSS***
  - ***NPSSv1 Capabilities***
  - Engineering Demonstrations
  - Planned Capabilities

NPSS Version 1.0.0 Capabilities

NPSS Version 1.0.0 can be used as an aerothermodynamic 0-dimensional cycle simulation tool:

- All model definition through input file(s)
- NIST (National Institute of Standards and Technology)-compliant thermodynamic gas-properties packages: Therm, Janaf, GasTbl
- Sophisticated solver with auto-setup, constraints, discontinuity handling
- Steady-state and transient engine system operation
- Flexible report generation
- Built-in object-oriented programming language for user-definable components and functions
- Support for distributed running of external code(s) via the common object request broker architecture (CORBA)
- Test data reduction and analysis
- Interactive debug capability
- Customer deck generation

Selected FY00 Highlights

- **Delivered NPSS V 1.0 in March (transient, dynamic linkable libraries, fully interpreted elements, data reduction, distributed objects). V2 requirements completed.**
- **Demonstrated a 547:1 reduction in combustion simulation time and a 400:1+ reduction in turbomachinery simulation time relative to a 1992 baseline.**
- **Initial coupling methodology for 3-D high-pressure core engine simulation completed.**
- **Completed the GE 90 fan/booster subsystem and combustor in preparation for the 3-D primary flowpath engine simulation.**
- **Demonstrated a 9.5:1 improvement in the performance/cost ratio for PC clusters relative to 1999 technology.**
- **NASA/industry team formed and implemented to define requirements and FY01 task for NPSS for space transportation.**
- **NPSS V1 proposed for use in GP 7000 and JSF engine development programs.**

NPSS Development Kit

FY00 Accomplishments

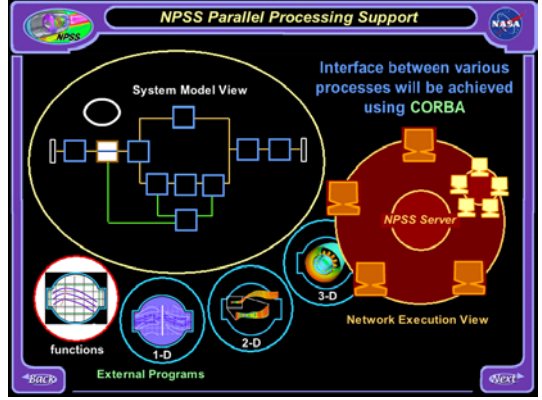

Integrating Codes Through CORBA Wrapping

- **Direct FORTRAN support**

  Allows converting FORTRAN code to a CORBA object without reverting to file I/O & attendant startup/shutdown overheads.

- **Single-precision floating-point variables**
- **'Meta' variables**

  i.e., Shaft, Nmech mapped to multiple boundary conditions.

- **Variable access via functions**

  For parallel codes where the CORBA process doesn't own storage of referenced data.

- **Circumferential averaging**
- **1-D array support**

NPSS Development Kit

FY00 Accomplishments

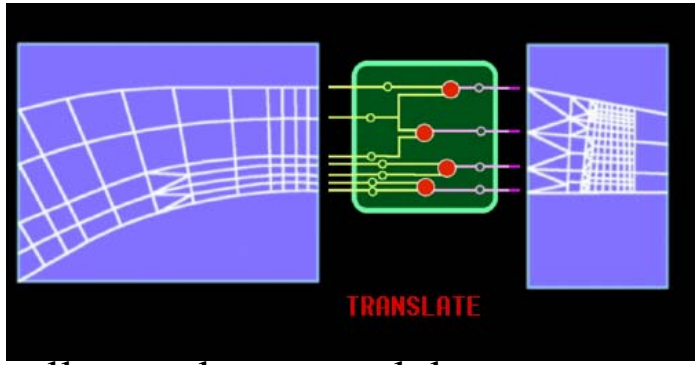

Coupling

- 2-D/3-D/Axi-symmetric mismatched grids, with cell or node centered data
- Interpolation method is internally unstructured, currently the only API uses structured grids
- Rolls-Royce ADPAC-NPSS-ANSYS sensitivity project
  - Will likely require unstructured support. Current interpolator has this, but API and messaging formats need to be defined
  - Likely wrap ANSYS via Java using file I/O
  - ANSYS optimizer loop to be emulated by Java client application
- Examining "best practices in coupling" for recovery into Dev. Kit
  - ASCI project coupling
  - Overflow-Vulcan-ANSYS
  - Haha3d-ANSYS
  - APNASA-TFLOW

NPSS Development Kit

FY00 Accomplishments

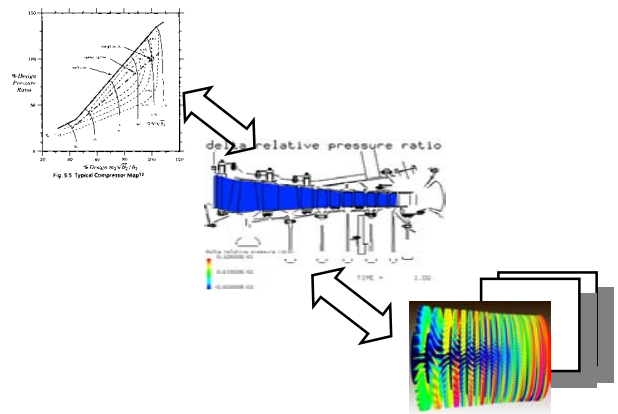

Zooming

- ’Natural' C++ access to remote variables
- PW 1-D zooming to compressor code
  - GRC 1-D compressor code wrapped with NPSS Dev. Kit
  - NPSS model built
  - What remains is to connect everything up
- PW 3-D/3-D zooming/coupling
  - Demonstration was expected for Annual Planning & Review Meeting
  - ADPAC wrapped in NPSS Dev. Kit
  - PW, NASA code review/examination conducted to appropriate codes to wrap
- 1-D Turbine code wrapped using NPSS Dev. Kit

NPSS Development Kit

FY00 Accomplishments

CORBA Security

- CORBA Security Workshop summary
  - Defined NPSS security policy
- CORBA Security Quick Start Hands-On Training Summary
  - Hitachi TPBroker SS architecture & administration GUI charts
- Defined NPSS CORBA Security testbed
  - Plans and testbed architecture
  - Purchases and network
  - Relative standards
  - Integration approach
- CORBA Security integration into NPSS schedule-3/01

NPSS Development Kit

FY00 Accomplishments

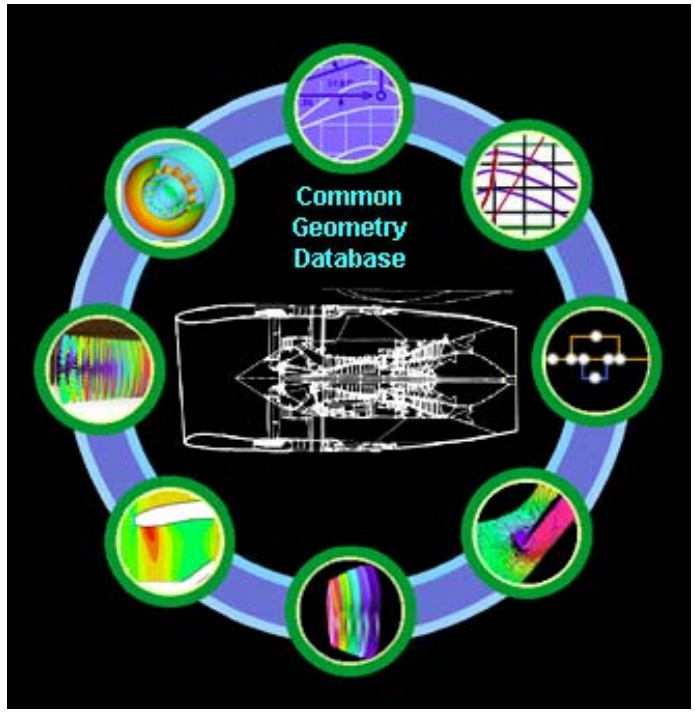

CAD Access & Interoperability Through Common Interface

- MIT grant for CAPRI: added CV port, enhanced IDEAS port
- OMG process
  - Requirements gathering (RFI), **complete**
  - Formal RFP (CAD Services V1.0, **6/00**)
  - Vendors and end users letter of intent (LOI, **9/18/00**)
  - Vendors seek common "ground" for response
  - Develop joint submission, **1/15/01**
  - Submission reviewed and approved as standard
  - Vendor provides commercial support for the standard

NPSS, OMG Shared Vision

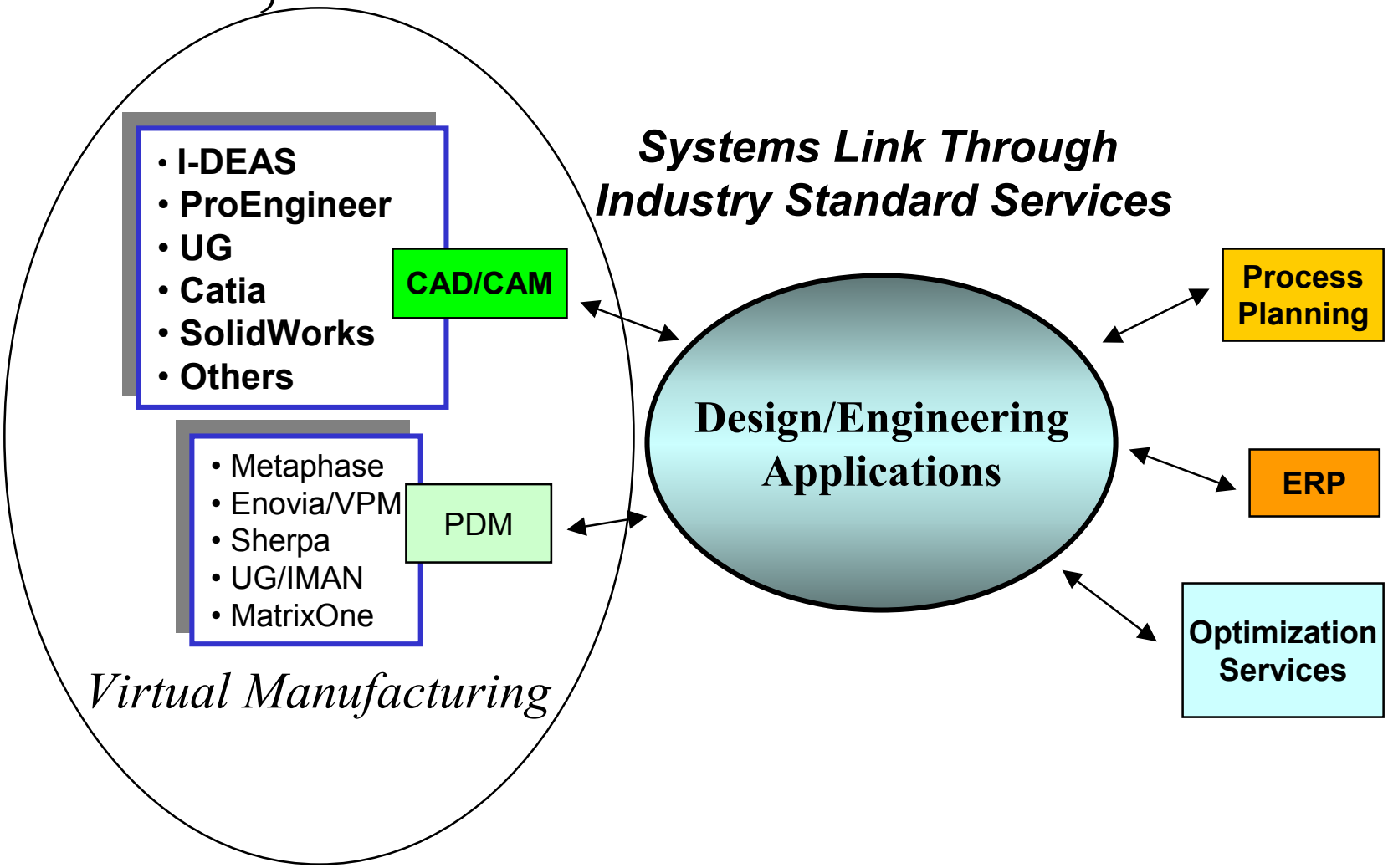

CAPRI FY00:

	UniGraphics	ProE	I-DEAS	CATIA V4	CV	Native - Felisa
Alpha	**X**					**X**
HP	**X**					**X**
IBM RS6K	**X**			**X**		**X**
SGI	**X**	**X**	**X**	**X**	**X**	**X**
SUN	**X**					**X**
LINUX	**X**					**X**
Windows NT/2000	**X**	**X**			**X**	**X**

CATIA V5 will be examined during this contract, but the best approach for the programming interface is not clear. An AutoCAD geometry reader will not yet be implemented.

A CV (CompterVision's CADDS V) interface has been written in support of NPSS work with Allison/Rolls Royce and ICEM-CFD.

CAPRI FY01: Geometry Creation

The most significant change for **CAPRI** this year is the addition of Boolean operations on solids. This allows for the specification of fluid passages where the blade is the solid. The blade is simply subtracted from the passage to get the geometry for the CFD calculation. In general very complex shapes can be obtained through a few operations. The current status is as follows:

	Parasolid	ProE	I-DEAS	CATIA V4	CV
Simple Solid Creation	X			X	X
Subtraction	X		X	X	X
Intersection	X			X	X
Union	X			X	X

FY01 Major Milestones

- Release NPSS V2 (real time ORB, CORBA security, limited zooming, dynamic load balancing, initial visual assembly language) (4Q).
- **Demonstrate full 3-D compressor analysis in 3 hours and full 3-D combustor analysis in 2.5 hours (>1000:1 reduction relative to a 1992 baseline)(4Q).**
- **Demonstrate 100:1 reduction in unsteady turbomachinery analysis time relative to 1999 baseline with MSTURBO on the HPCCP parallel testbed (4Q).**
- **Complete 3-D primary flowpath simulation of an advanced aircraft engine (4Q).**
- **Complete 3-D aero/structural/probabilistic analyses. Initiate implementation into the NPSS architecture (4Q).**
- **Initial release of NPSS for space transportation propulsion (4Q)**

Presentation Outline

- Definition of NPSS
- NPSS Program Structure
- ***Current Status of NPSS***
  - NPSSv1 Capabilities
  - ***Engineering Demonstrations***
  - Planned Capabilities

NPSS Multidisciplinary Integration and Analysis

NASA Contract NAS3-98003
Task 5

Edward J. Hall

Supervisor, Aerothermal Methods

Rolls-Royce, Indianapolis, IN

NPSS On-Site Review

March 21-22, 2001

Computing and Interdisciplinary Systems Office
Glenn Research Center

Geometry Challenges

- Industry interacting with multiple CAD systems
- Need to produce CAD data from within non CAD-based design systems
- Access to geometry required by multiple disciplines (aero/heat transfer/stress/dynamics/acoustics)
- Simulation procedures

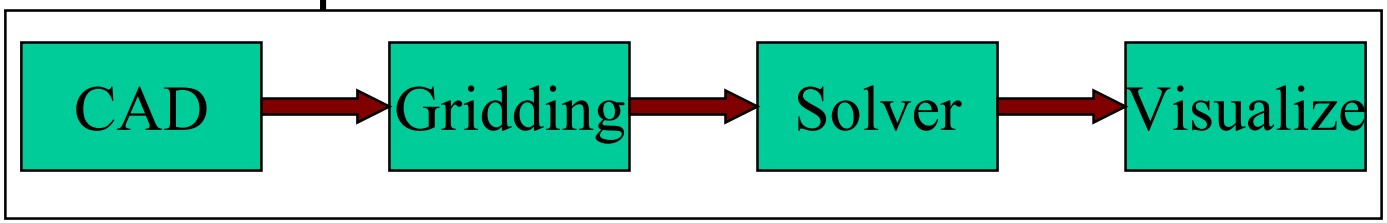

  - File based
  - Requires “good geometry”
  - One way communication
  - Difficult to introduce reverse engineering

CAPRI

- CAD vendor neutral application programming interface
- Allow access to geometry from within all modules of an analysis system
- Reliance on standards is minimized
- Modular system
- Multiple languages
- Transient solutions
- Allow multi-disciplinary coupling and zooming
- CAPRI combines geometry and topology

Multidisciplinary Integration and Analysis

- Objective
  - The objective of this task order is to enhance the NPSS core capabilities by expanding its reach into the high fidelity multidisciplinary analysis area. The intent is to investigate techniques to integrate structural and aerodynamic flow analyses, and provide benchmark by which performance enhancements to NPSS can be baselined.
- Approach
  - Couple high fidelity aerodynamic and structural/thermal analysis codes to enable multidisciplinary evaluation of NPSS components
- Strategy for Success
  - Data processing elements employ standard interface definitions to ensure commonality and modularity
    - CGNS - CFD General Notation System (CFD standard)
    - CAPRI - CAD data access API (Geometry interface standard)

Aero/Structural Coupling

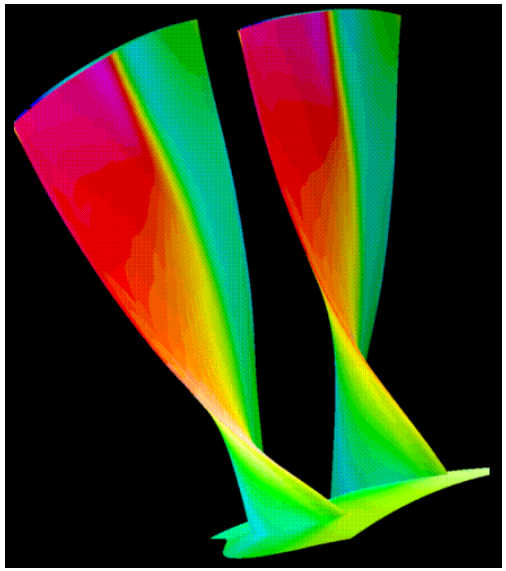

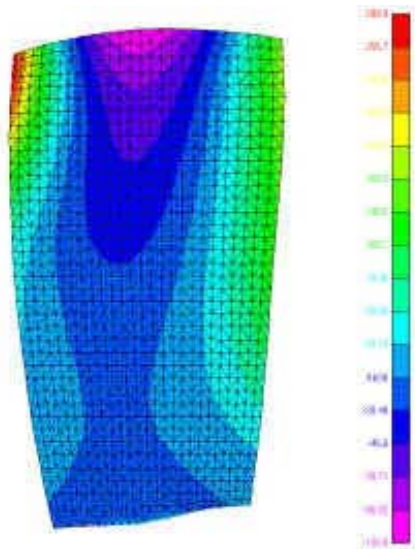

ADPAC CFD Analysis

Input:
geometry, operating conditions

Output:
pressure, temperature

ANSYS Structural Analysis

Input:
geometry, operating condition,
pressure, temperature

Output:
deformations, stress

ANSYS Multidisciplinary Implementation

- Flow chart of automated process

Aero design system

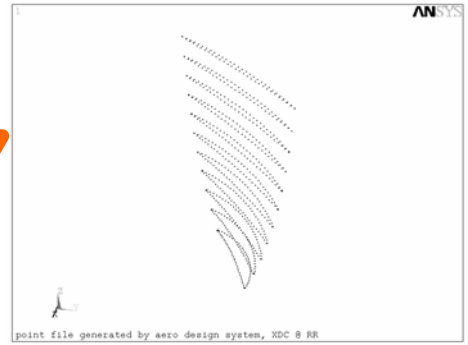

•Point file is created by Aero design system, read into 3D CAD or ANSYS
•History file is kept for re-runs of different designs of the airfoil
•The number of points and stream sections must be kept constant, location of points can change.

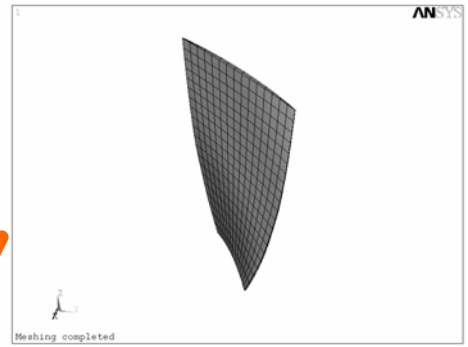

•ADPAC results are mapped onto mesh
• structural analysis is run for first guess on un-wrap of blade. Deflected shape is used to calculate the initial guess on cold geometry. The mesh is morphed using an iterative process to get the cold mesh geometry.

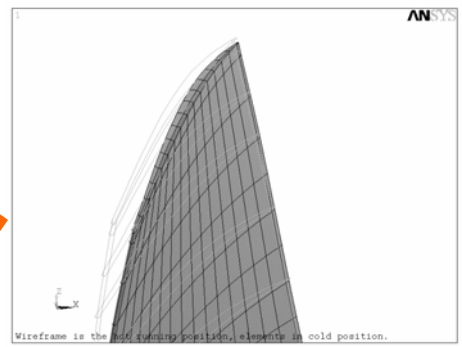

•The cold mesh node locations and the original nodal locations are used to generate a deflection file.
•Deflection file is used to generate new Aero data input which is used to analyze off design point configurations

Multidisciplinary Demo

- Hot to cold coordinate conversion via ANSYS
- Point-based airfoil definition input
- Fully automated (based on existing hot aero CFD data)
- Demo system delivered to NASA
- Expanding system for automated cold to warm conversion including CFD meshing/solution operations

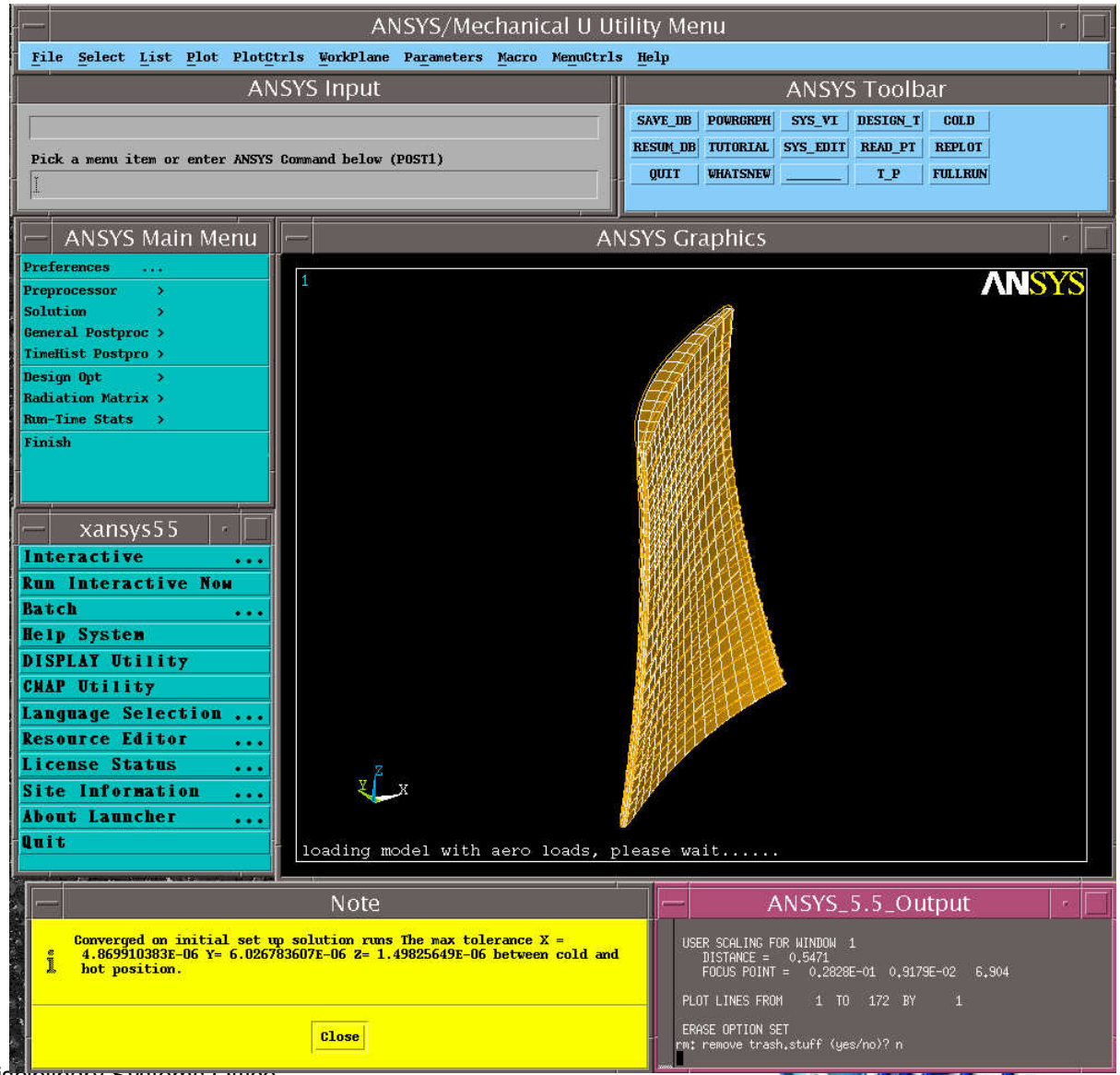

Rolls-Royce

Probabilistic Tip-Gap Study

Objective

- Determine Effect Of Tip Gap Variability On Aerodynamic Loss Factor And Mean Stress Distribution

Approach

- Select PDF for tip gap
- Perform ADPAC analysis for three values of tip gap (μ, $+k\sigma$, $-k\sigma$)
- Develop ANSYS FE Mesh
- Input , FE Mesh, Blade Pressure, Aero Loss Factor into NESTEM
- Predict Cumulative Distribution Function for Mean Stress and Aero Loss Factor

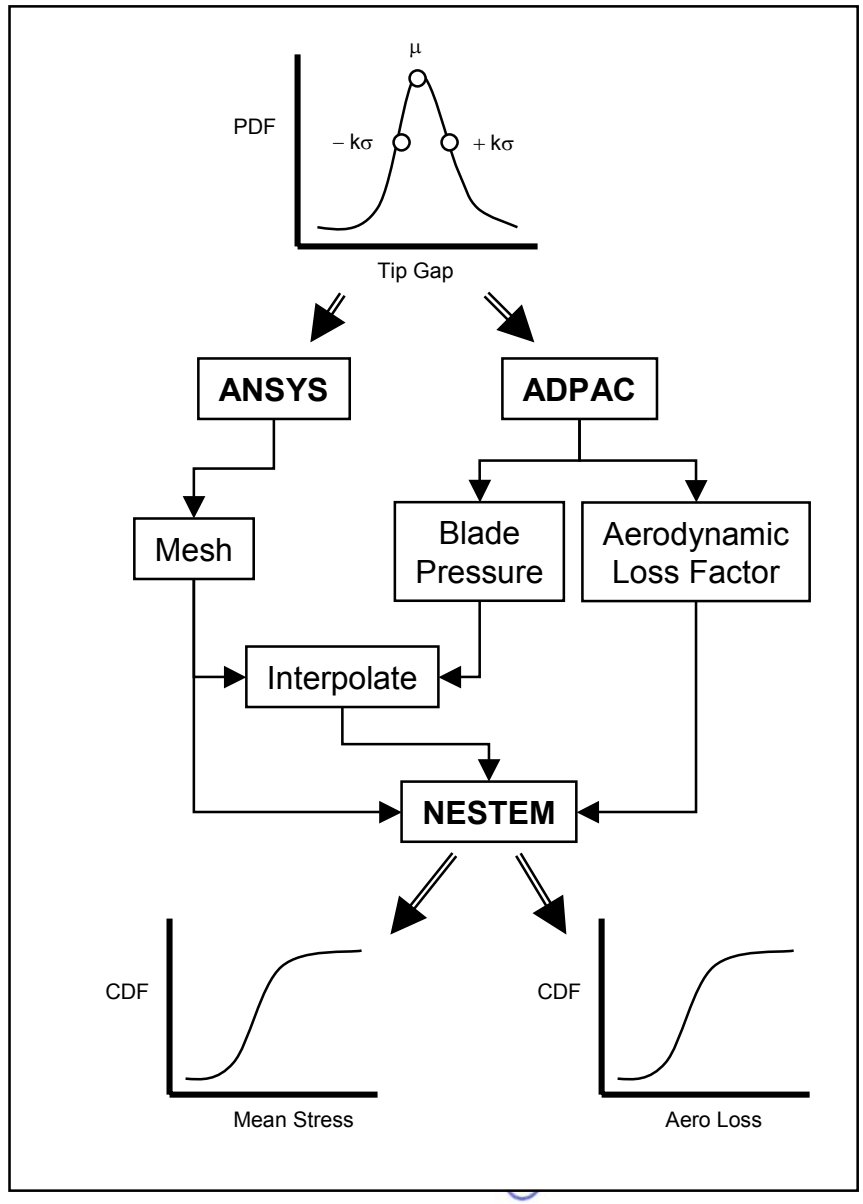

Rolls-Royce

Computing and Interdisciplinary Systems Office
Glenn Research Center

MultiDisciplinary Pump Development

- Unsteady 3D Fluid (NS) Structural Simulation
- Uses Hah3D and Ansys
- Designed to Mature Code Coupling Developers Kit (CCDK) Tool

Computational Grid

- 160x34x265 for single-passage IGV-impeller-diffuser.
- Simplified analysis:
  - 5 IGV passages
  - 2 impeller passages
  - 8 diffuser passages
- Final analysis:
  - 15 IGV passages
  - 6 impeller passages
  - 23 diffuser passages
- 7-10 cycles used for convergence.

Computational Grid

Initial Condition Pressure Contours at Midspan

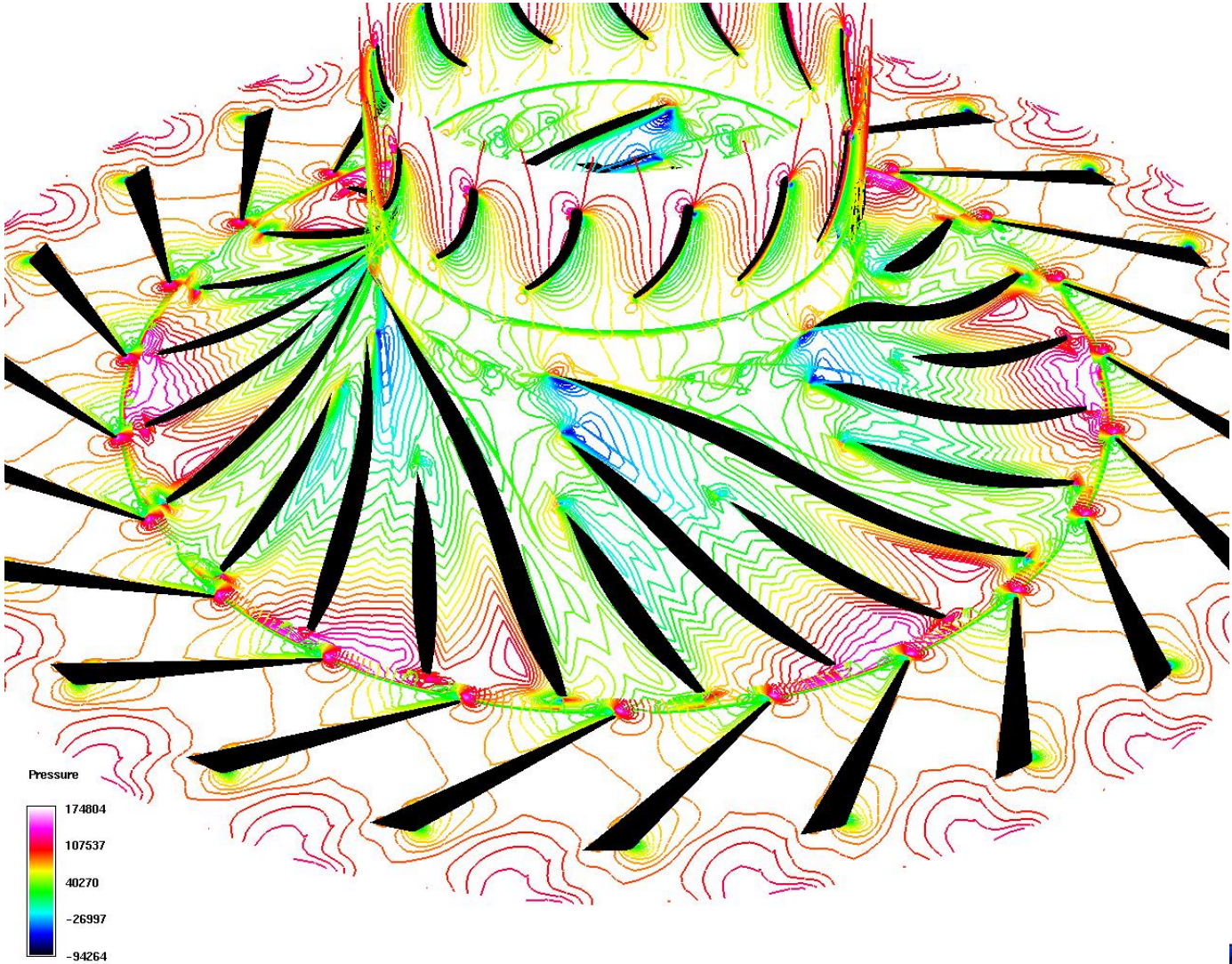

Turbopump Model:

IGV blades: 5

Nodes 7200

Elements 3245

Impeller blades: 8

Nodes 12336

Elements 5566

Diffuser blades: 8

Nodes 8640

Elements 3872

FEA model: SOLID45 | **Total Intensity STRAIN**

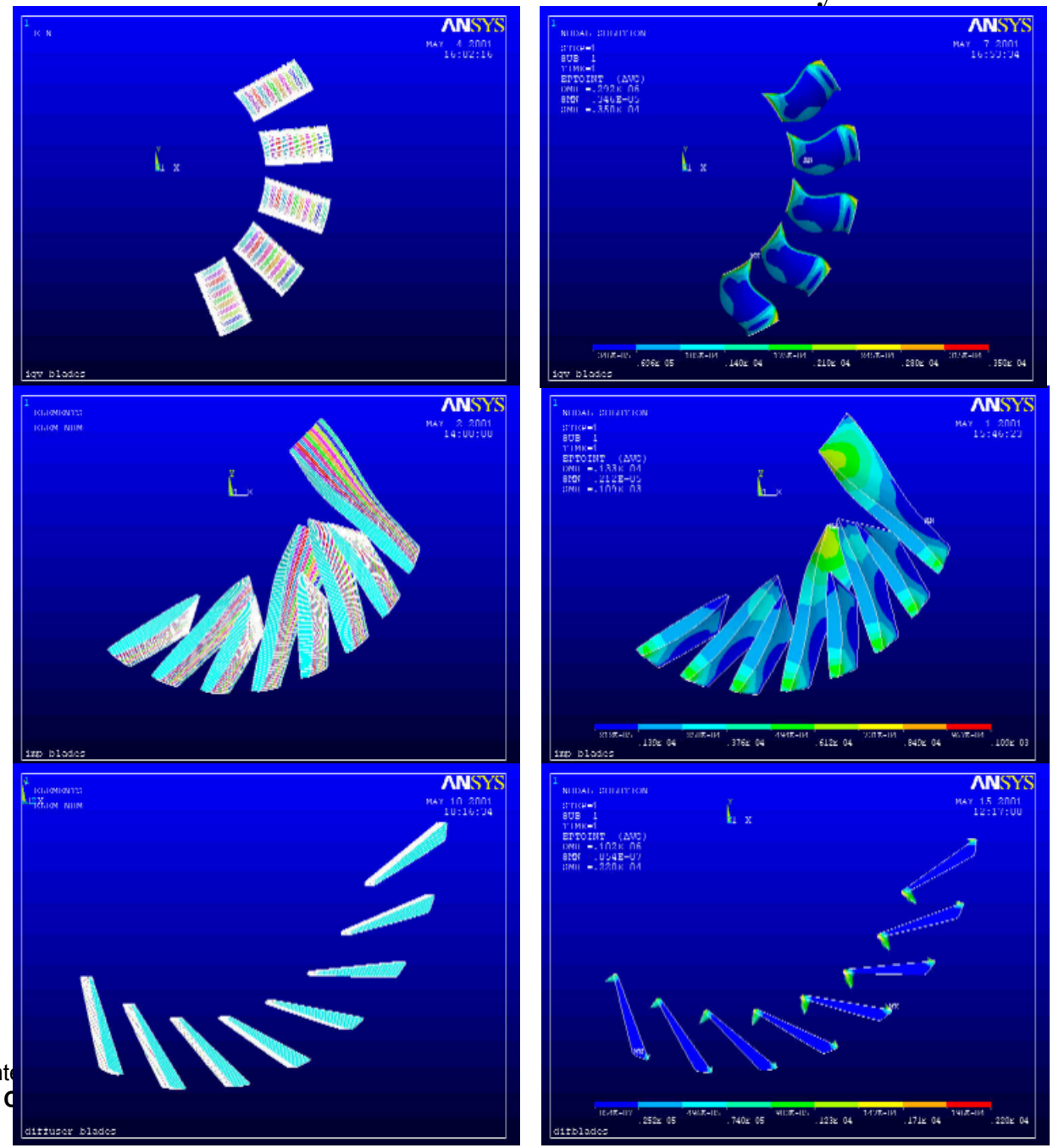

MultiDisciplinary ISTAR Simulation

- 3D Fluid (NS) Structural Simulation
- Uses Overflow, Vulcan, and Ansys
- Supports ISTAR Team and Oversight Team
- Designed to Mature Code Coupling Developers Kit (CCDK) Tool

ISTAR Engine Multidisciplinary Analysis

- Simulation of Approach Flow & Scram Flow for ISTAR Engine.
- Inflow Simulated with OVERFLOW; Scram Simulated with VULCAN. Structures with ANSYS
- Prelude to Aero/Thermal/Structural Simulation
- CFD Solution Delivered Aug. 2001
- Supports ISTAR Team and Oversight Team
- Designed to Mature Code Coupling Developers Kit (CCDK) Tool

Mach Distribution for ISTAR Engine Approach Flow

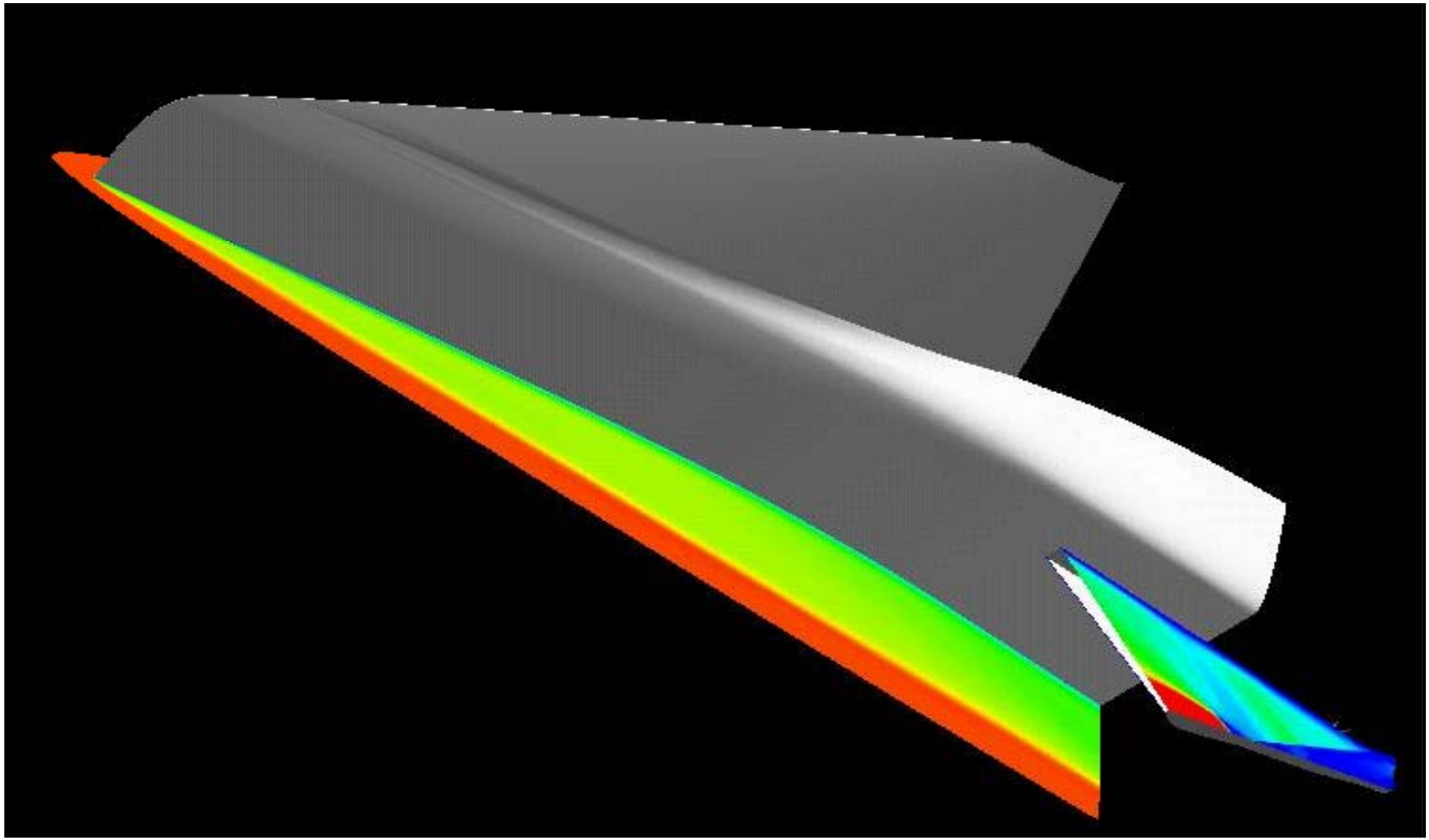

Fuel Mass Fraction in ISTAR Scram Combustor

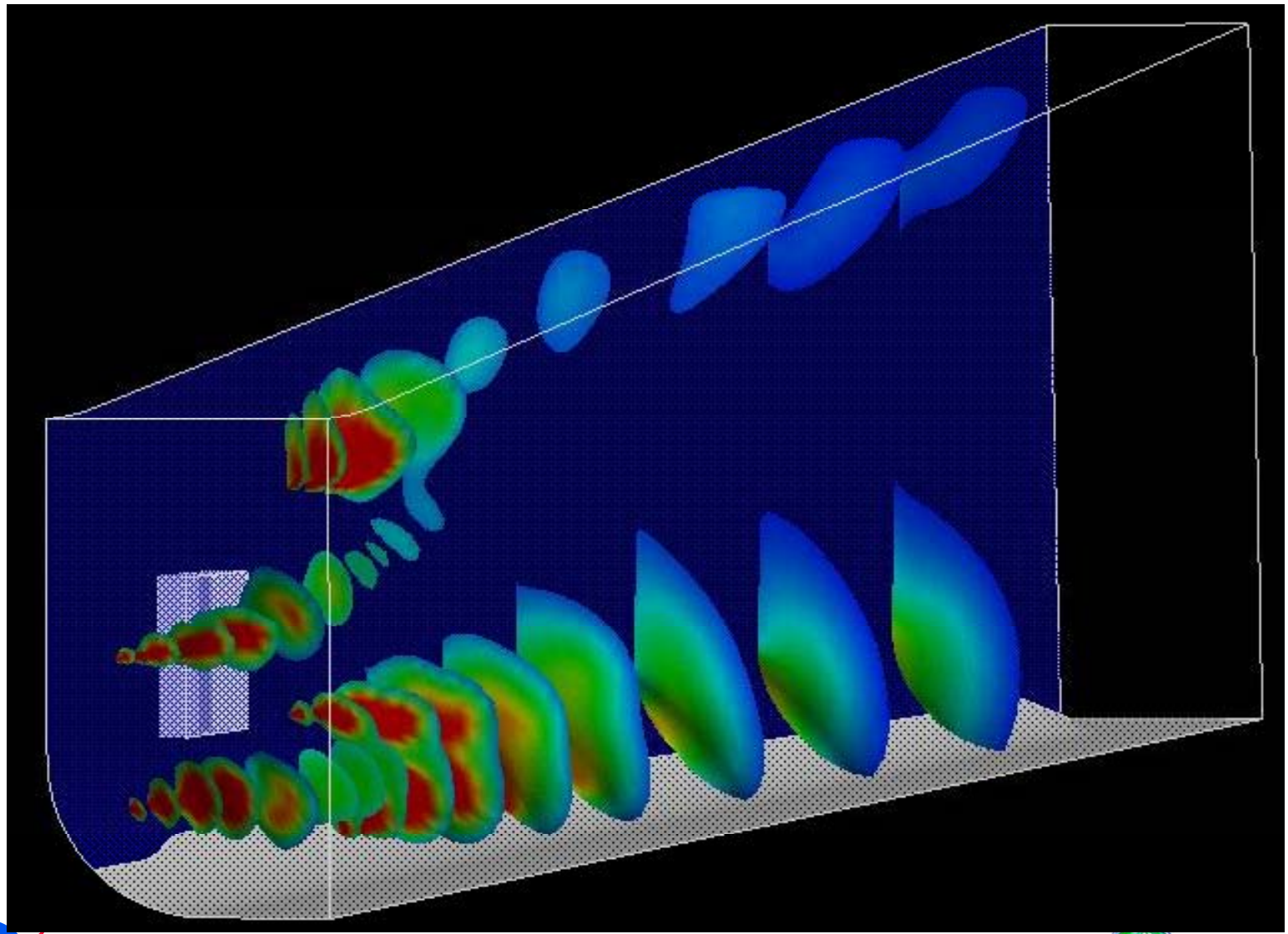

Fuel Iso-Surfaces Colored by Temperature

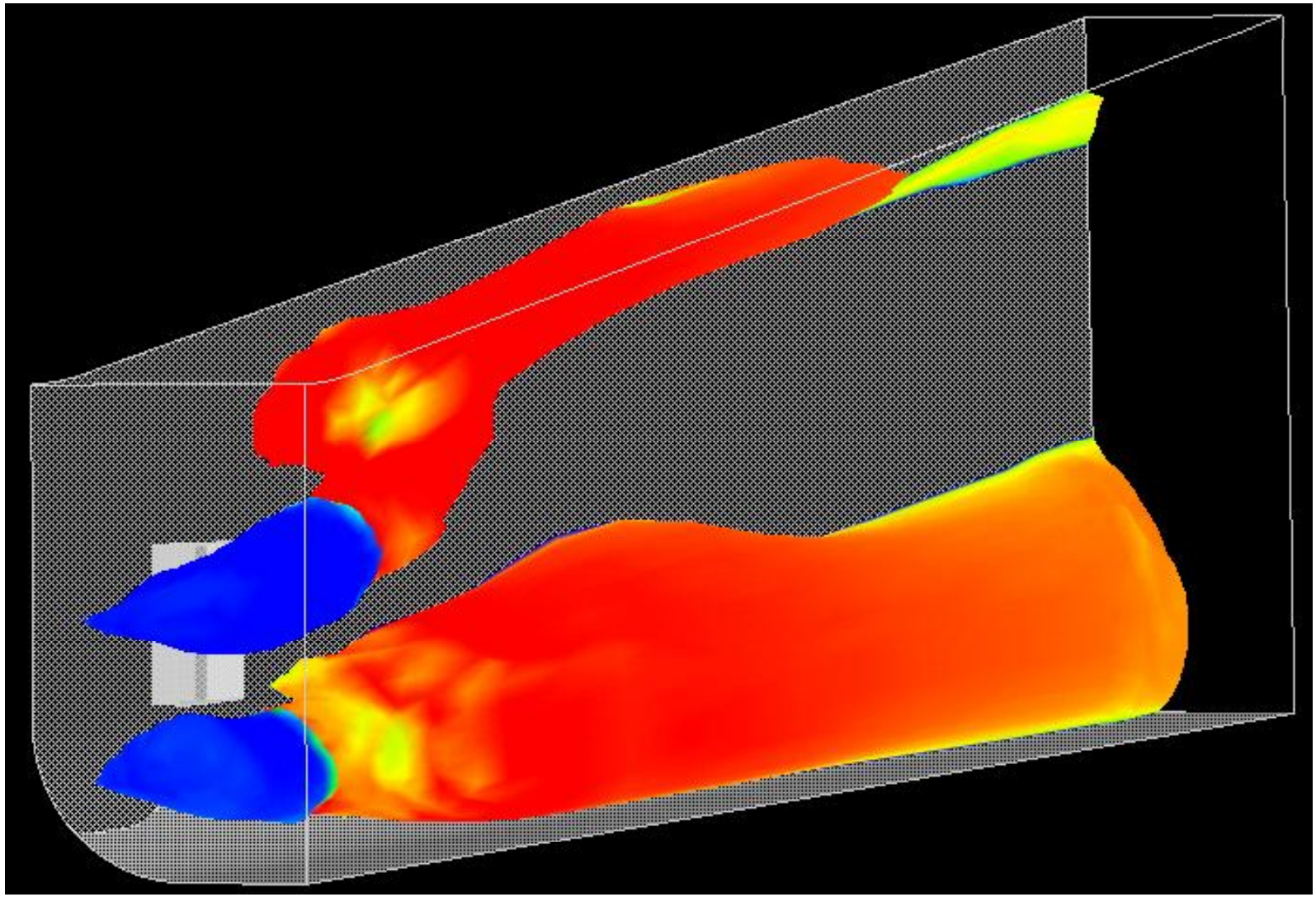

Future Work: Aero/Thermal/Structural Simulation

- Thermal/Structural Simulation and Coupling with Existing Aerodynamic/Combustion Code
- Heat Fluxes for Active Cooling Requirements
- Structural Deflections: Balancing Aerodynamic and Structural Requirements
- Thermal Effects on Seals

GE90 Engine Simulation

- Full Core 3D Simulation
- Uses APNASA and NCC
- Designed to Demonstrate Overnight Computation Capabilities
- Engineering Demonstration of 3D Code Coupling Capability

Turbofan Core Engine

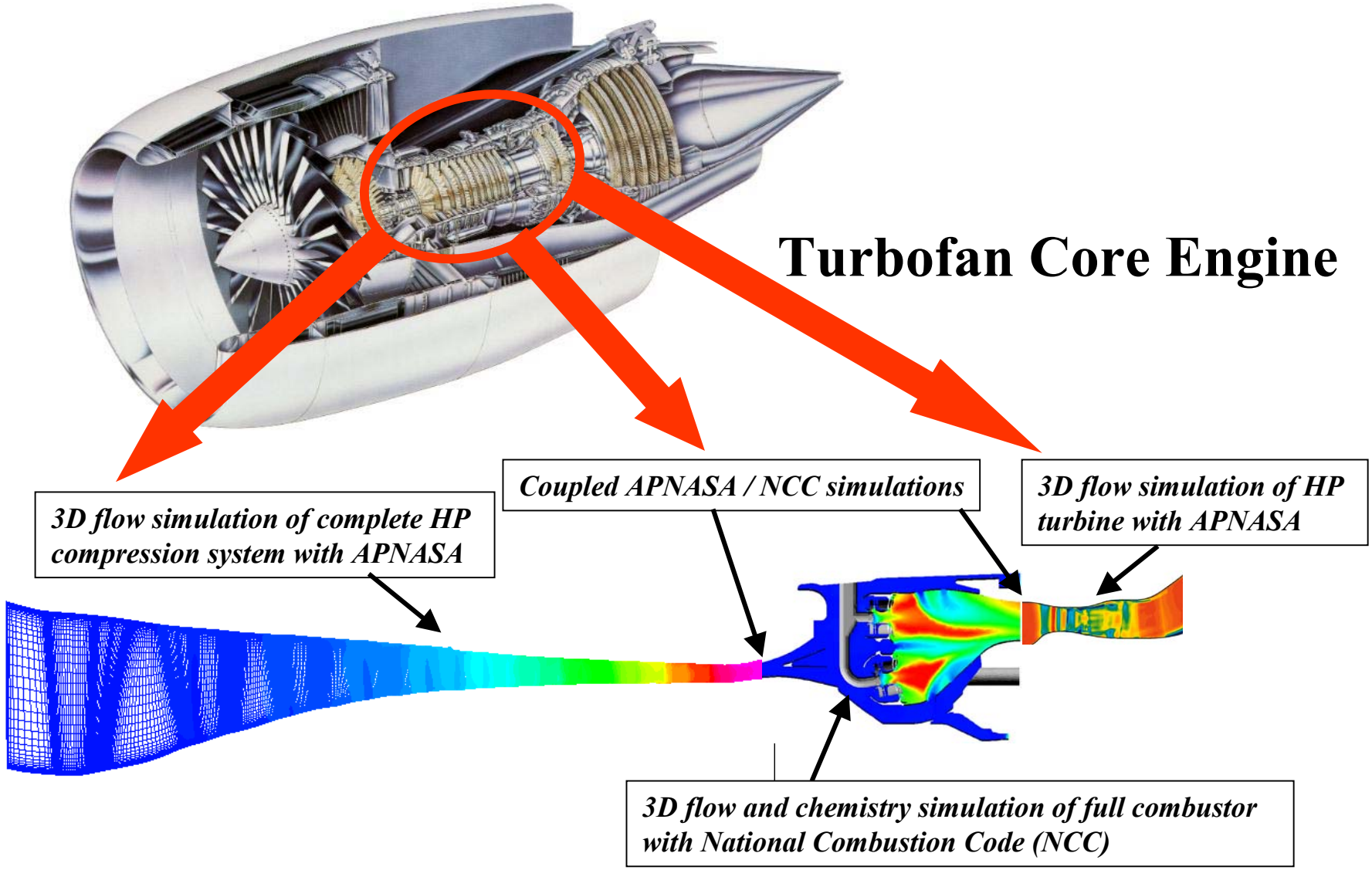

Presentation Outline

- Definition of NPSS
- NPSS Program Structure
- Current Status of NPSS
  - NPSSv1 Capabilities
  - Engineering Demonstrations
  - ***Planned Capabilities***

Numerical Propulsion System Simulation Roadmap

	'00 CY	'01	'02	'03	'04	'05	'06
	V.1		V.2	V.3		V.4	
CAPABILITIES	Steady-State, Transient, Low fidelity Dynamic, Reduced order & data reduction, Low Fidelity Flowpath, Geometry Design		Mid Fidelity Dynamic, Mid Fidelity Geometry Access CAD Systems		Full Performance Envelope 2D/3D Euler, Mid Fidelity Dynamic, Mid Fidelity Geometry Access across CAD systems	Full Engine Performance 3D Navier-Stokes Steady State, Unsteady, Transient, High Fidelity Geometry generation	
INTEROPERABILITY	Zooming 0D<->1D Single component, CORBA multi-ORBs, Distributed Objects		Zooming 0D<->1D/2D, 0D<-3D, Single components, CORBA Security		CORBA Security with SecurID, Probabilistic sensitivity analysis	Zooming 3D<->0D/1D/2D, Multiple components. Couple Multiple disciplines: structures, thermal	
PORTABILITY	Sun, SGI, HP	NT, Linux				Miniaturization of hardware	
RELIABILITY	High-Control Formal Software Development Process with Verification and Validation for each incorporation						
RESOURCE MGT	Globus, LSF		Information Power Grid aware load balancing, networked clusters		Information Power Grid Dynamic load balancing	Distributed gathering of simulation data for monitoring, convergence, visualization	
USABILITY	Script assembly language, Dynamic linkable libraries, Fully interpreted elements, interactive debug		Visual assembly language		Web Based Visual assembly language tools	Web Aware Visual assembly language tools	
PERFORMANCE		1000:1 reduction in execution time of 3D Turbo Machinery & Combustion simulation	24:1 reduction in 0D-1D zooming		Real-time ORB 100:1 reduction in 3D-3D coupling simulation		

Computing and Systems Office
Glenn Research

NPSS Version 2.0.0 Capabilities

- 1-D dynamic engine system operation
- Aircraft installation effects
- Improved thermo architecture and capability
- New components, including combustion, compression, turbine expansion
- Units conversion
- Initial visual-based syntax stand-alone tools (graphical & command)
- Input and output enhancements
- Enhanced NPSS Developer Kit
- Enhanced C++ converter, interactive debugger, and commands
- CORBA Security
- NPSS running in CORBA server mode
- Common geometry interface
- Initial rockets capabilities
- Zooming from low to high fidelity as defined in the NPSS SRS
- New user documentation: Installation Guide and Training Guide

NOTE:See NPSS SRS for detailed Version 2 requirements.

NPSS Architecture FY02 Milestones

- 3-D/3-D coupling of ANSYS and ADPAC wrappers incorporated into Development Kit.
- CORBA-based geometry services incorporated into Development Kit.
- CORBA Security services integrated with GLOBUS and incorporated into Development Kit.
- Fast probabilistic integration (FPI) deployed with Development Kit.

NPSS Wins 2001 NASA Software of the Year Award

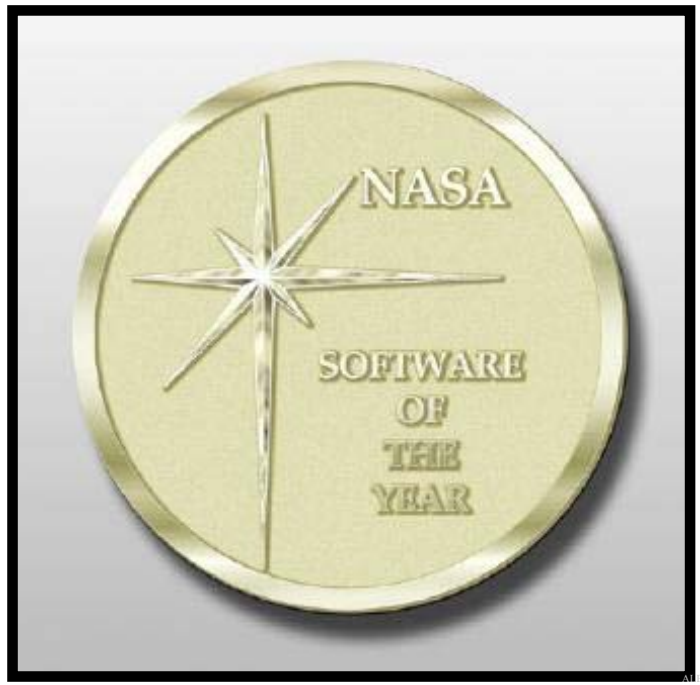

NPSS Wins NASA 2001 Turning Goals Into Reality Award (TGIR)

Computing and Interdisciplinary Systems Office
Glenn Research Center

International Space Systems, Inc.

RECIPE©
Collaborative Engineering Environment

Prepared for

MDA Panel Session

Thermal Fluids Analysis Workshop

September 12, 2001

500 Wynn Drive, NW, Suite 306 Huntsville, Alabama 35816
Tel (256)890-1178, Fax (256)890-1174

Agenda

- History of RECIPE© – What we set out to do
- Current Activities – ISSI and RECIPE©
- Requirements – What user needs in a system
- System Overview – Capabilities of RECIPE©

History of RECIPE©

Early History (Up to Spring 1999)

- Began with idea for RBCC vehicle design (coupled design)
- Phase-I STTR
  - All rocket TSTO
  - SSTO RBCC
- Thermal Analysis TestBed
  - Incorporated MINIVER and SINDA
  - Added robust database
  - User operated distributively

Recent History (Spring 1999 – Present)

- Demonstration of collaborative process for TGIR 2000 Conference
- Intercenter Systems Analysis Team (ISAT) technology assessments
  - September 2000
  - November 2000
  - March 2001
  - April 2001
  - June 2001
- Received several Phase III contracts

Current Activities

Recent History (Spring 1999 – Present)

- Continuing RECIPE© development
- Intercenter Systems Analysis Team (ISAT) participation
- Advanced Engineering Environment (AEE)

Requirements

RECIPE© Top Level Requirements

- System must be simple to use!
- Accommodate any model needing inputs from and/or providing outputs to other models
- Data to be easily retrieved and placed under configuration management
- Provide traceability of requirements/inputs and assumptions
- Provide a system that will work in Windows, Macintosh, and Unix environments
- Accommodate distributed computing via internet
- Provide reporting/summarization capabilities

System Overview

System Overview – System Goals

- Provide a system that can be used from preliminary design through production
- Provide a system that will permit data transfer between programs of any fidelity
- Provide a system that will allow engineers to work in parallel
- Provide a system that will allow engineers to work with their models in a familiar manner

System Overview – User Goals

- Make life easier for the manager
  - Provide security of mind about data
  - Provide method of tracking and recovering from problems
  - Provide progress tracking of projects
  - Provide method to view data transferred between models
  - Provide automated comparison report of important data which is portable to other presentations
- Make life easier for the engineer
  - Simplify process of exchanging data with other engineers
  - Simplify process of working with data
  - Simplify process of working with engineering tools

Example

RECIPE© Main Screen

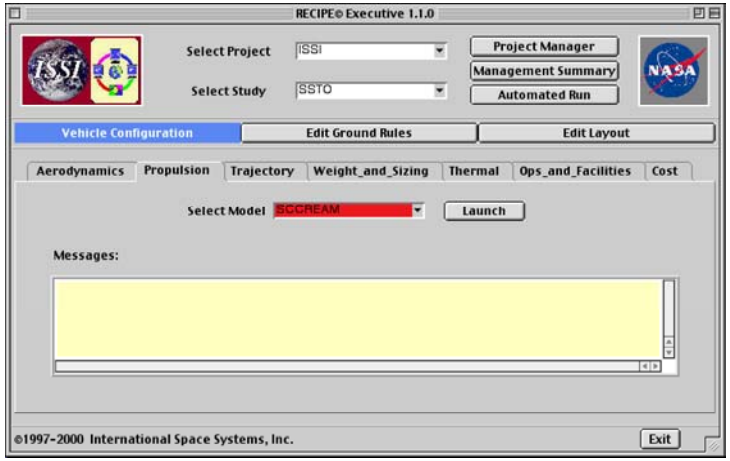

Engineer selects INTROS

System Weights And Sizing

INTROS Manager

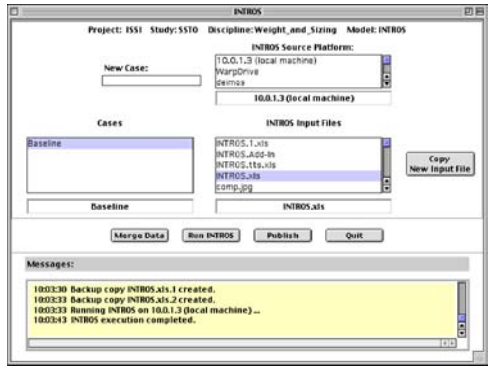

Engineer uses Technology Inputs In Model

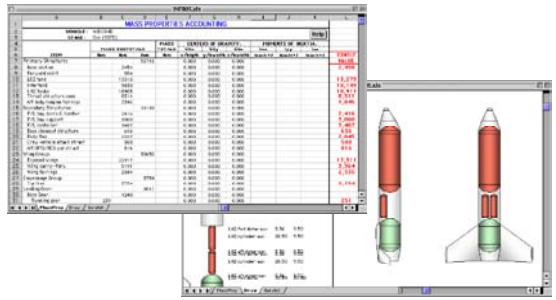

Next Engineer(s) uses Results for their analysis
+
Technology Inputs

All results are stored in and recalled from RECIPE© Database

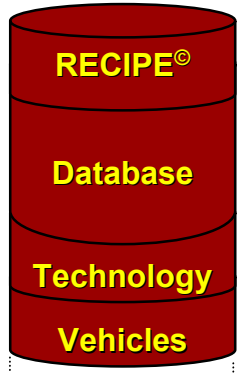

RECIPE© Server Saves Results

RECIPE© Database seamless to User

Trajectory

Facilities & Operations Costs

Development & Unit Costs

Economics

Quantitative Assessment

Management Summary

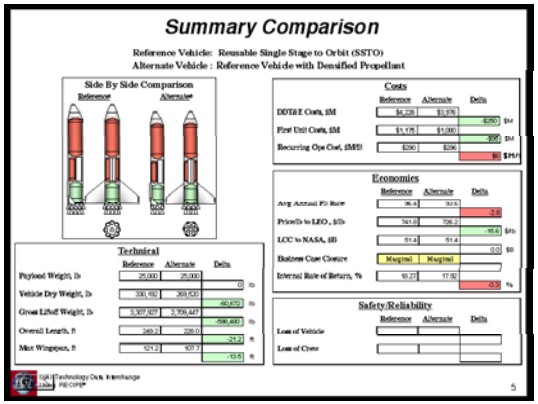

System Overview – Managing Data

- Projects are organized by a three tier hierarchy
  - Project
  - Study
  - Case
- Published data can be stored in a distributed manner or in a central “Mirror” location and archived for permanent storage
- Secure shell can be used for secure transfer of data through firewalls
- The VRC can be used as a permanent restricted storage location which supports ITAR classifications

RECIPE© Example Set-Up

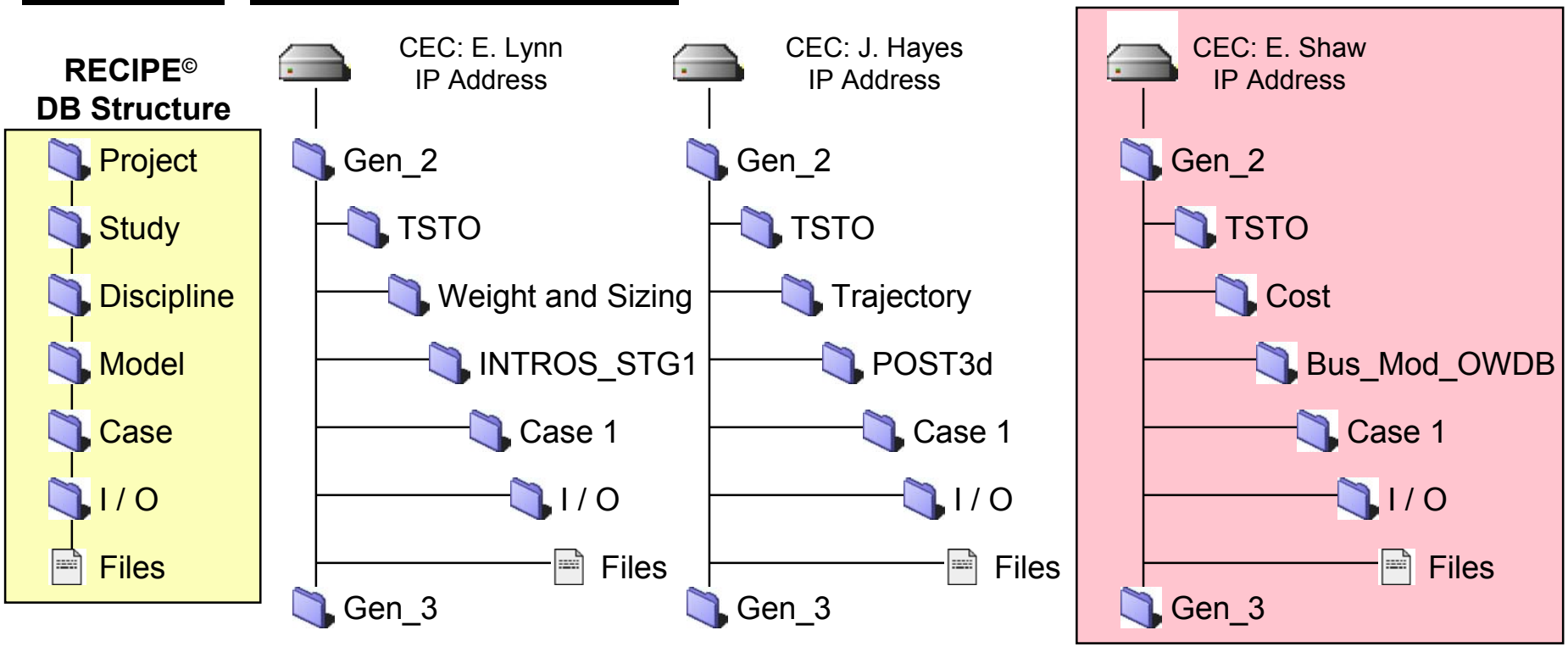

ISAT Example

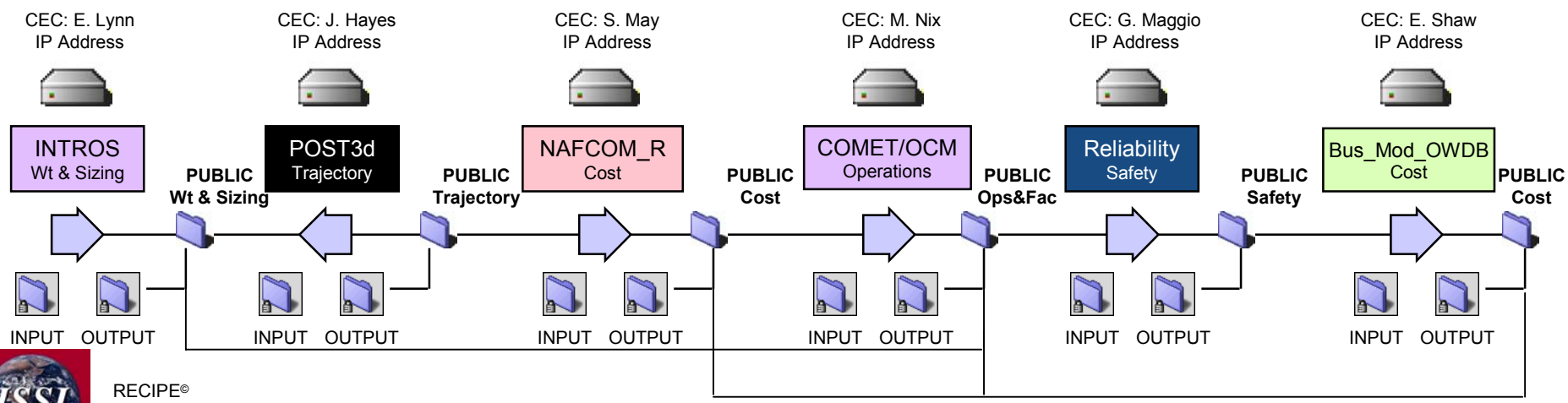

System Overview – Configuration Management

- Hierarchy makes it easy for engineer/manager to find previous work and retrieve/review data
- Final Publish functionality ensures data is not changed after initial work
  - “Freeze” model data so it cannot be changed in the future
  - Data can only be changed by “unpublishing” data after obtaining permission

System Overview – Traceability

- All input files (along with backups) and output files are stored locally
- All input files and published data are stored on “mirror” site via internet
- Logs provide history of actions on each RECIPE© workstation for tracking problems
- RECIPE© will capture
  - Which models have exchanged data for a specific project/study/case
  - What new or different inputs have been entered in a model

System Overview – Management Tools

- Project Status tracks project/study/case
  - Interdiscipline Publish
  - Final Publish
  - Unpublished

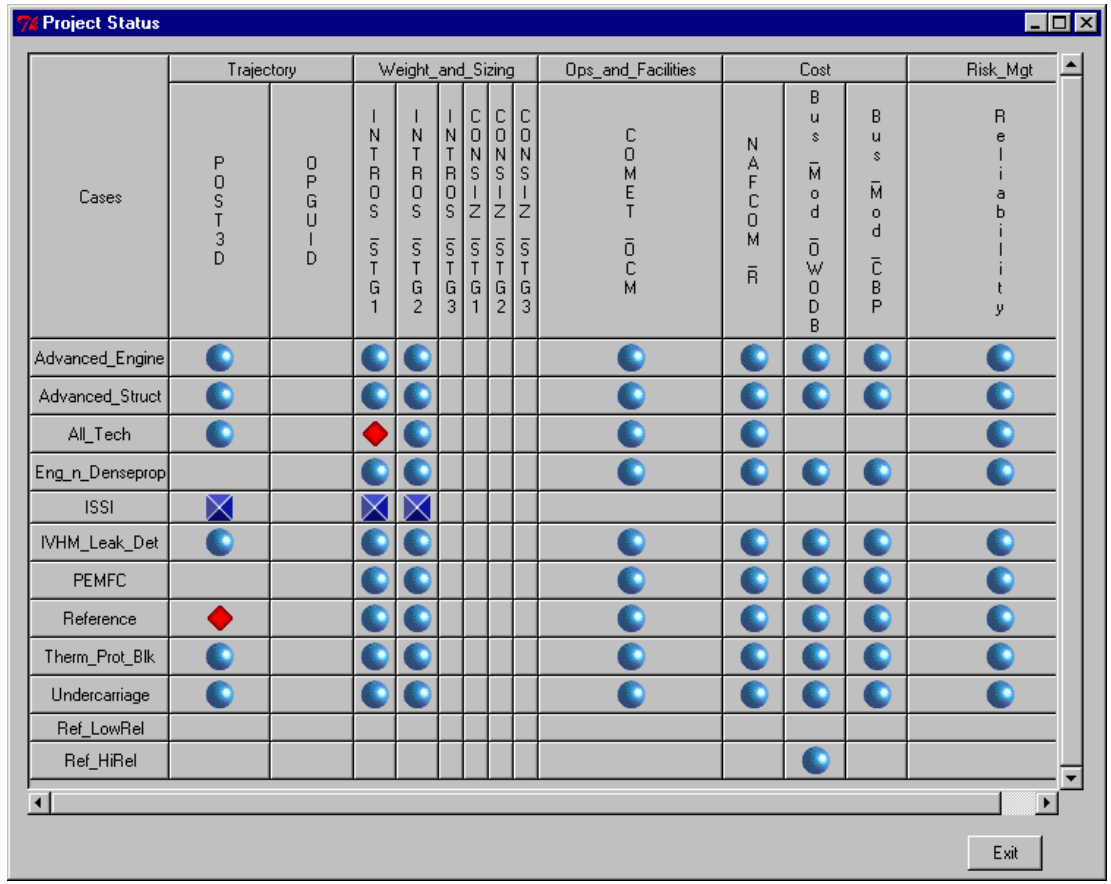

Cases	Trajectory		Weight_and_Sizing						Ops_and_Facilities	Cost			Risk_Mgt
	POST3D	OPGUID	INTROS_STG1	INTROS_STG2	INTROS_STG3	CONSIZ_STG1	CONSIZ_STG2	CONSIZ_STG3	COMET_OCM	NAFCOM_R	Bus_Mod_OWODB	Bus_Mod_CBP	Reliability
Advanced_Engine	●		●	●					●	●	●	●	●
Advanced_Struct	●		●	●					●	●	●	●	●
All_Tech	●		◆	●					●	●			●
Eng_n_Denseprop			●	●					●	●	●	●	●
ISSI	✕		✕	✕									
IVHM_Leak_Det	●		●	●					●	●	●	●	●
PEMFC			●	●					●	●	●	●	●
Reference	◆		●	●					●	●	●	●	●
Therm_Prot_Blk	●		●	●					●	●	●	●	●
Undercarriage	●		●	●					●	●	●	●	●
Ref_LowRel													
Ref_HiRel											●		

System Overview – Management Tools

- Access published data
  - Server(s) polled across internet for all published data
  - Project/study/case tree provides method to
    - View published data from any model for any project/study/case
    - Generate "Management Summary"

Management Summary

Reference Vehicle : TSTO Bimese- Reference
Technology Vehicle: TSTO Bimese- New Technology

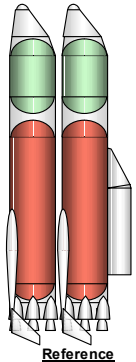

Reference

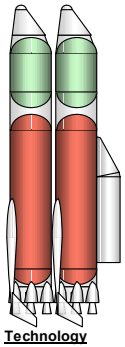

Technology

Cost

		Reference	Technology	Difference	
Technology Cost, Min	$B	1.0	1.4	40.0	%
Technology Cost, Max	$B	1.0	1.8	80.0	%
DDT&E Costs, Pes.	$M	100	99	-1.2	%
DDT&E Costs, Opt.	$M	100	106	5.7	%
First Unit Costs, Pes.	$M	100	84	-17.1	%
First Unit Costs, Opt.	$M	100	75	-25.0	%
Recurring Ops Cost/Flt, Pes.	$M	100	70	-30.4	%
Recurring Ops Cost/Flt, Opt.	$M	100	69	-30.6	%

Economics

		Reference	Technology	Difference	
Annual Flt Rate, Pes.		10.0	13.8	37.8	%
Annual Flt Rate, Opt.		20.0	24.2	41.8	%
Price/lb to LEO, Pes.	$	100	74	-26.7	%
Price/lb to LEO, Opt.	$	200	150	-25.2	%
NASA LCC Save, Pes.	$B	(10.0)	(7.0)	7.0	%
NASA LCC Save, Opt.	$B	(1.0)	(0.8)	13.3	%
Industry IRR, Pes.		1.0%	1.1%	12.7	%
Industry IRR, Opt.		10.0%	10.9%	9.6	%

Technical

		Reference	Technology	Difference	
Payload Weight	lbm	100	100	0.0	%
Vehicle Dry Weight	lbm	100	81	-19.3	%
Gross Liftoff Weight	lbm	100	83	-17.0	%
Overall Length	ft	100.0	95.1	-5.9	%
Max Wingspan	ft	100.0	95.3	-5.7	%

Safety

	Reference	Technology	Difference	
Loss of Vehicle- mean	1:01	1:02	15.22	%
Loss of Vehicle- 25th %tile	1:01	1:02	34.22	%
Loss of Vehicle- 50th %tile	1:01	1:02	28.52	%
Loss of Vehicle- 75th %tile	1:01	1:02	20.20	%

Example Only

System Overview –Using Tools

- Engineer can always see what project/study/case is being worked
- Files can easily be copied from other project/study/cases
- Engineer works with models in a familiar paradigm
  - Batch Programs with input and output files
    - Programs run local or remote
    - All functions accessible with single click
  - Excel workbooks are launched with a single click (even if multiple workbooks)

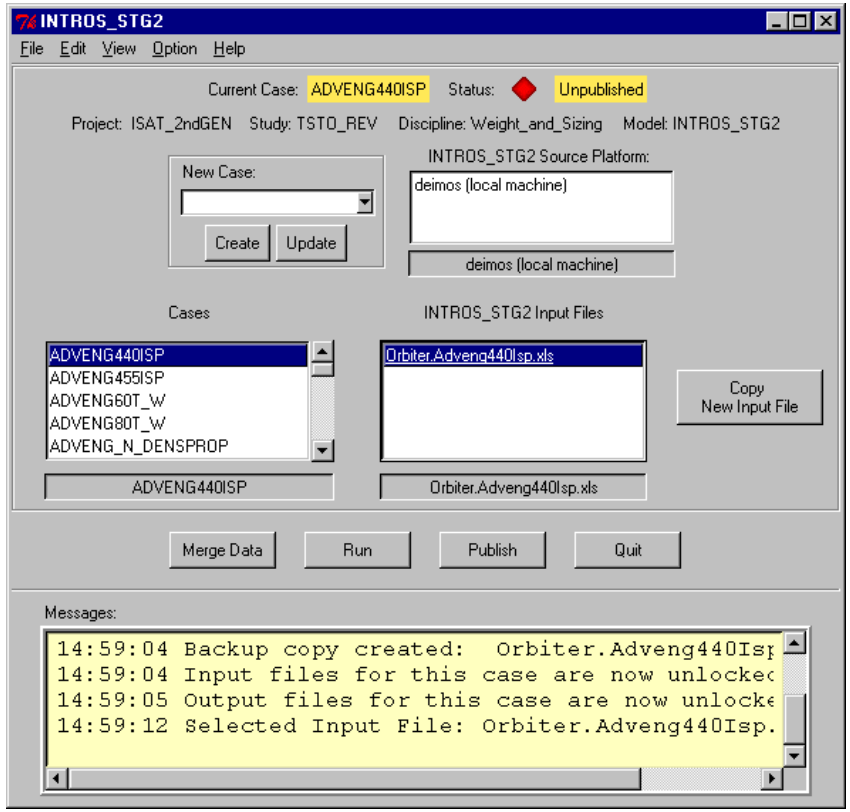

System Overview – Connecting Tools

- Data can be “merged” into the model input file
  - Engineer tells RECIPE© to poll server(s) and identify data from other models which is available for current model to use
  - Engineer tells RECIPE© to insert data into model
  - Can apply
    - Unit conversions
    - Arithmetic conversions
- Data is “Published”
  - Interdiscipline for preliminary publishes while iterating with other models
  - Final when data is available for rest of team
- Several models have been integrated and studies performed

ISAT and RECIPE© : NASA-MSFC CEC & NASA-LaRC CEC

RECIPE©: File Management System and Data Management System

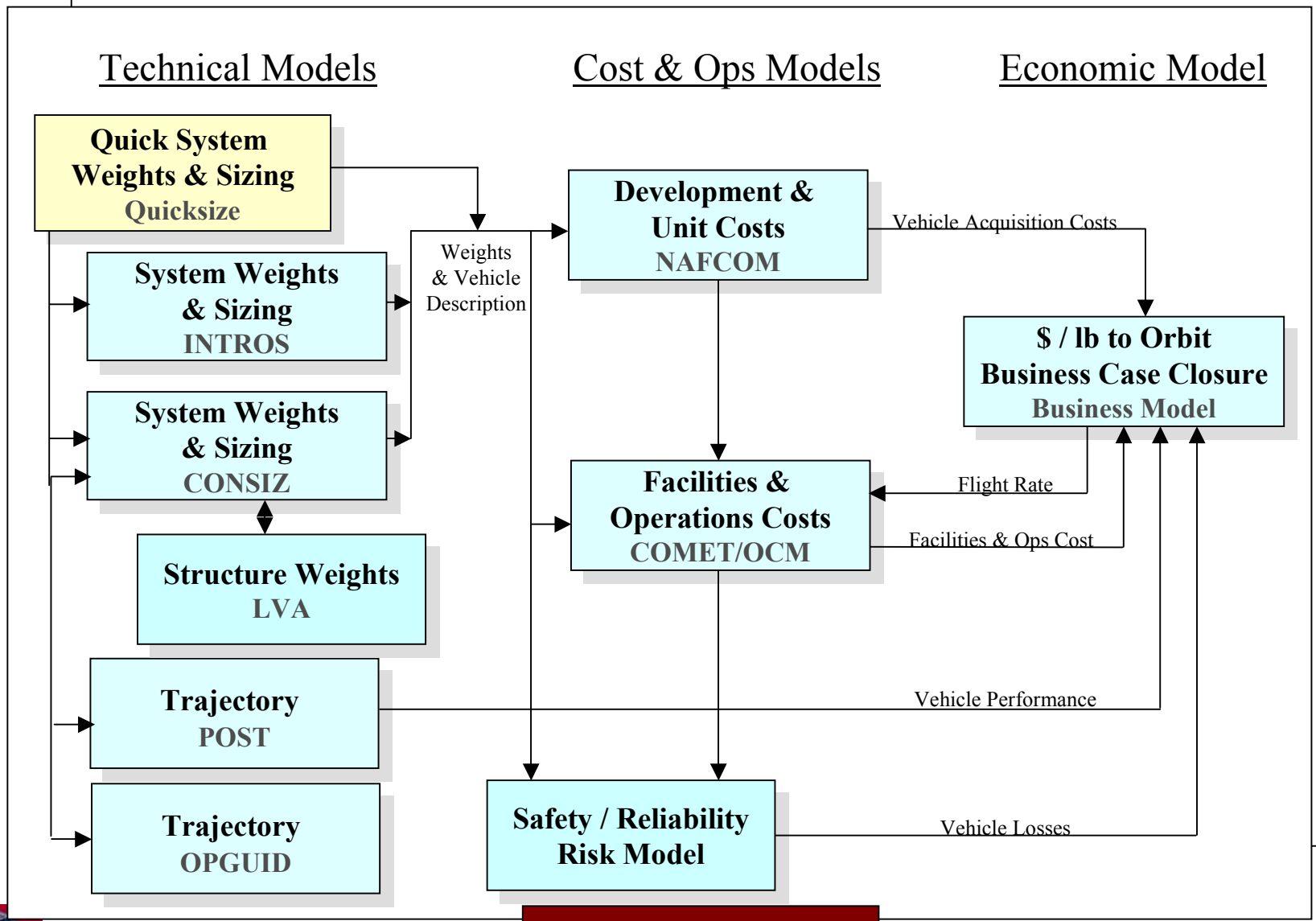

2ndGen ISAT Application

ISSI Assessment System

- Alternate Models in RECIPE©

Geometry / Chemical	Weights & Sizing	Aero / Thermal	Propulsion / Structures	Trajectory	Ops	Cost	Reliability
Pro-E	INTROS	APAS	SCCREAM	POST3d	NROC	NAFCOM _R	SAIC Reliability
CEA	CONSIZ	HYFIM	EPSURBCC	OTIS	Spaceliner 100	Spaceliner 100	RANT/ RAVE
	Quicksize	SINDA	LVA	OPGUID		IEM	
		MINIVER					

System Overview – Future Enhancements

- User Authorization will provide method to permit access to specific project/study/cases and prevent access to others
- Two step plan to simplify process of adding a model
  - "Easy Wrapper" to define RECIPE© model interface, how to run, what data to "Publish", what data and models to "Merge" data
  - "Automatic Wrapper" to aid identification of data and models from which to "Merge"
- Bounds for variables with flagging of variables outside
- Automatic processing of models with optimization capability
- Interface with PDM's including MSFC's IMAN

System Summary

- Makes life easier for the manager
  - Provide security of mind about data
    - Easy to retrieve
    - Not changing (without consent)
    - Archived
    - ITAR restricted (if stored in VRC)
  - Provide method of tracking and recovering from problems
  - Provide progress tracking of projects
  - Provide method to view data transferred between models
  - Provide automated comparison report of important data which is portable to other presentations

System Summary

- Make life easier for the engineer
  - Simplify process of exchanging data with other engineers
    - Receive data
    - Send data
  - Simplify process of working with data
    - Easy to find current data
    - Easy to find old data
  - Simplify process of working with engineering tools
    - Allow engineer to work in familiar paradigm without usual overhead
      - Edit input and output files with a single click
      - Generate desired plots of a program run with a single click
    - Make programs easy to use
      - Reduce manual work
        - » Typing
        - » Data manipulation
      - Launch programs with a single click
        - » Run local
        - » Run remote

System Summary

- What are the top five reasons to use RECIPE©?
  - 1) Engineers get to work with their models in a familiar atmosphere and can easily receive data from other models as soon as it is ready!
  - 2) Engineers and managers can trace problems and know that finished data is secure from tampering and easily retrieved!
  - 3) Engineers and managers can easily view results and easily export those results to other presentations!
  - 4) Engineers can easily retrieve important data from other models and insert that data into their models!
  - 5) ISSI will provide support and do everything possible to satisfy you, the customer!

Contacting ISSI

- Interested parties can contact us at

International Space Systems, Inc.
500 Wynn Drive
Suite 306
Huntsville, AL 35816

(256)890-1178

issi@issi-hsv.com

Rethinking the Design Process
iSIGHT Framework

Presentation to TFAWs 2001

Mark Prow

Dr. Therese Rhodes

Engineous Software
200 CentreGreen Way, Suite 100
Cary, NC 27513
919-677-6756 fax 919-677-8911
www.engineous.com
mark.prow@engineous.com
therese.rhodes@engineous.com

Engineous Software Inc.

Product Creation:
A Brutally Multidisciplinary Challenge!

Collaboration Across Engineering Disciplines, Organizations, Product Components and Lifecycle Stages

Airframe Structure

Aerodynamics
Heat Transfer
Structural Mechanics
Structural Dynamics

Propulsion

Engine Cycle
Aerodynamic
Structural Mechanics
Combustion
Structural Dynamics
Weight

Mission

Fuel Burn
Economic Analysis
Range
Takeoff Gross Weight

Noise

Airport Noise
Cabin Noise

Electronic

Guidance/Control
Communications
Electric Power Supply

Cost

Manufacturing Cost
Inventory/Financial Cost
Product Lifecycle Cost

Engineous Software Inc.

Copyright 2001 Engineous Software

Design Data Islands

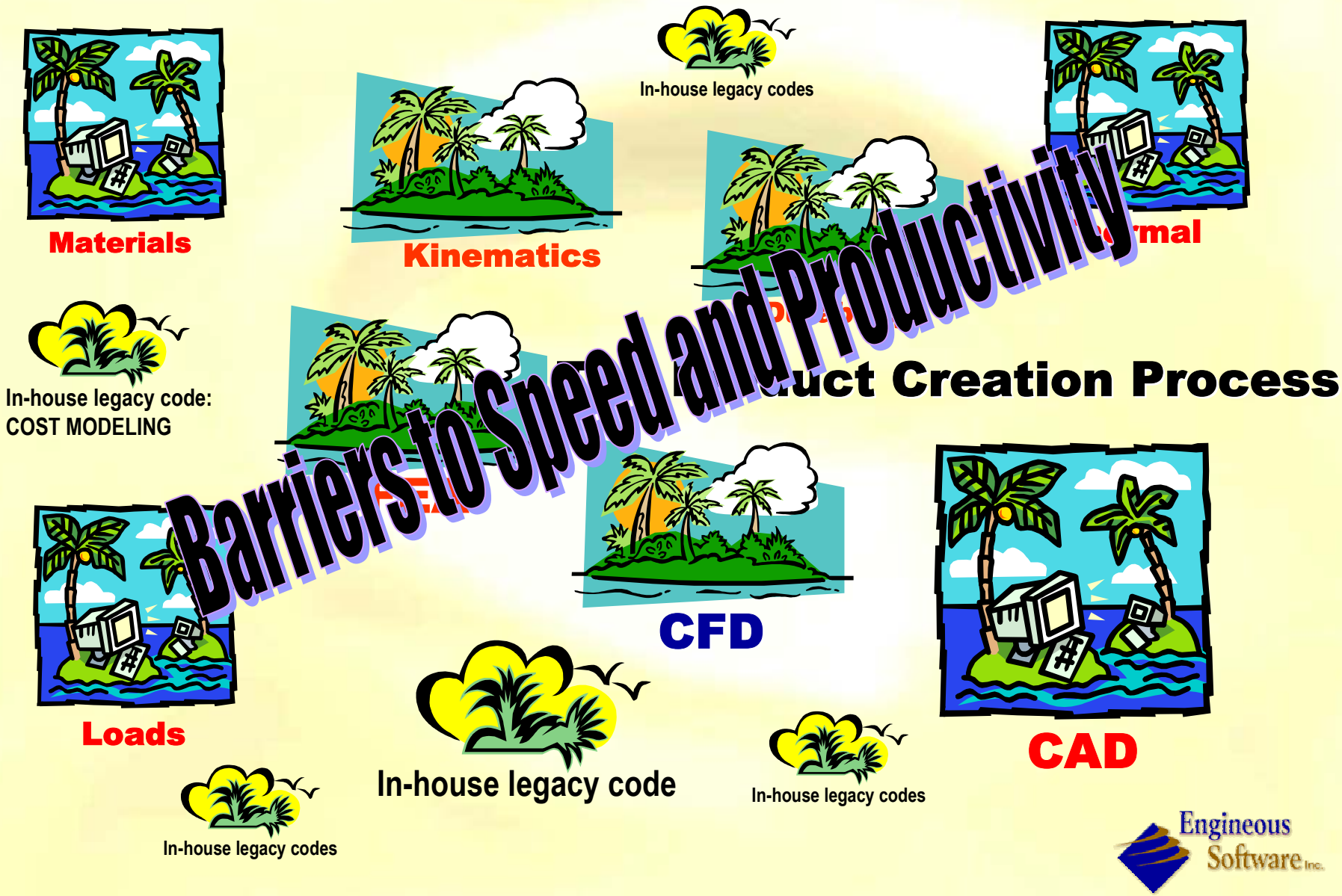

Copyright 2001 Engineous Software

Engineous History

A catalyst for engineering innovation!

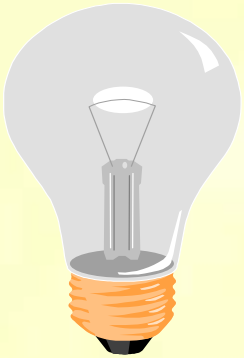

CR&D

Engineous

iSIGHT

"Software Robot" at MIT Invented by Dr. Tong	Engineous at GE >10 Years - $12 Million	1996 - Engineous founded 2001 - iSIGHT 6.0 released
1st. Generation	2nd Generation	3rd Generation

1979 — 1983 — 1996

Engineous Software Inc.

Copyright 2001 Engineous Software

Engineous People –Educational Snapshot

70 People Worldwide

- 61 Degreed Engineers
- 42 w/Advanced Engineering Degrees
- 10 Doctorate Level
- Industry Specific Experts- Automotive and Turbo Machinery. Substantial background at GM, GE, Cray Research, and NASA.
- Dr. Siu Tong – Founder and Chairman

  Over 20 years experience in the technology industry as a senior manager and in product research and development.

Engineous Software Inc.

Copyright 2001 Engineous Software

Helping Our Customers

Engineous Deploys Resources and Technology to:

1. **Help our clients integrate their diverse design tools**

2. **Automate their iterative design processes**

3. **Accelerate finding the best design solution**

Engineous Software Inc.

Copyright 2001 Engineous Software

Manual Design Evaluation Process

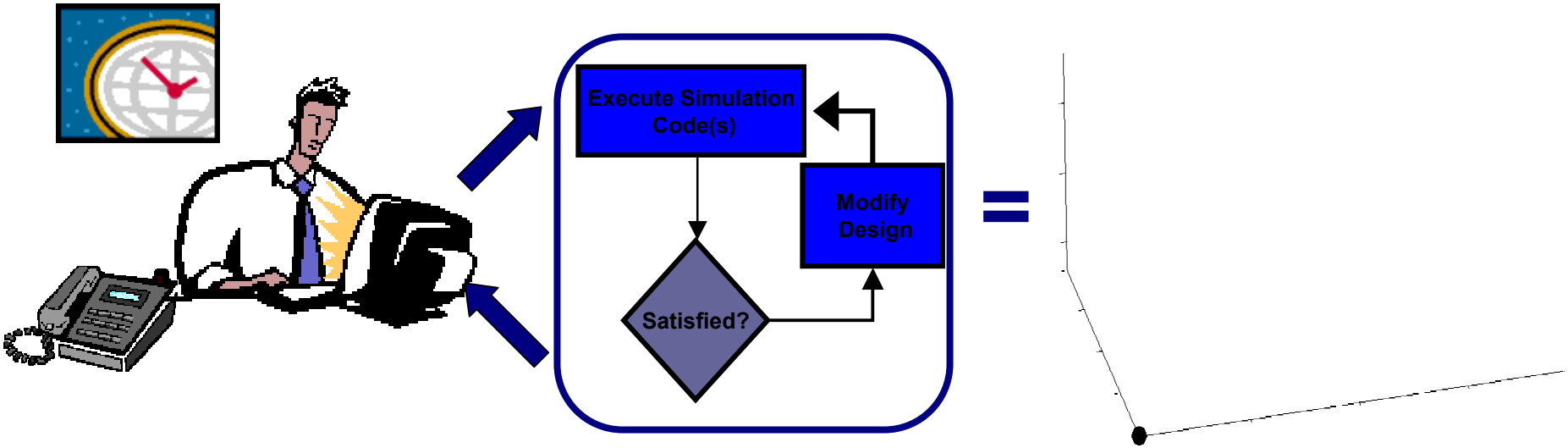

Manual Design Process

- Time consuming
- Error prone tasks
- Engineers spend more time preparing

Results

- Produces limited number of designs
- Produces questionable design quality
- Fewer design alternatives

Copyright 2001 Engineous Software

iSIGHT Software Robot

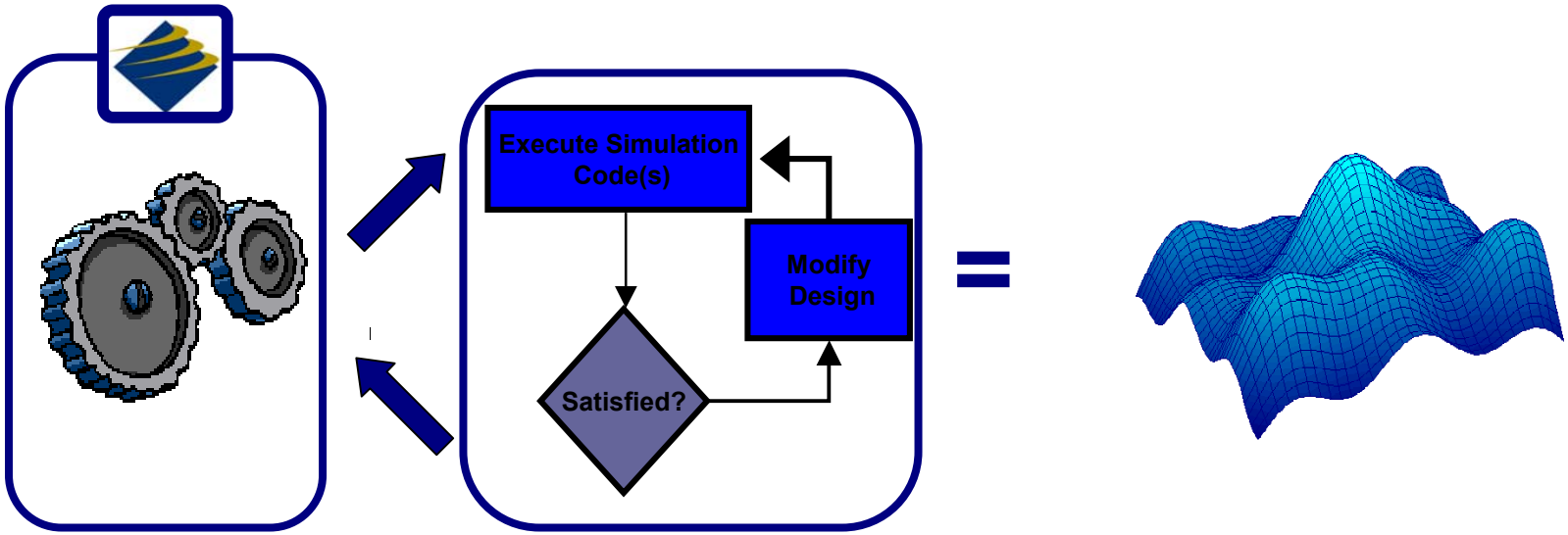

iSIGHT - Software Robot

- Engineer defines simulation process
- Engineer defines goals and constraints
- Robot applies design intelligence
- Automates and iterates design process
- 24 hour workday

Results

- Increased evaluations
- Improved quality
- Engineers spend more time evaluating
- Multiple design alternatives
- Saves valuable engineering time
- Greater product knowledge

Engineous Software Inc.

Copyright 2001 Engineous Software

Design Automation

iSIGHT

Integrates the Process

Automates the Execution

Evaluates the Alternatives

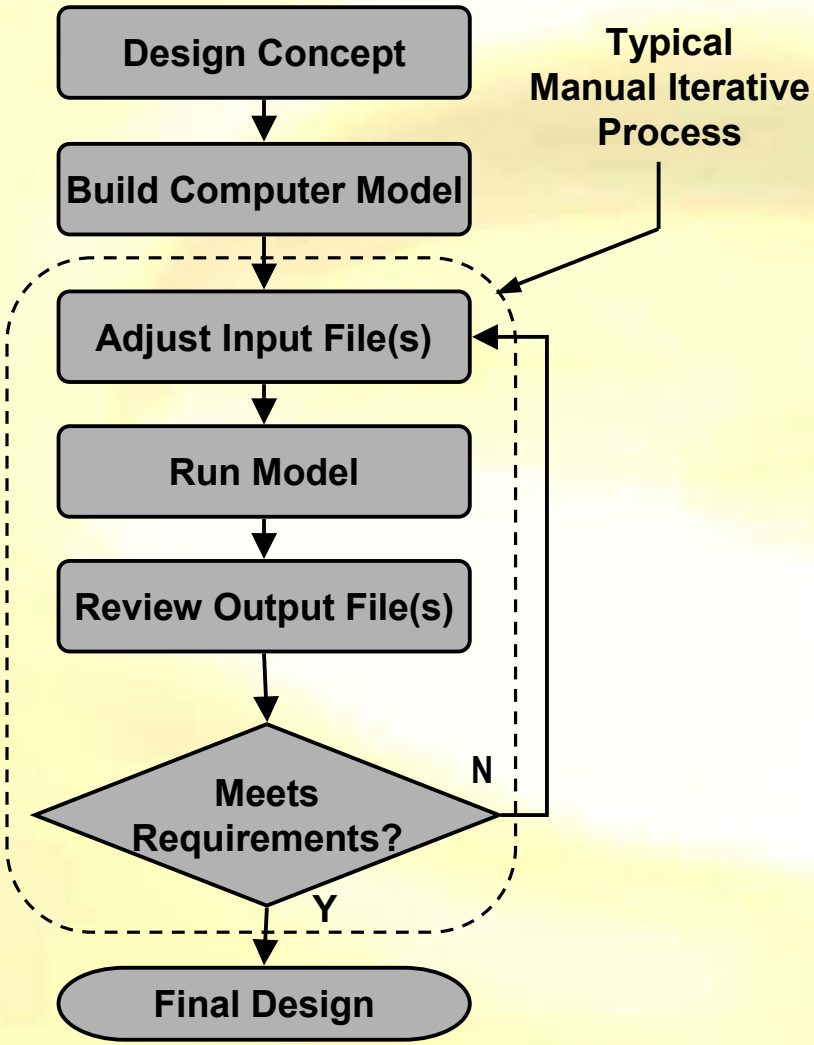

How does iSIGHT Modify Designs?

By Applying Design Intelligence to the iterative process through Design Study Tools

- *Deterministic*
- *Stochastic*

Copyright 2001 Engineous Software

Complete Design Exploration Engine

- Central Composite
- Full Factorial
- Orthogonal Array
- Latin Hypercube
- Parameter
- Database

- Rule-based
- Exploratory (GA etc)
- Gradient-based
- Mixed Variable

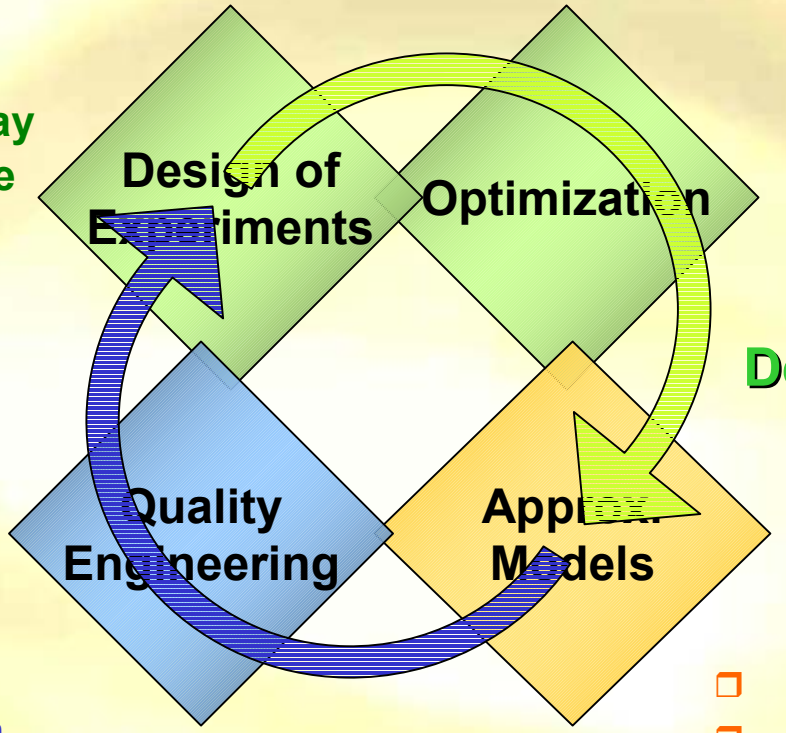

Deterministic Methods

- Monte Carlo
- Taguchi Robust Design
- Reliability Analysis
- Reliability-based Optimization
- Design for Six Sigma

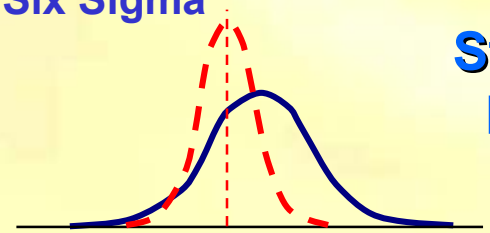

Stochastic Methods

- Taylor Series
- Response Surface
- Variable Complexity

Engineous Software Inc.

Copyright 2001 Engineous Software

New Design Process

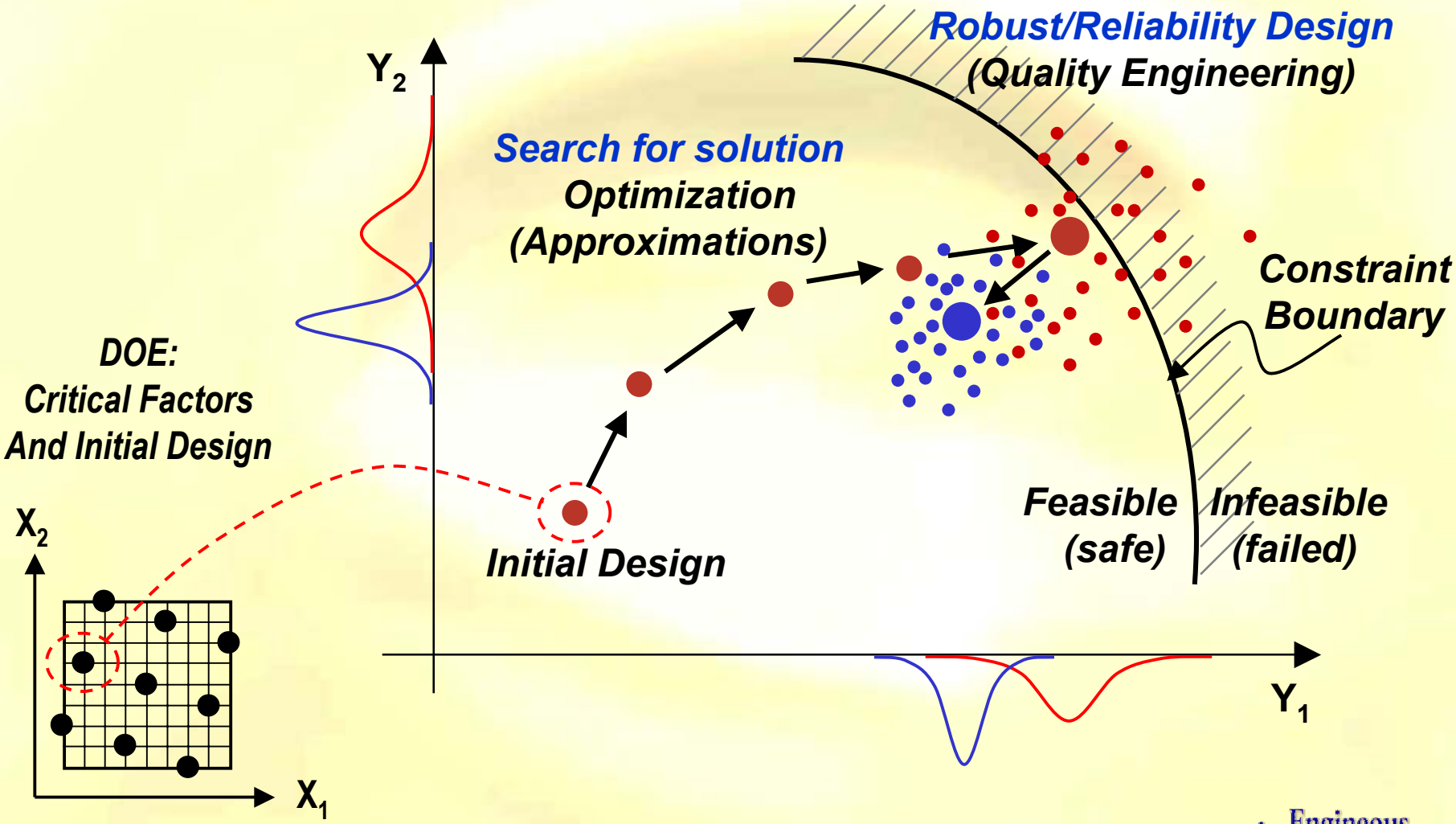

Copyright 2001 Engineous Software

GUI Interface

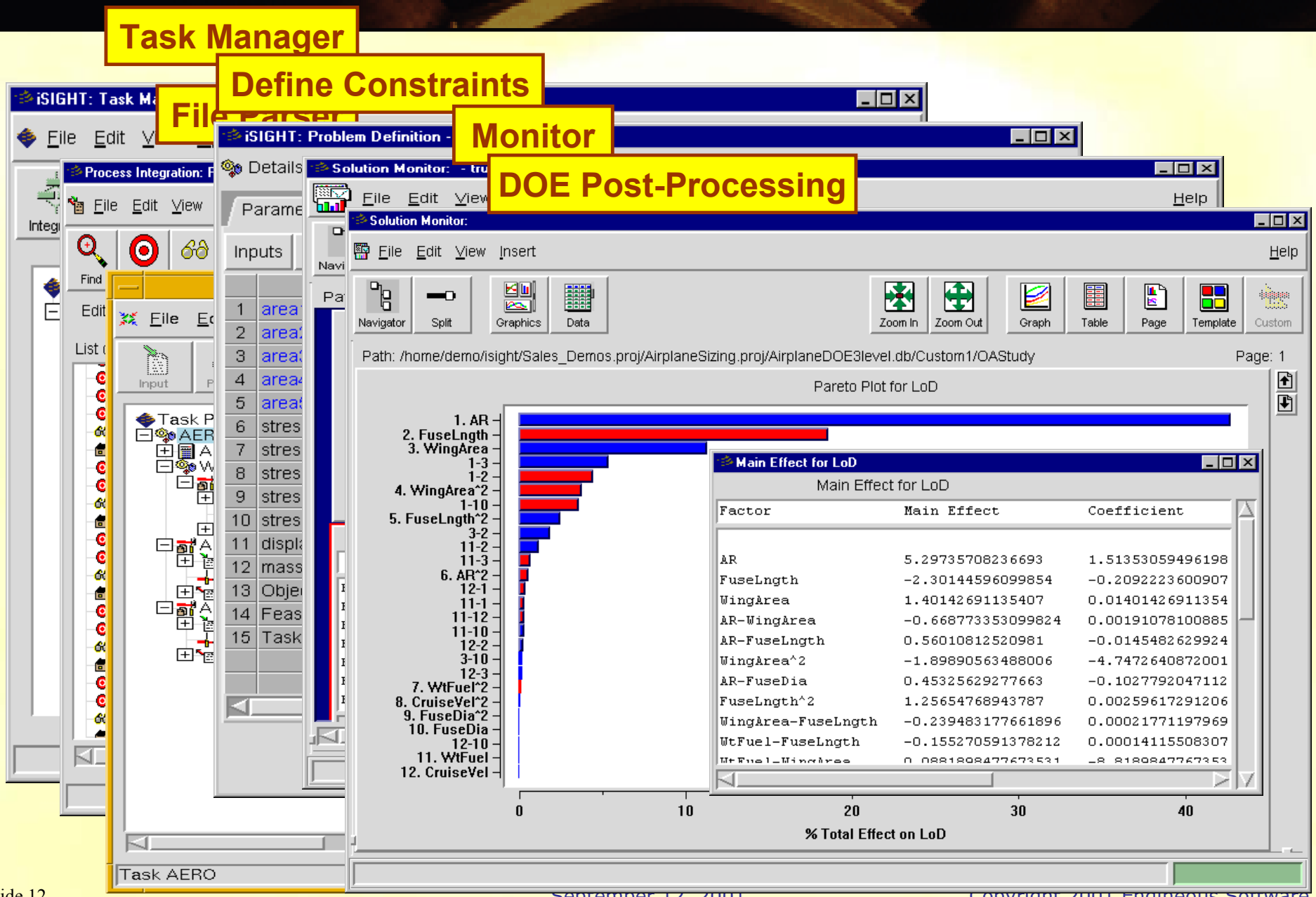

Copyright 2001 Engineous Software

Connectivity
A Sampling of Applications in Use at Our Customer Sites

- ASCII-based I/O Files using iSIGHT GUI

Structures:	**NASTRAN, MARC, ABAQUS, ANSYS**
Metal Forming:	**DEFORM, Procast**
CFD:	**STAR-CD, FLUENT, CFX, TASCflow, STREAM**
Crash/Impact:	**Pam-Crash, [illegible]**
Injection Molding	**[illegible]**
[illegible]	**[illegible]**
[illegible]	**ADAMS, DADS, Matlab, Matrix-X**
Engines:	**GT Power [illegible]**
Semiconductor [illegible]	**[illegible]**
CAD/[illegible]	**[illegible], Unigraphics, CATIA, PATRAN, Acumen, Hyper-Mesh, Gridgen, HICAD/CADAS etc.**
Turbomachinery	**Concepts NREC COMPAL, CCAD**
Thermo Cycle Analysis	**Legacy codes at GE, Toshiba, Honeywell, P&W, etc.**
General Math/Plotting:	**Mathcad, S-PLUS**
Many Internal Programs	

Virtually any Application Or Simulation Code

Engineous Software Inc.

Copyright 2001 Engineous Software

Platform Utilization

- Unix
  - Sun, SGI, HP, IBM, etc.
- Windows
  - NT, 2000
- Linux

- Parallel and Distributed Processing
  - Run multiple codes in parallel
  - Run parallel techniques (i.e., DOE, GA)
  - Distributed and enabled across heterogeneous network

Engineous Software Inc.

Copyright 2001 Engineous Software

Application Examples

- Multi-Stage Power Generator Steam Turbine
- DARPA: Integrated Disk Design & Manufacturing
- DARPA AIM (Project for Accelerated Insertion of Materials)
- Airframe/Propulsion Optimization
- Navy Propeller Conceptual Design
- Aerospike Nozzle Design
- America's Cup Yacht Design Prada's Luna Rossa

Engineous Software Inc.

Copyright 2001 Engineous Software

Multi-Stage Power Generator Steam Turbine

Problem: Reduce time required to design power plant turbines

Solution: Use Engineous software to integrate 29 codes

Result:

- **Design time reduced from 1 year to hours**
- **Major competitive advantage for GE Power Systems**

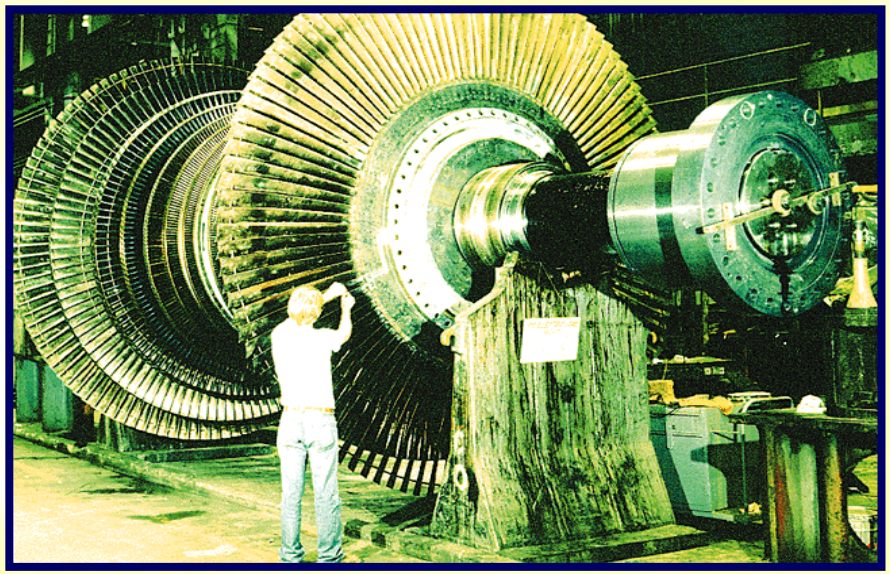

Engineous Software Inc.

Copyright 2001 Engineous Software

Multi-Stage Power Generator Steam Turbine

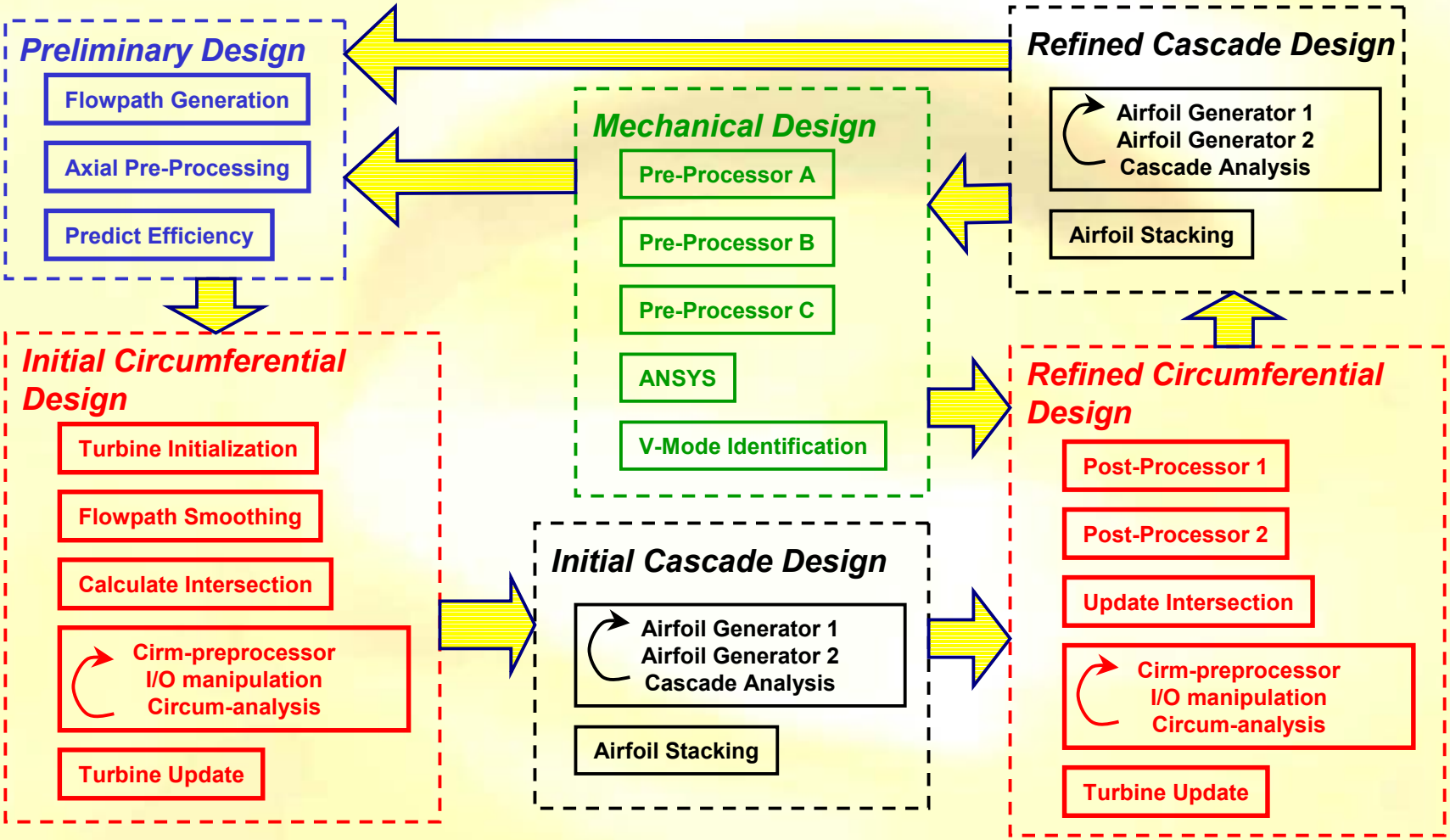

Engineous Software Inc.

Copyright 2001 Engineous Software

DARPA Program

- Integrated Turbine Disk Design

- Objective:
- Demonstrate geometry and finite element based multidisciplinary optimization (MDO) for complex product and process development

Copyright 2001 Engineous Software

DARPA: Integrated Disk Design & Manufacturing

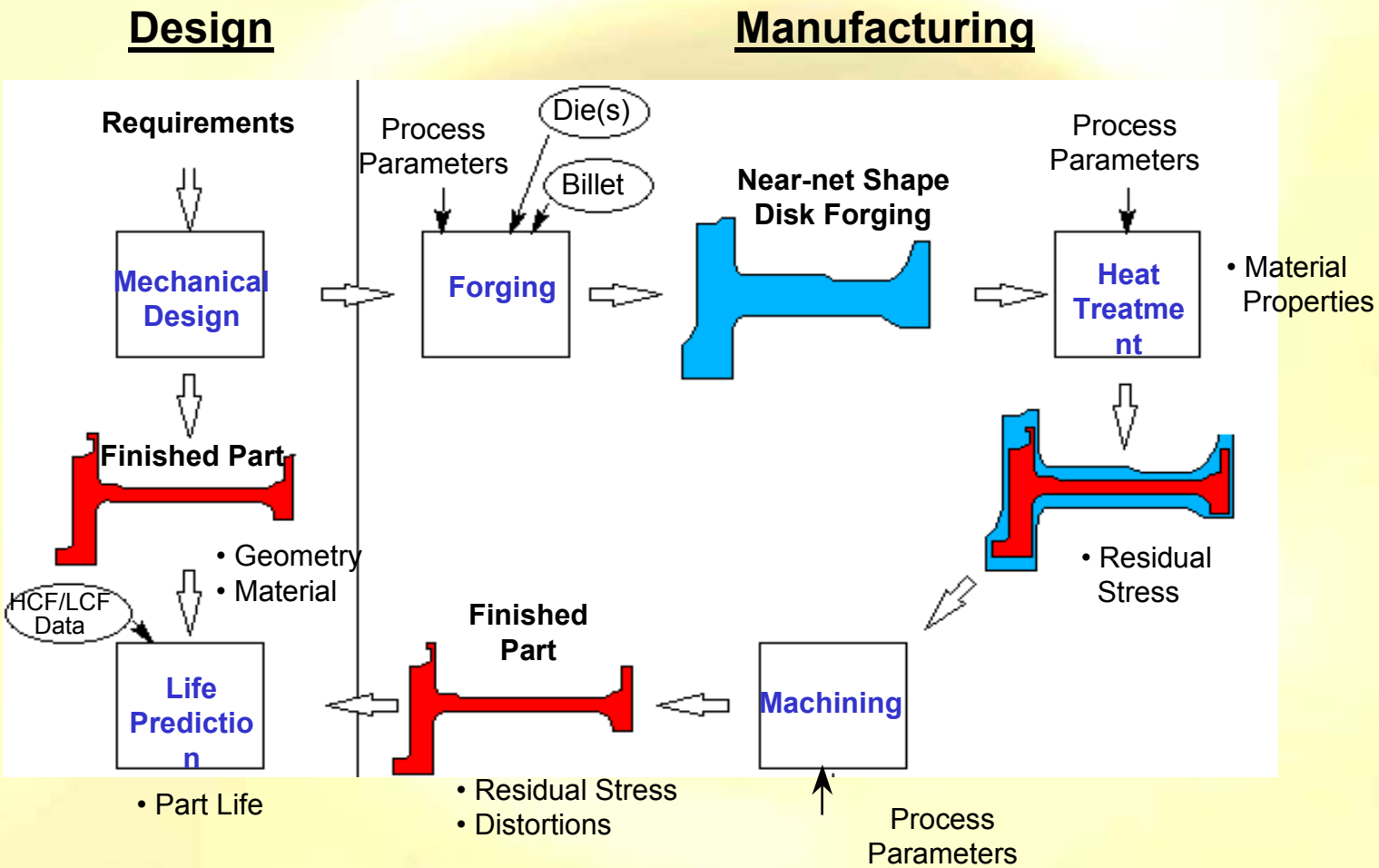

Copyright 2001 Engineous Software

DARPA: Integrated Disk Design & Manufacturing

- Mechanical Design
  - Meet Requirements
  - Minimize Weight
  - Minimize Cost
- Forging
  - Near Net Shape
  - Minimize Forging Operations
  - Formability
- Heat Treatment
  - Requisite Material Properties
  - Minimize Residual Stress
  - No Cracking
- Machining
  - Minimize Distortion
  - Minimize Number of Operations
- Life prediction
  - Required Life

Engineous Software Inc.

Copyright 2001 Engineous Software

DARPA: Integrated Disk Design & Manufacturing

The Problem:

Residual Stresses Introduced during Heat Treatment lead to distortions of the Finished Part

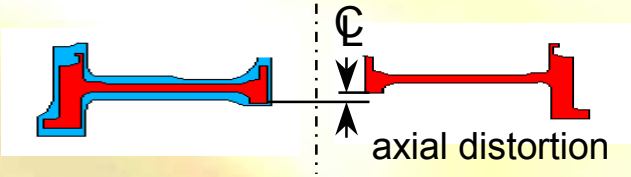

Minimize Non-uniform Cooling for Reduced Residual Stresses
Cooling Rate Constraints for Creep Performance
Surface Heat Transfer Coefficients h_i

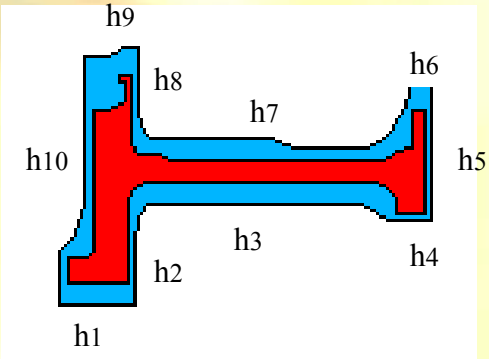

The Tools: **iSIGHT** **Finite Element Analysis (DEFORM)**

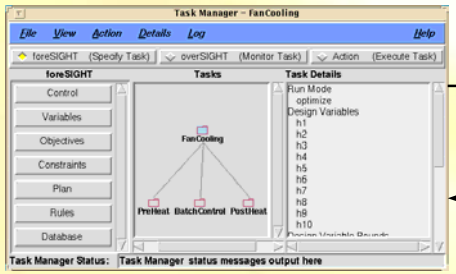

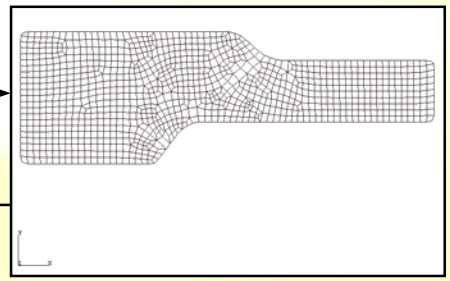

Cooling Rate Optimization

Engineous Software Inc.

Copyright 2001 Engineous Software

DARPA: Integrated Disk Design & Manufacturing

Initial Cooling Rates

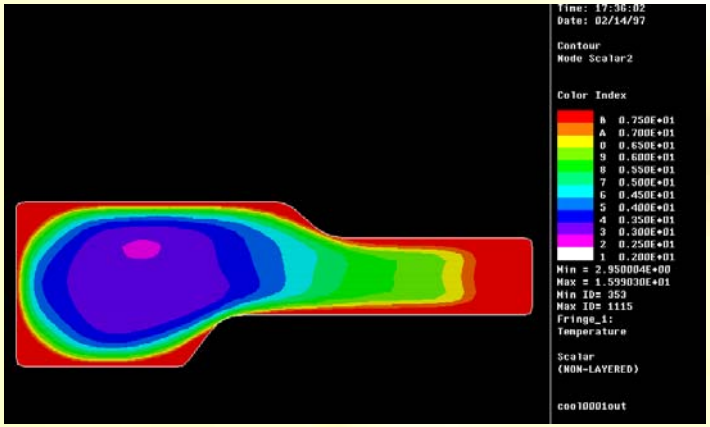

Initial Hoop Stress Distribution

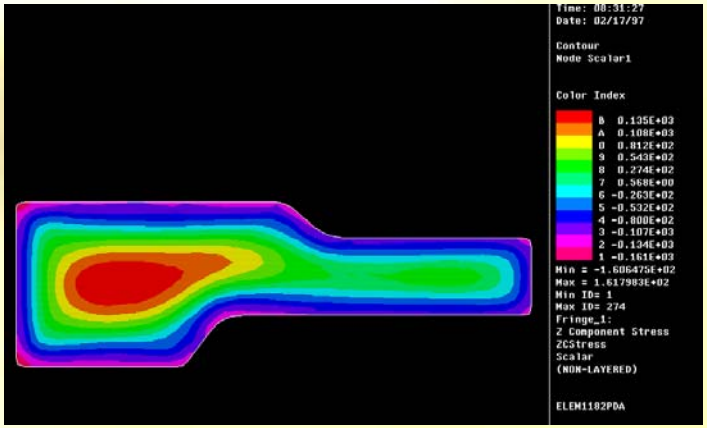

Final Cooling Rates

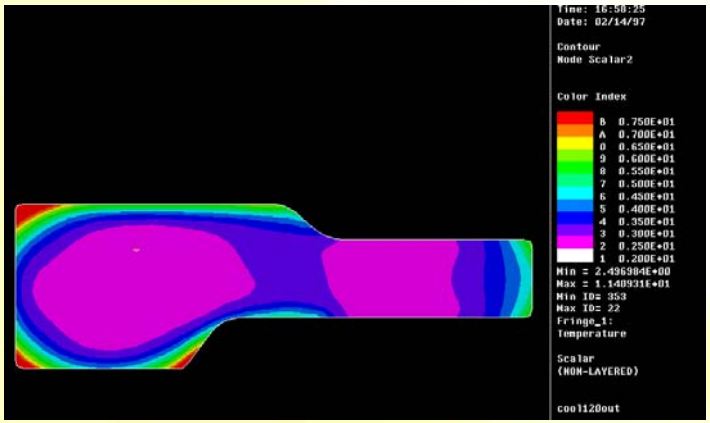

Final Hoop Stress Distribution

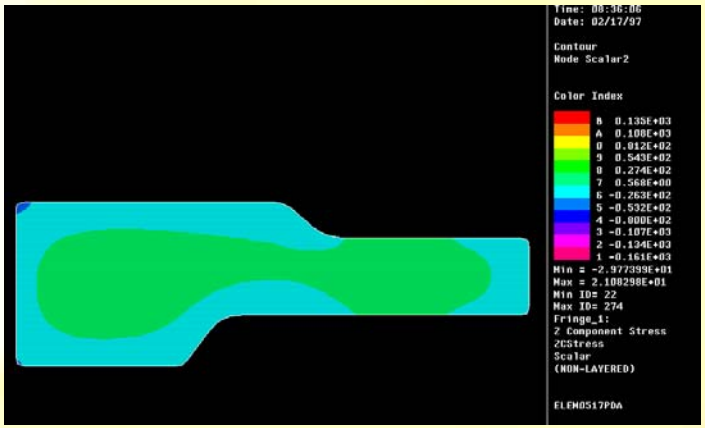

- Cooling Rate Distribution more Uniform
- Cooling Rate Target Met

Maximum Stresses Reduced by about 80 %

Cooling Rate and Stress Results

Engineous Software Inc.

Copyright 2001 Engineous Software

DARPA: Integrated Disk Design & Manufacturing

Forging Die Speed Optimization Objective:

To forge the billet into a high pressure turbine disk such that the maximum strain rate in the deformable work piece never exceeds 0.008 s^{-1} during forging.

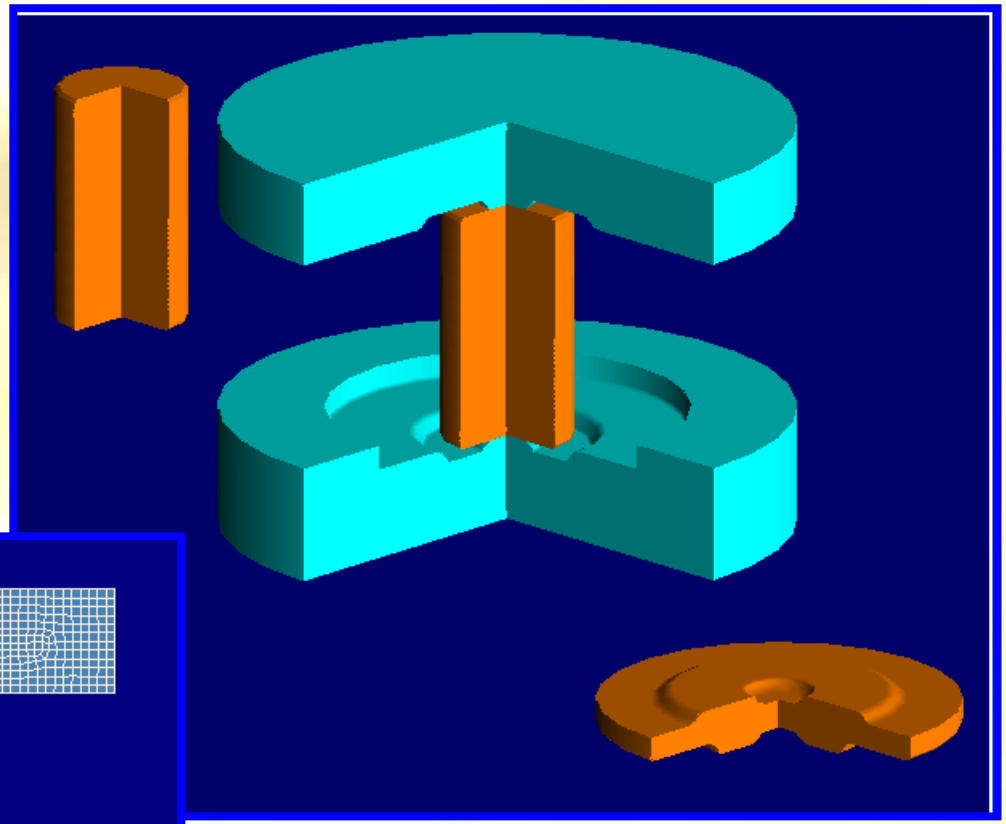

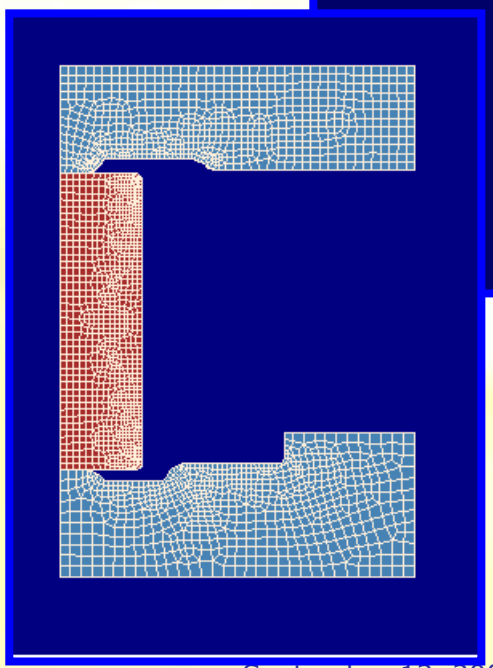

Engineous Software Inc.

Copyright 2001 Engineous Software

DARPA: Integrated Disk Design & Manufacturing

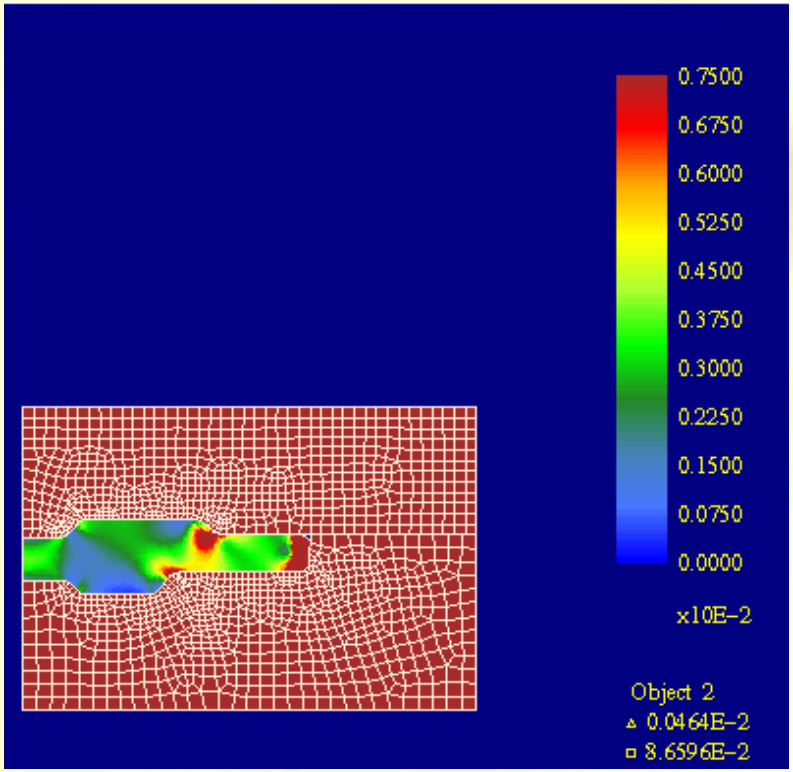

Conventional Approach Results

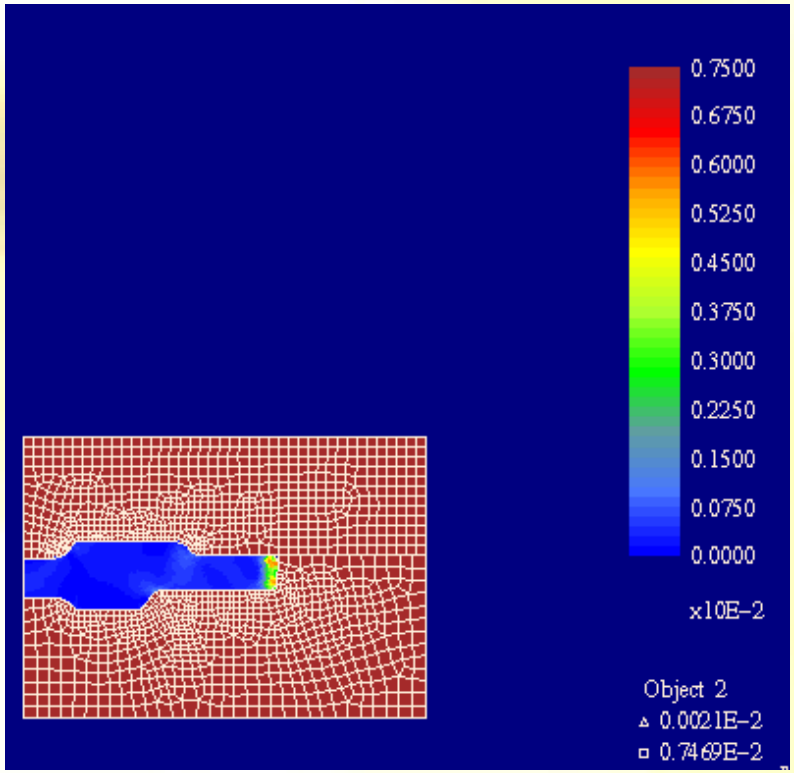

Optimized Approach Results

Forging Die Speed Optimization: Equivalent Strain Rate Contours

Engineous Software Inc.

Copyright 2001 Engineous Software

DARPA: Integrated Disk Design & Manufacturing

iSIGHT

Unigraphics

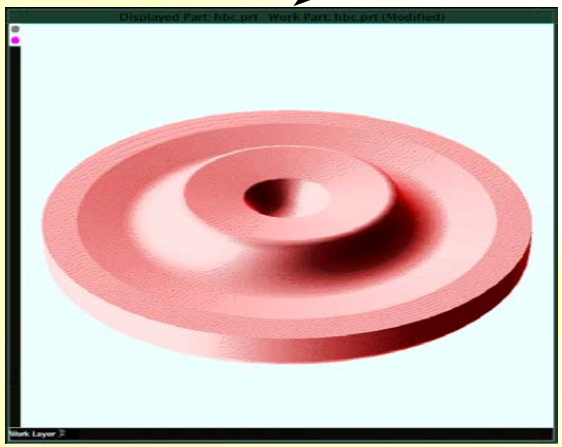

DEFORM

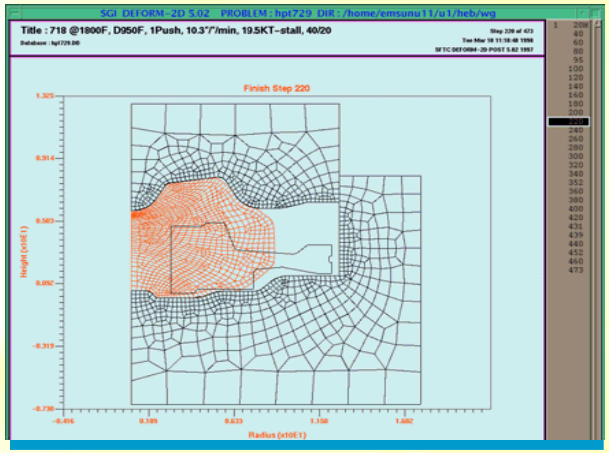

Forging Die Shape Optimization

Engineous Software Inc.

Copyright 2001 Engineous Software

DARPA: Integrated Disk Design & Manufacturing

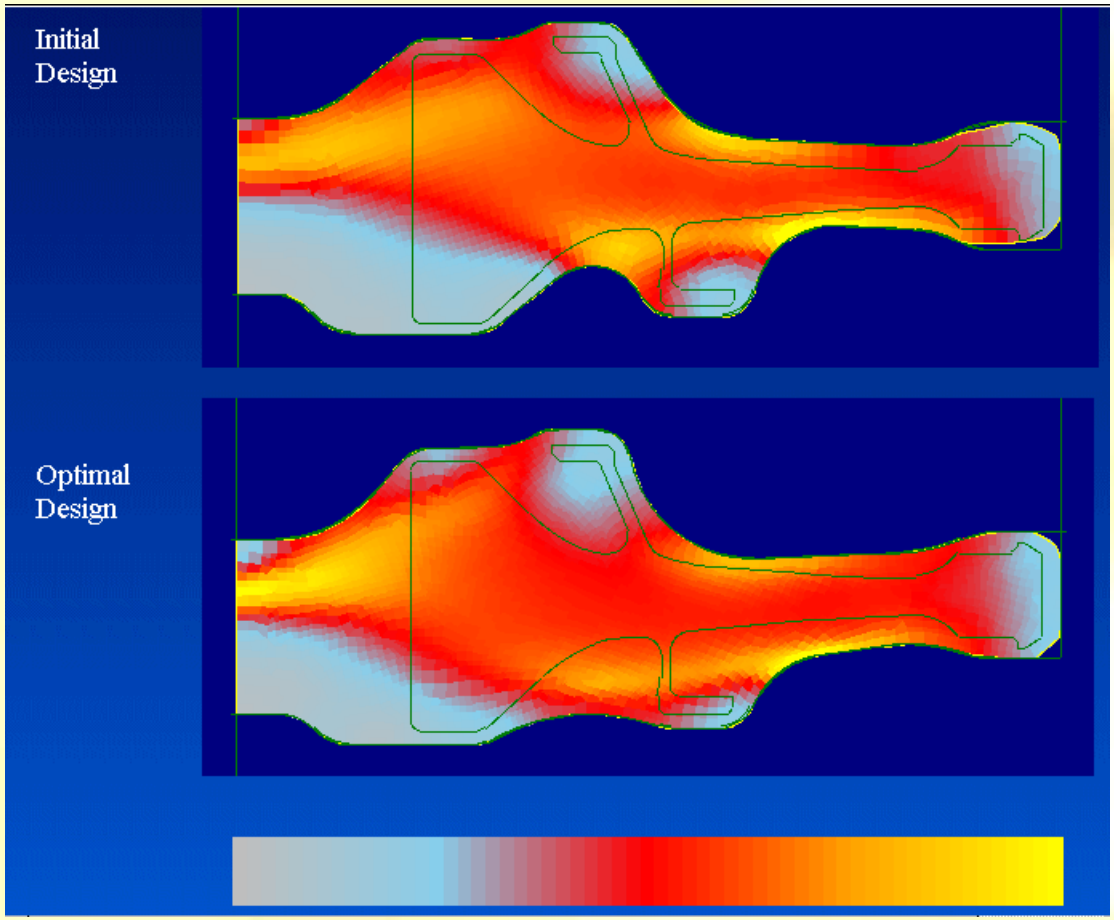

The strain distributions of the initial and optimal designs. The low strain region is reduced in the optimal design. All data is normalized.

Forging Die Shape Optimization:
Normalized Strain Distributions

Copyright 2001 Engineous Software

DARPA: Integrated Disk Design & Manufacturing

High Pressure Turbine Disk

Stage 9 Compressor Disk

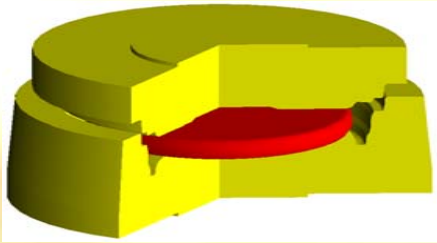

Summary:

- **Forging Optimization System Has Been Applied to Several Disks**
- **Demonstrated Weight Reductions of 11% (average) Over Manually Optimized Designs**
- **Transition of Software to Forging Vendors In-Progress**

Stage 1 Fan Disk

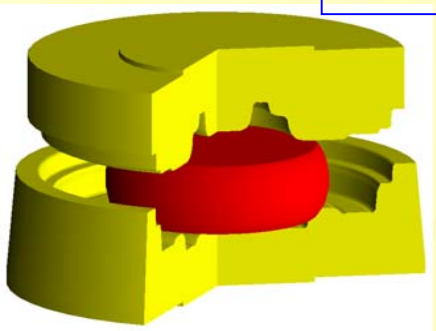

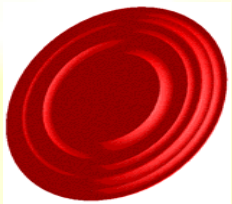

Forward Seal

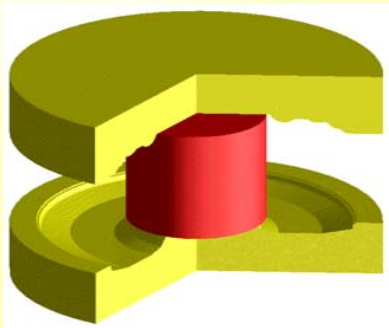

Engineous Software Inc.

Copyright 2001 Engineous Software

DARPA AIM (Project for Accelerated Insertion of Materials)

- **Goal:**
  - Develop a rotor component design system - called "aimSIGHT" - that allows material forming process parameters to be tuned automatically to achieve desired material properties and component performance, thereby dramatically reducing the time needed to develop new materials
  - Account for real world uncertainties in manufacturing process, material properties, tolerances, material behavior predictions, etc.

- **Team Members:**
  - Pratt & Whitney (Lead)
  - Scientific Forming Technologies Corp.
  - Ladish Co.
  - Engineous Software Inc.
  - Brown University
  - Carnegie-Mellon University
  - University of Connecticut
  - Drexel University
  - Lehigh University
  - University of Michigan
  - Michigan Technological University
  - MIT
  - Northwestern University
  - West Virginia University

Engineous Software Inc.

Copyright 2001 Engineous Software

“aimSIGHT” Design System

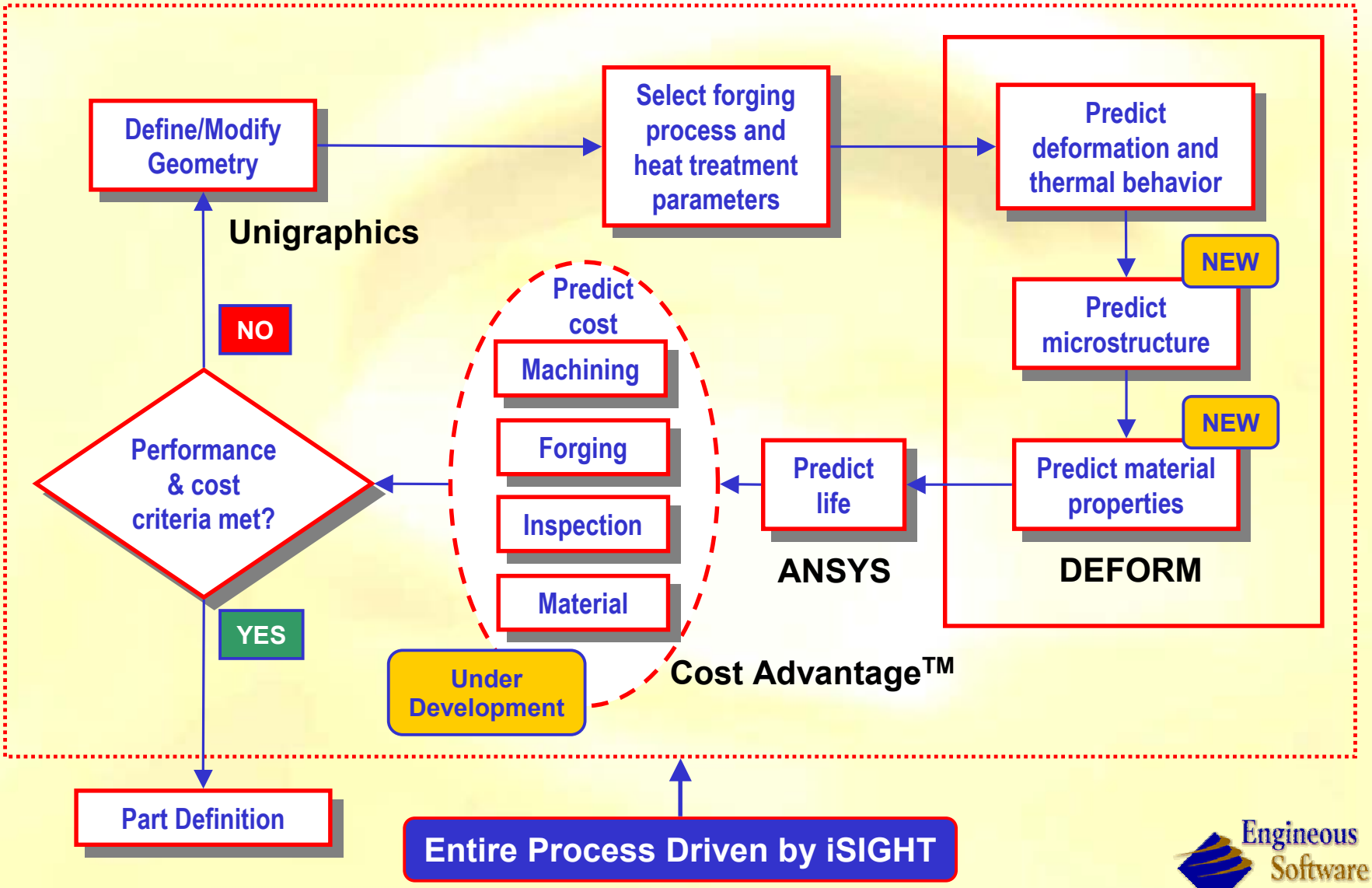

Copyright 2001 Engineous Software

Airframe/Propulsion Optimization

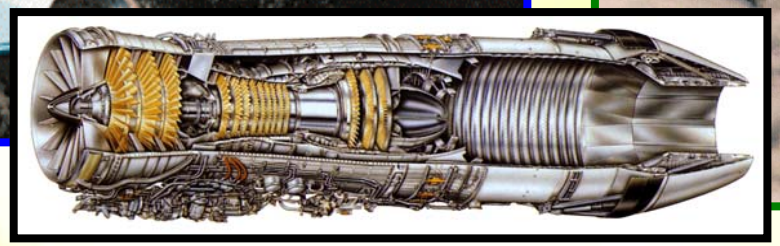

The Problem:

Determine the optimal cycle and minimum engine size to match a given engine to an airframe for optimal aircraft performance.

Engineous Software Inc.

Copyright 2001 Engineous Software

Integrated Airframe/Propulsion Optimization

Objective: **Determine the optimal cycle and minimum engine size to match a given engine to an airframe for optimal aircraft performance.**

Mission
- Maneuvers
- Cruise
- TO/LD

Engines
- F404
- F110
- F120

Airframes
- Commercial
- Fighter
- Bomber

Propulsion Installation → **Engine Sizing** ← **Inlet & Nozzle Selection**

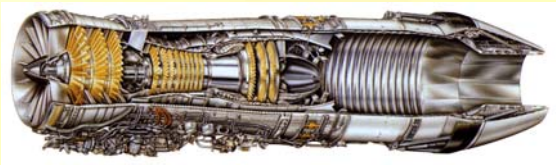

Optimum Aircraft Performance

Copyright 2001 Engineous Software

Integrated Airframe/Propulsion Optimization

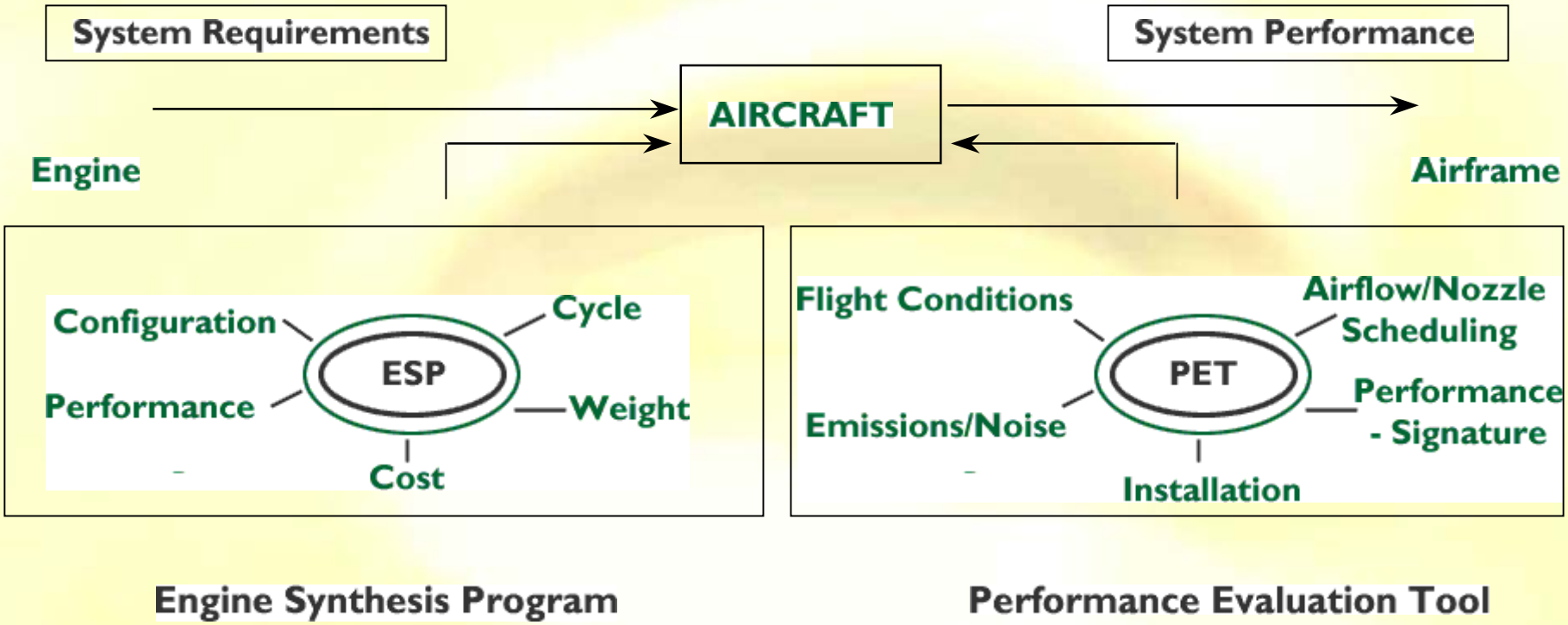

<u>Conclusion</u>: Design optimization using preliminary design tools allows efficient evaluation of complex engineering systems & scenarios that can improve designs to achieve enhanced performance and reduce cycle times at lower cost

Copyright 2001 Engineous Software

Integrated Airframe/Propulsion Optimization

Performance Optimization

Maximum Thrust

Subject to Constraints

0.0	<	ByPass Ratio	< 1.0
0.4	<	Fan Pressure Ratio	< 1.0
0.4	<	Overall Pressure Ratio	< 1.0
0.2	<	Inlet Airflow	< 1.0
0.8	<	Throttle Ratio	< 1.0

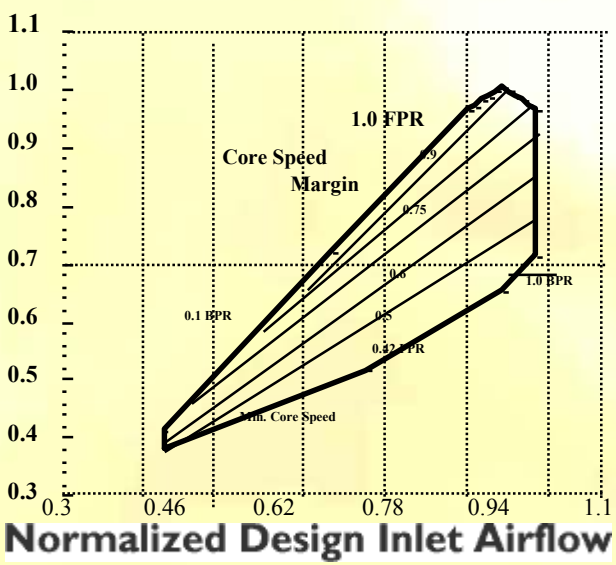

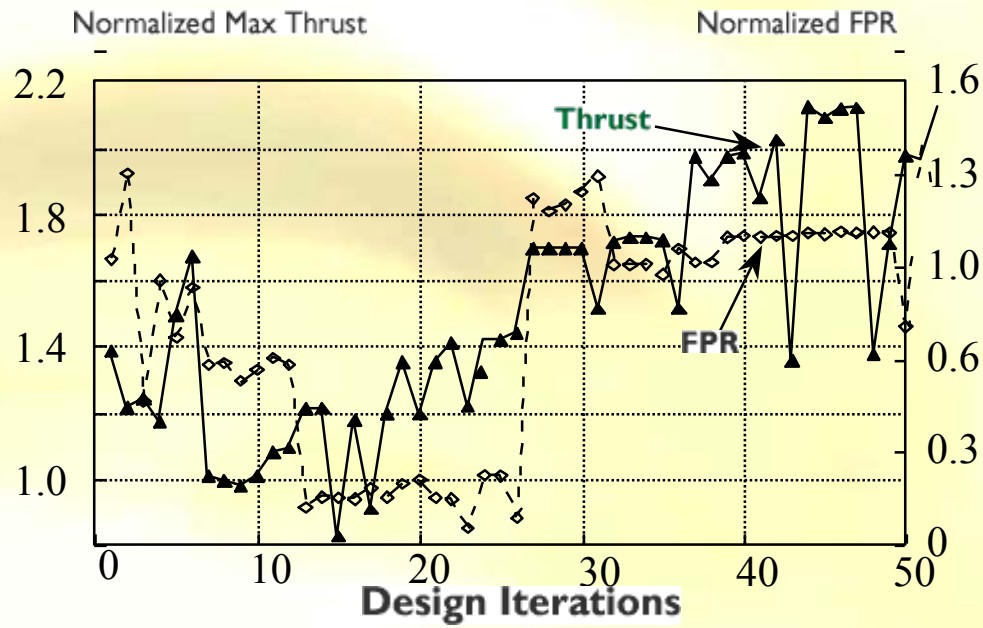

Initial Design

Thrust: 1.56, Weight: 1.08

Length: 1.25, Inlet Diameter: 1.2

Inlet Airflow: 1.5, FPR: 2.4

Final Design

Thrust: 2.0, Weight: 1.43

Length: 1.38, Inlet Diameter: 1.4

Inlet Airflow: 1.47, FPR: 1.7

Copyright 2001 Engineous Software

Navy Propeller Conceptual Design

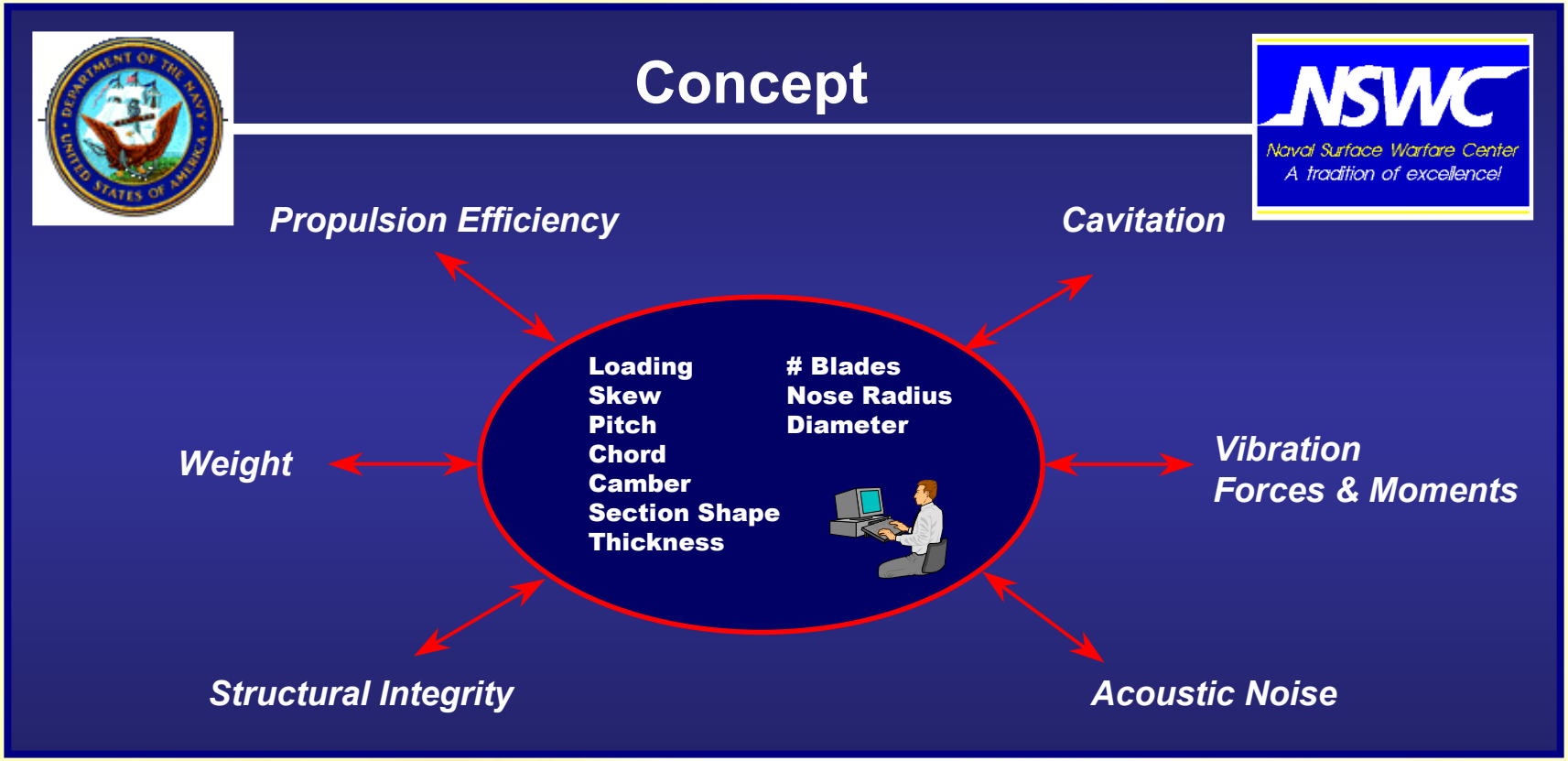

The Problem:

Balancing the <u>competing</u> design requirements and constraints of 6 engineering groups to create the best overall propeller

Engineous Software Inc.

Copyright 2001 Engineous Software

Navy Propeller Conceptual Design

Benefits

- Better Design in Reduced Time
  - Typical Single-Screw Propeller Design

Manual	*Engineous*
70% of Time Spent Preparing Design Alternatives *30% of Time Spent Evaluating and Engineering Design Alternatives*	*5% of Time Spent Preparing Design Alternatives* *95% of Time Spent Evaluating and Engineering Design Alternatives*
Average Preliminary Design Time: 2 Months	*Average Preliminary Design Time: 3 Weeks*
Limited Number of Design Alternatives Evaluated	*10-100 Times More Design Alternatives Evaluated*

Copyright 2001 Engineous Software

Aerospike Nozzle Design

NASA Langley

- **Problem:** Minimize the Gross Lift-off Weight. Requires modeling effects of 4 domains, namely structures, CFD, baseflow, and performance domains

  18 design variables, 564 constraints

- **Solution:** Coupled iSIGHT with multiple codes and implemented multidisciplinary feasible (MDF) strategy

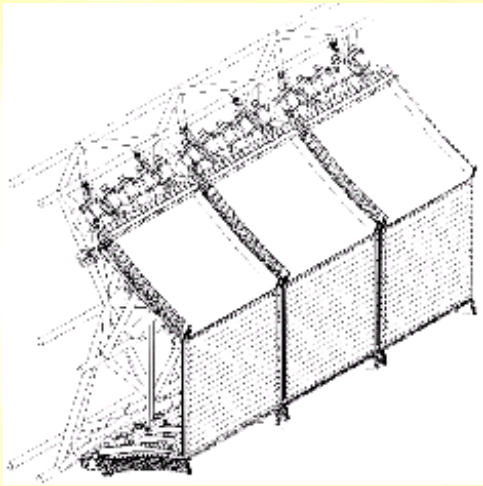

- **Results:**

  "iSIGHT reduces code and file management for the user"

  "iSIGHT reduces time required to explore variety of optimization schemes and design parameters"

Engineous Software Inc.

Copyright 2001 Engineous Software

Trim Optimization

- Optimize yacht position (trim) to minimize drag and maximize speed for given sea surface shape

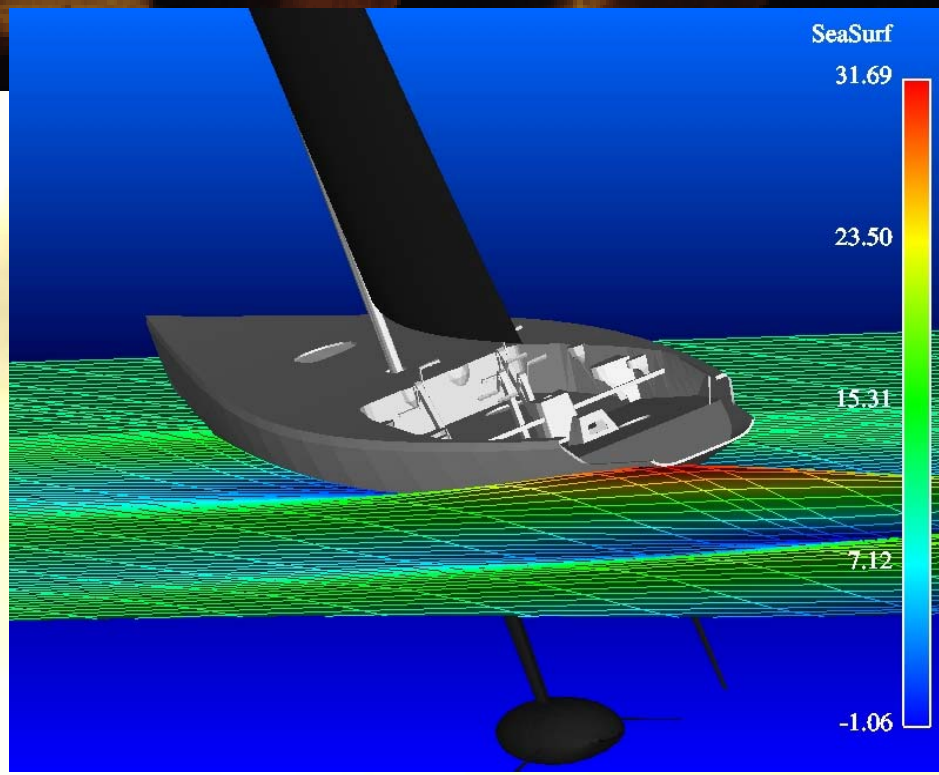

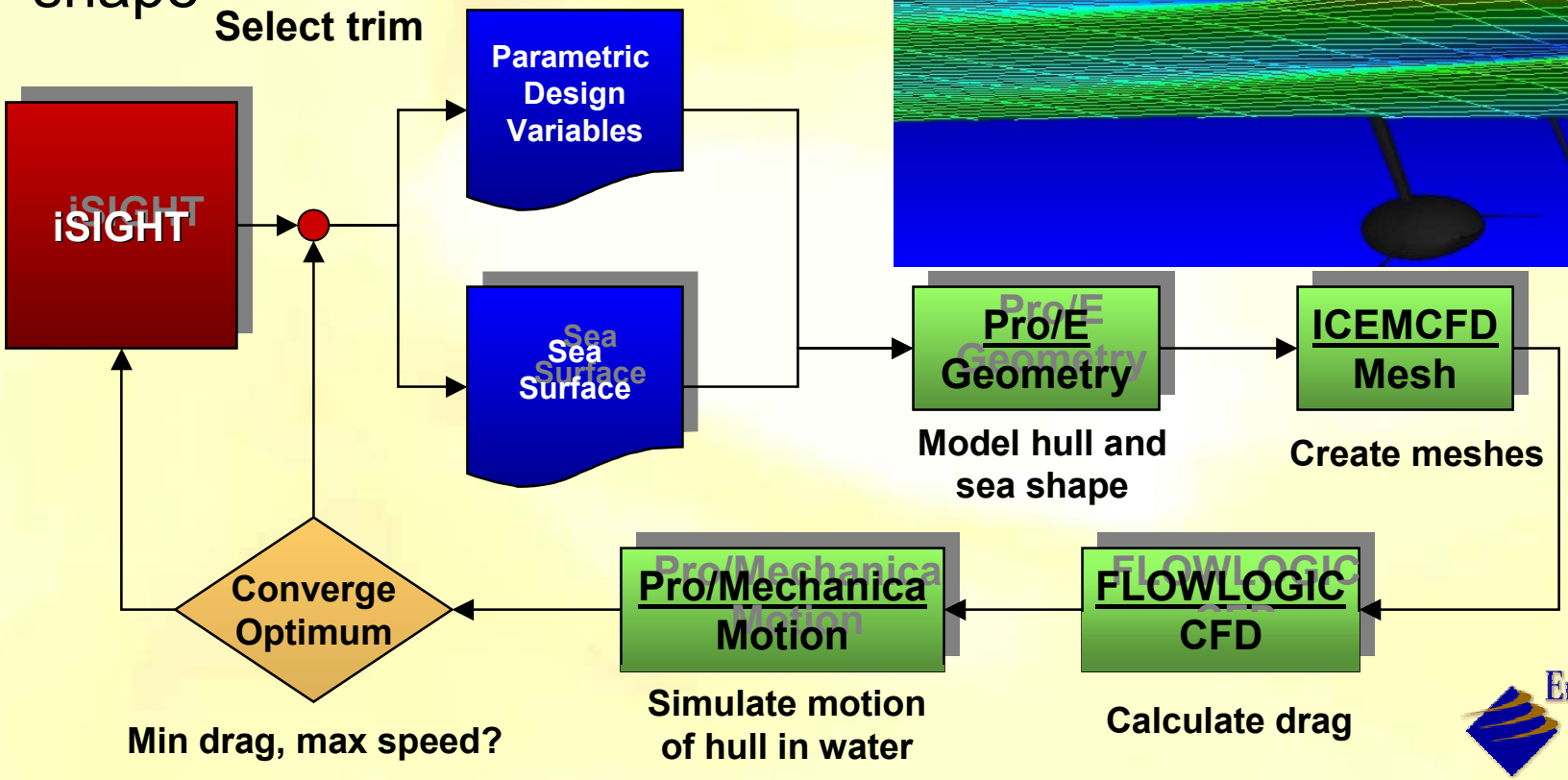

Copyright 2001 Engineous Software

Automating Hull Design

- 1000's of configurations analyzed in CFD
- *20-50* per day
- iSIGHT-based design system directly optimizes Pro/ENGINEER model
- <u>Final result:</u>

  Correct new 3-D Pro/E geometry for manufacturing, no prototyping!

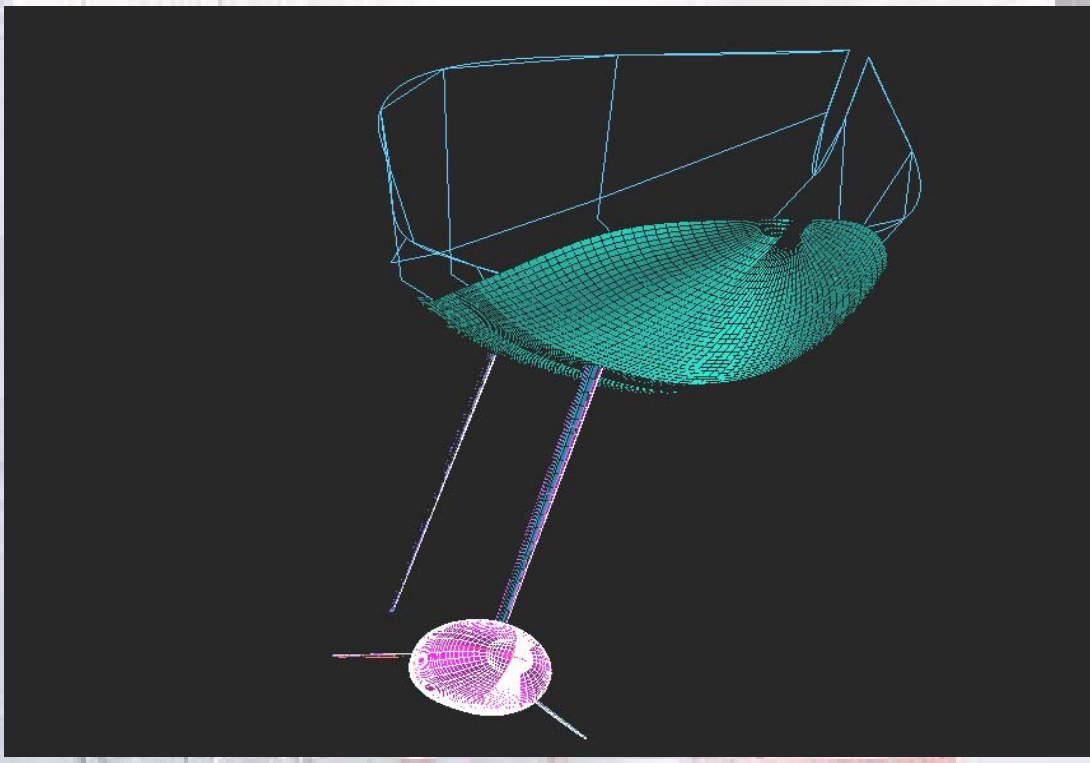

The Future is now!

Internet Design Collaboration

Engineous Software Inc.

Copyright 2001 Engineous Software

Engineering "Collaboration" through Shared Models

People interactively work with the same model, sharing control and seeing the execution results of other team members.

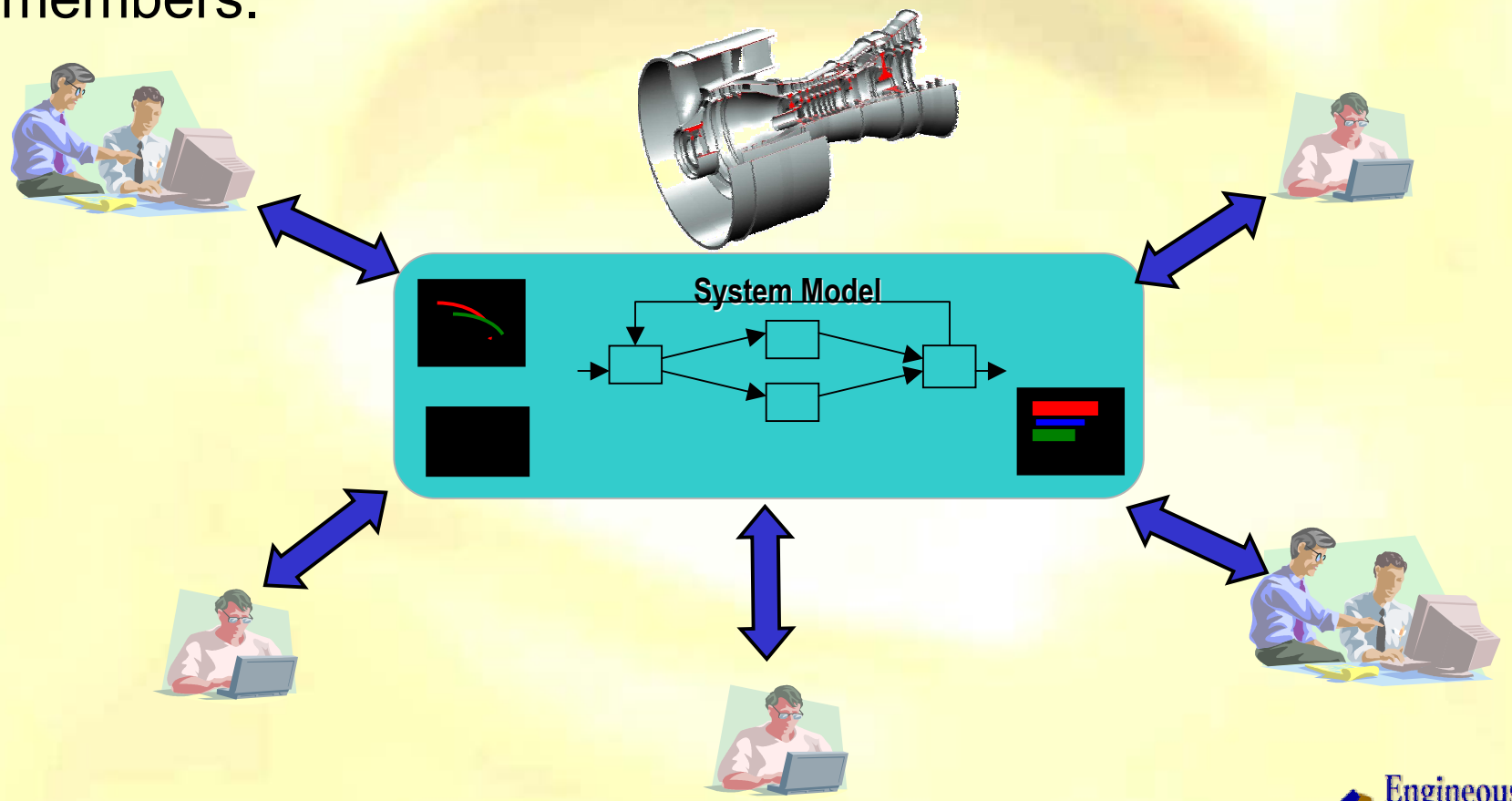

Copyright 2001 Engineous Software

iSIGHT Collaboration

- iSIGHT Collaborator (ISC)

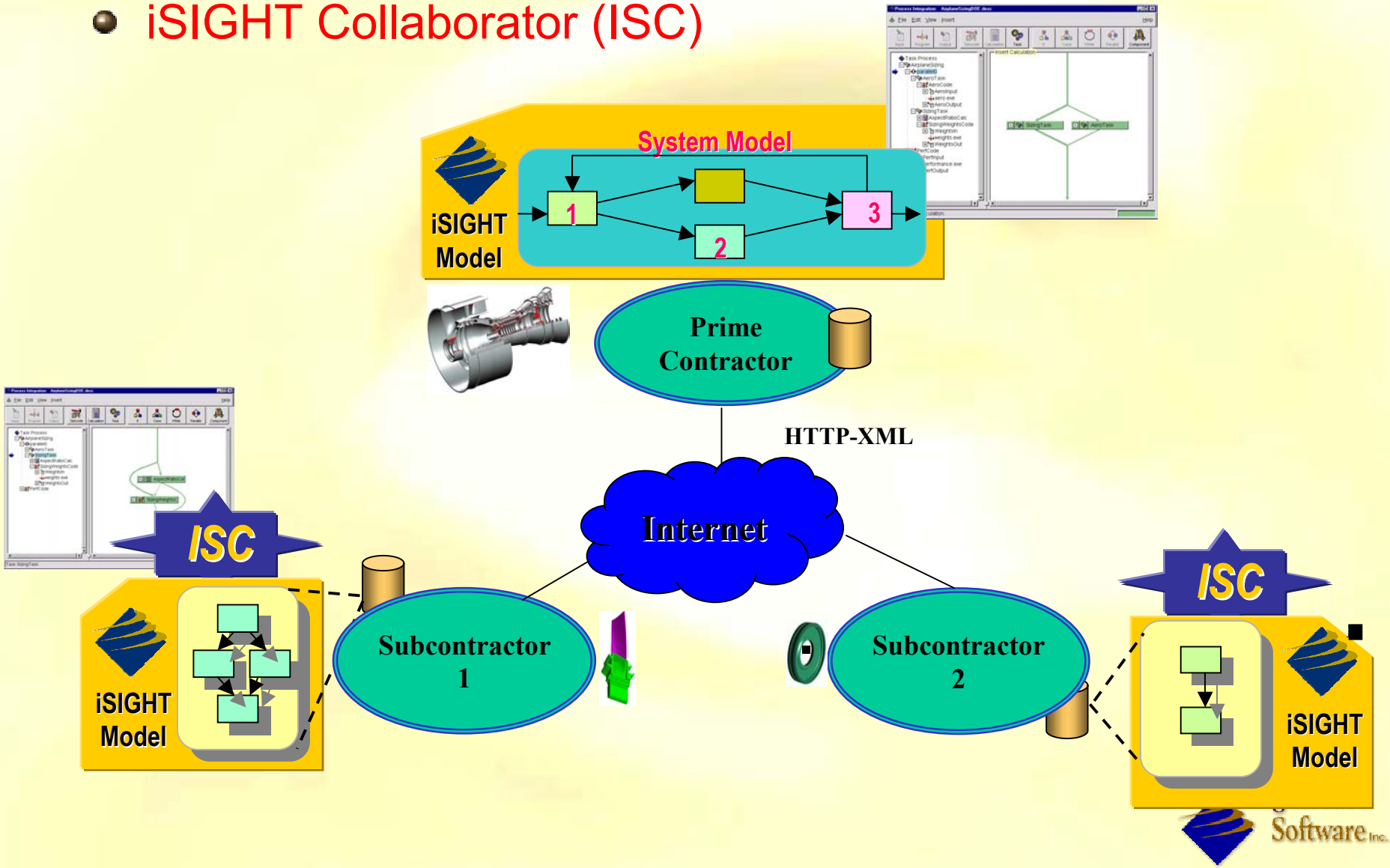

Copyright 2001 Engineous Software

Next Step

- Develop a “Federated Intelligent Product EnviRonment” (FIPER) that allows companies to globally —
  - Collaborate with dispersed design teams and business partners
  - Establish standard language protocol for all design tools, legacy data and systems
  - Access best-of-breed design and analysis tools
  - Automate non-creative tasks in the design process

Engineous Software Inc.

Copyright 2001 Engineous Software

What is FIPER

- A NIST sponsored and funded ($21.5M) project to develop:
- An internet-based distributed framework
  - Supports collaboration among geographically distributed engineering and business partners.
- A service-oriented product development environment
  - Provides an open flexible design environment which allows universal availability and incorporation of existing data, tools/methods and processes as services.
  - Provides a common way to model your analysis and design process in conjunction with your product data.

Engineous Software Inc.

Copyright 2001 Engineous Software

FIPER Consortium

FIPER

GE

Engineous Software Inc.

Parker

Rolls-Royce

NASA

Honeywell

GOODRICH

Stanford University

OHIO UNIVERSITY 1804

OAI

www.fiperproject.com

Engineous Software Inc.

Copyright 2001 Engineous Software

Summary

iSIGHT provides a framework which:

- Enables data exchange between applications in similar or diverse disciplines.
- Automates the iterative nature of the design process
- Applicable in all stages of the design process.
- Allows for automation and design exploration on the component, subsystem, and/or system level
- Allows users to quickly couple and drive their design and analysis tools of choice, use “best in class” for each discipline
- Provides a set of tools to explore design alternatives and improvements

Copyright 2001 Engineous Software

Conclusions

Utilization of the iSIGHT Framework throughout the design process (especially at the early conceptual design stage) has dramatic effects on:

- Lowering Costs
- Improving Safety and Reliability
- Reducing Design Cycle Time
- Improving Quality
- Improving Manufacturability

SLI (2nd gen) goals:

- *Reduce cost of launch to low earth orbit to $1,000 per pound of payload*
- *Improve safety of loss of crew to 1 in 10,000 flights*

Engineous Software Inc.

Copyright 2001 Engineous Software

powering collaborative commerce

i-man

TFAWS MDA Panel Session – September 12, 2001

Mitchell Bailey

PLM Technical Specialist

Mitchell.Bailey@ugs.com

agenda

- UGS Company introduction
- UGS Product offerings
- i-man detailed overview
- What the future holds

a new leader

Newswire May 23…EDS announced an agreement to purchase SDRC … EDS will offer to buy the 14 percent of its UGS subsidiary … to become EDS' fifth line of business. This move reshapes the CPC and CAPE landscapes with a services and software organization of over 5,000 employees and approximately $1.2 billion in revenues …

The merger will spur innovation and benefit all customers, both our customers and the customers of our competitors.

EDS PLM Solutions

Product Lifecycle Management

EDS

about UGS

… impeccable credentials

- Consistent performer
- Proven track record of partnerships
- Open technology and business culture
- Global execution
- Repeatable processes

global quality accreditation

ISO 9001

adding value across the enterprise

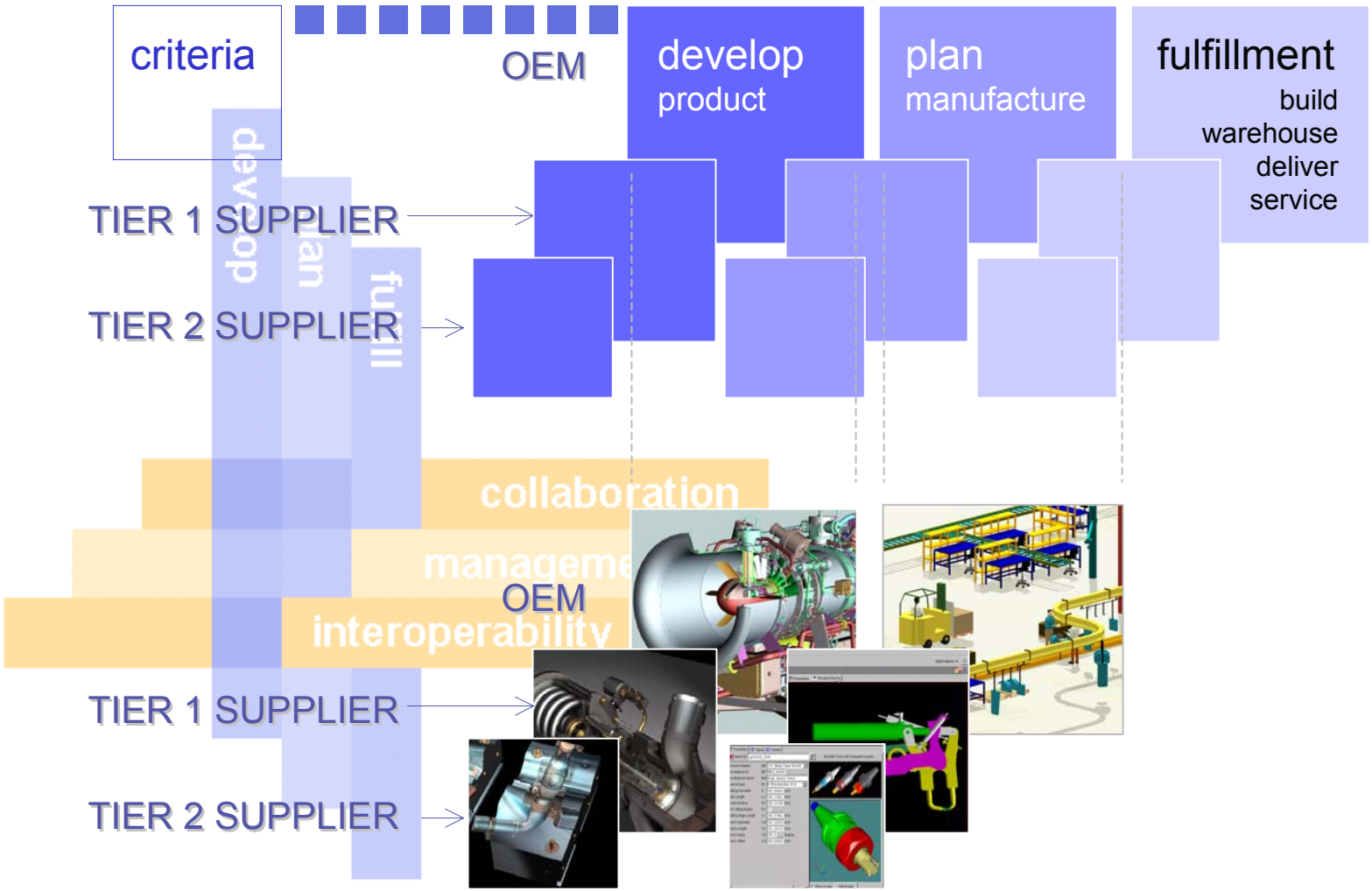

across the *extended* enterprise

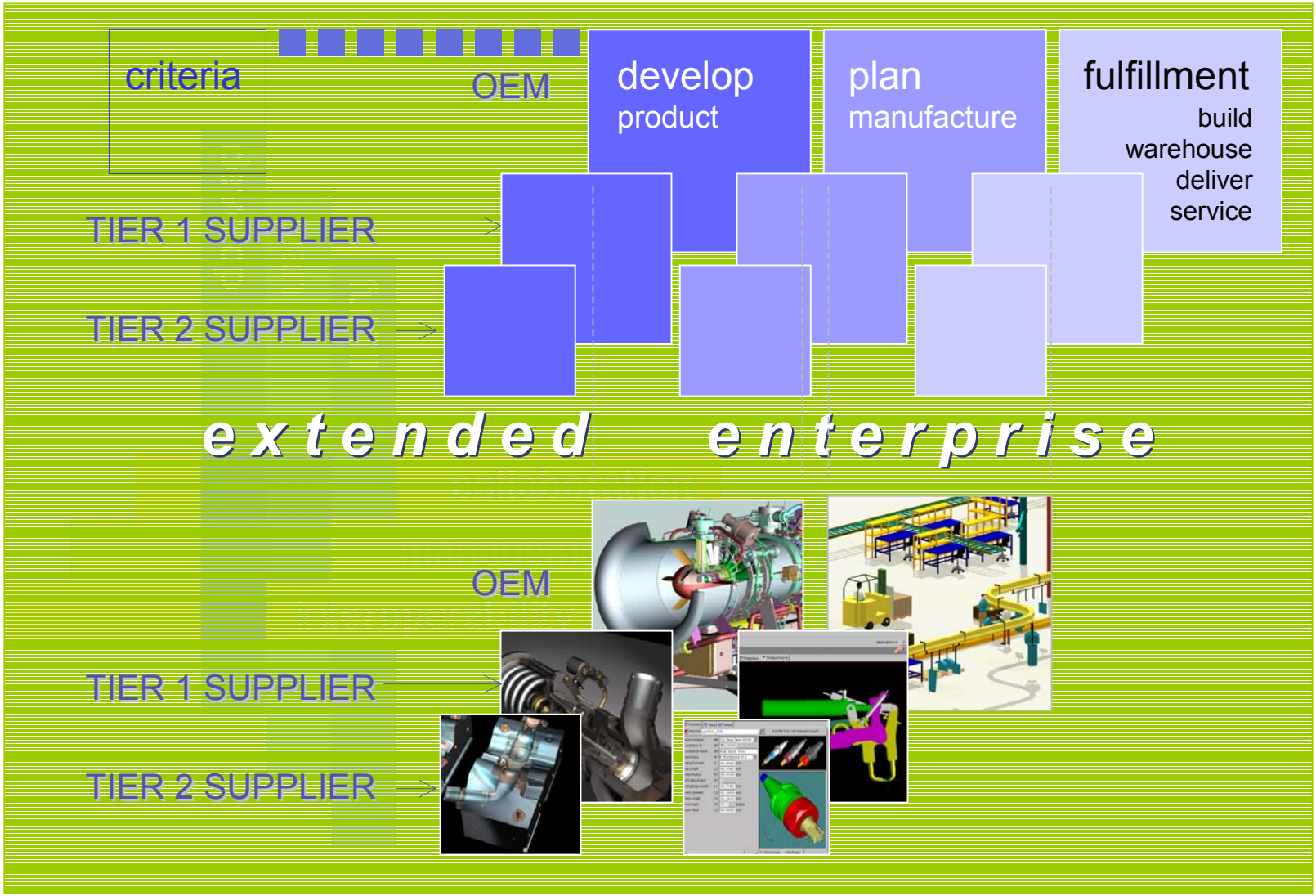

UGS… solutions & c-commerce platform

… the framework for our solutions

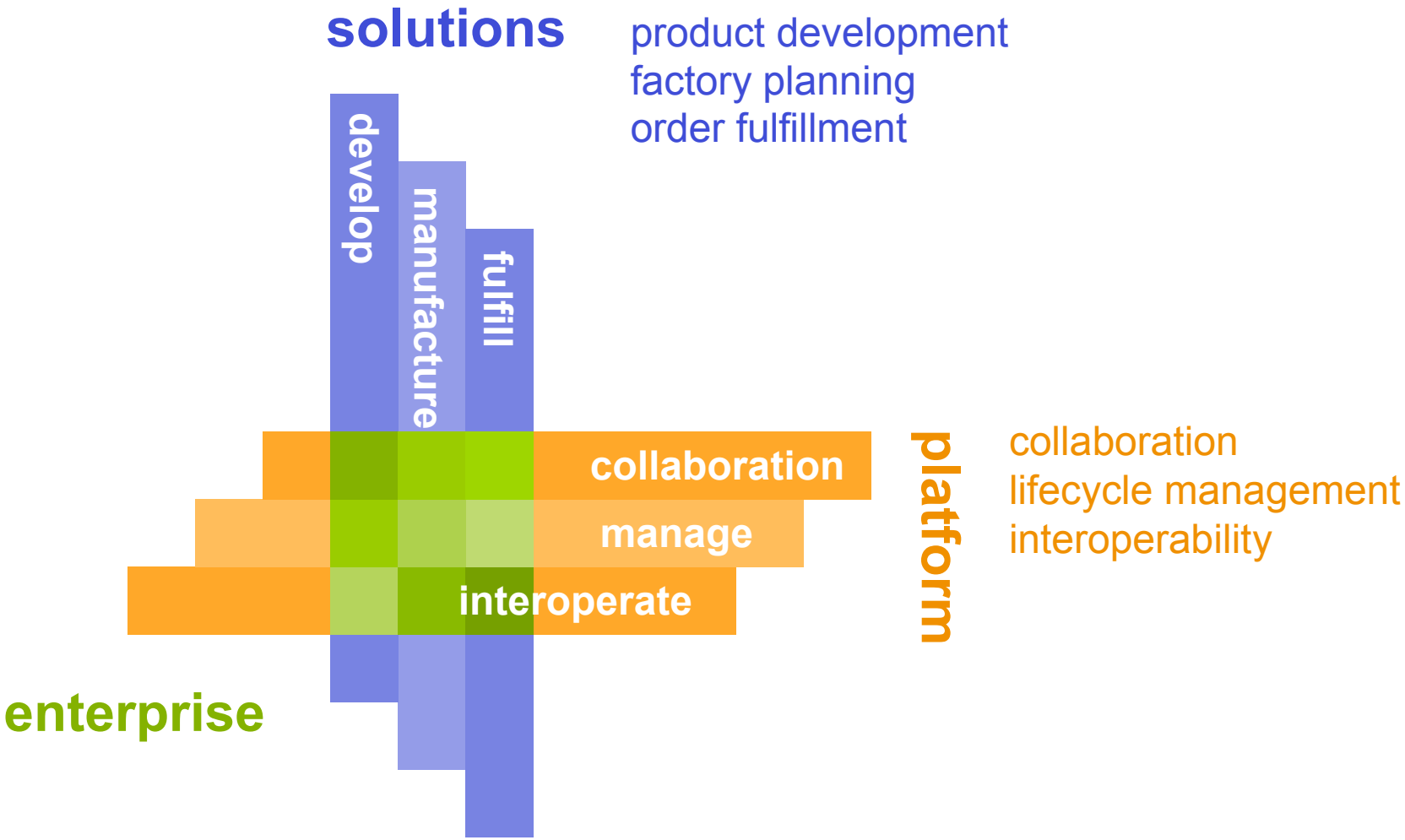

the products

unigraphics
- Product Modeling
- Knowledge Fusion
- Shape Studio
- Scenario CAE
- Mold Wizard
- Design Collaboration
- Product Vision

solid edge
- Product Modeling
- Sheetmetal
- Assembly
- Drafting
- Edge Exchange

e-factory
- NC Automation
- Factory CAD
- Factory Flow
- Jack Human Engineering
- dCADE Stamping
- Genius Tool Management
- Manufacturing Process Planning

develop

manufacture

fulfill

e-vis
- e-Procurement

i-man
- Sales Configurator

e-vis
- e-Vis Connect
- e-Vis Exchange
- e-Vis.com
- VisView
- VisMockup
- VisPublish

collaboration

manage

interoperate

i-man
- CAD Management
- Digital Validation
- Workflow
- Change Management
- Image Management
- Global i-Man
- Portal

parasolid
- XT modeling
- eXT product structure

e-vis
- JT visualization
- Visualization Toolkit

i-man
- ERP Connect
- e-Integrator

e-factory
- SDX plant definition

product development

unigraphics
- Product Modeling
- Knowledge Fusion
- Shape Studio
- Scenario CAE
- Mold Wizard
- Design Collaboration
- Product Vision

solid edge
- Product Modeling
- Sheetmetal
- Assembly
- Drafting
- Edge Exchange

develop

manufacture

fulfill

e-factory
- NC Automation
- Factory CAD
- Factory Flow
- Jack Human Engineering
- dCADE Stamping
- Genius Tool Management
- Manufacturing Process Planning

e-vis
- e-Procurement

i-man
- Sales Configurator

collaboration

e-vis
- e-Vis Connect
- e-Vis Exchange
- e-Vis.com
- VisView
- VisMockup
- VisPublish

manage

i-man
- CAD Management
- Digital Validation
- Workflow
- Change Management
- Image Management
- Global i-Man
- Portal

interoperate

parasolid
- XT modeling
- eXT product structure

e-vis
- JT visualization
- Visualization Toolkit

i-man
- ERP Connect
- e-Integrator

e-factory
- SDX plant definition

… making you uniquely successful

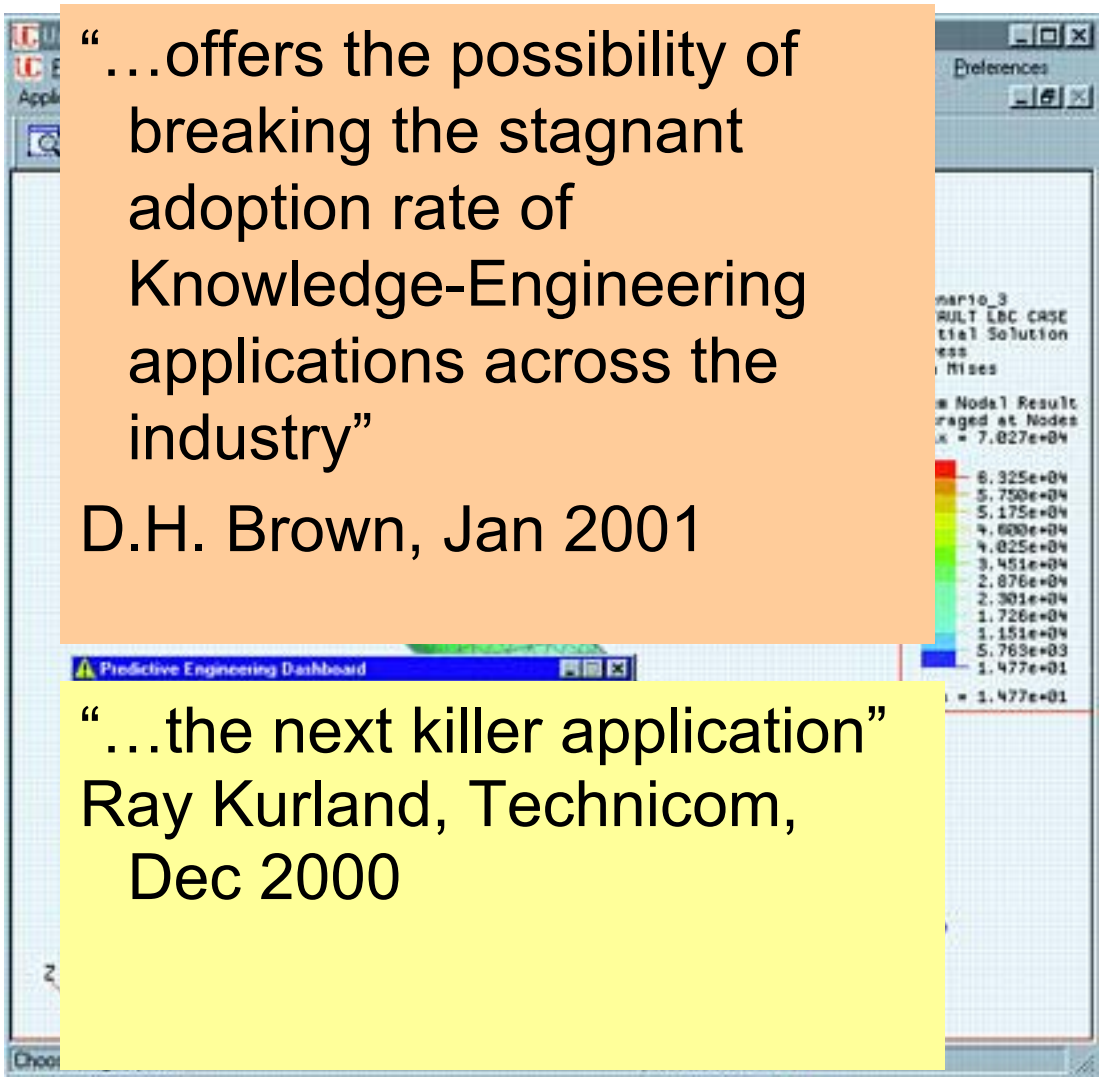

"…offers the possibility of breaking the stagnant adoption rate of Knowledge-Engineering applications across the industry"

D.H. Brown, Jan 2001

"…the next killer application"
Ray Kurland, Technicom, Dec 2000

- concept to production
- integrated analysis
- wizards
  - design
  - Analysis
  - manufacturing
- Knowledge Fusion

NEW!

solid edge

… proven 2D to 3D productivity jump

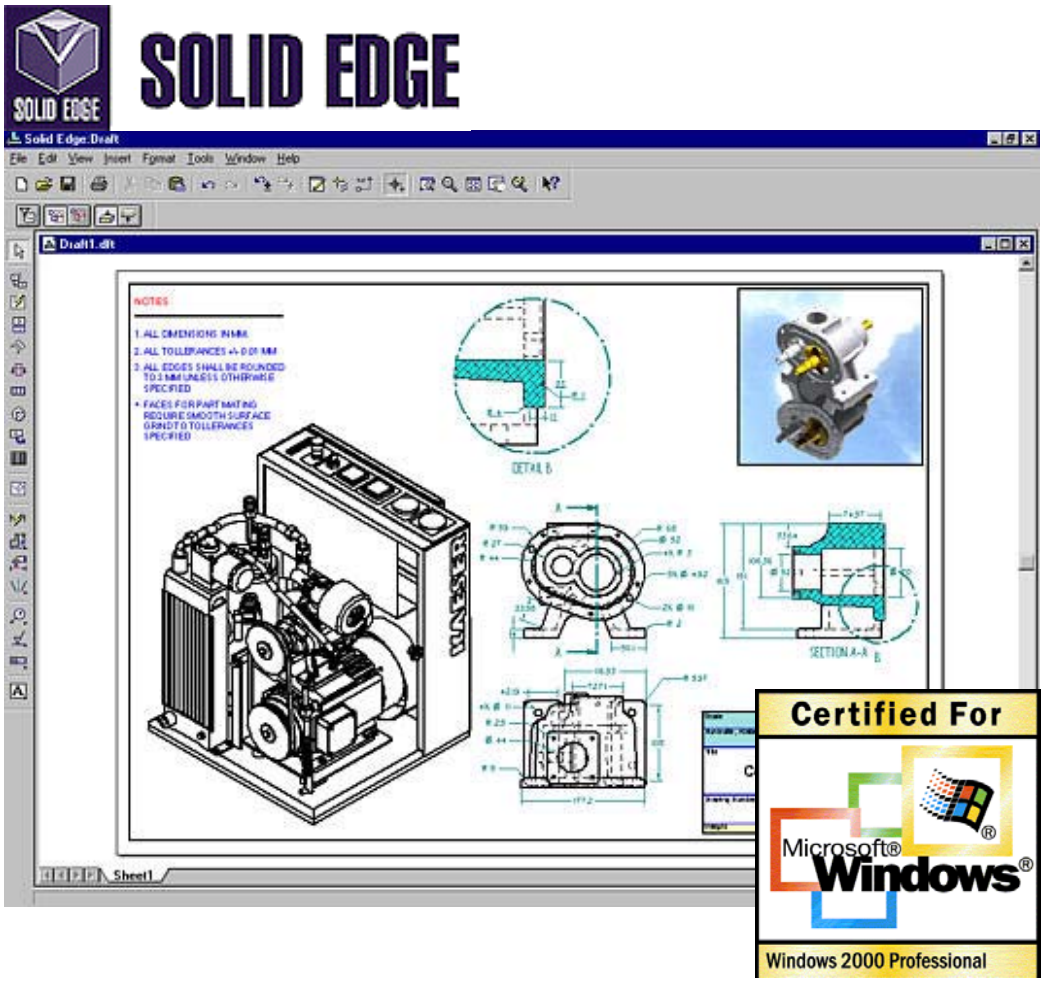

- benchmark ease of use
- productivity leader: stream
- best in class 2D drafting
- powerful applications
  - assemblies
  - weldments
  - sheet metal
  - tubing
  - drafting

manufacturing

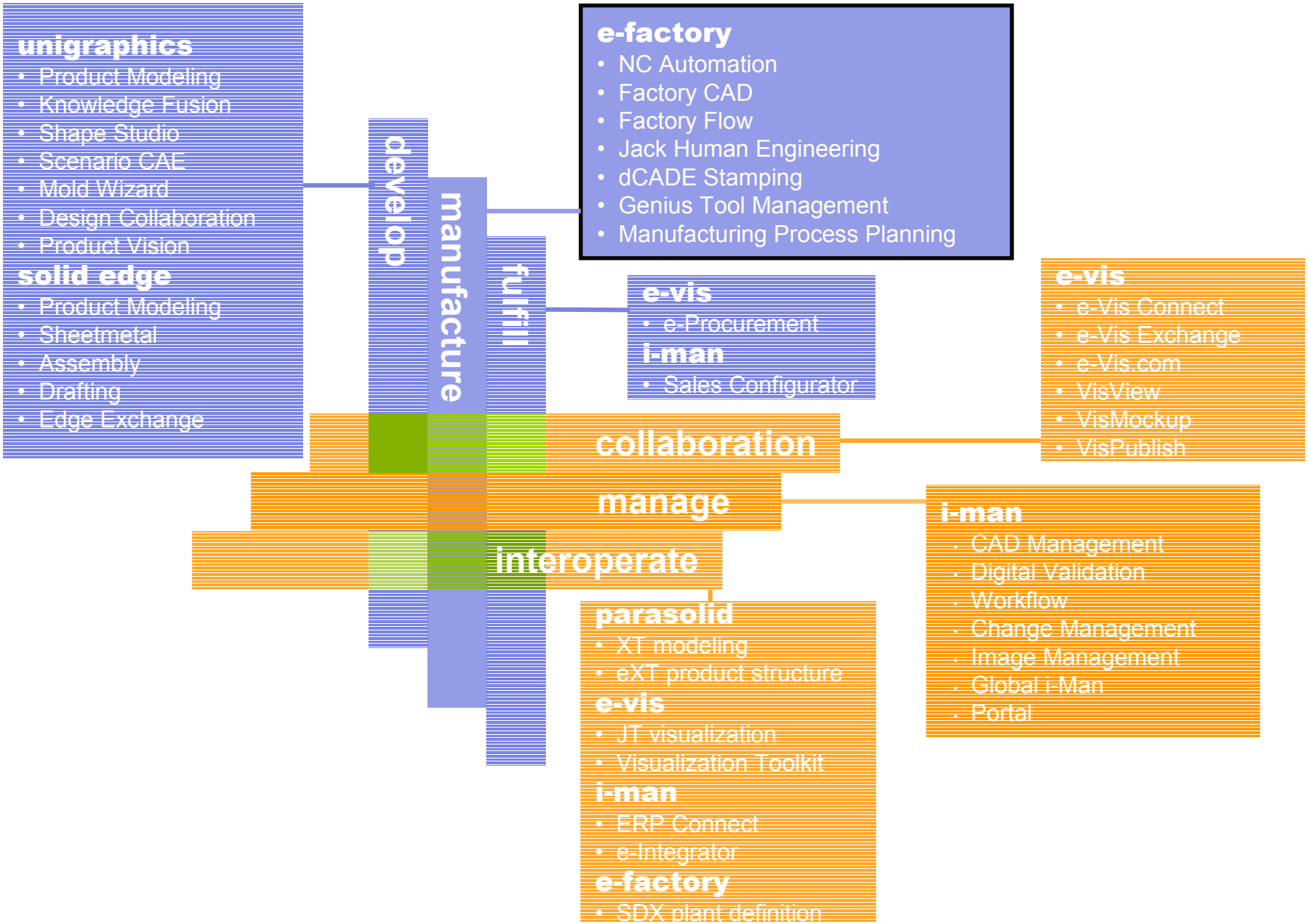

… applications for virtual manufacturing

- Product
- Process
- Plant
- Resource

P3R

making significant pre-production cost/time savings "reality"

interoperability

unigraphics
- Product Modeling
- Knowledge Fusion
- Shape Studio
- Scenario CAE
- Mold Wizard
- Design Collaboration
- Product Vision

solid edge
- Product Modeling
- Sheetmetal
- Assembly
- Drafting
- Edge Exchange

develop

manufacture

fulfill

e-factory
- NC Automation
- Factory CAD
- Factory Flow
- Jack Human Engineering
- dCADE Stamping
- Genius Tool Management
- Manufacturing Process Planning

e-vis
- e-Procurement

i-man
- Sales Configurator

e-vis
- e-Vis Connect
- e-Vis Exchange
- e-Vis.com
- VisView
- VisMockup
- VisPublish

collaboration

manage

interoperate

i-man
- CAD Management
- Digital Validation
- Workflow
- Change Management
- Image Management
- Global i-Man
- Portal

- XT modeling
- eXT product structure

e-vis
- JT visualization
- Visualization Toolkit

i-man
- ERP Connect
- e-Integrator

e-factory
- SDX plant definition

Parasolid

SOLID EDGE
PTC
Shaping Innovation
Armonicos
Pathtrace
CADKEY
MITSUBISHI
SDRC
Mastercam
Camtek
TOPCAD
DASSAULT SYSTEMES
SolidWorks
Deneb
ADAMS
ICAD-MX
MSC SOFTWARE
SIMULATING REALITY
BENTLEY
CADMAX
EAI
KNOWLEDGE TECHNOLOGIES INTERNATIONAL
IRON CAD
UNIGRAPHICS
GM
UNITED TECHNOLOGIES PRATT&WHITNEY
ANSYS
BOEING
ESPRIT
690,000 seats – 240 licensees – 230 applications

DirectModel

Unigraphics

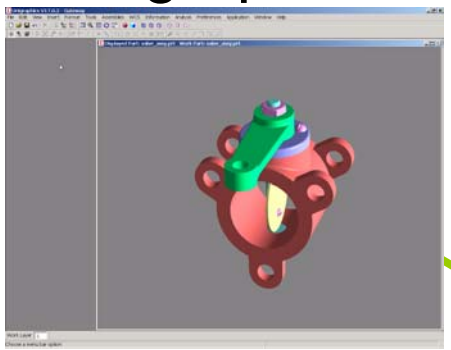

CATIA

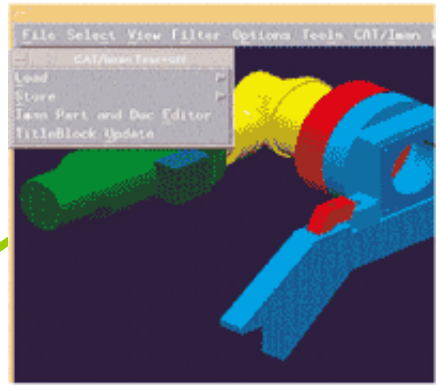

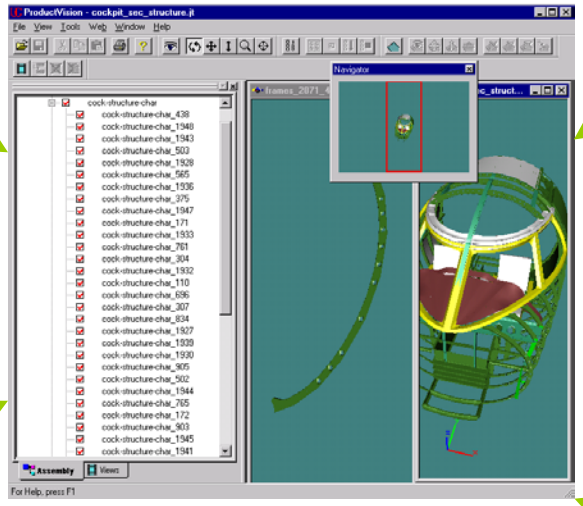

Pro/Engineer

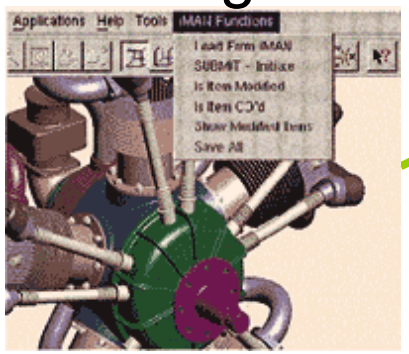

I-DEAS

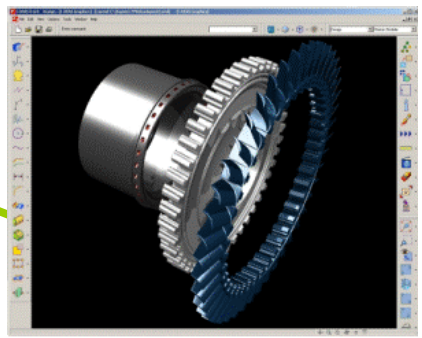

New Windows Interface for SDRC's I-DEAS
(click here for more info)

DirectModel

industry-standard CAD-neutral format

collaboration

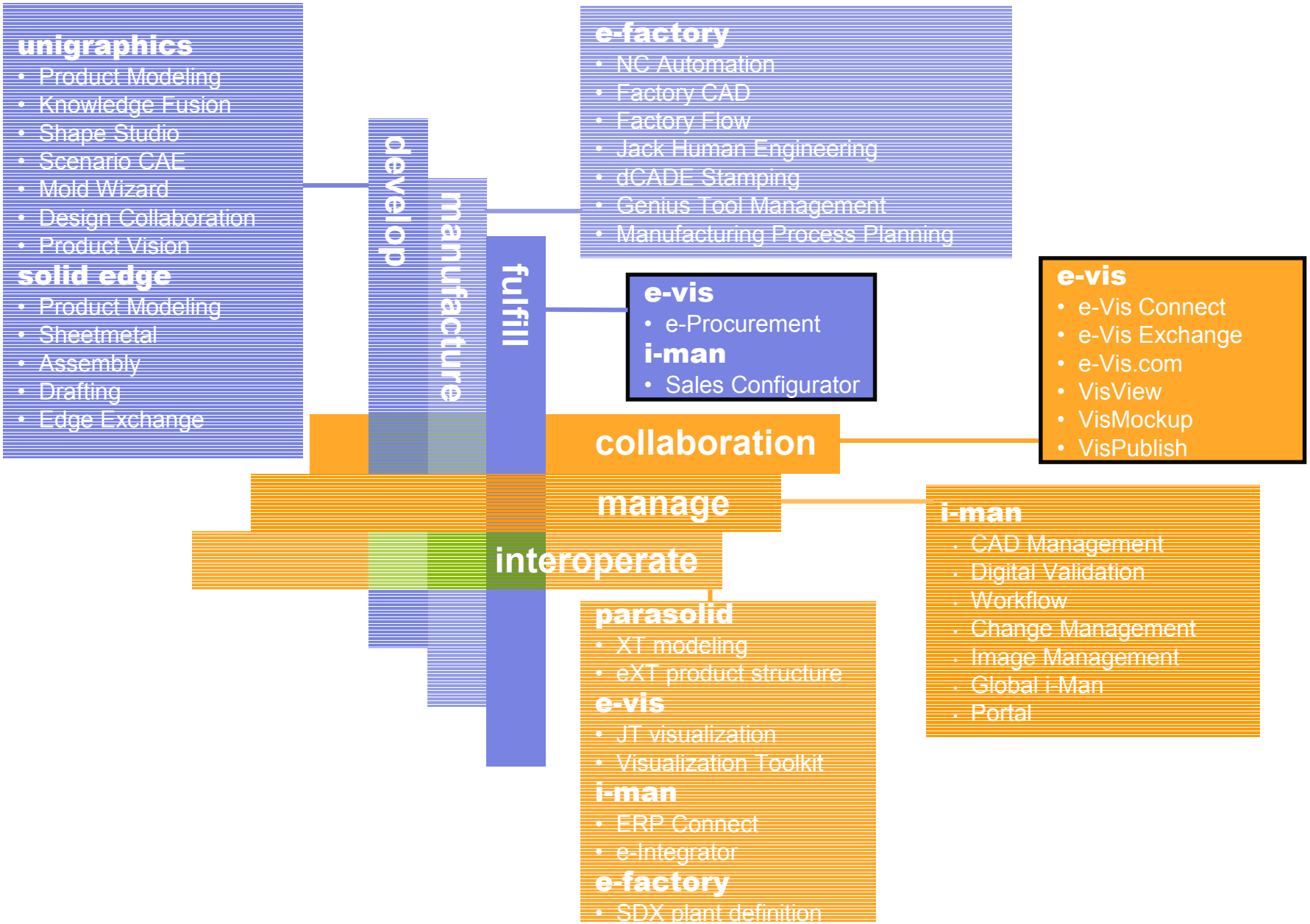

… most collaboration is still brute force

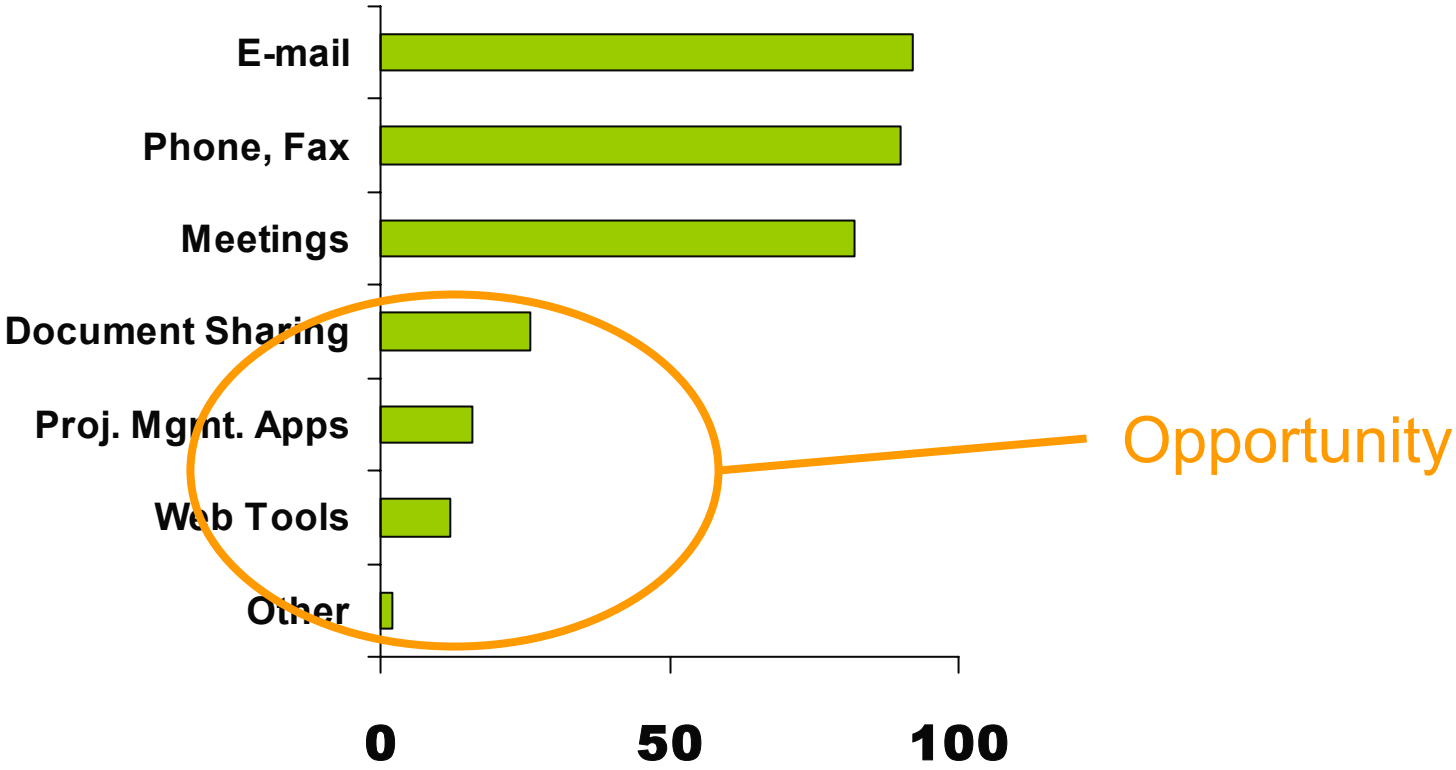

Percent of 50 Fortune 1000 Companies Interviewed
(multiple responses accepted)

Source: Forrester Research, Inc., March 2000

collaboration technology

Collaborative Applications

Product Design & Visualization

UNIGRAPHICS

SOLID EDGE

ProductVision

Virtual Collaboration Rooms (vRooms)

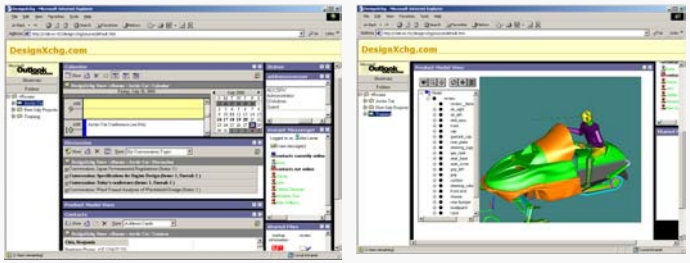

Geometry Pipeline

PARASOLID

XML

Visualization

Collaboration Server

i-man

Product Data Mgmt

E A I

visual collaboration

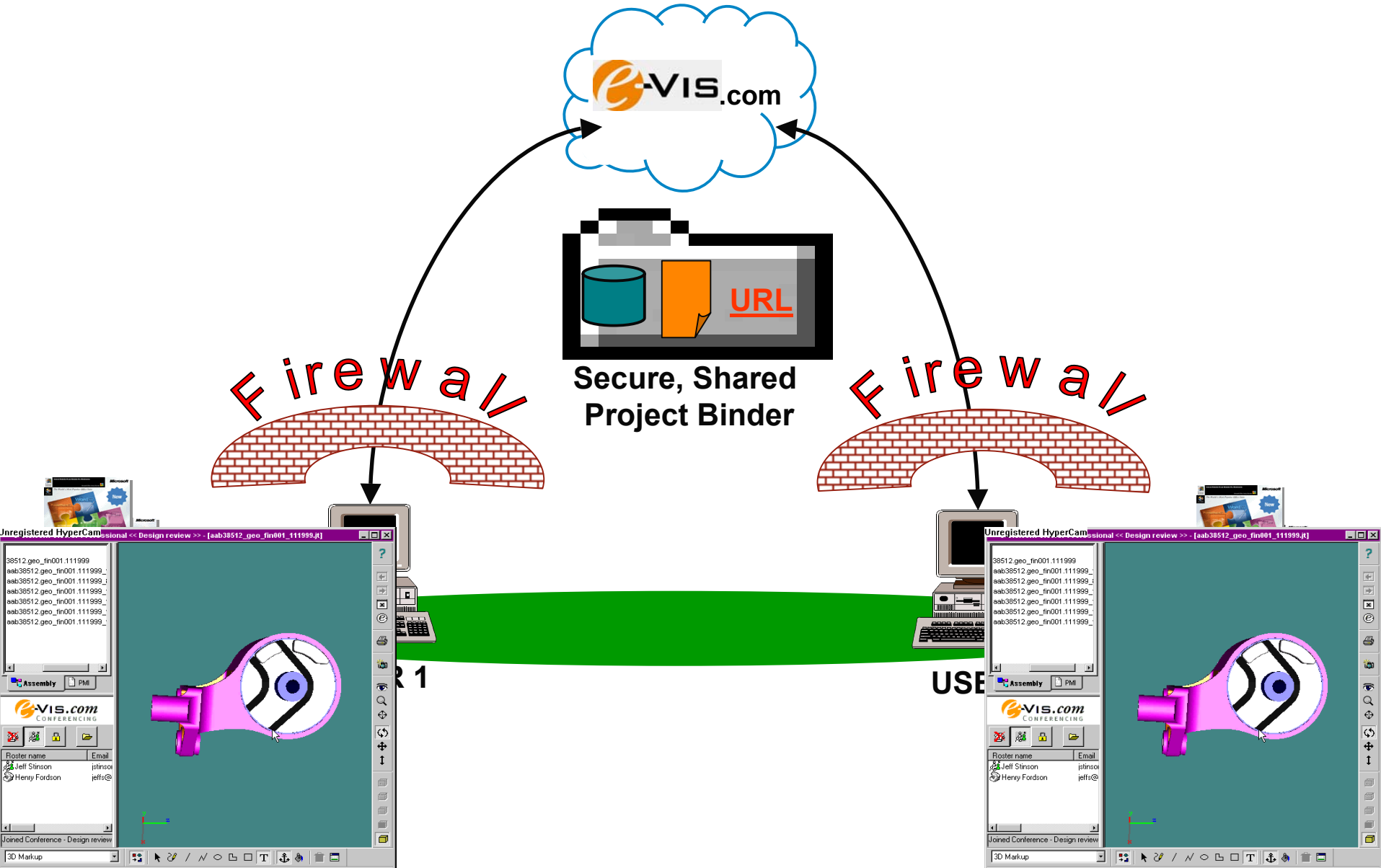

Visualization Pipeline

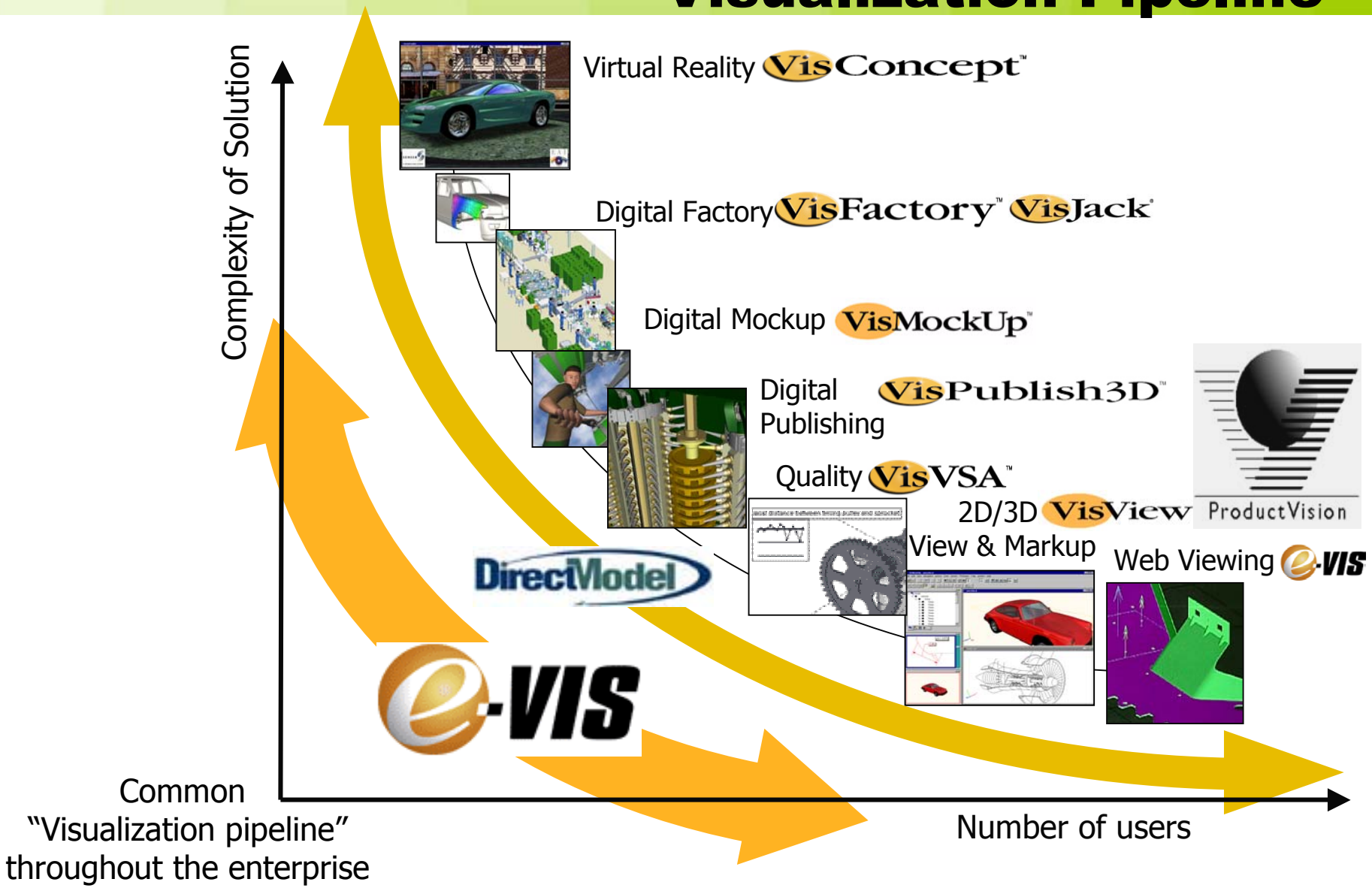

the best of both worlds:

Intranet and Internet collaboration

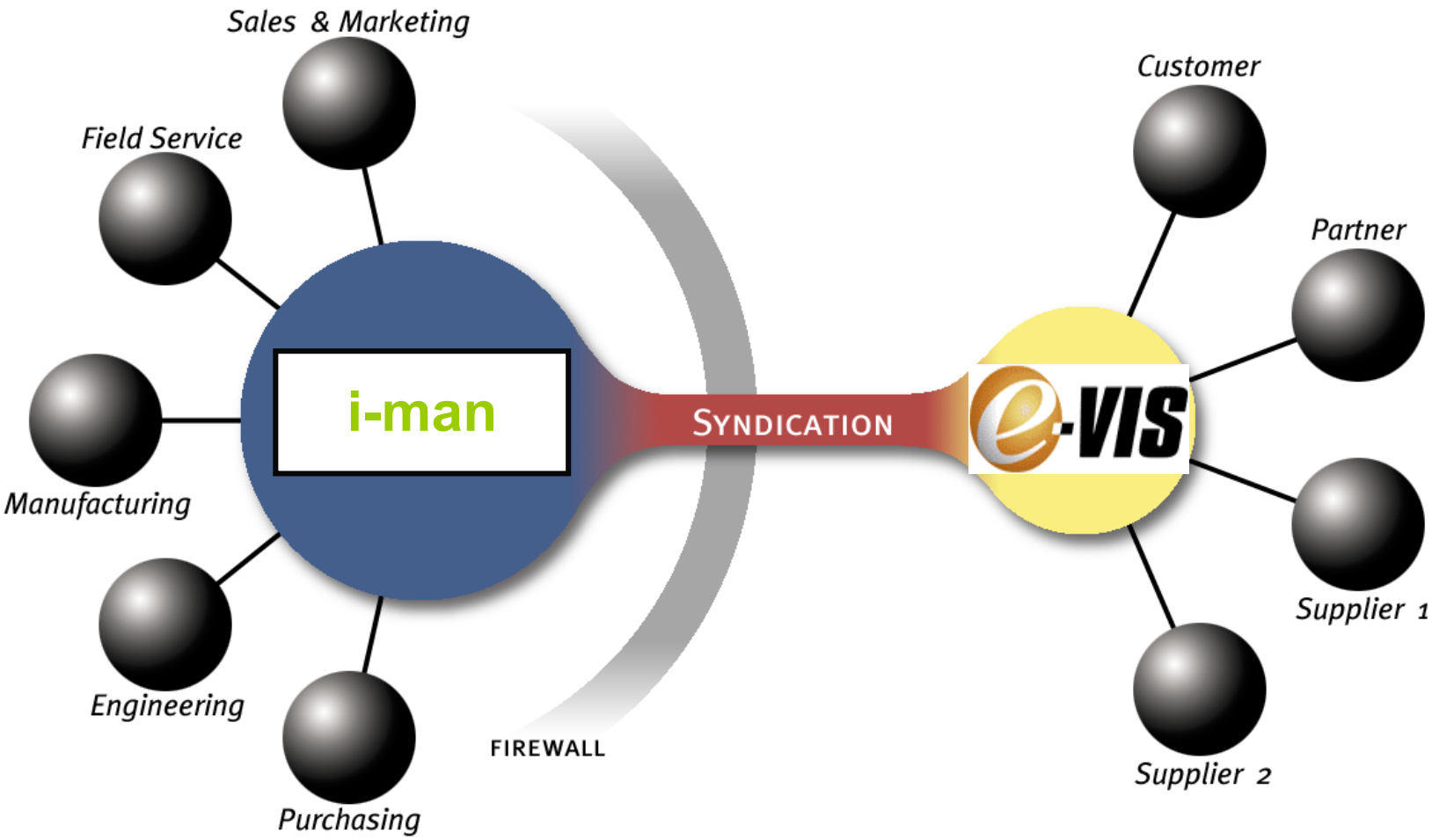

data management

unigraphics
- Product Modeling
- Knowledge Fusion
- Shape Studio
- Scenario CAE
- Mold Wizard
- Design Collaboration
- Product Vision

solid edge
- Product Modeling
- Sheetmetal
- Assembly
- Drafting
- Edge Exchange

develop

manufacture

fulfill

e-factory
- NC Automation
- Factory CAD
- Factory Flow
- Jack Human Engineering
- dCADE Stamping
- Genius Tool Management
- Manufacturing Process Planning

e-vis
- e-Procurement

i-man
- Sales Configurator

e-vis
- e-Vis Connect
- e-Vis Exchange
- e-Vis.com
- VisView
- VisMockup
- VisPublish

collaboration

manage

interoperate

i-man
- CAD Management
- Digital Validation
- Workflow
- Change Management
- Image Management
- Global i-Man
- Portal

parasolid
- XT modeling
- eXT product structure

e-vis
- JT visualization
- Visualization Toolkit

i-man
- ERP Connect
- e-Integrator

e-factory
- SDX plant definition

business drivers

- Some form of a **stage-gate** process is in place for new product development
- A recent Forrester Research interview of 50 Fortune 1000 Product Development executives found:
  - 96% have 3 or more departments actively involved in the product development process
  - 40% expect to work frequently with partners by 2002 - twice the number that do so today!

Source: Forrester Research, Inc., March 2000

business drivers

- A Deloitte Research study of 70 senior executives found that **only**:
  - **40% felt** that the **information** used in their Product Development Process was **reliable and accurate**
  - **27% felt** that the **information** was easily **accessible**

Source: Deloitte Consulting - Creating Unique Customer Experiences

future environment

Manage Product & Process Data in a Collaborative Product Development Environment Throughout the Extended Enterprise

i-man provides a scalable solution for managing, sharing, & viewing ALL product & process data

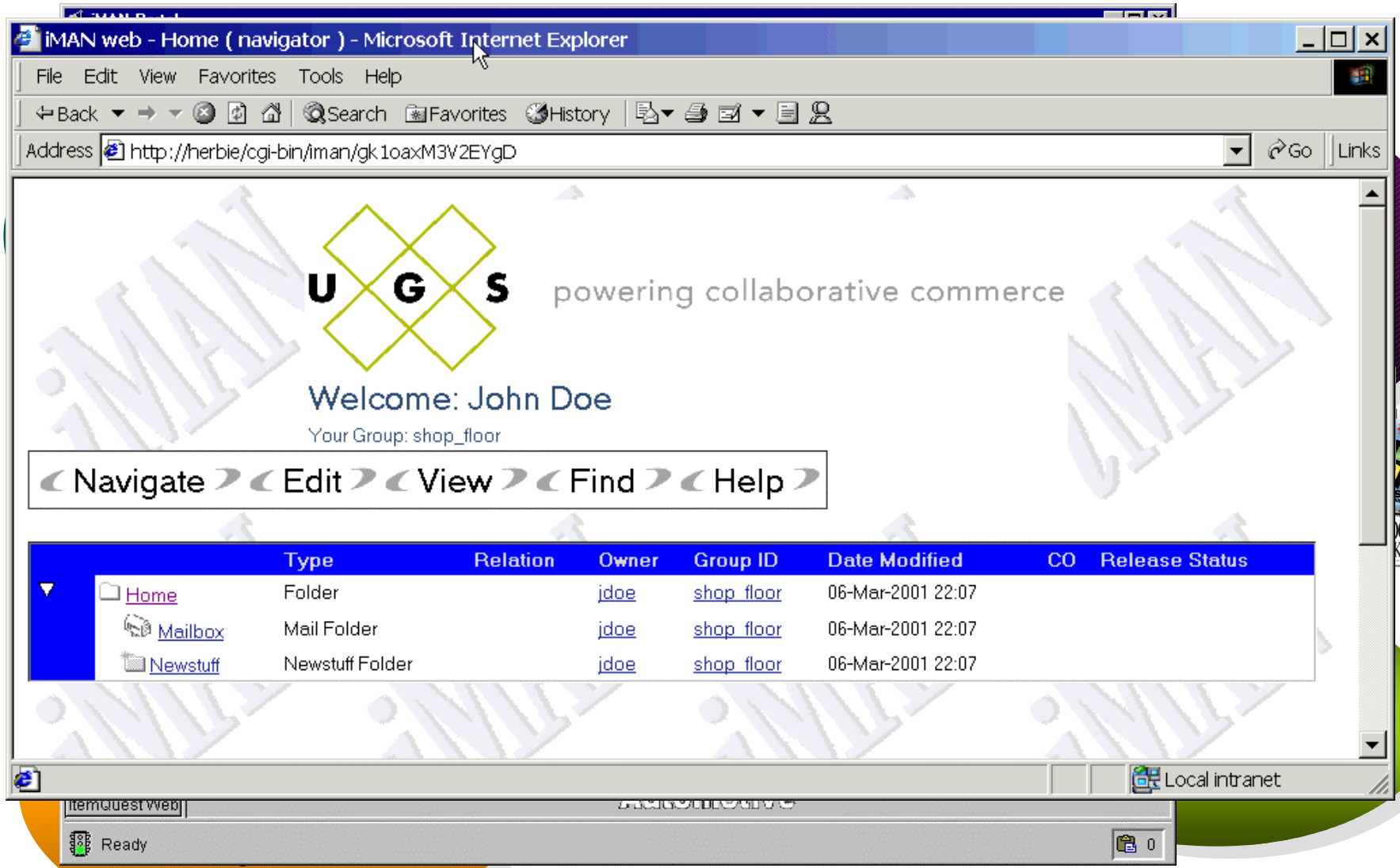

- As Built BOM

Open, standard architecture

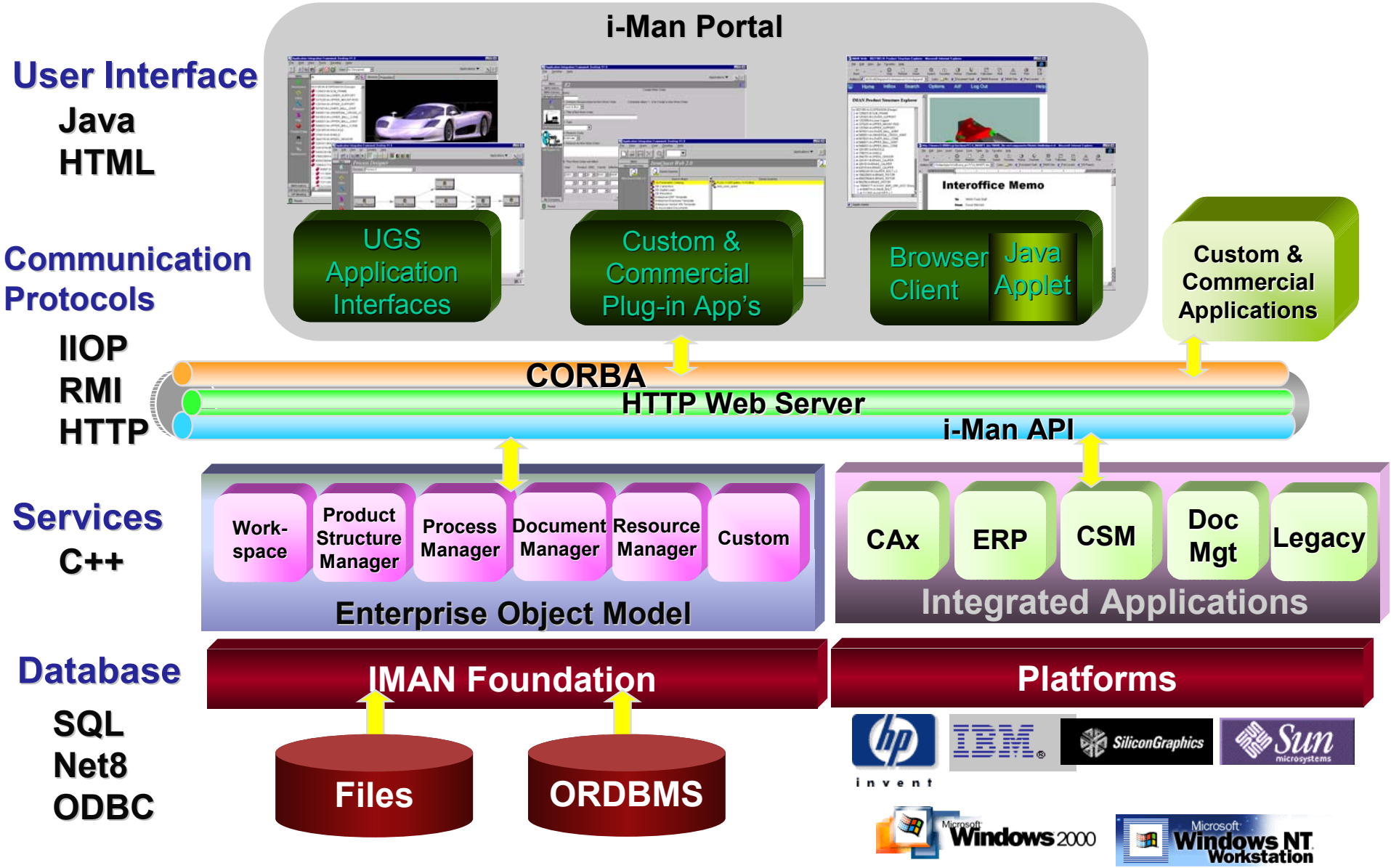

i-man product data management solutions

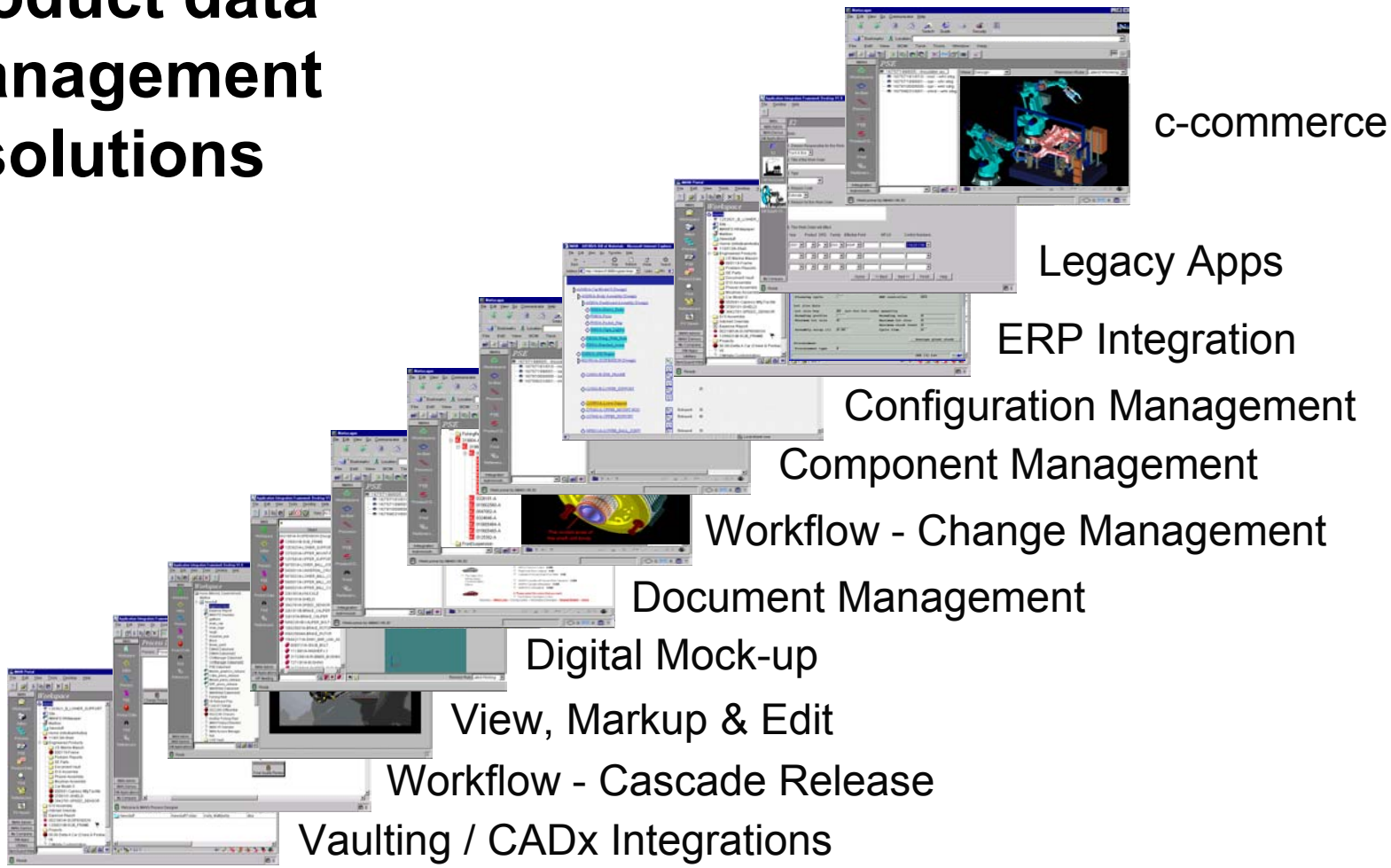

CAD integrations

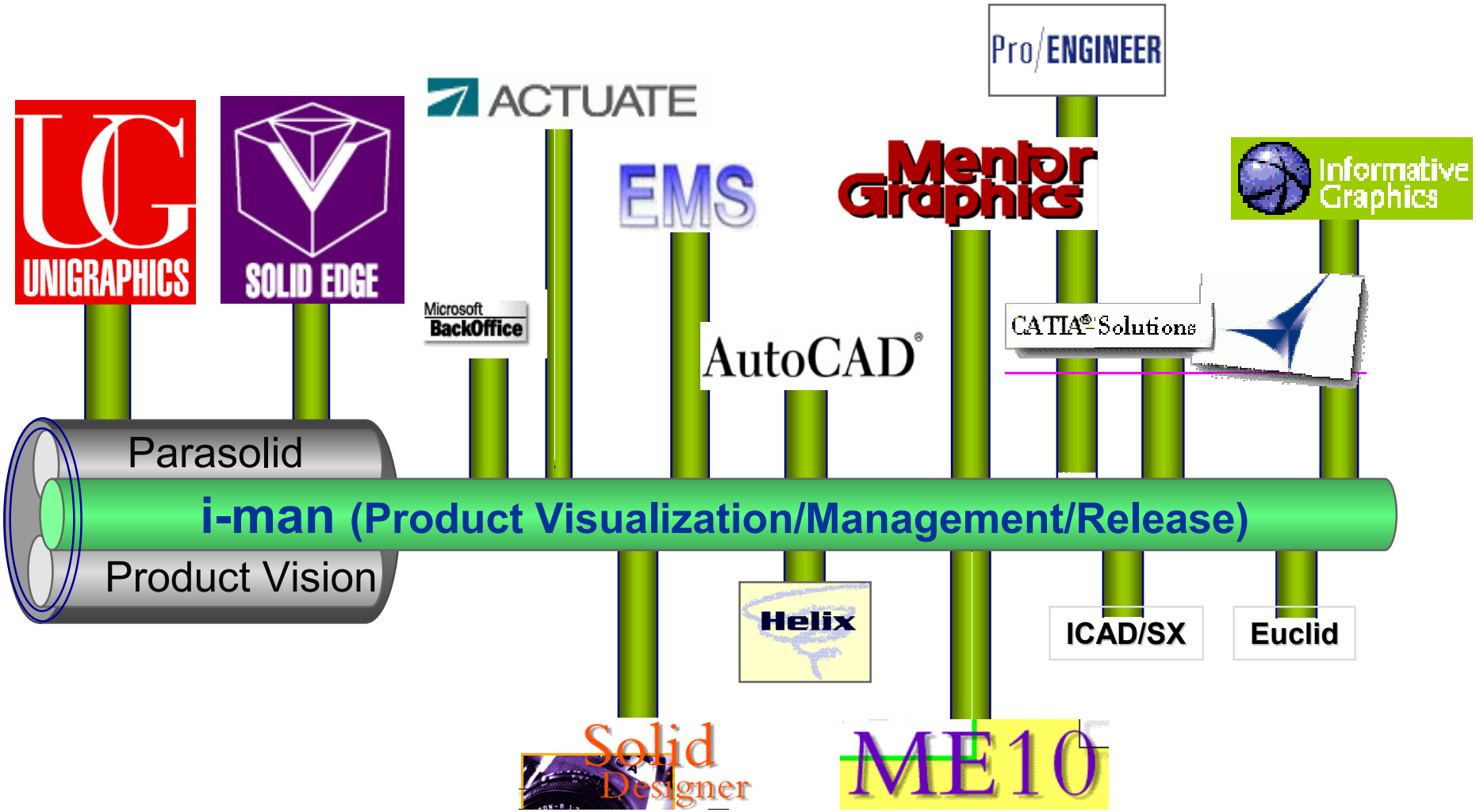

Analysis data management

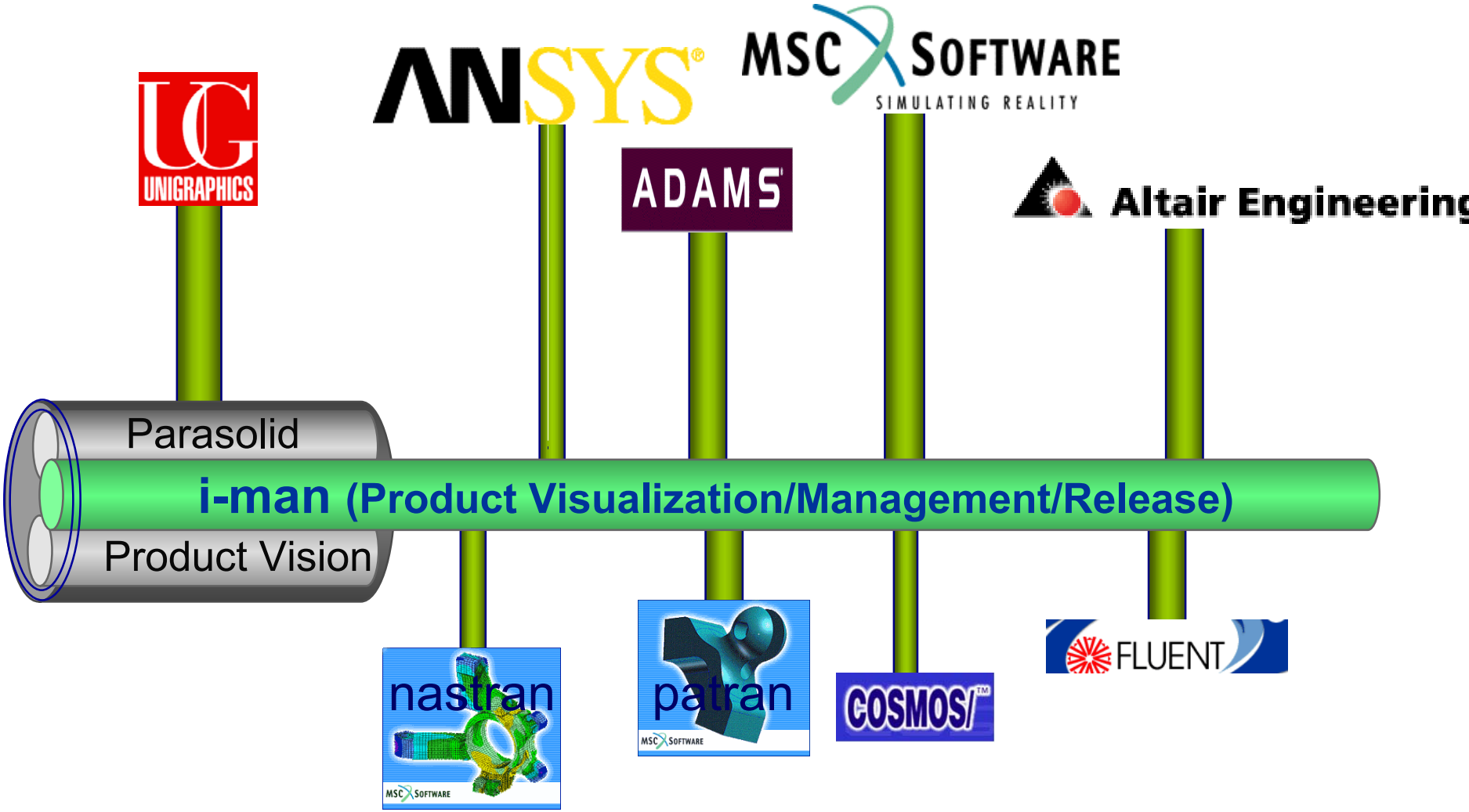

Workflow

i-man manages change → Integrates to other business functions

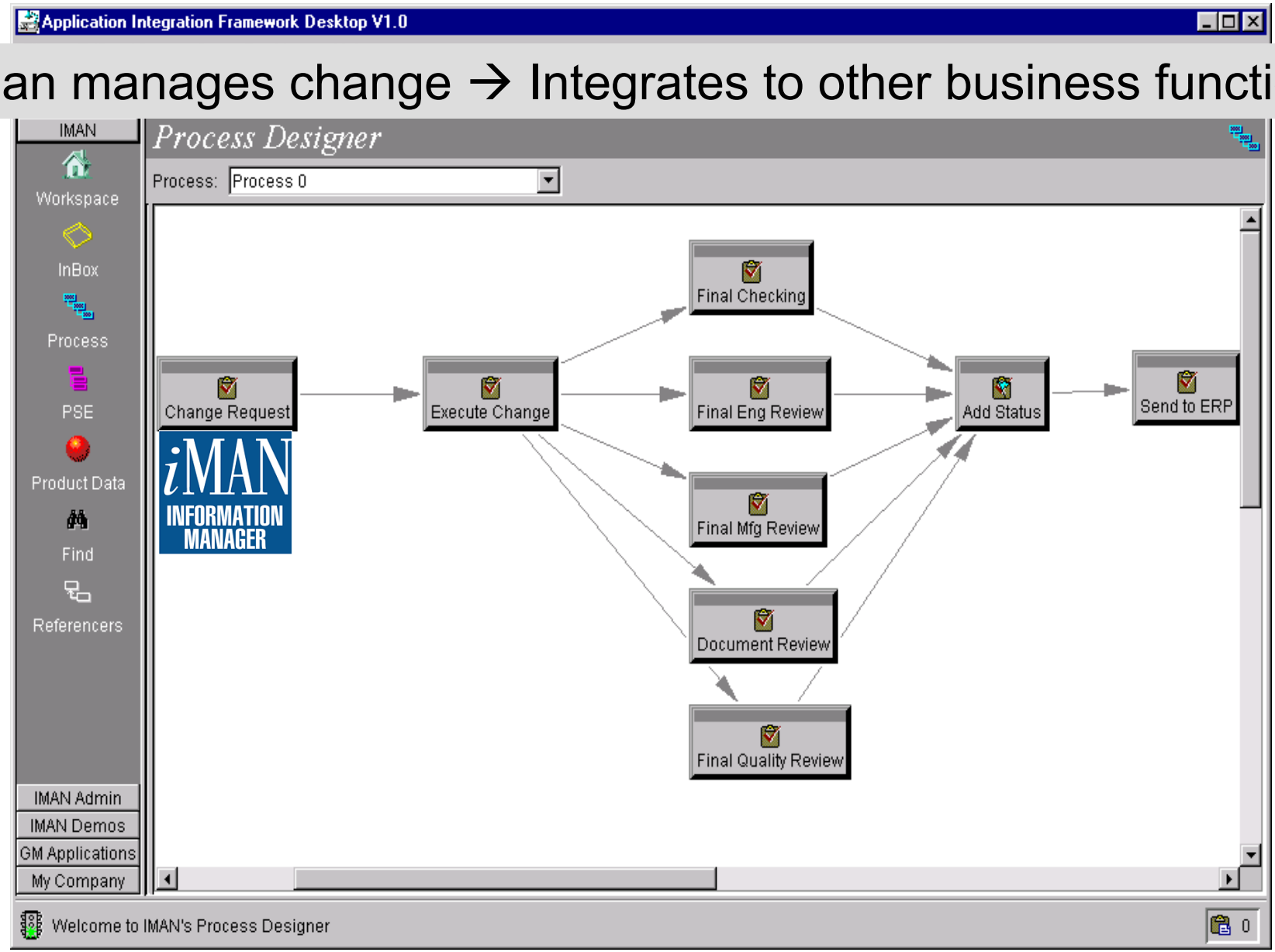

Change Management

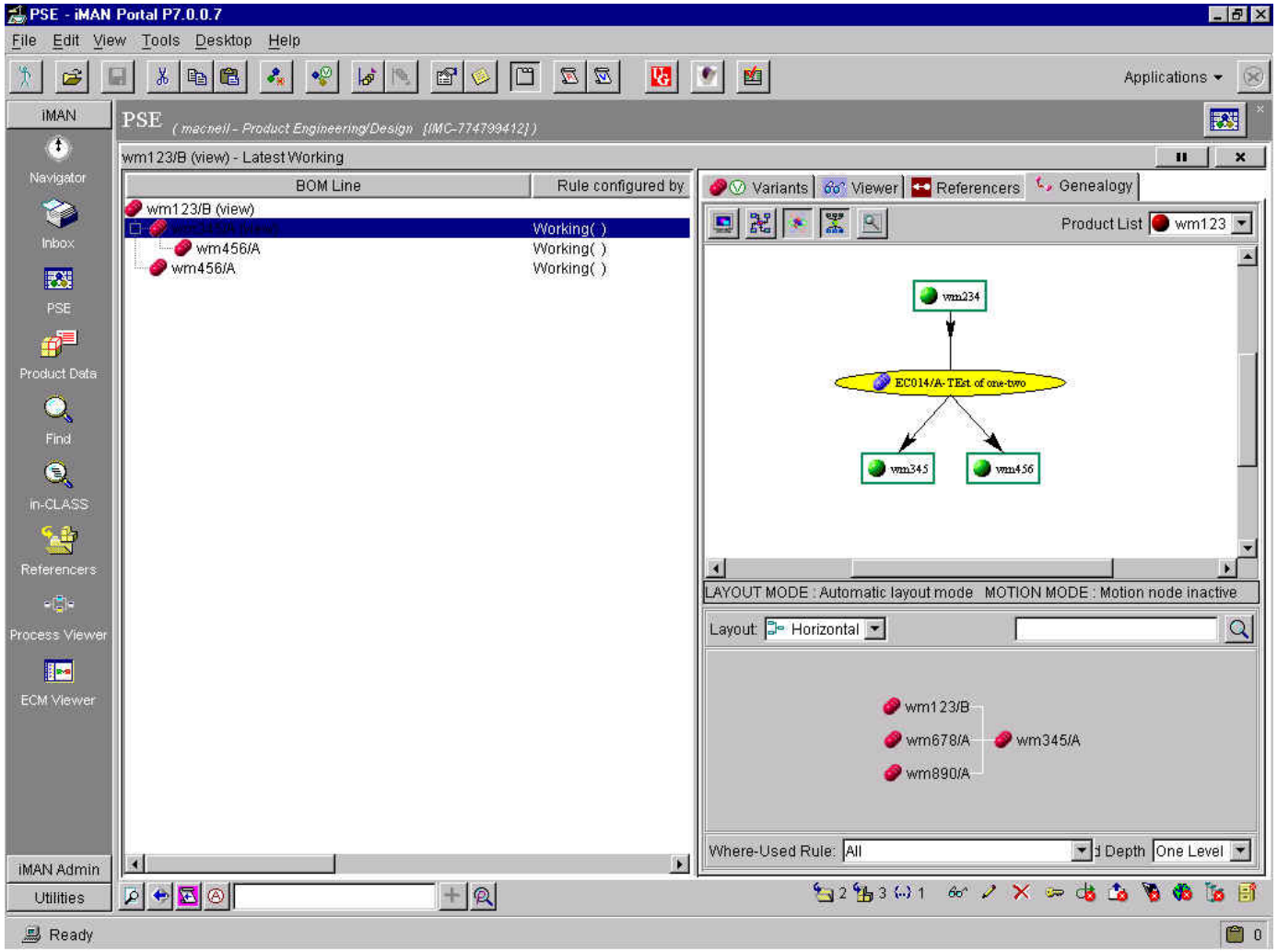

CMII Certified

Institute Of Configuration Management

Home Of CMII

Organizations Worldwide Are Using The CMII Principles To Upgrade
Their CM Practices, Adopting The CMII Model As Their Business
Process Infrastructure And Looking For CMII Compliant Tools

i-man V7.0

from UGS

Has Been Assessed Against The CMII Model And
Was Certified To Be CMII Compliant As Of

17 July 2001

Vincent C. Guess
Institute Of Configuration Management

Philip M. Wolfe
University Coalition For CMII

CERTIFIED

Integrated classification application i-man inClass

- Standard parts, documents
- Component Management
  - Classification
  - Multi-Media Display
- Promotes design reuse

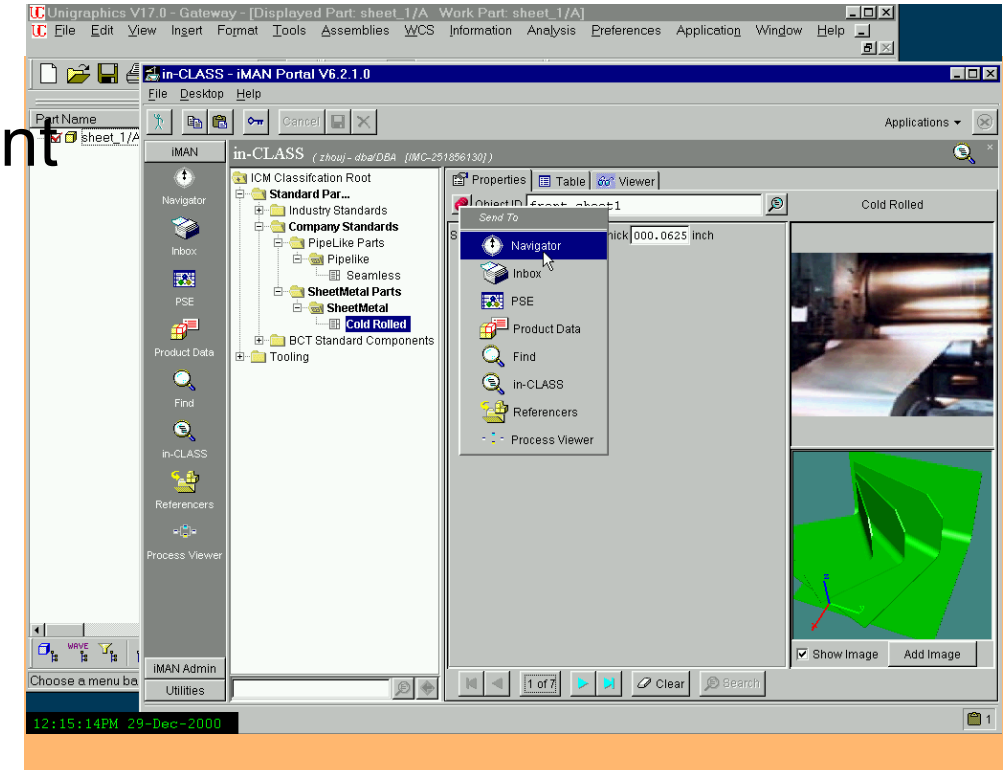

Configuration Management

- Ability to define options and constraints
- Generate BOM by filtering variations
- Pre-configured BOMs
- Integrated visualization

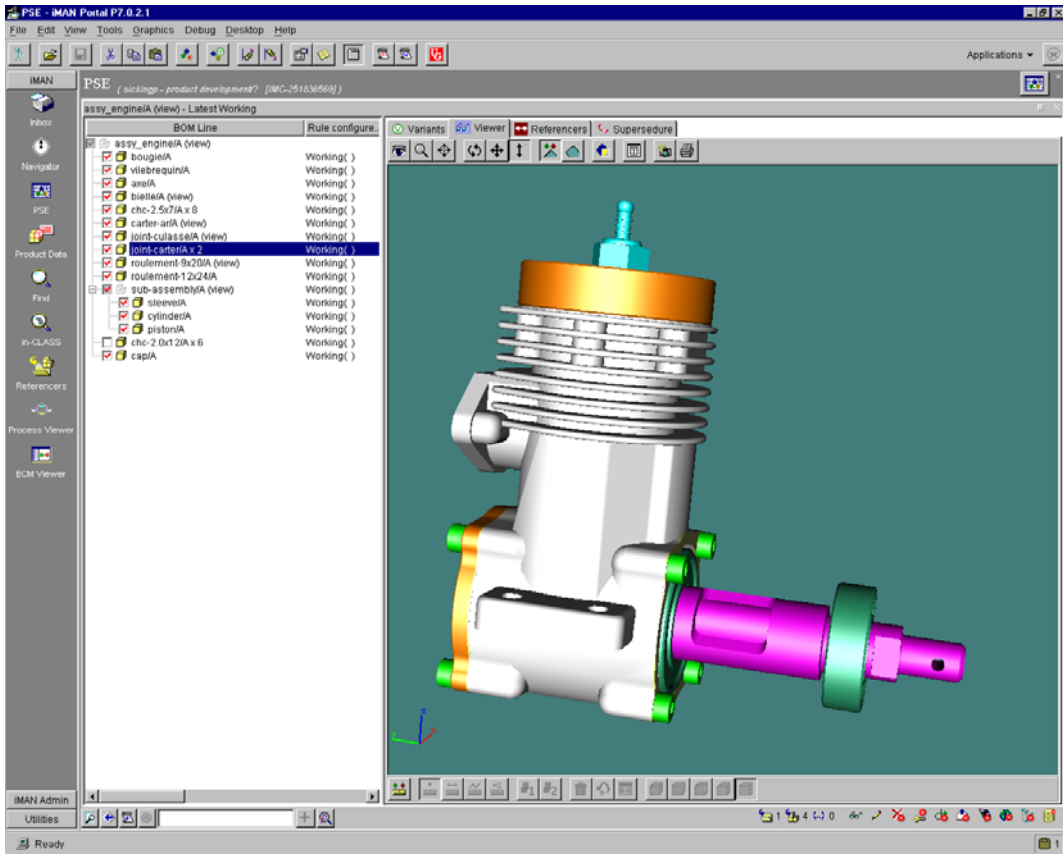

integrate with your ERP system

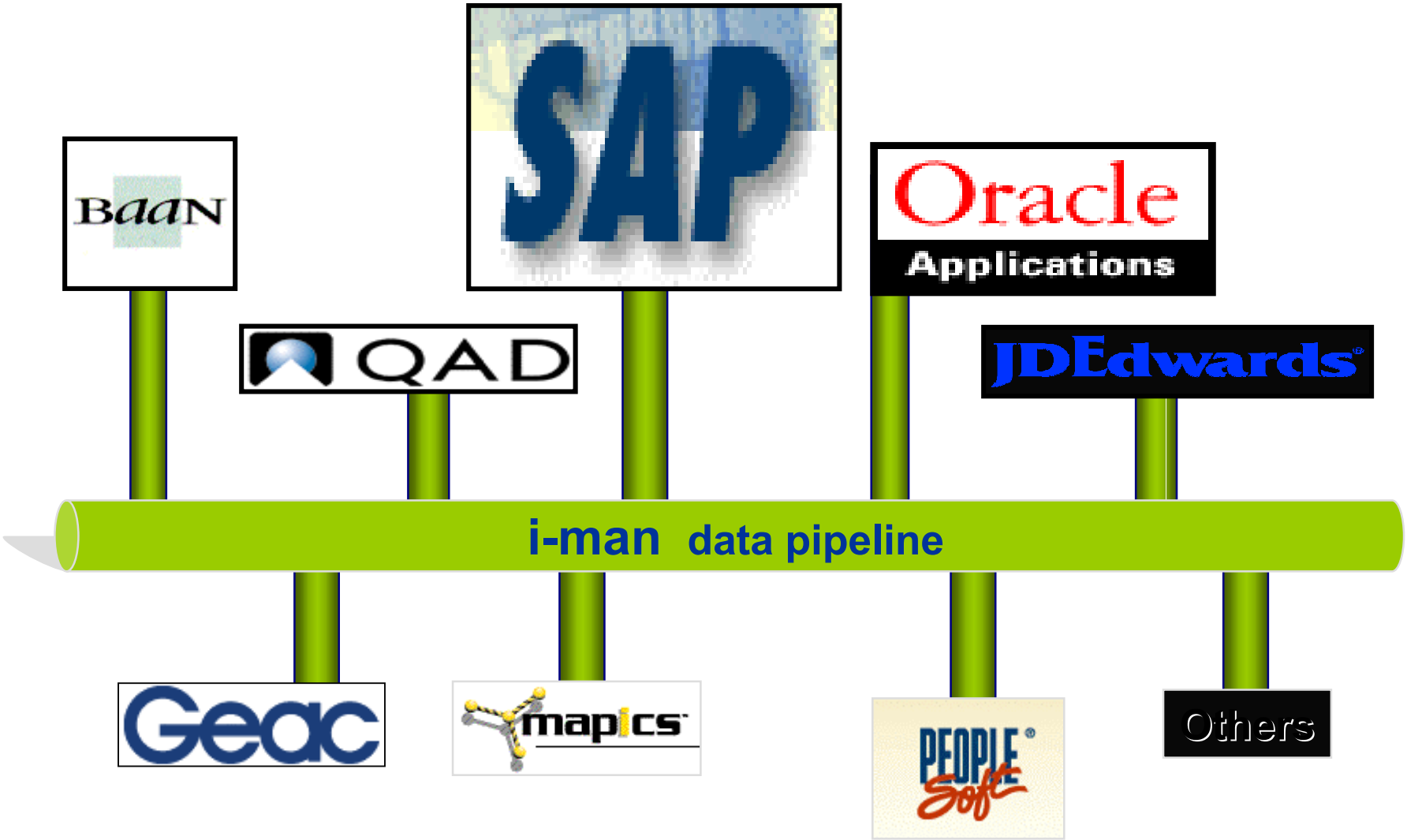

legacy systems integration

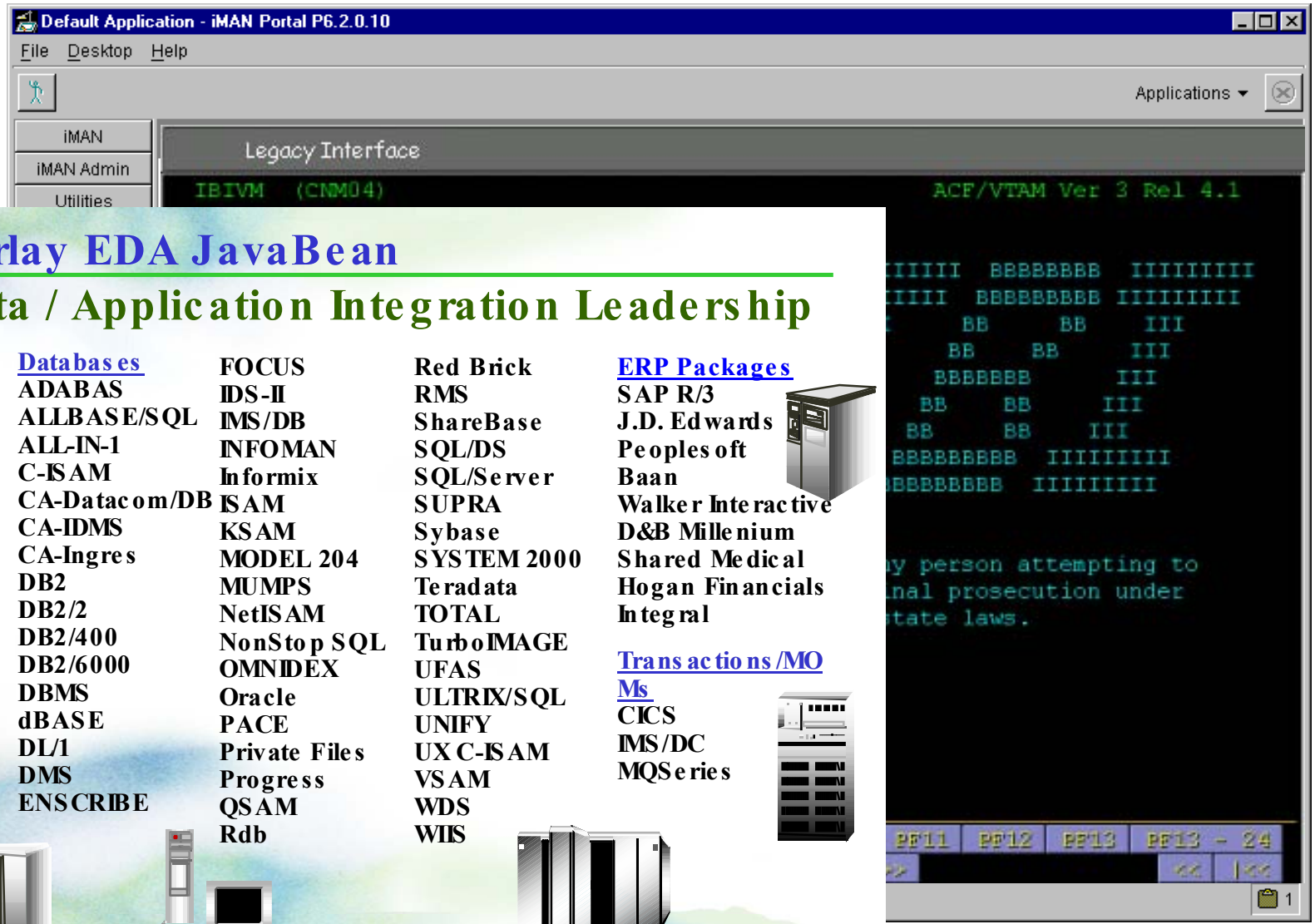

Parlay EDA JavaBean

Data / Application Integration Leadership

Databases

ADABAS
ALLBASE/SQL
ALL-IN-1
C-ISAM
CA-Datacom/DB
CA-IDMS
CA-Ingres
DB2
DB2/2
DB2/400
DB2/6000
DBMS
dBASE
DL/1
DMS
ENSCRIBE
FOCUS
IDS-II
IMS/DB
INFOMAN
Informix
ISAM
KSAM
MODEL 204
MUMPS
NetISAM
NonStop SQL
OMNIDEX
Oracle
PACE
Private Files
Progress
QSAM
Rdb
Red Brick
RMS
ShareBase
SQL/DS
SQL/Server
SUPRA
Sybase
SYSTEM 2000
Teradata
TOTAL
TurboIMAGE
UFAS
ULTRIX/SQL
UNIFY
UX C-ISAM
VSAM
WDS
WIIS

ERP Packages

SAP R/3
J.D. Edwards
Peoplesoft
Baan
Walker Interactive
D&B Millenium
Shared Medical
Hogan Financials
Integral

Transactions/MOMs

CICS
IMS/DC
MQSeries

i-man / e-integrator

Delivering Enterprise Connectivity

- Application for Quick Viewing of Information Located in External Data Sources
- Facilitates import of external database information to i-man
- Creates External Attribute Mapping to i-man Objects
- Leverages JDBC / ODBC Technologies

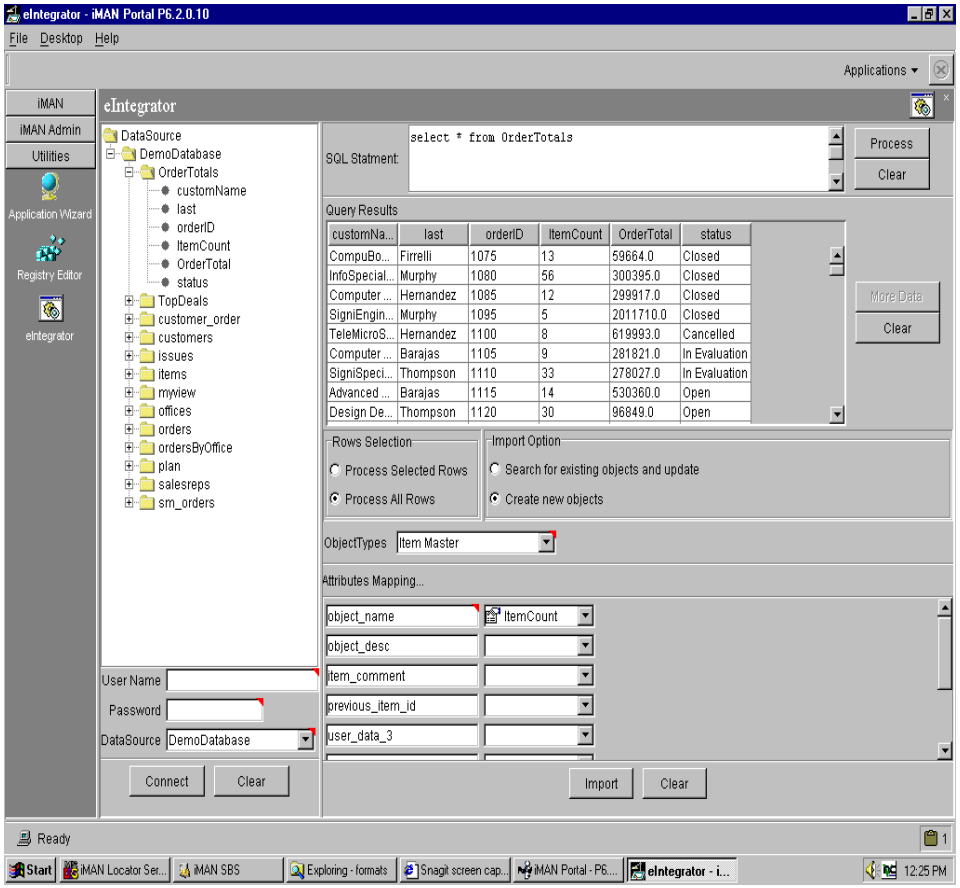

global i-man

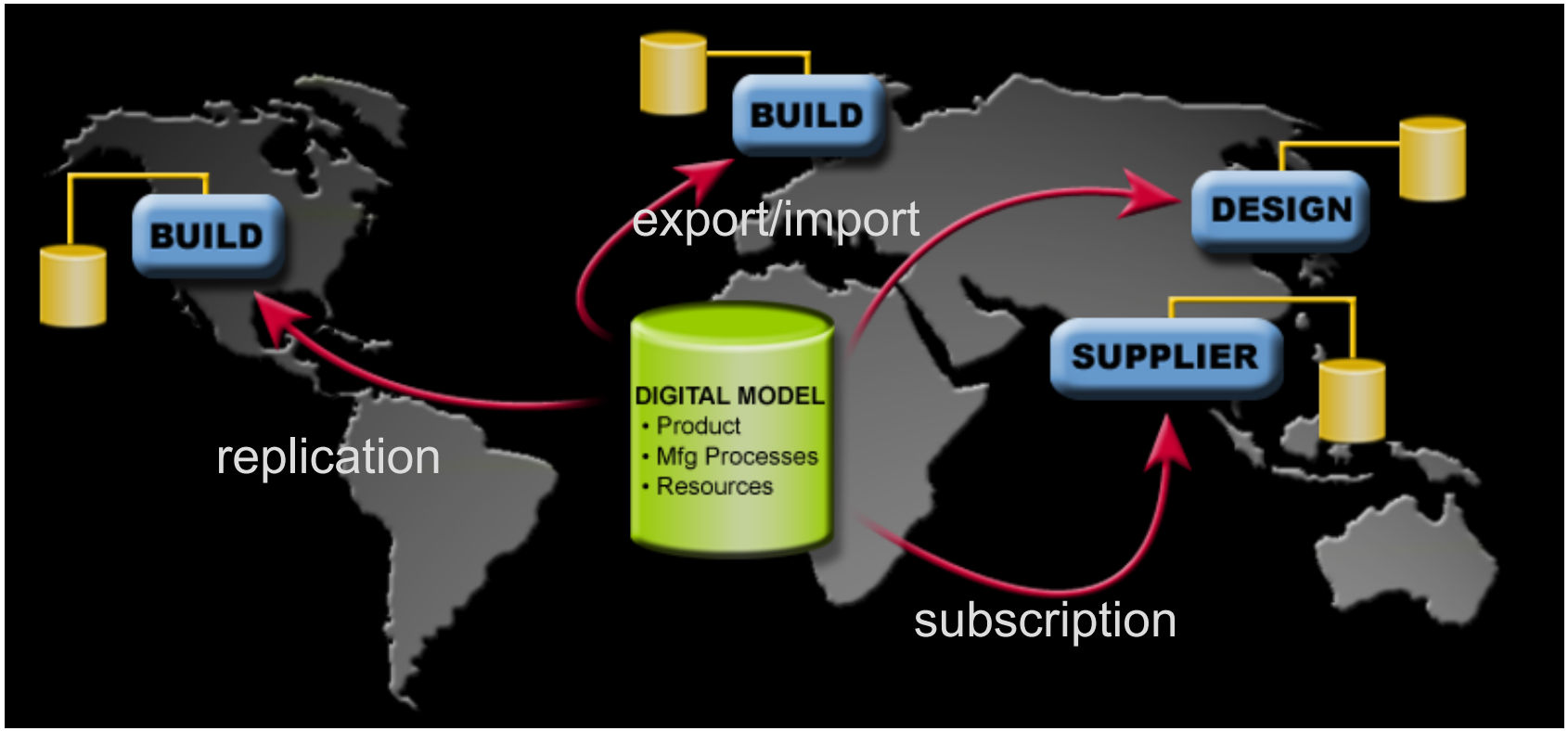

- Design collaboration
- Design anywhere, build anywhere
- Supplier collaboration

i-man

- Leading edge technology
- Robust applications
- Rapid deployment

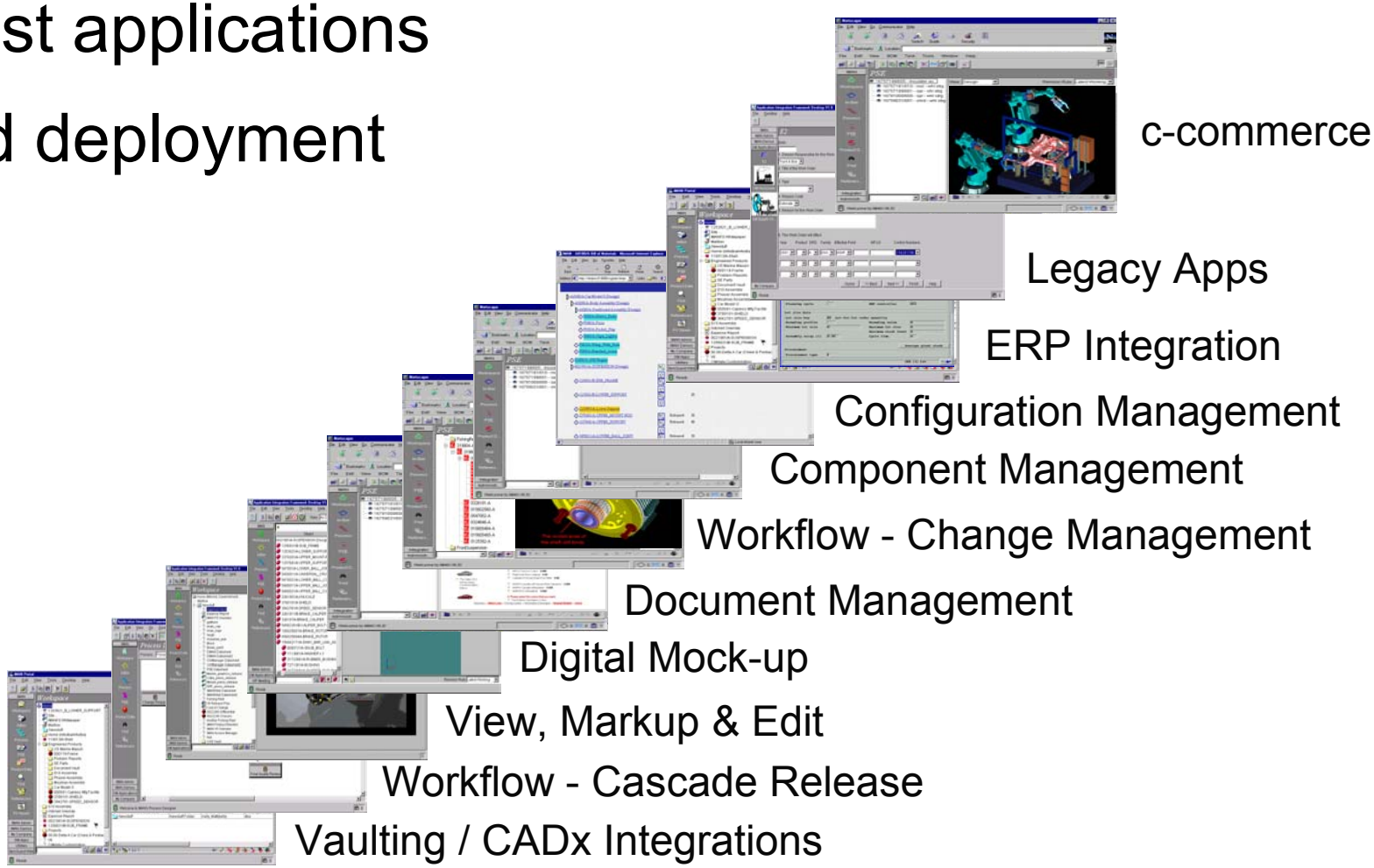

the future

Wasserstein-Perella report on automotive industry:

- Collaboration will facilitate $19 billion savings in product development costs for the Big 3 automakers alone.
- Product development time will be reduced by 50% over a five-year forecasting horizon.
- Production costs will be lower $900 to $1,300 per vehicle.

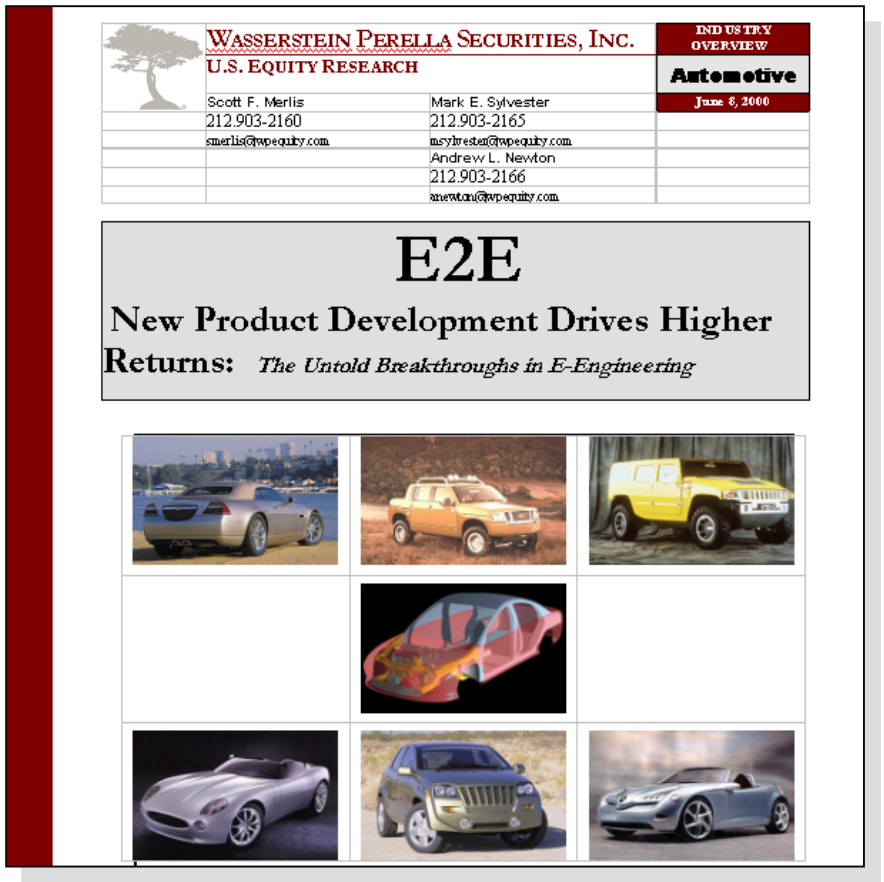

WASSERSTEIN PERELLA SECURITIES, INC.
U.S. EQUITY RESEARCH

INDUSTRY OVERVIEW
Automotive
June 8, 2000

Scott F. Merlis	Mark E. Sylvester
212.903-2160	212.903-2165
smerlis@wpequity.com	msylvester@wpequity.com
	Andrew L. Newton
	212.903-2166
	anewton@wpequity.com

E2E

New Product Development Drives Higher Returns: *The Untold Breakthroughs in E-Engineering*

the future

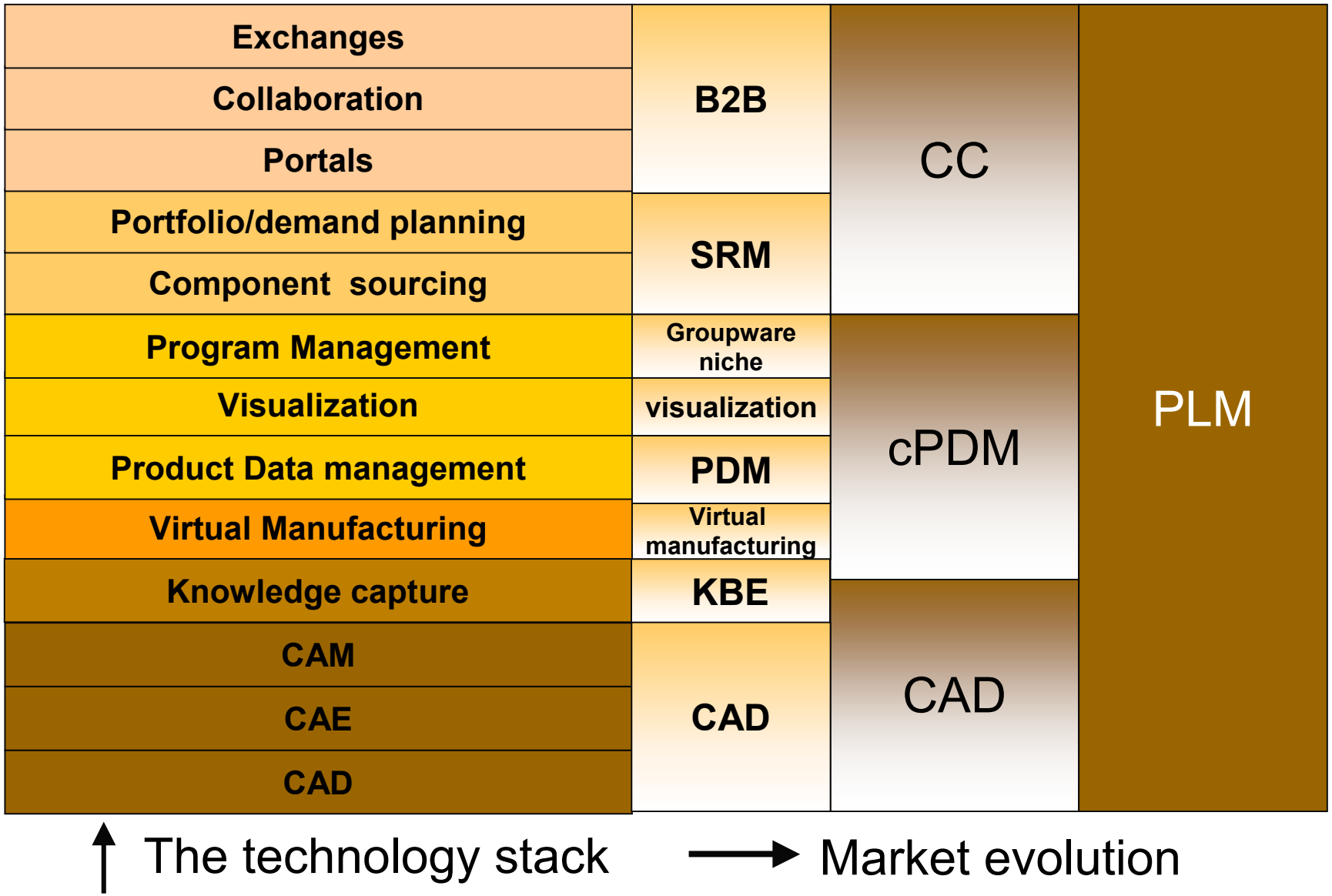
Exchanges
Collaboration
Portals
Portfolio/demand planning
Component sourcing
Program Management
Visualization
Product Data management
Virtual Manufacturing
Knowledge capture
CAM
CAE
CAD
B2B
SRM
Groupware niche
visualization
PDM
Virtual manufacturing
KBE
CAD
CC
cPDM
CAD
PLM
The technology stack
Market evolution

PLM ... market model

moving to internet-enabled collaboration

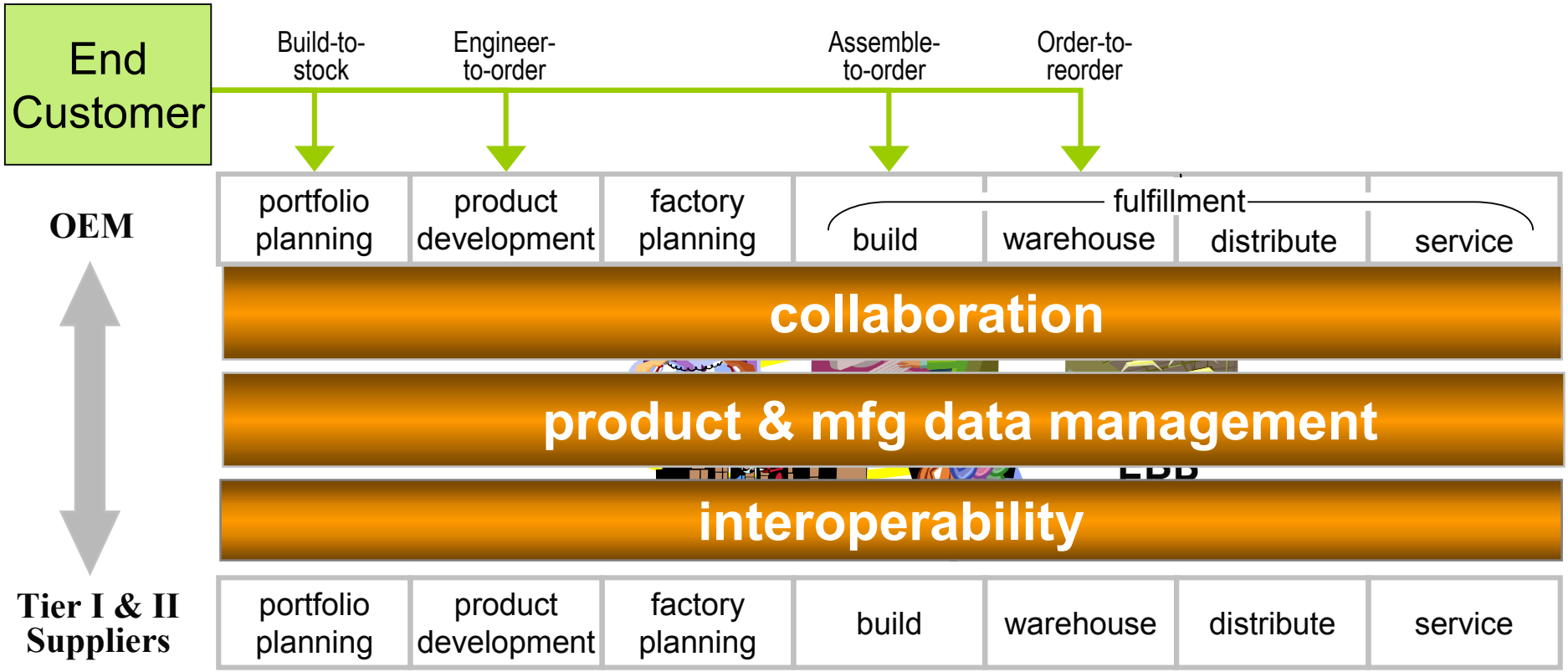

… solving the most

challenging business

problems with solutions

from UGS.

…THANK YOU

questions?

Robust Design Computational System (RDCS)

Kadambi (Raj) Rajagopal
Project Lead
Structures Technology

The Business Case for RDCS: Facilitate Low Cost Development

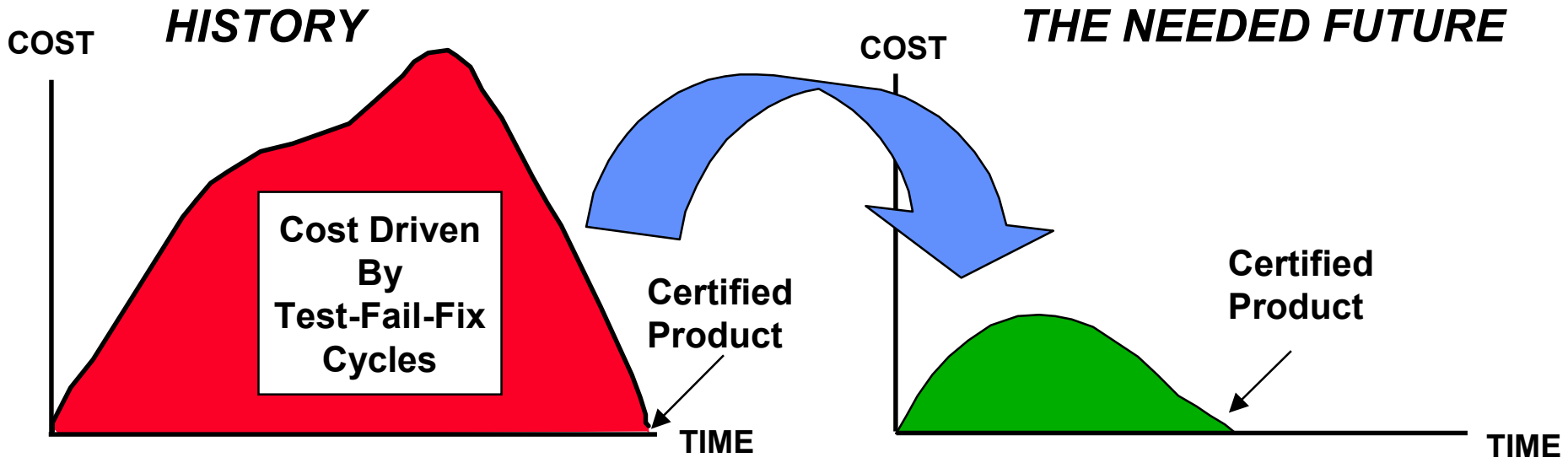

"Robust Design Computational System"

Capability Provided To:

- Fully Explore The Design Space
- Account For Variabilities
- Quantify Risks, Sensitivities Margins, Reliabilities

Detailed Design
Robust Design Process

Goal: Develop products insensitive to variation with an order of magnitude reduction in product development cost and cycle time.

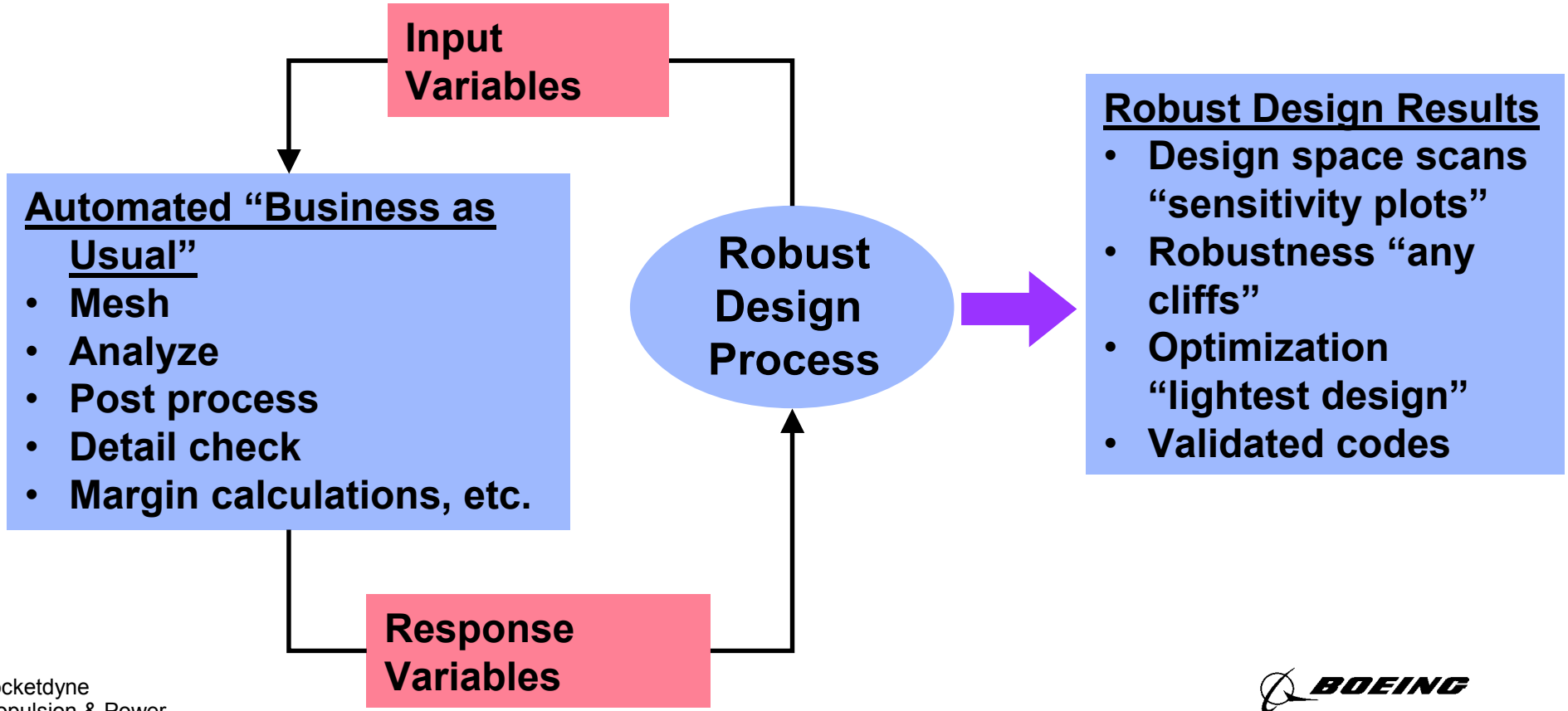

What is RDCS?
An Enterprise Wide Computational Tool

- An engineering code with built in strategies to perform standard deterministic design and advanced robust design methods such as: sensitivity quantification, design scanning, Taguchi signal-to-noise, deterministic optimization and probabilistic risk assessment

- A framework for performing automated design explorations using multi-disciplinary systems models distributed over a unix computing network

- Not just an analysis program such as finite element or discipline specific stress / thermal / fluid analysis

- A computational system that takes care of the mundane tasks of: setting up multi-disciplinary parametric analyses, running them on a network of computers, plotting the results, etc.

Robust Design Computational System

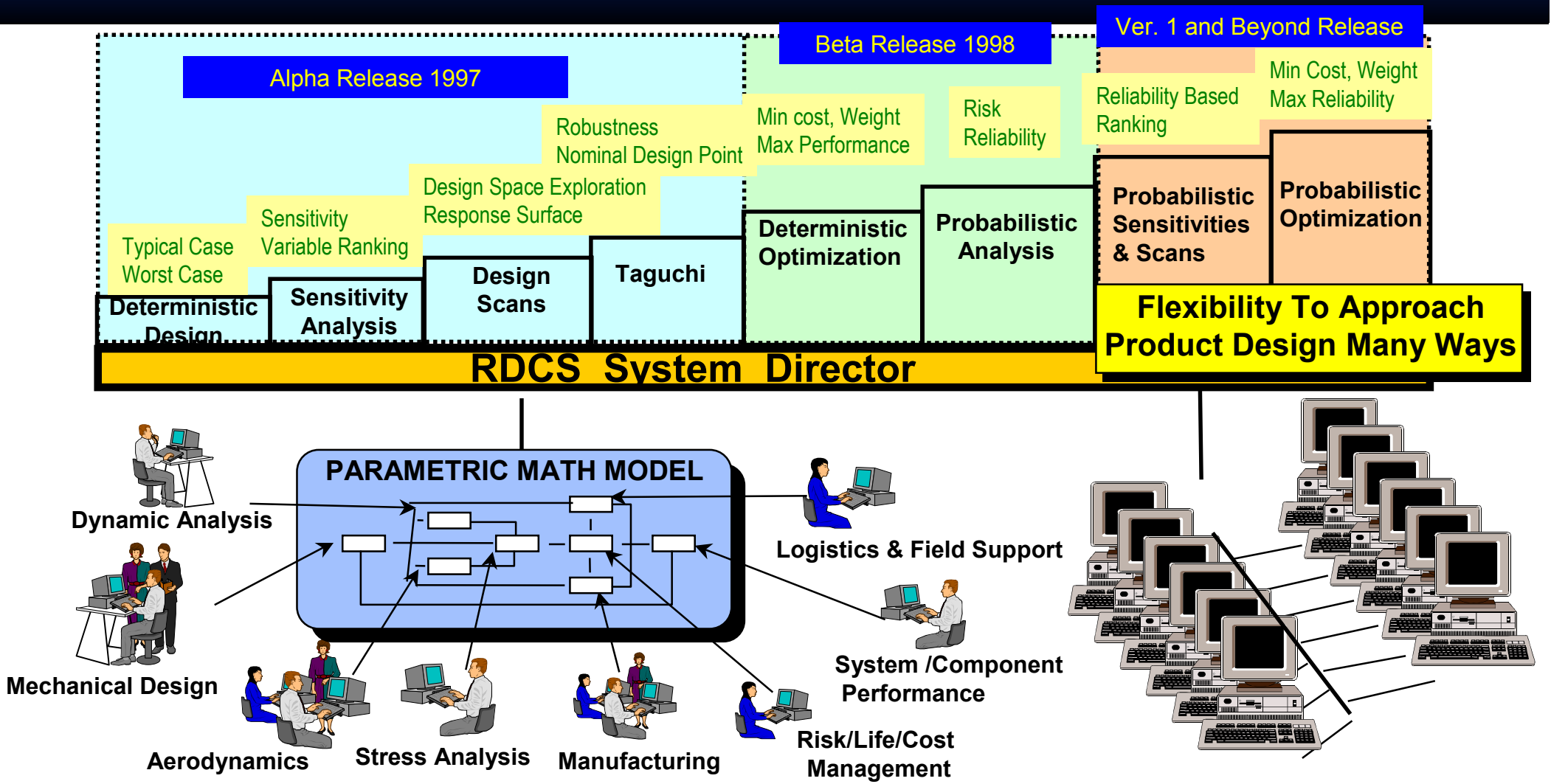

Capture analysis & design process

Rapid parallel computing

RDCS Workflow

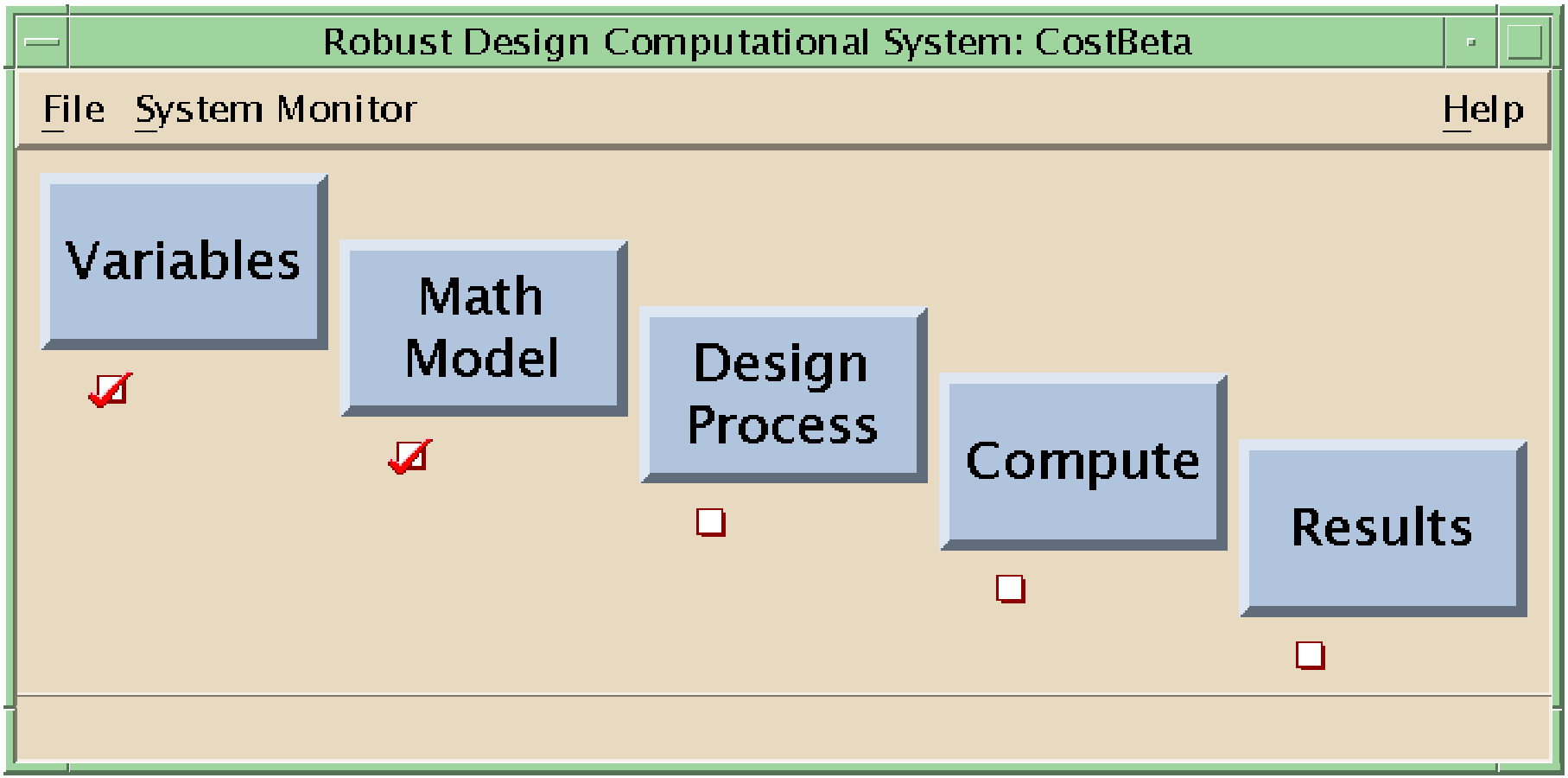

Definition of Global Variables & Responses

- **No Repetitive or Redundant Global Variable or Response Inputs**
- **Same Variables & Responses are Shared by All the Design Processes**

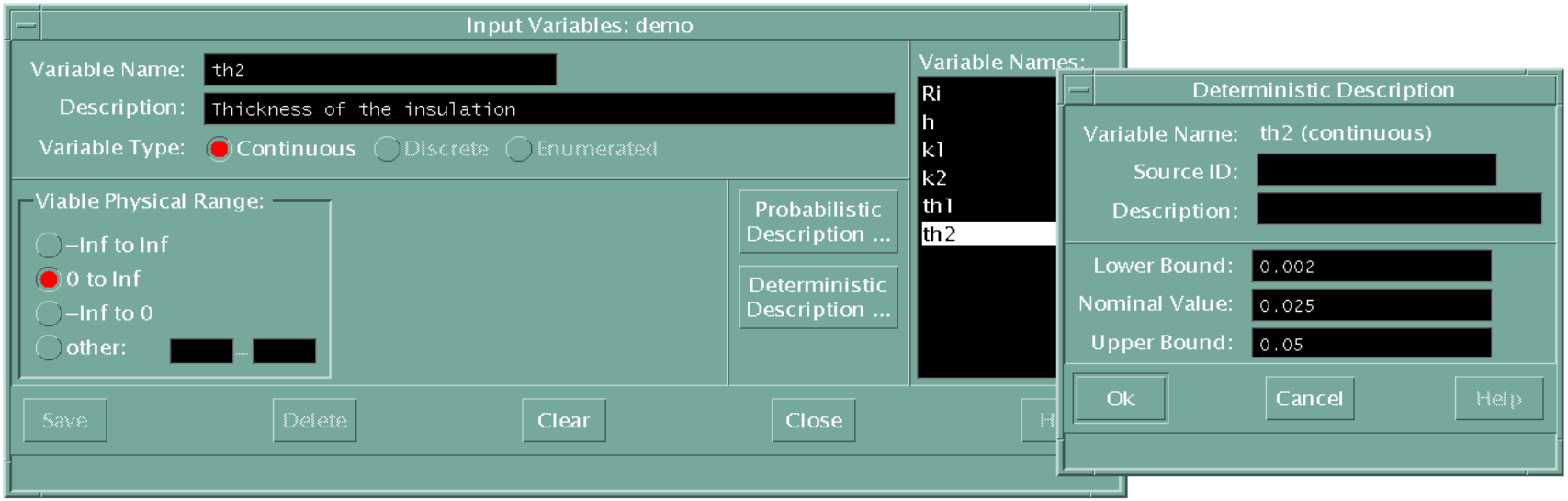

RDCS Allows Global Variables with Probabilistic Description

- **Numerous Probabilistic Distribution Models Such As Normal, LogNormal, Weibull etc. are available for Characterizing The Variations**

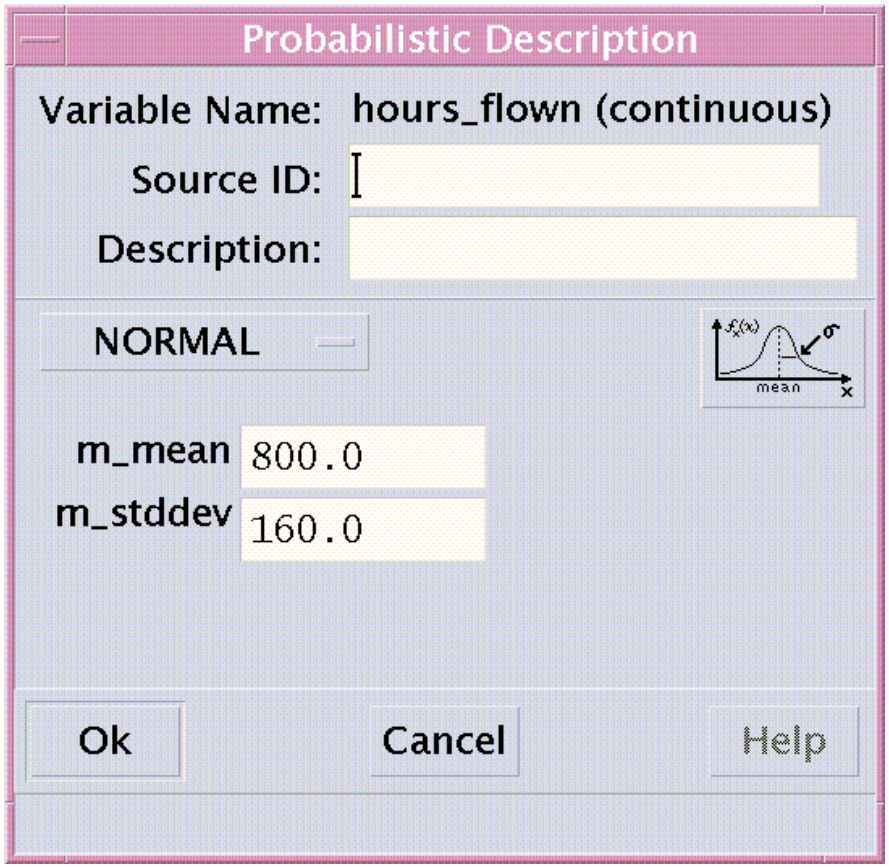

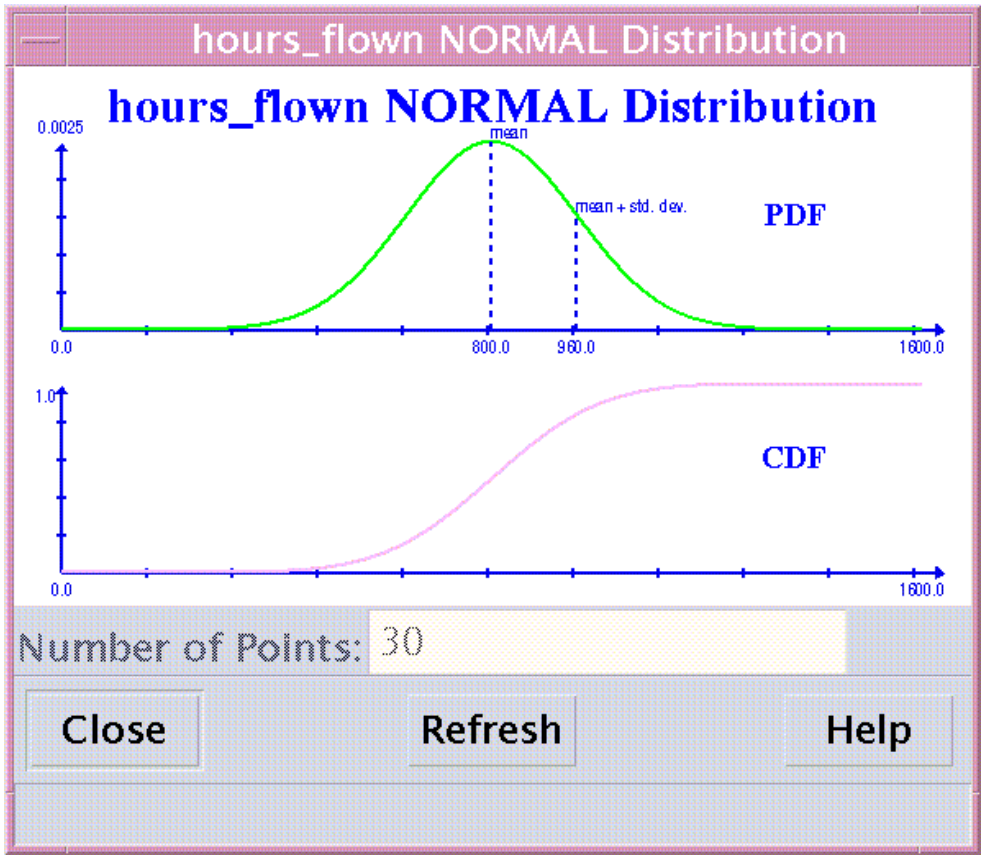

Graphical Definition of Multi-disciplinary Math Model

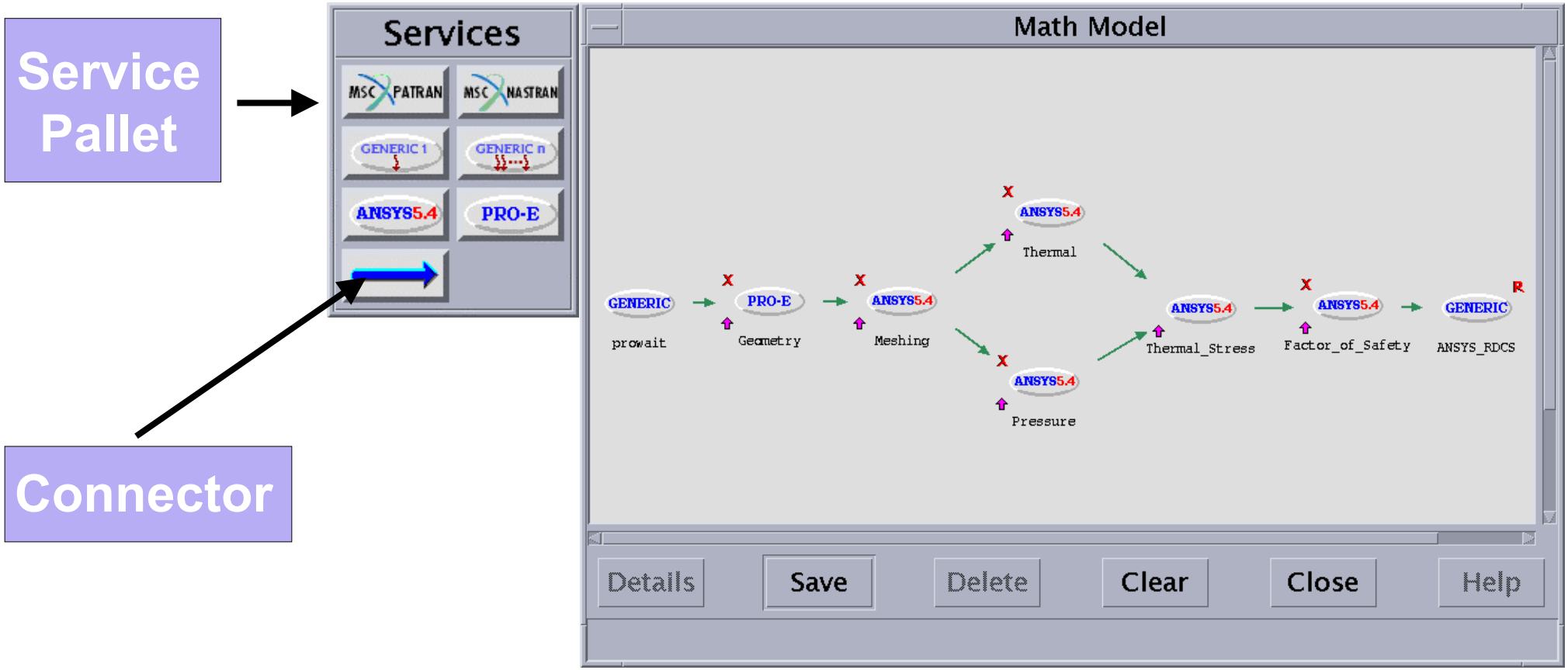

- **Customizable Service Pallet: Click and Drop Services**

Design Process Selection

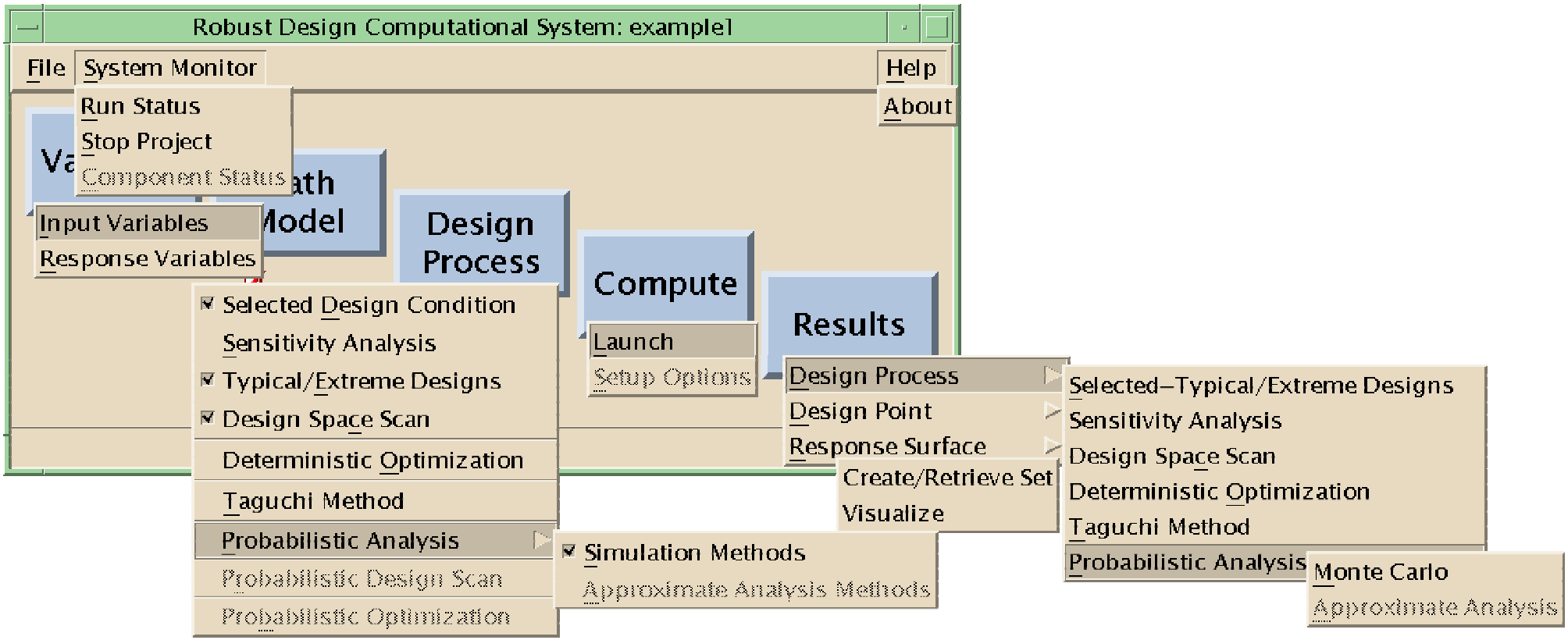

RDCS Design Visualization & Assessment

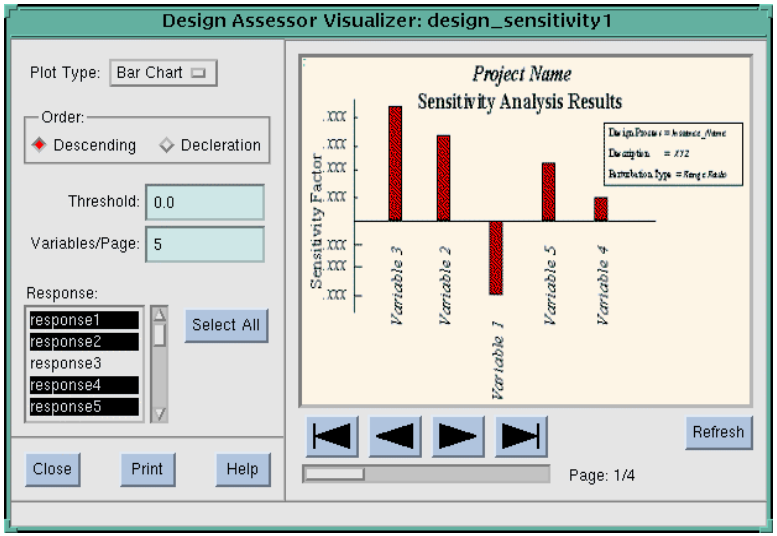

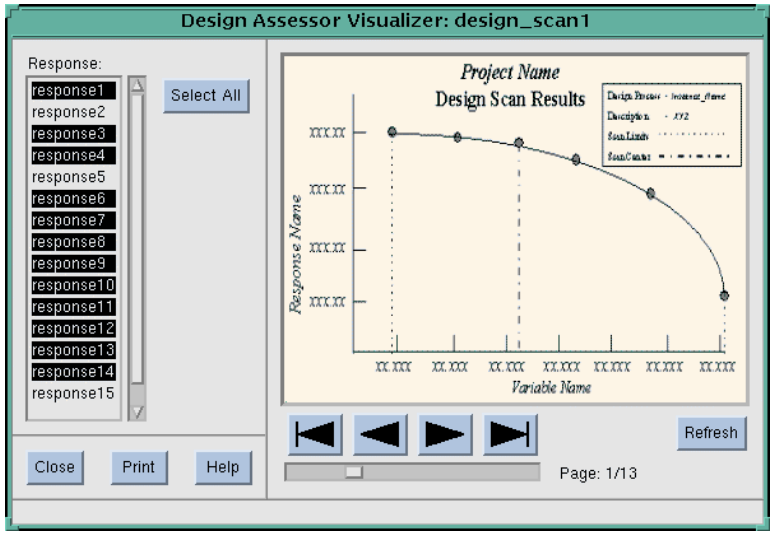

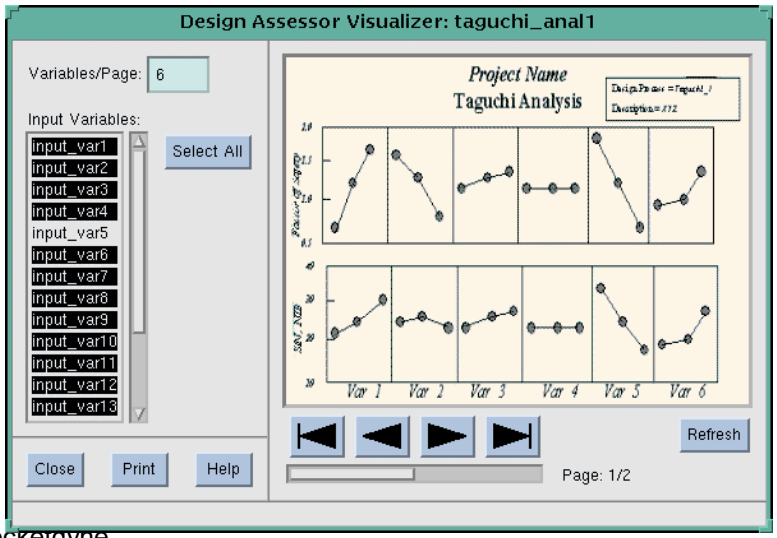

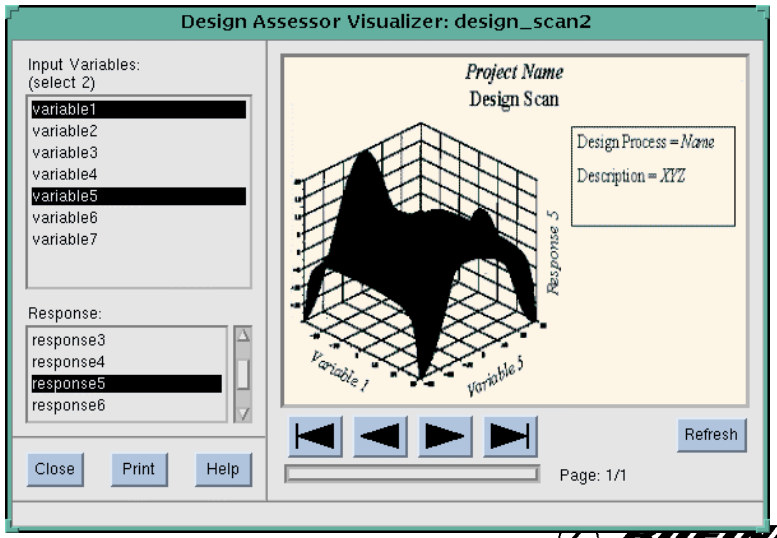

Applications Quantify Benefits of RDCS

1000 NONLINEAR ANSYS RUNS TO BALANCE 6 TURBINE BLADE SETS -- 200 RUNS/NIGHT

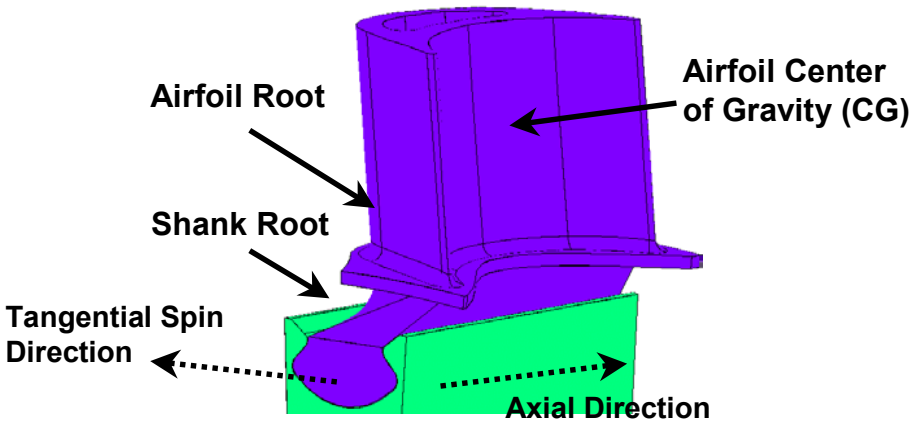

CHANGE ROCKET ENGINE HIGH PRESSURE JOINT DESIGN FOR ELV USING OVER 120 3D NON-LINEAR FEM MODEL CONFIGURATIONS

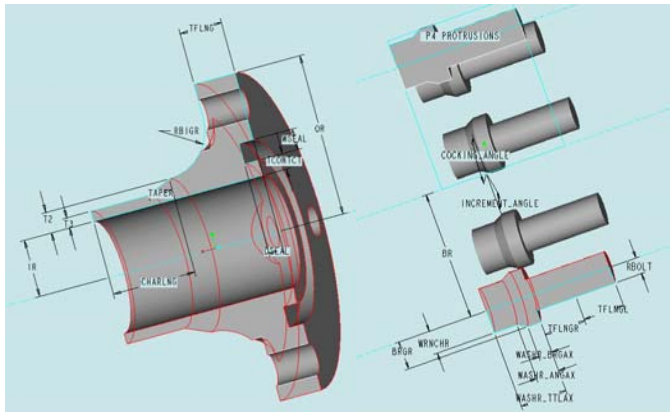

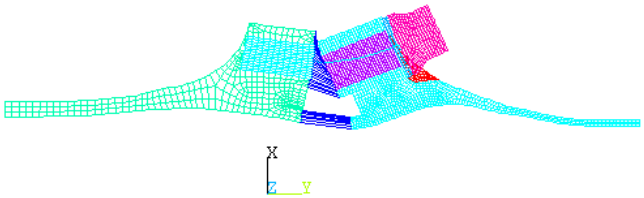

10% WEIGHT SAVINGS FOR RS-68 MANIFOLD FLANGE

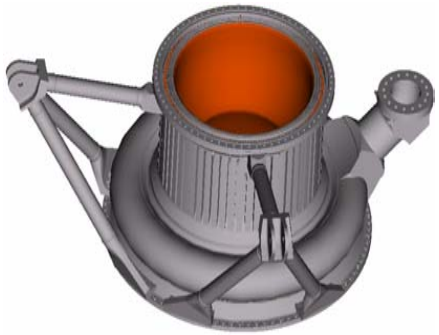

Software Architecture of RDCS
State Of The Art

- Graphical User Interface
  - Ease of Use
  - Minimal Training
- Client / Server
  - Distributed Computing
  - Major Cycle Time Improvement
  - Model for Internet/Intranet Operation
- Open Architecture
  - Adding New Design Processes
  - Permits Rapid Links To Other Codes
- Object Oriented Design
  - Ease of Maintenance
  - Reusability
  - Ease of Enhancement
- C++ Motif
  - Industry Standard
  - Supports Object Oriented Design

REPORT UNAVAILABLE

Thermal Technology Development Activities at the Goddard Space Flight Center - 2001

September 11, 2001

Dan Butler

Thermal Engineering Branch/Code 545

NASA/GSFC

http://watt-a-server.gsfc.nasa.gov/

Thermal Technology Development at GSFC

- Two-Phase Systems
  - Heat Pipes and Variable Conductance Heat Pipes
  - Capillary Pumped Loops
  - Loop Heat Pipes
  - Vapor Compression Systems (Heat Pumps)
  - Phase Change Materials
- Variable Emittance Surfaces
- Advanced Coatings
- High Conductivity Materials
- Electrohydrodynamic (EHD) Thermal Control Systems

Heat Pipes

- Heat Pipes use capillary forces generated by a wick structure and the latent heat of vaporization of a working fluid to transfer large amounts of heat at nearly constant temperature
- Heat is input to one end of the pipe where it vaporizes the working fluid
- The vapor is transported to the condenser end of the pipe where it is condensed and the heat is rejected
- The condensed fluid travels back to the evaporator section in a capillary wick structure, which can be grooves in the wall, screens, sintered metal, or other porous material

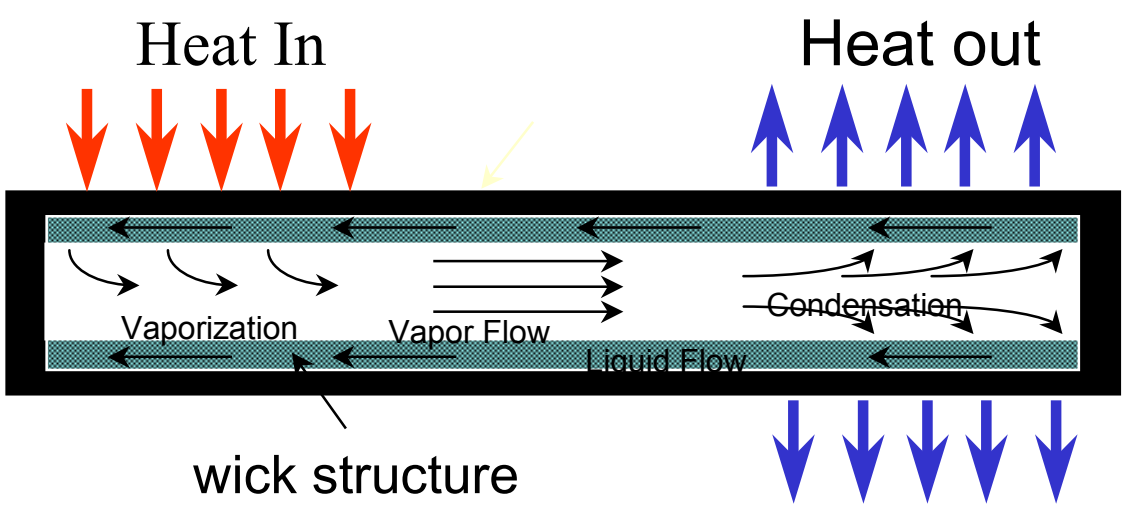

Heat Pipe Technology

1. Heat pipes are considered a standard off the shelf technology.
    1. Used routinely in many Spacecraft applications
    2. Copper/water pipes found in many laptops and video game consoles
2. Development efforts at GSFC
    1. Flight of HPP mid-deck experiment in early 90's, refinement of the GAP heat pipe analytical model
    2. Flight of cryogenic heat pipes on the shuttle in the mid 90's
    3. Qualification testing of Thermacore Copper/Water Heat Pipes in 2000
        1. Successfully completed Vibration and TV, including freeze/thaw cycles
        2. Promising diode action near 0 C as H2O freezes, demonstrated restart under load - Ideal for electronics cooling
    4. Use of an ethane heat pipe for the Swift XRT instrument 2002, operates at -50 C with a 10 watt heat load

Variable Conductance Heat Pipes VCHP's

- VCHP's utilize a reservoir containing inert gas (nitrogen) to block part or all of the condenser, thus providing temperature control of the heat pipe to +/- 2 C
- Requires electrical controller and heater on the reservoir, linked to a feedback thermistor
- VCHP's are off the shelf technology, but not extensively used
- GSFC applications on TPF flight experiment and Swift Loop Heat Pipe

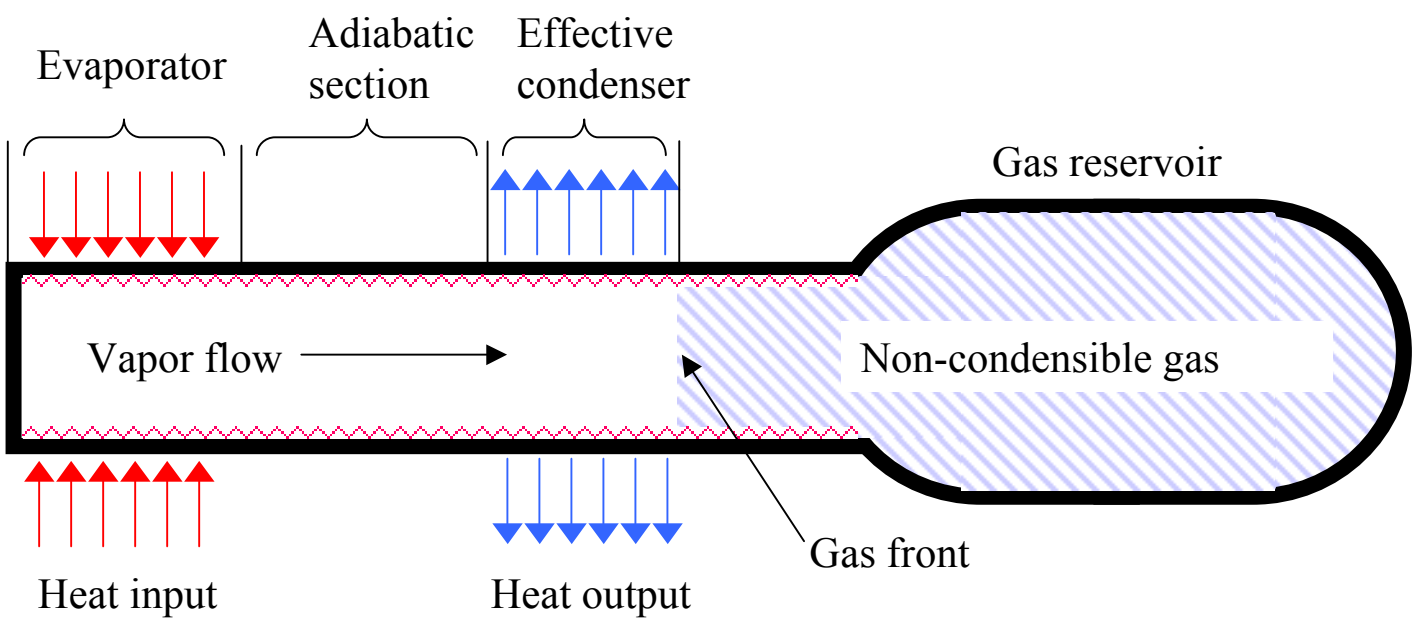

Capillary Pumped Loops

- Capillary pumped loops (CPL's) are two-phase heat transfer devices which use capillary forces for heat acquisition and fluid pumping with no moving parts
  - Transfers high heat loads over long distances with vibration free operation and passive control
  - Factor of 30x improvement in wicking height over conventional heat pipes - greatly improves ground testability and and eases spacecraft integration
  - Diode action offers shut down capability, minimize heater power requirements

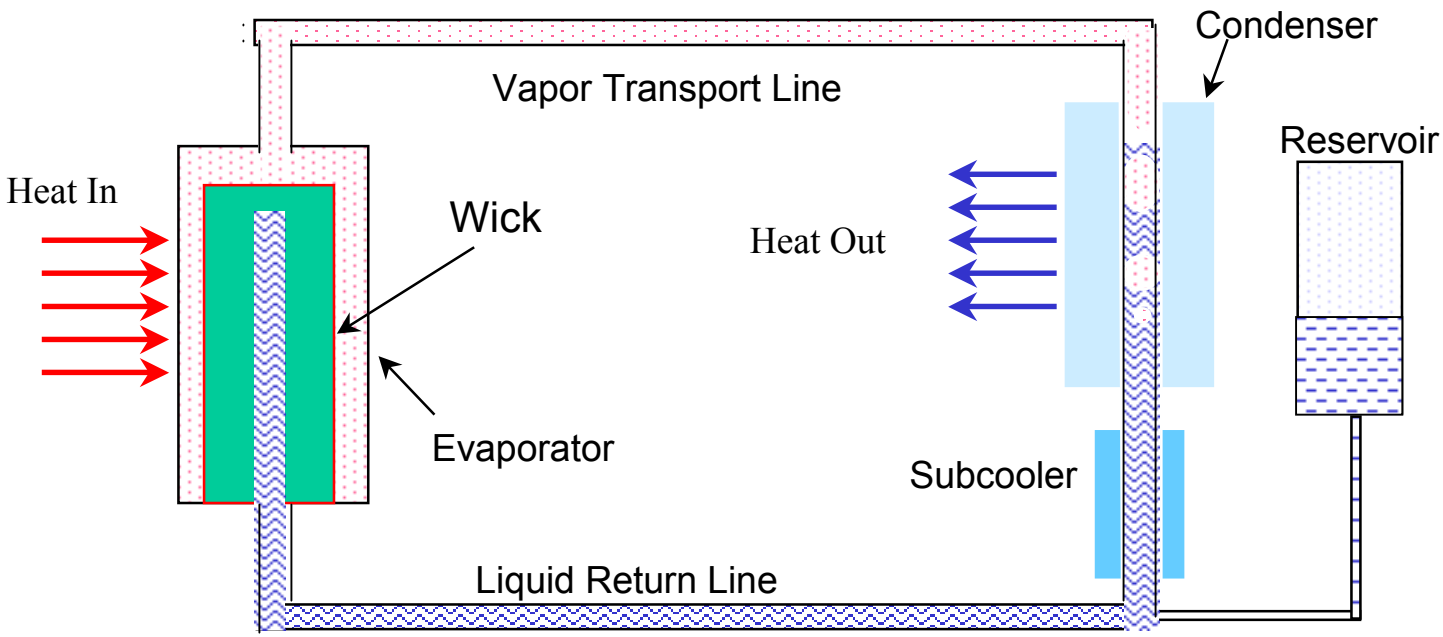

Capillary Pumped Loop Technology CPL

- CPL concept originated at the Lewis Research Center
- Developed at GSFC starting in the early 80's
- Numerous test beds and shuttle flight experiments
  - CPL GAS and Hitchhiker flight experiments in 1985 and 1986
    - Proof of Concept
  - CAPL 1 and CAPL 2 flight experiments in 1994 and 1995
    - Point Design for the EOS-AM (now TERRA) Spacecraft
    - Single pump CPL verified for flight applications - "Starter Pump CPL"
  - TPF Flight Experiment in 1997
    - Proof of Concept for multiple pump loop
  - Multiple pump CPL's
    - CAPL 3 flight experiment manifested on STS-108, Nov 2001
    - CCQ flight experiment (awaiting flight opportunity)

Starter Pump Capillary Pumped Loop

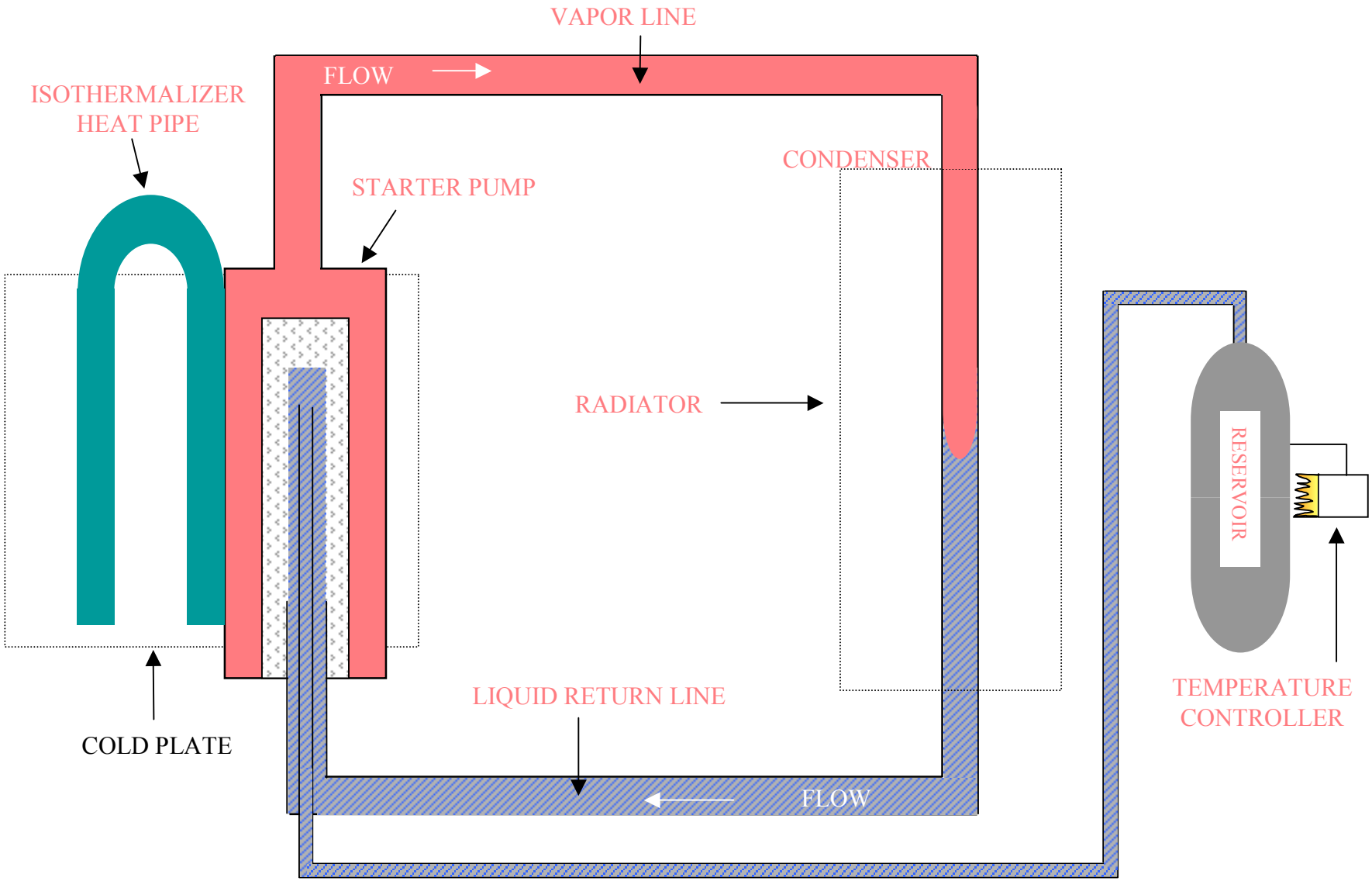

CPL's on TERRA (EOS-AM)

- **Terra launched December 18, 1999**
- **Two-phase loops (CPLs) are on SWIR, TIR and MOPPIT instruments**
- **On the next day, the first CPL system in a flight mission was started successfully.**
- **All 3 CPLs continue to demonstrate reliable, stable thermal control for their instruments**

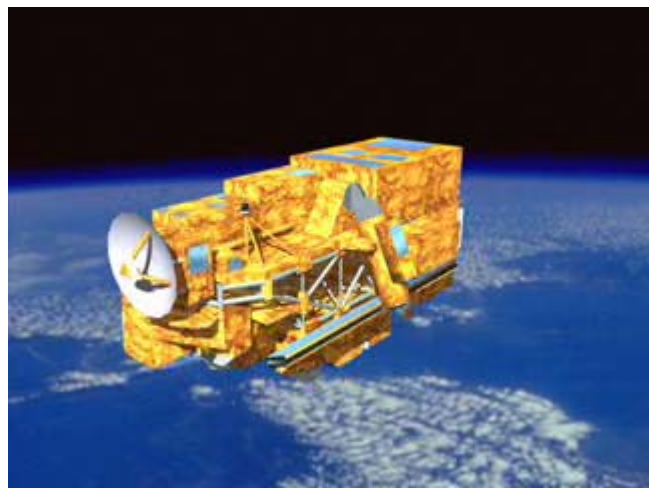

ASTER – TIR CPL CONFIGURATION

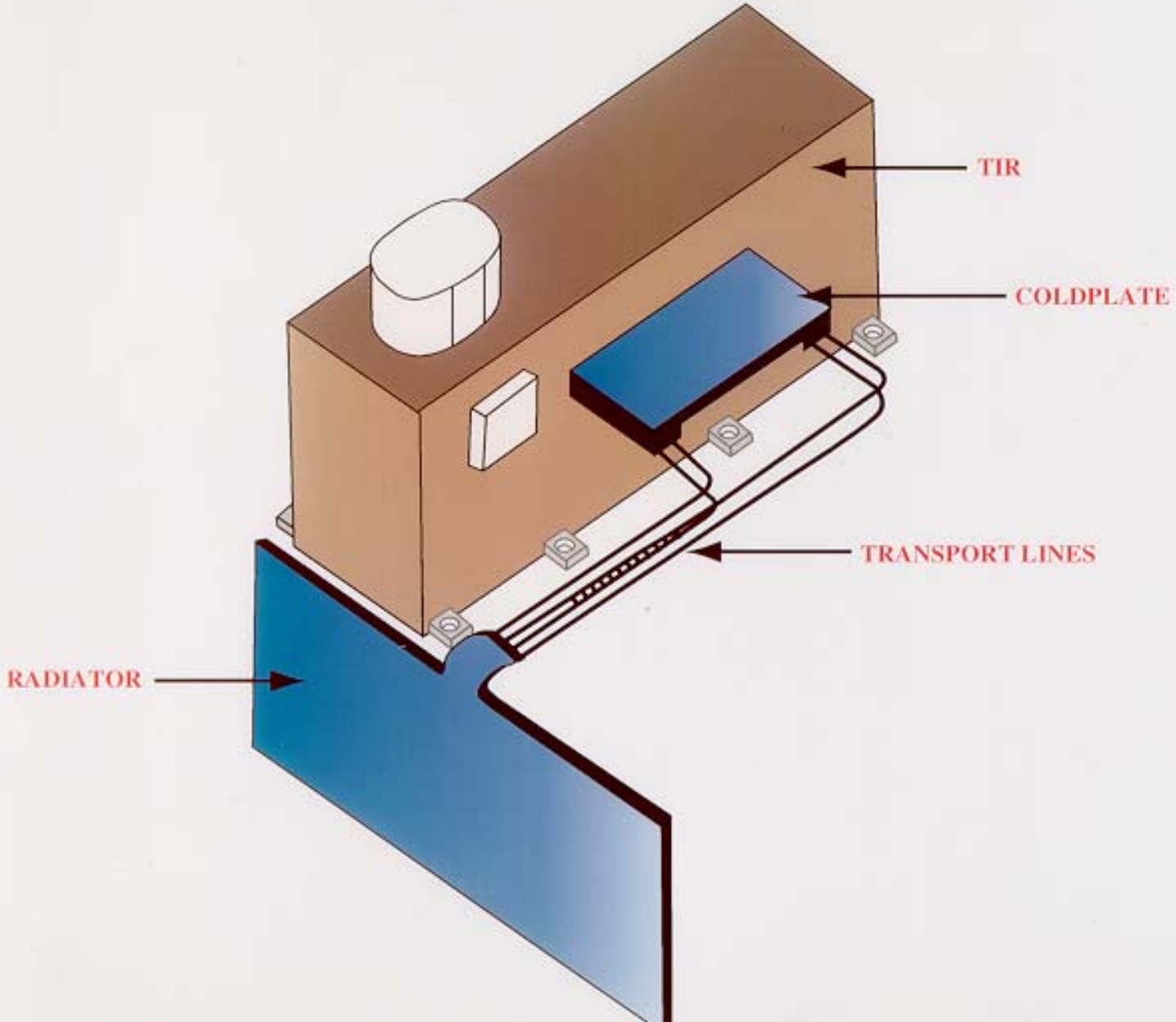

TERRA CPL Typical Layout

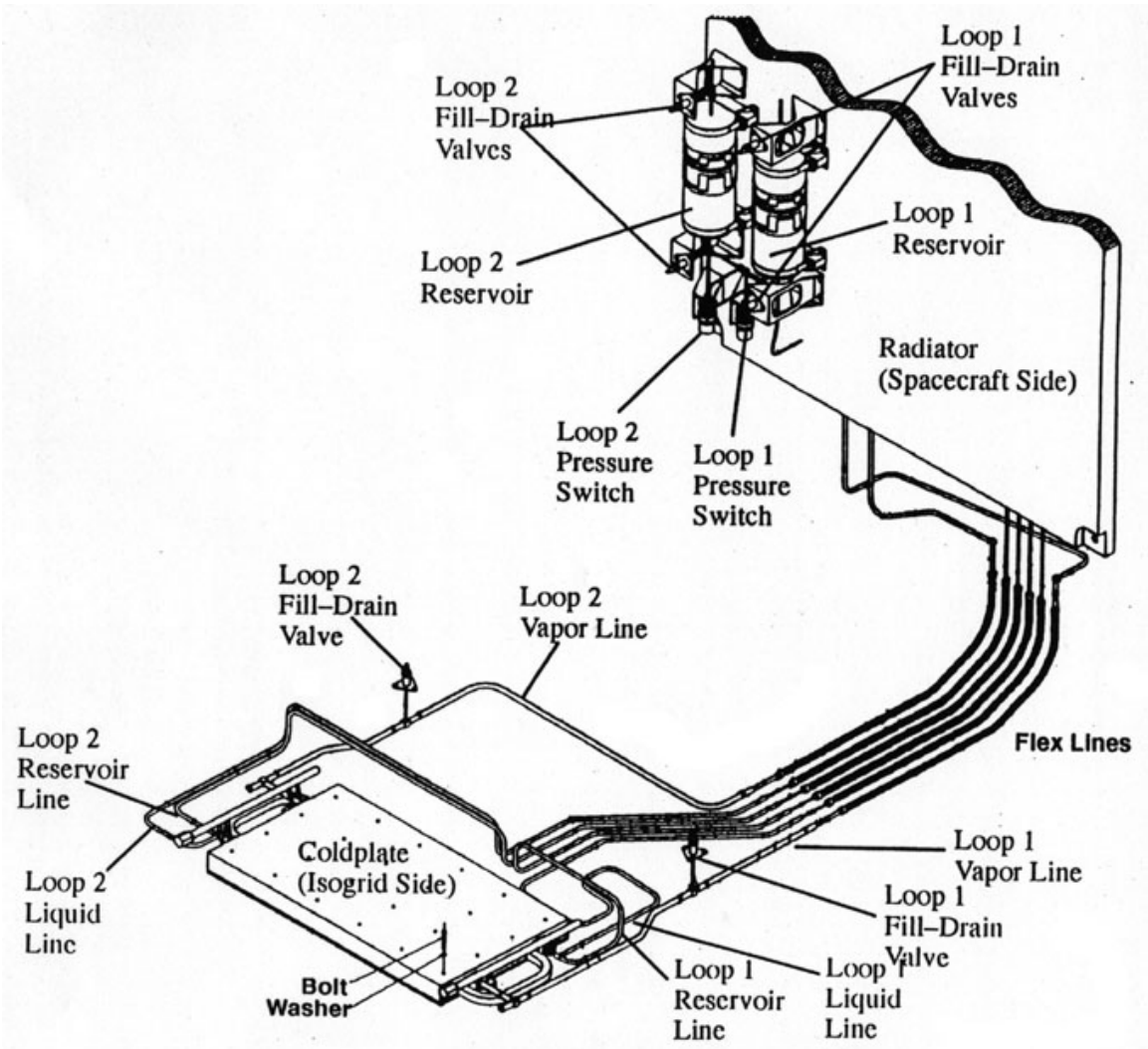

TERRA CPL - Coldplate

- Coldplate provides the thermal sink for the instrument.
- Contains the Capillary Starter Pump (Evaporator) that provides the capillary pumping head via porous wick.

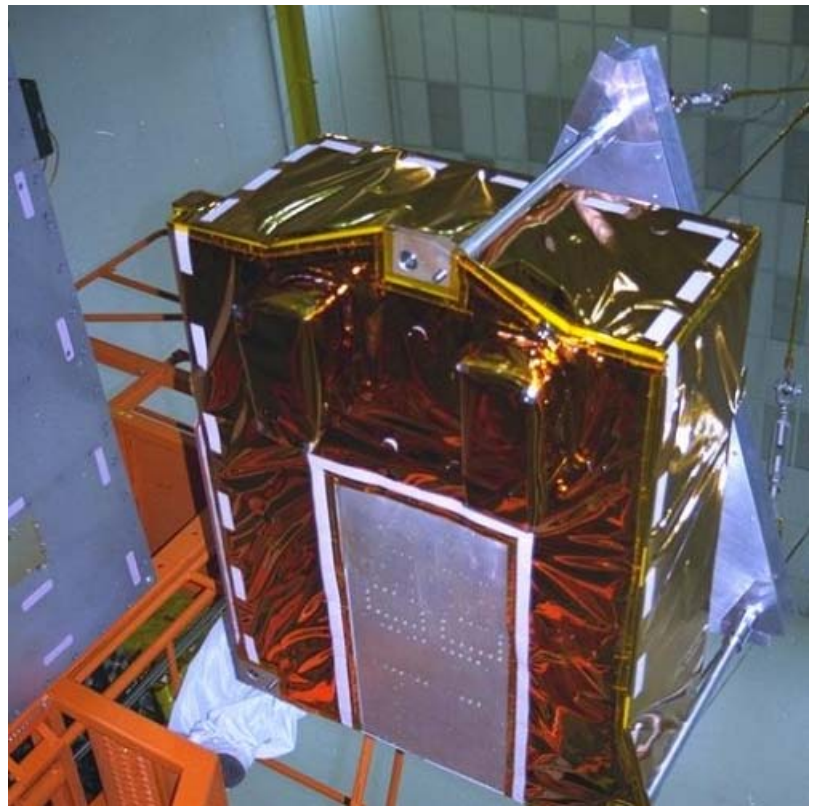

TERRA Normal Operations

The Radiator, Liquid Lines and Reservoir Lines have orbital variations and vary depending on the instrument activities. The coldplate remains at a constant temperature during all activities.

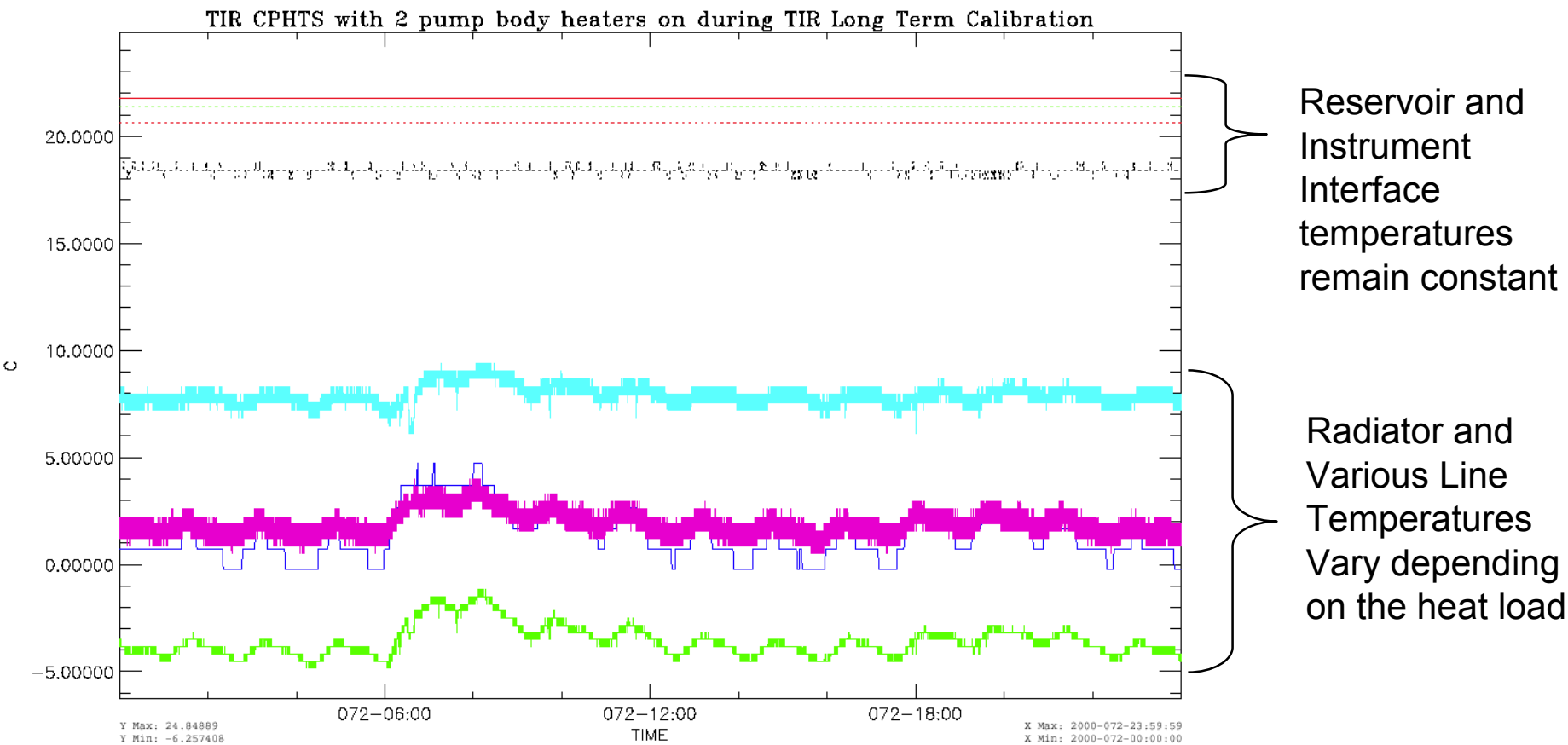

Reservoir Setpoint Change

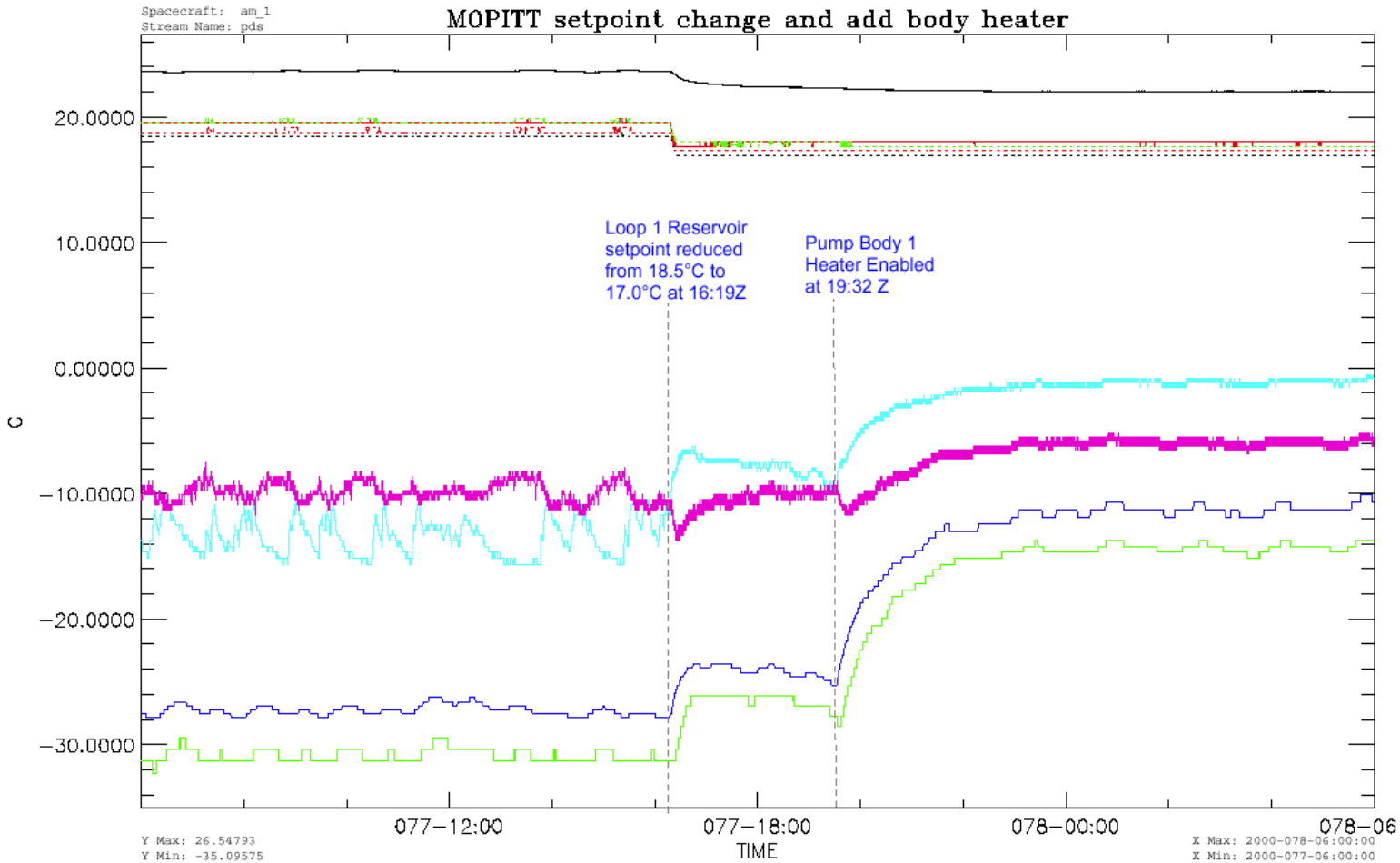

MNEMONIC NAME	SAMPLES	MINIMUM	MAXIMUM	AVERAGE	STD DEV	DESCRIPTION
MOP_TR_BPLT_2	10547	21.980	23.746	22.803	0.75298	Base Plate, Temperature P [C]
TCS_TR_M_CPPUMP1_MID	10547	17.659	19.907	18.662	0.76298	MOPITT Loop 1 Pump Middle [C]
TCS_TR_M_LIQLIN1_IN	10547	-32.294	-13.772	-23.678	7.4780	MOPITT Looop 1 Pump Liqui [C]
TCS_TR_M_RADSURF_HX1	1318	-27.879	-10.062	-20.456	7.2311	MOPITT Radiator Surface H [C]
TCS_TR_M_RESLIN1_IN	10546	-15.625	-0.49862	-7.5955	5.5600	MOPITT Loop 1 Reservoir L [C]
TCS_TR_M_RESLIN1_OUT	10547	-13.772	-5.1791	-8.5614	2.0194	MOPITT Loop 1 Reservoir L [C]
TCS_TR_M_RESV_LOOP1A	10547	16.908	18.784	17.557	0.74368	MOPITT Loop 1 Reservoir T [C]
TCS_TR_M_RESV_LOOP1B	10546	17.284	19.159	17.948	0.76644	MOPITT Loop 1 Reservoir T [C]
TCS_TR_M_VAPLIN1_FLX	10547	17.659	19.907	18.537	0.91956	MOPITT Loop 1 Vapor LIne [C]

Current Time:	2000-080-13:19:16
Req Start Time:	2000-077-06:00:00
Req Stop Time:	2000-078-06:00:00
Sample Rate:	All Points
Profile Name:	mop1_resvAB.abe
User Name:	abeuser

HST

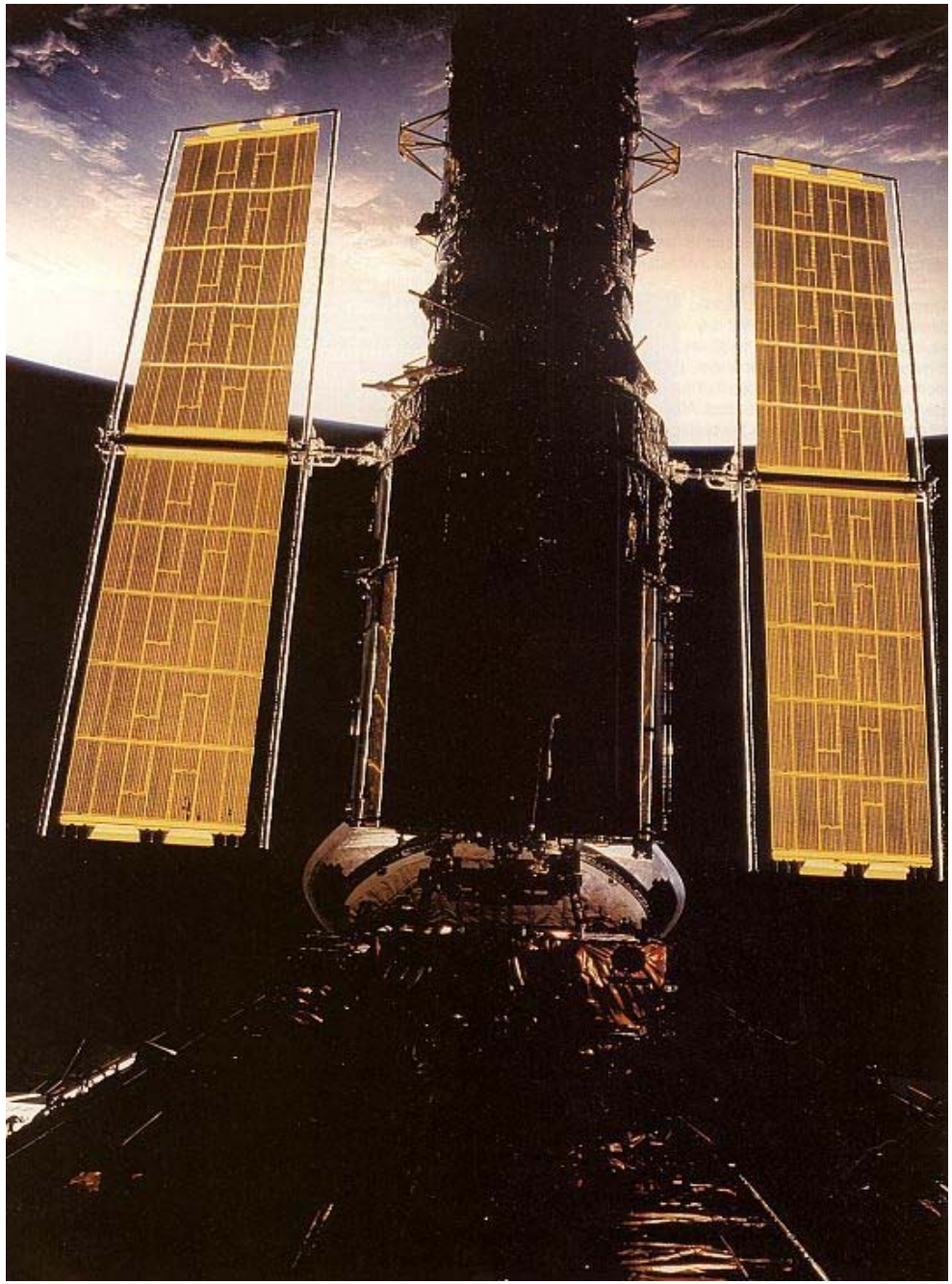

HST SM 3B Servicing Mission
STS - 109 Jan 2002

- **Near Infrared Camera and Multi Object Spectrometer (NICMOS) instrument installed on HST during Servicing Mission 2, Feb 1997**
  - Detectors cooled by nitrogen ice contained in a dewar
  - Thermal short in dewar detected shortly after SM2
  - Expected NICMOS lifetime of 4.5 years shortened to 1.7 years
- **On SM 3B, the astronauts will install a brayton cycle, mechanical cryo-cooler to cool NICMOS detectors and resume operations**
  - Mechanical refrigerator must be capable of developing in excess of 7 watts of cooling power at 70 K
  - Flexible Capillary Pump Loop built by Swales Aerospace selected to transfer energy from cryocooler to external radiator
- **Precursor check-out mission (HOST) flown on STS-95 in October 1998 to verify cryocooler and CPL operation in micro-gravity - Highly Successful.**

HST with CPL Radiators

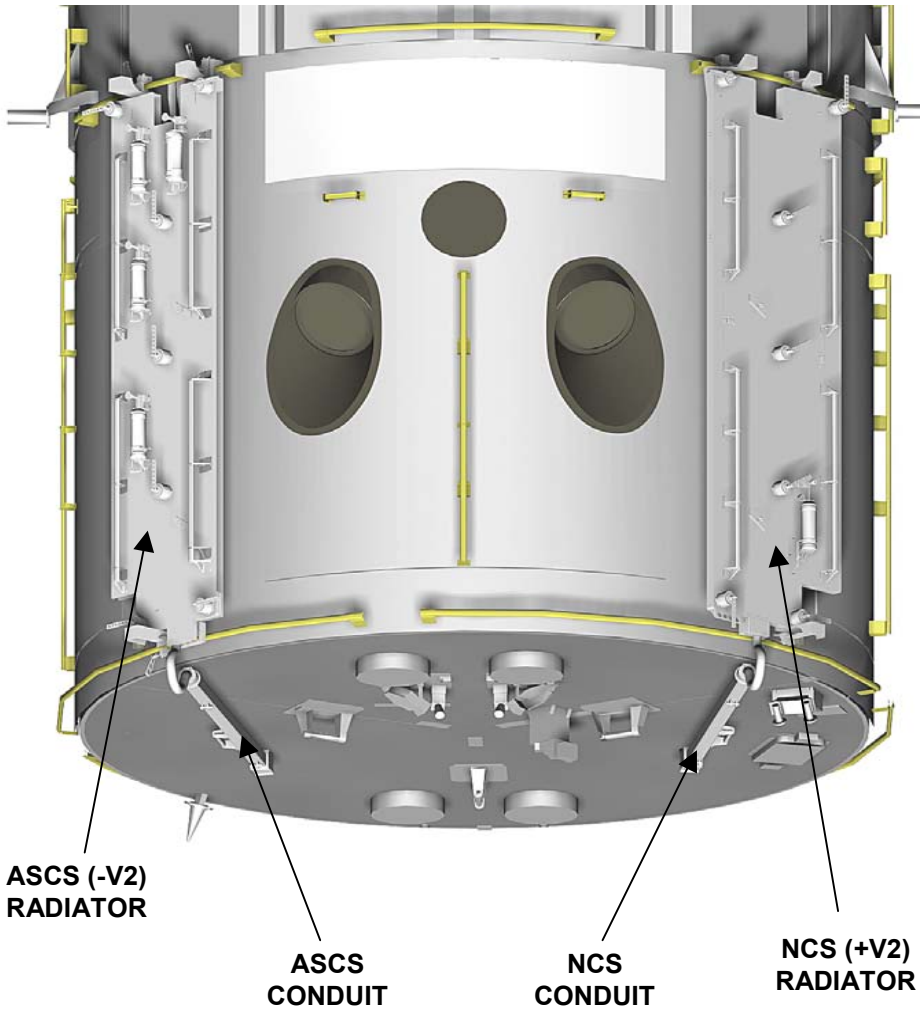

HST with CPL Installed

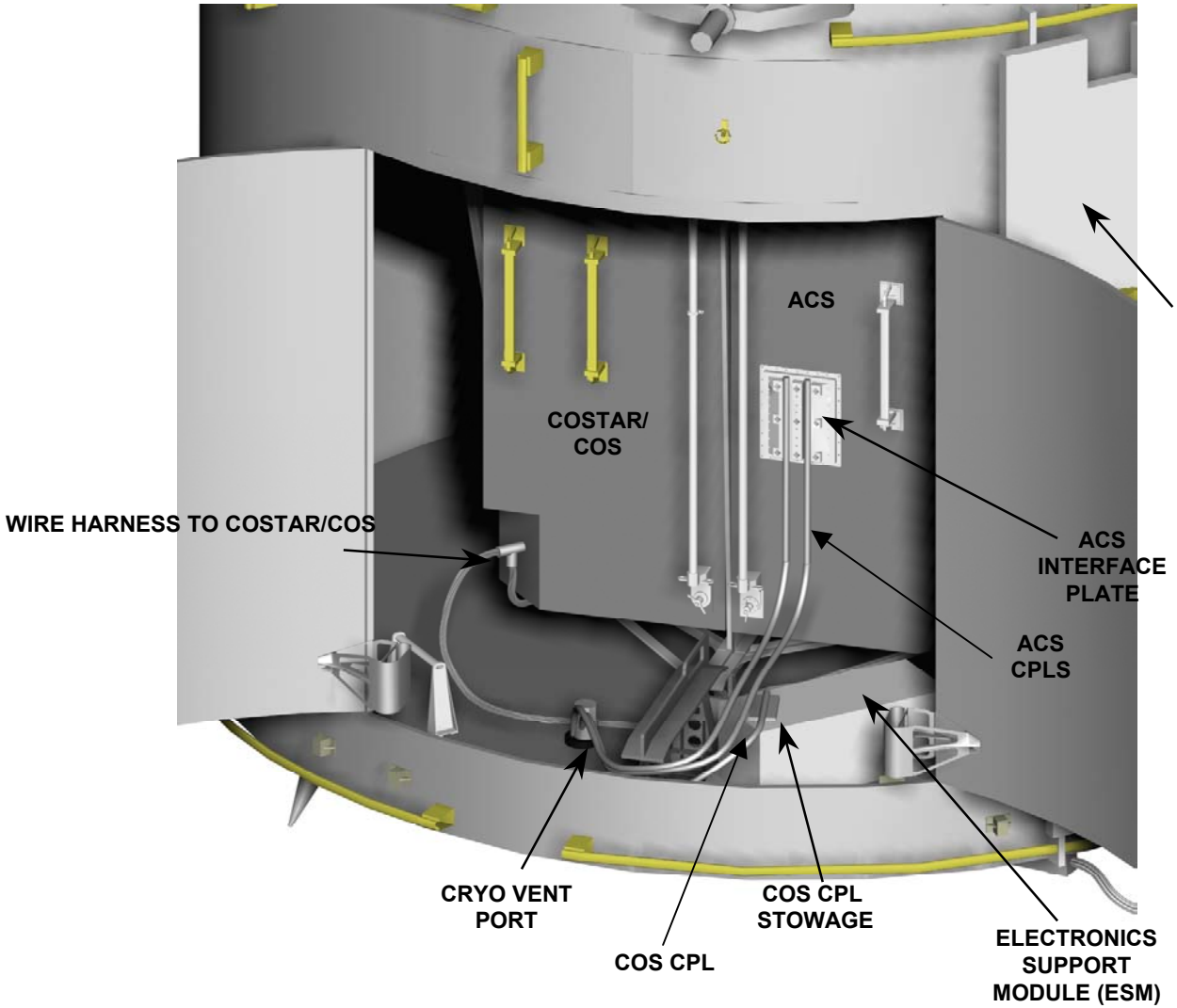

HST Thermal Components Assembly

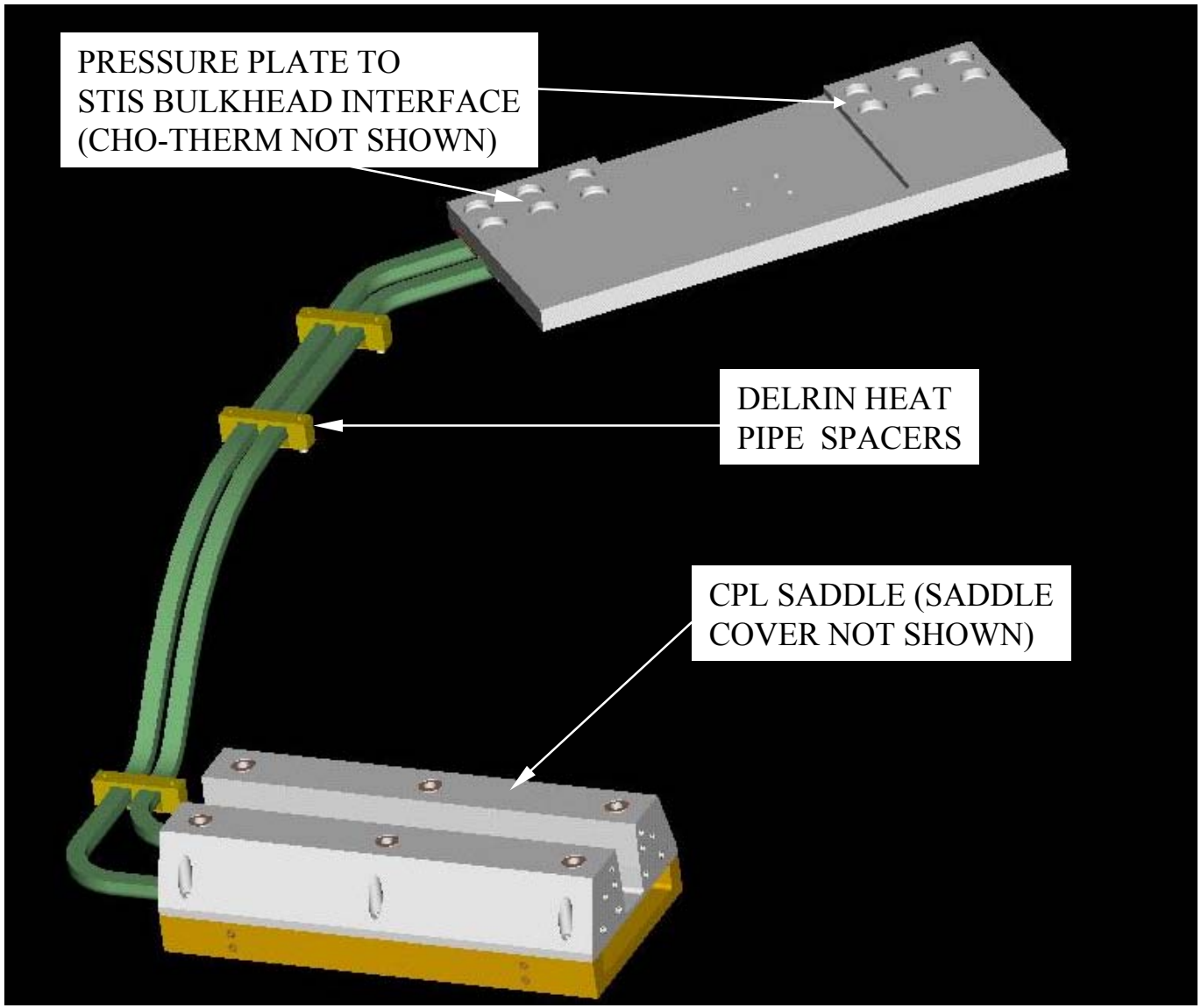

HOST Carrier Installed in the Payload Bay

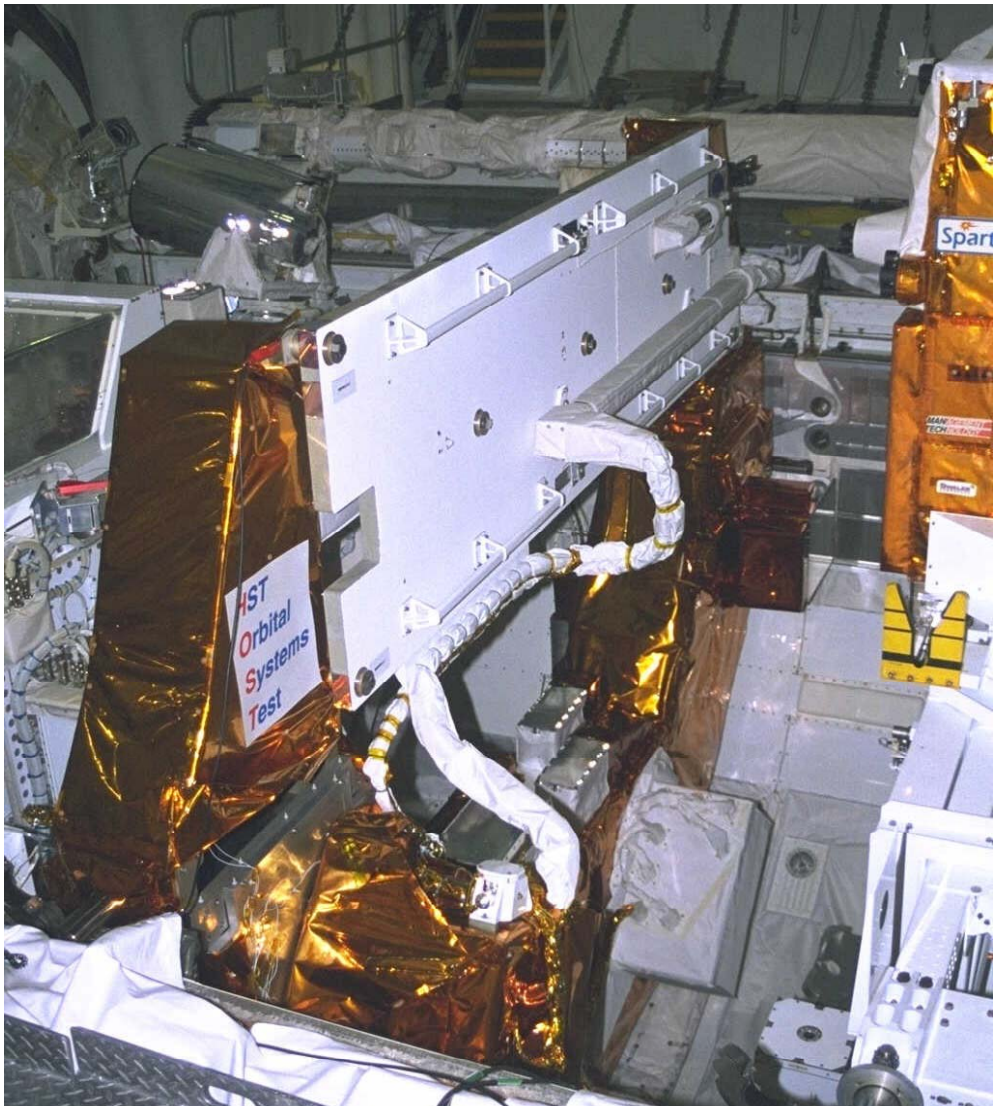

CPL Temperature Control Law Response

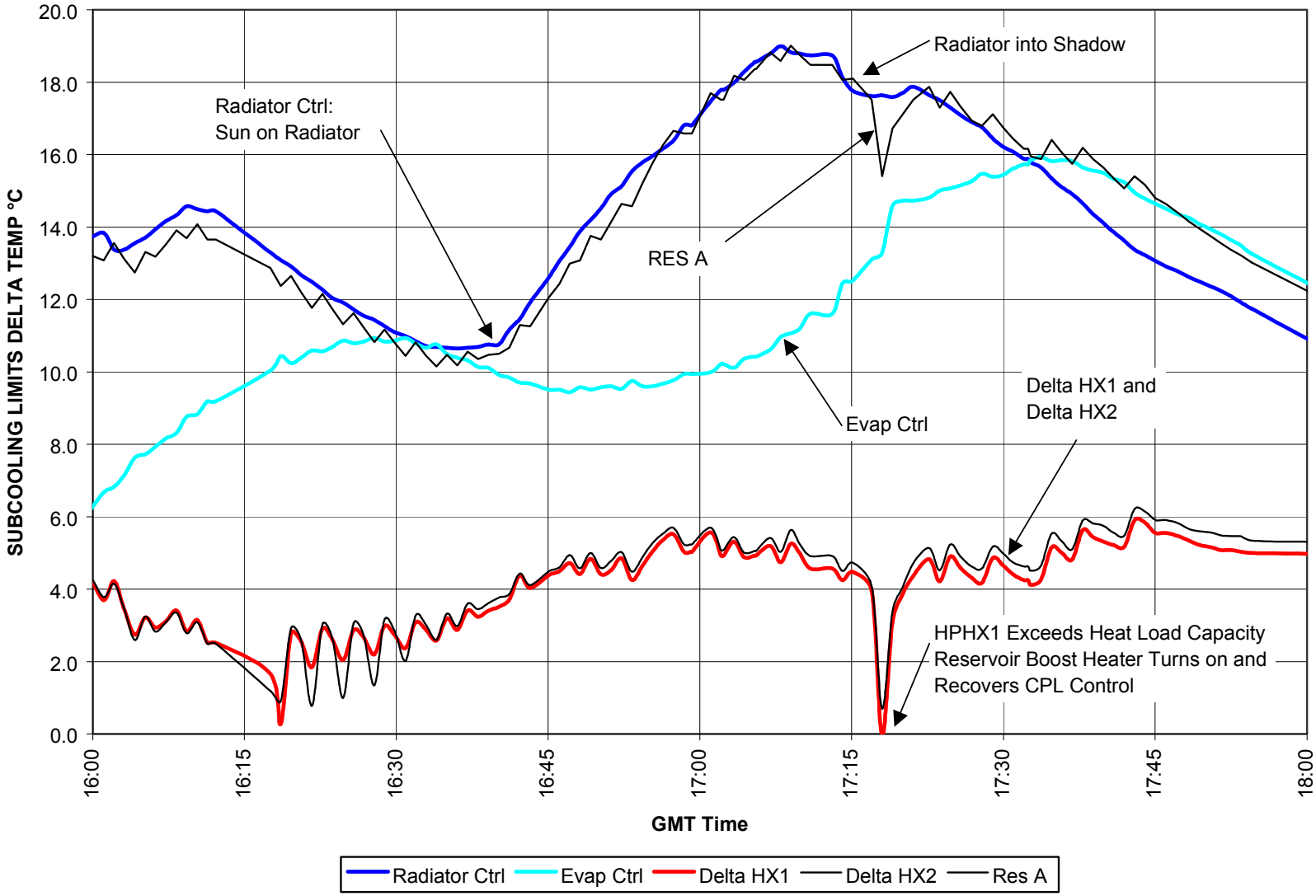

Multiple Evaporator Capillary Pumped Loop

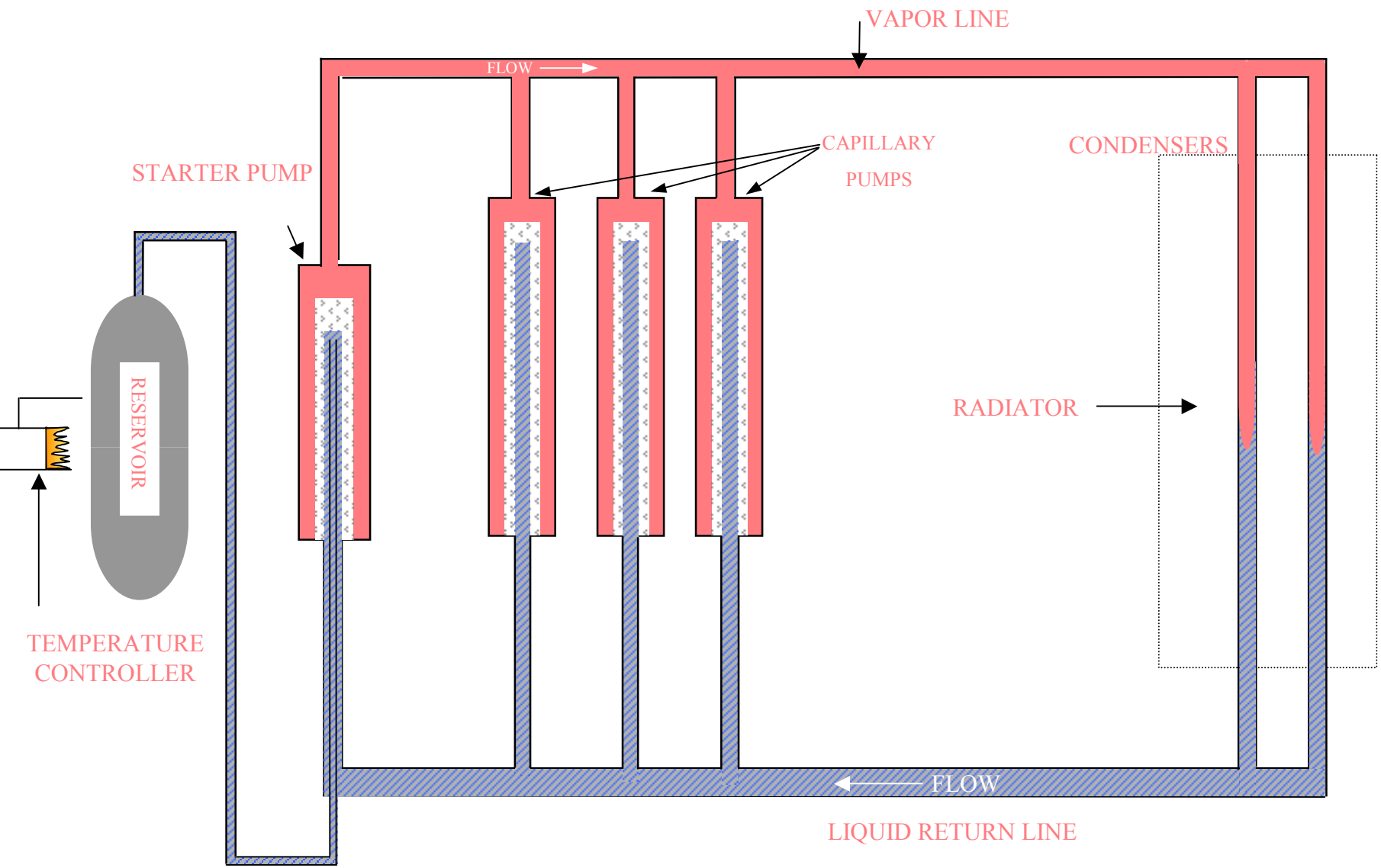

CAPL 3 Flight Experiment

NRL/NASA Experiment

CAPL 3 Flight Experiment

- Follow on to CAPL 1 (STS-60, 2/94) and CAPL 2 (STS-69, 9/95) flight experiments
- Joint Naval Research Lab (NRL)/NASA partnership which will meet technology objectives for both the Department of Defense and NASA
- Two-phase ammonia thermal control system consisting of a capillary pumped loop with multiple capillary evaporators and parallel direct condensation radiators
- Includes a capillary starter pump and a back pressure regulator to assist with start-up in micro-gravity
- Will demonstrate heat load sharing between evaporators which provides heating from the loop as well as cooling
- Currently manifested on STS-108 in Nov 2001

CAPL 3 Schematic

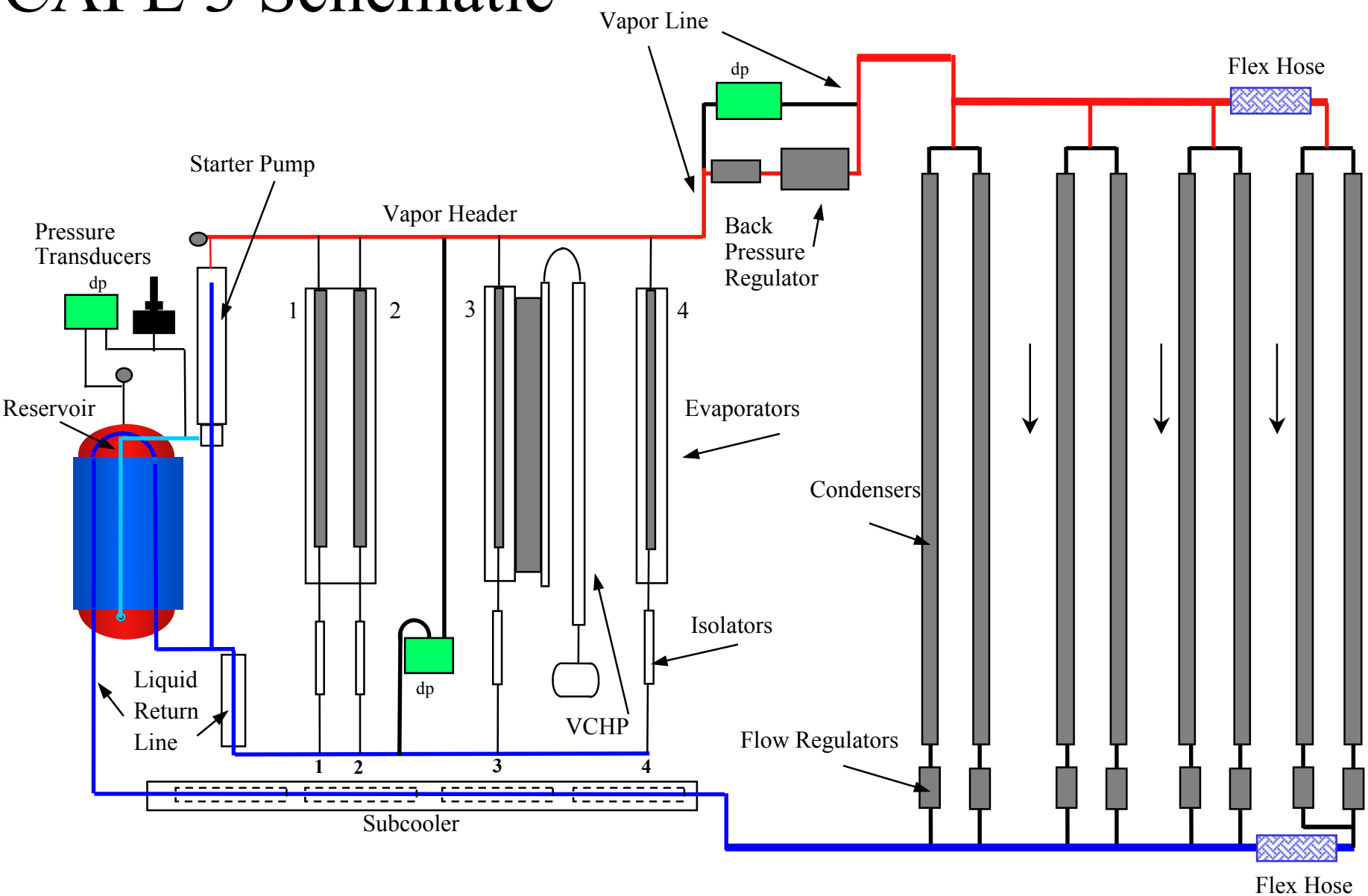

CAPL 3 Radiator Assembly (Upside Down)

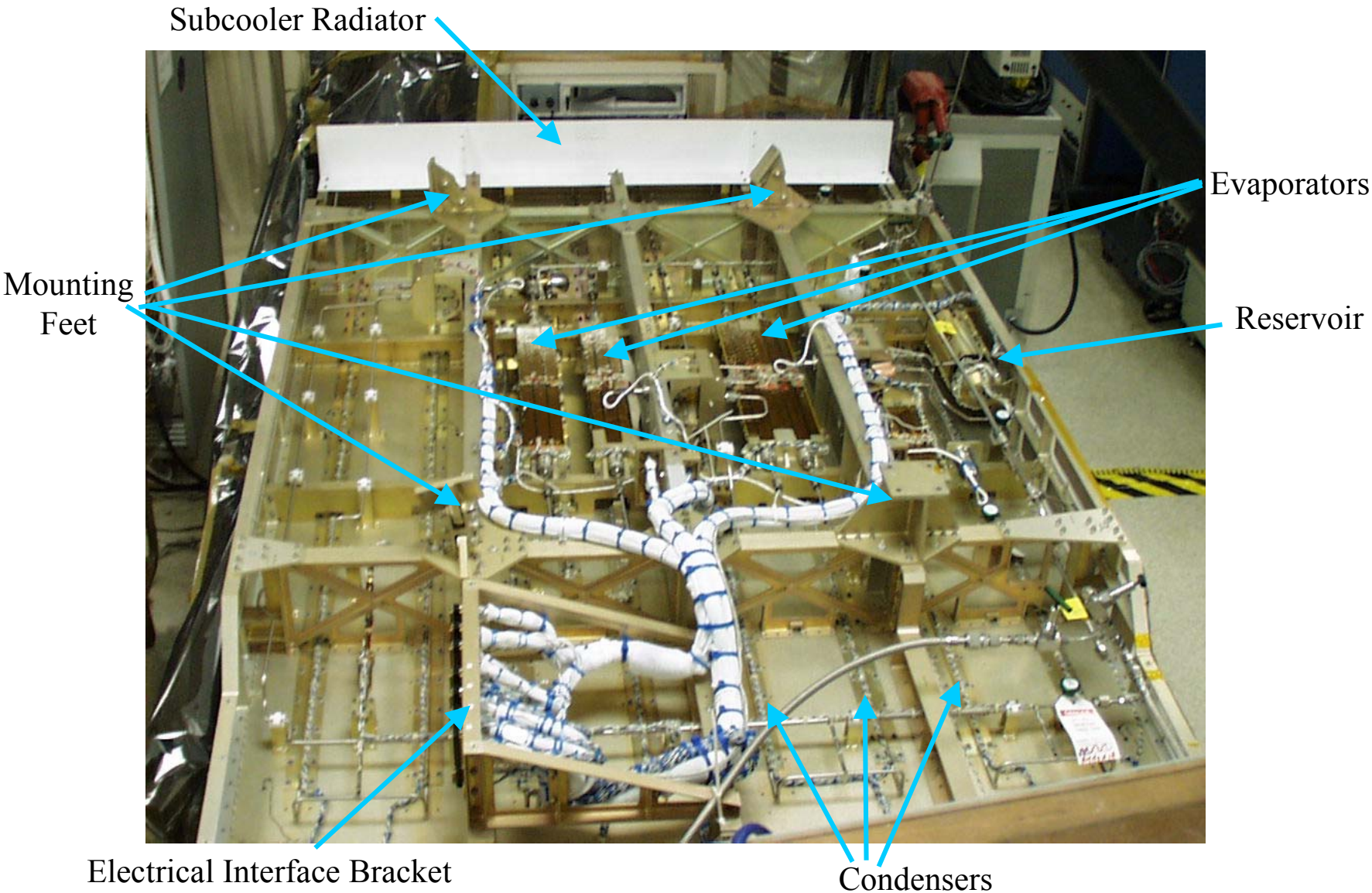

CAPL 3 Mission Description

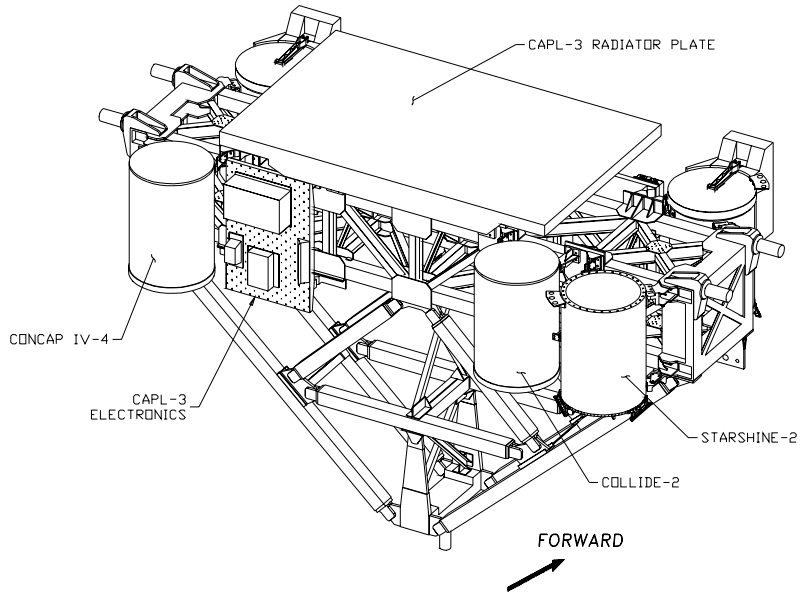

- Mounted aboard GAS bridge structure inside the shuttle bay
- 72 hour mission duration requested in SF1628
- Nominal power: 800 W, max power approximately 1600 W
- GSFC POCC for real-time Hitchhiker payload operation
- Shuttle bay nadir facing (-ZLV), or colder orientation, for at least 54 hours required, with 18 hours in bay to space attitude requested

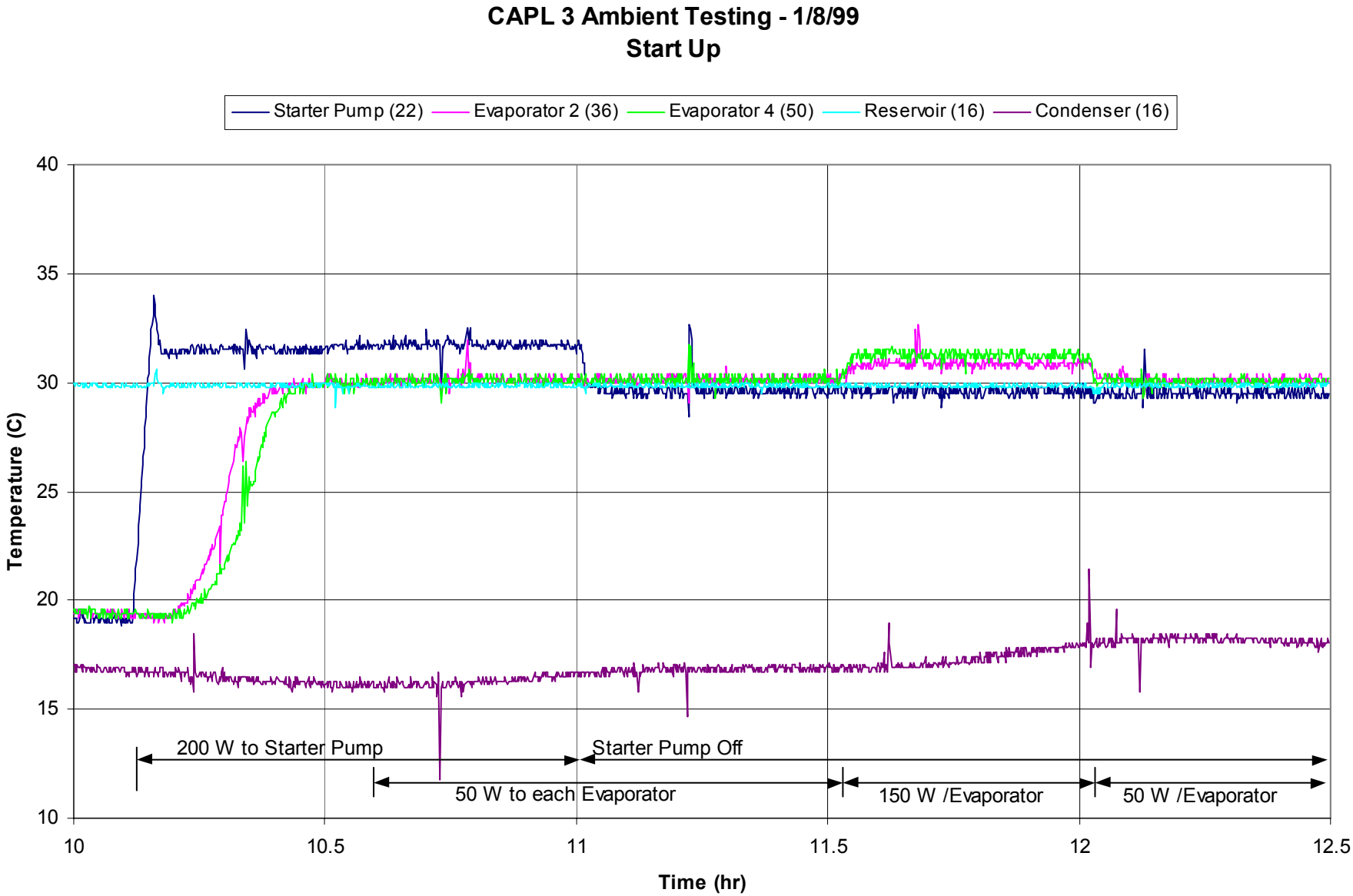
CAPL 3 Ambient Testing - 1/8/99
Start Up
Starter Pump (22)
Evaporator 2 (36)
Evaporator 4 (50)
Reservoir (16)
Condenser (16)
Temperature (C)
Time (hr)
40
35
30
25
20
15
10
10
10.5
11
11.5
12
12.5
200 W to Starter Pump
Starter Pump Off
50 W to each Evaporator
150 W /Evaporator
50 W /Evaporator

CCQ Objectives

- **Modify Two Phase Flow (TPF) experiment, flown in 1997**
  - Demonstrate proposed TRW CPL on the Shuttle using TPF CPL with an added evaporator and a capillary starter pump
  - Test new evaporator containing advanced wick which prevents vapor blow-by (Air Force Development) and increases pumping capability
  - Test mini-Loop Heat Pipes built by the Russians and provided by the Air Force
- **WHAT ARE WE GOING TO SHOW?**
  - High reliability CPL system suitable for use in spacecraft applications
  - Provide flight verification of mini-LHP design
- **WHEN?**
  - Actual flight date will depend on manifesting availability

TPF/*CCQ* Schematic

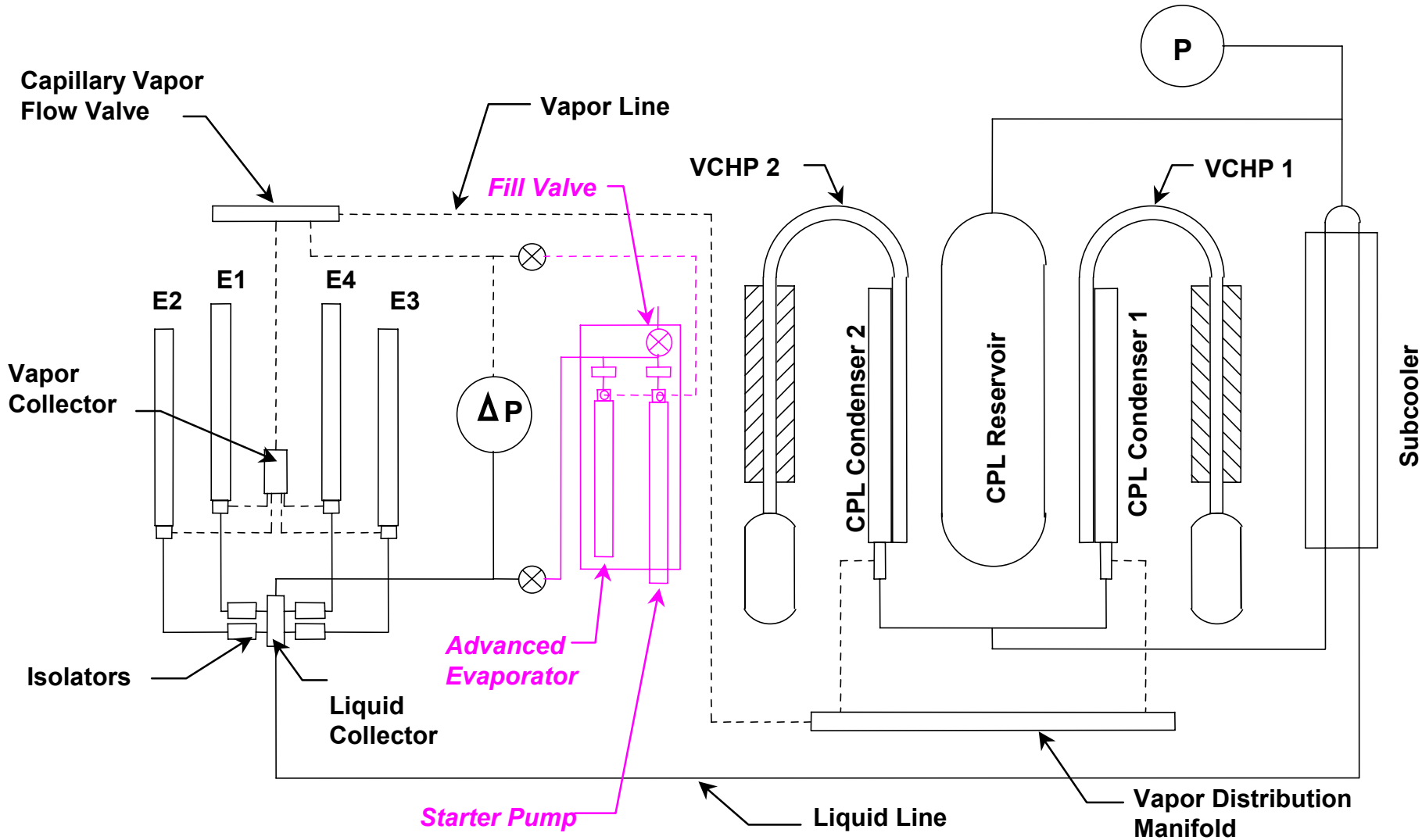

TPF Layout on Canister Lid

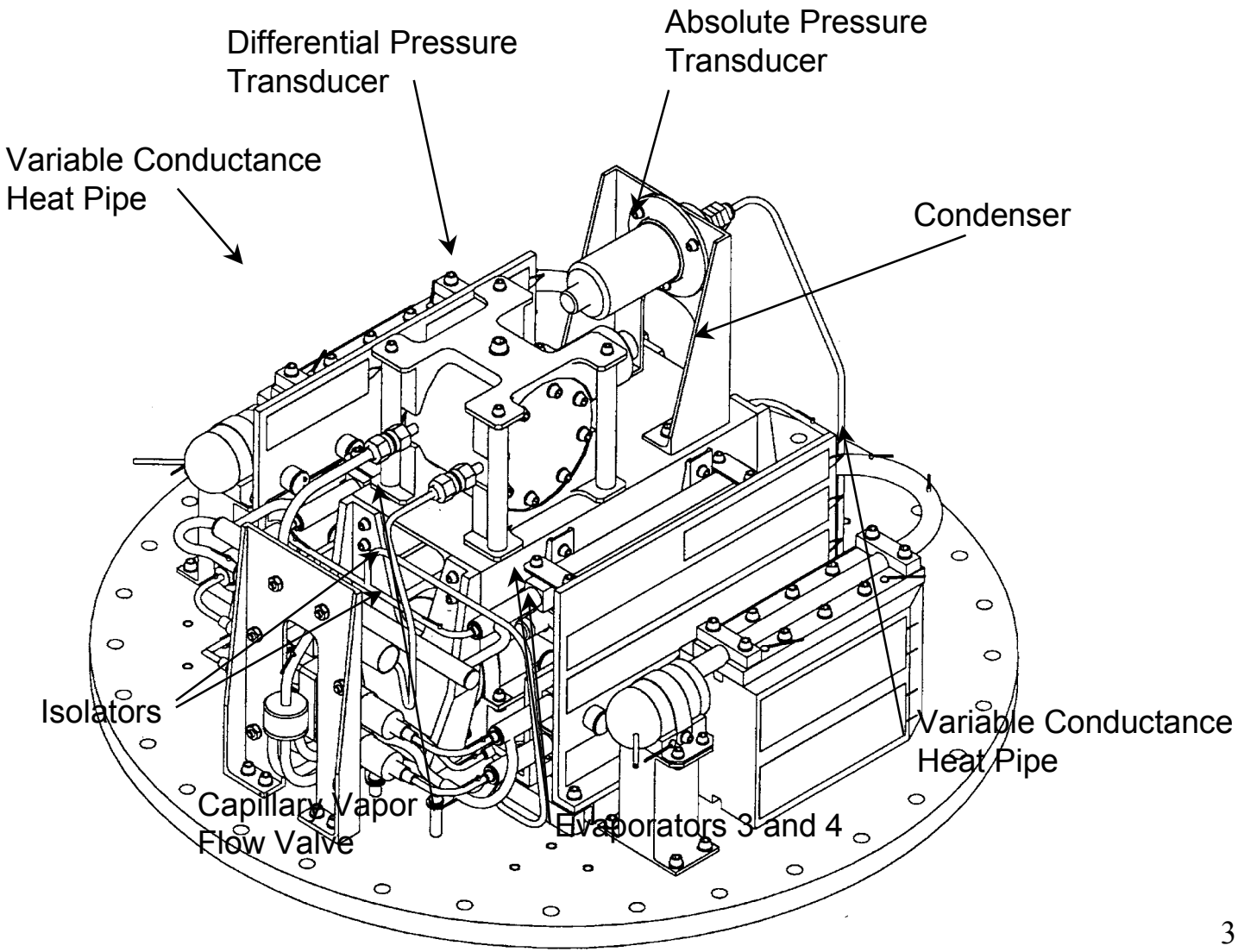

Cryogenic Capillary Pumped Loop (CCPL)

Capillary Pumped Loops (CPLs) are capable of transporting large amounts of heat over long distances and provide tight temperature control. They utilize capillary pumping forces (no moving parts).

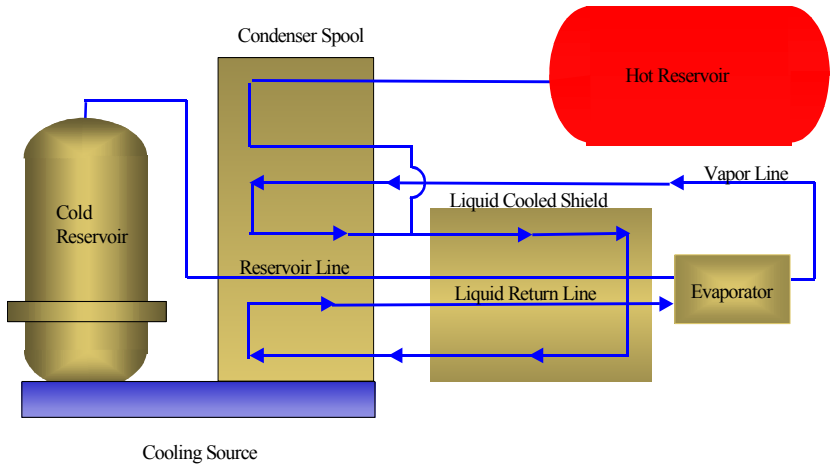

- **Several Cryogenic CPL's have been developed and tested**
  - **Transport of 0.5 to 12 watts in 80 to 100 Kelvin range with Nitrogen**
  - **Transport of 0.25 to 3.5 watts in 35 to 40 Kelvin range with Neon**
  - **Temperature can be controlled to any desired level within the operating range**
- **CCPL can be used in a cryogenic thermal bus or as a temperature control device**
- **CCPL flight experiment successfully flown on STS-95 in October 98**
  - **Demonstrated start-up and transport up to 2.5 W@ 80 to 100 Kelvin**
  - **Included breadboard superconductor bolometer from Code 690**
  - **Future development - Operation in the 2 to 4 Kelvin range with Helium**

CCPL Flight Unit Design

CCPL-5

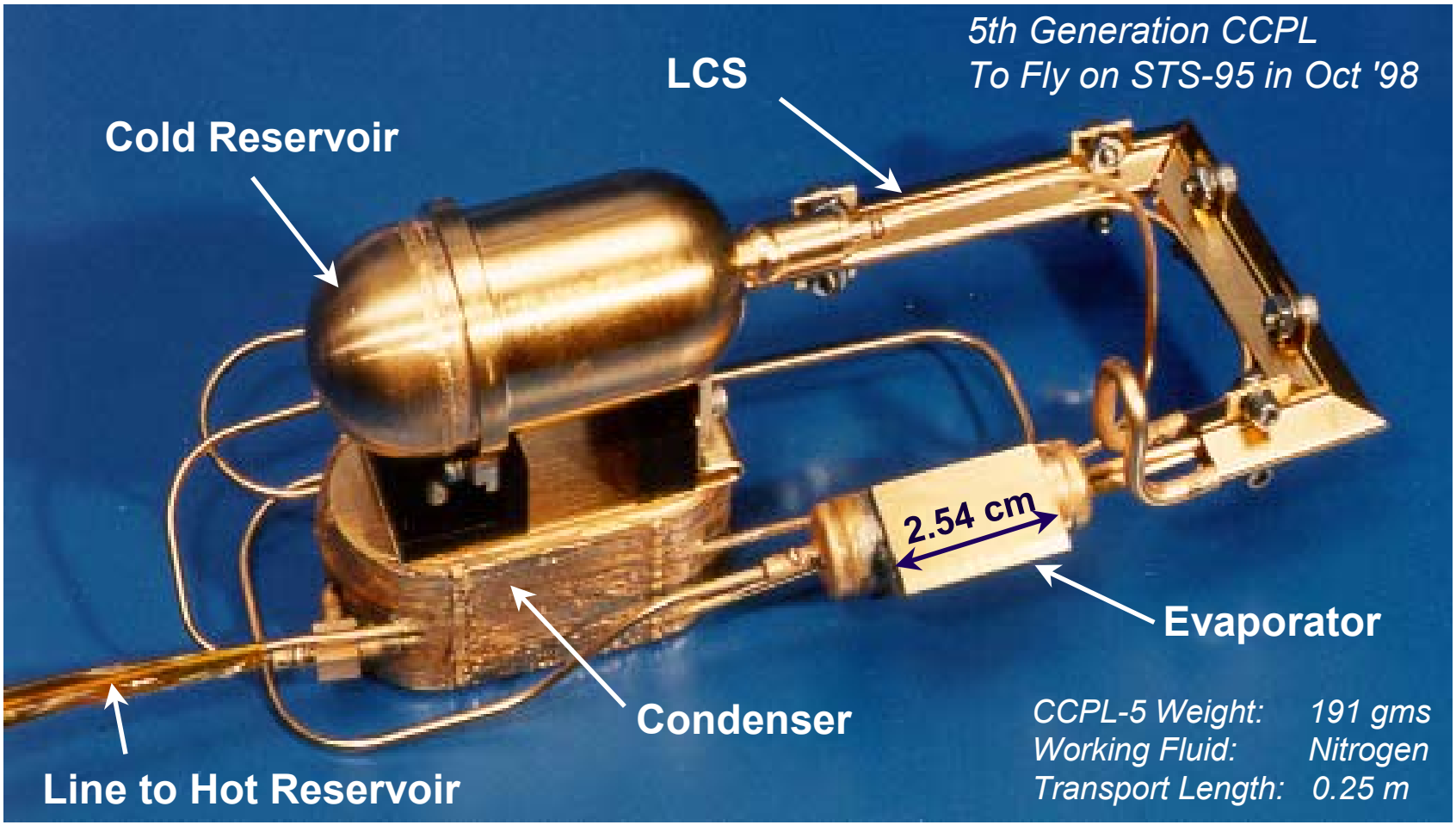

Neon CCPL

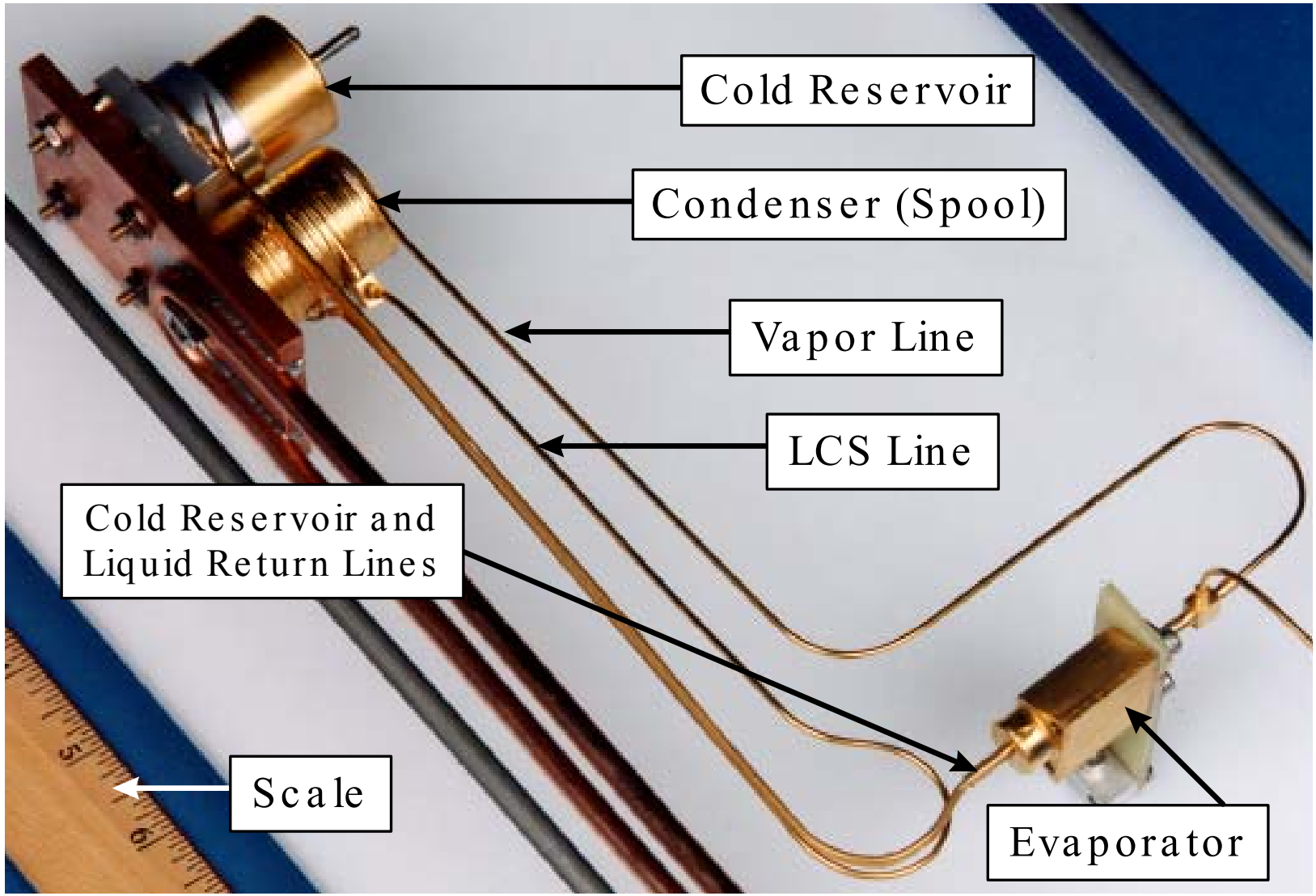
Cold Reservoir
Condenser (Spool)
Vapor Line
LCS Line
Cold Reservoir and
Liquid Return Lines
Scale
Evaporator

Ground Testing

CCPL-5 Results (Cont'd)

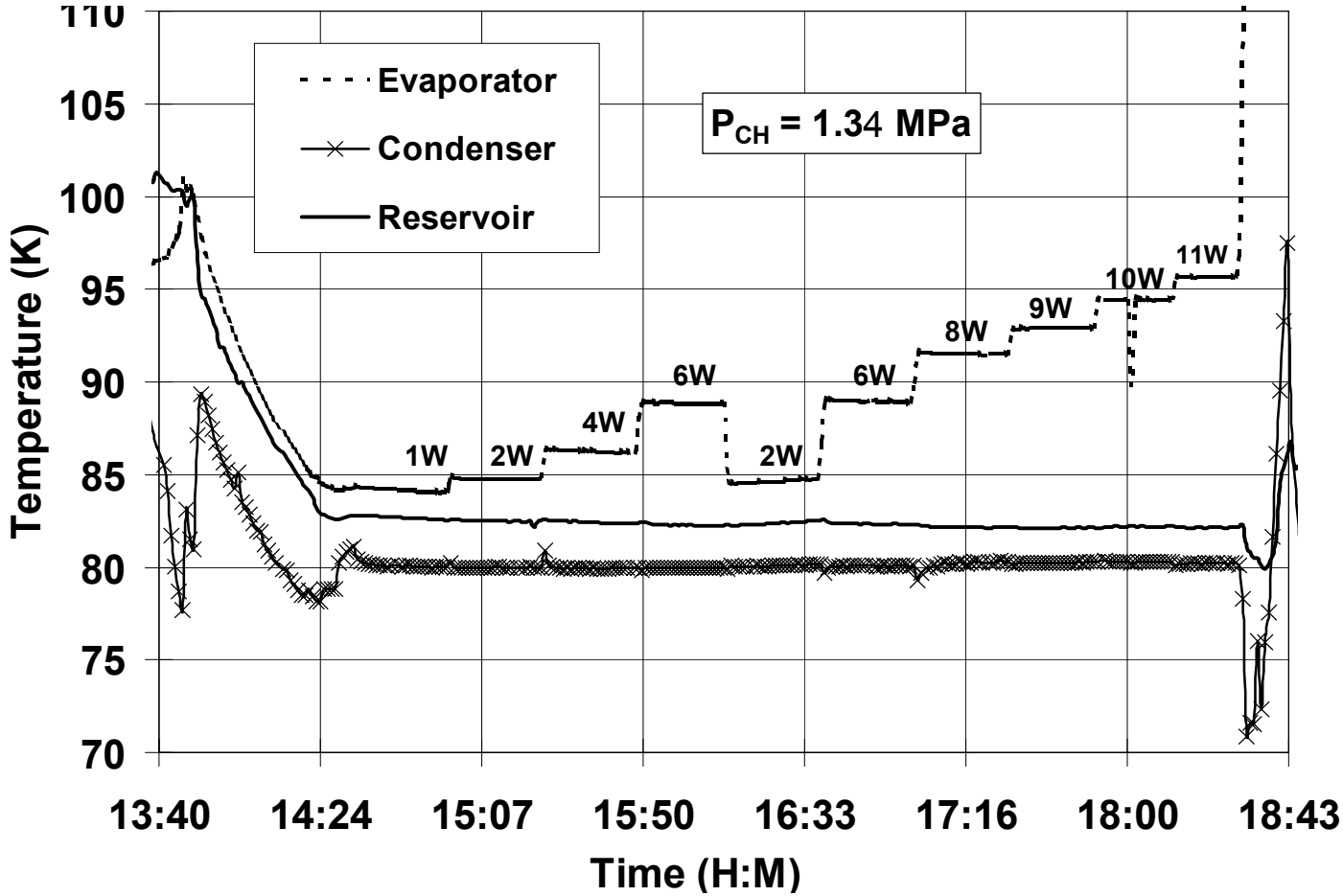

Loop Heat Pipes (LHP's)

- Description - LHP's are basically similar to CPL's - transfer large amounts of heat via the heat of vaporization of the working fluid, and can be shut down
- Invented in Russia in the 70's
- LHP's compensation chamber (reservoir) is attached directly to the evaporator, versus a remote location for CPL's

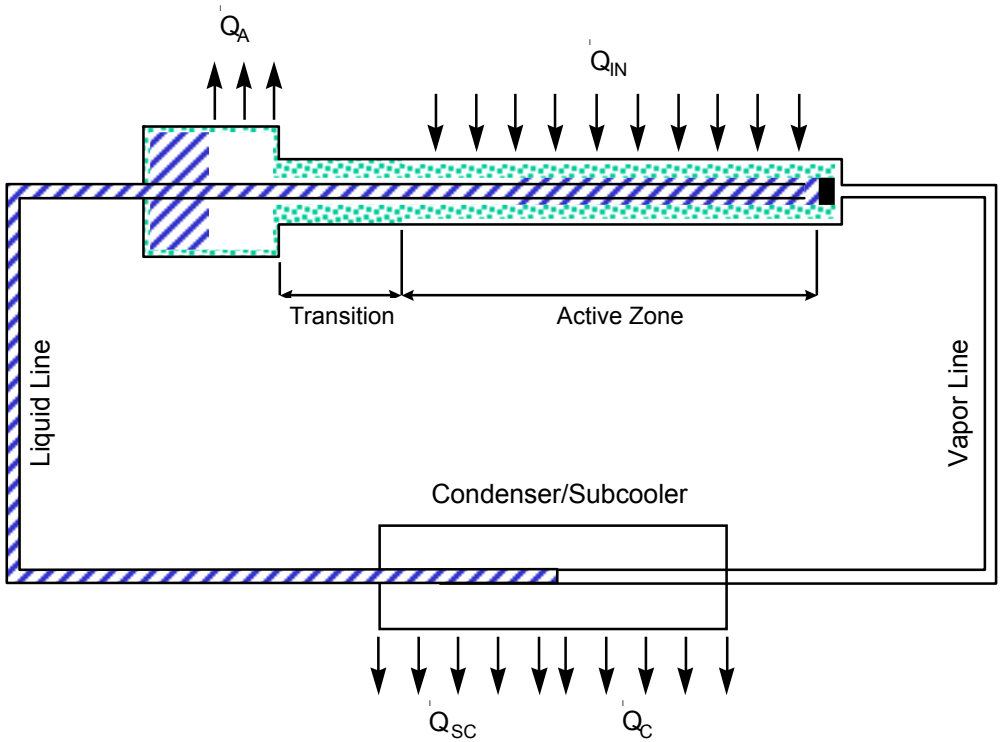

OPERATING TEMPERATURE

NO CONTROL OF COMPENSATION CHAMBER

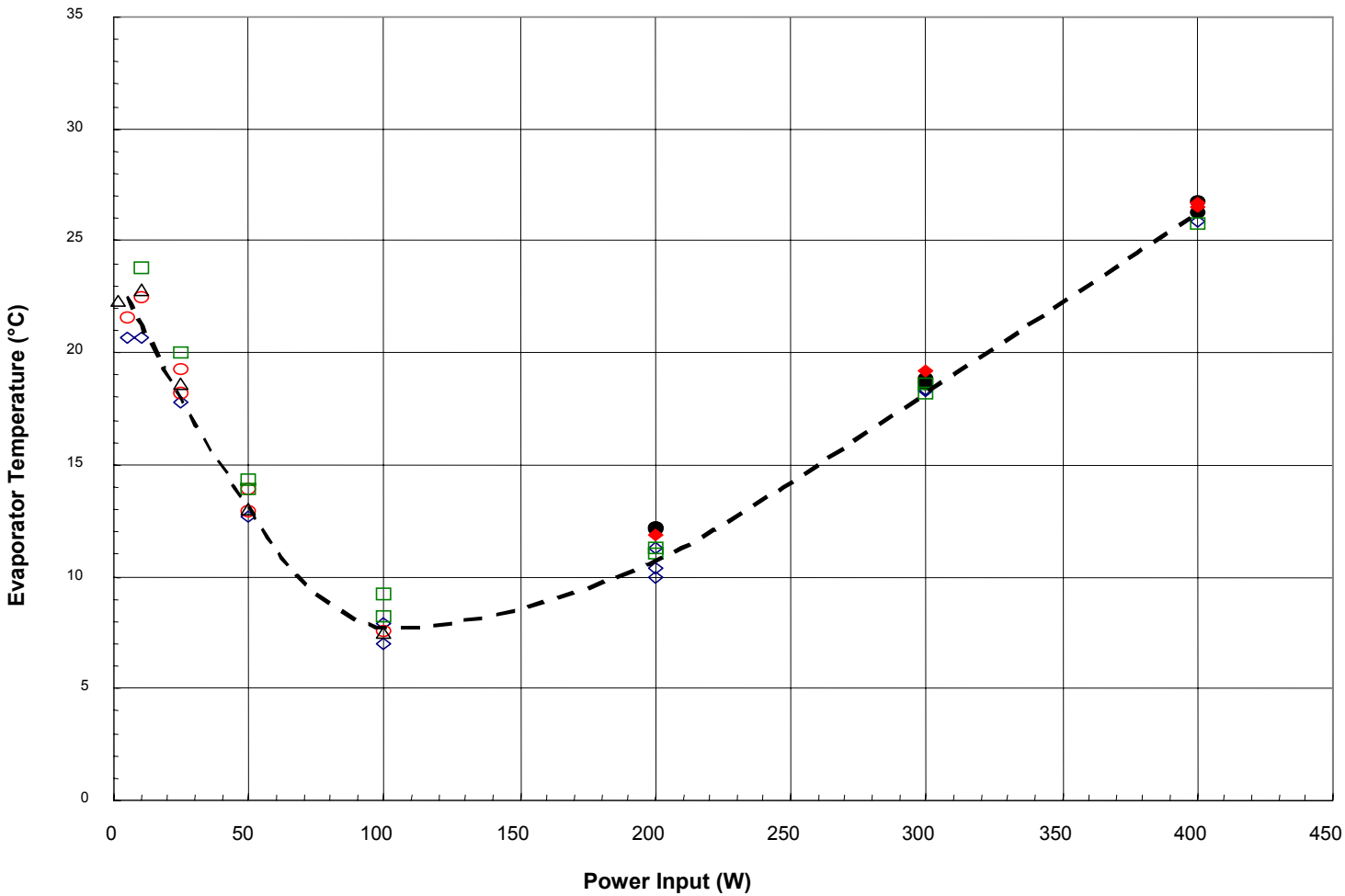

OPERATING TEMPERATURE

ACTIVE CONTROL OF COMPENSATION CHAMBER

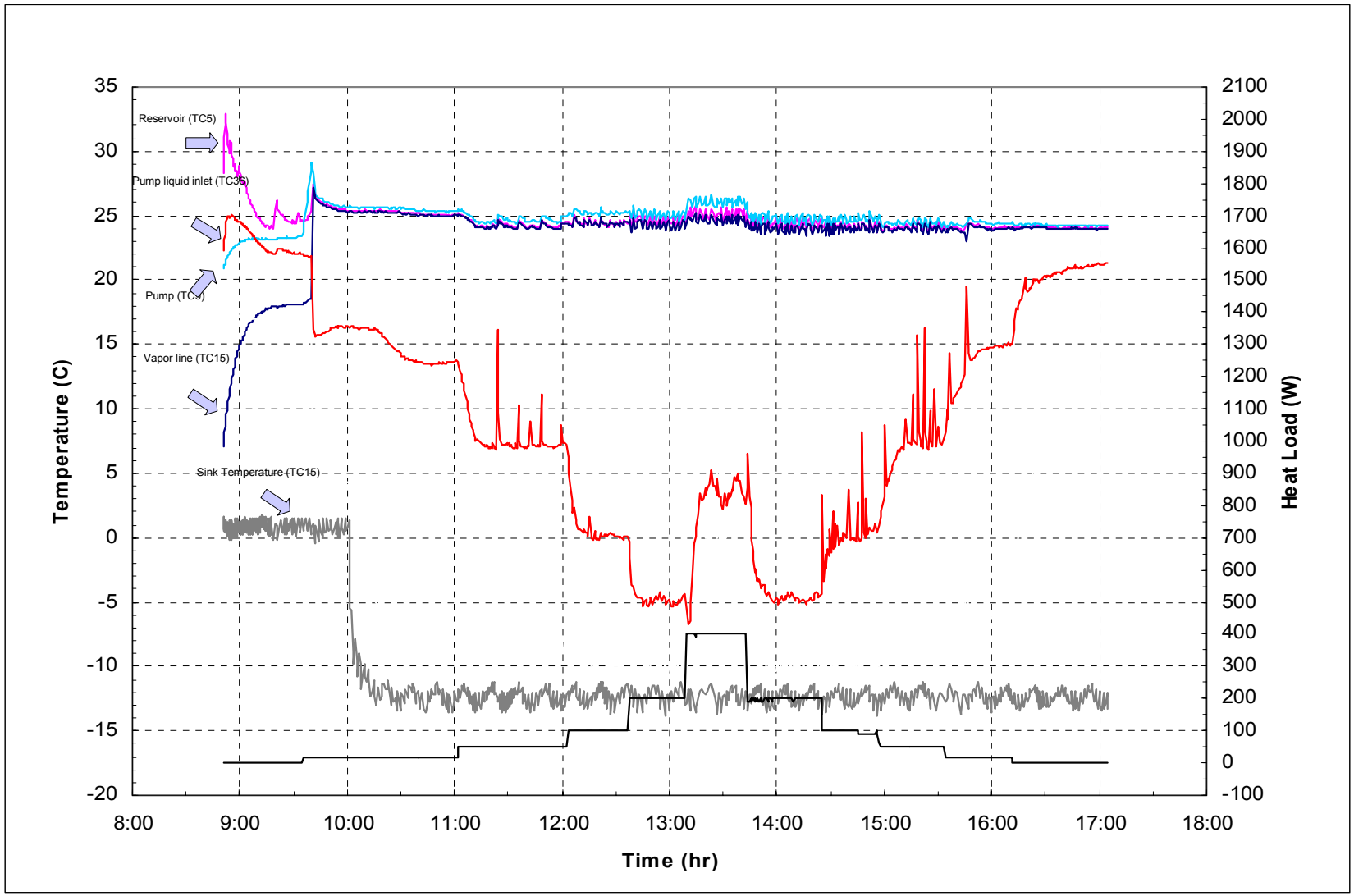

LHP Technology

- Both Swales and Dynatherm LHP designs were flown in 1997 shuttle experiments - Many Russian loops have also flown.
- Programs
  - GLAS Instrument (GSFC) - 2 LHP's for laser and electronics
  - EOS/AURA, TES instrument (JPL) - 5 LHP's for electronics, cryocooler
  - GOES/NEXT (Hughes) - 6 LHP's for star tracker, electronics
  - VASMIR (JSC) - high flux LHP for rocket cooling
  - M1 Tank (US Army) - electronics cooling, testing up to 5 G's
  - Nanosat & Mars Rover (JPL) - mini-LHP development
    - Baselined for the MARS 03 Rover mission
  - Swift BAT Instrument (GSFC)- 2 loops cool detector plate
  - Boeing/Hughes 702 satellites use LHP's with deployable radiators
    - Several on-orbit and operating
  - Mini-LHP development program

GLAS LOOP HEAT PIPE

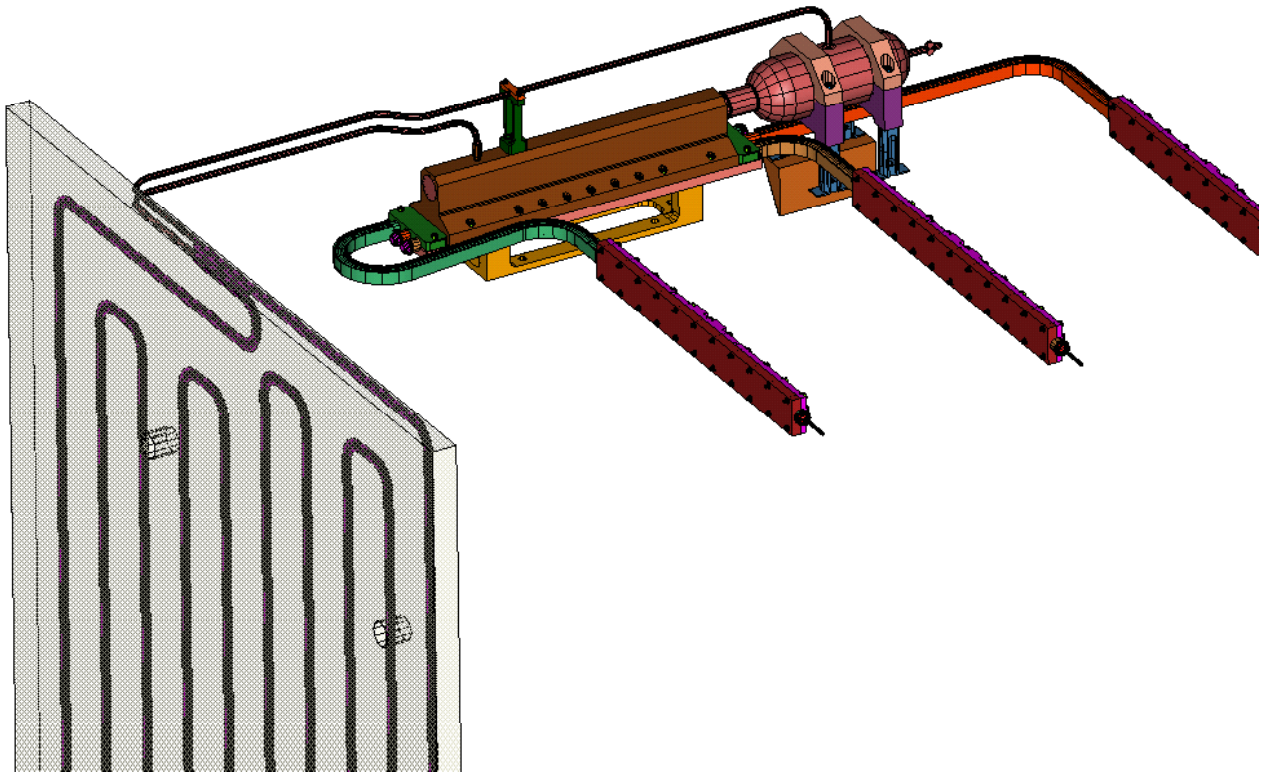

EOS-CHEM TES INSTURMENT
Loop Heat Pipe Layout

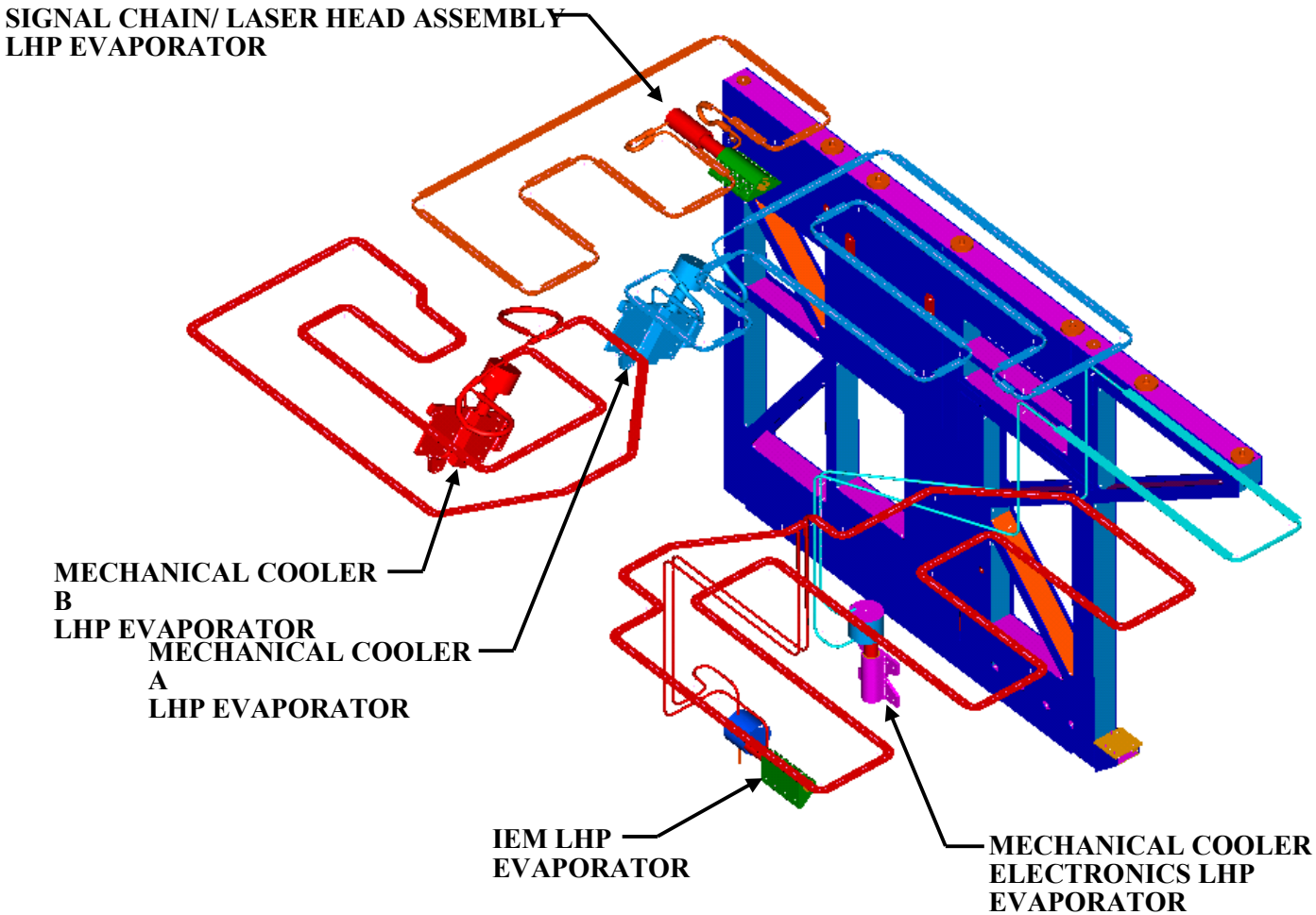

SWIFT/BAT LHP

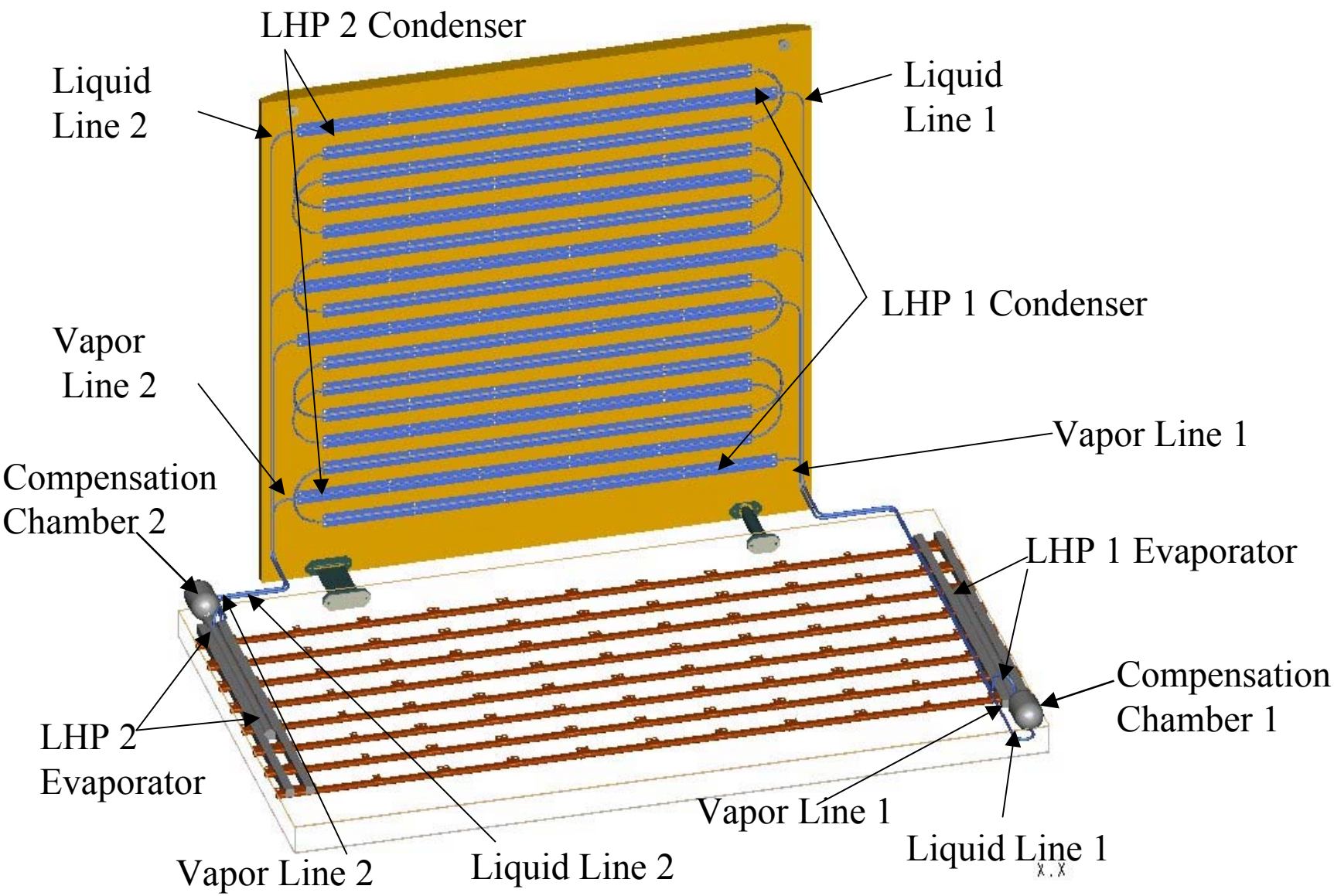

Mini-LHP

- **Miniaturization of existing technology**
  - currently have 1/2” dia evaporators
  - goal of 1/4” diameter evaporator
  - up to 10 of watt transport over < 1 meter length
- **Application to nanosats, electronics cooling**
  - allows isolation of spacecraft interior during cold case
  - especially suitable for fleets of S/C
- **Recent SBIR Phase 2 with TTH Research Inc./Thermacore**
- **HQ Award to GSFC (CETDP)**

Mini-Loop Heat Pipe

Russian mLHP's

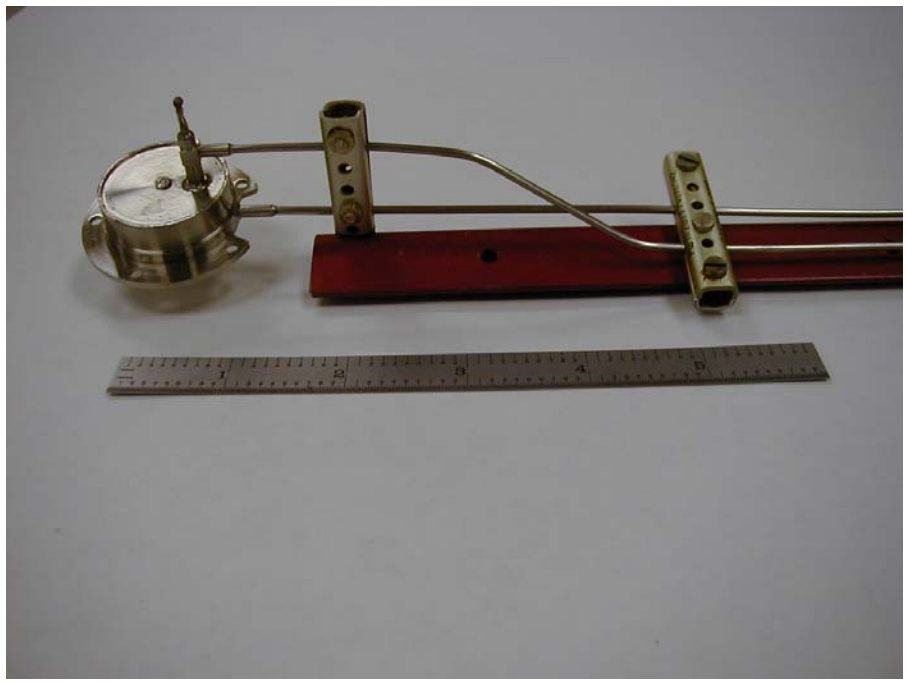

Mini-LHP Technology Issues

- mLHP performance does not scale linearly
  - Thermal coupling (heat leak) between compensation chamber and evaporator affects start-up capability and operating temperature
  - Previous experience on Capillary Pumped Loops shows that performance affected by size
- Manufacturing capabilities on a small scale
  - Wick fabrication and secondary wick installation
- Development of a high conductance condenser
- Thermal/Fluid dynamics on a small scale
- Gravitational affects on liquid/vapor fluid management

Heat Pumps

- Description - Heat pumps provide heat rejection at an elevated radiator temperature
  - Utilized in hot environments or to reduce radiator area (S/C real estate).
- Commercial units are unfit for vacuum and microgravity.
- Program in FY 99/00 - collaboration with the University of Maryland
  - Breadboard heat pump completed and tested in a vacuum environment
    - Upgrade of commercial unit for vacuum (approx 200 W)
    - Still need to address micro-gravity issues
  - Mini-heat pump development study (10 to 20 W) in FY 00
- Potential Applications - ULDB (balloon) thermal control in hot environments, ISS, Lunar Base, Hi-power Comsats, Laser cooling
- Penalty of weight and power

Heat Pump in Vacuum Test Chamber

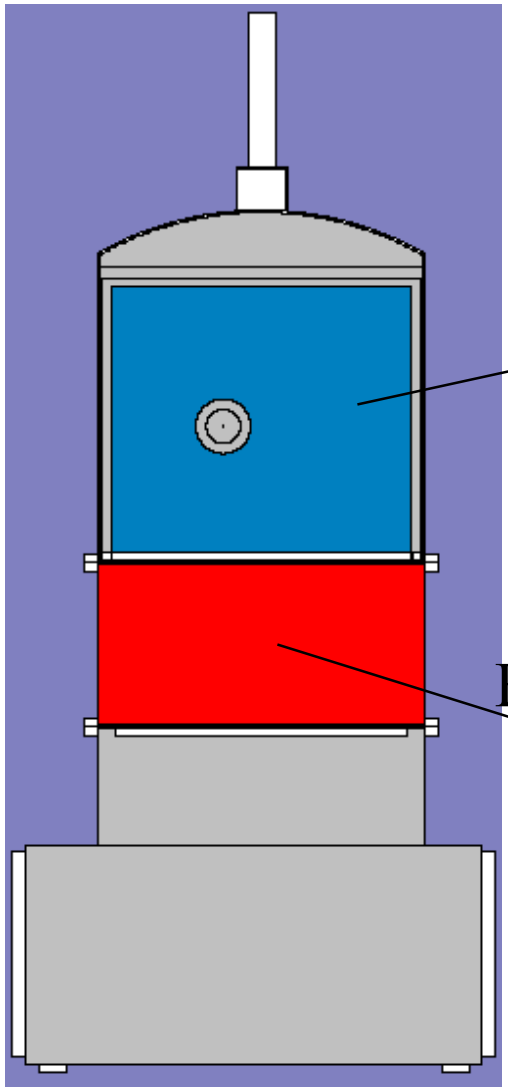

Cold Sink Environment

Gondola Environment

Phase Change Thermal Storage

VCL

Phase Change Module Design

Vegetation Canopy Lidar

- Prototype Phase Change Module Procured and Tested
- Dimensions - 10 x 10 x 0.4 inches thick

  PCM (Hexadecane Mass) ⇒ 430 grams

  PCM Melting Point ⇒ 18.2 °C

  Total Latent Heat Capacity ⇒ 30 Watt Hours

  Total Mass Per Module ⇒ 650 gram
- Overall geometry provides high heat transfer from heat pipe radiator to phase change module
- All four heat pipes located beneath laser chassis and phase change module footprints.
- Phase change module consists of a core assembly and face sheets.
- The core assembly consists of a fine pore structure fabricated out of aluminum honeycomb with embedded high conductivity K1100 carbon fibers that provide high through thickness conductance and freeze nucleation sites.
- Prototype face sheets are bonded to the core with EpoTek T7109 adhesive.

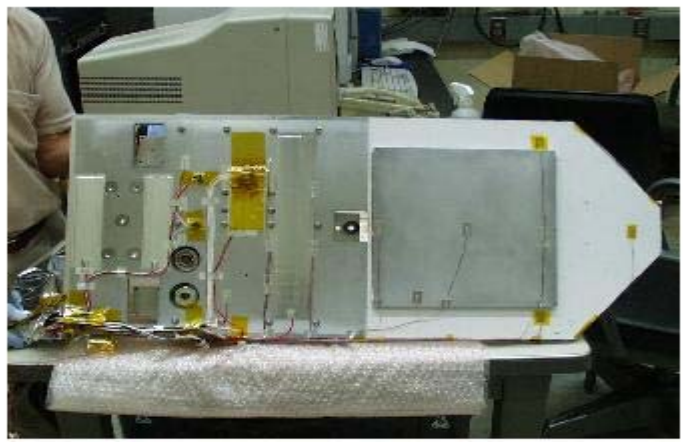

Variable Emittance Thermal Control Surfaces (VaryE)

- Variable emittance surfaces - Goal of 0.3 to 0.8 delta emissivity
  - Provides autonomous thermal control via a signal - “electronic louver”. Three technologies in work - electrochromic, electrophoretic, and MEMS mini-louvers.
- Program - Baselined for thermal control demo on ST-5 mission (‘04)
  - ST-5 funding from TRL Level 5 to flight
  - Air Force SBIR for electro-chromic (Ashwin-Uhas)
  - GSFC SBIR for electrophoretic (Sensortex)
  - CETDP for MEMS louver (APL/Sandia)
- Application/Payoff - Generic applicability to all S/C and instruments, large and small. Potentially very inexpensive as a solid state device

MEMS Louvers

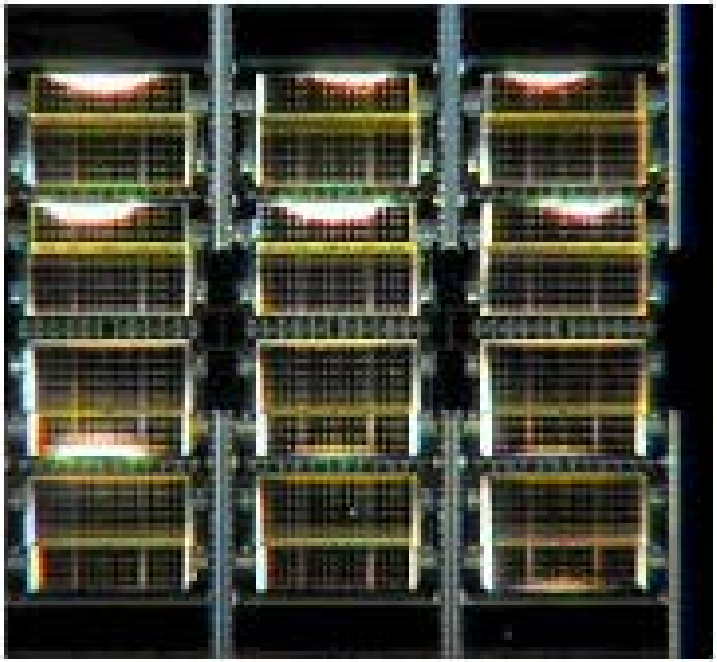

Figure 1 Louvers Closed

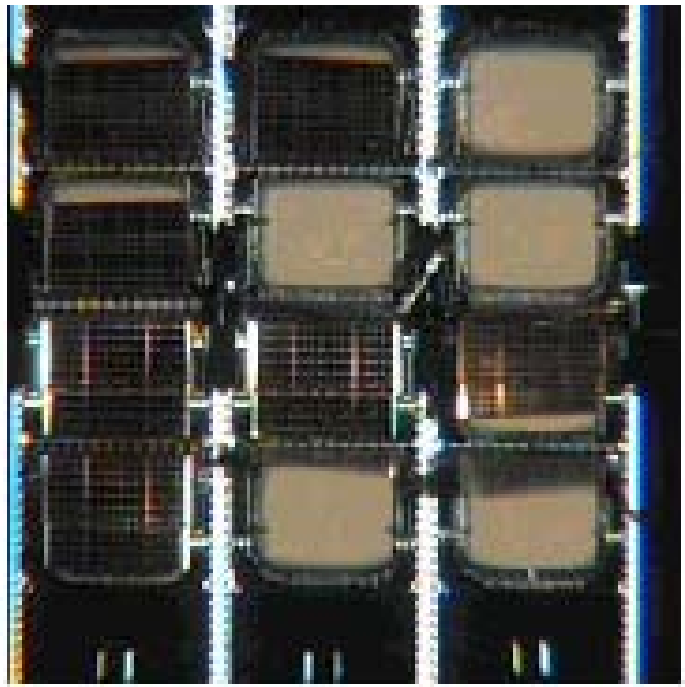

Figure 2 Louvers Open

Thermal Coatings Technology on the EO-1 S/C Launched in November 2000

- Two Flight Thermal Coatings – White Paint
  - Z93P White Paint: Calorimeter (S/N 032) Current technology - control sample
  - AZW/LA-II low alpha inorganic White Paint: Calorimeter (S/N 033) New technology
  - Both coatings developed by AZ Technology
- Z93P White Paint (S/N 032)
  - $\alpha = .17$, $\varepsilon_h = .87$
- AZW/LA-II White Paint (S/N 033)
  - $\alpha = .11$, $\varepsilon_h = .86$
- Flown on calorimeters built at GSFC (reduce S/C thermal effects)

Calorimeters on EO-1

- The Calorimeters are mounted on a bracket and attached to the C-C radiator (Bay 4)
- The LA-II coating ("low alpha") has a very low solar absorptance value when compared to other space application white paints.
  - A lower solar absorptance can provide improved radiator performance when exposed to UV. This improvement can lead to smaller radiator sizes, saving spacecraft mass.
- LA-II optical properties verified maintaining stability with improved solar absorptivity vs. Z93
- LA-II may provide cooler radiator temperatures when exposed to UV:
  - Data shows 5°C cooler in UV
- Baselined for the Swift Spacecraft (but it's expensive)

EO-1 Calorimeters

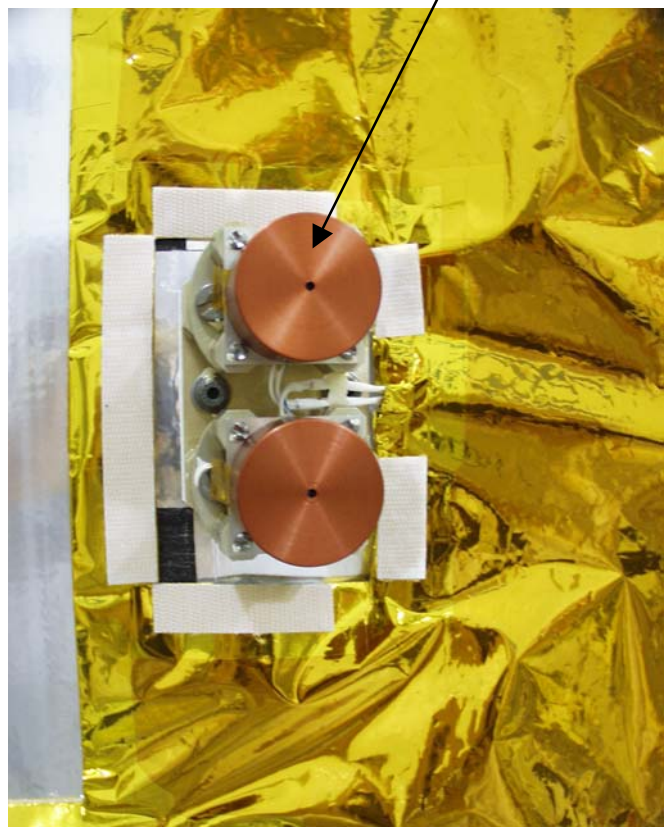

TSS Geometric Math Model

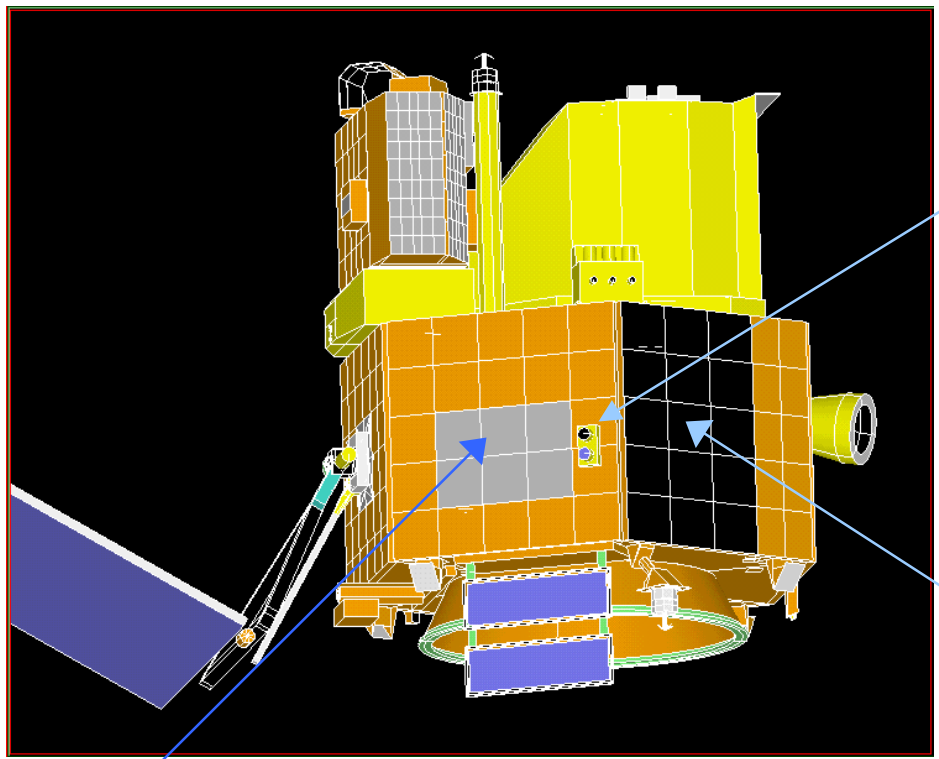

Transient Flight Data vs. Thermal Model Analysis

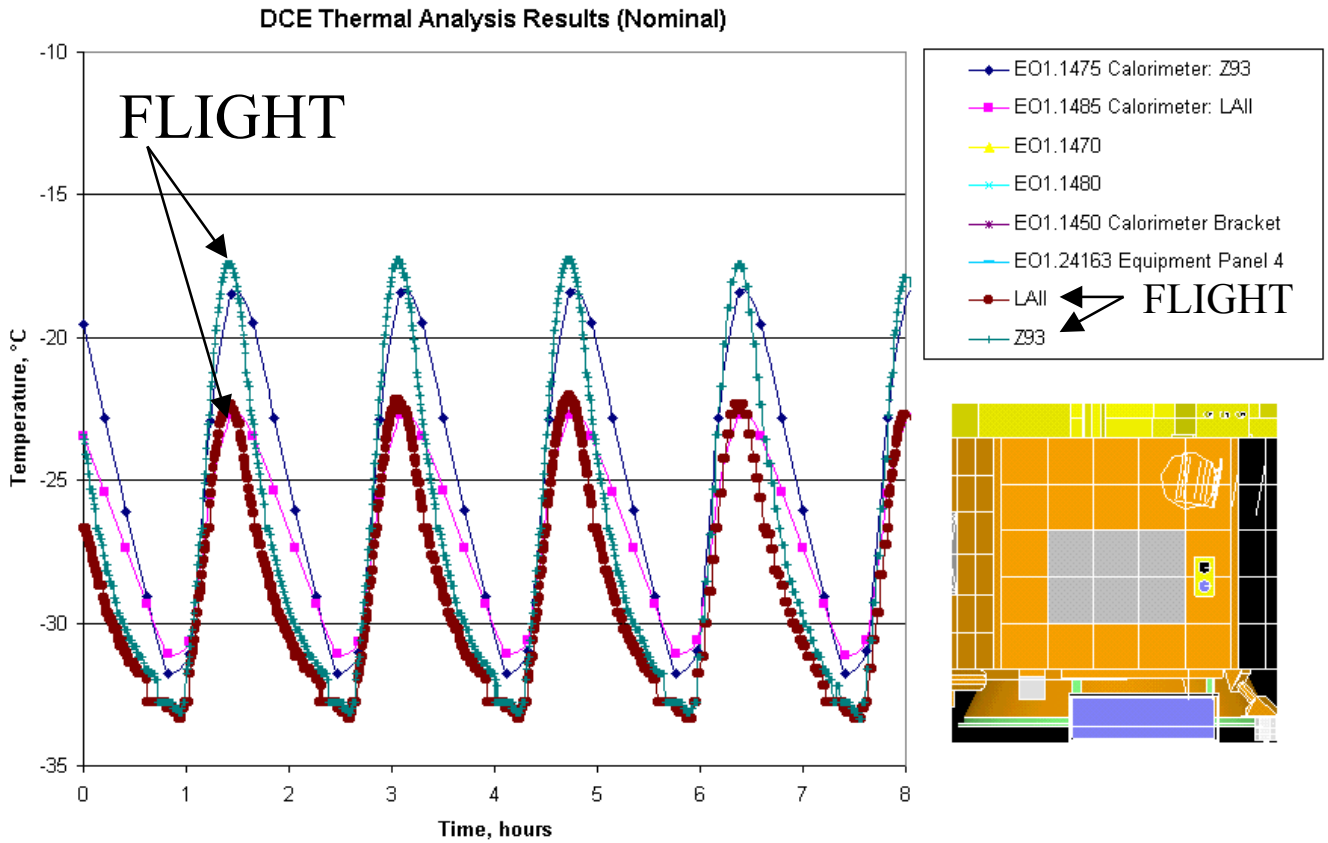

High Conductivity Materials

- Lightweight electronics box (K1100) - IRAD exercise
- Incorporated K1100 composite panels as electrical box mounting panels/radiators on WIRE (1999)
- MAP - gamma alumina at low temperatures (2001)
- Carbon-Carbon radiator on EO-1 (2000)
- Diamond Material for electronics cooling
- SBIR's with Ktech for Annealed Pyrolitic Graphite (APG)
  - Thermal Straps
  - Cryogenic Radiators for possible NGST application

Carbon-Carbon

- Carbon-Carbon (C-C) - Composite material that uses carbon for both the fiber and the matrix material
  - produced in a high temperature furnace in a lengthy process
- C-C has high thermal conductivity, good strength, and is lighter than Aluminum
  - C-C used in high temperature applications such as aircraft brakes, Space Shuttle wing leading edge
- Limited applications elsewhere to date, primarily due to cost and production lead time
- Carbon-Carbon Spacecraft Radiator Partnership (CSRP) formed to promote the use of Carbon-Carbon as a radiator material
  - informal partnership with members from government and industry

C-C Radiator on EO-1

- The New Millenium Program's EO-1 mission provided an opportunity for the CSRP to fly a C-C radiator
  - C-C radiator provided by CSRP at "no cost" to NMP
- The C-C radiator replaced one of 6 structural panels on the EO-1 Spacecraft - It is both a radiator and a structural member
- C-C Radiator consists of 1" Al honeycomb with 0.020" C-C face-sheets, approximately 28" by 28"
  - Utilizes 2 plies of P30X carbon fibers with carbon matrix established by Chemical Vapor Infiltration
  - Epoxy coated for strength and contamination protection
  - Aluminum inserts bonded to honeycomb core for mounting of electronics boxes and attachment to the S/C
  - Exterior coated with Silver Teflon for heat rejection
  - Flight qualification testing completed at GSFC

EO-1 C-C RADIATOR

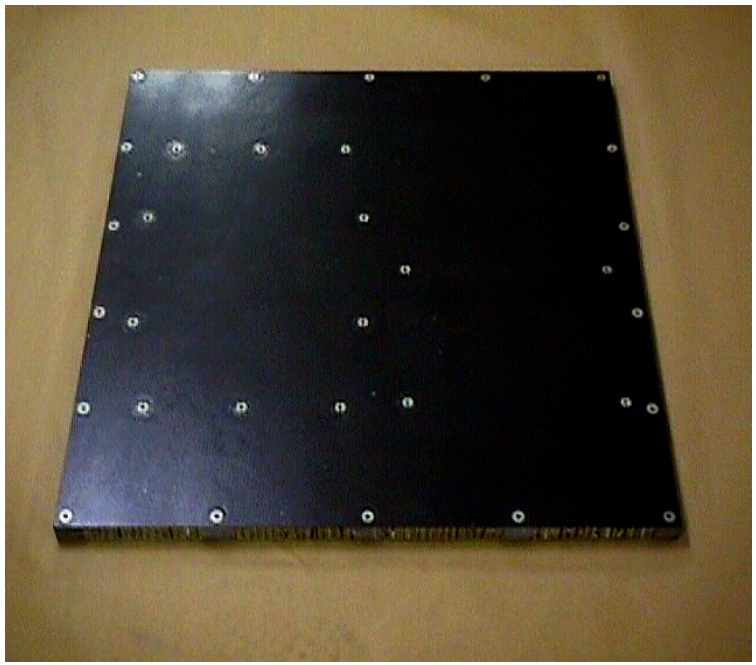

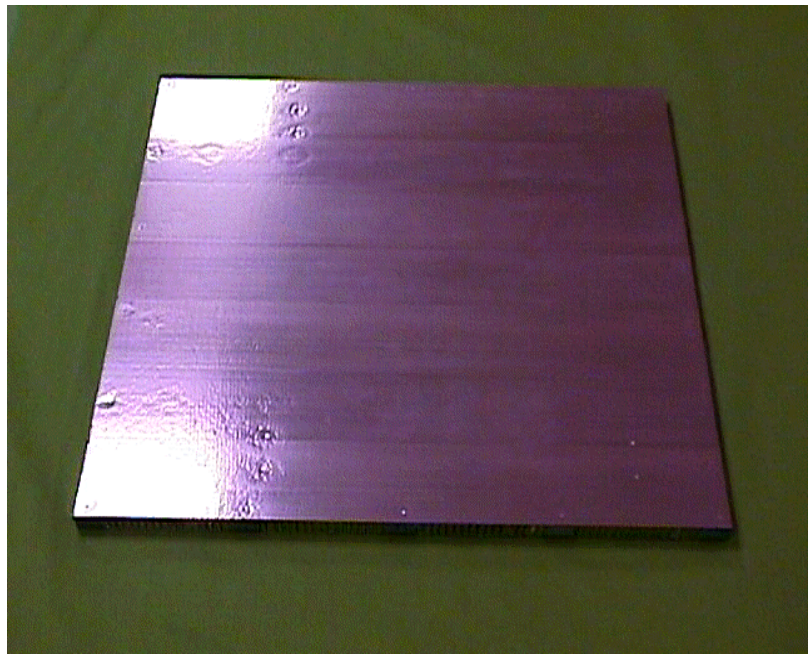

CC Radiator Thermistor Layout

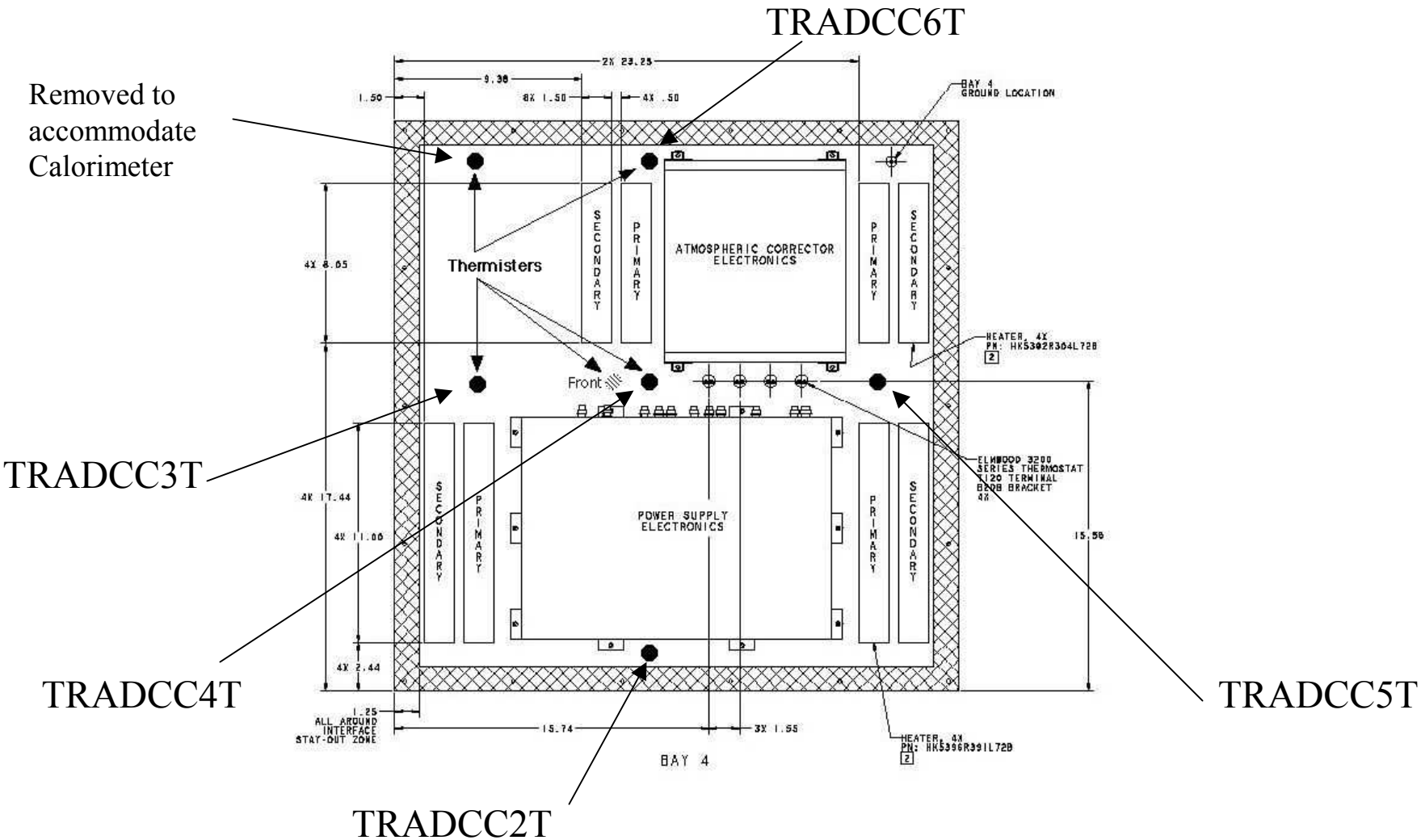

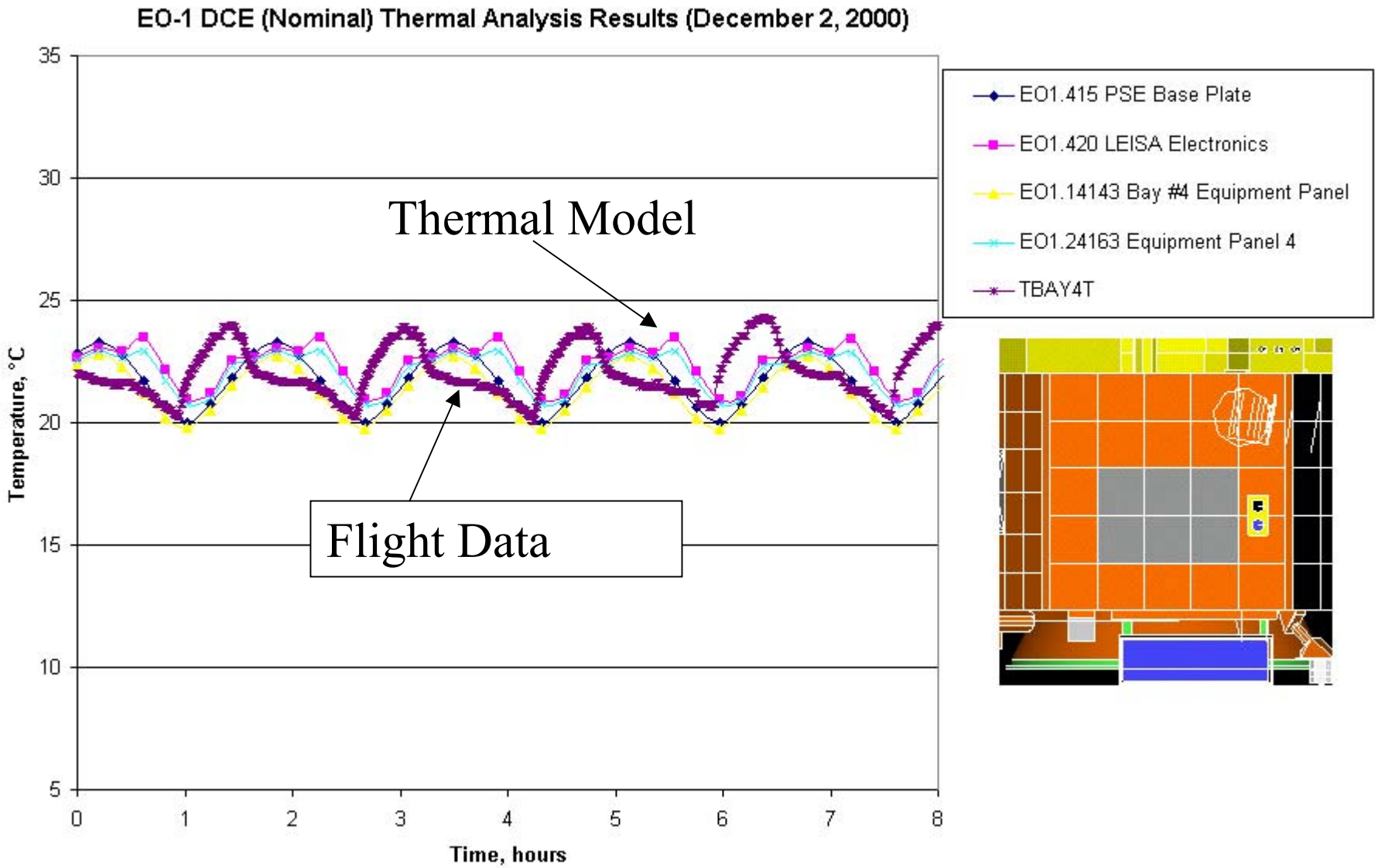
EO-1 DCE (Nominal) Thermal Analysis Results (December 2, 2000)
Temperature, °C
Time, hours
35
30
25
20
15
10
5
0
1
2
3
4
5
6
7
8
EO1.415 PSE Base Plate
EO1.420 LEISA Electronics
EO1.14143 Bay #4 Equipment Panel
EO1.24163 Equipment Panel 4
TBAY4T
Thermal Model
Flight Data

C-C Radiator Lessons Learned

- C-C Radiator technology was successfully validated
  - C-C radiator panels can be used to reduce S/C weight
  - They can also be used as part of the S/C structure
- C-C has a niche, especially for high temperatures
  - Application on the Solar probe
- C-C still needs further development (my opinion)
  - Reduction in fabrication time and cost - high conductivity "traditional" composites are competitive
  - CTE Interface issues with heat pipes
- Redundancy a good idea - we flew the spare panel
- Possible follow-on missions: C-C foam for low CTE mirrors/optical benches

CVD Diamond as a Heat Spreader

- Diamond is a unique substance.
  - Hardest known material
  - High thermal conductivity
  - Excellent mechanical strength
  - Electrical isolator, and may be used as a semiconductor.
- Recently received funding from HST to evaluate sample application as diode heat spreader
- Testing of Hi-K Diamond Underway (Norton Diamond)
  - TV testing for conductivity measurements completed - conductivity approx. 1000 W/mK
  - Vibration test in sample application in work (HST relay cooling)

Encapsulated APG Material System

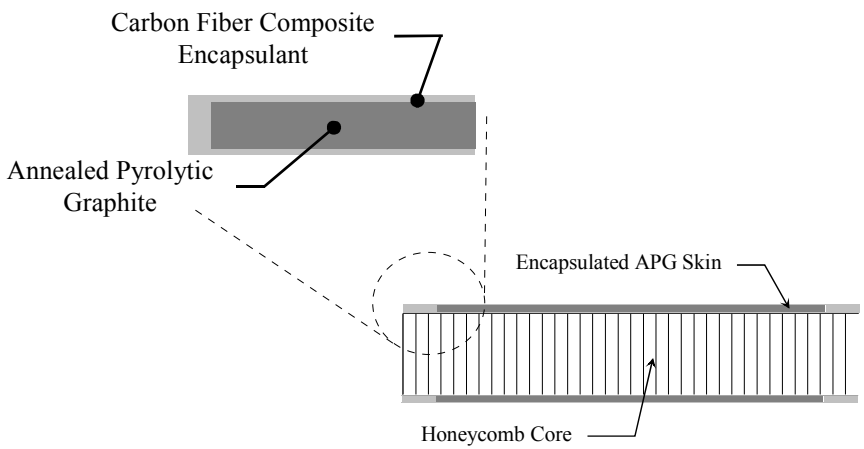

- Skin thermal conductivity
  - 1300 W/mK (273 K)
  - 2500 W/mK (120 K)
- Density less than 2.0 g/cm^3
- Stiffness and strength equivalent to baseline designs

APG Properties

Property	Room Temperature (25°C)	Cryogenic (100°K)
Thermal Conductivity	1700 W/mK (a & b - Axis) 10 W/mK (c - Axis)	3400 W/mK (a & b - Axis) 50 W/mK (c - Axis)
Mass Density	2.26 g/cc	2.26 g/cc
Coefficient of Thermal Expansion	-1.0 ppm/K (a & b - Axis) 25.0 ppm/K (c - Axis)	-1.0 ppm/K (a & b - Axis) 25.0 ppm/K (c - Axis)
Thermal Diffusivity	9.8 cm^2/s	-
Specific Heat	0.84 kJ/kgK	-
Tensile Strength	1,000 ksi (a & b - Axis) 0 Ksi (c - Axis)	1,100 ksi (a & b - Axis) 0 Ksi (c - Axis)

Basal plane thermal conductivity of APG

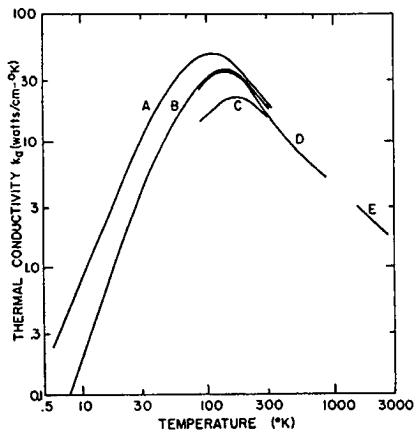

Flexible Thermal Strap

Fabrication

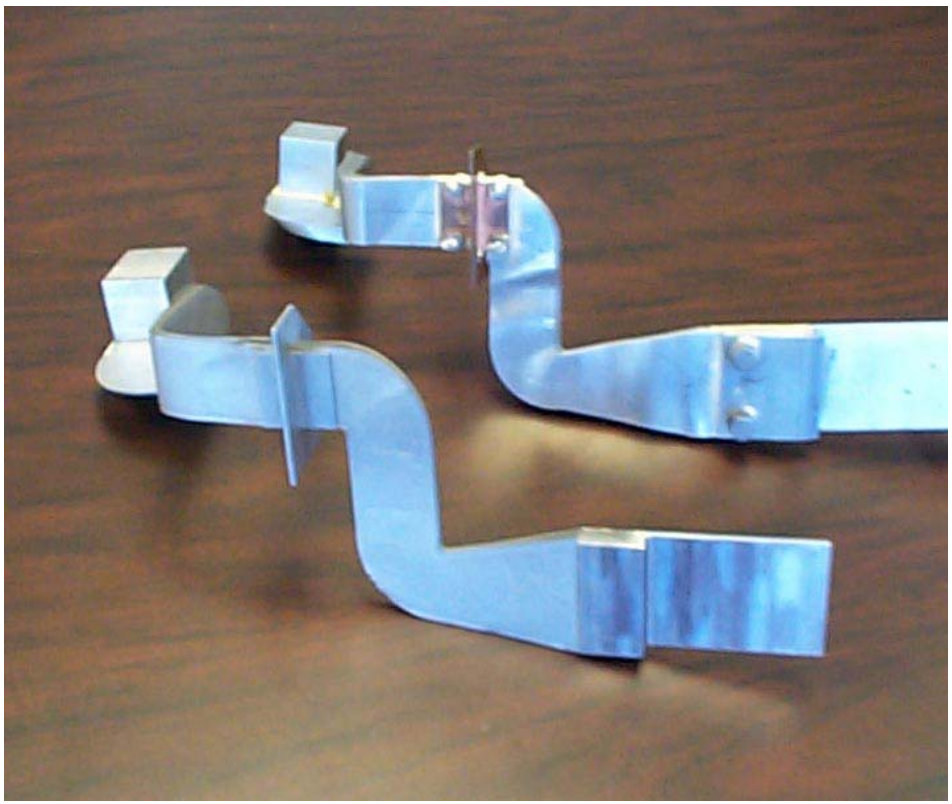

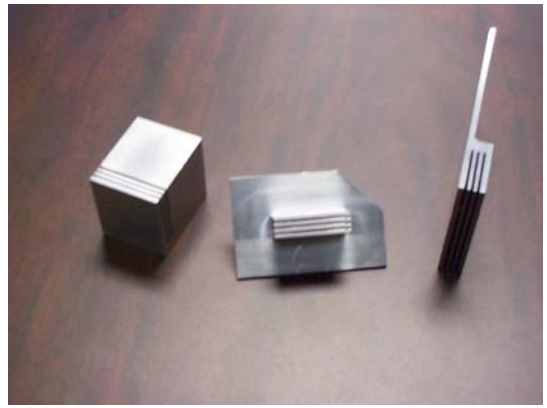

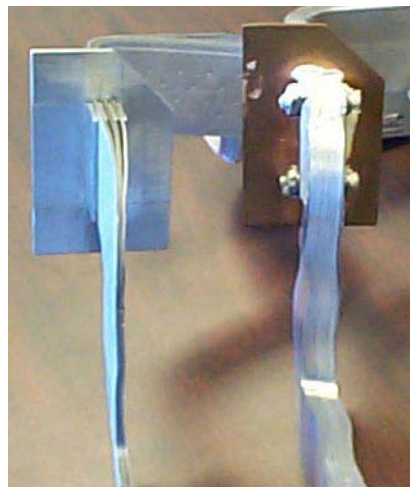

Thermal Strap
Performance

Mass Comparison

	Mass	Reduction %
APG	218.00	58%
Aluminum	518.00	

Thermal Performance Comparison

	Power	Resistance (K/w)	Conductance (w/K)
Aluminum	20.68	3.16	0.32
APG	21.04	2.96	0.34

Thermal Outgassing Properties

	% TML *	% CVCM **	% WVR ***	Limits (%)
APG/Foil	0.024	0.010	0.020	1.000
Supreme 10ANHT	0.770	0.060	0.100	0.100

* Total Mass Loss
** Collected Volatile Condensable Materials
*** Water Vapor Regain

Next Generation Space Telescope - GSFC Concept

Fabrication of Radiator Panels

Phase I Results

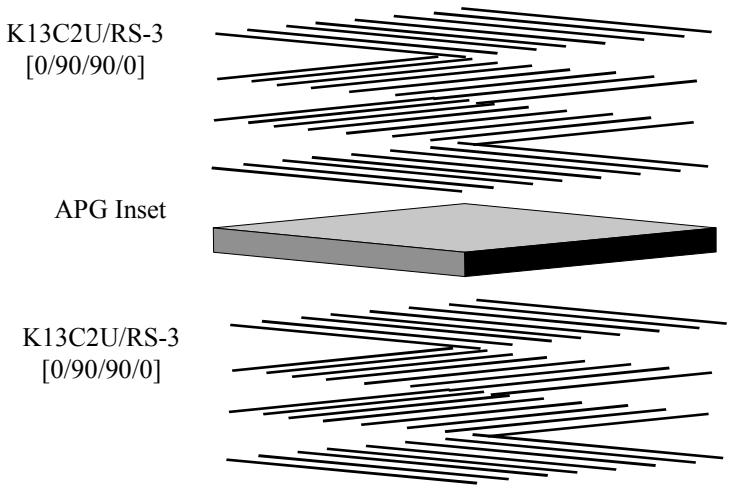

Part Number	Panel Thickness Nominal/Measured (inch)	Panel Width (inch)	Panel Length (inch)
KTC/IN10176A-01	.088/.092	2.999	5.999
KTC/IN10176A-02	.064/.068	3.001	6.000
KTC/IN10176A-03	.048/.050	3.001	6.000
KTC/IN10177-01	.088/.093	3.001	6.000

Panel Evaluation -- Measured Properties

Phase I Results

Conductivity -- Cryogenic Temperatures

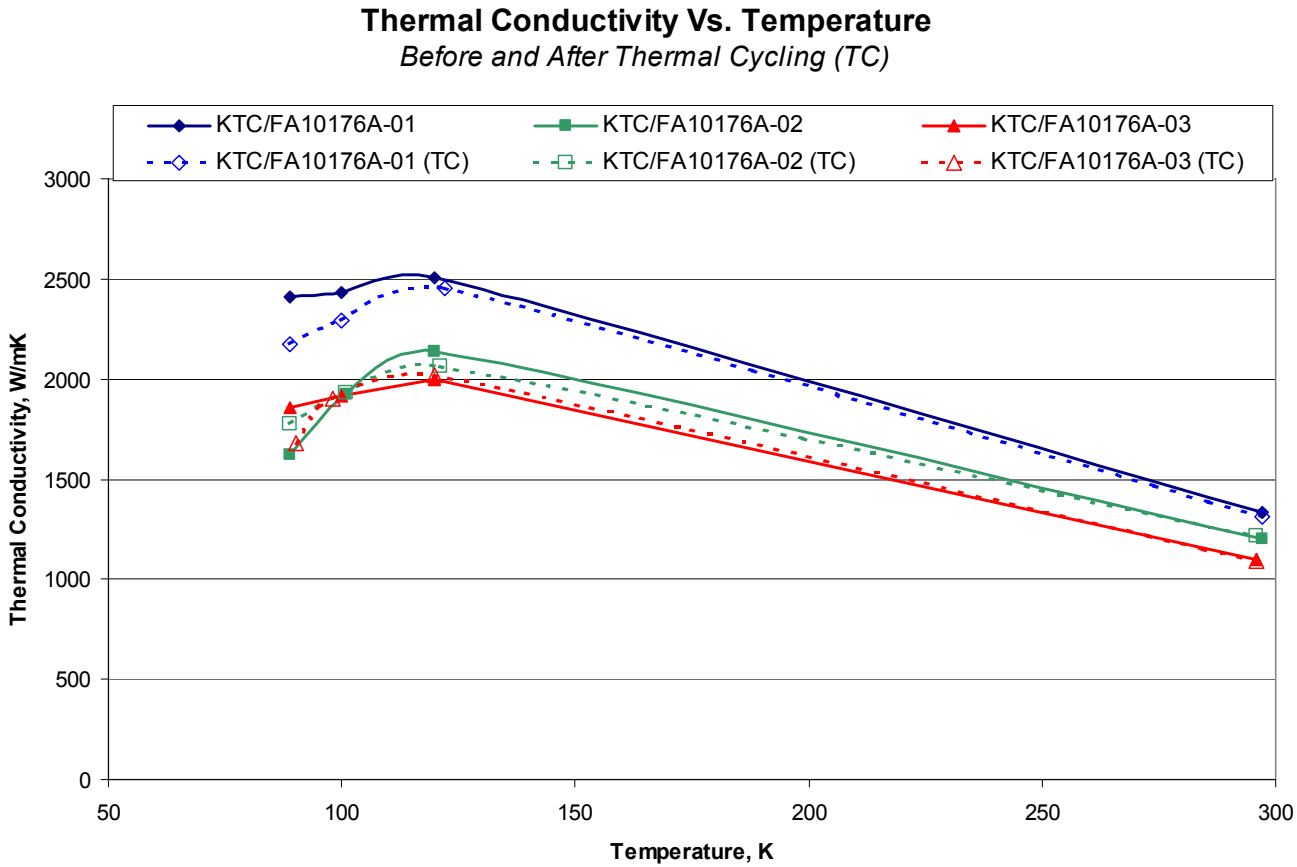

Max Average Values

Item	Measured k (W/mK)
IN10176A-01	2504
IN10176A-02	2134
IN10176A-03	1998

Electrohydrodynamic Pumping (EHD)

- Description - EHD forces can be used to enhance heat transfer, provide fluid management, separate gas/liquid mixtures, and pump fluids. Utilizes electrical forces only, with no mechanical moving parts.
- Working fluids - Dielectric refrigerant such as freon 134a, hydrocarbon, or nitrogen (cryogenic)
- Program includes partnerships with the University of Maryland and Texas A & M
  - EHD flow management test bed
  - EHD single phase and two-phase thermal control loops
  - Cryogenic EHD pumping test (LN2)
  - MEMS level cooling
- Application - Heat exchangers, ISS environmental systems, thermal control systems, MEMS level micro-channel cooling of electronics

EHD PHENOMENA

- Electrohydrodynamics (EHD) is an interdisciplinary phenomena dealing with the interactions between electric fields and flow fields

$$\vec{f}_e = \underbrace{q\vec{E}}_{\text{Coulomb Force}} - \underbrace{\tfrac{1}{2}E^2\nabla\varepsilon}_{\text{Permittivity Gradient Force}} + \underbrace{\tfrac{1}{2}\nabla\left[E^2\left(\frac{\partial\varepsilon}{\partial\rho}\right)\rho\right]}_{\text{Polarization Force}}$$

EHD PUMP DESIGN

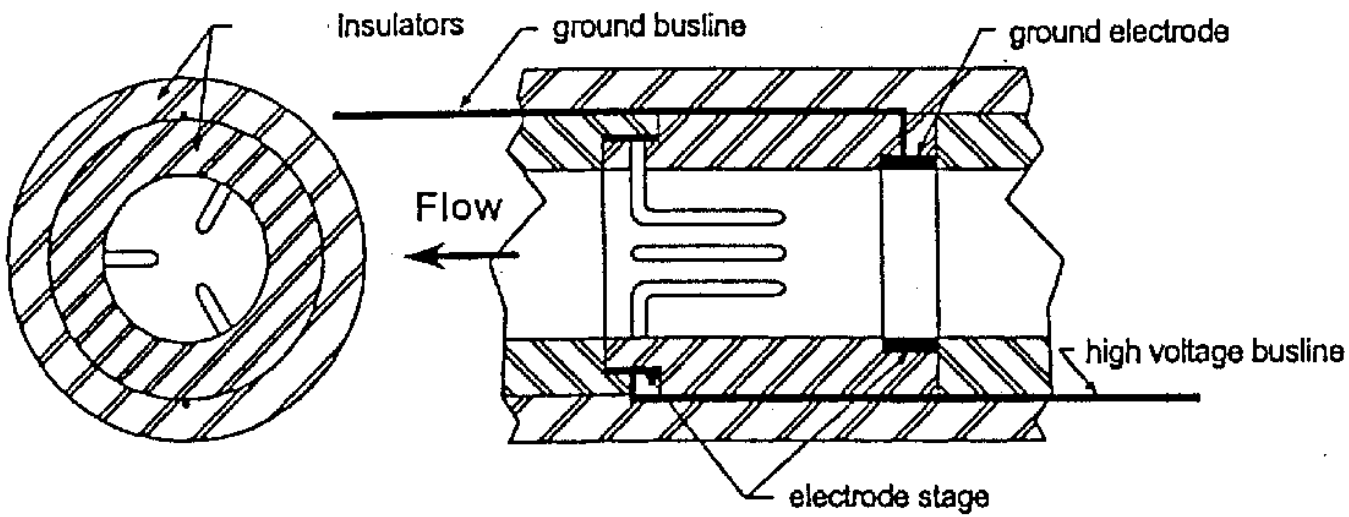

HOLLOW TUBE - RING ELECTRODE DESIGN

Electric Field

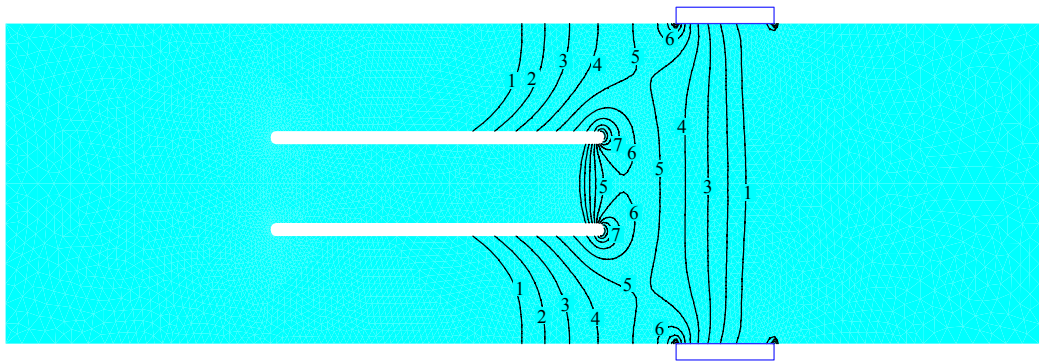

	(V/mm)
10	15500
9	11431
8	8430
7	6217
6	4585
5	3381
4	2493
3	1839
2	1356
1	1000

EHD Pump Design

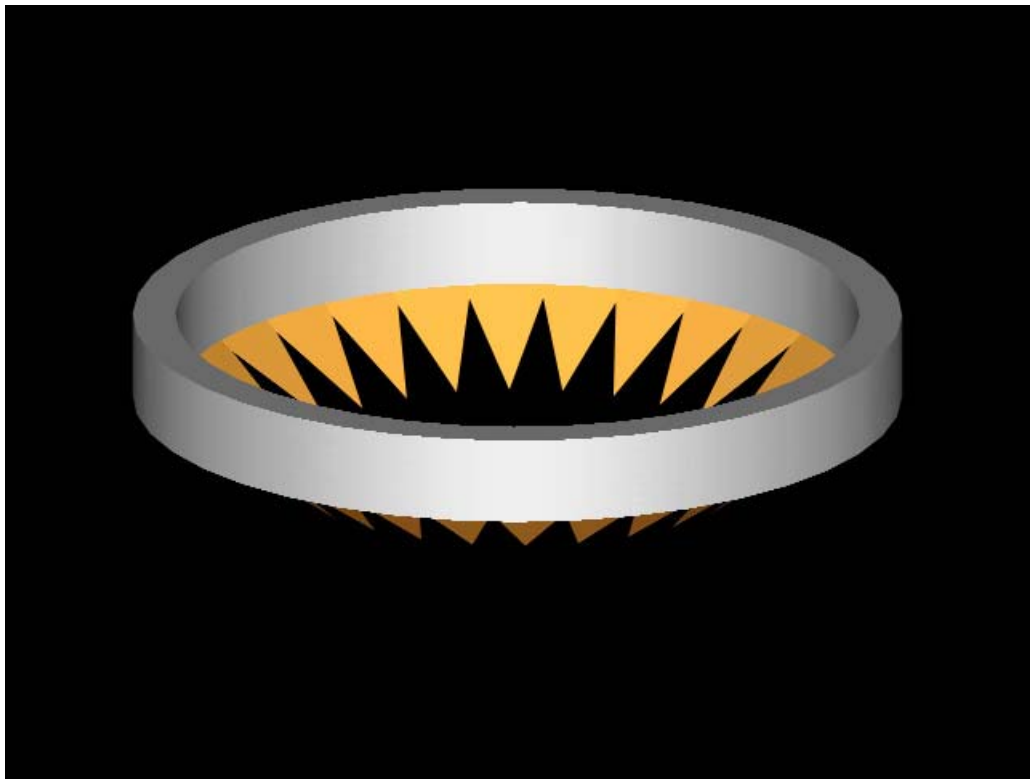

EHD Cryo/Loop Design

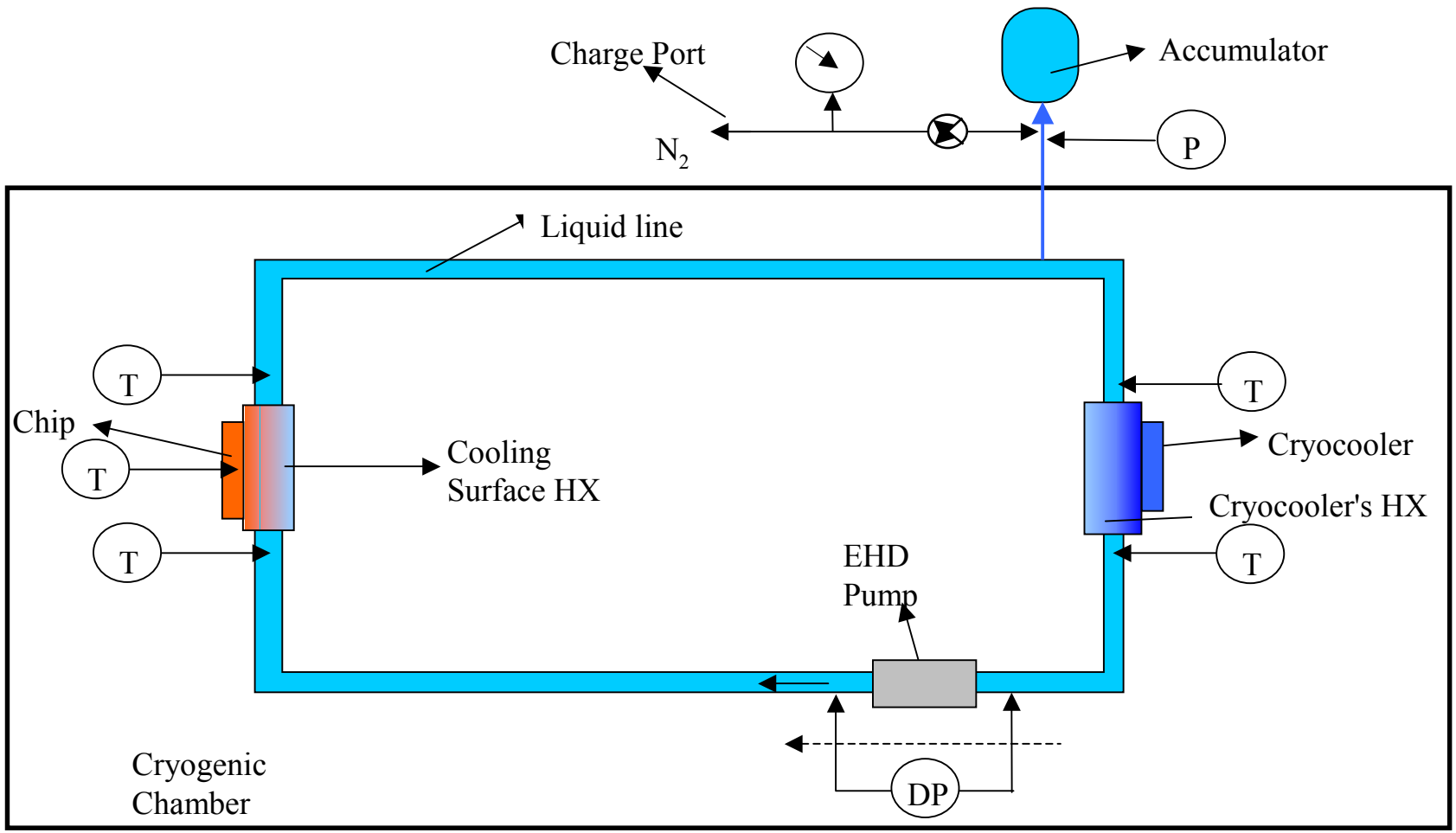

Prototype EHD Ambient Temperature Loop

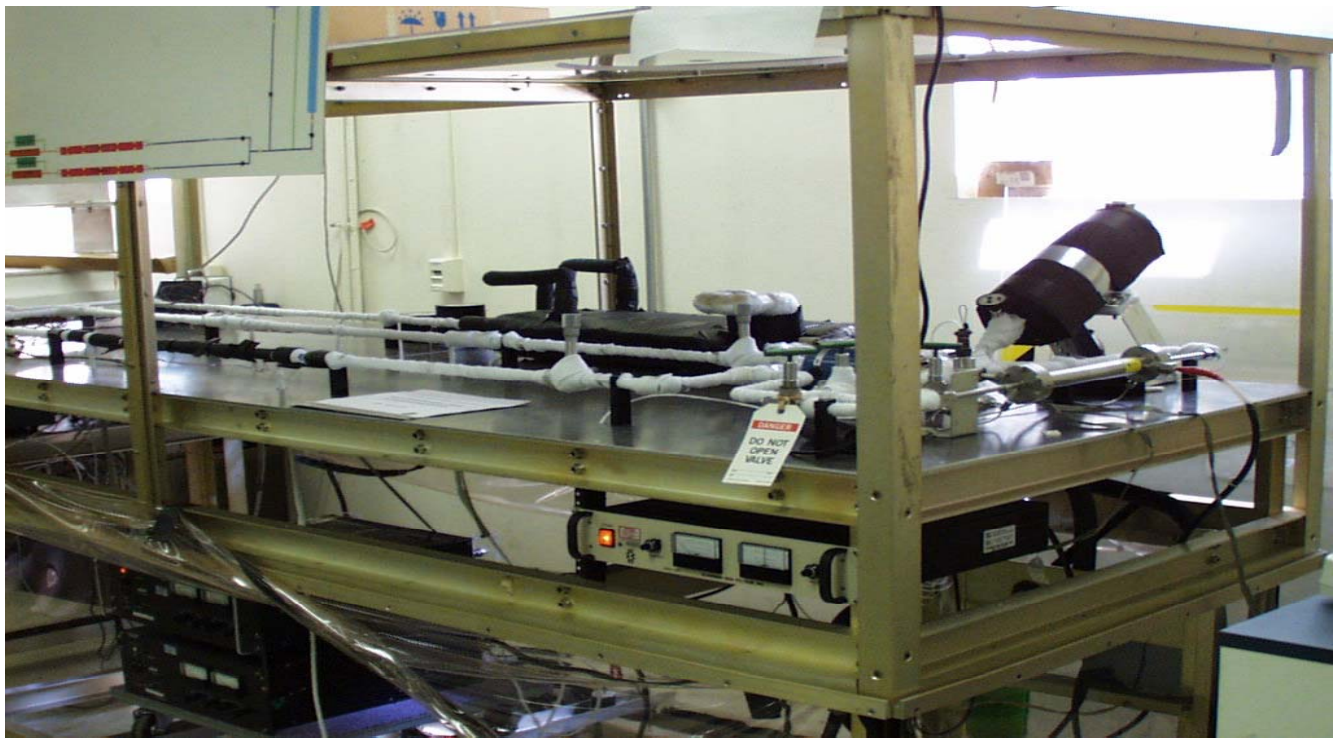

Conduction Pump Performance Ambient Temperature Loop

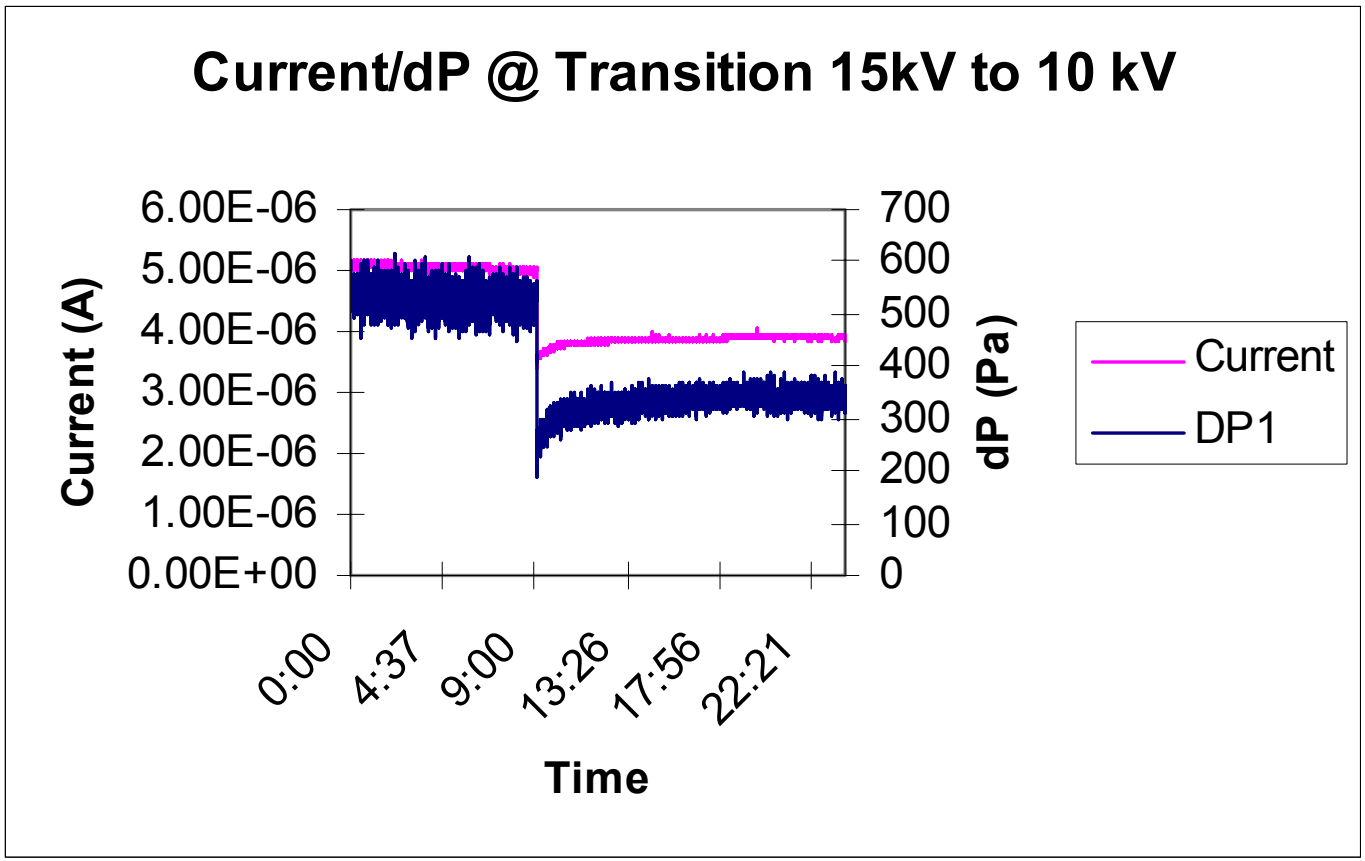

Cryogenic - Loop Pump Results with LN2

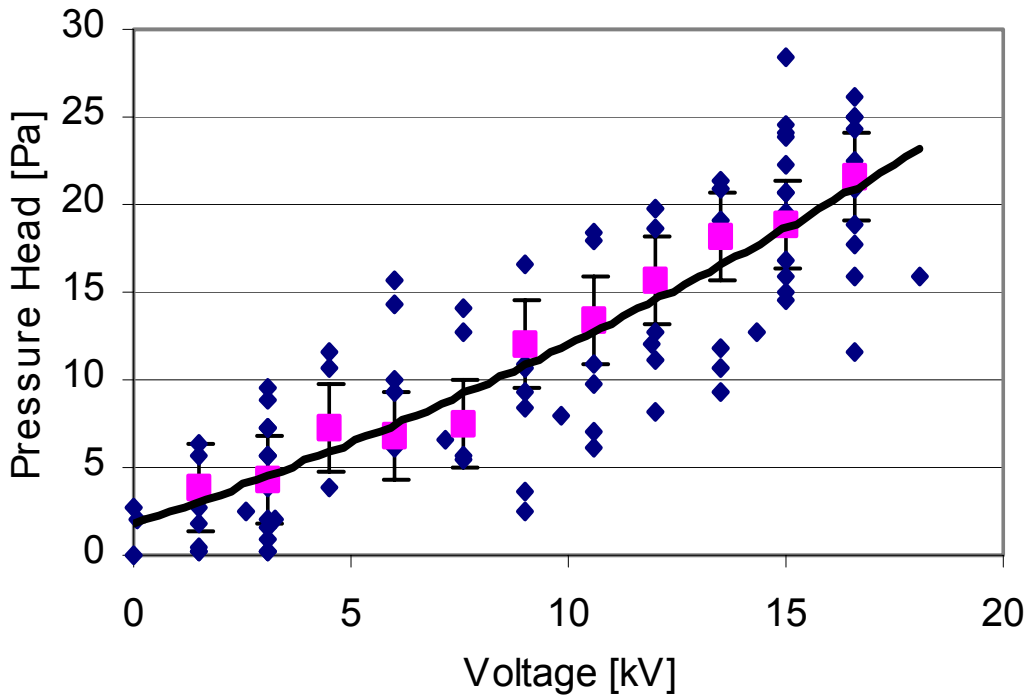

EHD MEMS Cooling Concept

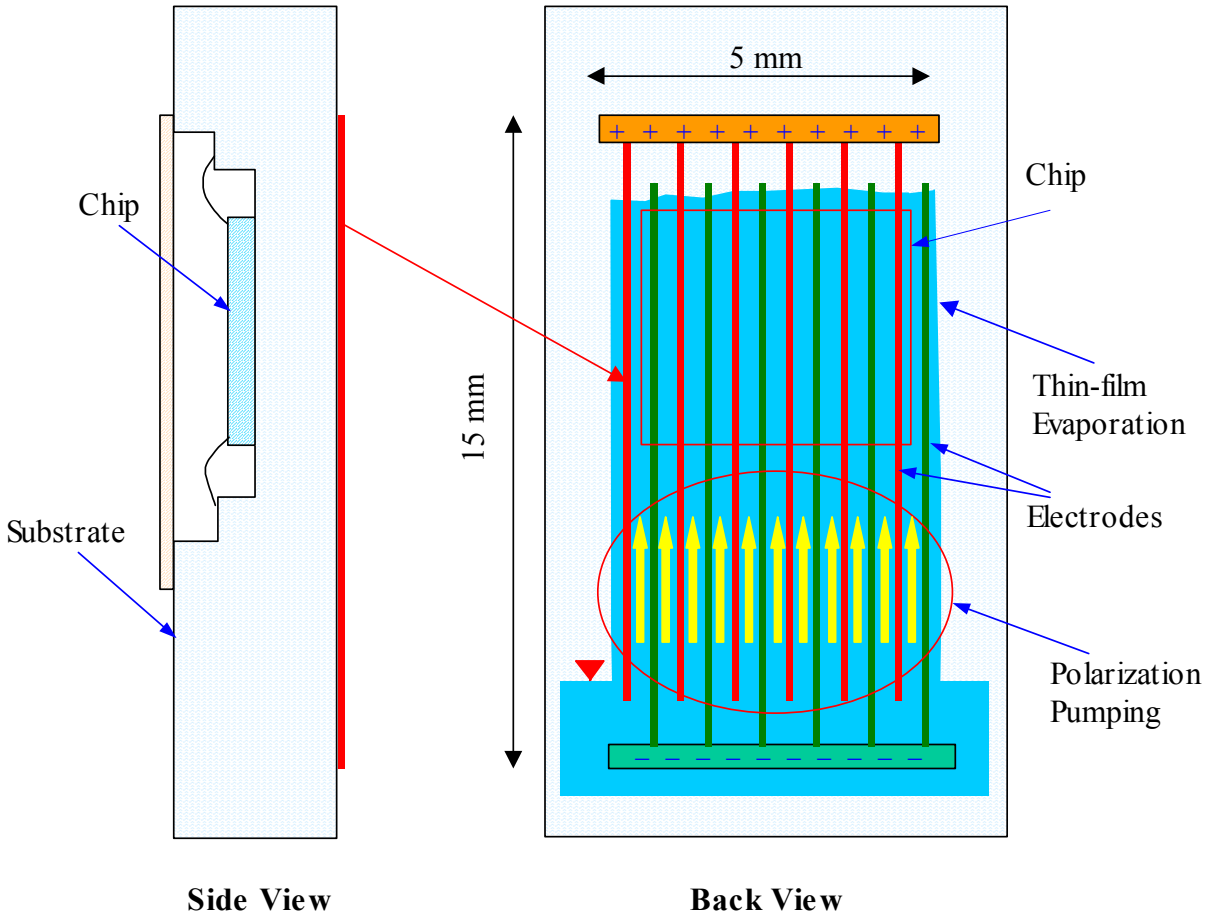

Future Technology Needs

- Dimensional stability of very large structures
- Diode action to minimize heater requirements
- Higher heat flux
  - lasers, electronics, propulsion systems
- Cryogenic temperature regime
  - that's where the science is headed
- Increasingly integrated designs (e.g., NGST)
- Fleets of micro/nano spacecraft have special problems
  - small C_p and need for common design (e.g.,ST5)
- Challenging thermal sinks (e.g., Solar Probe, ULDB flights)

ANALYSIS OF POOL BOILING IN MICROGRAVITY DURING LOSS OF COOLING FOR THE QUENCH MODULE INSERT (QMI)

Richard D. Horton
Tec-Masters, Inc.

ABSTRACT

In support of the thermal design of the quench module insert (QMI) microgravity experiment, a thermal/fluid math model was created with SINDA/FLUINT in order to simulate a loss of cooling scenario and the resultant pool boiling in the cooling lines. The objectives of the analysis were to determine whether critical components would surpass maximum temperature, what affect would phase change have on the component temperatures, and how much liquid volume would be expelled during the phase change. While developing the model, concerns were raised about the validity of phase change correlations used in SINDA/FLUINT when applied in the microgravity environment. This paper discusses the results of the thermal/fluid math model and the impact of microgravity on the pool boiling heat transfer coefficient.

INTRODUCTION

The QMI is a high gradient vacuum furnace, which will be used to perform directional solidification experiments in a microgravity environment. It will be installed in the Microgravity Science Laboratory (MSL) housed within the Materials Science Research Rack-1 (MSRR-1) aboard the International Space Station (ISS). This will be one of the first science facilities installed on the ISS[1]. The QMI is made up of four heated zones and one water-cooled zone, which produces a high thermal gradient in a metal/alloy sample rod. The overall QMI design consists of a hot zone, a cold zone, a gradient zone, a quench zone, an insulation jacket, and coolant loops[1]. The hot zone is made up of four independently controlled heaters insulated by alumina core sleeves within a Tantalum core housing (see figure 1). The hot zone assembly is designed to operate at a maximum temperature of 1400°C. The cold zone consists of a water-cooled copper outer-sleeve (chill block) coupled to an aluminum inner-sleeve through a conical interface. The inner-sleeve, known as the Thermal Interface Collar (TIC), interfaces with the Sample/Ampoule/Cartridge Assembly (SACA) through a high conductance material known

as Veltherm™. A variable flow rate water loop provides cooling to the chill block. The gradient zone consists of twenty molybdenum radiation shields, which provide axial isolation between the hot and cold zones. The quench zone is attached to the TIC of the cold zone and consists of a phase change device and actuation mechanism as shown in figure 1. The quench zone provides for a rapid cooling of the SACA material; however, for the purposes of this analysis, a non-quench TIC was used. The insulation jacket consists of two ten-layered spirally wrapped jackets of molybdenum foil. The hot zone, gradient zone, and insulation jacket are all mounted within the furnace housing. The furnace housing is cooled by a constant flow rate water loop that is brazed onto the housing jacket in a helical pattern (figure 1).

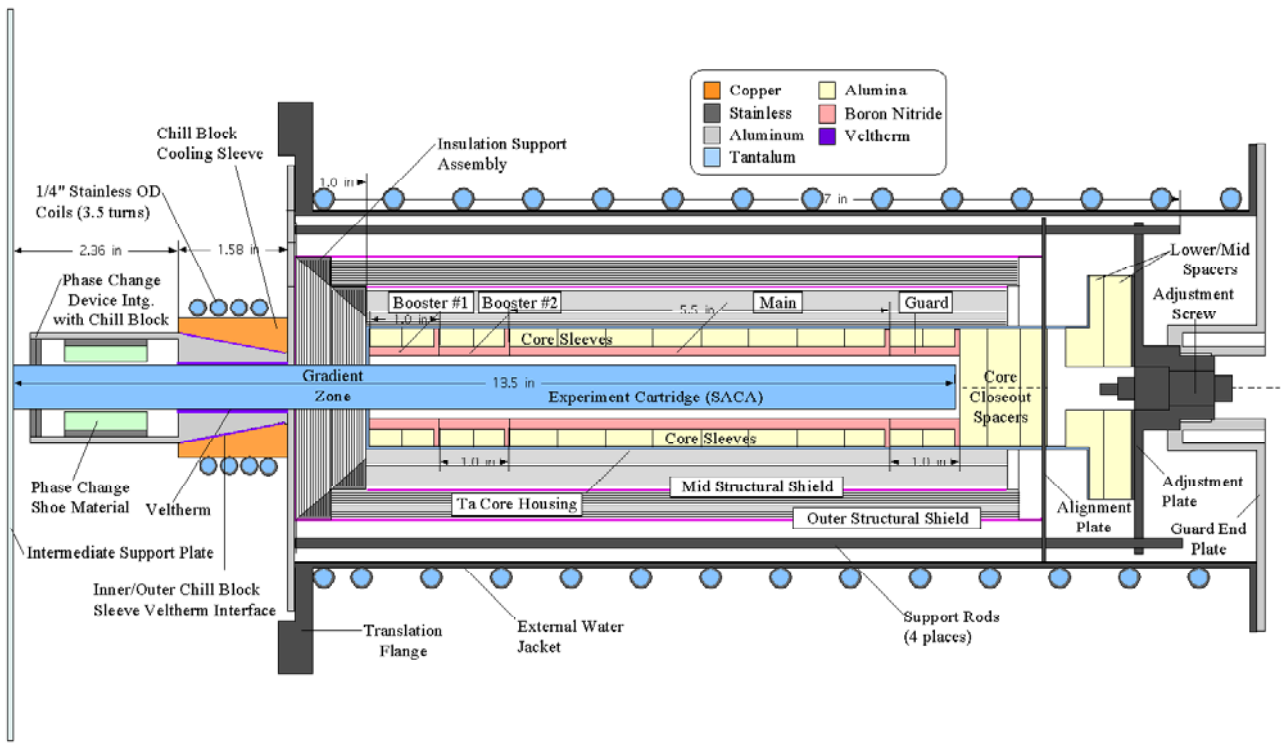

Figure 1: QMI cross-section[1]

A requirement of the QMI design is that the furnace does not cause any damage to the vacuum chamber during a loss of cooling event. The loss of cooling scenario that was envisioned was one in which a failure of the cooling loop pump halts the coolant flow. The heaters remain operational until a set point is reached by one of several monitored thermocouples placed on or near critical components. Critical temperatures for these components are reached almost immediately after the water flow stops. Thus, a loss of cooling quickly results in a loss of power. Once the power has been shut off, the furnace is then allowed to cool through radiation and conduction to the experiment chamber walls.

To ensure that a loss of cooling event would not damage the experiment chamber, a thermal math model was developed to simulate the loss of cooling scenario. Furthermore, it was hoped that the math model results could be used to develop possible design solutions that would enable the furnace to survive the loss of cooling event and maintain subsequent operational capability. The math model results were used to obtain maximum heat fluxes from the furnace to the experiment chamber and maximum furnace component temperatures.

MODEL DESCRIPTION

The original thermal math model for the QMI was developed using SINDA/G and TRASYS. The fluid portion of the model consisted of one-way conductors whose values were updated through the use of Fortran subroutines. Two simple FLUINT models, one for each cooling loop, had also been developed separately from the SINDA/G thermal model. These two models used heat flux arrays generated from the thermal model to impose heat loads directly onto the fluid lumps. This method allowed for an estimate of water volume expulsion and an approximation of when boiling in the cooling lines would begin to occur after the pump failure. To simulate loss of cooling, the steady state temperatures from the SINDA/G thermal model were used as initial conditions and radial conduction replaced the film coefficient calculations from the tube wall nodes to the fluid nodes. The model was then run using a transient solution routine until maximum temperatures for the critical components were reached. At that point, the heaters shut off and the transient run terminated. The results from this solution were then used as initial conditions for a second transient solution in which the water nodes were completely removed. This model was then used to simulate the transient heat up and eventual cool down of the furnace after the water had completely boiled. This conservative method of simulating phase change ignores the energy storage experienced due to the latent heat of vaporization.

In an effort to produce less conservative results that would more realistically predict maximum temperatures, a fully integrated thermal/fluid model was developed using SINDA/FLUINT. Since the two cooling loops for the furnace share a common outlet, a single fluid network was created to allow fluid exchange from one loop to another. The thermal and fluid models were integrated through the use of heat transfer ties[2]. Theoretically, this technique would provide a more accurate simulation of the phase change heat transfer as well as the volume expulsion that would take place in the cooling lines as the water flow stopped and the furnace begins to overheat. In addition to the heat transfer and thermal expansion of the fluid, this method would simulate the transient affects produced by the energy storage due to the heat of vaporization.

The thermal nodalization of the coolant tubing consists of three parts: an inner surface arithmetic node, a centerline diffusion node and an outer surface arithmetic node. The water jacket tubing is represented by four node groups for every 360° loop and one node group each for inlet and outlet routing. The chill block tubing is represented by a single node group for every 360° loop while the inlet and outlet routing is represented by an additional ten node groups, which includes the combined outlet tubing for the chill block and water jacket (figure 2). The diffusion nodes are connected by linear conductors to provide axial conduction within the tubing. The fluid model consists of fluid tank lumps, which correspond to each inner surface thermal node and are connected by inter-model heat transfer ties[2]. The tanks are connected by tubes that provide a flow path for thermal expansion of the water during conductive heating and expulsion of the water during boiling. Plenums were used to represent the supply and outlet of the cooling system. The thermal model is much more complex and a full description is beyond the scope of this paper. Due to science requirements imposed by the experiments for which the QMI was designed, the thermal model consists of nearly 5000 nodes. One of the keys to the directional solidification experiment is knowing the exact location of the solid/liquid interface. The accuracy required to locate the solid/liquid interface resulted in an axial nodal resolution of 2 millimeters.

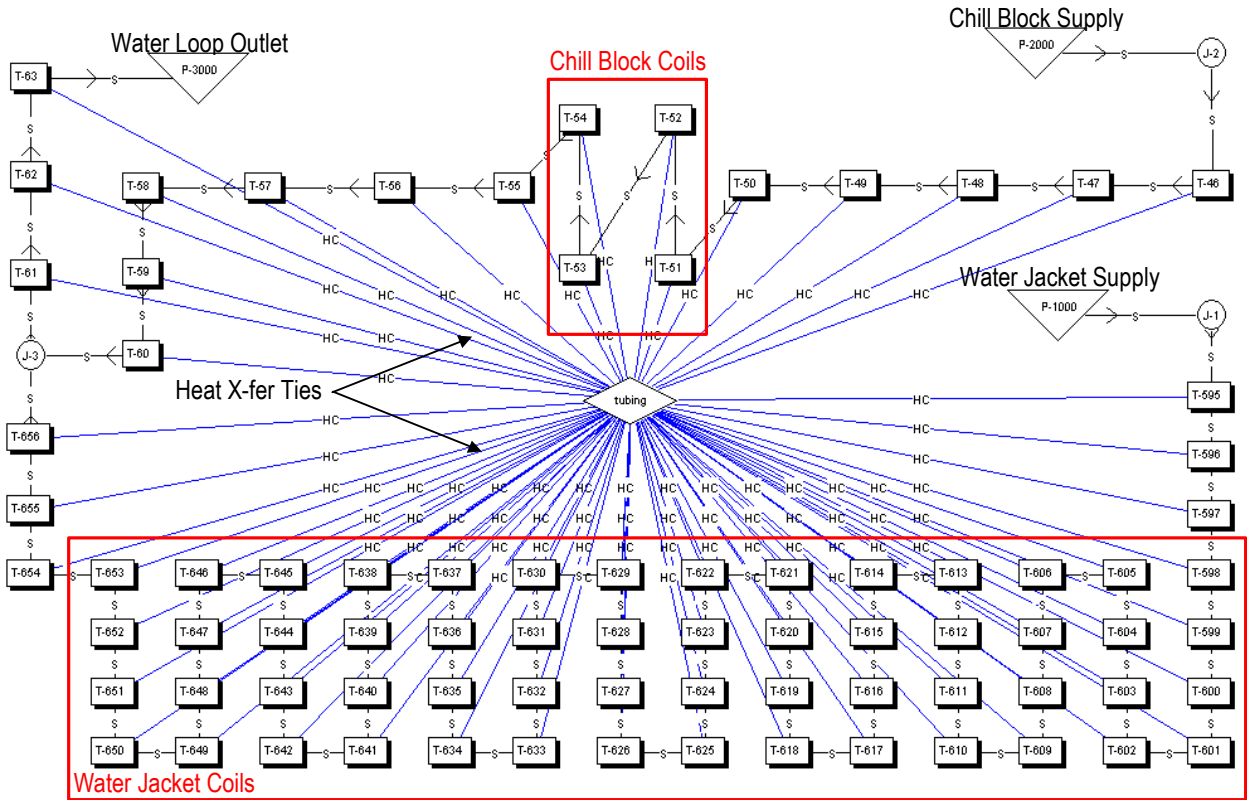

Figure 2: Fluid Model Network Diagram

POOL BOILING HEAT TRANSFER

As was mentioned in the preceding section, phase change provides a means of energy storage. During a loss of cooling scenario, the heat transfer rates from the furnace to the chamber become critical. By using the energy storage of the water in the cooling loops, it may be possible to reduce the maximum heat transfer rates and spread the heat transfer over a longer time period so as to avoid over heating the chamber as well as the furnace. However, it was unknown what differences may exist between boiling on Earth and boiling in low Earth orbit (LEO) or what affects any differences may have on the boiling heat transfer coefficients.

CORRELATIONS IN EARTH GRAVITY

The subject of pool boiling in a 1-g environment has been covered extensively in engineering research and testing. Numerous correlations have been developed for the purpose of describing the effects of phase change heat transfer analytically. Since these correlations were empirically derived from test data, they are very specific with respect to the geometry and conditions under which the tests were performed. Thus, any analysis performed with these

correlations on conditions other than those for which the correlations were derived will produce additional uncertainty in the results on top of that which is inherent to this type of analysis. Unfortunately, pool boiling inside tubes is not a situation that has received much if any attention by the research community. While correlations may exist for pool boiling in tubes, the only correlations that were found in preparation for this analysis pertained to forced convection or flow boiling. Therefore, the correlations for a flat plate will be used for this analysis.

Before beginning a discussion on the various correlations for all phases of boiling heat transfer, a discussion of the various boiling regimes is warranted. These regimes can best be described through an examination of the boiling curve (see figure 3)[4]. For the segment AB in the boiling curve, single-phase convection is the only form of heat transfer that occurs. As the heated surface temperature exceeds the saturation temperature of the liquid, bubbles begin to form in surface cavities and nucleate boiling begins. As the bubbles are removed from the surface by buoyancy forces, cooler liquid flows back into the cavity and the process continues. The sudden increase in heat transfer due to the removal of latent heat during vaporization results

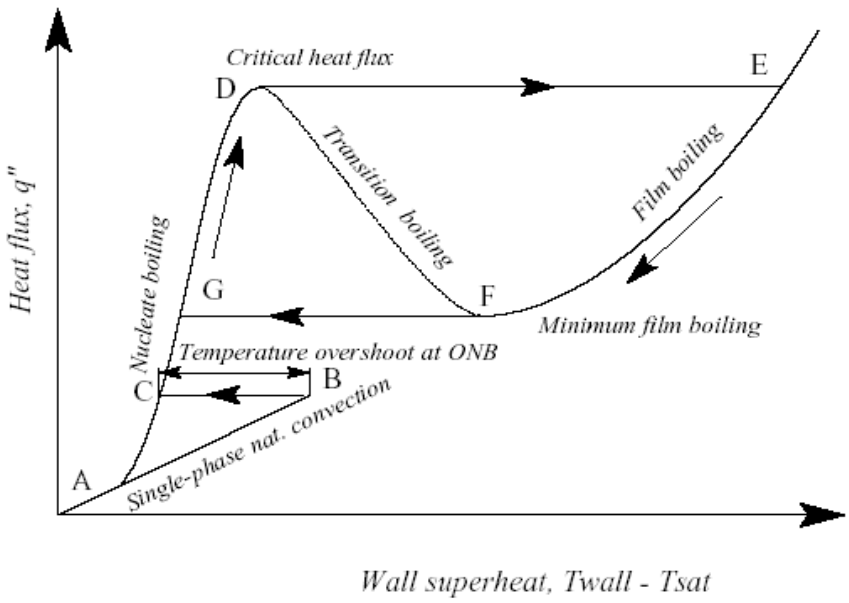

Figure 3: Typical Boiling Curve[4]

in a sudden drop in wall superheat at the onset of nucleate boiling (ONB) which is denoted by path BC in the curve. Path CD represents the nucleate boiling regime and during this period more and more bubbles are formed at the surface. As can be seen from the curve, in the nucleate boiling regime the wall superheat changes very slowly for a rapid increase in surface heat flux. As the wall superheat reaches the critical heat flux (CHF), a transition to film boiling begins represented by path DF. If the wall superheat is increased rapidly up to the critical heat flux, a direct jump to full film boiling may occur (path DE). The transition boiling regime is very unstable, and at any point on the surface the process can oscillate between nucleate and film boiling. This phenomenon is known as a hysteresis loop and can cause significant problems when attempting to model this transition boiling[5]. As can be gathered from the previous description, the phenomena that occur during boiling heat transfer are very complex and some aspects are still not very well understood. Analytical and empirical investigations into these phenomena are the subject of ongoing research.

The analytical process for the nucleate boiling phase begins with Newton's law of cooling[3],

$$q_s'' = h(T_{wall} - T_{sat})$$

where q_s'' is the surface heat flux and $\Delta T_e = (T_{wall} - T_{sat})$ is the excess temperature. If these two values are known then the heat transfer coefficient, h, can be calculated from the above equation. Using the flat plate as the geometry baseline, the surface heat flux can be calculated from the well-known correlation that was developed by Rohsenow[3].

$$q_s'' = \mu_l h_{fg}\left[\frac{g(\rho_l - \rho_v)}{\sigma}\right]^{1/2}\left(\frac{c_{p,l}\Delta T_e}{C_{s,f} h_{fg} Pr_l^n}\right)^3$$

The coefficient $C_{s,f}$ and the exponent n are dependent upon the surface-liquid combination. For stainless steel tubes filled with water, representative values are 0.06 and 1.0 respectively[3]. An important point on the boiling curve is the critical heat flux (CHF) at which point nucleation begins to be replaced by a constant vapor film between the surface and the liquid. Knowing when this phenomenon will begin to occur is of vital importance in preventing "burnout" which can damage the heating surface, as the vapor will act as an insulator. This is not a concern in the loss of cooling situation for QMI. However, the critical heat flux is important in that it is a signal that the correlation for nucleate boiling can no longer be used to calculate heat transfer. Through a hydrodynamic stability analysis, Zuber obtained an expression for determining the critical heat flux, which was independent of surface material and only weakly dependent on geometry[3]. Through experimentation and approximation the correlation was later refined to:

$$q_{max}'' = 0.149 \cdot h_{fg}\rho_v\left[\frac{\sigma g(\rho_l - \rho_v)}{\rho_v^2}\right]^{1/4}$$

The transition boiling regime is generally only obtainable by controlling the heated surface temperature, and no reliable correlation for predicting heat transfer exists at this time[6]. It is more widely assumed that at the CHF, film boiling begins. This phase of boiling is a combination of heat transfer through a vapor layer and radiation to fluid from heated surface. During film boiling, the temperature of the heated surface begins to increase rapidly since the heat transfer path is now primarily through the insulating vapor layer. The correlation for film boiling that was available in the text is for the geometry of horizontal cylinders immersed in a fluid and was developed by Bromley[5].

$$Nu_D = \frac{h_b D}{k_v} = 0.62\left[\frac{g\rho_v(\rho_l - \rho_v)(h_{fg} + 0.4c_{p,v}\Delta T_e)D^3}{\mu_v k_v \Delta T_e}\right]^{1/4}$$

Vapor properties in the above equation are evaluated at the film temperature and the liquid density is evaluated at the saturation temperature. The variable, h_b, is the boiling heat transfer

coefficient as opposed to the radiation heat transfer coefficient, h_r, which becomes a more significant contributor to the overall heat transfer at surface temperatures above about 300°C. The radiation heat transfer coefficient can be calculated from the equation[5],

$$h_r = \frac{\sigma\varepsilon\left(T_{wall}^4 - T_{sat}^4\right)}{T_{wall} - T_{sat}}$$

where σ is the Stefan-Boltzmann constant and ε is the surface emissivity. The total heat transfer coefficient is then calculated from[3],

$$h = h_b + \frac{3}{4}h_r \qquad \text{for } h_r < h_b$$

After all of the water in the tubes has boiled, the heat transfer becomes a function of free convection of a vapor similar to the free convection of the liquid state experienced prior to the onset of nucleate boiling.

CORRELATIONS IN REDUCED GRAVITY

As the thermal/fluid model was being developed, the question was raised as to the effects that microgravity may have on boiling heat transfer. Thus, a search of the relevant text was initiated. One of the first observations that were made after the research began was that the issue of boiling in a reduced gravity environment has been a topic of great debate among researchers. Testing has been conducted dating back to the 1950's when the only means of testing in a reduced gravitational field was in the form of drop towers[7]. These early drop towers were on the order of a few meters in height and provided barely a second of free fall simulating reduced gravity. However, later drop towers and drop shafts, which use abandoned mining shafts, increased dramatically in height. Many of these facilities now reach over a hundred meters or more in height, providing several seconds of quality reduced gravity on the order of 10^{-5}g with relatively little g-jitter (small oscillations in the mean g value). As an example, the JAMIC drop shaft in Hokkaido, Japan extends 790 meters into the ground and provides 10 seconds of free fall[4]. Other methods employed in simulating reduced gravity include parabolic flights aboard aircraft and sounding rockets which both provide even longer test periods on the order of 20 seconds for parabolic flights and up to 20 minutes for sounding rockets. While the sounding rockets provide good quality reduced gravity on the order of 10^{-4}g, they are more expensive and the experimental apparatus must be fully automated. The parabolic flights provide relatively poor quality reduced gravity on the order of 10^{-2}g with an excessive amount of g-jitter; however, the experimental apparatus may be monitored and changed as needed during the experiment. In the last decade, experiments have been placed onboard space shuttle flights, which provide good levels of reduced gravity on the order of 10^{-4} to 10^{-5}g with jitter levels depending on crew movements and operation of onboard systems[4].

Most of the experiments have been performed using a heated wire or horizontal flat plate immersed in a liquid, usually refrigerants such as R-113. However, some experiments have been

performed using water as the test liquid[8]. The results of the various experiments are often conflicting. One example of this is found when comparing the results produced by Lee et al.[9] and Lee and Merte[10] to the results produced by Oka et al.[8]. The results from the first two sources show an enhancement in the heat transfer coefficient in reduced gravity while the results of the later group show degradation in heat transfer. It is hard to compare the results of these two separate studies since the conditions under which they were obtained were so different. The experimental data produced by Lee and Merte[10] were obtained for R-113 on 5 separate space shuttle missions as part of the NASA Get Away Special (GAS) program. These experiments were able to achieve multiple long duration steady state boiling test runs at various surface heat flux levels for saturated and sub-cooled boiling.

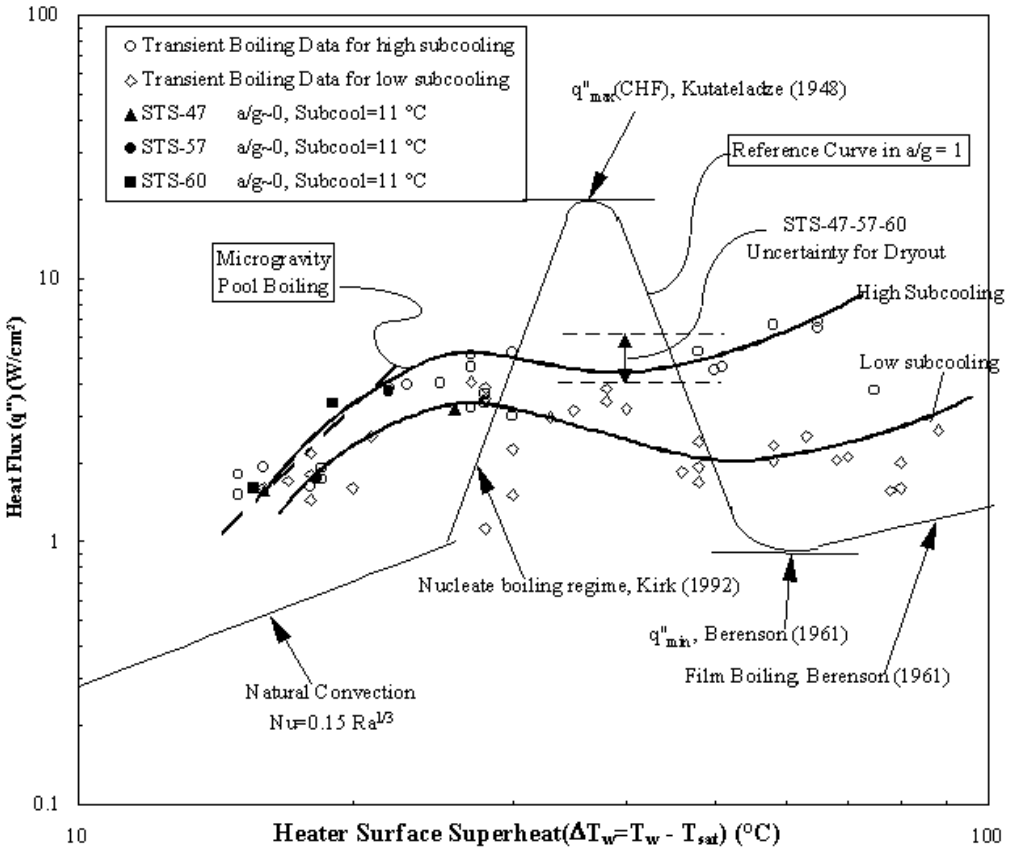

Figure 4: Reduced Gravity Pool Boiling Curve for R-113.[9]

Figure 4 shows the boiling curve produced by Lee et al.[9] over the course of several shuttle missions. Lee and Merte[10] have even produced a curve showing the derived heat transfer coefficient for reduced gravity as compared to terrestrial values (see figure 5). The experimental results produced by Oka et al.[8] were obtained for both R-113 and water by using the drop shaft at the Japan Microgravity Center (JAMIC). The nature of these experiments did not allow for long duration test runs and thus steady state nucleation was not achievable. Both experiments were performed on a flat heating surface as opposed to a wire heater immersed in a fluid, which has shown yet another set of characteristics according to additional research teams[4]. One would

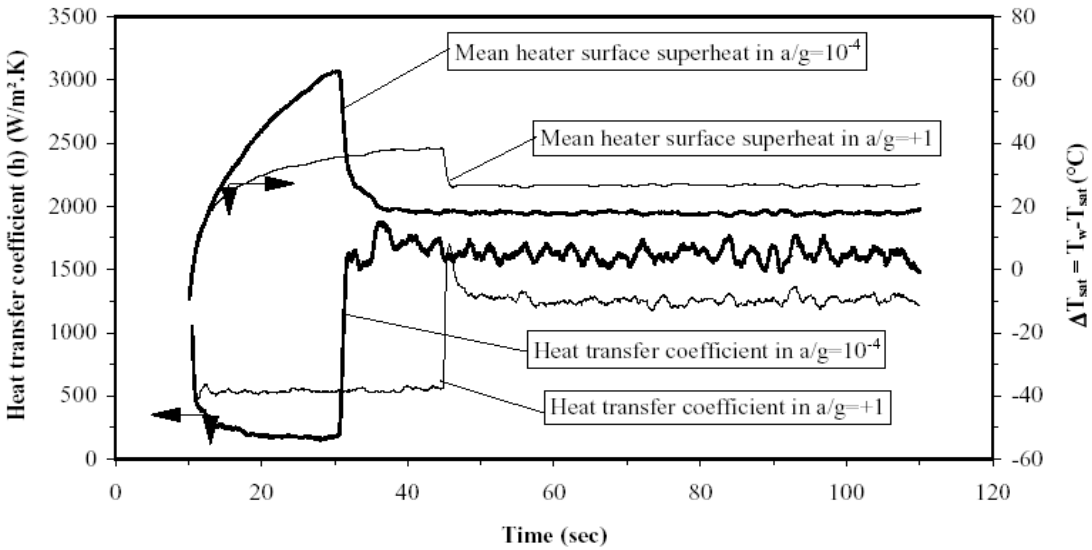

Figure 5: Mean Heater Surface Temperature and Derived Heat Transfer Coefficient

tend to be more confident in the results produced by Lee and Merte[10] since their test data was produced in the same environment that the QMI will experience, i.e. low Earth orbit (LEO). The results of their experiment found that the onset of nucleate boiling occurs sooner in reduced gravity and that as much as a 32% enhancement in the heat transfer was observed and as much as 40% for high levels of sub-cooling, and the critical heat flux is substantially reduced[9]. Figure 6 shows a sequence of images of the experimental apparatus during nucleate boiling.

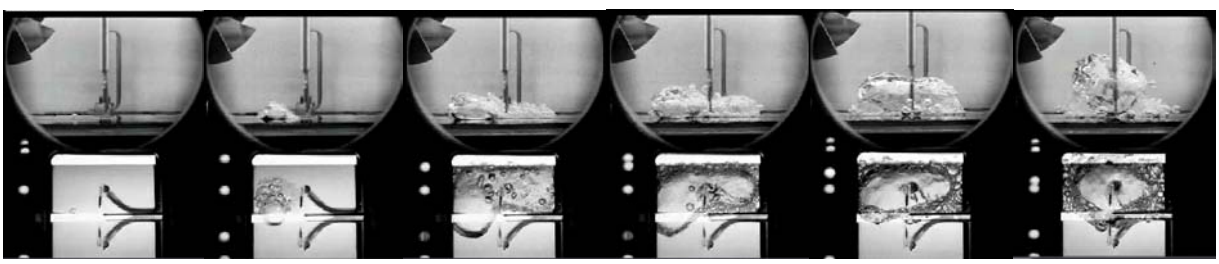

Figure 6: Sequence of Images of R-113 During Sub-cooled Boiling

Figure 7 is a sequence of images taken from the same experiment only with very low levels of surface heat flux. In this sequence of images the coalescence of the bubbles into a large single bubble is witnessed. The larger vapor bubble acts as reservoir for the smaller vapor bubbles, maintaining its size through the dual action of condensation and coalescence[10].

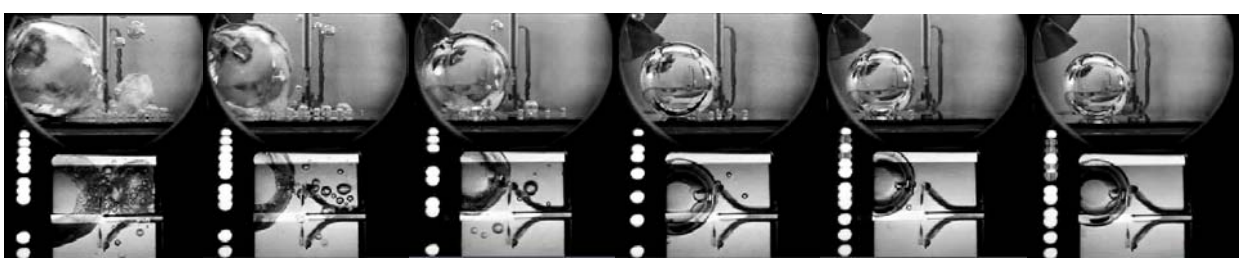

Figure 7: Sequence of Images of R-113 During Sub-cooled Boiling at Low Heat Flux Levels.

Unfortunately, most researchers are in mutual agreement that the heat transfer coefficients and the effect of reduced gravity vary for different fluids as well as for different surface geometry. Since the data produced by Lee and Merte[10] is for R-113, it cannot be applied to the configuration of the QMI with any confidence. Since water has a surface tension roughly four times that of R-113 and a heat of vaporization on the order of 14 times greater, it stands to reason that the two liquids would behave very differently in reduced gravity where heat transfer is driven by surface tension effects on bubble formation and detachment behavior. As it stands in the current state of pool boiling reduced gravity research, the quantity of experimental data is insufficient to support the derivation of any form of heat transfer correlations. One researcher suggested that those types of correlations are still a decade away. Even then, any correlations that may be derived will continue to be updated as more and more research is conducted. This is still occurring with Earth based correlations today, some 60 years after the first correlations were developed.

While the desired analytical correlations are not available, what can be taken from this investigation is a general picture of the behavior of fluid heat transfer in reduced gravity. This information will allow ground-based analysis to be tailored as much as possible towards a more accurate solution. For example, in a reduced gravity environment, the convection phase prior to the onset of nucleate boiling will be replaced by pure conduction through the fluid. Furthermore, knowing that in reduced gravity the critical heat flux is lower and the transition to film boiling occurs more quickly enables us to determine in which direction the actual results will deviate from the analytical results. Knowing these characteristics can give us a better idea of what to expect during an actual "on-orbit" loss of cooling event.

MODELING RESULTS

While the reduced gravity research was very interesting, we are still left with the modeling issues of phase change heat transfer. Apart from actually placing the QMI test unit on the shuttle and performing a loss of cooling experiment, the ground-based correlations will have to suffice. As stated in the preceding paragraph, the single-phase convection correlations can be replaced with conduction through the fluid. This will at least simulate the effects of a microgravity environment prior to the onset of nucleate boiling. In SINDA/FLUINT, as the flow rate in tubes approaches zero, single-phase heat transfer conductances are applied assuming a laminar Nusselt number and a constant surface temperature defined by the equation[2]

$$Nu_D \equiv \frac{h \cdot D}{k} = 3.66 \; ; \; \text{Laminar}$$

To simulate the conduction through the fluid in a microgravity environment the heat transfer is calculated from the radial conduction equation[3].

$$hA = \frac{2\pi \cdot L \cdot k}{Ln(r_2 / r_1)}$$

To simulate pool boiling, SINDA/FLUINT applies the above laminar Nusselt number equation to single-phase *vapor*, and to simulate condensation, the same equation is applied to single-phase *liquid*. This is a conservative method of calculating the heat transfer and greatly over-simplifies the boiling condition. SINDA/FLUINT does not perform a critical heat flux calculation; nor does it handle the case of sub-cooled boiling[2]. These conservative methods used by the SINDA/FLUINT processor would produce results that are nearly the same as those produced by the original technique that was employed using the SINDA/G thermal model. In order to try and produce less conservative results that more realistically simulate the boiling heat transfer phenomenon, the internal correlations that are automatically called by the SINDA/FLUINT processor were replaced. The convection heat transfer ties described above were replaced by user heat transfer ties[2]. By using these heat transfer ties in SINDA/FLUINT, the correlations discussed in the boiling section for Earth gravity could be incorporated. Prior to developing this model, a baseline case using the automated calculations of the SINDA/FLUINT processor was needed. This would allow the results from the user supplied correlation case to be compared to the results produced by the internal SINDA/FLUINT correlations. Attempts to obtain results from the baseline thermal/fluid model resulted in catastrophic failures of the SINDA/FLUINT processor. Whether using automated calculations or user inputs, the solution routine would not converge once phase change began in the fluid tanks. All attempts to resolve this issue had little or no effect. As the fluid in the tanks representing the chill block coil began to boil, increasingly smaller time-steps were taken by the FWDBCK solution routine. The model was allowed to run for several days to get past this transition at which point large fluctuations in the vapor temperature were observed. This pattern continued until boiling began to occur in the tanks around the furnace housing at which point the model began experiencing fluid property routine errors and the solution routine failed. Numerous modeling variations of Junction/Tank combinations were implemented in an attempt to resolve this issue. Attempts were also made using twinned paths and twinned tanks with ifaces. None of the methods employed had any positive effect (some actually made the problem worse). The control constants FRAVER, DTSIZF, RMFRAC, and RMRATE were adjusted in attempts to force the solution routine to smoothly pass through the phase change transition. This too had little or no effect. It was concluded that due to the overwhelming size and complexity of the thermal model the solution was unattainable with the current configuration. A model of this size requires a significant amount of processor time even without the added complication of a fluid submodel with phase change heat transfer. The SINDA/FLUINT manual warns users of the possible pitfalls of modeling phase change using tanks, stating, *"Small, two-phase or vapor (soft) tanks can significantly slow the solution."* [2]. Since one of the desired uses of this model was to track liquid volumes and associated expulsion rates during phase change, using junctions instead of tanks was not an option. Furthermore, junctions have no associated mass, and as a result no energy storage effects would be observed.

CONCLUSIONS

So what does all this mean for the situation of boiling in the cooling tubes on QMI? Essentially, there isn't enough data at this time to reliably incorporate any kind of analytical solution for reduced gravity boiling heat transfer. Furthermore, since the current configuration of the thermal/fluid model will not successfully run to completion in SINDA/FLUINT, the more

conservative approach will continue to be used were the assumption is that the water boils instantly with no phase change energy storage. Currently in development is a reduced order thermal model. The thermal nodalization has been reduced to fewer than 200 nodes. Once the reduction is complete and the model has been correlated to test data, the fluid model can then be integrated with the reduced model and another attempt will be made to achieve a solution with phase change heat transfer. Prior to this task, a stand alone fluid model representing both cooling loops will need to be run to ensure that the SINDA/FLUINT processor can effectively simulate simultaneous boiling in two separate locations in the water loop. Additional research is also needed in order to find more relevant ground based correlations for pool boiling in tubes. If the reduced version of the model is successful in simulating phase change, then the internal correlations will be replaced with the most appropriate ground correlations available. The results can then be compared to the baseline loss of cooling analysis and possibly presented in a future technical paper.

ACKNOWLEDGEMENTS

The author wishes to acknowledge the contributions of Shawn Breeding and Julia Khodabandeh, of the Marshall Space Flight Center, for their past modeling efforts from which the thermal/fluid model discussed in this paper was constructed.

REFERENCES

1. Breeding, S., et al., "Quench Module Insert Critical Design Review: Thermal Design Data Book", June 2000.
2. Cullimore, B.A., Ring, S.G. and Johnson, D.A., SINDA/FLUINT User's Manual, Version 4.3, June 2000.
3. Incropera, F.P. and DeWitt, D.P., Fundamentals of Heat and Mass Transfer, 3rd edition, John Wiley and Sons, 1990.
4. Di Marco, P. and Grassi, W., "Overview and Prospects of Boiling Heat Transfer Studies in Microgravity", *Proceedings of IN SPACE 97*, Tokyo (J), 18-19 November 1997.
5. Chapman, Alan J., Heat Transfer, 4th edition, Prentice Hall, 1984.
6. Collier, John G., Convective Boiling and Condensation, 2nd edition, McGraw-Hill, 1981.
7. Straub, J., Zell, M. and Vogel, B., "Pool Boiling in a Reduced Gravity Field", *Proceedings of the 9th International Heat Transfer Conference* (Jerusalem, Israel), Vol. 1, Hemisphere, New York, 1990, pp. 91-112.
8. Oka, T., Abe, Y., Mori, Y.H. and Nagashima, A., "Pool Boiling Heat Transfer in Microgravity", *JSME International Journal, Series B: Fluids and Thermal Engineering*, Vol. 39, No. 4, 1996, pp. 798-807.
9. Lee, H.S., Merte, H. and Chiaramonte, F., "Pool Boiling Curve in Microgravity", *Journal of Thermophysics and Heat Transfer*, Vol. 11, No. 2, April-June 1997, pp. 216-222.
10. H.S. Lee and H. Merte, Jr., 1999, "Pool Boiling Mechanisms in Microgravity", *Proceedings of the Engineering Foundation Conference on Microgravity Fluid Physics and Heat Transfer*, Ed. V. K. Dhir, Oahu, Hawaii, September 19-24, 1999.

NOMENCLATURE, ACRONYMS, ABBREVIATIONS

Acronyms

CHF	Critical Heat Flux
ISS	International Space Station
LEO	Low Earth Orbit
MSRR-1	Materials Science Research Rack-1
MSL	Microgravity Science Laboratory
ONB	Onset of Nucleate Boiling
QMI	Quench Module Insert

Symbols

c_p	Constant Pressure Specific Heat
C_{sf}	Empirical Constant
D	Diameter
g	Acceleration of Gravity
h_{fg}	Heat of Vaporization
h	Heat Transfer Coefficient
k	Thermal Conductivity
L	Length
Ln	Natural Logarithm
n	Empirical Constant
Nu	Nusselt Number
Pr	Prandtl Number
q_s''	Surface Heat Flux
r	Radius
T_{wall}	Wall or Surface Temperature
T_{sat}	Saturation Temperature of the Liquid
ΔT	Temperature Difference
μ	Viscosity
ρ	Density
σ	Surface Tension, Stefan-Boltzmann Constant
ε	Surface Emissivity

Subscripts

b	boiling
l	liquid
r	radiation
v	vapor

THERMAL EXAMINATION OF AN ORBITING CRYOGENIC FUEL DEPOT

Name of Author(s)
Patrick V. Hull
Steven L. Canfield
Tennessee Technological University

Name of Co-Author(s)
Connie Carrington
John Fikes
NASA/MSFC

ABSTRACT

For many years NASA has been interested in the storage and transfer of cryogenic fuels in space. Lunar, L2 and other chemical propulsive space vehicle missions now have staged refueling needs that a fuel depot would satisfy. The depot considered is located in lower earth orbit. Many considerations must go into designing and building such a station. Multi-layer insulation systems, thermal shielding and low conductive structural supports are the principal means of protecting the system from excessive heat loss due to boiloff.

This study focuses on the thermal losses associated with storing LH2 in a passively cooled fuel depot in a lower earth equatorial orbit. The corresponding examination looks at several configurations of the fuel depot. An analytical model has been developed to determine the thermal advantages and disadvantages of three different fuel depot configurations. Each of the systems consists of three Boeing rocket bodies arranged in various configurations. The first two configurations are gravity gradient stabilized while the third one is a spin-stabilized concept. Each concept was chosen for self-righting capabilities as well as the fuel settling capabilities, however the purpose of this paper is to prove which of the three concepts is the most efficient passively cooled system.

The specific areas to be discussed are the heating time from the fusion temperature to the vaporization temperature and the amount of boiloff for a specific number of orbits. Each of the previous points is compared using various sun exposed surface areas of the tanks.

INTRODUCTION

For many years NASA has been interested in the storage and transfer of cryogenic fuels in space. Lunar, L2 and other chemical propulsive space vehicle missions now have staged refueling needs that a fuel depot would satisfy. The depot considered is located in lower earth orbit. Many considerations must go into designing and building such a station. Multi-layer insulation

systems, thermal shielding and low conductive structural supports are the principal means of protecting the system from excessive heat loss due to boiloff.

This study will focus on the thermal losses associated with storing liquid hydrogen (LH_2) in a passively cooled fuel depot in a lower earth equatorial orbit. Three candidate designs will be analyzed and discussed, each resulting from a different depot configuration. Each design is based on a Boeing Delta IV Heavy Rocket. The specific analyses used to evaluate the designs are the heating time from the fusion temperature to the vaporization temperature and the boiloff losses. Multi-layer insulation systems, thermal shielding and low conductive structural supports are the principal passive means of reducing boiloff in systems storing cryogenic fuels.

An extensive analytical model has been developed and tested to determine the thermal losses for the three different fuel depot configurations. Each system is shown in figure 1

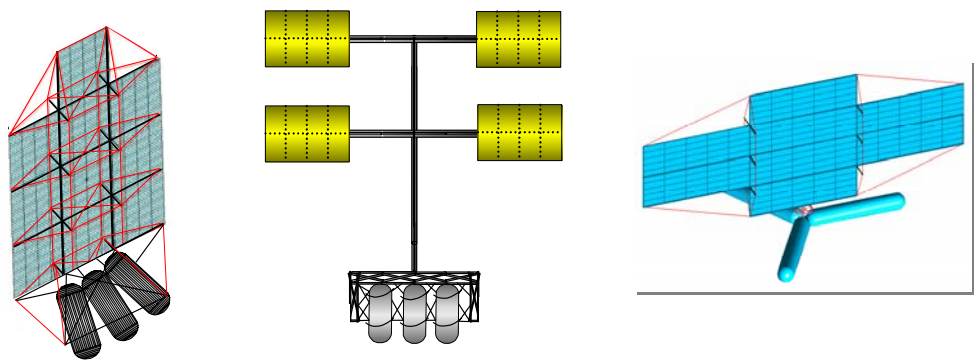

Figure 1: Abacus Tail Feather Concept, b) Four Wing Concept and c) Spinner Concept

ANALYTICAL MODEL

The vaporization temperature for LH_2 is 20.4K; the corresponding fusion temperature is 14K. Storage of LH_2 within this range will prevent slushing and boiloff. The greater concern is boiloff. Boiloff is mass loss due to phase changes from a solid to a gaseous state. Boiloff causes two severe problems within the system: (1) fuel loss and (2) over pressurization of the tank. Fuel loss due to vaporization is very expensive considering the mass transfer rate to LEO is $10,000/lb. Over pressurization of the tank from fuel vaporization is due density change in the fuel. This increase in volume could rupture the tank.

Analysis Assumptions

Design of the model required the development of several assumptions to govern the process: They are as follows:

1. All potential and kinetic energy changes are considered negligible
2. Neglect the heating of the boiloff vapor, it is small enough too become negligible.
3. Storage depot should maintain an Lower earth equatorial orbit,
4. Assume steady state surface conditions of the following
    (a) 1/10 of tank is considered against dark space

(b) 2/5 of tank is covered by the Earth
(c) The Sun and the thermal shield are combined to cover ½ the area of the tank

5. Isothermal conditions for each area section of the tank

CONTROL VOLUME

Analysis of the storage tank shown in Figure 2 begins by the application of the first law of thermodynamics to the control volume shown. The control volume in this case is the cryogenic tank itself as shown below.

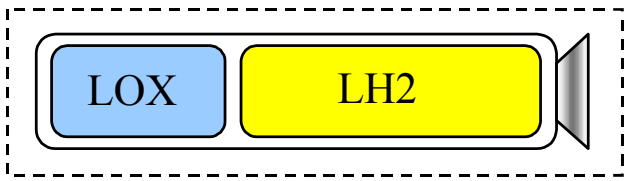

Figure 2: Control volume of the system

This is a passive system, meaning that no additional heat comes in or is taken away by thermal control system. The corresponding energy balance equation is $E_{in,dot} + E_{g,dot} + E_{out,dot} = E_{st,dot}$

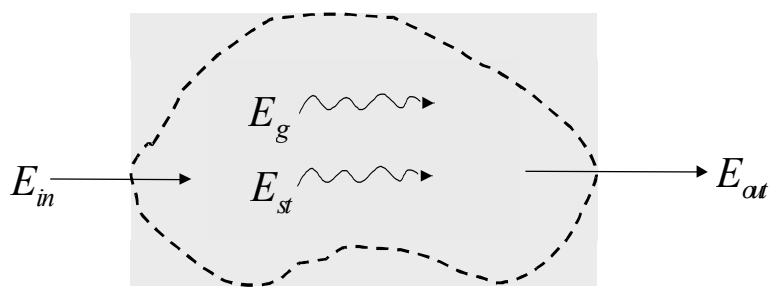

$$E_{in} + E_g - E_{out} = E_{st}$$

Figure 3: Theoretical control volume of the system

where E_{in} is the energy into the system from outside sources, E_{out} is the energy loss from the system. Each of these energy components is associated only with the surface of the control volume, meaning the radiation added and lost to the system. E_g is the thermal energy generation and E_{st} is the rate of energy stored within the system. The energy stored is in the form of increasing LH_2 temperature.

The control volume and energy balance theory stated above is attributed to the specific problem of the cryogenic fuel tank. A orbiting space vehicle experiences three sources of heat

addition, E_{in} , radiation from the sun, radiation from the earth and the radiation from the vehicle itself. The vehicle radiation in this case is from the thermal shield and or support structure.

The core problem of cooling cryogenic fluids is to combat the radiant heating by direct and indirect means. The effective radiation heat transfer constant used for the sun is 1143 W/m^2. Radiation emitted from the earth at LEO of 400Km is given by the radiation constant of q_{earth}= 60 W/m^2 for the lighted portion and q_{earth}= 20 W/m^2 for the shadow. Radiation absorption occurs from the thermal shield also. The thermal shield blocks some % of the sunlight from direct heat transfer to the tanks but in turn the shield is heated and thus emits radiation. The radiation constant is assumed to be 10 W/m^2.

E_{in} results from the sum of the sources:

$$E_{in} = Q_{radSun} + Q_{radEarth} + Q_{radShield} \tag{1}$$

Heat is also lost from the system from the tank surface. The effective radiation from the tank takes the form as radiation:

$$Q_{radTank} = e \cdot \sigma \cdot A \cdot T_S^{\ 4} \tag{2}$$

Where e is the emmissivity and σ is the Stefan-Boltzman constant. Other heat transfer mechanisms and heat lost due to the heat sink in boiloff are neglected:

$$E_{out} = Q_{radTank} \tag{3}$$

Figure 4 depicts the control volume of the tank with the heat additions and losses due to radiation heat transfer:

The total heat balance for the surface of the control volume is:

$$Q_{radTot} = Q_{radSun} + Q_{radEarth} + Q_{radShield} - Q_{radTank} \tag{4}$$

SURFACE TEMPERATURE CALCULATION

To calculate the surface temperature of the tanks requires the determination of the roots of a forth degree polynomial. Equating the conduction and radiation heat transfer rates and the polynomial is shown in Eqn 9-12.

$$\begin{aligned}
&Q_{Cond} = Q_{Rad} \\
&\frac{(T_S - T_i)}{R_{EQ}} = Q_{TOT} - e\sigma A T_S^{\ 4} \\
&(Q_{TOT})R_{EQ} - e\sigma A T_S^{\ 4} R_{EQ} - T_S + T_i = 0 \\
&Q = \left[R_{EQ} e\sigma A T_S^{\ 4} \ 0 \quad 0 \quad -T_S \quad (Q_{TOT})R_{EQ} + T_i\right]
\end{aligned} \tag{5-8}$$

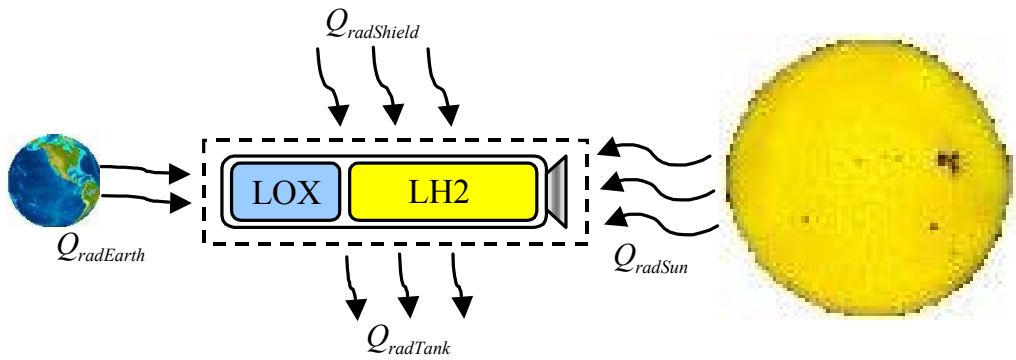

Figure 4: Control volume for radiation absorbed by the tank from the sun, earth and the shield and radiation emitted by the tank

The properties of the tank skin and substructure affect the thermal heating and cooling. The assumed tank absorbivity and emmissivity are assumed $\alpha = 0.4$ and $e = 0.018$. Another strong factor contributing to the heating and cooling of the cryogenic tanks is the time spent in the sun. The assumptions are made that the time spent in earth's shadow is equivalent to 40% of the time in orbit, as shown below.

TANK CONDUCTION HEAT TRANSFER

Now that the surface heat exchange has been established the thermal resistance throught the tank wall must be established. Thermal resistance is the ratio of the driving potential to the corresponding transfer rate. The driving potential for heat transfer through the tank is the outside surface temperature inside fuel temperature, ($T_i - T_s$). Thermal resistance for conduction through multi-layered insulation (MLI) is modeled as follows:

$$R_{Fuel} = \frac{1}{h_{Fuel} \cdot A}, \; R_A = \frac{L_A}{k_A \cdot A}, R_F = \frac{L_F}{k_F \cdot A} \tag{9-11}$$

Where h is the convection heat transfer coefficient, k is the thermal conductivity and L is the wall thickness.

Equivalent thermal resistance through tank wall:

$$R_{EQ} = R_{Fuel} + R_A + R_F \tag{12}$$

The resulting conductance equation is as follows:

$$Q_{Cond} = \frac{(T_S - T_i)}{R_{EQ}} \tag{13}$$

A visual model of the tank wall and the corresponding resistance is seen below.

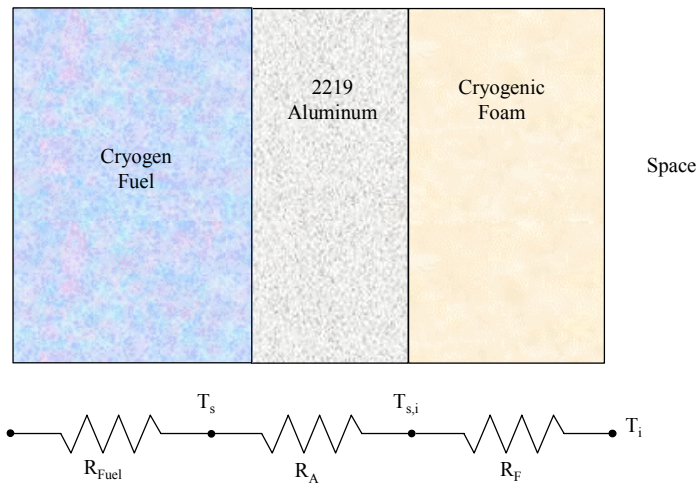

Figure 5: Equivalent thermal circuit for a series resistance wall of the Delta IV Tank

BOILOFF

The description for the rate at which energy is stored in the system is in terms of the temperature increase in the fuel and tank wall. This phenomenon occurs succeeding the radiation transfer due to small transport delays. Once the inner surface of the tank, T_s, changes the results are directly related to the changing temperature in the fuel, through natural convection heat transfer. The nucleate pool boiling equation to evaluate the heat transfer to the fuel from the tank wall is as follows:

$$q_s = A\mu_l h_{fg}\left[\frac{g(\rho_l - \rho_v)}{\sigma}\right]^{\frac{1}{2}}\left(\frac{c_{pl}\Delta T_e}{C_{sf} h_{fg}\,\mathrm{Pr}_l^n}\right)^3 \tag{14}$$

Where A is area, C_{sf} is the coefficient for surface tension combination, C_P is the specific heat at constant pressure, g gravity at lower earth orbit, h_{fg} latent heat of vaporization, P_r is the Prandtl number, μ is theViscosity, ρ is density of liquid fuel and σ is the Stefan-Boltzman constant.

Once the boiling heat transfer rate has been determined, assuming temperature and surface area does not change, all heat addition to the tanks will result in raising the temperature and or boiloff. Determination of the boiloff rate is accomplished using Eq. 15.

$$m_{b,dot} = \frac{q_s}{h_{fg}} \tag{15}$$

q_s is the boiling heat transfer rate and latent heat of vaporization.

MODELS

As mentioned this paper addresses three different types of models, abacus tail feather concept, four wing concept and spinner concept. Each of the three concepts possesses certain similar

thermal characteristics. All three of the concepts are based on construction of Delta IV Boeing rocket tanks. Thus, the thermal properties and geometry of the tanks are the same. In addition to the thermal and geometric similarities of the concepts, a thermal shield is used with each design.

The shield and the sun combined are assumed to cover approximately 50% of the total area of the fuel tanks, while the remaining 50% of the surface area is exposed to either the earth or space. The ratio of sun-exposed area to the shaded area depends solely on the area of the tank in direct sunlight. For example, if the sun hits 10% of the total area, the shield will shade the remaining 40%. This is true for the abacus and four wing concepts. An exception, however is the spinning concept, for which the amount of sunlight is dependent on rotation period of the tanks.

The abacus concept has three tanks situated at the bottom of the thermal shield. The shield will cover each tank for a portion of the time in orbit. Forty-percent of the orbit time is spent in the shadow of the earth and the remaining sixty-percent of the time is a constant exposure to sunlight. The percentage of exposure can vary from 2% to 50% of the total area of the tanks. Naturally, the less time in the sun the lower the heat gains.

The spinner concept also consists of three tanks. The tanks are attached to a central hub located beneath the thermal shield. The tanks are spun for cooling and fluid collation purposes. The spin rate of the tanks to this point is not valued; however, an assumed value is used here for calculation purposes. This value is calculated as follows

Acceleration due to spinning is:

$$a = \omega^2 \cdot r = \omega \times \omega \times (-\vec{r}) \tag{16}$$

Solving for get an effective artificial gravity of ¼ g gives:

$$\omega = \sqrt{\frac{5\% \cdot g}{r}} rad / \sec \tag{17}$$

Thus the total rotation speed for the system is:

$$T_{rotational} = \frac{60}{\frac{2 \cdot \pi}{\omega}} Hz \tag{18}$$

The tail feather / gravity gradient concept uses a series of arrays mounted on the system. Even if the solar cells double as a thermal shield, it will not likely cover a large enough area to effectively block the sun's radiation heat.

RESULTS

The gravity gradient is surprisingly the design with the most massive thermal penalties. The spinner concept proved to be the best design for reducing mass boiloff in a passively cooled system. The abacus and spinner concepts were compared directly using the same time in equatorial orbit, and altitude. In addition, the concepts varied exposure to the sun from 2% to 50% of the total surface area. However, the spinner concept had an opportunity to cool the tanks during the period of rotation in the shade while the abacus ant gravity gradient did not.

From figure 5 the heating time from the fusion temperature to vaporization temperature is shown for the three concepts for different sun exposed surface areas. The spinner concept is the best for the majority of the time, however the abacus method the better for the smaller exposed surface area. And the tail feather concept is better for the greatest exposed surface area.

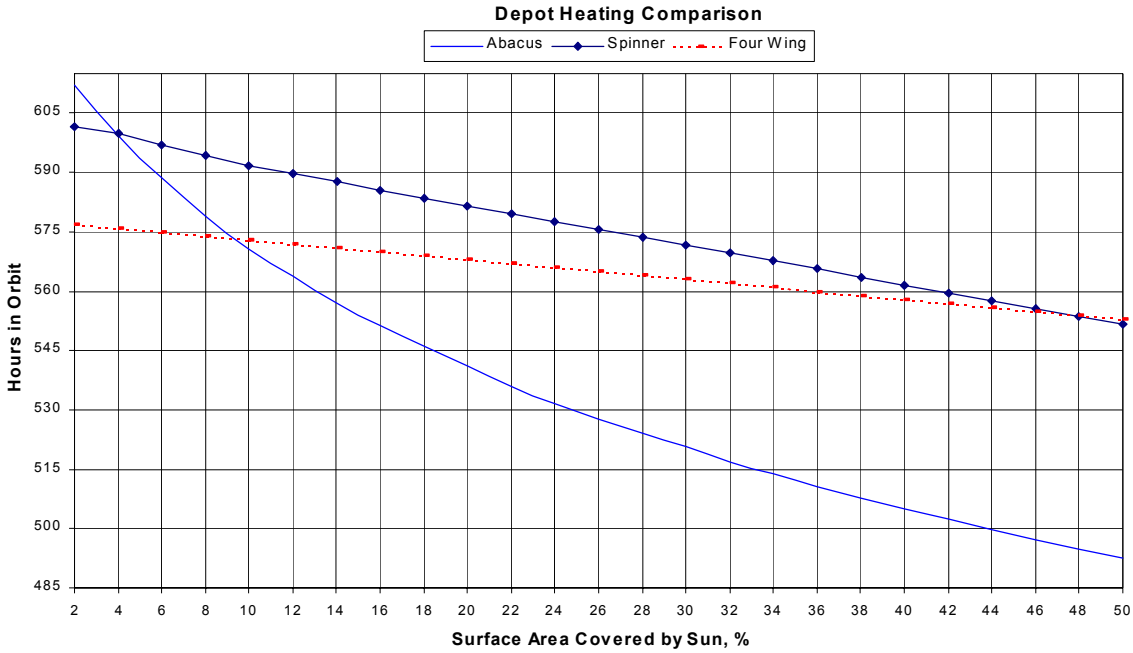

Figure 6: Fuel depot heating comparison chart. At any given sun exposed surface percentage the heating time from fusion temperature to vaporization temperature is known.

The analysis of boiloff rates for the three designs showed some staggering results. The spinner concept is by far the best design thermally of the three proposed, followed by the abacus concept and, last, the gravity gradient concept. The abacus concept had a boiloff amount of 119 times greater than the spinner concept for 450 orbits. From this analysis it is apparent that a system of these types cannot exist with passive cooling in orbit, active cooling must be employed.

CONCLUSION

Consideration must be taken for the energy balance using the first law of thermodynamics. In the design of cryogenic storage the minimum boiloff rates of systems in LEO should be optimized. Several recommendations for making this project work effectively are:

1. Increase the insulation thickness on the Delta IV tanks. Do not shave any off for weight considerations; allow the insulation system to be the payload itself,

2. Decrease the time the fuel depot spends in the sun while subsequently increasing the thermally shielded surface

3. Attach an active cooling system to reduce the effective boiloff

4. Use the boiloff gasses to cool the thermal shield, cooling the tank surface and possibly, use to cool the MLI

5. Use a spherical storage; surface tension dictates that a body of fluid neutrally floating in a gas will assume the smallest shape possible. Thus a spherical tank has the smallest effective surface area.

6. Design the system such that it has low conductive structural supports.

ACKNOWLEDGEMENTS

I would like to thank the Summer Faculty program at NASA/MSFC for funding this research.

REFERENCES

1. Dorsey, J. W. and Kleder C. L.: "Thermal Mass Penalties associated with Cryogenic Propellant Storage on Manned Mars and Venus Missions, Propulsion and Thermodynamics Department", Conference on Long-Term Cryo-Propellant Storage in Space, pp1-29, October 1966.

2. Knoll, R. H., Bartoo, E. R. and Boyle, R. J., "Shadow Shield Experimental Studies, Lewis Research Center, Conference on Long-Term Cryo-Propellant Storage in Space", October 1966, pp 83-93.

3. Fendell, F. E., "Heat Transfer to Rotating Cryogenic Fuel Tanks in Orbit, TRW Systems, Conference on Long-Term Cryo-Propellant Storage in Space" pp 195-211, October 1966.

4. Kittel, P. NASA Ames Research Center Moffet Field, CA and Parmley, R. T., Lockheed Palo Alto Research Laboratory, Palo Alto, CA., "Long Term Cryogen Storage in Space: A Feasibility Study", 679-686, 1996.

5. Anderson, J. E., Fester, D. A. and Czysz, P. M., "Evaluation of Long-Term Cryogenic Storage System Requirements", Martin Marietta Space Systems, Denver, CO., Advances in Cryogenic Engineering, Vol 35, pp 1725-1731, 1988.

6. Beduz, C., Rebiai, R. and Scurlock, R. G., Institute of Cryogenics University of South Hampton, South Hampton, UK, "Thermal Overfill, and the Surface Vaporization of Cryogenic Liquids Under Storage Conditions", pp 795-803, 1981.

7. Gursu, S., Sherif, S. A., Veziroglu, T. N. and Sheffield, J. W., "Optimizing Liquid Hydrogen Storage Systems", 13th Canadian Congress of Applied Mechanics, pp 540-541, 1991.

8. Cunningham, G. R., "Thermodynamic optimization of a Cryogenic Storage System for Minimum Boiloff", American Institute of Aeronautics and Astronautics, 1982

9. Harrison, J. K., "Thermal Characteristics of a Storage Vessel on the Moon", NASA-N-D-3785, 1967.

10. Incropera, F.P. and DeWitt, D.P., Fundamentals of Heat and Mass Transfer, 1990, John Wiley & Sons.

NOMENCLATURE, ACRONYMS, ABBREVIATIONS (STYLE=PAPERHEADINGS)

A	area, m^2
a	absorbivity of the fuel tanks
C_{sf}	coefficient for surface tension combination
C_P	specific heat at constant pressure, J/kg*K
e	emissivity of the fuel tanks W/m^2*K
g	gravity at lower earth orbit, m/s^2
h_{fuel}	convection heat transfer coefficient
h_{fg}	latent heat of vaporization, J/kg
k_A	thermal conductivity, W/m*K
L_F	thickness ofinsulation, m
m_{dot}	mass boiloff rate, kg/sec
n	exponent for surface tension combination
Orbit	number of orbits in analysis
P_r	Prandtl number
Q	overall heat delivery to the system, W
q	Radiation constant, W/m^2
R	Resistance
T	Temperature, K
μ	Viscosity, kg/s*m
ρ_l	density of liquid fuel, kg/m^3
ρ_g	density of gaseous fuel, kg/m^3
σ	Stefan-Boltzman constant,W/m^2 *K^4

X-38 De-orbit Propulsion Stage MLI Performance Test

Sept 10-14, 2001

Ken Kittredge
NASA/MSFC

Background

- X-38 is Pathfinder for Space Station Crew Return Vehicle
- X-38 Launched in Space Shuttle
- De-Orbit Propulsion System (DPS) Maneuvers X-38 in Descent Trajectory and is Jettisoned Prior to Re-entry
- X-38 DPS design hot biased to reduce power and energy requirements
- Black Beta Cloth selected as outer layer on MLI
- Analytical Margin is Small and no DPS Thermal Testing Planned.

X-38

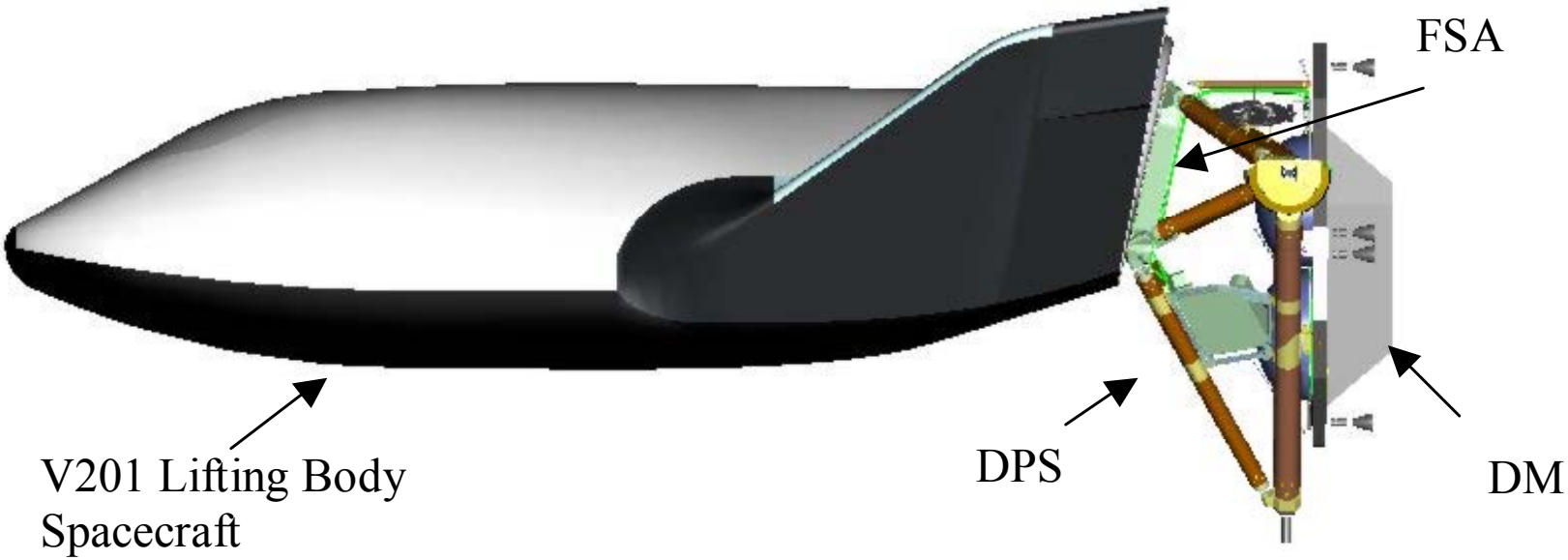

Objective

- Test DPS MLI
  - Sample Available
  - Test Facilities Available
    - Performed in MSFC Thermal Development Facility
- Determine if MLI Performance Meets or Exceeds that Assumed in Thermal Analyses
- Determine Performance Degradation due to Seams

Prep Work

- Literature Search of Potential Test Methods
- Test Fixture Conceptual Design
- Thermal Modeling and Analysis
- Design Modification
- Procurement/Manufacturing and Assembly
- Optical Property Measurement
- Instrumentation Acquisition
- Data Acquisition System Setup

Initial Test Methodology

- Guarded Heat Flow Technique Loosely Based on ASTM-177-97
- Use Temperature Difference Between Primary Heater Plate and Coldplate, Measured Emissivity for the Primary Heater and MLI, and the Primary Heater Power Draw to Calculate Effective Emittance (ε*)
- Black Anodized Aluminum Heater Plate, $\varepsilon = 0.83$
- MLI Black Beta Cloth Outer Surface, $\varepsilon = 0.87$, $\alpha = 0.96$

Test Fixture

- Test Fixture Composed of Polysulfone Plastic Frame and two Black Anodized Aluminum Heater Plates
- Mounted to Space Station –1 Coldplate with Teflon Isolators
- Insulated with four inches of Cryolite Fiberglass Matte
- MLI Sandwiched in Interface Between Heater Plates and Coldplate
- One Square Foot Test Area

Test Fixture Cross-Section

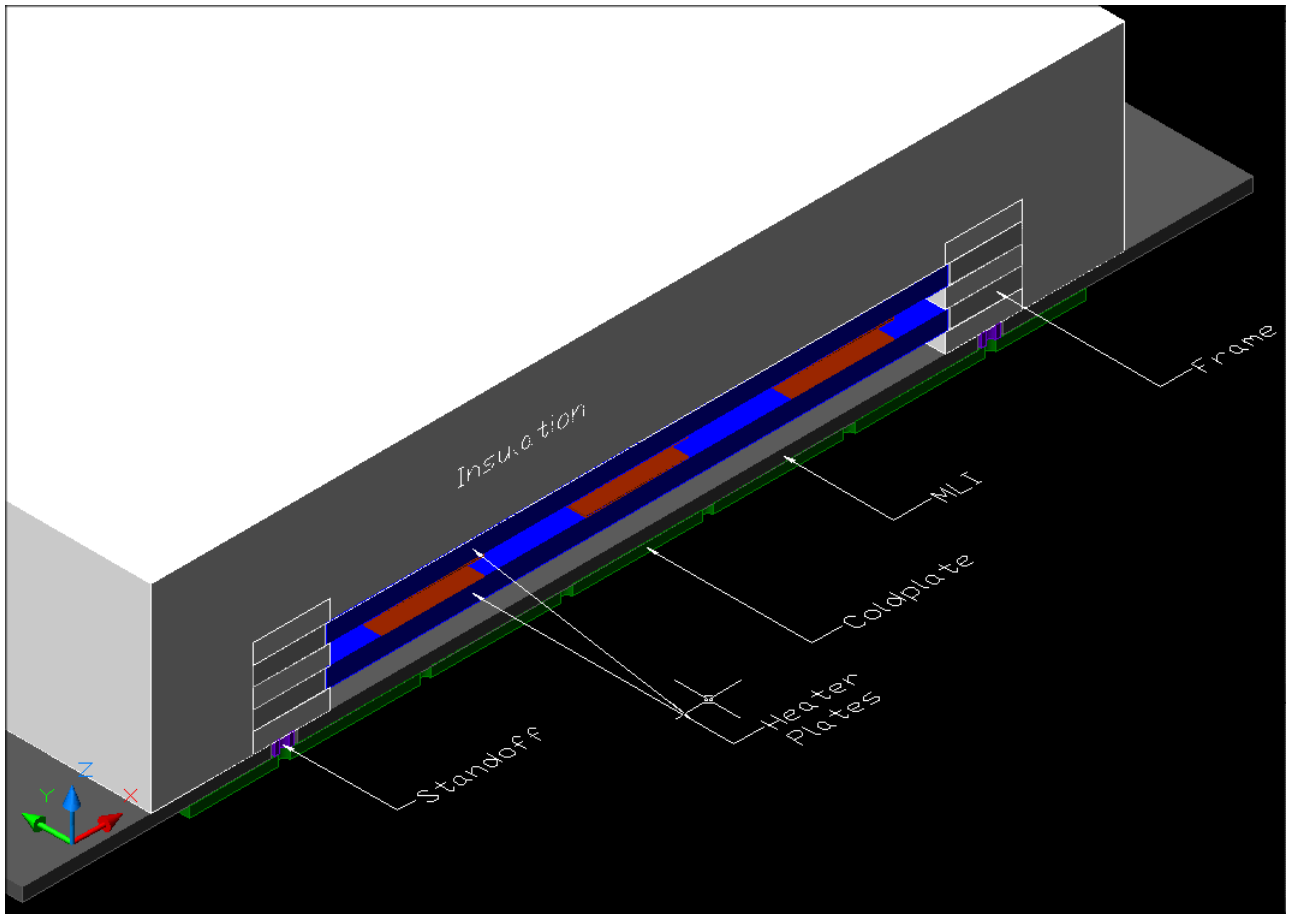

Test Setup

- 9 Minco Thermofoil Heaters per Heater Plate
- Temperature Sensors Mounted on Heater Plates, Coldplate, Frame, and Chamber Shell
- Fixture Isolated from Coldplate with Teflon Standoffs
- MLI Between Test Fixture and Coldplate
- Vacuum Chamber
- Johns Manville Cryo-lite Fiberglass Insulation
- ISS –1 Coldplate and Neslab Low Temperature Chiller
- Residual Gas Analyzer
- DAQ System and Power Supplies

Test Setup

Test Setup

Test Procedure

- Assemble MLI, Test Fixture, Insulation, and Coldplate in Vacuum Chamber
- Evacuate Chamber – Control Heaters to 300ºF, Chiller set to 5ºF.
- Adjust Heater Power so that Heater Plates are at the Same Temperature
- Record Primary Heater Plate Temperatures and Voltage and Current and Coldplate Temperature

Modifications

- Heater Plate Thermocouples Replaced with RTD's wired to HP DAQ System
- RTD's Bonded to the Heater Plates using Conductive Epoxy
- Fixture Re-oriented on Coldplate so the Open End was to the Left Rather than Top
- Aluminized Kapton Tape Applied to Fixture Exterior

Retest

- Reconfigured Test Yielded more Uniform Temperatures
- Primary Heater Temperature of 297ºF and Coldplate Temperature of 12ºF yielded ε^* of 0.028 based on full heat load of 13.0 btu/hr across MLI
- ε^* of 0.016 – 0.019 used in DPS Thermal Analyses.
- Assessment of Test Results Indicates much more Heat Leak from Test Fixture than Expected Causing Over-Estimation of ε^*

Reconfiguration for Seam Test

- Removed MLI from Test Fixture and Quartered it.
- Each Piece was then Reversed and laid out so the Seams of Adjacent Pieces Overlap then Taped in Place
- 8 RTD’s added to MLI side of Test Fixture Frame.
- Configuration then Reassembled.

MLI Configuration for Seam Test

Seam Test

- Primary Heater Temperature of 295ºF and Coldplate Temperature of 22.1ºF yielded ε^* of 0.044 based on full Heat Load of 19.1 btu/hr across MLI
- Assessment of Test Results Indicates much more Heat Leak from Test Fixture than Expected Causing Over-Estimation of ε^*
- Frame Temperatures of 235ºF Appreciable Higher than Expected

Post-Test Analysis

- Updated Thermal Model to as-Tested Configuration
- Identified Modeling Assumptions that Might Affect Results
  - Insulation k and Thickness
  - Heater Plate to Frame Heat Transfer
  - Frame (Polysulfone) k
  - Contact Conductance, Heater Plates to Frame and Frame to Frame
- Varied each Parameter to Determine Sensitivity
  - Results Insensitive to Frame k, Contact Conductance
- Looked for Combination that Matched Test Results
  - Apparently only 1
  - Insulation G * 3.8 Plate to Frame G * 0.49
- Seam Test $\varepsilon^* = 0.026$ MLI Test $\varepsilon^* = 0.011$

Error Analysis

- Look at Analysis Uncertainty due to Potential Instrumentation Errors
  - Assess Potential Errors due to RTD's, Thermocouples, Voltage & Current Measurements and DAQ System
- Rerun Model Correlation with each Error Applied in Both + and – Directions and Determine Effect on ε^* Prediction
  - Primary Heater Plate Temperature, +/- 0.828ºF
  - Guard Heater Plate Temperature, +/- 0.828ºF
  - Frame Temperatures, +/- 0.828ºF
  - Coldplate Temperature, +/- 2.7ºF
  - Chamber Temperature, +/- 2.7ºF
  - Heater Voltage, +/-(0.0003V+0.012) volts
  - Heater Current, +/-(0.002I+0.00025) amps

Results

- The Expected ε^* Range was Computed by Taking the Square Root of the Sum of the Squares of the Variances Induced by the Potential Error Cases and Applying those to the Nominal Values
  - Seam Test $\varepsilon^* = 0.017 – 0.035$
  - MLI Test $\varepsilon^* = 0.003 – 0.019$
- Assuming the Overlapped Seams Affect an Area 0.5" Wide and the Remainder of the Area in the Seam Test has the same ε^* as Computed for the MLI Test, an ε^* for just the Seam Area was Computed
  - $\varepsilon^* = 0.175 – 0.215$
  - This Value can be Combined with the ε^* from the MLI Test in an Area Weighted Manner to Estimate the Overall Performance of the X-38 MLI Blanket System.

Lessons Learned/Conclusions

- It's Difficult to Effectively Insulate an Effective Insulator
- Polysulfone is Easily Machinable, Vacuum Stable, and has a Good Temperature Range (-150ºF to +350ºF)
- Cryolite is a Fiberglass Matte Insulation with a Vacuum Stable Melamine Resin, Rated for –450ºF to +450ºF
  - It does have Quite an Affinity for Water Vapor.
  - The Thermal Conductivity is Apparently Higher than the Manufacturer's Value.
- A Horizontal Test Setup is much Preferable to Vertical
- A Guard Heater Complicates Model Correlation
- Testing a Larger Sample Area would have Improved Results

Space Station Environmental Control & Life Support System Pressure Control Pump Assembly Modeling and Analysis

September 10, 2001

R. Gregory Schunk
NASA Marshall Space Flight Center
Thermal and Fluid Systems Group/ED26

- Overview
- Integrated PCPA/Manifold Analyses
- Manifold Performance Analysis
- PCPA Motor Heat Leak Study
- Conclusions/Future Plans

Simplified Distillation Assembly/PCPA Block Diagram

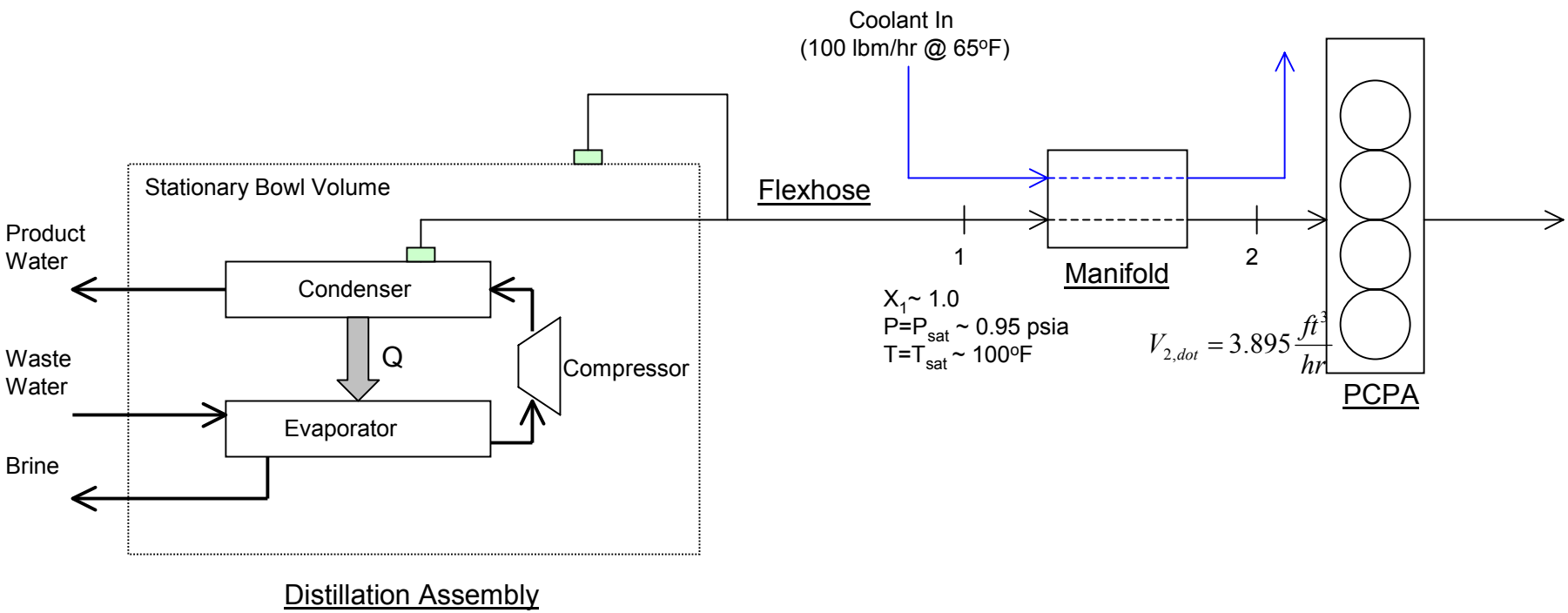

Distillation Assembly Cut-away View

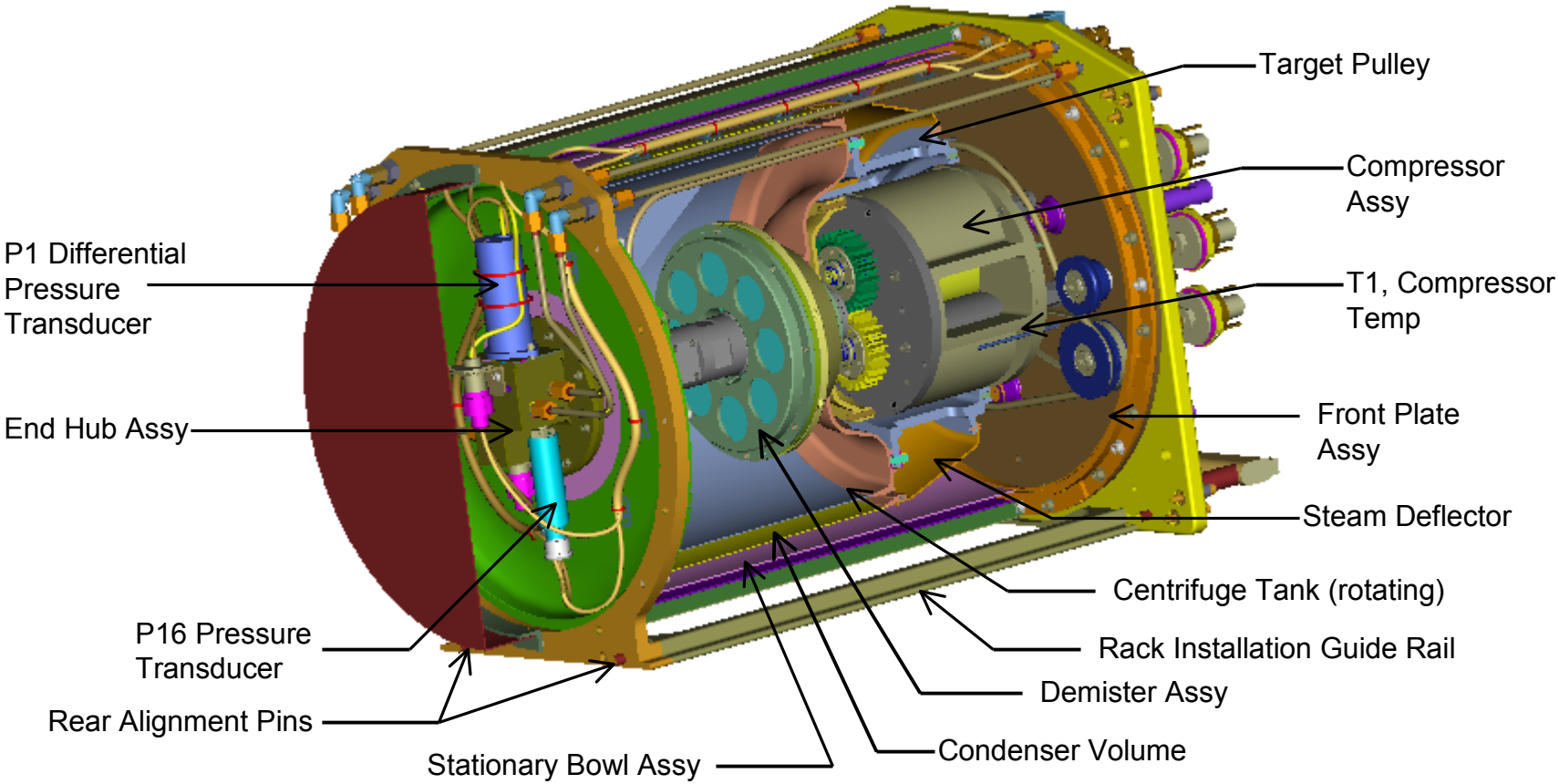

Pressure Control Pump Assembly

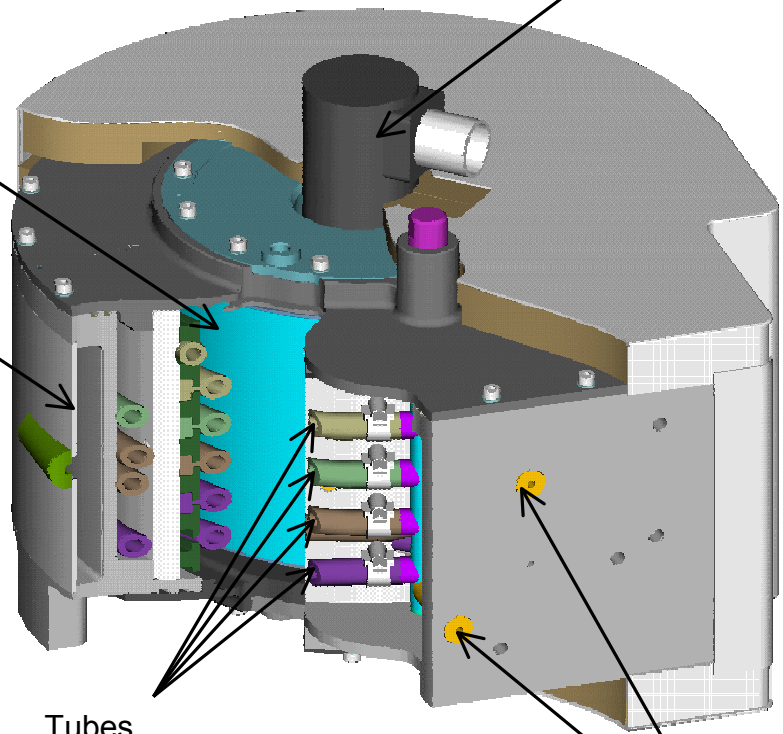

PCPA Chiller Block and Attachment

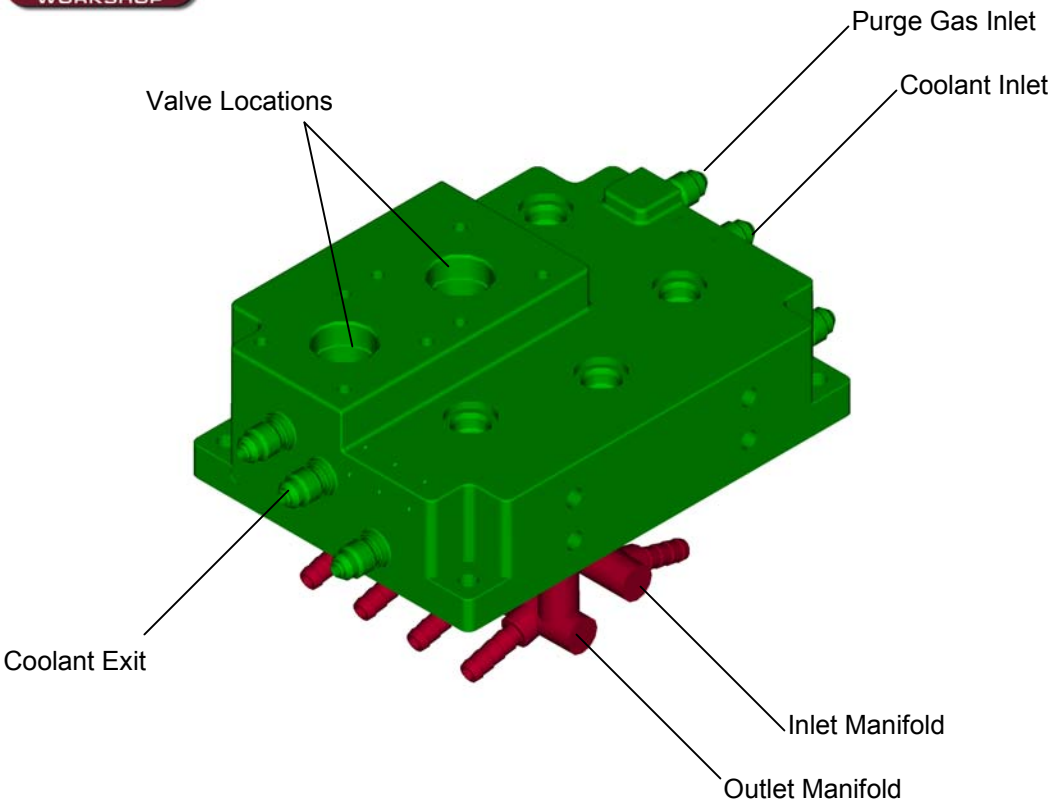

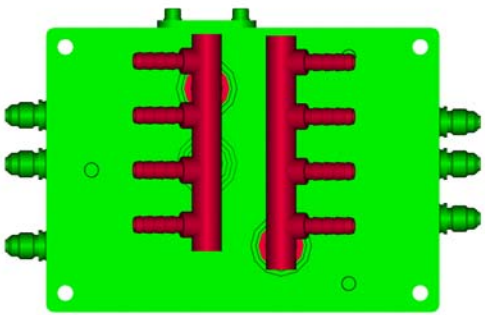

Bottom View

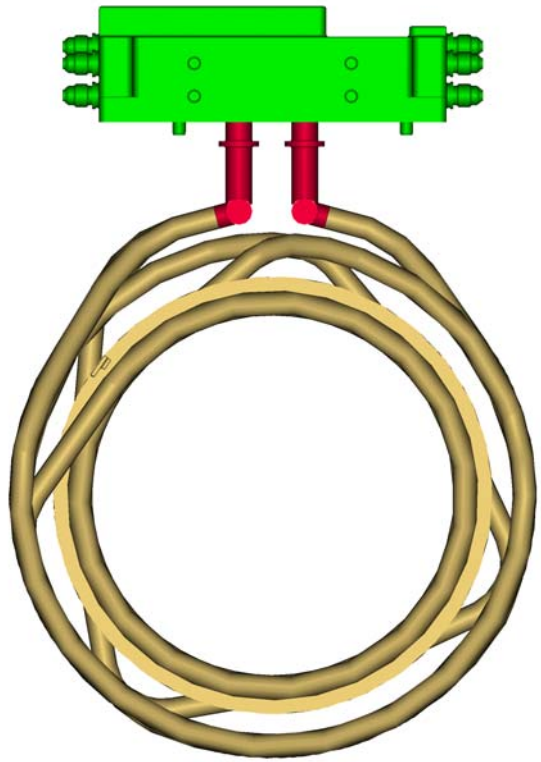

Chiller Block Attachment to the Pump

Inside the PCPA

Tubes and Mounting Hub

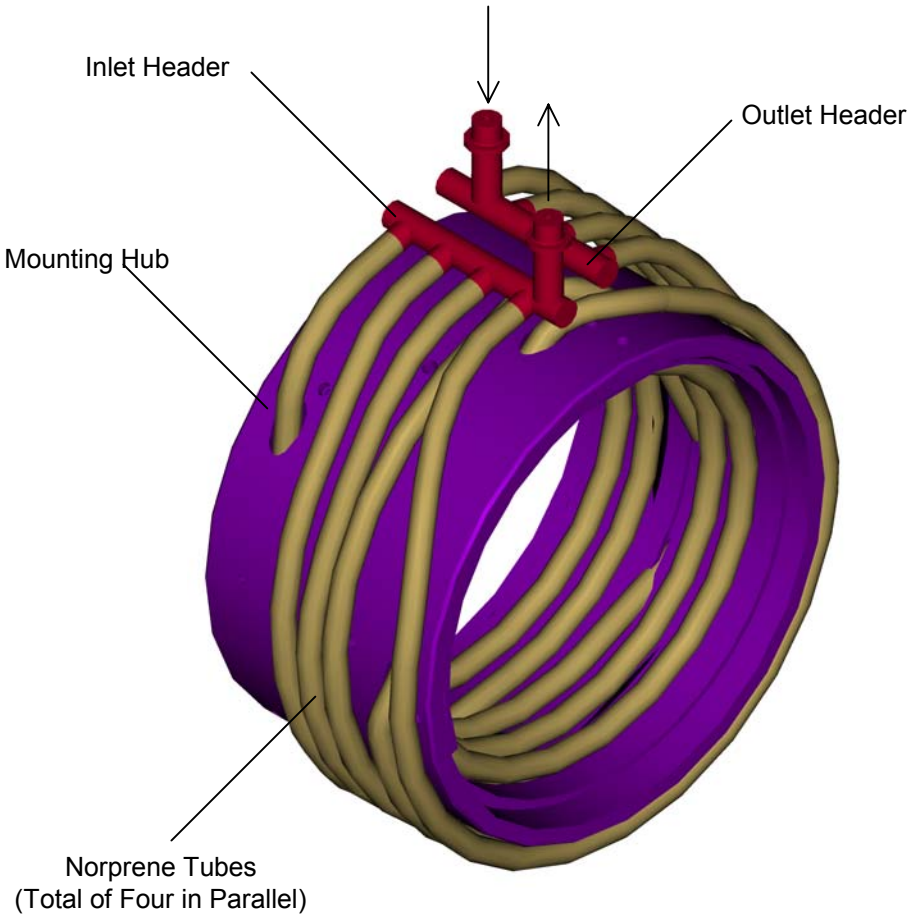

Individual Tube

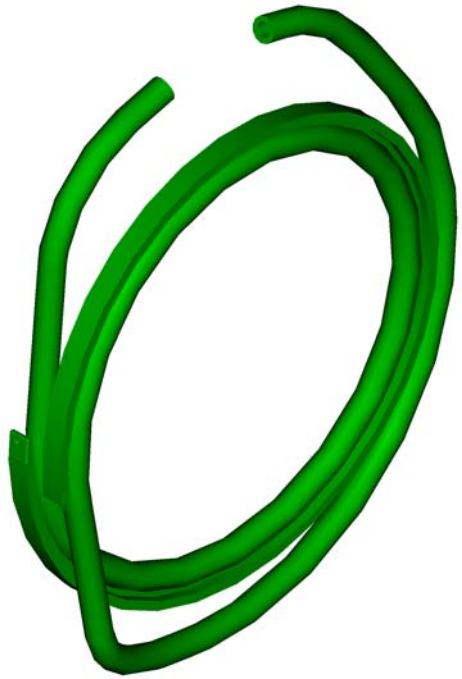

Fluid Volume per tube=1.167in^3

Volumetric displacement per tube (@24 rpm)=0.466in^3/sec

Total displacement (4 tubes)= 1.87in^3/sec

PCPA Pump Cycle

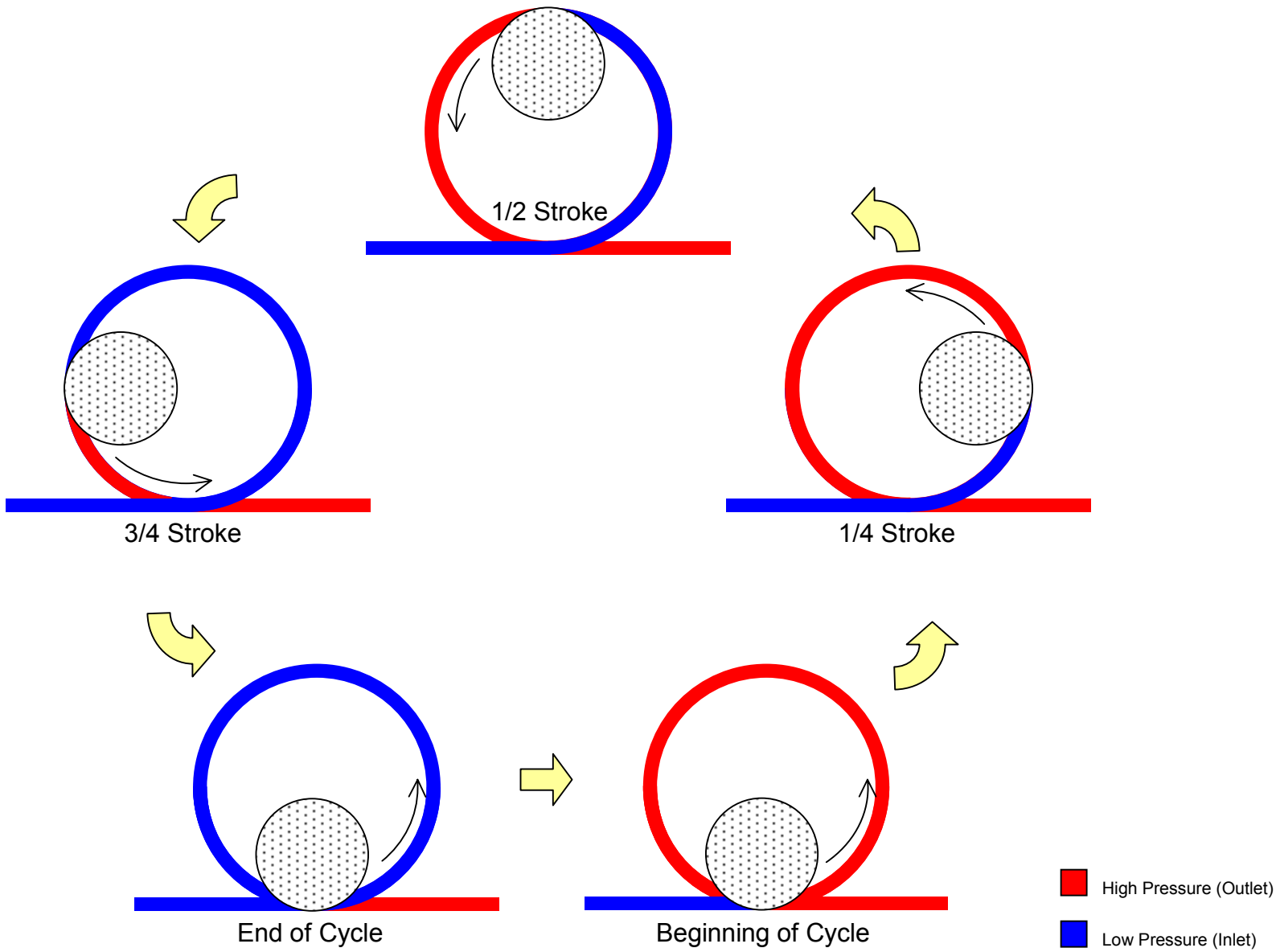

Opposing Piston-Cylinders used to Model Pump Cycle

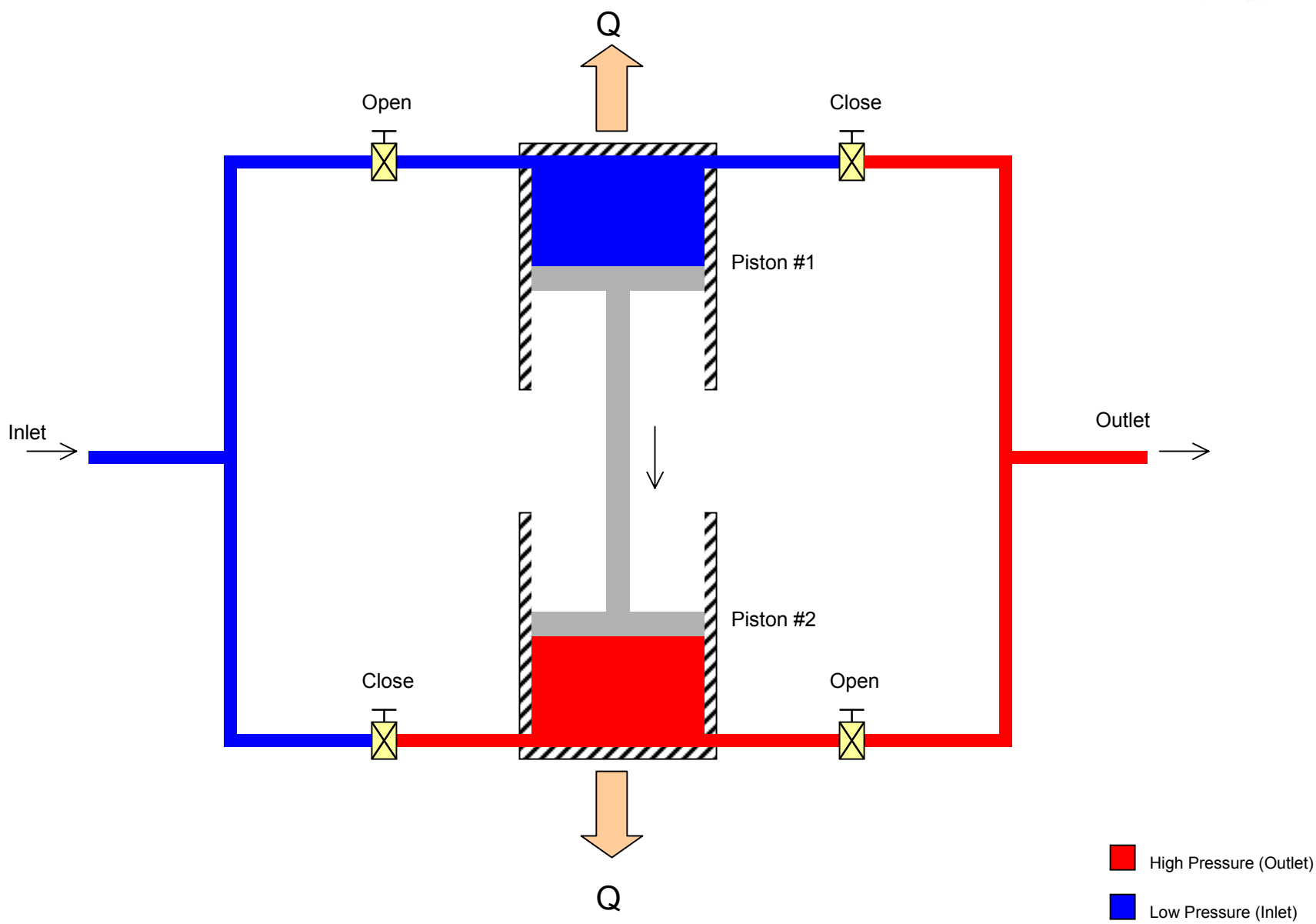

Piston-Cylinder Analogy for a Complete Cycle

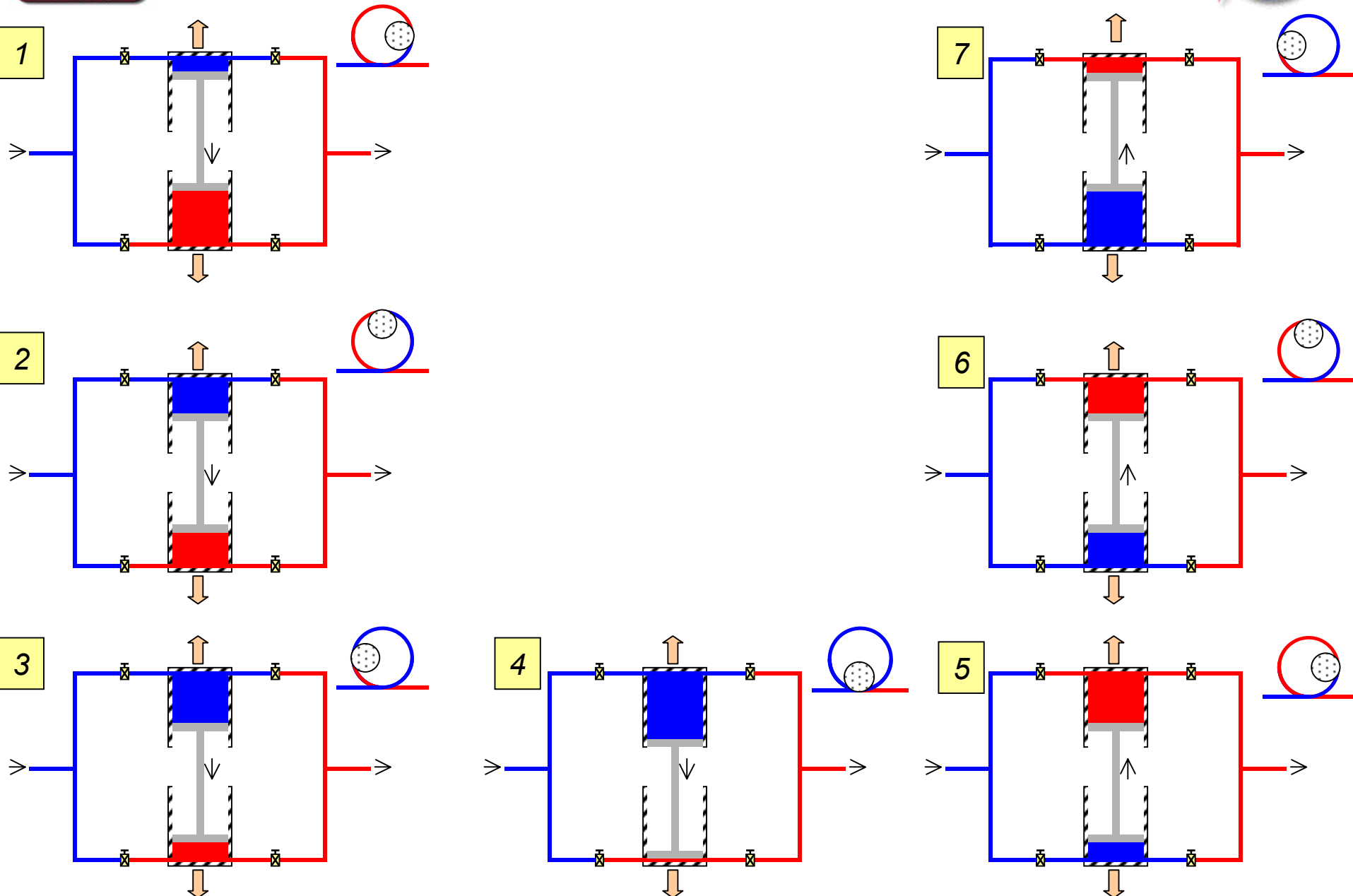

Derivation of the Pump Performance Equation

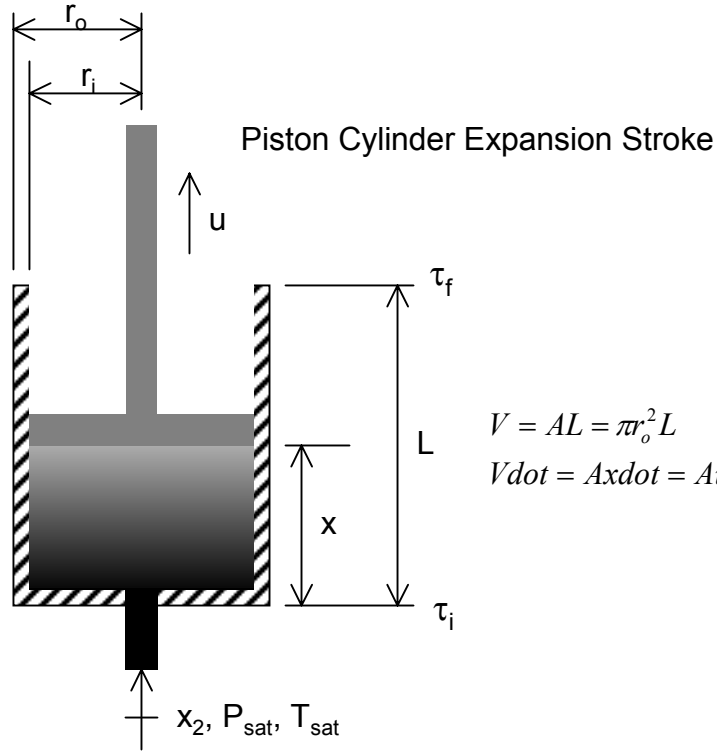

$$Qdot = \frac{2\pi k_{Norprene} x}{\ln(\frac{r_o}{r_i})}(T_{Piston} - T_{Coolant})$$

$$V = AL = \pi r_o^2 L$$

$$Vdot = Axdot = Au$$

Assume P,T inside the piston remain at P_{sat}, T_{sat}. The mass drawn into the volume over a timestep, $\Delta\tau$, is equal to:

$$\Delta M = \int \frac{Vdot}{v_f + x_2 v_{fg}} d\tau + \int \frac{2\pi k x \Delta T}{\ln(\frac{r_o}{r_i}) h_{fg}} d\tau = \frac{Vdot}{v_f + x_2 v_{fg}} \int d\tau + \frac{2\pi k \Delta T}{\ln(\frac{r_o}{r_i}) h_{fg}} u \int \tau d\tau \therefore (x = u\tau, Vdot = const)$$

$$\Delta M = \frac{Vdot}{v_f + x_2 v_{fg}} \Delta\tau + \frac{2\pi k \Delta T}{\ln(\frac{r_o}{r_i}) h_{fg}} u \frac{(\tau_f^2 - \tau_i^2)}{2} = \frac{Vdot}{v_f + x_2 v_{fg}} \Delta\tau + \frac{2\pi k \Delta T}{\ln(\frac{r_o}{r_i}) h_{fg}} u \frac{(\tau_f + \tau_i)}{2} \Delta\tau$$

$$\frac{\Delta M}{\Delta\tau} \rightarrow \boxed{Mdot = \frac{Vdot}{v_f + x_2 v_{fg}} + \frac{\pi k L \Delta T}{\ln(\frac{r_o}{r_i}) h_{fg}}} \therefore \frac{L}{2} = u \frac{(\tau_f + \tau_i)}{2}$$

Derivation of Manifold (Chiller Block) Performance Equation

Heat transfer between the coolant and purge gas passages in the manifold:

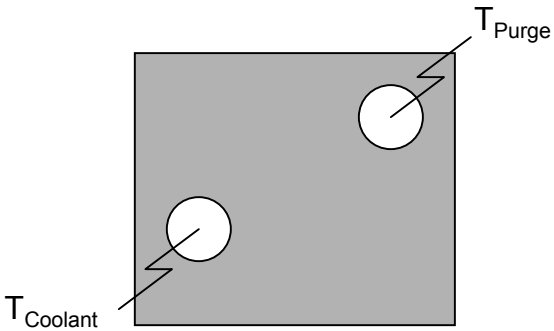

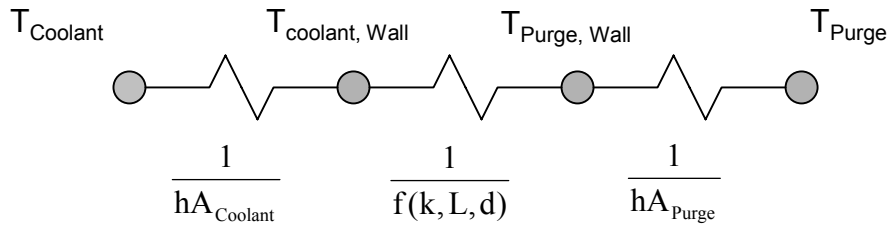

$$Qdot = \left\{ \frac{1}{hA_{Coolant}} + \frac{1}{f(k,L,d)} + \frac{1}{hA_{Purge}} \right\}^{-1} (T_{Purge} - T_{Coolant})$$

$$Qdot = \overline{G}\Delta T$$

Mass flow in the purge gas passage is inversely proportional to the condensation rate:

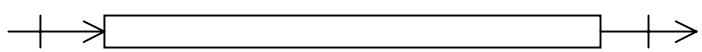

x_1, P_{sat}, T_{sat} x_2, P_{sat}, T_{sat}

$$Qdot = \overline{G}\Delta T = (x_1 - x_2) h_{fg} Mdot$$

$$Mdot = \frac{\overline{G}\Delta T}{h_{fg}(x_1 - x_2)}$$

$$\zeta = \frac{\overline{G}\Delta T}{h_{fg}}$$

Let ξ=heat transfer rate/heat of condensation; expected values range between 0.02 and 0.1 for the chiller block per hand calculation; larger value indicates higher heat transfer rate.

$$\boxed{Mdot = \frac{\zeta}{(x_1 - x_2)}}$$

Pump versus Manifold Parametric
X_1=100%, T_1=100°F

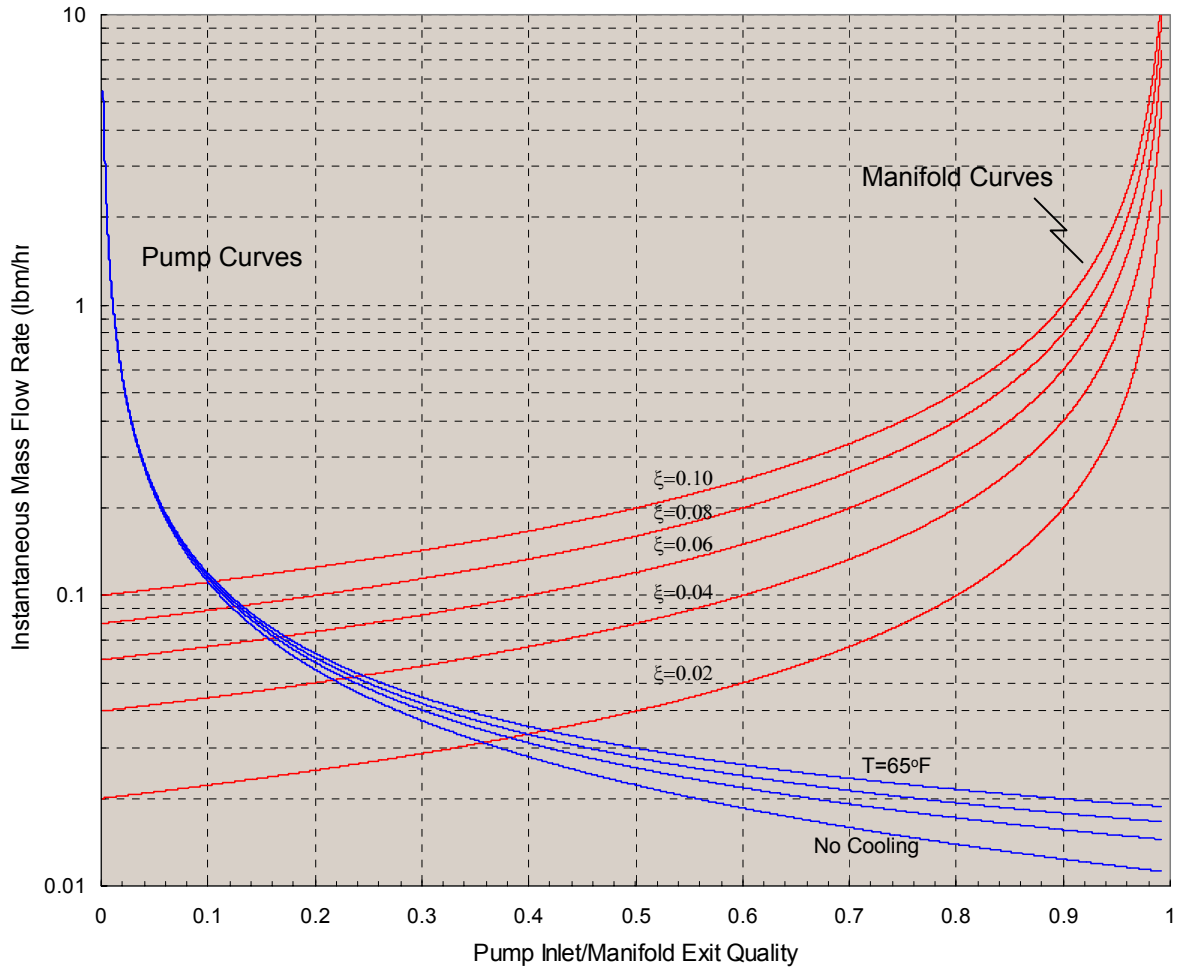

$$\xi = \frac{\overline{G}\Delta T}{h_{fg}}$$

- ξ is a dimensional parameter (units of mass flow rate) that describes the thermal performance of the manifold.
- A larger value of ξ indicates a higher heat transfer rate between the coolant and purge lines.
- Per hand calculations, ξ is expected to range between 0.02 and 0.1 for the manifold.

DA/PCPA Rack Interface Tubing Model

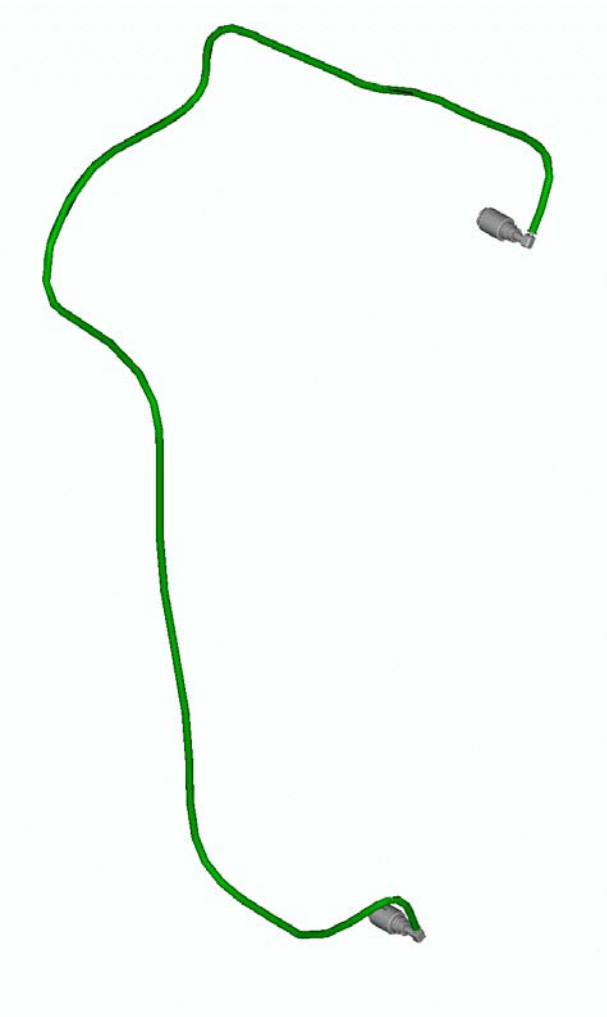

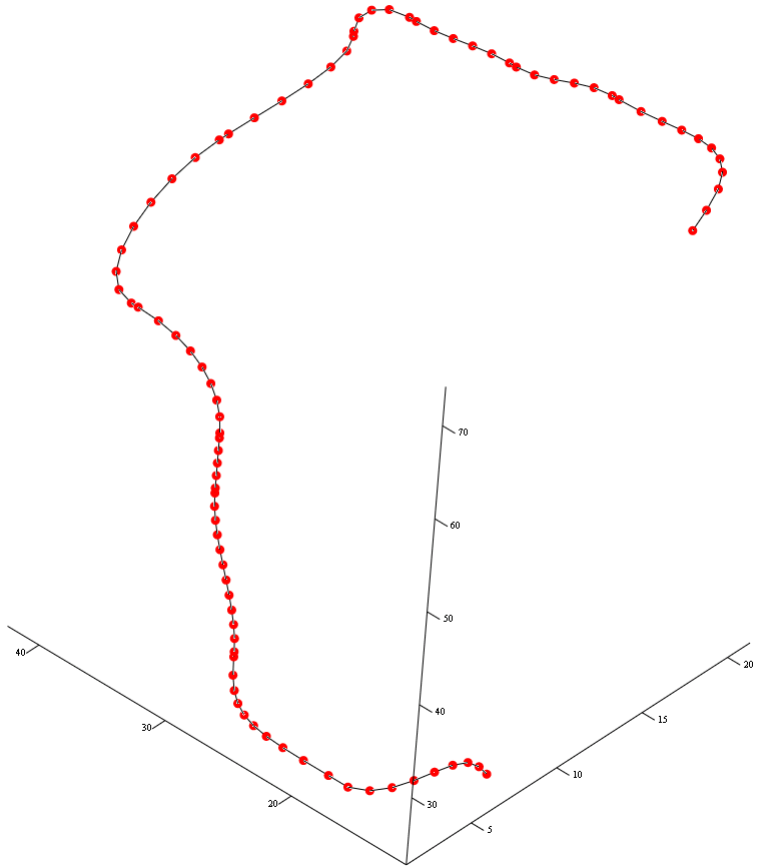

Steady State Results

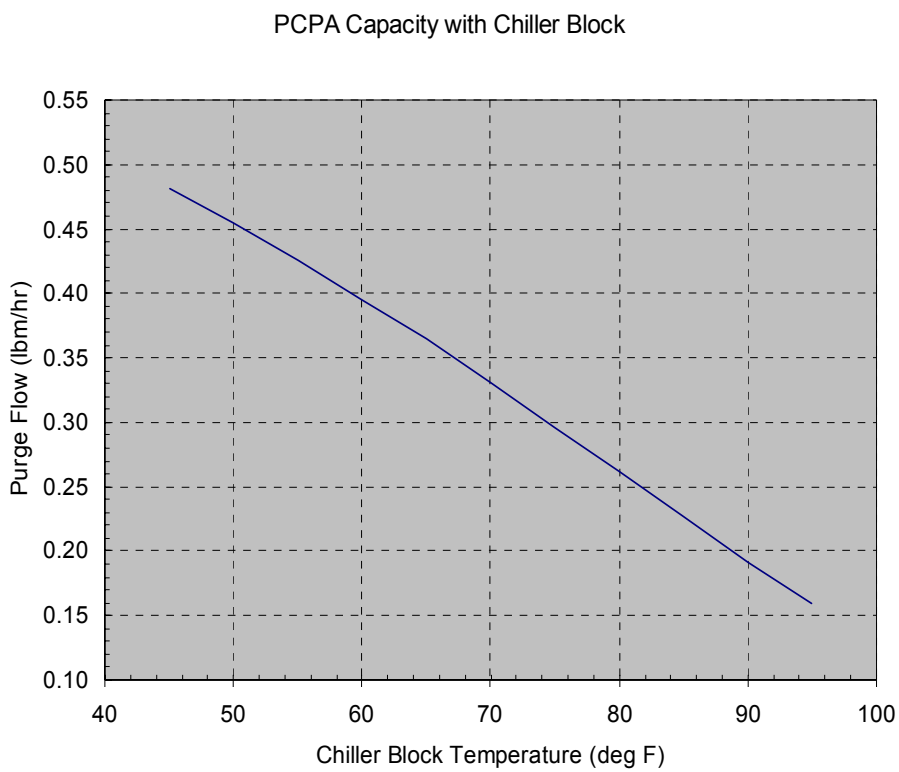

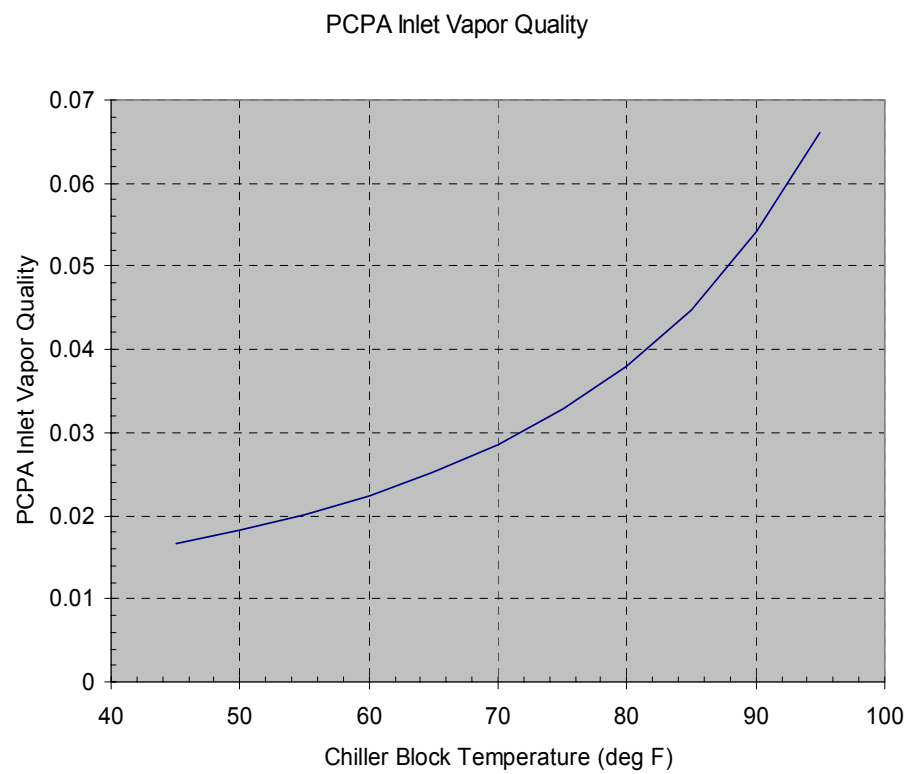

Steady State Results (Cont'd)

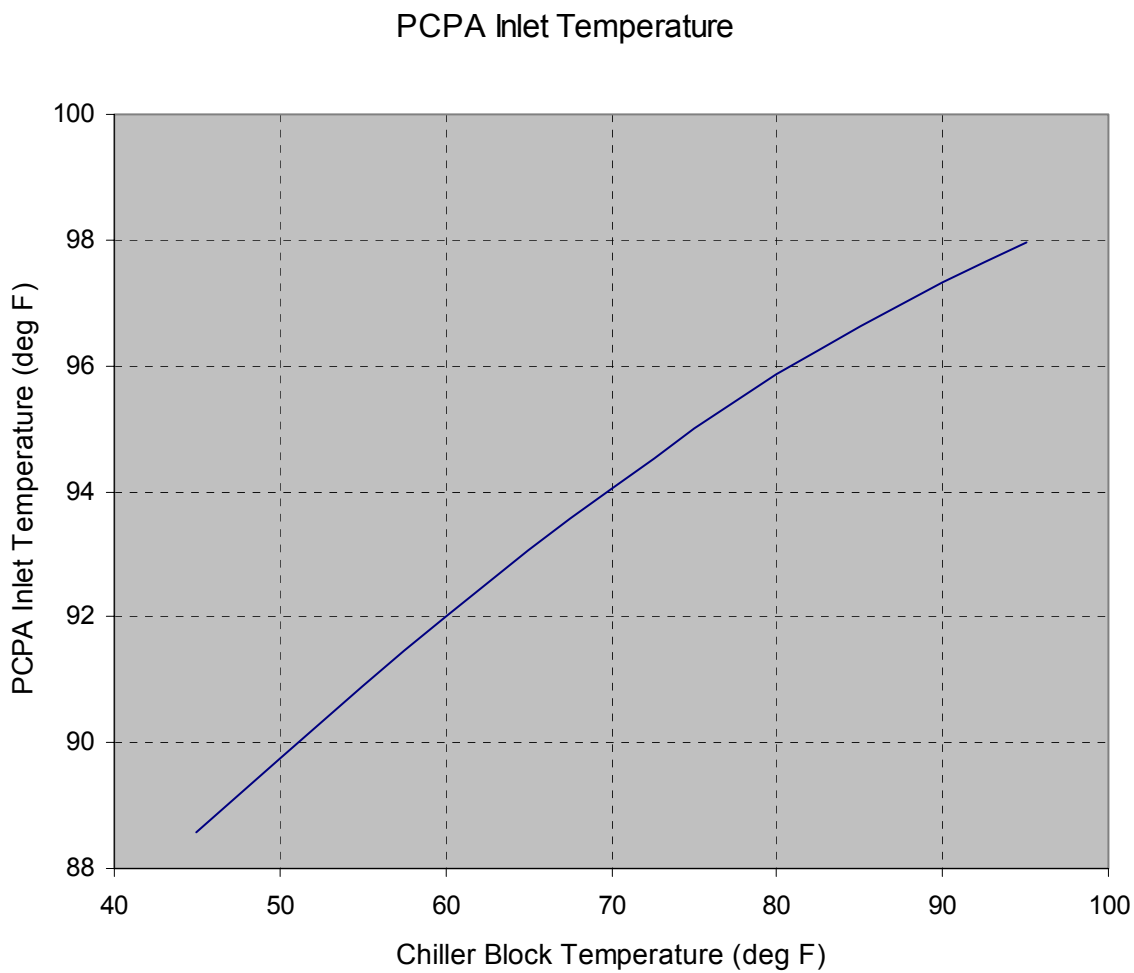

PCPA Chiller Block Thermal Model

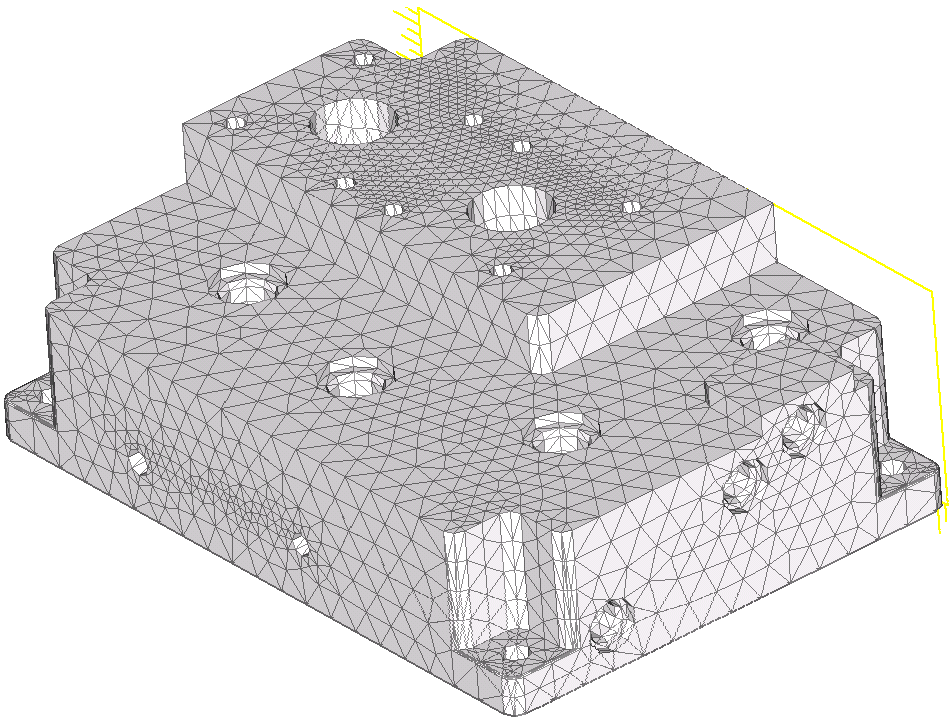

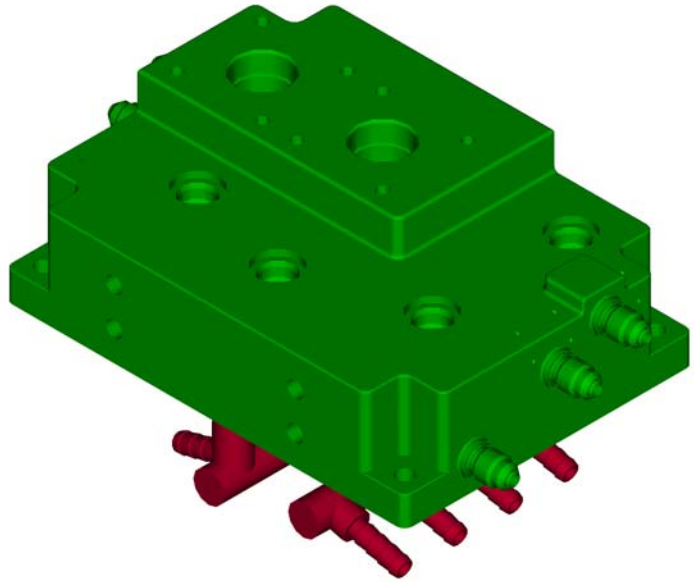

- Imported chiller block model directly from CAD file (stereo-lithography translation).
- Meshed as a solid with 10970 nodes and 43619 tetrahedrals.

PCPA Chiller Block Thermal Model Development

CAD Representation

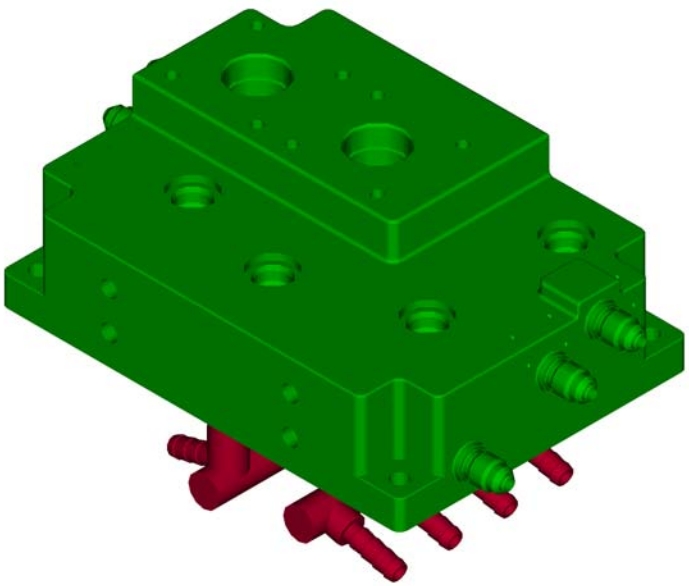

Stereo Lithography

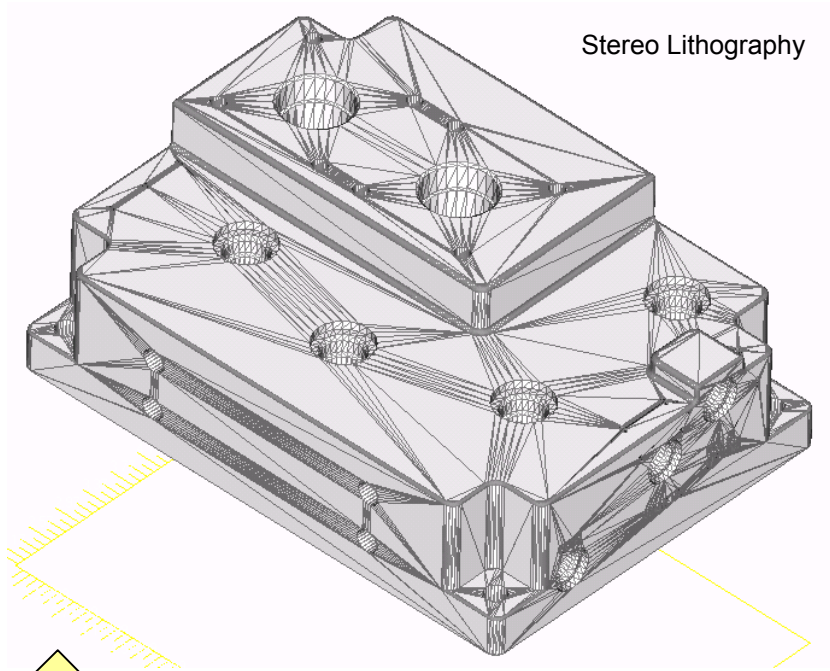

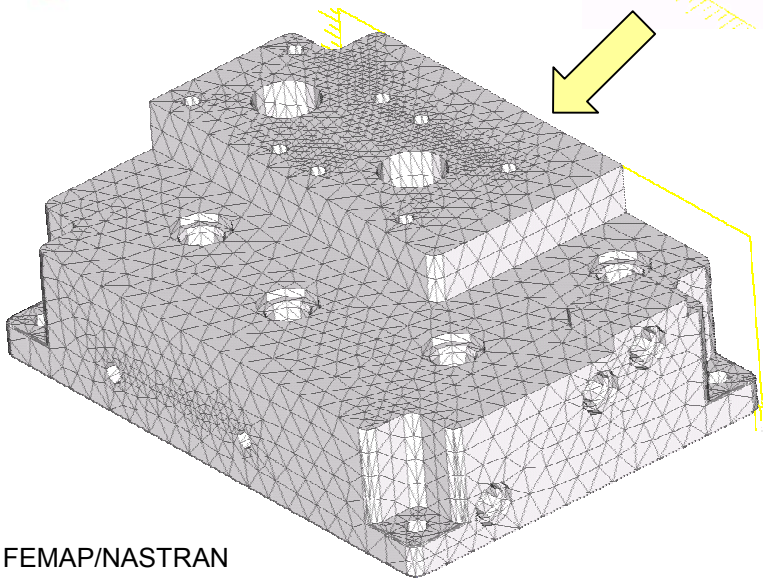

Final Mesh FEMAP/NASTRAN

- Imported chiller block model directly from CAD file (stereo-lithography translation).
- Meshed as a solid with 10970 nodes and 43619 tetrahedrals.

PCPA Chiller Block Thermal Analysis Results

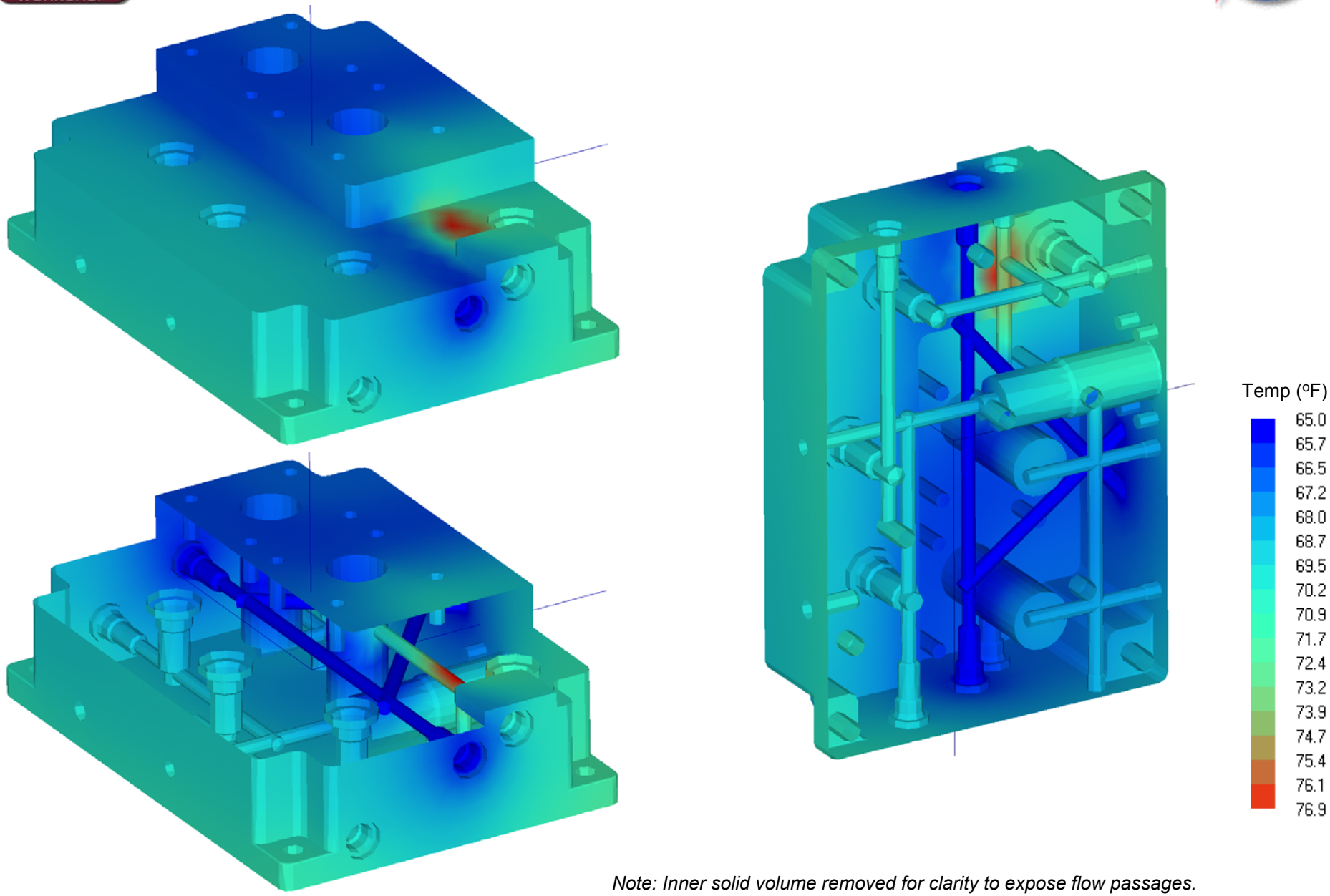

Note: Inner solid volume removed for clarity to expose flow passages.

Boundary Conditions for PCPA Motor Heat Leak Study

Cold Case (Motor Dissipation=18 watts)

	Motor Dissipation	Fluid Dissipation	Motor Cooling Jacket Temp	Outer Cooling Jacket Temp
	(watts)	(watts)	(F)	(F)
Nominal Operational	4.5	0.85	67	66
Worst Case Operational	18.0	3.38	72	71
Loss of Cooling	18.0	3.38	95	95

Hot Case (Motor Dissipation=55 watts)

	Motor Dissipation	Fluid Dissipation	Motor Cooling Jacket Temp	Outer Cooling Jacket Temp
	(watts)	(watts)	(F)	(F)
Nominal Operational	13.8	0.85	65+ 6=71	65+ 4=69
Worst Case Operational	55.0	0	65+22=87	65+18=83
Loss of Cooling	NA	NA	NA	NA

PCPA Thermal Model

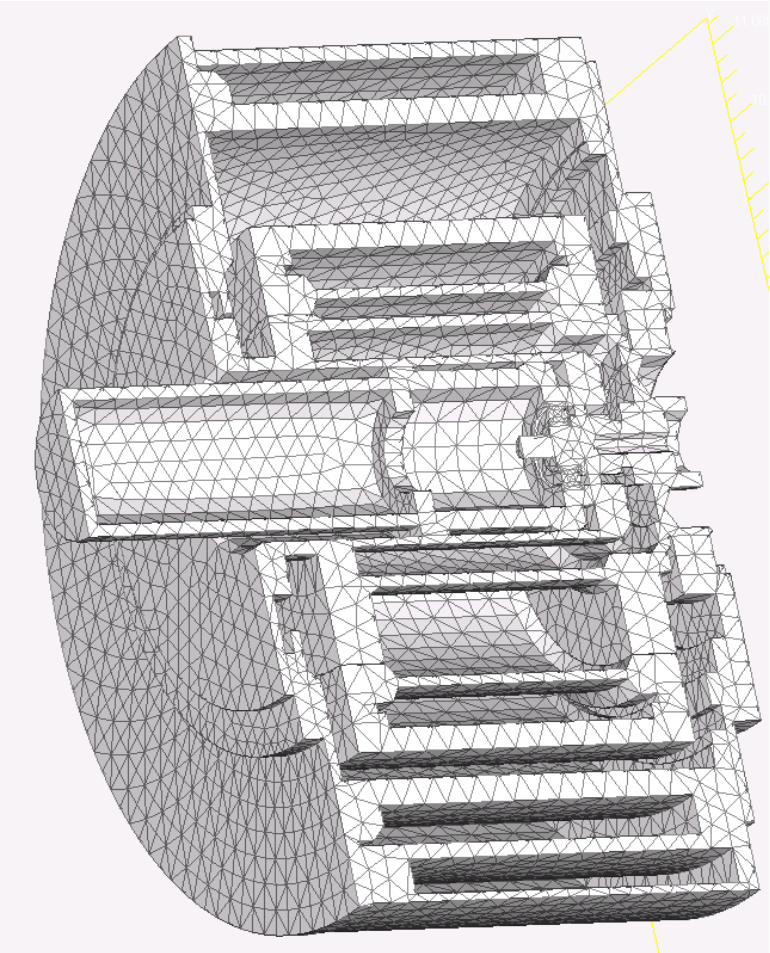

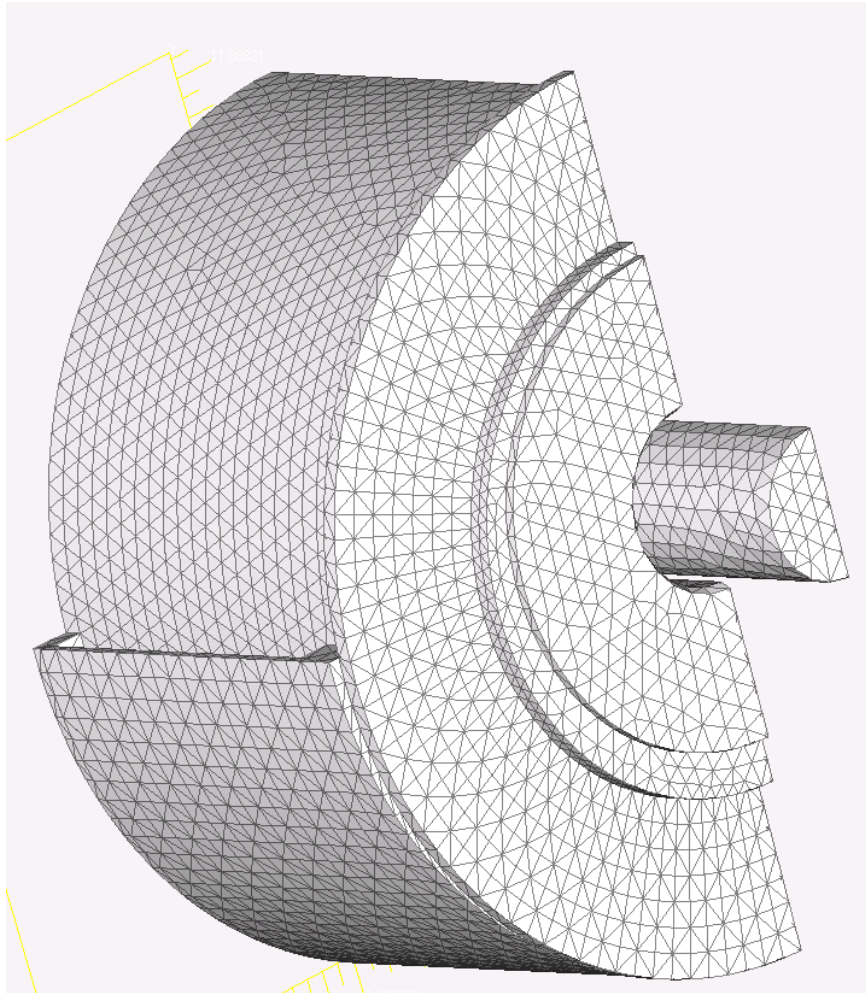

Nodes: 14612
Elements: 45508

PCPA Temperature Distribution for the Worst Case Operational Scenario

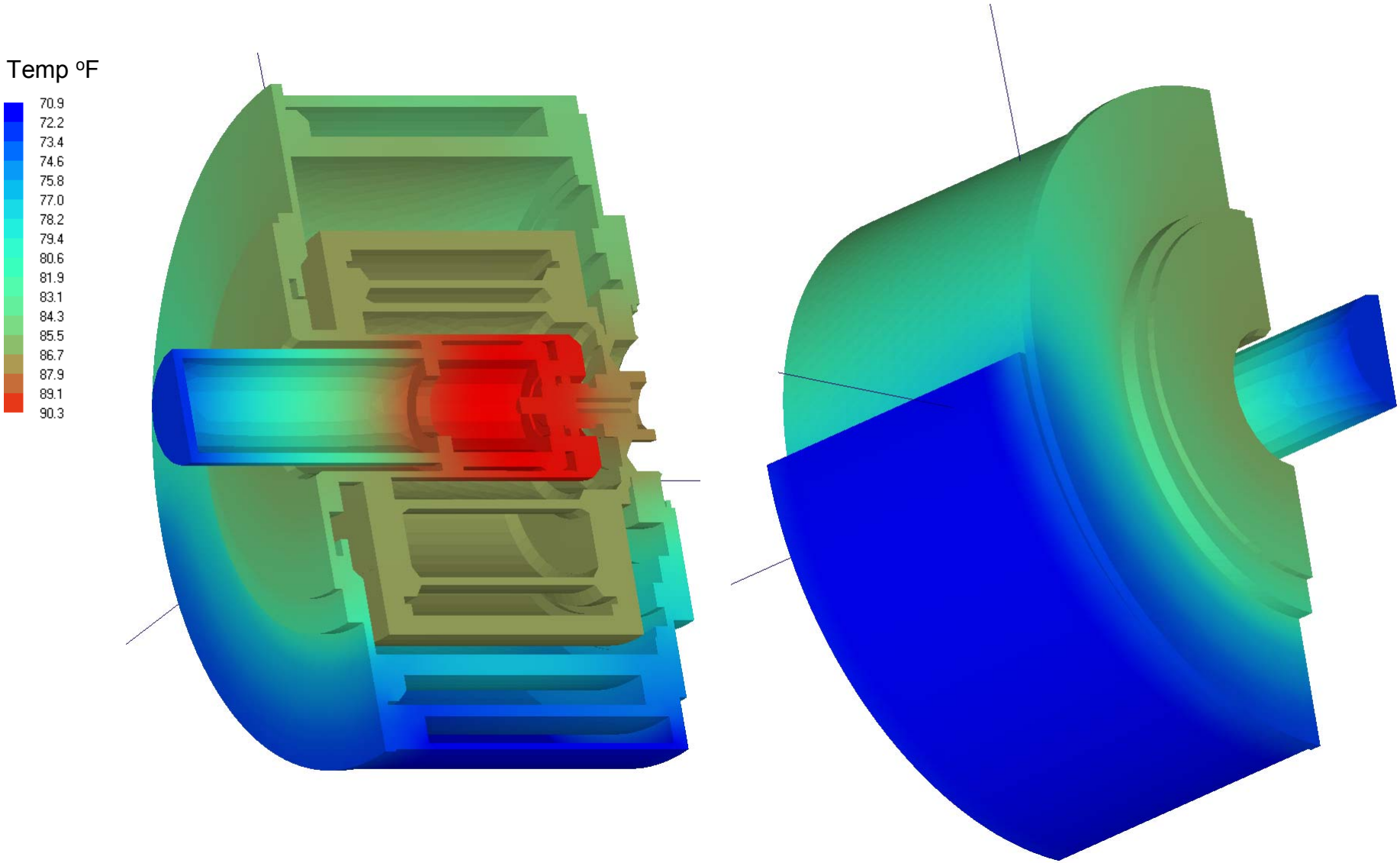

Steady State PCPA Motor Heat Leak Study Results

Cold Case (Motor Dissipation=18 watts)

	Harmonic Drive Outer Temp	Minimum Peristaltic Tubing Temp	Maximum Peristaltic Tubing Temp	Motor Temp
	(F)	(F)	(F)	(F)
Nominal Operational *(25% Duty Cycle)*	70.2	67.6	69.9	71.2
Worst Case Operational *(100% Duty Cycle)*	86.2	76.4	85.5	91.6
Loss of Cooling	109.8	100.3	109.3	113.8

Hot Case (Motor Dissipation=55 watts)

	Harmonic Drive Outer Temp	Minimum Peristaltic Tubing Temp	Maximum Peristaltic Tubing Temp	Motor Temp
	(F)	(F)	(F)	(F)
Nominal Operational *(25% Duty Cycle)*	78.5	72.3	77.8	80.4
Worst Case Operational *(100% Duty Cycle)*	126.8	92.3	110.3	137.5
Loss of Cooling	NA	NA	NA	NA

Conclusions/Future Plans

- Preliminary results from a thermal/flow analysis of the PCPA indicate that the pump performance (mass flow rate) is enhanced via cooling of the housing and lowering of the inlet vapor quality.

- Under a nominal operational profile (25% duty cycle or less), at the maximum motor dissipation, it appears that the peristaltic tubing temperature will still remain significantly below the expected UPA condenser temperature (78°F max versus ~105°F in the condenser) permitting condensation in the pump head.

- Future plans include the development of numerical models to characterize the integrated behavior of the PCPA/Manifold with the Distillation Assembly.

Thermal Analysis of Next Generation Space Telescope (NGST) Mirrors During Optical Testing in the X-Ray Calibration Facility (XRCF)

September 2001

Tim Page
NASA/MSFC

Steven Sutherlin
Raytheon ITSS/SvT MSFC Group

NGST Spacecraft Concept

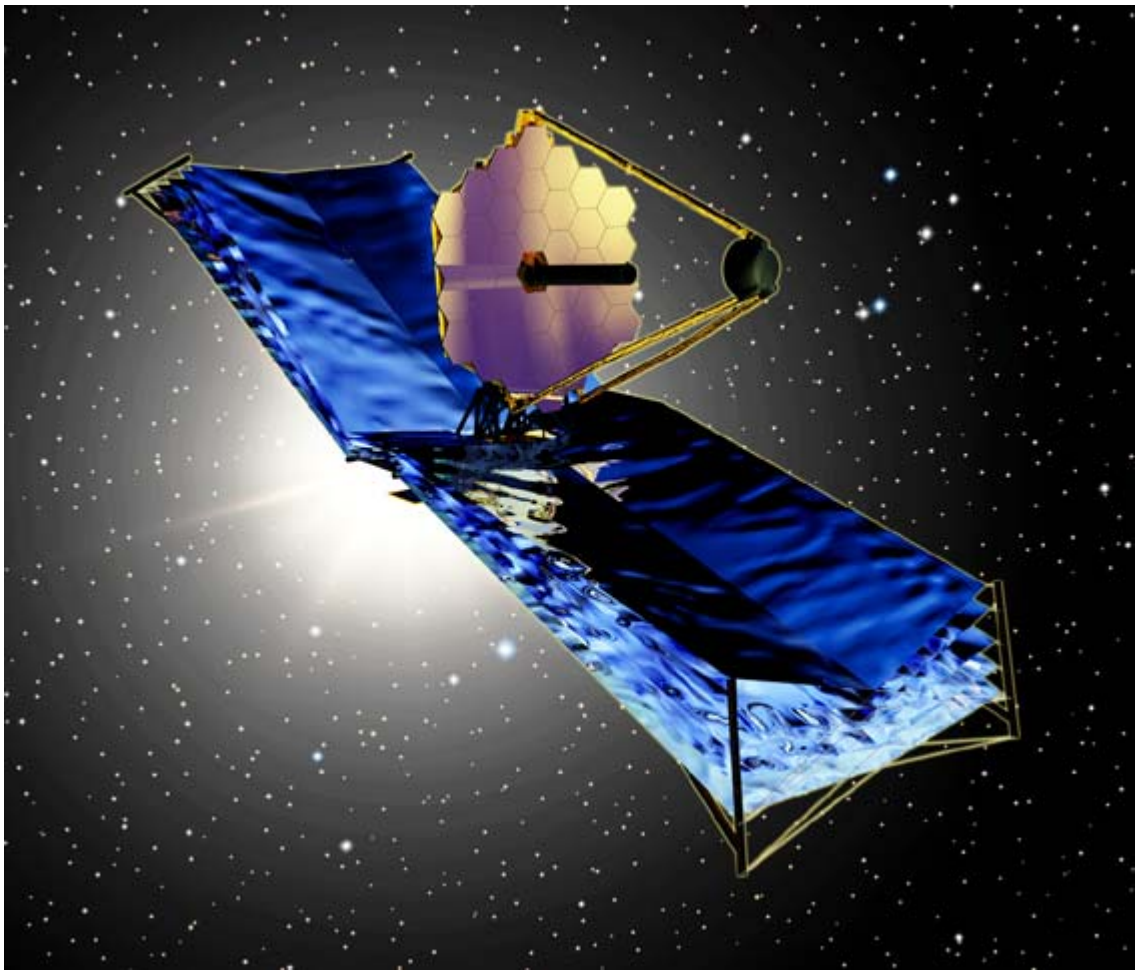

NGST Mirror Development Testing

- The NGST program and industry partners are developing extremely light-weight mirror designs.
- NGST development mirrors are being tested at MSFC.
- Target temperature for development mirror testing is 35 K.
- Conduction and radiation are not sufficient to conduct thermal vacuum testing in a reasonable time.
- Helium gas is injected into the vacuum chamber to accelerate temperature transitions during testing.
- Free-molecular conduction can be modeled by adapting present thermal analysis techniques.

NGST Mirror in the XRCF

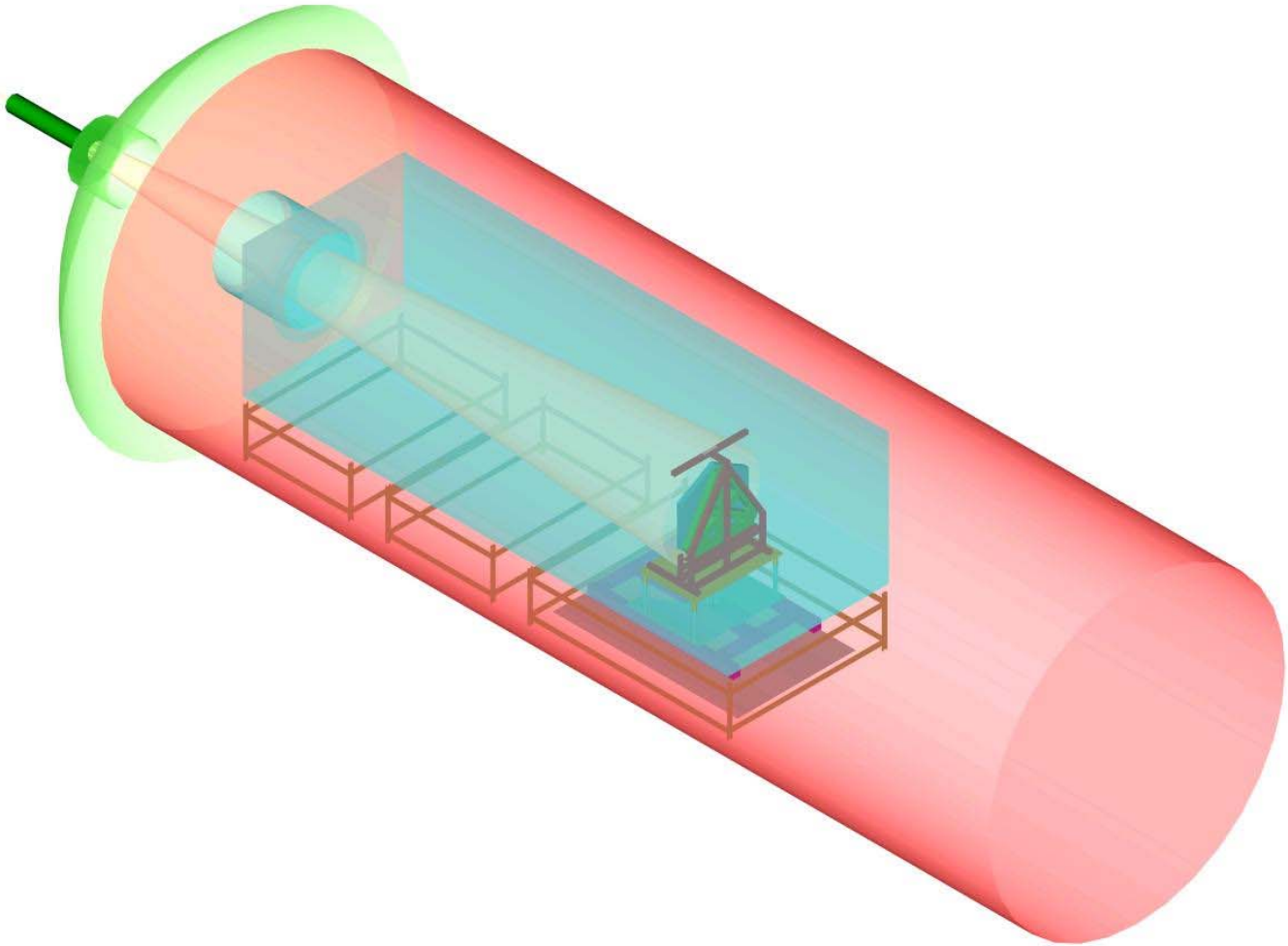

NGST Test Article

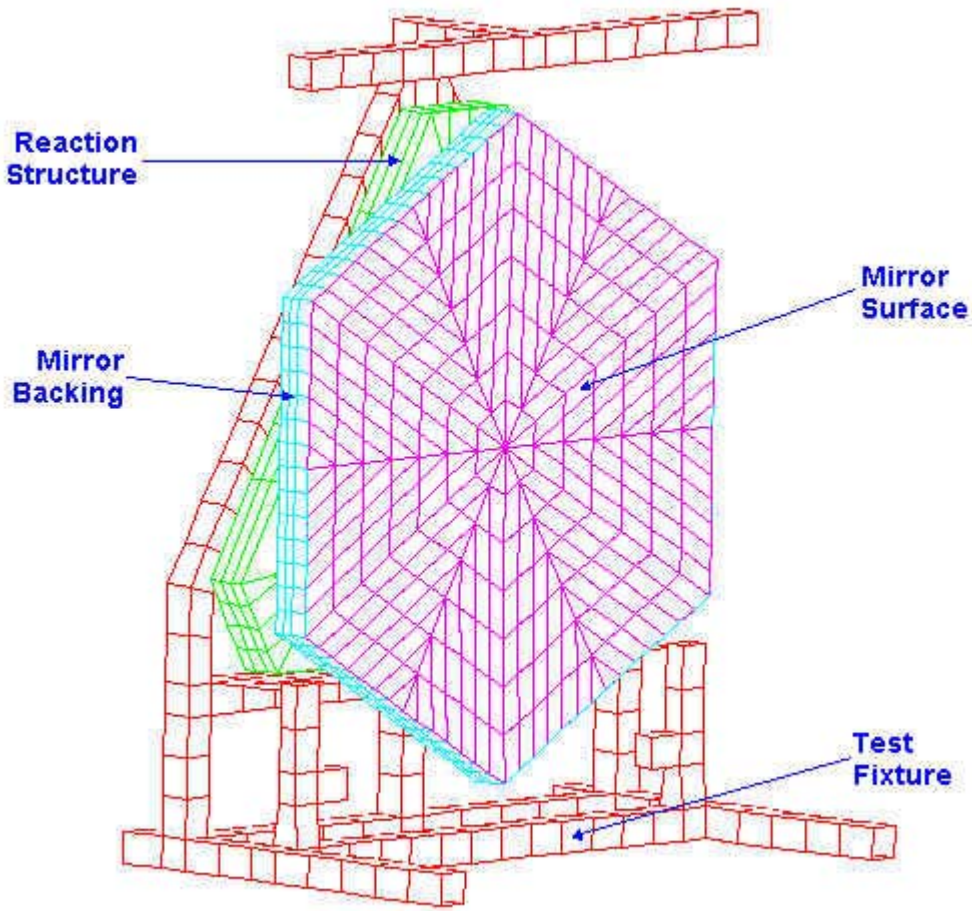

NGST Development Mirror

Knudsen Number

Knudsen Number	$\mathrm{Kn} = \lambda / L_e$	Ratio of Mean Free Path to Characteristic Dimension
Mean Free Path	$\lambda = \frac{\mu}{p}\sqrt{\frac{\pi R_u T}{2 g_c M}}$	μ = Gas Viscosity p = Gas Absolute Pressure R_u = Universal Gas Constant T = Gas Absolute Temperature M = Gas Molecular Weight
Characteristic Dimension	$L_e = 4V/A_w$	V = Enclosure Volume A_w = Enclosure Surface Area

Heat transfer and flow regimes are defined in terms of the Knudsen number.

Continuum	$\mathrm{Kn} < 0.01$
Mixed	$0.01 < \mathrm{Kn} < 0.30$
Free-molecular	$\mathrm{Kn} > 0.30$

Free-Molecular Conduction

The radiation heat transfer between two gray surfaces may be represented by:

$$Q = \sigma F_e F_{12} A_1 (T_2^4 - T_1^4).$$

Similarly, the free-molecular conduction between the two surfaces may be represented by:

$$Q = G\, p\, F_a F_{12} A_1 (T_2 - T_1),$$ in which

$$G = \frac{\gamma + 1}{\gamma - 1}\sqrt{\frac{g_c R_u}{8\pi M T}}$$

R_u = Universal Gas Constant
M = Gas Molecular Weight
T = Pressure Gauge Absolute Temperature

p = Gas Absolute Pressure and

F_a = Accommodation Coefficient Factor.

Accommodation Coefficient

The Accommodation Coefficient, **a**, is analogous to the Emissivity, **ε**, and its value depends on the specific gas/surface combination and the surface temperature. It represents the degree of approach of the gas molecules to thermal equilibrium with the bounding surfaces.

Accommodation Coefficients for Gases of Interest

Temp. (K)	**He**	**Air**	**Ne**	**H_2**
20	0.59	1.00	1.00	0.97
78	0.42	1.00	0.83	0.53
300	0.29	0.8-0.9	0.66	0.29

F_a , the Accommodation Coefficient Factor, is analogous to the Emissivity Factor, F_e. All expressions for F_e may be applied directly by substituting **a** for **ε**.

Results

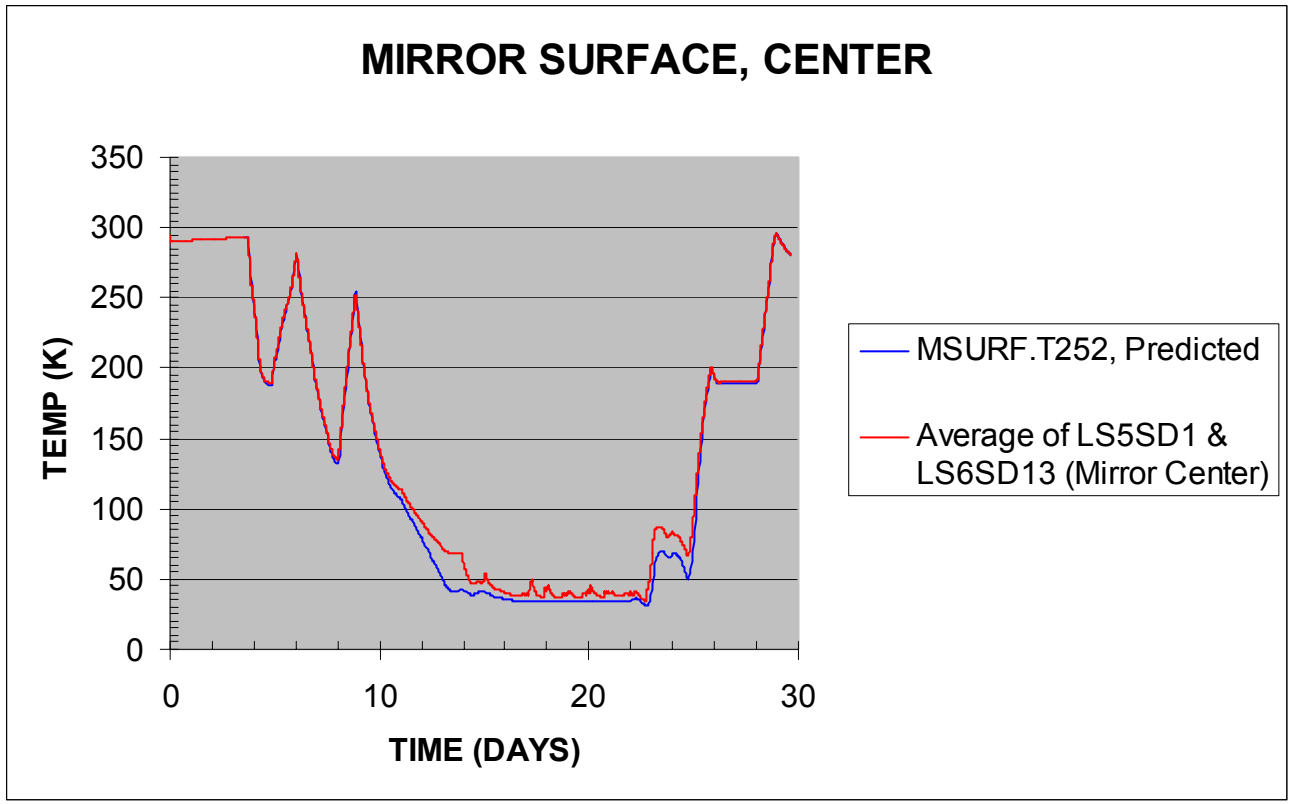
MIRROR SURFACE, CENTER
TEMP (K)
350
300
250
200
150
100
50
0
0
10
20
30
TIME (DAYS)
MSURF.T252, Predicted
Average of LS5SD1 & LS6SD13 (Mirror Center)

Results

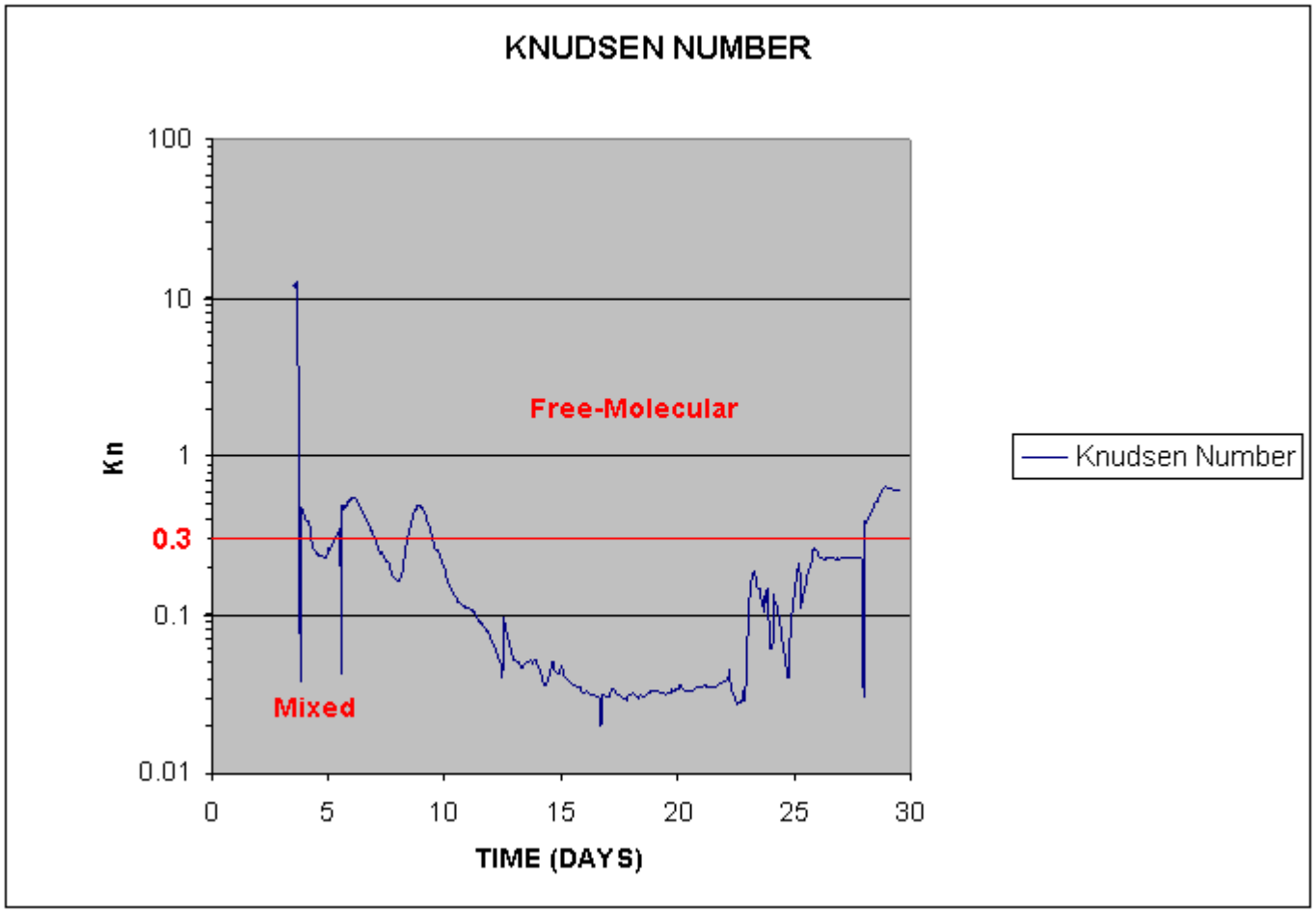
KNUDSEN NUMBER
100
10
1
0.3
0.1
0.01
Kn
Free-Molecular
Mixed
0
5
10
15
20
25
30
TIME (DAYS)
Knudsen Number

Results

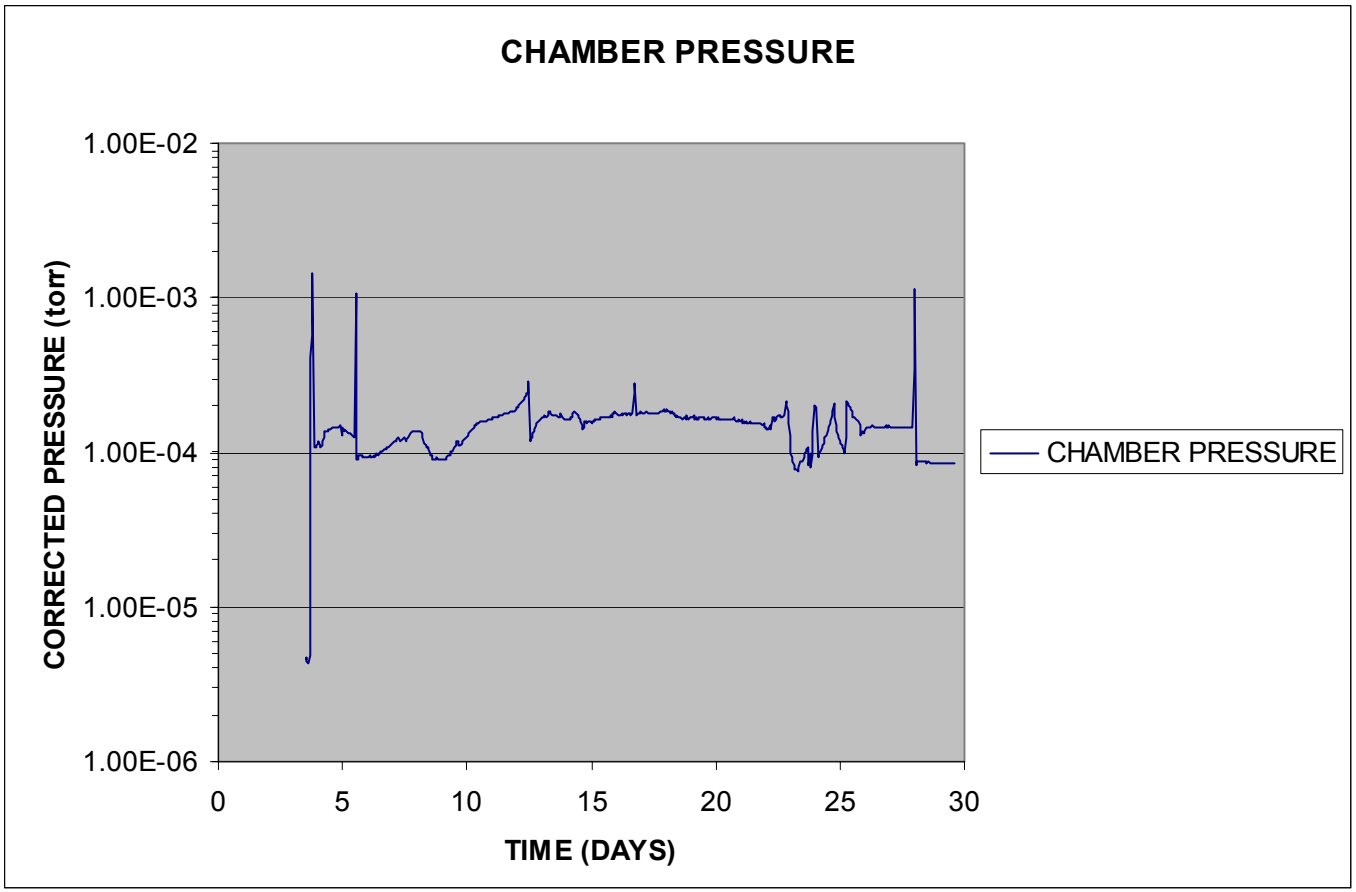
CHAMBER PRESSURE
1.00E-02
1.00E-03
1.00E-04
1.00E-05
1.00E-06
CORRECTED PRESSURE (torr)
0
5
10
15
20
25
30
TIME (DAYS)
CHAMBER PRESSURE

Recommendations

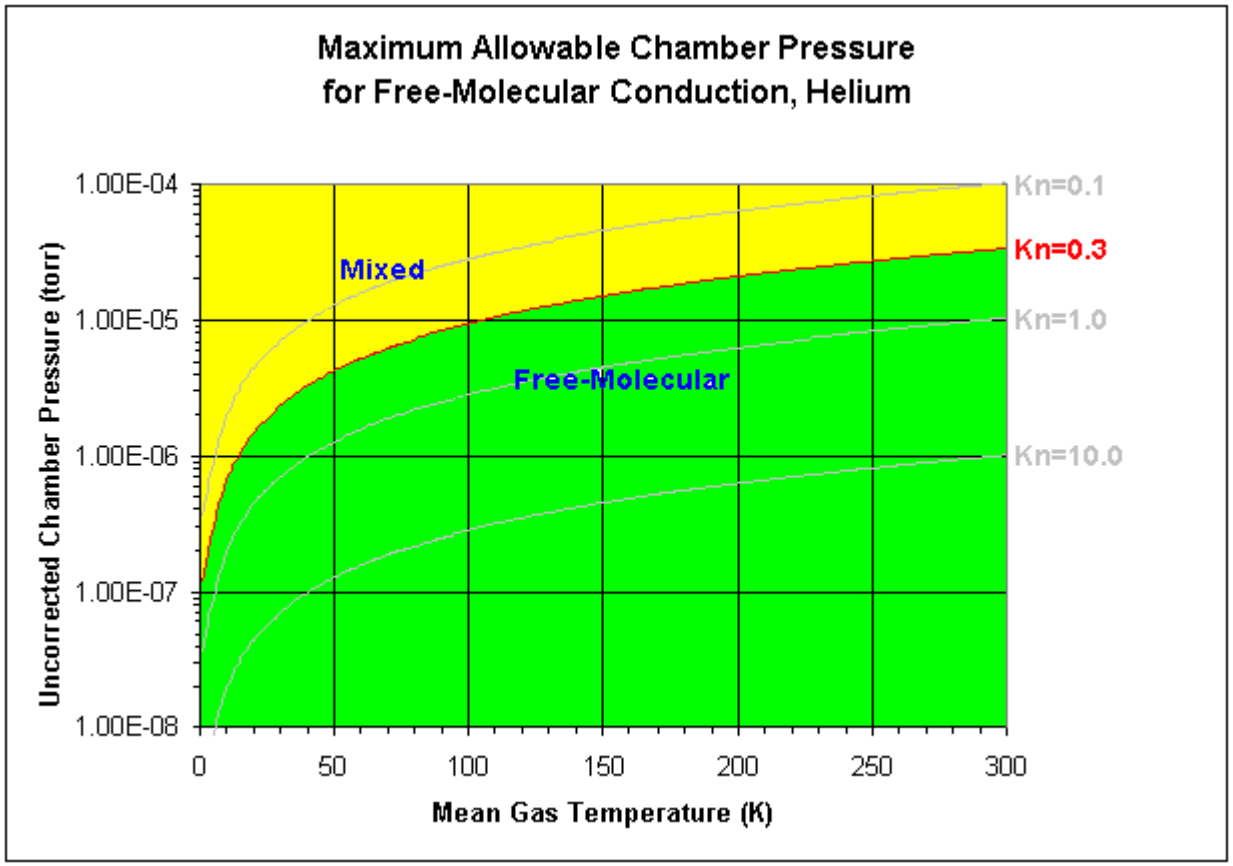

References

1. Randall F. Barron, *Cryogenic Heat Transfer*, Taylor & Francis, 1999, pp. 243 – 257.
2. Steven Sutherlin, *The Composite Optics, Inc. (COI) Development Mirror Thermal Analysis Final Report*, MG-01-498, May 30, 2001.

COMPARISON OF ANALYTICAL AND NUMERICAL PERFORMANCE PREDICTIONS FOR AN INTERNATIONAL SPACE STATION NODE 3 INTERNAL ACTIVE THERMAL CONTROL SYSTEM REGENERATIVE HEAT EXCHANGER

Stephen A. Wise
Qualis Corporation, MSFC Group / ED 25

James M. Holt
National Aeronautics and Space Administration / ED 25
Marshall Space Flight Center

ABSTRACT

The complexity of International Space Station (ISS) systems modeling often necessitates the concurrence of various dissimilar, parallel analysis techniques to validate modeling. This was the case with a feasibility and performance study of the ISS Node 3 Regenerative Heat Exchanger (RHX). A thermo-hydraulic network model was created and analyzed in SINDA/FLUINT. A less complex, closed form solution of the systems dynamics was created using an Excel Spreadsheet. The purpose of this paper is to provide a brief description of the modeling processes utilized, the results and benefits of each to the ISS Node 3 RHX study.

INTRODUCTION

Node 3 enhances the ISS stand-alone (without orbiter) crew capacity from a maximum of three to a maximum of seven by providing dedicated utilities supporting crew habitability functions at Station level. Of these dedicated utilities, the most critical are the Environmental Control and Life Support System (ECLSS) racks which condition the internal atmosphere. To provide for continuous operation, the Node 3 Thermal Control System (TCS) Low Temperature Loop (LTL) and Moderate Temperature Loop (MTL) collect and reject waste heat from the ECLSS racks. Requirements exist to ensure that during a single failure of the External Active Control System (EATCS) Loop B (LTL heat rejection capability) or power domain 2/3 (LTL equipment power) TCS function would continue to provide cooling to the critical ECLSS racks. In order to sustain operation for this contingency case the nominally dual loop mode TCS must accommodate a Loop Crossover Assembly (LCA) to allow the two loops to operate as one in series, utilizing the MTL to provide coolant for LTL heat rejection.

ENVIRONMENTAL CONTROL AND LIFE SUPPORT SYSTEM (ECLSS) DESCRIPTION

The Environmental Control and Life Support Systems (ECLSS) controls the atmosphere of the internal pressurized volume in terms of air pressure, temperature, humidity, particulate and microbial concentrations, and velocity. Additionally, the ECLSS racks provide for crew waste management and hygiene. The following rack assemblies achieve these ECLSS functions:

- Atmosphere Revitalization System (ARS) rack
    - Sample Delivery System (SDS) – to allow proper air flow distribution inside the rack
    - Trace Contaminant Control Subassembly (TCCS) – processes the cabin air to remove the gaseous trace contaminants that could be hazardous for the crew
    - Major Constituent Analyzer (MCA) – continuously monitors the partial pressures of the major atmospheric constituents in the Node 3 cabin and from other modules of the ISS.
    - Area smoke detection and fire indication
    - Carbon Dioxide Removal Assembly (CDRA) – processes the cabin air to remove carbon dioxide
    - Avionics Air Assembly (AAA) – provides air circulation for fire detection and provides air cooling for rack components
- Oxygen Generation System (OGS) rack – Contains the Oxygen Generator Assembly (OGA) to produce oxygen for atmospheric supply
- Water Recovery System (WRS) #1 & #2 racks – Waste water processing to potable water and pre-treated urine to urine distillate processing
- Waste & Hygiene Compartment (W&HC) #1 & #2 racks – Crew personal hygiene and crew urine and fecal collection
- Common Cabin Air Assembly (CCAA) – Air/Water Heat Exchanger (HX) that transfers environmental heat loads to the LTL for rejection

NODE 3 INTERNAL ACTIVE THERMAL CONTROL SYSTEM (IATCS) DESCRIPTION - NOMINAL OPERATION

The Node 3 Internal Active Thermal Control System (IATCS) consists of two loops that employ single-phase water as a heat transport fluid: the Node 3 Low Temperature Loop (LTL) and the Node 3 Moderate Temperature Loop (MTL). The Node 3 LTL and MTL collect and transport waste heat from the subsystems avionics equipment, the environmental control system and from subsystems and payloads within elements attached to Node 3.

The collected heat load is rejected by means of two separate single-phase ammonia loops A and B, via two dedicated NH_3/H_2O Heat Exchangers (HX), mounted on the external shell of the Node 3 Zenith Cone. The collected heat is transferred from the ammonia loops to the Station radiators for rejection.

Each loop contains various components that provide pressure and temperature control. The functional diagram of the Node 3 IATCS is depicted in Figure 1.

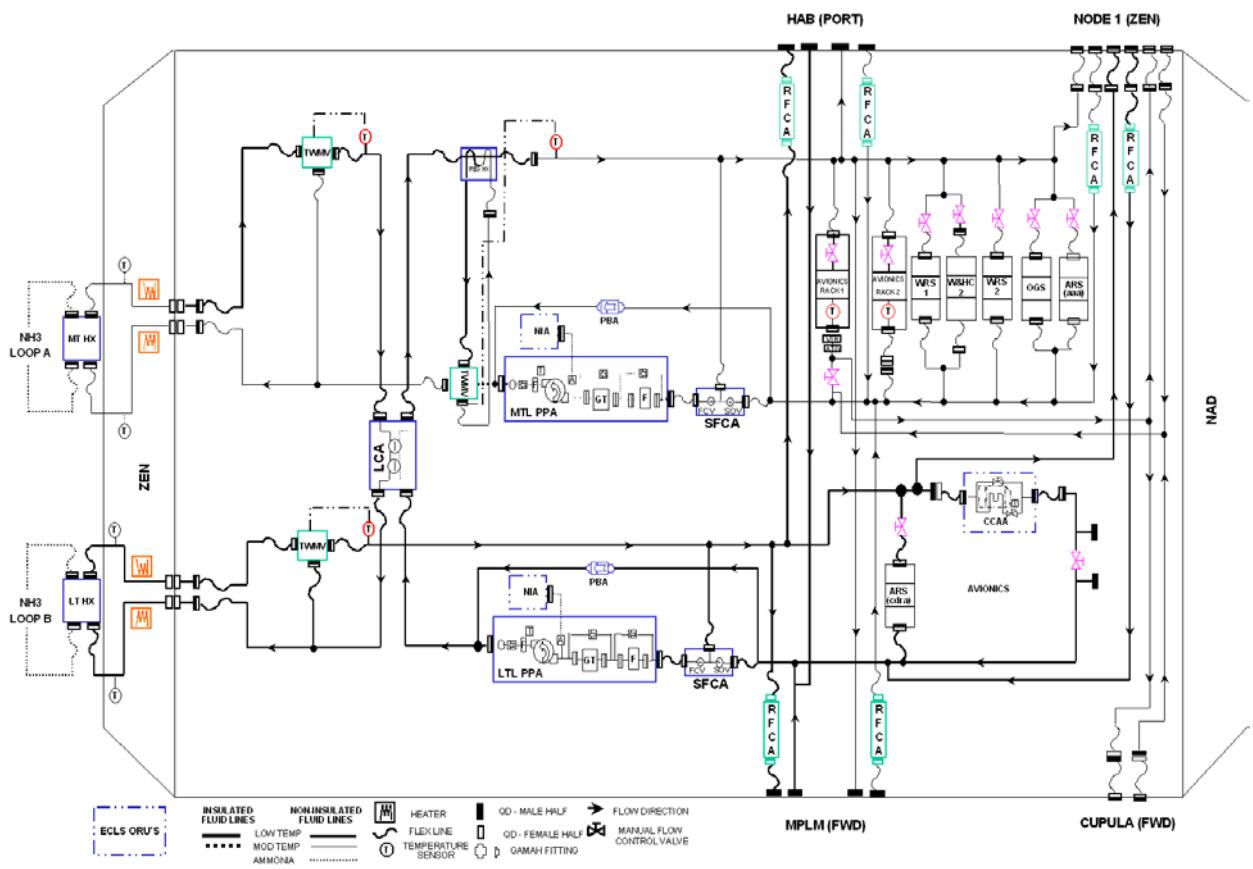

Figure 1 – Node 3 IATCS

LOW TEMPERATURE LOOP (LTL)

At a non-selectable temperature range from 38˚ – 43˚F, the LTL guarantees the correct flow rate distribution and removes waste heat from the attached modules Multi-Purpose Logistics Module (MPLM), Node 1 and Habitation Module (HAB) LT loop, the ECLSS CCAA, the ARS – CDRA rack, and the internal Cold Plate HXs located on the external side of the Zenith cone shell.

MODERATE TEMPERATURE LOOP (MTL)

At a non-selectable temperature range from 61˚ - 65˚F, the Moderate Temperature Loop (MTL) guarantees the correct flow rate distribution and removes waste heat from the attached Modules MPLM scar, Node 1 MT & High Temperature (HT) loop and Cupola, the ARS – AAA rack, WRS-#1 & -#2, W&HC-#1 & -#2, OGS – OGA rack and Cold Plate cooled electronic equipment located in Avionics Racks #1 & #2.

NODE 3 INTERNAL ACTIVE THERMAL CONTROL SYSTEM (IATCS) DESCRIPTION - CONTINGENCY OPERATION

A single failure of the EATCS loop B or power domain 2/3 would result in the loss of LTL coolant flow, creating a condition where CO_2 removal capability would be lost in both the United States Laboratory (USL) module and Node 3. To combat this Node 3 TCS will accommodate a LCA to connect the two loops in series to operate as a single loop, utilizing the MTL to provide coolant for LTL heat rejection.

In view of the fact that the MTL will be providing coolant for LTL use, the temperature of the MTL transport fluid must be adjusted to match the need of the equipment on the LTL. This is accomplished by adjusting the set point of the MTL Common Thermal Bus (CTB) Three Way Mix Valve (TWMV) from 65.0˚F (MTL nominal) to 50.0˚F. Consequently, as the transport fluid re-enters the MTL, the LTL equipment heat load may not have been enough as to raise the fluid above the dew point (65.0˚F). Therefore, the system ensures the fluid temperature is raised above the dew point with a RHX in conjunction with a TWMV (65.0˚F set point) to preclude condensation upon the MTL coolant lines and equipment.

REGENERATIVE HEAT EXCHANGER (RHX) FEASIBILITY AND PERFORMANCE

As previously stated, the RHX must ensure the temperature of the MTL fluid is above the dew point to preclude condensation. A study was made to determine if the condensation preclusion requirement could be met under a “low load” scenario (no attached modules). The scope of this case is based on estimated heat dissipation values ascertained from the Node 3 Design Review Thermal Budget[1]. The estimated values were derived from the equipment that were considered to be operational after a single failure of the EATCS loop B power domain 2/3. The heat loads utilized for the analysis are shown in Table 1. The analysis also shows the allowable performance envelope for condensation preclusion and heat rejection.

CLOSED FORM SOLUTION

A closed form solution was developed to ascertain RHX performance based on Node 3 single loop mode architecture. Figure 2 shows the layout and nomenclature used for the closed form solution.

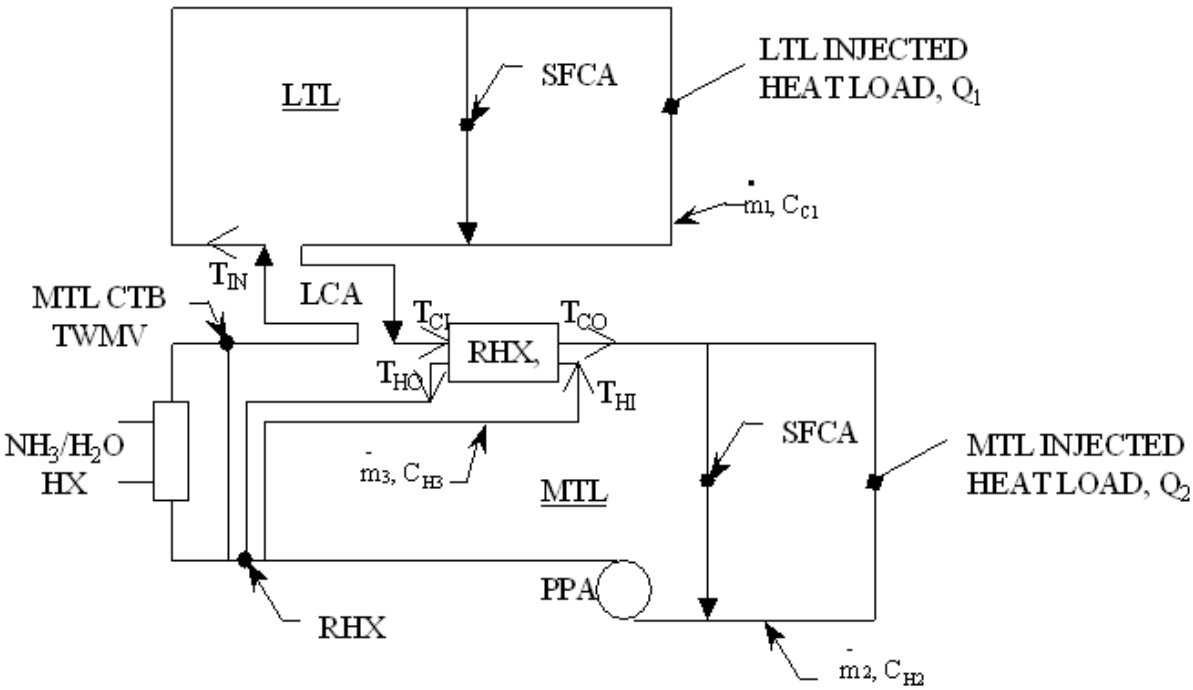

Figure 2 – Closed Form Solution Schematic

The Pump Package Assembly (PPA) total flowrate considered in the calculation was 2300 lbm/hr due to single loop mode pump performance degradation from the nominal 3000 lbm/hr. MTL Common Thermal Bus (CTB) Three Way Mix Valve (TWMV) temperature set point (T_{IN}) was changed from 65.0˚F (MTL nominal) to 50.0˚F, and the RHX TWMV outlet temperature (T_{CO}) was set to 65.0˚F to avoid condensation. The knowns, LTL and MTL (Q_1 and Q_2) injected heat loads and RHX hotside flowrate ($mdot_3$) were varied in the analysis to ascertain the useful working envelope for the system. T_{CO} and T_{IN} were also specified in the study. Assumptions made include the following; H_2O constant specific heat, c_p = 1.0 Btu/lbm˚F, $C_{MIN} = C_{H3} = mdot_3 c_p$, and $C_{H2} = C_{C1}$ = 2300 Btu/hr˚F.

As shown in Figure 3[2],linear interpolation about a cold side water flowrate of 2300 lbm/hr yields an equation for the RHX hotside effectiveness of:

Effectiveness equation: $$\varepsilon \approx \left(\frac{-0.28}{1500}\right)\left(\dot{m}_3 - 1500\right) + 0.93 \qquad (1)$$

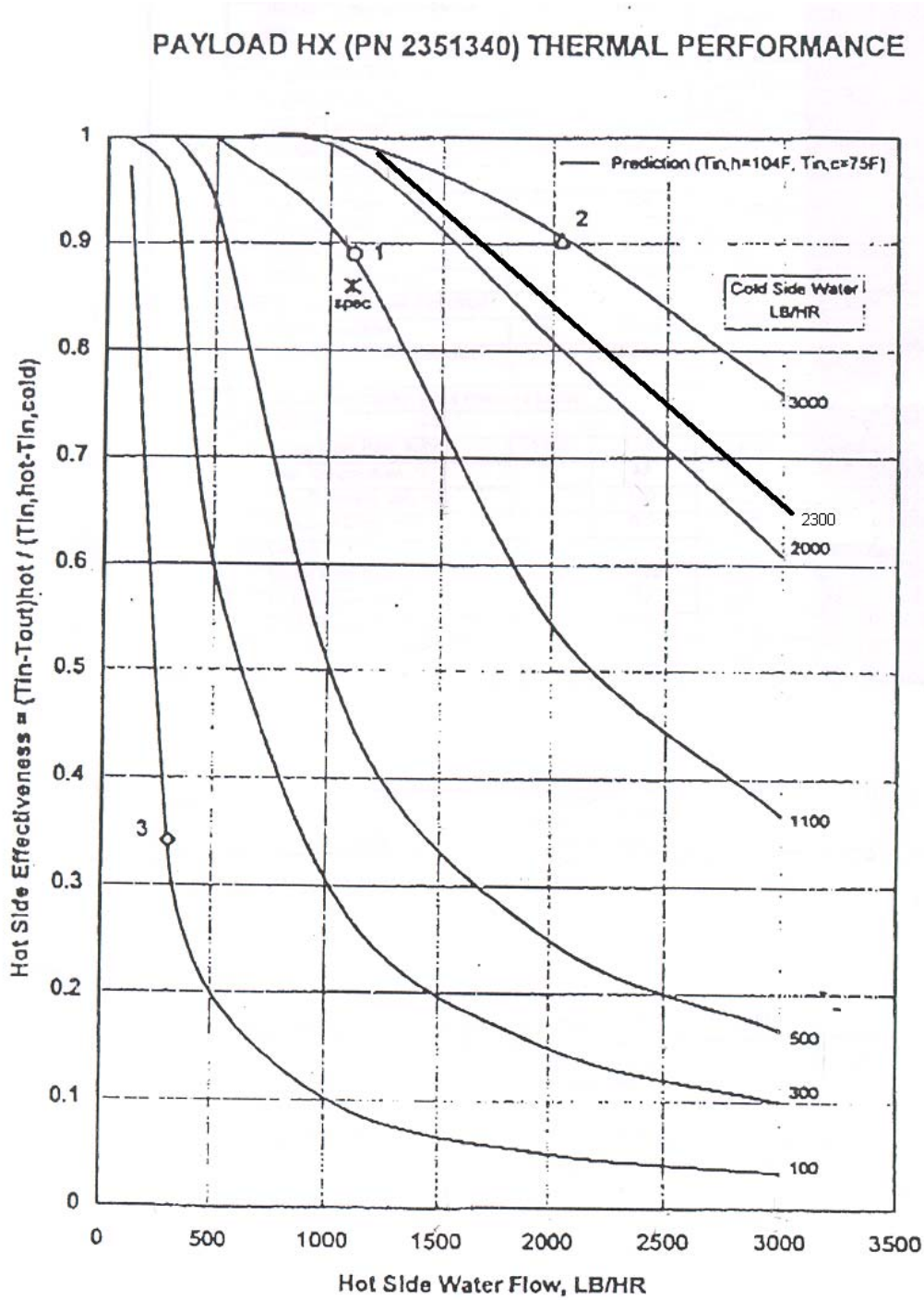

Figure 3 – Regenerative Heat Exchanger Performance Curves

The following relationships[3] are appropriate for the effectiveness - NTU method of heat exchanger analysis.

$$Q_{MAX} = Q_T / \varepsilon \tag{2}$$

$$T_{CI} = T_{IN} + Q_1 / C_{C1} \tag{3}$$

$$T_{CI} = - Q_{MAX} / C_{MIN} + T_{HI} \tag{4}$$

$$T_{HI} = T_{CO} + Q_2 / C_{H2} \tag{5}$$

$$T_{CO} = T_{CI} + Q_T / C_{C1} \tag{6}$$

$$Q_T = \varepsilon (C_{MIN})(T_{HI} - T_{CI}) \tag{7}$$

Combining equations. 1-7 and solving for $mdot_3$ in terms of Q_1, Q_2, T_{CO}, and T_{IN} with assumptions 1-3 yields:

$$\dot{m}_3 = \frac{-1347.92\left\{\left[-\left(Q_1 + 5.78\left(Q_2 - 397.81\left(T_{CO} - T_{IN}\right)\right)\right)\right]^{(1/2)} - 2.41\left[Q_1 - Q_2 - 2300\left(T_{CO} - T_{IN}\right)\right]^{(1/2)}\right\}}{\left[Q_1 - Q_2 - 2300\left(T_{CO} - T_{IN}\right)\right]^{(1/2)}}$$

With the aforementioned relationships, an Excel Spreadsheet was developed to perform trade studies for the system. With the Excel "solver" function, it was possible to determine either flow rates or heat loads necessary for the system to operate successfully. Table 1 gives the thermal loads associated with the various components and Figure 4 shows the input interface to the Excel Spreadsheet.

SOURCE OR COMPONENT	THERMAL LOAD [Watts]	
	LTL	**MTL**
ARS / CDRA	**725.0**	-
ARS / AAA	-	**229.0**
OGA	-	**2320.0**
MTL PPA	-	**470.0**
TWMV	-	**1.0**
SFCA	-	**2.0**
Cold biased attitude producing a negative environmental heat load with cabin air temperature at 80°F	*-720.0	-
2 crew members	*270.0	-
Avionics Racks #1	*17.3	**557.7**
CCAA Water Separator	*44.7	-
CCAA Temp. Control Valve	*1.0	-
CCAA EIB	*6.5	-
Air Smoke Detect. (ASD)	*6.0	-
Harness	*20.0	-
THC Cabin Fan	*191.0	-
General Luminary Assy.	*300.0	-
ELPS	*10.0	-
UOP – 1, 2, 3, & 4	*36.0	-
Pressure Control Panel	*20.0	-
Nitrogen Introduction Assy.	*14.4	-
IMV Fan	*110.0	-
IMV Valve	*4.0	-
PCS	*100.0	-
CCAA	**430.9**	-
TOTALS	**1155.9**	**3579.7**

* - Air Load: total value incorporated for CCAA

Table 1 – Single Loop Mode Thermal Budget (est.)

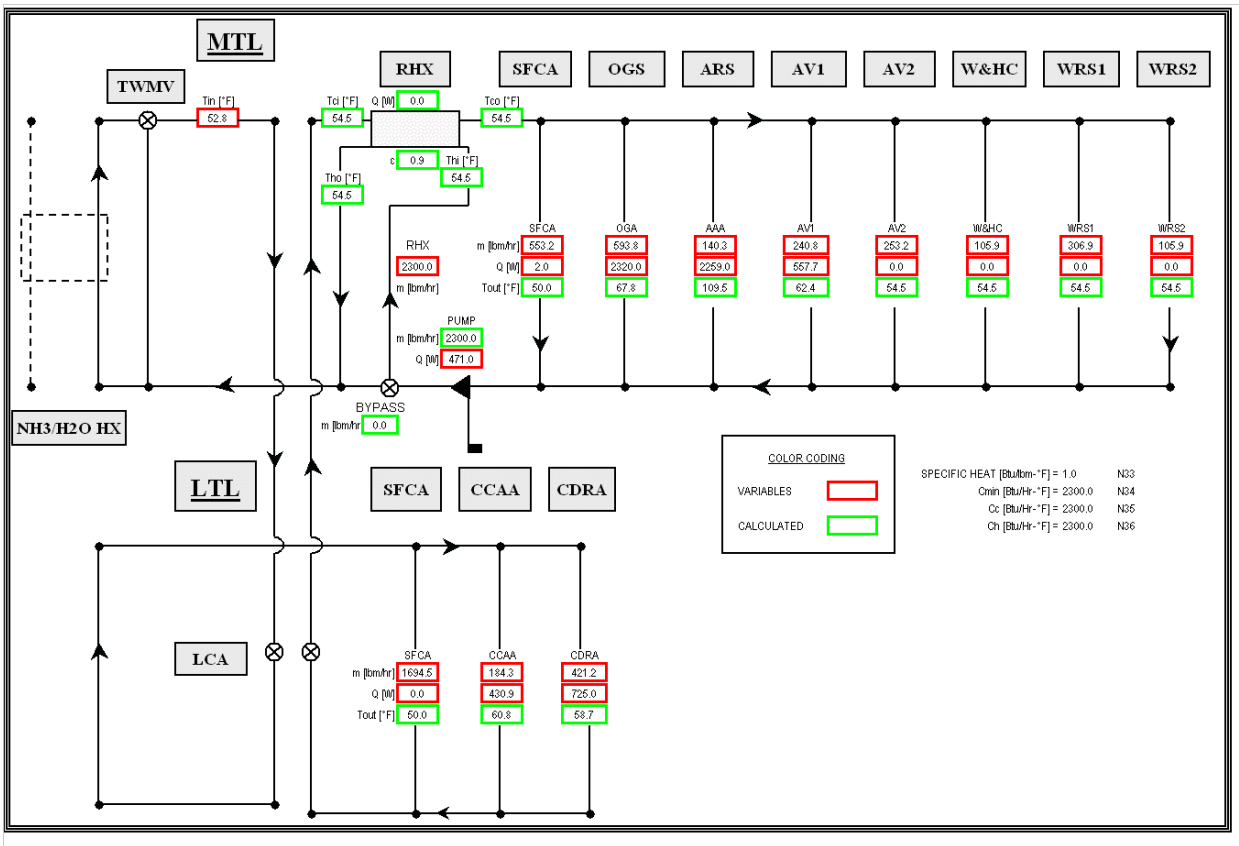

Figure 4 – Excel Spreadsheet Interface

The flow distribution in the parallel branches of the LTL was determined separately by the SINDA/FLUINT model. Details of this model are noted in the next section. Closed form results illustrate the RHX hotside flowrates corresponding to MTL and LTL injected heat loads which are required to maintain the RHX cold side exit temperature above the dew point (65.0˚F). Trends show that the MTL heat load must increase when the LTL heat load is decreased. The boundary of acceptable performance is also shown, based on total flowrate of 2300 lbm/hr. Figure 5 shows the closed form solution.

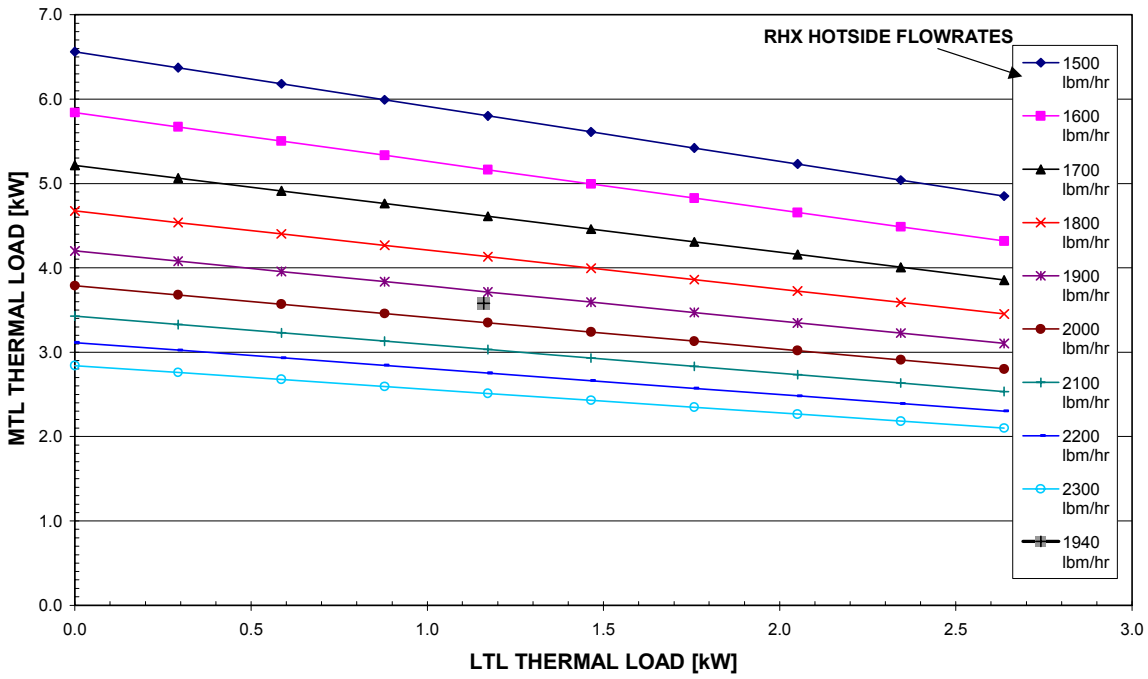

Figure 5 – Closed Form Results

SINDA/FLUINT

A simplified SINDA/FLUINT mathematical model, representing the Node 3 single loop configuration (Node 3 core only, no resources provided to Node 1 Airlock or HAB), was developed to determine the RHX performance independent of the close form solutions. This model was based on the current Node 2 thermal/hydraulic model and incorporates common IATCS components' hydraulic characteristics as well as software control algorithms. Modifications were made to the Node 2 model to account for effects from additional racks, pipe lengths, MTL/LTL single loop configuration and RHX thermal/hydraulic performance parameters [2]. Figure 6 shows the SINDA/FLUINT model.

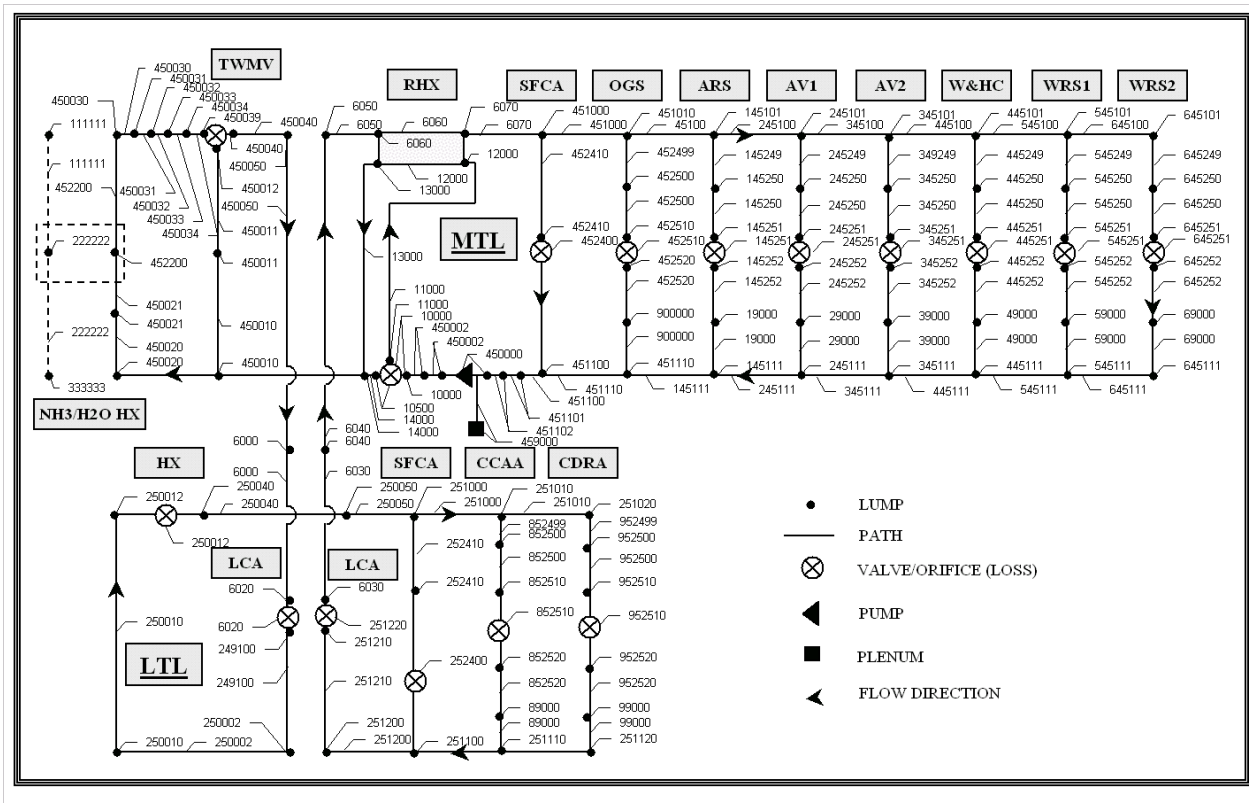

Figure 6 – Node 3 IATCS Math Model

Additional modeling parameters of interest include racks, the LTL System Flow Control Assembly (SFCA) valve and the LTL CTB TWMV. The current plan is not to manipulate Manual Flow Control Valves (MFCV) during the failure; therefore, all rack simulated "LOSS" input values remained constant based on nominal design flowrates. A failure of power domain 2/3 or Loop B ammonia would result in the SFCA remaining in the last commanded position, which was assumed to be nominal. Therefore, the LTL SFCA valve coefficient was set to a constant based on the calculated value for the nominal LTL flowrate and a setpoint of 13 psid. The LTL CTB TWMV valve loss coefficient was set to a value corresponding to the full bypass condition. It was assumed that in case of the aforementioned failure, the TWMV would be manually set to this position. The MTL PPA was set to a constant flowrate of 2300 lbm/hr based on performance degradation from the nominal 3000 lbm/hr. Setpoints used in the analysis for the MTL CTB TWMV and RHX TWMV were 47.5 ºF and 62.5 ºF respectively, and a loop A ammonia inlet temperature of 40.0ºF.

When compared, the trends of the SINDA/FLUINT and closed form solution differed only slightly due to the control algorithm software error band, which translates to a ±5˚F tolerance, CTB MTL TWMV single mode set point of 47.5˚F vs. 50.0˚F, and RHX TWMV set point of 62.5˚F vs. 65˚F.

CONCLUSION

This study was made to determine if the condensation preclusion requirement could be met while the TCS is in single loop mode under a "low load" scenario. Currently, the heat loads are not guaranteed accurate or final in the Node 3 design. This ambiguity makes it difficult to modify the more complex SINDA/FLUINT model. The closed form solution allows for a much timelier analysis and trade study capability without sacrificing accuracy.

REFERENCES (STYLE=PAPERHEADINGS)

1. Node 3 DR-1, Torino, Italy, July 1999

2. Allied Signal Aerospace Equipment Systems, Doc. No. 97-69186 pg. 3.3.2-4

3. Frank P. Incropera and David P. DeWitt, "Heat and Mass Transfer," Chap.11, John Wiley & Sons, New York, 1996

Thermal Design, Analysis, and Testing of the Quench Module Insert Bread Board

July 31, 2001

Shawn Breeding and Julia Khodabandeh

ED25/ NASA/MSFC

Quench Module Insert (QMI) Microgravity Materials Processing

- *What is microgravity materials processing?*
  - *Creating desired thermal gradient and solid/liquid interface front movement for a given processing temperature in a microgravity environment*

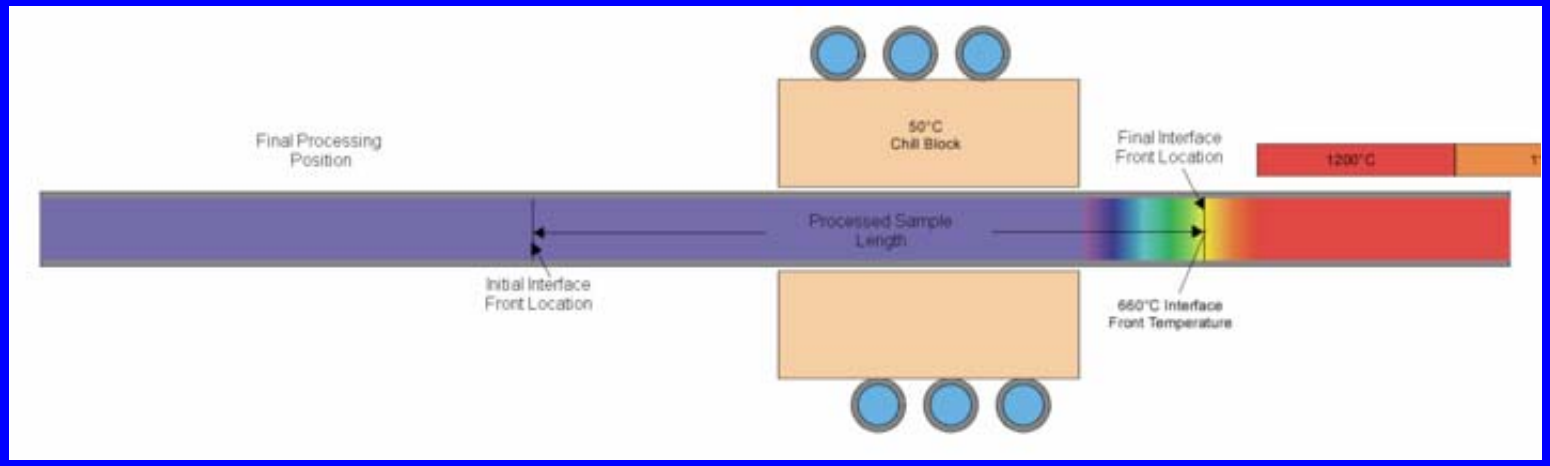

Quench Module Insert (QMI) Science Requirements

- *Metals and Alloys Processing*
  - *Currently Supporting Two Investigators*
  - *Sample Processing from 600°C to 1400°C*
  - *Various Sample Materials up to 1cm diameter*
  - *Sample Gradients up to 150°C/cm for a 1cm aluminum sample at 1100°C processing*
  - *Sample Isothermality of ±10°C over a 10cm length of a 1cm dia. aluminum sample*
  - *20cm hot zone; four independently controlled zones; 20cm of translation; approximately 18cm of sample processing*
  - *Sample Quench rates providing solidification of a 2cm length of a 1cm diameter aluminum sample in 2seconds*

Quench Module Insert (QMI) Interfaces

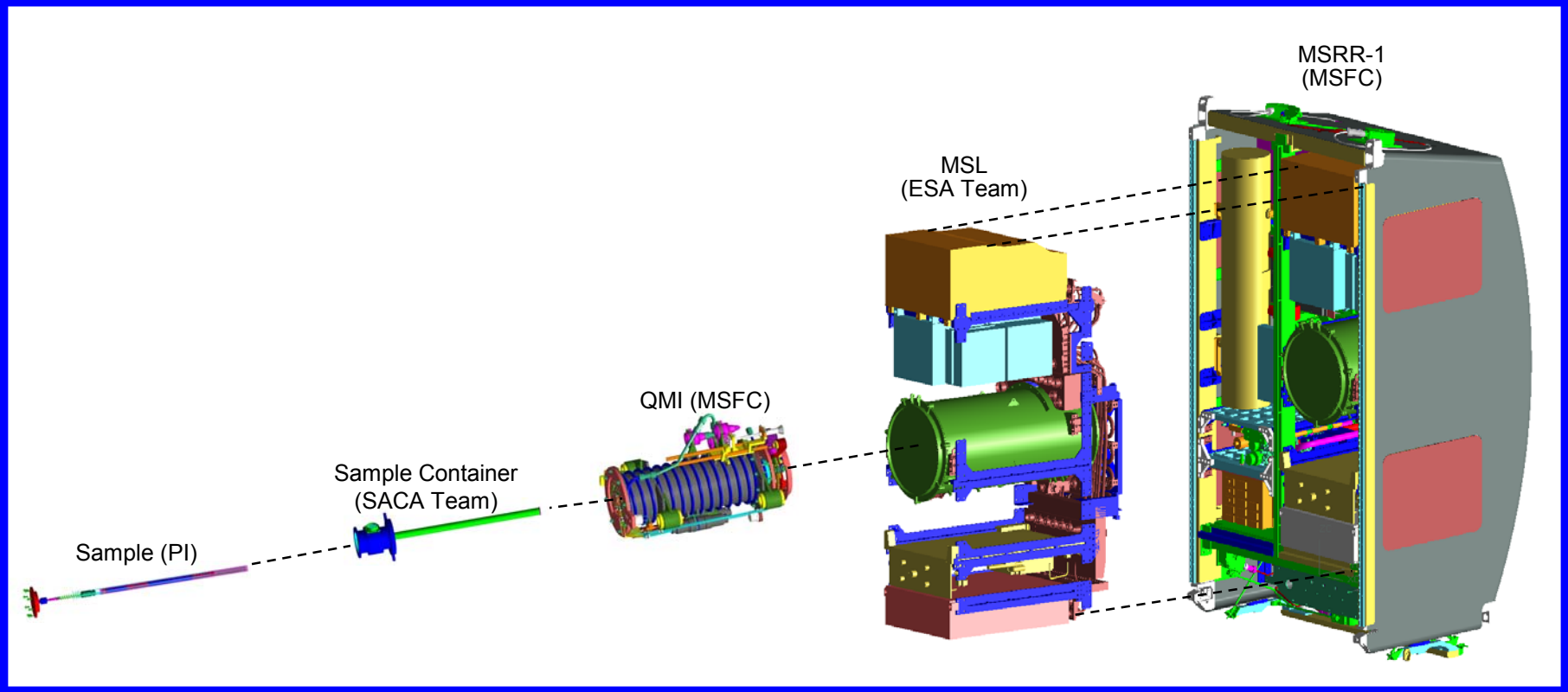

Quench Module Insert (QMI) Interface Requirements

- *Integration in the ESA's Materials Science Laboratory*
  - *3kW Max. Power/Cooling Allocation (currently showing a max. power requirement of less than 450W at 1400°C)*
  - *Fail Safe Loss of Cooling (max. 600ml of expelled volume)*
  - *Touch Temperature (>49°C) during all phases of processing*
  - *Limits on waste heat losses to the ESA thermal chamber (100W)*
  - *Max. Shell temperatures*
  - *Max. Coolant return temperatures*
  - *190mbar pressure drop at max. coolant flow conditions*

Quench Module Insert (QMI) Design Layout

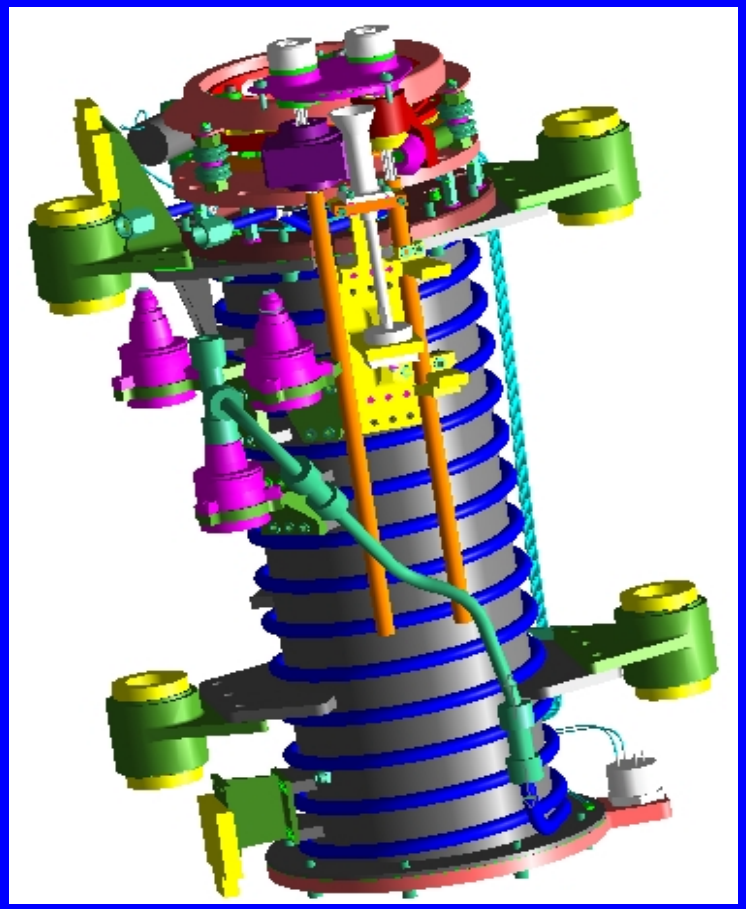

- *Bridgman-type, Vacuum Furnace*
- *Four heated zones*
- *One interchangeable cold zone*
- *Phase Change Quench System*
- *Highly Efficient Insulation Design*

Quench Module Insert (QMI) Design Layout

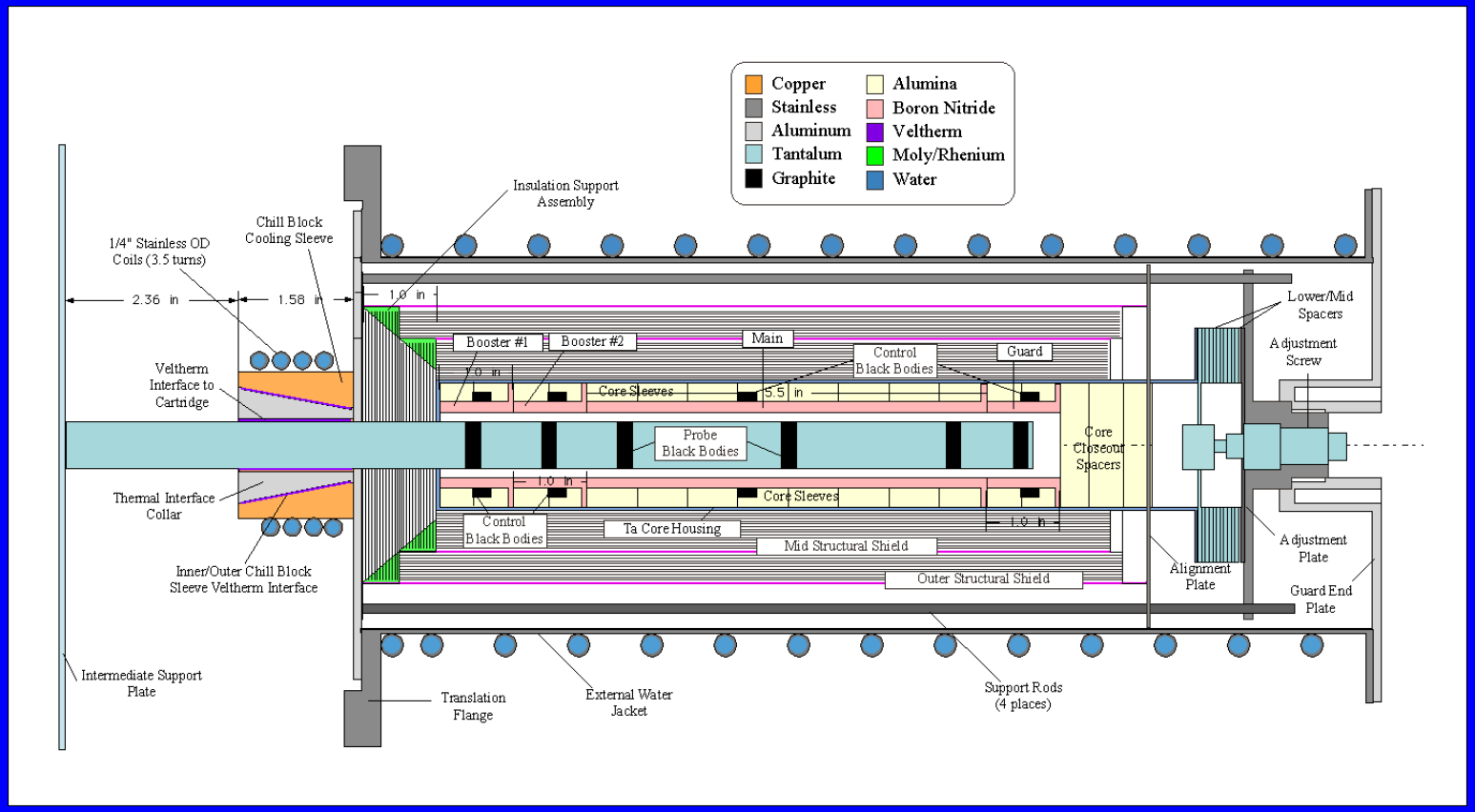

Quench Module Insert (QMI) Design Layout

QMI Thermal Analysis and Design Methodology

- *Modeling via TRASYS II, SINDA/G, and SINDA85*
  - *One overall axi-symmetric SINDA/G model (>5000 nodes) per Unit*
    - *Easily reconfigured for any translation position via user constants*
    - *Detailed component level temperature summary tables and plots generated for each case*
    - *User defined sinroutines for helical heat transfer coefficient, uniform power distribution, summary tables, plot files*
  - *Three TRASYS II models (translatable bore, jacket, and PCD)*
    - *Easily reconfigured for any translation position or SACA geometry/surface properties via users constants*
- *Preliminary Hot Zone Test Article to verify insulation and thermal performance in a static test condition (heavily instrumented)*
- *Hot Zone Test Article model correlation results and lessons learned are applied to Bread Board and Flight models*
- *Bread Board model correlation results and lessons learned are applied to both the Bread Board and Flight models*

QMI Thermal Analysis and Design Methodology

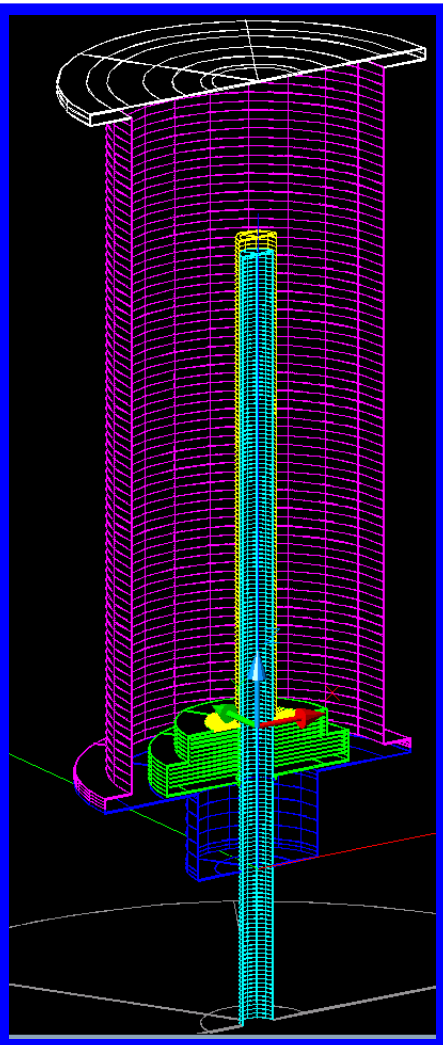

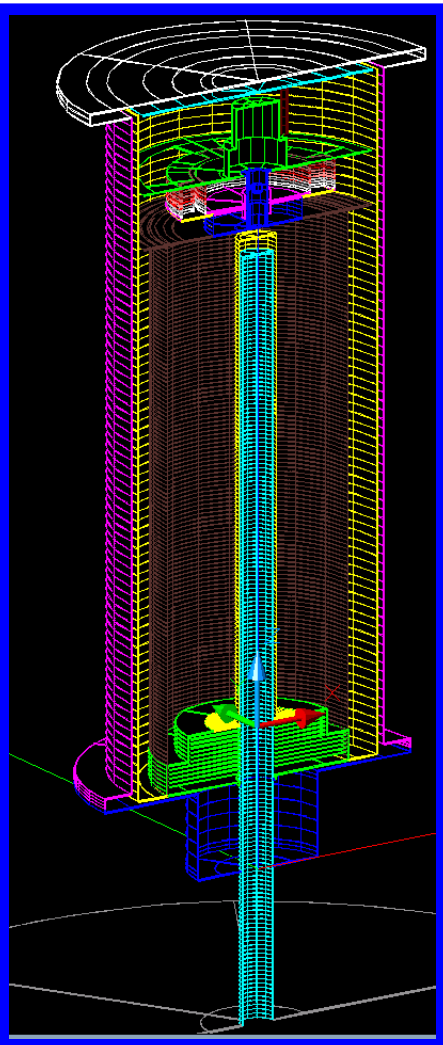

QuickTime™ and a
QuickDraw decompressor
are needed to see this picture.

QMI Thermal Analysis and Design Methodology

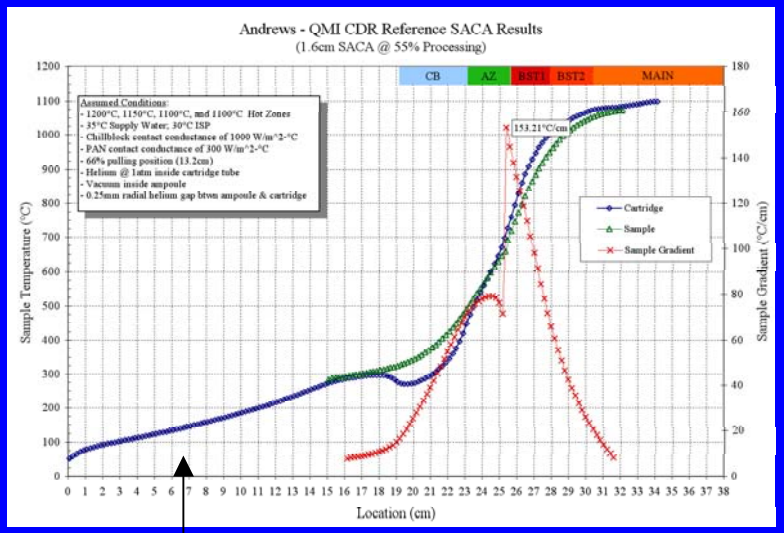

Science Requirements Temperature Plots

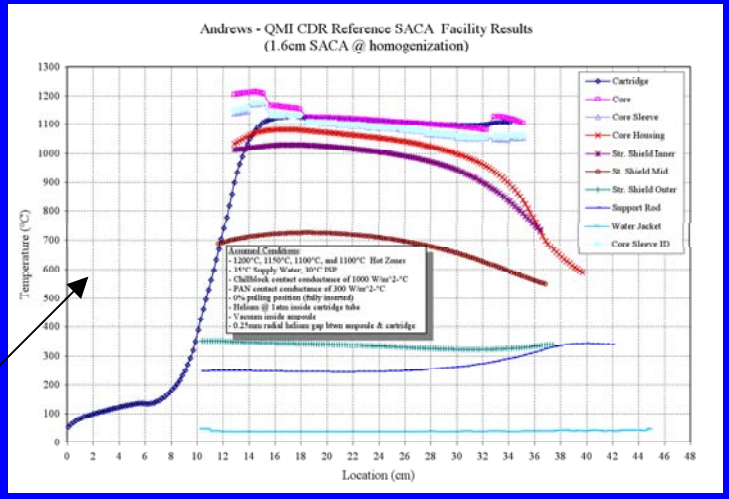

Component Level Temperature Plots

Updated Thermal Model Results for Heater Control Temperatures at 1200 °C, 1150 °C,1100 °C, 1100 °C

BOUNDARY CONDITIONS

Cartridge Position: 0.00cm (fully inserted; Refrence SACA with pure Aluminum Sample)

Hot Zone Settings:			Coolant Water Settings:		
Booster #1 Temp :	1200	°C	Chill Block Inlet:	35	°C
Booster #2 Temp:	1150	°C	Chill Block flow Rate:	50	kg/hr
Main Temperature:	1100	°C	Pan Conductance:	300	W/m ^{2}-°C
Guard Temperature:	1100	°C	Water Jacket Inlet:	35	°C
			Water Jacket flow rate:	40	kg/hr

Temperature Results

Components	Max. (°C)	Min. (°C)	Avg. (°C)	Components	Max. (°C)	Min. (°C)	Avg. (°C)
Quench Zone				**Hot Zone**			
Housing	N/A	N/A	N/A	**Booster #1 Overall**	1213.3	1184.4	1203.8
Shoe	N/A	N/A	N/A	Booster #1 Bore	1202.8	1184.4	1196.5
				Booter #1 Lead	1191.4	107.6	922.0
Chill Block:				Booter #1 Solder	95.8	62.0	71.0
Bore Temp	56.5	50.2	52.6	**Booster #2 Overall**	1164.4	1145.8	1156.7
Inner Sleeve	56.5	49.6	52.2	Booster #2 Bore	1160.2	1148.1	1155.5
Outer Sleeve	40.0	39.0	39.6	Booter #2 Lead	1142.9	104.8	893.5
Water	36.6	35.0	35.9	Booter #2 Solder	93.6	61.6	70.2
				Main Overall	1124.3	1073.3	1105.9
Chill Block Plate				Main Bore	1124.3	1080.4	1106.5
Plate	61.4	60.4	60.8	Main Lead	1071.5	105.4	618.8
Bore	61.4	N/A	N/A	Main Solder	94.1	61.7	70.4
Chill Block Interface	61.3	N/A	N/A	**Guard Overall**	1127.1	1081.6	1113.5
AZ Interface	61.3	N/A	N/A	Guard Bore	1125.0	1096.1	1115.1
Rod Interface	60.4	N/A	N/A	Guard Lead	1068.7	106.9	473.7
				Guard Solder	95.2	61.8	70.7
Adiabatic Zone							
Disks	785.5	299.8	566.2	**Core Sleeves**			
Ints Support Structure	609.3	121.7	406.9	Booster #1	1199	1128	1156
Shield #2	700.2	687.6	693.4	Booster #2	1150	1125	1130
Shield #3	352.3	351.1	351.9	Main	1107	1045	1079
Core Housing	1013.9	N/A	N/A	Guard	1099	1038	1051
Guard Zone Closeout				**Core Housing**			
Adjustment Plate	448.1	397.8	427.5	Overall	1081	557	966
Adjustment Screw	438.3	426.2	433.8	Booster #1 Area	1078	1034	1060
Lower Spacer	506.6	483.7	495.2	Booster #2 Area	1081	1080	1081
Mid. Spacer	468.3	457.8	463.6	Main Arrea	1078	949	1034
Top Plate Closeout	61.9	59.4	60.6	Guard Area/Flange	937	557	671
Inner Closeout Spacer	1032.9	896.4	915.4				
Mid Closeout Spacer	749.7	738.3	743.9	**Structural Shields**			
Outer Closeout Spacer	600.8	591.5	596.9	Layer #1 (inner)	1030	737	964
Devo Plate	459.4	422.3	449.5	Layer #2	725	550	678
Core housing Intf.	556.9	N/A	N/A	Layer #3 (outer)	352	322	336
Ext Water Jacket				**Support Rods**			
Cylinder	55.9	36.3	38.9	Rod #1	343	244	273
Flange, CB side	59.1	59.1	59.1	Rod #2	343	244	273
Flange, Guard side	59.3	59.2	59.3	Rod #3	343	244	273
Water	38.6	35.2	36.8	Rod #4	343	244	273
CB Plate Intf	59.1	N/A	N/A				

Heater Wire Informations

Heater Wire Losses (W)		Heater Wire Currents (Amp)	
Booster #1	1.1	Booster #1	3.37
Booster #2	0.2	Booster #2	1.62
Main	0.2	Main	2.11
Guard	0.1	Guard	2.16

Component Level & Housekeeping Summary Tables

QMI Bread Board Testing and Instrumentation Approach

- *HZTA Testing focused on determination of insulation performance and verification of heat flow mapping (losses, contact coefficients)*
- *Bread Board focused on overall insert performance, chill block performance, hot zone control, and heat flow mapping*
  - *Furnace instrumentation placed to map the flow of heat from the heaters at various areas to obtain a total energy balance and evaluation of the system performance*
  - *Overall energy balance was obtained real-time by adding calculations to the data system for coolant loops to compare to power draw*
  - *Heat flow between components was verified by measuring temperature at the components know conductive heat flow paths*
  - *Detailed understanding of zone-to-zone interaction as a function of set points was required. Needed to assess what actual average bore temperature was obtained for a given zone's set point*
  - *Assess the ability to maximize the booster#1 set point temperature and maintain control of booster#2 to maximize gradient capability*

QMI Bread Board Testing and Instrumentation Approach

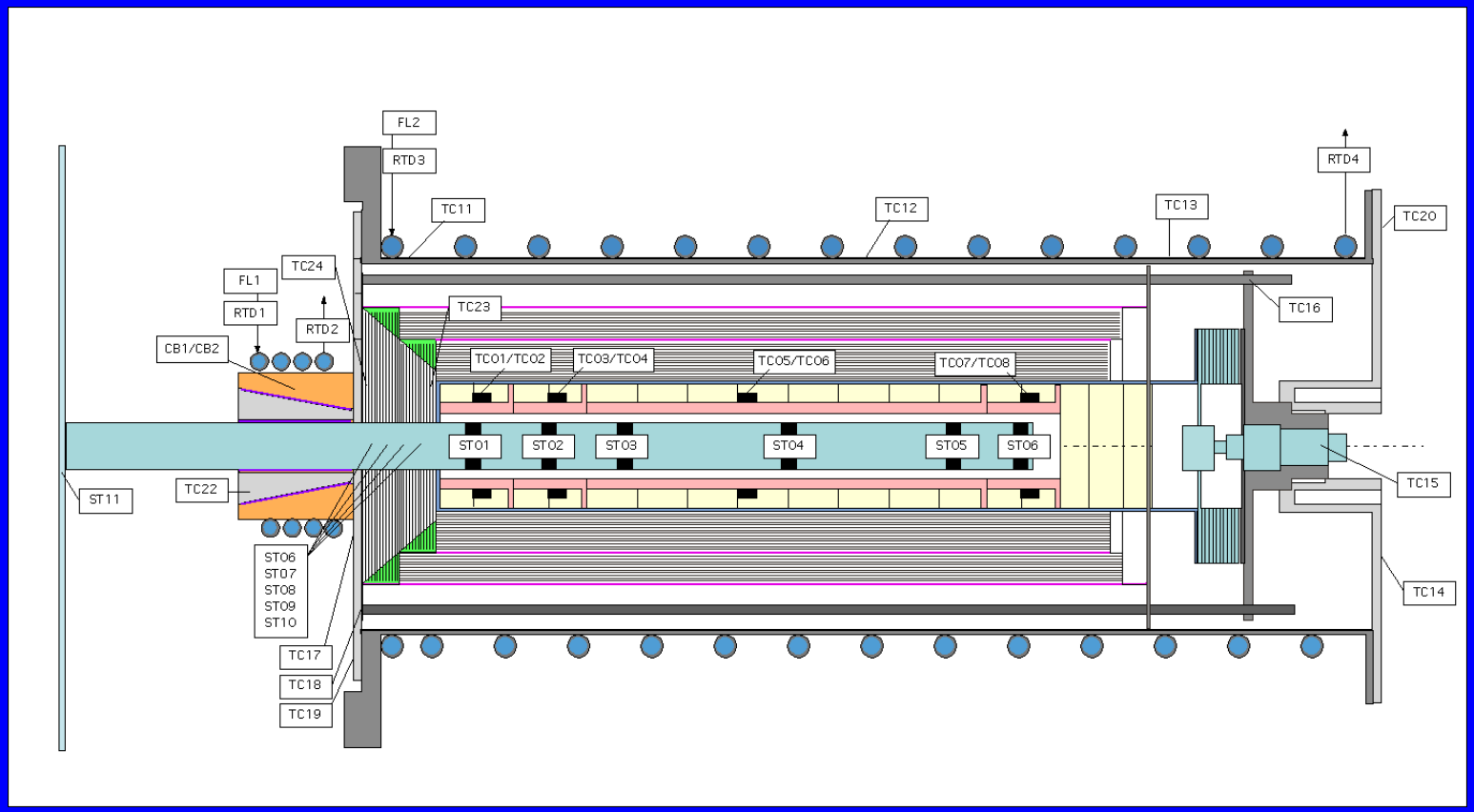

QMI Breadboard Thermal Probe Requirements

- *Provide repeatable and accurate measurements of furnace performance*
  - *Thermal gradient measurement*
    - *Surface properties*
    - *Material thermal conductivity*
    - *Gradient zone instrumentation location and spacing*
  - *Heated zone measurements*
    - *Surface properties*
    - *Heated zone instrumentation location*
    - *Instrumentation isolation*
- *Provide performance measurements while simulating a science sample*
  - *Heater power*
  - *Cold zone heat load*

QMI Thermal Probe Design Parameters

- *Surface properties*
  - *High emissivity preferred*
  - *Stable under vacuum*
- *Materials selection*
  - *Low thermal conductivity*
  - *1400°C processing temperature*
- *Instrumentation*
  - *Location and spacing in the gradient zone*
  - *Location and isolation in the heated zone*
- *Science sample loading*

Preliminary Thermal Probe Designs

- *High Gradient Furnace with Quench (HGFQ)*
  - *1.6cm OD stainless steel probe*
  - *Performance at 1100 °C processing*
    - *169 - 218 °C/cm gradient*
    - *1100W steady state heater power (inert gas furnace)*
- *Hot Zone Test Article (HZTA)*
  - *1.6cm OD stainless steel probe*
  - *Performance at 1200/1150/1100/1100°C processing*
    - *182°C/cm gradient*
    - *342W steady state heater power*
- *QMI PDR Probe Design*
  - *1.3cm OD aluminum nitride probe*
  - *Performance at 1200/1150/1100/1100°C processing*
    - *132°C/cm gradient*
    - *298W steady state heater power*

Design Features for Gradient Measurement

- *1.6cm solid tantalum thermal probe*
  - *Surface emissivity of 0.2*
  - *Low thermal conductivity of 2.8 Btu/hr in °F*
- *Four Type C tantalum sheath thermocouples*
  - *Thermocouple spacing of 0.3 in*
  - *Sheaths run along surface grooves*
  - *Beads positioned at probe centerline with a 30° entry angle*
  - *Beads potted into position with epoxy*

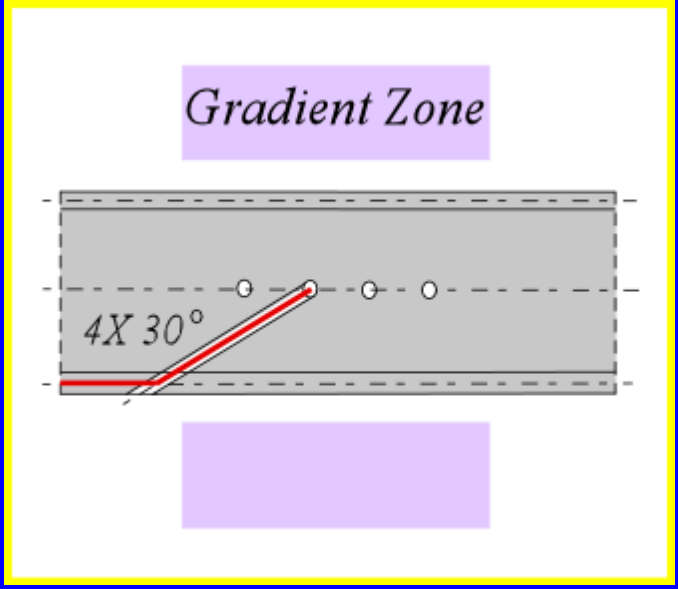

Design Features for Heated Zone Measurements

- *Graphite ring black body sensors*
  - *Surface emissivity of 0.9*
  - *Maximize heat transfer to sensors without compromising heat transfer to probe*
- *Sensors isolated from probe*
  - *Dimpled tantalum shields wrapped to cut radial losses*
  - *Multiple tantalum disks cut axial losses*
- *Type C tantalum sheath thermocouples*
  - *Sheaths run along surface grooves*
  - *Beads potted into graphite rings with epoxy*

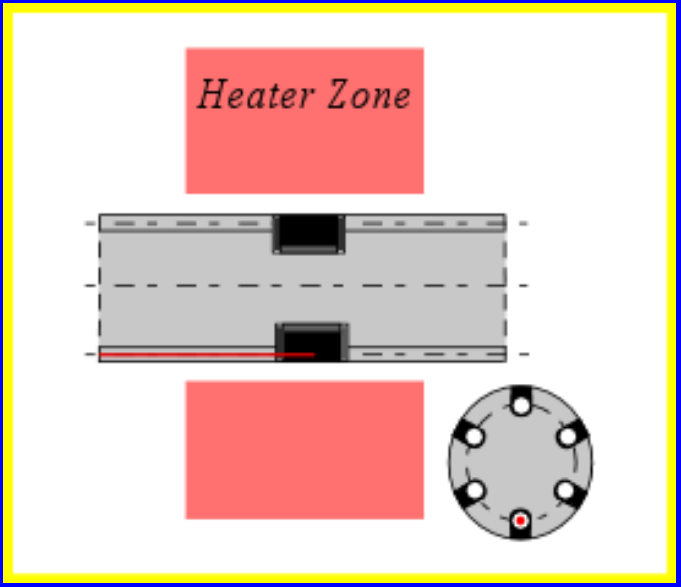

Thermal Gradient Analysis Results

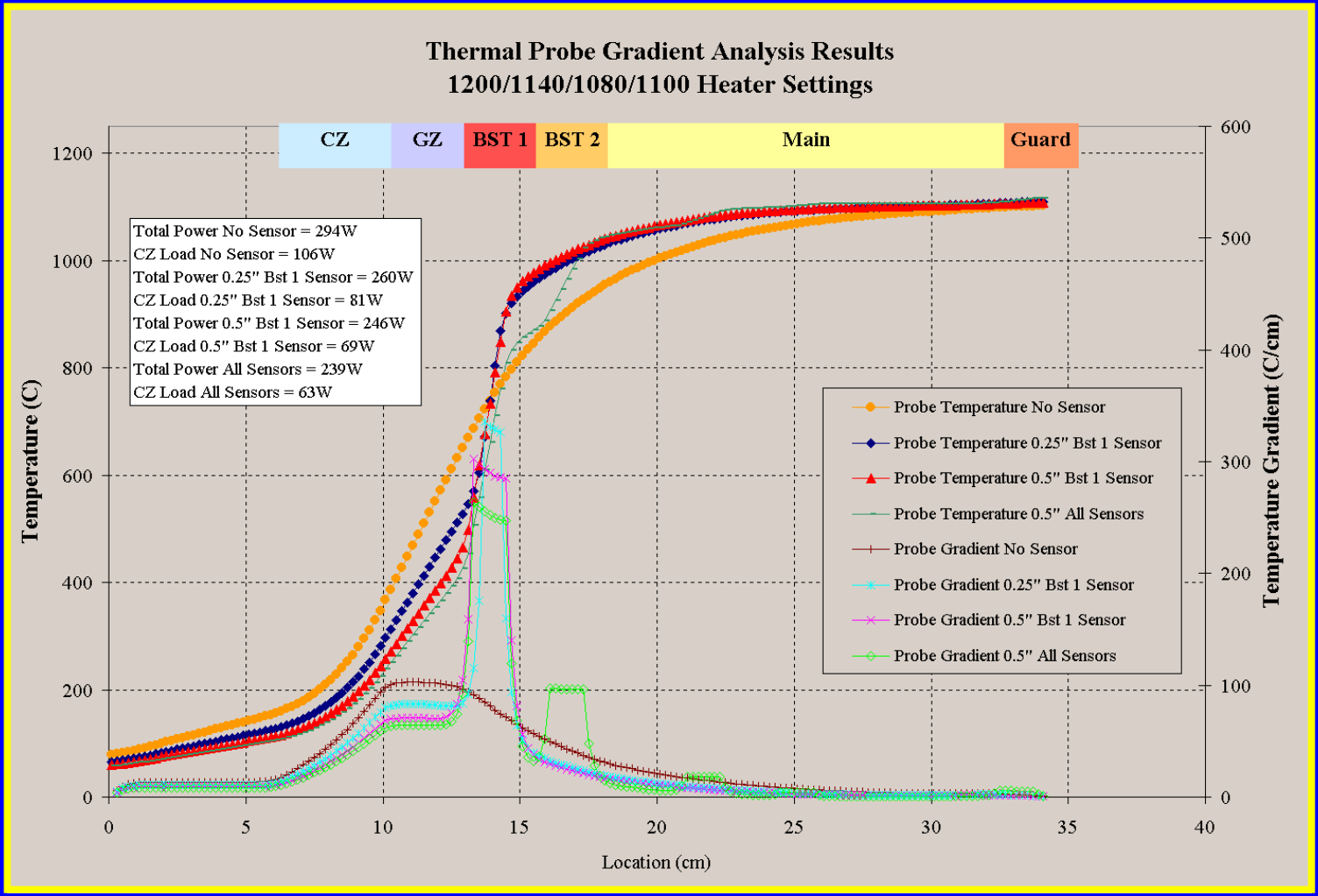

Heated Zone Analysis Results

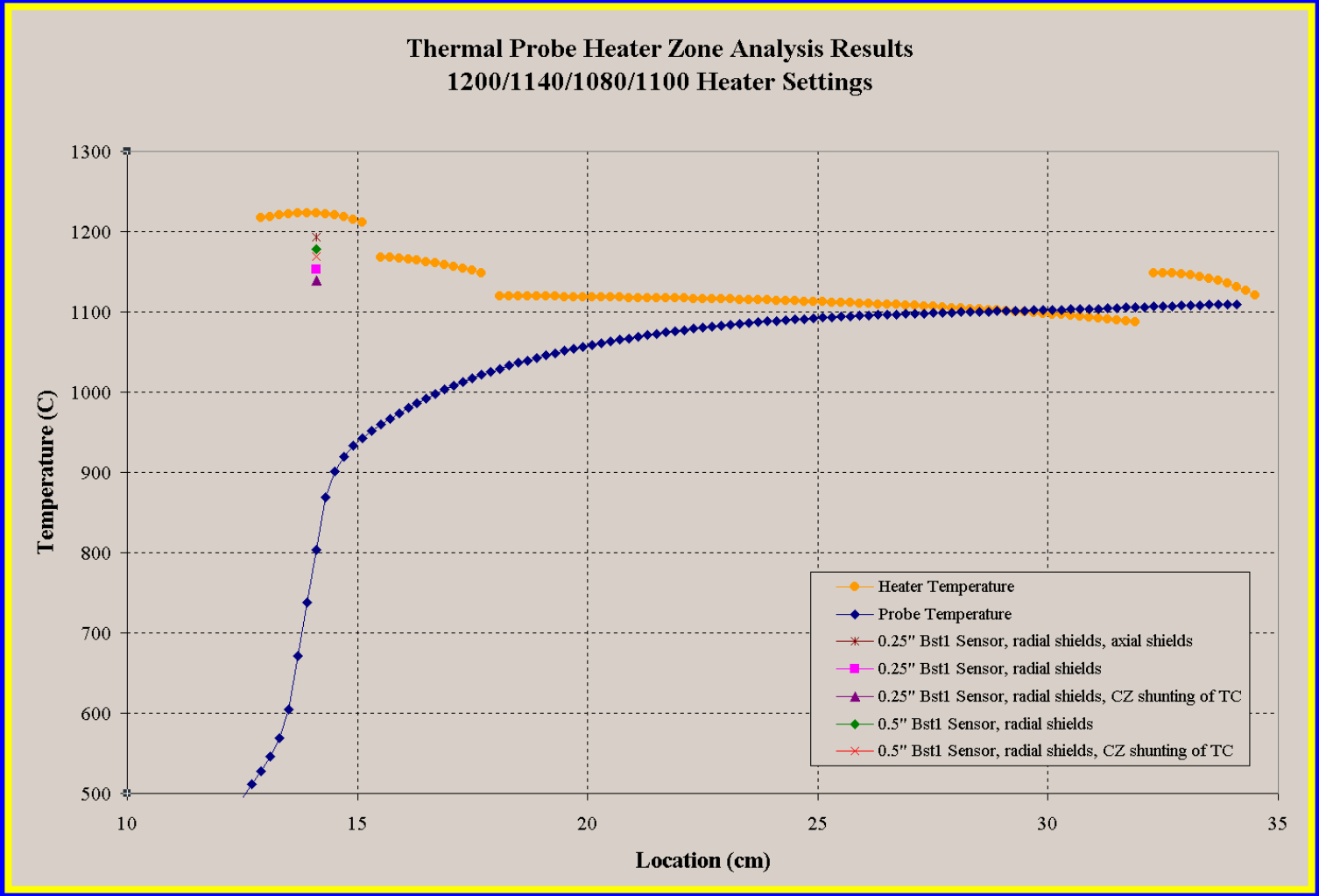

Breadboard Thermal Probe Layout

- *Four centerline thermocouples in gradient zone*
- *Six isolated 0.25 inch blackbody sensors in heated zones*
  - *One sensor in Bst1, Bst2, and guard and three sensors in longer main*
  - *One thermocouple per sensor*

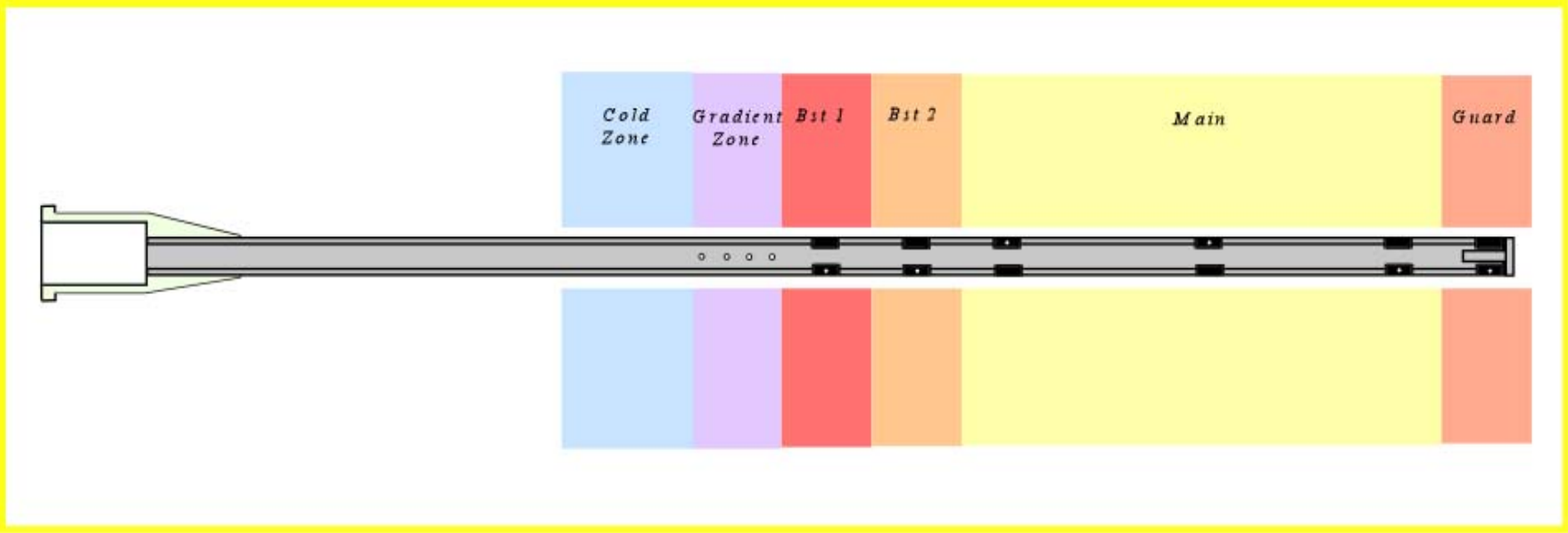

Flight Thermal Probe Requirements

- *Provide repeatable and accurate measurements of heated zone*
  - *Blackbody sensor design concept*
  - *Limited to 12 thermocouples by MSL*
- *Incorporate MSL required safety thermocouple*
- *Maximize probe life*
  - *Eliminate gradient measurement*
  - *Cold zone performance monitored by PT1000s*
- *Minimize weight*
  - *Decrease use of tantalum material*

Flight Thermal Probe Design Features

- *Six 0.5 inch blackbody sensors in heated zones*
  - *Graphite or silicon carbide coated boron nitride rings*
  - *Redundant thermocouples in each sensor except main central sensor*
  - *Sensors isolated from one another by axial shielding*
- *Weight reduction*
  - *Tantalum shaft with thin walled tantalum brackets*
  - *Substitution of stainless steel where temperatures allow*

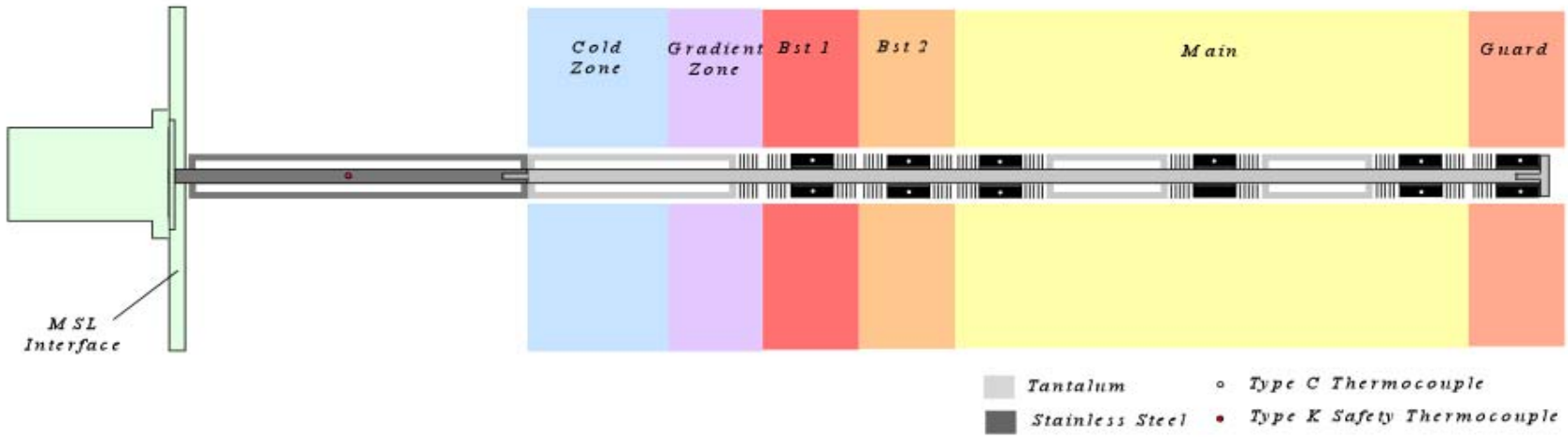

QMI Bread Board Correlation and Performance

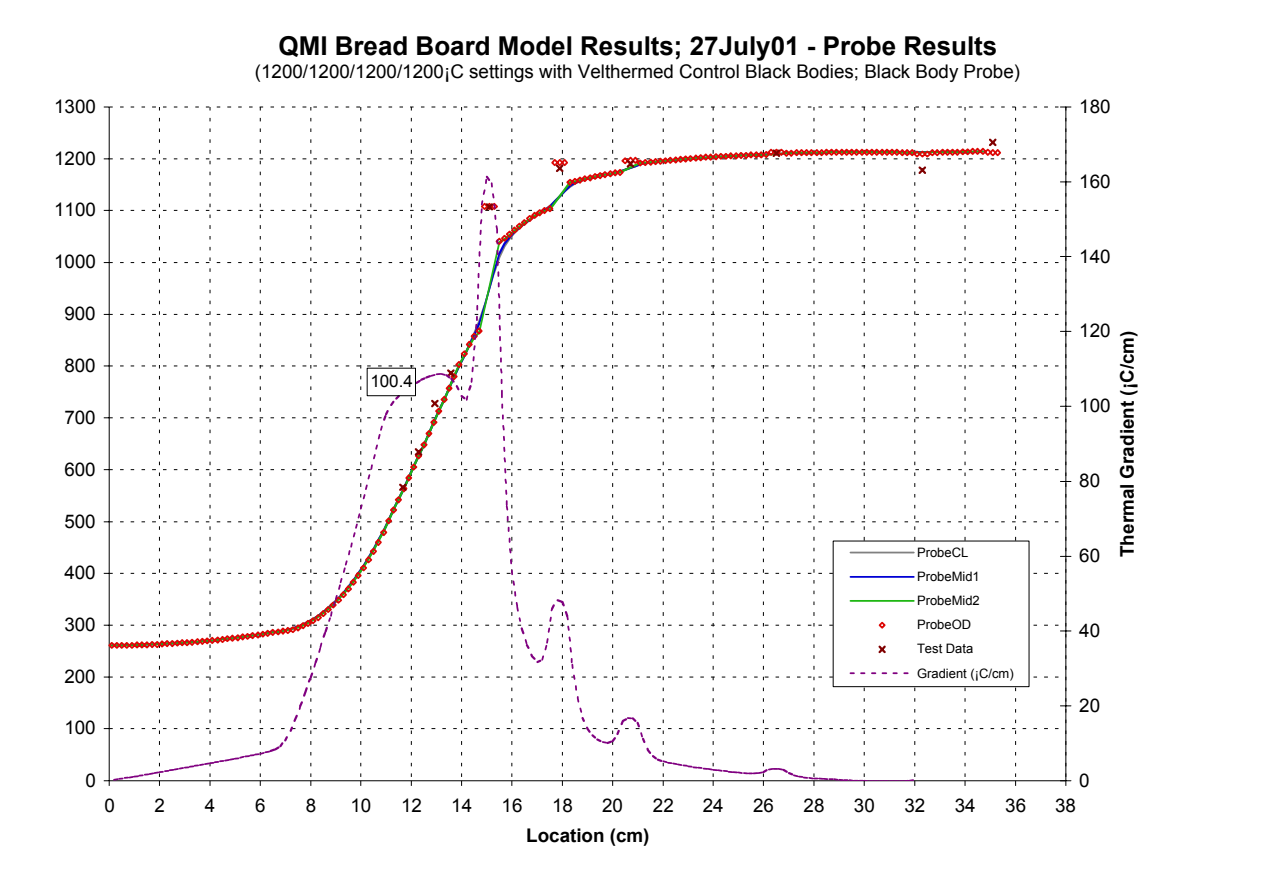

QMI Bread Board Correlation and Performance

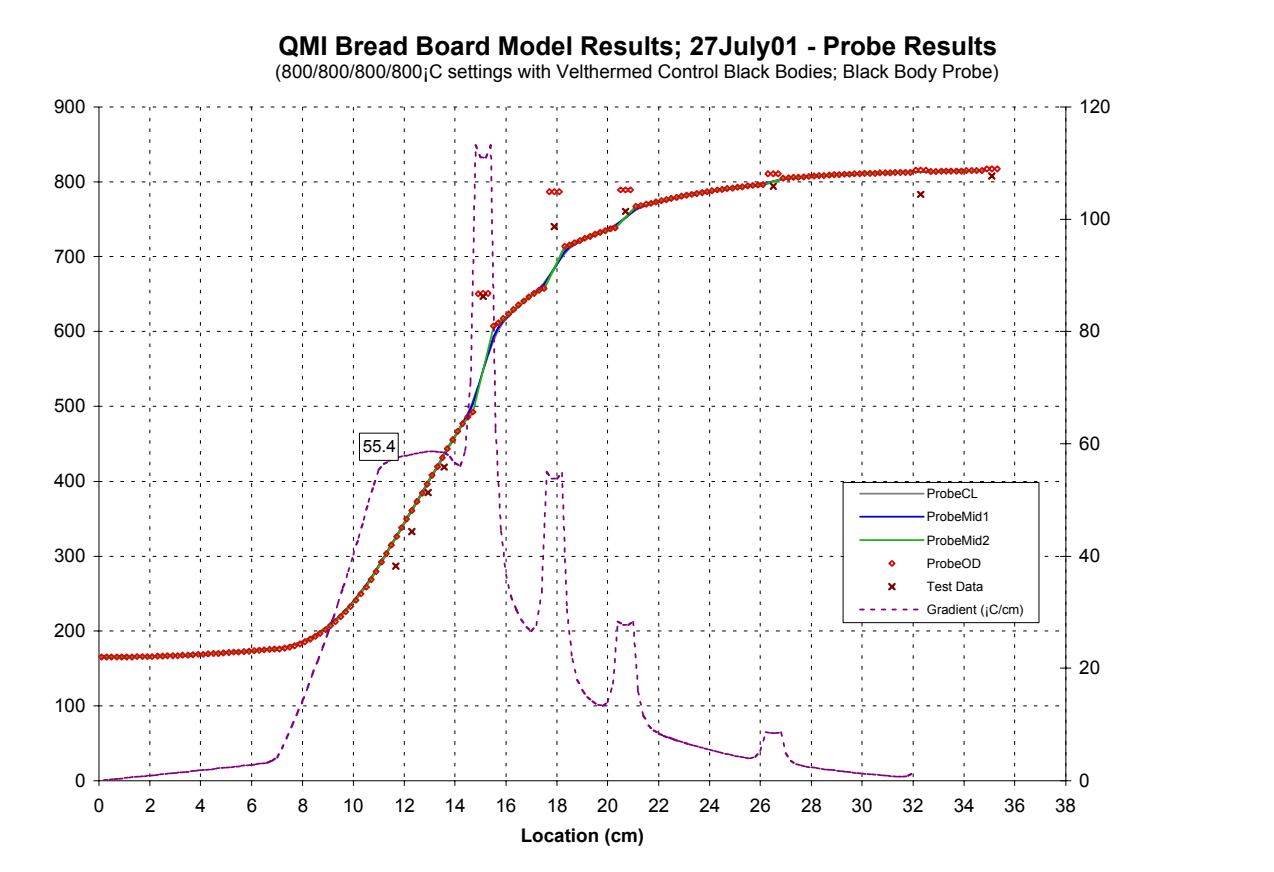

QMI Bread Board Correlation and Performance

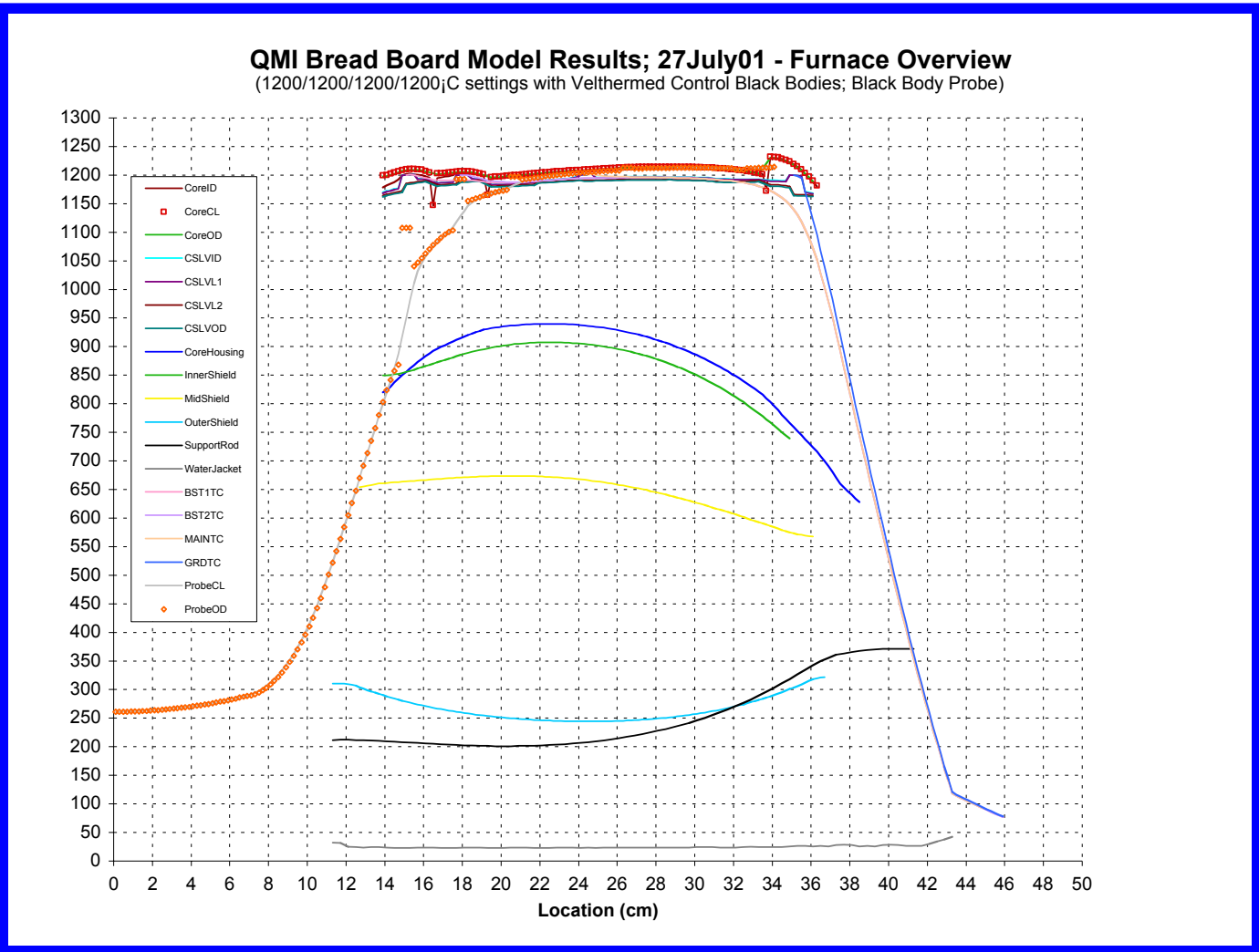

QMI Bread Board Correlation and Performance

Location	ID		05May01 600degC Bbody Cntrl (no chead cooling)	Model Results: bbc00-03l @ 600¡C	Differences	05May01 800degC Bbody Cntrl (no chead cooling)	Model Results: bbc00-03l @ 800¡C	Differences	07May01 1000¡C Bbody Control	Model Results: bbc00-03l @ 1000¡C	Differences	07May01 1200¡C Bbody Control	Model Results: bbc00-03l @ 1200¡C	Differences
CB Outer Sleeve	CB1	degC	26.2	25.8	2%	29.2	28.1	4%	32.47	30.6	6%	35.68	33.2	7%
CB Outer Sleeve	CB2	degC	25.7	25.4	1%	28.5	27.5	4%	31.69	29.7	6%	34.75	32.0	8%
CB Flow	FL1	kg/hr	49.0	50.3	3%	48.8	50.3	3%	49.16	50.3	2%	49.03	50.3	3%
WJ Flow	FL2	kg/hr	38.5	38.3	0%	37.1	38.3	3%	39.00	38.3	2%	38.35	38.3	0%
	FL3	kg/hr	88.8	N/A		86.6	N/A		89.30	N/A		88.54	N/A	
Booster#1 Power	PW1	W	25.3	19.8	22%	50.3	39.7	21%	86.54	67.8	22%	134.03	105.2	21%
Booster#2 Power	PW2	W	11.3	11.7	3%	21.1	21.5	2%	32.11	31.9	0%	42.03	41.9	0%
Main Power	PW3	W	24.2	24.5	1%	35.9	34.1	5%	49.29	43.4	12%	69.55	57.8	17%
Guard Power	PW4	W	16.6	11.8	29%	30.6	22.5	26%	55.94	37.3	33%	90.53	58.2	36%
Total Power	PW	W	77.4	67.8	12%	137.8	117.8	15%	223.87	180.4	19%	336.14	263.0	22%
CB Inlet	RTD1	degC	21.4	21.5	0%	21.4	21.5	1%	21.50	21.5	0%	21.68	21.5	1%
CB Outlet	RTD2	degC	22.0	22.2	1%	22.4	22.5	1%	22.96	22.9	0%	23.60	23.3	1%
WJ Inlet	RTD3	degC	21.5	21.6	1%	21.5	21.6	0%	21.68	21.6	0%	21.90	21.6	1%
WJ Outlet	RTD4	degC	22.0	22.2	1%	22.7	22.8	1%	23.77	23.7	0%	25.52	24.9	2%
	RTD5	degC	26.2	N/A		26.5	N/A		27.00	N/A		27.73	N/A	
B1 Bbody	ST01	degC	423.2	425.5	1%	647.2	650.2	0%	872.80	881.2	1%	1107.35	1106.6	0%
B2 Bbody	ST02	degC	524.7	585.4	12%	740.4	786.8	6%	959.56	989.7	3%	1181.19	1193.0	1%
Main/B2 Bbody	ST03	degC	548.8	590.5	8%	760.4	789.2	4%	972.97	992.2	2%	1190.56	1196.7	1%
Main/Mid Bbody	ST04	degC	579.6	609.5	5%	794.3	810.9	2%	1001.06	1012.3	1%	1210.59	1212.7	0%
Main/Guard Bbody	ST05	degC	580.8	616.1	6%	783.2	815.7	4%	980.67	1013.0	3%	1178.00	1209.1	3%
Guard Bbody	ST06	degC	598.0	618.7	3%	808.0	817.3	1%	1017.54	1014.5	0%	1231.64	1212.1	2%
GZ TCs - CB	ST07	degC	183.4	226.1	23%	286.4	338.0	18%	419.41	459.7	10%	566.51	584.9	3%
GZ TCs	ST08	degC	212.5	240.9	13%	332.6	361.2	9%	477.22	492.1	3%	634.50	627.3	1%
GZ TCs	ST09	degC	245.2	255.9	4%	384.5	384.5	0%	550.55	524.9	5%	727.79	670.2	8%
GZ TCs - BST	ST10	degC	269.2	270.9	1%	418.6	407.9	3%	595.47	557.8	6%	786.42	713.6	9%
SACA Mtg. Plate	ST11	degC	34.2	20.0		42.1	20.0		51.91	20.0		65.05	20.0	
B1 Control	TC01	degC	595.9	599.5	1%	794.6	800.3	1%	993.45	1000.4	1%	1200.04	1200.3	0%
B1 Redunt.	TC02	degC	600.0	599.5	0%	800.0	800.3	0%	999.99	1000.4	0%	1204.94	1200.3	0%
B2 Control	TC03	degC	600.0	600.2	0%	800.0	800.2	0%	1000.00	1000.0	0%	1200.00	1199.9	0%
B2 Redunt	TC04	degC	598.5	600.2	0%	798.5	800.2	0%	997.84	1000.0	0%	1199.32	1199.9	0%
Main Control	TC05	degC	596.1	601.6	1%	796.1	799.2	0%	996.18	999.9	0%	1199.53	1201.0	0%
Main Redunt.	TC06	degC	600.0	601.6	0%	800.0	799.2	0%	999.99	999.9	0%	1200.01	1201.0	0%
Guard Control	TC07	degC	600.0	599.7	0%	800.0	800.5	0%	1000.00	1000.3	0%	1200.00	1199.6	0%
Guard Redunt.	TC08	degC	595.1	599.7	1%	793.6	800.5	1%	990.93	1000.3	1%	1194.10	1199.6	0%
WJ Upper	TC11	degC	29.6	25.3	15%	36.1	28.2	22%	45.45	32.1	29%	58.35	37.2	36%
WJ Mid	TC12	degC	22.5	22.2	1%	23.3	22.8	2%	24.86	23.7	5%	27.30	25.1	8%
WJ Lower	TC13	degC	28.4	30.6	8%	32.3	35.2	9%	37.23	40.8	10%	43.72	47.4	8%
Guard Plate	TC14	degC	32.0	31.5	2%	37.8	36.5	3%	44.88	42.6	5%	53.94	49.7	8%
Adj. Screw	TC15	degC	267.1	249.0	7%	347.7	341.4	2%	429.03	422.2	2%	498.48	494.7	1%
Support Rod	TC16	degC	234.9	305.7	30%	297.1	457.7	54%	352.98	603.4	71%	409.88	739.3	80%
CB Plate 1	TC17	degC	34.7	34.8	0%	44.7	46.2	3%	58.49	62.6	7%	76.83	85.8	12%
CB Plate 2	TC18	degC	48.5	63.8	31%	67.9	100.6	48%	92.09	146.8	59%	117.97	201.2	71%
CB Plate 3	TC19	degC	32.1	25.6	20%	40.3	28.8	29%	51.83	33.0	36%	67.64	38.5	43%
Power Trans.	TC20	degC	38.4	30.8	20%	45.5	35.5	22%	53.54	41.2	23%	63.30	47.9	24%
TIC	TC22	degC	27.8	28.6	3%	31.7	32.4	2%	36.12	36.6	1%	40.19	40.8	1%
Devo/BST	TC23	degC	300.4			462.6			640.10			808.41		
Devo/CB	TC24	degC	226.3			348.5			482.30			609.71		
Furnace Flange	TC25	degC	26.0			28.2			30.51			35.05		
Transl. Bkt.	TC26	degC	29.0			33.0			37.80			44.60		
Total Cooling	Qt	W	55.7	65.8	18%	107.6	112.7	5%	178.27	174.1	2%	270.69	253.7	6%
Chill Block Cooling	Qcb	W	31.5	38.4	22%	57.9	59.5	3%	83.75	82.1	2%	109.48	105.3	4%
Water Jacket Cooling	Qwj	W	24.2	27.4	13%	49.7	53.2	7%	94.52	92.0	3%	161.21	148.4	8%

Summary and Conclusions

- *Current Bread Board testing indicates that the QMI thermal design models and methods are very accurate*
  - *Probe gradient zone temperature results have been used to judge initial furnace positioning measurement and have aided in trouble-shooting 5-8mm offsets of the furnace/probe positioning*
  - *Thermal probe black body zone readings have been used to troubleshoot the temperature control system. Control thermocouple attachment methods have been evaluated based upon the black body temperature readings obtained in the main/guard zones*
  - *One simplified SACA prototype run has shown the ability to produce greater than 90°C/cm thermal gradients in an 11.7mm diameter pure aluminum sample at a 900°C sample processing temperature*
- *Results obtained and design lessons learned from the bread board testing are being "flowed up" to the flight design. The QMI bread board is providing invaluable information on the capabilities and evaluation of the flight design.*
- *Currently retrofitting the control instrumentation for the hot zones*
- *Additional testing is soon to begin and will include quench testing*

Thermal Design Overview of the Mars Exploration Rover Project

Glenn Tsuyuki

Jet Propulsion Laboratory

California Institute of Technology

Pasadena, CA

September 10, 2001

Agenda

- Mission Overview
- Thermal Environments
- Driving Thermal Requirements
- Thermal Design Approach
- Thermal Control Block Diagram
- Thermal Design Description
- Thermal Analysis Results Summary
- Testing Plans
- Issues & Concerns

Flight System Configuration

Mars Exploration Rover

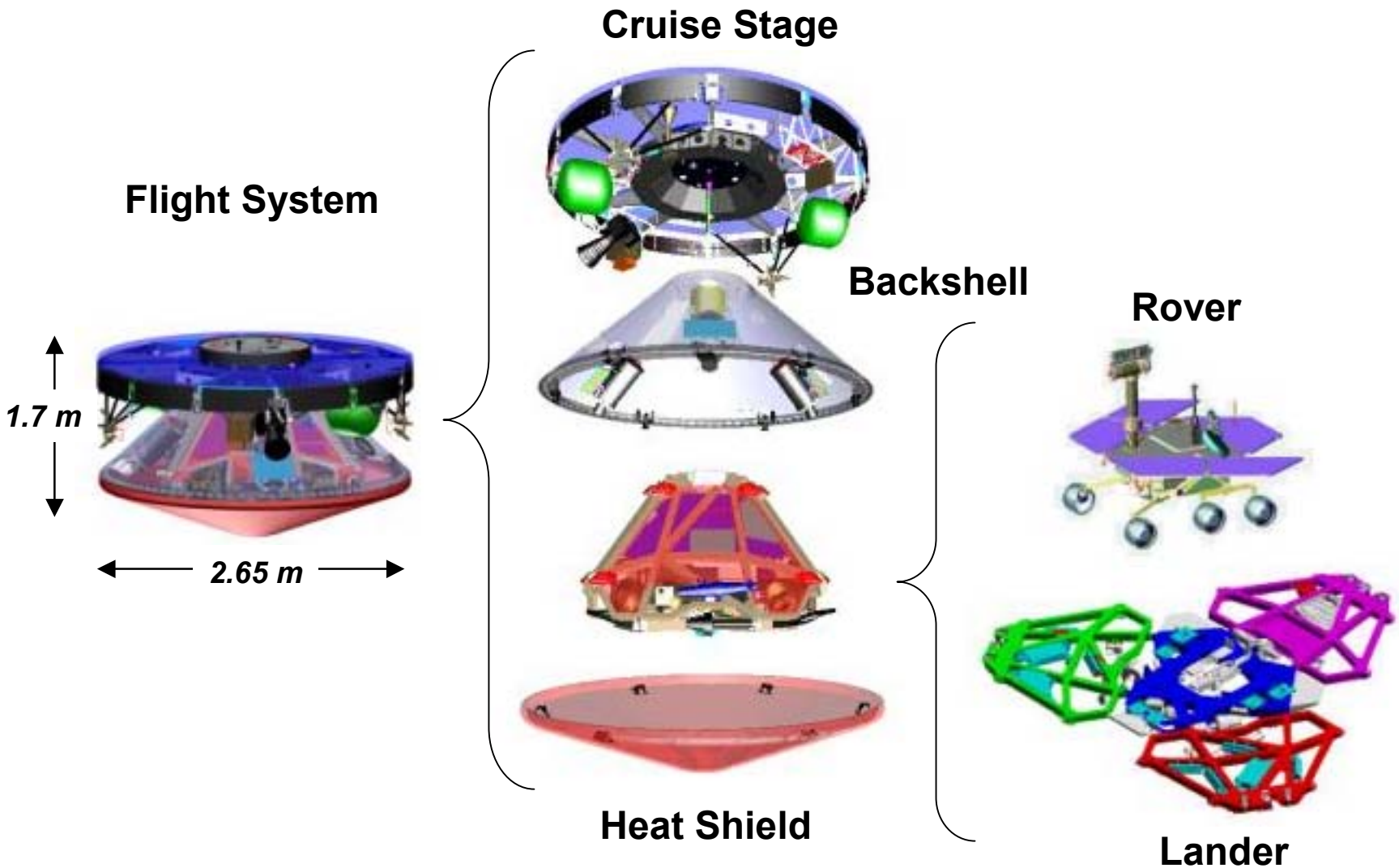

MER-A Cruise Scenario

Mars Exploration Rover

View from Ecliptic North Pole
20 Day Tic Marks

MER-A
Launch Date = 5/30/03
Arrival Date = 1/4/04

MER-B
Launch = 6/25/03
Arrival = 1/25/04

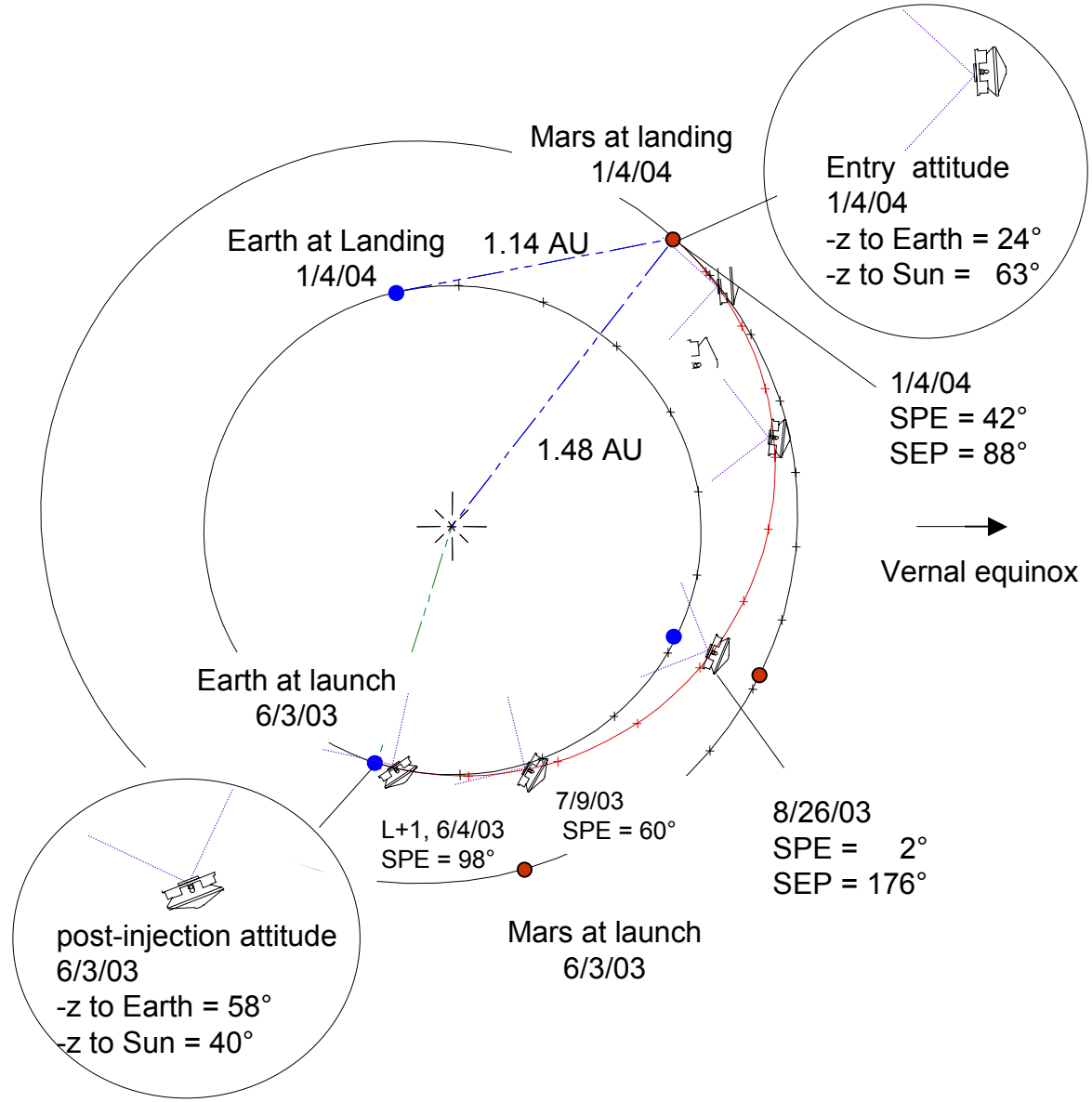

-z axis
- antenna boresight
- panel normal axis
- spin axis

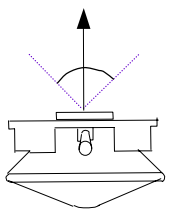

90° cone around -z axis
- ±45° offset antenna
- ±45° panel normal axis

Entry, Descent & Landing (EDL) Scenario

Mars Exploration Rover

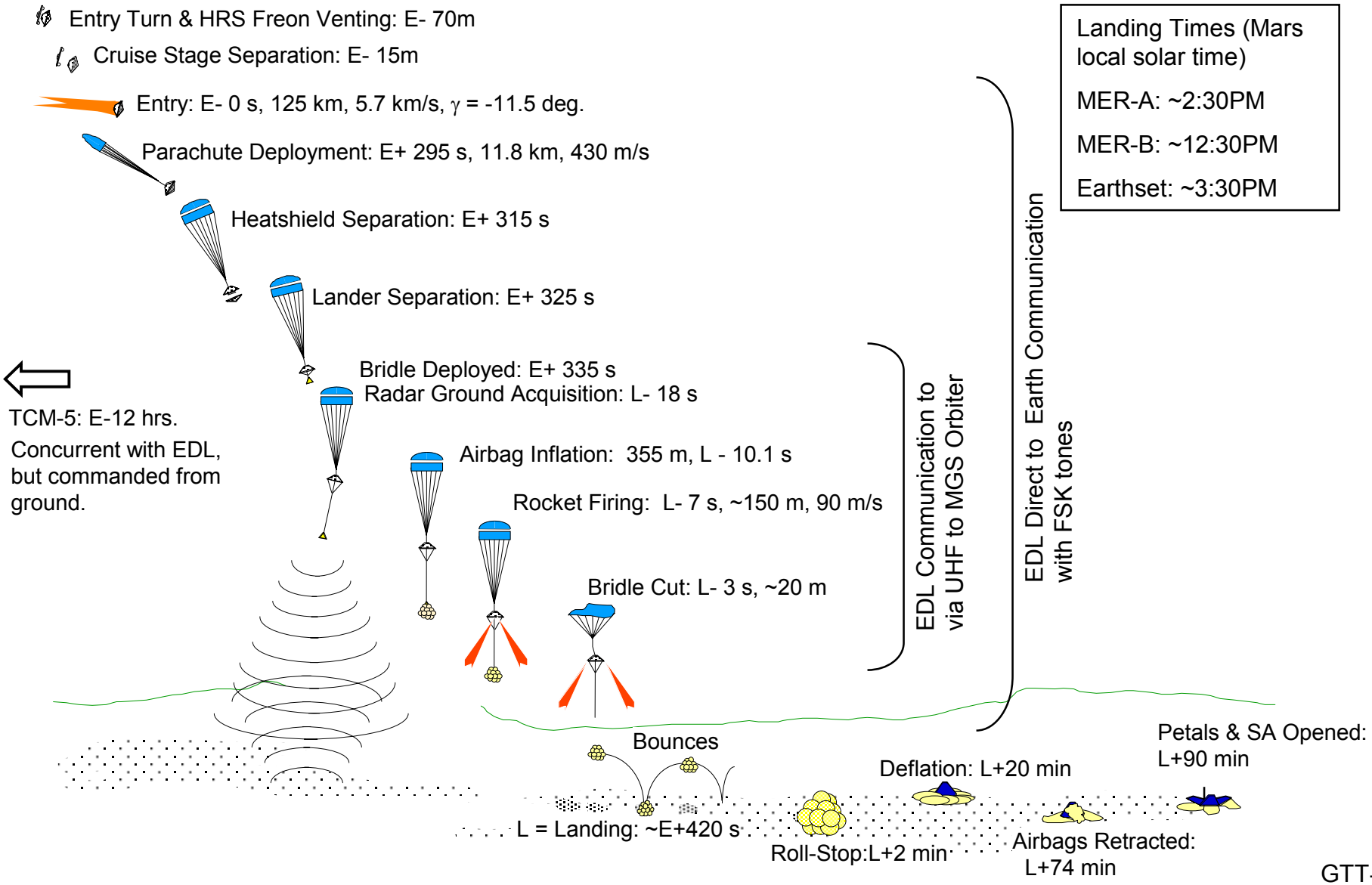

Landing Times (Mars local solar time)
MER-A: ~2:30PM
MER-B: ~12:30PM
Earthset: ~3:30PM

Impact to Egress Scenario

Mars Exploration Rover

Sol 1

Solar Array Deploy
PMA Deploy & Imaging
HGA Deploy

Airbag Retraction / Petal Deploy / Egress Aid Deploy

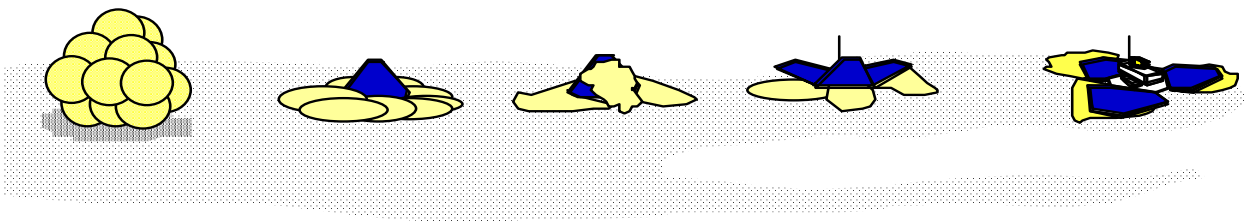

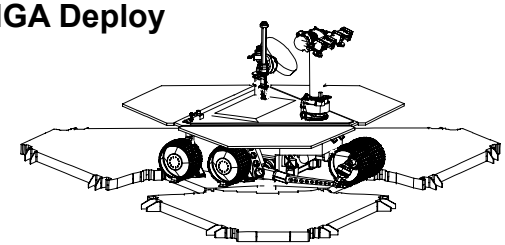

Sol 2-3

Petal / Airbag Adjustments
Pancam/Mini-TES

Lift Rover / Lock Rockers

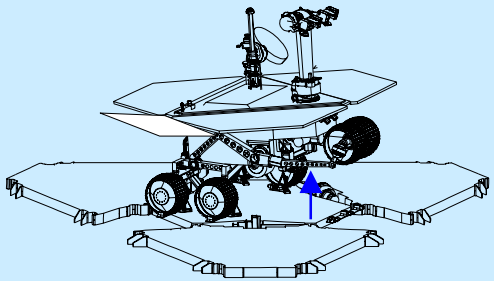

Deploy Rockers

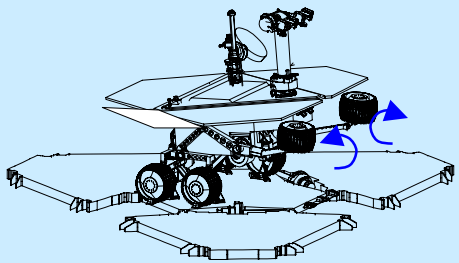

Lower Lift Mechanism & Deploy Bogies

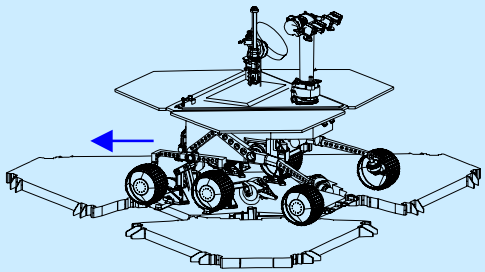

Sol 4

Drive Petals to final Configuration

Release Middle Wheels & Fire 3rd Cable Cutter

Turn in Place

Drive Off Lander Deck

Surface Scenario

Mars Exploration Rover

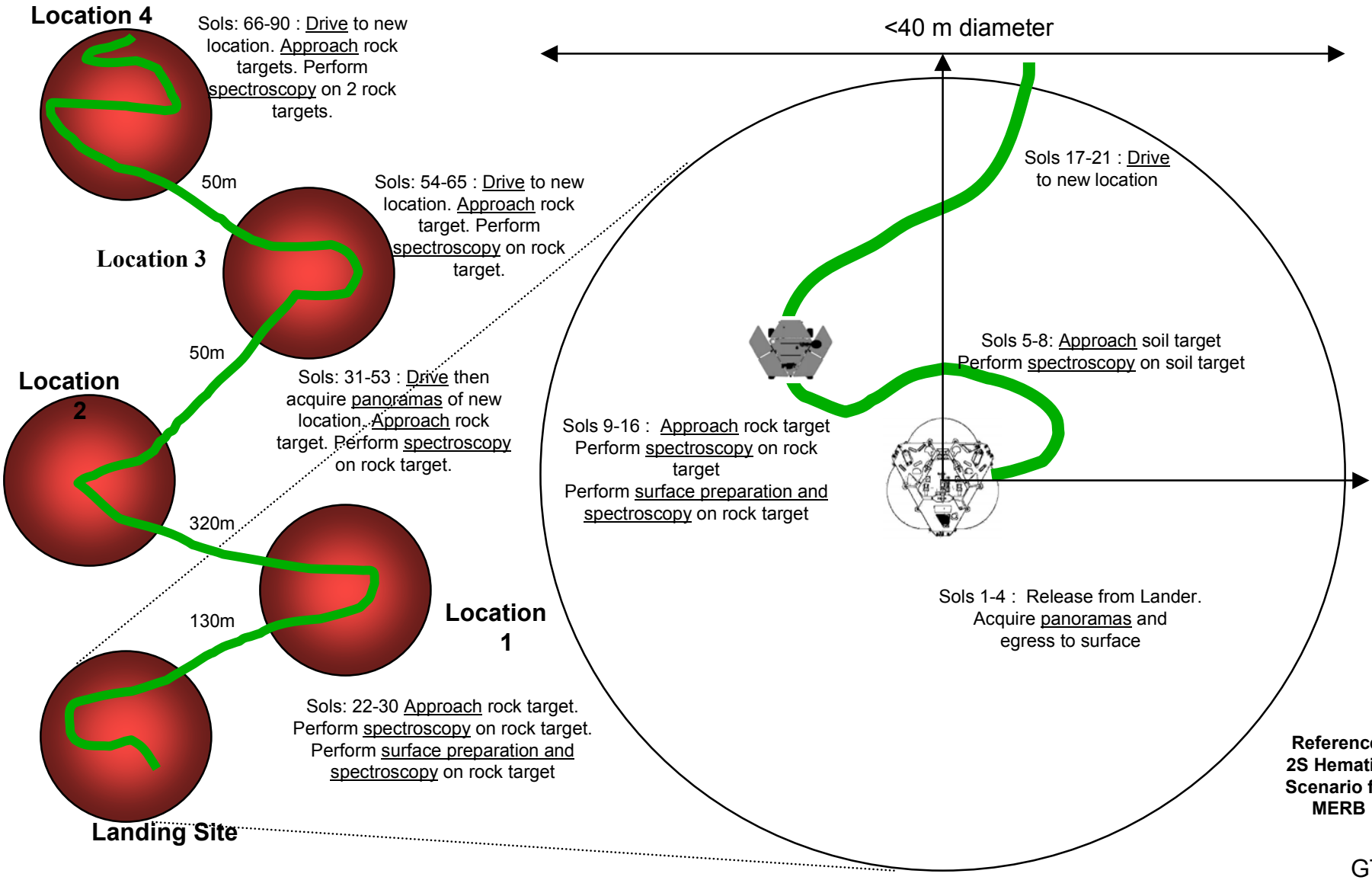

Reference: 2S Hematite Scenario for MERB

Spacecraft Cruise Configuration

Mars Exploration Rover

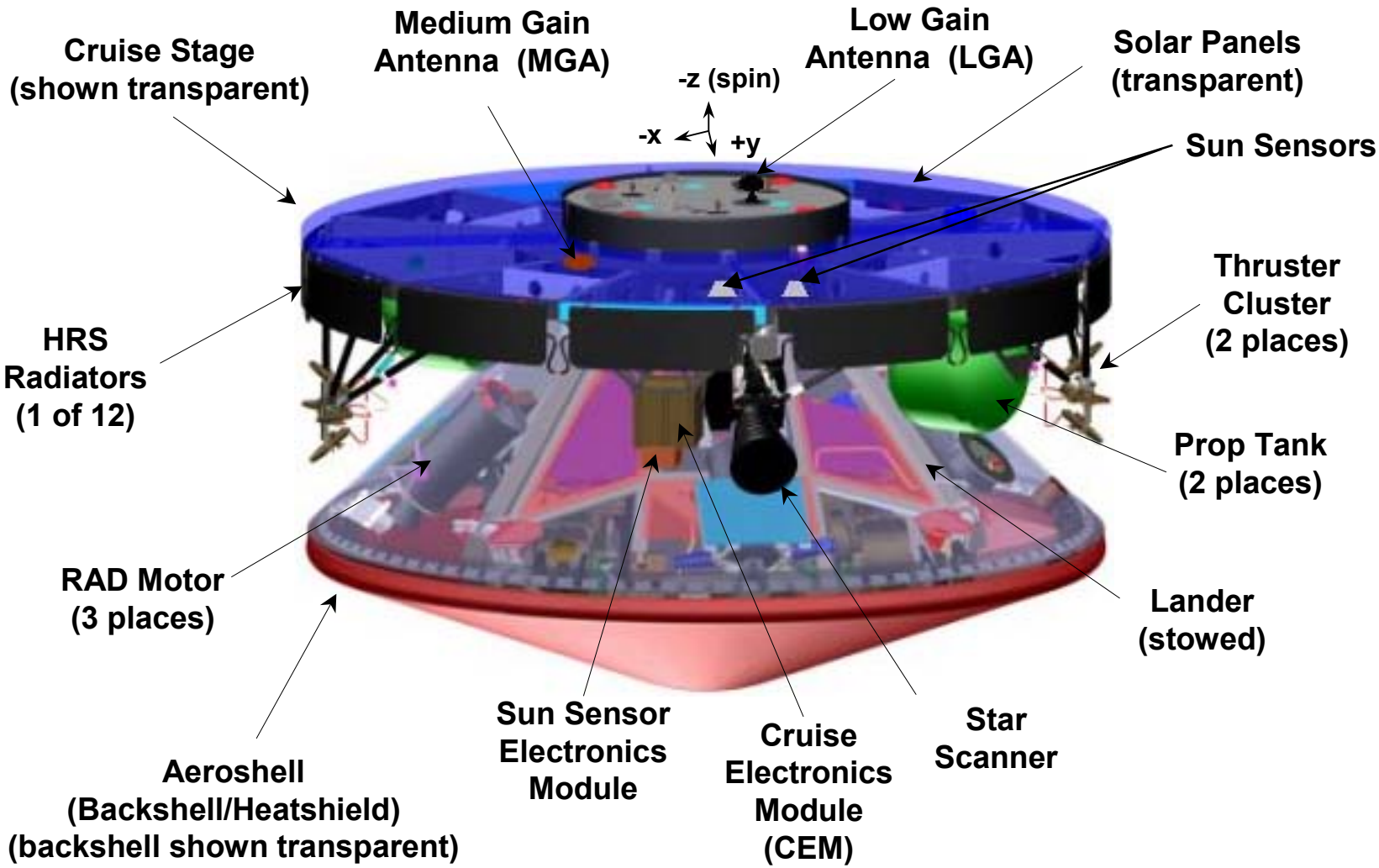

Cruise Stage Configuration

Mars Exploration Rover

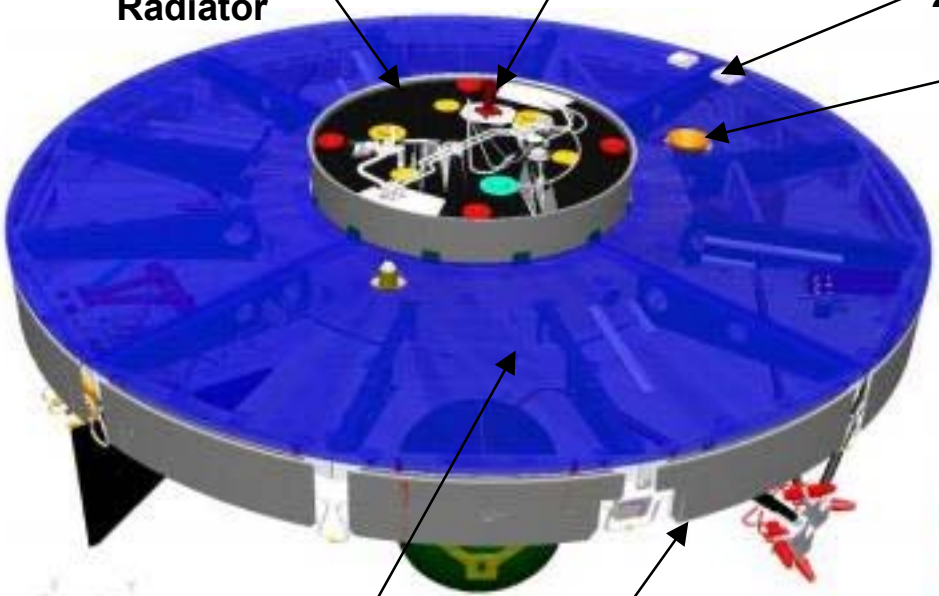

Not shown:
Lighting Suppression Assembly

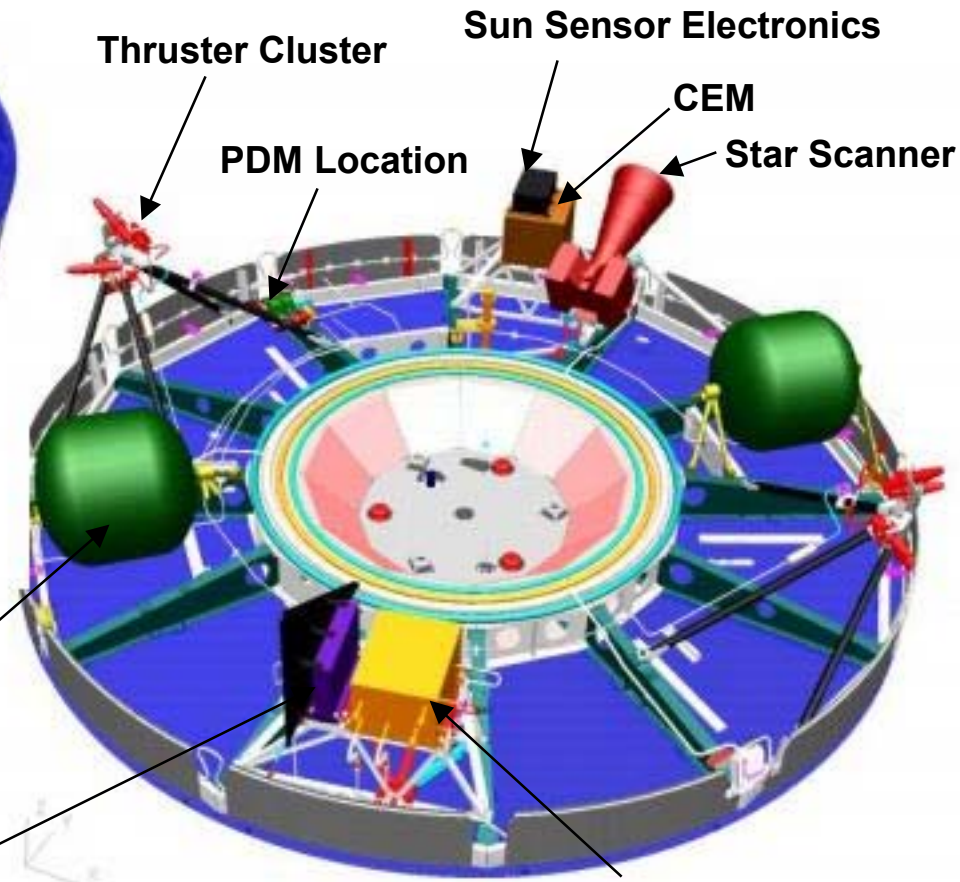

Aeroshell Configuration

Mars Exploration Rover

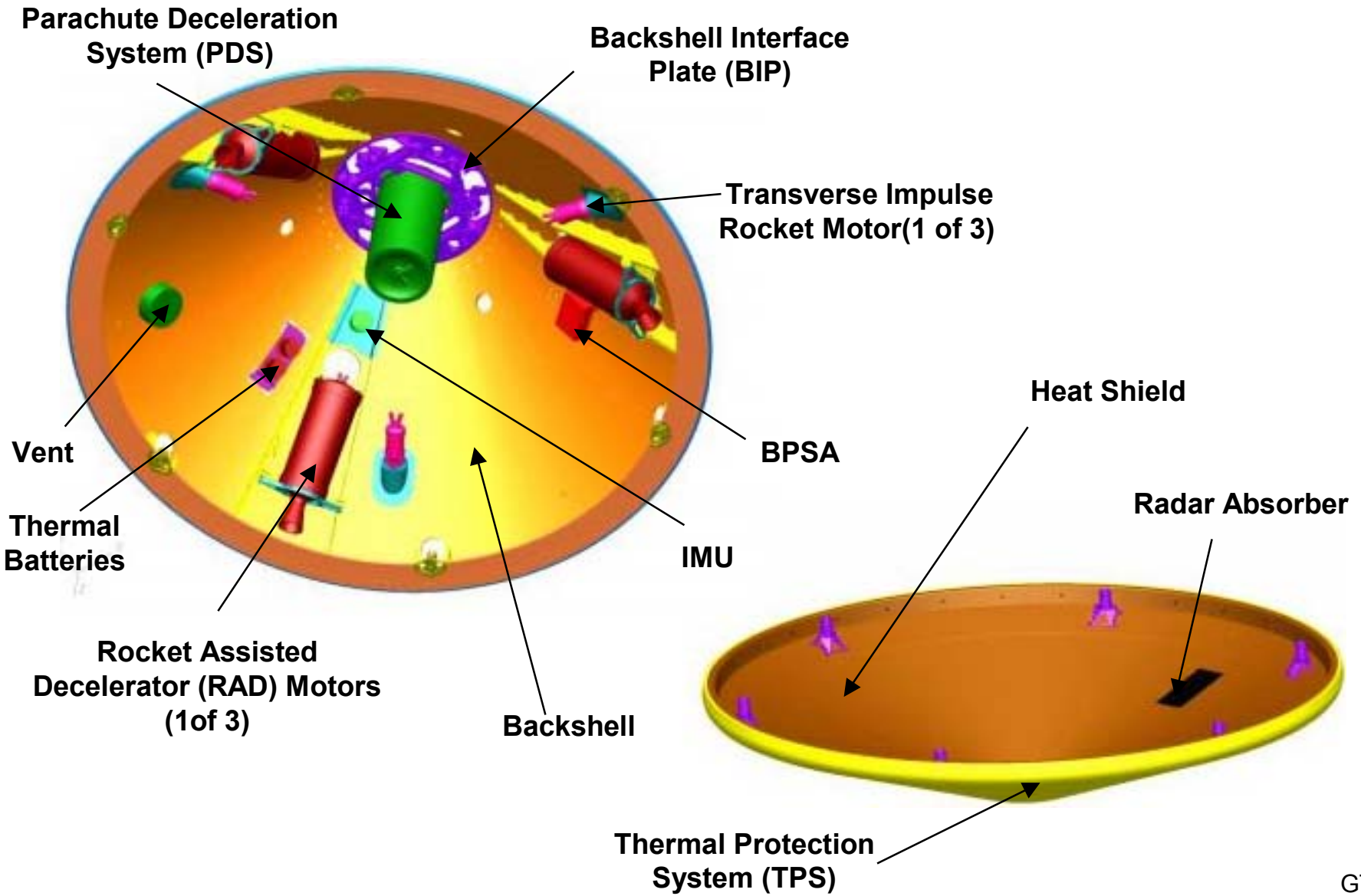

Lander Assembly - Stowed

Mars Exploration Rover

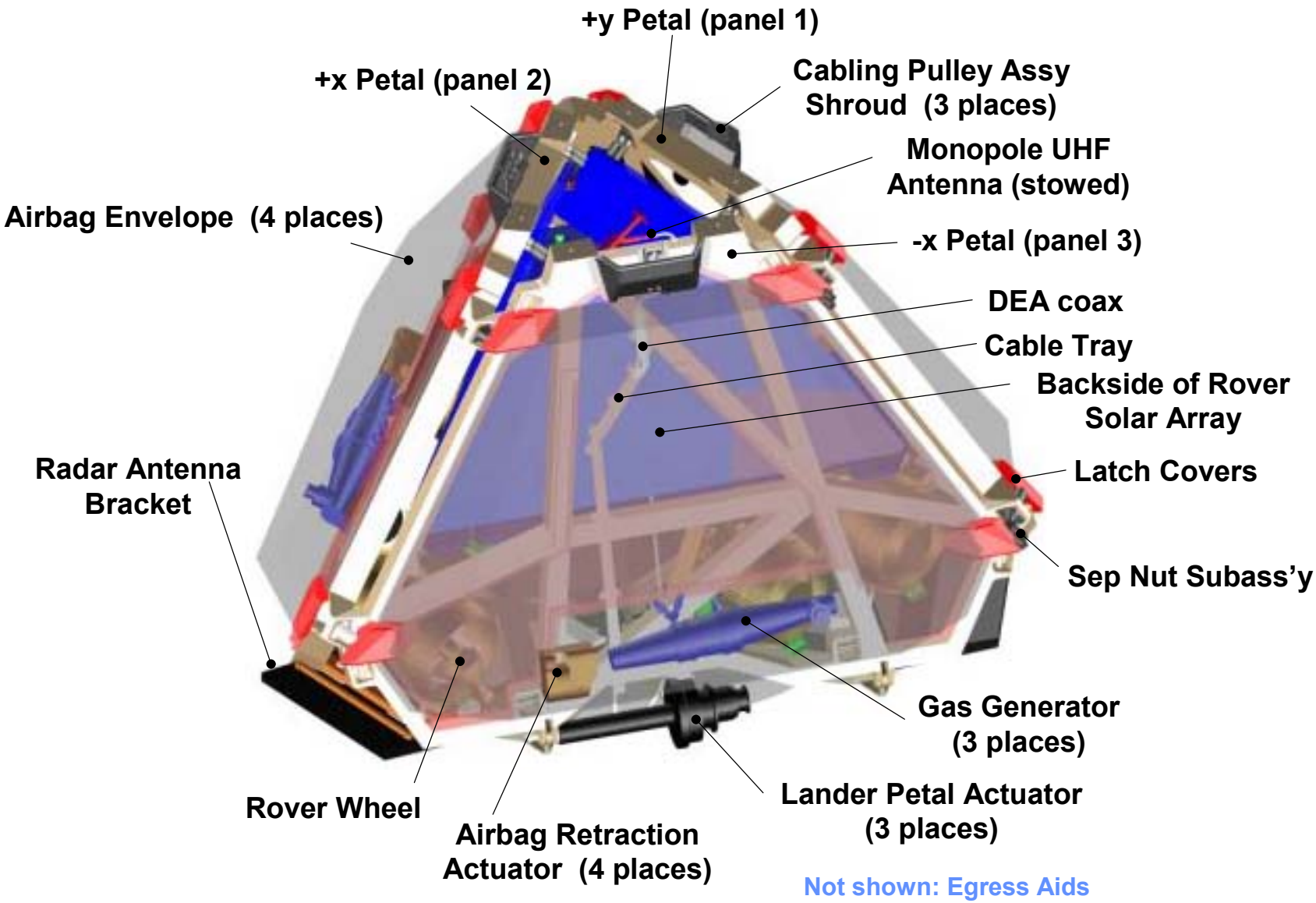

Not shown: Egress Aids

Lander Assembly - Deployed

Mars Exploration Rover

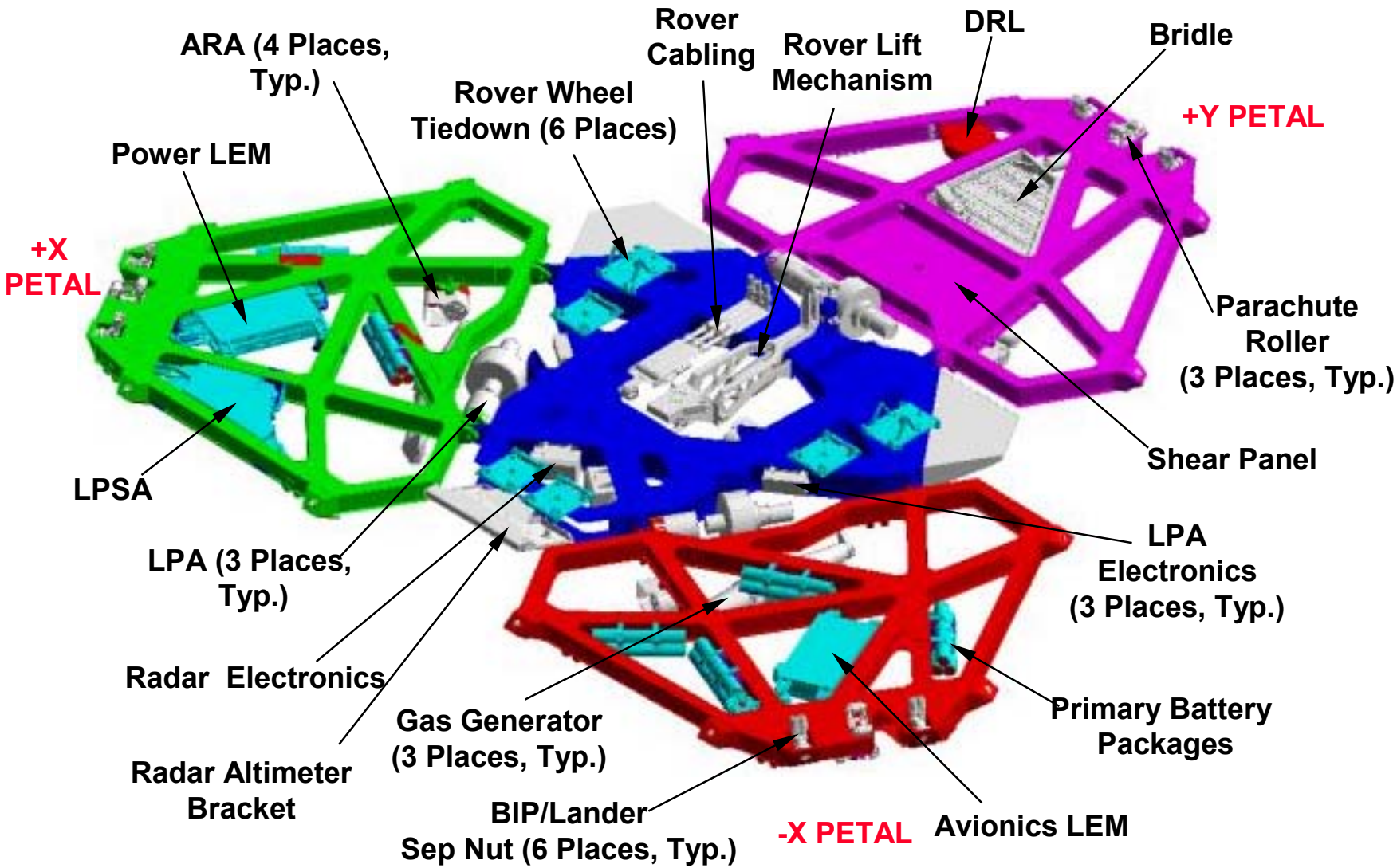

Rover - Stowed Configuration

Mars Exploration Rover

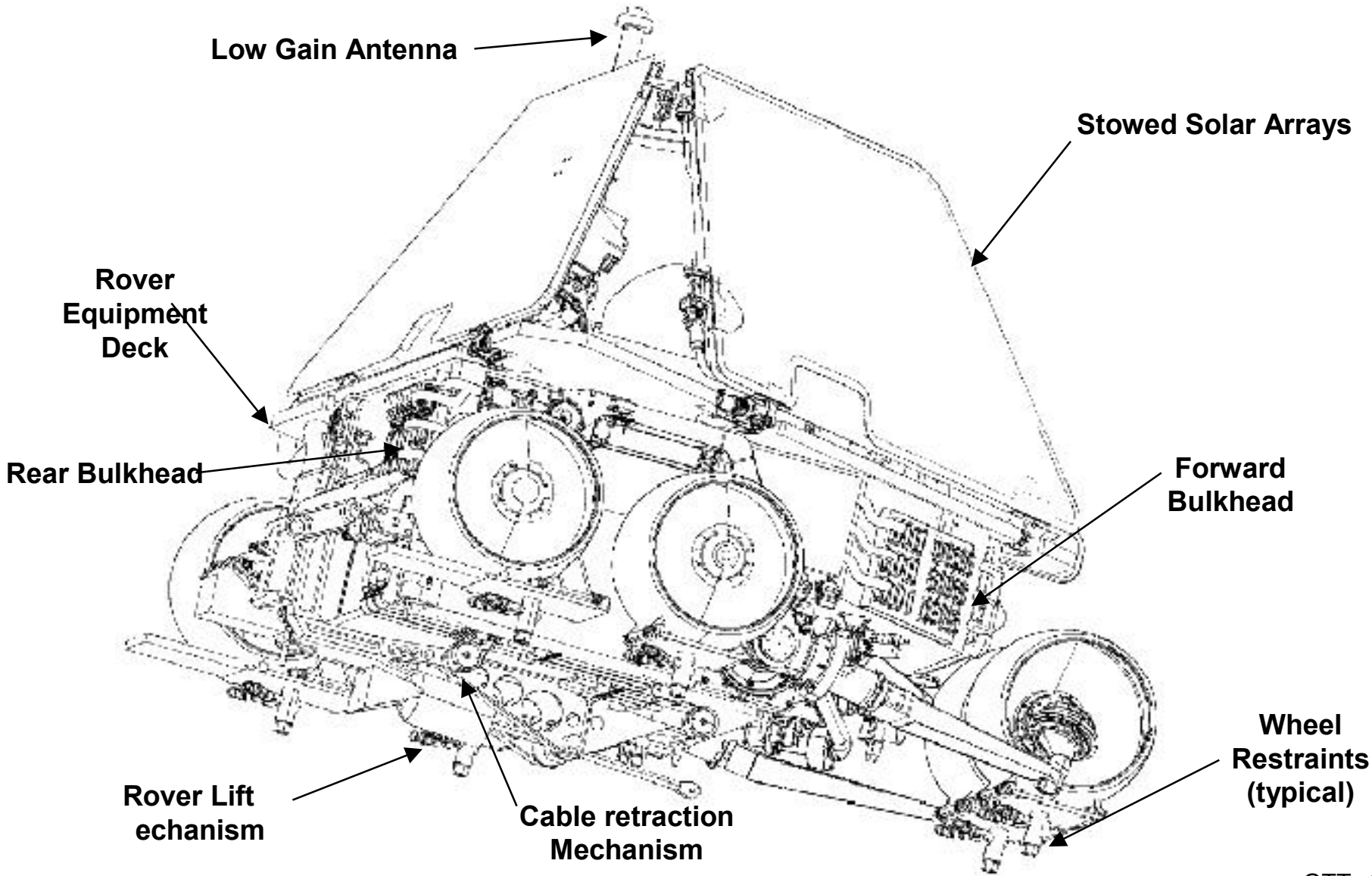

Shaded Isometric Views of the Stowed Rover

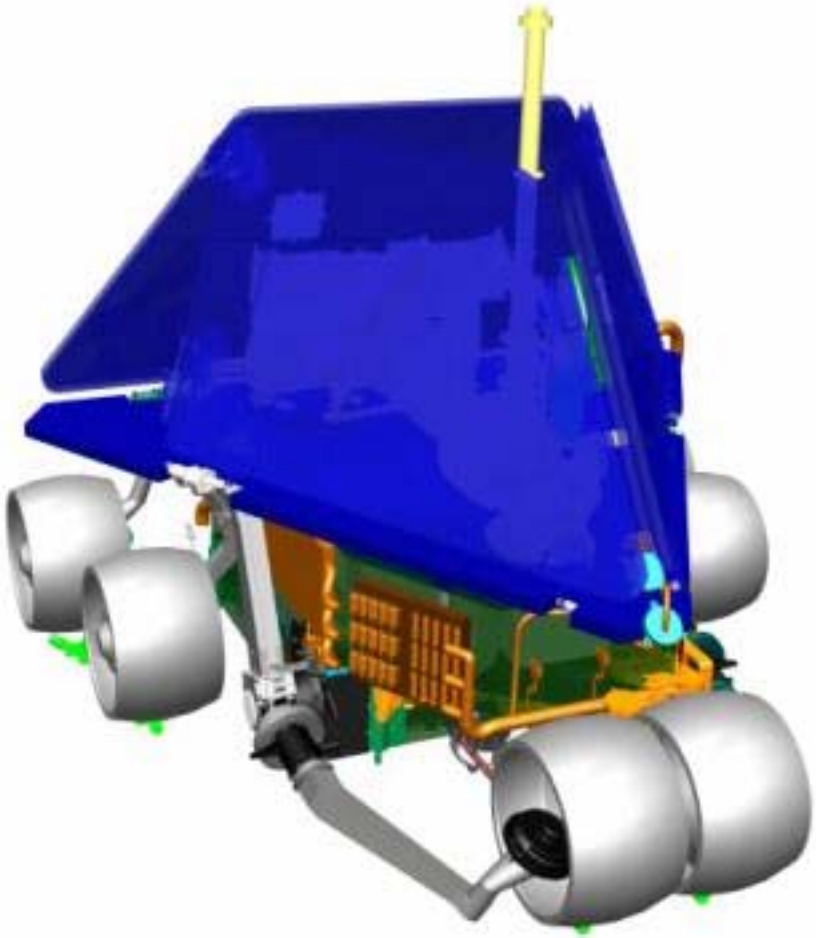

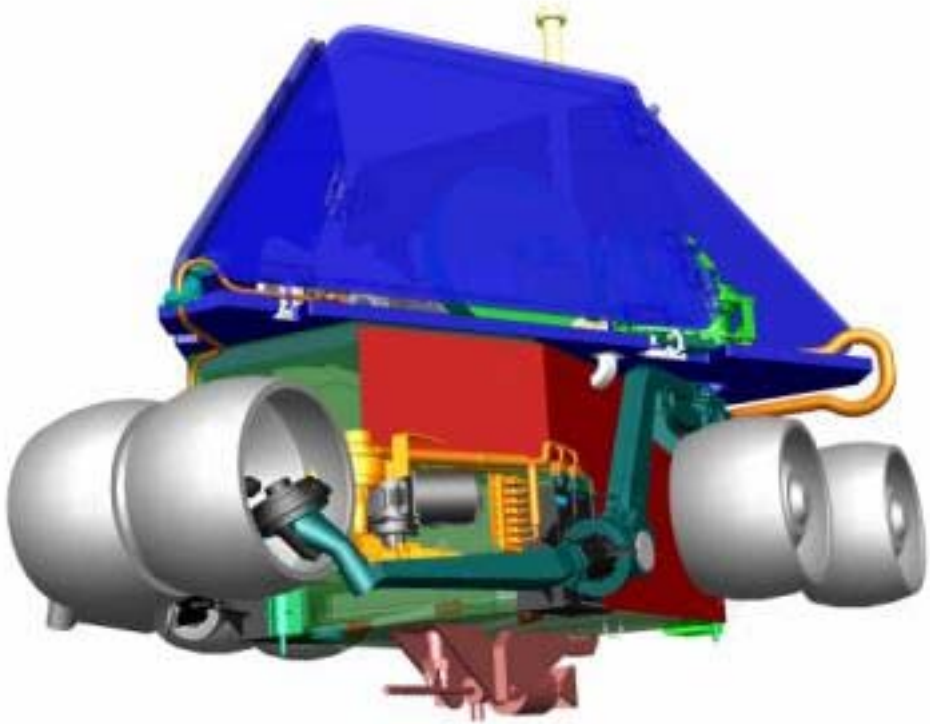

Deployed Rover on the Lander

Mars Exploration Rover

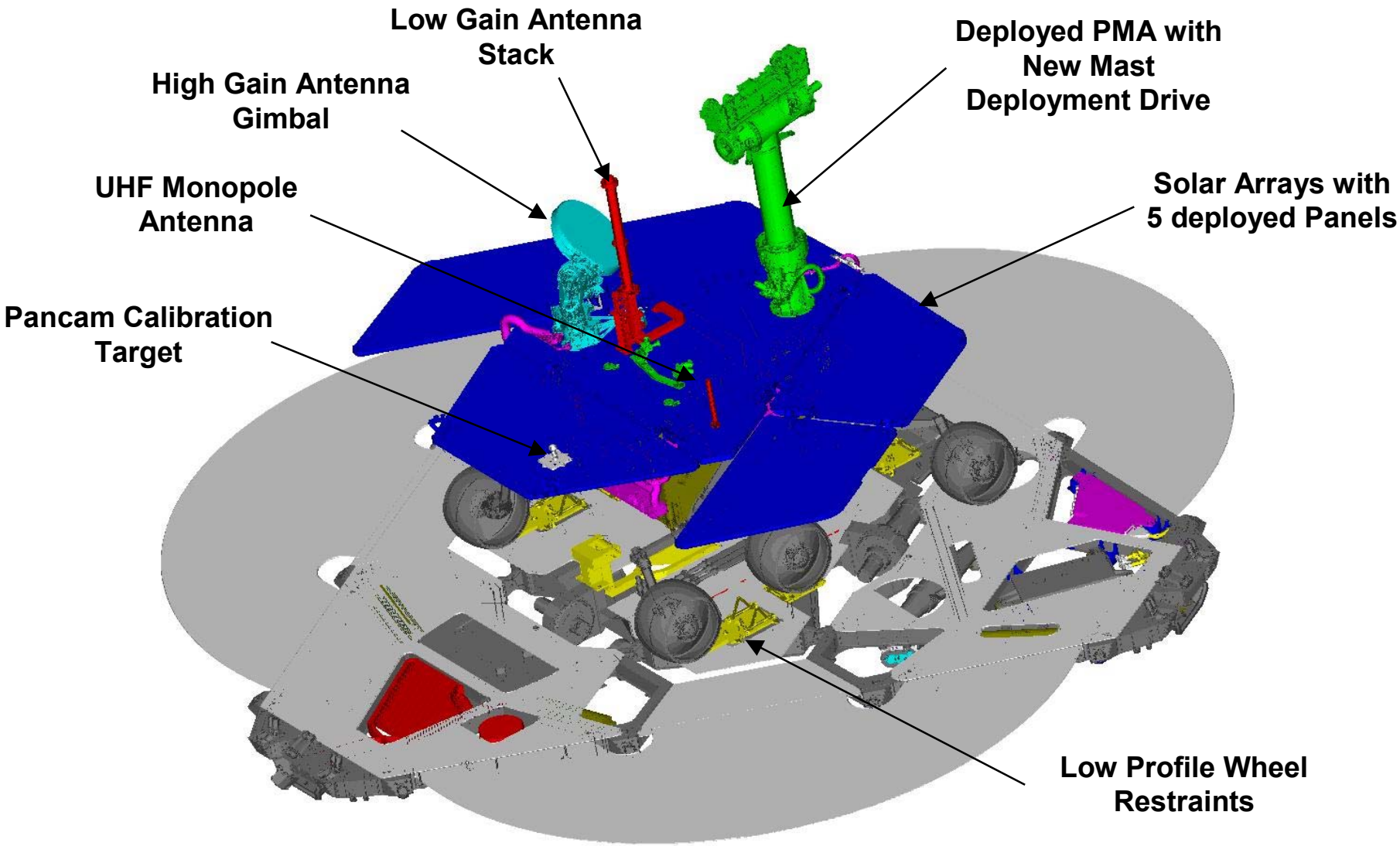

Rover Configuration - Deployed

Mars Exploration Rover

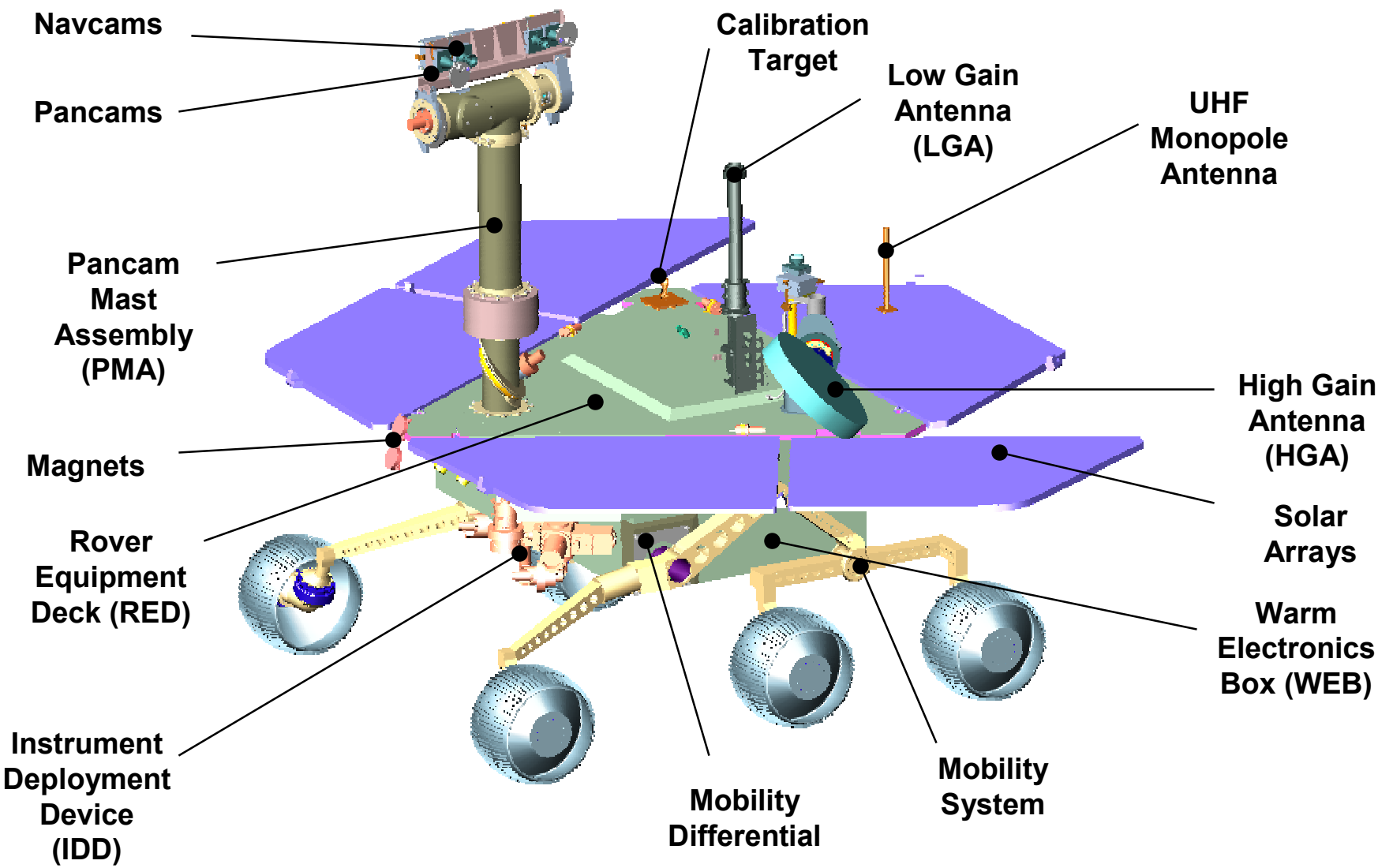

Isometric View of the WEB

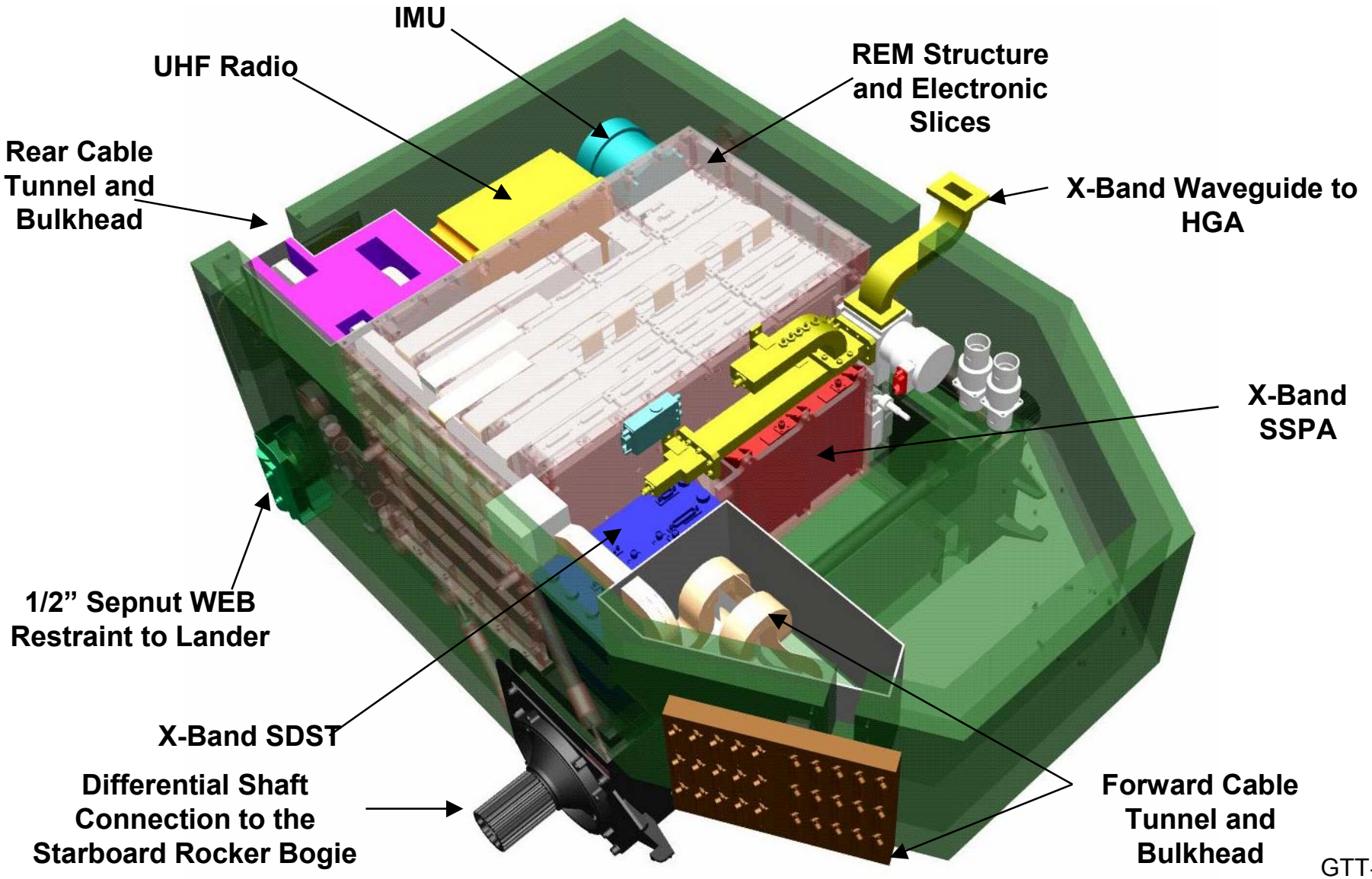

Remote Sensing Science Instruments

Mars Exploration Rover

Pancams - Mast mounted stereo panoramic cameras with color filters on pan/tilt gimbal

- **1024x1024x12bit CCD**
- **~16deg FOV**

Mini-TES - Miniature Thermal Emission Spectrometer

- **Near and mid-IR point spectrometer (6 to 25 µm with resolution of 10 cm^{-1}) to determine mineralogy of Martian surface**
- **20/8mrad FOV raster scanned to produce thermal emission "images"**

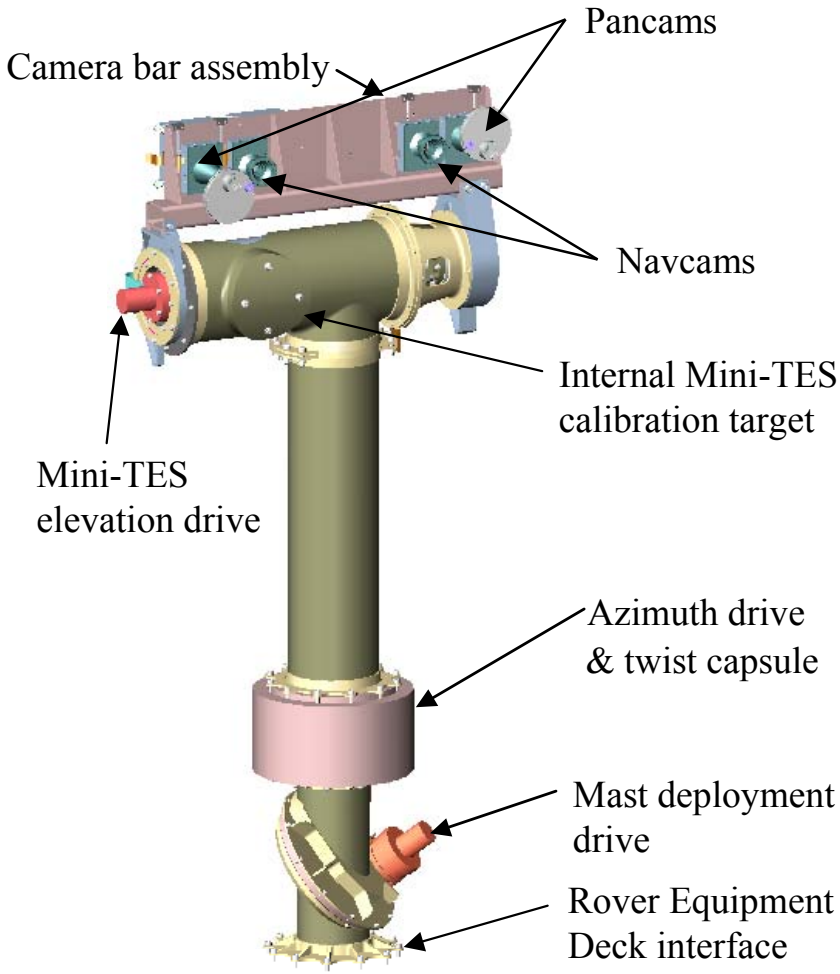

Pancam Mast Assembly (PMA)

In situ Science Instruments

- Instrument Deployment Device (IDD) - a 5 DOF robotic arm for deployment of 3 in situ science instruments and a Rock Abrasion Tool (RAT) against rock and soil targets
  - Microscopic Imager (MI)- 1024x1024x12bit camera with 30 μm/pixel resolution with 3 mm depth of field
  - Alpha Particle X-ray Spectrometer (APXS) - determine elemental chemistry of target
  - Moessbauer Spectrometer (MB) - detects nanophase and amorphous hydrothermal Fe minerals, identifies Fe carbonates, sulfates, nitrates, and determines oxidation state of Fe minerals
- The front HAZCAMs provide imaging of workspace for ground planning of instrument deployments

Instrument Deployment Device (IDD)

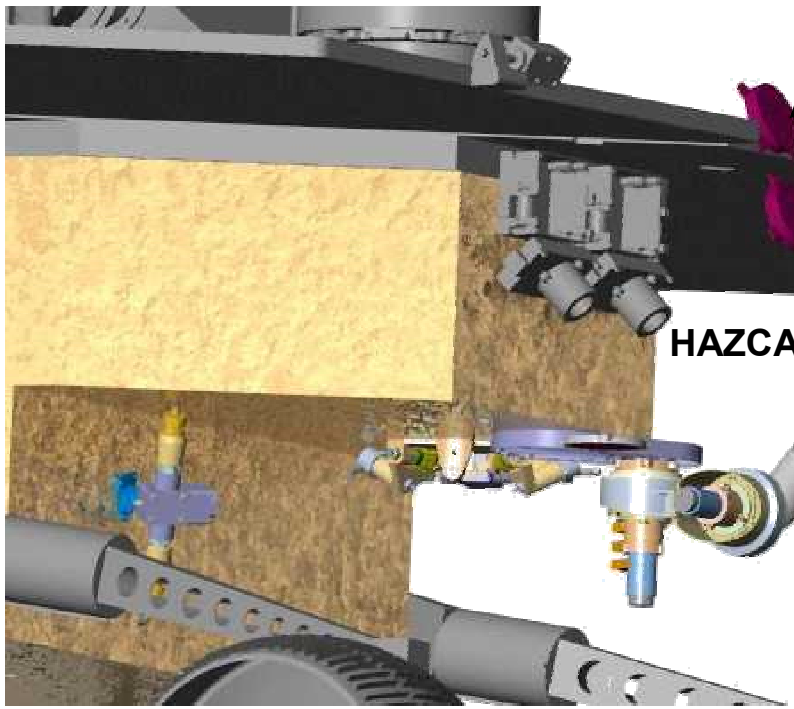

Rock Abrasion Tool

- **Rock Abrasion Tool (RAT)**
  - **Penetrates through dust & surface alteration that might be present on rocks, exposing materials more likely to preserve evidence of environmental conditions at the time of their formation**

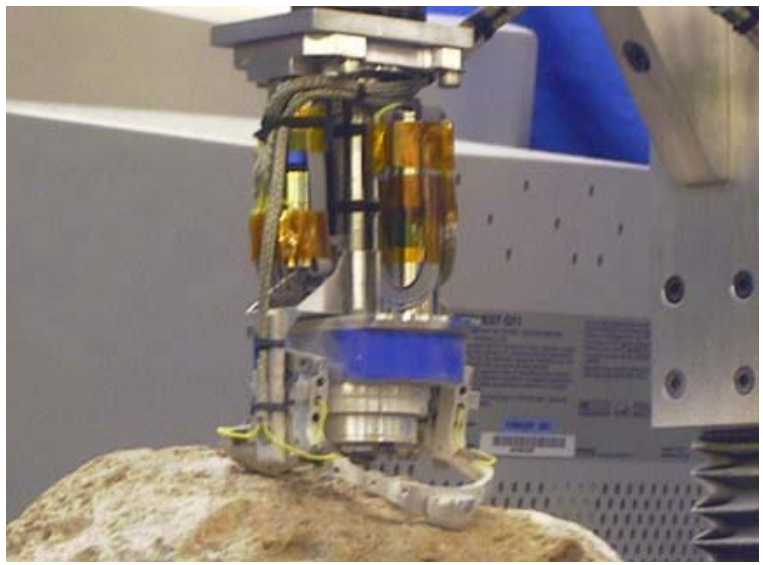

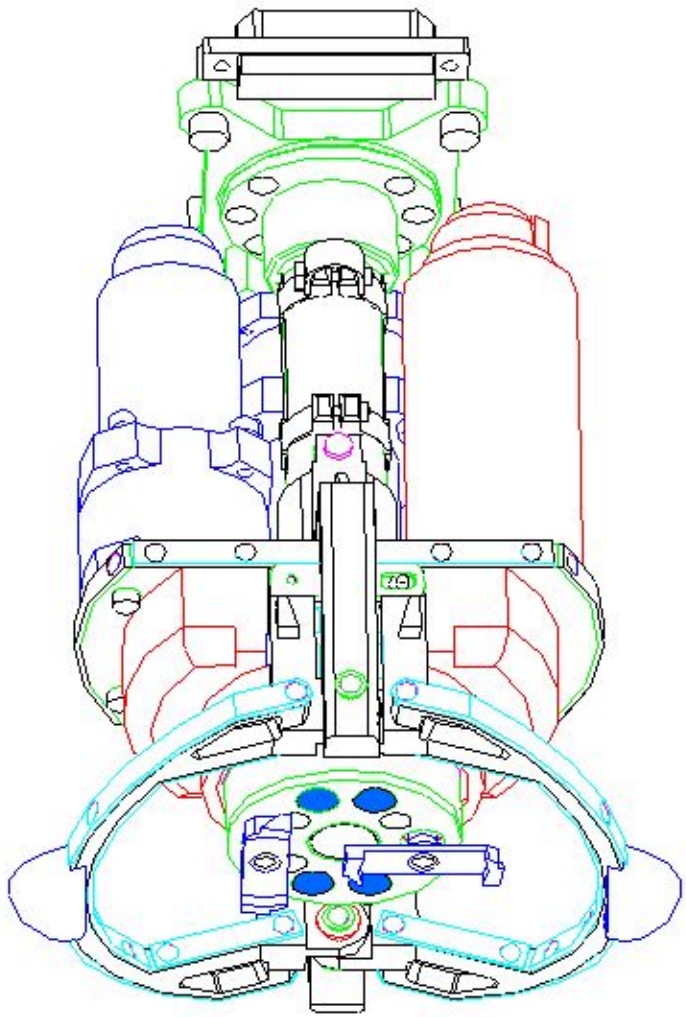

Thermal Environment

- **Off-sun during cruise requirements:**
  - **Continuous: 0° to 51° off-sun cone angle**
    - **Launch to Launch + 21 days: up to 51°**
    - **Launch + 22 day to Mars turn-to-Entry: 0° to 46°**
  - **Transient off-sun cone angles & durations**
    - **TCM1: 90° for up to 110 minutes at 1.02 AU**
    - **Mars turn-to-Entry: 83° for up to 70 minutes**

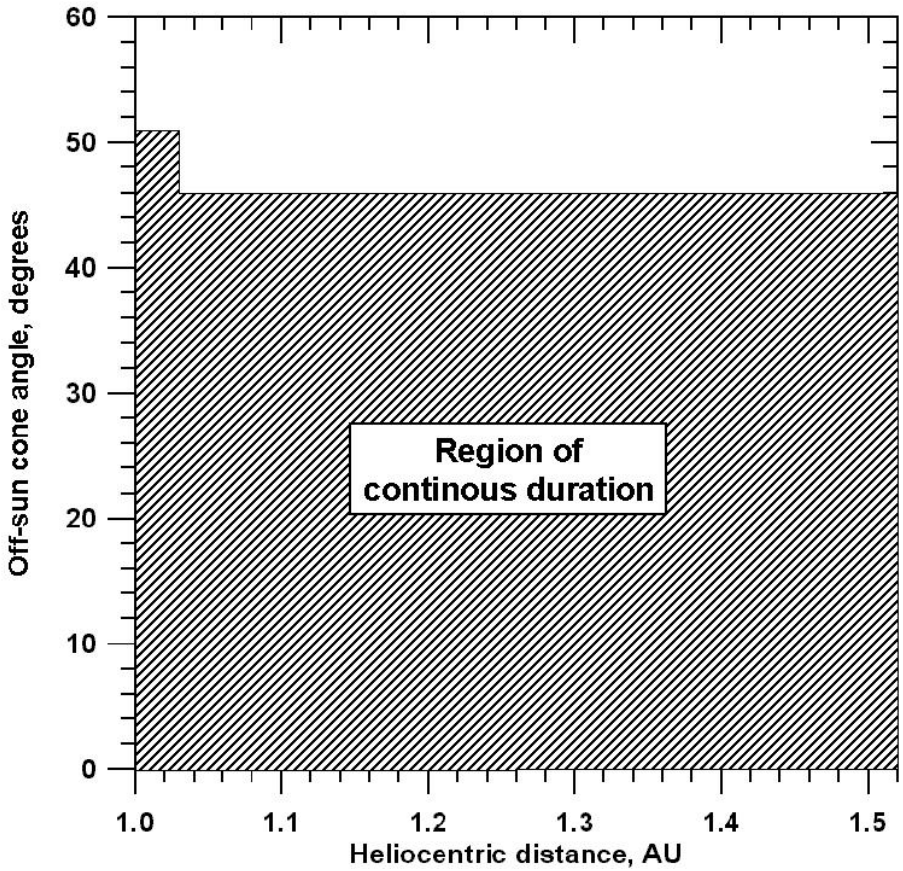

Thermal Environment (cont'd)

- **Mission requirements (encompasses MER-A & MER-B) :**
  - Cruise Heliocentric distance: 1.01 AU to 1.52 AU
  - Areocentric longitude during surface operations (L_s): 328 to 40°
  - Landing site: 15S to 10N
  - Surface operations duration: 90 Sols

- **Mars surface environmental requirements (MER ERD, Rev A):**
  - Surface temperature (min/max): -97°C / 26°C
  - Atmosphere temperature (min/max): -95°C / 2°C
  - Solar flux at the surface (min/max): 0 / 600 W/m^2
  - Sustained wind speed at 1 m above surface:
    - 8:00 LST to 17:00 LST: 3 to 15 m/s
    - 17:00 LST to 8:00 LST (next day): 0 to 15 m/s
    - Wind speed at elevations below 1m will be less

Key Driving Level 3 Requirements

- **Driving allowable flight temperature (AFT) requirements:**
  - **REM avionics/telecom maximum (op & non-op) AFT limit: 50°C**
    - **Limiting factor for DTE requirement & nighttime battery energy usage**
    - **Drives need for heat rejection system (HRS)**
    - **Drives EDL thermal design**
  - **Rover battery - operating AFT limits: -20/30°C**
    - **Tighter temperature limits than REM governed RHU & thermal switch usage for Martian surface operation**
  - **Lander battery - cruise storage (non-op) AFT limits: -40/10°C**
    - **Tighest limits of all non-HRS controlled hardware**
  - **Backshell IMU maximum operating AFT limit: 51°C**
    - **Constrains operation at launch (for calibration purposes) & during EDL**
  - **Propellant line minimum (op & non-op) AFT limit: 15°C**

Key Driving Level 3 Requirements (cont'd)

- **Surface communication requirements:**
  - **2 hours of continuous DTE operation per Sol and up to 3 total hours per Sol**

DOORS ID	*Requirement*	*Status*
888	The Thermal Control System shall maintain all specified flight hardware within the limits listed in the Temperature Requirements Table for 2 hrs of continuous DTE X-band per sol, starting no later than 11:00am and for 3 hr total of DTE X-band transmission per sol, subject to availability of power	Comply by design & analysis

  - **Capability to operate the HGA actuators at 10 am Mars local time without additional warm-up heater**

DOORS ID	*Requirement*	*Status*
607	The Flight System shall be capable of operating the HGA actuators at 10 am Mars local time without additional warmup.	Comply by design & analysis

Blue text denotes changes from Project PDR

System Thermal Block Diagram

Mars Exploration Rover

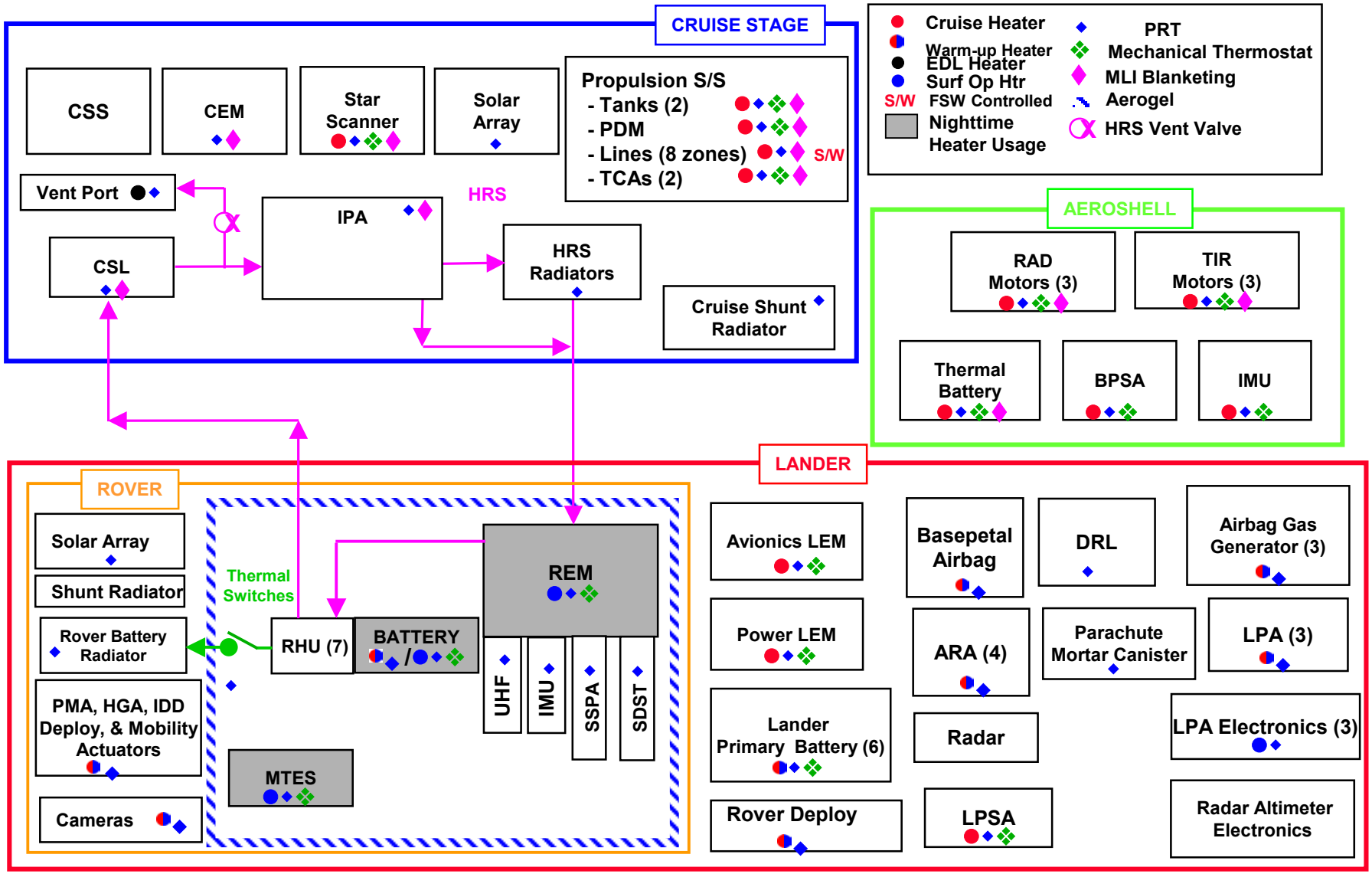

Cruise Stage Thermal Design Overview

Mars Exploration Rover

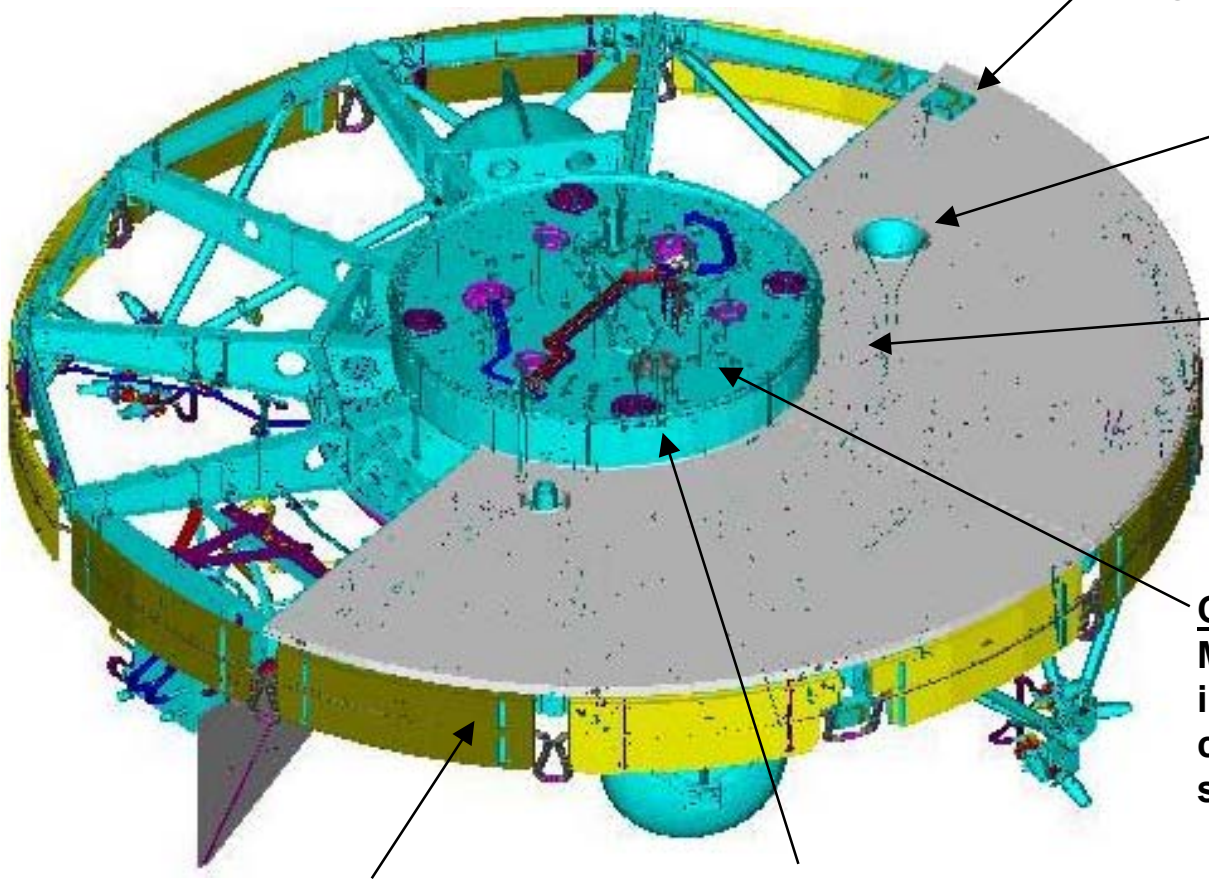

Sun Sensors:
Ag/FEP tape on top

MGA:
S13-GLO (white) paint on back

Solar Array:
Ag/FEP tape on inner ring, S13-GLO (white) paint on substrate backside

Cruise Shunt Radiator:
M1 (white) paint including sep. spring covers, anodized L/V spring pads

HRS Radiators:
M1 (white) paint on both sides

LVA:
S13-GLO (white) paint on lateral side

Cruise Stage Thermal Design Overview (cont'd)

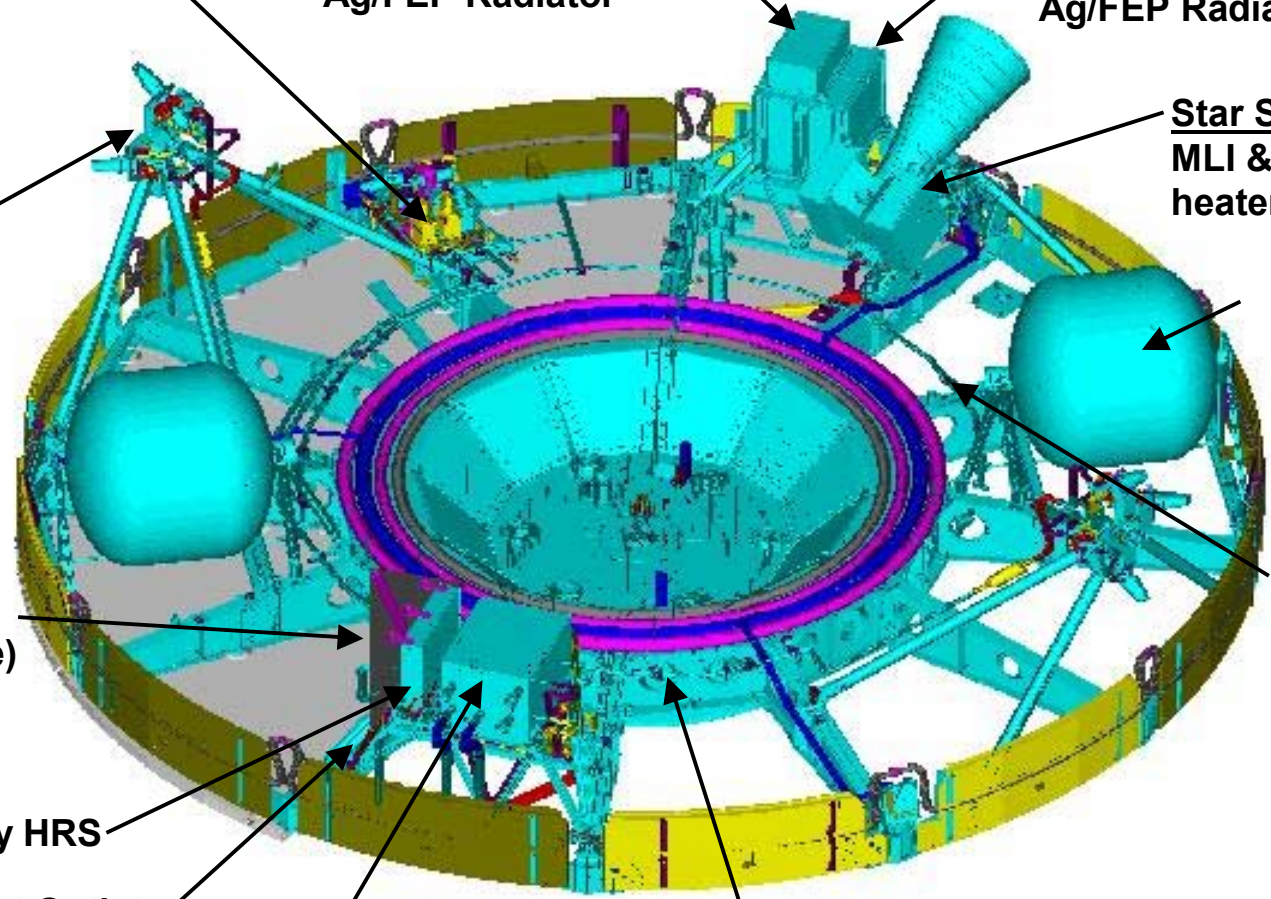

PDM: MLI & thermostatic heaters

Sun Sensor Elect.: MLI & Outward Ag/FEP Radiator

CEM: MLI & Outward Ag/FEP Radiator

Star Scanner: MLI & thermostatic heater

TCAs: MLI & thermostatic heaters

Propellant Tanks: MLI & thermostatic heaters

Propellant Lines: MLI, aluminum cladding, thermostatic FSW heater control for 8 zones

CSL Radiator: S13-GLO (white) paint

CSL: Controlled by HRS

HRS Vent Outlet: Warm-up heater

IPA: MLI & HRS

Intercostals: S13-GLO (white) white paint

HRS Overview

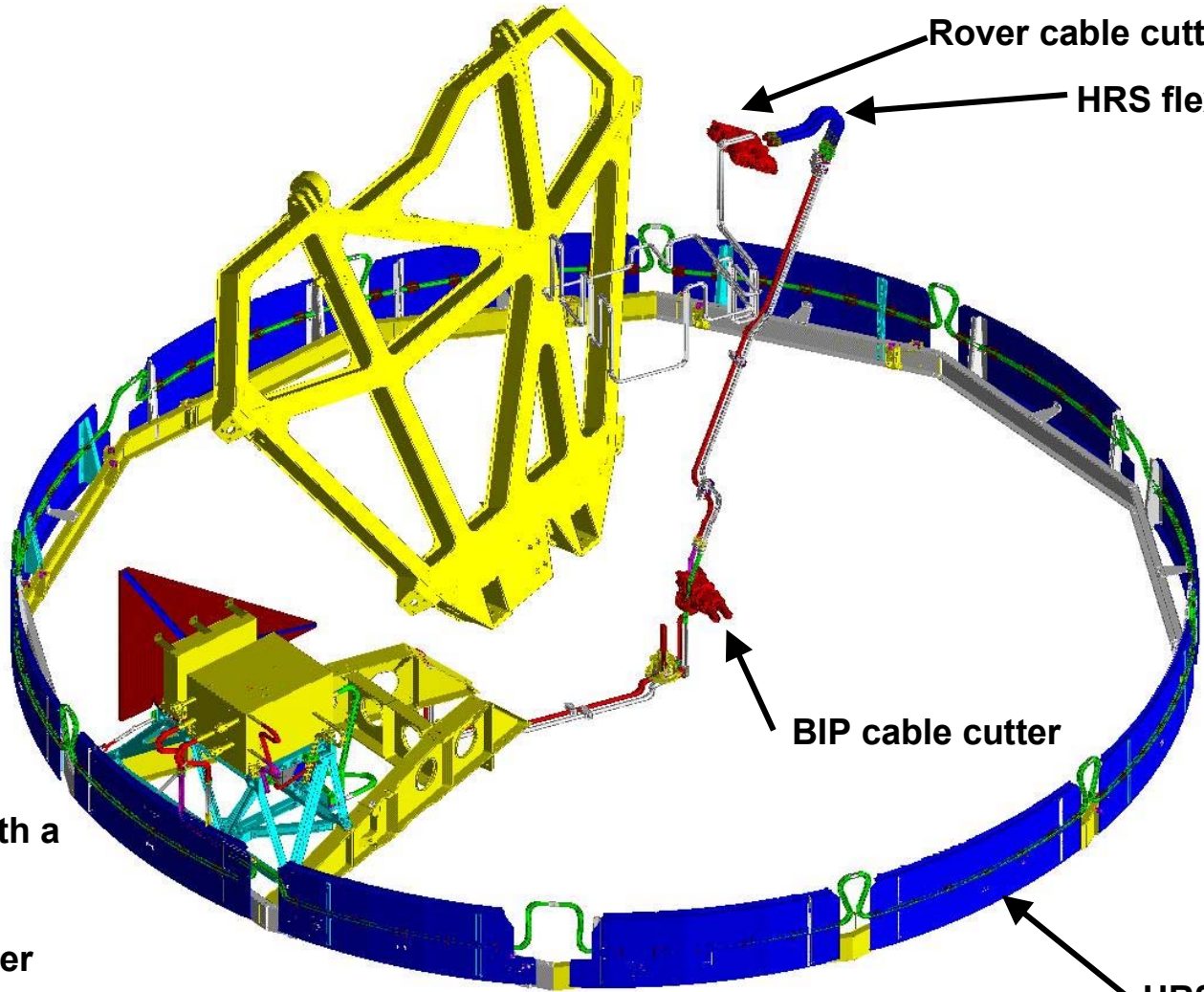

IVSR consists of:
- IVSR structure
- IPA
- 2 Pyro valves
- Filter in parallel with a relief valve
- Vent outlet
- Pressure transducer
- CSL heat exchanger
- CSL “shark fin” radiator

HRS Schematic

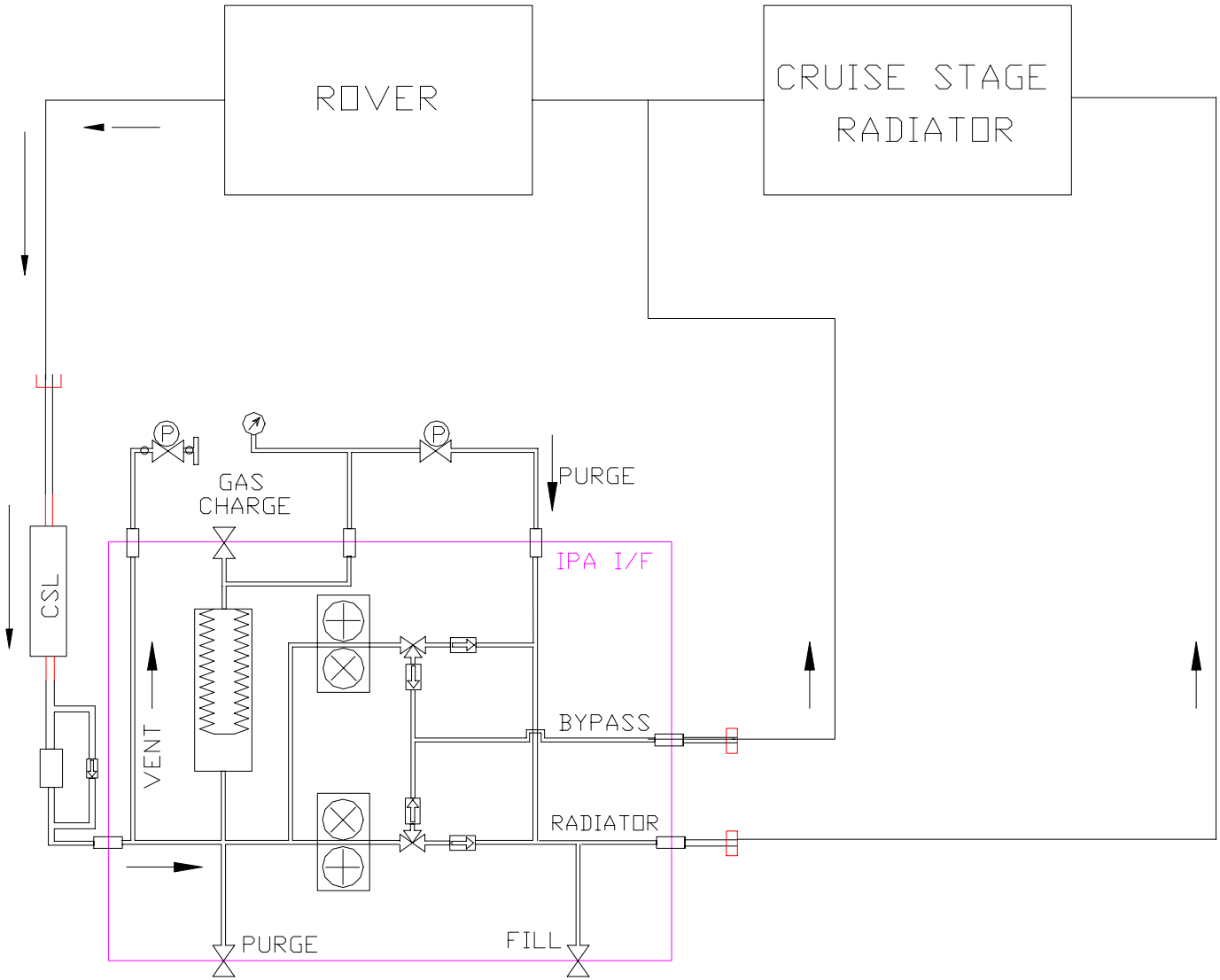

Integrated Pump Assembly

- **Mars Pathfinder IPA shown**
- **MER adopted a Mars Pathfinder build-to-print approach for the IPA**

IPA Schematic

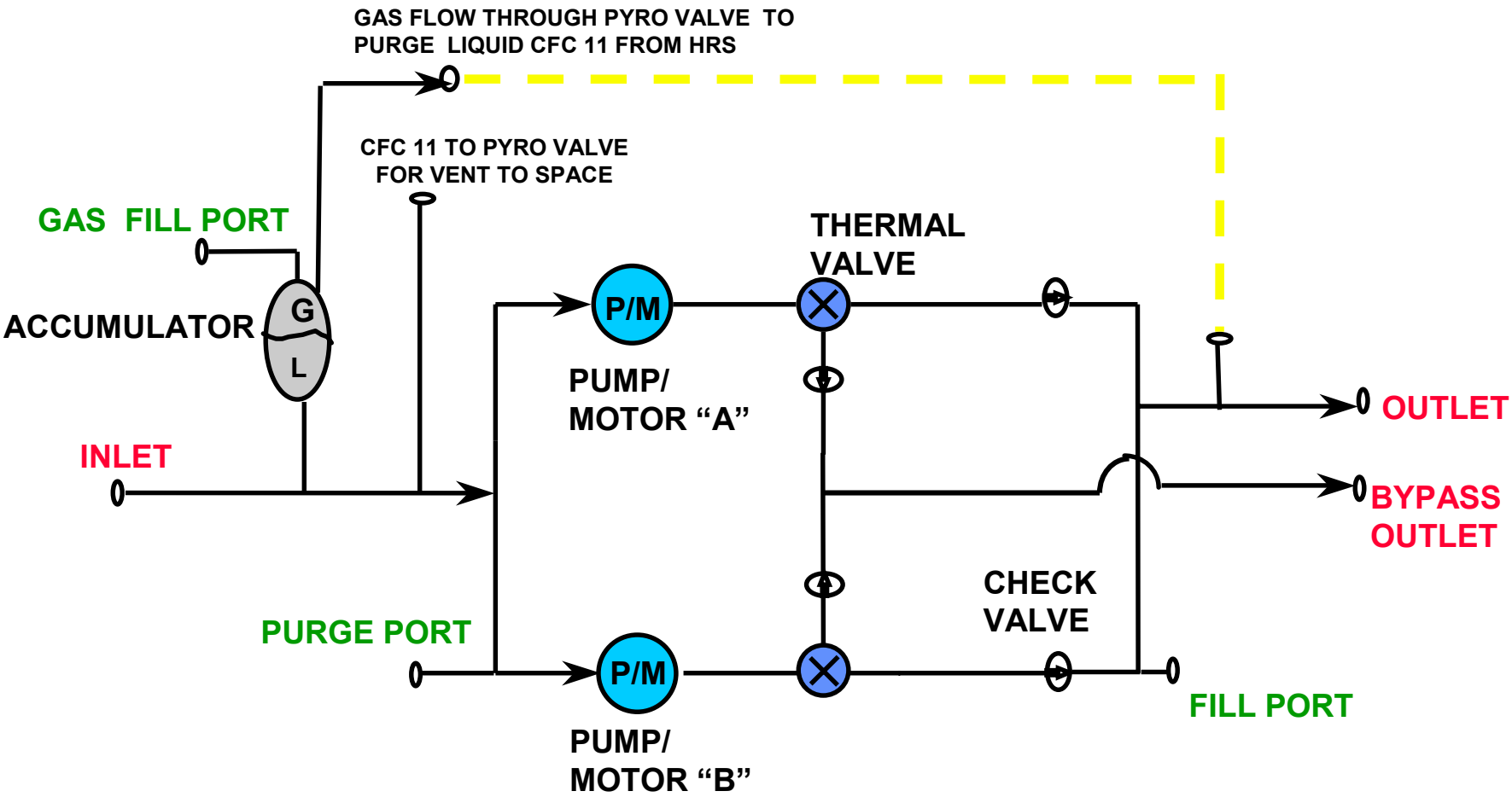

Aeroshell Thermal Design Overview

Mars Exploration Rover

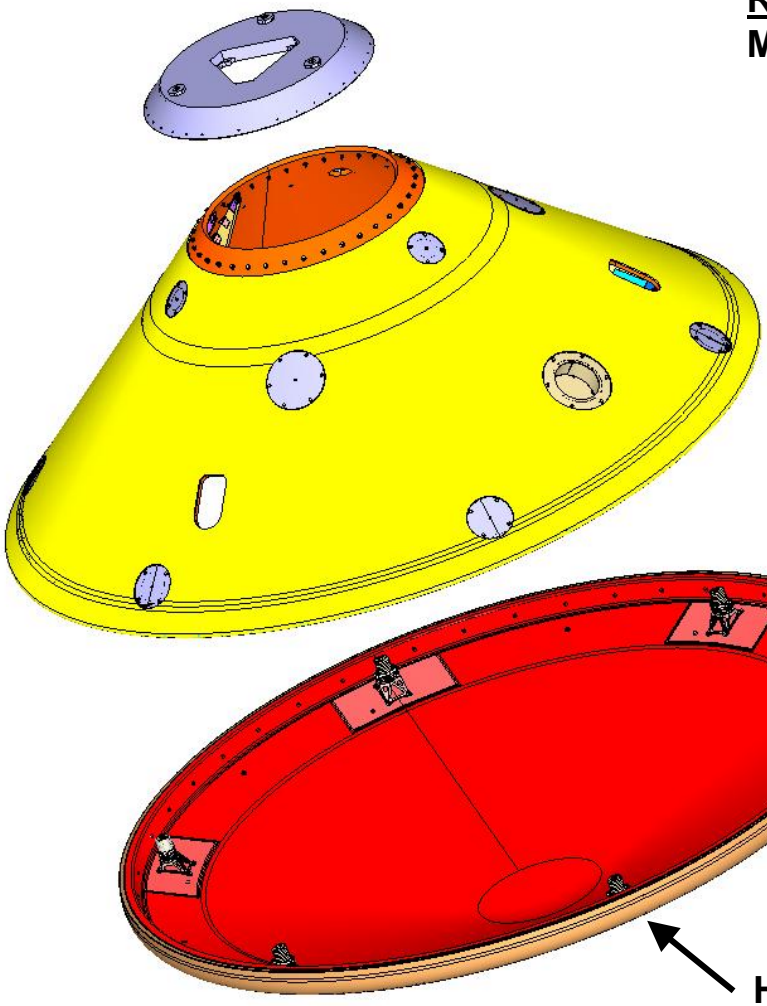

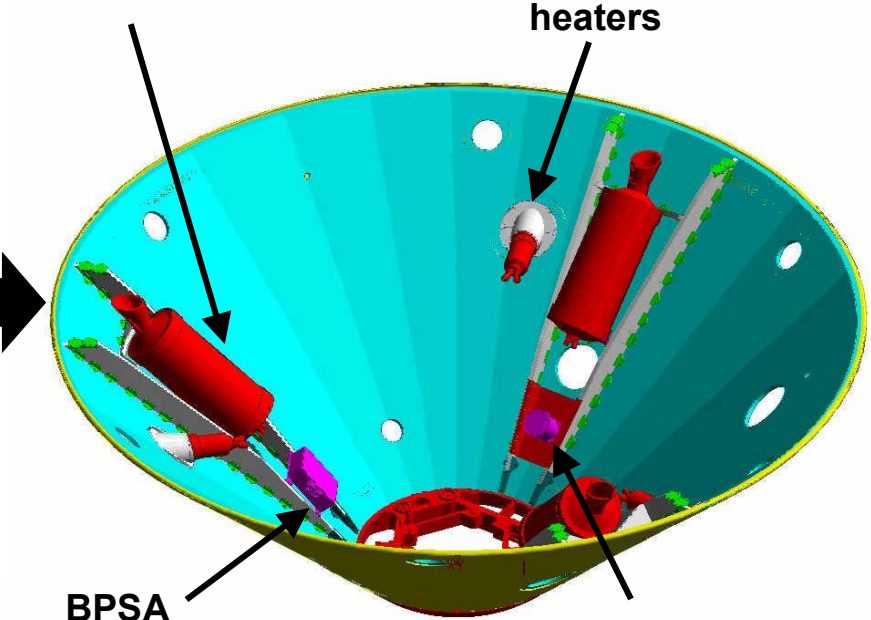

RAD Motors (3)
MLI & thermostatic heaters

TIRS Motors (3)
MLI & thermostatic heaters

BPSA
Thermostatic heaters
High ε finish

BS IMU
Thermostatic heaters
Mounting plate mass

Thermal Battery (hidden)
MLI & thermostatic heaters

Heat Shield
Interior MLI
Exterior radiation shield

Lander Thermal Design Overview

Mars Exploration Rover

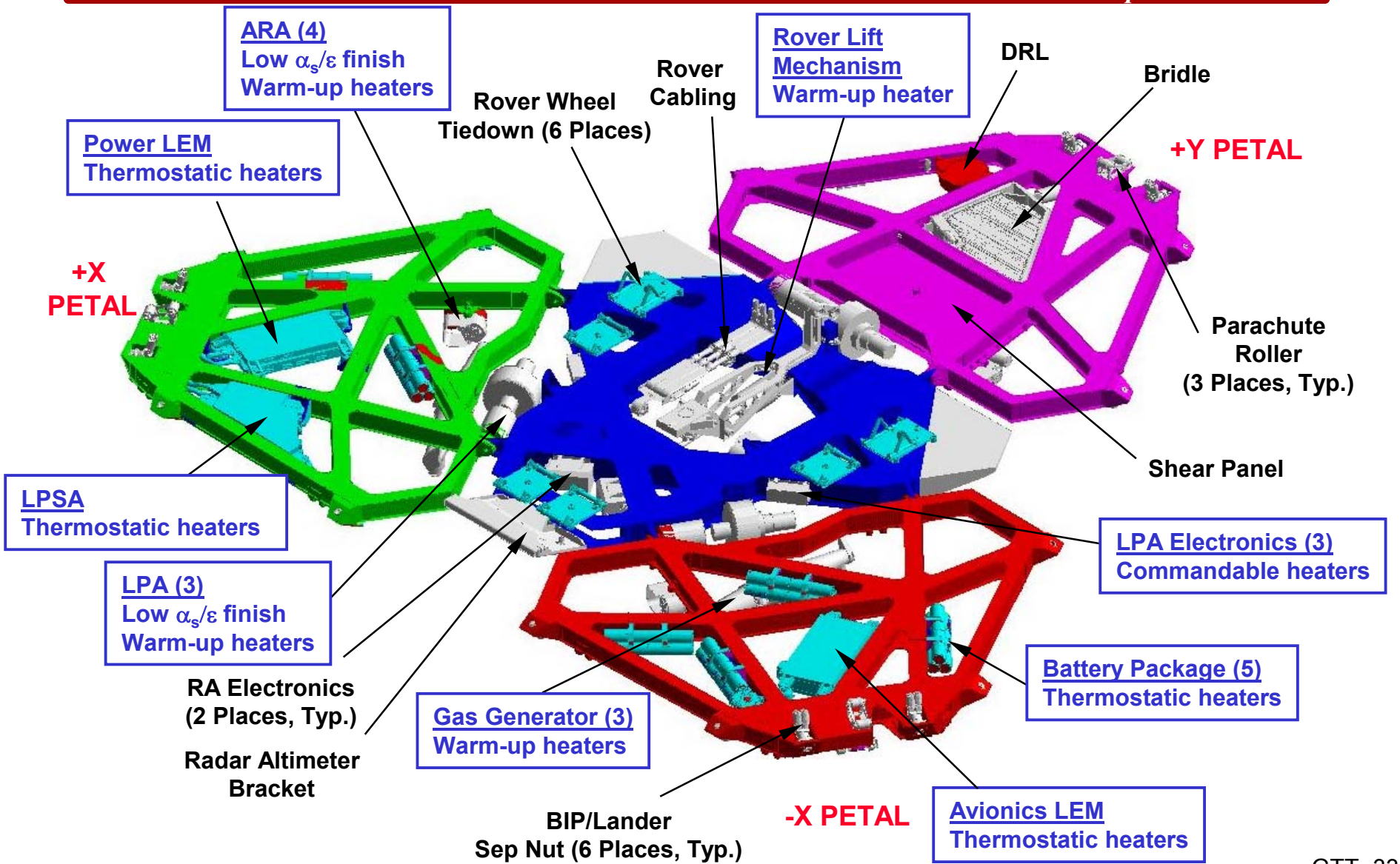

Rover Thermal Design Overview

Mars Exploration Rover

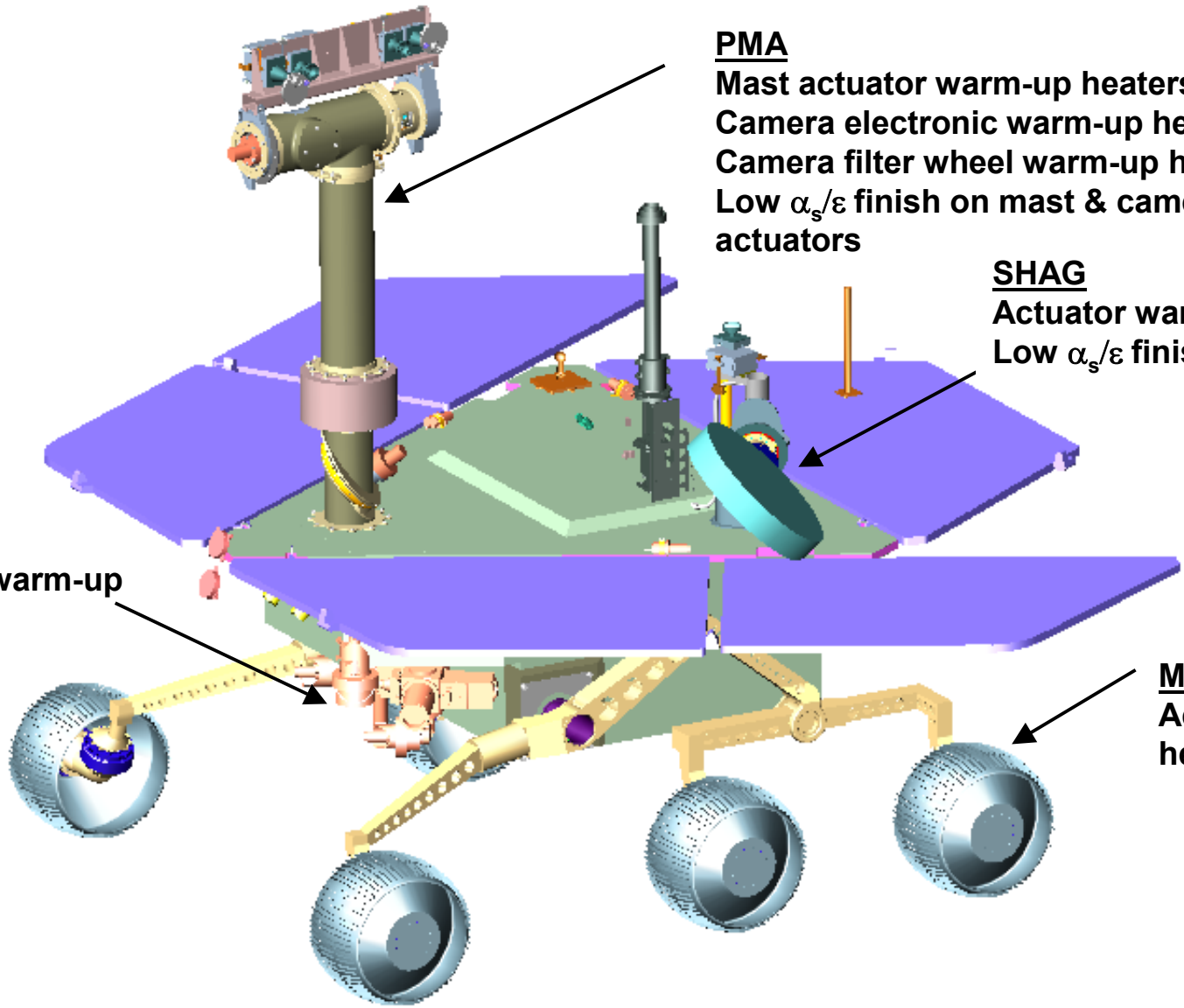

PMA
Mast actuator warm-up heaters
Camera electronic warm-up heaters
Camera filter wheel warm-up heaters
Low α_s/ε finish on mast & camera actuators

SHAG
Actuator warm-up heater
Low α_s/ε finish on actuator

IDD
Actuator warm-up heaters

Mobility
Actuator warm-up heaters

Rover Thermal Design Overview (cont'd)

WEB DESIGN FEATURES

- Aerogel attached to interior of WEB structure
- Thermostatic heaters on battery, REM, & mini-TES
- Thermal switches for battery
- HRS tubing on REM for cruise

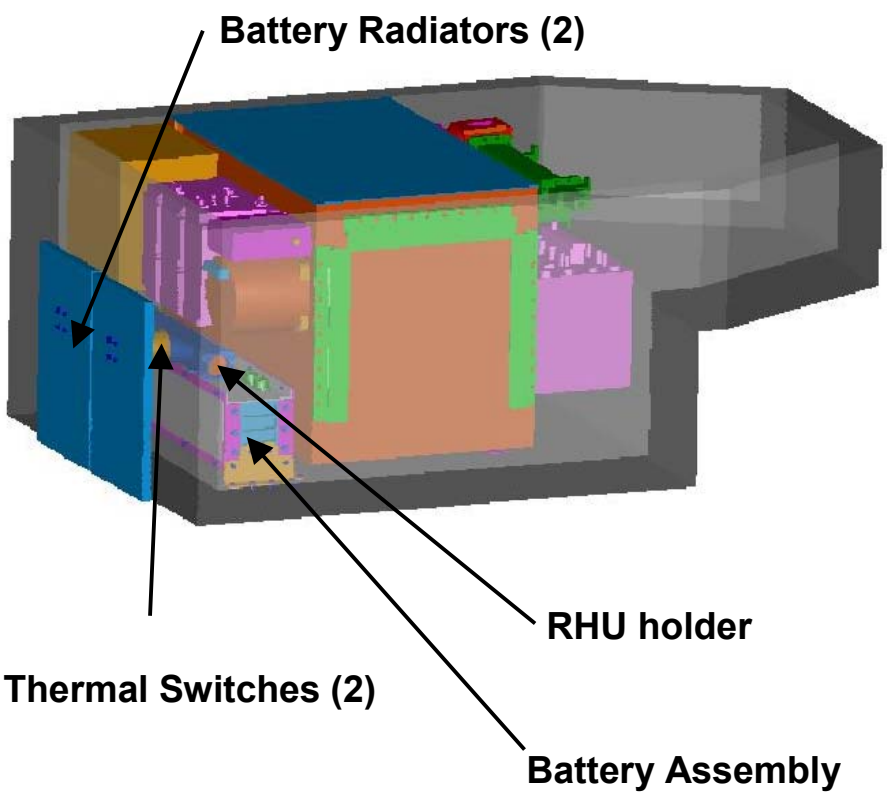

HRS tubing on REM

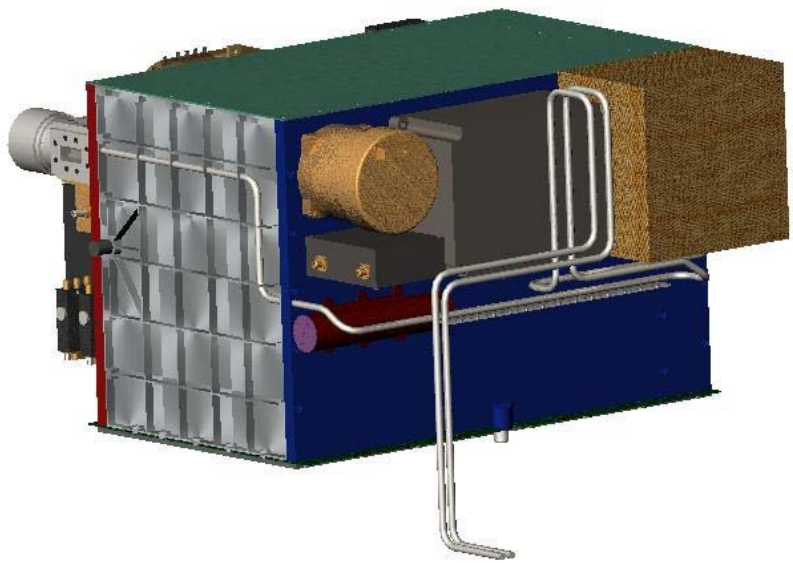

Thermal Switch

- **Heat switch assembly:**
  - **Heat switch unit**
    - **Passive, variable thermal conductance mechanism which is mounted between the radiator &RHU holder on Rover battery**
    - **Variable conductance achieved via temperature activated paraffin wax which expands/contracts to mechanically close/open the switch**
  - **Wobblefram seal**
    - **Teflon PFA diaphragm used to seal off hole in WEB wall**

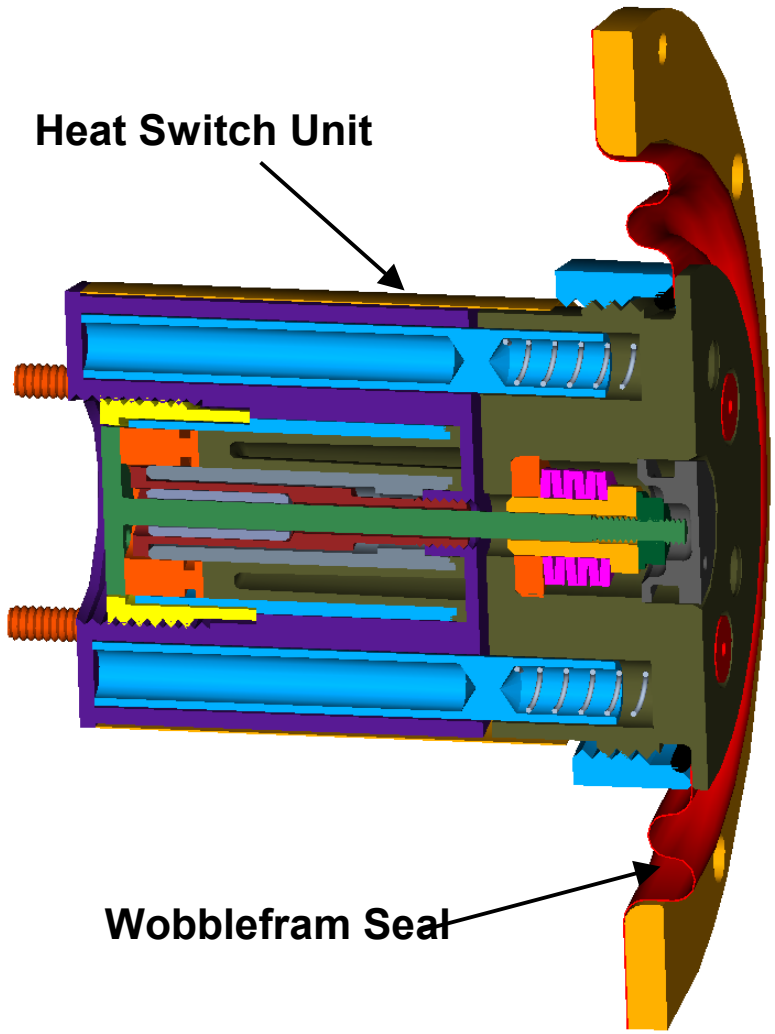

Cruise Thermal Analysis - Cruise Stage

Mars Exploration Rover

	TEMPERATURE (°C)											
	ALLOWABLE FLIGHT				PREDICTED FLIGHT				Margin			
	OP		NOP		OP		NOP		OP		NOP	
	min	max	min	max	min	max	min	max	min	max	min	max
CRUISE STAGE												
Cruise Solar Array average	-50	90	-70	110	-17	71	n/a	n/a	33	18	n/a	n/a
Cruise Shunt Limiter Assembly	-25	40	n/a	50	-12	2	n/a	n/a	12	38	n/a	n/a
Propellant Tanks (includes gas service valves)	15	30	15	30	23	23	n/a	n/a	8	6	n/a	n/a
Tanks during ground operations	n/a	n/a	n/a	40			n/a	n/a			n/a	n/a
Thruster Valve, 1 lbf	20	110	20	50	24	24	n/a	n/a	4	26	n/a	n/a
PDM	15	50	15	50	23	23	n/a	n/a	8	26	n/a	n/a
service valve outside PDM make it a unit	n/a	n/a	n/a	n/a			n/a	n/a			n/a	n/a
filter	n/a	n/a	n/a	n/a			n/a	n/a			n/a	n/a
latch valve	n/a	n/a	n/a	n/a			n/a	n/a			n/a	n/a
pressure transducer	n/a	n/a	n/a	n/a			n/a	n/a			n/a	n/a
CEM Assembly	-40	50	-40	50	3	22	n/a	n/a	43	27	n/a	n/a
Star Scanner head & electronics	-14	**50**	n/a	n/a	0	27	n/a	n/a	14	23	n/a	n/a
Sun Sensor electronics	-30	50	n/a	n/a	3	22	n/a	n/a	32	28	n/a	n/a
Sun Sensor Heads (2 on -Z, 3 on X/Y)	-25	85	n/a	n/a	-3/-22	28/67	n/a	n/a	22/3	53/18	n/a	n/a
5/8" Ti Bolt, Bushing & Sep. Spring	-60	60	-60	60	-20	51	n/a	n/a	40	8	n/a	n/a
IPA	-20	40	-20	40	-3	6	n/a	n/a	16	34	n/a	n/a
IPA electronics	-20	50	-20	50	-3	6	n/a	n/a	16	44	n/a	n/a
Pyro valve-HRS purge	-30	66	-30	66	-3	6	n/a	n/a	26	60	n/a	n/a
HRS radiator	-90	n/a	n/a	n/a	-40/-65	-7/-16	n/a	n/a	50/24	n/a	n/a	n/a
Cruise Shunt Radiator	-40	100	-40	100	-14	67	n/a	n/a	25	33	n/a	n/a
LVA	n/a	n/a	n/a	n/a	-20	51	n/a	n/a	n/a	n/a	n/a	n/a

Cruise Thermal Analysis - Aeroshell

Mars Exploration Rover

	TEMPERATURE (°C)											
	ALLOWABLE FLIGHT				PREDICTED FLIGHT				Margin			
	OP		NOP		OP		NOP		OP		NOP	
	min	max	min	max	min	max	min	max	min	max	min	max
AEROSHELL												
BIP:					n/a	n/a	-34	9	n/a	n/a	n/a	n/a
5/8" Cable Cutter (BIP)	-100	30	-100	60	n/a	n/a	-34	9	n/a	n/a	65	50
1" Cable Cutter in (BIP)	-100	30	-100	60	n/a	n/a	-34	9	n/a	n/a	65	50
5/8" Pyro Sep Nut, Cruise Stage Sep. (BIP)	-100	30	-100	60	n/a	n/a	-34	9	n/a	n/a	65	50
Parachute Canister & Mortar	-45	45	-45	45	n/a	n/a	-35	9	n/a	n/a	10	36
Backshell:												
BS Thermal Batteries	-40	35	-40	35	n/a	n/a	-29	6	n/a	n/a	11	29
Backshell Pyro Switch Assembly (BPSA)	-40	50	-40	50	n/a	n/a	-29	0	n/a	n/a	11	50
IMU-Litton LN 200S (Rover & Backshell)	-39	51	-47	65	n/a	n/a	-29	-1	n/a	n/a	18	66
3/8" Pyro Sep Nut, B/S side	-120	30	-120	60	n/a	n/a	-94	3	n/a	n/a	26	56
3/8" Ti Bolt & Sep Mech. (LMA Supplied)	-120	30	-120	60	n/a	n/a	-94	3	n/a	n/a	26	56
RAD Rockets	-40	-20	-40	40	n/a	n/a	-24	2	n/a	n/a	16	38
TIRS Motors	-40	-20	-40	40	n/a	n/a	-24	5	n/a	n/a	16	35
Backshell-outer surface (TPS)	-150	n/a	-150	n/a	n/a	n/a	-36/-97	-6/10	n/a	n/a	114/53	n/a
Backshell-Bond line	-100	150	-100	150	n/a	n/a	-35/-95	-4/7	n/a	n/a	64/5	154/143
Heatshield:												
Heatshield-outer surface (SLA561)	-150	n/a	-150	n/a	n/a	n/a	-81	-7	n/a	n/a	69	n/a
Heatshield-Bond line	-150	250	-150	250	n/a	n/a	-81	-6	n/a	n/a	69	256

Cruise Thermal Analysis - Lander

Mars Exploration Rover

	TEMPERATURE (°C)											
	ALLOWABLE FLIGHT				PREDICTED FLIGHT				Margin			
	OP		NOP		OP		NOP		OP		NOP	
	min	max	min	max	min	max	min	max	min	max	min	max
LANDER												
Descent antenna	-110	45	-110	45	n/a/	n/a	-38	4	n/a/	n/a	72	41
Radar Altimeter X-mit Antennas	-85	45	-85	45	n/a/	n/a	-38	4	n/a/	n/a	47	41
Radar Altimeter Rec Antennas	-85	45	-85	45	n/a/	n/a	-38	4	n/a/	n/a	47	41
Radar Altimeter electronics	-40	40	-40	40	n/a/	n/a	-38	4	n/a/	n/a	2	36
Coax tansfer switch (CxS4)	-35	50	-35	50	n/a/	n/a	-39	4	n/a/	n/a	-4	45
Lander Primary Battery (LiSO2)												
Cruise (non-op)	n/a	n/a	-40	10	n/a/	n/a	-38	5	n/a/	n/a	2	5
Lander Pyro Switch Assembly (LPSA)	-50	50	-50	50	n/a/	n/a	-38	5	n/a/	n/a	12	45
Power-LEM Assembly	-40	50	-50	50	n/a/	n/a	-37	4	n/a/	n/a	13	46
Avionics-LEM Assembly	-40	50	-50	50	n/a/	n/a	-38	5	n/a/	n/a	12	45
3/8" Release Nuts	-120	30	-120	60	n/a/	n/a	-35	9	n/a/	n/a	85	51
5/8"Lander Cable Cutter	-105	30	-105	60	n/a/	n/a	-35	9	n/a/	n/a	70	51
1" Cable Cutter w/HRS on Base Petal	-105	30	-105	60	n/a/	n/a	-38	4	n/a/	n/a	67	56
Lander Petal Actuator (+Y, +X, -X)	-45	15	-105	40	n/a/	n/a	-39	4	n/a/	n/a	66	36
Airbag Retraction Actuator (+Y, +X, -X, basepetal	-45	15	-105	40	n/a/	n/a	-38	5	n/a/	n/a	67	35
Rover Deploy (lift) Actuator Assembly	-45	15	-105	40	n/a/	n/a	-38	4	n/a/	n/a	67	36
Airbag material, cruise	n/a	n/a	-85	80	n/a/	n/a	-58	5	n/a/	n/a	27	75
Gas Generator (+Y, +X, -X)	-40	0	-50	50	n/a/	n/a	-39	-1	n/a/	n/a	11	51
Bridle cutter assy (B/S)	-120	30	-120	60	n/a/	n/a	-38	5	n/a/	n/a	82	55
Bridle Descent Rate Limiter	-55	30	-55	40	n/a/	n/a	-38	5	n/a/	n/a	17	35
Bridle Assy	-60	30	-60	40	n/a/	n/a	-38	5	n/a/	n/a	22	35
Lander Structure	-55	40	-55	40	n/a/	n/a	-39	9	n/a/	n/a	16	31

Cruise Thermal Analysis - Rover

Mars Exploration Rover

	ALLOWABLE FLIGHT				PREDICTED FLIGHT				Margin			
	OP		NOP		OP		NOP		OP		NOP	
	min	max	min	max	min	max	min	max	min	max	min	max
ROVER												
SSPA	-25	50	-40	50	0	7	-9	-3	25	43	31	53
SDST	-25	50	-40	50	na	na	-3	3	na	na	37	47
UHF Transceiver	-40	55	-40	55	na	na	-4	3	na	na	36	52
Rover Solar Array (3J)	-125	90	-125	90	na	na	-37	5	na	na	88	85
Li-Ion Battery												
Cruise	-20	10	n/a	n/a	na	na	-8	-1	na	na	na	na
REM Assembly	-40	50	-40	50	-4	3	n/a	n/a	25	43	n/a	n/a
Web Structure												
WEB Bumper Limit Switches	-105	50	-105	50	na	na	-31	5	na	na	74	45
Solar Array Bumper Limit Switches	-105	50	-105	50	na	na	-31	5	na	na	74	45
RHU	-100	300	n/a	n/a	-31.0	5.0	n/a	n/a	25	43	n/a	n/a
SCIENCE												
Mini TES	-40	35	-40	45	na	na	-19	4	na	na	21	41
IMU-Litton LN 200S (Rover & Backshell)	-39	51	-47	65	na	na	11	17	na	na	58	48

Rover 2 Hour of Continuous DTE

Mars Exploration Rover

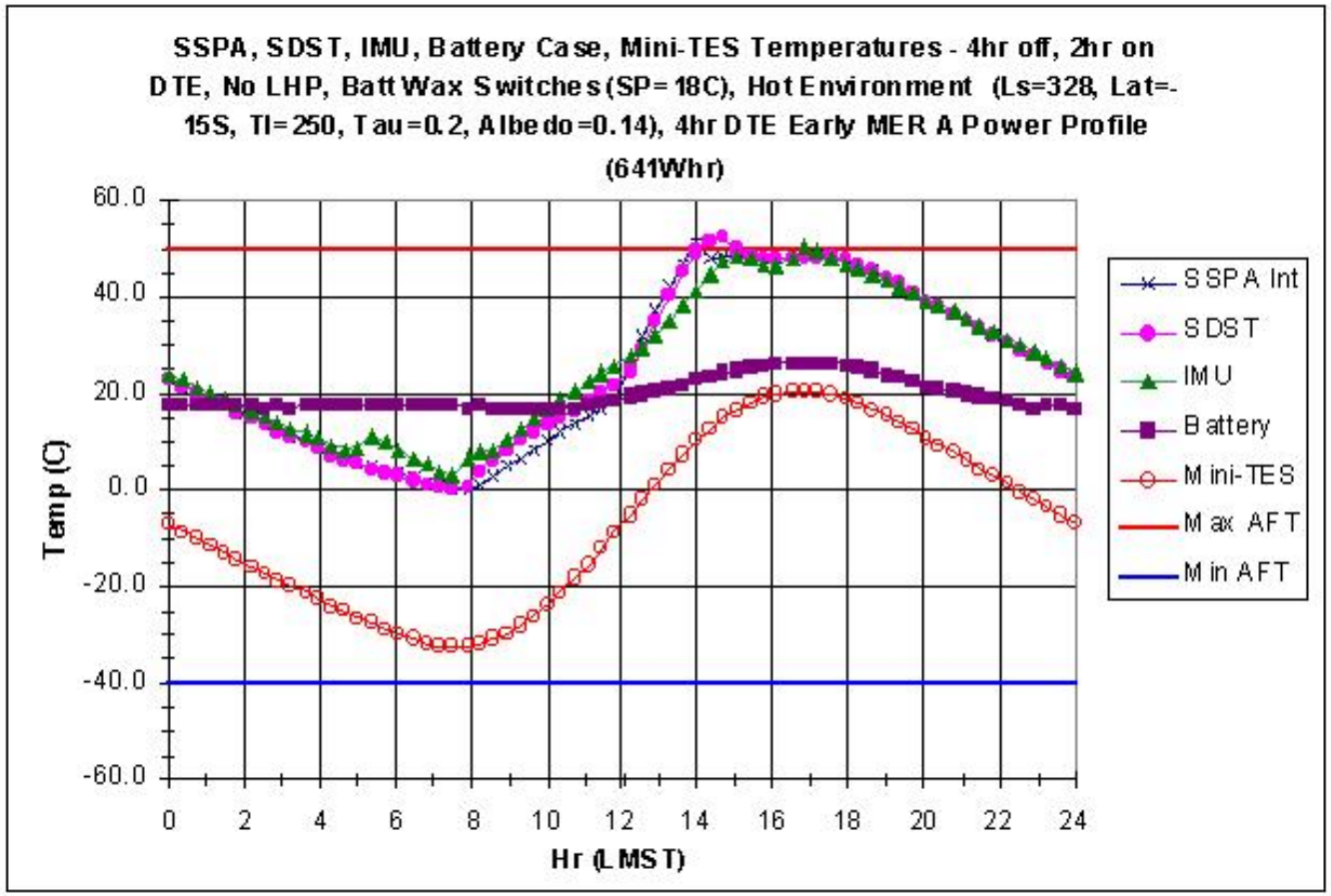

Max SSPA Interface Temp = 51°C

Max UHF Interface Temp = 52°C

Max Battery Temp = 26C

Rover Cold Surface Scenario

Mars Exploration Rover

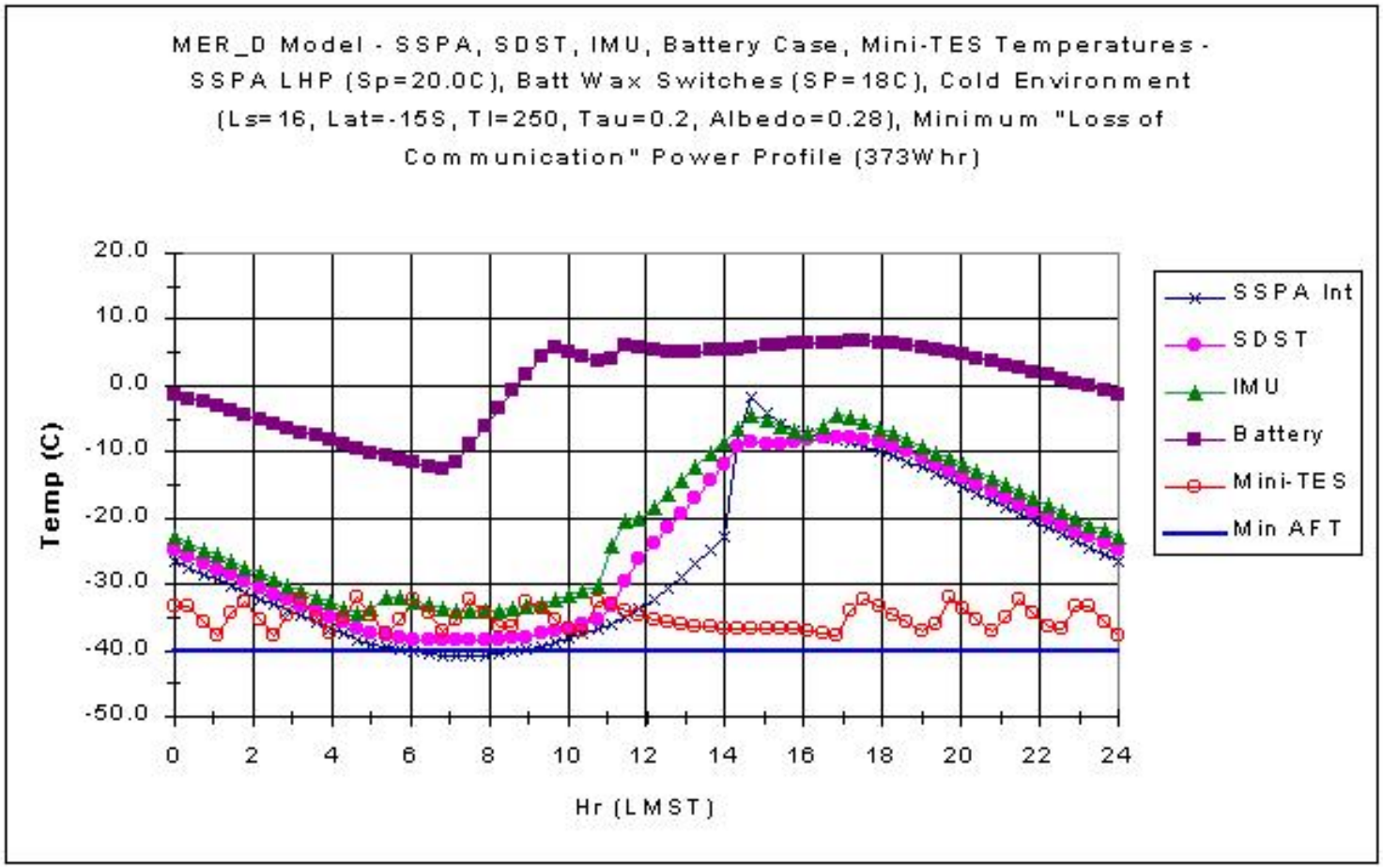

Subsystem Test Plans

- **Rover/HRS Thermal Characterization Test Overview**
  - Test start delayed (11/15/01 → 2/23/02) due to EM H/W delivery slip (10/1/01 → 1/18/02)
  - 30 day test is performed in Bldg. 248 10-foot vertical chamber
  - Test article is a combination of EM & TMM H/W (no flight H/W)
  - This is a preview of the integrated system thermal performance
    - Identify & correct potential thermal design defects prior to system thermal test
    - Examine HRS performance during cruise
    - Examine WEB/RED & thermal switch performance for Mars landed environment

Subsystem Test Plans (cont'd)

- System T/B Test Overview

– S/C Cruise 1	9/10/02	B150 25' chamber	12 days
– S/C Cruise 2	11/5/02	B150 25' chamber	5 days
– Rover 1	1/10/03	B248 10' chamber	12 days
– Rover 2	1/22/03	B248 10' chamber	5 days

- First & third tests are thermal design verification
  - No thermal margin testing planned
- Second & fourth tests are workmanship tests
- IR lamps used in B150 25' chamber for off-sun environmental heating during cruise
- IR lamps used in B248 10' for Mars solar environmental heating during landed operations

Issues & Concerns:
CEDL Design & Analysis

Issue/Concern	Resolution Plan
Difficult to quantify uncertain parameters for BS IMU thermal analysis. Absolute worst-case results only permit 60 minutes of operation	Review analysis & assumptions to determine if a realistic worst-case can be confidently established. If so, determine if IMU operational time is acceptable. If not, inform Systems that only 60 minutes of operation is permissible.

Issues & Concerns:
Thermal Testing

Issue/Concern	Resolution Plan
Schedule for Rover thermal vacuum/thermal balance tests too close to one another to permit assessment of test data & to institute design fixes, if necessary	Work with ATLO to inject sufficient margin between both Rover tests.
Separate flight lander test not part of ATLO thermal test baseline	Currently carried as a reserve request. Consider a descoped test where: Lander is tested in a smaller chamber OR only critical elements are tested.

USE OF BLACKBODY OPTICAL FIBER THERMOMETERS IN HIGH TEMPERATURE ENVIRONMENTS

Matthew R. Jones and David G. Barker
Department of Mechanical Engineering
Brigham Young University

ABSTRACT

A blackbody optical fiber thermometer consists of an optical fiber whose sensing tip is given a metallic coating. The sensing tip of the fiber forms an isothermal cavity, and the emission from this cavity is approximately equal to the emission from a blackbody. Temperature readings are obtained by measuring the spectral intensity at the end of the fiber at two wavelengths. The ratio of these measurements is used to infer the temperature at the sensing tip. However, readings from blackbody optical fiber thermometers are corrupted by self-emission when extended portions of the probe are exposed to elevated temperatures. This paper describes two possible methods for correcting the problem due to self-emission by the fiber. The first method is two-fiber optical fiber thermometry. In this method, a second fiber is positioned parallel to the original fiber. The fibers are identical except that the second fiber has a reflecting coating instead of a blackbody cavity at its tip. Since both the emitting and reflecting fibers are exposed to the same thermal environment, measurements of the intensity at the end of the reflecting fiber can be used to eliminate error due to emission by the fiber. The second approach is spectral remote sensing. In this method, the intensity exiting the fiber is measured in portions of the visible and infrared spectrum. The measured spectral intensities are used to reconstruct the temperature profile along the fiber. Application of these techniques to the thermal control system of a microgravity furnace is discussed.

INTRODUCTION

Optical fiber thermometers (OFT) are devices that use photonic signals to sense temperatures. Compared to other temperature sensors, OFT have the following advantages:

- Long-term stability
- Immunity to electromagnetic interference
- High precision
- Capable of withstanding harsh environments

Several types of OFT have been developed (Kreider 1985). Interferometric sensors use the thermal expansion of an optical fiber to perturb a laser signal, and the temperature is inferred using interferometry. Fluoropitc sensors have a photoluminescent material attached to the active end of an optical fiber. An excitation pulse from a pulsed laser or flash lamp activates the sensing

tip, and the temperature is inferred from the decay time of the photoluminescent signal. Blackbody sensors consist of a high-temperature optical fiber with an opaque cavity attached to the sensing tip. The spectral radiative flux detected at the end of the fiber is related to the temperature of the cavity via Planck's law (Dils 1983). Fluoroptic and interferometric sensors are very precise, but their temperature ranges are limited by material properties. Blackbody sensors can operate over a wide range of temperatures, so blackbody sensors are generally used in high temperature applications.

An example of an application in which the use of blackbody OFT is highly desirable is in the thermal control system of microgravity furnaces that will fly on the International Space Station. The design of these furnaces is similar to that of a Bridgman furnace and consists of a heater core, insulation jacket, instrumentation, coolant loop components, a cold zone for directional solidification, and a quench zone for rapid quenching. A sketch of a preliminary design for a typical furnace's hot zone is shown in Fig. 1. The heater core contains four heated zones: Booster 1, Booster 2, Main and Guard. The sensor plate is cooled in order to maintain sensors and other instrumentation at acceptable operating temperatures. The cold zone is a water-cooled chill block (not shown) that is located adjacent to Booster 1. This design produces the high thermal gradients required for directional solidification experiments.

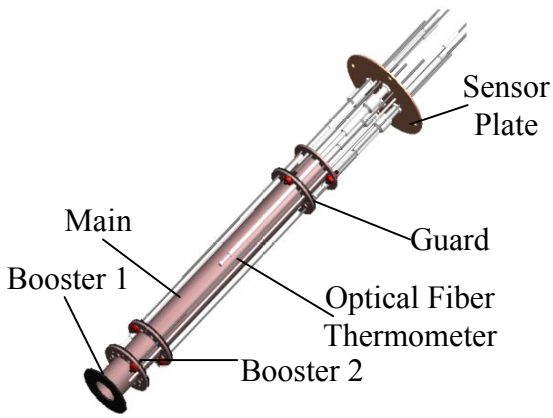

Figure 1. Hot zone assembly for a microgravity furnace

As shown in Fig. 1, the OFT are aligned with the axis of the furnace in these preliminary designs, and an extended portion of the fiber is exposed to elevated temperatures. Jones et al. (1999) showed that emission from portions of the fiber other than the sensing tip corrupt the temperature measurements under these conditions.

This paper describes two possible methods for correcting the problem due to self-emission by the fiber. The first method is two-fiber optical fiber thermometry (Jones et al. 2000). In this method, a second fiber is positioned parallel to the original fiber. The fibers are identical except that the second fiber has a reflecting coating instead of a blackbody cavity at its tip. Since both the emitting and reflecting fibers are exposed to the same thermal environment, measurements of the intensity at the end of the reflecting fiber can be used to eliminate error due to emission by the fiber. The second approach is motivated by previous studies in which spectral remote sensing

was used to determine the temperature profiles in semitransparent solids and high temperature gases (Chupp and Viskanta 1974, Hommert et al. 1975, Viskanta et al. 1975, Hommert and Viskanta 1978). In this method, the intensity exiting the fiber is measured in portions of the visible and infrared spectrum. The measured spectral intensities are used to reconstruct the temperature profile along the fiber.

BLACKBODY OPTICAL FIBER THERMOMETRY

A typical blackbody OFT is illustrated in Fig. 2 (Dils 1983). The probe consists of a sapphire (Al_2O_3) fiber whose sensing tip is given a metallic coating. The sensing tip of the fiber forms an isothermal cavity, so emission from this cavity is approximately equal to the emission from a blackbody. The other end of the fiber is attached to the detection system.

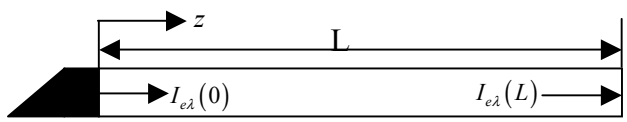

Figure 2. Schematic diagram for a blackbody optical fiber thermometer. The sensing tip $(z=0)$ is coated with a thin metallic film to create a small isothermal cavity at a temperature of T_0. The radiative flux emitted by the cavity, $I_\lambda(0)$, is approximately equal to the spectral emissive power of a blackbody, $I_{b\lambda}(T_0)$

An equation relating the spectral intensity at the end of the fiber to the spectral intensity emitted from the cavity is needed to infer the temperature at the sensing tip. The required relationship is obtained by modeling the fiber as an absorbing, emitting and non-scattering medium. The spectral intensity at each point along the fiber is given by the solution of Eq. 1 with the boundary condition specified by Eq. 2 (Brewster 1992).

$$\frac{dI_{e\lambda}}{dz} = -K_{a\lambda} I_{e\lambda} + K_{a\lambda} I_{b\lambda}\left(T(z)\right) \tag{1}$$

$$I_{e\lambda}(0) = I_{b\lambda}(T_0) \tag{2}$$

Solving for $I_{b\lambda}(T_0)$ gives

$$I_{b\lambda}(T_o) = I_{e\lambda}(t_{\lambda L})\exp\{t_{\lambda L}\} - \int_0^{t_{\lambda L}} I_{b\lambda}\left(T(t_\lambda)\right)\exp\{t_\lambda\}\,dt_\lambda \tag{3}$$

where $t_\lambda = K_{a\lambda} z$ and $t_{\lambda L} = K_{a\lambda} L$. The exponential in the first term on the right hand side of Eq. 3 corrects for the attenuation due to absorption of the intensity as it propagates along the fiber. The

integral on the right hand side of Eq. 3 represents noise due to emission by the fiber. The usual procedure is to assume that this integral is negligible.

$$I_{b\lambda}\left(T_o\right) \approx I_{b\lambda}\left(T_{bf}\right) = I_{e\lambda}\left(t_{\lambda L}\right)\exp\left\{t_{\lambda L}\right\} \tag{4}$$

Note that the estimate of the spectral blackbody intensity given by Eq. 4 is greater than the true value, so the measured temperature, T_{bf}, will be greater than the actual temperature, T_o.

The spectral radiative flux leaving the fiber is measured by the detector. The relationship between the measured value and the spectral intensity at the end of the fiber is

$$I_{e\lambda}\left(t_{\lambda L}\right) = \beta_\lambda M_{e\lambda} \tag{5}$$

where β_λ is a calibration factor and $M_{e\lambda}$ is the output from the detector. For the temperatures and the wavelengths of interest, Wien's limit may be used to approximate the spectral intensity of a blackbody,

$$I_{b\lambda}\left(T\right) \approx \frac{c_1}{\pi n^2 \lambda^5 \exp\left\{c_2/n\lambda T\right\}} \tag{6}$$

where c_1 and c_2 are the radiation constants and n is the refractive index of the fiber at the specified wavelength.

The temperature is obtained by making measurements at two wavelengths, λ_1 and λ_2. Using Eqs. 4 - 6, the ratio of $M_{e\lambda_1}$ to $M_{e\lambda_2}$ is

$$\frac{M_{e\lambda_1}}{M_{e\lambda_2}} = \frac{n_2^2 \lambda_2^5 \beta_{\lambda_2} \exp\left\{t_{\lambda_2 L}\right\} \exp\left\{\dfrac{c_2}{n_2 \lambda_2 T_{bf}}\right\}}{n_1^2 \lambda_1^5 \beta_{\lambda_1} \exp\left\{t_{\lambda_1 L}\right\} \exp\left\{\dfrac{c_2}{n_1 \lambda_1 T_{bf}}\right\}} \tag{7}$$

The measured temperature is obtained by solving Eq. 7 for the estimated temperature, T_{bf}.

$$T_{bf} = \frac{c_2\left(\dfrac{1}{n_2\lambda_2} - \dfrac{1}{n_1\lambda_1}\right)}{\ln\left[\left(\dfrac{n_1}{n_2}\right)^2 \left(\dfrac{\lambda_1}{\lambda_2}\right)^5 \dfrac{\beta_{\lambda 1} \exp\left\{t_{\lambda_1 L}\right\} M_{e\lambda_1}}{\beta_{\lambda 2} \exp\left\{t_{\lambda_2 L}\right\} M_{e\lambda_2}}\right]} \tag{8}$$

Recall that the integral in Eq. 3 represents the portion of the detected radiative flux that is due to emission by the fiber. This integral is negligible when the temperature of the fiber is low ($I_{b\lambda}\left(T\left(t_\lambda\right)\right) \approx 0$ for $t_\lambda \neq 0$) or the optical depth of the fiber is small $\left(t_{\lambda L} \approx 0\right)$. In situations similar to the furnace design illustrated in Fig. 1, the emission represented by the fiber is not negligible (Jones et al. 1999). This paper focuses on two possible methods of accounting for the effects due to emission by the fiber. The first approach is two-fiber optical fiber thermometry, and the second approach is spectral remote sensing.

TWO-FIBER OPTICAL FIBER THERMOMETRY

One possible method to accounting for the integral in Eq. 3 is to position a second fiber next to the original fiber as illustrated in Fig. 3. The fibers are identical except that the second fiber has a reflecting coating instead of a blackbody cavity at its tip. The first fiber is referred to as the emitting fiber, and the second fiber is referred to as the reflecting fiber.

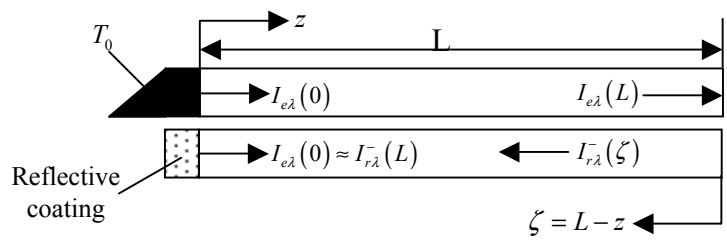

Figure 3. Schematic diagram for a two-fiber optical fiber thermometer

Since both the emitting and reflecting fibers are exposed to the same thermal environment, measurements of the spectral intensity at the end of the reflecting fiber can be used to eliminate error due to emission by the fiber. Three possible methods of using the data from the reflecting fiber to correct the temperature measurements have been developed (Jones et al. 2000). The most promising method is described below

The governing equation and boundary condition for the spectral intensity propagating along the reflecting fiber are given by Eqs. 9 and 10.

$$\frac{dI_{r\lambda}}{dz} = -K_{a\lambda} I_{r\lambda} + K_{a\lambda} I_{b\lambda}\left(T\left(z\right)\right) \tag{9}$$

$$I_{r\lambda}\left(0\right) = \rho_\lambda I_{r\lambda}^{-}\left(L\right) + \left(1-\rho_\lambda\right) I_{b\lambda}\left(T\left(0\right)\right) \tag{10}$$

Reflecting fibers can be fabricated by masking all but the tip of the fiber and sputtering a layer of MgO onto the fiber. The normal spectral reflectance of MgO is approximately 0.97 in the 0.4 μm to 1 μm spectral region (Touloukian and DeWitt 1972). Therefore, assuming $\rho_\lambda \approx 1$ the solution of Eqs. 9 and 10 gives

$$I_{r\lambda}(0) = I_{r\lambda}(t_{\lambda L})\exp\{t_{\lambda L}\} - \int_0^{t_{\lambda L}} I_{b\lambda}(T(t_\lambda))\exp\{t_\lambda\}\,dt_\lambda \tag{11}$$

Since $I_{r\lambda}(0) = \rho_\lambda I_{r\lambda}^-(L) \approx I_{r\lambda}^-(L)$, a second expression for $I_{r\lambda}(0)$ is obtained by solving for the spectral intensity propagating along the reflecting fiber in the direction of the reflecting tip. The appropriate equation and boundary condition are

$$\frac{dI_{r\lambda}^-}{d\zeta} = -K_{a\lambda} I_{r\lambda}^- + K_{a\lambda} I_{b\lambda}(T(\zeta)) \tag{12}$$

$$I_{r\lambda}^-(0) = 0 \tag{13}$$

The boundary condition given by Eq. 13 is appropriate, because the end of the fiber connected to the detection system is maintained at a low temperature. Therefore, emission at the wavelengths of interest is negligible. Solving Eqs. 12 and 13 gives

$$I_{r\lambda}(0) \approx I_{r\lambda}^-(t_{\lambda L}) = \int_0^{t_{\lambda L}} E_{b\lambda}(T(t_{\lambda L} - t_\lambda))\exp\{-t_\lambda\}\,dt_\lambda \tag{14}$$

Combining Eqs. 11 and 14 gives

$$\int_0^{t_{\lambda L}} I_{b\lambda}(T(t_\lambda))e^{t_\lambda}dt_\lambda = I_{r\lambda}(t_{\lambda L})e^{t_{\lambda L}} - \int_0^{t_{\lambda L}} I_{b\lambda}(T(t_{\lambda L} - t_\lambda))e^{-t_\lambda}dt_\lambda \tag{15}$$

Substituting Eq. 15 into Eq. 3 gives

$$I_{b\lambda}(T_0) = I_{e\lambda}(t_{\lambda L})e^{t_{\lambda L}} - \left[I_{r\lambda}(t_{\lambda L})e^{t_{\lambda L}} - \int_0^{t_{\lambda L}} I_{b\lambda}(T(t_{\lambda L} - t_\lambda))e^{-t_\lambda}dt_\lambda \right] \tag{16}$$

As in Eq. 3., the first term on the right hand side of Eq. 16 corrects for the attenuation of the spectral intensity as it propagates along the fiber. The terms in brackets on the right hand side of Eq. 16 represent noise due to emission by the fiber. The integral represents the spectral intensity emitted by the fiber toward the reflecting tip that is subsequently reflected and transmitted to the detection system.

Subtracting Eq. 3 from Eq. 16 gives

$$I_{r\lambda}(t_{\lambda L})\mathrm{e}^{t_{\lambda L}} = \int_0^{t_{\lambda L}} \left[I_{b\lambda}(T(t_\lambda))e^{t_\lambda} + I_{b\lambda}(T(t_{\lambda L} - t_\lambda))e^{-t_\lambda} \right] dt_\lambda \tag{17}$$

An average temperature is defined such that

$$I_{b\lambda}\left(T_a\right)=\frac{1}{e^{t_{\lambda L}}-e^{-t_{\lambda L}}}\int_0^{t_{\lambda L}}\left[I_{b\lambda}\left(T\left(t_\lambda\right)\right)e^{t_\lambda}+I_{b\lambda}\left(T\left(t_{\lambda L}-t_\lambda\right)\right)e^{-t_\lambda}\right]dt_\lambda \tag{18}$$

Next, the average temperature is used to approximate the integral in Eq. 3. That is,

$$I_{b\lambda}\left(T_o\right)\approx I_{b\lambda}\left(T_{2f}\right)=I_{e\lambda}\left(t_{\lambda L}\right)e^{t_{\lambda L}}-I_{b\lambda}\left(T_a\right)\int_0^{t_{\lambda L}}e^{t_\lambda}dt_\lambda=I_{e\lambda}\left(t_{\lambda L}\right)e^{t_{\lambda L}}-I_{b\lambda}\left(T_a\right)\left(e^{t_{\lambda L}}-1\right) \tag{19}$$

Combining Eqs. 17 - 19 gives

$$I_{b\lambda}\left(T_o\right)\approx I_{b\lambda}\left(T_{2f}\right)=I_{e\lambda}\left(t_{\lambda L}\right)e^{t_{\lambda L}}-\frac{e^{t_{\lambda L}}-1}{e^{t_{\lambda L}}-e^{-t_{\lambda L}}}I_{r\lambda}\left(t_{\lambda L}\right)e^{t_{\lambda L}} \tag{20}$$

Similar to Eq. 5, the relationship between the spectral intensity at the end of the reflecting fiber and the measured value is

$$I_{r\lambda}\left(t_{\lambda L}\right)=\beta_\lambda M_{r\lambda} \tag{21}$$

Again, an approximate temperature is obtained by making measurements at two wavelengths, λ_1 and λ_2. Combining Eqs. 5-6 and Eqs. 20-21 gives

$$T_{2f}=\frac{c_2\left(\frac{1}{n_2\lambda_2}-\frac{1}{n_1\lambda_1}\right)}{\ln\left[\left(\frac{n_1}{n_2}\right)^2\left(\frac{\lambda_1}{\lambda_2}\right)^5\frac{\beta_{\lambda_1}e^{t_{\lambda_1 L}}\left(M_{e\lambda_1}-\frac{e^{t_{\lambda_1 L}}-1}{e^{t_{\lambda_1 L}}-e^{-t_{\lambda_1 L}}}M_{r\lambda_1}\right)}{\beta_{\lambda_2}e^{t_{\lambda_2 L}}\left(M_{e\lambda_2}-\frac{e^{t_{\lambda_2 L}}-1}{e^{t_{\lambda_2 L}}-e^{-t_{\lambda_2 L}}}M_{r\lambda_2}\right)}\right]} \tag{22}$$

SPECTRAL REMOTE SENSING

In this method, the intensity exiting the fiber is measured in portions of the visible and infrared spectrum. The measured spectral intensities are used to reconstruct the temperature profile along the length of the fiber. Based on Eq. 3, the temperature profile is related to the measured values through an integral equation.

$$\beta_{\lambda_i}M_{e\lambda_i}=I_{e\lambda}\left(t_{\lambda L}\right)=\exp\left\{-t_{\lambda_i L}\right\}\left[I_{b\lambda_i}\left(T_o\right)+\int_0^{t_{\lambda_i L}}\exp\left\{t_{\lambda_i}\right\}I_{b\lambda_i}\left(T\left(t_{\lambda_i}\right)\right)dt_{\lambda_i}\right] \tag{23}$$

An estimate of the temperature profile is obtained by inverting Eq. 23. This equation is classified as a Fredholm integral equation of the first kind. This type of equation is frequently encountered in the solution of inverse problems involving radiative transfer (Howell et al. 2000), and it is known that the solution to an equation of this type is not unique (Jones 2001).

Because there is not a unique solution, conventional gradient-based search methods are likely to become trapped in local minima and are generally ineffective in finding optimal solutions in cases such as this. A directed random search method such as a genetic algorithm is capable of finding the global optimal solution in complex, multi-dimensional search spaces. Genetic algorithms are based on the principle of natural selection or survival of the fittest. The structure of a typical genetic algorithm is shown in Fig. 4. The following paragraphs briefly describe the aspects of the implementation unique to this study. Detailed discussions of the fundamentals of genetic algorithms and descriptions of the wide variety of optimization problems successfully treated using genetic algorithms are available in the literature (Goldberg 1989, Pham and Karaboga 2000).

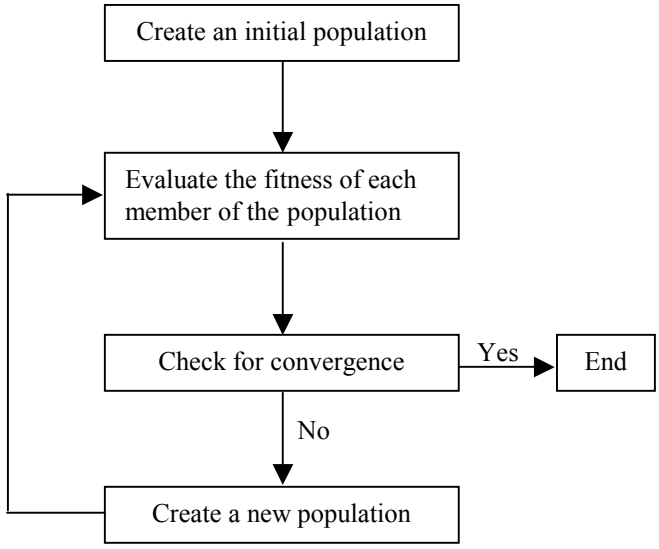

Figure 4. Flowchart for a simple genetic algorithm

SELECTION OF AN INITIAL POPULATION

An initial population of 100 possible temperature profiles was created by randomly perturbing an initial estimate of the temperature profile along the optical fiber.

THE FITNESS FUNCTION

The error for the jth possible temperature profile in the population is the rms value of difference between the measurements and the value of $\left(\beta_{\lambda_i} M_{\lambda_i}\right)_j$ obtained from Eq. 9 using the jth temperature profile.

$$\varepsilon_j = \frac{1}{N_\lambda} \sum_{i=1}^{N_\lambda} \sqrt{\left(\frac{\left(\beta_{\lambda_i} M_{\lambda_i}\right)_{measured} - \left(\beta_{\lambda_i} M_{\lambda_i}\right)_j}{\left(\beta_{\lambda_i} M_{\lambda_i}\right)_{measured}} \right)^2} \tag{24}$$

The smoothness of each temperature profile was quantified using the second finite differences.

$$s_j = \frac{2}{N_p - 2} \sum_{k=2}^{N_p - 1} \left| \frac{\left(T(z_{k+1}) - T(z_k)\right)\left(z_k - z_{k-1}\right) - \left(T(z_k) - T(z_{k-1})\right)\left(z_{k+1} - z_k\right)}{\left(z_{k+1} - z_{k-1}\right)\left(z_{k+1} - z_k\right)\left(z_k - z_{k-1}\right)} \right| \tag{25}$$

The fitness of the jth possible temperature profile was defined as

$$f_j = \frac{\varepsilon_{\max} - \varepsilon_j}{\varepsilon_{avg}} + \frac{s_{\max} - s_j}{s_{avg}} \tag{26}$$

where $\varepsilon_{\max}$ and ε_{avg} are the maximum and average values for the current generation and $s_{\max}$ and s_{avg} are the maximum and average values of the smoothness criterion for the current generation.

CREATION OF A NEW POPULATION

The possible temperature profile with the greatest fitness value and the possible temperature profile with the minimum error from the previous generation were copied directly into the new generation. If the most fit solution happened to be the solution with minimum error, two copies of the same solution would be placed in the new generation. This was necessary to avoid losing the solution with minimum error. The rest of the new generation was created using the two methods described below.

The first approach used the crossover and mutation operators to create the remaining possible temperature profiles (Goldberg 1989, Pham and Karaboga 2000). The crossover operation consists of selecting two possible temperature profiles according to their fitness values. A crossover site for each point in the temperature profile was randomly selected, and the portion of the temperature profile above the crossover site in the first possible profile was combined with the remaining portion of the second possible profile to create a new possible temperature profile. The mutation operator was applied after the new generation had been filled. The mutation operator consists of randomly selecting 1% of all the temperature values and then randomly perturbing it within a range of 800 K.

In the second approach, a smoothing operator was repeatedly applied to the possible temperature profile with the minimum error. Ten new possible profiles were created using the average of the temperature at a point with its two nearest neighbors. The next ten new possible profiles were created using the average of the temperature at a point with its four nearest neighbors. The remaining 78 new possible temperature profiles were created using the crossover and mutation operators as described above.

OPTICAL PROPERTIES OF SAPPHIRE

The spectral refractive index and absorption coefficient of Al_2O_3 must be known in order to evaluate the temperature at the sensing end of the OFT using Eq. 8 or Eq. 22 or to reconstruct the temperature profile along the OFT using Eq. 23. Maltison (1962) measured the refractive index of sapphire at 46 wavelengths between 0.2652 μm and 5.577 μm at room temperature. A three-term Sellmeier dispersion equation was developed based on these measurements, and this equation was used to calculate the refractive index as a function of wavelength. Brewster (1992) compiled a table of data regarding the imaginary part of the refractive index of sapphire from a variety of sources. The spectral absorption coefficients were calculated using Eq. 27 and linear interpolation of this data.

$$K_{a\lambda} = \frac{4\pi k}{\lambda} \tag{27}$$

Figure 5 shows the spectral refractive indices and absorption coefficients used in this study. Since the wavelength at which the peak emission occurs increases as the average temperature decreases, it is necessary to make measurements at longer wavelengths to reconstruct temperature profiles with lower average temperatures. Obtaining measurements at longer wavelengths is difficult due to increased absorption, so it is expected that the reconstruction of the temperature profile will be more difficult as the average temperature decreases.

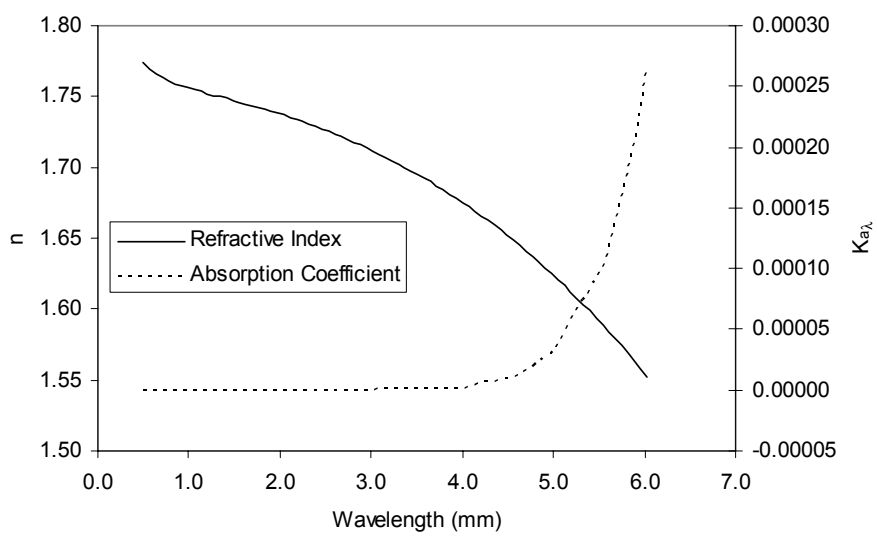

Figure 5. Refractive Index (n) and Absorption Coefficient ($K_{a\lambda}$) as a function of wavelength for Al_2O_3

Gryvnak and Burch (1965) reported significant increases in the absorption coefficient with temperature above 1200 C. However, data regarding the variation of the absorption coefficient with temperature below 1200 C is not available for the spectral range of interest, so it was assumed that the absorption coefficient was independent of temperature in this study.

SIMULATED TEMPERATURE MEASUREMENTS

Three typical axial temperature profiles for the microgravity furnace illustrated in Fig. 1 were obtained from a detailed thermal model (NASA-MSFC et al. 1999). Simulated measurements of the spectral radiative flux were calculated using these temperature profiles and Eq. 23 for a number of wavelengths. The spectral radiative flux is defined as the product of the spectral intensity and the solid angle defined by the numerical aperture of the optical fiber.

$$E_{e\lambda} = I_{e\lambda}\left(t_{\lambda L}\right)\Delta\Omega = \beta_{\lambda} M_{e\lambda}\Delta\Omega \tag{28}$$

For Cases 1 and 2, 50 different wavelengths between 0.5 μm and 4.0 μm were used. This spectral region includes all the wavelengths for which the emission was significant. For Case 3, 65 wavelengths between 0.5 μm and 5.0 μm were used to account for the peak wavelength shift. The wavelengths used in the two-fiber approach were 0.8 μm and 0.95 μm. The temperature measured using the standard approach to blackbody optical fiber thermometry is compared with the temperatures obtained using two-fiber optical fiber thermometry and remote sensing in Table 1.

Table 1. Simulated Temperature Measurements

Case	T_o (K)	T_{bf} (K)	T_{2f} (K)	T_{rs} (K)
1	1440	1458	1438	1441
2	1169	1200	1169	1169
3	877	895	877	878

The errors in the measured temperatures obtained using the standard approach to blackbody OFT vary between 1% to 3%. The larger errors occur when portions of the fiber are at temperatures greater than the temperature of the sensing tip (Cases 2 and 3). Note that, as predicted by comparing Eqs. 3 and 4, the measurements obtained using the standard approach are biased toward higher values.

The two-fiber approach eliminated the errors in Cases 2 and 3 and greatly reduced the error in Case1. The tip temperature was also accurately measured (to within 0.1%) using the remote sensing approach in each of the three cases.

The reconstructed temperature profiles obtained using the remote sensing approach are compared with the actual temperature profiles in Figs. 6 - 8. The initial estimates used to obtain these results are also shown in these figures. As expected, the reconstructed temperature profile is more accurate when the profile has a higher average temperature. In the worst case (Case 3), the maximum deviation of the reconstructed temperature profile from the actual temperature profile

was 5.3% in the high temperature region and 16.1% in the low temperature region. The average deviation between the actual temperature profile and the reconstructed temperature profile was 2.6% in this case.

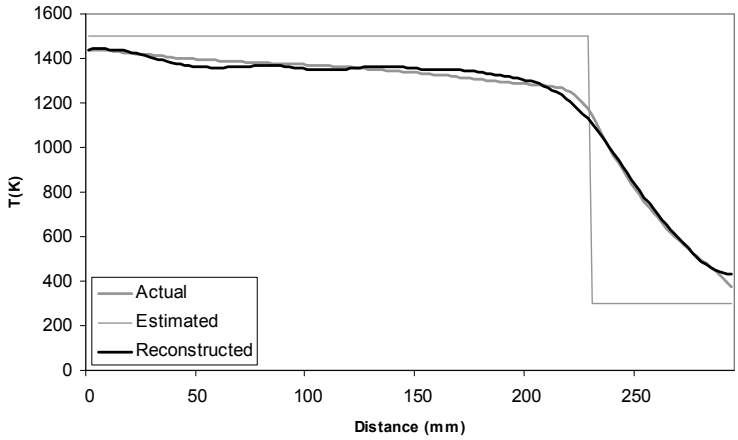

Figure 6. Reconstructed temperature profile for Case 1

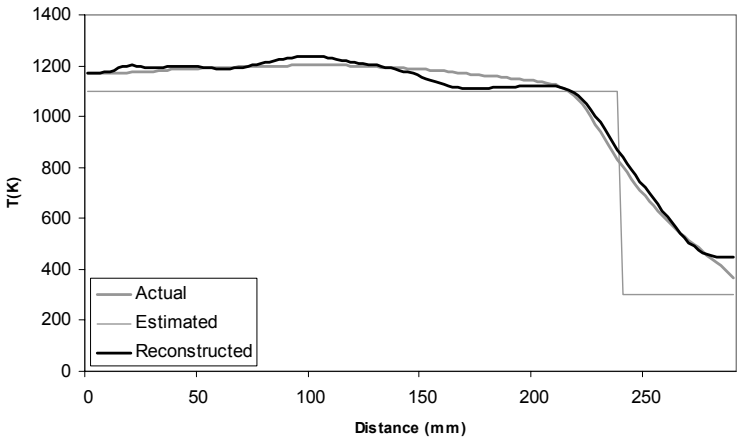

Figure 7. Reconstructed temperature profile for Case 2

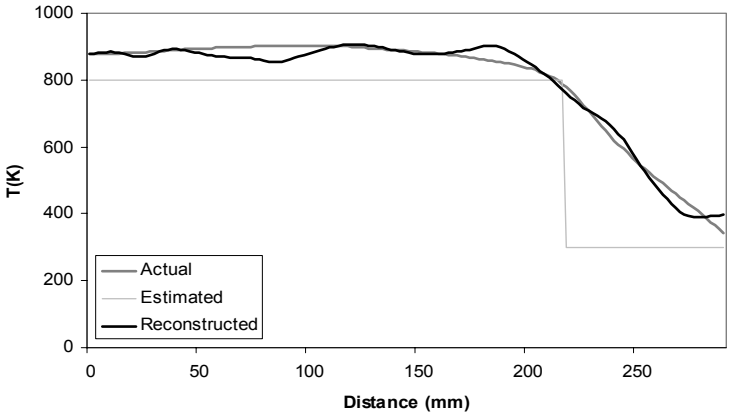

Figure 8. Reconstructed temperature profile for Case 3

Although the reconstructed temperature profiles differ from the actual temperature profile, the spectral radiative fluxes calculated using the actual temperature profile are in nearly perfect agreement with the spectral radiative fluxes calculated using the reconstructed temperature profile. Figure 9 compares the spectral radiative fluxes for the actual temperature profile and the reconstructed profile obtained for Case 3. The maximum deviation was 1.98% at 4.77 μm. The average deviation was 0.44%. The kink in Figure 9 is due to the rapid increase in the spectral absorption coefficient for wavelengths greater than 4.0 μm (see Figure 5).

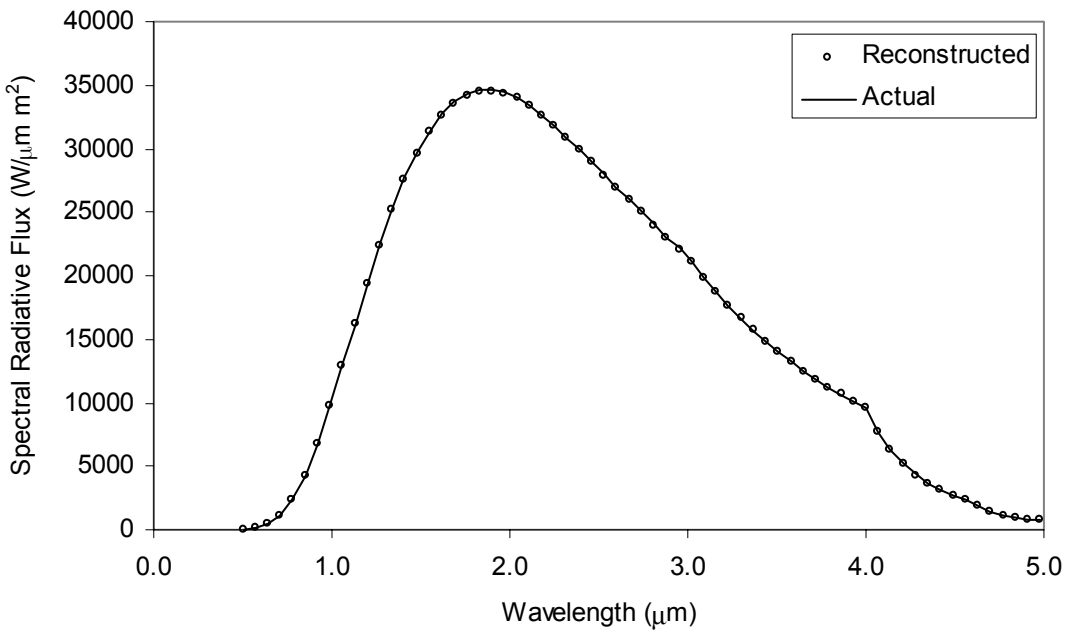

Figure 9. Spectral radiative flux for the reconstructed profile of Case 3

SUMMARY AND CONCLUSIONS

The use of blackbody optical fiber thermometers offers a number of advantages, but errors due to self-emission by the fiber prevent the use of the standard approach in applications where extended portions of the fiber are exposed to elevated temperatures. This paper described two methods that eliminate the errors due to emission by the fiber.

Two-fiber OFT uses a second fiber with a reflecting tip to estimate the spectral intensity emitted by the fiber. This approach eliminates the bias toward higher temperatures that occurs when the standard approach to blackbody OFT is employed.

The remote sensing method can be used to accurately determine the temperature at the tip of a blackbody OFT. The approach may also be used to estimate the temperature profile along the entire length of the fiber. For the cases considered in this paper, the reconstructed temperature profile was accurate to within approximately 5% in the high temperature region and to within approximately 16% in the low temperature region.

REFERENCES

Brewster, M. Q. 1992, *Thermal Radiative Transfer & Properties*, John Wiley & Sons, New York.

Dils, R. R. 1983, "High-temperature optical fiber thermometry," *Journal of Applied Physics*, Vol. 54 No. 3, pp. 1198 - 1201.

Chupp, R. E. and Viskanta, R. 1974, "Development and Evaluation of a Remote Sensing Technique for Determining the Temperature Distribution in Semitransparent Solids," *ASME Transactions – Journal of Heat Transfer,* Vol. 96, No. 3, pp. 391-397.

Gryvnak, D. A. and Burch, D. E. 1965, "Optical and Infrared Properties of Al_2O_3 at Elevated Temperatures," *Journal of the Optical Society of America*, Vol. 55 No. 6, pp. 625 - 629.

Goldberg, D. E., 1989, *Genetic Algorithms in Search, Optimization, and Machine Learning*, Addison-Wesley, Reading MA.

Hommert, P. J., Viskanta, R., and Chupp, R. E. 1975, "Application of Spectral Remote-Sensing Method for Recovering Temperature Distribution in Glass," *Journal of the American Ceramic Society*, Vol. 58, pp. 58-62.

Hommert, P. J. and Viskanta, R. 1978, "High Temperature Gas Diagnostics by Spectral Remote Sensing," International Journal of Heat and Mass Transfer, Vol. 21, pp. 769 – 781.

Howell, J. R., Ezekoye, O. A., and Morales, J. C. 2000, "Inverse Design Model for Radiative Heat Transfer," ASME Transactions – Journal of Heat Transfer, Vol. 122, No. 3, pp. 492 – 502.

Jones, M. R., Farmer, J. T., and Breeding, S. P. 1999, "Evaluation of the use of optical fiber thermometers for thermal control of the quench module insert," *Proceedings of the Thermal & Fluids Analysis Workshop*, Sep. 13 – 17, Huntsville, AL.

Jones, M. R., Farmer, J. T., and Breeding, S. P. 2000, "Two-Fiber Optical Fiber Thermometry," *Proceedings of IMECE: 2000 International Mechanical Engineering Congress and Exposition*, Nov. 5-10, Orlando, FL.

Jones, M. R. 2001, "Reconstruction of the Temperature Profile Along an Optical Fiber Thermometer," to appear in *Proceedings of IMECE: 2001 International Mechanical Engineering Congress and Exposition*, Nov. 11-16, New York, NY.

Kreider, K. G. 1985, "Fiber-Optic Thermometry," *Applications of Radiation Thermometry, ASTM STP 895*, J. C. Richmond and D. P. DeWitt, Eds. American Society of Testing and Materials, Philadelphia, pp. 151 -161.

Maltison, I. H. 1962, "Refraction and Dispersion of Synthetic Sapphire," *Journal of the Optical Society of America*, Vol. 52 No. 12, pp. 1377 – 1379.

NASA-MSFC, Tec-Masters Inc., Sverdrup Technologies 1999, *Thermal Design Data Book, Quench Module Insert, Preliminary Design Review*.

Pham, D. T. and Karaboga, D. 2000, *Intelligent Optimisation Techniques: Genetic Algorithms, Tabu Search, Simualted Annealing and Neural Networks*, Springer, London.

Touloukian, Y. S. and DeWitt, D. P. (eds.) 1972, *Thermal Radiative Properties: Nonmetallic Solids*, vol. 8 of *Thermophysical Properties of Matter*, Plenum Press, New York.

Viskanta, R., Hommert, P. J., and Groninger, G. L. 1975, "Spectral Remote Sensing of Temperature Distribution in Semitransparent Solids Heated by an External Radiation Source," Applied Optics, Vol. 14, No. 2, pp. 428 – 437.

CONTACT

Matthew R. Jones is an Assistant Professor in the Department of Mechanical Engineering at Brigham Young University. His email address is mrjones@et.byu.edu, and his phone number is 801-378-3070. David G. Barker is a senior majoring in mechanical engineering at Brigham Young University. His email address is dbarker@byu.edu, and his phone number is 801-378-3051.

NOMENCLATURE

c_1, c_2	Radiation constants
$E_{e\lambda}$	Spectral radiative flux
f	Fitness function
$I_{b\lambda}$	Spectral blackbody intensity
$I_{e\lambda}$	Spectral intensity in the emitting fiber
$I_{r\lambda}$	Spectral intensity in the reflecting fiber
i, j, k	Indices
$K_{a\lambda}$	Spectral absorption coefficient for the optical fiber
L	Length of the optical fiber
$M_{e\lambda}$	Measurement from the detector output
N_p	Number of points in the temperature profile
N_λ	Number of wavelengths
n	Real part of refractive index for Al_2O_3
k	Imaginary part of refractive index for Al_2O_3
s	Smoothness criterion
t_λ	Spectral optical length of the optical fiber
$t_{\lambda L}$	Total spectral optical depth of the optical fiber
$T(t_\lambda)$	Temperature profile
T_{bf}	Measured temperature obtained using the standard method
T_o	True temperature of the sensing tip
T_{rs}	Measured temperature obtained using the remote sensing method
T_{2f}	Measured temperature obtained using the two-fiber method

T_m	Measured temperature of the sensing tip
z	Distance along the axis of the fiber
β_λ	Calibration factor
$\Delta\Omega$	Solid angle defined by the numerical aperture of the fiber
ε	RMS difference between the measured and calculated radiative fluxes.
λ	Wavelength
ρ_λ	Spectral reflectivity of the reflective coating

REPORT DOCUMENTATION PAGE

Form Approved
OMB No. 0704-0188

Public reporting burden for this collection of information is estimated to average 1 hour per response, including the time for reviewing instructions, searching existing data sources, gathering and maintaining the data needed, and completing and reviewing the collection of information. Send comments regarding this burden estimate or any other aspect of this collection of information, including suggestions for reducing this burden, to Washington Headquarters Services, Directorate for Information Operation and Reports, 1215 Jefferson Davis Highway, Suite 1204, Arlington, VA 22202-4302, and to the Office of Management and Budget, Paperwork Reduction Project (0704-0188), Washington, DC 20503

1. AGENCY USE ONLY *(Leave Blank)*	2. REPORT DATE	3. REPORT TYPE AND DATES COVERED
	July 2002	Conference Publication

4. TITLE AND SUBTITLE

The Twelfth Thermal and Fluids Analysis Workshop

5. FUNDING NUMBERS

6. AUTHORS

Alok Majumdar, Compiler

7. PERFORMING ORGANIZATION NAMES(S) AND ADDRESS(ES)

George C. Marshall Space Flight Center
Marshall Space Flight Center, AL 35812

8. PERFORMING ORGANIZATION REPORT NUMBER

M–1049

9. SPONSORING/MONITORING AGENCY NAME(S) AND ADDRESS(ES)

National Aeronautics and Space Administration
Washington, DC 20546–0001

10. SPONSORING/MONITORING AGENCY REPORT NUMBER

NASA/CP—2002–211783

11. SUPPLEMENTARY NOTES

Proceedings of a workshop held at NASA Marshall Space Flight Center, September 10–14, 2001.
Workshop organizers: Bruce Tiller, Marshall Space Flight Center.
Prepared for Structures, Mechanics, and Thermal Department, Engineering Directorate

12a. DISTRIBUTION/AVAILABILITY STATEMENT

Unclassified-Unlimited
Subject Category 34
Standard Distribution

12b. DISTRIBUTION CODE

13. ABSTRACT *(Maximum 200 words)*

The Twelfth Thermal and Fluids Analysis Workshop (TFAWS 01) was held at the Bevill Center, The University of Alabama in Huntsville, Huntsville, Alabama, September 10–14, 2001. The theme for the hands-on training workshop and conference was “Engineering Excellence and Advances in the New Millenium.” Forty-five technical papers were presented in four sessions: (1) Thermal Spacecraft/Payloads, (2) Thermal Propulsion/Vehicles, (3) Interdisciplinary Papers, and (4) Fluids Papers. Thirty-nine papers were published in these proceedings. The remaining six papers were not available in electronic format at the time of publication. In addition to the technical papers, there were (a) nine hands-on classes on thermal and flow analyses softwares, (b) thirteen short courses and product overview lectures, (c) five keynote lectures and, (d) panel discussions consisting of eight presentations. The workshop resulted in participation of 195 persons representing NASA Centers, Government agencies, aerospace industries, academia, software providers, and private corporations.

14. SUBJECT TERMS

thermal analysis, computational fluid dynamics, numerical heat transfer, network flow analysis, thermal protection system, interdisciplinary analysis

15. NUMBER OF PAGES

1047

16. PRICE CODE

17. SECURITY CLASSIFICATION OF REPORT	18. SECURITY CLASSIFICATION OF THIS PAGE	19. SECURITY CLASSIFICATION OF ABSTRACT	20. LIMITATION OF ABSTRACT
Unclassified	Unclassified	Unclassified	Unlimited